Transactions of the ASME®

Transactions of the ASME, Journal of Heat Transfer (ISSN 0022-1481) is published quarterly (Feb., May, Aug., Nov.) for $160.00 per year by The American Society of Mechanical Engineers, 345 East 47th Street, New York, NY 10017. Second class postage paid at New York, NY and additional mailing offices. POSTMASTER: Send address changes to Transactions of the ASME, Journal of Heat Transfer, c/o THE AMERICAN SOCIETY OF MECHANICAL ENGINEERS, 22 Law Drive, Box 2300, Fairfield, NJ 07007-2300.
CHANGES OF ADDRESS must be received at Society headquarters seven weeks before they are to be effective. Please send old label and new address.
PRICES: To members, $36.00, annually; to nonmembers, $160.00. Add $15.00 for postage to countries outside the United States and Canada.
STATEMENT from By-Laws. The Society shall not be responsible for statements or opinions advanced in papers or . . . printed in its publications (B7.1, para. 3).

INDEXED by Applied Mechanics Reviews and Engineering Information, Inc.
Canadian Goods & Services Tax Registration #126148048

Journal of Heat Transfer

Published Quarterly by The American Society of Mechanical Engineers

VOLUME 113 • NUMBER 3 • AUGUST 1991

ANNOUNCEMENTS

TECHNICAL PAPERS

(Contents Continued)

TECHNICAL NOTES

Fractal Network Model for Contact Conductance

A. Majumdar
Department of Mechanical and Aerospace Engineering,
Arizona State University,
Tempe, AZ 85287

C. L. Tien
A. Martin Berlin Professor,
Office of the Chancellor,
University of California,
Berkeley, CA 94720

The topography of rough surfaces strongly influences the conduction of heat and electricity between two surfaces in contact. Roughness measurements on a variety of surfaces have shown that their structure follows a fractal geometry whereby similar images of the surface appear under repeated magnification. Such a structure is characterized by the fractal dimension D, *which lies between 2 and 3 for a surface and between 1 and 2 for a surface profile. This paper uses the fractal characterization of surface roughness to develop a new network model for analyzing heat conduction between two contacting rough surfaces. The analysis yields the simple result that the contact conductance* h *and the real area of contact* A_t *are related as* $h \sim A_t^{D/2}$ *where* D *is the fractal dimension of the surface profile. Contact mechanics of fractal surfaces has shown that* A_t *varies with the load* F *as* $A_t \sim F^{\eta}$ *where* η *ranges from 1 to 1.33 depending on the value of* D. *This proves that the conductance and load are related as* $h \sim F^{\eta D/2}$ *and resolves the anomaly in previous investigations, which theoretically and experimentally obtained different values for the load exponent. The analytical results agreed well with previous experiments although there is a tendency for overprediction.*

Introduction

When a compressive load is applied between two nominally flat surfaces, the presence of surface roughness produces imperfect contact at their interface. Such an imperfect contact is characterized by a large number of contact spots of various sizes, spread over the whole contact interface. The degree of imperfect contact is measured by both the size distributions of these contact spots as well as the actual area of contact, which is a fraction of the apparent or nominal surface area. The prediction of the degree of contact is of great importance to several engineering problems such as thermal and electrical contact resistance as well as sealing, friction, wear, and lubrication. For surfaces in thermal contact, an imperfect junction results in a sharp temperature rise across the interface, as shown in Fig. 1. Such a temperature jump plays a significant role in the thermal performance of composite materials, porous insulations, as well as biomedical and aerospace instrumentation (Fletcher, 1988). In microelectronics, several layers of materials are used for packaging of electronic devices. Imperfect contact between these layers seriously affects the electrical and thermal performance of these devices.

Previous studies on thermal contact resistance (Tien, 1968; Cooper et al., 1969; Mikic, 1974; Yovanovich, 1987) have all concluded that the nondimensional conductance in vacuum and the load are related as

$$\frac{h\sigma}{\lambda} = \xi\sigma' \left(\frac{F}{HA_a}\right)^x \tag{1}$$

where σ is the standard deviation of the surface height, σ' the mean surface slope, ξ is a constant, h is the thermal contact conductance, F is the compressive load between the surfaces, H is the hardness of the softer surface, and A_a is the apparent area of contact. Although it is clear that surface topography is an important element in a contact process, the validity of such a relation between conductance and the load is a subject of question in this study. The question is raised because it has been experimentally observed that the mean slope σ' varies with the resolution of the roughness measuring instrument. Also, several empirical and theoretical studies have reported different values of the load exponent x ranging from 0.85 to 0.99, as listed in Table 1. This work takes a fundamental look at the geometric structure of rough surfaces and explains why the mean slope σ' cannot be used in such a relation. Instead, it proposes a new model to analyze contact resistance that uses intrinsic surface properties to obtain a relation that will provide physical insight to the origins of the exponent x.

The structure of a rough surface is usually quite disordered and often assumed to be random. Nayak (1971) proposed a

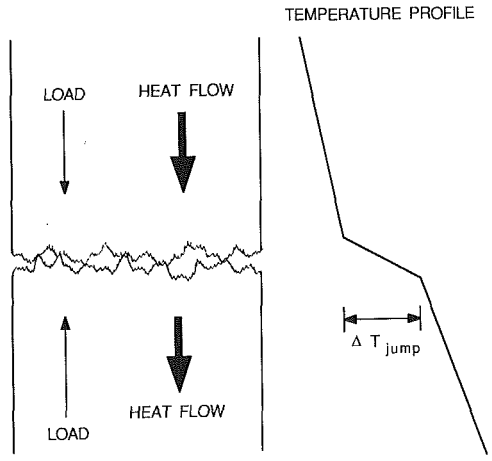

Fig. 1 Heat conduction across two rough surfaces in imperfect contact produces a temperature jump

Table 1 Comparison of load exponents of previous investigations

Reference	Load exponent
Tien (1968)	0.85
Cooper et al. (1969)	0.99
Thomas and Probert (1970)	0.92
Yovanovich (1987)	0.95

Contributed by the Heat Transfer Division and presented at the ASME-AIChE National Heat Transfer Conference, Philadelphia, Pennsylvania, August 6-9, 1989. Manuscript received by the Heat Transfer Division May 16, 1990; revision received January 12, 1991. Keywords: Conduction, Direct-Contact Heat Transfer, Modeling and Scaling.

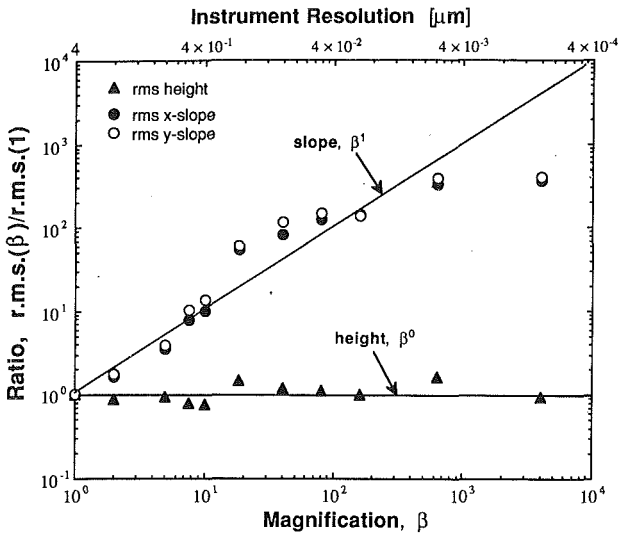

Fig. 2 Scale dependence of statistical roughness parameters for a magnetic tape. Roughness measurements for $\beta < 10$ were made by optical interferometry (Bhushan et al., 1988) whereas for $\beta > 10$ atomic force microscopy was used (Oden et al., 1991)

statistical characterization of rough surfaces, which used parameters like variances of the height, slope, and curvature of a surface. These parameters are extensively used in models of surface contact (Bhushan, 1990). However, later studies have indicated that surface topography is a nonstationary random phenomenon for which the variance of the height distribution is related to the length of the sample (Sayles and Thomas, 1978) and therefore not unique. Roughness measurements also show that the variances of slope and curvature depend strongly on the resolution of the roughness-measuring instrument or any other form of filter and hence are not unique (Bhushan et al., 1988; Bhushan and Blacksman, 1990). This can be observed in Fig. 2 where the statistical parameters rms height and slope are plotted against the magnification of a magnetic tape surface (Majumdar and Bhushan, 1990a). It is clear that instruments with different resolutions yield different values of the rms slope for the same surface. Therefore the use of the rms slope σ' in Eq. (1) is not valid.

Roughness measurements show that surfaces contain roughness features at several length scales ranging from millimeters to nanometers (Majumdar and Bhushan, 1990b). To characterize such a multiscale structure one must use parameters that are independent of any length scale. This study introduces a new method of characterizing rough surfaces by fractal geometry. The fractal characteristics of a rough surface are then used to develop a model to predict contact conductance. Before discussing the details of this model it is necessary briefly to discuss the theory of fractal geometry.

Fractal Geometry

Fractal geometry is a mathematical language that describes the structural disorder and chaos of a number of objects found in nature (Mandelbrot, 1982). Examples of such objects include the shapes of coastlines, clouds, and mountains. The unique property of these objects is that as one looks closer and closer, increasing details of the object keep appearing. These details tend to follow the same structural pattern at several length scales of observation. It is common to use Euclidean objects such as spheres, cubes, flat planes, and smooth curves to describe such objects approximately and then study the physical phenomena relevant to them. However, Euclidean geometry relies on integer values of dimension that characterize *smooth* shapes and fails to describe the structural complexity of natural objects. On several occasions, however, it is crucial to know the structural details of the object at the length scales relevant to a physical phenomenon. This is where fractal geometry becomes important.

The following subsections provide a mathematical description of fractal geometry that is relevant to engineering problems such as contact conductance.

Hausdorff Dimension. The length of a line is measured by breaking the line into small units of length ϵ and then adding the number of units in the form

$$L = \Sigma \epsilon^1 \tag{2}$$

Similarly the area of surface is measured by breaking up the

Nomenclature

a = area of a contact island, m^2
A = area, m^2; $A^* = A/A_a$
b = discretization parameter, Eq. (22)
d = distance between two contact islands, m
D = fractal dimension of surface profile or island coastline
D_s = fractal dimension of a rough surface
F = load on a surface, N; $F^* = F/HA_a$
G = surface characterization parameter, m, Eq. (10)
h = contact conductance, $Wm^{-2}K^{-1}$; $h^* = h\sigma/\lambda$
H = hardness of a material, Nm^{-2}; an exponent in Eq. (8)
l = characteristic length of a contact island, m
L = apparent characteristic length of a surface, m
m = magnification; or exponent defined in Eq. (25)
n = number of islands in Eq. (18)
M = measure of an object
$P(\omega)$ = power of the spectrum, m^3
q = order associated with the size of an island, Eq. (22)
R = effective thermal resistance for a set of contact spots, $W^{-1}K$
$\mathbf{R}$ = total thermal resistance, $W^{-1}K$
$S(\tau)$ = structure function, m^2
X = self-affine function
β = magnification
γ = scaling factor in Eq. (5)
Γ = gamma function
ϵ = unit of measurement
η = load-exponent for contact area-load relation, Eq. (41)
λ = thermal conductivity, $Wm^{-1}K^{-1}$
ξ = constant in Eq. (1)
ρ = thermal resistance of a surface asperity, $W^{-1}K$
σ = standard deviation of surface height, m
σ' = standard deviation of surface slope
τ = spatial interval in the lateral direction of a surface, m
ψ = constant in Eq. (12)
ω = frequency of roughness, m^{-1}

Subscripts

a = apparent area
c = cavity
L = largest island or cavity
q = q islands defined in Eq. (22)
s = series resistance, Eq. (26)
t = total area of contact spots

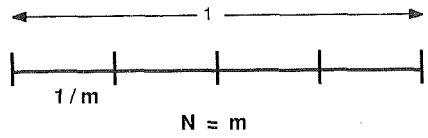

Figure 3a

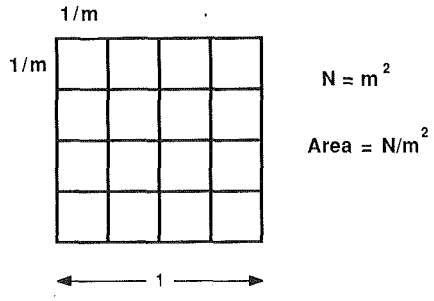

Figure 3b

Fig. 3 Concept of self-similarity based on Euclidean objects: (*a*) line, $D = 1$, (*b*) square, $D = 2$

surface into small squares of size $\epsilon \times \epsilon$ and then adding the number of units as

$$A = \Sigma \epsilon^2 \tag{3}$$

It should be noted that in Eqs. (2) and (3) the exponents 1 and 2 correspond to the dimensions of the objects. The unique property of these measures, length and area, is that they are independent of the unit of measurement ϵ and in the limit $\epsilon \to 0$ these measures remain finite and nonzero. This is apparent in Euclidean objects such as a smooth straight line where the length is independent of whether a centimeter or a micrometer scale is used. The concept of Euclidean measure and dimension can be generalized to the form

$$M = \Sigma \epsilon^D \tag{4}$$

where M is the measure and D is a real number. The exponent D is the dimensions of an object if it makes the measure M independent of the unit of measurement ϵ in the limit of $\epsilon \to 0$. This is a simple definition of the *Hausdorff dimension* whereas a more rigorous one can be found in Mandelbrot (1982). Contrary to common understanding, this generalization allows the dimension of an object to take noninteger values.

Self-Similarity. Consider a one-dimensional line of unit length as shown in Fig. 3(*a*). Each segment of the line, of size $1/m$, is *similar* to the whole line and needs a magnification of m to be an exact replica of the whole line. Since the length of the line remains independent of $1/m$, it follows that the number of units is $N \sim m$. Now consider a square in Fig. 3(*b*), which has a side of unit length. Each small square of side $1/m$ is similar to the whole square and needs a magnification of m to be an exact replica of the whole square. However, the number of small squares in the whole is $N \sim m^2$. In general, for an object of dimension, D, it follows from the above argument that

$$N \sim m^D \tag{5}$$

Hence the dimension of the object can be obtained as

$$D = \frac{\log N}{\log m} \tag{6}$$

This definition of dimension, which is based on the self-similarity of an object, is called the *similarity dimension* (Mandelbrot, 1982).

To perceive what an object of a noninteger dimension looks like, follow the recursive construction in Fig. 4, which yields the Koch curve of dimension 1.26. The first step in this construction breaks a straight line into three parts and replaces the middle portion by two segments of equal length. In the subsequent stages each straight segment is broken into three parts and the middle portion of each segment is replaced by two parts. If this recursion is done infinite times then the Koch curve is obtained. The mathematical properties of this curve are that, firstly, it is continuous but not differentiable anywhere. This is because if the curve is repeatedly magnified, more and more details of the curve keep appearing. This implies that a tangent cannot be drawn at any point and therefore the curve cannot be differentiated. Secondly, the curve is exactly self-similar because if a small portion of the curve is appropriately magnified, it will be an exact replica of the whole Koch curve. Thirdly, although the curve contains roughness at a large number of scales the dimension of the curve remains constant at all scales.

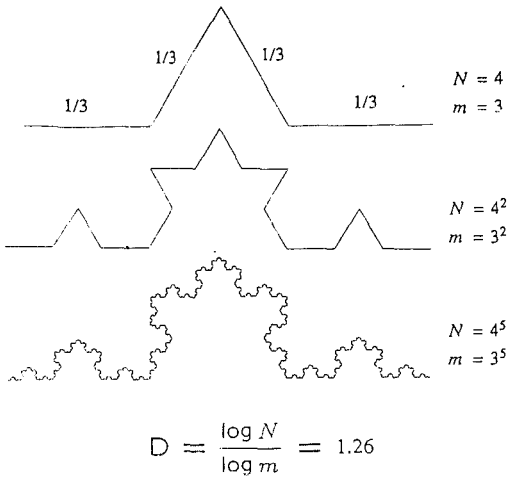

Fig. 4 Recursive construction of the Koch curve of dimension $D = 1.26$

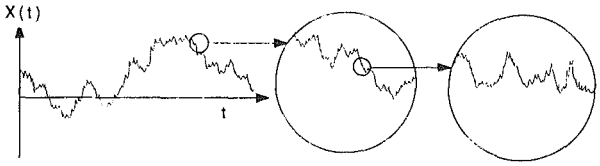

Fig. 5 Qualitative description of self-affinity of a function *x(t)*

Self-Affinity. The definition of self-similarity is based on the property of *equal* magnification in all directions as described in Fig. 3(*b*). However, there are many objects in nature that have unequal scaling in different directions. For example, consider the function $X(t)$, which represents the x location of a particle in Brownian motion as a function of time, t, as shown in Fig. 5. If this curve is repeatedly magnified, more and more details keep appearing, which suggests that it is in some sense similar to the Koch curve. However, since the time t and the location X are two different physical entities, they usually scale differently. Therefore the function $X(t)$ is not self-similar but *self-affine*. A simple mathematical definition states that if the point (x, z) is scaled as $(\gamma_1 x, \gamma_2 z)$ by unequal scaling factors (γ_1, γ_2), such that the probability distributions of (x, z) and $(\gamma_1 x, \gamma_2 z)$ are congruent, then (γ_1, γ_2) is an affine transformation and (x, z) is self-affine. A more rigorous definition is available from Mandelbrot (1982). This concept can be quantitatively shown by the statistics of the Brownian function, which follows the relation (Mandelbrot, 1985)

$$\overline{X}(\gamma t) = \gamma^{1/2}\overline{X}(t) \quad \text{assuming } X(0)=0 \tag{7}$$

where $\overline{X}$ is the probability distribution of X. Equation (7) shows that if time t scales by γ then the position X scales by $\gamma^{1/2}$. Since the time and the position scale differently, the Brownian function $X(t)$ is statistically self-affine.

The statistics of Brownian motion can be generalized to a whole class of functions called *fractional Brownian motion* or fBm (Mandelbrot and van Ness, 1968). The statistics of fBm follow the relation

$$S(\tau) = \langle (X(t+\tau) - X(t))^2 \rangle \sim |\tau|^{2H} \tag{8}$$

where $S(\tau)$ is called the structure function and $\langle\,\rangle$ implies temporal average. For fBm the value of H can vary between 0 and 1. Brownian motion is a special case of this function when $H = 1/2$. The fractal dimension of self-affine fractals cannot be obtained from Eq. (6), which is valid only for self-similar fractals (Mandelbrot, 1985, 1986). Voss (1985) showed that the dimension of a self-affine function is related to the parameter H as $D = E + 1 - H$ where E is equal to the number of arguments of the function X. In the above example since t is the only argument of X, the dimension of the function is $D = 2 - H$.

With this mathematical background of fractal geometry, a scale-invariant characterization of rough surfaces is now presented.

Fractal Characterization of Rough Surfaces

Roughness measurements by instruments at different resolutions have shown that when a surface profile $z(x)$ is repeatedly magnified, more and more roughness keeps appearing, as shown in Fig. 5 (Thomas, 1982; Majumdar, 1989; Bhushan and Blackman, 1990; Majumdar and Bhushan, 1991). Unless artificially textured the roughness appears disordered and random. Due to the multiscale nature of surface roughness as evident in Fig. 5, a profile $z(x)$ can be considered to be composed of a superposition of waves of all wavelengths and random phases. To characterize such a profile it is necessary to determine the amplitude of the roughness at each wavelength. This is typically obtained by finding the power spectrum of the profile by the relation

$$P(\omega) = \frac{1}{L}\left(\int_0^L z(x)\, e^{i\omega x}\, dx\right)^2 \tag{9}$$

where $P(\omega)$ is the power of a wave of frequency ω. Here frequency is the reciprocal of the wavelength and has units of inverse length. The integral in Eq. (9) is the Fourier transform of $z(x)$, which provides the amplitude of waves of frequency ω whereas P is the square of the amplitude.

Consider an isotropic and homogeneous rough surface of dimension D_s. The property of isotropy relates to the invariance of the probability distribution under the rotation of the coordinate axes and reflection on any plane. The homogeneity of a surface implies that the probability distribution of the heights is independent of the location on the surface. The profile, $z(x)$, of such a surface along a straight line and in any arbitrary direction is of dimension $D = D_s - 1$ (Mandelbrot, 1986) and is a statistically valid representation of the surface. Such a profile is typically obtained by stylus measurements or by optical techniques.

In all generality, the scaling in the z direction will not be the same as in the x direction, implying that the function $z(x)$ is self-affine. For a self-affine fractal profile $z(x)$, the power spectrum follows the relation (Majumdar and Tien, 1990; Majumdar and Bhushan, 1990a; Voss, 1988)

$$P(\omega) = \frac{G^{2(D-1)}}{\omega^{(5-2D)}} \tag{10}$$

The structure function $S(\tau)$ can be found as (Berry, 1978)

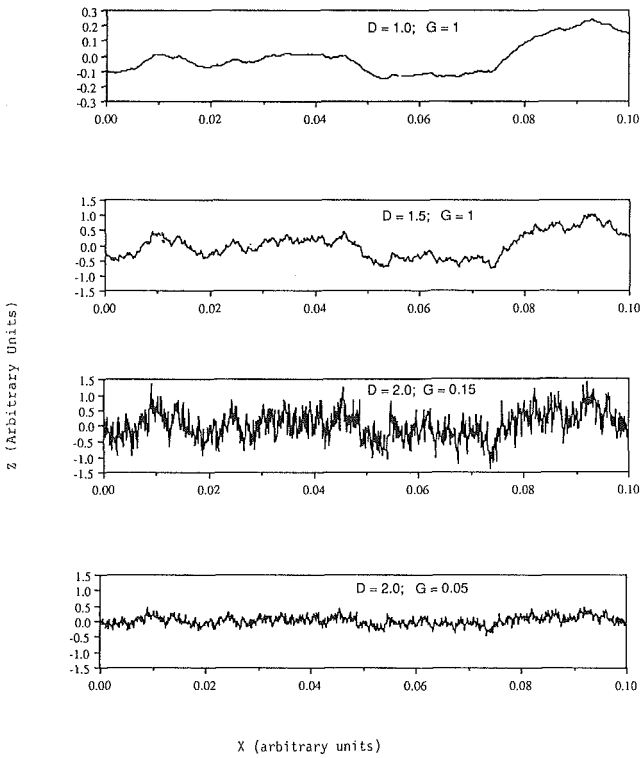

Fig. 6 Comparison of simulated fractal profiles of different values of D and G

$$S(\tau) = \langle (z(x+\tau) - z(x))^2 \rangle = \int_{-\infty}^{\infty} P(\omega)\,(e^{i\omega\tau} - 1)\,d\omega = \psi G^{2(D-1)}\tau^{(4-2D)} \tag{11}$$

where ψ is a constant

$$\psi = \frac{\Gamma(2D-3)\sin((2D-3)\pi/2)}{2-D} \tag{12}$$

Comparison of Eq. (11) with Eq. (7) shows that $S(\tau)$ satisfies the criterion of an fBm of dimension D.

The fractal nature of a real surface profile can be verified either by finding its power spectrum and then comparing with Eq. (10) or calculating its structure function and comparing it with Eq. (11). Before doing so, however, it is instructive to understand the interpretation of the parameters D and G that characterize the spectrum and the structure function. Figure 6 shows four fractal profiles that were generated artificially by the Weierstrass–Mandelbrot function (Voss, 1988; Majumdar and Tien, 1990; Majumdar and Bhushan, 1990a). The first profile shows that when $D = 1$, the profile is smooth, suggesting that the low-frequency components are dominant in amplitude. As D is increased, the high-frequency components become comparable in amplitude with the low-frequency ones. Comparison of the third and the fourth profiles shows that as G is reduced, the amplitude of roughness is reduced over all frequencies. Note that the vertical scale of the first profile is less than other profiles, suggesting that when D is increased, the amplitude is also increased.

It is important to note that the two parameters G and D that characterize the spectrum are independent of ω and therefore scale independent. This is in contrast with conventional methods of roughness characterization by rms height σ and slope σ'. Once the power spectrum is known, these parameters can be derived by taking different moments of the spectrum. For the spectrum of Eq. (10) they are

$$\langle (z)^2 \rangle = \sigma^2 = \int_{\omega_l}^{\omega_h} S(\omega)\, d\omega = \frac{G^{2(D-1)}}{(4-2D)} \left(\frac{1}{\omega_l^{(4-2D)}} - \frac{1}{\omega_h^{(4-2D)}} \right) \quad (13)$$

$$\left\langle \left(\frac{dz}{dx} \right)^2 \right\rangle = \sigma'^2 = \int_{\omega_l}^{\omega_h} \omega^2 S(\omega)\, d\omega = \frac{G^{2(D-1)}}{(2D-2)} \left(\omega_h^{(2D-2)} - \omega_l^{(2D-2)} \right) \quad (14)$$

Equations (13) and (14) provide the variances of the height and the slope, respectively, between the frequencies ω_l and ω_h. For roughness measurements by stylus profilometry, for example, the low-frequency limit, ω_l, corresponds to the length of the sample whereas the high-frequency limit, ω_h, corresponds to the Nyquist frequency, which is related to the resolution of the instrument. Equations (13) and (14) shows that these statistical parameters are functions of the two length scales and their dependence involves the fractal dimension of the surface.

If the dimension of the surface profile is chosen to be the limiting case of $D = 2$, the spectrum behaves as $P(\omega) \sim 1/\omega$. If it is assumed that $\omega_h \gg \omega_l$ then the rms height varies as $\ln(\omega_h/\omega_l)$ and the rms slope varies as ω_h. Now if the surface profile is magnified by a length-scaling factor $\beta > 1$, it transforms ω_l and ω_h to $\beta\omega_l$ and $\beta\omega_h$, respectively. Therefore, one would predict that the rms height would remain constant and the rms slope would increase as β. Figure 2 shows such trends for the rms height and rms slope for a magnetic tape surface (Majumdar and Bhushan, 1990a). The data for $1 < \beta < 10$ were obtained by roughness measurements using optical interferometry (Bhushan et al., 1988) whereas for $10 < \beta < 4000$, atomic force microscopy was used (Qden et al., 1991).

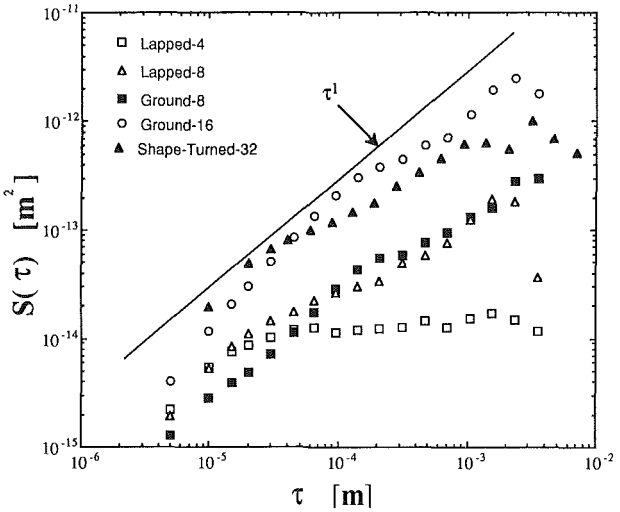

Fig. 7 Structure function of machined stainless steel surfaces. The numbers associated with each machining process correspond to average roughness (μin.) of the surface as specified for General Electric Roughness Specimen (Cat. No. 8651831G1).

The evidence of self-affinity of several machined stainless steel surfaces is shown in Fig. 7. The roughness was measured by stylus profilometry and is well described by Majumdar and Tien (1990). The nearly straight-line behavior of the structure function on a log-log plot suggests that the power-law behavior of Eq. (11) is satisfied. The slope of the straight line gives the dimension D whereas the intercept provides G. The straight line $S(\tau) \sim \tau^1$ corresponds to a Brownian profile of $D = 1.5$. The data in Fig. 7 indicate that at small scales all the surfaces profiles are nearly Brownian, whereas at larger scales they are non-Brownian. Comparison of $S(\tau)$ for Lapped-4 and Lapped-8 surfaces suggests that for length scales below 30 μm the roughness is the same whereas for larger scales, the amplitude of the Lapped-4 profile is much smaller than that of Lapped-8. This explains the apparent smoothness of the surface. Comparison of Lapped-8 and Ground-8 shows similar roughness behavior. The Ground-16 and Shape-Turned-32 profiles have a higher value of G suggesting that the roughness amplitudes are higher. However, since the slopes of $S(\tau)$ for Lapped-8, Ground-8, Ground-16, and Shape-Turned-32 are nearly the same, the dimensions of these surfaces are equal. Therefore, the relative amplitude of roughness at different scales will be the same.

Previous studies (Majumdar and Tien, 1990; Majumdar and Bhushan, 1990a) have shown that surface roughness can be deterministically simulated by the Weierstrass–Mandelbrot function, given as

$$z(x) = G^{(D-1)} \sum_{n=n_1}^{\infty} \frac{\cos 2\pi \gamma^n x}{\gamma^{(2-D)n}}; \quad 1 < D < 2; \quad \gamma > 1 \quad (15)$$

Here, the frequency modes are $\omega = \gamma^n$. The W-N function is self-affine and satisfies all the requirements of an fBm. The function suggests that for a lateral length scale $l = 1/\omega$ the amplitude of the roughness varies as

$$z(l) = G^{(D-1)} l^{(2-D)} \quad (16)$$

Equation (16) is important to this study since it provides a relation between vertical and the lateral scales of a rough surface.

Size Distribution of Contact Spots

Consider a rough surface $z(x, y)$ of dimension D_s for which its mean plane is defined by the average of the height distribution. The size distribution of contact spots for such a surface can be obtained by looking at the horizontal cross sections of the surface at various heights above the mean plane. The series

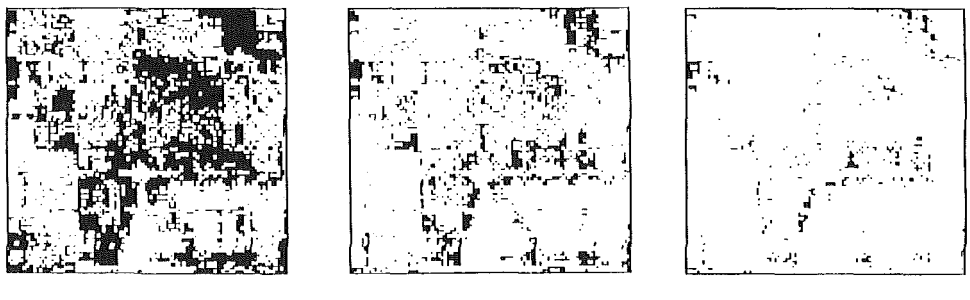

Fig. 8 Cross sections of a simulated rough surface of dimension D = 2.5 at different heights above the mean plane (Majumdar and Bhushan, 1990a)

of such cross sections of a simulated rough surface of dimension $D = 2.5$ (Majumdar and Tien, 1990), shown in Fig. 8, indicates that each section consists of a large number of "islands" of different sizes. Mandelbrot (1975, 1982), while studying the geomorphology of the earth, showed that the total number of islands of areas greater than a particular area, a, follows the power law $N(A>a)\sim a^{-B}$ where $B = D/2$ and $D = D_s - 1$. The equality in this equation can be invoked by using a_L to be the area of the largest island to yield

$$N(A \geq a) = a_L^B a^{-B} \tag{17}$$

which implies that there is only one largest island. From Eq. (17), the frequency distribution of islands of area lying between a and $a+da$ can be obtained as follows

$$n(a) = -\frac{dN}{da} = Ba_L^B a^{-(B+1)} \tag{18}$$

The total area of all the islands, A_t, can now be found to be

$$A_t = \int_0^{a_L} n(a)ada = \frac{B}{1-B}\, a_L = \frac{D}{2-D} a_L \tag{19}$$

The size distribution of Eq. (17) is for an unloaded surface. It is assumed in this study that the distribution remains unchanged upon loading. Although this is not valid for plastic deformation, it is a first approximation to the real distribution. Majumdar and Bhushan (1990) have recently shown that smaller spots are more likely to be in plastic deformation, and larger spots, which are dominant in heat conduction, are in elastic deformation. Moreover, repeated loading and unloading encountered in several engineering applications will tend to make the surface harder, thus promoting elastic deformation. Therefore, for analysis of thermal contact conductance, one can argue that the assumption of an unloaded size distribution is reasonable.

It is interesting to note that power laws, similar to that of Eq. (17), have been observed for nucleation sites during pool boiling (Lorenz et al., 1974). This behavior can possibly be explained by recognizing the fact that for horizontal sections below the mean plane, the distribution of "lakes" formed by the mouths of the cavities will follow the same power law as in Eq. (17). It will be shown later that the average distance between two neighboring islands, of a particular area a, is crucial for the prediction of contact resistance. This distance is related to the cavities existing at the plane of cross section. Imagine the fraction of the apparent area that is not occupied by the contact spots to be divided into cavities, the characteristic length of which is decided by the distance between the asperities. Since these cavities can be visualized as inverted asperities, the size distribution follows as

$$N_c(A_c \geq a_c) = a_{Lc}^{D/2}\, a_c^{-D/2} \tag{20a}$$

where

$$\frac{D}{2-D}\, a_{Lc} = A_a - \frac{D}{2-D}\, a_L \tag{20b}$$

The size distribution of contact spots and cavities can now be used to introduce a network model to predict the contact resistance between two rough surfaces.

Network Model

The contact between two rough surfaces can be modeled by an equivalent surface contacting a smooth plane (see Appendix). Such a contact process produces a large number of contact spots, whose size distribution follows Eq. (17). Each contact spot imposes a certain resistance to the flow of heat across the surface. This resistance is composed of a series of resistances due to small asperities stacked on bigger asperities in a self-similar fashion. However, since all the spots co-exist at the contact plane, these series of resistances act in parallel. Since in the limit of an infinitesimal area, the number of islands become infinite, the flow of heat follows an infinite and extremely complex network of resistances. The complexity of such a network can, however, be reduced by using the self-similarity of the geometry of rough surfaces. The model introduced now uses the feature of self-similarity to reconstruct the network of resistances by repeatedly adding a simple group of resistances infinite times in a self-similar pattern.

The basic element of either a series or a parallel network is the resistance of a single asperity. For the sake of simplicity consider an asperity to be a parallelopiped. As suggested in Eq. (16) the height z of an asperity of length $l = 1/\omega$ is $G^{(D-1)} l^{(2-D)}$. The resistance, ρ, of a single asperity is

$$\rho = \frac{z}{\lambda l^2} = \frac{C}{l^D} \tag{21}$$

where λ is the effective conductivity of the two surfaces in series and $C = G^{(D-1)}/\lambda$.

The characteristic lateral length l of an asperity is chosen such that its base area follows $a = l^2$. From Eq. (21) it can be concluded that the conductance $h \sim 1/\rho$ varies as $h \sim l^D$ or $h \sim a^{D/2}$. This power-law relation between the conductance h and area a is the essence of the fractal model and is the key to explain the experimentally observed behavior in Eq. (1).

Discretization of the Size-Distribution. The network model is developed by discretizing the size-distribution of Eq. (17) in the following way. An island of characteristic length l_q and area $a_q = l_q^2$ is defined to be a q-island and satisfies the relations

$$a_q = \frac{A_a}{b^{2q}} \text{ and } l_q = \frac{L}{b^q} \tag{22}$$

Here, $A_a = L^2$ is the apparent area of the surface and b is a real number greater than unity. The values of q range from $q_L \leq q < \infty$, where q_L corresponds to the largest island a_L such that $a_L = A_a/b^{2q_L}$. Therefore q_L satisfies the relation

$$q_L = \frac{\log(A_a/a_L)}{2\log b} = \frac{\log\left(\dfrac{D}{(2-D)A_t^*}\right)}{2\log b} \tag{23}$$

Following Eq. (21), the resistance of a q-island is

$$\rho_q = Cb^{qD}/L^D \tag{24}$$

The network model is based on finding an effective resistance of the set of all the q-islands, and then constructing a network of effective resistances for different values of q.

Effective Resistance of q-Islands. For a particular value of q, consider the set of all the q-islands co-existing on the contact plane, which form a parallel path for the heat flow. Each strand of this parallel network consists of a series of resistances that arise from each q-island stacked on a series of asperities. The series-parallel network of neighboring q-islands is shown in Fig. 9. Since the number of q-islands can be determined from the size distribution, the only unknown quantity is the number of series resistances in each strand of the parallel network. The number of asperities in series depends on the depth below the contact plane where each strand is joined in parallel with other strands. If two contact spots are separated by a distance, l, then the depth of the cavity between them follows Eq. (16). One now needs to determine the average distance between q-islands, which can be obtained by the size distribution of cavities in Eq. (20a).

The size distributions of Eqs. (17) and (20a) are uniquely determined by the area of the largest island or cavity, which are related through Eq. (20b). Since the number of both the largest island and the largest cavity is unity, the relation between the two size distributions lies in the equality, $N(A \geq a) = N_c\,(A_c \geq a_c)$. Using Eq. (20$b$) with this equality, the average

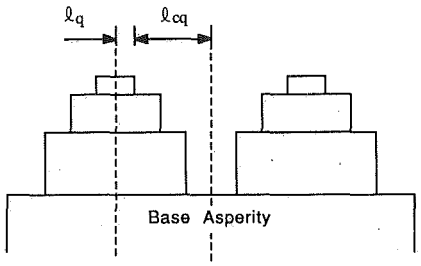

MODEL OF STACKED ASPERITIES

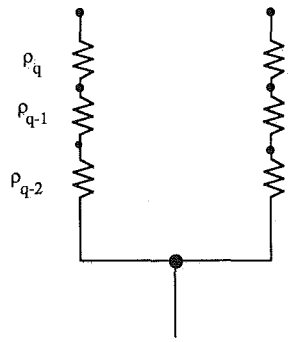

Fig. 9 Series-parallel resistance network for two neighboring q-islands

length of the cavity, $l_{cq} = a_{cq}^{1/2}$, between neighboring q-islands can be reduced

$$l_{cq} = \frac{L}{b^q}\left(\frac{D}{2-D}\right)^{1/2}\left(\frac{1-A_t^*}{A_t^*}\right)^{1/2} \tag{25}$$

Equation (25) shows that for small contact islands, that is for large values of q, the cavity sizes or the distance between the q-islands is small. Moreover, if the total contact area increases, the distance between islands is reduced as expected. The distance d_q between two q-islands is the sum of l_q and l_{cq} and is determined by the value of m_q that satisfies the relation $d_q = L/b^{m_q}$. Using Eq. (25), m_q can be determined to be

$$m_q = q - \frac{\log\left(1+\left(\frac{D(1-A_t^*)}{(2-D)A_t^*}\right)^{1/2}\right)}{\log b} \tag{26}$$

Here the exponent of m_q corresponds to the base of the two neighboring asperities in Fig. 9. Thus, the difference, $q - (m_q+1)$, is the number of resistances in series in each strand of the parallel network. Using the expressions for l_q and ρ_q, the total series resistance ρ_{sq} in each strand is

$$\rho_{sq} = C\sum_{i=m_q+1}^{q}\frac{1}{l_i^D} = \frac{C}{L^D}\left(\frac{b^{(q+1)D}-b^{(m_q+1)D}}{b^D-1}\right) \tag{27}$$

The number of strands of order q is obtained from the size distribution of the q islands and is given by

$$n(a_q) = N(A\geq a_q) - N(A\geq a_{q-1}) = b^{(q-q_L)D}\left(\frac{b^D-1}{b^D}\right) \tag{28}$$

Therefore, the effective resistance R_q, which represents the total series-parallel network for the whole set of q islands, can be determined by dividing the total series resistance of each strand ρ_{sq} by the number of parallel strands as given in Eq. (28). The expression for R_q follows as

$$R_q = \frac{Cb^{qL^D}}{L^D}\left(\frac{b^D}{b^D-1}\right)^2(1-b^{(m_q-q)D}) \tag{29}$$

It is interesting to note that since the difference $q-m_q$ is a

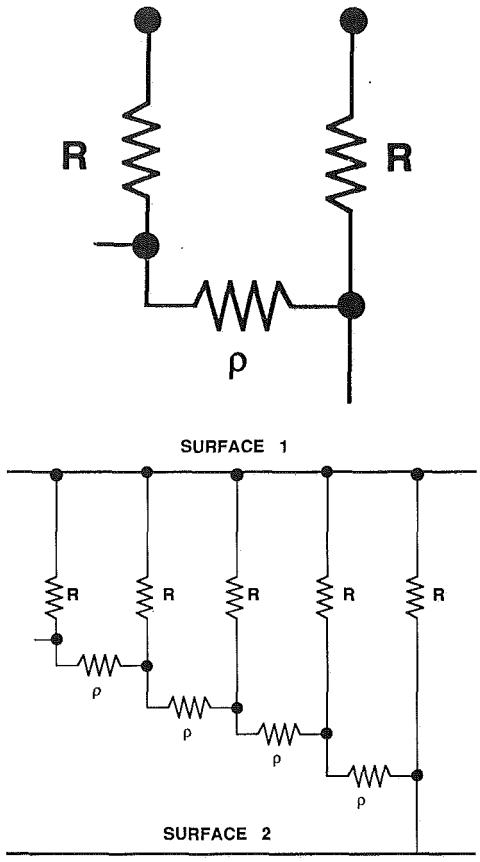

Fig. 10 Basic group of resistances (*a*) is repeatedly added to form a complete resistance network (*b*)

function of only the fractal dimension and the total contact area, the effective resistance R_q is independent of the size of the islands and can be called R. The reason for such an independence can be explained by a scaling argument. The resistance of a q-island is $\rho_q \sim a_q^{-D/2}$. The number of these q-islands conducting heat in parallel on the contact interface is $n(a_q) \sim a_q^{-D/2}$. Therefore, the effective resistance $R \sim r_q/n$ is independent of a_q.

Tree Network. It has been established that the series resistance of each q-island strand joins to form a parallel network at a depth corresponding to m_q. Below this depth the effective resistance R joins a network of resistances formed by islands of other values of q. For a particular contact area A_t^* and a fractal dimension, the difference $m_q - m_{q-1}$ is unity. This implies that the effective resistance R_{q-1} joins the network at a depth lower than that of R_q. Therefore, between respective junctions of R_q and R_{q-1} there must be a resistance in series. This resistance, which is the base in Fig. 9, is ρ_{m_q} and is in series with R_q and parallel with R_{q-1}. Since R_q is the effective resistance of q-island strands, one must find the effective resistance of ρ_{m_q} to be in series with R_q. The number of resistances used to find R_q was $n(a_q)$ and therefore the effective resistance of ρ_{m_q} can be found similarly as

$$\rho = \frac{\rho_{m_q}}{n(a_q)} = \frac{Cb^{qL^D}}{L^D}\left(\frac{b^D}{b^D-1}\right)b^{(m_q-q)D} \tag{30}$$

Equation (30) shows that analogous to R, ρ is also independent of the island sizes.

The combination of ρ and R can be used to construct a basic group of resistances as shown in Fig. 10(a). This group of

resistances can be recursively added to form an infinite network of resistances, for values of $q_L \leq q < \infty$ and $m_{qL} \leq m_q < \infty$. This constitutes the complete network for resistance during a contact process, as shown in Fig. 10(*b*). The treelike structure of this network indicates that when heat flows from the lower surface to the upper, the path branches at each stage and in the limit, forms an infinite number of resistive elements.

The total resistance, **R**, which arises from the series-parallel combination of resistances, can be computed from

$$\frac{1}{\mathbf{R}}=\frac{1}{R}+\cfrac{1}{\rho+\cfrac{1}{\cfrac{1}{R}+\cfrac{1}{\rho+\cdots}}} \tag{31}$$

This reduces to the simple form

$$\mathbf{R}=\frac{R(\rho+r)}{R+\rho+r} \tag{32}$$

where r is given by

$$r=\frac{R(\rho+r)}{R+\rho+r} \tag{33}$$

It is clear from Eqs. (32) and (33) that the resistances can be computed by a recursive algorithm. Solving for r Eq. (33) and substituting into Eq. (32), the total resistance is obtained to be

$$\mathbf{R}=\frac{R[1+\sqrt{1+4(R/\rho)}]}{2(R/\rho)+[1+\sqrt{1+4(R/\rho)}]}=Rf(R/\rho) \tag{34}$$

The ratio R/ρ follows from Eqs. (29) and (30) as

$$\frac{R}{\rho}=\left(\frac{b^D}{b^D-1}\right)(b^{(m_q-q)D}-1) \tag{35}$$

Assuming $b^D \gg 1$, this reduces to

$$\frac{R}{\rho}=\left(\frac{D(1-A_t^*)}{(2-D)A_t^*}\right)^{1/2} \tag{36}$$

In terms of the real area of contact, the resistance R can be written as

$$R=\frac{C}{L^D}\left(\frac{D}{(2-D)A_t^*}\right)^{D/2}\left[1-\frac{1}{1+\left(\frac{D(1-A_t^*)}{(2-D)A_t^*}\right)^{1/2}}\right] \tag{37}$$

Usually it is found that the real area of contact is less than 10 percent of the apparent area. In such a case, Eq. (37) can be approximated to be

$$R=\frac{C}{L^D}\left(\frac{D}{(2-D)A_t^*}\right)^{D/2} \tag{38}$$

Therefore the total resistance **R** can now be written as

$$\mathbf{R}=\frac{f(R/\rho)C}{L^D}\left[\frac{D}{(2-D)A_t^*}\right]^{D/2} \tag{39}$$

Equation (39) shows that as the area of contact increases the total resistance to the flow of heat decreases as expected. The nondimensional contact conductance can be defined as $h^*=\sigma/(\lambda A_a \mathbf{R})$, where the standard deviation σ of the surface is used as the characteristic length scale. It should be noted that the variance of the equivalent surface is the sum of the variances of each surface. The variance can be obtained by integrating the power spectrum between the limits $1/L$ and infinity to yield the following:

$$\sigma=\frac{G^{(D-1)}L^{(2-D)}}{\sqrt{4-2D}} \tag{40}$$

Using Eq. (40) the nondimensional contact conductance can be found to be

$$h^*=\frac{1}{f(R/\rho)\sqrt{4-2D}}\left(\frac{(2-D)A_t^*}{D}\right)^{\frac{D}{2}} \tag{41}$$

Results and Discussion

The fractal network model of contact resistances uses a deterministic approach to analyze the random phenomenon of contact conductance. The use of self-similarity in such an approach considerably reduces the complexity of the problem and yields the simple and powerful result of Eq. (41).

To obtain the conductance as a function of load F, it is necessary to establish a relation between the real area of contact A_t and F. Majumdar and Bhushan (1990b) recently developed a model of elastic-plastic contact between two fractal surfaces. The analysis showed that the area-load relation follows a power law as

$$A_t^* \sim F^{*\eta} \tag{42}$$

The area-load exponent η varies between 1 and 1.33 for the following conditions: (*a*) When $D = 1$ the deformation is likely to be plastic and so $\eta = 1$; (*b*) when $D = 1.5$, the deformation is elastic and then $\eta = 1.33$; (*c*) when $D = 2$, the deformation is plastic and $\eta = 1$. It is clear that there is a reversal behavior in η as the dimension is increased. The conductance-load relation follows from this as

$$h^* \sim F^{*\eta/D2} \tag{43}$$

Equation (43) shows the origins of the exponent x in Eq. (1).

It is necessary now to determine the reason for the conductance-area exponent to be $D/2$. Equation (21) indicates that the resistance of the basic element of the network is $\rho \sim l^{-D}$. In terms of the area of the resistive element the conductance is therefore $h \sim a^{D/2}$. Since the basic element is linearly added to form the complete network of resistances, the exponent in Eq. (41) is therefore $D/2$. This result is independent of network model proposed in this study, and depends only on the fractal characterization of the surface profiles.

It should be noted that as the dimension of the surface increases the contact conductance decreases. The reason for this lies in relation between A_t and a_L of Eq. (19). For a given area of contact, the area of the largest island decreases as the dimension of the surface is increased. The largest island of area a_L fully determines the size distribution of islands as shown in Eq. (17). Therefore, as the dimension is increased, the sizes of all the islands decrease. Since smaller islands impose greater resistance to heat flow, an increase in dimension results in lower conductance.

Previous studies have indicated that the load-exponent usually lies between 0.85 and 0.99 as shown in Table 1. Since the relation between the fractal dimension and the load exponent has been established, it is now possible to explain why this exponent lies between 0.85 and 0.99. Figure 7 shows that when surfaces are ground, the fractal dimension D is close to 1.5. For $D = 1.5$ the value of $\eta = 1.33$. Therefore, the conductance-load exponent $\eta D/2$ is equal to unity. As the value of D is increased toward 2, the value of η decreases toward 1, thus maintaining the product $\eta\, D/2$ to be close to or slightly less than unity. The lower limit of $\eta D/2$ occurs when both D and η go to unity and then $\eta D/2 = 0.5$.

Figure 11 shows a comparison of the present analysis with some experimental results obtained from previous studies. For

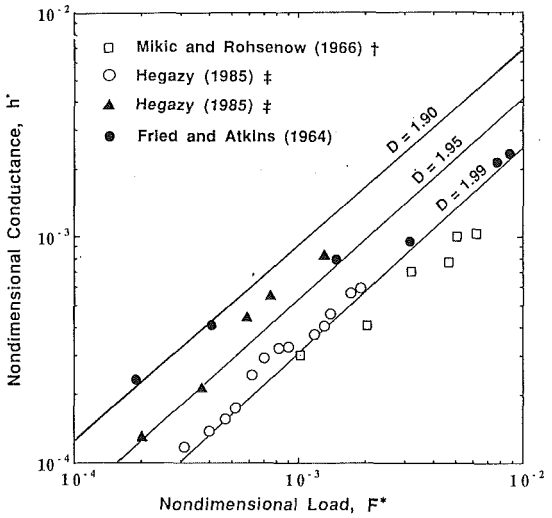

Fig. 11 Comparison of network model with previous experimental data: † from Tien (1968); ‡ from Yovanovich (1987)

lack of surface material properties such as hardness and elastic modulus, an assumption of purely plastic deformation corresponding to $\eta = 1$ has been made. The data of Fried and Atkins (1964) were obtained for SS304 stainless steel specimens of size 5.08 cm × 7.62 cm and of standard deviation $\sigma = 1.56$ μm. Tien (1968) showed that these data could be correlated with a load exponent of 0.85, which corresponds to $D = 1.7$. However, this value of the dimension in Eq. (32) overpredicted the data that span the predictions corresponding to dimensions between 1.9 and 1.99. Although the agreement was better with the data of Mikic and Rohsenow (1966), the present theory still seemed to overpredict. Hegazy (1985) obtained data for specimens of nickel Ni200 (solid triangles) with a standard deviation of $\sigma = 8.48$ μm and used a load-exponent of 0.95 to correlate his data. The data were in excellent agreement with the predictions for $D = 1.95$ instead of 1.9. Hegazy (1985) also obtained experimental data for stainless steel 304 specimens (open circles) of $\sigma = 6.29$ μm, which are in excellent agreement with the predictions for $D = 1.99$. In general, although the theory is in reasonable agreement with experiments, it tends to overpredict. It is now necessary to explore the reasons for this overprediction.

It should be noted firstly that the present theory deals with isotropic surfaces. Machining processes such as grinding produce anisotropic roughness for which the values of the characterization parameters D and G will vary with direction in the (x, y) plane. Comparison with theory and experiments therefore may not be reasonable. However, it can be argued that a comparison will yield equivalent values of D and G that will lie between their corresponding maximum and minimum values for an anisotropic surface.

As shown earlier, the variance or the mean slope of a surface, which are provided by previous studies, cannot uniquely characterize the spectra of rough surfaces. Since none of these investigations provided information about the spectra of the surfaces, it is difficult to verify the relation between the dimension of those surfaces and the contact conductance. Although the present results match the experiments well, a complete verification would require information on both the spectrum and the contact conductance of the surface in addition to the actual hardness of the surface. Currently, experiments are being performed to check the validity of the network model. Nevertheless, a functional relationship between the conductance, load, and the fractal dimension has been established in this study.

Previous experimental studies have all indicated that in addition to the variation of the load exponent, the actual (dimensional) contact conductance may vary considerably even for specimens of the same material. This variation was generally attributed to the variation in mean slope, which was then used to nondimensionalize the conductance and collapse the data into one power law. Earlier in this paper, it was shown that mean slope is an instrument-dependent parameter and cannot be responsible for variation in contact conductance data. This suggests that other material or topographical properties of rough surfaces produce uncertainty in the experimental data. In particular, if a surface work hardens during surface machining or the contact process, the actual hardness of the surface is greater than the bulk value. This tends to promote elastic deformation and increase the exponent η in Eq. (42). The present model also neglects the presence of any oxide film on the surface. Unless carefully prepared, such films are always present on the surface and can impose considerable resistance to heat flow. For thermal contact conductance, one also needs to include the effect of phonon transmission through thin films. A source of overprediction in this model is that the resistance to lateral heat flow is assumed to be zero. The present study introduces a framework for predicting contact conductance in which the lateral heat flow resistance can be included in the future.

Conclusions

The fractal nature of rough surfaces suggests that statistical parameters like the mean slope or the standard deviation of the height are not unique for a surface. Instead, they depend strongly on the roughness measuring instrument or the length of the sample, respectively. This is mathematically proved in this study and experimentally shown for over three decades of length scales for a magnetic tape surface. Therefore, the use of the mean slope to correlate contact conductance data will lead to ambiguity.

This work introduces a new fractal model to predict contact resistance as a function of the load on the surfaces. During a contact process a large number of contact spots are created at the contact plane. These spots form an infinite and complex network of resistances. The complexity of this network is largely reduced by using the self-similarity of rough surfaces, which allows the addition of a simple group of resistances to build an infinite network. The analysis of this network yields the sample and powerful result that the conductance is related to the load by a power law where the load exponent is a function of the fractal dimension of the surface profile. Results of this model agree well with experimental data of previous studies, although the theory tends to overpredict the data.

References

Berry, M. V., 1978, "Diffractals," *Journal of Physics A*, Vol. 12, pp. 781–797.

Berry, M. V., and Lewis, Z. V., 1980, "On the Weierstrass-Mandelbrot Fractal Function," *Proceedings of the Royal Society of London*, Vol. A 370, pp. 459–484.

Bhushan, B., Wyant, J. C., and Meiling, J., 1988, "A New Three-Dimensional Non-contact Digital Optical Profiler," *Wear*, Vol. 122, pp. 301–312.

Bhushan, B., 1990, *Tribology and Mechanics of Magnetic Storage Devices*, Springer-Verlag, New York.

Bhushan, B., and Blackman, X. X., 1990, "Atomic Force Microscopy of Magnetic Rigid Disks and Sliders and Its Applications to Tribology," ASME Paper No. 90-Trib-5, ASME *Journal of Tribology*, in press.

Cooper, M. G., Mikic, B. B., and Yovanovich, M. M., 1969, "Thermal Contact Conductance," *International Journal of Heat and Mass Transfer*, Vol. 12, pp. 279–300.

Fletcher, L. S., 1988, "Recent Developments in Contact Conductance Heat Transfer," ASME JOURNAL OF HEAT TRANSFER, Vol. 110, pp. 1059–1070.

Fried, E., and Atkins, H., 1964, "Interface Thermal Conductance in a Vacuum," *Journal of Spacecraft and Rockets*, Vol. 2, p. 591.

Hegazy, A. A., 1985, "Thermal Joint Conductance of Conforming Rough Surfaces: Effect of Surface Micro-Hardness Variation," Ph.D. Thesis, University of Waterloo, Canada.

Lorenz, J. J., Mikic, B. B., and Rohsenow, W. M., 1974, "The Effect of Surface Conditions of Boiling Characteristics," *Proceedings of the 5th International Heat Transfer Conference*, Tokyo, Vol. IV, pp. 35-39.

Majumdar, A., 1989, "Fractal Surfaces and Their Applications to Surface Phenomena," Ph.D. Thesis, Department of Mechanical Engineering, University of California, Berkeley.

Majumdar, A., and Tien, C. L., 1990, "Fractal Characterization and Simulation of Rough Surfaces," *Wear*, in press.

Majumdar, A., and Bhushan, B., 1990a, "Role of Fractal Geometry in Roughness Characterization and Contact Mechanics of Surfaces," ASME *Journal of Tribology*, Vol. 112, pp. 205-216.

Majumdar, A., and Bhushan, B., 1990b, "Fractal Model for Elastic-Plastic Contact Between Rough Surfaces," ASME *Journal of Tribology*, Vol. 113, pp. 1-11.

Majumdar, A., and Bhushan, B., 1991, "Role of Fractal Geometry in Tribology," in: ASME *Advances in Information Storage Systems*, Vol. 1,in press.

Mandelbrot, B. B., and van Ness, J. W., 1968, "Fractional Brownian Motions, Fractional Noise and Applications," *SIAM Review*, Vol. 10, pp. 422-437.

Mandelbrot, B. B., 1975, "Stochastic Models for the Earth's Relief, the Shape and Fractal Dimension of the Coastlines, and the Number-Area Rule for Islands," *Proceedings of the National Academy of Science, USA*, Vol. 72, pp. 3825-3828.

Mandelbrot, B. B., 1982, *The Fractal Geometry of Nature*, W. H. Freeman, New York.

Mandelbrot, B. B., 1985, "Self-Affine Fractals and Fractal Dimension," *Physica Scripta*, Vol. 32, pp. 257-260.

Mandelbrot, B. B., 1986, "Self-Affine Fractal Sets, I, II, and III," in: *Fractals in Physics*, L. Pietronero and E. Tosatti, eds., North-Holland Publishers, Amsterdam, pp. 3-28.

Mikic, B. B., and Rohsenow, W. M., 1966, "Thermal Contact Resistance," *Technical Report No. 4542-41*, Department of Mechanical Engineering, Massachusetts Institute of Technology, Cambridge, MA.

Mikic, B. B., 1974, "Thermal Contact Conductance; Theoretical Considerations," *International Journal of Heat and Mass Transfer*, Vol. 17, pp. 205-214.

Nayak, P. R., 1971, "Random Process Model of Rough Surfaces," ASME *Journal of Lubrication Technology*, Vol. 93, pp. 398-407.

Oden, P. I., Majumdar, A., and Bhushan, B., 1991, "Atomic Force Microscopy and Contact Mechanics of Magnetic Tapes," submitted to ASME *Journal of Tribology*.

Sayles, R. S., and Thomas, T. R., 1978, "Surface Topography as a Nonstationary Random Process," *Nature*, Vol. 271, pp. 431-434.

Thomas, T. R., and Probert, S. D., 1970, "Thermal Contact Resistance: The Directional Effect and Other Problems," *International Journal of Heat and Mass Transfer*, Vol. 13, pp. 789-807.

Thomas, T. R., 1982, *Rough Surfaces*, Longman Inc., New York.

Tien, C. L., 1968, "A Correlation for Thermal Contact Conductance of Nominally-Flat Surfaces in Vacuum," *Proceedings of the 7th Thermal Conductivity Conference*, U.S. Bureau of Standards, pp. 755-759.

Voss, R. F., 1985, "Random Fractal Forgeries," in: *Fundamental Algorithms for Computer Graphics*, R. A. Earnshaw, ed., pp. 805-835.

Voss, R. F., 1988, "Fractals in Nature: From Characterization to Simulation," in: *The Science of Fractal Images*, H. O. Peitgen and D. Saupe, eds., Springer-Verlag, New York, pp. 21-70.

Yovanovich, M. M., 1987, "Theory and Applications of Constriction and Spreading Concepts for Microelectronic Thermal Management," Keynote Address, *Proceedings of the International Symposium on Cooling Technology for Electronic Equipment*, Honolulu, HI.

APPENDIX

The contact between two rough surfaces can be modeled as contact between one equivalent rough surface with a flat plane, as shown in Fig. A1. For the equivalent surfaces, the structure function $S(\tau)$ is given as:

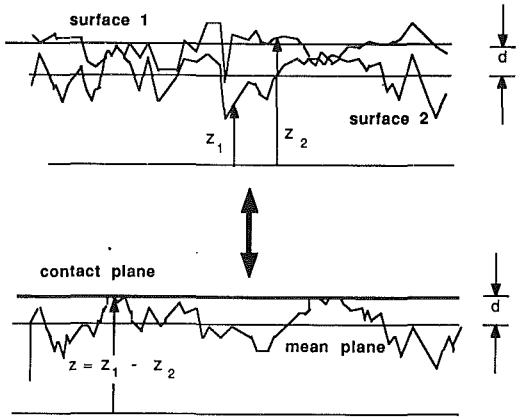

Fig. A1 Static contact between two surfaces is equivalent to the contact between a composite surface and a flat plane

$$S(\tau) = \langle (z(x+\tau) - z(x))^2 \rangle \tag{A1}$$

where

$$z(x) = z_1(x) - z_2(x) \tag{A2}$$

Substituting Eq. (A2) into (A1) one gets

$$S(\tau) = \left\langle \begin{array}{c} (z_1(x+\tau) - z_1(x))^2 - 2(z_1(x+\tau) - z_1(x))(z_2(x+\tau) - z_2(x)) + \\ (z_2(x+\tau) - z_2(x))^2 \end{array} \right\rangle \tag{A3}$$

Since the two surfaces are statistically uncorrelated, the cross-product term $\langle 2(z_1(x+\tau) - z_1(x))(z_2(x+\tau) - z_2(x)) \rangle$ goes to zero. The equation then becomes

$$S(\tau) = \langle (z_1(x+\tau) - z_1(x))^2 + (z_2(x+\tau) - z_2(x))^2 \rangle \tag{A4}$$

which reduces to

$$S(\tau) = S_1(\tau) + S_2(\tau) \tag{A5}$$

Therefore the structure function of the equivalent surface is the sum of the structure functions of the individual surfaces.

Since the power spectrum $P(\omega)$ is related to the surface function $S(\tau)$ as

$$S(\tau) = \int_{-\infty}^{\infty} P(\omega)\ (\exp(-i\omega\tau) - 1)\ d\omega \tag{A6}$$

it is evident that the power spectrum of the equivalent surface is the sum of the power spectra of the individual surfaces, $P\omega = P_1(\omega) + P_2(\omega)$. For the contact between a rough surface and a flat plane one must derive the value of the dimension D and the scaling constant G from the spectrum or the structure function of the equivalent surface.

G. Pagliarini
Associate Professor,
Istituto di Fisica Tecnica,
Università degli Studi di Bologna,
40136 Bologna, Italy

G. S. Barozzi
Full Professor,
Istituto di Fisica Tecnica,
Università degli Studi di Trieste,
34127 Trieste, Italy

Thermal Coupling in Laminar Flow Double-Pipe Heat Exchangers

Thermal interaction between the streams of laminar flow double-pipe heat exchangers is investigated theoretically by accounting for axial conduction along the wall separating the fluids. In a countercurrent arrangement, thermal coupling is demonstrated to have a definite influence on all the more important heat transfer parameters, such as the wall temperature, the heat flux density, the local entropy production rate, and the Nusselt number distributions. The overall performance of the device is considered under a second law point of view, and a complete parametric study is carried out.

1 Introduction

Parallel plate and double pipe heat exchangers find current application in industrial processes for energy conversion. The need for accurate sizing of the equipment and its thermodynamic optimization increases when the temperature difference between the fluids decreases and becomes paramount when a very high efficiency is demanded.

A basic unit essentially consists of two flow passages separated by a conducting wall. Through this, the two heat carriers thermally interact, flowing either concurrently or countercurrently. A double-pipe device can therefore be schematized into a couple of concentric tubes, the inner one providing the heat transfer surfaces.

As discussed in classical thermal engineering textbooks (Kays and London, 1984; Kakac et al., 1981; Spalding, 1984), two essential assumptions are customarily made in the design of heat exchangers: (*i*) The film coefficients are considered to be insensitive to the longitudinal distribution of both the heat flux and the surface temperature; and (*ii*) they are taken to be uniform, irrespective of the heat exchanger length. There is substantial evidence (Stein, 1966a) that based upon the above assumptions, the sizing of the heat transfer surfaces is satisfactory for turbulent flow conditions. The local heat transfer rate is scarcely influenced by the thermal boundary conditions in those cases, and the thermal inlet region usually covers a small part of the heat transfer length. When dealing with laminar flow conditions, however the thermal inlet length can often be of the same order of magnitude as the heat exchanger length. Film coefficients are by no means uniform and also become very sensitive to the thermal boundary condition. Since the two streams are thermally coupled by the conducting wall, the boundary condition for each of them is not defined a priori. It is instead dependent on the geometry and the thermal properties of the wall, other than the operating conditions of the device. The problem is made even more complex when axial conduction along the wall is taken into account. Axial wall conduction affects both the distributions of the heat transfer coefficients and the overall thermal performance of the device.

In this paper, the effects of thermal coupling in double-pipe heat exchangers are dealt with. Heat conduction along the wall is accounted for in the analysis and its influence on heat exchanger effectiveness and entropy production is discussed.

2 Literature Survey

The earliest investigations on double current laminar heat exchangers are due to Stein (1964, 1965a, 1965b) who presented an analytical solution for concurrent flow. The mathematical aspects associated with countercurrent flow were first discussed by Nunge and Gill (1965). They also presented extensive results for double-pipe heat exchangers (Nunge and Gill, 1966). The approach was based upon the reduction of the primitive double-region problem into a couple of one-region Sturm–Liouville problems. Coupling conditions had to be matched at the common boundary, and an equivalent of the orthogonality condition devised over both regions. This constitutes a major difficulty in orthogonal expansion solutions and the accuracy of the procedure used by Nunge and Gill has actually been questioned (see Stein, 1966b, and Blanco et al., 1968, for discussion). Stein (1966a, 1966c) presented a generalization of the method for both concurrent and countercurrent flow. The method was extended by Blanco and Gill (1967) to the case of slug flow rather than fully developed laminar flow, while the effects of axial conduction in the fluids were considered by Nunge et al. (1967). The superposition of known solutions in the form of the Duhamel theorem was applied to the concurrent case by Gill et al. (1968). An alternative approach is based on the expression of the temperature field in each stream in terms of unknown functions of the heat flux across the walls, thus creating a system of cross-linked integral equations to be solved numerically. This was adopted by Bentwich (1970, 1973) to deal with two-stream and multistream parallel-flow heat exchangers. An original general methodology for conjugated problems was presented by Papoutsakis and Ramkrishna (1981). The energy equation was decomposed into a system of first-order differential equations, which again gave a Sturm–Liouville problem. Sample temperature distributions in concurrent and countercurrent heat exchangers were presented on account of axial heat conduction in the two streams. An efficient algorithm for solving two Sturm–Liouville equations coupled at a common boundary was given by Mikhailov (1972, 1973a). The analytical solution was based upon a finite integral transform and applies to a wide class of conjugated boundary value problems. A specialized version of the method for conjugated Graetz problems was formulated by Mikhailov (1973b, 1983) and illustrative examples were presented by Mikhailov and Shishedjiev (1976), among which the case of concurrent double pipe heat exchanger was treated. The same problem has recently been treated by Cotta and Ozisik (1986) using a more refined version of the same method. Finally, a fully numerical solution for developing flow in countercurrent double-pipe heat exchangers has been presented by Lin and Tsay (1986).

Under the assumptions of fully developed laminar flow and constant property fluids, a few general comments can be made on the thermal behavior of double-stream heat exchangers.

With concurrent flow:

(*i*) A thermally developed region always exists asymptotically. This may or may not be attained in practical cases, depending on the heat exchanger length. The length of the

Contributed by the Heat Transfer Division for publication in the JOURNAL OF HEAT TRANSFER. Manuscript received by the Heat Transfer Division July 5, 1989; revision received November 9, 1990. Keywords: Conjugate Heat Transfer, Heat Exchangers, Thermodynamics and Second Law.

thermal inlet region is a function of the wall thermal resistance, fluid properties and the operating conditions.

(*ii*) Asymptotic values of the heat transfer coefficient can be significantly less than those corresponding to the boundary condition of uniform wall temperature, condition (T), for single-stream cases. They cannot be larger than values corresponding to the boundary condition of uniform heat flux, condition (H) (Stein, 1965a). Such behavior is consistent with single-stream heat transfer results when imposing an exponentially decreasing heat flux at the duct wall (Shah and London, 1978).

(*iii*) Distributions of the heat transfer coefficient in the thermal inlet region show good agreement with single-stream solutions for case (T). Despite this, the wall temperature can exhibit significant longitudinal variations (Gill et al., 1968).

With countercurrent flow:

(*i*) The heat transfer rate decreases monotonically from the extremities to the central part of the heat transfer length where a minimum is always achieved. Eventually, a central region of thermally developed flow can occur, according to the heat exchanger geometry and the operating conditions.

(*ii*) Asymptotic values of the heat transfer coefficients are never less than values corresponding to case (T), but can be significantly larger than reference values for the boundary condition (H) (Stein, 1966a).

(*iii*) For each stream, the heat transfer coefficient is bounded by single-stream solutions (T) and (H) close to the entrance (Lin and Tsay, 1986). It may be worth noting that in spite of the influence of thermal coupling on the distributions of film coefficients an overall heat transfer coefficient can still be defined. According to the Seban et al. (1972) approximate method, this can be used with sufficient accuracy.

(*iv*) The effect of axial heat conduction in fluids is generally negligible for Peclet numbers greater than 100 (Nunge et al., 1967).

In all the above literature, the effect of axial conduction along the wall separating the two streams was overlooked. This has been recognized to have a definite effect on heat transfer

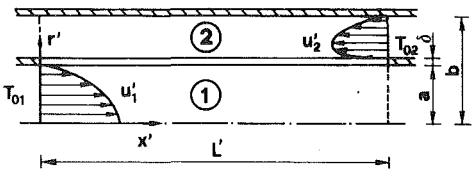

Fig. 1 Schematic of the double-pipe heat exchanger

efficiency in countercurrent flow (Kroeger, 1966; Barron and Yeh, 1976) and crossflow (Chiou, 1983) heat exchangers. Very accurate results for the laminar flow case were given by Mori et al. (1980) for parallel plate countercurrent heat exchangers. Sample data for both concurrent and countercurrent double pipe heat exchangers were presented by the authors (1984a).

Double-stream heat exchangers have also been extensively investigated from a thermodynamic point of view, and many valuable second law analyses can be mentioned (see, for example, Bejan, 1977; Golem and Brzustowski, 1976; Ciampi and Tuoni, 1979). In all of them, however, the lumped system approach has been employed, while assuming a uniform heat transfer coefficient and omitting axial wall conduction. The latter effect was considered by Chowdhury and Sarangi (1983), who also derived a simple formula to optimize the thermal conductivity of the wall. That criterion has been found to be valid even in the case of laminar balanced counterflow heat exchangers (Pagliarini and Barozzi, 1984b, 1985).

3 Analysis

The system under consideration is schematically depicted in Fig. 1. Two Newtonian constant property fluids are assumed to flow under steady and laminar conditions through the equipment with fully developed velocity profiles. Internal heat generation, viscous dissipation, and axial heat conduction in the fluids are neglected.

According to the notation in the figure, indexes 1 and 2, respectively, designate the inner and outer stream. It is assumed that heat is transferred from stream 2 to stream 1. The fluid

Nomenclature

a = internal radius of the inner duct (Fig. 1)
b = internal radius of the outer wall of the outer duct (Fig. 1)
B = radius ratio $= b/a$
c_p = specific heat at constant pressure
d_h = hydraulic diameter
H = ratio between the flow-stream capacity rate of outer and inner flow $= (m\ c_p)_2/(m\ c_p)_1$
(H) = thermal boundary condition referring to uniform wall heat flux
k = thermal conductivity
K = nondimensional thermal conductivity $= k/k_1$
K_{opt} = optimum K value $= \mathrm{Pe}_1/[2(1+H^{-1})]$, from Chowdhury and Sarangi (1983, equation (11))
L' = dimensional length of the heat exchanger
L = nondimensional length of the heat exchanger $= L'/a$
L^* = nondimensional length of the heat exchanger $= L'/(2\ a\ \mathrm{Pe}_1)$
m = mass flow rate
Nu = Nusselt number (equations (8))
Pe = Peclet number $= U\ d_h\ (c_p\ \rho/k)_f$
q = nondimensional heat flux at the solid–fluid interface (equations (6))
Q = heat transferred per unit time from stream 2 to stream 1
r' = dimensional radial coordinate
r = nondimensional radial coordinate $= r'/a$
s = rate of entropy production per unit volume
S = rate of entropy production
T = absolute temperature
T_0 = absolute inlet temperature
(T) = thermal boundary condition referring to uniform wall temperature
u' = dimensional axial velocity
u = nondimensional axial velocity $= u'/U$
U = fluid mean axial velocity
x' = dimensional axial coordinate
x^* = nondimensional axial coordinate $= x'/(2\ a\ \mathrm{Pe}_1)$
z^* = nondimensional axial coordinate $= L^* - x^*$
Γ = nondimensional inlet temperature of the outer stream $= T_{02}/T_{01}$
δ = wall thickness
Δ = nondimensional wall thickness $= (\delta/a)$
ϵ = heat exchanger effectiveness (equation (14))
Θ = nondimensional temperature $= T/T_{01}$
Θ_b = nondimensional bulk fluid temperature (equation (7))
Θ_w = nondimensional temperature at the wall–fluid interface
ρ = density
σ = nondimensional rate of entropy production per unit volume (equation (9))
Σ = nondimensional rate of entropy production

Subscripts

f = fluid
s = solid
x = local value
w = wall-fluid interface
1 = inner stream
2 = outer stream

temperature is uniform at the inlet sections; the condition $T_{02} > T_{01}$ therefore holds.

For the sake of brevity, the mathematical problem is directly stated in nondimensional terms. Use is made of symbols and definitions given in the Nomenclature. The system is subdivided into three physically homogeneous regions, namely, stream 1, stream 2, and the solid wall separating the fluids.

For each region the energy equation is written:

Stream 1:

$$u_1 \frac{\partial \Theta_1}{\partial x^*} = 4\left(\frac{1}{r}\frac{\partial \Theta_1}{\partial r} + \frac{\partial^2 \Theta_1}{\partial r^2}\right) \qquad 0 \le x^* \le L^*, \quad 0 \le r \le 1 \tag{1}$$

$$\Theta_1(0, r) = \Theta_{01} \tag{1a}$$

$$\frac{\partial \Theta_1}{\partial r}(x^*, 0) = 0 \tag{1b}$$

Solid Wall:

$$4\,\mathrm{Pe}_1^2\left(\frac{1}{r}\frac{\partial \Theta_s}{\partial r} + \frac{\partial^2 \Theta_s}{\partial r^2}\right) + \frac{\partial^2 \Theta_s}{\partial x^{*2}} = 0 \quad 0 \le x^* \le L^*, \quad 1 \le r \le 1+\Delta \tag{2}$$

$$\frac{\partial \Theta_s}{\partial x^*}(0, r) = \frac{\partial \Theta_s}{\partial x^*}(L^*, r) = 0 \tag{2a}$$

Stream 2:

$$u_2 \frac{\partial \Theta_2}{\partial x^*} = 4\frac{K_f}{H}(B^2 - (1+\Delta)^2)\left(\frac{1}{r}\frac{\partial \Theta_2}{\partial r} + \frac{\partial^2 \Theta_2}{\partial r^2}\right) \qquad 0 \le x^* \le L, \quad 1+\Delta \le r \le B \tag{3}$$

$$\Theta_2(0, r) = \Theta_{02} \quad \text{(concurrent case)}$$
$$\Theta_2(L^*, r) = \Theta_{02} \quad \text{(countercurrent case)} \tag{3a}$$

$$\frac{\partial \Theta_2}{\partial r}(x^*, B) = 0 \tag{3b}$$

In equations (1) and (3), u_1 and u_2 are nondimensional distributions of the fluid velocity, as given in the literature (e.g., Shah and London, 1987, Chap. 5, p. 78, and Chap. 12, p. 205, for circular and annular ducts, respectively). Pe_1 is the Peclet number for the inner stream, H is the thermal capacity ratio of the streams, $H = (mc_p)_2/(mc_p)_1$, and Δ is the nondimensional wall thickness.

Continuity conditions for the temperature and the heat flux apply at the interfaces:

$$\Theta_1(x^*, 1) = \Theta_s(x^*, 1), \qquad \frac{\partial \Theta_1}{\partial r}(x^*, 1) = K_s \frac{\partial \Theta_s}{\partial r}(x^*, 1) \tag{4a}$$

$$\Theta_2(x^*, 1+\Delta) = \Theta_s(x^*, 1+\Delta), \qquad \frac{\partial \Theta_2}{\partial r}(x^*, 1+\Delta) = \frac{K_s}{K_f}\frac{\partial \Theta_s}{\partial r}(x^*, 1+\Delta) \tag{4b}$$

The wall temperature and the heat flux at the solid-fluid interfaces, as well as the bulk fluid temperature and the local Nusselt number, have practical significance. They are defined as

$$\Theta_{w1} = \Theta_s(x^*, 1) \tag{5a}$$

$$\Theta_{w2} = \Theta_s(x^*, 1+\Delta) \tag{5b}$$

$$q_1 = \left(\frac{\partial \Theta_1}{\partial r}\right)_w \tag{6a}$$

$$q_2 = K_f(1+\Delta)\left(\frac{\partial \Theta_2}{\partial r}\right)_w \tag{6b}$$

$$\Theta_{b1} = 1 + 8\int_0^{x^*} q_1\, d\xi^* \tag{7a}$$

$$\Theta_{b2} = \Gamma + \frac{8}{1+\Delta}\frac{B}{H}\int_0^{z^*} q_2\, d\zeta^* \tag{7b}$$

$$\mathrm{Nu}_{x1} = 2\frac{q_1}{\Theta_{w1} - \Theta_{b1}} \tag{8a}$$

$$\mathrm{Nu}_{x2} = \frac{2}{K_f}\frac{B-(1+\Delta)}{1+\Delta}\frac{q_2}{\Theta_{w2} - \Theta_{b2}} \tag{8b}$$

By definition equation (6*b*), the heat flux density q_2 is referred to the inner wall surface ($r = 1$) to allow direct comparison with q_1. Equations (5*b*), (6*b*), and (8*b*) hold for both the concurrent and the countercurrent flow case. Equation (7*b*) is written for countercurrent flow heat exchangers. The proper form for the concurrent flow case is obtained by changing the variables z^* and ζ^* with $x^* = L^* - z^*$ and $\xi^* = L^* - \zeta^*$, respectively. Finally, Γ in equation (7*b*) is the ratio of the inlet fluid temperatures T_{02} and T_{01} measured on the thermodynamic Kelvin scale.

The overall rate of entropy production, S, will be used to quantify the heat transfer process according to a second law point of view. Following London and Shah (1983), this quantity is nondimensionalized as

$$\Sigma = \frac{S\,T_{01}}{Q}$$

where Q is the total amount of heat transferred per unit time from stream 2 to stream 1.

The local entropy production rate per unit volume, s, is nondimensionalized and is expressed as follows (de Groot and Mazur, 1962):

$$\sigma = \frac{k_s\, a\, T_{01}}{Q}\frac{1}{\Theta^2}\left(\left(\frac{1}{2\,\mathrm{Pe}_1}\frac{\partial \Theta}{\partial x^*}\right)^2 + \left(\frac{\partial \Theta}{\partial r}\right)^2\right) \tag{9}$$

Equation (9) holds for the solid wall. It applies to the fluid regions as well, viscous dissipation in the fluids having been disregarded. The total entropy production rate can be split into three terms Σ_1, Σ_2, and Σ_s, pertaining to the fluid streams and the wall, respectively. One therefore has

$$\Sigma = \Sigma_1 + \Sigma_2 + \Sigma_s \tag{10}$$

The latter term is given as:

$$\Sigma_s = 4\pi\,\mathrm{Pe}_1 \int_1^{1+\Delta}\int_0^{L^*} \sigma_s r\, dr\, dx^* \tag{11}$$

Similar expressions can be written for Σ_1 and Σ_2. However, the following alternative forms have been used here:

$$\Sigma_1 = 4\pi\,\mathrm{Pe}_1 \int_0^{L^*} q_1\left(\frac{1}{\Theta_{b1}} - \frac{1}{\Theta_{w1}}\right) dx^* \tag{12a}$$

$$\Sigma_2 = 4\pi(1+\Delta)\mathrm{Pe}_1 \int_0^{L^*} q_2\left(\frac{1}{\Theta_{w2}} - \frac{1}{\Theta_{b2}}\right) dx^* \tag{12b}$$

These or equivalent expressions are commonly found in the literature (see, e.g., equation (5) from Bejan, 1982), to calculate the entropy production rate in pipe flow heat transfer. Equations (12) are used here for convenience, since Θ_b, Θ_w, and q are known at the end of the computational procedure, while the temperature distributions in the fluids are not. Also, equations (12) allow the numerical results to be checked against the integral entropy balance. This reads

$$\Sigma = \frac{1}{\Theta_{b1}(L^*) - 1}\left(\ln \Theta_{b1}(L^*) + H \ln\left(\Theta_{b2}(L^*)/\Gamma\right)\right) \tag{13}$$

The thermodynamic performance of heat exchangers is usually expressed in terms of the effectiveness, ϵ, and defined as:

$$\epsilon = \frac{Q}{(m\,c_p)_{\min}\,(T_{02} - T_{01})} \tag{14}$$

From equations (13) and (14), the following relations between Σ and ϵ are easily demonstrated:

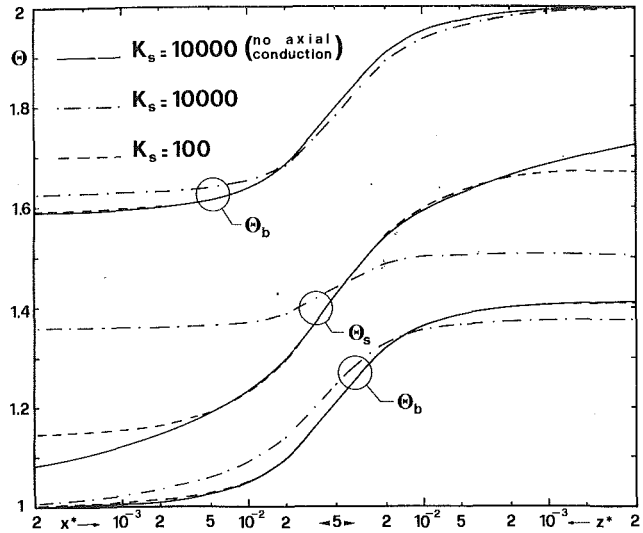

Fig. 2 Axial distributions of bulk fluid and wall (radially averaged) nondimensional temperatures; $H=1$, $Pe_1=500$, $L=100$, $B=6$, $\Delta=0.5$, and $K_f=1$

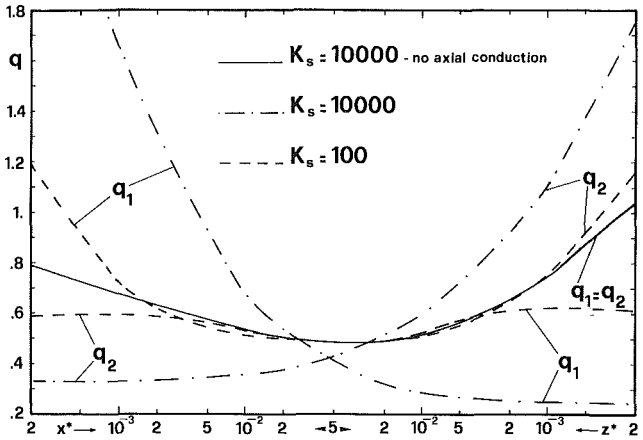

Fig. 3 Axial distributions of the nondimensional heat flux at wall-to-fluid interfaces; $H=1$, $Pe_1=500$, $L=100$, $B=6$, $\Delta=0.5$, and $K_f=1$

$$\frac{\Sigma}{1-1/\Gamma}=\frac{1}{\epsilon}\frac{\Gamma}{(\Gamma-1)^2}\left\{\ln\left[1+\epsilon(\Gamma-1)\right]+H\ln\left[1-\frac{\epsilon}{H}\left(1-\frac{1}{\Gamma}\right)\right]\right\} \quad (15a)$$

for $H>1$, and

$$\frac{\Sigma}{1-1/\Gamma}=\frac{1}{\epsilon}\frac{\Gamma}{(\Gamma-1)^2}\left\{\frac{1}{H}\ln\left[1+\epsilon H(\Gamma-1)\right]+\ln\left[1-\epsilon\left(1-\frac{1}{\Gamma}\right)\right]\right\} \quad (15b)$$

for $H<1$. The quantity $(1-1/\Gamma)$ is used here as a normalization factor for Σ.

4 Procedure and Accuracy

A seminumerical method had been suggested (Barozzi and Pagliarini, 1984, 1985) to deal with conjugated heat transfer in pipe flow. This has been extended to the case of parallel flow heat exchangers. The technique relies upon the application of the superposition principle at the solid–fluid interfaces, and the numerical solution of the energy equation in the wall, by a finite element method. A detailed description of the method having been given elsewhere (Barozzi and Pagliarini, 1985), the procedure will be simply outlined here.

By applying the Duhamel theorem at the solid wall boundaries, one has

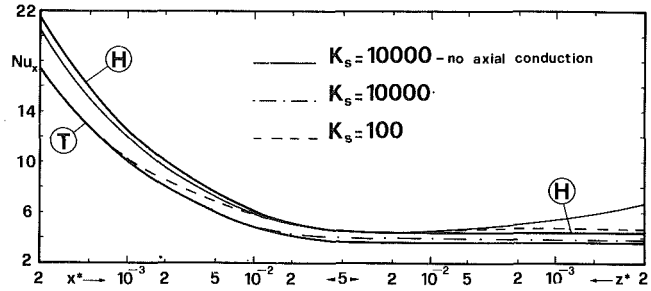

Fig. 4 Axial distributions of the local Nusselt number for inner stream, and reference one-stream data for boundary conditions (H) and (T); $H=1$, $Pe_1=500$, $L=100$, $B=6$, $\Delta=0.5$, and $K_f=1$

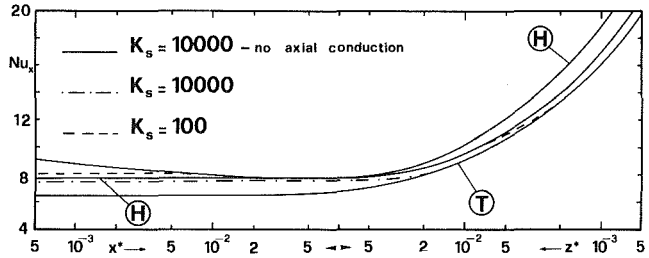

Fig. 5 Axial distributions of the local Nusselt number for outer stream, and reference one-stream data for boundary conditions (H) and (T); $H=1$, $Pe_1=500$, $L=100$, $B=6$, $\Delta=0.5$, and $K_f=1$

$$\Theta_w(x^*)-\Theta_{b1}(x^*)=q_1(0)\frac{2}{\mathrm{Nu}_H(x^*)}+\int_0^{x^*}\frac{2}{\mathrm{Nu}_H(x^*-\xi^*)}\frac{dq_1(\xi^*)}{d\xi^*}\,d\xi^* \quad (16)$$

The expression holds for both streams 1 and 2. In the case of countercurrent flow, however, x^* and ξ^* must be replaced by z^* and ζ^*, respectively, when referring to the outer stream. Nu_H designates the local Nusselt number distribution for a uniformly heated circular (stream 1) or annular (stream 2) duct. Nu_H values are from the literature (Shah and London, 1978). Equation (16) allows the wall-to-fluid temperature differences to be computed for arbitrary distributions of the heat flux.

The computational procedure is iterative. It is initialized with guessed distributions of Θ_b and Nu_x. These complete the set of boundary conditions for equation (2). The energy equation in the wall is solved numerically, by a finite element method. Triangular elements with linear temperature distribution are used in the discretization procedure. From the distribution of Θ_s, updated values of q_1, q_2, Θ_{b1}, and Θ_{b2} are obtained through equations (6) and (7) respectively. Wall-to-fluid temperature differences are then computed by equation (16) and Nu_x distributions obtained from equations (8) to start a new run. The prescribed convergency level was based on the total heat transfer rate, Q, and set equal to 0.001 percent. In all the cases considered, convergence was achieved in less than 14 iterations. Distributions of Nu_x, q, Θ_w, and Θ_b are available at the end of the computational process. The entropy production rates are thus computed by equations (9)–(12). Temperature distributions in the fluid streams are not needed and not computed. However, they can be obtained by superposition, when necessary.

Previous numerical experiments with single-stream problems (Barozzi and Pagliarini, 1984, 1985) showed that the accuracy of Nu_x values is better than 2 percent. Direct comparison with results for the two-stream case is more difficult, since no tabulated data have been found in the open literature. Two checks have been attempted against the available results given in graphic form for the countercurrent case. Omitting axial conduction in the wall, Θ_w and Nu_x distributions have been compared with Nunge and Gill's (1966, Figs. 5 and 7) results.

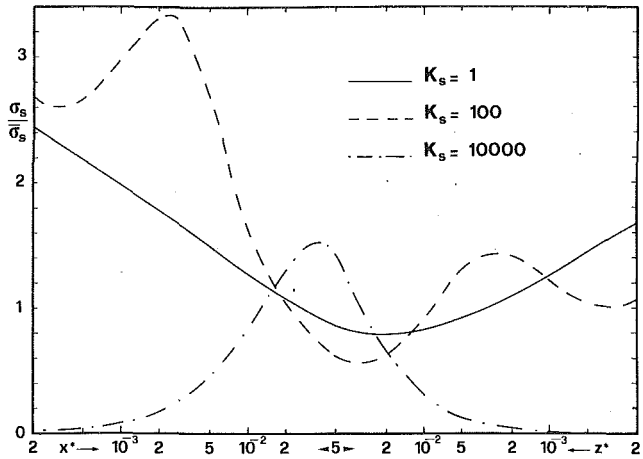

Fig. 6 Axial distributions of local entropy production rate (radially averaged) for the wall; values referred to the mean values of σ_s; $\Gamma = 2$, $H = 1$, $Pe_1 = 500$, $L = 100$, $B = 6$, $\Delta = 0.5$, and $K_f = 1$

Maximum deviations of 6 and 10 percent have been found, respectively. This can be considered acceptable in view of the moderate level of accuracy of the results given by Nunge and Gill (1966), as discussed by Stein (1966b, 1966c). No results being available on account of axial wall conduction in double-pipe heat exchangers, a version of the program has been specifically prepared to provide comparison with the data of Mori et al. (1980) for parallel plate heat exchangers. The agreement with the results shown by Mori et al. (1980, Fig. 10) has been very good.

5 Results

Both the concurrent and countercurrent flow configurations have been investigated. However, only results for the countercurrent case will be presented and discussed in detail.

From the above analysis, the nondimensional groups relevant to the problem are K_s, K_f, B, Δ, L, H, and Pe_1. The absolute temperature ratio Γ also appears in the formulation as far as the problem is considered under a second law point of view. Throughout this analysis, Γ is kept constant at a value of $\Gamma = 2$. It is worth pointing out that, for any value of Γ, Σ can be computed by equations (15) from given values of ϵ and H. Note that the effectiveness concept derives from first law considerations; thus ϵ is independent of Γ. The range covered by the present investigation is as follows: $L = 10$ and 100; $\Delta = 0.5$ and 2; $B = 3$ and 6; $K_s = 1$, 10, 100, 1000, and 10,000; $K_f = 0.1$, 1, and 5; $Pe_1 = 500$, 1000, and 10,000; $H = 0.5$, 1, and 2.

The effect of thermal coupling of the two streams is well illustrated by the distributions of heat flux and temperature at the wall interfaces, as well as the fluid bulk temperature and the Nusselt number for the two streams. Plots of those quantities are presented in Figs. 2, 3, 4, and 5 for a relatively long ($L = 100$), balanced ($H = 1$) heat exchanger. All these quantities are independent of Γ. Data for that single case allow the general trend of the results to be described. Note that in the figures use is made of two separate scales for x^* and $z^* = L^* - x^*$, one running left to right and one running right to left, from the extremities to the middle of the device length.

When overlooking axial heat conduction in the wall, heat transfer results are characterized as follows (Pagliarini and Barozzi, 1984a); (*i*) The temperature of the incoming fluid coincides with the wall temperature at the inlet section; (*ii*) the nondimensional heat flux density is point by point equal on the two sides of the wall, and, typically, its distribution shows a minimum in the central part of the heat transfer region; and (*iii*) for each stream, the distribution of the Nusselt number rapidly decreases near the inlet section of the stream, Nu_x ranging between Nu_T and Nu_H distributions (i.e., single-stream

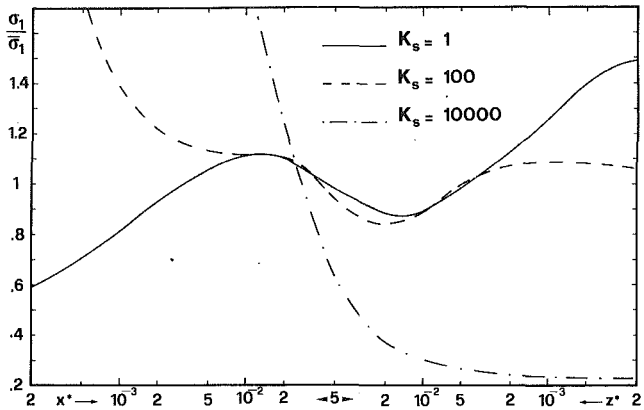

Fig. 7 Axial distributions of local entropy production rate (radially averaged) for the inner stream; values referred to the mean value of σ_1; $\Gamma = 2$, $H = 1$, $Pe_1 = 500$, $L = 100$, $B = 6$, $\Delta = 0.5$, and $K_f = 1$

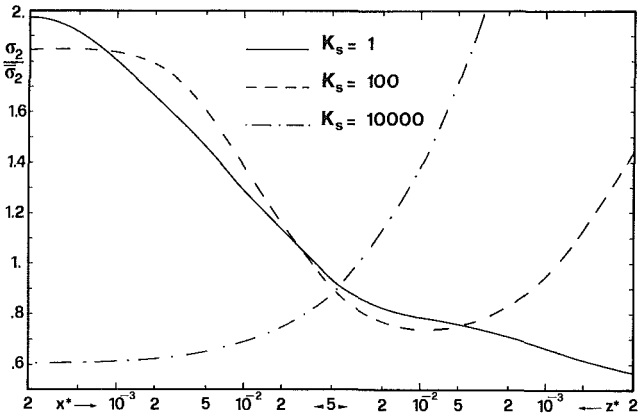

Fig. 8 Axial distributions of local entropy production rate (radially averaged) for the outer stream; values referred to the mean value of σ_2; $\Gamma = 2$, $H = 1$, $Pe_1 = 500$, $L = 100$, $B = 6$, $\Delta = 0.5$, and $K_f = 1$

results for boundary condition (T) and (H), respectively). Nu_x plots take on a minimum, and eventually show a constant value region in the central part of the heat exchanger.

All the above trends are modified in the presence of axial conduction in the wall:

(*i*) Two isothermal areas are created at the wall-to-fluid interfaces, close to the extremities, and the wall temperature does not coincide any further with the inlet fluid temperatures at $x^* = z^* = 0$. The wall-to-fluid temperature difference and the length of the isothermal zones both increase for increase of axial conduction effects. This is well illustrated in Fig. 2 where the effect of the wall conductivity is stressed. It is observed that for increasing K_s, the wall temperature tends to become more uniform, and the outlet temperature of the internal stream, $\Theta_{b1}(x^* = L^*)$ decreases while $\Theta_{b2}(z^* = L^*)$ increases correspondingly. As a consequence, the total heat flux and the effectiveness of the heat exchanger reduce.

(*ii*) Axial wall conduction also uncouples the heat transfer processes on the two sides of the wall. Plots in Fig. 3 still display a general trend similar to the one observed in the absence of axial conduction up to $K_s = 100$: A central zone is found, where the heat flux density is uniform and equal over the two sides of the wall. The situation completely changes for high K_s, the q plots taking on a monotonically decreasing trend from the inlet to the outlet with one single crossing point.

(*iii*) The effect of axial wall conduction on the distributions of the Nusselt number is demonstrated by the coincidence of Nu_x with the corresponding (circular duct or annulus) single-stream solution, case (T), near the inlet section. Farther downstream, both Nu_x and q reach an asymptotic value in the cases shown in Figs. 4 and 5. For low K_s values this may be higher

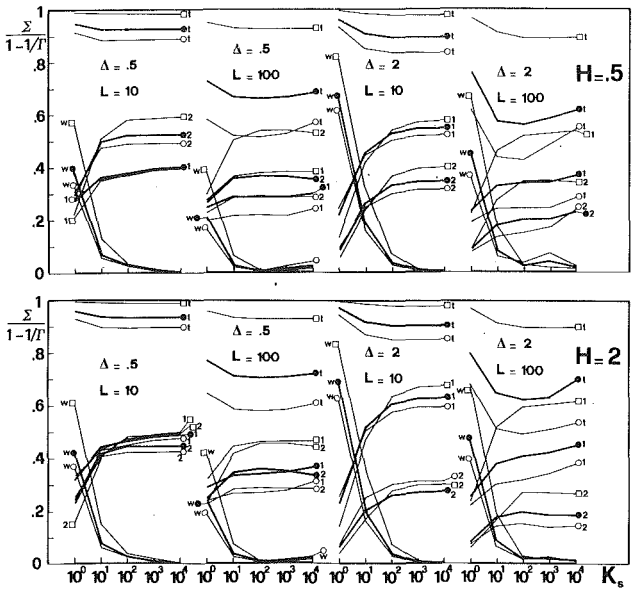

Fig. 9 Normalized nondimensional entropy production rate, as a function of nondimensional thermal conductivity of the wall, K_s; $\Gamma = 2$, $B = 6$, and $K_f = 1$; legend: *w*: in the wall; 1: in the inner stream; 2: in the outer stream; *t*: total value; ○: $Pe_1 = 500$; ●: $Pe_1 = 1000$; □: $Pe_1 = 10{,}000$

than the fully developed one-stream value, case (H), but approximates solution (T) for increasing K_s.

Distributions of the local entropy production rate in the streams and the wall are presented in Figs. 6, 7, and 8 for $\Gamma = 2$. Here, σ has been averaged radially over the section of the region (stream or wall) concerned, and referred to the mean entropy generation rate in the region itself. The results allow some insight to be attained into the irreversible nature of the heat transfer process.

It can be observed first, that distributions of σ in the wall and the streams are quite sensitive to variations in the wall conductivity. For $K_s = 10{,}000$, the local entropy production in the fluids is maximum at the inlet sections, and decreases monotonically downstream. For reducing K_s, the plots of σ_1 and σ_2 take on a less regular trend, eventually presenting intermediate maxima and minima, and the values decrease progressively at the inlet, while increasing in the outlet regions. The local entropy generation rate in the fluids is related to q, Θ_w, and Θ_b as from equations (12). The above behavior can therefore be interpreted in the light of Figs. 2 and 3 from which it is possible to deduce that the maxima in σ_1 and σ_2 correspond to axial positions where either the heat flux density or the wall-to-fluid temperature difference are relatively high.

Distributions of σ_s indicate that the effect of the radial thermal resistence of the wall is dominant when K_s is low. Entropy generation is a minimum in the central region and a maximum at the extremities for $K_s = 1$. Such a trend is typical in the absence of axial conduction (Pagliarini and Barozzi, 1984b). The situation is completely reversed when K_s is very high. For $K_s = 10{,}000$ a maximum is found in the middle of the wall length, where the axial temperature gradient is higher. The entropy production falls to zero at the wall extremities, where the wall is isothermal. Case $K_s = 100$ represents an intermediate situation where the entropy production rates due to the axial and radial conduction tend to be in balance. All the above trends are not substantially modified by variations of H over the range covered by this analysis.

The role of the wall conductivity, K_s, has been particularly stressed by the results. However, the significance of the observations is more general, results for low K_s values being representative of situations where the effect of heat conduction along the wall is moderate, and vice versa.

Table 1 Effectiveness of countercurrent heat exchangers, $B = 6$ and $K_f = 1$

Δ=0.5	L=10	|	ε						
Pe_1 ⇓	H ⇓	K_{opt} ⇓	K_s= 1	10	100	1000	10000	10000*	K_{opt}
500	0.5	83	.115	.155	.157	.153	.153	.163	.157
	1	125	.063	.088	.090	.087	.087	.094	.089
	2	167	.069	.100	.102	.099	.098	.107	.101
1000	0.5	167	.067	.095	.098	.095	.095	.101	.097
	1	250	.037	.055	.056	.055	.054	.058	.056
	2	333	.040	.062	.064	.062	.062	.067	.063
10000	0.5	1667	.010	.019	.020	.020	.020	.021	.020
	1	2500	.005	.011	.012	.012	.012	.012	.012
	2	3333	.006	.012	.014	.014	.013	.014	.013
Δ=0.5	L=100	|	ε						
Pe_1 ⇓	H ⇓	K_{opt} ⇓	K_s= 1	10	100	1000	10000	10000*	K_{opt}
500	0.5	83	.572	.655	.662	.647	.597	.666	.662
	1	125	.340	.403	.409	.401	.376	.412	.409
	2	167	.378	.457	.465	.457	.431	.468	.464
1000	0.5	167	.378	.456	.464	.459	.438	.467	.464
	1	250	.214	.266	.272	.268	.257	.273	.271
	2	333	.234	.298	.305	.302	.289	.307	.304
10000	0.5	1667	.067	.096	.100	.100	.098	.101	.100
	1	2500	.037	.055	.058	.058	.056	.058	.057
	2	3333	.040	.063	.066	.066	.065	.067	.066
Δ=2	L=10	|	ε						
Pe_1 ⇓	H ⇓	K_{opt} ⇓	K_s= 1	10	100	1000	10000	10000*	K_{opt}
500	0.5	83	.092	.207	.227	.227	.227	.249	.227
	1	125	.048	.115	.128	.128	.128	.141	.128
	2	167	.050	.125	.142	.142	.142	.156	.142
1000	0.5	167	.050	.128	.146	.146	.146	.159	.146
	1	250	.026	.070	.082	.082	.082	.090	.082
	2	333	.027	.077	.091	.091	.091	.100	.091
10000	0.5	1667	.006	.023	.032	.033	.033	.035	.033
	1	2500	.003	.013	.018	.018	.018	.020	.018
	2	3333	.003	.014	.020	.021	.021	.022	.021
Δ=2	L=100	|	ε						
Pe_1 ⇓	H ⇓	K_{opt} ⇓	K_s= 1	10	100	1000	10000	10000*	K_{opt}
500	0.5	83	.525	.765	.781	.702	.628	.808	.783
	1	125	.305	.488	.511	.475	.437	.525	.509
	2	167	.330	.552	.584	.557	.524	.597	.582
1000	0.5	167	.335	.570	.605	.571	.529	.620	.602
	1	250	.184	.337	.364	.351	.331	.373	.362
	2	333	.194	.372	.406	.395	.376	.415	.403
10000	0.5	1667	.050	.130	.155	.155	.149	.159	.153
	1	2500	.026	.072	.087	.087	.084	.090	.086
	2	3333	.027	.078	.097	.097	.093	.100	.095

*: no axial conduction.

The number of the relevant nondimensional quantities being so large, their influence on the thermal behavior of the device cannot be considered in terms of the local entropy production rate. The effect of each parameter is more conveniently estimated by resorting to the total entropy production rate Σ, or the heat exchanger effectiveness, ϵ.

The nondimensional entropy generation rate Σ, and its components, Σ_1, Σ_2, and Σ_s, are shown in Fig. 9. Values of ϵ for changing Δ, L, Pe_1, H, and K_s are presented in Table 1. Values of effectiveness corresponding to the optimum value of the wall conductivity, K_{opt}, have also been computed by the same procedure for all the cases considered, and results listed in Table 1. K_{opt} is defined according to Chowdhury and Sarangi (1983, equation (11)) and is a function of Pe_1 and H. Finally, results in the absence of axial wall conduction are given for the sake of comparison. These are for $K_s = 10{,}000$.

It is pointed out that the effectiveness of the heat exchanger

no longer increases monotonically with K_s, as it would do in the absence of axial conduction in the wall. Instead, for any choice of Pe_1 and H, a minimum can be identified for Σ, and a corresponding maximum for ϵ at an intermediate value of K_s.

For low K_s, most of the entropy production is concentrated in the wall, due to the effect of radial heat conduction. In a short heat exchanger ($L = 10$), while increasing K_s the contribution of the wall decreases monotonically, the wall approaches an isothermal condition, Σ_s goes to zero, and Σ_1, Σ_2 approach a constant value independent of K_s. In a long device ($L = 100$), however, the increase in the entropy production due to axial conduction in the wall competes with the reduction in the radial contribution for increasing K_s. Thus, a minimum is observed in Σ_s for K_s of order 100. This is found to be representative of a condition of maximum effectiveness and minimum total entropy production. Neither a situation of the wall being isothermal nor Σ having a constant value is usually found in a long heat exchanger for K_s up to 10,000.

From data in Table 1, it is observed that ϵ is a minimum for $H = 1$ irrespective of the choice of other nondimensional quantities. When analyzing the results in terms of the entropy production rate, however, it is found that Σ_1 decreases and Σ_2 increases systematically for increasing H from 0.5 to 2. Overall, the total entropy production rate, Σ, is practically insensitive to variations of H for short heat exchangers ($L = 10$). Variations of Σ with H are less than 1 percent in those cases. The same holds true for long heat exchangers ($L = 100$), provided that $Pe_1 \geq 1000$. For lower values of Pe_1 and $L = 100$, however, changing H from 0.5 to 2 produces a definite increase in Σ (from 5 to 20 percent). From a second law point of view, then, operating conditions corresponding to values of H higher than one should be avoided in high-performance devices.

Increasing Pe_1 always reduces the negative influence of longitudinal heat conduction, but also causes deterioration in the overall performance of the device.

Long heat exchangers are found to be more sensitive to the variation of the wall conductivity than short devices. This finding looks contradictory since the effect of axial heat conduction is expected to be more pronounced when L is low. However, it must be emphasized that short heat exchangers are basically characterized by a very high rate of entropy production. Any additional contribution to it is thus of moderate importance in relative terms.

Table 1 indicates that values of ϵ are higher for $\Delta = 2$ than for $\Delta = 0.5$. When interpreting such a behavior, it should be born in mind that increasing Δ at equal Pe_1 and H produces a relative increase of the mean fluid velocity of the external stream, the flow rate remaining unchanged. The effectiveness of the heat exchanger increases as a consequence. The same holds true for reducing B as can be seen by comparing data in Table 1 with results given in Table 2. The percentage reduction in effectiveness due to axial wall conduction definitely increases for increasing wall thickness, while it is little influenced by variations in the pipe diameter ratio. It is worth pointing out, however, that the entropy production inherent in the fluid-dynamic process is not taken into account in this analysis. That term increases for an increase in the mean velocity of flow.

All other quantities being fixed, the effectiveness also increases monotonically for increasing K_f, as from Table 3. That behavior should be ascribed to the reduction of the convective thermal resistence of the external stream that occurs for increasing K_f.

The criterion given by Chowdhury and Sarangi (1983) to predict the optimum value of the wall conductivity was based on some crude approximation. Nonetheless it is found to agree very favorably with the results of the present analysis. From data in Table 1, the values of ϵ obtained for $K_s = K_{opt}$ systematically approach the maximum. The criterion tends to become slightly less accurate and reliable when the effectiveness is very low.

Table 2 Effectiveness of countercurrent heat exchangers, $B = 3$ and $K_f = 1$

Δ=0.5	L=100				ϵ			
Pe_1 ⇓	H ⇓	K_{opt} ⇓	K_s= 1	10	100	1000	10000	K_{opt}
500	0.5	83	.676	.792	.802	.775	.682	.802
	1	125	.414	.511	.521	.510	.466	.521
	2	167	.460	580	.593	.585	.549	.593
1000	0.5	167	.472	.601	.616	.605	.561	.615
	1	250	.270	.359	.370	.366	.346	.369
	2	333	.292	.398	.412	.408	.391	.411
10000	0.5	1667	.088	.147	.158	.158	.154	.157
	1	2500	.047	.082	.089	.089	.087	.089
	2	3333	.050	.091	.099	.099	.097	.098

Table 3 Effectiveness of countercurrent heat exchangers for different values of K_f; $B = 6$ and $Pe_1 = 500$

Δ=0.5	L=100				ϵ		
Pe_1 ⇓	H ⇓	K_s= 1	10	100	1000	10000	
500	0.5	.192	.200	.201	.199	.195	K_f=0.1
	1	.113	.119	.120	.119	.116	
	2	134	.142	.143	.141	.137	
500	0.5	.572	.655	.662	.647	.597	K_f=1
	1	.340	.403	.409	.401	.376	
	2	.378	.457	.465	.457	.431	
500	0.5	.725	.857	.867	.833	.707	K_f=5
	1	.451	.568	.581	.568	.508	
	2	.501	.642	.659	.652	.614	

As far as concurrent flow heat exchangers are concerned, computations have been restricted to the case of balanced flow, $H = 1$. Results have been presented elsewhere (Pagliarini and Barozzi, 1984a). They indicate that the effects of axial conduction in the wall are minor, with respect to the corresponding counterflow cases. Local quantities, such as the wall and the fluid temperatures, are actually only moderately influenced. The overall effectiveness of the device is totally unaffected by the presence of heat conduction along the wall.

6 Concluding Remarks

Local and overall effects of thermal coupling in laminar counterflow double-pipe heat exchangers have been considered on account of axial heat conduction in the wall separating the streams. The range covered by this analysis has been deliberately limited, in view of the considerable number of geometric, thermal, and flow parameters involved in the problem. A few conclusions of a general validity are however permitted.

It is observed first that conduction along the thermally active wall may have a definite effect upon the distributions of the most important thermal quantities, such as the wall temperature, the heat flux, the bulk fluid temperature, and the Nusselt number. The extent of such an influence depends however on a number of geometric, thermal, and flow variables, forming a set of seven independent nondimensional groups. Therefore, local effects of thermal coupling and axial wall conduction have been mainly concerned with the effect of the wall conductivity parameter, K_s. The presence of axial wall conduction is revealed by the wall temperature tending to become longitudinally uniform. The effect starts at the wall extremities, where two isothermal regions are observed, however low the value of K_s is. These lengthen progressively for increasing K_s, finally covering the entire heat transfer section as the wall conductivity tends to infinity. Correspondingly, the two streams become thermally uncoupled in the sense that each current approaches the thermal behavior typical of a single-stream

case, subject to the boundary condition of uniform wall temperature. In the limit of high K_s values, then, single-stream Nu_T correlations apply.

The thermodynamic behavior of the equipment can either be considered under a traditional first law point of view, or expressed in terms of the entropy production rate following a second law approach. It is observed that the two methods lead to perfectly equivalent results as far as the overall performance of the equipment is concerned. In fact, the heat exchanger effectiveness, ϵ, and the total entropy production rate, Σ, are related in a very simple way. The second law approach, however, gives a deeper insight into the irreversible nature of the heat transfer process, and therefore offers a more reliable design tool.

The performance of countercurrent heat exchangers has been investigated, as affected by the operative conditions, the thermal properties of the wall and the fluids, and the geometry of the equipment.

Results indicate that increasing the Peclet number, e.g., by increasing the flow rate, while leaving constant the heat capacity ratio, H, always produces a reduction in the heat exchanger effectiveness. On the other hand, for increasing H from 0.5 to 2, a minimum is observed in ϵ, for balanced heat exchangers. In terms of the entropy production rate, however, it is found that the performance of the device is influenced negatively by high values of H. That conclusion is of chief concern for devices whose effectiveness is basically very high, as is the case of a long heat exchanger. Increasing the fluid conductivity ratio, K_f, has a strong and positive effect on effectiveness. Changing the wall thickness or the diameter of the outer duct, i.e., changing Δ or B, all other conditions being unchanged, corresponds to considering a quite different physical situation. The results must therefore be interpreted with some care. In any case they indicate a reduction of the performance in the case of a long and very efficient heat exchanger, both for decreasing Δ and increasing B. Also note that relatively high values for the wall thickness have been used in the present analysis to emphasize the influence of axial wall conduction on local quantities. Results are however of practical significance, since they offer clear directions for conduction-penalty minimization.

The effects of the wall conductivity have been particularly stressed in the analysis. It is found that a region of minimum entropy production always exists in the range of variability considered for K_s. The need for optimizing the wall conductivity becomes the more stringent as the equipment effectiveness increases. In this connection, the simple criterion suggested by Chowdhury and Sarangi (1983) has been proved to give reliable indications over a wide range of operative conditions. Thus, the analysis indicates that a proper choice of the wall material is needed for the thermal performance optimization of laminar flow double pipe heat exchangers. To exemplify, if heat is exchanged between two countercurrent water streams separated by a copper wall ($K_s \approx 600$), axial conduction in the wall is expected to produce a small, but definite, decrease in the effectiveness. The optimum value could be attained using a steel wall, characterized by a K_s value of about 100. If, instead, a glass wall is used, the order of magnitude of K_s drops to 1, and the effectiveness decreases sharply due to the introduction of a high radial thermal resistance. The effects of axial wall conduction are more pronounced when gaseous fluids are considered. If, indeed, two air streams and a cooper wall are used, K_s becomes higher than 10,000. A reduction of a few percentage units in the device effectiveness can result, with respect to the optimum value. Once again, the latter can be approximated using a steel wall ($K_s \approx 1000$).

As far as concurrent flow heat exchangers are concerned, previous work (Pagliarini and Barozzi, 1984a) has demonstrated that the effects of wall conductivity are minor.

This conclusion, however, is restricted to the case of balanced heat exchangers, and further analyses are needed to generalize it.

Acknowledgments

The authors acknowledge the useful remarks of the Referees, and the help of Dr. M. W. Collins, The City University, London, during the revision of the paper. The research has been supported by M.P.I., and C.N.R. under grant No. 89.03276.07.

References

Barozzi, G. S., and Pagliarini, G., 1984, "Conjugated Heat Transfer in a Circular Duct With Uniform and Non-uniform Wall Thickness," *Heat and Technology*, Vol. 2, pp. 72–91.

Barozzi, G. S., and Pagliarini, G., 1985, "A Method to Solve Conjugate Heat Transfer Problems: the Case of Fully Developed Laminar Flow in a Pipe," ASME JOURNAL OF HEAT TRANSFER, Vol. 107, pp. 77–83.

Barron, R. F., and Yeh, S. L., 1976, "Longitudinal Conduction in Three-Fluid Heat Exchangers," ASME Paper No. 76-WA/HT-9.

Bejan, A., 1977, "The Concept of Irreveribility in Heat Exchanger Design: Counterflow Heat Exchangers for Gas-to-Gas Applications," ASME JOURNAL OF HEAT TRANSFER, Vol. 99, pp. 374–380.

Bejan, A., 1982, "Second-Law Analysis in Heat Transfer and Thermal Design," in: *Advances in Heat Transfer*, Vol. 15, T. F. Irvine and J. P. Hartnett, eds., Academic Press, New York, pp. 1–58.

Bentwich, M., 1970, "Concurrent and Countercurrent Parabolic Flow Heat Exchangers," *Israel Journal Technology*, Vol. 8, pp. 197–207.

Bentwich, M., 1973, "Multistream Countercurrent Heat Exchangers," ASME JOURNAL OF HEAT TRANSFER, Vol. 95, pp. 458–463.

Blanco, J. A., and Gill, W. N., 1967, "Analysis of Multistream Turbulent Forced Convection Systems," *Chemical Engineering Progress Symposium Series 77*, Vol. 63, pp. 66–79.

Blanco, J. A., Gill, W. N., and Nunge, R. J., 1968, "Computational Procedures for Recent Analyses of Counterflow Heat Exchangers," *AIChE Journal*, Vol. 14, pp. 505–507.

Chiou, J. P., 1983, "Thermal Performance Deterioration in Crossflow Heat Exchanger Due to Longitudinal Heat Conduction and Nonuniform Inlet Fluid Temperature Distribution," *Proceedings ASME-JSME Thermal Engineering Joint Conference*, Honolulu, HI, Vol. 2, pp. 451–458.

Chowdhury, K., and Sarangi, S., 1983, "A Second Law Analysis of the Concentric Tube Heat Exchanger: Optimization of Wall Conductivity," *International Journal of Heat and Mass Transfer*, Vol. 26, pp. 783–786.

Ciampi, M., and Tuoni, G., 1979, "Considerazioni Termodinamiche sugli Scambiatori di Calore (On the Thermodynamic Behavior of Heat Exchangers)," *La Termotecnica*, Vol. 33, pp. 186–197.

Cotta, R. M., and Ozisik, M. N., 1986, "Thermally Developing Concurrent-Flow Circular Double-Pipe Heat Exchanger Analysis," *Proceedings Eighth Heat Transfer Conference*, Vol. 6, San Francisco, pp. 2805–2810.

de Groot, S. R., and Mazur, P., 1962, *Non-Equilibrium Thermodynamics*, North Holland, Amsterdam, Netherlands.

Gill, W. N., Porta, E. W., and Nunge, R. J., 1968, "Heat Transfer in the Thermal Entrance Region of Concurrent Flow Heat Exchangers With Fully Developed Laminar Flow," *International Journal of Heat and Mass Transfer*, Vol. 11, pp. 1408–1412.

Golem, P. J., and Brzustowski, T. A., 1976, "Second-Law Analysis of Energy Processes, Part II: the Performance of Simple Heat Exchangers," *Trans. Can. Soc. Mech. Engrs.*, Vol. 4, pp. 219–226.

Kakac, S., Bergles, A. E., and Mayinger, F., 1981, *Heat Exchangers, Thermal-Hydraulic Fundamentals and Design*, Springer-Verlag, Berlin, Germany.

Kays, W. M., and London, A. L., 1984, *Compact Heat Exchangers*, 3rd ed., McGraw-Hill, New York.

Kroeger, P. G., 1966, "Performance Deterioration in High Effectiveness Heat Exchangers Due to Axial Heat Conduction Effects," *Advances Cryogenic Engineering*, Vol. 12, pp. 364–372.

Lin, T. F., and Tsay, Y. L., 1986, "Thermal Interactions in Countercurrent-Flow Double-Pipe Heat Exchangers," *Proceedings Eighth Heat Transfer Conference*, Vol. 6, San Francisco, pp. 2811–2816.

London, A. L. and Shah, R. K., 1983, "Costs of Irreversibilities in Heat Transfer Exchanger Design," *Heat Transfer Engineering*, Vol. 4, pp. 59–73.

Mikhailov, M. D., 1972, "General Solutions of the Heat Equations in Finite Regions," *International Journal of Engineering Science*, Vol. 10, pp. 577–591.

Mikhailov, M. D., 1973a, "General Solutions of the Diffusion Equations Coupled at Boundary Conditions," *International Journal of Heat and Mass Transfer*, Vol. 16, pp. 2155–2164.

Mikhailov, M. D., 1973b, "General Solutions of the Coupled Diffusion Equations," *International Journal of Engineering Science*, Vol. 11, pp 235–241.

Mikhailov, M. D., 1983, "Mathematical Modelling of Heat Transfer in Single Duct and Double Pipe Exchangers," in: *Low Reynolds Number Flow Heat Exchangers*, S. Kakac, R. K. Shah, and A. E. Bergles, eds., Hemisphere Publ. Corp., Washington, DC.

Mikhailov, M. D., and Shishedjiev, B. K., 1976, "Coupled at Boundary Mass or Heat Transfer in Entrance Concurrent Flow," *International Journal of Heat and Mass Transfer*, Vol. 19, pp. 553–557.

Mori, S., Kataya, M., and Tanimoto, A., 1980, "Performance of Counterflow, Parallel Plate Heat Exchangers Under Laminar Flow Conditions," *Heat Transfer Engineering*, Vol. 2, pp. 28–38.

Nunge, R. J., and Gill, W. N., 1965, "Analysis of Heat or Mass Transfer in Some Countercurrent Flows," *International Journal of Heat and Mass Transfer*, Vol. 8, pp. 873–886.

Nunge, R. J., and Gill, W. N., 1966, "An Analytical Study of Laminar Counterflow Double-Pipe Heat Exchangers," *AIChE Journal*, Vol. 12, pp. 279–286.

Nunge, R. J., Porta, E. W., and Gill, W. N., 1967, "Axial Conduction in the Fluid Streams of Multistream Heat Exchangers," *Chemical Engineering Progress Symposium Series*, Series 77, Vol. 63, pp. 80–91.

Pagliarini, G., and Barozzi, G. S., 1984a, "Effetti di Accoppiamento Termico negli Scambiatori Tubo in Tubo a Correnti Laminari (Thermal Coupling in Laminar Double Stream Heat Exchangers)," *Proceedings Second National Conference on Heat Transfer*, Bologna, Italy, pp. 103–113.

Pagliarini, G., and Barozzi, G. S., 1984b, "Produzione di Entropia per Conduzione Termica nella Parete di Scambiatori di Calore a Correnti Contrapposte Bilanciate (Entropy Generation Due to Thermal Conduction Along the Wall of Balanced Counterflow Heat Exchangers)," *Proceedings 39th A.T.I. National Conference*, L'Aquila, Italy, Vol. I, pp. 191–200.

Pagliarini, G., and Barozzi, G. S., 1985, "Ulteriori Considerazioni sulla Produzione di Entropia in Scambiatori di Calore a Correnti Laminari Contrapposte (Further Considerations on Entropy Production in Laminar Countercurrent Heat Exchangers)," *Proceedings Third National Conference on Heat Transfer*, Palermo, Italy, pp. 164–176.

Papoutsakis, E., and Ramkrishna, D., 1981, "Conjugated Graetz Problems," *Chemical Engineering Science*, Vol. 36, pp. 1381–1391, 1393–1399.

Seban, R. A., Hsieh, T. C., and Greif, R., 1972, "Laminar Counterflow Exchangers: an Approximate Account of Wall Resistance and Variable Heat Transfer Coefficients," ASME JOURNAL OF HEAT TRANSFER, Vol. 94, pp. 391–396.

Shah, R. K., and London, A. L., 1978, *Laminar Flow Forced Convection in Ducts*, Academic Press, New York.

Spalding, D. B., 1984, *Heat Exchanger Design Handbook*, Hemisphere, Washington, DC.

Stein, R. P., 1964, "The Graetz Problem in Concurrent-Flow Double-Pipe, Heat Exchangers," ANL Rept. 5889, Argonne National Lab.

Stein, R. P., 1965a, "The Graetz Problem in Concurrent Flow Double Pipe Heat Exchangers," *Chemical Engineering Progress Symposium Series 59*, Vol. 61, pp. 76–87.

Stein, R. P., 1965b, "Heat Transfer Coefficients in Liquid Metal Concurrent Flow Double Pipe Heat Exchangers," *Chemical Engineering Progress Symposium Series 59*, Vol. 61, pp. 64–75.

Stein, R. P., 1966a, "Liquid Metal Heat Transfer," in: *Advances in Heat Transfer*, Vol. 3, T. F. Irvine and J. P. Hartnett, eds., Academic Press, New York.

Stein, R. P., 1966b, "Computational Procedures for Recent Analyses of Counterflow Heat Exchangers," *AIChE Journal*, Vol. 12, pp. 1216–1219.

Stein, R. P., 1966c, "Mathematical and Practical Aspects of Heat Transfer in Double Pipe Heat Exchangers," *Proceedings Third International Heat Transfer Conference*, AIChE, New York, Vol. 1, pp. 139–148.

An Analysis of Heat Transfer in Josephson Junction Devices

A. S. Lavine

C. Bai

University of California, Los Angeles,
Los Angeles, CA 90024-1597

Josephson junctions are electronic devices made from superconducting materials that cycle between resistive and nonresistive states. Heat generated in the resistive state causes a temperature rise, which may adversely affect electrical behavior, by reducing the critical Josephson current. In this work, temperature distributions and resulting reductions in critical current are calculated for Josephson junctions made from low and high-temperature superconductors. It is found that an unacceptable reduction in critical current may occur for junctions made from high-temperature materials. This problem can almost certainly be overcome, but perhaps at the expense of one advantage of Josephson junctions, namely compactness.

Introduction

Josephson junctions are electronic devices fabricated from superconductors. They have tremendous potential because of their fast switching speeds and low power dissipation. In the past, the major drawback of Josephson junction devices was that they had to be cooled to below the critical temperature of the superconducting materials, usually by immersion in liquid helium. With the recent developments in new higher temperature superconductors, there has been a resurgence in the interest in Josephson junctions. This paper addresses the thermal behavior of Josephson junctions as it relates to their electrical behavior.

One typical configuration for a Josephson junction, known as a Josephson tunnel junction, consists of a sandwich of two thin superconducting layers with a "barrier" of normal metal or insulating material in between. When a current flows through this sandwich, the electrical behavior depends on the value of the current (see Fig. 1). If it is below some critical value, I_c, superconducting pairs will tunnel through the barrier material; the sandwich will then display zero resistance, and hence, zero voltage drop. If the current exceeds the critical value, there will then be a nonzero resistance and a voltage drop across the sandwich. It is important to note that the critical Josephson current is *not* the same as the critical current at which the bulk superconducting material becomes normal. For instance, for niobium nitride, the critical Josephson current density is on the order of 2000 A/cm^2 (it is junction dependent), whereas the bulk critical current density is on the order of 10^5 A/cm^2 (at temperatures on the order of 0.8 T_c).

Josephson junction logic devices work by switching rapidly between the nonresistive and resistive states. When in the resistive state, heat is generated, which will raise the temperature of the junction. Temperature control is very important, because the critical Josephson current is temperature dependent (see Fig. 2). An increase in temperature causes a decrease in critical current, which can adversely affect the electrical behavior of the device. It is anticipated that this self-heating effect will be exacerbated for high-temperature superconductors at higher operating temperatures, because the rate of heat generation is expected to be higher. This will be discussed in more detail later.

There has been a considerable amount of research on Josephson tunnel junctions using low-temperature superconductors. Recent research has generally concentrated on junctions made of niobium nitride (NbN) rather than lead, because of NbN's mechanical hardness, large gap voltage, and high (relative to lead) superconducting transition temperature (15–16 K). In this paper, NbN will be used as a representative low-temperature superconductor. There has been some research on the thermal aspects of Josephson tunnel junctions, which is particularly relevant to the work reported here. Arnett (1983) experimentally determined the critical power density at which a particular niobium edge junction ceased to operate because its transition temperature was exceeded. Ketchen (1979) per-

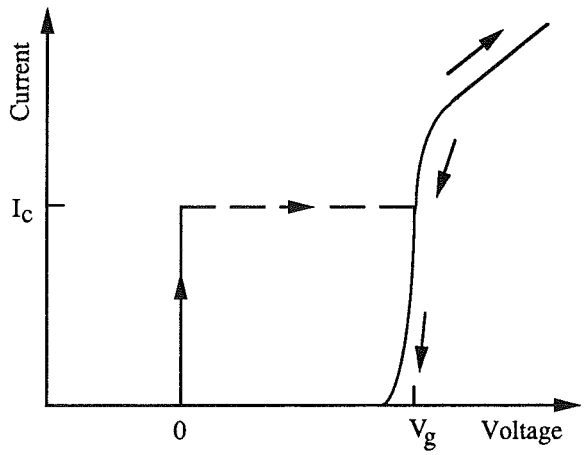

Fig. 1 I-V behavior of a Josephson junction

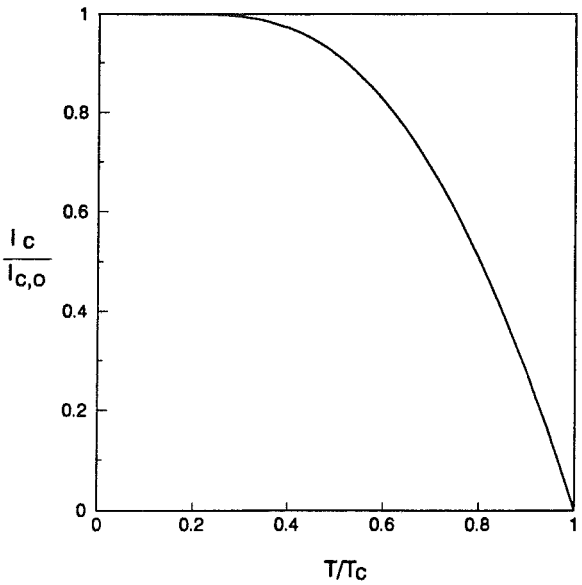

Fig. 2 Typical temperature dependence of the critical Josephson current

Contributed by the Heat Transfer Division and presented at the ASME Winter Annual Meeting, San Francisco, California, December 10–15, 1989. Manuscript received by the Heat Transfer Division. October 10, 1989; revision received December 3, 1990. Keywords: Conduction, Cryogenics, Electronic Equipment.

formed a similar experiment for lead alloy junctions. Shoji et al. (1987) experimentally investigated the temperature dependence of the electrical characteristics of a NbN tunnel junction. There has also been research on thermal aspects of point contact junctions (Iwanyshyn and Smith, 1972), microbridges (Skopcol et al., 1974; Dharmadurai, 1980), and coplanar electrode junctions (Jennings and Rubinsky, 1986).

Since high-temperature superconductors were discovered, there have been many efforts to observe the Josephson effect in these materials and to produce Josephson junctions with them for possible applications. Some researchers have reported successful fabrication of "crack" (Iguchi et al., 1987; Sugishita et al., 1987), weak link (Wu et al., 1987; Wiener-Avnear et al., 1989; Rogers et al., 1989), or edge (Laibowitz et al., 1990) Josephson junctions from $YBa_2Cu_3O_{7-x}$ (YBCO). The results of Sugishita et al. show a linear temperature dependence of the Josephson critical current, rather than the usual BCS-type dependence shown in Fig. 2 (Ambegaokar and Baratoff, 1963). To our knowledge there has not been a successful sandwich-type Josephson junction fabricated with high-temperature superconductors and operated at liquid nitrogen temperatures.

There has been a tremendous amount of research on thermal modeling of electronic devices, which is certainly relevant to the present work (see, for instance, Bar-Cohen and Kraus, 1988; Ellison, 1989). It is not the intent of this study to advance the science of thermal modeling of electronics, but rather to show how the temperature distribution in a Josephson junction affects its electrical behavior.

Background and Problem Statement

The intent of this study is to (*a*) calculate the temperature distribution in a Josephson junction as a function of the various governing parameters, (*b*) evaluate the effect of the temperature distribution on the critical Josephson current, and (*c*) assess the important differences between junctions made from low and high-temperature superconductors.

Heat is generated in the barrier region when it is in the resistive state. The heat flux can be evaluated from the product of the current density and voltage. Depending on how the junction is operated, the current density and voltage could take on a large range of values. The worst realistic case would be for the current density to equal the critical current density, J_c, and the voltage to equal the gap voltage, V_g (see Fig. 1). For NbN, with critical current density on the order of 2000 A/cm^2 and gap voltage of 4.5 mV, the heat flux is on the order of 10^5 W/m^2. The heat flux is expected to increase for high-temperature superconductors (Van Duzer, 1989). One reason is that the gap voltage scales proportionally with transition temperature, T_c, so that:

$$q'' = J_c V_g \propto J_c T_c \tag{1}$$

This alone will account for at least a sixfold increase in the heat flux, since T_c is approximately 15 and 92 K for NbN and YBCO, respectively. Another consideration is that higher operating temperatures cause greater thermal noise. To enable stable operation in the presence of the increased noise, the current will have to scale proportionally with operating temperature, T_∞ (Van Duzer, 1989). That is:

$$I_c = J_c A_b \propto T_\infty \tag{2}$$

where A_b is the barrier area. High-temperature superconductors are typically operated in liquid nitrogen (T_∞ = 77 K), whereas low-temperature superconductors are operated in liquid helium (T_∞ = 4.2 K). Thus there is more than an order of magnitude increase in operating temperature. The thermal noise criterion, equation (2), may or may not affect the heat flux, depending on the critical current density that can be achieved in Josephson junctions made from the new high-temperature materials. If the critical current density in the new materials is roughly the same as in the old low-temperature materials, then the thermal noise criterion will not affect the heat flux (cf. equation (1)), but the junction area will have to scale up with operating temperature (cf. equation (2)). This would be a significant disadvantage, because compactness and the associated speed have always been strong points of Josephson junctions. If it is possible to maintain the same size junctions by increasing the critical current density by an order of magnitude over the low-temperature materials then the heat flux will increase accordingly (cf. equation (1)).

The geometry of an electronic device made from Josephson junctions is considerably more complicated than the simple sandwich described earlier. In practice, a typical low-temperature Josephson junction device consists of a silicon substrate with multiple sandwich junctions arranged on its surface, and a wiring pattern of additional superconducting material on top of the junctions. The low-temperature material considered here is niobium nitride (NbN). The entire device is put into some sort of package and immersed in liquid helium. For lack of better information, it is assumed here that device geometries for high-temperature superconductors will not change substantially from the low-temperature technology, but that YBCO replaces NbN as the superconductor, MgO replaces silicon as

Nomenclature

A_b = area of barrier = L_b^2
A_e = area of bottom electrode = L_e^2
A_s = area of substrate associated with a single junction = L_s^2
Bi = Biot number = $h_{\text{eff}} H_e / k_y$
h = coolant heat transfer coefficient
h_{eff} = effective heat transfer coefficient, equation (3)
H_e = electrode thickness
H_s = substrate thickness
I_c = critical Josephson current
J_c = critical Josephson current density = I_c/A_b
k_s = substrate thermal conductivity
k_x, k_y, k_z = thermal conductivity of electrode in x, y, z directions
L_b = barrier lateral dimension
L_e = electrode lateral dimension
L_s = lateral dimension of substrate associated with a single junction
$\hat{L}$ = $(L_e/2H_e)\sqrt{k_y/k_x}$
$\overline{q}$ = time-averaged rate of heat conducting into bottom electrode
$\overline{q}''$ = time-averaged heat flux based on barrier area = $\overline{q}/A_b$
Q = $\overline{q}'' H_e / k_y (T_c - T_\infty)$
R = thermal resistance
t_p = period of time varying heat input
T = temperature
T_c = superconducting transition temperature
T_t = temperature at top of electrode
T_∞ = coolant temperature
V_g = gap voltage
x, y, z = coordinate directions
α = thermal diffusivity
γ = $\sqrt{\omega/2\alpha}$
ζ = $(z/H_e)\sqrt{k_y/k_x}$
η = y/H_e
θ = $(T - T_\infty)/(T_c - T_\infty)$
θ_t = θ evaluated at top of electrode
$\overline{\theta_t}$ = θ_t averaged over barrier area
ξ = $(x/H_e)\sqrt{k_y/k_x}$
ω = frequency of oscillations of heat input = $2\pi/t_p$

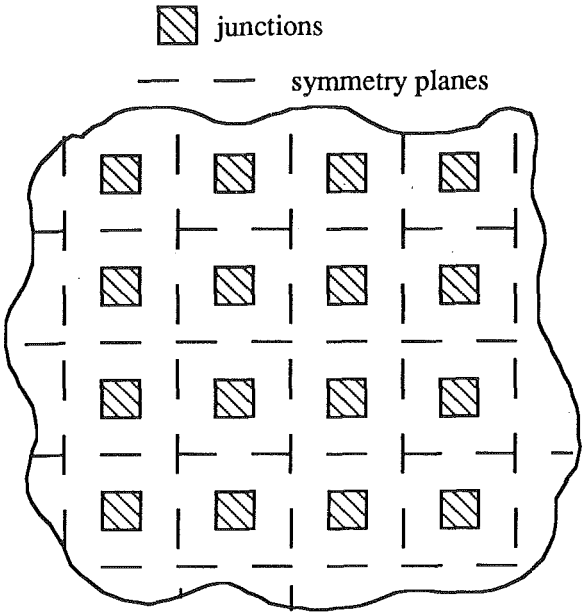

Fig. 3 Infinite square array of square Josephson junctions

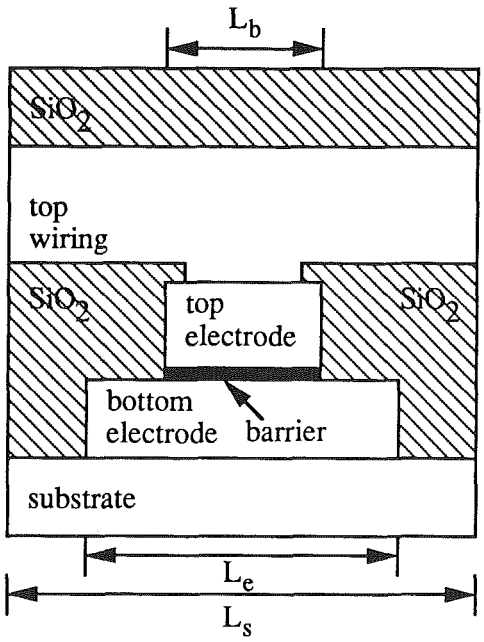

Fig. 4 A typical device showing the various material layers

the substrate, and nitrogen replaces helium as the coolant. A "generic" geometry is defined below, with dimensions that can be varied in the analysis.

The generic geometry considered here is an infinite square array of square Josephson junctions on a substrate, as shown in Fig. 3. Since the array is infinite, the planes midway between adjacent junctions are symmetry planes, and are therefore adiabatic. Thus, the problem can be reduced to modeling a single junction. The geometry of a single junction module is shown in Fig. 4 (not drawn to scale). The junction itself consists of a bottom electrode and a smaller top electrode, separated by an extremely thin barrier (dark region). This sandwich is placed on top of the substrate. The top electrode is connected to another superconducting layer (the wiring). The cross-hatched regions are electrical insulation. Typical dimensions of the various layers for NbN technology (Spargo and Kerber, 1989) are given in Table 1. It can be seen from the table that the barrier is extremely thin compared to the electrodes, and the electrodes are very thin compared to the substrate.

Table 1 Dimensions of various material layers

Layer From Bottom to Top:	Thickness (μm)
Substrate	300
Bottom Electrode	0.1
Barrier	0.001
Top Electrode	0.1
Top Wiring	0.4
Electrical Insulation	0.3

A number of simplifications are made in analyzing this device. The major ones are stated now, and will be discussed in the next section. The major simplifications are:

1 The problem is treated as steady-state.

2 The problem is reduced to consideration of the bottom electrode only, with specified heat input at the barrier and heat transfer to the substrate at the bottom face.

3 Heat transfer from the bottom electrode to the substrate is modeled using an effective heat transfer coefficient, which accounts for all resistances between the electrode and the coolant.

Analysis

Steady-State Assumption. During operation, Josephson junctions typically cycle between a resistive and nonresistive state. The heat generation in the barrier is therefore a periodic function of time, with a period on the order of nanoseconds. Nonetheless, a steady-state analysis can be justified. To demonstrate this, a simple one-dimensional model problem is considered. In the next section it will be argued that most of the heat conducts downward through the bottom electrode, substrate, and package to the coolant. The model problem is therefore chosen to consist of a slab of thickness H and thermal diffusivity α, which is intended to correspond in an approximate fashion to the bottom electrode, substrate, and package. This slab is exposed to a periodic heat flux at the upper surface, $q''(t) = \bar{q}''(1 + \cos \omega t)$, and a specified temperature, T_∞, at the lower surface. After the initial transient has passed, the solution consists of a steady part corresponding to the average heat flux, $\bar{q}''$, and a fluctuating part corresponding to the fluctuating heat flux, $\bar{q}'' \cos \omega t$. The temperature is highest at the top of the electrode, and the amplitude of the fluctuations is also largest there. Furthermore, the temperature at the top of the electrode governs the electrical behavior of the junction. For these reasons, this temperature is used as the criterion to determine whether the problem can be treated as steady-state. It can be shown that the amplitude of the fluctuating part of this temperature (normalized by the steady part) is a function of γH, where $\gamma = \sqrt{\omega/2\alpha}$. In particular, for $\gamma H > 3$, this function is approximated by $(\sqrt{2}\gamma H)^{-1}$, accurate to within 0.5 percent. Now, an *extremely* conservative estimate of γH can be made by taking H to be the substrate thickness of 300 μm (even though the package is orders of magnitude larger), and taking α to be the value for the silicon substrate at 4.2 K, namely $\alpha = 3$ m^2/s (Touloukian et al., 1970). (This is higher than for most materials, and is orders of magnitude higher than the value at 77 K.) Then, with $\omega = 2\pi/t_p$, where t_p is the period (on the order of 10^{-9} s), $(\sqrt{2}\gamma H)^{-1}$ is less than 0.1. This says that even for this extremely conservative estimate, the fluctuating part of the temperature is less than 10 percent of the steady part, and a steady-state analysis is therefore well justified. Put another way, the thermal time constant of the device, H^2/α, is so large compared to the period of the fluctuations, t_p, that the fluctuations are almost completely damped

out, *even* at the location of the periodic heat input. The steady-state temperature should then be calculated based on the time-averaged value of the heat flux, $\overline{q}''$, not the maximum value that occurs when the junction is in its resistive state.

Justification for Considering Bottom Electrode Only. The heat generated in the barrier may conduct upward into the top electrode or downward into the bottom electrode. The partitioning of the total heat generation between the two directions is determined by the thermal resistances in the two directions. In practice, the substrate is typically bonded to a heat sink or package, which has a large area exposed to the coolant. In this case, the thermal resistance is much less in the "downward" than the "upward" direction, and most of the heat conducts into the bottom electrode. This is the situation modeled here. However, if the upper surface of the junction were also in contact with a large heat sink exposed to the coolant, then the thermal resistances in the two directions would be comparable, and roughly half of the heat would conduct downward into the bottom electrode. It should be noted that the magnitude of the heat generation in junctions made from the new materials is not yet known to within an order of magnitude, so a factor of two uncertainty is not cause for concern. Later in the paper, the heating rate (in nondimensional form) will be varied over a broad range.

Heat Transfer Coefficient at Bottom of Electrode. An effective heat transfer coefficient is now defined that describes the rate of heat transfer leaving the bottom of the electrode. This accounts for all thermal resistances between the bottom of the electrode and the coolant. It is defined as:

$$h_{\text{eff}} = \frac{\overline{q}}{A_e(T_{eb} - T_\infty)} \tag{3}$$

where A_e is the electrode area, and T_{eb} is the temperature at the bottom of the electrode. Now:

$$T_{eb} - T_\infty = (T_{eb} - T_{st}) + (T_{st} - T_{sb}) + (T_{sb} - T_\infty) \tag{4a}$$

$$= \overline{q}[R_b + R_s + R_p] \tag{4b}$$

where T_{st} and T_{sb} are the temperatures at the top and bottom of the substrate, respectively, R_b is the thermal boundary resistance between the electrode and the substrate, R_s is the resistance of the substrate, and R_p is the resistance between the substrate and coolant, which depends strongly on the design of the package. The orders of magnitude of the various resistances are now considered.

1 Thermal Boundary Resistance, R_b. At very low temperatures, thermal resistance occurs at the interface between two different substances due to phonon scattering. According to acoustic mismatch theory, the resistance (times area), R_bA_e, is inversely proportional to T^3, where T is absolute temperature. The constant of proportionality is on the order of 10^{-3} m^2-K^4/W for a variety of pairs of materials (Swartz and Pohl, 1987; Swartz, 1987; Schmidt, 1977). Thus at T = 4.2 K, R_bA_e is on the order of 10^{-5} m^2-K/W, while at T = 77 K, R_bA_e is on the order of 10^{-9} m^2-K/W. Experimental data for a variety of different materials show excellent agreement with the acoustic mismatch theory at temperatures below about 30 K, but at higher temperatures the measured thermal resistances are about an order of magnitude higher than the predictions, that is, R_bA_e is on the order of 10^{-8}m^2-K/W at 77 K (Swartz and Pohl, 1987).

2 Substrate Resistance, R_s. The substrate resistance consists of a conduction resistance and a constriction resistance. The conduction resistance is given by $R_{\text{cond.}} = H_s/k_sA_s$, where $A_s = L_s^2$ is the substrate area associated with a single junction (see Fig. 4). The constriction resistance is $R_{\text{const.}} = \Psi/k_sL_e$, where Ψ is a constant, which is order one or less for a variety of different geometries (Yovanovich and Antonetti, 1988). The ratio of these resistances is:

$$\frac{R_{\text{const.}}}{R_{\text{cond.}}} = \frac{\Psi A_s}{H_s L_e} \approx \frac{L_e}{H_s}\frac{A_s}{A_e} \tag{5}$$

The electrode dimension, L_e, is typically on the order of 10 μm, and H_s is approximately 300 μm. Since one advantage of Josephson junctions is their compactness, the ratio A_s/A_e is typically not large, perhaps between 1 (the minimum possible value) and 10. Therefore, $R_{\text{const.}}/R_{\text{cond.}}$ is generally less than one, which says that the constriction resistance does not dominate. Thus, the substrate resistance is the same order of magnitude as the conduction resistance, which can be written (for later convenience) as:

$$R_sA_e = \frac{H_s}{k_s}\frac{A_e}{A_s} \tag{6}$$

The thermal conductivity of silicon at 4.2 K is about 150 W/m-K (Touloukian et al., 1970), and the thermal conductivity of MgO at 77 K is about 490 W/m-K (from the equation in Flik et al., 1990, which is a fit to the data of Slack, 1962). Thus, with A_s/A_e ranging once again between 1 and 10, R_cA_e varies between order 10^{-7} and 10^{-6} m^2-K/W for both materials.

3 Resistance Between Substrate and Coolant, R_p. This resistance depends strongly on the design of the package. A crude upper bound on R_p can be found by assuming that there is no package, that is, that the substrate is in direct contact with the coolant. Assuming nucleate boiling, the heat transfer coefficient h for boiling helium on a silicon surface is on the order of 10^4 to 10^5 W/m^2-K (Flint et al., 1982) and for nitrogen it is the same order of magnitude (Merte and Clark, 1964). The corresponding resistance is $R_p = 1/hA_e$, or:

$$R_pA_e = \frac{1}{h}\frac{A_e}{A_s} \tag{7}$$

which is at most 10^{-4} m^2-K/W. However, a well-designed package could reduce this value by orders of magnitude.

It is now possible to estimate the range of values of the effective heat transfer coefficient defined by equation (3). Equation 4(b) is rewritten here, and the orders of magnitude of the various terms inside the brackets are given beneath it (in m^2-K/W):

$$T_{eb} - T_\infty = \frac{\overline{q}}{A_e}[\underset{\substack{10^{-5}\text{ at 4.2 K}\\ 10^{-8}\text{ at 77 K}}}{R_bA_e} + \underset{10^{-7}\text{ to }10^{-6}}{R_sA_e} + \underset{10^{-4}\text{ or less}}{R_pA_e}] \tag{8}$$

If the substrate is directly exposed to the coolant or if the package is not well-designed, the resistance R_p could dominate, and the total resistance could be as large as 10^{-4} m^2-K/W. However, if the package is well designed, then this resistance could possibly become negligible compared to the remaining resistances. In this case, at 4.2 K, the thermal boundary resistance dominates, and the total resistance is order 10^{-5} m^2-K/W. At 77 K, the substrate conduction resistance dominates, and the total resistance could be as low as 10^{-7} m^2-K/W. The substrate conduction resistance (equation (6)) could be reduced still further by increasing the spacing between junctions (i.e., increasing A_s/A_e), but this would probably be unacceptable from the viewpoint of compactness and the associated speed. Finally, then, the effective heat transfer coefficient defined by equation (3) could take on the following ranges:

$$h_{\text{eff}} = \begin{cases} 10^4 \text{ to } 10^5 \text{ W/m}^2\text{-K, at 4.2 K} \\ 10^4 \text{ to } 10^7 \text{ W/m}^2\text{-K, at 77 K} \end{cases} \tag{9}$$

Three-Dimensional Temperature Distribution in Bottom Electrode. Finally, the problem has been reduced to one of finding the temperature distribution in the bottom electrode

(see Fig. 5, not drawn to scale). There is a specified constant heat flux into the top face of the bottom electrode over the barrier region. The remainder of the top and the sides are insulated. The bottom face loses heat to the coolant. The thermal conductivity will be allowed to be anisotropic, since this is true for YBCO. However, in the interest of simplicity, it is assumed that the thermal conductivity is the same in the x and z directions, that the electrode is square, and that the barrier dimension L_b is half the electrode dimension L_e. Then the governing differential equation and boundary conditions are, in nondimensional form:

$$\frac{\partial^2\theta}{\partial\xi^2}+\frac{\partial^2\theta}{\partial\eta^2}+\frac{\partial^2\theta}{\partial\zeta^2}=0 \tag{10}$$

$$\text{At } \xi=0,\ \hat{L}\text{:}\quad \frac{\partial\theta}{\partial\xi}=0 \tag{11a}$$

$$\text{At } \zeta=0,\ \hat{L}\text{:}\quad \frac{\partial\theta}{\partial\zeta}=0 \tag{11b}$$

$$\text{At } \eta=0\text{:}\quad \frac{\partial\theta}{\partial\eta}=\mathrm{Bi}\,\theta \tag{12a}$$

$$\text{At } \eta=1\text{:}\quad \frac{\partial\theta}{\partial\eta}=\begin{cases} Q & 0<\xi<\frac{1}{2}\hat{L} \text{ and } 0<\zeta<\frac{1}{2}\hat{L} \\ 0 & \frac{1}{2}\hat{L}<\xi<\hat{L} \text{ or } \frac{1}{2}\hat{L}<\zeta<\hat{L} \end{cases} \tag{12b}$$

The solution is:

$$\theta=Q\Bigg\{\sum_{n=1}^{\infty}\sum_{m=1}^{\infty}a_{mn}\cos\lambda_n\xi\cos\lambda_m\zeta\Big[\sqrt{\lambda_n^2+\lambda_m^2}\cosh\sqrt{\lambda_n^2+\lambda_m^2}\eta+\mathrm{Bi}\sinh\sqrt{\lambda_n^2+\lambda_m^2}\eta\Big]+\sum_{n=1}^{\infty}b_n\cos\lambda_n\xi[\lambda_n\cosh\lambda_n\eta+\mathrm{Bi}\sinh\lambda_n\eta]+\sum_{m=1}^{\infty}c_m\cos\lambda_m\zeta[\lambda_m\cosh\lambda_m\eta+\mathrm{Bi}\sinh\lambda_m\eta]+\frac{1}{4}\left(\frac{1}{\mathrm{Bi}}+\eta\right)\Bigg\} \tag{13}$$

where

$$\lambda_n=n\pi/\hat{L} \tag{14}$$

$$a_{mn}=\frac{4\sin\lambda_n\hat{L}/2\sin\lambda_m\hat{L}/2}{mn\pi^2\sqrt{\lambda_n^2+\lambda_m^2}\left[\sqrt{\lambda_n^2+\lambda_m^2}\sinh\sqrt{\lambda_n^2+\lambda_m^2}+\mathrm{Bi}\cosh\sqrt{\lambda_n^2+\lambda_m^2}\right]} \tag{15}$$

$$b_n=\frac{\sin\lambda_n\hat{L}/2}{n\pi\lambda_n(\lambda_n\sinh\lambda_n+\mathrm{Bi}\cosh\lambda_n)} \tag{16}$$

$$c_m=\frac{\sin\lambda_m\hat{L}/2}{m\pi\lambda_m(\lambda_m\sinh\lambda_m+\mathrm{Bi}\cosh\lambda_m)} \tag{17}$$

It can be seen that the solution for the nondimensional temperature $\theta=(T-T_\infty)/(T_c-T_\infty)$ depends on $\mathrm{Bi}=h_{\mathrm{eff}}H_e/k_y$, $Q=\bar{q}''H_e/k_y(T_c-T_\infty)$, and $\hat{L}=(L_e/2H_e)\sqrt{k_y/k_x}$. It can be noted that θ is directly proportional to Q. A different nondimensional temperature θ/Q could have been defined, thereby eliminating the parameter Q from the problem. However, the present nondimensional temperature is more physically meaningful, since it is a measure of how close the temperature is to the transition temperature. Also, when it comes to evaluating the effect of the temperature on the critical current, the parameter Q becomes necessary, and the present nondimensionalization is more convenient. It can also be seen from the parameter $\hat{L}$ that the effect of anisotropic thermal conductivity is comparable to changing the aspect ratio of the electrode, i.e., increasing the thermal conductivity in the x–z plane is equivalent to decreasing the electrode dimension L_e.

Evaluation of Critical Current. The critical Josephson current density is determined by the temperature of the barrier, which is approximately equal to the temperature at the top of the electrode, T_t (neglecting Kapitza and contact resistance between the electrode and barrier). If the temperature locally exceeds the transition temperature, then the superconductor (electrode) will go normal at that location. The current will flow only through the portion of the superconductor that remains below the transition temperature, so there will not be any Joule heating within the superconducting material, only in the barrier itself. The critical current that can pass through the entire barrier is found by integrating the critical current density over the barrier area:

$$I_c=4\int_0^{L_b/2}\int_0^{L_b/2}J_c(T_t)\,dx\,dz \tag{18}$$

In the interest of simplicity, a linear relationship between critical current density and temperature is assumed here. A linear relationship is a reasonable approximation to the BCS-type dependence shown in Fig. 2, in the range between T_∞ and T_c, especially for YBCO, for which $T_\infty/T_c = 0.84$. Furthermore, some preliminary experimental results have shown that the critical current density depends linearly on temperature for a crack junction made from YBCO (Sugishita et al., 1987). (This will not necessarily carry over to a sandwich-type junction). At any rate, it will be assumed that $J_c(T) = \max[\beta(T_c-T), 0]$, where β is a constant of proportionality. Then the reduction in critical current relative to the critical current at the coolant temperature is given by:

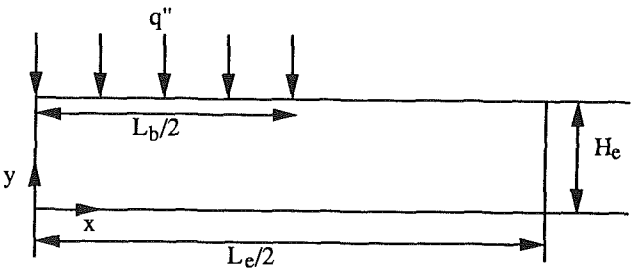

a) Side View

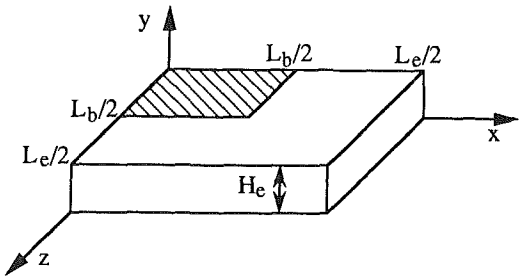

b) Perspective View

Fig. 5 Bottom electrode

Table 2 Low and high temperature examples

Case	Q	$\hat{L}$	Bi	$\bar{\theta}_t$	$I_c/I_{c,\infty}$
Low T_c	0.00021	50	0.0045	0.025	0.975
1st High T_c	0.017	50	0.0045	2.02	0.0
2nd High T_c	0.017	16	0.0045	1.15	0.001
3rd High T_c	0.00093	215	0.0045	0.176	0.824
4th High T_c	0.017	50	0.45	0.050	0.950

$$\frac{I_c}{I_c(T_\infty)} = \frac{4}{L_b^2}\int_0^{L_b/2}\int_0^{L_b/2} \frac{\max[T_c - T_{t,0}]}{T_c - T_\infty}\, dxdz = \frac{4}{L_b^2}\int_0^{L_b/2}\int_0^{L_b/2} (1 - \min[\theta_t, 1])\, dxdz \tag{19}$$

It can be seen that if θ_t is less than unity over the entire barrier area, then $I_c/I_{c,\infty}$ is simply equal to $1 - \bar{\theta}_t$, where $\bar{\theta}_t$ is the average value of θ_t over the barrier area. If θ_t exceeds unity over some portion of the barrier area, this simple relation no longer holds. If θ_t exceeds unity over the entire barrier area, the critical current will go to zero. This technique for calculating the critical current reduction in a superconductor due to a temperature rise has been used previously by Flik and Tien (1988), with regard to the *bulk* critical current.

Results and Discussion

Temperature Distributions. Some sample comparisons of low and high-temperature superconductors are now presented. Table 2 shows the parameter values (Q, $\hat{L}$, and Bi), and two results of the analysis, namely $\bar{\theta}_t$ and $I_c/I_{c,\infty}$. Recall that $\bar{\theta}_t$ is the average value of θ_t over the barrier area, and if θ_t is less than unity over the entire barrier area, then $I_c/I_{c,\infty}$ is simply equal to $1 - \bar{\theta}_t$.

First, typical values of the nondimensional parameters are determined for the low-temperature case. For NbN, it was noted earlier that the heat flux in the resistive state is of order 10^5 W/m^2. The time-averaged heat flux would be roughly half as much, or 5×10^4 W/m^2. The effective heat transfer coefficient is taken equal to the largest plausible value, 10^5 W/m^2-K. The difference between the transition and coolant temperatures is $T_c - T_\infty = 11$ K, and the geometric parameters are taken to be $L_e = 10$ μm, $H_e = 0.1$ μm. After a thorough search of the literature, national laboratories, and private industry, we have been unable to find a value for the thermal conductivity of NbN in the superconducting state. Based on data for other niobium alloys (Touloukian et al., 1970) it appears that the thermal conductivity is of order 1–10 W/m-K at 4.2 K. For simplicity, the thermal conductivity of NbN is taken to be 2.2 W/m-K, the value that is later used for YBCO. It should be noted that the problem is solved in nondimensional form, and the values of the nondimensional parameters are later varied over broad ranges, so that the results are not limited to this particular value for the thermal conductivity of NbN. Finally, then, using the above values, and assuming that the thermal conductivity is isotropic, the parameter values for the low-T_c case are as given in Table 2.

Now for the high-temperature case, the most important difference is the higher heat flux. In this first high-T_c case, the Biot number is held the same as for the low-temperature case, since this is within the range possible for the high-temperature situation. The dimensions are also assumed to be the same as for the low-temperature case, and the thermal conductivity is assumed isotropic, so that $\hat{L}$ is the same as for the low-temperature case. (The effects of Biot number and $\hat{L}$ will be explored later.) If the dimensions are the same, then the current density must scale up with operating temperature (recall equation (2)). Then the heat flux scales up with the product of transition temperature and operating temperature (cf. equations (1) and (2)), so the heat flux is $5 \times 10^4 \cdot (92 \cdot 77)/(15 \cdot 4.2) = 5.6 \times 10^6$ W/m^2. The thermal conductivity of YBCO is 2.2 W/m-K at 77 K (Hagen et al., 1989). (This is the out-of-plane thermal conductivity. The effect of anisotropy will be discussed later.) The temperature difference is $T_c - T_\infty = 15$ K. Then, with the same dimensions as the low-temperature case, the parameters for the first high-T_c case are as given in Table 2.

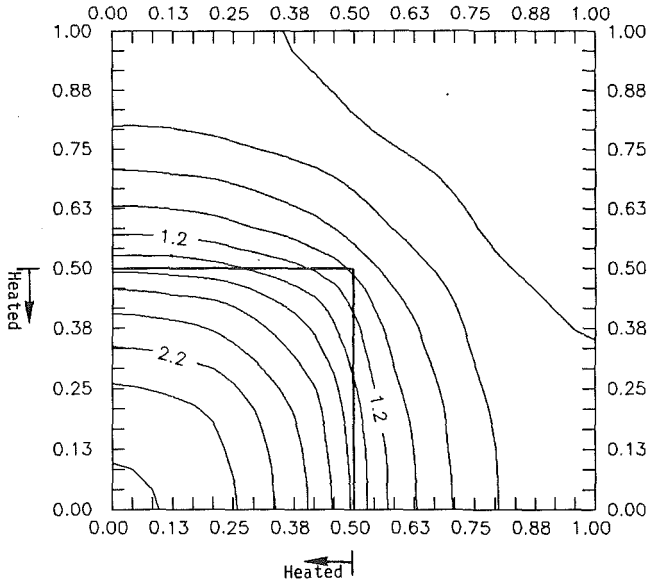

Fig. 6 Isotherms at top of bottom electrode, first high-T_c case, Q = 0.017, $\hat{L}$ = 50, Bi = 0.0045

Since the only parameter that differs between the low-T_c and first high-T_c cases is Q, and θ is directly proportional to Q, there is no need to show detailed results for both cases. For the first high-T_c case, the temperature distribution at the top of the electrode is shown as an isotherm plot in Fig. 6. Only the temperature at the top surface of the electrode is presented, since this is what determines the critical current. Because of symmetry, only one quarter of the electrode is shown, and the heated area is only a quarter of that. The temperature rise is quite large; over the entire heated area (the barrier area) the temperature exceeds the superconducting transition temperature ($\theta > 1$). This causes the critical current to decrease to zero (cf. equation (19)), so that the junction would not be able to switch into the nonresistive state. For the low-T_c case, the isotherms would look identical, but the temperature is smaller by a factor of 81. In that case, the temperature is not elevated significantly above the coolant temperature, and the critical current would only be reduced to $I_c/I_{c,\infty} = 0.975$ (see Table 2). To summarize, in the low-T_c case the critical current is only reduced by 2.5 percent, whereas in the first high-T_c case the critical current is reduced to zero as a result of the heat flux being higher by about two orders of magnitude.

The thermal conductivity of YBCO is anisotropic due to the crystal structure. Hagen et al. (1989) measured the thermal conductivity of crystals of YBCO, and found that the conductivity in the in-plane (ab) direction is typically four to five times greater than in the out-of-plane (c) direction. In addition, the thermal conductivity of a thin film is both anisotropic (with a higher conductivity in the plane of the film than normal to it) and size dependent (Flik and Tien, 1988). The thermal conductivities in the three coordinate directions would therefore depend on the orientation of the crystals and the film thickness. As an example, the thermal conductivity in the x–z plane is taken to be 10 times greater than that in the y direction. Thus, Bi and Q remain unchanged, but $\hat{L}$ decreases to 16. The parameters for this second high-T_c case are given

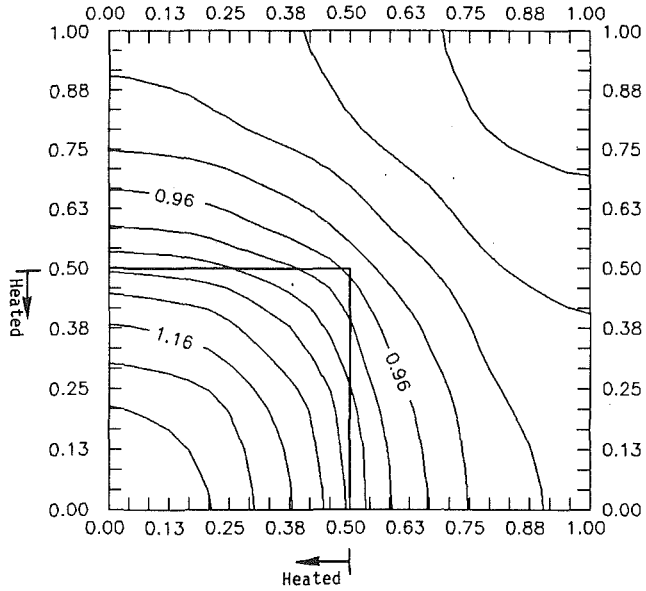

Fig. 7 Isotherms at top of bottom electrode, second high-T_c case, Q = 0.017, $\hat{L}$ = 16, Bi = 0.0045

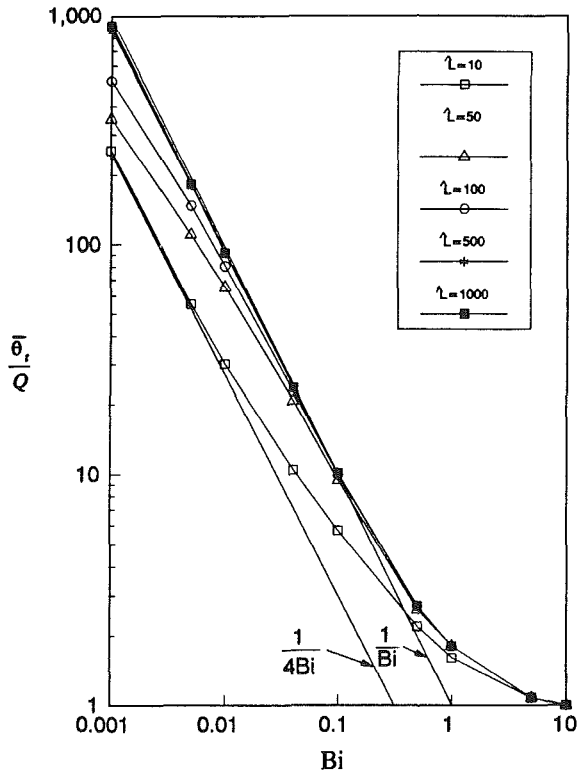

Fig. 8 $\bar{\theta}_t/Q$ as a function of Bi and $\hat{L}$

in Table 2, and an isotherm plot is shown in Fig. 7. The results are as expected, namely that there is enhanced conduction in the x–z plane, which increases the temperature in the unheated region and decreases the temperature in the heated region. However, the temperature still exceeds the transition temperature over nearly the entire barrier area, so the critical current would be almost zero (see Table 2).

The first high-T_c case discussed earlier assumed that high-temperature junctions could be fabricated such that the current density scales up with operating temperatures. Let us now consider what happens if instead the current density is the same as for low-temperature junctions. Then the barrier area will have to scale up with operating temperature (equation (2)). Maintaining the same ratio of barrier to electrode area, the electrode dimension must increase relative to the old value of 10 μm as $L_e = 10\ \mu\text{m} \cdot (77/4.2)^{1/2} = 43\ \mu$m, and $\hat{L} = 215$. If the current density is unchanged from the low-temperature case, then the heat flux does not scale up with operating temperature, only with transition temperature, so $\bar{q}'' = 5 \times 10^4 \cdot (92/15) = 3.1 \times 10^5\ \text{W/m}^2$, and $Q = 9.3 \times 10^{-4}$. This is less than five times greater than the low-T_c case, and is almost twenty times less than the first high-T_c case. The parameters for this third high-T_c case are given in Table 2. The reduction in Q is a tremendous advantage. In the first high-T_c case, $\bar{\theta}_t = 2.0$, whereas in the third high-T_c case $\bar{\theta}_t = 0.18$ (see Table 2). In this latter case, the temperature would nowhere exceed the transition temperature, and the critical current would be reduced to $I_c/I_{c,\infty} = 0.82$, compared to zero in the first high-T_c case. Therefore, from the perspective of temperature control, it is clearly advantageous to use larger electrodes with lower current densities, and hence lower heat fluxes. However, this might not be acceptable from the point of view of compactness and speed.

It is conceivable that, for the high-temperature case, the effective heat transfer coefficient might be two orders of magnitude higher than the value assumed so far of $10^5\ \text{W/m}^2\text{-K}$ (recall equation (9)). This would mean that the Biot number would also be larger by two orders of magnitude, i.e., Bi = 0.45. This is the fourth high-T_c case. From Table 2, the increase in Bi would cause a very significant decrease in the temperature, to $\bar{\theta}_t = 0.050$. The critical current would only be reduced by 5 percent, i.e., $I_c/I_{c,\infty} = 0.95$.

The effects of the parameters Bi and $\hat{L}$ will now be discussed in a more general manner. Figure 8 shows the value of $\bar{\theta}_t$ divided by Q, as a function of Bi and $\hat{L}$. An increase in the Biot number corresponds to an increased heat transfer coefficient, and therefore causes a decrease in temperature. A decrease in $\hat{L}$ causes $\bar{\theta}_t$ to decrease. The reason is that a decrease in $\hat{L}$ corresponds to a decrease in the aspect ratio L_e/H_e or in the conductivity ratio k_y/k_x. In either case, conduction in the x–z plane is enhanced, causing heat to spread out more in the electrode, thereby reducing the average temperature over the heated section. However, for $\hat{L}$ greater than about 50 there is little effect of this parameter, except for very low Bi.

It is also interesting to consider some limiting cases. For small Bi and large $\hat{L}$, heat conducts from the barrier area straight through the electrode without spreading out (since large $\hat{L}$ implies negligible lateral conduction), and the external resistance dominates (due to the small Biot number). Therefore, $\bar{T}_t - T_\infty = \bar{q}''/h_{\text{eff}}$, or $\bar{\theta}_t/Q = 1/\text{Bi}$. This line is shown in Fig. 8, and the approximation is seen to hold very accurately for Bi less than about 0.3 and $\hat{L}$ greater than about 50. For small Bi and small $\hat{L}$, the temperature rise is less than this simple prediction, because of enhanced conduction in the x–z plane. As $\hat{L}$ goes to zero (still for small Bi), the heat can be assumed to conduct through the entire electrode area, rather than just the barrier area, so that $\bar{T}_t - T_\infty = \bar{q}'' A_b/h_{\text{eff}} A_t$, or $\bar{\theta}_t/Q = (1/\text{Bi})(A_b/A_e) = 1/4\text{Bi}$ for the case considered here. This is seen to be reasonably accurate for $\hat{L} = 10$ and Bi less than about 0.01. For Bi greater than about 0.3, the temperature exceeds both of these predictions, because the thermal resistance of the electrode is significant and there is a nonnegligible temperature rise between the bottom and top of the electrode. For large Bi, the resistance of the electrode dominates the external resistance, and heat conducts straight through the electrode without spreading out regardless of the value of $\hat{L}$. Therefore, $\bar{T}_t - T_\infty = \bar{q}'' H_e/k_y$, or $\bar{\theta}_t/Q = 1.0$. This is confirmed in Fig. 8 for large Bi.

These three limiting cases are summarized in Table 3 in both nondimensional and dimensional form. From the dimensional expressions, it is clear that a large effective heat transfer coefficient is desirable (as expected), since for small Bi, the temperature rise decreases with increasing h_{eff}, and in the limit of

Table 3 Limiting cases

	$\bar{\theta}_t/Q$	$T_t - T_\infty$
Large Bi	1	$\frac{\bar{q}''H_e}{k_y} = \frac{\bar{q}H_e}{k_y A_b}$
Small Bi, large $\hat{L}$	$\frac{1}{Bi}$	$\frac{\bar{q}''}{h_{eff}} = \frac{\bar{q}}{h_{eff}A_b}$
Small Bi, small $\hat{L}$	$\frac{A_b}{A_e Bi}$	$\frac{\bar{q}''}{h_{eff}}\frac{A_b}{A_e} = \frac{\bar{q}}{h_{eff}A_e}$

large h_{eff} (large Bi), the temperature rise reaches its minimum value of $\bar{q}H_e/k_yA_b$. A large value of h_{eff} can be achieved through careful design of the package, and/or by increasing the spacing between junctions (although this latter may be unacceptable from the viewpoint of compactness and the associated speed). A large area (A_b or A_e) also reduces the temperature rise by decreasing the heat flux, but again this may not be an acceptable design. Finally, it can also be seen from these expressions that the electrode thickness, H_e, has a somewhat complicated effect on the temperature. For small Bi, an increase in H_e (decrease in $\hat{L}$) decreases the temperature, due to enhanced conduction in the x-z plane, which causes an increase in the area through which heat conducts (from A_b to A_e). For large Bi, however, an increase in H_e increases the temperature, due to the increased temperature rise between the bottom and top of the electrode. The small Biot number situation is more typical of the low-temperature case, since the thermal boundary resistance is significant, but it may be possible (and essential) to achieve a larger Biot number in the high-temperature case.

Reduction in Critical Josephson Current. Figure 9 shows the effect of the nondimensional parameters on the critical Josephson current. A value of $I_c/I_{c,\infty}$ of unity means that the critical current is equal to its value at the coolant temperature, that is, no reduction in critical current has occurred due to self heating. A value of $I_c/I_{c,\infty}$ of zero means that the temperature at the barrier has everywhere exceeded the critical temperature, and therefore the critical current has gone to zero. In other words, the junction will not be able to switch to the nonresistive state. Curves are shown for $Q = 2.1 \times 10^{-4}$ and 1.7×10^{-2}, the representative values for low and high-temperature superconductors, respectively. The trends are as expected, namely that there is a far greater reduction in critical current for the larger value of Q, and that an increase in Bi or a decrease in $\hat{L}$ is advantageous in avoiding a reduction in critical current. The reduction in critical current can be substantial, especially for the high-temperature case, and therefore it is essential to address thermal issues in the design of Josephson junction devices made from high-temperature superconductors.

Conclusions

The thermal aspects of a Josephson junction have been investigated. The situation considered is fairly general, since the combination of coolant, package, substrate, and thermal boundary resistance is represented by an effective heat transfer coefficient, which can take on a wide range of values. The temperature distribution and resulting reduction in critical Josephson current were calculated as functions of the nondimensional parameters Q, $\hat{L}$, and Bi. The parameter Q has the largest effect, since the temperature rise is proportional to Q. The Biot number also has a large effect, since for small Biot (Bi less than about 0.3) the temperature rise is inversely proportional to Bi. The parameter $\hat{L}$ has a lesser effect; this parameter must be less than about 50 for enhanced conduction to play a significant role in reducing the temperature rise, and

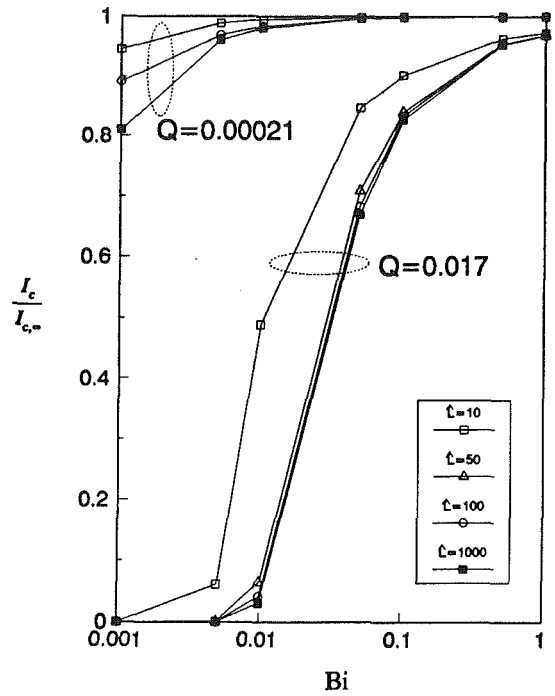

Fig. 9 $I_c/I_{c,\infty}$ as a function of Q, Bi, and $\hat{L}$

even then the effect is not huge. The ratio of temperature rise for infinite $\hat{L}$ to the temperature rise for $\hat{L} = 0$ is A_e/A_b, which is typically not a large number (the value four was used as an example in this paper).

The main difference between Josephson junctions made from low and high-temperature superconductors is that the high-temperature junctions are expected to have a higher value of heat flux. If the heat flux is in fact larger by two orders of magnitude, great care will have to be taken to ensure that the critical Josephson current is not adversely affected. Fortunately, in the high-temperature situation the Kapitza resistance is not dominant, and with careful design it may be possible to increase the effective heat transfer coefficient by orders of magnitude over the low-temperature case (as explored in the fourth high-T_c case). However, it may only be possible to achieve such a large effective heat transfer coefficient by spacing the junctions farther apart. Alternatively, by enlarging the junctions the heat flux can be lowered (for the same heating rate), as in the third high-T_c case. Both of these alternatives would reduce the compactness of Josephson junction devices, which would reduce their electrical speed. As demonstrated by the second high-T_c case, a larger thermal conductivity in the plane of the electrode yields only a minor improvement. If the Biot number is less than about 0.3, some advantage can be gained by increasing the electrode thickness, which enhances lateral conduction in the electrode. However, for larger Bi, the increase in temperature rise between the bottom and top of the electrode outweighs the advantage of enhanced lateral conduction.

In conclusion, this analysis of heat transfer in Josephson junction devices indicates that, for junctions made from high-temperature superconductors, the temperature rise may be sufficient to cause unacceptable reductions in critical current. These problems can almost certainly be overcome (since they are less severe than for semiconductor devices), but it may be at the expense of certain of the supposed advantages of Josephson junctions, such as their compactness and associated speed.

Acknowledgments

The authors would like to thank Hughes Aircraft Company, the University of California, and the National Science Foun-

dation for their support. Special thanks are due to Drs. Hunter, Spargo, and Kerber for their advice and assistance.

References

Ambegaokar, A., and Baratoff, A., 1963, "Tunneling Between Superconductors," *Physics Rev. Lett.*, Vol. 10, pp. 486–489; also see Erratum, *Physics Rev. Lett.*, Vol. 11, p. 104.

Arnett, P. C., 1983, "Heating in Nb Edge Junctions," *IEEE Trans. Magnetics*, Vol. MAG-19, No. 3, pp. 1151–1154.

Bar-Cohen, A., and Kraus, A. D., 1988, *Advances in Thermal Modeling of Electronic Components and Systems*, Vol. 1, Hemisphere, New York.

Dharmadurai, G., 1980, "Self-Heating-Induced Phenomena in Long Thin-Film Superconductors and Their Applications," *Phys. Stat. Sol. A*, Vol. 62, No. 11, pp. 11–33.

Ellison, G. N., 1989, *Thermal Computations for Electronic Equipment*, Robert E. Krieger Publishing Co., Malabar, FL.

Flik, M. I., and Tien, C. L., 1988, "Intrinsic Thermal Stability of Anisotropic Thin-Film Superconductors," *Superconductivity Applications and Developments*, ASME MD-Vol. 11, pp. 39–45.

Flik, M. I., Phelan, P. E., and Tien, C. L., 1990, "Thermal Model for the Bolometric Response of High-T_c Superconducting Films to Optical Pulses," *Cryogenics*, Vol. 30, No. 12, pp. 1118–1128.

Flint, E., Van Cleve, J., Jenkins, L., and Guernsey, R., 1982, "Heat Transport to He I from a Polished Silicon Surface," *Advances in Cryogenic Engineering*, Vol. 27, pp. 283–292.

Hagen, S. J., Wang, Z. Z., and Ong, N. P., 1989, "Anisotropy of the Thermal Conductivity of $YBa_2Cu_3O_{7-y}$," *Physical Review B*, Vol. 40, No. 13, pp. 9389–9392.

Iguchi, I., Sugishita, A., and Yanagisawa, M., 1987, "DC SQUID Operation at 77 K Using All Ceramics Josephson Junctions," *Japanese Journal of Applied Physics*, Vol. 26, No. 6, pp. L1021–L1022.

Iwanyshyn, O., and Smith, H. J. T., 1972, "Thermal Effects at Superconducting Point Contacts," *Physical Review B*, Vol. 6, No. 1, pp. 120–130.

Jennings, R., and Rubinsky, B., 1986, "A Finite Element Study of a Coplanar Electrode Josephson Junction With Respect to Electric Potential and Temperature," *Int. Comm. Heat Mass Transfer*, Vol. 13, pp. 55–65.

Ketchen, M. B., 1979, "Power Supply Regulators for Josephson Latching Logic," *Technical Digest of IEDM*, pp. 489–492.

Laibowitz, R. B., Koch, R. H., Gupta, A., Koren, G., Gallagher, W. J., Foglietti, V., Oh, B., and Viggiano, J. M., 1990, "All High T_c Edge Junctions and SQUIDs," *Appl. Phys. Lett.*, Vol. 56, No. 7, pp. 686–688.

Merte, H., and Clark, J. A., 1964, "Boiling Heat Transfer With Standard, Fractional and Near Zero Gravity," ASME JOURNAL OF HEAT TRANSFER, Vol. 86, pp. 351–360.

Rogers, C. T., Inam, A., Hegde, M. S., Dutta, B., Wu, X. D., and Venketesan, T., 1989, "Fabrication of Heteroepitaxial $YBa_2Cu_3O_{7-x}$-$PrBa_2Cu_3O_{7-x}$-$YBa_2Cu_3O_{7-x}$ Josephson Devices Grown by Laser Deposition," *Appl. Phys. Lett.*, Vol. 55, No. 19, pp. 2032–2034.

Schmidt, C., 1977, "Thermal Boundary (Kapitza) Resistance at Niobium-Epoxy Interfaces in Superconducting and Normal States," *Physical Review B.*, Vol. 15, No. 9, pp. 4187–4192.

Shoji, A., Aoyagi, M., Kosaka, S., and Shinoki, F., 1987, "Temperature-Dependent Properties of Niobium Nitride Josephson Tunnel Junction," *IEEE Trans. Magnetics*, Vol. MAG-23, No. 2, pp. 1464–1471.

Skopcol, W. J., Beasley, M. R., and Tinkham, M., 1974, "Self-heating Hotspots in Superconducting Thin-Film Microbridges," *J. Appl. Phys.*, Vol. 45, No. 9, pp. 4054–4066.

Slack, G. A., 1962, "Thermal Conductivity of MgO, Al_2O_3, $MgAl_2O_4$, and Fe_3O_4 Crystals from 3° to 300°K," *Physical Review*, Vol. 126, No. 2, pp. 427–441.

Spargo, J., and Kerber, G., 1989, Hughes Aircraft Company, personal communication.

Sugishita, A., Yanagisawa, M., and Iguchi, I., 1987, "Macroscopic Quantum Interference Effect for High-T_c YBaCuO and GdBaCuO Josephson Junctions," *Japanese Journal of Applied Physics*, Vol. 26, No. 9, pp. L1472–L1474.

Swartz, E. T., 1987, "Solid-Solid Thermal Boundary Resistance," Ph.D. Thesis, Cornell University, Ithaca, NY.

Swartz, E. T., and Pohl, R. O., 1987, "Thermal Resistance at Interfaces," *Appl. Phys. Lett.*, Vol. 51, No. 26, pp. 2200–2202.

Touloukian, Y. S., Powell, R. W., Ho, C. Y., and Klemens, P. G., 1970, *Thermophysical Properties of Matter*, Vol. I, IFI/Plenum, NY.

Van Duzer, T., 1989, "Superconductor Electronic Device Application," *IEEE J. Quantum Electronics*, Vol. 25, No. 11, pp. 2365–2377.

Wiener-Avnear, E., Cooper, J. E., Kerber, G. L., Spargo, J. W., Toth, A. G., Josefowicz, J. Y., Rensch, D. B., Clemens, B. M., and Hunter, A. T., 1989, "Laser Patterning of YBaCuO Weak Link Bridges," *IEEE Trans. Magnetics*, Vol. 25, No. 2, pp. 935–938.

Wu, P. H., Cheng, Q. H., Yang, S. Z., Chen, J., Li, Y., Ji, Z. M., Song, J. M., Lu, H. X., Gao, X. K., Wu, J., and Zhang, X. Y., 1987, "The Josephson Effect in a Ceramic Bridge at Liquid Nitrogen Temperature," *Japanese Journal of Applied Physics*, Vol. 26, No. 10, pp. L1579–L1580.

Yovanovich, M. M., and Antonetti, V. W., 1988, "Application of Thermal Contact Resistance Theory to Electronic Packages," in: *Advances in Thermal Modeling of Electronic Components and Systems*, Vol. 1, Chap. 2, Hemisphere, New York.

Electrostatic Cooling of a Horizontal Cylinder

M. E. Franke
Professor.
Mem. ASME

L. E. Hogue[1]
Lieutenant Colonel, USAF.

Air Force Institute of Technology,
Wright-Patterson AFB, OH 45433

The effects of corona wind on the heat transfer rate from a heated horizontal cylinder are described. Corona discharge and a corona wind are developed when a high voltage is applied to an electrode (emitter) near a grounded surface. In this study the corona wind is directed toward the lower region of the grounded cylinder by placing either a positively charged single-wire emitter or multipoint emitter parallel to and directly below the heated cylinder. Heat transfer rates from the heated cylinder under free convection conditions with and without a corona wind are obtained by measuring the power input to the cylinder. Free convection rates are also obtained from interferometer photographs. Free convection heat transfer rates are increased several times by the corona wind.

Introduction

Numerous studies have been conducted on the effects of electrostatic fields on free convective heat transfer rates. Many of these studies have shown that corona discharge resulting from intensive electrostatic fields around various types of electrodes/emitters (sharp points or small diameter wires) enhances the free convective heat transfer rate from adjacent surfaces. Emitters have been located on the surfaces or near the surfaces, either within or outside the thermal boundary layers. The corona wind, which develops from these intense electrostatic fields, is caused by the Coulomb force exerted on the ions and collisions of ions and neutral molecules of gas as described by Yabe et al. (1978), which extends the work of Robinson (1961) and Velkoff (1962). As a result, corona wind can provide significant cooling in free convection and is particularly advantageous if other means of cooling are inappropriate or not available.

Examples of studies related to increases in the free-convection heat transfer rate on vertical surfaces include those of Marco and Velkoff (1963), O'Brien and Shine (1967), and Franke and Hudson (1984). These investigations involved the cooling of heated surfaces with discharge electrodes (emitters) composed of stretched-wire or multipoint electrodes. While the studies showed significant increases in heat transfer rates, the geometric configurations were such that the corona wind did not always provide the best possible flow enhancement.

The purpose of this study was to enhance the flow around a horizontal circular cylinder in air by corona wind and determine the effect on the free convection heat transfer rate. The cylinder was maintained at ground potential with respect to a positive high-voltage emitter. Corona discharge occurred on the emitter, allowing a corona wind to develop between the emitter and the cylinder and act like a jet of air directed at the cylinder from below. Baseline free convection heat transfer rates were calculated and determined experimentally. Increases in the heat transfer rate from the cylinder were determined quantitatively by a heat-balance method and qualitatively with a Mach-Zehnder interferometer.

Experimental Apparatus

The experimental apparatus consisted of a heated horizontal cylinder, heater circuit, instrumentation and controls, high-voltage apparatus and emitters, Mach-Zehnder interferometer, camera system, and a system for blowing air.

The 2.5-cm-dia cylinder was 25 cm long and was constructed from 2024 aluminum with the surface machined to a smooth, nearly polished finish. The cylinder was suspended by cotton cord in the test section of the interferometer. The cylinder was constructed in two halves with a center cavity to facilitate installation of a coiled, nichrome-wire heater element and thermocouples. The heater was connected to an a-c circuit that contained a variable transformer and a digital multimeter.

The surface temperature of the cylinder was measured with twelve, 30-gage, copper-constantan thermocouples located 1.9 mm below the cylindrical surface. The thermocouples were located 90 deg apart, four at each end and four at center span. The thermocouple readings were weighted to account for the lower temperatures at the ends of the cylinder in determining the average temperature of the cylinder. Two additional thermocouples were used to measure the ambient temperature in the test section. The thermocouples were connected to an automated data acquisition system consisting of a scanner, system controller, and a digital voltmeter.

The Mach-Zehnder interferometer had 20-cm-dia optics and a light source consisting of a 100-W mercury vapor lamp with a Wratten No. 77A filter. Interference photographs were obtained with a Polaroid camera back and Type 42 film. A high-voltage d-c power supply was used to provide the high voltage to the emitters at a positive potential with respect to ground. The emitter voltage and current were measured with an electrostatic voltmeter and a microammeter.

Two types of emitters were used to establish the corona discharge: a single stretched-wire emitter and a multipoint emitter. The emitters together with the test cylinder are illustrated in Fig. 1. The wire emitter was either nichrome wire with a diameter of 0.32 mm or chromel wire with a diameter of 0.1 mm. The emitter wire was mounted and stretched between two copper rods parallel to the axis of the cylinder. The distance between the emitter and the cylinder was varied from 6.4 to 31.8 mm.

The multipoint emitter consisted of 21 0.1-mm-dia by 6.3-mm-long chromel wires mounted in 3-mm-dia by 0.1-m-long copper rods that were, in turn, mounted in a Plexiglas holder. The wires were spaced 12.7 mm apart and positioned beneath the cylinder as shown in Fig. 1.

A jet of air from a wedged-shaped plenum was also directed at the cylinder to compare its effect with that of the corona wind. Each side of the plenum was 30 cm square. The sides converged from a base width of 10.5 cm to form a slot 0.4 mm wide and 30 cm long. The slot was positioned below the cylinder at distances from the cylinder equivalent to the emitter-to-cylinder spacings. Air input to the plenum was through two quick-disconnect fittings at the base of the plenum. The pressure near the plenum base was measured with a 0–172 kPa (gage) pressure transducer. The air velocity was measured with

[1]Present affiliation: Air Force Systems Command.

Contributed by the Heat Transfer Division and presented at the 2nd ASME/JSME Thermal Engineering Joint Conference, Honolulu, Hawaii, March 22–27, 1987. Manuscript received by the Heat Transfer Division May 6, 1987; revision received February 11, 1991. Keywords: Augmentation and Enhancement, Electronic Equipment, Natural Convection.

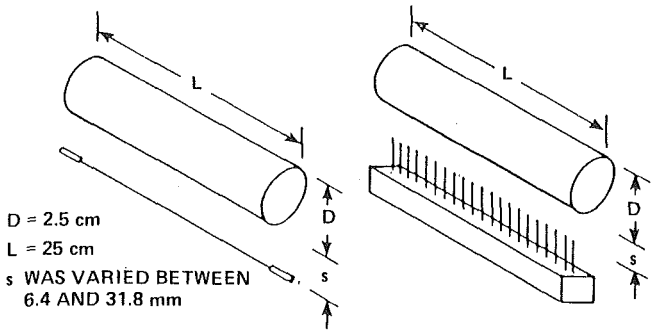

Fig. 1 Test configurations

a calibrated direct-reading air flow meter. The meter is designed to measure velocities in ducts or in open spaces. The meter was also used to measure the corona wind velocity.

Energy Balance and Calculation Procedure

Experimental Procedure. The cylinder was heated to a fixed ΔT by adjusting the variable transformer in the a-c heater circuit. The total heat transfer rate in free convection Q_{to} and any increase in heat transfer rate ΔQ_t due to electrostatic corona discharge were determined from a-c power input measurements with and without corona discharge while maintaining a constant surface-to-ambient temperature difference ΔT. The increase in heat transfer ΔQ_t, at constant ΔT, was determined from changes in heater current since the heater resistance R was assumed constant. In equation form

$$\Delta Q_t = Q_t - Q_{to} = R\Delta(I^2) \tag{1}$$

The temperatures were monitored by the data acquisition system, which was programmed to sample each thermocouple sequentially, measure its voltage, and compute a temperature. The measured temperatures were then automatically weighted to obtain an average temperature difference between the cylinder and ambient.

With the interferometer, the heat transfer rate was determined by measuring the spacing of the fringes on an interferogram at a number of locations around the cylinder. The temperature gradients were then obtained from the fringe spacing, and the average heat transfer rate from the cylinder was obtained from the average of the gradients around the cylinder (Kennard, 1932). These measurements were only possible in the free convection case, because with electrostatic corona discharge the boundary layer became too thin to obtain accurate measurements.

Calculation Procedure. The heat transfer rate from the horizontal cylinder without electrostatic corona discharge was obtained by the two experimental methods previously described and also by calculations based on available free convection heat transfer equations given by, for example, Kreith (1958) and Rohsenow and Choi (1961). The total heat transfer rate Q_{to} from the cylinder in free convection includes that due to convection and radiation from the cylindrical surface (Q_{co} and Q_{ro}) and from the ends (Q_{eo}):

$$Q_{to} = Q_{co} + Q_{ro} + Q_{eo} \tag{2}$$

The free convection part of the heat transfer rate Q_{co} is given by

$$Q_{co} = \bar{h}_o A \Delta T \tag{3}$$

where the average convection coefficient $\bar{h}_o$ for a long cylinder is given by

$$\bar{h}_o = \frac{k}{D}(0.53)(\mathrm{Gr}_D\,\mathrm{Pr})^{1/4} \tag{4}$$

The radiation heat transfer rate for a small gray body of constant emissivity in black surroundings was calculated in the accepted way using the fourth power of temperature. The heat transfer rate from the ends was calculated assuming small vertical plates.

With electrostatic cooling, the total heat transfer rate Q_t is determined by Q_c, Q_r, and Q_e:

$$Q_t = Q_c + Q_r + Q_e \tag{5}$$

Since the temperature of the cylinder was held constant during the tests, it was assumed the heat transfer rate from the cylindrical surface due to radiation and the total heat transfer rate through the ends did not change; i.e., $Q_r = Q_{ro}$ and $Q_e = Q_{eo}$. Therefore, the increase in heat transfer rate due to electrostatic cooling results from an increase in convection heat transfer about the cylindrical surface. From Eqs. (1), (2), and (5)

$$\Delta Q_t = Q_c - Q_{co} \tag{6}$$

By dividing Eq. (6) by Eq. (3), the increase in heat transfer rate can be expressed as a ratio of the average convection coefficient $\bar{h}$ to the average free convection coefficient $\bar{h}_o$, which becomes

$$\bar{h}/\bar{h}_o = 1 + \Delta Q_t/Q_{co} \tag{7}$$

when A and ΔT are constant.

Results and Discussion

Free Convection. The convection heat transfer rate Q_{co} from the cylinder at a ΔT_o of 27.8°C was calculated as 4.34 W using Eqs. (3) and (4). The corresponding average Nusselt

Nomenclature

A = area
c_p = specific heat at constant pressure
D = cylinder diameter
d = emitter diameter
E = electrostatic potential, d-c
g = acceleration due to gravity
Gr_D = Grashof number = $g\beta\Delta TD^3/\nu^2$
h = average convection coefficient = $Q_c/A\Delta T$
I = electrical current, a-c or d-c
k = thermal conductivity
L = cylinder length
$\overline{\mathrm{Nu}}_D$ = average Nusselt number = $\bar{h}_o D/k$
P = emitter power = EI, d-c
Pr = Prandtl number = $\mu c_p/k$
Q = heat transfer rate
Q_{ro} = radiation heat transfer rate = $\sigma\epsilon A(T_w^4 - T_a^4)$
R = electrical resistance
Re_D = Reynolds number = $\rho VD/\mu$
s = emitter-to-cylinder spacing
T = temperature
ΔT = temperature difference = $T_w - T_a$
V = velocity
β = thermal expansion coefficient
ϵ = emissivity
μ = dynamic viscosity
ν = kinematic viscosity
ρ = density
σ = Stefan-Boltzmann constant

Subscripts

a = ambient
c = convection (cylindrical surface)
e = ends of cylinder
o = no electrostatic field (free convection)
r = radiation (cylindrical surface)
t = total
w = surface of cylinder

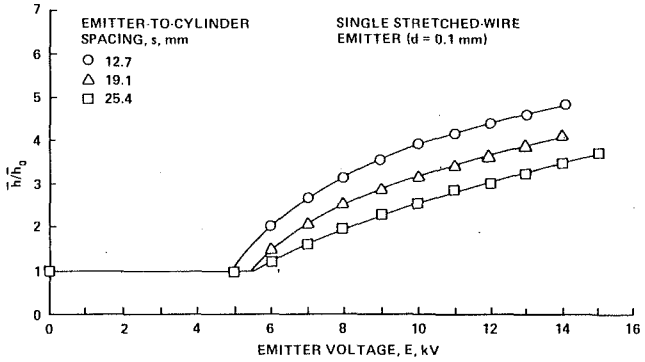

Fig. 2 Effect of wire emitter voltage and spacing on heat transfer rate

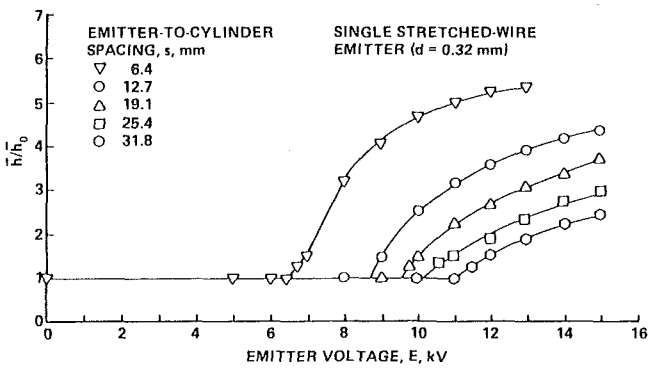

Fig. 3 Effect of wire emitter voltage and spacing on heat transfer rate

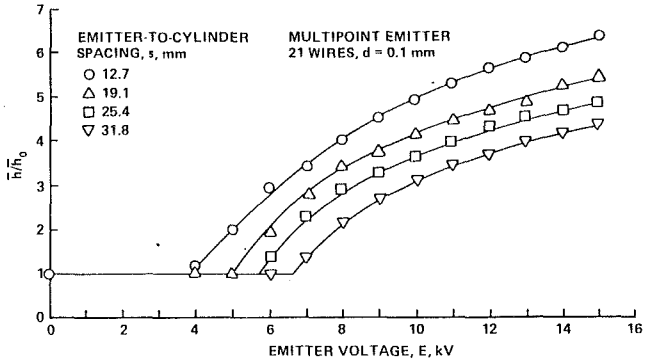

Fig. 4 Effect of multipoint emitter voltage and spacing on heat transfer rate

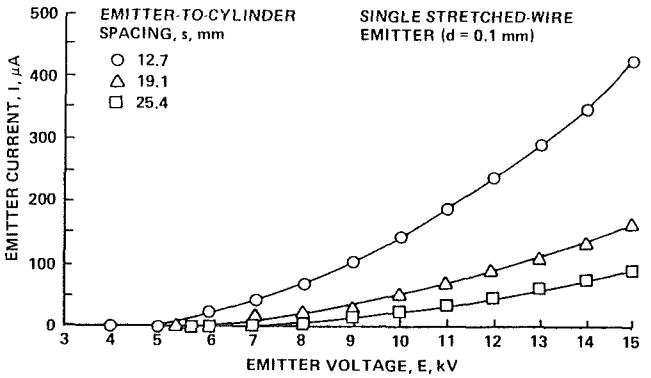

Fig. 5 Emitter voltage-current characteristics

number $\overline{\mathrm{Nu}}_D$ was 7.2 and the heat transfer coefficient $\bar{h}_o$ was 7.7 W/m^{2}K.

The radiation heat transfer rate Q_{ro} from the aluminum cylinder based on an emissivity of 0.07 was calculated to be 0.27 W. The heat transfer rate Q_{eo} from the ends of the cylinder was calculated as 0.23 W. Together, the radiation and end losses amounted to 0.5 W. Thus, the calculated total heat transfer rate from the cylinder in free convection was Q_{to} = 4.84 W. This calculated value was within 2 percent of the measured heater power input rate of 4.91 W. Also, almost 90 percent of the heat transfer was by convection from the cylindrical surface.

The average heat transfer rate from the cylinder in free convection measured with the interferometer was 4.6 W. This value also compares favorably (within 6 percent) with the calculated convection rate of 4.34 W. This is quite good considering the effect of the thermal boundary layer from the ends of the cylinder on the measurement. With the relatively good agreement between the experimental and calculated values, the free convection baseline values appear reasonably accurate. This also substantiates that the radiation and end losses were relatively small compared with the convection heat transfer from the cylindrical surface.

Corona Wind. Heat transfer results for three different emitters are shown in Figs. 2–4 for several different emitter-to-cylinder spacings. The results are presented in terms for the ratio $\bar{h}/\bar{h}_o$ as a function of emitter voltage. Increases in heat transfer rate as high as five to six times the free convection rate were obtained. The amount of increase depended on the emitter-to-cylinder spacing and the emitter voltage. The shapes of the curves were similar for all test configurations.

In all cases, a voltage greater than breakdown voltage was required before the heat transfer rate was affected. The breakdown voltage is considered as that value of voltage when current begins between the emitter and the cylinder. The breakdown voltage decreased as emitter diameter was decreased and as the spacing between the emitter and the cylinder was decreased. Voltage-current characteristics for the 0.1-mm-dia emitter are shown in Fig. 5. Increases in emitter voltage beyond breakdown increased the current, the corona wind, and the heat transfer rate from the cylinder.

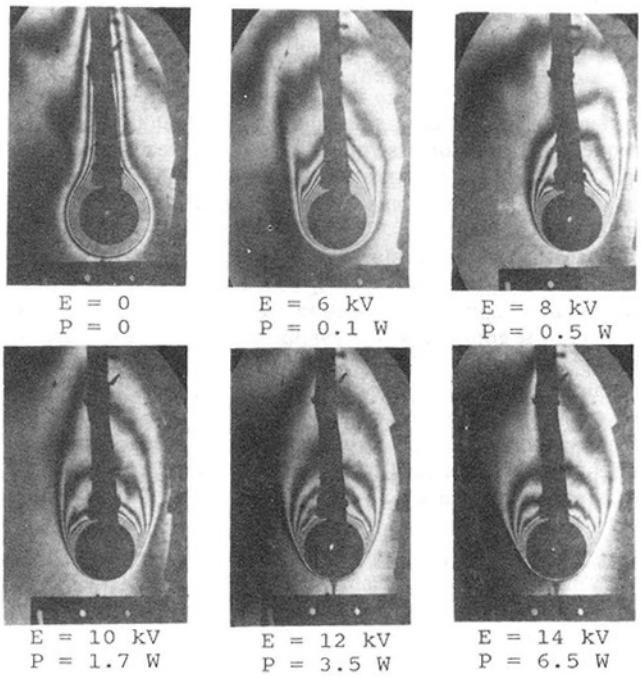

Fig. 6 Interferometer photographs of effect of corona wind on the thermal boundary layer with stretched-wire emitter (d = 0.1 mm, s = 12.7 mm)

Interferometer photographs illustrating the thermal boundary layer around the cylinder at selected values of emitter voltage are shown in Fig. 6. The photographs are for the 0.1-mm-dia wire emitter at an emitter spacing of 12.7 mm and correspond to the upper curve in Fig. 2. No effect on the boundary layer was observed until breakdown voltage was

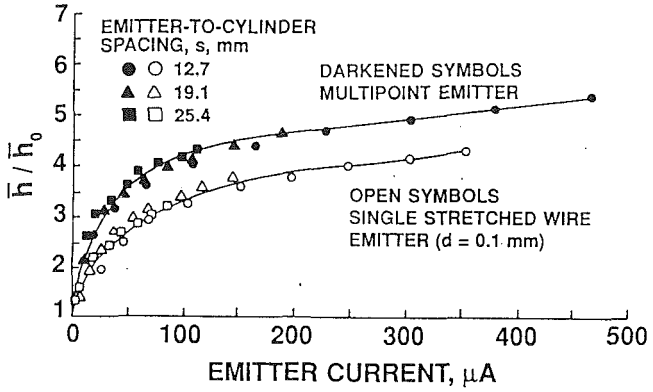

Fig. 7 Effect of emitter current on heat transfer rate

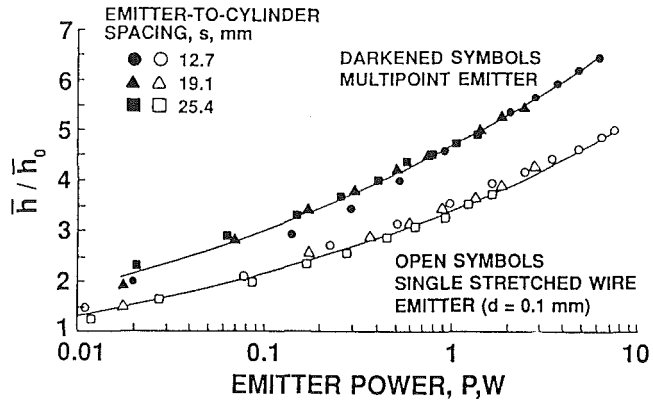

Fig. 8 Effect of emitter power on heat transfer rate

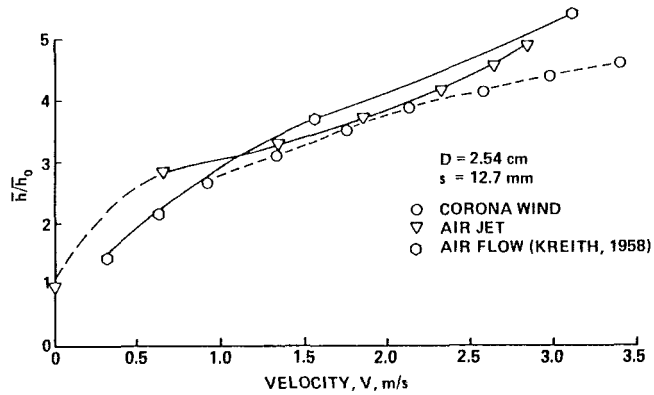

Fig. 9 Cooling effectiveness of corona wind, blowing air jet, and uniform air flow

reached. At an emitter voltage of 6 kV and above, the boundary layer on the lower surface of the cylinder is visibly thinner, indicating increased temperature gradients and increased heat transfer rates. At voltages at 12 kV and above, a thermal effect of the electrostatic discharge below the cylinder can be seen in the photographs. The emitter cannot be seen in the photographs because the brackets holding it block it from view. The slight asymmetry for the 8 kV case in Fig. 6 was probably due to a small ambient disturbance at the instant the photograph was taken.

The heat transfer results in Figs. 2 and 4 are correlated with emitter current and power in Figs. 7 and 8, respectively. For a given emitter the heat transfer rates are relatively independent of emitter-to-cylinder spacing. Also, for a given current or power level, the multipoint emitter was more effective than the wire emitter in increasing the heat transfer rate. Even at the highest emitter power input, the power requirement was still less than the increase in heat transfer rate.

The corona wind velocity was measured at 12.7 mm from the wire without the cylinder present for various values of voltage. The discharge was realized in this case by grounding the probe of the direct-reading air flow meter. By correlating the voltage with those in Fig. 2, corresponding heat transfer rates were related to velocity (Fig. 9). Correlation of the results in Fig. 9 with those in Fig. 7 shows that the ratio of $V/\sqrt{I}$ is relatively constant over the range shown. These results agree with those of Yabe et al. (1978), who found that the velocity of the corona wind increased with the square root of current. Thus, the results in Fig. 7 suggest that the multipoint emitter was more effective in increasing the velocity of the corona wind for a given current.

Blowing Air Jet. The effectiveness of blowing air issuing from a slot approximately 0.4 mm wide and 30 cm long on cooling the cylinder was obtained over a range of air velocities up to approximately 3 m/s. The velocities were measured at 12.7 mm from the slot over a range of plenum pressures without the cylinder present. The same pressure conditions were reestablished in the plenum with the cylinder present and heat transfer rates were obtained. The cooling effectiveness of the blowing air jet is shown in Fig. 9. For an equivalent velocity, the heat transfer rate of the air jet was approximately the same as that of the corona wind. Based on measured velocity, the Reynolds number Re_D ranged up to approximately 5000 at 3 m/s.

Heat transfer rates given by Kreith (1958) for uniform air flow over a 2.54-cm-o.d. pipe are also plotted in Fig. 9. The heat transfer rates with uniform air flow were somewhat higher than those obtained with the corona wind and the blowing air, as shown in Fig. 9. This higher heat transfer rate might be expected since the velocities measured with the corona wind and the air jet were centerline or maximum velocities. The results of Yabe et al. (1978) are also of interest here. Yabe measured the dynamic pressure due to the oncoming flow on a 0.1-m-square flat plate located 0.02 m above the wire and found that a corona wind velocity of 1.4 m/s at centerline decreased to an estimated 0.8 m/s at 0.013 m from the centerline. The velocity magnitudes found by Yabe are in the same range as those in this study. Also the distance from the centerline noted above is equivalent to the radius of the cylinder in this study. The overall agreement of the three methods indicates that corona wind cooling is somewhat similar to air jet cooling and to air in uniform crossflow over a cylinder for the range of velocities considered.

Conclusions

Heat transfer rates from a horizontal cylinder were increased as much as six times the free convection rate by electrostatic cooling. No increase in the heat transfer rate was observed until breakdown voltage occurred and there was a current between the emitter and the cylinder. Emitter size and distance from the cylinder affected the value of the breakdown voltage and the heat transfer rate. For a given emitter, the heat transfer rate varied with emitter current or power. Compared with the stretched-wire emitter, the multipoint emitter was more effective in increasing heat transfer rates at a given power level. For the same velocity, the heat transfer rates due to air jet cooling and electrostatic cooling were approximately the same. Based on the heat transfer results, the velocity of the corona wind was found to increase with the square root of the current.

References

Franke, M. E., and Hutson, K. E., 1984, "Effects of Corona Discharge on Free-Convection Heat Transfer Inside a Vertical Hollow Cylinder," ASME JOURNAL OF HEAT TRANSFER, Vol. 106, pp. 346–351.

Kennard, R. B., 1932, "An Optical Method for Measuring Temperature Distribution and Convection Heat Transfer," *Bureau of Standards Journal of Research*, Vol. 8, pp. 787–805.

Kreith, F., 1958, *Principles of Heat Transfer*, International Textbook Company, Scranton, PA.

Marco, S. M., and Velkoff, H. R., 1963, "Effect of Electrostatic Fields on Free-Convection Heat Transfer From Flat Plates," ASME Paper No. 62-HT-9.

O'Brien, R. J., and Shine, A. J., 1967, "Some Effects of an Electric Field on Heat Transfer From a Vertical Plate in Free Convection," ASME JOURNAL OF HEAT TRANSFER, Vol. 89, pp. 114–115.

Robinson, M., 1961, "Movement of Air in the Electric Wind of the Corona Discharge," *AIEE Transactions*, Vol. 80, pp. 143–150.

Rohsenow, W. M., and Choi, H., 1961, *Heat, Mass, and Momentum Transfer*, Prentice-Hall, Inc., Englewood Cliffs, NJ.

Velkoff, H. R., 1962, "Electrofluidmechanics: A Study of Electrokinetic Actions in Fluids," Report No. ASD-TR-61-642, Propulsion Laboratory, Aeronautical Systems Division, Wright Patterson AFB, OH.

Yabe, A., Mori, Y., and Hijikata, K., 1978, "EHD Study of the Corona Wind Between Wire and Plate Electrodes," *AIAA Journal*, Vol. 16, No. 4, pp. 340–345.

ERRATA

We are sorry to report an error that has carried into the following two ASME papers:

> Y. Elkassabgi and J. H. Lienhard, "Influences of Subcooling on the Burnout of Horizontal Cylindrical Heaters," ASME JOURNAL OF HEAT TRANSFER, Vol. 110, No. 2, 1988, pp. 479–486,

where it appears in Eqs. (19) and (21), and again in the abscissa of Fig. 8, and

> J. H. Lienhard, "Burnout on Cylinders," ASME JOURNAL OF HEAT TRANSFER, 50th Anniversary Issue, Vol. 110, No. 4B, 1988, pp. 1271–1286,

where it appears in Eqs. (29) and (31), and again in the abscissa of Fig. 14.

In each case:

> $Ja/Pe^{1/4}$ should be changed to $Ja/Pe^{1/2}$.

Inverse Heat Conduction Applied to the Measurement of Heat Transfer Coefficient on a Cylinder: Comparison Between an Analytical and a Boundary Element Technique

D. Maillet
Maître de Conférence.
Assoc. Mem. ASME

A. Degiovanni
Professeur.

Laboratoire d'Energétique et de Mécanique Théorique et Appliquée,
Institut National Polytechnique de Lorraine,
Ecole Nationale Supérieure d'Electricité et de Mécanique,
54516 Vandoeuvre les Nancy Cedex, France

R. Pasquetti
Chargé de Recherche CNRS,
Laboratoire de Mathématiques,
Université de Nice, Faculté des Sciences,
06034 Nice, France

A new method using either an analytical or a boundary element inverse technique, is developed for measurement of local heat transfer coefficients. The direct model calculates the temperature field inside a cylindrical pipe. This is submitted to a given heat transfer coefficient angular profile on its outer radius and on an uniform temperature on its inner radius. Experimental temperature measurements inside the cylinder are processed by two techniques. Their results are very close and coherent with those of other authors. Variation of the cylinder conductivity with temperature, implemented by the boundary element technique, seems to show that the averaging of its value yields a regularization effect.

1 Introduction

Measuring the local heat transfer coefficient h by a direct method between a point M on a wall and a fluid at temperature T_e, poses a difficult problem: One has to measure at the same spot both a wall temperature T and a heat flux Q, which passes through section of area ΔS centered at M as shown in Fig. 1.

In the case of cylindrical geometry, typical of a crossflow heat exchanger for instance, this problem is easier to solve since the sensor section can be moved by revolving the cylinder. Heat flux is generally produced by an electrical resistance. This is either a metal foil rolled around the cylinder (uniform heat flux density) as used by Zukauskas and Ziugzda (1985) or it is located at M with guard rings, compensation resistances, and heat generation on the cylinder axis; see Martin and Gosse (1968). In these experiments the probe is unable to measure the local wall temperature with precision if it is not uniform. Moreover heat loss evaluation proves to be difficult.

Another method has been recently developed by Maillet and Degiovanni (1989). It involves estimating the Fourier boundary condition on the outer surface of the cylinder (the h coefficient), starting from temperature measurements inside the cylinder and a known boundary condition on an inner surface. This inverse conduction method is based on an analytical solution of the energy equation. It has been successfully tested on experimental temperature measurements. Its main limitation stems from the linear character of the direct model used. The purpose of this paper is to examine whether a nonlinear phenomenon—a temperature-dependent conductivity of the cylinder material—has a significant effect on the transfer coefficient profile on the cylinder. The results of Maillet and Degiovanni are compared with results obtained from the same experimental measurements using a boundary element solution developed by Pasquetti and Le Niliot (1990).

The direct model for both techniques will be presented first. The inverse problem will then be examined and the two inversion procedures will be implemented starting from the same experimental measurements.

Contributed by the Heat Transfer Division for publication in the JOURNAL OF HEAT TRANSFER. Manuscript received by the Heat Transfer Division June 12, 1990; revision received February 1, 1991. Keywords: Conduction, Measurement Techniques, Numerical Methods.

2 Direct Heat Transfer Problem

Temperature T at a point P inside a cylindrical pipe, limited by two surfaces of radii r_1 and r_2, is sought as a function of polar coordinates (r, Φ) as shown in Fig. 2. A uniform temperature T_1 is fixed on the inside radius r_1 and a heat transfer coefficient h, which varies with angle Φ, is given on the outer radius r_2. We were interested in cases where h shows a symmetry with respect to the plane $\Phi = 0$.

Analytical Solution. The temperature field is the solution of the heat equation associated with its boundary, parity, and periodicity conditions:

$$\frac{\partial^2 T}{\partial r^2} + \frac{1}{r}\frac{\partial T}{\partial r} + \frac{1}{r^2}\frac{\partial^2 T}{\partial \Phi^2} = 0 \tag{1}$$

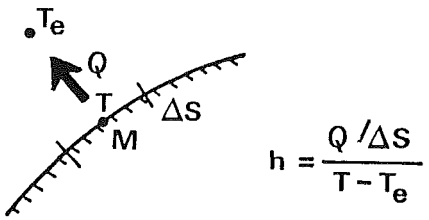

Fig. 1 Direct measurement of local heat transfer coefficient

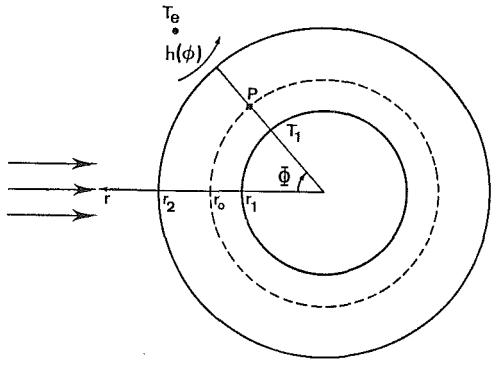

Fig. 2 Model geometry

$$\begin{cases} T \text{ even function in } \Phi & (2) \\ T \text{ periodical of period } 2\pi \text{ in } \Phi & (3) \\ T = T_1 \text{ at } r = r_1 & (4) \\ -k\dfrac{\partial T}{\partial r} = h(\Phi)[T - T_e] \qquad \text{at } r = r_2 & (5) \end{cases}$$

Condition (5) forbids the use of the method of separation of variables because of the nonconstant value of coefficient h.

To overcome this difficulty it is possible to use the "interface flux method" already tested by Degiovanni et al. (1984). This is close to the "Heat-Flux-Based Unsteady Surface Element" method developed by Keltner and Beck (1981) in the transient regime. It consists, first, in fixing a condition of variable heat flux density φ $(= Q/\Delta S)$ at the outer surface and writing condition (5) in the following way:

$$-k\frac{\partial T}{\partial r} = \varphi\ (\Phi) \tag{5}$$

This problem can then be solved, temperature T being expressed in terms of the function φ (Φ). This heat flux density can be expressed in terms of the known function h (Φ), using the equality of the right-hand terms of Eqs. (5) and (6).

In order to make condition (4) homogeneous we made a change of function:

$$\theta\ (r, \Phi) = T_1 - T\ (r, \Phi) \tag{7}$$

The problem is now linear, with constant coefficients, and is homogeneous. It can be solved by separation of variables (see Ozisik, 1980):

$$\theta\ (r, \Phi) = \mu \sum_{n=0}^{\infty} a_n\, g_n(x) \cos n\,\Phi \tag{8}$$

with

$$\mu = 2r_2/k\pi \qquad x = r/r_2 \qquad e = r_1/r_2$$

$$g_0(x) = \frac{1}{2}\ell n\ (x/e)$$

$$g_n(x) = \frac{1}{nx^n}\,\frac{x^{2n} - e^{2n}}{1 + e^{2n}} \text{ if } n \geq 1$$

$$a_n = \int_0^{\pi} \varphi\ (\Phi')\, \cos n\,\Phi'\, d\Phi' \tag{9}$$

The function φ is the solution of the following integral equation:

$$\varphi(\Phi) = h(\Phi)[\theta_e - \theta_2\ (\Phi)] \tag{10}$$

with

$$\theta_e = T_1 - T_e \qquad \theta_2(\Phi) = \theta(r_2, \Phi)$$

It can be put as follows:

$$\mu \int_0^{\pi} Q(\Phi, \Phi')\varphi(\Phi')\, d\Phi' + \varphi(\Phi) = \theta_e h(\Phi)$$

with

$$Q(\Phi, \Phi') = h(\Phi) \sum_{n=0}^{\infty} g_n(1) \cos n\Phi \cos n\Phi'$$

This problem is solved in the particular case where φ is a piecewise constant function of angle Φ on N intervals:

Nomenclature

a_n = coefficient in direct analytical model (DAM)
A = DAM matrix
B = inverse analytical model (IAM) matrix
Bi = Biot number $= h_m r_2/k$
C = DAM matrix
c = specific heat
$\mathbf{d}$ = vector in DAM
e = coefficient in DAM
e_h = norm in IAM
E, F, M = matrices
g_n = coefficient in DAM
$G\ G'$ / $H\ H'$ = BEM matrices
h = local heat transfer coefficient
k = thermal conductivity
K = Kirchhoff transformation
L = number of boundary elements in BEM
L' = number of domain internal points in BEM
N = number of surface intervals in DAM
N_1 = number of equations in BEM
N_2 = number of unknowns in inverse BEM
$\mathbf{n}$ = outward pointing normal unit vector
$\mathbf{p}$ = vector in IAM
$\mathbf{P}$ = vector in IBEM
q = temperature normal derivative
Q = wall heat flux $(r = r_2)$
$\mathbf{Q}$ = vector-temperature normal derivative
r = radius
R = regularization matrix in IBEM
R_T = temperature residual in IAM
S, S' = least-square sums
$T, \mathbf{T}$ = temperature and temperature vector
U = matrix in IBEM
$\mathbf{u}$ = vector in Analytical Model (AM)
x = reduced radius $= r/r_2$
X = sensitivity matrix in AM
$\mathbf{X}, \hat{\mathbf{X}}$ = vector of the unknowns and its estimate in IBEM
X_T, X_r = sensitivity coefficients
$\mathbf{y}$ = measured temperature vector
α = coefficient in BEM
γ = regularization coefficient
Γ = domain boundary in BEM
δ_{ij} = Kronecker symbol
δ_M = Dirac impulse at point M
Δ = variation, or Laplacian
ϵ = temperature error vector
θ = temperature difference $(T_1 - T)$
μ = coefficient in DAM
ρ = mass density
Φ, Φ' = polar angle
$\boldsymbol{\Phi}$ = polar angle vector
$\varphi, \boldsymbol{\varphi}$ = wall heat flux density $(r = r_2)$ and corresponding vector
ψ = function: case of temperature-dependent conductivity
∇ = nabla operator

Subscripts

0 = relative to measurement radius
1 = denotes cylinder internal radius
2 = denotes cylinder external radius
e = denotes gaseous environment
m = average value over boundary (perimeter)
M = relative to point M
ϵ = depending on the measurement noise
γ = depending on the regularization coefficient

Superscripts

$*$ = Green function
$\hat{}$ = estimated value
$\bar{}$ = average value over one boundary interval in DAM
t = transpose of a matrix
c = one-dimensional corrected value

$$\varphi(\Phi)=\varphi_i \quad \text{for} \quad \Phi_{i-1}\le\Phi<\Phi_i$$

with

$$\Phi_i=i\pi/N \quad \text{and} \quad 1\le i\le N$$

The a_n coefficients can then be expressed using Eq. (9) and the discrete values φ_i. Temperature θ is thus a linear combination of these φ_i's:

$$\theta(r,\ \Phi)=\sum_{i=0}^{N} d_i\ (x,\ \Phi)\ \varphi_i=\mathbf{d}^t\varphi \tag{11}$$

The average heat transfer coefficient on each interval is

$$h_i=\varphi_i/(\theta_e-\bar{\theta}_{2i}) \tag{12}$$

The average temperature $\bar{\theta}_{2i}$ on interval number i is calculated by integration of Eq. (11) at the outside radius ($x=1$):

$$\bar{\theta}_{2i}=\sum_{j=1}^{N} C_{ij}\ \varphi_j \tag{13}$$

Equations (12) and (13) show that the heat flux densities φ_i are the solution of the following equation:

$$A\ \varphi=\mathbf{u} \tag{14}$$

with

$$A_{ij}=(C_{ij}+\delta_{ij}/h_i)/\theta_e \quad \text{for } 1\le i\le N$$
$$u_i=1 \quad \text{and } 1\le j\le N$$

δ_{ij} being the Kronecker symbol.

The approximate solution of the direct problem is thus:

$$\theta(r,\ \Phi)=\mathbf{d}^t\ A^{-1}\ \mathbf{u} \tag{15}$$

Boundary Element Solution. In this section continuous and discrete expressions of the boundary element method (BEM) are reviewed in the case of the Laplace equation ($\Delta T=0$). The extension of this method is also considered for the case of a temperature-dependent conductivity.

Let us consider a domain Ω of boundary Γ. For linear steady heat conduction, the fundamental equation of BEM is derived starting from the fact that the integral of the product of the residual of the Laplace equation by a weight function T^* must be equal to zero. It can be shown (see Brebbia, 1978) after double integration of this expression and the choice of a Green function for T^* that any point M of Ω verifies:

$$\alpha\ T_M+\int_\Gamma T\ q^*\ d\ \Gamma=\int_\Gamma q\ T^*\ d\ \Gamma \tag{16}$$

with $q=\partial T/\partial n$; $\alpha=1$ if M belongs to Ω without being located on Γ; $\alpha=0.5$ if M belongs to Γ and if Γ is smooth on a neighborhood of M. T^* is any function such that:

$$\Delta T^*+\delta_M=0\ (\delta_M\text{: Dirac impulse at point } M)$$

T^* $(P;\ M)$ is the so-called "fundamental solution" and q^* stems from its derivative; both expressions depend on the dimension of the space of Ω and on the distance r between points M and P. It can be shown (see Carslaw and Jaeger, 1959) that in our two-dimensional case one can choose

$$T^*=\frac{1}{2\pi}\ell n\ (1/r) \qquad q^*=\nabla T^*\cdot\mathbf{n}=-\frac{\mathbf{r}\cdot\mathbf{n}}{2\pi r^2}$$

$\mathbf{n}$ is the normal outer unit pointing vector.

Only boundary integrals are present in Eq. (16), which means that only a mesh of Γ under the form of "boundary elements" is necessary. The simplest way to proceed is therefore to assume uniform temperature T_j and flux q_j on each element Γ_j. The definitions of coefficients H_{ij} and G_{ij} are

$$H_{ij}=\int_{\Gamma_j} q^*(P;\ M_i)d\Gamma \qquad G_{ij}=\int_{\Gamma_j} T^*(P;\ M_i)d\Gamma$$

leading to the following form of Eq. (16) for boundary element i, L being the total number of elements:

$$\frac{1}{2}T_i+\sum_{j=1}^{L} H_{ij}\ T_j=\sum_{j=1}^{L} G_{ij}\ q_j$$

This equation can be written for each element of Γ. Introducing matrices H and G such as:

$$[H]_{ij}=H_{ij}+\frac{1}{2}\delta_{ij} \qquad \text{and} \qquad [G]_{ij}=G_{ij}$$

leads to the construction of the following system of algebraic equations:

$$H\mathbf{T}=G\mathbf{Q} \tag{17}$$

In the case of the direct problem, taking boundary conditions into account allows a separation between data and unknowns.

If unknowns are gathered into an $\mathbf{X}$ vector, Eq. (17) can be rewritten under the form of a system of linear equations whose solution is $\mathbf{X}$. Once this system is solved, $\mathbf{T}$ and $\mathbf{Q}$ are known and it is possible to determine temperature at any internal point M' introducing coefficients H'_{ij} and G'_{ij} as already defined, but with $\alpha=1$ instead of $\alpha=0.5$:

$$T'_i+\sum_{j=1}^{L} H'_{ij} \quad T_j=\sum_{j=1}^{L} G'_{ij}\ q_j$$

This equation, written at L' internal points, can be shown as follows, using matrices H' and G' of elements H'_{ij} and G'_{ij}:

$$\mathbf{T}'=-H'\ \mathbf{T}+G'\ \mathbf{Q} \tag{18}$$

If thermal conductivity depends on temperature the problem becomes nonlinear in the domain. The use of Kirchoff transformation allows return to the linear case:

$$\psi=K(T)=\int_0^T k(T')dT'$$

with its consequence on the heat equation:

$$\nabla\ (k\ \nabla\ T)=\Delta\psi$$

The use of Kirchoff transformation substitutes a mixed nonlinear boundary condition to the Fourier condition of our problem. But this type of condition is no harder to handle by BEM than by any traditional numerical method, because the variables are located precisely at the boundary. Our approach uses local linearization, which means, after discretization, linearizations specific to each boundary element; see Pasquetti and Caruso (1990).

Direct Model Results. The analytical direct model was tested for a function h (Φ) representative of crossflow convective cooling of a cylinder in the subcritical regime: constant value equal to 250 $\mathrm{Wm^{-2}K^{-1}}$ on [0, 40 deg] followed by a linear decrease until 100 $\mathrm{Wm^{-2}K^{-1}}$ on [40, 80 deg] and a linear increase until 200 $\mathrm{Wm^{-2}K^{-1}}$ on [80, 180 deg]. $\Phi=0$ is the direction of the upstream flow and the parameters are

$$r_1=8\ \text{mm} \quad r_2=16\ \text{mm} \quad k=0.26\ \mathrm{Wm^{-1}K^{-1}} \quad \theta_e=40^\circ\mathrm{C}$$

An inner temperature profile obtained by the analytical solution for a radius r_o equal to 14 mm was plotted in Fig. 3 for a choice of 18 intervals. It should be noted that temperature variations can be measured (about 2.5°C amplitude). It has been shown that the sensitivity to the number of intervals is weak for this optimum value of N; when N was given the successive values 5, 9, 18, and 36, the maximum temperature difference was reduced from 0.15 to 0.12 and then to 0.02°C, while the mean quadratic difference was reduced from 0.072 to 0.030 and then to 0.005°C.

The temperature profile obtained from the boundary element solution was very similar to the previous one, differences being always lower than 0.05°C for a single angle.

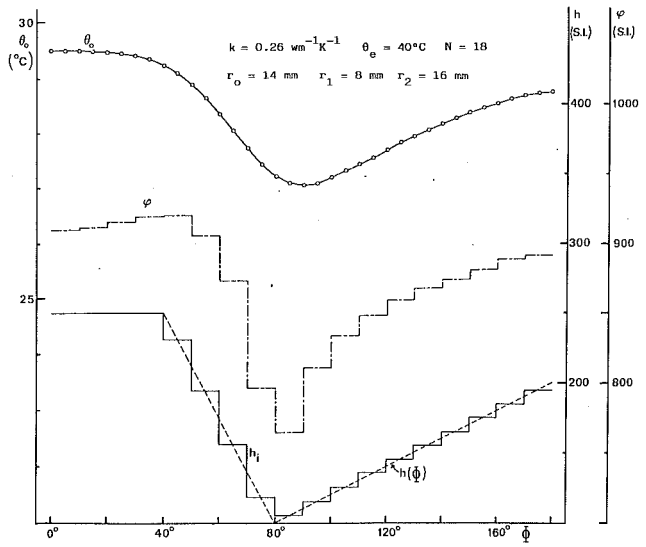

Fig. 3 Results of the direct model

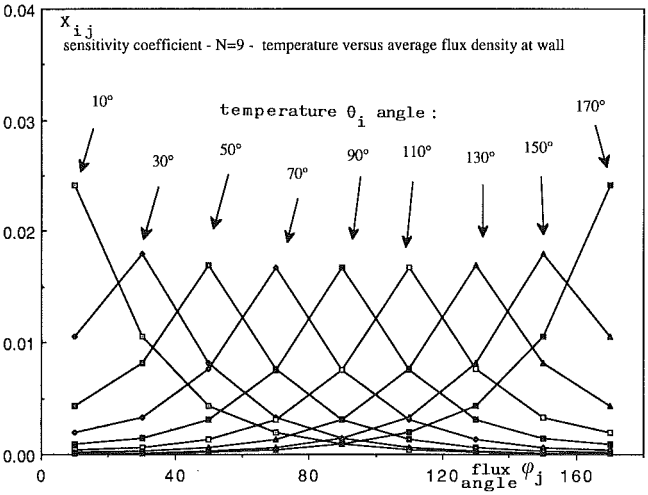

Fig. 4 Wall sensitivity coefficient X_{ij}

We can notice that Eq. (13) gives us a valuable insight into the difficulty of separate measurements of ΔT and φ at the wall. By use of the Beck and Arnold method (1977) we can define the sensitivity coefficient X_{ij} of the average wall temperature $\bar{\theta}_{2i}$ on the ith interval to the average heat flux density $\bar{\varphi}_j$ at the jth interval:

$$X_{ij} = \frac{\partial \bar{\theta}_{2i}}{\partial \varphi_j} = C_{ij} \tag{19}$$

This sensitivity coefficient is independent of the boundary conditions of the temperature field in the cylindrical pipe, the problem being linear in φ. We plotted X_{ij} for nine intervals, a shape factor e of 0.5 and preceding values of radius r_2 and conductivity k in Fig. 4. It shows the rather strong thermal coupling between different sections at the outer surface of the cylinder when the Biot number Bi ($=r_2 h_m/k$) is high enough. φ_j can be normalized by φ_m and $\bar{\theta}_{2i}$ by θ_e in Eq. (19). The average heat transfer coefficient h_m is defined in the following way:

$$h_m = \varphi_m/(\theta_e - \theta_{2m}) \tag{20}$$

φ_m and θ_{2m} being the average values of φ and θ_2 on $[0, \pi]$.

The dependence of X_{ij} on angle Φ_j for different values of i and j and the not-too-weak values of Bi shows the impossibility of measuring a local value of h by a single measurement of temperature and flux at the same location. This effect stems from the tangential conductive transfer at the wall.

3 Inverse Problem

Analytical Method. In this problem conditions (2)–(4) remain unchanged while condition (5) is replaced by a fixed temperature condition at $(N+1)$ points on an internal radius r_o of the pipe:

$$\theta(r_o, \Phi_i) = \theta_{oi} \quad \text{for } 0 \le i \le N \tag{21}$$

Equation (11), valid for a linear problem, can be written in the following way:

$$\theta_o = B\,\varphi \text{ with } B_{ij} = d_j(x_o, \Phi_i) \tag{22}$$

If measured temperatures are exact, Eq. (22) can be solved to find heat flux densities.

Actually experimental temperature measurements always present some uncertainty, and the abovementioned method is no longer valid. We call $y_{\epsilon i}$ the value of θ_{oi} measured at radius r_o and angle Φ_i, θ_{oi} the exact corresponding value, and ϵ_i the random error that is assumed to be additive:

$$y_{\epsilon i} = \theta_{oi} + \epsilon_i \tag{23}$$

To take this noise into account it is possible to use a least-squares method, which consists of minimizing the sum S of the quadratic differences ϵ_i^2 with respect to the fluxes φ_i that are unknowns. The drawback of this method is that $\varphi(\Phi)$ does not continuously depend on the data y. To assure a certain regularity to the angular variation of φ, a regularization term is added to the previous sum. A second-order term, which represents, under a discrete form, the second derivative of function $\varphi(\Phi)$, has been chosen here. It smoothes the flux fluctuations and stabilizes the problem as Beck et al. (1985) have shown:

$$S = \sum_{i=0}^{N} (y_{\epsilon i} - \theta_{oi})^2 + \gamma \sum_{i=2}^{N-1} (\varphi_{i+1} - 2\varphi_i + \varphi_{i-1})^2 \tag{24}$$

The fluxes are solutions of the following equation:

$$\frac{\partial S}{\partial \varphi_\ell} = 0 \quad \text{for } 1 \le \ell \le N \tag{25}$$

which can be put into the form:

$$E\,\varphi_{\epsilon,\gamma} = \mathbf{p}_\epsilon \tag{26}$$

with $E = B^t B + \gamma F^t F$ and $\mathbf{p} = B^t y_\epsilon$, F being a tridiagonal matrix of dimensions (N, N).

System (26) can be solved in φ and heat transfer coefficients can be calculated as before.

Analytical Inversion From Simulated Measurements. In order to test this inverse method we have implemented it on simulated measurements for various values of the regularization parameter γ. These simulated measurements come from the temperature profile θ_0, the output of the direct model (see Fig. 3), which was modified by a random additive noise ϵ, of standard deviation σ, according to Eq. (23). The output $\hat{h}$ of this model was an estimate of the heat transfer coefficient profile h, the input of the direct model. The results are presented in Fig. 5.

In the absence of regularization ($\gamma = 0$), a low noise level ($\sigma = 0.05$°C) led to important oscillations of $\hat{h}$ after the minimum value of h ($\Phi = 80$°C). Therefore it justifies the choice of the second-order regularization, which limits the $\hat{\varphi}$ oscillations (and hence the $\hat{h}$ ones) as Beck et al. (1985) have shown.

In the case of nonzero values for γ (10^{-4} and 10^{-8}), for the same noise level, agreement between the $\hat{h}$ and h profiles becomes quite good, especially in the last case. It should be noted that in that case with noise ten times higher ($\sigma = 0.5$°C), the

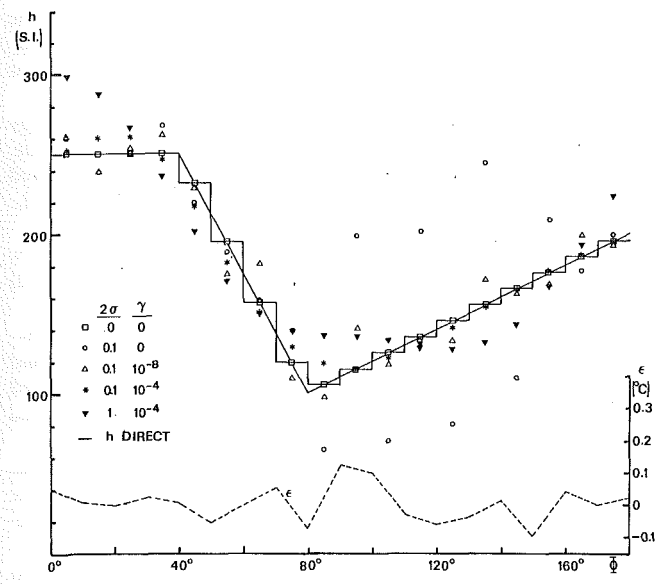

Fig. 5 Inversion from simulated measurements

inverse model still yields the general shape of the direct h profile.

The choice of γ is a point of very practical importance: Its level must be adjusted as a function of the noise in the data. In this preliminary work we have chosen to minimize the following norm based on the estimated and exact heat transfer coefficients (average square error):

$$e_h^2 = \frac{1}{N}\sum_{i=1}^{N}(\hat{h}_i - h_i)^2$$

The temperature residual R_T can also be calculated starting from the estimated temperature profile $\hat{\theta}_0$ calculated as a function of the estimated heat-flux densities $\hat{\varphi}$ (output of the inverse model):

$$R_T^2 = \frac{1}{N}\sum_{i=0}^{N}(\hat{\theta}_{0i} - y_i)^2$$

For a noise ϵ of standard deviation $\sigma = 0.05°C$, applied on the temperature profile of Fig. 3 ($r_0 = 14$ mm), the adjusted value of γ that minimized e_h is the following:

$$\gamma = 1.5 \times 10^{-6}$$

with $e_h = 2.68$ W m^{-2} K^{-1} and $R_T = 0.045$ K.

It should be noted that the temperature residual R_T, that is, the fraction of temperature not justified by the model, is very close to the measurement error standard deviation σ. This is the recommendation made by Tikhonov and Arsenine (1976) for the selection of the regularization parameter.

Simulated measurements without any noise were used as an input of the inverse model for that adjusted value of γ. The identified h profile was very close to the original one ($e_h = 1.67$ W m^{-2} K^{-1}), which shows that the determinist bias is very small.

Boundary Element Method. Equations (17) and (18) can be rewritten in the following way:

$$\begin{bmatrix} H \\ H' \end{bmatrix} \mathbf{T} = \begin{bmatrix} G \\ G' \end{bmatrix} \mathbf{Q} + \begin{bmatrix} 0 \\ -T' \end{bmatrix} \tag{27}$$

This matrix relationship is the base equation of the BEM approach of inverse heat conduction problems as shown by Pasquetti and Le Niliot (1990). As for the direct problem, it is possible to rearrange this equation in order to gather the unknowns into an $\mathbf{X}$ vector and to construct a system of algebraic equations:

$$U\,\mathbf{X} = \mathbf{P} \tag{28}$$

Let $N_1 = L + L'$ be the number of equations and N_2 the number of unknowns of system (28). This system can be solved if N_1 and N_2 are equal. If N_1 is smaller than N_2 no solution can be found and if the opposite is true the system is overdetermined. This last assumption is the one generally met. A suitable solution can be found according to a minimization of the quadratic norm:

$$\|U\,\mathbf{X} - \mathbf{P}\| = (U\,\mathbf{X} - \mathbf{P})^t\,(U\,\mathbf{X} - P) \tag{29}$$

As already underlined, the main difficulty lies in the high sensitivity of measurements to additive noise. Numerical solutions of this type of problem can be stabilized using regularization techniques (see Tikhonov and Arsenine, 1976); form (29) is replaced by:

$$\|U\mathbf{X} - \mathbf{P}\|^2 + \gamma\|R\mathbf{X}\|^2 = (U\mathbf{X} - \mathbf{P})^t\,(U\mathbf{X} - \mathbf{P}) + \gamma X^t\,R^t R\mathbf{X} \tag{30}$$

where the second term of the right member of this equation represents the regularization term, which is added to quadratic form (29).

Matrix R is a function of the regularization order and of the arrangement of the $\mathbf{X}$ components. In the symmetrical problem studied in this article we have chosen a second-order regularization on peripheral fluxes as was done in the analytical approach.

The solution of this optimization problem verifies the following system (N_2 equations with N_2 unknowns), which states that the gradient of functional (30) is equal to zero:

$$(U^tU + \gamma R^tR)\hat{\mathbf{X}} = \mathrm{U}^t\mathbf{P} \tag{31}$$

The solution, which obviously depends on noise ϵ, will be more or less regular depending on the level of the regularization coefficient γ:

$$\hat{\mathbf{X}} = \hat{\mathbf{X}}\,(\epsilon, \gamma)$$

It should be noted that the two inverse models—analytical and boundary elements—rely on the minimization of different functionals. Functional (24) is minimized with respect to the unknown flux densities φ at the outside wall. Functional (30) depends strongly on the boundary element formulation itself. It depends on vector $\mathbf{X}$, which is composed not only of the same flux densities φ or, which is similar, of the same temperature normal derivatives, but also of the temperatures and fluxes that are unknown at the L points of the boundary Γ of the domain; see section 4 for a complete description of domain Ω.

4 Experimental Measurements

Experimental Setup. A cylindrical pipe made out of epoxy resin of 500 mm length, 8 mm inside radius and 16 mm outside radius was built through casting and turning on a copper pipe of diameters 14.0 and 16.0 mm. Three chromel-alumel thermocouples of 0.12 mm diameter were implanted parallel to the cylinder axis. Their junctions were shifted about 120 deg between each other and were located in the transverse plane of symmetry of the cylinder. Nominal radii of implantation were the following:

$$r_o = 14 \text{ mm} \qquad r'_o = 12 \text{ mm} \qquad r''_o = 10 \text{ mm}$$

and the actual radii, measured after destruction of the pipe, were:

$$r_o = 14.02 \pm 0.25 \text{ mm} \qquad r'_o = 12.62 \pm 0.18 \text{ mm}$$
$$r''_o = 9.61 \pm 0.06 \text{ mm}$$

A flow of hot water at 65°C, produced by a thermostat, passed through the central copper pipe to fix the inner boundary condition. The temperature of the copper pipe was also monitored by a thermocouple in that transverse cross section.

The measurement cylinder was set in the channel of a wind

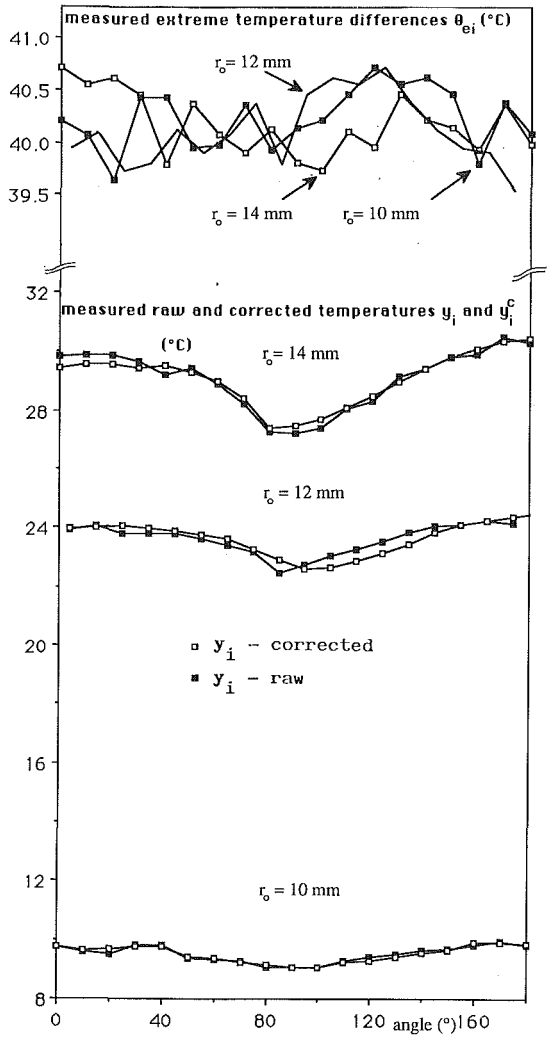

Fig. 6 Experimental temperature measurements

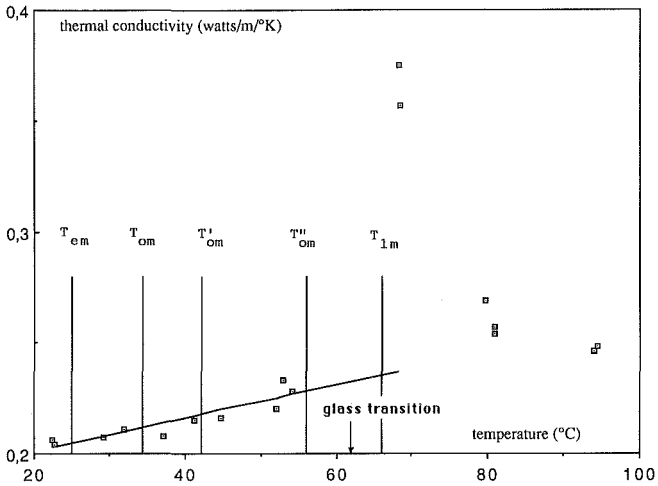

Fig. 7 Thermal conductivity of the resin: variation with temperature and average levels of measured temperatures at different radii

tunnel whose section was 400 × 400 mm and whose turbulence rate was of the order of 1 percent. Air temperature was also measured upstream from the cylinder.

Experimental Procedure. Measurements were made for an upstream air velocity of 30.7 m/s, which corresponds to a Reynolds number of 64,250.

A rotation of the cylinder with a 10 deg step allowed the measurement of a new point for the three probes once a steady regime had been set, which required from 30 to 40 mn (18 or 19 measured temperatures).

Due to the experimental duration and the heat produced by the fan engine, the ambient temperature did not stay constant. For the analytical approach, each measurement must be related to the same extreme temperature difference in the system θ_e. We chose a one-dimensional temperature correction:

$$y_i^c = y_i + \frac{\text{Bi ln } (x_o/e)}{1+\text{Bi ln } (1/e)}(\theta_e - \theta_{ei}) \tag{32}$$

θ_e is the average of the measured extreme temperature differences θ_{ei} for each measurement y_i of θ_{oi} and y_i^c is the corrected value of y_i for a Biot number equal to 10. Raw and corrected temperature profiles as well as the variations of θ_{0i} are presented for each thermocouple in Fig. 6.

For the BEM approach, θ_e is taken as a function of the polar angle without any correction for y_i. For this approach the boundary of the domain has been discretized into $L = 52$ elements. On the internal circle ($r_i \simeq 8$ mm) divided into 18 quadratic elements, temperature is known (Dirichlet condition). At the planes of symmetry ($\Phi = 0$ and 180 deg), divided into 2×8 linear elements, the surface heat flux is equal to zero (Neuman homogeneous condition). On the external circle ($r_2 \simeq 16$ mm), divided into 18 quadratic elements, temperature and surface heat flux are unknown. Measurements have provided $L' = 18$ internal temperatures at points regularly distributed on a circle of radius r_o. Each temperature was interpolated between two measurements, the same being true for θ_{ei} (no one-dimensional correction). System (31) is square, N_1 and N_2 being both equal to 70.

Thermal conductivity of the epoxy resin (Ciba-Geigy CY 1301 + Hardener HY932) was measured indirectly: Calorimetry gave us the specific heat $c(T)$ curve while the flash method yielded the thermal diffusivity $a(T)$ curve. Measurement of the resin density produced the conductivity versus temperature relationship presented in Fig. 7:

$$k(T) = \rho\, c(T)\, a\, (T)$$

The $c(T)$ curve shows that this resin presents a glass transition around 62°C. This transformation can affect the temperature field around the radius r''_o of the most internal probe in these measurements. It can be noted from Fig. 7 as well that the resin's conductivity varies slightly with temperature, about 14 percent between ambient and copper pipe temperature. We therefore had the choice of taking for conductivity k either an average value: $\bar{k} = 0.224$ W/m°K, or a linear variation with T (in °C) obtained by a least-squares regression: $k(T) = 0.186 + 7.52 \times 10^{-4}\, T$.

5 Inversion From Experimental Measurements

Comparison of Techniques. Both techniques—analytical and boundary element—were used to estimate heat transfer coefficients starting from the raw temperature profiles of Fig. 6. A regularization coefficient γ of 10^{-6} and a constant value of 0.224 W/m K for thermal conductivity were used. Results for both techniques are presented in Fig. 8; analytical inversion yields two profiles with the same minimum, the noise being mainly located at the first 50 deg, while boundary element inversion produces three profiles with a minimum shifted to higher angular values when r_o decreases. When compared, the results of the two techniques were close for the highest value (14 mm) of radius r_o. There was a higher dispersion for its lowest value (10 mm), even if the general shape was the same.

Comparison Between Fixed and Temperature-Dependent Conductivity Results. The boundary element technique allows the use of a temperature variable conductivity during

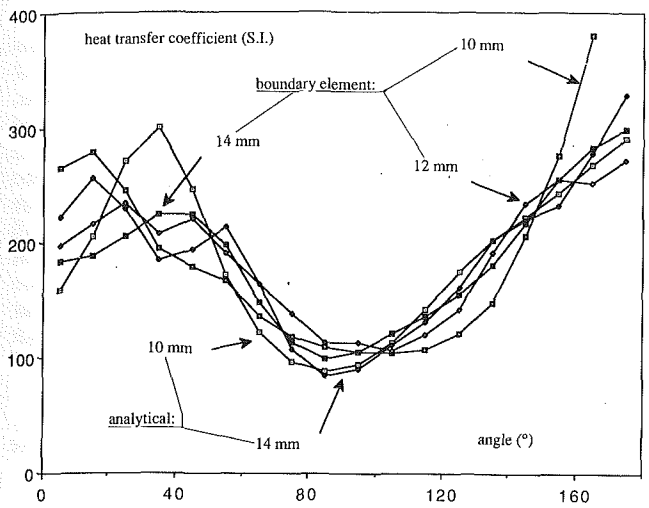

Fig. 8 Inversion from raw measurements

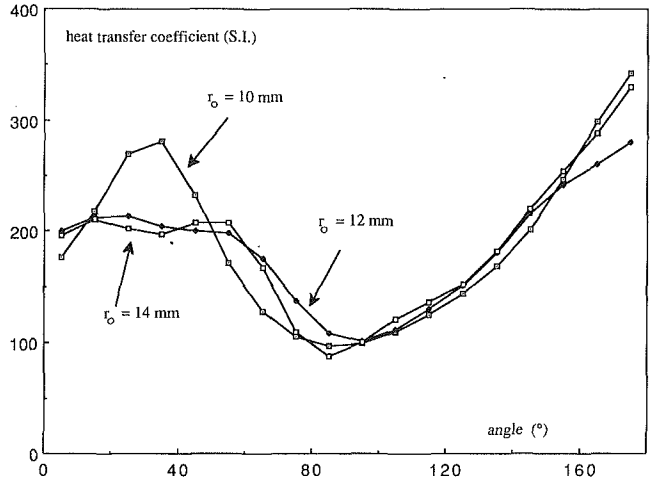

Fig. 10 Analytical inversion t from one-dimensional corrected measurements

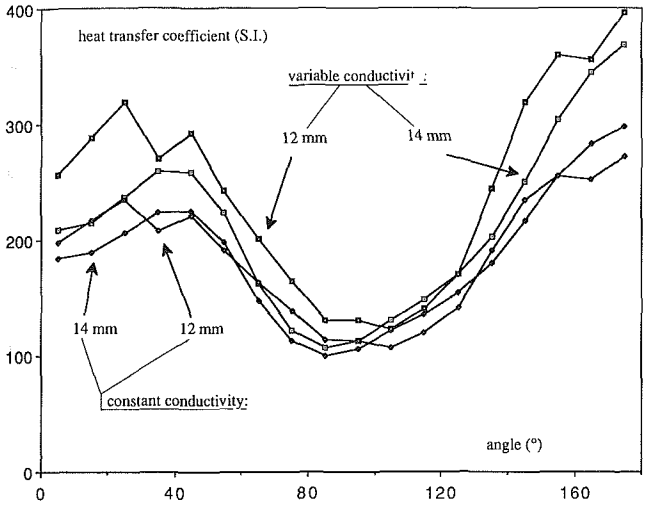

Fig. 9 Boundary element inversion from raw measurements: comparison between constant and temperature-dependent conductivity cases

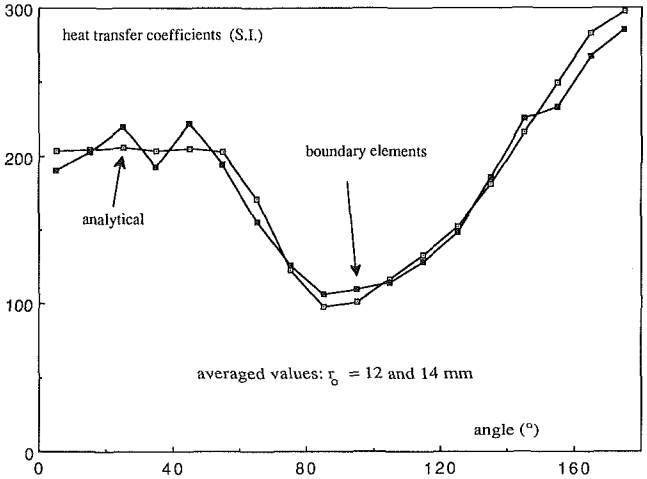

Fig. 11 Comparison of analytical (corrected measurements) and boundary element (raw measurements) inversions

inversion. It is possible to plot in Fig. 9 these h profiles with those obtained in Fig. 8 for a constant conductivity by the boundary element technique. It is interesting to notice that, for a same measurement radius, the two assumptions for conductivity k lead to nearly the same profile, if starting from the variable conductivity case the average value $\bar{k}$ is decreased (h being proportional to k) while the slope of the $k(T)$ relationship is decreased to damp the angular variation of h.

Inversion From Corrected Temperature Profiles. Analytical inversion from a one-dimensional corrected temperature profile was implemented for the three radii and is presented in Fig. 10. The results were close for the two independent temperature profiles measured at 14 and 12 mm: The h coefficient presented a nearly constant value for the first 50 deg, then a minimum close to 90 deg followed by a quasi-linear increase up to 180 deg. It should be noticed that the profile corresponding to 12 mm seems smoother than the 14 mm one because of the interpolation that was made to bring back temperatures to angles that are multiples of 10 deg, the original 12 mm profile being taken at 4 deg, 14 deg, ... Results yielded by the most internal probe at 10 mm depart from the other two between 0 and 50 deg. It could stem from the behavior of the resin in the measured temperature range of this probe (54 to 57°C): The glass transition detected in Fig. 7 occurred between the radius of this probe and the copper pipe close to 66°C. This transformation is not relevant once the steady regime is reached; however, any fluctuation of temperature yields a fluctuation of the degree of advancement of this transformation, which creates a local heat source term, either positive or negative, in the heat equation (1) and modifies the temperature field in the vicinity of this probe.

Comparison of h profiles estimated from raw and corrected measurements by the analytical technique (see Figs. 8 and 10) shows that one-dimensional correction did not produce any distortion on the profile but a smoothing of deviations produced by variations of the ambient temperature.

One can notice in Fig. 10 that the slope of $h(\Phi)$ is not equal to zero at the rear stagnation point. This is contrary to our assumption of symmetry with respect to the direction of the velocity vector on the front side. This may be caused by an effect of natural convection on the horizontal cylinder or by the absence of symmetric measurement points for the analytical approach. In order to take them into account, we added to the sum S defined by Eq. (24) a regularization term S' of the first order, on the two extreme angular intervals where the second derivative cannot be evaluated:

$$S' = (\varphi_2 - \varphi_1)^2 + (\varphi_N - \varphi_{N-1})^2$$

This term was used to flatten the h profile around 0 and 180 deg where the derivative of $h(\Phi)$ should be equal to zero because of symmetry.

Global Results Using the Two Techniques. An average of

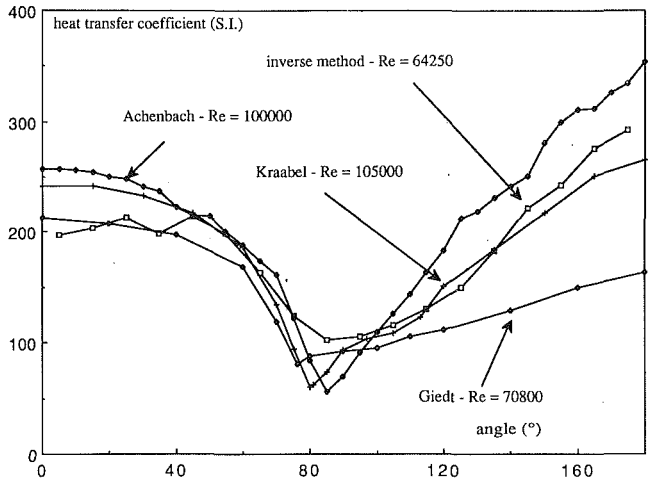

Fig. 12 Comparison with previous measurements

the h profiles with one-dimensional correction for the analytical approach and the presence of this S' term for 12 and 14 mm radii is presented in Fig. 11. One can notice a zero slope near 0 deg and a lower slope than previously at 180 deg.

On the same plot is presented the average of the h profiles for the same two radii by the boundary element technique with constant conductivity; it is interesting to note the total agreement of the two profiles, which means that our approach does not depend on the inverse technique, analytical or boundary elements, used to process the experimental temperatures.

Sensitivity to Temperature Error and Error on the Probe's Location. It has been shown by Maillet and Degiovanni that integration of the heat equation (1) on the [0, π] angular interval produced an r-dependent average temperature θ_m for a given average heat flux density φ_m:

$$\theta_m(r) = \frac{r_2}{k} \ln\left(\frac{r}{r_1}\right) \varphi_m \tag{33}$$

The average heat transfer coefficient h_m (see Eq. (20)) can thus be derived with respect to the average temperature θ_{om} at measurement radius r_o and with respect to r_o to yield analytical expressions for the two relative sensitivity coefficients:

$$X_T = \frac{\Delta h_m}{h_m} \Big/ \frac{\Delta \theta_{om}}{\theta_e} = \frac{(1 + \mathrm{Bi} \ln 1/e)^2}{\mathrm{Bi} \ln x_o/e} \tag{34}$$

$$X_r = \frac{\Delta h_m}{h_m} \Big/ \frac{\Delta r_o}{r_o} = \frac{1 + \mathrm{Bi} \ln 1/e}{\ln x_o/e} \tag{35}$$

For a Biot number Bi equal to 10, a shape factor e of 0.5 and r_o equal to 10, 12, then 14 mm X_T takes the following values: 28, 15, and 11. This means that an absolute error of 0.05°C on temperature at radius 10 mm implies a 3.5 percent relative error on h_m for a temperature difference θ_e of 40°C. For the three radii and identical values of the other parameters X_r takes the following values: 35, 20, and 14, which means that a 0.25-mm error on the measured radius of the external couple (14 mm) will produce a 25 percent error of the average heat transfer coefficient. The only way of getting rid of this error would be to measure the total heat flux leaving the cylinder by calorimetry and then to use Eq. (33) to determine the probe's radius.

Comparison With Previous Measurements. We have plotted on Fig. 12 the average of the two profiles presented in Fig. 11 for the two inversion techniques as well as results obtained by Giedt (1949), Achenbach (1975), and Krabel et al. (1980) for slightly higher Reynolds numbers. The Nusselt number measurements of these three authors have been converted to h values using the radius r_2 of our experiment and the air thermal conductivity. These four profiles present the same qualitative variation but differences may stem from experimental conditions: turbulence rate, blockage factor, and wall boundary condition as Zukauskas and Ziugzda (1985) showed. These differences also come from the intrinsic limitations of measurement methods based on energy balances as shown above. To emphasize this last point one can notice that the three authors' profiles present a very sharp minimum in the vicinity of the separation point of the boundary layer ($\simeq$ 80 deg). This comes from the fact that a local balance cannot take into account tangential conduction at the wall. These methods modify the internal field in the cylinder, in a different way for each measurement point; each measurement does not correspond to the same problem. On the contrary an inverse model allows the experimenter to get rid of this problem.

7 Advantages and Disadvantages of This Inverse Method

The advantages of this inverse method for the calculation of the angular evolution of the local heat transfer coefficient on a cylinder, compared to a method based on energy balances, are the following:

- no distortion of the flux lines: The homogeneity of the measurement cylinder is preserved.
- easy experimental part: no electrical adjustment necessary.
- no need for heat loss estimation.
- knowledge of sensitivity to temperature measurement errors for average values of h.

Many other advantages can be noted:

- exact inversion from errorless measurements (for $\epsilon = \gamma = 0$).
- only one adjustable parameter, γ, the regularization parameter that can be given an adjusted value.
- final profile is independent of the inversion technique—either analytical or boundary element, although these two techniques do not minimize the same functional.
- the constant conductivity assumption leads to a good approximation to the temperature dependent case if this dependence is weak: besides, preliminary study seems to show that a representative average value of this conductivity has a regularization effect.
- very fast computational time: inversion takes a few seconds of computation time on a 386 Personal Computer once matrices of linear systems (26) or (31) have been constructed.

The extension to the case where the heat transfer coefficient angular profile is not symmetric or to a case where it is the inner boundary condition, which is unknown, does not present any particular problem.

One limiting requirement for a precise use of this method is the need to measure separately by calorimetry either the total heat flux leaving the cylinder with the same measurement pipe or the Nusselt number for the global heat transfer under similar conditions. In both cases a calculation of the average wall heat flux density will remove the uncertainty on the temperature probe location (see Eq. (35)), which has a tremendous effect on the average level of h, and will allow a precise choice of the representative thermal conductivity if this parameter varies slightly with temperature. As in other inverse methods an estimate of the errors is quite delicate to obtain (see Groetsch, 1984).

8 Conclusion

A steady-state two-dimensional heat transfer model, which allows the calculation of the inner temperature field starting from a profile of the wall heat transfer coefficient, has been established for a cylindrical geometry. Transfer coefficient measurement feasibility has been studied on a test case using either an analytical or a boundary element solution. An inverse procedure has been developed: It takes a regularization term

into account in order to overcome the problem of random measurement errors. A simulation of measurements has been processed using a noisy temperature profile as input. The value of the regularization parameter has been adjusted for this test case.

Experimental measurements were taken and processed using either the analytical or the boundary element technique. The h profiles are coherent for the three measurement radii and do not depend on the technique used. Effect of temperature dependence of the thermal conductivity of the cylinder material was studied. The experimental profile estimated by the inverse model was compared to profiles obtained by other authors for close conditions. Advantages and disadvantages of this method have been presented.

References

Achenbach, E., 1975, "Total and Local Heat Transfer From a Smooth Cylinder in Cross-Flow at High Reynolds Number," *International Journal of Heat and Mass Transfer*, Vol. 18, pp. 1387–1396.

Beck, J. V., and Arnold, K. J., 1977, *Parameter Estimation in Engineering and Science*, Wiley, New York.

Beck, J. V., Blackwell, B., and St. Clair, C. J., Jr., 1985, *Inverse Heat Conduction—Ill-posed Problems*, Wiley, New York.

Brebbia, C. A., 1978, *The Boundary Element Method for Engineers*, Pentech Press.

Carslaw, H. S., and Jaeger, J. C., 1959, *Conduction of Heat in Solids*, 2nd ed., Oxford University Press, United Kingdom.

Degiovanni, A., Sinicki, G., Gery, A., and Laurent, M., 1984, "Un Modèle de Résistance Thermique de Contact en Régime Permanent," *Revue Générale de Thermique*, Vol. 267, pp. 161–175.

Giedt, W. H., 1949, "Investigation of Variation of Point Unit-Heat-Transfer Coefficient Around a Cylinder Normal to an Air Stream," *Transaction of the ASME*, Vol. 71.

Groetsch, W. C., 1984, *The Theory of Tikhonov Regularization for Fredholm Equations of the First Kind*, Pitman.

Keltner, N. R., and Beck, J. V., 1981, "Unsteady Surface Element Method," ASME JOURNAL OF HEAT TRANSFER, Vol. 103, pp. 759–764.

Krabel, J. S., Baughn, J. W., and McKillop, A. A., 1980, "An Instrument for the Measurement of Heat Flux From a Surface With Uniform Temperature," ASME JOURNAL OF HEAT TRANSFER, Vol. 102, pp. 576–578.

Maillet, D., and Degiovanni, A., 1989, "Méthode Analytique de Conduction Inverse Appliquée à la Mesure du Coefficient de Transfert Local sur un Cylindre en Convection Forcée," *Revue de Physique Appliquée*, Vol. 24, pp. 741–759.

Martin, M. G., and Gosse, J., 1968, "Etude de la Convection Thermique autour des Cylindres par un Ecoulement Pulsé," *Comptes rendus de l'Académie des Sciences*, Paris, série A, Vol. 266, pp. 1107–1110.

Ozisik, M. N., 1980, *Heat Conduction*, Wiley, New York.

Pasquetti, R., and Le Niliot, C., 1990, "Conduction Inverse par Eléments de Frontière. Cas stationnaire," *Revue de Physique Appliquée*, Vol. 25, pp. 99–107.

Pasquetti, R., and Caruso, A., 1990, "Boundary Element Approach for Transient and Non-linear Thermal Diffusion," *Numerical Heat Transfer*, Part B, Vol. 17, pp. 83–89.

Pasquetti, R., and Le Niliot, C., 1990, "Boundary Element Approach for Inverse Heat Conduction Problems: Application to Transient Bidimensional Numerical Experiment," *Numerical Heat Transfer*, in press.

Tikhonov, A., and Arsenine, V., 1976, *Méthode de résolution des problèmes mal posés*, Editions de Moscou.

Zukauskas, A., and Ziugzda, J., 1985, *Heat Transfer of a Cylinder in Crossflow*, G. F. Hewitt, ed., Hemisphere Publishing Corporation, Springer-Verlag, New York.

Solution for Transient Conjugated Forced Convection in the Thermal Entrance Region of a Duct With Periodically Varying Inlet Temperature

J. S. Travelho
Associate Researcher.

W. F. N. Santos
Assistant Researcher.

Instituto de Pesquisas Espaciais,
Laboratório Associado de Combustão e Propulsão,
Cachoeira Paulista—SP, 12630 Brazil

This work presents an analytical solution of the transient conjugated laminar forced convection problem of a slug flow in the thermal entrance region inside a parallel plate duct. A solution in series form is already known for this kind of problem. This solution leads to a complex eigenvalue problem with transcendental equations. The present solution obtained by using the Laplace transform completely eliminates this problem. The amplitudes and phase lags with respect to the inlet conditions are determined for the complex wall temperature, fluid bulk temperature, and wall heat flux from this solution. The results are plotted for comparison with the results obtained with the series solution.

Introduction

The unsteady state forced convection heat transfer problem, subjected to periodic time variation of the inlet condition, has been the subject of study for many years now. One of the motivations is its importance for heat exchanger control. For most engineering applications, the initial transients are neglected and a quasi-stationary solution is normally used to predict the thermal response of the device.

Important contributions for the solution of this problem were presented by Sparrow and de Farias (1968) and Cotta et al. (1987). Sparrow and de Farias analytically studied the transient conjugated problem inside a parallel plate duct assuming a slug flow velocity profile, and obtained a solution in series form. The solution presented by these authors leads to a complex eigenvalue problem, which depends on the wall and fluid physical properties on the oscillation frequency of the temperature. A trial and error procedure was employed by Sparrow and de Farias for the numerical evaluation of the real and imaginary parts of the eigenvalues. The number of eigenvalues needed depends on the position being considered, increasing for points close to the inlet (thermal entrance). Cotta et al. advanced the analysis presented by Sparrow and de Farias by considering transient forced convection both in parallel plate channel and circular ducts, and adopted the sign-count method to obtain the complex eigenvalues.

The principal difficulty in the analysis of this problem has been the solution of the resulting complex eigenvalue problem. Therefore, Travelho and Santos (1988) presented an alternative way to solving this problem with the same physical conditions presented by Sparrow and de Farias and Cotta et al., without the need of determining the complex eigenvalues. These eigenvalues are avoided by applying the Laplace transform to the equation and to the boundary conditions of the problem. The inverse transform, which is the solution of the original problem, was obtained numerically. In the present work we further advance the analysis of Travelho and Santos by analytically obtaining the inverse Laplace transform.

The analytical evaluation of the general solution provides a variety of results of engineering interest. These include local quantities such as the wall temperature, the fluid bulk temperature, and wall heat flux, which vary with time and with axial position to an extent that depends on the physical parameters of the problem.

Contributed by the Heat Transfer Division for publication in the JOURNAL OF HEAT TRANSFER. Manuscript received by the Heat Transfer Division January 3, 1990; revision received November 22, 1990. Keywords: Conjugate Heat Transfer, Forced Convection, Transient and Unsteady Heat Transfer.

Problem Formulation

Consider laminar forced convection inside a parallel plate duct separated by a distance $2L$ and whose walls are each of thickness l. The fluid entering the duct has a temperature that varies periodically with time. The wall temperature variation is not specified in advance, but is dynamically determined by a balance of the heat transfer rate and the energy stored. The wall and fluid transport properties are assumed to be constant and the axial conduction and viscous dissipation are neglected. The parallel plate duct under consideration is shown in Fig. 1. Under such conditions, the energy equation has the form

$$\frac{\partial T(x, z, t)}{\partial t} + u\frac{\partial T(x, z, t)}{\partial z} = \alpha\frac{\partial^2 T(x, z, t)}{\partial x^2} \qquad (1a)$$

for $0 \le x \le L$, $z \ge 0$, and $t \ge 0$. The initial and boundary conditions are given by

$$T(x, 0, t) = T_0 + \Delta T_0 e^{i\omega t} \qquad 0 \le x \le L,\ t \ge 0 \qquad (1b)$$

$$\left.\frac{\partial T(x, z, t)}{\partial x}\right|_{x=0} = 0 \qquad z \ge 0,\ t \ge 0 \qquad (1c)$$

$$-k\left.\frac{\partial T(x, z, t)}{\partial x}\right|_{x=1} = \rho_w c_w l\frac{\partial T(1, z, t)}{\partial t} \qquad (1d)$$

An initial condition is not necessary because this work interest is the periodic part of the solution. The slug flow model (U = const) is assumed and the following dimensionless groups are introduced into equations (1a)-(1d):

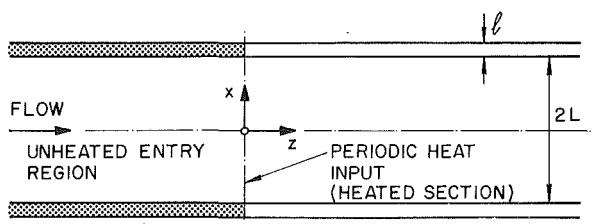

Fig. 1 Geometry of parallel plate duct

$$X=\frac{x}{L} \tag{2a}$$

$$Z=\frac{\alpha z}{UL^2} \tag{2b}$$

$$\tau=\frac{\alpha t}{L^2} \tag{2c}$$

$$\theta(X, Z, \tau)=\frac{T(x, z, t)-T_0}{\Delta T_0} \tag{2d}$$

$$\Omega=\frac{\omega L^2}{\alpha} \tag{2e}$$

$$a^*=\frac{\rho c_p L}{\rho_w c_w l} \tag{2f}$$

Consequently, equations (1*a*)–(1*d*) expressed in dimensionless form are

$$\frac{\partial\theta(X, Z, \tau)}{\partial\tau}+\frac{\partial\theta(X, Z, \tau)}{\partial Z}=\frac{\partial^2\theta(X, Z, \tau)}{\partial X^2}$$

$$\text{in } 0\le X\le 1,\ Z\ge 0,\ \tau\ge 0 \tag{3a}$$

$$\theta(X, 0, \tau)=e^{i\Omega\tau} \tag{3b}$$

$$\left.\frac{\partial\theta(X, Z,\tau)}{\partial X}\right|_{X=0}=0 \tag{3c}$$

$$a^*\left.\frac{\partial\theta(X, Z,\tau)}{\partial X}\right|_{X=1}+\frac{\partial\theta(1, Z, \tau)}{\partial\tau}=0 \tag{3d}$$

In order to obtain a periodic solution the temperature is assumed to have the form

$$\theta(X, Z, \tau)=\psi(X, Z)e^{i\Omega(\tau-Z)} \tag{4}$$

Equations (3*a*)–(3*d*) together with equation (4) give

$$\frac{\partial\psi(X, Z)}{\partial Z}=\frac{\partial^2\psi(X, Z)}{\partial X^2} \text{ in } 0\le X\le 1,\ Z\ge 0 \tag{5a}$$

$$\psi(X, 0)=1 \tag{5b}$$

$$\left.\frac{\partial\psi(X, Z)}{\partial X}\right|_{X=0}=0 \tag{5c}$$

$$\left.\frac{\partial\psi(X, Z)}{\partial X}\right|_{X=1}+ib^*\psi(1, Z)=0 \tag{5d}$$

The dimensionless parameter b^* that appears in equation (5*d*) characterizes the effects of wall capacitance to heat transfer, and is defined by

$$b^*=\frac{\Omega}{a^*}=\frac{\omega L\rho_w c_w l}{k} \tag{6}$$

Method of Solution

Equations (5*a*)–(5*d*) can be solved by using the Laplace transform technique. Thus, by applying the Laplace transform to the variable Z, equations (5*a*)–(5*d*) become

$$\frac{\partial^2\tilde{\psi}(X,s)}{\partial X^2}=s\tilde{\psi}(X, s)-1 \text{ for } 0\le X\le 1. \tag{7a}$$

$$\left.\frac{\partial\tilde{\psi}(X, s)}{\partial X}\right|_{X=0}=0 \tag{7b}$$

$$\left.\frac{\partial\tilde{\psi}(X, s)}{\partial X}\right|_{X=1}+ib^*\tilde{\psi}(1, s)=0 \tag{7c}$$

where $\tilde{\psi}(X, s)$ is defined as

$$\tilde{\psi}(X, s)=\lim_{Z\to s}\psi(X, Z)=\int_0^\infty\psi(X, Z)e^{-sZ}dZ \tag{8}$$

and s is the Laplace transform parameter.

The solution of equation (7*a*) is

$$\tilde{\psi}(X, s)=C_1(s)e^{\sqrt{s}X}+C_2(s)e^{-\sqrt{s}X}+\frac{1}{s} \tag{9}$$

The integration constants C_1 and C_2 can be calculated by using equations (7*b*) and (7*c*). Therefore, the function $\tilde{\psi}(X, s)$ is expressed by

$$\tilde{\psi}(X, s)=\frac{1}{s}-\frac{ib^*}{s}\left[\frac{e^{\sqrt{s}X}+e^{-\sqrt{s}X}}{\sqrt{s}(e^{\sqrt{s}}-e^{-\sqrt{s}})+ib^*(e^{\sqrt{s}}+e^{-\sqrt{s}})}\right] \tag{10}$$

which can be rearranged to give

$$\tilde{\psi}(X, s)=\frac{1}{s}-\frac{ib^*}{s}\frac{e^{-\sqrt{s}}(e^{\sqrt{s}X}+e^{-\sqrt{s}X})}{(\sqrt{s}+ib^*)}\left[\frac{1}{1-\left(\frac{\sqrt{s}-ib^*}{\sqrt{s}+ib^*}\right)e^{-2\sqrt{s}}}\right] \tag{11}$$

Nomenclature

A = amplitude
a^* = heat capacity defined by equation (2*f*)
b^* = parameter defined by equation (6)
$C_1(s)$, $C_2(s)$ = defined by equation (9)
c_p = fluid specific heat
c_w = wall specific heat
G = defined by equation (12)
i = $\sqrt{-1}$
Im = imaginary part of
k = thermal conductivity of fluid
L = half-spacing between plate
l = wall thickness
n = number of terms in the series
Re = real part of
s = Laplace transform parameter
$T(x, z, t)$ = fluid temperature
T_0 = cycle mean temperature
t = time
U = mean velocity
u = flow velocity
$W(r)$ = function related to error function of complex argument and defined by equation (16)
X = dimensionless normal coordinate
x = normal coordinate
Z = dimensionless axial coordinate
z = axial coordinate
α = thermal diffusivity of fluid
ΔT_0 = amplitude of inlet oscillations
$\theta(X, Z, \tau)$ = dimensionless temperature
ρ = fluid mass density
ρ_w = wall density
τ = dimensionless time
ϕ = phase lag
$\psi(X, Z)$ = dimensionless periodic part of
Ω = dimensionless frequency of oscillations
ω = frequency of oscillations

Superscript

~ = Laplace transform of

Subscripts

b = bulk temperature
h = heat flux
w = wall temperature

The term in the brackets can be written in series form by using

$$\frac{1}{1-G}=1+G+G^2+\cdots\sum_{n=0}^{\infty}G^n \tag{12}$$

where the condition $|G|<1$ should be satisfied to obtain convergence. This way the function $\tilde{\psi}(X, s)$ can be written as

$$\tilde{\psi}(X, s)=\frac{1}{s}-\frac{ib^*}{s}\frac{e^{-\sqrt{s}}(e^{\sqrt{s}X}+e^{-\sqrt{s}X})}{(\sqrt{s}+ib^*)}\left[\sum_{n=0}^{\infty}\left(\frac{\sqrt{s}-ib^*}{\sqrt{s}+ib^*}\right)^n e^{-2n\sqrt{s}}\right] \tag{13}$$

Rearranging this equation one obtains

$$\tilde{\psi}(X, s)=\frac{1}{s}-ib^*\sum_{n=0}^{\infty}\left[\frac{e^{-\sqrt{s}(2n+1\pm X)}}{s(\sqrt{s}+ib^*)}\left(\frac{\sqrt{s}-ib^*}{\sqrt{s}+ib^*}\right)^n\right] \tag{14}$$

where the $\pm$ sign means that ib^* multiplies two series, one with the + sign and the other with the − sign. The inverse transform of equation (14), which is the periodic solution of the proposed problem, is obtained with the aid of tables of transform (Roberts and Kaufman, 1966). In this work, only the first two terms were considered, because they already give a good approximation for Z smaller or of the order of 0.5. The function $\tilde{\psi}(X, s)$ then becomes

$$\psi(X, Z)=1-\operatorname{erfc}\left(\frac{1\pm X}{2\sqrt{Z}}\right)+\operatorname{erfc}\left(\frac{3\pm X}{2\sqrt{Z}}\right)-4ib^*\sqrt{\frac{Z}{\pi}}e^{-(3\pm X)^2/4Z}+e^{(1\pm X)ib^*-b^{*2}Z}\operatorname{erfc}\left(\frac{1\pm X}{2\sqrt{Z}}+ib^*\sqrt{Z}\right)-[1-2ib^*(3\pm X+2ib^*Z)]e^{(3\pm X)ib^*-b^{*2}Z}\cdot\operatorname{erfc}\left(\frac{3\pm X}{2\sqrt{Z}}+ib^*\sqrt{Z}\right) \tag{15}$$

The function $W(r)$ (Abramowitz and Stegun, 1964) is often used instead of the error function when the latter has a complex argument. This function is defined as

$$W(r)=e^{-r^2}\operatorname{erfc}(-ir) \tag{16}$$

The introduction of this function in equation (15) gives

$$\psi(X, Z)=1-\operatorname{erfc}\left(\frac{1\pm X}{2\sqrt{Z}}\right)+\operatorname{erfc}\left(\frac{3\pm X}{2\sqrt{Z}}\right)-4ib^*\sqrt{\frac{Z}{\pi}}e^{-(3\pm X)^2/4Z}+e^{-(1\pm X)^2/4Z}W\left[-b^*\sqrt{Z}+\frac{(1\pm X)}{2\sqrt{Z}}i\right]-[1-2ib^*(3\pm X+2ib^*Z)]e^{-(3\pm X)^2/4Z}W\left[-b^*\sqrt{Z}+\frac{(3\pm X)}{2\sqrt{Z}}i\right] \tag{17}$$

Equations (4) and (17), taken together, constitute the solution for the time-dependent temperature field in the fluid. As usual, one is interested in evaluating such quantities as the dimensionless wall temperature, wall heat flux, and fluid bulk temperature as function of Z and τ.

The dimensionless wall temperature $\theta_w(Z, \tau)$ is given by

$$\theta_w(Z, \tau)\equiv\theta(1, Z, \tau)=\psi(1, Z)e^{i\Omega(\tau-Z)} \tag{18}$$

while the wall heat flux $\theta_h(Z, \tau)$ is given by

$$\theta_h(Z, \tau)\equiv-\left.\frac{\partial\theta(X, Z, \tau)}{\partial X}\right|_{X=1}=-\left.\frac{\partial\psi(X, Z)}{\partial X}\right|_{X=1}e^{i\Omega(\tau-Z)} \tag{19}$$

and the dimensionless fluid bulk temperature $\theta_b(Z, \tau)$ by

$$\theta_b(Z, \tau)=\int_0^1\theta(X, Z, \tau)dx=\left[\int_0^1\psi(X, Z)dx\right]e^{i\Omega(\tau-Z)} \tag{20}$$

The periodic parts of the dimensionless wall temperature, wall heat flux, and fluid bulk temperature are determined by using the approximated analytical solution of equation (17), so

$$\psi_w(Z)\equiv\psi(1, Z)=\operatorname{erfc}\left(\frac{2}{\sqrt{Z}}\right)-4ib^*\sqrt{\frac{Z}{\pi}}(e^{-1/Z}+e^{-4/Z})+W(-b^*\sqrt{Z})+4ib^*(1+ib^*Z)e^{-1/Z}W\left(-b^*\sqrt{Z}+\frac{i}{\sqrt{Z}}\right)-(1-8ib^*+4b^{*2}Z)e^{-4/Z}W\left(-b^*\sqrt{Z}+\frac{2i}{\sqrt{Z}}\right) \tag{21}$$

$$\psi_h(Z)\equiv-\left.\frac{\partial\psi(X, Z)}{\partial X}\right|_{X=1}=4b^{*2}\sqrt{\frac{Z}{\pi}}(e^{-1/Z}+e^{-4/Z})+ib^*W(-b^*\sqrt{Z})+4ib^*(1+ib^*Z)e^{-1/Z}W\left(-b^*\sqrt{Z}+\frac{i}{\sqrt{Z}}\right)-ib^*(1+8ib^*-4b^{*2}Z)e^{-4/Z}W\left(-b^*\sqrt{Z}+\frac{2i}{\sqrt{Z}}\right) \tag{22}$$

$$\psi_b(Z)\equiv\int_0^1\psi(X, Z)dx=1+\frac{1}{ib^*}-2\sqrt{\frac{Z}{\pi}}(1-4e^{-1/Z}+3e^{-4/Z})-4\left(1+\frac{1}{ib^*}\right)\operatorname{erfc}\left(\frac{1}{\sqrt{Z}}\right)+\left(4+\frac{3}{ib^*}\right)\operatorname{erfc}\left(\frac{2}{\sqrt{Z}}\right)-\frac{1}{ib^*}W(-b^*\sqrt{Z})-4\left(1+ib^*Z-\frac{1}{ib^*}\right)e^{-1/Z}W\left(-b^*\sqrt{Z}+\frac{i}{\sqrt{Z}}\right)+\left(8+4ib^*Z-\frac{3}{ib^*}\right)e^{-4/Z}W\left(-b^*\sqrt{Z}+\frac{2i}{\sqrt{Z}}\right) \tag{23}$$

As mentioned before, the amplitudes and phase lags of the quantities of interest are used to visualize the final solution. These quantities are $A_w(Z)$, $A_h(Z)$, $A_b(Z)$, and the phase lags $\phi_w(Z)$, $\phi_h(Z)$, and $\phi_b(Z)$ corresponding, respectively, to the amplitudes and phase lags of wall temperature, wall heat flux, and fluid bulk temperature. They are given by

$$A_w=|\psi_w|=\{[\operatorname{Re}(\psi_w)]^2+[\operatorname{Im}(\psi_w)]^2\}^{1/2} \tag{24}$$

$$\phi_w=\operatorname{tg}^{-1}\left[\frac{\operatorname{Im}(\psi_w)}{\operatorname{Re}(\psi_w)}\right]-\Omega Z \tag{25}$$

where $\operatorname{Re}(\psi_w)$ and $\operatorname{Im}(\psi_w)$ are the real and imaginary parts of $\psi_w(Z)$ given by equation (21). A_h, A_b, ϕ_h, and ϕ_b are obtained from equations (22) and (23) using equations similar to equations (24) and (25).

Results and Discussion

Amplitudes and phase lags calculated with the present solution and the series solution given in the literature are shown in Figs. 2(*a*)-4(*b*). As shown in these figures, the agreement between these solutions is very good in the thermal entrance region. One should notice that the extent of this region depends on the parameter b^*. As b^* decreases, the thermal entrance region extends up to larger values of the variable Z. The agreement between the solutions for smaller b^* is also very good up to values of Z larger than one. The corresponding physical distance is, of course, a function of such other physical quan-

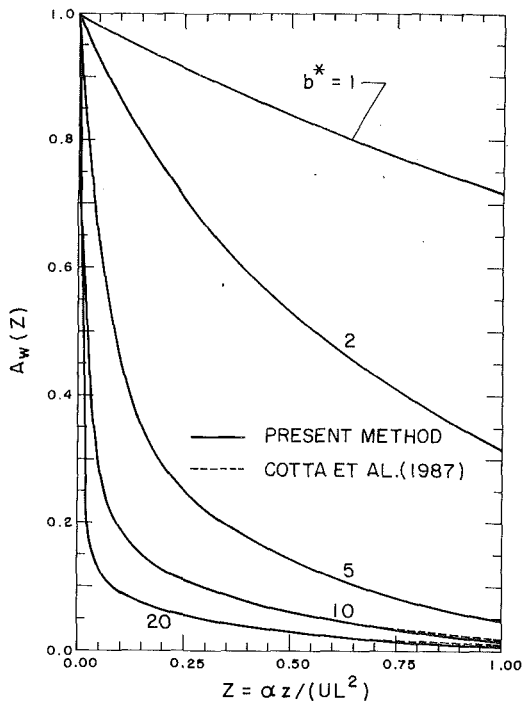

Fig. 2(*a*) Comparison between wall temperature amplitudes, as a function of *Z*, calculated by using the present method and by using series solution

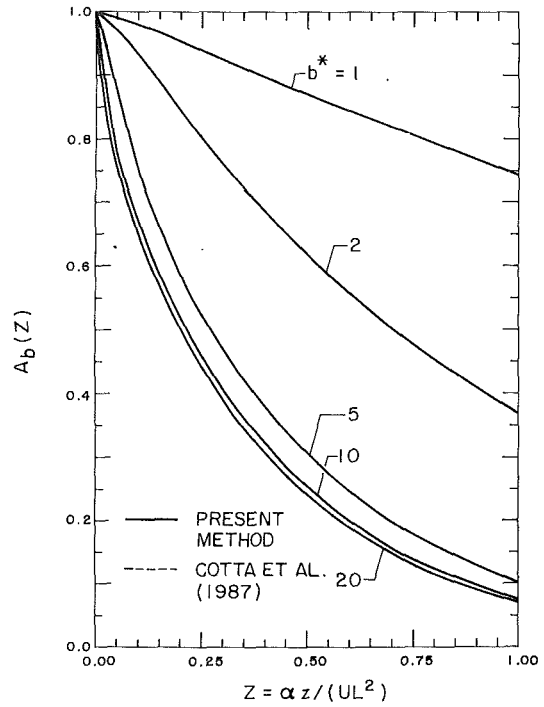

Fig. 3(*a*) Comparison between bulk temperature amplitudes, as a function of *Z*, calculated by using the present method and by using series solution

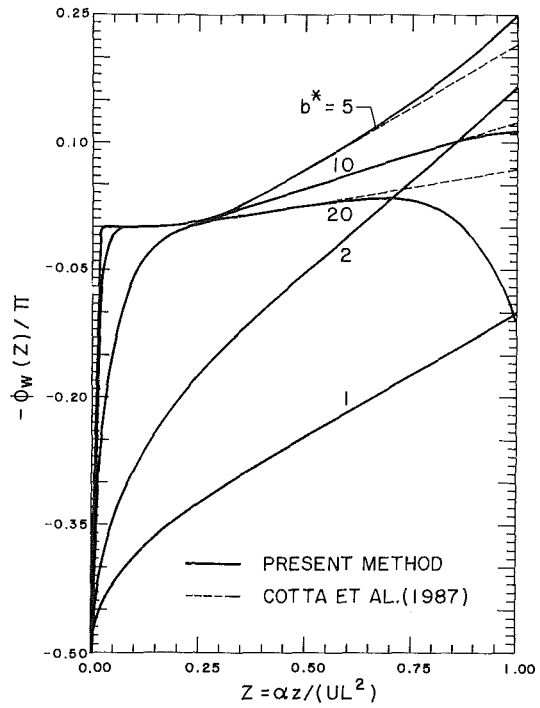

Fig. 2(*b*) Comparison between wall temperature phase lags by using the two methods

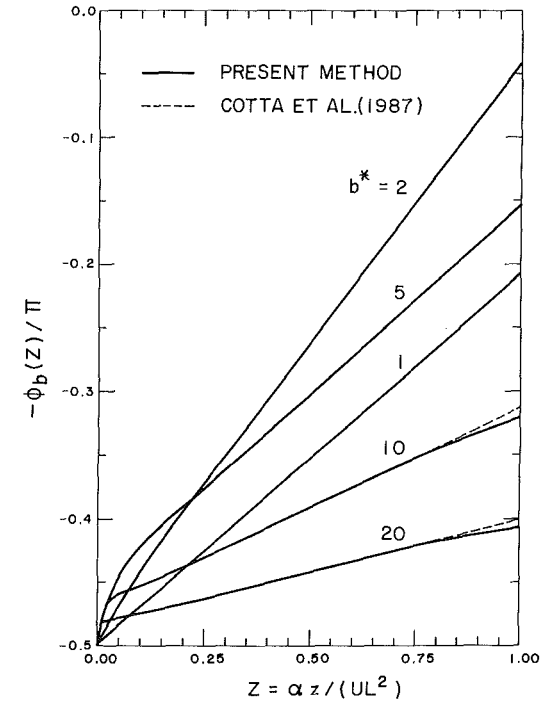

Fig. 3(*b*) Comparison between bulk temperature phase lags by using the two methods

tities as the fluid velocity. By adopting reasonable values for the physical quantities, Z equal to or bigger than one would mean a larger physical distance. However, as mentioned by Sparrow and Farias, practical value of b^* are larger than one. For values of b^* equal to or bigger than 5, the amplitudes of various quantities studied drop very quickly. As b^* increases, the thermal entrance region becomes smaller in terms of Z. For larger b^*, the agreement between the present solution and the one given in the literature is shown in Figs. 2(*a*)–4(*b*) to be very good, up to the point where the amplitude decreased enough for the oscillations to be neglected. Therefore, one can see, with the aid of Figs. 2(*a*)–4(*b*), that, in any case of practical importance, the present solution is very accurate.

The present solution also behaves differently from the ones obtained by Sparrow and Farias and Cotta et al. Their solutions converge more rapidly for larger values of Z, and need more terms for small values of Z. The present solution is obtained, on the other hand, by neglecting terms in equation (14). This approximation becomes better as s increases, which implies that the present solution becomes a better approximation as Z becomes smaller. The reader should notice the increase in the difference between the solutions as Z goes to 1.

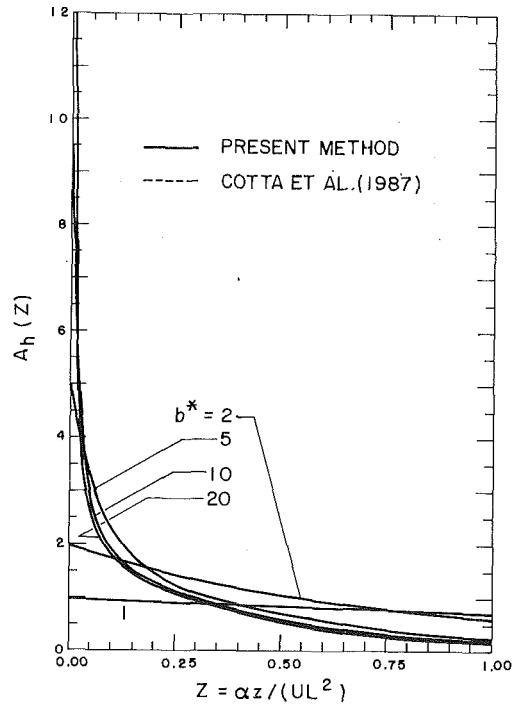

Fig. 4(*a*) Comparison between wall heat flux amplitudes, as a function of *Z*, calculated by using the present method and by using series solution

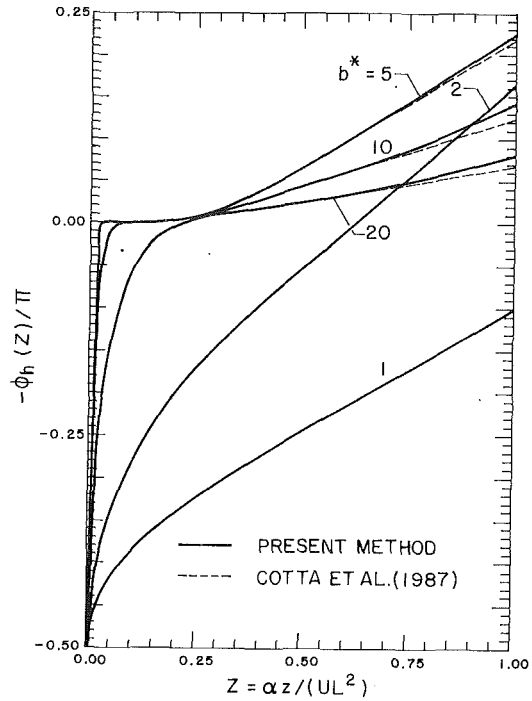

Fig. 4(*b*) Comparison between wall heat flux phase lags by using the two methods

Conclusion

An alternative solution has been found for the wall temperature, wall heat flux, and fluid bulk temperature in a parallel plate duct for a transient forced convection situation caused by a periodical variation in the inlet temperature. Equations (18), (19), and (20), which give the above-cited quantities, are of direct application. They only require elementary functions that are tabulated in the literature, e.g., Abramowitz and Stegun (1964). Their utilization does not involve the solution of any other equation, while for the series solution it is necessary to solve the transcendental equation, which yields the complex eigenvalues as a function of the parameter b^*.

The present solution starts to become inaccurate as Z becomes equal to or larger than one. However, this nondimensional coordinate is obtained by dividing the axial coordinate by half of the distance between the plates and by the Peclet number. The Peclet number in an actual system is, usually, very large and, therefore, in many cases, Z equal to one means a distance much larger than the equipment itself. Another point is that for the control of equipment it is convenient to work with a large amplitude of oscillations, which occurs for small values of Z.

References

Abramovitz, M., and Stegun, I. A., 1964, *Handbook of Mathematical Function With Formulas, Graphs and Mathematical Tables,* National Bureau of Standards Appl. Math. Ser. 55.

Cotta, R. M., Mikhailov, M. D., and Özişik, M. N., 1987, "Transient Conjugated Forced Convection in Ducts With Periodically Varying Inlet Temperature," *International Journal of Heat and Mass Transfer,* Vol. 30, pp. 2073–2082.

Roberts, G. E., and Kaufman, H., 1966, *Tables of Laplace Transforms,* W. B. Sounders and Co., Philadelphia, PA.

Sparrow, E. M., and de Farias, F. N., 1968, "Unsteady Heat Transfer in Ducts With Time-Varying Inlet Temperature and Participating Walls," *International Journal of Heat and Mass Transfer,* Vol. 11, pp. 837–853.

Travelho, J. S., and Santos, W. F. N., 1988, "Transient Heat Transfer in Duct With Periodically Varying Inlet Temperature" [in Portuguese], *Proceedings, 2nd National Meeting on Thermal Sciences,* Aguas de Lindoia, Brazil, pp. 315–317.

Convective Heat and Mass Transfer in the Stagnation Region of a Laminar Planar Jet Impinging on a Moving Surface

D. A. Zumbrunnen
Thermal/Fluids Laboratory,
Department of Mechanical Engineering,
Clemson University,
Clemson, SC 29634-0921

Manufacturing processes frequently employ impinging jets to cool or dry a material. Materials are often in motion since many manufacturing processes are designed to produce large quantities of a product. In some cases, the surface velocity can exceed or be comparable to the jet impingement velocity. In this study, the stagnation region of a laminar, planar jet is considered where surface motion is directed perpendicular to the jet plane. A similarity solution to the Navier-Stokes equations is formulated to determine the flow velocity in the stagnation region. Heat and mass transfer distributions are determined from numerical solutions to the conservation equations for energy and species, where velocity components are calculated from the similarity solution. Restrictions regarding the use of heat and mass transfer correlations, which are commonly developed with experimental apparatuses where the impingement surface is stationary, are provided.

Introduction

Manufacturing methods frequently involve complexities that are difficult to duplicate in the laboratory. In some cases, the influence of complicating aspects is deemed, a priori, to be negligible. A salient example concerns the use of impinging jets to cool or dry materials in motion. Heat and mass transfer correlations, which are employed by engineers to develop specifications for jet cooling or drying systems, rarely account for surface motion effects. Such correlations are often developed with an experimental apparatus in which the impingement surface is stationary. For example, a widely referenced and comprehensive review of correlations for impinging gas jets (Martin, 1977) does not include restrictions regarding the use of correlations with respect to the importance of surface motion.

An example of jets impinging on a moving surface is shown in Fig. 1. In the hot-rolling process (Kohring, 1985), hot steel plate is reduced to a final thickness by a series of counterrotating rollers. After rolling, the plate is cooled by planar water jets, which are mounted above and below a runout table and which span the plate surface. Water from the nozzles divides on the plate, where it flows either opposite to or in the direction of plate motion. The transport of fluid away from the stagnation line (the line of symmetry for the dividing flow spanning the plate surface) is facilitated on the side of the jet where the jet flow and plate move in the same direction. However, where the jet flow and plate motion are opposed, fluid is entrained and re-enters the impingement region. Since the plate speed can exceed the jet impingement velocity by a factor of nearly ten, flow velocity profiles are significantly affected, which, in turn, influence convective heat transfer. Entrainment is reduced at the lower plate surface in Fig. 1 since jet effluent falls away from the surface. Similarly, entrainment is less significant near the trailing edge of the moving plate, where effluent is lost and cannot re-enter the impingement region. Air is frequently used in similar configurations to dry or cool paper, textiles, and polymer films (Martin, 1977; Sineath and Pavelchek, 1971).

Relatively few studies have considered the effect of surface motion on heat or mass transfer due to impinging jets. Flow visualization and overall heat transfer measurements were performed for a circular submerged air jet impinging on the face of a rotating disk in a large air-filled enclosure (Metzger and Grochowsky, 1977). At high rotational speeds, a rotationally dominated flow pattern was observed near the disk surface and the influence of the impinging jet flow on heat transfer was reduced. A similar study was later conducted by Popiel and Boguslawski (1986). Results indicated that the impinging jet flow can become severely disrupted due to the entrainment of surrounding air by the rotating disk motion. These studies are not directly applicable to the case considered here since this work primarily concerns a free-surface jet, in which the influence of a surrounding fluid is negligible, and since a rotationally dominated flow pattern does not arise. Results apply directly to submerged jets, such as those considered by Martin (1977), only when the impinging flow is not disrupted by the motion imparted to the surrounding fluid. It should be noted that flow disruption of a submerged jet by fluid entrained by surface motion demonstrates the importance of surface motion in affecting heat or mass transfer rates.

An experimental study of a turbulent, planar air jet impinging on a moving surface was performed by van Heiningen et al. (1977). Their apparatus consisted of a large rotating drum heated and cooled by two externally mounted and oppositely facing nozzles. Local heat transfer coefficients were in close agreement with jet impingement studies employing stationary flat plates. Surface motion effects were deemed therefore to be negligible for the conditions of their experiments in which the plate speed was less than 1.5 percent of the jet impingement velocity. The effect of surface motion on forced convection heat transfer due to an impinging, turbulent, planar gas jet was modeled numerically by Huang et al. (1984) for an isothermal plate. A crossflow of fluid (moving in the same direction as the plate) was incorporated to simulate flow from neighboring jets and to reduce ambiguity associated with fluid entrainment due to surface motion. Numerical results showed little change in the location of the peak Nusselt number due to surface motion for ratios of surface-to-jet velocities from 0 to 0.5. However, the peak Nusselt number decreased slightly at higher surface velocities, but this decrease was only dis-

Contributed by the Heat Transfer Division and presented at the Joint AIAA/ASME Thermophysics and Heat Transfer Conference, Seattle, Washington, June 18-20, 1990. Manuscript received by the Heat Transfer Division May 5, 1990; revision received September 27, 1990. Keywords: Forced Convection, Jets, Materials Processing and Manufacturing Processes.

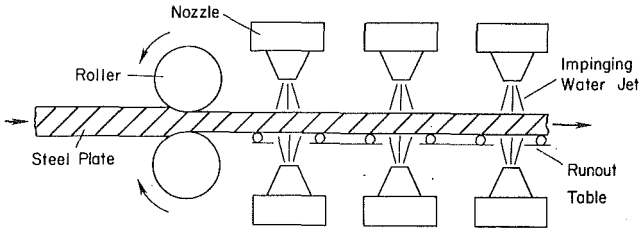

Fig. 1 Cooling of steel plate by planar water jets subsequent to hot rolling

cernible in their results when the crossflow was high. Thus, the slight decrease in peak Nusselt number beneath the jet may have been due to a perturbation in the crossflow velocity profile caused by the wall motion. It is difficult generally to determine from their results the importance of surface motion, since the surface motion affected the imposed crossflow and also since a moving surface may not be isothermal.

In this study, attention is focused on the stagnation region of a laminar, planar jet where surface motion is directed perpendicular to the jet plane. In order to estimate the effect of surface motion, a similarity analysis is performed with the Navier–Stokes equations to determine the flow velocity. Heat and mass transfer distributions are determined from numerical solutions to the conservation equations for energy and species, where velocity components are calculated from the similarity solution. Determining flow velocity from the similarity solution reduces ambiguity associated with fluid entrained by the moving surface. This reduction in ambiguity is made possible by assuming that the entrained fluid only alters the impinging flow in regions adjacent to the moving surface.

Analysis

Model Restrictions and Assumptions. The stagnation region beneath a planar jet is depicted in Fig. 2. In this region, the vertical velocity components of the fluid in the central portions of the jet become smaller near the surface. The flow bifurcates symmetrically along a stagnation *line* subtending the plate in the spanwise direction. A stagnation region is formed where the flow is characterized by a nearly constant gradient du_∞/dx in the horizontal free-stream velocity component u_∞ (i.e., the component parallel to the impingement surface) due to a change in static pressure with the distance x from the stagnation line. Boundary layer analyses are often performed to calculate heat and mass transfer coefficients in the stagnation region (White, 1974). For the case where the impingement surface is

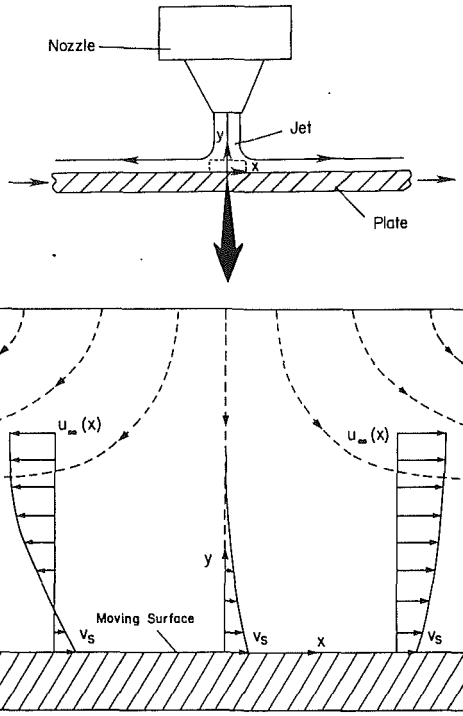

Fig. 2 Variation in the flow velocity component directed parallel to the moving surface within the stagnation region of a planar jet

in motion as in Fig. 2, the boundary layer equations for $x < 0$ are not applicable, since fluid is entrained by the surface motion and information is thereby propagated against the free-stream flow direction. A boundary layer flow does develop for $x > 0$ where the surface and free-stream motions are in the same direction. However, boundary conditions for the boundary layer problem at $x = 0$ are difficult to specify, and solutions are facilitated by considering the region enclosed by the dashed lines in Fig. 2 as a single elliptic problem.

Velocity profiles for the velocity component directed parallel to the impingement surface are shown in Fig. 2 at the stagnation line and at equal distances from the stagnation line. For $x < 0$, fluid near the surface is entrained by the surface motion, while fluid farther from the surface is more greatly influenced by the free-stream velocity component u_∞. Fluid at the stagnation line ($x = 0$), where $u_\infty = 0$, is propelled only by the surface motion. For $x > 0$, the flow velocity and surface

Nomenclature

c_p = specific heat at constant pressure
C = free-stream velocity gradient near stagnation line [equation (7)]
$\overline{C}$ = dimensionless velocity gradient $= wC/v_j$
C_f = coefficient of friction [equation (20)]
D = mass diffusivity
h = function related to flow velocity [equation (6)]
h_q = convective heat transfer coefficient [equation (24*a*)]
h_m = convective mass transfer coefficient [equation (24*b*)]
H = dependent variable governing flow velocity $= h(v/C)^{-1/2}$
I = dependent variable related to flow velocity on moving impingement surface $= L/v_s$
k = thermal conductivity
L = function related to flow velocity on moving impingement surface [equation (11)]
Nu_w = Nusselt number $= h_q\, w/k$
Nu_* = ratio of Nusselt number for moving plate to Nusselt number for stationary plate
P = static pressure
P_0 = stagnation pressure
Pr = Prandtl number $= \mu c_p/k$
q = heat flux
Re_w = Reynolds number $= v_j w/\nu$
Sc = Schmidt number $= \nu/D$
Sh = Sherwood number $= h_m w/D$
Sh_* = ratio of Sherwood number for moving plate to Sherwood number for stationary plate
T = temperature
T_s = local temperature of impingement surface
T_{s0} = temperature of impingement surface at stagnation line ($\overline{x} = 0$)
T_∞ = free-stream temperature (jet temperature)
u = x component of velocity
$\overline{u}$ = dimensionless velocity component $= u/v_j$
u_∞ = x component of free-stream velocity

motion are in the same direction and flow symmetry ensures that the magnitude of the free-stream velocity component u_∞ is equal to the magnitude of u_∞ at the same distance from the stagnation line where $x < 0$. It is therefore assumed that surface motion effects are restricted to a small entrained fluid layer located adjacent to the moving surface. In addition, in order to maintain the characteristics of the impinging flow, effluent located above the entrained layer cannot collect on the moving surface and create a backwash against the incident jet. These assumptions should be generally valid for curved impingement surfaces such as rotating drums, for upwardly discharging jets, or for short moving plates, where effluent cannot readily reenter the stagnation region due to geometric considerations. However, if a backwash of fluid disrupts the impinging flow, the model would no longer directly apply.

Flow is often turbulent in many industrial jet cooling, heating, or drying systems. Since little work has been done to ascertain the importance of surface motion in impinging flows, laminar flow conditions are considered in order to reveal many underlying physical mechanisms. Specific assumptions are: (*i*) steady, incompressible laminar flow, (*ii*) constant thermophysical properties, (*iii*) negligible viscous heating, (*iv*) negligible body forces in comparison to viscous forces, (*v*) impinging flow not disrupted by flow entrainment, (*vi*) impermeable impingement surface, and (*vii*) low mass transfer rates such that the mass fraction of the diffusing species is much less than unity.

In the following analysis, the flow velocity on the moving surface is determined by modifying and extending an existing analytical solution pertaining to stagnation flow on stationary surfaces. Velocity components are then used with the conservation equations for energy and species to determine heat and mass transfer distributions numerically. Employing an analytical flow solution to obtain numerical solutions to the energy equation is advantageous since ambiguity associated with fluid entrainment on the moving surface is reduced.

Determination of Flow Velocity. Equations for the conservation of mass and momentum that correspond to the assumptions are (Burmeister, 1983)

$$\frac{\partial u}{\partial x}+\frac{\partial v}{\partial y}=0 \tag{1}$$

$$u\frac{\partial u}{\partial x}+v\frac{\partial u}{\partial y}=\frac{-1}{\rho}\frac{\partial P}{\partial x}+\nu\left[\frac{\partial^2 u}{\partial x^2}+\frac{\partial^2 u}{\partial y^2}\right] \tag{2}$$

$$u\frac{\partial v}{\partial x}+v\frac{\partial v}{\partial y}=\frac{-1}{\rho}\frac{\partial P}{\partial y}+\nu\left[\frac{\partial^2 v}{\partial x^2}+\frac{\partial^2 v}{\partial y^2}\right] \tag{3}$$

The flow velocity is subject to conditions at the impingement surface and far above the impingement surface.

Impingement surface ($y = 0$)*:*

$$u=v_s \tag{4a}$$

$$v=0 \tag{4b}$$

Far above impingement surface ($y\to\infty$)*:*

$$u=u_\infty \tag{5a}$$

$$v=v_\infty \tag{5b}$$

A solution method to equations (1)–(3) was developed to incorporate a moving impingement surface (Zumbrunnen, 1990). The method was subsequently found to have been presented earlier by Rott (1956) in an investigation of unsteady flow past airfoils, but its pertinence to impinging jets used in materials processing appears to have been unrecognized. The method is related to the analytical solution for two-dimensional stagnation flows on stationary impingement surfaces by K. Hiemenz (Schlichting, 1979), which for clarity must be considered first. Near the stationary impingement surface, the velocity components of a fluid element directed normal and parallel to the stagnation streamline are given respectively by

$$u=Cxh'(y) \tag{6a}$$

$$v=-Ch(y) \tag{6b}$$

In equation (6), $h(y)$ is a function only of y, C is a positive constant, and the distances from the stagnation line perpendicular and parallel to the stagnation streamline are x and y, respectively. The constant C can be determined from potential flow solutions (Inada et al., 1981) or from static pressure measurements (Zumbrunnen et al., 1989). Far from the surface, the free-stream velocity components are

$$u_\infty=Cx \tag{7a}$$

$$v_\infty=-Cy \tag{7b}$$

The velocity components given by equations (6) and (7) satisfy mass conservation [equation (1)] as required. The magnitude of the free-stream velocity vector **V** is related simply to u_∞ and v_∞ by $V=(u_\infty^2+v_\infty^2)^{1/2}$ and can be used with Bernoulli's equation to find the corresponding pressure distribution in the free stream [equation (8*a*)]. Since viscous effects become more significant near the impingement surface, equation (8*a*) is used to suggest the proper functional form for the pressure distribution in the viscous flow [equation (8*b*)].

$$P_0-P=\frac{1}{2}\rho C^2[x^2+y^2] \tag{8a}$$

Nomenclature (cont.)

$\bar{u}_\infty$ = dimensionless free-stream velocity component = u_∞/v_j
v = y component of velocity
$\bar{v}$ = dimensionless velocity component = v/v_j
v_j = impingement velocity
v_s = velocity of impingement surface
v_∞ = y component of free-stream velocity
$\bar{v}_s$ = dimensionless surface velocity = v_s/v_j
$\bar{v}_\infty$ = dimensionless free-stream velocity component = v_∞/v_j
w = jet width
x = horizontal distance from stagnation line (Fig. 2)
$\bar{x}$ = dimensionless distance = x/w
$\bar{x}_{\max}$ = largest magnitude of $\bar{x}$ (Fig. 4)
y = vertical distance above impingement surface (Fig. 2)
$\bar{y}$ = dimensionless distance = y/w
β = dimensionless surface temperature or surface mass fraction gradient [equation (23)]
δ = velocity boundary layer thickness
η = dimensionless coordinate = $y(\nu/C)^{-1/2} = \bar{y}(\bar{C}\,\mathrm{Re}_w)^{1/2}$
θ = dimensionless temperature = $(T - T_\infty)/(T_{s0} - T_\infty)$
θ_s = dimensionless surface temperature = $(T_s - T_\infty)/(T_{s0} - T_\infty)$
μ = dynamic viscosity
ν = kinematic viscosity = μ/ρ
ρ = mass density
τ_s = shear stress at impingement surface
ω = mass fraction of diffusing species
ω_s = local mass fraction at impingement surface
ω_{s0} = mass fraction at stagnation line on impingement surface
ω_∞ = free-stream mass fraction of diffusing species
Ω = dimensionless mass fraction = $(\omega - \omega_\infty)/(\omega_{s0} - \omega_\infty)$
Ω_s = dimensionless surface mass fraction = $(\omega_s - \omega_\infty)/(\omega_{s0} - \omega_\infty)$

$$P_0 - P = \frac{1}{2}\rho C^2[x^2 + F(y)] \tag{8b}$$

Boundary conditions for $h(y)$ in equation (6) are readily found by comparing equations (6) and (7) at the stationary impingement surface where $u = v = 0$ and far from the surface where $u \to u_\infty$ and $v \to v_\infty$.

$$y = 0 : h = \frac{dh}{dy} = 0 \tag{9a}$$

$$y \to \infty : \frac{dh}{dy} \to 1 \tag{9b}$$

A governing ordinary differential equation for $h(y)$ can be found from equation (2), where u, v, and P are given by equations (6) and (8*b*)

$$\left(\frac{dh}{dy}\right)^2 - h\frac{d^2h}{dy^2} - \frac{\nu}{C}\frac{d^3h}{dy^3} - 1 = 0 \tag{10}$$

Utilizing boundary conditions given by equation (9), u and v are determined from the solution to equation (10). With the velocity components known, equations (3) and (8*b*) are utilized to evaluate $F(y)$, with $F(y = 0) = 0$ at the stagnation line ($\bar{x} = 0$) according to equation (8*a*).

For the *moving* impingement surface, viscous effects require that the horizontal flow velocity u near the surface at each point x approach the surface speed v_s. In particular, at the stagnation line ($x = 0$) where $u_\infty = 0$, the flow velocity must be largest at the plate surface ($y = 0$) and become smaller away from the surface, as in Fig. 2. Equation (6*a*) is modified to give an expression for the horizontal velocity component that includes surface motion effects

$$u = C\,x\,h'(y) + L(y) \tag{11}$$

As will be shown in the subsequent analysis, the function $L(y)$ incorporating surface motion effects is dependent on $h(y)$. No attempt is made to linearize the Navier–Stokes equations and equation (11) is thereby not a statement of superposition, but is found to be a general solution to the Navier–Stokes equations. At this point, $h(y)$ and $L(y)$ may be regarded as unknown functions, which must satisfy specified matching conditions that are discussed below. The corresponding expression for the vertical velocity component v on the moving surface is found from equations (1) and (11). Since $v = 0$ at the impingement surface [assumption (*vi*)], the expression for v is readily shown to be identical to equation (6*b*).

Equation (11) must become identical to equation (7*a*) far from the surface and, at the surface, $u = v_s$. With boundary conditions for $h(y)$ given by equation (9), the function $L(y)$ is subject to

$$y = 0 : L = v_s \tag{12a}$$

$$\text{as } y \to \infty : L \to 0 \tag{12b}$$

With equations (6*b*) and (11), equation (2) gives

$$C^2 x\left[\left(\frac{dh}{dy}\right)^2 - h\frac{d^2h}{dy^2} - \frac{\nu}{C}\frac{d^3h}{dy^3} - 1\right] + C\left[L\frac{dh}{dy} - h\frac{dL}{dy} - \frac{\nu}{C}\frac{d^2L}{dy^2}\right] = 0 \tag{13}$$

The solution to $L(y)$ can be found from equation (13) by noting that the first expression in brackets is identical to equation (10) pertaining to the stationary impingement surface. Since the boundary conditions [equation (9)] for $h(y)$ remain unchanged, both expressions in brackets are identically equal to zero and the governing ordinary differential equation for L is

$$\frac{\nu}{C}\frac{d^2L}{dy^2} + h\frac{dL}{dy} - L\frac{dh}{dy} = 0 \tag{14}$$

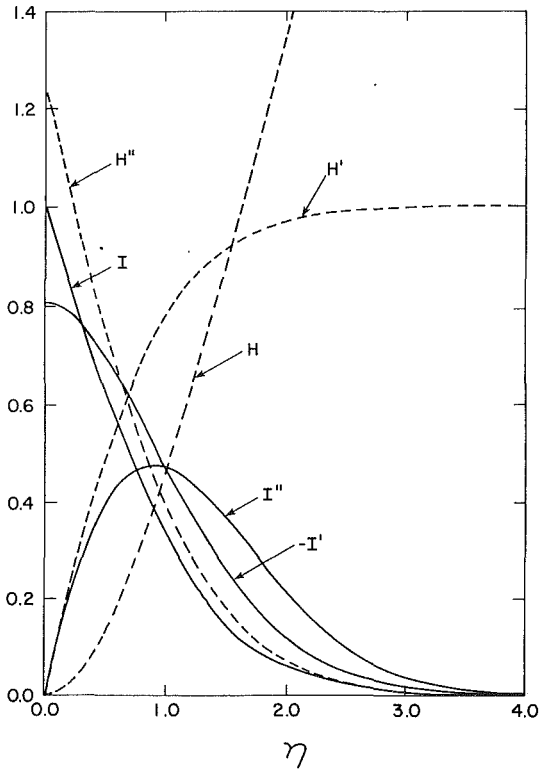

Fig. 3 Solutions to the differential equations governing flow velocity in the stagnation region

In terms of the dimensionless variables $\bar{C}$, $\bar{u}$, $\bar{v}$, H, I, and η (see Nomenclature), equations (11), (6*b*), (10), and (14) become

$$\bar{u} = \bar{C}\bar{x}\frac{dH}{d\eta} + \bar{v}_s I(\eta) \tag{15}$$

$$\bar{v} = -H(\eta)\left[\frac{\bar{C}}{\mathrm{Re}_w}\right]^{1/2} \tag{16}$$

$$\frac{d^3H}{d\eta^3} + H\frac{d^2H}{d\eta^2} - \left[\frac{dH}{d\eta}\right]^2 + 1 = 0 \tag{17}$$

$$\frac{d^2I}{d\eta^2} + H\frac{dI}{d\eta} - I\frac{dH}{d\eta} = 0 \tag{18}$$

Equations (17) and (18) are subject to the conditions given by equations (9) and (12), which in terms of H, I, and η, are

$$\eta = 0 : \quad H = \frac{dH}{d\eta} = 0; \quad I = 1 \tag{19a}$$

$$\eta \to \infty : \quad \frac{dH}{d\eta} \to 1; \quad I \to 0 \tag{19b}$$

Solutions to equation (17) are available graphically and in tabulated form (White, 1974; Schlichting, 1979). Values of H from these solutions can be used with equation (19) to determine $I(\eta)$ by numerical integration of equation (18). However, in order to ensure adequate accuracy, equations (17) and (18) were both written as systems of first-order differential equations and then each system was solved by the fourth-order Runge–Kutta method. A step size of 0.02 was used for η to ensure accuracy to six decimal places. Initial values for $d^2H/d\eta^2$ and $dI/d\eta$ were assumed and integration was performed for $0 \le \eta \le 10$. The initial values were successively improved by using the secant method until the conditions given by equation (19*b*) were satisfied at $\eta = 10$. This maximum value of η was selected since larger values did not affect the integrated results, indicating that $\eta = 10$ is effectively infinity in equation (19*b*).

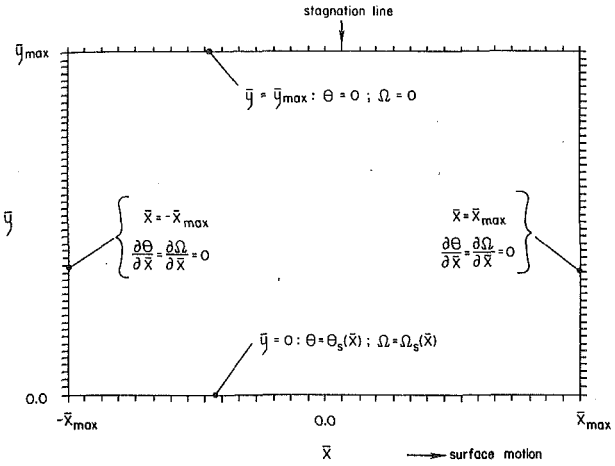

Fig. 4 Computational domain and boundary conditions used in numerical solution to conservation equations for energy and species

Results of the numerical integration are plotted in Fig. 3, wherein the primes denote differentiation with respect to η. Although available elsewhere (White, 1974; Schlichting, 1979), the solution to equation (17) is included since it is required to solve equation (18). Along the stagnation line ($\bar{x} = 0$) where $u_\infty = 0$, the flow velocity on the moving surface is governed by $I(\eta)$ according to equation (15), which rapidly approaches zero as η increases. Thus, for $\eta \gtrsim 3$, surface motion has a small effect on the flow. Adjacent to the stagnation line, $\bar{u}$ in equation (15) depends on both $dH/d\eta$ and $I(\eta)$. The influence of the free stream is governed by $dH/d\eta$, which is close to unity for $\eta \gtrsim 3$. The functions $dH/d\eta$ and $I(\eta)$ are, therefore, countervailing and the importance of surface motion depends on the distances from the stagnation line and from the surface.

The coefficient of friction C_f can be determined from the flow solution and is defined by

$$C_f = \frac{\tau_s}{\rho v_j^2/2} = \frac{\mu\left(\frac{\partial u}{\partial y} + \frac{\partial v}{\partial x}\right)\Big|_{y=0}}{\rho v_j^2/2} \tag{20}$$

where τ_s is the shear stress at the impingement surface. In accordance with equations (6*b*) and (16), $\partial v/\partial x = 0$ in equation (20). In terms of the dimensionless position $\bar{x}$ and the dimensionless parameters $\overline{C}$, Re_w, and $\bar{v}_s$, the shear stress distribution on the moving impingement surface is with equation (15)

$$C_f \mathrm{Re}_w^{0.5} = 2\sqrt{\overline{C}}\left[\overline{C}\bar{x}\frac{d^2H}{d\eta^2} + \bar{v}_s\frac{dI}{d\eta}\right]\Bigg|_{\eta=0} \tag{21}$$

where $d^2H/d\eta^2|_{\eta=0} \approx 1.232588$ and $dI/d\eta|_{\eta=0} \approx -0.804752$.

Determination of Heat and Mass Transfer Distributions. In terms of the dimensionless variables θ, Ω, $\bar{x}$, and $\bar{y}$ (see Nomenclature), equations for the conservation of energy and species (Burmeister, 1983), which correspond to the assumptions, are

$$\mathrm{Pr}\mathrm{Re}_w\left[\bar{u}\frac{\partial\theta}{\partial\bar{x}} + \bar{v}\frac{\partial\theta}{\partial\bar{v}}\right] = \frac{\partial^2\theta}{\partial\bar{x}^2} + \frac{\partial^2\theta}{\partial\bar{y}^2} \tag{22a}$$

$$\mathrm{Sc}\mathrm{Re}_w\left[\bar{u}\frac{\partial\Omega}{\partial\bar{x}} + \bar{v}\frac{\partial\Omega}{\partial\bar{y}}\right] = \frac{\partial^2\Omega}{\partial\bar{x}^2} + \frac{\partial^2\Omega}{\partial\bar{y}^2} \tag{22b}$$

Equations (22*a*) and (22*b*) were solved numerically for the boundary conditions and computational domain given in Fig. 4. Central difference approximations (Gerald, 1978) were used to represent the partial derivatives, and the velocity components $\bar{u}$ and $\bar{v}$ were calculated from equations (15) and (16). The resulting system of finite difference equations was solved using the line-by-line method and the tridiagonal matrix algorithm (Patankar, 1980). At $\bar{y} = 0$, piecewise linear variations in θ_s and Ω_s are specified in equation (23), where β is the dimensionless gradient in surface temperature or mass fraction in the vicinity of the stagnation line

$$-\bar{x}_{max} \le \bar{x} < -0.2, \quad \bar{y} = 0: \quad \theta_s = \Omega_s = 1 - 0.2\beta \tag{23a}$$

$$-0.2 \le \bar{x} \le 0.2, \quad \bar{y} = 0: \quad \theta_s = \Omega_s = 1 + \beta\bar{x} \tag{23b}$$

$$0.2 < \bar{x} \le \bar{x}_{max}, \quad \bar{y} = 0: \quad \theta_s = \Omega_s = 1 + 0.2\beta \tag{23c}$$

For heat transfer:

$$\beta = \left[\frac{w\dfrac{dTs}{dx}}{T_s - T_\infty}\right]_{x=0} = \frac{d\theta_s}{d\bar{x}}\Big|_{\bar{x}=0} \tag{23d}$$

For mass transfer:

$$\beta = \left[\frac{w\dfrac{d\omega}{dx}}{\omega_s - \omega_\infty}\right]_{x=0} = \frac{d\Omega_s}{d\bar{x}}\Big|_{\bar{x}=0} \tag{23e}$$

A linear variation near the stagnation line was deemed to be appropriate in that such a local variation was measured experimentally for a moving plate cooled by a turbulent, planar water jet (Zumbrunnen et al., 1990) and since only variations near the stagnation line are considered. Since θ_s and Ω_s are constant for $\bar{x} < -0.2$ and $\bar{x} > -0.2$, the boundary conditions in Fig. 4 at $\bar{x} = -\bar{x}_{max}$ and $\bar{x} = \bar{x}_{max}$ (i.e., $\partial\theta/\partial\bar{x} = \partial\Omega/\partial\bar{x} = 0$) are consistent with equation (23). This consistency decreases the sensitivity to the proximity of the boundary condition at $\bar{x} = -\bar{x}_{max}$, where the temperature distribution of the fluid traveling with the surface (Fig. 2) is generally not known. At $\bar{y} = \bar{y}_{max}$, the distance from the impingement surface is sufficiently large that free-stream conditions prevail, giving $\theta = \Omega = 0$.

The computational domain in Fig. 4 was subdivided using a uniform grid with 31 grid points in the $\bar{x}$ direction and 41 grid points in the $\bar{y}$ direction. A greater number of divisions was employed in the $\bar{y}$ direction for which velocity, species, and temperature gradients were higher. Values for $\bar{x}_{max}$ and $\bar{y}_{max}$ were carefully chosen to minimize sensitivity to the boundary conditions. For the dimensionless surface speeds considered ($0 \le \bar{v}_s \le 4$), results were determined to be insensitive to the boundary conditions at $\bar{x}_{max}$ with $\bar{x}_{max} = 0.3$. A value of 0.4 was used for $\bar{y}_{max}$ in order to ensure that changes in temperature and mass fraction were confined to the computational domain for the Prandtl and Schmidt numbers considered.

In accordance with the heat/mass transfer analogy and given the similarity in the boundary conditions, $\theta(\bar{x}, \bar{y}) = \Omega(\bar{x}, \bar{y})$ when Pr = Sc. Local Nusselt and Sherwood numbers, with the jet width w as a characteristic length, were calculated from central difference representations (Gerald, 1978) of equations (24*a*) and (24*b*)

$$\mathrm{Nu}_w(\bar{x}) = \frac{h_q(\bar{x})w}{k} = \frac{-1}{\theta_s(\bar{x})}\frac{\partial\theta}{\partial\bar{y}}\Big|_{\bar{y}=0} \tag{24a}$$

$$\mathrm{Sh}_w(\bar{x}) = \frac{h_m(\bar{x})w}{D} = \frac{-1}{\Omega_s(\bar{x})}\frac{\partial\Omega}{\partial\bar{y}}\Big|_{\bar{y}=0} \tag{24b}$$

Model Verification

The Nusselt number Nu_w at the stagnation line for a planar jet impinging on a stationary, isothermal surface can be calculated from the similarity solution for laminar flow past a wedge (White, 1974). Model-predicted values for Nu_w with $\bar{v}_s$

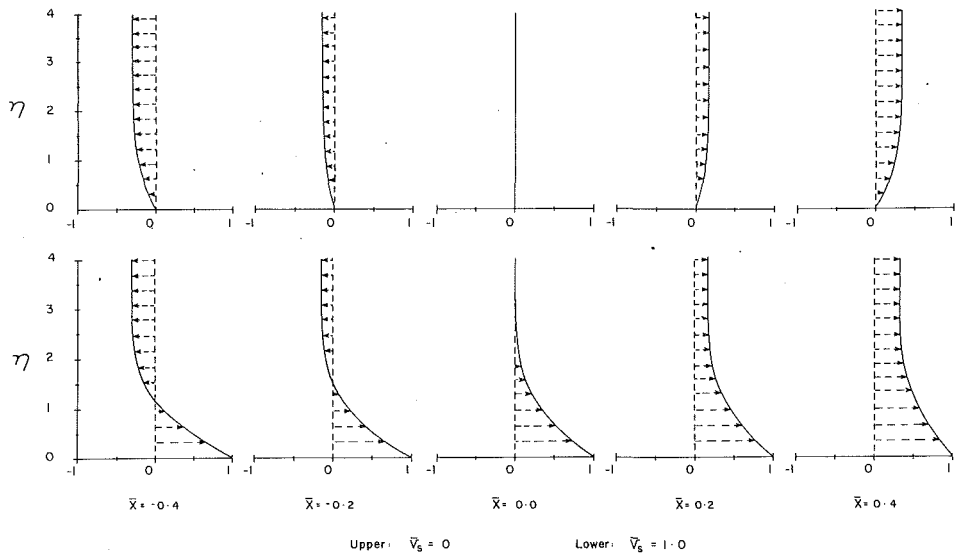

Fig. 5 Dimensionless flow velocity component $\bar{u}$ in the vicinity of a stationary and moving impingement surface with $\bar{C} = 0.7854$

$= 0$ and $\bar{x} = 0$ were within 0.4 percent of values calculated from the wedge flow solution for the Prandtl number range considered in this study ($0.5 \leq Pr \leq 3.0$). Experimental heat transfer results for a laminar, planar jet impinging on a stationary ($\bar{v}_s = 0$) surface with $Pr = 7.5$ are given by Inada et al. (1981). Their specified correction for Prandtl number ($Nu_w \propto Pr^{0.37}$) was applied to adapt their results to $Pr = 3.0$. A comparison is provided in Fig. 8, wherein excellent agreement is evident. Comparisons to the numerical results reported by Huang et al. (1984) were not possible since a crossflow of fluid was imposed in their work to simulate flow from neighboring jets.

Results and Discussion

The effect of surface motion on heat and mass transfer in the stagnation region is clarified by first considering the flow velocity solution. In equation (15), the dimensionless velocity component $\bar{u}$ depends on the dimensionless free-stream velocity gradient $\bar{C}$, the dimensionless distance from the stagnation line $\bar{x}$, and on the dimensionless surface velocity $\bar{v}_s$. The product $\bar{C}\bar{x}$ is recognized from equation (7*a*) to be the dimensionless free-stream velocity $\bar{u}_\infty$. The influence of surface motion relative to the free stream in determining $\bar{u}$ is governed by the functions $dH/d\eta$ and $I(\eta)$ in Fig. 3. Near the surface ($\eta \approx 0$), $I(\eta) \gg dH/d\eta$ and $\bar{u}$ is most greatly influenced by surface motion. The influence of surface motion diminishes at larger η, and $\bar{u}$ approaches the value corresponding to a stationary surface. The velocity component $\bar{v}$ in equation (16), however, is independent of the surface motion. This result can be surmised intuitively by noting that the surface motion in the symmetrically dividing flow is directed perpendicular to the flow direction for $\bar{v}$.

The dimensionless flow velocity component $\bar{u}$ is presented in Fig. 5 for a stationary surface ($\bar{v}_s = 0$) and for a moving surface ($\bar{v}_s = 1.0$). The specified value for $\bar{C}$ pertains to planar jets where the discharge velocity is uniform across the nozzle width (Inada et al., 1981). Velocity profiles are presented only for $-0.4 \leq \bar{x} \leq 0.4$, where the free-stream velocity in the planar jet is closely described by equation (7). For $\bar{v}_s = 0$, the flow velocity profiles are symmetric about the stagnation line ($\bar{x} = 0$) and indicate the flow acceleration commonly associated with stagnation flow. The velocity profiles for the moving impingement surface differ markedly from those for the stationary surface. At the stagnation line, flow is induced near the surface ($\eta \approx 0$) as a consequence of the surface motion. The flow velocities near the surface for $\bar{x} = 0.2$ and $\bar{x} = 0.4$ are higher than the flow velocities far from the surface, since the fluid acceleration in the free stream is not complete. For $\bar{x} < 0$, the flow velocity close to the surface is directed opposite to the flow far from the surface. The region containing fluid moving in the direction of surface motion becomes larger as the distance from the stagnation line decreases and the free-stream velocity diminishes. The case where $\bar{v}_s \ll 1$ is shown in Fig. 2. The case where $\bar{v}_s \gg 1$ is qualitatively similar to Fig. 5 with $\bar{v}_s = 1.0$.

Further understanding of the flow on the moving surface can be gained by considering the expression for friction coefficient C_f given by equation (21). It is evident from Fig. 5 that the dimensionless velocity gradient $d\bar{u}/d\eta|_{\eta=0}$ is greatly affected by surface motion. According to equation (21), the magnitudes of the friction coefficients for the stationary surface are equal at equal values of $\bar{x}$ from the stagnation line. However, as the surface velocity $\bar{v}_s$ increases, the friction coefficient distribution is displaced downward ($dI/d\eta|_{\eta=0} = -0.804752$) since the gradient in the flow velocity component $\bar{u}$ is increasingly influenced by the surface motion as Fig. 5 indicates.

A well-known characteristic of impinging flows, where the impingement surface is stationary, is the constancy of the velocity boundary layer thickness δ within the impingement region (Schlichting, 1979). Equation (15) was used to determine values for η where $y = \delta$ [i.e., $\eta(y = \delta)$] for the moving surface according to the criterion $|(\bar{u}_\infty - \bar{u})/\bar{u}_\infty| = 0.01$. This criterion reduces to $\bar{u}/\bar{u}_\infty = 0.99$ used to establish δ for the stationary surface. (The criterion $\bar{u}/\bar{u}_\infty = 0.99$ is not generally appropriate for the moving surface since $|\bar{u}|$ can be larger than $|\bar{u}_\infty|$.) The solution to equation (10) is readily used to show that $\eta(y = \delta) = 2.4$ for the stationary surface. For the moving impingement surface, calculations indicate that the velocity boundary layer thickness is largest near the stagnation line and increases with the surface velocity $\bar{v}_s$. The spatial variation in the boundary layer thickness and the dependence on $\bar{v}_s$ are attributed to the differing relative influence of the functions $dH/d\eta$ and $I(\eta)$ (Fig. 3) in determining the flow velocity in equation (15). However, the difference between the flow velocity component $\bar{u}$ and the free-stream velocity $\bar{u}_\infty$ is small for $\eta \gtrsim 2.4$, since changes in $dH/d\eta$ and $I(\eta)$ are very nearly completed in Fig. 3. Thus, the distance over which the velocity changes on the moving plate is largely represented by the ve-

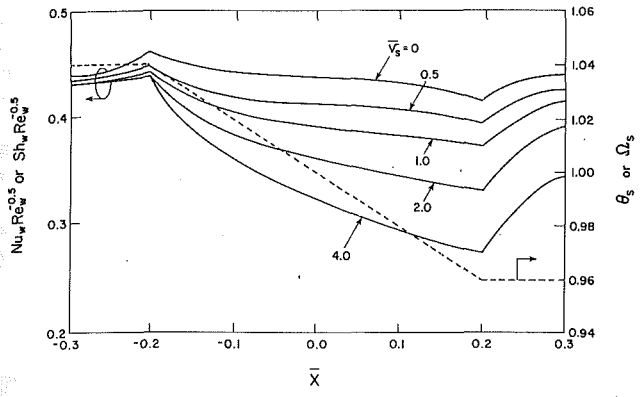

Fig. 6 Heat and mass transfer distributions on a moving impingement surface characterized by a varying surface temperature or surface mass fraction with $\bar{C} = 0.7854$, Pr = Sc = 0.7, and $\beta = -0.2$

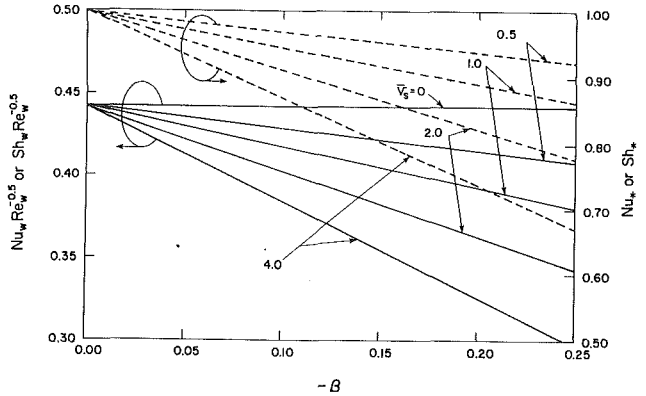

Fig. 7 Influence of local surface temperature gradient or local mass fraction gradient on heat and mass transfer at the stagnation line ($\bar{x} = 0$) with $\bar{C} = 0.7854$ and Pr = Sc = 0.7

locity boundary layer thickness on the stationary surface, for which $\eta = 2.4$.

The numerical model was used to generate local heat and mass transfer distributions for a moving surface with a constant surface temperature or constant mass fraction [$\beta = 0$ in equation (23)]. Heat and mass transfer distributions in terms of $Nu_w Re_w^{-0.5}$ or $Sh_w Re_w^{-0.5}$ varied with surface velocity by less than 0.1 percent over the range $0 \le \bar{v}_s \le 4.0$ for $0.5 \le Pr \le 3.0$ and $0.5 \le Sc \le 3.0$. This insensitivity to surface velocity arises when $\beta = 0$ since under this condition, as commonly noted in analytical stagnation flow solutions (White, 1974), $\partial\theta/\partial\bar{x} \ll \partial\theta/\partial\bar{y}$, $\partial^2\theta/\partial\bar{x}^2 \ll \partial^2\theta/\partial\bar{y}^2$, $\partial\Omega/\partial\bar{x} \ll \partial\Omega/\partial\bar{y}$, and $\partial^2\Omega/\partial\bar{x}^2 \ll \partial^2\Omega/\partial\bar{y}^2$. Equation (22) then becomes

$$\mathrm{PrRe}_w \bar{v} \frac{\partial\theta}{\partial\bar{y}} = \frac{\partial^2\theta}{\partial\bar{y}^2} \tag{25a}$$

$$\mathrm{ScRe}_w \bar{v} \frac{\partial\Omega}{\partial\bar{y}} = \frac{\partial^2\Omega}{\partial\bar{y}^2} \tag{25b}$$

Solutions to equation (25) are independent of the flow velocity component $\bar{u}$ [equation (15)] and dependent on the flow velocity component $\bar{v}$ [equation (16)]. Since values of $\bar{v}$ given by equation (16) remain unchanged on the moving surface, the solutions to equation (25) do not depend on the surface velocity $\bar{v}_s$. Consequently, heat and mass transfer correlations or analyses for stationary impingement surfaces can be used to determine heat or mass transfer rates for moving impingement surfaces when the moving surface is characterized by a constant surface temperature or constant surface mass fraction for the diffusing species. These restrictions are seldom satisfied in cooling processes since the surface temperature of a material in motion generally decreases as the material passes through an impinging jet. In drying applications, surface mass fraction can also decrease if the moving material is simultaneously cooled.

The effect of a decreasing surface temperature or surface mass fraction on the local heat and mass transfer distributions for a uniform ($\bar{C} = 0.7854$) planar jet impinging on a moving surface is shown in Fig. 6. The values for Pr and Sc are representative of applications where air is used for cooling or where air is used to evaporate water. All distributions shown in Fig. 6 pertain to the single variation for θ_s or Ω_s given by equation (23) with $\beta = -0.2$. Of primary interest in this study is the influence of surface motion on heat and mass transfer near the stagnation line ($\bar{x} \le |0.2|$). As discussed earlier, linear variations in θ_s and Ω_s were specified near the stagnation line since such variations closely approximate the local surface temperature distribution on a moving plate (Zumbrunnen et al., 1990). Local Nusselt and Sherwood numbers farther from the stagnation line ($\bar{x} > |0.2|$) correspond to regions where constant surface temperature and surface mass fraction are prescribed, in order to obtain heat and mass transfer results that are independent of the boundary conditions at $\bar{x} = |0.3|$ in Fig. 4. Results for this region are presented in Fig. 6 for completeness and to show the importance of the local gradient in θ_s and Ω_s for a moving impingement surface. The general behavior in local Nusselt and Sherwood numbers for $\bar{x} > |0.2|$ is consistent with the discussion related to equation (25), since single values of Nusselt and Sherwood numbers are approached near $\bar{x} = |0.3|$ once the surface gradient is removed. Closer to the stagnation line, local Nusselt and Sherwood numbers with the linear surface variation decrease with increasing surface velocity. Decreases occur, since warmer or higher concentration fluid near the surface is transported by the surface motion to regions located downstream with respect to the surface motion direction. The temperature or mass fraction gradients directed perpendicular to the surface are thereby reduced. The decrease is most significant for $\bar{x} > 0$ where the surface motion and fluid flow are in the same direction. For $x < 0$, the surface motion and fluid flow are oppositely directed and the larger relative velocity between the surface and flow leads to a smaller reduction in the Nusselt and Sherwood numbers.

The influence of a decreasing surface temperature or surface mass fraction is examined further at the stagnation line ($\bar{x} = 0$) in Fig. 7. For the *stationary* surface ($\bar{v}_s = 0$), the Nusselt and Sherwood numbers are independent of the dimensionless surface temperature gradient or surface mass fraction gradient. This independence is due to the symmetry of the dividing flow at the stagnation line, where fluid approaches the surface only along the stagnation line. A dependence on surface temperature gradient at the stagnation line has been suggested by boundary layer similarity analyses, which utilize surface temperature variations of the functional form $T_s - T_\infty = Ax^\gamma$ (Levy, 1952; Eckert and Drake, 1972), where A and γ are positive constants to approximate physical temperature variations. However, although mathematically satisfying conditions needed to achieve similarity solutions, this functional form is inappropriate in impinging flows since, in contradiction with $T_s - T_\infty = Ax^\gamma$, $T_s \ne T_\infty$ for $x = 0$ where a finite heat transfer coefficient applies (Zumbrunnen et al., 1989).

For the *moving* impingement surface, Nusselt and Sherwood numbers in Fig. 7 are smaller for larger magnitudes of the parameter β. Reductions are greater at higher values of the dimensionless surface velocity $\bar{v}_s$, but become vanishingly small for $\beta = 0$. In terms of Nu_* (the ratio of Nu_w for a moving surface to Nu_w for a stationary surface), Nusselt numbers can be reduced by more than 30 percent for $\bar{v}_s \approx 4.0$ and $\beta \approx -0.25$. Analogous reductions for Sherwood numbers are given in terms of Sh_*. Nusselt or Sherwood numbers decrease by less than 10 percent for small surface velocities ($\bar{v}_s \le 0.5$) with $-\beta < 0.25$. This result is consistent with the aforedescribed study conducted by van Heiningen et al. (1977), in which heat

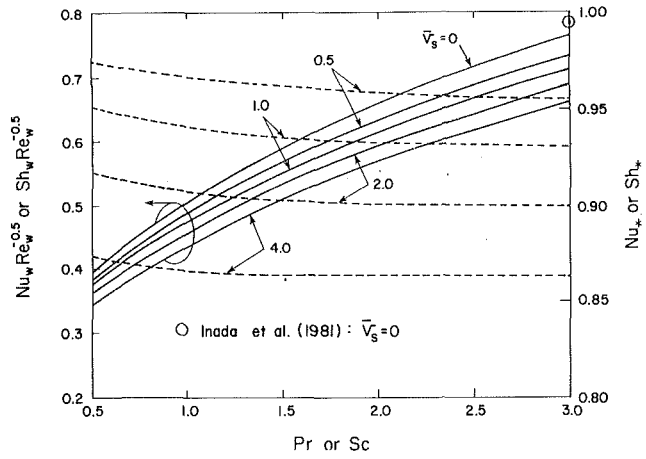

Fig. 8 Influence of Prandtl and Schmidt numbers on heat and mass transfer at the stagnation line ($\bar{x} = 0$) with $\bar{C} = 0.7854$ and $\beta = -0.1$

transfer results for $\bar{v}_s < 0.015$ were in close agreement with results from studies employing stationary plates.

In Fig. 8, Nusselt and Sherwood numbers at the stagnation line ($\bar{x} = 0$) with $\beta = -0.1$ are larger at higher Prandtl and Schmidt numbers, but decrease with increasing surface velocity as in Fig. 7. The distance from the moving surface over which flow velocity varies relative to the distance for which temperature and mass fraction vary is governed by the Prandtl and Schmidt numbers. At higher Prandtl and Schmidt numbers, the region adjacent to the surface affected by surface motion extends farther into the flow. Consequently, temperature and mass fraction profiles are more greatly influenced by the surface motion at the higher Prandtl and Schmidt numbers, which is indicated in Fig. 8 by the correspondingly smaller values of Nu_* and Sh_* at the higher surface velocities. However, reductions in heat or mass transfer in Fig. 8 are only weakly dependent on the Prandtl or Schmidt numbers. This result suggests that surface motion effects at the stagnation line can be succintly expressed in terms of Nu_* and Sh_* for large ranges in Pr and Sc by the format employed in Fig. 7. The importance of surface motion can be assessed by first estimating β and $\bar{v}_s$ from entrance and exit conditions for a specified cooling or drying application. The corresponding value for Nu_* or Sh_* can then be determined from Fig. 7.

Conclusions

The influence of surface motion on fluid flow is confined to a thin region, which, although larger, is effectively represented by the velocity boundary layer thickness for a planar jet impinging on a stationary surface. Convective heat and mass transfer are unaffected by surface motion when the surface temperature and surface mass fraction are spatially constant along the impingement surface. However, in situations where surface temperature or surface mass fraction vary with distance from the stagnation line, convective heat and mass transfer are dependent on the dimensionless surface velocity $\bar{v}_s$. Surface temperature and surface mass fraction typically decrease in the direction of surface motion in applications where impinging jets are employed. Consequently, comparatively warmer or higher concentration fluid is entrained by the surface motion, decreasing heat and mass transfer rates at positions downstream with respect to the surface motion direction. Empirical heat and mass transfer correlations for impinging jets, which are often developed with stationary impingement surfaces, may provide inaccurate estimates in manufacturing processes where the cooled or dried material is in motion. Values of Nu_* and Sh_*, which are shown in Figs. 7 and 8, can be used to assess the importance of surface motion and the applicability of empirical correlations to particular jet cooling or drying applications.

Acknowledgments

Support for this work was provided by the Clemson University Research Office and is gratefully acknowledged. I would also like to extend my gratitude to the reviewers and to Professor Tah-teh Yang of Clemson University for their comments and assistance.

References

Burmeister, L. C., 1983, *Convective Heat Transfer*, Wiley, New York, pp. 737–747.

Eckert, E. R. G., and Drake, R. M., Jr., 1972, *Analysis of Heat and Mass Transfer*, McGraw-Hill, New York, pp. 306–314.

Gerald, C. F., 1978, *Applied Numerical Analysis*, Addison Wesley, New York, pp. 194–201.

Huang, P. G., Mujumdar, A. S., and Douglas, W. J. M., 1984, "Numerical Prediction of Fluid Flow and Heat Transfer Under a Turbulent Impinging Slot Jet With Surface Motion and Crossflow," ASME Paper No. 84-WA/HT-33.

Inada, S., Miyasaka, Y., and Izumi, R., 1981, "A Study on the Laminar-Flow Heat Transfer Between a Two-Dimensional Water Jet and a Flat Surface With Constant Heat Flux," *Bulletin of the JSME*, Vol. 24, pp. 1803–1810.

Kohring, F. C., 1985, "Waterwall Water-Cooling Systems," *Iron and Steel Engineer*, June, pp. 30–36.

Levy, S., 1952, "Heat Transfer to Constant-Property Laminar Boundary Layer Flows With Power-Function Freestream Velocity and Wall-Temperature Variation," *Journal of the Aeronautical Sciences*, Vol. 19, pp. 341–348.

Martin, H., 1977, "Heat and Mass Transfer Between Impinging Gas Jets and Solid Surfaces," in: *Advances in Heat Transfer*, Vol. 13, Academic Press, New York, pp. 1–60.

Metzger, D. E., and Grochowsky, L. D., 1977, "Heat Transfer Between an Impinging Jet and a Rotating Disk," ASME JOURNAL OF HEAT TRANSFER, Vol. 99, pp. 663–667.

Patankar, S. V., 1980, *Numerical Heat Transfer and Fluid Flow*, McGraw-Hill, New York, pp. 52–54, 64–66.

Popiel, C. O., and Bogusłowski, L., 1986, "Local Heat Transfer From a Rotating Disk to an Impinging Round Jet," ASME JOURNAL OF HEAT TRANSFER, Vol. 108, pp. 357–364.

Rott, N., 1956, "Unsteady Viscous Flow in the Vicinity of a Stagnation Point," *Quarterly of Applied Mathematics*, Vol. 13, pp. 444–451.

Schlichting, H., 1979, *Boundary-Layer Theory*, 7th ed., McGraw-Hill, New York, pp. 95–99.

Sineath, H. H., and Pavelchek, W. R., 1971, "Cellophane," in: *The Science and Technology of Polymer Films*, Vol. II, Wiley-Interscience, New York, pp. 395–400.

van Heiningen, A. R. P., Mujumdar, A. S., and Douglas, W. J. M., 1977, "Flow and Heat Transfer Characteristics of a Turbulent Slot Jet Impinging on a Moving Wall," in: *Abstracts of the Symposium on Turbulent Shear Flows*, Pennsylvania State University, University Park, PA, Vol. I, pp. 3.9–3.15.

White, F. M., 1974, *Viscous Fluid Flow*, McGraw-Hill, New York, pp. 273–284, 172–184.

Zumbrunnen, D. A., Incropera, F. P., and Viskanta, R., 1989, "Convective Heat Transfer Distributions on a Plate Cooled by Planar Water Jets," ASME JOURNAL OF HEAT TRANSFER, Vol. 111, pp. 889–896.

Zumbrunnen, D. A., 1990, "Convective Heat and Mass Transfer in the Stagnation Region of a Planar Jet Impinging on a Moving Surface," *Proceedings, 5th AIAA/ASME Thermophysics and Heat Transfer Conference*, K. Vafai et al., eds., ASME HTD-Vol. 129, pp. 11–20.

Zumbrunnen, D. A., Incropera, F. P., and Viskanta, R., 1990, "Method and Apparatus for Measuring Heat Transfer Distributions on Moving and Stationary Plates Cooled by a Planar Liquid Jet," *Experimental Thermal and Fluid Science*, Vol. 3, pp. 202–213.

Convective Heat Transfer by Impingement of Circular Liquid Jets

X. Liu
Student Mem. ASME

J. H. Lienhard V
Mem. ASME

J. S. Lombara[1]

Department of Mechanical Engineering,
Massachusetts Institute of Technology,
Cambridge, MA 02139

The impingement of circular, liquid jets provides a convenient method of cooling surfaces. Here, jet impingement cooling of uniformly heated surfaces is investigated analytically and experimentally for stable, unsubmerged, uniform velocity laminar jets in the absence of phase change. Analytical and numerical predictions are developed for a laminar radial film flow. Experiments using undisturbed laminar jets were performed to determine local Nusselt numbers from the stagnation point to radii of up to 40 diameters. Turbulent transition in the film flow is observed experimentally at a certain radius. Beyond this transition radius, a separate turbulent analysis is constructed. Integral method results are compared to numerical results, and Prandtl number effects are investigated. The predictions are found to agree well with the measurements for both laminar and turbulent flow. Predictive formulae are recommended for the entire range of radii.

Introduction

Cooling a surface with an impinging liquid jet is an attractive technique because of its high efficiency and unsophisticated hardware requirements. Applications of jet impingement cooling are varied, and include processing of both metals and molded plastics, cooling of high-efficiency (aircraft) generator coils, and cooling of certain electronic modules. Such jets lend themselves to either convective boiling or to nonevaporative convection, but in both situations the cooling efficiency varies with the radial distance from the point of impact. In this study, we consider the impingement of a circular, unsubmerged, laminar liquid jet on a surface of uniform heat flux. Convective transport, without change of phase, is analyzed theoretically and experimentally, taking account of both the initial laminar flow and the downstream turbulent flow.

An axisymmetric, laminar impinging jet spreads into a thin, laminar liquid film when it impacts a plane surface normal to its axis (Fig. 1). The hydrodynamics of this film have previously been studied theoretically by Watson (1964) and experimentally by Azuma and Hoshino (1984a, 1984b, 1984c, 1984d) and by Olsson and Turkdogan (1966). Watson divided the flow radially into a stagnation region, a boundary layer region with surface velocity equal to jet speed, and a region of viscous similarity with decreasing surface velocity; he noted that the film flow would be terminated by a hydraulic jump at a location independently controlled by downstream conditions. The thickness of the film initially decreases and then increases with radius as viscous wall effects slow the spreading film. Watson employed both viscous similarity and momentum integral solutions.

Watson's theoretical expressions for the laminar boundary layer and similarity region velocity profiles and film thickness were experimentally verified by Azuma and Hoshino (1984b, 1984c) using laser-Doppler measurements. This is in contrast to the results of Olsson and Turkdogan (1966), who measured the surface velocity by dropping bits of cork onto the liquid. Olsson and Turkdogan found poor agreement with Watson's predictions, observing a constant surface velocity lower than the jet speed, and their results have sometimes been used to deny the presence of a similarity region. However, no conclusive evidence showed that the dropped, buoyant cork actually moved at the liquid surface speed. Since the experimental approach of Azuma and Hoshino is clearly more accurate, we are inclined to give their conclusions greater weight. For the details of Watson's flow field, the reader is referred to his paper. His expressions, and those of a later independent study by Sharan (1984), are quoted hereinafter when needed.

Azuma and Hoshino measured the turbulent transition radius in their system (which used an annular orifice mounted on the plate, rather than an actual impinging jet) and also measured the subsequent velocity profiles. The turbulent film was well characterized by standard boundary layer results, but it did appear to show relaminarization farther downstream as the film slowed and its stability increased.

Using Watson's similarity solution, Chaudhury (1964) analyzed the heat transfer from an isothermal wall in terms of a series solution for the similarity region and an integral solution for the boundary layer region; Carper (1989) has also presented a solution to that problem. Liu and Lienhard (1989) developed predictions of the Nusselt number for uniform heat flux using an integral method and presented limited comparisons to ex-

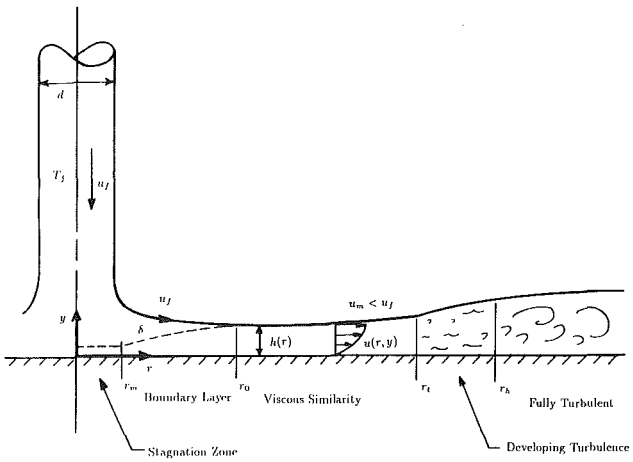

Fig. 1 Jet and film flow field showing hydrodynamic evolution (not to scale)

[1]Present address: Leutron Corporation, Allentown, PA.

Contributed by the Heat Transfer Division for publication in the JOURNAL OF HEAT TRANSFER. Manuscript received by the Heat Transfer Division July 4, 1990; revision received September 29, 1990. Keywords: Forced Convection, Jets, Thin Film Flow.

perimental data. Wang et al. (1989a, 1989b, 1989c) gave detailed theoretical solutions for heat transfer in the stagnation and boundary layer regions; these solutions account for variable wall conditions as well as for conjugate heat transfer between the jet and the wall. They did not consider the downstream similarity region, in which surface velocity declines with radius; at common Reynolds numbers, the stagnation zone and boundary layer regimes are confined to radii of 3 to 7 diameters from the point of impact. When a jet is used to cool large areas, the similarity region and turbulent transition must also be accounted for.

Experimental studies have been few, particularly in regard to local, rather than average, heat transfer. Ishigai et al. (1977) measured local heat transfer coefficients in the hydraulic jump region and presented a limited, graphic set of data for the local heat transfer coefficient in the plane of impact. They mentioned that the data showed a downstream transition from laminar to turbulent flow; their jets were produced by a short tube, three diameters in length. Stevens and Webb (1989) investigated turbulent impinging jet heat transfer experimentally and developed a correlation for Nu_d. Their data are confined to $r/d < 15$ and their correlation is accurate in a region $r/d < 5$ for $d = 2.2$ mm and a smaller region for larger diameter of jets. The radial transition from laminar to turbulent flow was not mentioned, but it must be noted that their jets were deliberately made turbulent prior to impact.

Nakoryakov et al. (1978) used electrodiffusion to obtain local mass transfer coefficients beneath a laminar jet and compared them to an appropriate boundary layer analysis. Their study applies to very high Schmidt number ($\mathrm{Sc} \gg 1$) and a boundary condition of uniform wall concentration, correspondent to uniform wall temperature conditions at $\mathrm{Pr} \gg 1$. Their experiments showed the mass transfer coefficient to rise above the laminar prediction downstream, and they argued this to result from surface waves. However, the present results suggest that transition to turbulence is a more likely cause in their range of Reynolds number. The incoming jet velocities for their experiments were calculated on the basis of the apparently theoretical stagnation zone result

$$\mathrm{Nu}_l = 0.753\ \mathrm{Pr}^{1/3}\ \mathrm{Re}_l^{1/2} \tag{1}$$

where l is the radius of their electrodiffusion probe. However, this correlation was not independently corroborated in their paper.

The present paper develops radially complete results for the liquid film heat transfer with uniform heat flux; most of these results are analytically derived, and all are validated experimentally. Particular attention is devoted to the similarity region, employing numerical solutions for the uniform flux condition (which is not self-similar) to investigate the role of wall boundary conditions, simplified correlations, and the integral method prediction of a critical Prandtl number above which the thermal boundary layer does not reach the free surface (Liu and Lienhard, 1989). Our previous integral method solutions are extended to include $\mathrm{Pr} < 1$. The laminar predictions are then compared to new experimental data from an experimental apparatus configured to achieve very clean, stable, laminar jets. The laminar predictions are generally found to agree very well with the data. In addition, turbulent transition is observed in the similarity region, and separate analytical predictions are developed to account for the turbulent augmentation of the heat transfer. A correlation is given for the turbulent transition point.

Nomenclature

c_p = heat capacity
C_c = jet contraction coefficient = 0.611
C_f = friction factor
d = contracted jet diameter = $\sqrt{C_c} \times$ (diameter of orifice)
$f'(\eta)$ = similarity function, equation (24)
h = local thickness of liquid sheet
h_{r1} = liquid sheet thickness at the position where thermal boundary layer reaches the free surface
h_t = liquid sheet thickness at transition point from laminar to turbulence
h_{T0} = liquid sheet thickness at r_{T0}
k = thermal conductivity of the liquid
k_w = thermal conductivity of the heater
Nu_d = Nusselt number = $q_w d/k(T_w - T_f)$
Nu_r = Nusselt number based on r, = $q_w r/k(T_w - T_f)$ = $\mathrm{Nu}_d(r/d)$
Pr = Prandtl number
q_w = wall heat flux
Q = volume flow rate of jet = $u_f \pi d^2/4$
r = radius measured from point of jet impact
r_h = hump radius, at which turbulence is fully developed
r_o = radius at which δ reaches the surface of the liquid sheet
r_1 = radius where thermal boundary layer reaches the free surface for $\mathrm{Pr} > 1$
$r_{T,i}$ = location of the initial temperature profile given
r_{T0} = radius where thermal boundary layer reaches the free surface for $\mathrm{Pr} < 1$
$r_{u,i}$ = location of the initial velocity profile given
r_t = radius at transition point from laminar to turbulent flow
R = Reynolds number defined by Watson = $2Q/d\nu$ = $(\pi/2)\ \mathrm{Re}_d$
Re_d = Reynolds number of the jet = $u_f d/\nu$
St = Stanton number = $q_w/\rho c_p u_{\max}\ (T_w - T_{sf})$
t = heater sheet thickness
$T(r, y)$ = liquid temperature distribution
T_f = jet temperature at impingement
T_m = measured temperature on the back of the heater
T_{sf} = free surface temperature
T_{sat} = liquid saturation temperature
T_w = wall temperature on the liquid side of the heater
$u(r, y)$ = radial velocity distribution in liquid film
u_f = velocity of impinging jet
$u_{\max}$ = local maximum film velocity (liquid free surface velocity), equal to u_f in regions 2, 2l, and 3l
y = distance normal to the wall
z = distance between nozzle and target plate
δ = viscous boundary layer thickness
δ_t = thermal boundary layer thickness
$\Delta = \delta/h$
Δ_{T0} = Δ at r_{T0}
$\epsilon = (t/d); \epsilon^2$ is the order of radial to vertical conduction in the heater sheet
η = similarity variable
θ = nondimensional temperature
μ = dynamic viscosity
ν = kinematic viscosity
ρ = density
$\phi = \delta/\delta_t$

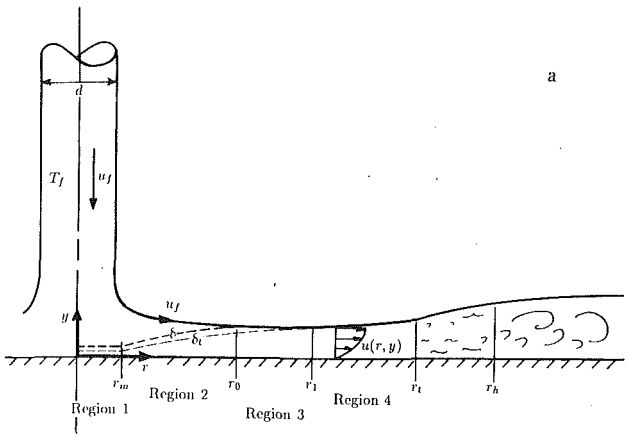

(a)

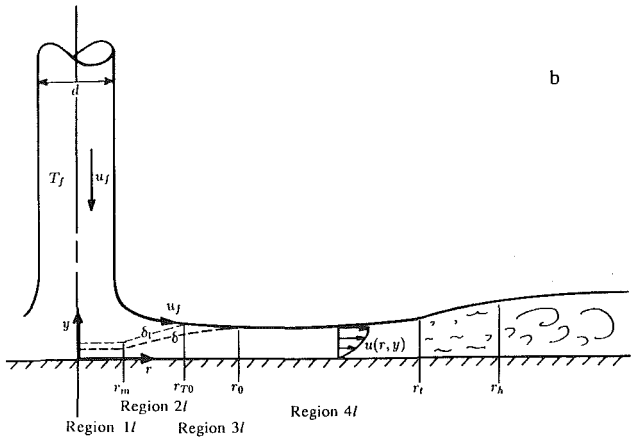

(b)

Fig. 2 Development of the thermal boundary layer: (*a*) Pr > 1; (*b*) Pr < 1 (not to scale)

2 Predictions From the Laminar Theory

2.1 Integral Solutions for the Heat Transfer: Pr ≥ 1. In a previous study (Liu and Lienhard, 1989), we obtained integral solutions for the heat transfer in the boundary layer and similarity regions for Prandtl number greater than the unity. The regions identified and results found are as follow (see Fig. 2*a*):

Region 1. The stagnation zone.

Region 2. $\delta < h$ region: Neither the thermal nor viscous boundary layer reach the free surface; surface temperature and velocity, T_{sf} and u_{max}, are the inlet temperature and velocity, T_f and u_f.

Region 3. $\delta = h$ and $\delta_t < h$ region: The viscous boundary layer has reached the free surface. The velocity outside the viscous boundary layer decreases with radius, but the surface temperature remains at the inlet temperature, T_f.

Region 4. $\delta = h$, $\delta_t = h$, and $T_w < T_{sat}$ region: In this region, the thermal boundary layer has reached the surface of the liquid sheet, and the temperature of the liquid surface increases with radius.

For region 2, the boundary layer region follows the stagnation zone:

$$\mathrm{Nu}_d = 0.632\ \mathrm{Re}_d^{1/2}\ \mathrm{Pr}^{1/3}\left(\frac{d}{r}\right)^{1/2} \tag{2}$$

Region 2 ends and region 3 begins where the viscous boundary layer reaches the film surface at $r = r_0 = 0.1773 d\ \mathrm{Re}_d^{1/3}$. In region 3:

$$\mathrm{Nu}_d = \frac{0.407\ \mathrm{Re}_d^{1/3}\ \mathrm{Pr}^{1/3}\left(\frac{d}{r}\right)^{2/3}}{\left[0.1713\left(\frac{d}{r}\right)^2 + \frac{5.147 r}{\mathrm{Re}_d d}\right]^{2/3}\left[\frac{1}{2}\left(\frac{r}{d}\right)^2 + C_3\right]^{1/3}} \tag{3}$$

where[2]

$$C_3 = \frac{0.267(d/r_0)^{1/2}}{\left[0.1713\left(\frac{d}{r_0}\right)^2 + \frac{5.147 r_0}{\mathrm{Re}_d d}\right]^2} - \frac{1}{2}\left(\frac{r_0}{d}\right)^2 \tag{4}$$

Region 3 ends and region 4 begins where the thermal boundary layer reaches the liquid surface at $r = r_1$; equations defining r_1 are given in our previous paper. In region 4:

$$\mathrm{Nu}_d = \frac{0.25}{\frac{1}{\mathrm{PrRe}_d}\left(1 - \frac{r_1^2}{r^2}\right)\left(\frac{r}{d}\right)^2 + 0.130\frac{h}{d} + 0.0371\frac{h_{r1}}{d}} \tag{5}$$

where h is given by equation (20) below. Note that region 4 will occur only for Pr less than a critical value near five[3]; otherwise, the thermal boundary layer does not grow fast enough to reach the surface of the liquid film, which thickens at increasing radius owing to viscous retardation. This Prandtl number prediction is of particular interest, and we shall explore it further using numerical solutions for the viscous flow regime below. Regions 3 and 4 correspond to Watson's self-similar viscous flow regime.

2.2 Integral Solutions for the Heat Transfer: Pr < 1. As noted in our previous paper, the region map changes for small Prandtl number (see Fig. 2*b*):

Region 1l. The stagnation zone.

Region 2l. $\delta_t < h$ region: Neither the thermal nor viscous boundary layer reaches the free surface; surface temperature and velocity, T_{sf} and u_{max}, are the inlet temperature and velocity, T_f and u_f.

Region 3l. $\delta_t = h$ and $\delta < h$ region: The thermal boundary layer has reached the free surface. The surface temperature increases with radius, but the velocity outside the viscous boundary layer is still the jet velocity, u_f.

Region 4l. $\delta = h$, $\delta_t = h$, and $T_w < R_{sat}$ region: In this region, the viscous boundary layer has reached the surface of the liquid sheet, and the velocity of the liquid surface decreases with radius.

The integral energy equation may be used to estimate the Nusselt number:

$$\frac{d}{dr}\int_0^{\delta_t} ru(T - T_f)dy = \frac{q_w}{pc_p} r \tag{6}$$

In region 2l, we approximate the velocity and temperature profiles as

$$T - T_w = (T_f - T_w)\left[\frac{3}{2}\frac{y}{\delta_t} - \frac{1}{2}\left(\frac{y}{\delta_t}\right)^3\right] \tag{7}$$

$$u = u_{\max}\left[\frac{3}{2}\frac{y}{\delta} - \frac{1}{2}\left(\frac{y}{\delta}\right)^3\right] \quad y < \delta$$
$$= u_f \quad y \geq \delta \tag{8}$$

These profiles satisfy no slip at the wall, have no shear or heat flux at the free surface (i.e., negligible evaporation; Liu and Lienhard, 1989), and match the local wall temperature. Integration of equation (6) with these profiles yields

[2] We have here corrected a minor typographical error in the expression for C_3 appearing in our previous paper.

[3] Our previous paper gave this value as 4.86. If the higher-order terms in the integral analysis are retained, the value becomes 5.23, which is 7 percent higher than the previous one.

$$\mathrm{Nu}_d = \left[\frac{\frac{9}{16}\mathrm{Re}_d \mathrm{Pr}\left(\frac{r}{d}\right)\left(1-\phi+\frac{2}{5}\phi^2-\frac{1}{35}\phi^4\right)}{\frac{1}{2}\left(\frac{r}{d}\right)^2 + C} \right]^{1/2} \tag{9}$$

$$\phi = \frac{\delta}{\delta_t} = 1.786\,\mathrm{Nu}_d \left(\frac{r}{d\,\mathrm{Re}_d}\right)^{1/2} \tag{10}$$

and C is a constant used to match to the stagnation zone. (The stagnation zone is discussed in Section 4.4 below.) If we assume that at the match point r_m, $\mathrm{Nu}_d = \mathrm{Nu}_{d,m}$ and $\phi = \phi_m$, then

$$C = \frac{9}{16}\frac{\mathrm{Re}_d \mathrm{Pr}}{\mathrm{Nu}_{d,m}^2}\left(\frac{r_m}{d}\right)\left(1-\phi_m+\frac{2}{5}\phi_m^2-\frac{1}{35}\phi^4\right)-\frac{1}{2}\left(\frac{r_m}{d}\right)^2 \tag{11}$$

If δ/δ_t is very small and C is also negligible (as shown in section 4), equation (11) can be further simplified to

$$\mathrm{Nu}_d = 1.06\,\mathrm{Re}_d^{1/2}\mathrm{Pr}^{1/2}\left(\frac{d}{r}\right)^{1/2} \tag{12}$$

Region 2l ends where the thermal boundary layer reaches the surface of the liquid sheet at $r = r_{T0}$:

$$\frac{r_{T0}}{d} = \frac{0.1984\mathrm{Re}_d^{1/3}\mathrm{Pr}^{1/3}}{\left(1-0.7107\,\mathrm{Pr}^{1/2}\right)^{2/3}} \tag{13}$$

In region 3l, $\delta_t = h$ and the temperature of the liquid surface, T_{sf}, is an increasing function of r. The temperature profile in this region is

$$T - T_w = (T_{sf} - T_w)\left[\frac{3}{2}\frac{y}{h}-\frac{1}{2}\left(\frac{y}{h}\right)^3\right] \tag{14}$$

At r_{T0}, the beginning of region 3l, $\mathrm{Nu}_d = \mathrm{Nu}_{d,T0}$, $h = h_{T0}$, and $\delta = \delta_{T0}$, where h and δ can be computed from Sharan's equations (1984):

$$\frac{h}{d} = 0.125\left(\frac{d}{r}\right) + 1.005\left(\frac{r}{\mathrm{Re}_d d}\right)^{1/2} \tag{15}$$

$$\frac{\delta}{d} = 2.679\left(\frac{r}{\mathrm{Re}_d d}\right)^{1/2} \tag{16}$$

Integration of equation (6) from $r = r_{T0}$ with equations (8) and (14) gives

$$\left(\frac{\mathrm{Nu}_d}{2(1-\frac{3}{8}\Delta)}\right)^{-1} = \frac{r}{\mathrm{Re}_d \mathrm{Pr} h}\left(1-\left(\frac{r_{T0}}{r}\right)^2\right) + \frac{4}{3}\frac{h}{d}\left(\frac{5}{8}-\frac{3}{20}\Delta^2+\frac{3}{280}\Delta^4\right) - \frac{4}{3}\frac{h_{T0}}{d}\left(\frac{5}{8}-\frac{3}{20}\Delta_{T0}^2+\frac{3}{280}\Delta_{T0}^4\right) + 2\frac{r_{T0}h_{T0}}{rh}\left(1-\frac{3}{8}\Delta_{T0}\right)\frac{1}{\mathrm{Nu}_{T0}} \tag{17}$$

where $\Delta = \delta/h$. If the terms in Δ are neglected, this simplifies to

$$\mathrm{Nu}_d = \frac{2}{\frac{r}{\mathrm{Re}_d \mathrm{Pr} h}\left(1-\left(\frac{r_{T0}}{r}\right)^2\right) + 0.833\frac{h}{d} - 0.833\frac{h_{T0}}{d} + 2\frac{r_{T0}h_{T0}}{rh}\frac{1}{\mathrm{Nu}_{T0}}} \tag{18}$$

Region 4l begins at $r_0 = 0.1773\,d\mathrm{Re}_d^{1/3}$, where the viscous boundary layer reaches the surface; here, the surface velocity decreases with radius. Sharan's integral analysis (1984) shows that

$$u_{\max} = \frac{1}{5}\frac{u_f d^2}{hr} \tag{19}$$

where

$$h = 0.1713\left(\frac{d^2}{r}\right) + \frac{5.147}{\mathrm{Re}_d}\left(\frac{r^2}{d}\right) \tag{20}$$

(Equation (20) is in good agreement with Watson's expression for h, which is based on velocity profile of the similarity solution.) The velocity profile is equation (8) with $\delta = h$ and u_{max} from equation (19), while the temperature profile is still equation (14). At $r = r_0$, $h = h_0$ and $\mathrm{Nu}_d = \mathrm{Nu}_{d,0}$. Integration of equation (6) from $r = r_0$ yields

$$\mathrm{Nu}_d = \frac{0.25}{\frac{1}{\mathrm{Re}_d \mathrm{Pr}}\left(\frac{r^2}{d^2}-\frac{r_0^2}{d^2}\right) + 0.130\left(\frac{h_0}{d}-\frac{h}{d}\right) + 0.25\frac{1}{\mathrm{Nu}_{d,0}}} \tag{21}$$

2.3 Numerical Integration in the Viscous Similarity Region. In the region of viscous similarity, we may solve the nonsimilar boundary-layer energy equation numerically in order to evaluate the accuracy of the integral method solutions for regions 3 and 4 ($\mathrm{Pr} > 1$) and for region 4l ($\mathrm{Pr} < 1$). In addition, we may probe the predicted critical Prandtl number for the occurrence of region 4 and the general differences between regions 3 and 4.

Chaudhury (1964) used Watson's velocity similarity to transform the energy equation in the film into the following form:

$$\frac{\partial^2 T}{\partial \eta^2} = \mathrm{Pr} f' \frac{(r^3+l^3)}{r^2}\frac{\partial T}{\partial r} \tag{22}$$

Here, the velocity similarity profile is (Watson, 1964)

$$\frac{2}{c^2}f'(\eta) = \sqrt{3} + 1 - \frac{2\sqrt{3}}{1+cn\,[3^{1/4}c(1-\eta)]} \tag{23}$$

where cn is a Jacobi elliptic function, $c = 1.402$, the similarity coordinate is

$$\eta = \frac{y}{h} = \frac{3\sqrt{3}Qr}{2\pi^2\nu(r^3+l^3)}y \tag{24}$$

and the length l is

$$l = 0.3243 d\,\mathrm{Re}_d^{1/3} \tag{25}$$

We may nondimensionalize r and l in equation (22) with r_0, the radius at which the viscous boundary layer reaches the liquid surface ($0.1833 d\,\mathrm{Re}_d^{1/3}$, according to Watson's analysis[4]). Temperature is nondimensionalized as

$$\theta = \frac{T - T_f}{\Delta T} \tag{26}$$

where ΔT is chosen for convenience as $\Delta T = (2\pi^2\nu q_w r_0^2)/(3\sqrt{3}kQ)$ for uniform wall heat flux and as $\Delta T = T_w - T_f$ for uniform wall temperature. The differential equation is then

$$\frac{\partial^2\theta}{\partial\eta^2} = \mathrm{Pr} f'(\eta)\frac{\bar{r}^3+\bar{l}^3}{\bar{r}^2}\frac{\partial\theta}{\partial\bar{r}} \tag{27}$$

The thermal boundary condition at the wall is

$$\left.\frac{\partial\theta}{\partial\eta}\right|_{\eta=0} = -\frac{\bar{r}^3+\bar{l}^3}{\bar{r}} \tag{28}$$

for uniform flux and

$$\theta|_{\eta=0} = 1 \tag{29}$$

for uniform temperature. The free surface is assumed to experience negligible evaporation or convection, so that

[4]Watson found a Blasius velocity profile upstream of the similarity region. The integral method's algebraic velocity profile gives a constant of 0.1773, rather than 0.1833 (3.4 percent lower). To maintain consistency within each approach, we apply 0.1773 with our integral solutions and 0.1833 with the differential equation solutions.

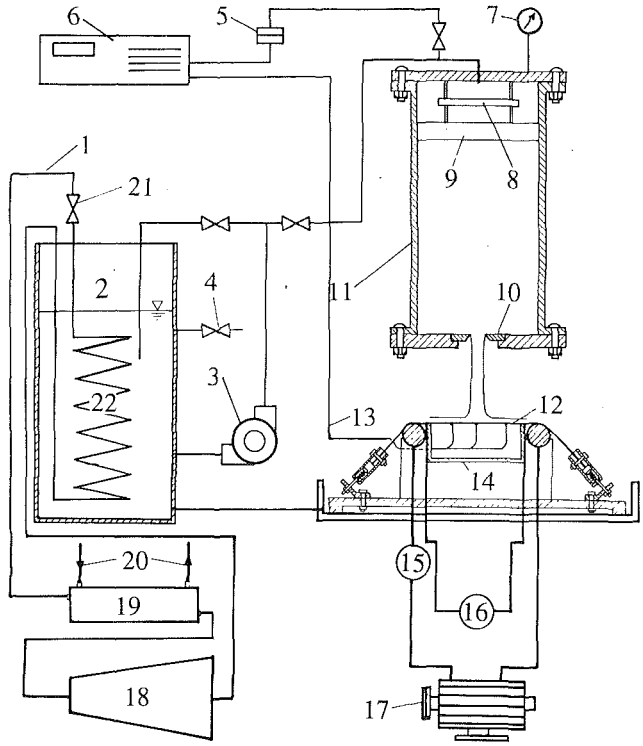

Fig. 3 Experimental apparatus: 1. Freon line; 2. chilled water tank; 3. pump; 4. water supply line; 5. pressure transducer; 6. digital voltmeter; 7. pressure gage; 8. momentum dissipating plate; 9. honeycomb; 10. sharp-edged orifice plate; 11. plenum; 12. steel heater sheet; 13. thermocouple leads; 14. pressurized plastic box; 15. ammeter; 16. voltmeter; 17. 30 kW generator; 18. compressor; 19. heat exchanger; 20. cooling water; 21. throttling valve; 22. evaporator

$$\left.\frac{\partial\theta}{\partial\eta}\right|_{\eta=1} = 0 \tag{30}$$

This approximation is valid for low liquid surface temperatures (Liu and Lienhard, 1989).

The numerical integration begins at $\bar{r} = 1$ ($r = r_0$). The temperature profile at this station is the initial condition for the solution; tests (see below) show that the initial profile is quickly damped and has little influence on the Nusselt number downstream. The following initial profile was employed:

$$\frac{T-T_f}{T_w-T_f} = 1-\frac{3_y}{2\delta_t}+\frac{1}{2}\left(\frac{y}{\delta_t}\right)^3 \quad y\le\delta_t \tag{31}$$

$$= 0 \qquad \delta_t\le y\le\delta \tag{32}$$

which again satisfies the boundary conditions (no surface flux and matching to T_w). The wall temperature and boundary layer thickness were selected to match those of the upstream boundary layer as calculated from the integral solution. The differential equation was integrated using the Crank–Nicholson procedure.

3 Experiments

Experiments were performed to determine the wall temperature distribution and Nusselt number that actually occur in jet impingement cooling. The experimental arrangement is shown in Fig. 3. The apparatus is in three primary parts: a water jet loop, a refrigerating system, and an electrical heating system.

In our previous paper, the experimental jets showed significant disturbances and sometimes splattered. To prevent splattering, a new apparatus was built specifically to produce uniform velocity-profile, laminar jets free of the surface disturbances that produce splattering (Vasista, 1989). A large plenum with an inlet momentum-breakup plate and turbulence dissipating honeycomb was used to create a pressurized liquid supply free of disturbances from the incoming flow. The jets studied were produced at the bottom of the plenum. The stability of liquid jets is very sensitive to the type of nozzle producing the jet. Pipelike nozzles provide turbulent liquid to the jet when the Reynolds number exceeds a relatively small value (2000–4000); this turbulence generally leads to disturbances in the liquid surface, which are unstable and which are strongly amplified when the jet impacts a flat surface (Errico, 1986). In the present experiments, carefully machined sharp-edged orifice plates were used, rather than pipelike nozzles. Sharp-edged orifices yield laminar, undisturbed jets of high stability. Thus, splattering was entirely suppressed in the present experiments.

The liquid supply was chilled by a mechanical refrigerator before being pumped to the plenum. The water was cooled to near 4°C. This cooling served two purposes. The first was to ensure that the liquid free-surface temperature would not become high enough to produce significant evaporative heat loss at any point along the heater surface (Liu and Lienhard, 1989). The second was to increase the accuracy of the experiments: The requirement of low evaporative loss necessitates relatively low heat fluxes and consequently small differences between wall and inlet temperatures. Subcooling the liquid supply maximized the measured ΔT, without creating evaporative loss, and thus decreased the uncertainty in the measured Nusselt number.

The liquid jets impinge on a heater made of 0.10-mm-thick, 15.2-cm-wide stainless steel sheet. The sheet is stretched over the open top of a 15.2 cm by 17.7 cm plexiglass insulation box and over 2.54-cm-dia. copper rods, which serve as electrodes; springs maintain the tension in the sheet as it expands thermally and prevent its vibration or deflection. The insulation box keeps water away from the underside of the heater sheet, and restricts underside heat losses to a negligible natural convection loss. The box is slightly pressurized with compressed air to prevent liquid inflow. A 15 V, 1200 amp generator powers the sheet directly; the generator was run at up to 20 percent of full power.

The wall temperature distribution is measured by 0.076 mm J-type thermocouples attached to the underside of the sheet and electrically insulated from it by high-temperature Kapton tape. Starting at the stagnation point of the jet, the thermocouples are placed at radial increments of 1.27 cm along the arcs of circle centered at the stagnation point, within a sector of very small angle. The azimuthal symmetry of the flow is very high, and the mechanical convenience of this arrangement was found to introduce no error.

Radial conduction in the heater sheet may be shown to be of order $\epsilon^2 = (t/l)^2$ relative to vertical conduction, where l is the length scale associated with radial changes in the heat transfer coefficient. For the jets, l is essentially the jet diameter, d, so that $\epsilon^2 \approx 0.001$. Radial conduction is thus negligible in comparison to vertical conduction; a formal perturbation solution of the heat equation substantiates this conclusion.

Convective backloss, via natural convection below the heater, is likewise negligible relative to the convective cooling at the upper surface of the heater; the back is essentially adiabatic. At the stagnation point, backloss is less than 0.2 percent of the total flux, owing to the very high liquid-side Nusselt number. The backloss increases downstream, as the Nusselt number declines, but even in the worst case, at the largest radius, this loss is less than 4 percent. Because the backloss is so small, the temperature drop through the 0.06 mm thick Kapton tape (which electrically isolates the thermocouples) was entirely negligible and required no temperature correction.

The vertical conductive temperature drop through the electrical heater, however, can be appreciable in regions where the surface heat transfer coefficient becomes large, principally the stagnation zone. Solution of the heat equation, through terms

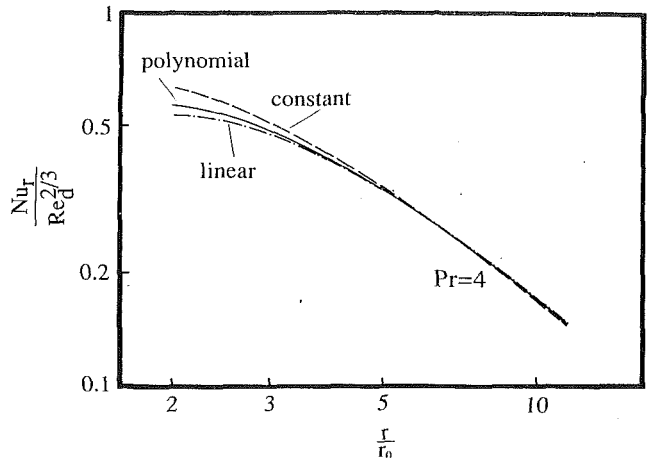

Fig. 4 Effect of initial conditions on the solution of the differential equations in the viscous similarity region for Pr = 4

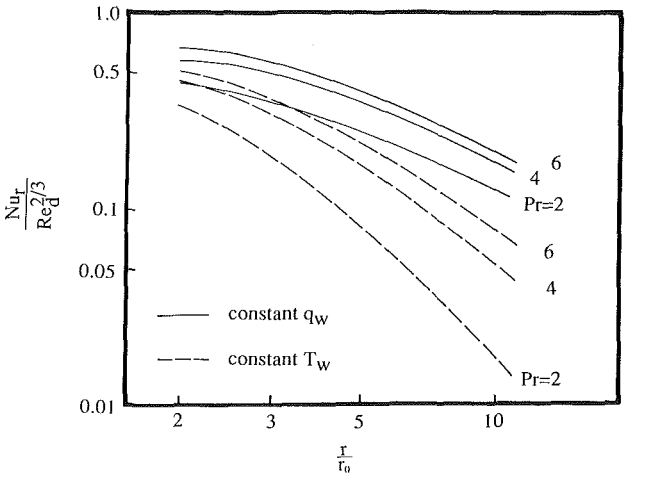

Fig. 5 Comparison of uniform heat flux and uniform temperature wall conditions in the viscous similarity region (from differential equation)

of order $\epsilon = t/d$, shows that the ratio of the true Nusselt number, based on liquid-side temperature ($Nu_t = q_w d/k(T_w - T_f)$) to the measured Nusselt number, based on temperature at the back of the heater ($Nu_m = q_w d/k(T_m - T_f)$) is

$$\frac{Nu_t}{Nu_m} = \frac{1}{1 - \zeta Nu_m/2} \tag{33}$$

where $\zeta = tk/k_w d$ relates the Biot number to the true Nusselt number. This temperature correction was applied in reducing the measured data. For the majority of our measurements, the correction is less than 10 percent of the Nusselt number. However, in the stagnation region, particularly when using the smallest orifice (3.18 mm), the correction could be as large as 30 percent.

For each thermocouple measurement, a number of values were taken to reduce random error. These measured values were averaged to get the actual values for the calculations. The thermocouples were also calibrated under isothermal conditions before and after each run to reduce systematic errors. The wall temperature increases with radius and the local Nusselt number is based on the temperature differences between the wall and the incoming jets. At the stagnation point, the temperature differences are smallest and the uncertainty is largest. For 3/8 in. (9.5 mm) diameter orifice it is ±30 percent. The uncertainty goes down very rapidly as radius increases and for most positions uncertainty is less than ±5 percent. Further reduction of stagnation zone uncertainty, by increasing the heat flux, was untenable as a result of the requirement of minimizing downstream evaporation. The uncertainty for Re_d is less than ±2 percent and that for r is less than ±0.25 mm.

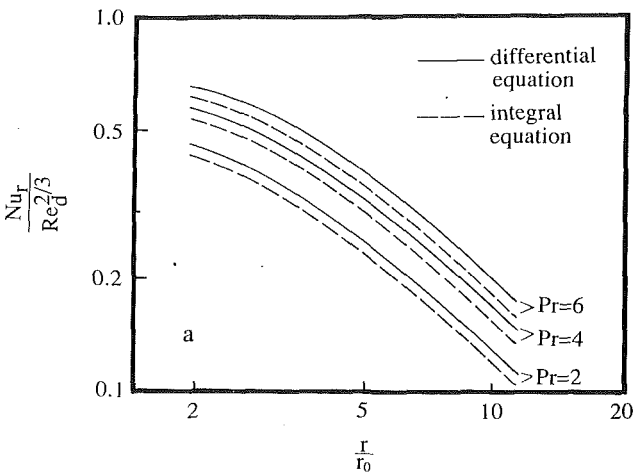

(a)

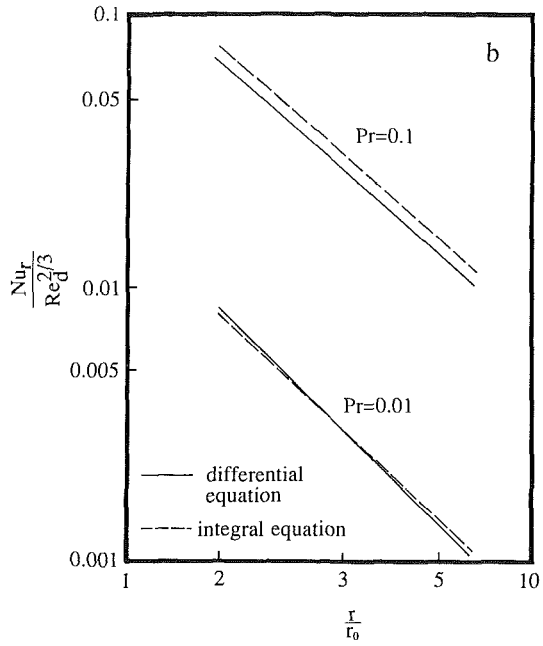

(b)

Fig. 6 Comparison of the solutions from differential and integral analysis of the viscous similarity region at $Re_d = 10^4$ for: (a) Pr > 1; and (b) Pr < 1

Discussion

4.1 Comparison of Integral and Differential Solutions. Numerical integration of the differential equation (22) requires the temperature distribution at the beginning of the similarity region. The exact temperature distribution depends on the upstream stagnation and boundary layer regions. In our calculations, that distribution is based on the polynomial solution from the integral method. However, to test the effects of this initial condition, the computation was also run with an initially linear temperature distribution, between T_w and T_f, in the boundary layer and with a uniform initial temperature, at T_f. The bulk temperatures of these two profiles are larger and smaller, respectively, than that of the polynomial, while the initial slopes of the profiles near the wall are smaller and larger, respectively. Thus, the linear profile gives a lower initial Nu_d and the uniform profile gives a higher initial Nu_d. Figure 4 compares the computations for the different initial temperature profiles. By $r/r_0 = 3$, the difference between the linear, polynomial, and constant initial temperature profiles has decreased to less than 10 percent, and the profiles are indistin-

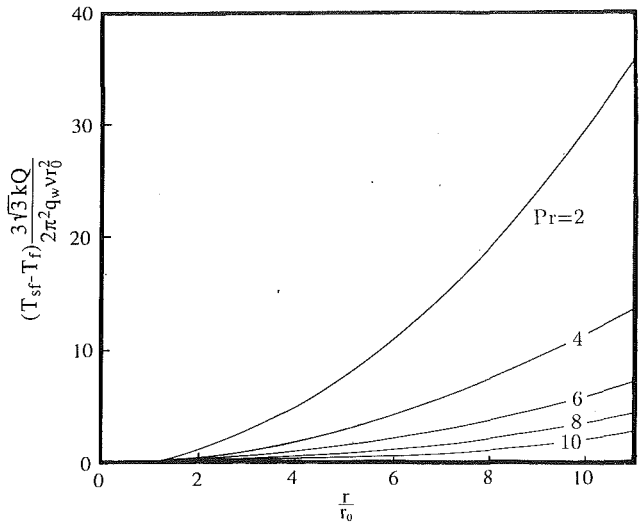

Fig. 7 Effect of Prandtl number on the free surface temperature in the viscous similarity region (from differential equation)

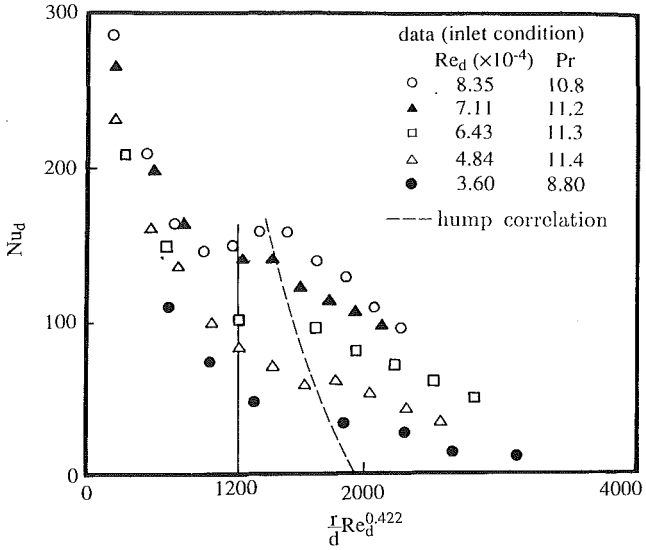

Fig. 9 Turbulent transition as manifested in the Nusselt number

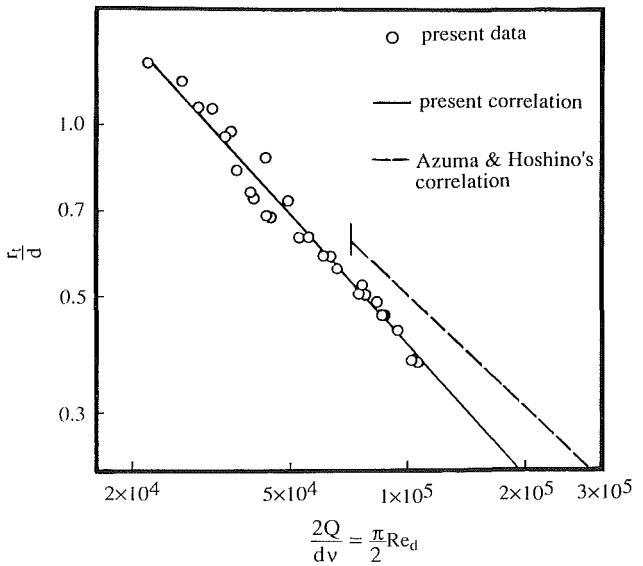

Fig. 8 Radii for transition from laminar to turbulent flow

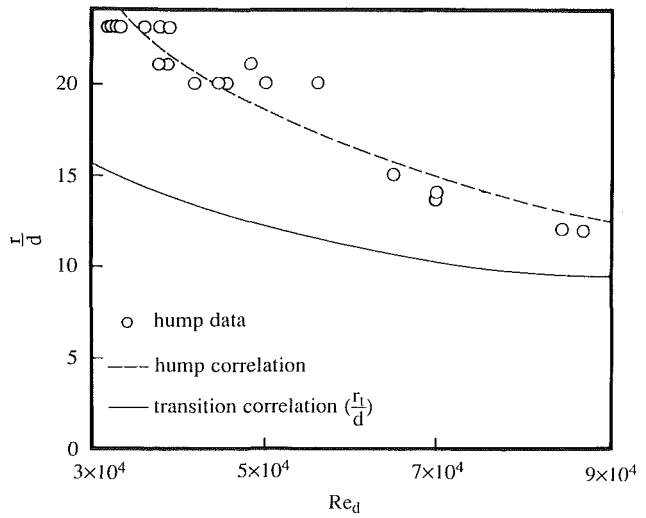

Fig. 10 Transition and hump radii

guishable at larger r/r_0. Thus, the initial temperature distribution has minimal influence on the Nusselt number in the region far from the center, and results based on the polynomial initial distribution are clearly satisfactory. Moreover, these tests show that the heat transfer in the stagnation zone and boundary layer regimes have little effect on the wall temperature at large radii.

Figure 5 compares heat transfer coefficients for uniform wall heat flux (UHF) to those for uniform wall temperature (UWT) from the differential equation solution. In our previous paper, we noted that, in the boundary layer region, the heat transfer coefficient for UHF was 25 percent higher than that for UWT. By contrast, in the similarity region, the difference between boundary conditions increases with increasing radius. Once the thermal boundary layer reaches the free surface, the energy from the wall is absorbed by the entire film, a situation comparable to fully developed duct flow. However, the UHF condition for the radial film differs markedly from the duct flow, in that the heat transfer surface increases linearly with radius. The UHF condition of the jet is akin to a duct flow with flux increasing linearly with axial position, and such a condition is known to produce a higher heat transfer coefficient. This conclusion is not altered by our definition of Nu_d in terms of incoming, rather than bulk, temperature.

The figure shows that, for small Prandtl numbers, the UWT Nusselt number decreases more rapidly than for large Prandtl number, since the driving temperature difference between wall and surface temperature dwindles much faster at low Pr. At $r/r_0 = 10$, the UWT Nusselt number for Pr = 2 is only 9 percent as large as that UHF, and that for Pr = 6 is only 40 percent.

Nusselt numbers from the integral and differential equations are compared in Figs. 6(*a*, *b*) for Pr>1 and Pr<1, respectively.[5] For Pr > 1, the maximum difference between the integral and differential solutions is about 10 percent. The integral solution is lower than the differential equation solution as a result of the assumed shape of the temperature distribution. The integral solution neglects the higher order terms in δ_t/δ, which should cause more error as Pr decreases toward unity, but the comparison shows better agreement with the differential equation solution at lower Pr. Apparently, the neglect of higher order terms compensates for the somewhat smoother profile of the integral procedure. For Pr<1, Fig.

[5]The ordinate $Nu_r/Re_d^{2/3}$ follows naturally from the scaling of the differential equation, but does not carry the full dependence on Re_d.

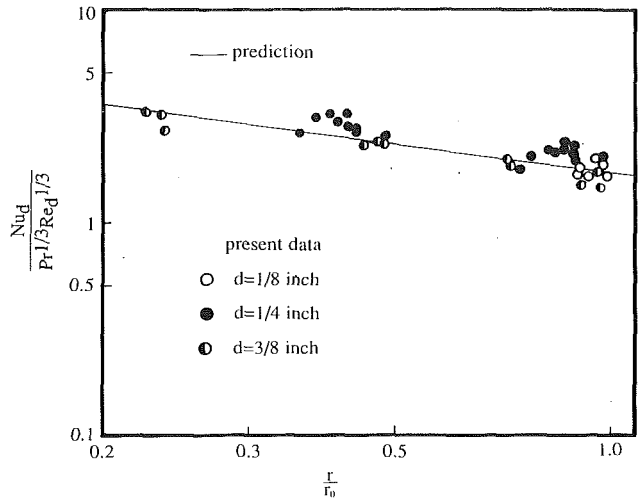

Fig. 11 Measured and predicted Nusselt number in region 2: data for several diameters of orifice

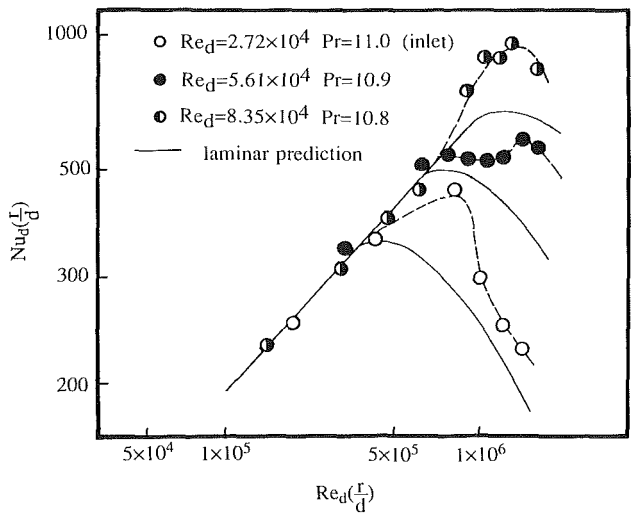

Fig. 12 Nu_r from data and laminar theory for regions 2 and 3 (— — —: faired curves)

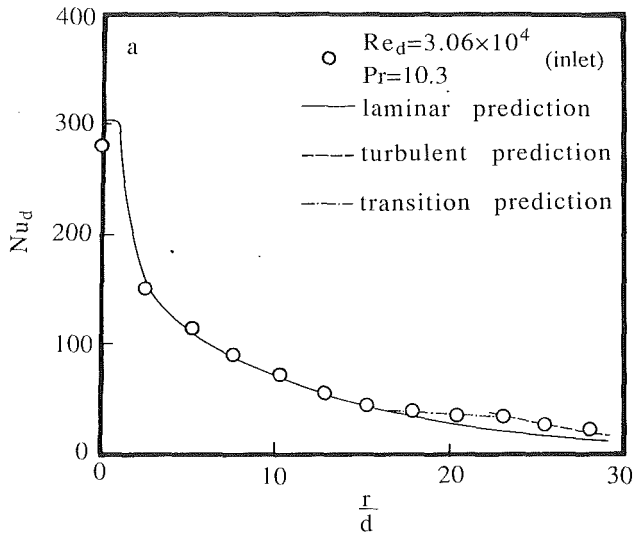

(a)

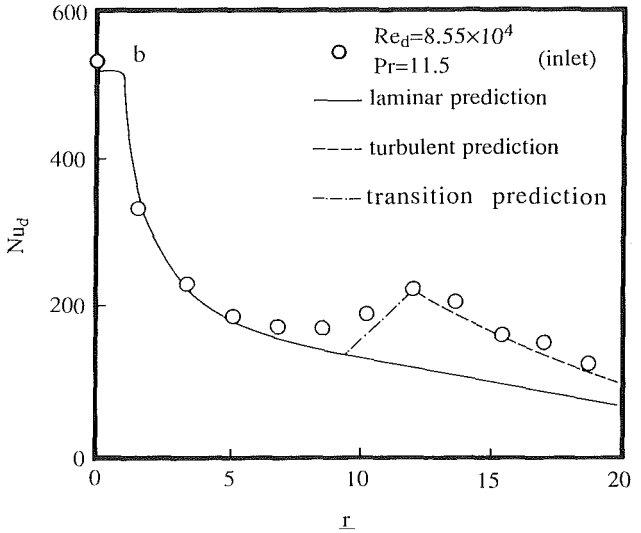

(b)

Fig. 13 Comparison of data to the laminar and turbulent predictions (predictions follow Table 1)

6(*b*) shows the simplified integral results, which neglect all terms in ϕ or Δ. In contrast to Pr > 1, for Pr < 1 the neglected terms are as large as the terms retained when Pr approaches unity. The comparison shows that for Pr = 0.1 the disagreement between the integral and differential equations is more than 20 percent. Fortunately, most liquid metals have Pr near 0.01, and for this case the simplified integral results agree with the differential results to better than 5 percent. For larger Prandtl numbers, the higher order terms should be retained when calculating Nu_d.

From the integral analysis, we previously found that the thermal boundary layer would not reach the free surface for Pr > 5.2. Therefore, for Pr > 5.2, the free surface temperature remains at T_f for all r according to the integral analysis. Of course, this is an approximation based on the assumption of a sharply defined boundary layer. Figure 7 shows the dimensionless free surface temperature from the differential equation solution as function of r/r_0 and illustrates the strong influence of the Prandtl number. For Pr = 2, the surface temperature is more than 11 times higher than for Pr = 10. For Pr > 5.2, the free surface temperature increases much more slowly. However, the surface temperature does rise above the inlet value for Pr > 5.2, and this is another cause of differences between integral and differential solutions for Nu_d.

For engineering purposes, it is convenient to construct a simplified version of the integral or differential predictions. First, we note that, in the Prandtl number range between 1 and 5.2 (for which region 4 is possible), the difference between the integral solutions for region 3 and region 4, if applied at the same Reynolds number and radius, amounts to less than 3 percent. Thus, the equation derived for region 3 can usually be applied as a good approximation in region 4 as well.

For futher simplification, we may consider $r/d \gg 0.322\,Re^{1/3}$ and neglect the terms in d/r and C_3 in the integral result for region 3 (equation (3)):

$$Nu_d = 0.172\,Re_d\,Pr^{1/3}\left(\frac{d}{r}\right)^2 \tag{34}$$

Correlation of the differential equation solutions (accurate to ±9 percent) leads to the following, similar result for 1 < Pr < 100 and 2.5 < r/r_0 < 100:

$$Nu_d = 0.195\,Re_d^{0.98}\,Pr^{0.38}\left(\frac{d}{r}\right)^{1.95} \tag{35}$$

For the range 2.5 < r/r_0 < 10, a slightly better fit (to ±5 percent) is

$$\mathrm{Nu}_d = 0.15\,\mathrm{Re}_d^{0.93}\,\mathrm{Pr}^{0.38}\left(\frac{d}{r}\right)^{1.80} \tag{36}$$

Since a turbulent transition and a hydraulic jump usually occur downstream, the latter equation is more useful. However, neither correlation is reliably accurate in the range $1 \le r/r_0 \le 2.5$; this range is important in practice, and we recommend use of the theoretical prediction, equation (3), in region 3. The integral prediction for region 2 is equation (2). For laminar flow, equations (2) and (3) can be used to estimate the local Nusselt number. These predictions are compared with our experimental data below.

The preceding results do not mean that the identification of regions 3 and 4 is unimportant. In region 4, liquid surface temperature increases rapidly with radius, and evaporation can become very significant. Conversely, in region 3, evaporation can be less important for low initial liquid temperature. Thus, for lower Prandtl numbers, the surface temperature should always be estimated, and, if necessary, the adiabatic surface condition should be dropped in favor of an evaporating surface condition. Surface evaporation was carefully suppressed in the present experiments by cooling the incoming liquid and by limiting the heat flux, but in engineering applications, evaporation will almost always occur. Evaporation will tend to raise Nu_d (Liu and Lienhard, 1989), since it offers an additional heat sink, unless it leads to film dryout downstream, in which case Nu_d will drop disastrously.

The numerical solutions with constant Prandtl number suggest Nusselt number is proportional to Prandtl number to the 0.38 power over Prandtl number from 1 to 100. However, most liquids of high Prandtl number show a rapid decrease in Prandtl number with increasing temperature. Streamwise variations in Pr, as bulk temperature rises, are certainly important and probably outweigh any finer adjustments of the Prandtl number exponents. Best agreement with experimental data was obtained when the values of viscosity (i.e., Re_d) and Pr used in the equations were those corresponding to temperatures at the radial midpoint of the film.

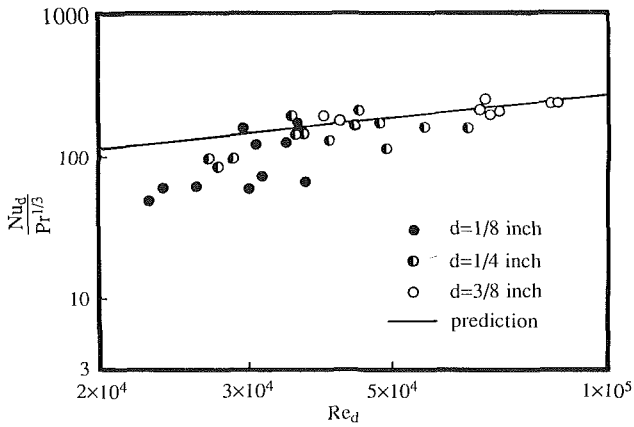

Fig. 14 Measured stagnation point Nusselt number compared to prediction for Pr > 3: data for several diameters of orifice

4.2 Turbulent Transition. The preceding analyses are based on laminar flow and consider neither surface waves nor turbulent transition. Plainly, it is important to know the location of transition from laminar to turbulent flow. If, in addition, turbulence significantly raises the Nusselt number above the laminar prediction, a separate analysis of the turbulent transport is necessary.

Figure 8 shows measurements of the turbulent transition radius in the present system. The transition point is easily identified, since the laminar liquid sheet is smooth and transparent, while the turbulent liquid sheet has a rough surface, which reflects light and appears bright. The associated surface waves are described by Azuma and Hoshino (1984a) as "lattice-shaped" waves. A curve fit of our data (Gabour, 1991) gives the transition radius as

$$\left(\frac{r_t}{d}\right)\mathrm{Re}_d^{0.422} = 1.2\times 10^3 \tag{37}$$

In their own system, Azuma and Hoshino measured

$$\left(\frac{r_t}{d}\right)\mathrm{Re}_d^{0.315} = 0.73\times 10^3 \tag{38}$$

which shows a slightly weaker dependence on Reynolds number, but turbulent transition points normally depend on the disturbances present in a specific system. Equation (37) suggests a coordinate of $(r/d)\,\mathrm{Re}_d^{0.422}$. Using this coordinate, some of the present heat transfer data are shown in Fig. 9. At the transition point, the figure shows a clear shift in the slope of the Nusselt number, which becomes more pronounced at higher Reynolds number. The Nusselt number increases above the laminar trend, as direct comparisons (below) illustrate. Note that the abscissa here is chosen to illustrate the turbulent transition, not the functional dependence of Nu_d on Re_d and Pr; thus, the curves do not collapse to a single line. Moreover, the streamwise changes in the Re_d and Pr dependencies make it impossible to present all of our data, for many different conditions, on a single graph. In this and following figures, we present enough data to illustrate the general behavior without attempting to be exhaustive.

The Nusselt numbers show a hump downstream of the turbulent transition point. This hump corresponds to the point at which the turbulence has become fully developed (see heat transfer predictions below). As the Reynolds number increases, the hump becomes more pronounced and occurs after shorter distance. The transition and hump radii are shown as a function of jet Reynolds number in Fig. 10. The data for the hump position can be correlated as

Table 1 Suggested formulae for local Nusselt number for Pr ≥ O(1)

Region	Range	Nu_d
Stagnation zone	$0 \le r/d < 0.787,\quad 0.15 \le \mathrm{Pr} \le 3$	$0.715\,\mathrm{Re}_d^{1/2}\mathrm{Pr}^{0.4}$
	$\mathrm{Pr} > 3$	$0.797\,\mathrm{Re}_d^{1/2}\mathrm{Pr}^{1/3}$
Transition: stagn. to b.l.	$0.787 < r/d < 2.23$	$\left(\frac{\frac{27}{80}\mathrm{Re}_d\mathrm{Pr}\frac{r}{d}}{\frac{1}{2}\left(\frac{r}{d}\right)^2-0.2535}\right)^{1/3}$
b.l. region (2)	$2.23 < r/d < 0.1773\,\mathrm{Re}_d^{1/3}$	$0.632\,\mathrm{Re}_d^{1/2}\mathrm{Pr}^{1/3}\left(\frac{d}{r}\right)^{1/2}$
Similarity region (3 & 4)	$0.1773\,\mathrm{Re}_d^{1/3} < r/d < 1200\,\mathrm{Re}_d^{-0.422}$	$\frac{0.407\,\mathrm{Re}_d^{1/3}\mathrm{Pr}^{1/3}\left(\frac{d}{r}\right)^{2/3}}{\left[0.1713\left(\frac{d}{r}\right)^2+\frac{5.147}{\mathrm{Re}_d d}\frac{r}{d}\right]^{2/3}\left[\frac{1}{2}\left(\frac{r}{d}\right)^2+C_3\right]^{1/3}}$
	$(r_0/d < r/d < r_t/d)$	$\left(C_3 = \frac{0.267\,(d/r_0)^{1/2}}{\left[0.1713\left(\frac{d}{r_0}\right)^2+\frac{5.147\,r_0}{\mathrm{Re}_d d}\right]^2} - \frac{1}{2}\left(\frac{r_0}{d}\right)^2\right)$
Transition: laminar/turb	$1200\,\mathrm{Re}_d^{-0.422} < r/d < 2.86\times 10^4\,\mathrm{Re}_d^{-0.68}$	$\mathrm{Nu}_{lam}(r_t) + [\mathrm{Nu}_{turb}(r_h) - \mathrm{Nu}_{lam}(r_t)]\frac{(r-r_t)}{(r_h-r_t)}$
Turbulent region	$r/d > 2.86\times 10^4\,\mathrm{Re}_d^{-0.68}$	$\frac{8\,\mathrm{Re}_d\mathrm{Pr}\,f(C_f,\mathrm{Pr})}{49(h/r)(r/d)+28(r/d)^2 f(C_f,\mathrm{Pr})}$

$$\left(\frac{r_h}{d}\right)\mathrm{Re}_d^{0.68}=2.86\times10^4 \tag{39}$$

Recall that the border of region 2 is $r_0/d = 0.1773\mathrm{Re}_d^{1/3}$. This implies that if $\mathrm{Re}_d > 1.1 \times 10^5$, the transition will take place in region 2. For the present Reynolds number range, transition always occurs in the similarity region (region 3). Indeed, the stability analysis of Azuma and Hoshino (1984d) suggests that the flow will always be most unstable near the border of regions 2 and 3, with waves or turbulence commencing in the similarity region.

Figure 11 shows a comparison of the data to the integral solution (equation (2)) in region 2. The agreement is generally within the uncertainty of the data. This region is relatively small. In this region, small concentric ripples can be observed (called "disturbance" waves by Azuma and Hoshino). These waves do not develop significantly, and they appear to have no strong effect on the heat transfer.

In the similarity region, our heat transfer data show a clear transition from laminar to turbulent flow. Azuma and Hoshino (1984a) report a critical (transition) discharge Reynolds number, based on the jet diameter, of 4.8×10^4. From our data this critical discharge Reynolds number is much lower (less than 2×10^4). This discrepancy may be caused by the definition of the critical discharge Reynolds number adopted by Azuma and Hoshino. They regarded the flow to be turbulent when the so-called "sandpaperlike" waves are present over 50 percent of the azimuthal direction, and took that discharge Reynolds number as the critical value. That type of situation never occurs in the present experiments; here with increasing Reynolds number, waves and disturbances inside the liquid sheet intensify, but the transition circle stays essentially circular and symmetric at all Re_d.

The laminar analysis predicts that for a given Re_d, $\mathrm{Nu}_r = (r/d)\,\mathrm{Nu}_d$ reaches a peak value and then decreases. Figure 12, however, shows two features that differ from the prediction. The first is that the data break from the initially linear portion of the laminar prediction at a higher value of Nu_r than predicted. The other is a sharp peak in Nu_r downstream of the change in slope. The first feature suggests, from our observations and those of Azuma and Hoshino's (1984a, 1984d), that the disturbance waves have intensified in this portion of the film. They appear to increase the heat transfer coefficients by up to 20 percent in this short region, which is just ahead of the transition radius where sandpaperlike waves occur (see also Fig. 13*b*). The second feature, the peak, is simply the hump at full development of turbulence, as previously discussed.

The friction coefficient measurements and mass transfer data of Nakoryakov et al. show a very similar behavior. The primary difference is that turbulent transition, as deduced from their friction coefficient measurements, occurs in the boundary layer region (region 2). Their data show a single peak rather than the pair of features seen here. This suggests that the sheet has become turbulent before surface waves can contribute significantly to the heat transfer. They attribute the peak to waves rather than turbulent transition. However, for their Reynolds number range, the turbulent transition is a more likely explanation.

4.3 Prediction of Turbulent Heat Transfer. The Nusselt number turbulent flow may be calculated using the thermal law of the wall. The Stanton number is defined as

$$\mathrm{St}=\frac{q_w}{\rho c_p u_{\max}(T_w-T_{sf})} \tag{40}$$

and the law of the wall may be written in the standard internal-flow form

$$\mathrm{St}=\frac{C_f/2}{1.07+12.7(\mathrm{Pr}^{2/3}-1)\sqrt{C_f/2}}=f(C_f,\ \mathrm{Pr}) \tag{41}$$

The skin friction coefficient is calculated from the Blasius law

$$C_f=0.045\left(\frac{\nu}{u_{\max}h}\right)^{1/4}=0.073\mathrm{Re}_d^{-1/4}\left(\frac{r}{d}\right)^{1/4} \tag{42}$$

where the 1/7 power turbulent velocity distribution produces a maximum velocity

$$u_{\max}=\frac{1}{7}\frac{u_f d^2}{hr} \tag{43}$$

and a film thickness h of

$$h=d\left(\frac{0.02091}{\mathrm{Re}_d^{1/4}}\left(\frac{r}{d}\right)^{5/4}+C\frac{d}{r}\right) \tag{44}$$

with

$$C=0.1713+\frac{5.147}{\mathrm{Re}_d}\frac{r_t}{d}-\frac{0.02091}{\mathrm{Re}_d^{1/4}}\left(\frac{r_t}{d}\right)^{1/4} \tag{45}$$

From the above, the Nusselt number for turbulent flow may be calculated:

$$\mathrm{Nu}_d=\frac{8\mathrm{Re}_d\mathrm{Pr}f(C_f,\ \mathrm{Pr})}{49\left(\frac{h}{r}\right)\left(\frac{r}{d}\right)+28\left(\frac{r}{d}\right)^2 f(C_f,\ \mathrm{Pr})} \tag{46}$$

When $\mathrm{Pr} \gg 1$, the equation simplifies to

$$\mathrm{Nu}_d=0.0052\mathrm{Re}_d^{3/4}\left(\frac{d}{h}\right)\left(\frac{d}{r}\right)^{3/4}\left(\frac{\mathrm{Pr}}{1.07+12.7(\mathrm{Pr}^{2/3}-1)\sqrt{C_f/2}}\right) \tag{47}$$

The turbulent Nusselt number is substantially higher than the laminar Nu_d.

Figures 13(*a*, *b*) show the laminar and turbulent predictions together with experimental data for two runs at different Reynolds numbers. In both cases, agreement is excellent. The increasing strength of turbulent augmentation with increasing Reynolds number is also quite apparent. The only significant disagreement observed is in the stagnation zone for lower Reynolds number. Data and predictions for the stagnation zone are discussed in the next section.

4.4 Stagnation Zone Heat Transfer. In the stagnation zone of a body passing through an infinite fluid medium, White (1974) finds

$$\mathrm{Nu}_d=G(\mathrm{Pr},\ 3)\left(\frac{Bd^2}{\nu}\right)^{1/2} \tag{48}$$

where

$$G(\mathrm{Pr},\ 3)=\begin{cases}0.53898\mathrm{Pr}^{0.4} & 0.15\le\mathrm{Pr}\le3.0\\ 0.6010\mathrm{Pr}^{1/3}-0.05085 & \mathrm{Pr}\ge3.0\end{cases}$$

The value of $B = 2\partial u/\partial r$ at the stagnation point of an inviscid impinging liquid jet was calculated approximately by Schach (1935)[6]

$$B=1.76\frac{u_f}{d} \tag{49}$$

This value should be applicable for reasonably large jet Reynolds numbers.

From these results

$$\mathrm{Nu}_d=\begin{cases}0.715\,\mathrm{Re}_d^{1/2}\mathrm{Pr}^{0.4} & 0.15\le\mathrm{Pr}\le3\\ 0.797\,\mathrm{Re}_d^{1/2}\mathrm{Pr}^{1/3} & \mathrm{Pr}>3\end{cases} \tag{50}$$

Figure 14 compares the data to the above equations, illustrating generally good agreement. The data appear to fall below the

[6]Schach's Figs. 9 and 10 are a bit garbled. This often-quoted value is obtained from his $\partial v/\partial z$ and continuity.

prediction at lower Reynolds numbers. This behavior may be related to a decrease in the stagnation zone velocity gradient owing to viscous effects, but further study is required.

Nakoryakov et al. (1978) measured the Nusselt number for mass transfer beneath an impinging jet at high Schmidt number with uniform wall concentration. They did not directly test a relation for the stagnation zone transport. Instead, they used a relation for Nu (equation (1)) to calculate their jet velocities. The relation they used seems to be quite close to that suggested above, although its origin remains obscure (it does not appear in the reference they cite). Nakoryakov et al. also measured wall shear stress in the stagnation zone, but the calibration of their stress probe was similarly based on an assumed value of $\partial u/\partial r$.

Stevens and Webb (1989) used a pipe-type nozzle producing turbulent incoming jets, and their measured Nusselt numbers are in the same general range, although a bit higher, than the present data. They represented their stagnation zone results by a correlation that accounts for the Reynolds number dependence of the stagnation velocity gradient with a dimensional correlating factor of u_f/d

$$\mathrm{Nu}_d = 2.67\mathrm{Re}_d^{0.57}\left(\frac{z}{d}\right)^{-1/30}\left(\frac{u_f}{d}\right)^{-1/4}\mathrm{Pr}^{0.4} \tag{51}$$

where z is the distance of their nozzle from the heater. This correlation shows a somewhat different dependence on jet diameter and velocity than is found for the present laminar jets. Stevens and Webb present a second correlation for the radial variation Nu_d, which does not represent the present data well at the large radii of interest to us, although it does represent their own data very well for r/d less than about 5.

The size of the stagnation zone may be estimated by calculating the radius at which the stagnation boundary layer and the region 2 boundary layer have the same thickness (i.e., $2.107\,d\,\mathrm{Re}_d^{1/2} = 2.679\,(rd/\mathrm{Re}_d)^{1/2}$; White, 1974; Sharan, 1984). The result is

$$\frac{r_m}{d} = 0.787 \tag{52}$$

Similarly, Stevens and Webb found the stagnation region beneath a turbulent jet to reach to roughly $r/d = 0.75$. Our crude estimate shows that the stagnation zone is very small. Its primary importance is that it possesses the maximum local heat transfer coefficient (lowest wall temperature) in the flow. It contributes little, however, to overall heat removal or downstream Nusselt numbers as may be seen from the full integral result for region 2 (Liu and Lienhard, 1989), which does not neglect the stagnation zone heat flow as does equation (2):

$$\mathrm{Nu}_d = \left(\frac{\frac{27}{80}\mathrm{Re}_d\mathrm{Pr}\frac{r}{\delta}}{\frac{1}{2}\left(\frac{r}{d}\right)^2 + C_2}\right)^{1/3} \tag{53}$$

with $\delta = 2.679\,(rd/\mathrm{Re}_d)^{1/2}$. At $r = r_m$, the Nusselt number should equal the stagnation zone Nusselt number; thus,

$$C_2 = -0.2535 \tag{54}$$

The error in Nu_d caused by neglecting the stagnation zone is less than 10 percent for $r/d > 2.23$.

4.5 Recommendations for Nusselt Number Estimation. Table 1 summarizes the suggested relations for estimating local Nusselt number for impinging, circular, free liquid jets. For most regions, deviations are less than 10 percent. For laminar convection in the similarity region, however, waves can enhance the heat transfer, and Nu_d may exceed the estimate by up to 20 percent; as the waves are damped, the heat transfer goes back down. The wavy region is relatively small, however, because it is limited by subsequent turbulent transition. In the region of transition from laminar to turbulent flow, between r_t and r_h, we tentatively recommend a line fit between the laminar predictions at r_t and the turbulent prediction at r_h. This fit is shown in Figs. 13 (*a*, *b*) and can be seen not to account properly for the wave effects that occur in that region at larger Reynolds number. With the exceptions of this line fit and the correlation for r_t/d, all equations in Table 1 are analytical predictions; each is substantiated by experiment.

4.6 Additional Studies Required. In jet impingement cooling applications, turbulent incoming jets are likely to be produced, since upstream disturbances are not usually damped and the jets often issue from pipes. While turbulence may enhance stagnation point heat transfer, it is damped sharply as the film spreads. We are currently conducting experimental studies of turbulent jet heat transfer.

Impinging jets will splatter if the jet surface is even slightly disturbed or the thin liquid sheet is disturbed beyond a certain magnitude. Disturbances to the incoming jet are often caused by irregularities in the orifice or by turbulence in the liquid supply. Roughness of the target surface can also disturb the liquid film. Splattering removes liquid from the liquid film, and thus lowers the Nusselt number; Liu and Lienhard (1989) estimated reductions of 20 percent or more. We are also investigating the role of splattering in jet impingement cooling.

Finally, the behavior of the stagnation zone at lower Reynolds number will be further investigated, owing to surface tension effects and a possible viscous decrease of the stagnation velocity gradient as Re_d becomes smaller.

Conclusions

Convective heat removal by liquid jet impingement has been investigated for uniform wall flux and circular, laminar jets. Both theoretical and experimental results are given.

- The radial distribution of Nusselt number is accurately predicted by the formulae in Table 1 for Prandtl numbers of order unity or greater.
- Laminar heat transfer in the film for $\mathrm{Pr} \geq O(1)$ may be calculated from equation (2) in the boundary layer region (region 2) and by equation (3) in the laminar portion of the similarity region (regions 3 and/or 4). These regions are described in Section 2.1.
- Laminar heat transfer predictions for $\mathrm{Pr} < 1$ are developed in Section 2.2.
- Comparison of the integral predictions to numerical solutions in the similarity region supports conclusions previously drawn from the integral approach for $\mathrm{Pr} > 1$ as well as the new results for $\mathrm{Pr} < 1$.
- Turbulent transition occurs at a radius given by equation (37). Turbulence becomes fully developed at a radius given by equation (39). Turbulent heat transfer in the film is given by equation (46).
- The stagnation point Nusselt number is reasonably well represented by equation (50).

Acknowledgments

The authors are grateful to Ms. Laurette A. Gabour for her measurements of the turbulent transition radius and to Mr. Vittal K. Vasista for construction of the flow loop. This project was supported by grants from the A. P. Sloan Foundation and the National Science Foundation (grant No. CBT-8858288).

References

Azuma, T., and Hoshino, T., 1984a, "The Radial Flow of a Thin Liquid Film, Part 1: Laminar-Turbulent Transition," *Trans. Japan Soc. Mech. Engrs.*, Vol. 50, p. 974.

Azuma, T., and Hoshino, T., 1984b, "The Radial Flow of a Thin Liquid Film, Part 2: Film Thickness," *Trans. Japan Soc. Mech. Engrs.*, Vol. 50, p. 902.

Azuma, T., and Hoshino, T., 1984c, "The Radial Flow of Thin Liquid Film, Part 3: Velocity Profile," *Trans. Japan Soc. Mech. Engrs.*, Vol. 50, p. 1126.

Azuma, T., and Hoshino, T., 1984d, "The Radial Flow of Thin Liquid Film, Part 4: Stability of Liquid Film and Wall Pressure Fluctuation," *Trans. Japan Soc. Mech. Engrs.*, Vol. 50, p. 1136.

Carper, H. J., 1989, "Impingement Cooling by Liquid Jet," presented at the ASME Winter Annual Meeting, San Francisco, CA.

Chaudhury, Z. H., 1964, "Heat Transfer in a Radial Liquid Jet," *J. Fluid Mech.*, Vol. 20, pp. 501–511.

Errico, M., 1986, "A Study of the Interaction of Liquid Jets With Solid Surfaces," Doctoral Thesis, University of California at San Diego.

Gabour, L. A., 1991, "Heat Transfer to Turbulent and Splattering Impinging Liquid Jets," S. B. Thesis in Mechanical Engineering, MIT, Cambridge, MA.

Ishigai, S., Nakanishi, S., Mizuno, M., and Imamura, T., 1977, "Heat Transfer of the Impinging Round Water in the Interference Zone of Film Flow Along the Wall," *Bulletin of the JSME*, Vol. 20, No. 139.

Liu, X., and Lienhard V, J. H., 1989, "Liquid Jet Impingement Heat Transfer on a Uniform Flux Surface," *Heat Transfer Phenomena in Radiation, Combustion, and Fires,* ASME HTD-Vol. 6, pp. 523–530.

Lombara, J. S., 1990, "An Experimental Investigation of Liquid Jet Impingement Heat Transfer Theories," S. B. Thesis in Mechanical Engineering, MIT, Cambridge, MA.

Nakoryakov, V. E., Pokusaev, B. G., and Troyan, E. N., 1978, "Impingement of an Axisymmetric Liquid Jet on a Barrier," *Int. J. Heat Mass Transfer*, Vol. 21, pp. 1175–1184.

Olsson, R. G., and Turkdogan, E. T., 1966, "Radial Spread of a Liquid Stream on a Horizontal Plate," *Nature*, Vol. 211, No. 5051, pp. 813–816.

Schach, W., 1935, "Umlenkung eines kreisförmigen Flussigkeitsstrahles an einer ebenen Platte senkrecht zur Strömungsrichtung," *Ing.-Arch.*, Vol. 6, pp. 51–59.

Schlichting, H., 1979, *Boundary-Layer Theory*, 7th ed., McGraw-Hill, New York.

Sharan, A., 1984, "Jet-Disc Boiling: Burnout Predictions and Application to Solar Receivers," Master's Thesis in Mechanical Engineering, University of Houston, TX.

Stevens, J., and Webb, B. W., 1989, "Local Heat Transfer Coefficients Under an Axisymmetric, Single-Phase Liquid Jet," *Heat Transfer in Electronics—1989*, ASME HTD-Vol. 111, pp. 113–119.

Vasista, V. K., 1989, "Experimental Study of the Hydrodynamics of an Impinging Liquid Jet," Bachelor's Thesis in Mechanical Engineering, MIT, Cambridge, MA.

Wang, X. S., Dagan, Z., and Jiji, L. M., 1989a, "Heat Transfer Between a Circular Free Impinging Jet and a Solid Surface With Nonuniform Wall Temperature or Wall Heat Flux—1. Solution for the Stagnation Region," *Int. J. Heat Mass Transfer*, Vol. 32, No. 7, pp. 1351–1360.

Wang, X. S., Dagan, Z., and Jiji, L. M., 1989b, "Heat Transfer Between a Circular Free Impinging Jet and a Solid Surface With Nonuniform Wall Temperature or Wall Heat Flux—2. Solution for the Boundary Layer Region," *Int. J. Heat Mass Transfer*, Vol. 32, No. 7, pp. 1361–1371.

Wang, X. S., Dagan, Z., and Jiji, L. M., 1989c, "Conjugate Heat Transfer Between a Laminar Impinging Liquid Jet and a Solid Disk," *Int. J. Heat Mass Transfer*, Vol. 32, No. 11, pp. 2189–2197.

Watson, E. J., 1964, "The Radial Spread of a Liquid Over a Horizontal Plane," *J. Fluid Mech.*, Vol. 20, pp. 481–499.

White, F. M., 1974, *Viscous Fluid Flow*, McGraw-Hill, New York.

Starting Flow and Heat Transfer Downstream of a Backward-Facing Step

F. K. Tsou
Department of Mechanical Engineering,
Drexel University,
Philadelphia, PA 19104

Shih-Jiun Chen
Department of Mechanical Engineering,
Temple University,
Philadelphia, PA 19122

Win Aung
National Science Foundation,
Washington, DC 20550

Experiments are performed to study the starting process of heat transfer downstream of a backward-facing step. A Ludwieg tube wind tunnel is employed to produce the incompressible flow, which accelerates from a zero velocity to a steady state value with an accelerating period of 7 ms and a steady-state period of 12 ms. Hot-wire anemometry and heat flux gages are used to measure the flow and heat transfer history, respectively. The onset of transition in the free shear layer shows that the disturbance originates from the top corner of the step, then propagating to the free stream. The velocity and turbulence profiles in the free shear layer reach steady-state values after the leading edge disturbance traverses to the measurement locations. In regions upstream and far downstream of the step, heat flux history data suggest the transformation of the flow from laminar to transitional and finally to turbulent flow. Hot-wire anemometry measurements indicate high-frequency turbulence with a short characteristic time. In the recirculating region, however, a longer characteristic time is observed because of the existence of large-scale eddies. The dimensionless reattachment length (x_r/H) is shown to increase with time from the bottom corner ($x_r/H = 0$) in the laminar regime to a maximum value of 13.6 in the transitional regime, and decreases to a constant value of 7.6 in the turbulent regime. The steady-state flow field and heat transfer compare favorably with existing data obtained using steady-state techniques.

1 Introduction

Reattaching separated flow has a variety of engineering applications, such as flow encountered in heat exchangers and buildings, on microelectronic circuit boards, and in combustors in jet and rocket engines. Two-dimensional flow past a backward-facing step, which represents one of the simplest geometries for producing separation and reattachment of turbulent shear layer flow, has been studied extensively. Aung (1983) and Eaton and Johnston (1981) have reviewed and discussed the effects of system parameters, including Reynolds numbers, free-stream turbulence, initial boundary layer type and thickness, and channel expansion ratio, on flow separation and reattachment.

Recent investigations on the reattachment process include the effects of separation point excitation (Roos and Kegelman, 1987), initial shear layer (Adams and Johnston, 1988; Aung et al., 1985), step Reynolds number (Chen et al., 1988), and the inlet turbulence intensity (Isomoto and Honami, 1989). Numerical computations were carried out by Gooray et al. (1985) for turbulent heat transfer and by Ghoniem and Sethian (1987) for laminar flow structure. All the aforementioned studies were based on steady-state conditions. Reattaching separated flow downstream of an abrupt pipe expansion has been studied by Baughn et al. (1989).

A typical steady-state flow pattern of separation and reattachment is shown in Fig. 1. Here, an initial turbulent boundary layer flow (Region I) passes over the corner of a backward-facing step, creating a free shear layer (Region IV) and a recirculating region (II). A dividing streamline separates the downstream flowing fluid and the fluid in the recirculating region. The dividing streamline intersects the downstream wall at the reattachment point. Downstream of that point, the flow redevelops into a boundary layer type flow (Region III). The

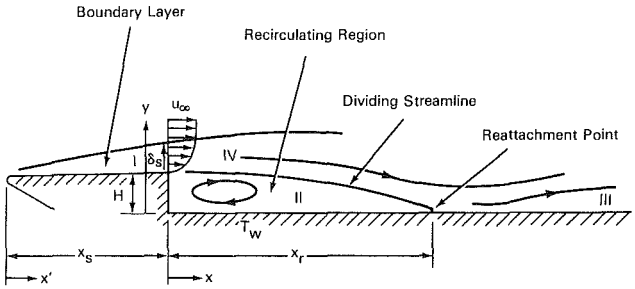

Fig. 1 Sketch for flow over a backward-facing step: H = 3.3 mm; x_s = 254 mm; Region I: initial layer; Region II: recirculating flow; Region III: redeveloping boundary layer; Region IV: separated shear layer

separating streamlines are concave downward, causing a thinning initial boundary layer, and in region II large scale eddies prevail (Troutt et al., 1984).

Since thermal system components often fail as a result of too many on-off cycles (i.e., start-up and shut-down), the starting process of separation and reattachment may be of equal or greater importance in design than the corresponding steady-state conditions. Transient phenomena, however, have not received adequate attention. Two available studies are the laminar flow study carried out by Honji (1975) and by Durst and Pereira (1988). In the experimental study performed by Honji (1975), he identified two characteristic lengths: the length of the formation region (step height) and the diffusion length of the free shear layer. Before the leading edge disturbance reaches the step, the flow is governed by the step height and thus the dimensionless time ($u_\infty t/H$) and the Reynolds number ($u_\infty H/\nu$) control the flow pattern. The same dimensionless time has been used by Durst and Pereira (1988) in a numerical study of the starting flow down a step in a two-dimensional channel flow. Both studies report that the recirculating region grows with time until steady state is reached. There has not been, however, any study on the leading edge effect on separation

Contributed by the Heat Transfer Division for publication in the JOURNAL OF HEAT TRANSFER. Manuscript received by the Heat Transfer Division October 10, 1989; revision received November 21, 1990. Keywords: Flow Separation, Forced Convection, Transient and Unsteady Heat Transfer.

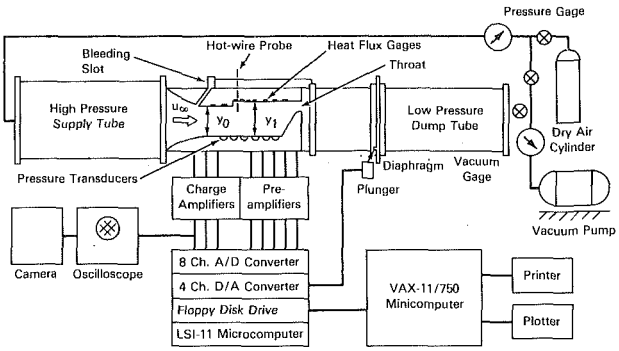

Fig. 2 Ludwieg tube wind tunnel and measurement system

and reattachment. Furthermore, no data are available on turbulent flow and heat transfer in a starting process.

The objective of the present paper is to investigate the *fluid flow* and *heat transfer* associated with the starting flow past a backward-facing step. Special attention is given to the free shear layer and the recirculating region including the reattachment point. This study shows that the structure of flow in the starting process, consisting of flow initiation, acceleration, and boundary layer and free shear layer development from an initially unsteady laminar flow to an eventually steady turbulent flow, is an inherently complicated flow that is little understood. To study this starting process and flow development, it is necessary to accelerate a flow from zero velocity to a steady-state value. To accomplish this, a short-duration flow facility, i.e., an 11-m-long Ludwieg tube wind tunnel, has been designed, constructed, and installed in the Department of Mechanical Engineering and Mechanics at Drexel University. A schematic diagram of this facility is shown in Fig. 2.

2 Experimental Apparatus and Procedure

2.1 Ludwieg Tube Wind Tunnel. In the present study, the subsonic flow behind expansion waves in a Ludwieg tube wind tunnel (Fig. 2) is utilized to produce the starting flow past a backward-facing step. The tunnel consists of three sections: a 127 mm i.d. by 3 m long high-pressure supply tube; a test section of 127 mm width, 50.8 mm height, and 700 mm length; and a 89 mm i.d. by 7 m long low-pressure dump tube. While the tubes are made of stainless steel, the test section is made of aluminum for easy machining. A diaphragm, placed 2.4 m downstream of the test section, is ruptured by a pin to start the flow. The test section is located at a sufficient distance from the diaphragm to insure the existence of one-dimensional isentropic flow. In the test section, an initial convergent section is designed to produce a cross-section-wide uniform flow, which is further aided by bleeding part of the flow downstream as indicated in Fig. 2. The straight portion, 47.5 mm high (y_o) by 127 mm wide, has a length of 254 mm to ensure that the initial boundary layer at the step is turbulent. The step height is 3.3 mm so that the expansion ratio (y_1/y_o) is 1.07. The aspect ratio of 38.5 is sufficient to give an essentially two-dimensional flow. At the end of the test section, a nozzle 25.4 mm in height is installed to choke the flow.

At the beginning of each experimental run, the entire tunnel is evacuated. Dry air is then supplied. The high-pressure tube and the test section are then pressurized to 202 kPa, which is sufficient to choke the flow at the throat. The data acquisition begins after the diaphragm is ruptured by a solenoid-actuated pin. At the same time, a shock wave travels downstream while an expansion wave propagates upstream, causing the free-stream temperature to drop. The flow behind the expansion wave in the test section accelerates until the flow is choked at the throat. A steady-state subsonic flow with a Mach number of 0.3, as determined by the area ratio of the test section to the nozzle throat, is then reached. This is confirmed by pressure and hot-wire measurements (Chen, 1985). The steady-state flow has a temperature of 16–18°C below the wall temperature. In the test section, the combined value of momentum thicknesses on upper and lower walls is less than 5 percent of the test section height, so that an external flow rather than a channel flow situation may be assumed.

It should be emphasized that the present experiments require no heating of the test section, since heat transfer is produced by a temperature difference $T_w - T_\infty = 16$–$18°C$ induced by the expansion wave. The heat transfer causes the wall temperature to drop, albeit negligibly, as will be shown in Fig. 8. That is, the experiments are conducted at essentially constant wall temperature. Further details concerning the operating procedures of the wind tunnel are available in existing literature (Chen, 1985; Tsou et al., 1983), and will not be repeated here.

2.2 Measurement System. Measurements of pressure as a function of time are made using Kistler Model 603B1 piezoelectric pressure transducers with 503D charge amplifiers. Six transducers, mounted along the centerline and flush with the lower wall (Fig. 2), are located at $x = 0$, 25.35, 50.80, 76.22, 114.3, and 165.1 mm, respectively. The response time of these transducers is on the order of 1 μs.

Measurements of velocity or speed of flow, turbulence, and temperature of the flow field are performed using a TSI-1050 constant temperature hot-wire anemometer having a wire diameter of 5 μm. The hot wire has a dynamic response of 3 kHz as a temperature sensor. Temperature measurement has been found to be in good agreement with that obtained using the isentropic relation coupled with the pressure measurement. It is found that the wall temperature is essentially constant during each test run. In order to obtain the profiles for velocity, turbulence intensity, and temperature, the probe has been designed to translate along a vertical direction using a model

Nomenclature

h = heat transfer coefficient
H = step height = 3.3 mm
k = thermal conductivity of the flow
M = Mach number
Nu = Nusselt number = hH/k
p = pressure transducers
q, q_w = wall heat fluxes
Re_H = step height Reynolds number = $\rho u_\infty H/\mu$
t = time
T = temperature
ΔT = surface temperature drop
u = instantaneous velocity in x direction
$|u|$ = instantaneous flow speed
u' = fluctuation component of u
$\bar{u}$ = mean component of u
x, x' = streamwise coordinate as defined in Fig. 1
x_r = reattachment length
x_s = initial length as defined in Fig. 1
y = cross-stream coordinate as defined in Fig. 1
y_o, y_1 = distance as defined in Fig. 2
δ = boundary layer thickness
μ = dynamic viscosity of flow
ν = kinematic viscosity of flow
ρ = density of flow
τ = dimensionless time defined in equation (1)

Subscripts

s = at the step or separation
w = at the wall
∞ = free stream

430-M (Newport Corp.) translation stage with a resolution of 0.01 mm.

Heat fluxes are measured using thin film platinum gages 5 mm in length, 0.5 mm in width, and 1000 Å in thickness coated on Pyrex substrates. The recorded surface temperature history is postprocessed based on one-dimensional unsteady heat conduction theory (Tsou et al., 1983) to yield time-varying heat fluxes. Heat flux gages are mounted flush with the upper wall and along the centerline at locations of $x/H = -33.6, -20.3, 0.30, 1.22, 2.13, 3.04, 3.94, 4.85, 5.76, 6.67, 7.59, 13.6, 22.7, 40.9$, with two gages in the initial boundary layer region, nine gages in the recirculating region, and three gages in the redeveloping boundary layer region. These gages have extremely fast response times (less than 1 μs) and, hence, are capable of detecting whether the boundary layer is laminar, transitional, or turbulent. In order to convert resistance changes (due to the time-varying surface temperatures) to voltage signals, constant currents of 3 mamp are passed through the gages to minimize the effect of electric heating. The signals are amplified with gains of 1000 and filtered at cut-off frequencies of 3 kHz before being sent to the A/D converter. The details of the signal conditioning circuits such as filters and amplifiers as well as heat flux processing are discussed elsewhere (Chen, 1985; Tsou et al., 1983).

An LSI-11/2 microcomputer with an eight-channel A/D converter (12-bit resolution) has been developed for data acquisition. The recorded data are transferred to a VAX-11/750 minicomputer for further processing and analysis including the use of a statistical software package RS1. A sampling rate of 40 kHz is employed to measure the turbulence characteristics giving a frequency spectrum up to 20 kHz. Sampling rates of 5 kHz are used for all other properties including mean velocities, temperatures, pressures, and wall heat fluxes. These sampling rates are properly chosen to avoid the aliasing effect. The system description and software have been given by Chen (1985).

Obviously, the single hot-wire approach employed in this study can be used to indicate velocities only if the flow direction is predetermined. In spite of this, the approach has been employed successfully in previous investigations of separated flow. In the present study, the method is used to measure the speed of the flow, insofar as the recirculating region is concerned. For simplicity of data presentation, however, the speed of the flow is denoted by the symbol $|u|$ in the present paper. For the free shear layer and the free stream flow, the hot-wire probe gives the flow in the x direction.

2.3 Tunnel Qualifications. Velocities at five spanwise locations and five vertical (outside of the boundary layers) locations are measured to check the two dimensionality and the vertical uniformity of the flow, respectively. The scattering in all measurements is less than 2 percent for mean velocities and less than 5 percent for turbulence intensities. The turbulence intensities at steady state are evaluated with at least 300 data points. The time-dependent mean velocities are determined using the moving time average method. The initial length (x_s in Fig. 1) is sufficiently long to give a turbulent boundary layer at the step. All pressure transducers and heat flux gages are located at the center of the tunnel to minimize edge effects. Chen and Tsou (1984) have reported that the measured heat fluxes at steady state are within 5 percent of the flat plate solution (Holman, 1986) for all upstream locations ($x/H < 0$) and the locations far downstream of the step, i.e., $x/H > 25$.

3 Results and Discussions

In the present investigation, we employ the following steady-state system parameters: (1) Mach number: M = 0.3; (2) step Reynolds number: $Re_H = 38{,}800$; (3) turbulent boundary layer thickness at the step: $\delta_s/H = 1.4$; (4) free-stream turbulence intensity: 0.4 percent; and (5) temperature difference between the wall and the free stream; $T_w - T_\infty = 16$–$18°C$. The latter, relatively small temperature difference is chosen to minimize the variable-property effect.

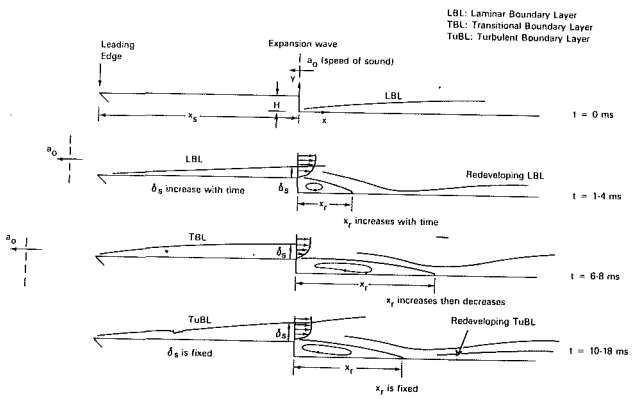

Fig. 3 Flow development during a starting flow past a step

3.1 Transient Flow Field. As stated previously, the present study employs a Ludwieg tube wind tunnel to generate the accelerating flow. In our experience, this tunnel is uniquely suited for the purpose of this study. The development of the transient flow field, however, is not commonly understood. A fundamental characteristic of the tunnel is the generation of an expansion wave once the diaphragm is ruptured. The accelerating flow behind the expansion wave is initially a one-dimensional frictionless flow. For flow behind the expansion wave over a flat plate without a leading edge, Tsou et al. (1983) have studied the heat transfer in the unsteady boundary layer, which is formed and growing on the flat plate, as the boundary layer changes from laminar, to transitional, and finally to turbulent flow, while the Reynolds number increases with time. The earlier work of Chen et al. (1988) has shown that the flow structure during the starting process consists of four stages. They are depicted in Fig. 3. The flow is laminar in the beginning, but is primarily turbulent in the steady state. As indicated by the dashed lines and arrows in Fig. 3, the expansion wave head travels upstream (to the left) at the speed of sound (a_o), while the flow behind the wave accelerates downstream (Tsou et al., 1983). The flow is similar to the starting flow initiated by a suction fan.

Soon after time $t = 0$, which corresponds to the time when the expansion wave head reaches the step, an unsteady free shear layer begins to develop downstream of the step ($x > 0$). This leads to flow separation at the top corner, and a recirculating zone forms at the lower corner. Up to the time $t =$ 1 ms, the flow behind the step behaves like a free jet. The time for the wave to propagate through the test section is about 1 ms. Therefore, at $t = 1$–4 ms when the expansion wave head leaves the leading edge, a laminar boundary layer grows with time behind the leading edge. Simultaneously, the recirculating region elongates gradually as the reattachment length increases with time. Downstream of the reattachment point, the flow redevelops into a boundary layer type flow. At $t = 6$–8 ms, the initial boundary layer near the step becomes transitional and the reattachment length increases to a maximum. At $t =$ 10–18 ms the leading edge effect propagates to the step, and the initial boundary layer becomes fully turbulent while the reattachment length decreases and attains a relatively constant value at steady state.

Instantaneous flow speeds at three representative locations downstream of the step are shown in Fig. 4. These locations are situated in the free stream, within the free shear layer, and in the recirculating region, respectively. Beginning at $t = 0$ ms and up to approximately $t = 7$ ms, the free-stream flow (curve

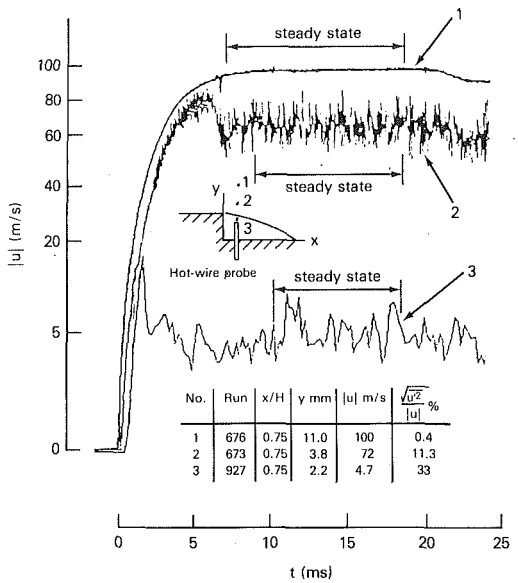

Fig. 4 Instantaneous velocity/speed measurements at three locations

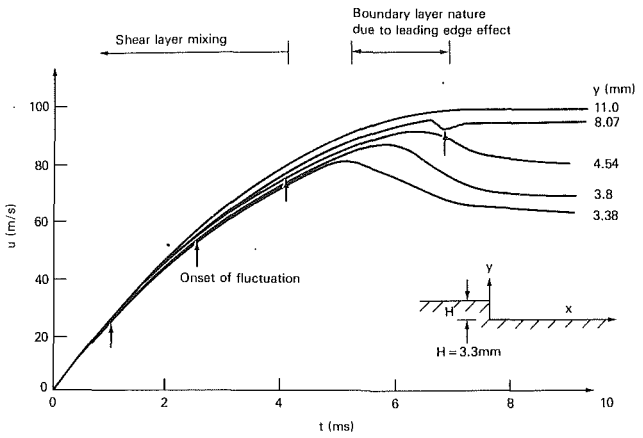

Fig. 5 Time-dependent mean velocities in free shear layer

1) accelerates from a quiescent state to a steady state. The steady-state flow has a velocity of 100 m/s and a turbulence intensity of 0.4 percent from $t = 7$ to $t = 19$ ms. The free-stream velocity agrees with the value predicted using one-dimensional frictionless flow analysis (Tsou et al., 1983). Curve 2 shows that from $t = 0$ to $t = 2.5$ ms, the separated shear layer is laminar but becomes transitional at $t = 2.5$ ms when small fluctuations are observed as a result of convective mixing through the separated shear layer. The velocity finally drops (between $t = 6$ and 8 ms) to a steady-state value when the leading edge disturbance reaches the step. Note that the shear layer approaches steady state shortly after the free stream becomes steady. Turbulence with high-frequency fluctuations and a short characteristic time as shown in curve 2 is also observed in the boundary layer (Region I in Fig. 1). In the recirculating region (Region II), however, the time required for the flow to develop and to reach a steady state is found to be longer because of the existence of large-scale eddies (and thus a longer characteristic time) as indicated by the lower frequency fluctuations (curve 3). Since a single-wire probe is used in the present study, the velocity in the recirculating region (curve 3) is indicated only qualitatively. Flow visualization study in the recirculating region (Troutt et al., 1984) has also indicated that the turbulent shear layer rolled into large-scale vortices, which give rise to overall flow unsteadiness in the recirculating region.

In order to provide more insight into the mechanisms of flow development in the shear layer ($x/H = 0.75$), time-dependent mean velocities at various y locations are shown in Fig. 5. The upper curve representing the free steam is the same as curve 1 in Fig. 4. The four arrows, from left to right at $t = 1, 2.5, 4, 6.5$ ms, indicate the onset of transition (as indicated by velocity fluctuations) at $y = 3.38$, 3.8, 4.54, 8.07 mm, respectively. These fluctuations originate from the top corner (i.e., $x = 0$ and $y = 3.3$ mm) of the step and diffuse in the downstream as well as in the transverse directions throughout the separated free shear layer.

The lower four curves in Fig. 5 show that the velocities increase and then decrease to steady-state values at t values between 5 and 7 ms. This decrease in velocities at the hot-wire locations is caused by the combined effect of the time-wise growth of the boundary layer and the propagating leading edge disturbance. This combined boundary layer and leading edge effect is not completely understood and requires additional study. Some conjectures, however, are possible regarding the observations shown in Fig. 5. For convenience, we define a dimensionless time, τ, as

$$\tau = \frac{\int_0^t u_\infty dt}{x_s} \tag{1}$$

The time needed for the boundary layer effect to reach the probe location, i.e., for the leading edge disturbance to arrive at the step, may be estimated using $\tau = 1$ in equation (1). The estimated time is about 5–6 ms, which agrees well with the measured values as shown in Fig. 5.

The boundary layer grows with time until the hot wire is submerged in the boundary layer causing the velocities to drop. It is observed that the velocity nearest to the wall at $y = 3.38$ mm begins to decrease at $t = 4.5$ ms. The boundary layer effect continues to propagate upward, resulting in subsequent velocity drops at $y = 3.8$, 4.54, and 8.07 mm. The flow at $y = 11$ mm is essentially frictionless since it is located outside of the boundary layer at all times. After $t = 7$ ms, the velocities as well as the turbulence intensities at all locations attain steady-state values.

3.2 Steady-State Flow Field. Figure 6 shows the mean velocity profile at $x/H = 0.75$ in the steady state. The curve for the "1/7th power law" at the step is also shown. The data are below the theoretical curve, indicating that the streamline is concave downward, resulting in a boundary layer thinning effect near the step. Figure 6 suggests that the velocity profile, in the free shear layer in the late stage of temporal development, resembles the typical distribution in a steady-state turbulent boundary layer in attached flow. Figure 7 depicts the turbulence intensity distribution at $x/H = 0.75$ in steady state. The maximum value of 18 percent is attained immediately downstream of the step ($y/H = 1$) and it is in agreement with data obtained in continuous wind tunnels (Moss and Baker, 1980; Isomoto and Honami, 1989). It is seen from Fig. 7 that the present data deviate from those of others (Moss and Baker, 1980; Vogel and Eaton, 1985) at $y/H > 1$ because of the difference in the initial boundary layer thicknesses. The reason for the discrepancy at $y/H < 1$ is not clear at this time and needs further investigation, since the single wire used here is inadequate for measurements in the recirculating flow. One possible explanation is that the turbulence is very sensitive to the x/H locations in the recirculating region. When Adams and Johnston (1989) compared several studies for turbulence intensities at the reattachment region, they only reported qualitative agreement.

3.3 Transient Heat Fluxes and Reattachment. The measured surface temperature variations in heat flux gages (ΔT) and calculated wall heat fluxes (q_w) versus time are shown in

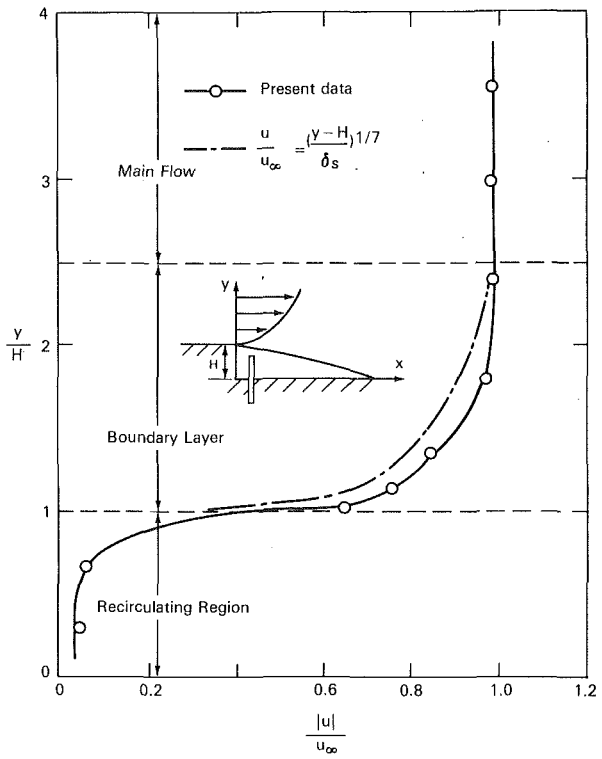

Fig. 6 Steady-state mean velocity/speed profile at $x/H = 0.75$

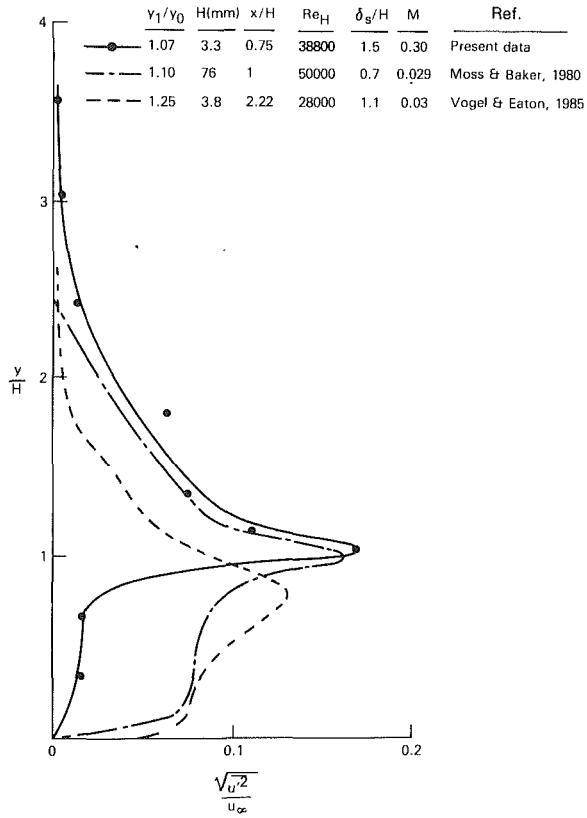

Fig. 7 Steady-state turbulence intensity distribution at $x/H = 0.75$

Fig. 8. The lower curves (ΔT) show that the surface temperature change is about 0.5°C or less so that the wall temperature is essentially constant. The upper curves (q_w) demonstrate that steady-state conditions are obtained for a period of several milliseconds. A typical pattern of heat flux in the turbulent boundary layer is shown in Fig. 8(*a*). The flow starts at t = 0 ms and an unsteady laminar boundary layer develops up to t = 3.5 ms when transition to turbulence takes place with an abrupt increase of heat flux, as indicated by the arrow. Steady state heat flux is obtained between t = 7 and 19 ms immediately after the free stream becomes steady (see Figs. 4 and 5). This temporal variation of heat flux is similar to the flow variation suggested by curve 2 in Fig. 4. After the boundary layer transition takes effect at the heat flux gage location, the time required for the boundary layer to develop (i.e., the time required for the turbulent diffusion through the boundary layer) can be estimated by dividing the turbulent energy by the production rate of turbulent energy. The time constant, which is estimated by Bradshaw (1975) to be 10 δ/u_∞, is found to be 0.5 ms at the location of $x/H = -20.3$. This time constant is a good estimate as shown by comparing the steady-state times associated with the free stream in Fig. 4 (curve 1) and the heat fluxes of the turbulent boundary layer in Fig. 8(*a*).

Figure 8(*b*) shows the representative wall heat flux and surface temperature information for the recirculating region (Region II in Fig. 1). Compared with Region I, it takes a longer time for the heat flux in Region II to become steady. The reason is that the large eddies (which lead to curve 3 of Fig. 4) have longer characteristic times than those associated with the conventional attached boundary layer. In Fig. 8(*c*) where the flow is in the redeveloping boundary layer region (Region III), the time (t > 10 ms) for the heat flux to become steady is longer yet than that in Fig. 8(*b*). In general, the heat flux versus time curves in region I and III show fluctuations with higher frequency and smaller amplitudes, while the curve in region II shows fluctuations with lower frequency and larger amplitudes. In addition, boundary layer transition is observed in both Regions I and III but not in Region II (arrowheads in

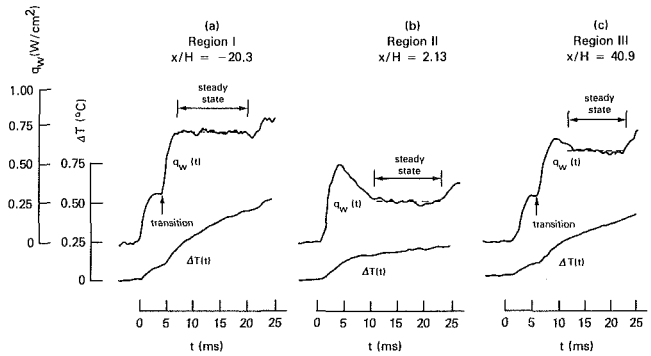

Fig. 8 Measured surface temperature variations in heat flux gages (ΔT) and wall heat fluxes (q_w) versus time (t) in three regions (Region I: initial boundary layer; Region II: recirculating flow; Region III: redeveloping boundary layer)

Figs. 8(*a*) and 8(*c*) indicate the time when transition takes place). These results provide support for the flow pattern description given in conjunction with Figs. 1 and 3.

A cross plot of heat transfer using Nu/Nu_s versus x/H at various times is shown in Fig. 9. The value of Nu_s is obtained using the steady-state turbulent boundary layer solution for flow over a flat plate at the step (Holman, 1986). At t = 0 (see Fig. 3), the heat fluxes are nearly zero everywhere. At t = 1 ms, when the recirculating region begins to grow downstream, the heat flux is maximum near the bottom corner at x/H = 0.3. During the second and the third stages (Fig. 3), the locations of the maximum heat fluxes shift downstream to x/H = 2.1, 4.0, 5.8, and 13.6 at times t = 2, 4, 6, and 8 ms, respectively. It is noted that the free stream and initial boundary layer become steady at t = 7 ms. After t = 10 ms, the overall flow field as depicted in Fig. 1 reaches a steady state and so do the heat fluxes. At the steady state, the present maximum (peak) value of 1.10 for Nu/Nu_s is slightly less than

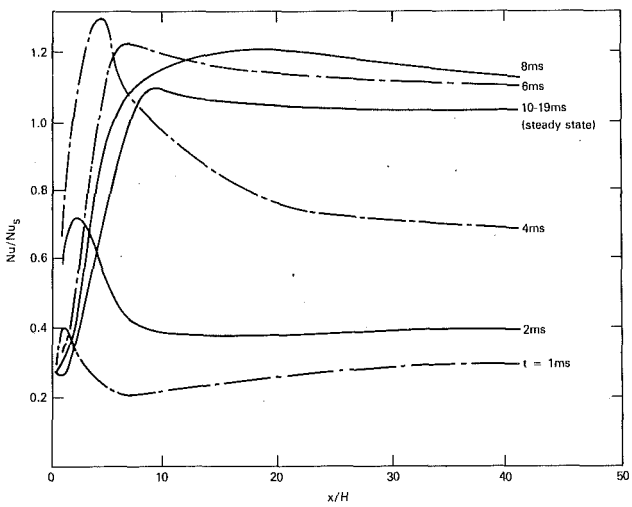

Fig. 9 Normalized Nusselt number Nu/Nu$_s$ versus *x/H* with increasing time

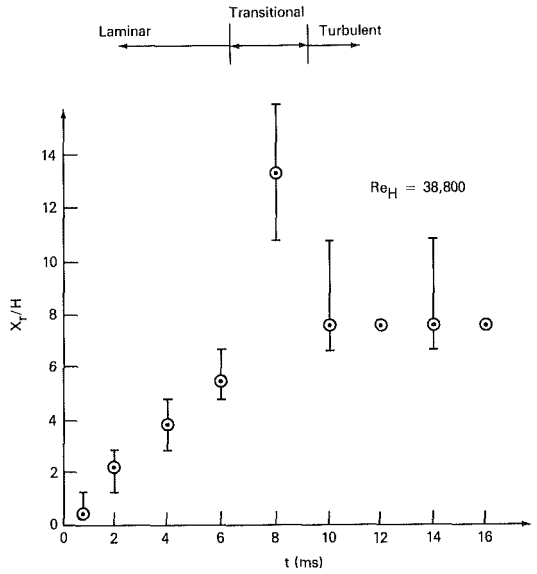

Fig. 10 Dimensionless reattachment length versus time

the value of 1.15 (Seban, 1964) and 1.20 (Aung and Goldstein, 1971) obtained in other studies.

Although peak values of heat transfer do not exactly correspond to the reattachment points, the locations of the peak values are often used to estimate reattachment lengths (Aung and Goldstein, 1971; Vogel and Eaton, 1985). As shown in Fig. 10, the reattachment length x_r/H, as inferred by the location of maximum q_w, increases gradually from 0.3 to 5.8 in the laminar flow regime. A maximum of 13.6 is attained in the transitional regime before finally settling down to a steady value of 7.6 in the turbulent regime. This reattachment flow pattern provides further support for the overall flow structure depicted in Fig. 3. The uncertainty bars shown in Fig. 10 are basically due to the discrete heat flux gage locations available in the present study. More heat flux gages between $x/H = 0$ and $x/H = 14$ are needed to improve the spatial resolution of the reattachment points.

3.3 Steady-State Heat Transfer and Reattachment. Since the wall temperature drops in all three regions are usually less than 0.5°C as indicated in Fig. 8, the wall temperature may be assumed to be constant. Steady-state wall heat fluxes upstream and far downstream of the step (i.e., Regions I and III in Fig. 1) have been reported (Chen and Tsou, 1984; Chen et al., 1988) to be in good agreement with the solution of turbulent

y_1/y_0	H(mm)	x_r/H	Re_H	δ_s/H	M	REF
○ 1.07	3.3	7.9	38800	1.4	0.30	Present data
— — — 1.25	38	6.67	28000	1	0.033	Vogel and Eaton, 1985
—·— 1.29	25.4	6	73000	2	0.13	Seban, 1964

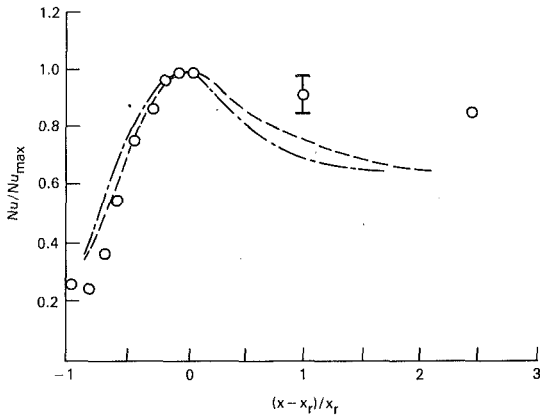

Fig. 11 Comparison of normalized Nusselt number Nu/Nu$_{max}$ versus dimensionless distance, $(x - x_r)/x_r$

boundary layer over a flat plate. Here, heat transfer data in the near corner region are presented. Local heat transfer coefficients (h) and Nusselt numbers (Nu) have been determined using the steady-state wall heat fluxes described previously, i.e.,

$$h = q_w/(T_w - T_\infty) \tag{2}$$

$$\mathrm{Nu} = hH/k \tag{3}$$

A plot of Nu/Nu$_{max}$ is shown in Fig. 11, where Nu$_{max}$ is the maximum Nusselt number at the reattachment point. Good agreement is shown with the data of Seban (1964) and Vogel and Eaton (1985) in the recirculating region. Near the corner where x/H approaches zero, Nu/Nu$_{max}$ is found to be 0.25. This suggests the existence of a secondary recirculating vortex in the corner. The present data downstream of the reattachment point are higher than those of Seban (1964) and Vogel and Eaton (1985) because of the smaller expansion ratio used in the present study, i.e., 1.07 compared to 1.25 and 1.29 for Seban (1964) and Vogel and Eaton (1985), respectively.

The reattachment length in the present study is $x_r/H = 7.6$, which is higher than the previous values of 6.6 (Vogel and Eaton, 1985) and 4.5 (Aung and Goldstein, 1971). The reason may be traced in part to the large steady-state Reynolds number ($Re_H = 38{,}800$) employed in the present research. The reattachment length is found to increase with the Reynolds number by Chen et al. (1988) and Roos and Kegelman (1987). The uncertainty of the present data is estimated to be 3, 5, and 8 percent for Re_H, q_w, and Nu, respectively.

4 Conclusions

Based on the present experimental study of the time history of both the flow field and the heat flux in separated flow beyond a backward-facing step, the following conclusions may be drawn:

1 The short duration flow, which accelerates from a zero velocity to a steady-state subsonic flow, is useful for studying the development of flow field and heat transfer in separated regions. A constant wall temperature boundary condition is attained using this approach without any difficulty.

2 Transient flow patterns in the separated free shear layer indicate early fluctuations, which are caused by flow mixing in the free jet boundary layer. In the late stages of flow, the velocities approach steady-state turbulent boundary layer distributions.

3 The steady-state flow structure depicted in Fig. 1 has been verified with the present measurements. Large-scale eddies with low-frequency fluctuations characterize the flow in the recirculating region, while high-frequency turbulence fluctuations dominate the flow in the turbulent boundary layer and free shear layer.

4 Transient heat flux variations indicate the transformation of the flow from laminar through transitional to turbulent flow in the initial and the redeveloping boundary layer regions, but not in the recirculating region, which requires longer time for the heat flux to become steady.

5 During the flow development, the Reynolds number increases with time causing the reattachment length to increase with time in the laminar regime. In the transitional regime, the reattachment length reaches a maximum and finally decreases to a steady-state value in the fully turbulent regime. The experimental observations are consistent with the flow structure for the starting process shown in Fig. 3.

6 Steady-state Nusselt numbers in the recirculating region compare well with values in existing literature. The heat transfer approaches a finite nonzero value at the corner.

7 In order to investigate the flow and turbulence characteristics further in the recirculating region, a two-component LDA system is recommended.

Acknowledgments

This study constitutes a part of Drexel/National Cheng Kung University-IAA cooperative research activity.

References

Adams, E. W., and Johnston, J. P., 1988, "Effects of the Separating Shear Layer on the Reattachment Flow Structure, Part 1: Pressure and Turbulence Quantities," *Experiments in Fluids*, Vol. 6, pp. 400–408.

Aung, W., and Goldstein, R. J., 1971, "Heat Transfer in Turbulent Separated Flow Downstream of a Rearward Facing Step," *Israel J. Technology*, Vol. 10, No. 1-2, pp. 35–41.

Aung, W., 1983, "Separated Forced Convection," *Proceedings of the ASME-JSME Thermal Engineering Joint Conference*, Vol. 2, pp. 499–515.

Aung, W., Baron, A., and Tsou, F. K., 1985, "Wall Independency and Effect of Initial Shear Layer Thickness in Separated Flow and Heat Transfer," *Int. J. Heat Mass Transfer*, Vol. 28, No. 9, pp. 1757–1771.

Baughn, J. W., Hoffman, M. A., Launder, B. E., Lee, Daehee, and Yap, C. W., 1989, "Heat Transfer, Temperature, and Velocity Measurements Downstream of an Abrupt Expansion in a Circular Tube at a Uniform Wall Temperature," ASME JOURNAL OF HEAT TRANSFER, Vol. 111, pp. 870–876.

Bradshaw, P., 1975, *An Introduction to Turbulence and Its Measurements*, Pergamon Press, Oxford, United Kingdom.

Chen, S. J., and Tsou, F. K., 1984, "Computer-Based Data Acquisition of Heat Transfer in Short-Duration Flow Over a Backward-Facing Step," ASME Paper No. 84-HT-47.

Chen, S. J., 1985, "The Effect of Injection-Stream Turbulence on Film Cooling Effectiveness and Heat Transfer Coefficients," Ph.D. Thesis, Drexel University, Philadelphia, PA.

Chen, S. J., Tsou, F. K., Duan, X. R., and Aung, W., 1988, "Flow Development and Heat Transfer for Short-Duration Flow Over a Backward-Facing Step," *3rd International Symposium on Transport Phenomena in Thermal Control*, Taipei, Taiwan, pp. 313–324.

Durst, F., and Pereira, J. C. F., 1988, "Time-Dependent Laminar Backward-Facing Step Flow in a Two-Dimensional Duct," ASME *Journal of Fluids Engineering*, Vol. 110, pp. 289–296.

Eaton, J. K., and Johnston, J. P., 1981, "A Review of Research on Subsonic Turbulent Flow Reattachment," *AIAA Journal*, Vol. 19, No. 9, pp. 1092–1100.

Ghoniem, A. F., and Sethian, J. A., 1987, "Effect of Reynolds Number on the Structure of Recirculating Flow," *AIAA Journal*, Vol. 25, No. 1, pp. 169–171.

Gooray, A. M., Watkins, C. B., and Aung, W., 1985, "Turbulent Heat Transfer Computation for Rearward-Facing Steps and Sudden Pipe Expansions," ASME JOURNAL OF HEAT TRANSFER, Vol. 107, pp. 70–76.

Holman, J. P., 1986, *Heat Transfer*, 6th ed., McGraw-Hill, New York.

Honji, H., 1975, "The Starting Flow Down a Step," *J. Fluid Mech.*, Vol. 69, Part 2, pp. 229–240.

Isomoto, K., and Honami, S., 1989, "The Effect of Inlet Turbulence Intensity on the Reattachment Process Over a Backward-Facing Step," ASME *Journal of Fluids Engineering*, Vol. 111, pp. 87–92.

Moss, W. D., and Baker, S., 1980, "Recirculating Flows Associated With Two-Dimensional Steps," *Aeronautical Quarterly*, Aug., pp. 151–171.

Roos, F. W., and Kegelman, J. T., 1987, "Structure and Control of Flow Over a Backward-Facing Step," *Forum on Unsteady Flow Separation*, ASME FED-Vol. 52, pp. 215–223.

Seban, R. A., 1964, "Heat Transfer to the Turbulent Separated Flow of Air Downstream of a Step in the Surface of a Plate," ASME JOURNAL OF HEAT TRANSFER, Vol. 42, pp. 259–264.

Troutt, T. R., Scheelke, B., and Norman, T. R., 1984, "Organized Structures in a Reattaching Separated Flow Field," *J. Fluid Mech.*, Vol. 143, pp. 413–427.

Tsou, F. K., Chen, S. J., and Ko, S. Y., 1983, "Measurements of Heat Transfer Rates Using a Transient Technique," ASME Paper No. 83-HT-87.

Vogel, J. C., and Eaton, J. K., 1985, "Combined Heat Transfer and Fluid Dynamics Measurements Downstream of a Backward-Facing Step," ASME JOURNAL OF HEAT TRANSFER, Vol. 107, pp. 922–929.

Augmented Heat Transfer in Square Channels With Parallel, Crossed, and V-Shaped Angled Ribs

J. C. Han
Professor.
Fellow ASME

Y. M. Zhang
Research Associate.

Turbine Heat Transfer Laboratory,
Department of Mechanical Engineering,
Texas A&M University,
College Station, TX 77843

C. P. Lee
Senior Staff Engineer,
General Electric Company,
Cincinnati, OH 45215
Mem. ASME

The effect of the rib angle orientation on the local heat transfer distributions and pressure drop in a square channel with two opposite in-line ribbed walls was investigated for Reynolds numbers from 15,000 to 90,000. The square channel composed of ten isolated copper sections has a length-to-hydraulic diameter ratio of 20; the rib height-to-hydraulic diameter ratio is 0.0625; the rib pitch-to-height ratio equals 10. Nine rib configurations were studied: 90 deg rib, 60 and 45 deg parallel ribs, 60 and 45 deg crossed ribs, 60 and 45 deg V-shaped ribs, and 60 and 45 deg Λ-shaped ribs. The results show that the 60 deg (or 45 deg) V-shaped rib performs better than the 60 deg (or 45 deg) parallel rib and, subsequently, better than the 60 deg (or 45 deg) crossed rib and the 90 deg rib. The V-shaped rib produces the highest heat transfer augmentation, while the Λ-shaped rib generates the greatest pressure drop. The crossed rib has the lowest heat transfer enhancement and the smallest pressure drop penalty.

Introduction

Applying turbulence promoters inside cooling passages is an effective technique to enhance the heat transfer rate inside turbine blades. The effects of rib configurations (such as rib height, spacing, angle of attack) and flow Reynolds number on the average heat transfer and pressure drop in the fully developed region of a uniformly heated square channel with two opposite rib-roughened walls were investigated systematically (Han, 1984; Han et al., 1985). The effects of the above parameters on the local heat transfer and pressure drop in developing (entrance) and fully developed regions of foil-heated, ribbed rectangular channels with five different aspect ratios were reported (Han, 1988; Han and Park, 1988; Han et al., 1989). The results show that the angled ribs provide a better heat transfer performance than the transverse ribs, and the narrow aspect ratio channels (near the leading edge of the airfoil) perform better than the broad aspect ratio channels (near the trailing edge of the airfoil). In a two-pass square channel, in addition to the rib turbulators and the flow Reynolds number, the effects of the sharp 180 deg turn on the distributions of the local mass transfer (using naphthalene sublimation technique) and pressure drop right after the sharp turn are significant (Han et al., 1988; Chandra et al., 1988; Chandra and Han, 1989). Effects of the rib-angle orientations on the local mass transfer (using naphthalene sublimation technique) and pressure drop distributions in three-pass rectangular channels have also been reported (Han and Zhang, 1989; 1991). These previous studies show that rib angle orientation on two opposite walls of a cooling channel has a significant impact on the local heat transfer and pressure drop distributions. To identify the better rib angle orientation in a cooling channel, it requires some systematic heat transfer measurements for various rib turbulator configurations.

Several questions still remained after the previous studies: (1) The previous results are obtained primarily for parallel ribs (the ribs on two opposite walls of the cooling channels are in parallel orientations). It is questionable whether the crossed ribs (the ribs on two opposite walls of the cooling channels are in crossed orientations) can provide a better heat transfer performance than the parallel ribs. (2) The previous studies show that the angled ribs provide a better heat transfer performance than the transverse ribs because of the secondary flow induced by the rib angle. It is of interest whether the V-shaped ribs can perform even better than the angled ribs because of the double secondary flow induced by the V-shaped rib angle. (3) The previous studies have used the foil-thermocouple method and the naphthalene sublimation technique to determine the detailed distributions of the local heat/mass transfer coefficients between every two ribs, but the number of thermocouples used and the number of mass transfer points measured are still limited. To obtain the true average heat transfer coefficients for turbine cooling design, it is better to have a test section that can determine the regionally averaged heat transfer coefficients in the channel streamwise flow direction. The regionally averaged heat transfer method has been used to study the effect of channel entrance on the regionally averaged heat transfer coefficient in a square duct with two opposite ribbed walls (Burggraf, 1970), and also to study the effect of the channel geometry on the regionally averaged heat transfer coefficient in two-pass smooth rectangular channels (Metzger and Sahm, 1986).

The objective of this study is to investigate the effect of rib orientation on local heat transfer distributions and pressure drop in a square channel with two opposite ribbed walls for Reynolds numbers 15,000 to 90,000. The square channel length-to-hydraulic diameter ratio (L/D) is 20; the rib height-to-hydraulic diameter ratio (e/D) is 0.0625; the rib pitch-to-height ratio (p/e) equals 10. Table 1 lists the nine rib configurations studied: 90 deg rib, 60 deg parallel rib, 60 deg crossed rib, 60 deg V-shaped rib, 60 deg Λ-shaped rib, 45 deg parallel rib, 45 deg crossed rib, 45 deg V-shaped rib, 45 deg Λ-shaped rib. Note that the 60 and 45 deg ribs on two opposite walls of the square channel can be parallel or crossed to each other. Also note that ribs on two opposite walls of the square channel are directly opposite to each other (i.e., in-line arrays) for all nine configurations studied. The square channel has ten isolated copper sections in the axial direction. The regionally averaged heat transfer coefficients on both the ribbed-side and the smooth-side walls of the channel are determined from the channel entrance to the downstream region. The channel-av-

Contributed by the Heat Transfer Division for publication in the JOURNAL OF HEAT TRANSFER. Manuscript received by the Heat Transfer Division June 14, 1990; revision received October 1, 1990. Keywords: Augmentation and Enhancement, Finned Surfaces, Turbines.

Table 1 Configurations of ribs on channel walls

CASE	DESCRIPTION IN THE TEXT	NOTATION IN THE FIGURES
1	90° rib	90°
2	60° parallel rib	60°//
3	60° crossed rib	60°X
4	60° ∨-shaped rib	60°∨
5	60° ∧-shaped rib	60°∧
6	45° parallel rib	45°//
7	45° crossed rib	45°X
8	45° ∨-shaped rib	45°∨
9	45° ∧-shaped rib	45°∧

eraged heat transfer coefficients are obtained, and the heat transfer versus pressure drop performances are compared for the nine rib configurations studied. The semi-empirical friction and heat transfer correlations are also provided.

Experimental Apparatus and Data Reduction

Experimental Apparatus. Figure 1(*a*) shows a cross section for the test duct. The square test duct consisted of heated parallel copper plates. The test duct is 101.6 cm (40 in.) long and has a cross section of 5.08 cm by 5.08 cm (2 in. by 2 in.). The copper plate is 0.635 cm (0.25 in.) thick. The test duct orientation was such that the two opposite rib-roughened walls of the square cross sections were vertical and the two opposite smooth walls horizontal. These ribbed walls were made by gluing square brass ribs to the copper plate surface in a required distribution. The ribs serve as turbulence promoters to trip the laminar sublayer of the turbulent flow. The glue thickness was estimated to be 0.0127 cm (0.005 in.) or less. The foil heaters were embedded in double-sided tape and uniformly adhered between the copper plate and a wood plate to insure good contact. Each wall of the test duct had one foil heater; each foil heater could be independently controlled by a variac transformer and provided a controllable constant heat flux for each wall of the test duct. The entire heated test duct, including the unheated end duct (outlet section), was centrally mounted in a long horizontal enclosure of cross-sectional dimensions 30.5 cm by 30.5 cm (12 in. by 12 in.). The enclosure was filled with fiberglass insulating material.

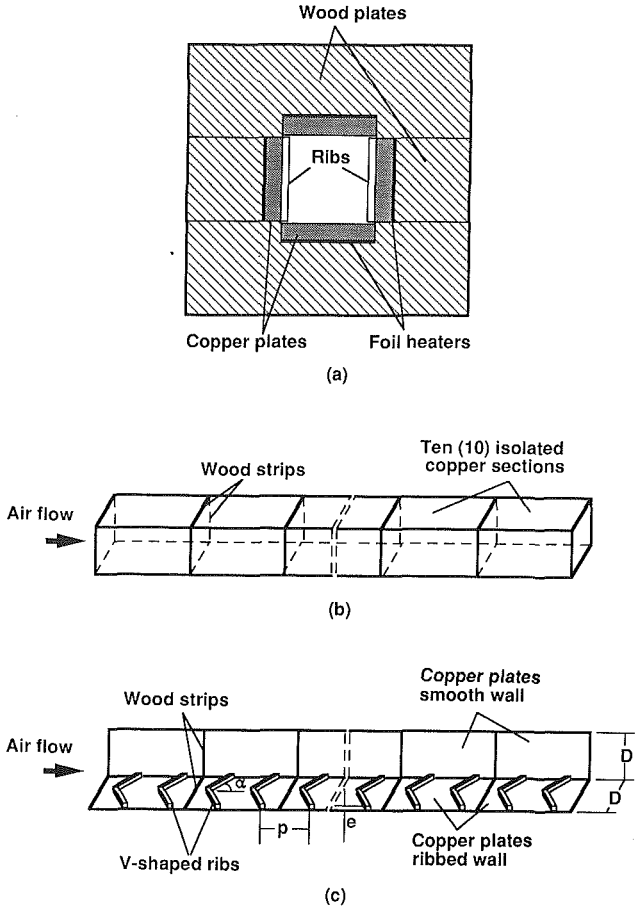

Fig. 1 *(a)* **Cross section of the test duct;** *(b)* **test duct composed of ten copper sections;** *(c)* **∨-shaped rib orientation**

The test duct was divided into 10 short copper sections as shown in Fig. 1(*b*). Each copper section is 10.16 cm (4 in.) long and has a cross section of 5.08 cm by 5.08 cm (2 in. by 2 in.). There are thin wood strips (0.159 cm thickness) as insulation to prevent the possible heat conduction between copper sections. These wood strips were adhered along the periphery contact surface between short copper sections. The unheated entrance duct had the same cross section and length

Nomenclature

A = heat transfer surface area
D = square channel width or height
e = rib height
e^+ = roughness Reynolds number, equation (9)
f = friction factor in a channel with two opposite ribbed walls
f_o = friction factor in fully developed tube flow
f_r = friction factor for four-sided ribbed channel
G = heat transfer roughness function; also mass velocity = ρV
$\overline{G}$ = average heat transfer roughness function
g_c = conversion factor
h = heat transfer coefficient
K = thermal conductivity of air
L = channel length
Nu = Nusselt number = hD/K
Nu_o = Nusselt number in fully developed tube flow
Nu_r = ribbed-side wall Nusselt number
Nu_s = smooth-side wall Nusselt number
P = rib pitch
Pr = Prandtl number of air
ΔP = pressure drop across the test section
q = heat generation rate from foils
q_{loss} = heat loss rate through insulation
R = friction roughness function
Re = Reynolds number = $\rho DV/\mu$
St = Stanton number = Nu/RePr
St_o = Stanton number in fully developed tube flow
St_r = ribbed-side-wall Stanton number
St_s = smooth-side-wall Stanton number
T_b = bulk mean temperature
T_w = local wall temperature
V = average velocity of air
X = axial distance from heated channel inlet
μ = average dynamic viscosity of air
ρ = average density of air

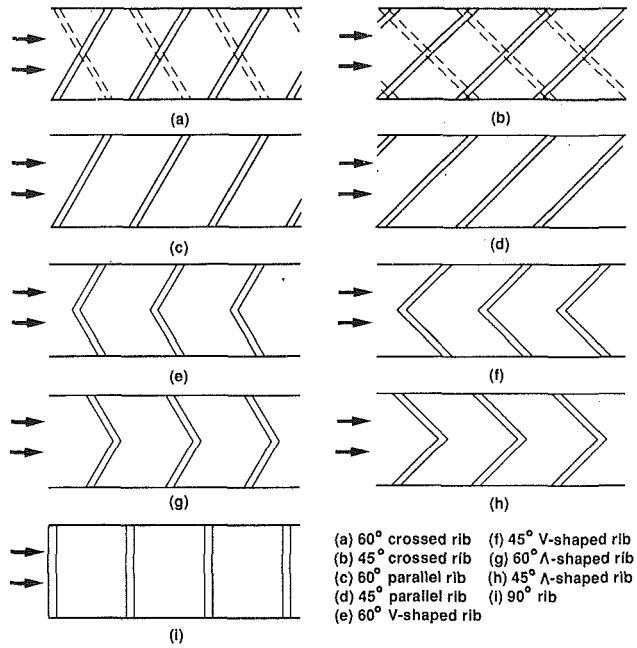

Fig. 2 Top view for the nine rib configurations studied

as those of the test duct, although the entrance duct was of plexiglass plates. This entrance duct served to establish hydrodynamically fully developed flow at the entrance to the heated duct. The wall temperature of the test section was measured by 40 copper-constantan thermocouples distributed along the length and across the span of the copper plates. Thermocouples were also used to measure the bulk mean air temperature entering and leaving the test duct. A Fluke 2285B Data Logger and a Texas Instruments Personal Computer were used for temperature readings and data storage. Two pressure taps were used for the static pressure drop measurements between the inlet and outlet of the test duct. Figure 1(*c*) shows a schematic of the V-shaped rib geometry. Table 1 lists the nine rib configurations studied. Figure 2 shows the top view of the nine rib orientations studied.

Data Reduction. A micromanometer connected to pressure taps was used to measured the pressure drop across the test duct. In fully developed duct flow, the friction factor can be determined by measuring the pressure drop across the flow channel and the mass velocity of the air. The friction factor can be calculated from

$$f = \Delta P/[4(L/D)(G^2/2\rho g_c)] \tag{1}$$

The friction factor f is based on the isothermal conditions (tests without heating). The maximum uncertainty in the friction factor is estimated to be less than 8 percent for Reynolds numbers greater than 10,000 by using the uncertainty estimation method of Kline and McClintock (1953). The friction factor f of the present study was normalized by the friction factor for fully developed turbulent flow in smooth circular tubes ($10^4 < \mathrm{Re} < 10^6$) proposed by Blasius as

$$f/f_o = f/[0.046\mathrm{Re}^{-0.2}] \tag{2}$$

The local heat transfer coefficient was calculated from the local net heat transfer rate per unit surface area to the cooling air, the local wall temperature on each copper plate, and the local bulk mean air temperature as

$$h = (q - q_{\mathrm{loss}})/[A(T_w - T_b)] \tag{3}$$

Equation (3) was used for the ribbed-side wall and the smooth-side wall heat transfer coefficient calculations. The local net heat transfer rate was the electrical power generated from the foil heaters minus the heat loss outside the test duct. The electrical power generated from the foil was determined from the measured foil resistance and the voltage on each wall of the test duct. The effect of the local wall temperature variation on the local foil resistance was estimated to be very small and negligible. The effect of axial wall conduction between copper sections on the local net heat transfer rate was small but included in the data reduction. To place the results on a common basis, the heat transfer area used in equation (3) was always that of a smooth wall. The foil heaters provided a nearly uniform heat flux on each wall of the test duct. The heat loss from the test duct was determined separately under a no-flow condition. The maximum heat loss from the ribbed-side wall and the smooth-side wall was estimated to be less than 3 and 4 percent, respectively, for Reynolds numbers greater than 10,000.

The local wall temperatures used in equation (3) were read from each copper plate thermocouple output. The local wall temperatures on both the ribbed-side and the smooth-side walls were close to each other, within 1°C. The bulk mean air temperatures entering and leaving the test duct were measured by thermocouples. The local bulk mean air temperature used in equation (3) was calculated assuming a linear air temperature rise along the flow duct. The total net heat transfer rate from the test duct to the cooling air agreed well with the cooling air enthalpy rise along the test duct. The inlet bulk mean air temperature was 27° to 31°C (81° to 88°F) depending on the test conditions. The maximum uncertainty in the Nusselt number was estimated to be less than 8 percent for Reynolds numbers larger than 10,000 by using the uncertainty estimation method of Kline and McClintock (1953).

The local Nusselt number of the present study was normalized by the Nusselt number for fully developed turbulent flow in smooth circular tubes correlated by McAdams/Dittus-Boelter as:

$$\mathrm{Nu}/\mathrm{Nu}_o = (hD/K)/(0.023\mathrm{Re}^{0.8}\mathrm{Pr}^{0.4}) \tag{4}$$

The friction data for turbulent flow in a square duct with two opposite ribbed walls can be correlated by the following equations (Han, 1988):

$$R(e^+) = (f_r/2)^{-1/2} + 2.5\ \ln\ (2e/D) + 2.5 \tag{5}$$

where

$$f_r = 2f - f_o \tag{6}$$

$$e^+ = (e/D)\mathrm{Re}(f_r/2)^{1/2} \tag{7}$$

Similarly the heat transfer data for fully developed turbulent flow in a square duct with two opposite ribbed walls can be correlated by the following equations (Han, 1988):

$$G = (f_r/2)^{1/2}/\mathrm{St}_r + 2.5\ \ln\ (2e/D) + 2.5 \tag{8}$$

and

$$\overline{G} = [(f_r/2)^{1/2}]/\overline{\mathrm{St}} + 2.5\ \ln\ (2e/D) + 2.5 \tag{9}$$

where

$$\overline{\mathrm{St}} = (\mathrm{St}_r + \mathrm{St}_s)/2 \tag{10}$$

In the present data reduction program, equations (5)–(10) were used to calculate the friction roughness function $R(e^+)$ and the heat transfer roughness function G and $\overline{G}$.

Experimental Results and Discussion

Regionally Averaged Heat Transfer Data. The local (regionally averaged) heat transfer results are presented as the axial distributions of a normalized Nusselt number ratio. Figure 3 shows the Nusselt number ratio distribution for the smooth channel and for 90 deg ribs. The Nusselt number ratio decreases with increasing the axial distance and then reaches a constant value in the fully developed region at a given flow Reynolds number. The local Nusselt number ratio decreases slightly with increasing Reynolds numbers. For the smooth channel the

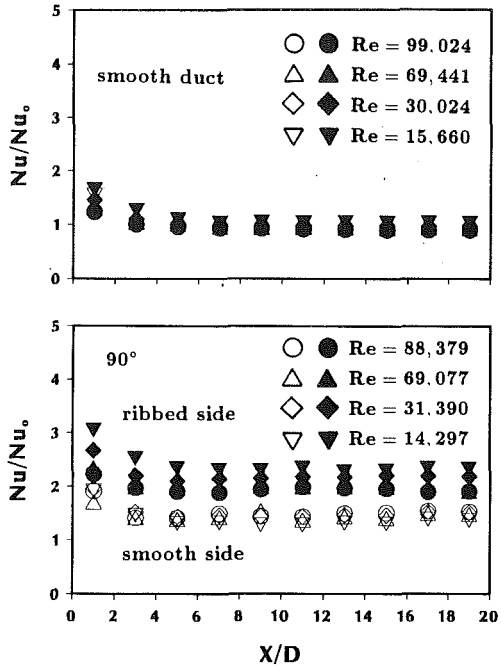

Fig. 3 Local Nusselt number ratio distributions for smooth channel and 90 deg rib

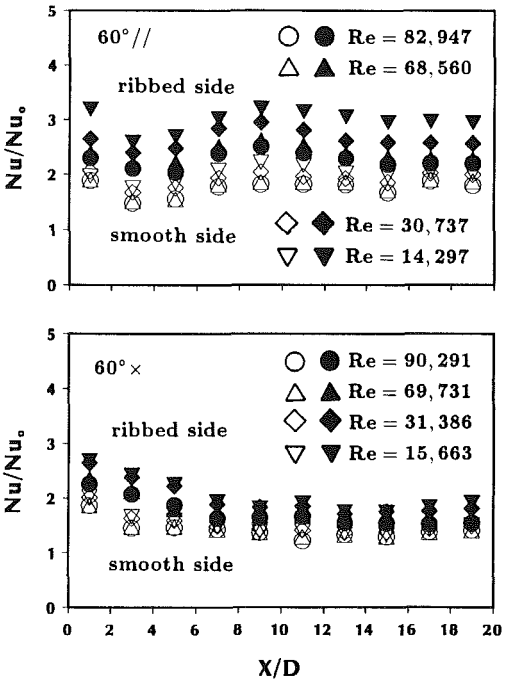

Fig. 4 Local Nusselt number ratio distributions for 60 deg parallel and crossed ribs

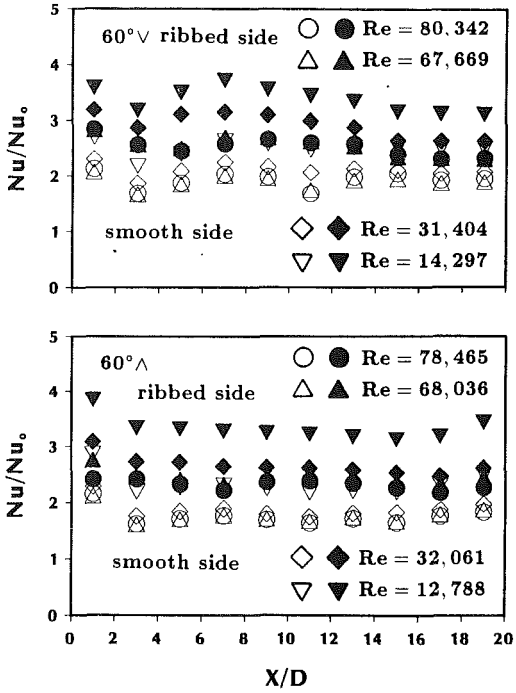

Fig. 5 Local Nusselt number ratio distributions for 60 deg ∨-shaped and ∧-shaped ribs

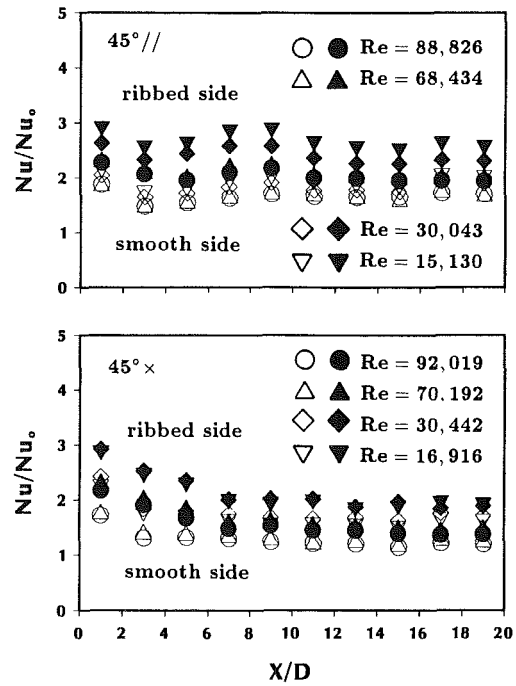

Fig. 6 Local Nusselt number ratio distributions for 45 deg parallel and crossed ribs

maximum deviation of the Nusselt number from the McAdams/Dittus-Boelter correlation is 10 percent.

Figures 3–7 present the test results for the ribbed channel. These figures represent the ribbed-side Nusselt number ratio distributions and the corresponding smooth-side Nusselt number ratio distributions for 90, 60, and 45 deg ribs. It was found from the experimental raw data that the local temperatures on two opposite walls are about the same at the same axial distance from the inlet of the heated channel. Therefore, the local ribbed-side Nusselt number in these figures is the average value of the two opposite ribbed-wall Nusselt numbers at a given location, and the local smooth-side Nusselt number is the average value of the two opposite smooth-wall Nusselt numbers at a given location. The results show that for each case the local Nusselt number ratio decreases with increasing Reynolds number. For the cases of 90 deg rib, 60 deg crossed rib, 60 deg ∧-shaped rib, 45 deg crossed rib, and 45 deg ∧-shaped rib, the Nusselt number ratio (ribbed-side or smooth-side) decreases while increasing the axial distance, and reaches a constant value in the fully developed region at a given flow Reynolds number. However, for the cases of 60 deg parallel rib, 60 deg ∨-shaped rib, 45 deg parallel rib, and 45 deg ∨-shaped rib, the Nusselt

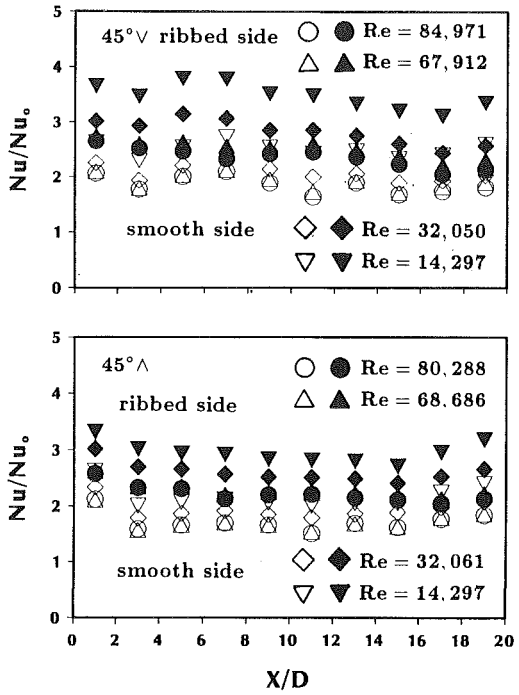

Fig. 7 Local Nusselt number ratio distributions for 45 deg ∨-shaped and ∧-shaped ribs

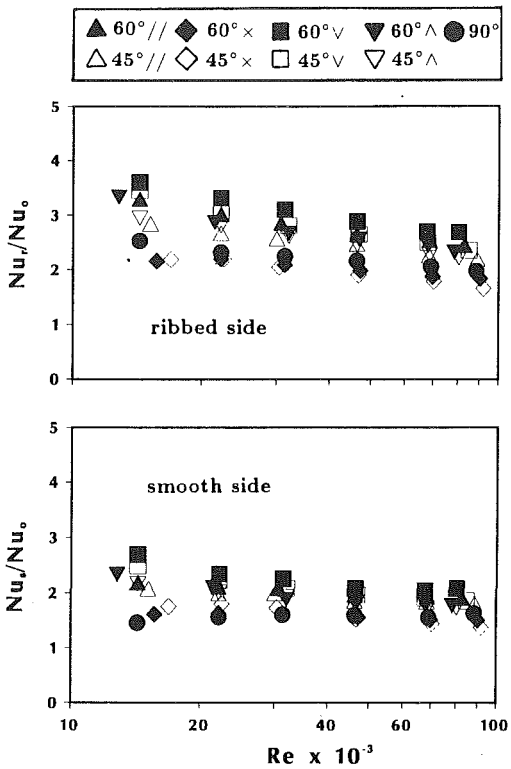

Fig. 8 Average Nusselt number ratio versus Reynolds number for the nine rib configurations studied

number ratio (ribbed-side or smooth-side) decreases to reach a minimum value of X/D around 4 and then increases to reach a maximum value at X/D around 9 for the 60 deg parallel rib, at X/D around 8 or 7 for the 60 deg ∨-shaped rib or 45 deg parallel and ∨-shaped ribs, due to the secondary flow induced by the rib orientation. After the maximum value the Nusselt number ratio decreases again in the farther downstream region.

The lower Nu/Nu$_o$ ratios for the crossed rib orientation may be caused by the cancellation of the secondary flow induced by the rib axes on the two opposite walls of the square channel. The lower heat transfer coefficients obtained with crossed ribs as opposed to parallel ribs are similar to those reported by Metzger and Vedula (1987) in a straight triangular cross-sectional channel with a transient heat transfer method (paint-coated surface), and also reported in the previous studies (Han et al., 1989; Han and Zhang, 1991). It is conjectured that the flow pattern generated by the 60/45 deg crossed ribs contains a single cell of secondary flow whereas the 60/45 deg parallel ribs induce a pair of counterrotating cells. The similar secondary flow patterns for 60/45 deg ∨-shaped and for 60/45 deg ∧-shaped ribs may occur in this study. The 60/45 deg ∨-shaped ribs may generate two pairs of counterrotating cells along each divergent axis of ∨-shaped ribs and cause a higher heat transfer. On the other hand, the two pairs of counterrotating cells may cancel each other because of the convergent axis of the ∧-shaped ribs (i.e., the reverse ∨-shaped ribs) and cause a higher pressure loss (see Fig. 9) and lower heat transfer. These secondary flow effects diminish at the downstream region of the flow channel.

Channel-Averaged Heat Transfer and Pressure Drop Data. Figure 8 shows the Nusselt number ratio (ribbed-side or smooth-side) versus Reynolds number for 90, 60, and 45 deg ribs. The ribbed-side Nusselt number ratio is the average value of the entire ribbed-wall Nusselt number from the channel inlet to the outlet. Similarly, the smooth-side Nusselt number ratio is the average value of the entire smooth-wall Nusselt number from the inlet to the outlet of the heated channel.

The results show that the 60 deg ∨-shaped rib provides higher Nusselt number ratios than those of the 60 deg parallel rib, 60 deg ∧-shaped rib, 90 deg rib, and 60 deg crossed rib. The same trend shown in Fig. 8 suggests that the 45 deg ∨-shaped rib gives higher Nusselt number ratios than 45 deg parallel, 45 deg ∧-shaped, and 45 deg crossed ribs. The 60 or 45 ∨-shaped ribs provide higher heat transfer coefficients on both the ribbed-side and smooth-side walls than other rib configurations. This is because the forward ∨-shaped ribs induce a favorable secondary flow mixing on the ribbed-side wall and toward both smooth-side walls. Note that the 60 and 45 deg crossed ribs give the lowest heat transfer coefficients, even slightly lower than the 90 deg rib. The 60 deg (or 45 deg) parallel and ∧-shaped ribs have about the same heat transfer coefficients, and both are lower than the corresponding ∨-shape rib but higher than the corresponding crossed and 90 deg rib. Figure 8 also shows that the Nusselt number ratio decreases slightly with increasing Reynolds numbers.

Figure 9 compares the friction factor ratio between 90, 60, and 45 deg ribs. The pressure drops across the test channel are measured at the unheated flow conditions. The results show that the 60 deg (or 45 deg) ∧-shaped rib provides higher friction factor ratios than those of 60 deg (or 45 deg) ∨-shaped rib, 60 deg (or 45 deg) parallel rib, 90 deg rib, and 60 deg (or 45 deg) crossed rib. The 60 deg (or 45 deg) ∧-shaped rib gives the highest pressure drop due to flow toward the mid-line of the ribbed-side wall induced by the reverse ∨ rib (i.e., the ∧-shaped rib). Note that the 60 deg (or 45 deg) crossed rib gives both the lowest heat transfer coefficients and the smallest pressure drops compared to other rib configurations. Figure 9 also shows that the friction factor ratio increases with increasing Reynolds numbers.

Heat Transfer Performance Comparison. Figure 10 represents the Nusselt number ratio (ribbed-side and smooth-side) versus the friction factor ratio for 90, 60, and 45 deg ribs over a range of studied Reynolds numbers. The results show the Nusselt number ratio decreases but the friction factor increases with increasing Reynolds number as discussed in the previous section. This means that the heat transfer performance decreases with increasing Reynolds number. The results also show

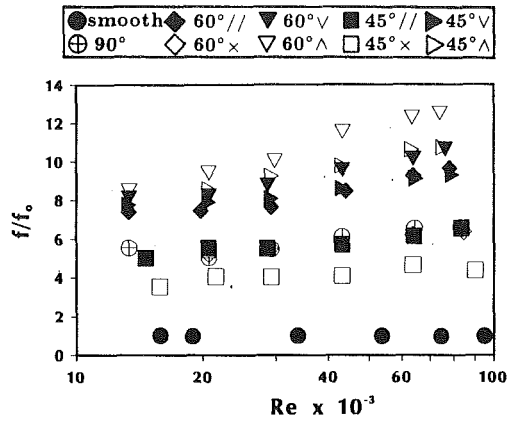

Fig. 9 Average friction factor ratio versus Reynolds number for the nine rib configurations studied

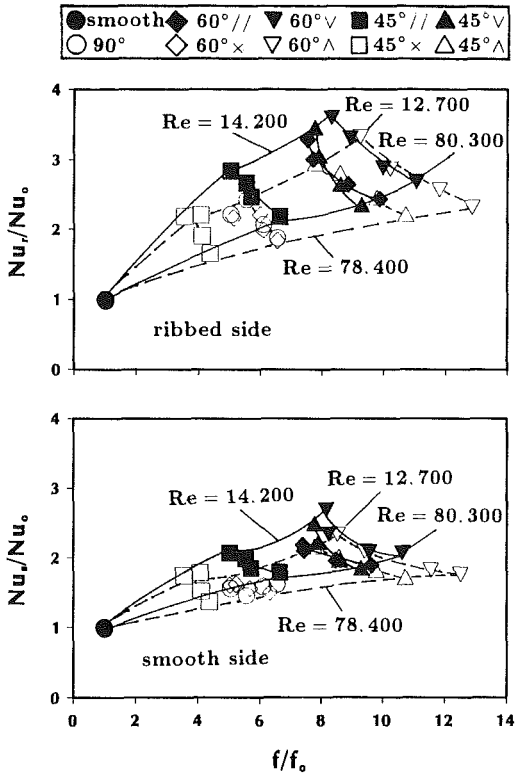

Fig. 10 Average Nusselt number ratio versus average friction factor ratio for the nine rib configurations studied

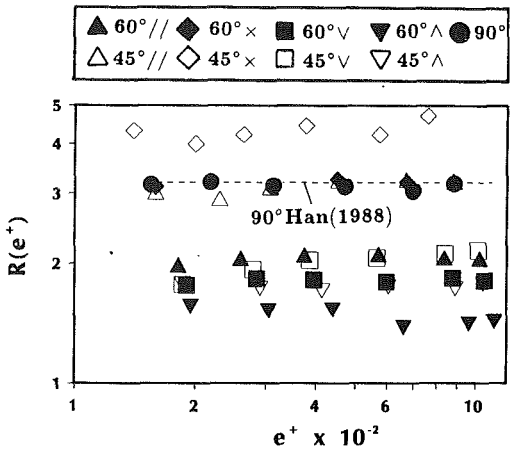

Fig. 11 Friction factor correlation

Table 2 Coefficients and exponents for friction and heat transfer roughness functions

$R(e^+) = a(e^+)^b$ $G(e^+) = a(e^+)^b$ $\bar{G}(e^+) = a(e^+)^b$

Case	a	b	a	b	a	b
90°	3.18	0.0	3.97	0.28	4.86	0.28
60°//	2.05	0.0	1.52	0.41	2.41	0.36
60°X	3.18	0.0	3.24	0.32	4.57	0.28
60°∨	1.72	0.0	1.35	0.42	1.76	0.40
60°∧	1.42	0.0	1.59	0.43	2.12	0.41
45°//	3.05	0.0	2.07	0.36	3.01	0.32
45°X	4.40	0.0	2.11	0.37	2.43	0.37
45°∨	2.04	0.0	1.36	0.43	1.93	0.40
45°∧	1.70	0.0	1.83	0.41	2.49	0.38

that, in general, the Nusselt number ratio increases with increasing friction factor ratio. The 60 deg forward ∨-shaped rib provides 2.7 to 3.5 times the ribbed-side heat transfer enhancement with 8 to 11 times the pressure drop penalty. The 60 deg crossed rib gives 1.8 to 2.2 times the ribbed-side heat transfer augmentation with 5 to 7 times the pressure drop increment. The 90 deg rib gives about the same heat transfer augmentation as the 60 deg crossed rib. The 60 deg ∧-shaped rib provides slightly lower heat transfer but much greater pressure drop than the 60 deg ∨-shaped rib. The 60 deg parallel rib gives slightly lower heat transfer than the 60 deg ∨-shaped rib with about the same amount of pressure drop penalty. The ribbed-side heat transfer enhances 2.3 to 3.5 times while the corresponding pressure drop increases 7.8 to 9.4 times for the case of the 45 deg ∨-shaped rib. The corresponding values are 1.7 to 2.2 times and 3.5 to 4.5 times, respectively, for the case of the 45 deg crossed rib. It can be concluded that the 60 deg ∨-shaped rib gives the best performance, the 60 deg parallel rib is second, while the 60 deg ∧-shaped, 90 deg rib, and the 60 deg crossed rib are about the same. The performance of the 45 deg ∨-shaped rib is about the same as the 45 deg parallel rib, which is better than those of 45 deg crossed rib, 45 deg ∧-shaped rib, and 90 deg rib.

Heat Transfer and Friction Correlations. Figure 11 shows the friction roughness function (R) versus the roughness Reynolds number (e^+) for 90, 60, and 45 deg ribs for a range of studied Reynolds numbers. The roughness functions for 90 deg rib, 60 deg crossed rib, and 45 deg parallel rib are about the same and checked with the previous correlation that was developed for the 90 deg rib (Han, 1988). The 60 deg ∧-shaped rib has the lowest roughness function, which implies the highest pressure drop. The 45 deg crossed rib has the highest roughness function, which means the lowest pressure drop when compared to other rib configurations. The roughness function is almost independent of the roughness Reynolds number for all rib configurations studied. Table 2 gives the coefficients and exponents in this function for all cases studied. For a given rib configuration and flow Reynolds number, the friction factor can be predicted from the roughness function (R) read from Table 2.

Figure 12 shows the heat transfer roughness function (G) versus the roughness Reynolds number (e^+) for 90, 60, and 45 deg ribs for a range of Reynolds number studied. Similar plots for the average heat transfer roughness function ($\bar{G}$), based on the average value of the ribbed-side and smooth-side heat transfer coefficients ($\bar{St}$), are also shown in Fig. 12. The

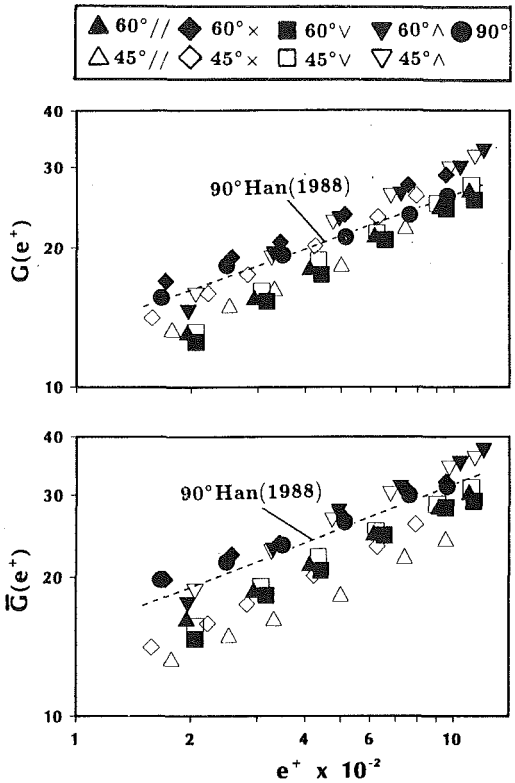

Fig. 12 Heat transfer correlation

heat transfer roughness function (G or $\overline{G}$) increases with increasing roughness Reynolds number (e^+) for all studied rib configurations. The heat transfer roughness functions for 90 deg rib are about the same as the previous correlation, which is developed for the 90 deg rib (Han, 1988). The 60 deg ∨-shaped rib has the lowest G value, which means the highest heat transfer. The 60 deg parallel rib has the next lower G value to the 60 deg ∨-shaped rib. The 45 deg ∨-shape rib and the 45 deg parallel rib have about the same lower G value, which means the heat transfer coefficients are higher. Table 2 gives the coefficients and exponents in this function for all cases studied. The slopes of G (or $\overline{G}$) versus e^+ for 60 and 45 deg, crossed, parallel, and ∨-shaped ribs are higher than the 90 deg rib. For a given rib configuration and flow Reynolds number, the Stanton number can be predicted from the heat transfer roughness function (G or $\overline{G}$) and roughness function (R) read from Table 2.

Concluding Remarks

Local heat transfer and pressure drop measurements have been performed in straight square channels with parallel, crossed, and ∨-shaped rib turbulators for Reynolds numbers from 15,000 to 90,000. The main findings of the study are given below.

1 For 90, 60, or 45 deg crossed ribs, and for 60 or 45 deg ∧-shaped ribs, the Nusselt number ratio decreases by increasing the axial distance, and reaches a constant value several ribs from the channel entrance. For 60 or 45 deg parallel ribs and for 60 or 45 deg ∨-shaped ribs, however, the Nusselt number ratio decreases to a minimum and then increases to a maximum value downstream due to favorable secondary flow induced by rib orientation.

2 For a range of studied Reynolds numbers, the 60 deg (or 45 deg) ∨-shaped rib gives higher heat transfer augmentation than other rib configurations while the 60 deg (or 45 deg) ∧-shaped rib produces the largest pressure drop. The 60 deg (or 45 deg) crossed rib gives the lowest heat transfer enhancement and the smallest pressure drop penalty.

3 The 60 deg ∨-shaped rib provides better heat transfer performance than the 60 deg parallel rib and subsequently better than the 60 deg ∧-shaped, and 90 and 60 deg crossed ribs, which have about the same performance. The 45 deg ∨-shaped rib has the same performance as the 45 deg parallel rib and is sequentially better than the 45 deg ∧-shaped rib, 45 deg crossed rib, and 90 deg rib.

4 The 60/45 deg ∨-shaped ribs perform better than the 60/45 deg parallel ribs. Both are recommended for turbine cooling design. The 60/45 deg ∧-shaped ribs, the 60/45 deg crossed ribs, and the 90 deg ribs are not recommended. The heat transfer performance decreases with increasing Reynolds number.

5 The semi-empirical correlations of the friction factor and Stanton number are developed for nine rib configurations, which can be used for turbine cooling design.

Acknowledgments

The investigation was supported by the General Electric Company.

References

Burggraf, F., 1970, "Experimental Heat Transfer and Pressure Drop With Two-Dimensional Turbulence Promoter Applied to Two Opposite Walls of a Square Tube," in: *Augmentation of Convective Heat and Mass Transfer*, A. E. Bergles and R. L. Webb, eds., ASME, New York, pp. 70–79.

Chandra, P. R., Han, J. C., and Lau, S. C., 1988, "Effect of Rib Angle on Local Heat/Mass Transfer Distribution in a Two-Pass Rib Roughened Channel," ASME *Journal of Turbomachinery*, Vol. 110, pp. 233–241.

Chandra, P. R., and Han, J. C., 1989, "Pressure Drop and Mass Transfer in Two-Pass Ribbed Channels," AIAA *Journal of Thermophysics and Heat Transfer*, Vol. 3, No. 3, pp. 315–320.

Han, J. C., 1984, "Heat Transfer and Friction in Channels With Two Opposite Rib-Roughened Walls," ASME JOURNAL OF HEAT TRANSFER, Vol. 106, pp. 774–781.

Han, J. C., Park, J. S., and Lei, C. K., 1985, "Heat Transfer Enhancement in Channels With Turbulence Promoters," ASME *Journal of Engineering for Gas Turbines and Powers*, Vol. 107, pp. 629–635.

Han, J. C., 1988, "Heat Transfer and Friction Characteristics in Rectangular Channels With Rib Turbulators," ASME JOURNAL OF HEAT TRANSFER, Vol. 110, No. 2, pp. 321–328.

Han, J. C., Chandra, P. R., and Lau, S. C., 1988, "Local Heat/Mass Transfer Distributions Around Sharp 180° Turns in Two-Pass Smooth and Rib-Roughened Channels," ASME JOURNAL OF HEAT TRANSFER, Vol. 110, No. 1, pp. 91–98.

Han, J. C., and Park, J. S., 1988, "Developing Heat Transfer in Rectangular Channels With Rib Turbulators," *International Journal of Heat and Mass Transfer*, Vol. 31, No. 1, pp. 183–195.

Han, J. C., Ou, S., Park, J. S., and Lei, C. K., 1989, "Augmented Heat Transfer in Rectangular Channels of Narrow Aspect Ratios With Rib Turbulators," *International Journal of Heat and Mass Transfer*, Vol. 32, No. 9, pp. 1619–1630.

Han, J. C., and Zhang, P., 1989, "Pressure Loss Distribution in Three-Pass Rectangular Channels With Rib Turbulators," ASME *Journal of Turbomachinery*, Vol. 111, pp. 515–521.

Han, J. C., and Zhang, P., 1991, "Effect of Rib-Angle Orientation on Local Mass Transfer Distribution in a Three-Pass Rib-Roughened Channel," ASME *Journal of Turbomachinery*, Vol. 113, pp. 123–130.

Kline, S. J., and McClintock, F. A., 1953, "Describing Uncertainties in Single-Sample Experiments," *Mechanical Engineering*, Vol. 75, pp. 3–8.

Metzger, D. E., and Sahm, M. K., 1986, "Heat Transfer Around Sharp 180° Turns in Smooth Rectangular Channels," ASME JOURNAL OF HEAT TRANSFER, Vol. 108, pp. 500–506.

Metzger, D. E., and Vedula, R. P., 1987, "Heat Transfer in Triangular Channels With Angled Roughness Ribs on Two Walls," *Experimental Heat Transfer*, Vol. 1, pp. 31–44.

Heat Transfer and Turbulent Flow Characteristics of Isolated Three-Dimensional Protrusions in Channels

P. T. Roeller

J. Stevens

B. W. Webb

Heat Transfer Laboratory,
Department of Mechanical Engineering,
Brigham Young University,
Provo, UT 84602

The flow structure and average heat transfer characteristics of single, isolated three-dimensional protrusions in a flow channel have been investigated experimentally. This configuration has relevance in the electronics industry. The study was designed to identify the influence of the three-dimensional flow around a heated protrusion on its average heat transfer. Heated protrusions varying in width between 0.12 and 1.0 channel widths for a fixed protrusion height and streamwise length were studied in the channel Reynolds number range $500 \leq Re \leq 10{,}000$. The channel wall spacing was also varied parametrically between 1.25 and 2.5 streamwise protrusion lengths. The study included both average heat transfer measurements, and detailed local velocity and turbulent flow structure measurements made using laser-Doppler velocimetry. The experimental results show that the Nusselt number increases with both decreasing channel wall spacing and decreasing protrusion width. The increase in heat transfer with decreasing wall spacing is explained by the accelerated flow due to the protrusion-obstructed channel. Increasing Nusselt number with decreasing protrusion width is a result of increased three-dimensional flow and associated turbulent mixing. Both of these flow-related phenomena are illustrated with local mean velocity and turbulence intensity measurements. The presence of recirculation zones both upstream and downstream of the module is revealed. The flow acceleration around the heated protrusions, and three dimensionality of the flow and heat transfer are competing mechanisms; the higher heat transfer due to flow acceleration around the protrusions for larger protrusions goes counter to the trend for higher heat transfer due to increased three-dimensional flow and transport for smaller protrusions. A Nusselt number correlation is developed as a function of channel Reynolds number and protrusion and channel geometric parameters, which describes the tradeoffs discussed.

Introduction

The increasing miniaturization of electronic components and resultant rise in heat flux at the chip level has motivated research aimed at improved understanding of the fundamentals of heat transfer in discrete heating situations. The intimate coupling between the complex flow structures and convective heat transfer in electronics packages is not yet fully understood. This is particularly true of channel flows with heated protrusions. The purpose of this study was to identify the fundamental factors influencing the convective transport from an isolated protrusion of variable dimensions in a channel—a configuration prototypical of many fan-cooled electronic systems. The study involves characterization of both the turbulent flow structure around the protrusion and the convective heat transfer.

Heat transfer characteristics of discretely heated protrusions in forced convection situations have been treated to some extent in the literature. Heat transfer from two-dimensional protrusions in channels was studied experimentally (Lehmann and Wirtz, 1984, 1985; Biber and Sammakia, 1986; Chang et al., 1987; McEntire and Webb, 1990). The strong influence of the geometric parameters was reflected in the heat transfer correlations, and underlines the importance of the flow structure on the convective transport. Three-dimensional arrays of heated protrusions have also been investigated (Sparrow et al., 1982; Moffat and Arvizu, 1982; Moffat et al., 1985). The effect of upstream protrusions on the transport characteristics of heated protrusions is particularly evident.

The problem of forced convection from discretely heated components has also received attention from the analytical perspective in laminar two-dimensional (Davalath and Bayazitoglu, 1987), turbulent two-dimensional (Knight and Crawford, 1987, 1988), and laminar three-dimensional (Asako and Faghri, 1987) geometries using finite difference techniques. Again, the intimate coupling between the flow patterns and the heat transfer was observed.

Despite the relatively broad coverage of the subject of heat transfer from protrusions in channel flows summarized in the foregoing, the fundamental turbulent flow structure and associated heat transfer from three-dimensional protrusions in channels are not yet fully understood. This paper reports on an experimental study designed to elucidate the mechanisms of flow and heat transfer in such a system. In particular, the geometric dimensions of the protrusion that influence the three dimensionality of the flow are explored. Detailed experimental heat transfer and velocity data to be presented are also critical in the evaluation of mathematical models used in the design of electronics packages. Detailed local experimental data are particularly critical for the development and evaluation of theoretical models in the transitional Reynolds number regime, where forced air-cooled electronic equipment is often designed to operate.

Contributed by the Heat Transfer Division for publication in the JOURNAL OF HEAT TRANSFER. Manuscript received by the Heat Transfer Division July 16, 1990; revision received November 28, 1990. Keywords: Electronic Equipment, Flow Separation, Forced Convection.

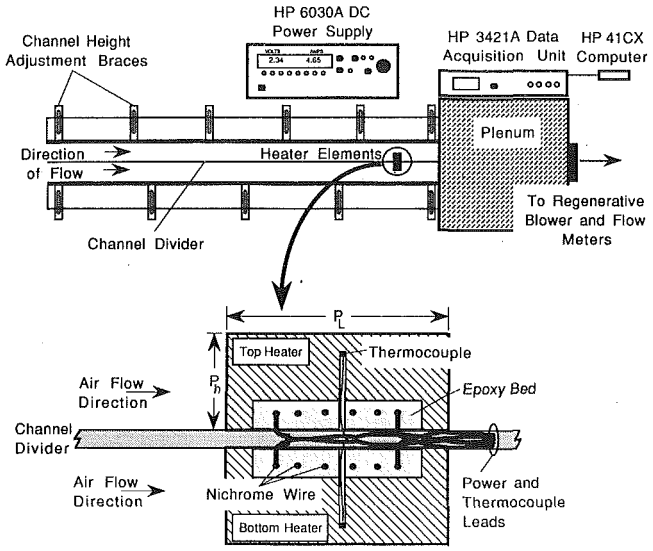

Fig. 1 Schematic of experimental apparatus and heater modules

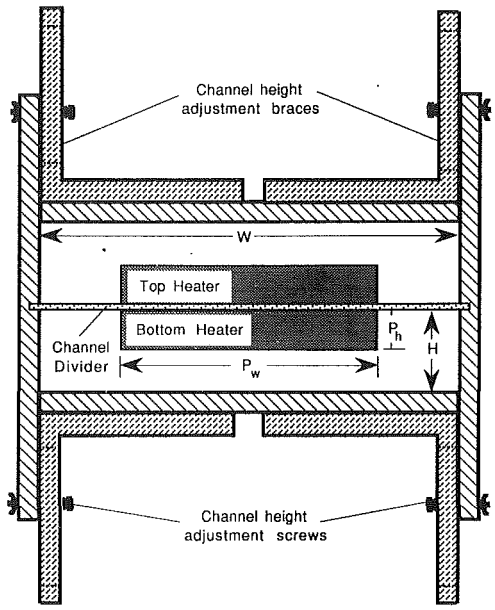

Fig. 2 End view of the experimental apparatus

Experimental Apparatus and Instrumentation

A channel and heater assembly were designed and constructed to permit velocity and heat transfer measurements over a broad range of experimental parameters. The channel walls were constructed of plexiglass to provide optical access in the test section and entrance length. The channel cross section was divided symmetrically in half by a thin divider, forming identical top and bottom channels, as shown in Fig. 1. Each of the two channels was equipped with an instrumented heater module for measurement. The purpose of the thermally symmetric channel design was to minimize conjugate heat transfer in the channel floor on which the heaters were mounted. The channel divider was constructed from a 2.2-mm-thick internally ribbed cardboard sheet. The cardboard sheet was chosen because of its rigidity and low thermal conductivity. Only absolutely flat divider sections were used. Additionally, the grooves into which the cardboard sheet were inserted were milled such that a tight fit existed, and no vibration of the divider was observed during the experiments. The channel was designed to have variable height capability. Four channel heights were investigated, $H = 15$, 20, 24, and 30 mm, with a fixed channel width of $W = 155$ mm. The channel height was adjusted by means of movable channel walls, as shown in the end view of Fig. 2. Based on the relationship for the entrance length corresponding to fully developed flow (Fox and McDonald, 1978), the channel was constructed to be 1520 mm in overall length, allowing approximately 200 mm between the heated protrusion and the channel exit.

As explained in the foregoing, high thermal conductivity modules, heated electrically at the same rate, were placed on opposite sides of the channel divider. A cross-sectional detail of the heater blocks is shown in the lower panel of Fig. 1. A small coil of nichrome wire, which was connected to electrical leads, was designed to fit inside a section milled in each module. This coil provided the electrical resistance needed to heat the module ohmically. Small voltage sensing leads were attached to the nichrome coil at the junction with the power leads. These were used to measure the voltage drop across each coil during each experiment. With the thermocouples installed and the resistor set in place with epoxy, an instrumented heater module was then attached to the opposite sides (top and bottom) of a section of the cardboard divider material. The thermocouple, power supply, and voltage sensing leads were drawn out of the channel toward the downstream plenum between the ribs on the interior of the cardboard channel divider. Thus, there was no disturbance in the channel cross section due to instrumentation wires. This section of cardboard with attached modules was designed to slide easily horizontally in and out of the channel test section and to fit snugly with the existing

Nomenclature

A^* = fraction of channel cross section open to flow at the protrusion, Eq. (2)
A_s = total convective surface area of the protrusion = $2P_hP_w + P_LP_w + 2P_hP_L$; the $2P_hP_L$ term vanishes for the two dimensional heaters
D_H = hydraulic diameter of the channel upstream of the test section
$\bar{h}$ = average heat transfer coefficient
H = channel height, Fig. 2
k = thermal conductivity
$\overline{\mathrm{Nu}}$ = average Nusselt number = $\bar{h}P_L/k$
P_h = protrusion height, Fig. 2
P_L = streamwise length of the protrusions, Fig. 1
P_w = protrusion width, Fig. 2
q = convective heat transfer from the protrusion
Re = channel Reynolds number = UD_H/ν
$\overline{T}_s$ = average heater module temperature
T_∞ = free-stream temperature
$\bar{u}$ = local average streamwise velocity
u' = local rms streamwise velocity fluctuation = $[\Sigma(\bar{u} - u_i)^2/N]^{1/2}$
U = average channel velocity upstream of the protrusion
W = channel width, Fig. 2
X = dimensionless streamwise coordinate referenced to the leading edge of the protrusion = x/P_L
Y = dimensionless vertical distance from the channel floor = y/H
Z = dimensionless spanwise coordinate referenced to spanwise center of the channel = $z/(W/2)$
ν = kinematic viscosity

length of divider in the upstream portion of the channel. Four of these sections with the different module protrusion widths were used to establish trends in the heat transfer coefficient as it varied with the module dimensions. Three pair of matching three-dimensional modules with protrusion widths $P_w = 19$ mm, 38 mm, and 75 mm with fixed protrusion height, $P_h = 12$ mm, and protrusion streamwise length, $P_L = 12$ mm, were used in the experimental study. A pair of matching two-dimensional blocks (spanning the full 155-mm width of the channel) with the same 12-mm protrusion height and streamwise length was also studied to contrast the two and three dimensionality of the flow and heat transfer.

Copper/constantan thermocouples were embedded in both top and bottom heater modules to monitor temperature gradients, if any, and to measure the heated module temperature needed in the calculation of the average heat transfer coefficient. The number of thermocouples used varied with protrusion width; two, three, four, and five thermocouples were used in the $P_w = 19$, 38, 75, and 155 mm modules, respectively. The variation in the temperature measurements on the module interior was never more than 6 percent of the difference between average module and free-stream temperature, $\overline{T}_s - T_\infty$. Additionally, the variation in $\overline{\mathrm{Nu}}$ between top and bottom heaters was always less than 4.0 percent, with the average difference being less than 2 percent. The protrusions were constructed of 6061-T6 aluminum alloy ($k = 172$ W/mK). Because the conduction resistance of aluminum is so much smaller than the convection resistance, the modules were considered isothermal; the block Biot number was determined to be less than 0.003, indicating negligible temperature gradients in the solid blocks. The exposed aluminum surfaces were highly polished to reduce the heat transfer by radiation. The emissivity was measured using an infrared radiometer to be approximately 0.05, which is consistent with published radiative property data for polished aluminum (Incropera and DeWitt, 1990). The maximum and average radiation heat loss for all experiments were 1.4 and 0.5 percent, respectively, of the total heat transfer for $\mathrm{Re} > 2000$. Losses were higher at lower Reynolds numbers, but these low-Re data were not included in the final heat transfer correlation. The radiation losses were therefore neglected.

Because of the dual channel symmetry, each heater module acted as a guard heater for the one opposite. However, an analysis of the conjugate heat transfer in the channel divider revealed that the conduction loss was nonnegligible. To estimate the heat loss, the channel divider was approximated as an annular fin whose base temperature was equal to the heated module temperature. The convective heat transfer coefficient prevailing over the "fin" surface was estimated to be 70 percent of the value measured for the heated protrusion. Such an approximate analysis is likely to overestimate the conduction loss. It was found that for the range of Reynolds number experiments for which the heat transfer was correlated ($\mathrm{Re} \geq 2000$), the maximum conduction loss was 6.9 percent of the total Ohmic dissipation. The average Nusselt numbers were corrected for this loss based on the results of the approximate analysis. A copper/constantan (Cu/Co) thermocouple was placed at the channel entrance to measure the ambient temperature (T_∞).

The room air was drawn into the channel entrance over the heated modules in the test section, into the plenum, and out through bypass flow meters to the regenerative blower, which was operated in suction mode. Three rotameters with different flow rate measurement ranges 14.2–70.8, 85.0–396.4, and 340.0–1529.1 1/m were used to meter the air flow rate. The flow meters have a calibrated accuracy of 5 percent. A thermocouple was placed at the entrance of the flow meters to measure the temperature necessary for corrected flow meter readings. Since the upper and lower channels were constructed to be symmetric in every way, it was assumed that the global and local flow characteristics of the upper and lower channels were identical. This is supported by the fact that the maximum difference between the average Nusselt number for the upper and lower heaters was only 4.0 percent in all of the experiments. Indeed, the average difference between upper and lower heated module Nusselt numbers was less than 2 percent. This is well within the experimental uncertainty in $\overline{\mathrm{Nu}}$ of 7.4 percent to be presented.

After the heat transfer data were collected, the channel was modified for measurement of the streamwise component of the local mean velocity and its fluctuating component using a laser-Doppler velocimeter (LDV). The laser-Doppler velocimetry study was carried out with a TSI Model 1980 LDV system operated in backscatter mode with Spectra-Physics Model 2016, 5 W laser. The ellipsoidal probe volume dimensions were 600 μm by 40 μm, given respectively as the major and minor axes of the ellipsoid. The direction of flow was resolved by using frequency shifting. Statistical data were based on a sample size of 8000 measurements, with a sampling frequency of approximately 1500 samples/s. A computer-controlled three-axis positioning table with a resolution of ± 0.1 mm in each axis was used to position the beam crossing in the channel flow at predetermined locations. Atomized water droplets generated by a Fairchild six-jet atomizer, which produced a mean droplet size of just under 1 μm (documented by the atomizer manufacturer), were used to seed the flow. The atomizer was placed at the channel entrance and the small water droplets were entrained into the channel with the incoming air. Velocity measurements were made without heating, since the flow was forced convection dominated. The cardboard channel divider was replaced with an aluminum divider to prevent warping when exposed to the atomized water. Exact replicas of the aluminum blocks used in the heat transfer portion of this study were machined and, as in the heat transfer portion, were attached to opposite sides of a section of the aluminum divider. Two of these sections were constructed. Replicas of the two-dimensional block ($P_w = W = 155$ mm) with the same 12-mm protrusion height were attached to the opposite sides of one of the sections, and replicas of the three-dimensional protrusion with the 38-mm protrusion width and 12-mm protrusion height were attached to the other section. The mean flow and turbulence structures were mapped for the two- and three-dimensional protrusions from these two sections at two Reynolds numbers for an intermediate channel height of $H = 20$ mm.

Experimental Uncertainty

An error analysis using the method of Kline and McClintock (1953) was performed to determine the uncertainty in the experimental data. The majority of the error in $\overline{\mathrm{Nu}}$ can be traced to the uncertainty in the convective heat transfer and temperature difference. The uncertainty in convective heat transfer is due largely to the simplified analysis for the conduction loss correction. Although the conduction loss through the channel divider can probably be determined only to within 20–25 percent accuracy, these losses are so small that the convective dissipation from the module is estimated accurate to 5 percent. The estimated error in the temperature difference is 0.5°C. Temperature differences ($\overline{T}_s - T_\infty$) ranged from a minimum of 11.7°C to a maximum of 76.4°C. The maximum uncertainty in ΔT was therefore 2.1 percent. The resulting maximum composite uncertainty in average Nusselt number is 7.4 percent.

The single largest contributor to uncertainty in the Reynolds number was the measurement of the volumetric flow rate. With the manufacturer-supplied calibration for the flow meters of 5 percent, an uncertainty in Reynolds number of 7.7 percent is estimated. This number includes an estimate of asymmetry in flow partitioning between the parallel channels in the experimental system (based on the average 2 percent difference

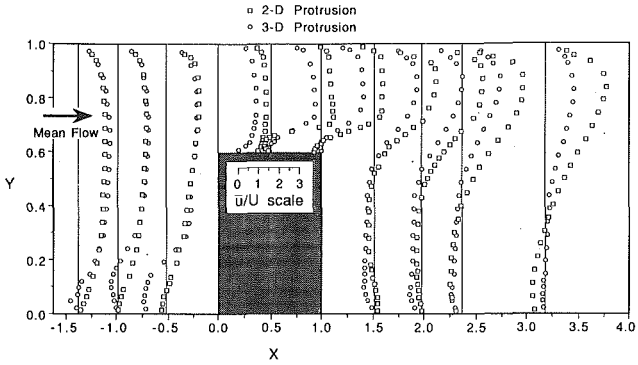

Fig. 3 Vertical profiles of the local streamwise mean velocity at the channel centerline ($Z=0$) at various streamwise locations for Re = 2300, $P_h/P_L=1.0$, $H/P_L=1.67$: two-dimensional protrusion, $P_w/W=1.0$; three-dimensional protrusion, $P_w/P_L=3.17$ ($P_w/W=0.25$); measurement profile locations: $X=-1.38$, -0.96, -0.54, 0.0, 0.5, 1.0, 1.54, 1.96, 2.38, and 3.21

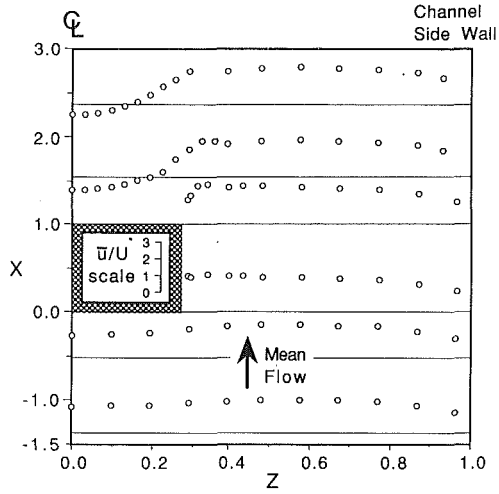

Fig. 4 Horizontal profiles of the local streamwise mean velocity at an elevation $y/P_h=0.5$, and at various streamwise locations for the three-dimensional protrusion, Re = 2300, $P_w/P_L=3.17$ ($P_w/W=0.25$), $P_h/P_L=1.0$, $H/P_L=1.67$; measurement profile locations: $X=-1.38$, -0.54, 0.0, 1.0, 1.54, 2.38

in Nusselt number for the top and bottom heaters). Laser velocimetry measurements were estimated to be accurate to 2.0 percent. The error in location of the LDV diagnostic volume relative to the channel wall is estimated at ± 0.15 mm.

Experimental Results

The parameters for the convective heat transfer from the protrusions were characterized in nondimensional form by the average Nusselt number and the channel Reynolds number. The streamwise length of the protrusion was chosen as the characteristic length in all dimensionless variables except the channel Reynolds number, which was based on the channel hydraulic diameter. Hence, the dimensionless channel height, protrusion height, and protrusion width are normalized as H/P_L, P_h/P_L, and P_w/P_L, respectively. To aid in visualizing the width of the protrusion relative to the total width of the channel, this parameter is also presented as a fraction of the channel width, P_w/W. Since P_L and W remained constant in all experiments, each value of P_w/W has a unique P_w/P_L counterpart. The experimental study included the effects of channel Reynolds numbers in the nominal range $500 \le \mathrm{Re} \le 10{,}000$, protrusion widths varying between $1.58 \le P_w/P_L \le 12.9$ ($0.12 \le P_w/W \le 1.0$), and channel height in the range $1.25 \le H/P_L \le 2.5$. The protrusion height was fixed at $P_h/P_L = 1.0$. In all, 136 experiments were run to assess the effect of the various operating parameters on the average heat transfer. The average Nusselt number was defined as $\overline{\mathrm{Nu}} = \bar{h}P_L/k$, where the average heat transfer coefficient was determined from the corrected heat transfer from the heater module, q, the average heater module temperature, $\overline{T}_s$, and the total convective surface area of the heater, as $\bar{h} = q/A_s(\overline{T}_s - T_\infty)$. Note that the surface area of the two-dimensional protrusions does not include the protrusion spanwise end areas. The results will be presented first as a discussion of the flow structure drawn from the LDV measurements. The heat transfer from the protrusions will then be presented.

Flow Structure. Figure 3 illustrates vertical profiles of the streamwise velocity component normalized by the channel average velocity (upstream of the protrusion), $\bar{u}/U$, for the two-dimensional ($P_w/W = 1.0$) and three-dimensional ($P_w/W = 0.25$) protrusions for the experimental conditions $P_h/P_L = 1.0$, $H/P_L = 1.67$, and Re = 2300. These profiles were taken at the spanwise center of the channel, $Z=0$, at exact streamwise locations noted in the figure caption. The streamwise and vertical coordinates are defined as $X = x/P_L$, were x is referenced to the leading edge of the heater module, and $Y = y/H$, referenced from the channel floor. The scale for each cross-stream profile of the streamwise velocity component is shown inside the block representing the heated protrusion. The vertical lines corresponding to each velocity profile pair (two-dimensional and three-dimensional) serve as reference points, indicating the streamwise locations at which the velocity measurements were taken. Sidewall velocity effects were confined to less than 10 percent of the channel width (Roeller, 1989).

Figure 3 shows that the flow is significantly accelerated by the presence of the channel obstruction presented by both two- and three-dimensional protrusions. Mean velocities above the protrusion are observed to be somewhat higher for the two-dimensional than for the three-dimensional module. This is explained by the fact that in the three-dimensional configuration, the flow has a greater tendency to bypass the accelerated flow region on top by traveling around the sides of the protrusion, to be illustrated shortly. The increased flow velocity resulting from the channel obstruction will be shown to have a significant effect on the heat transfer.

The flow over both two-dimensional and three-dimensional modules separates at the top upstream corner as it accelerates over the protrusion. Although no negative velocities are seen along the module top at $X=0$, recirculation with reverse flow velocities as high as half the channel average are seen downstream (e.g., $X=0.5$). The vertical extent of this reverse flow zone above the protrusion is greater for the two-dimensional than for the three-dimensional protrusion. The separated flow does not reattach before reaching the downstream edge of either the two-dimensional or three-dimensional protrusion.

A small recirculation zone upstream of the heater module is evident for both two- and three-dimensional configurations. This reverse flow region extends a full protrusion length upstream for both conditions. A similar recirculation zone was observed in flow visualization photographs in a study of a significantly larger three-dimensional protrusion (Olsen et al., 1989), and was seen to influence the local heat transfer along the impingement face. Interestingly, the recirculation zone upstream of the module is significantly larger for the three-dimensional protrusion, with reverse flow velocities as high as three times those found at corresponding locations for the two-dimensional module. The flow approaching the protrusion must either accelerate over the top, or reverse back upstream and eventually merge with the mean flow in the two-dimensional system. The alternative in the three-dimensional system is to bypass around the protrusion sides, which will be illustrated shortly.

A recirculation zone on the downstream side of both the two-dimensional and three-dimensional protrusions extends

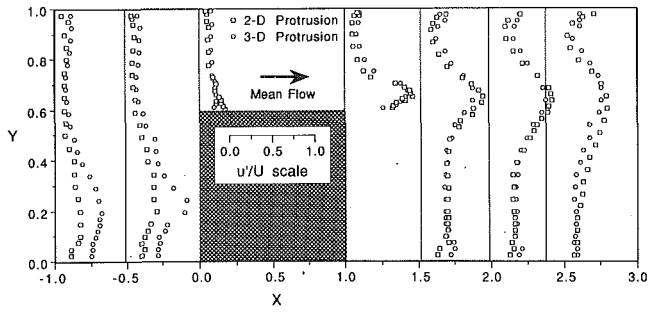

Fig. 5 Comparison of normalized rms velocity fluctuations at the channel centerline ($Z=0$) for the two-dimensional ($P_w/W=1.0$) and three-dimensional ($P_w/W=0.25$) protrusions corresponding to the mean velocity data of Fig. 3; measurement profile locations: $X=-0.96$, -0.54, 0.0, 1.0, 1.54, 1.96, 2.38

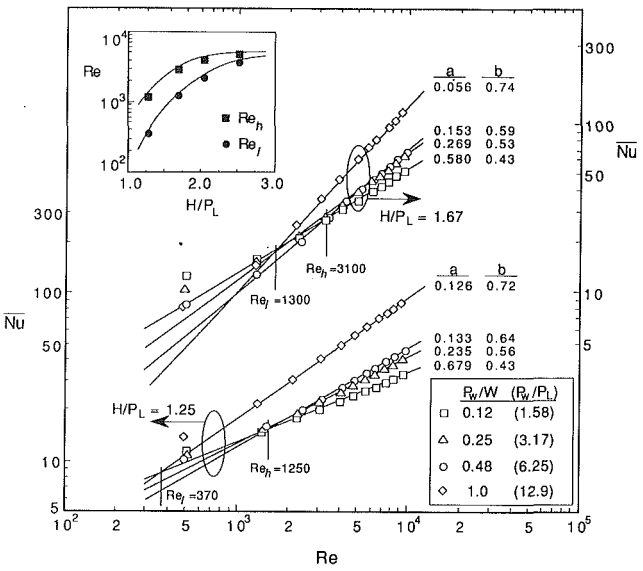

Fig. 6 Variation of the average Nusselt number with channel Reynolds number for all protrusion widths studied and two channel heights, $H/P_L=1.25$ and 1.67

well beyond $X=3$, as the reverse flow wraps around the protrusion in the conventional horseshoe structure. The recirculation zone occupies much of the height of the channel. The size of this leeward recirculation zone diminishes as one proceeds downstream. The recirculation zone is smaller for the three-dimensional configuration, although the reverse flow velocities immediately downstream of the protrusion are nearly twice that found for the two-dimensional module (see, for example, $X=1.54$). There exists a double eddy structure in the near-downstream region for the two-dimensional configuration, as evidenced by the velocity profile at $X=1.54$.

The flow around the sides of the three-dimensional protrusion at a vertical position halfway up the protrusion ($y/P_h=0.5$) for the conditions of Fig. 3 is illustrated in Fig. 4. The figure represents horizontal profiles of local mean streamwise velocity as viewed from the top of the channel. Again, the horizontal lines corresponding to each velocity profile indicate the streamwise measurement location. Velocity data are shown only from the channel centerline ($Z=0$) to the side wall ($Z=1$). Again, the increased flow velocities due to the presence of the protrusion are evident. Interestingly, the protrusion's influence is felt well upstream, evidenced by the normalized velocities nearly twice the channel average at $X=-1.38$ in the approximate region $0.3\le Z\le 0.9$. The accelerated bypass flow around the sides of the protrusion is also evident; the local mean flow is accelerated by approximately 25–30 percent over the channel average velocity at $X=0$ and 1. Also of interest is the recirculation on the leeward side of the three-dimensional module, which shrinks with increasing downstream position. Again, this is indicative of the horseshoe flow structure characteristic of flow around protrusions, and which strongly affects the heat transfer, particularly near the protrusion base and floor-mount (Eibeck and Eaton, 1987; Fisher and Eibeck, 1990; Goldstein et al., 1985; Goldstein and Karni, 1984; Ireland and Jones, 1986). The effects would be more evident for local heat transfer measurements in the present system. Although no separated flow is seen along the side of the protrusion at this elevation ($y/P_h=0.5$), such reverse flows were observed in other locations. However, these zones were much thinner than those observed along the top of the protrusion (thicknesses less than $0.04P_L$), with associated low negative velocities. The separated flow zone is clearly more pronounced along the top of the protrusion than along the sides.

A comparison of the turbulent fluctuation characteristics of the mean velocity corresponding to the data of Fig. 3 for the two- and three-dimensional protrusions is illustrated in Fig. 5. The two module configurations exhibit the same general turbulence behavior—higher fluctuations near the walls and in the shear layers separating the primary flow from the recirculation zones. In general, the fluctuations for the two- and three-dimensional protrusions are of the same order of magnitude. Notable exceptions are the location upstream of the module in the lower part of the channel, $Y\le 0.6$. The levels of turbulent fluctuation for the three-dimensional modules here are significantly higher; the rms fluctuation of the streamwise velocity component for the three-dimensional modules may be twice the value for the two-dimensional modules at the same location. The higher turbulent fluctuations for the three-dimensional protrusions may be explained in terms of strongly three-dimensional flow. Independent of the increased heat transfer area along the side faces parallel to the flow, the increased turbulence intensity for the three-dimensional module configuration is certain to provide more effective heat transport from the heated module.

Heat Transfer. Figure 6 illustrates the variation of the average Nusselt number with Reynolds number for the $H/P_L=1.25$ and 1.67 channel wall spacings, and for all heated module widths ranging from $P_w/W=0.12$ to 1.0 ($P_w/P_L=1.58$ to 12.9). These data are representative of the trends observed for the higher channel wall spacings ($H/P_L=2.0$ and 2.5) not shown. The figures show least-squares correlations of the experimental data for each protrusion width using a relationship of the form

$$\overline{\mathrm{Nu}}=a\ \mathrm{Re}^{b} \tag{1}$$

The maximum average deviation between correlation and experimental data in any one data set is 5 percent. The correlations are presented to illustrate more clearly the trends in the data and will be used to quantify what will be identified as competing effects in the heat transfer. Note that the experimental data for $\mathrm{Re}=500$ are not well represented by the correlation of the higher Reynolds number data. Laser-Doppler velocimetry measurements comparing hydrodynamic data reveal dramatically increased turbulence intensity for $\mathrm{Re}>2000$ over the $\mathrm{Re}=500$ case (Roeller, 1989). It is not surprising that the lower Reynolds number data, which apparently lie in the laminar flow regime, are governed by a different transport mechanism than the higher Re flow situation. For this reason the $\mathrm{Re}=500$ data were not included in the correlations shown.

Figure 6 shows that the heat transfer dependence on Reynolds number increases with protrusion width, illustrated by the higher slope of the correlation line. Indeed, the different slopes of the correlations for a given channel wall spacing result in an intersection in the $\overline{\mathrm{Nu}}$–Re lines for the different protrusion widths. The three-dimensional module correlations intersect at

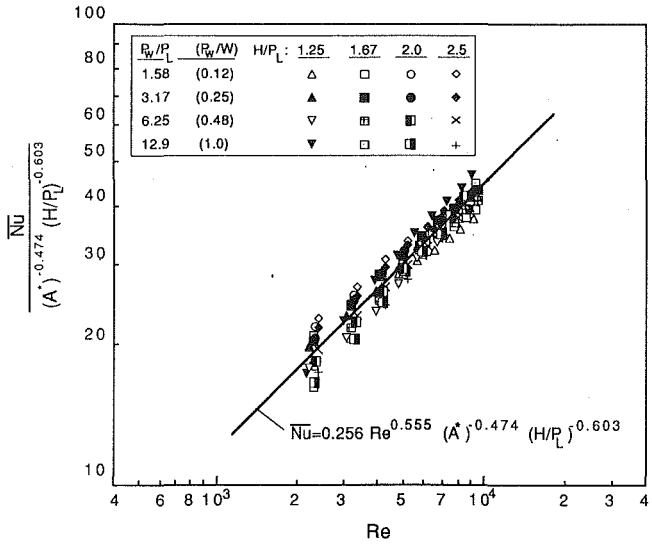

Fig. 7 Correlation of experimental average heat transfer data

approximately the same Reynolds number, while the two-dimensional data intersect the three-dimensional protrusion correlations at some lower value of Re. The values of Reynolds number at which these intersections occur are denoted Re_h and Re_l, respectively. Re_l is the Reynolds number at which the correlation for the two-dimensional protrusion ($P_w/W=1.0$) first intersects the correlations for the three-dimensional modules with increasing Re. Similarly, Re_h is the approximate Reynolds number at which the correlations for all three-dimensional modules intersect. At Reynolds numbers below these approximate intersection points, an increase in protrusion width results in a decrease in the average Nusselt number. The heat transfer is greater for the two-dimensional protrusion only at the Reynolds number above Re_l, and the narrowest three-dimensional protrusion is seen to have the greatest heat transfer at Re below Re_l. Conversely, at Re above the intersection points, an increase in P_w/W results in an *increase* in the average Nusselt number. This was perhaps more evident at the higher wall spacings reported elsewhere (Roeller et al., 1990; Roeller, 1989). While the selection of Re_l and Re_h is somewhat arbitrary, the trends are illustrated, and the observations relative to the relative magnitudes and slopes of the $\overline{Nu}$–Re lines for the different protrusion widths can be made for all channel heights, H/P_L. An increase in P_w/W results in a situation that is less influenced by three-dimensional flow and heat transfer; in the limit of $P_w/W=1.0$ the transport may be thought of as two dimensional (for sufficiently large channel aspect ratio). In this case, the flow is accelerated due to increased constriction of the channel. These observations suggest that the energy transport is governed by competing phenomena; wider protrusions and smaller channel wall spacings yield higher flow velocities at the protrusion, with associated intense convective cooling. On the other hand, narrower protrusions yield higher three dimensionality of the flow with its associated higher turbulence and three-dimensional transport. The accelerated flow and three-dimensional effects are thus competing.

The inset plot of Fig. 6 demonstrates graphically the change in the approximate intersection points, Re_l and Re_h, with the increase in channel wall spacing, H/P_L, for all experimental data. The data are joined by faired curves. The plot shows that as the channel wall spacing increases the intersection Reynolds numbers (Re_l and Re_h) increase as well. Therefore, for increasing H/P_L and at higher channel Reynolds numbers, accelerated flow effects dominate the heat transfer. The reverse is also true. As channel wall spacing decreases, the critical Reynolds number separating the region where three-dimensional effects dominate the heat transfer also decreases. The Re_l, Re_h–H/P_L data also illustrate that for increasing H/P_L, Re_l and Re_h appear to merge to a horizontal asymptote that is independent of channel wall spacing. This is intuitive, since for $H/P_L\rightarrow\infty$, the acceleration due to the constriction in the channel would vanish. It was also previously observed that the slope of the correlation lines for the two-dimensional modules approaches that of the three-dimensional heaters as H/P_L increases (Roeller et al., 1990). These two observations suggest that as the channel wall spacing increases, the competition between accelerated flow and three-dimensional effects becomes less important.

In summary, the results of Fig. 6 suggest that at low Reynolds number (below Re_l) and higher channel wall spacings, three-dimensional effects dominate the heat transfer (increased flow velocity effects are minimal). At high Reynolds number (above Re_h) and lower channel wall spacings, higher flow velocity dominates the heat transfer even for the three-dimensional heaters; the wider three-dimensional protrusions exhibit higher heat transfer. It should be clearly understood, however, that both effects, the increased mean velocity and the three dimensionality, play a role in the heat transfer in all regions, but one or the other appears to dominate in a given geometric and flow regime.

A composite correlation of the experimental heat transfer data for all channel wall spacings, protrusion widths, and channel Reynolds numbers was formulated. The fraction of channel cross section open to flow at the protrusion describes the acceleration due to the constriction. Hence, a parameter A^* is proposed for use in correlating the data. The parameter A^* represents the fraction of the channel cross section open to flow, and is defined as

$$A^*=1-(P_w/W)(P_h/H) \tag{2}$$

For a fixed channel width, W, the parameter A^* is seen to vary with protrusion width and height, and channel wall spacing. Values of A^* ranged from 0.20 for the two-dimensional protrusion and the smallest channel wall spacing, to 0.95 for the narrowest protrusion and highest channel wall spacing. The normalized channel height is also used in the correlation. All of the experimental data, with the exception of the laminar flow Re = 500 data, were then correlated with the equation

$$\overline{Nu}=0.256\ Re^{0.555}\ (A^*)^{-0.474}\ (H/P_L)^{-0.603} \tag{3}$$

The correlation is shown with all experimental data in Fig. 7. Equation (3) is valid for air flow with Reynolds numbers in the range $2000\le Re\le 10{,}000$, protrusion widths varying between $1.58\le P_w/P_L\le 12.9$ ($0.12\le P_w/W\le 1.0$), and channel wall spacings in the range $1.25\le H/P_L\le 2.5$. The empirical correlation predicts the experimental data with an average error of 6.0 percent and a maximum error of 20.3 percent. Although some grouping of the data is evident, the low error of Eq. (3) in representing the nearly 140 experiments attests to the utility and accuracy of the correlation. Previous correlations of heat transfer data for two-dimensional heated protrusions have exhibited a dependence on $Re^{0.6}$ for $700\le Re\le 3000$ and $0.5\le H/P_L\le 1.5$ (Lehmann and Wirtz, 1984), which is not significantly different from that found here. However, their study indicated only a weak dependence on channel wall spacing (less than 15 percent change in Nu over the range of H/P_L studied).

Conclusions

The flow structure and heat transfer characteristics of an isolated three-dimensional protrusion in channel flow have been investigated experimentally. The parameters varied experimentally included channel Reynolds number, protrusion width, and channel wall spacing. Laser-Doppler velocimetry was used to map detailed velocity and turbulent fluctuations around both two- and three-dimensional protrusions. The LDV

results show the presence of flow separation and strong recirculation zones, which vary in size and intensity for the two- and three-dimensional modules. The accelerated flow due to the obstruction of the channel by the protrusion is also apparent.

Average heat transfer results suggest that transport from the protrusions is dominated by competing phenomena—the increased flow velocity due to the contraction in the channel at the protrusions, and the three-dimensional effects as the air flow was forced around the finite width protrusions. Larger protrusion widths present greater channel obstruction with increased acceleration of the flow. The result is associated higher convective heat transfer. Conversely, smaller protrusion widths yield more intense three-dimensional transport and higher turbulence intensity, with resultant higher heat transfer. The average heat transfer for a given geometric and flow condition reflects the combined effects of both phenomena. A composite correlation was developed describing the experimental data as a function of channel Reynolds number, normalized channel wall spacing, and a parameter quantifying the fraction of channel cross section open to flow.

Acknowledgments

This work was supported in part by the U.S. National Science Foundation under grant No. CBT-8552493.

References

Asako, Y., and Faghri, M., 1987, "Three-Dimensional Heat Transfer and Fluid Flow Analysis of Arrays of Rectangular Blocks Encountered in Electronic Equipment," ASME Paper No. 87-HT-78.

Biber, C. R., and Sammakia, B. G., 1986, "Transport From Discrete Heated Components in a Turbulent Channel Flow," ASME Paper No. 86-WA/HT-68.

Chang, M. J., Shyu, R. J., and Fang, L. J., 1987, "An Experimental Study of Heat Transfer From Surface Mounted Components to a Channel Airflow," ASME Paper No. 87-HT-75.

Davalath, J., and Bayazitoglu, Y., 1987, "Forced Convection Cooling Across Rectangular Blocks," ASME JOURNAL OF HEAT TRANSFER, Vol. 109, pp. 321–328.

Eibeck, P. A., and Eaton, J. K., 1987, "Heat Transfer Effects on a Longitudinal Vortex Embedded in a Turbulent Boundary Layer," ASME JOURNAL OF HEAT TRANSFER, Vol. 109, pp. 16–24.

Fisher, E. M., and Eibeck, P. A., 1990, "The Influence of a Horseshoe Vortex on Local Convective Heat Transfer," ASME JOURNAL OF HEAT TRANSFER, Vol. 112, pp. 329–335.

Fox, R. W., and McDonald, A. T., 1978, *Introduction to Fluid Mechanics*, 2nd ed., Wiley, New York.

Goldstein, R. J., and Karni, J., 1984, "The Effects of a Wall Boundary Layer on Local Mass Transfer From a Cylinder in Crossflow," ASME JOURNAL OF HEAT TRANSFER, Vol. 106, pp. 260–267.

Goldstein, R. J., Chyu, M. K., and Hain, R. C., 1985, "Measurement of Local Mass Transfer on a Surface in the Region of the Base of a Protruding Cylinder With a Computer-Controlled Data Acquisition System," *International Journal of Heat and Mass Transfer*, Vol. 28, pp. 977–985.

Incropera, F. P., and DeWitt, D. P., 1990, *Introduction to Heat Transfer*, 2nd ed., Wiley, New York.

Ireland, P. T., and Jones, T. V., 1986, "Detailed Measurements of Heat Transfer on and Around a Pedestal in Fully Developed Passage Flow," *Proceedings of the 8th International Heat Transfer Conference*, Vol. 3, C. L. Tien et al., eds., Hemisphere Publishing Corp., Washington, DC, pp. 795–800.

Kline, S. J., and McClintock, F. A., 1953, "Describing Uncertainties in Single-Sample Experiments," *Mechanical Engineering*, Jan., pp. 3–12.

Knight, R. W., and Crawford, M. E., 1987, "Simulation of Convective Heat Transfer in Pipes and Channels With Periodically Varying Cross-Sectional Area," *Numerical Methods in Thermal Problems*, Vol. 5, R. W. Lewis, K. Mortan, and W. G. Habashi, eds., Pineridge Press, Swansea, pp. 512–523.

Knight, R. W., and Crawford, M. E., 1988, "Numerical Prediction of Turbulent Flow and Heat Transfer in Channels With Periodically Varying Cross-Sectional Area," in: *Proc. 1988 National Heat Transfer Conference*, Vol. 1, H. R. Jacobs, ed., ASME, New York, pp. 669–676.

Lehmann, G. L., and Wirtz, R. A., 1984, "Convection From Surface Mounted Repeating Ribs in a Channel Flow," ASME Paper No. 84-WA/HT-88.

Lehmann, G. L., and Wirtz, R. A., 1985, "The Effect of Variations in Streamwise Spacing and Length on Convection From Surface Mounted Rectangular Components," in: *Heat Transfer in Electronic Equipment—1985*, ASME, New York, pp. 39–47.

McEntire, A. B., and Webb, B. W., 1990, "Local Forced Convective Heat Transfer From Protruding and Flush-Mounted Two-Dimensional Discrete Heat Sources," *International Journal of Heat and Mass Transfer*, Vol. 33, pp. 1521–1533.

Moffat, R., and Arvizu, D. E., 1982, "The Use of Superposition in Calculating Cooling Requirements for Circuit Board Mounted Electronic Components," IEEE Paper No. CH 1781-4/82/0000-b133.

Moffat, R. J., Arvizu, D. E., and Ortega, A., 1985, "Cooling Electronic Components: Forced Convection Experiments With an Air-Cooled Array," in: *Heat Transfer in Electronic Equipment—1985*, ASME HTD-Vol. 48, pp. 17–27.

Olsen, J., Webb, B. W., and Queiroz, M., 1989, "Local Three-Dimensional Convective Heat Transfer From a Heated Cube," *Collected Papers in Heat Transfer 1989*, W. J. Marner et al., eds., ASME, New York, pp. 7–13.

Roeller, P. T., 1989, "An Experimental Study of Forced Convection Heat Transfer From Two- and Three-Dimensional Protrusions," M.S. Thesis, Department of Mechanical Engineering, Brigham Young University, Provo, UT, 84602.

Roeller, P. T., Stevens, J., and Webb, B. W., 1990, "Heat Transfer and Turbulent Flow Characteristics of Isolated Three-Dimensional Protrusions in Channels," in: *Thermal Modeling and Design of Electronic Systems and Devices*, R. A. Wirtz and G. L. Lehmann, eds., ASME, New York, pp. 7–13.

Sparrow, E. M., Niethammer, J. E., and Chaboki, A., 1982, "Heat Transfer and Pressure Drop Characteristics of Arrays of Rectangular Modules Encountered in Electronic Equipment," *International Journal of Heat and Mass Transfer*, Vol. 25, pp. 961–973.

An Experimental Study of Convective Heat Transfer in Radially Rotating Rectangular Ducts

C. Y. Soong[1]

S. T. Lin
Graduate Student.

G. J. Hwang
Professor.
Mem. ASME

Department of Power
Mechanical Engineering,
National Tsing Hua University,
Hsinchu, Taiwan 30043

The paper presents an experimental study of convective heat transfer in radially rotating isothermal rectangular ducts with various height and width aspect ratios. The convective heat transfer is affected by secondary flows resulting from Coriolis force and the buoyancy flow, which is in turn due to the centrifugal force in the duct. The growth and strength of the secondary flow depend on the rotational Reynolds number; the effect of the buoyancy flow is characterized by the rotational Rayleigh number. The aspect ratio of the duct may affect the secondary flow and the buoyancy flow, and therefore is also a critical parameter in the heat transfer mechanism. In the present work the effects of the main flow, the rotational speed, and the aspect ratio γ on heat transfer are subjects of major interest. Ducts of aspect ratios $\gamma = 5$, 2, 1, 0.5, and 0.2 at rotational speed up to 3000 rpm are studied. The main flow Reynolds number ranges from 700 to 20,000 to cover the laminar, transitional, and turbulent flow regimes in the duct flow. Test data and discussion are presented.

Introduction

Heat transfer in rotating ducts has been a major subject in the study of cooling technology for rotating machines in the past decades due to its importance in engineering applications, e.g., cooling channels in gas turbines and electrical generators. Considering the orientation of flow passages and the axis of rotation, they can be categorized into the following five rotation modes: (*a*) radial or orthogonal mode, (*b*) parallel mode, (*c*) axial mode, (*d*) slant mode, and (*e*) circumferential mode. Among these modes, the radial mode is the most interesting one for its application to rotor blade cooling in gas turbines.

In the radially rotating ducts, the rotationally induced Coriolis and centrifugal forces can be generated and consequently the flow and heat transfer characteristics are affected by these forces. The secondary flow, which is established by the Coriolis force in the cross plane of the duct, provides a beneficial effect on the heat transfer rate. This topic has been studied in many investigations, e.g., the analytical and experimental works by Mori and Nakayama (1968) and Mori et al. (1971); and the accumulated achievements of the earlier works have been collected in a review monograph by Morris (1981). Recently, Morris (1977, 1981) and Morris and Ayhan (1979) advocated the significance of the centrifugal-buoyancy effect, which has an advantageous effect on heat transfer for radially inward flow but an adverse effect for radially outward flow. This class of flows has an analogy to mixed convection, buoyancy-assisted and opposed, in a gravitational field (Eckert, 1979). Later, some theoretical analyses (Siegel, 1985; Soong and Hwang, 1990) corroborated this argument. Numerical simulation for this complicated convection problem is rather troublesome for its bifurcation nature in laminar flow with higher parameters (Spezial and Thangan, 1983; Hwang and Jen, 1990), and for lacking an adequate model in the turbulent flow regime to simulate the transport phenomena in the presence of both the Coriolis and centrifugal-buoyancy effects. Comparatively, experimental approach is a more reliable means to obtain the useful information on the flow and heat transfer in a rotating duct.

Table 1 lists the previous experimental investigations on heat transfer in radially rotating ducts. One can find that studies in most of the previous works are concerned with circular ducts, and new studies pertain to noncircular, i.e., triangular (Clifford et al., 1984; Harasgama and Morris, 1988), square (Hwang and Soong, 1989; Harasgama and Morris, 1988; Wagner et al., 1991), and rectangular (Guidez, 1989) ducts. In practice the utilizations of the circular, rectangular, and triangular ducts are all possible in a turbine blade. Near the leading edge, the circular duct may be employed as a coolant channel; but near the trailing edge, a triangular one is a best choice; and between them, rectangular channels are more appropriate. On the other hand, the rotational effect could be different for ducts of various cross sections. In rectangular ducts, for example, the cross-sectional aspect ratio may affect the strength of the secondary flow. Therefore the aspect ratio is also a critical parameter in the heat transfer mechanism. So far, however, there are no such data available in the literature.

In the present study, heat transfer in radially rotating isothermal rectangular ducts is investigated experimentally. The effects of forced flow, rotation, and aspect ratio γ on the heat transfer are subjects of major interest. Ducts of aspect ratio $\gamma = 5$, 2, 1, 0.5, and 0.2 at rotational speeds up to 3000 rpm are studied. The main flow Reynolds number ranges from 700 to 20,000 to cover laminar, transitional, and turbulent flow regimes in the duct flow. Three different wall-coolant temperature differences are used for square ducts ($\gamma = 1$) to explore the centrifugal-buoyancy effect on heat transfer. An automatically controlled test apparatus developed for heat transfer measurements in rotating isothermal systems is employed to perform a series of measurements. An appreciable amount of test data with discussion are presented.

Parametric Analysis

The physical configuration of convective heat transfer in radially rotating isothermal rectangular ducts considered in the present study is shown in Fig. 1. The duct of aspect ratio $\gamma = H/$

[1]Present address: Associate Professor, Department of Aeronautical Engineering, Chung Cheng Institute of Technology, Taoyuan, Taiwan 33509.

Contributed by the Heat Transfer Division for publication in the JOURNAL OF HEAT TRANSFER. Manuscript received by the Heat Transfer Division September 20, 1989; revision received October 1, 1990. Keywords: Forced Convection, Mixed Convection, Rotating Flows.

Table 1 Experimental investigation on heat transfer in radially rotating ducts

Authors	Year	Duct type	L/D	Rotational speed (rpm)	Reynolds No. ($\times 10^3$)	Thermal B.C.
Mori et al.	1971	o	56.67	0–1000	1–10.8	UWT*
Lokai and Limanskii	1975	o	26	0–5000	9–40	UHF
Zysina-Molozhen et al.	1976	o	25	0–2250	4–30	UHF
Metzger and Stan	1977	o	6, 12, 24	0–3000	0.7–3.1	UWT
Lokai and Gunchenko	1979	o	?	0–5500	12–37	UHF
Morris and Ayhan	1979	o	10, 20	0–2000	5–15.5	UHF
Clifford et al.	1984	△	20	0–1000	6.8–38	UHF
Iskakov and Trushin	1985	o	11.25	0–876	30–80	UHF
Harasgama and Morris	1988	o △ □	20	0–2000	7–25	UHF
Hwang and Soong	1989	□	30	0–3000	0.7–20	UWT
Guidez	1989	▭	11.5	0–5200	17–41	UHF
Wagner et al.	1991	□	14	0–1100	12.5–50	UWT

*Mass transfer analogy

B (height H denotes the sides parallel to the Coriolis force in the cross plane) rotates with a constant speed ω about an axis at a distance Z_o from the origin of the coordinate system. The thermal boundary condition of uniform wall temperature (UWT) is imposed on the duct walls. Due to the complexity of the problem, the governing parameters will be extracted through the nondimensionalization of the continuity, momentum, and energy equations.

To simplify the analysis, a steady and incompressible flow is assumed and gravitational force is neglected, for its magnitude is small compared to the centrifugal force. The governing equations are depicted as follows:

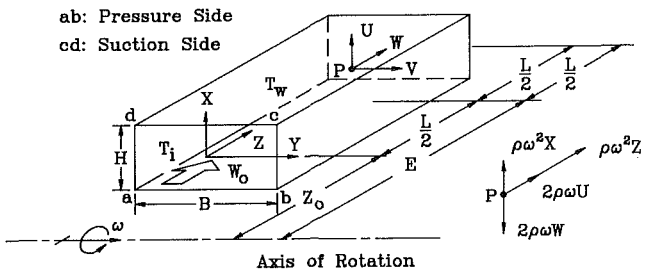

Fig. 1 Physical model of the problem

Nomenclature

B = duct width
C_p = specific heat
D = hydraulic diameter
E = semispan eccentricity
H = duct height
h_{lm} = heat transfer coefficient based on LMTD
k = specific heat ratio
L = duct length
l = dimensionless duct length = L/D
M = air flow Mach number
$\dot{m}$ = mass flow rate
Nu = mean Nusselt number
Nu_r = mean Nusselt number in rotation case
Nu_o = mean Nusselt number in stationary case
Nu_∞ = Nusselt number in fully developed case
P = static pressure
P' = pressure departure from the reference condition
p' = dimensionless quantity of P'
Pr = Prandtl number
Q = heat flux
R = position vector from the rotation center
Ra_ω = rotational Rayleigh number = $(\omega^2 E)/\beta(T_w - T_i)D^3\mathrm{Pr}/\nu^2$
Ra^*_ω = combined buoyancy parameter = $\mathrm{Ra}_\omega/\mathrm{Re}^2$
Re = main flow Reynolds number = $W_o D/\nu$
Re_{cr} = critical Reynolds number
Re_ω = rotational Reynolds number = $\omega D^2/\nu$
Ro = rotation number = $\omega D/W_o$
r = temperature recovery factor
$T_{b,e}$ = exit bulk temperature
$T_{b,f}$ = mean fluid temperature in duct
T_f = fluid temperature
T_i = inlet temperature of air
T_r = recovery temperature
T_w = wall temperature
ΔT = reference temperature difference = $T_w - T_i$
ΔT_{lm} = log-mean temperature difference (LMTD)
U, V, W = velocity components
u, v, w = dimensionless velocity components
UHF = uniform heat flux
UWT = uniform wall temperature
W_o = mean flow velocity in duct
X, Y, Z = coordinate system
x, y, z = dimensionless quantity of (X, Y, Z)
Z_o = distance from duct entrance to the axis of rotation
γ = duct aspect ratio (height/width) = H/B
ϵ = dimensionless semispan eccentricity = E/D
θ = dimensionless temperature = $(T - T_i)/\mathrm{Pr}(T_w - T_i)$
μ = viscosity
ν = kinematic viscosity
ρ = fluid density
ω = rotational speed

$$\nabla \cdot V = 0 \tag{1}$$

$$(\nabla \cdot V)V = \nu \nabla^2 V - \nabla P'/\rho - \omega \times \omega \times R - 2\omega \times V \tag{2}$$

$$(\nabla \cdot V)T = \alpha \nabla^2 T \tag{3}$$

By invoking the Boussinesq approximation, $\rho = \rho_r[1 - \beta(T - T_i)]$, to the centrifugal force terms and introducing the nondimensional variables

$$x = X/H, \quad y = Y/B, \quad z = Z/L, \quad u = U/\left(\frac{\gamma+1}{2l} W_o\right),$$

$$v = V/\left(\frac{\gamma+1}{2\gamma l} W_o\right), \quad w = W/W_o, \quad p' = P'/\rho_r W_o^2,$$

$$\theta = (T - T_i)/\mathrm{Pr}(T_w - T_i), \quad D = 2HB/(H+B), \quad l = L/D,$$

$$\epsilon = E/D, \quad \mathrm{Re} = W_o D/\nu, \quad \mathrm{Re}_\omega = \omega \cdot D^2/\nu,$$

$$\mathrm{Ro} = \mathrm{Re}_\omega/\mathrm{Re}, \quad \mathrm{Ra}_\omega = \omega^2 E\beta(T_w - T_i)D^3\mathrm{Pr}/\nu^2,$$

equations (1)–(3) can be expressed in the following dimensionless scalar form:

$$\frac{\partial u}{\partial x} + \frac{\partial v}{\partial y} + \frac{\partial w}{\partial z} = 0 \tag{4}$$

$$u\frac{\partial u}{\partial x} + v\frac{\partial u}{\partial y} + w\frac{\partial u}{\partial z} = \frac{1}{\mathrm{Re}} \nabla^{*2} u - \frac{4l^2}{(\gamma+1)^2}\frac{\partial p'}{\partial x} - \frac{4l^2}{\gamma+1}\mathrm{Ro} \cdot w - \frac{\mathrm{Ra}_\omega}{\mathrm{Re}^2}\frac{x\theta}{\epsilon} \tag{5}$$

$$u\frac{\partial v}{\partial x} + v\frac{\partial v}{\partial y} + w\frac{\partial v}{\partial z} = \frac{1}{\mathrm{Re}} \nabla^{*2} v - \frac{4\gamma^2 l^2}{(\gamma+1)^2}\frac{\partial p'}{\partial y} \tag{6}$$

$$u\frac{\partial w}{\partial x} + v\frac{\partial w}{\partial y} + w\frac{\partial w}{\partial z} = \frac{1}{\mathrm{Re}} \nabla^{*2} w - \frac{\partial p'}{\partial z} + (\gamma+1)\mathrm{Ro} \cdot u - \frac{\mathrm{Ra}_\omega}{\mathrm{Re}^2}\frac{l^2}{\epsilon}(z_o + z) \cdot \theta \tag{7}$$

$$u\frac{\partial \theta}{\partial x} + v\frac{\partial \theta}{\partial y} + w\frac{\partial \theta}{\partial z} = \frac{1}{\mathrm{PrRe}} \nabla^{*2} \theta \tag{8}$$

where $\nabla^{*2} = \frac{4l}{(\gamma+1)^2}\left[\frac{\partial^2}{\partial x^2} + \gamma^2\frac{\partial^2}{\partial y^2} + \frac{(\gamma+1)^2}{4l^2}\frac{\partial^2}{\partial z^2}\right]$.

In the above equations, one can find that the rotational effects are characterized by the dimensionless groups $\mathrm{Re}_\omega/\mathrm{Re}$ (or Ro) and $\mathrm{Ra}_\omega/\mathrm{Re}^2$. Physically, the former represents the ratio of the Coriolis force to the inertia force or the relative significance of the Coriolis-induced secondary flow effect to the forced flow effect. The latter is the ratio of the centrifugal-buoyancy force to the inertia force or the relative importance of the buoyancy to the forced convection effect. It is also seen that the main flow Reynolds number Re characterizes the forced convection effect.

The parametric analysis generates the following statements: (1) The parameters involved in the present problem are the Prandtl number Pr, the cross-sectional aspect ratio γ, the eccentricity ϵ, the duct length l, the main flow Reynolds number Re, the rotation number Ro ($=\mathrm{Re}_\omega/\mathrm{Re}$), and the buoyancy parameter $\mathrm{Ra}_\omega/\mathrm{Re}^2$. (2) The centrifugal-buoyancy effect ($\sim \mathrm{Re}^{-2}$) diminishes faster than the effect of the Coriolis-induced secondary flow ($\sim \mathrm{Re}^{-1}$) as the main flow Reynolds number increases. (3) From the x-momentum equations, it is very clear that the pressure gradient, and the Coriolis and viscous forces in the cross plane can be strongly affected by the aspect ratio γ as well as the duct length l.

Experimental Apparatus and Test Procedure

In the present study an experimental apparatus, shown in Fig. 2, is employed to conduct a series of measurements of the mean Nusselt number under various conditions. The apparatus consists of six major parts: (1) coolant air supply, (2) test section, (3) heater and temperature controller, (4) motor and speed controller, (5) data acquisition and reduction system, and (6) sequential controller and monitoring system. Two feedback controllers are used for the wall temperature and rotational speed regulations, and a sequential controller is for the experimental sequence control. A personal computer is used to play the role of center controller and monitor for the whole experimental system. The control and monitoring system is described in detail in a previous work (Hwang and Soong, 1989) and will not be repeated here.

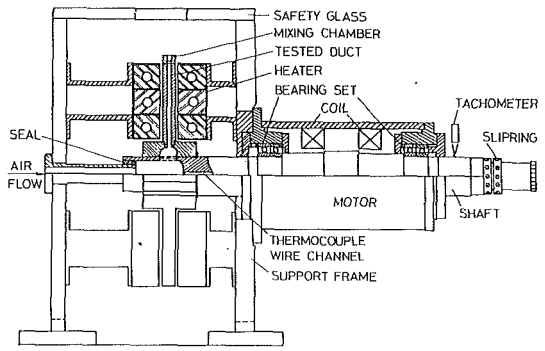

Fig. 2 Arrangement of experimental apparatus

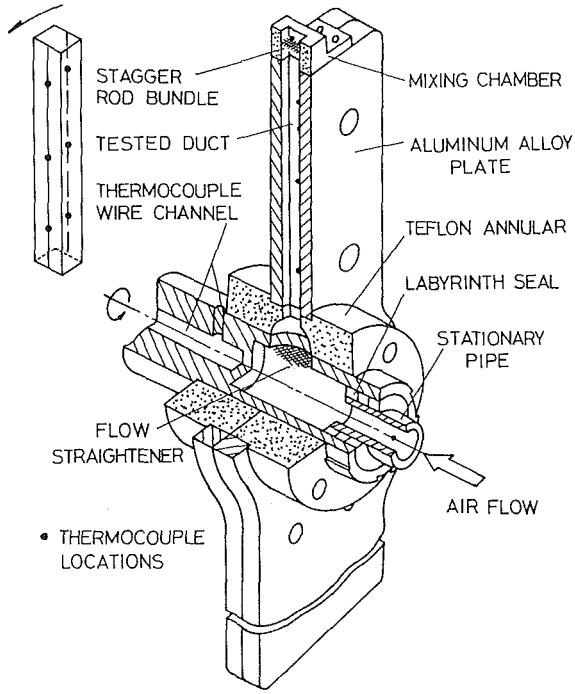

Fig. 3 Test section assembly

A schematic diagram of the test model assembly is shown in Fig. 3. The hydraulic diameter of the model ducts is 4 mm and the length-to-diameter ratio is 30. Considering the requirements of high thermal conductivity, light weight, high material strength, and machining feasibility, aluminum alloy (e.g., AA-6061 or 6101) is an appropriate choice. A channel in a half height and several slots for thermocouple installations are grooved on two pieces of well-finished aluminum alloy plates. The required rectangular duct can thus be formed by screwing the plates face to face. The outside surfaces of the plates are oxidized in black to increase the absorptivity of radiative heat from the heater system.

Along the duct axis, three pairs of T-type copper-constantan

thermocouples are embedded in the slots parallel to the duct. The wall temperature is measured at the axial locations of 1/6, 1/2, and 5/6 length of the duct from the inlet. A Teflon annular hub with spline keyways in the inner side is used for mounting the test section of the rotating shaft and also as a thermal insulator to insulate the shaft from the hot test section.

After passing through an electronic digital flowmeter, the coolant air flow enters the cylindrical plenum space in the hollow shaft and flows through the straightener fixed in the interior of the shaft to eliminate the initial swirl before entering the rectangular duct. A thermocouple is located at the inlet of the plenum space to measure the temperature of the inlet air flow. To pick up the bulk temperature reading at the ext, a mixing chamber made of Teflon is attached to the exit plane. A stagger rod bundle is installed in the chamber to provide a well-mixed condition. The whole model assembly is placed in a test cell enclosed by a support frame with safety glass plates and ventilation openings.

In the UWT thermal boundary condition, the local heat flux carried away by the coolant varies along the duct. A two-disk three-ring annular heater system with a total power of 1.2 kW is designed. The two-disk heaters are parallel with a 5-mm gap on each side of the test section. The power output from each of the three ring heaters (inner, middle, outer), which corresponds to a thermocouple on the duct wall, is controlled individually by using a mutlichannel temperature controller.

The rotational speed can be detected by a photo-electric tachometer and adjusted by a feedback controller to attain the present speed. The temperature readings from the rotating part are transferred to the recorder through a slip-ring assembly attached at the end of the shaft. The slip-ring assembly has 12 rings; its permitted speed for continuous duty is 6000 rpm. The raw data are processed by a built-in program once per minute until the criterion of steady-state, i.e., the variation of the mean Nusselt number is less than 1 percent in ten minutes, is satisfied. After setting a value for the wall temperature, usually, a period of one hour was allowed for warmup and additional 30 to 45 minutes was required to reach the steady-state condition. In the present work the inlet air temperature is about 25°C. Three wall temperatures, $T_w = 45$, 55, and 80°C, are posed to study the effect of temperature difference on heat transfer characteristics.

Preliminary Tests and Data Reduction

Preliminary tests were performed for data calibration and error estimations. The errors in the temperature measurement are due to the inaccuracies in the initial calibration of the thermocouples, the reading of recorder, and the connections in the slip ring. The three uncertainties are 0.1°C, 0.1°C, and 0.2°C, respectively. The total uncertainty in temperature is, therefore, 0.4°C. Radiation error in the temperature measurement of the exit air flow is estimated by following the analysis in Eckert and Drake's book (1972), and the maximum relative error in temperature reading is less than 1.65 percent.

In an experiment with a large flow rate, the compressibility correction for the measured temperature of the air flow is performed. By denoting the recovery temperature as T_r, the true fluid temperature T_f can be expressed as

$$T_f = T_r \Big/ \left[1 + \frac{k-1}{2} r \mathrm{M}^2 \right] \tag{9}$$

where k is the specific heat ratio, M is the Mach number of the air flow, and r is the temperature recovery factor (Schlichting, 1979) and

$$r = \mathrm{Pr}^{1/2} \quad \text{for laminar flow}$$

$$= \mathrm{Pr}^{1/3} \quad \text{for turbulent flow}$$

It is noted that a maximum temperature difference $T_r - T_f = 2.5$°C is found for the case of Re = 20,000 (M ≈ 0.21) in the present study. The uniformity of the wall temperature is also checked. A wall temperature difference of 0.5°C between the temperatures at 1/6 and 5/6 length of the duct and 0.2°C between the pressure and suction sides of the duct was found for $\gamma = 1$ at $\Delta T = T_w - T_i = 30$°C, Re = 8300, and $\mathrm{Re}_\omega = 200$. Considering the possible leakage of the air flow, a flow-rate calibration is conducted in the stationary case, and the calibration curve is used in data reduction. The maximum error in the flow rate is 5 percent, and in the rotational speed it is 1 percent. An error analysis in the measurement of temperature, flow rate, and physical properties was carried out. In the worst case of measurements, the uncertainty is about 13 percent in the value of the Nusselt number at $\Delta T = 30$°C, and 18 percent at $\Delta T = 20$°C.

The mean or the overall Nusselt number is based on the heat transfer coefficient derived from the energy balance over a duct length L

$$Q = h_{lm} \cdot 2(H+B) \cdot L \cdot \Delta T_{lm} = \dot{m} \cdot C_p (T_{b,e} - T_i) \tag{10}$$

In the calculation of heat transfer coefficient, net heat flux, and therefore the heat loss, must be accurately estimated; see, e.g., Wagner et al. (1991). To avoid the difficult task of heat-loss estimation, the log-mean temperature difference (LMTD) ΔT_{lm} rather than the net heat flux is used; ΔT_{lm} is defined as (Youset and Tarasuk, 1982)

$$\Delta T_{lm} = (T_{b,e} - T_i) / \ln[(T_w - T_i)/(T_w - T_{b,e})] \tag{11}$$

in which T_w denotes the measured average wall temperature, T_i is the inlet air temperature, and $T_{b,e}$ is the exit bulk temperature. The fluid properties are evaluated at the mean fluid temperature $T_{b,f}$ based on LMTD, i.e.,

$$T_{b,f} = T_w - (T_w - T_i)/\ln[(T_w - T_i)/(T_w - T_{b,e})] \tag{12}$$

Therefore, the mean Nusselt number is

$$\mathrm{Nu} = \frac{1}{4} \cdot \ln[(T_w - T_i)/(T_w - T_{b,e})] \cdot (\mathrm{PrReD}/L) \tag{13}$$

in which only Pr, Re, L/D, and the three measured temperatures T_i, T_w, and $T_{b,e}$ are involved.

Results and Discussion

In the present study the properties ρ, k, μ, and Pr are all assumed as constants due to the low temperature difference ΔT. From the previous parametric analysis, the enhancement of heat transfer rate, denoted by the ratio $\mathrm{Nu}_r/\mathrm{Nu}_o$, in the rotating rectangular ducts depends on the parameters Re, Re_ω, Ra_ω, γ, l, and ϵ. For fixed duct length and eccentricity, the Nusselt number ratio can be expressed as a function of Re, Re_ω, Ra_ω, and γ, or in terms of the combined parameters

$$\mathrm{Nu}_r/\mathrm{Nu}_o = f[\mathrm{Re}, \mathrm{Ro}, \mathrm{Ra}_\omega^*, \gamma] \tag{14}$$

where r and o denote rotational and stationary conditions, respectively, $\mathrm{Ro} = \mathrm{Re}_\omega/\mathrm{Re}$ is the rotation number, and $\mathrm{Ra}_\omega^* = \mathrm{Ra}_\omega/\mathrm{Re}^2$ is the parameter indicating the relative importance of the buoyancy to the forced convection effect.

Figure 4 shows the variation of the mean Nusselt number with the Reynolds number for a square duct $\gamma = 1$. The Reynolds number ranging from 700 to 20,000 covers the laminar, transitional, and turbulent flow regimes. It is seen that the stationary duct data obtained in the present experiment are quite reasonable when compared with previous results in the high Reynolds number regime (Deissler, 1953; Woods, 1975), but show higher values in the Nusselt number when compared with pure forced convection data in laminar flow regime (Shah and London, 1978). One may attribute this discrepancy to all possible secondary flow motion due to flow passage and natural convection. The data display different slopes in laminar and turbulent flow regimes as expected. In the stationary condition, the slope of the curve changes at Reynolds number near

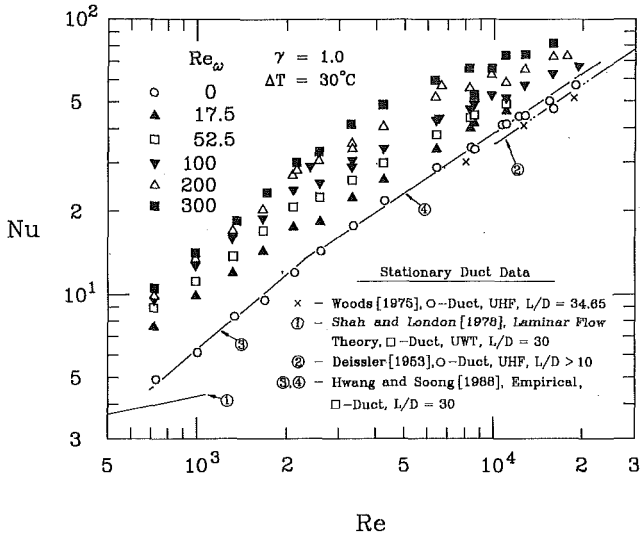

Fig. 4 Mean Nusselt number variation in rotating square duct ($\gamma = 1$)

2300. The data at $Re > 2300$ behave as typical turbulent flow data and those at $Re < 2300$ behave as laminar and transitional data. The rotating duct data show behavior similar to that of the stationary data. All the data for rotational cases tend to merge into the limiting curve as the Reynolds number increases. This is due to a relatively low secondary flow and buoyancy effects in a strong forced flow at high Reynolds number.

Figure 5 shows the experimental data for two low aspect ratio ducts ($\gamma = 0.2$ and 0.5) and two high aspect ratio ones ($\gamma = 2$ and 5). All of the data presented in Figs. 4 and 5 were measured in the thermal boundary condition of UWT with a temperature difference $\Delta T = T_w - T_i = 30°C$ or $\Delta T/T_w \approx 0.1$. It is seen that most of the rectangular duct data follow the same trend as that the square duct behaves, except the distinct behavior of the $\gamma = 5.0$ duct at $Re_\omega \geq 52.5$ presented in the high Reynolds number region. The relatively lower heat transfer rate in these cases will be discussed later.

The aspect ratio effect on the heat transfer enhancement at various rotational Reynolds numbers is presented in Fig. 6. The considerable enhancement of heat transfer in the laminar and transitional flow ($Re < 4000$) regimes is observed. Also, one can find that the secondary flow effect on the heat transfer enhancement in high γ ducts diminishes faster than that in low

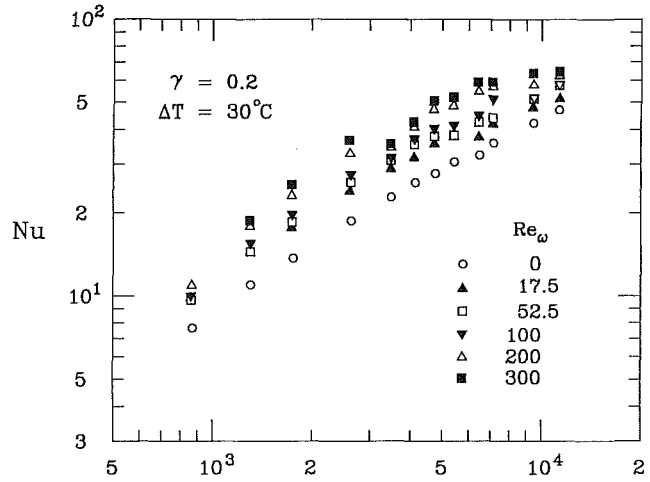

Fig. 5(*a*) $\gamma = 0.2$

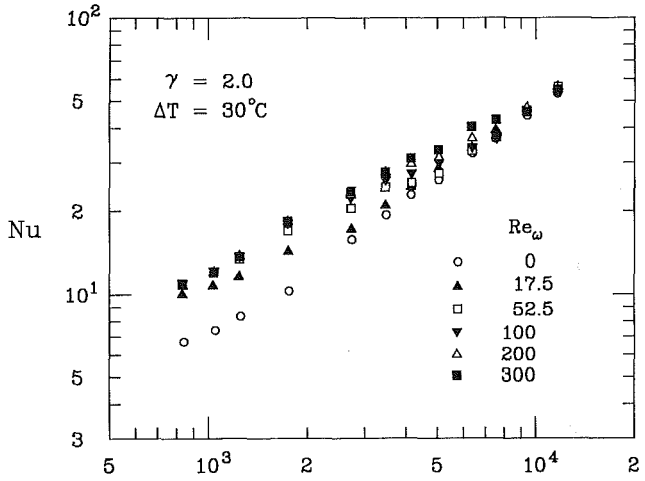

Fig. 5(*c*) $\gamma = 2.0$

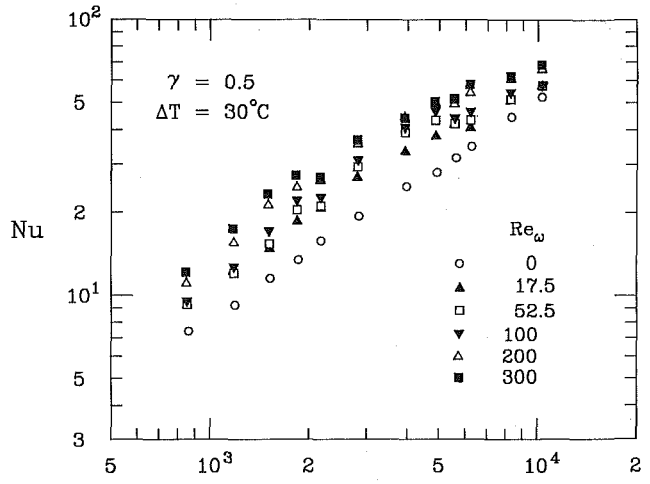

Fig. 5(*b*) $\gamma = 0.5$

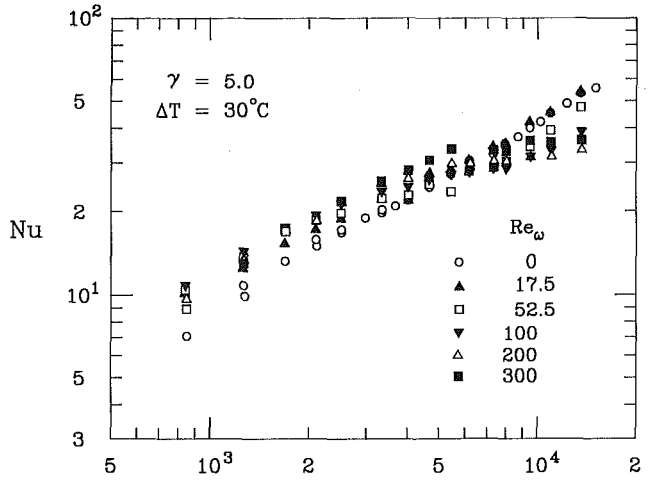

Fig. 5(*d*) $\gamma = 5.0$

Fig. 5 Mean Nusselt number variation in rotating rectangular ducts

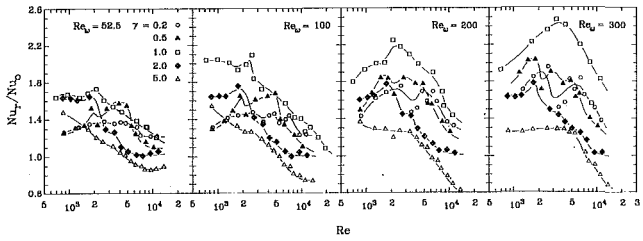

Fig. 6 Dependence of heat transfer enhancement on cross-sectional geometry and Coriolis effects

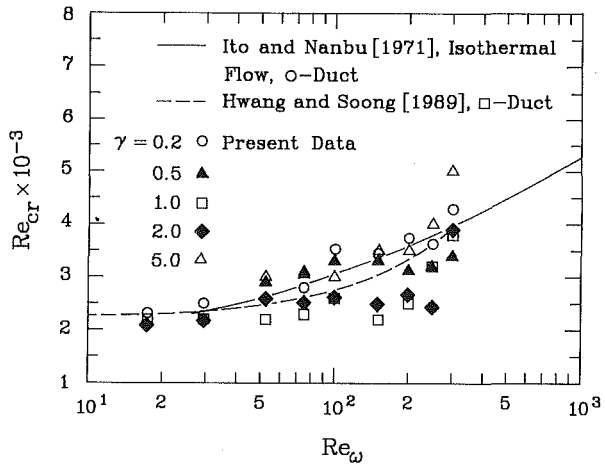

Fig. 7 Rotational effect on laminar-turbulent transition

γ ones. This is due to the relatively weak secondary flow effect in the high γ ducts. The heat transfer enhancement in a square duct is most remarkable. However, the data for ducts of $\gamma \neq 1$ are somewhat irregular in a low Reynolds number region. Almost all of the data follow a growing trend due to the increasing Coriolis effect, except the high aspect ratio duct of $\gamma = 5$. Similar behavior has been reported in previous works on laminar cases (Mori and Nakayama, 1968; Hwang and Soong, 1989). This beneficial effect is suppressed in the turbulent flow regime.

In the turbulent flow regime, the magnitude of Nu_r/Nu_o follows a regular order of square, low γ, and high γ ducts. It may be concluded that the rotational effect on heat transfer enhancement is the smallest in the high γ ducts, but is the strongest in a square one. The physical interpretation based on the dimensionless equations (4)–(8) can be stated as follows. In the low γ ducts ($\gamma < 1$), the Coriolis force $-4l^2 \cdot \mathrm{Ro} \cdot w/(1+\gamma)$ in x-momentum equation (5) seems to be slightly increased for the more convex main flow velocity distribution along the duct height (i.e., in the x direction); but the viscous force $4l(\partial^2 u/\partial x^2)/(\gamma+1)^2$ on the walls perpendicular to the Coriolis force also becomes large. The total effect of these forces weakens the secondary flow motion in the cross plane. In high γ ducts ($\gamma > 1$), the Coriolis force becomes smaller and approaches zero as $\gamma \to \infty$. The secondary flow is weakened by the higher viscous force on the longer sides, and then is difficult to increase in the high γ narrow duct. Consequently, buoyancy becomes the dominant effect. Even in a strong forced flow, therefore, the buoyancy still has the chance to reverse the beneficial effect of the secondary flow. This point can serve as a reasonable interpretation for the low heat transfer rate in the high γ ducts, while in the low γ ducts, the Coriolis force is more uniformly distributed along the duct width and this uniformity will not generate strong secondary flow. Therefore, one may expect to have a large Coriolis force effect on the heat transfer in a duct with the aspect ratio near $\gamma = 1$ and a smaller effect in a duct with $\gamma \to 0$ or ∞. This phenomenon can also be observed in

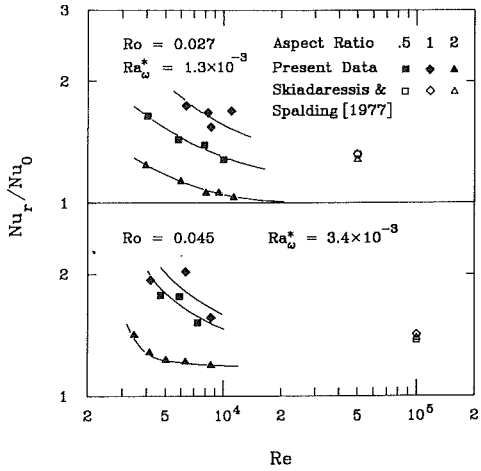

Fig. 8 Comparison of experimental and numerical results in turbulent flow regime

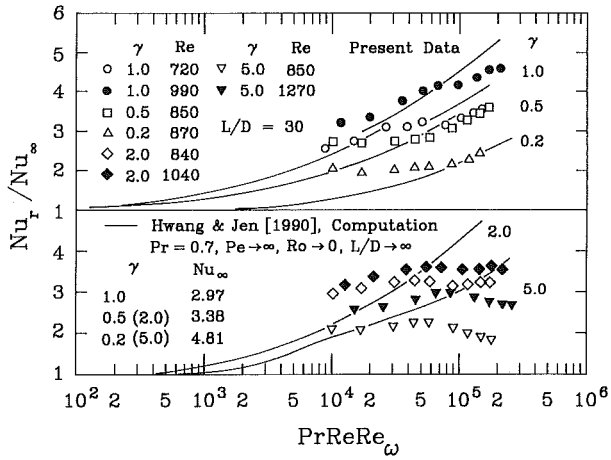

Fig. 9 Comparison of experimental and numerical results in laminar flow regime

heated horizontal rectangular ducts (Cheng and Hwang, 1969) and curved channels (Cheng and Akiyama, 1970).

To extract the information about the critical Reynolds number from the present data, the salient changes in slope of the heat transfer curves are used to deduce the occurrence of the laminar-turbulent transition. From the data shown in Fig. 6, it is found that the transition in the square duct is very clear but is blurred in some of the other ducts, e.g., $\gamma = 0.2$, 0.5, and 2.0. In these cases double peaks appear in the heat transfer curves; the average of the Reynolds number for two peaks is used as a representative value for identification of transition. This may be related to the beginning and the end of laminar-turbulent transitional regime. Figure 7 presents the rotational effect on the critical Reynolds number. In general, the rotational effect tends to delay transition in all of the cases and is stronger in narrow ducts, e.g., $\gamma = 0.2$ and 5. Qualitatively, the present results are reasonable in comparison with the earlier empirical formulas for an isothermal flow problem (Ito and Nanbu, 1971) and previous work on heat transfer in a square duct (Hwang and Soong, 1989).

In Fig. 8 selected data in the turbulent flow regime are compared with the numerical results interpreted from Skiadaressis and Spalding's computation (1977). Again, both the present data and the numerical results tend to merge into the limiting values as $\mathrm{Re} \to \infty$ and this observation confirms the argument presented in the previous sections. However, the numerical calculation was carried out by using the standard k–ϵ model without body force modification and ignoring the

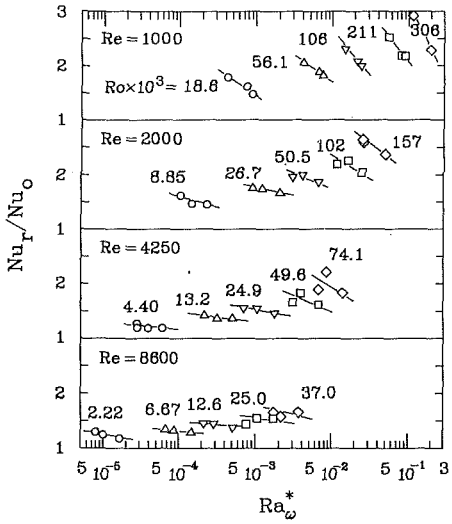

Fig. 10 Centrifugal-buoyancy effect on heat transfer in a rotating square duct ($\gamma = 1$)

centrifugal-buoyancy effect; therefore, the numerical results overestimate the rotational effects on the heat transfer enhancement.

The numerical calculation for laminar fully developed flow and heat transfer in radially rotating isothermal rectangular ducts was carried out by Hwang and Jen (1990). Some of the present data at Re near 1000 are compared with the numerical results. From Fig. 9 it is found that, at a given Reynolds number, the measured heat transfer data are slightly higher than the fully developed values due to the entrance effect. However, this dominance is reversed at large rotational speed or in this case, large value of PrReRe_ω with constant Re. It is attributed to the large centrifugal-buoyancy effect in the laminar (low Re) flow regime, which is not considered in the numerical simulation. For constant Re, the centrifugal-buoyancy effect is proportional to ω^2 (appears in definition of Ra_ω). The rapid growth of the buoyancy effect flattens the increasing trend of the heat transfer rate, and in the cases of weak secondary flow, e.g., high γ ducts, the reverse effect is quite remarkable.

Additionally, the velocity profiles in the cross plane in the entrance regions are more uniform than those in the fully developed case. Therefore, the larger Coriolis force and therefore secondary flow effect on heat transfer can be generated in the fully developed case or in a long duct. This gives another physical interpretation for the comparison of the measured data ($L/D = 30$) and the numerical results for the fully developed case ($L/D \to \infty$) in the high PrReRe_ω region in Fig. 9. Although the duct-length effect is not studied in the present work, the effect on the heat transfer may be deduced from the argument mentioned above.

It is very difficult to separate the Coriolis and the centrifugal buoyancy effects in an experimental condition of the constant main flow Reynolds number. In the present study, the square duct is chosen as a typical example to explore the centrifugal-buoyancy effect. Three different wall-to-inlet temperature differences $\Delta T = 20$, 30 and 55°C (i.e., $\Delta T/T_w \approx 0.063$, 0.091, and 0.156) are used to generate different buoyancy effects while retaining the other parameters unchanged. The measurements were performed at four Reynolds numbers, Re = 1000, 2100, 4250, and 8600. From Fig. 10, it is obvious that there is an adverse effect of centrifugal-buoyancy on heat transfer, i.e., the heat transfer enhancement decreases as the Ra^*_ω increases. The adverse effect of the Ra^*_ω tends to diminish as the Reynolds number increases. These results agree with those proposed by Morris and Ayhan (1979), Clifford et al. (1984), and Harasgama and Morris (1988). In a recent work by Guidez (1989), it was presented that the mean Nusselt number increases with buoyancy parameter. However, Ro is not a control variable for the data in Fig. 16 of Guidez's paper. It is believed that the growing trend is caused by the Ro effect rather than solely by the buoyancy effect. Meanwhile, it is obvious that the data in our Fig. 10 also present the same trend if the condition of constant Ro is ignored. In a more recent work (Wagner et al., 1991), the growing trend of the heat transfer enhancement with increasing $\Delta\rho/\rho$ (or $\Delta T/T_w$) for constant Ro was also reported. The data of Wagner et al. at Re = 25,000 seem to be in direct conflict with the buoyancy effects at the relatively low Reynolds number Re < 10,000 reported by Morris and Ayhan (1979), Clifford et al. (1984), Harasgama and Morris (1988), and the present work. One may attribute this phenomenon to an increasing velocity fluctuation in buoyancy opposing flow (Swanson and Catton, 1987). This effect is opposite to that in laminar and transitional flow regimes.

Concluding Remarks

The present experimental investigation provides the heat transfer data of radially rotating isothermal rectangular ducts of aspect ratio $\gamma = 5.0$, 2.0, 1.0, 0.5, and 0.2. The following conclusions can be drawn:

1 The Coriolis-induced secondary flow can provide a beneficial effect on the heat transfer enhancement, while the centrifugal buoyancy presents an adverse effect. Both of these effects will diminish in a strong forced flow field.

2 In the present study the physical model is very complicated. By performing a parametric analysis, six critical parameters are involved. They are the Prandtl number Pr, the cross-sectional aspect ratio γ, and the duct length l for the geometry, the rotational number $\mathrm{Ro} = \mathrm{Re}_\omega/\mathrm{Re}$ for the Coriolis effect, the buoyancy parameter $\mathrm{Ra}^*_\omega = \mathrm{Ra}_\omega/\mathrm{Re}^2$ for the centrifugal buoyancy effect, and the Reynolds number for the forced flow effect. The buoyancy effect diminishes faster than the Coriolis effect as $\mathrm{Re} \to \infty$, but the resultant overall rotational effect depends on individual value of the parameters in the problem.

3 The aspect ratio γ of the duct is a critical parameter in the mechanism of the secondary flow formation and strength. The significance of γ can be revealed in the dimensionless momentum equations. One may expect to have a larger Coriolis effect on heat transfer in a duct with the aspect ratio near 1.

4 Due to the complicated and interactive nature of the flow field and heat transfer, further studies on the local flow structure and heat transfer mechanism are necessary, especially for the high rotational speeds and/or Reynolds numbers.

Acknowledgments

The authors would like to thank the National Science Council, Taiwan, for their support of this work through Grant No. NSC-75-0201-P007-01R.

References

Cheng, K. C., and Akiyama, M., 1970, "Laminar Forced Convection Heat Transfer in Curved Rectangular Channels," *Int. J. Heat Mass Transfer,* Vol. 13, pp. 471-490.

Cheng, K. C., and Hwang, G. J., 1969, "Numerical Solution for Combined Free and Forced Laminar Convection in Horizontal Rectangular Channels," ASME JOURNAL OF HEAT TRANSFER, Vol. 91, pp. 59-66.

Clifford, R. J., Harasgama, S. P., and Morris, W. D., 1984, "An Experimental Study of Local and Mean Heat Transfer in a Triangular-Sectional Duct Rotating in the Orthogonal Mode," ASME *Journal of Engineering for Gas Turbines and Power,* Vol. 106, No. 3, pp. 661-667; also, *Int. J. Turbo. Jet Engines,* Vol. 2, 1985, pp. 93-106.

Deissler, R. G., 1953, "Analysis of Turbulent Heat Transfer and Flow in the Entrance Region of Smooth Passages," NACA TN 3016.

Eckert, E. R. G., 1979, "Simulation of Rotation by Gravity," *Letters Heat Mass Transfer,* Vol. 6, pp. 131-136.

Eckert, E. R. G., and Drake, R. M., Jr., 1972, *Analysis of Heat and Mass Transfer,* 1st ed., McGraw-Hill, New York, p. 694.

Guidez, J., 1989, "Study of the Convective Heat Transfer in a Rotating Coolant Channel," ASME *Journal of Turbomachinery,* Vol. 111, pp. 43-50.

Harasgama, S. P., and Morris, W. D., 1988, "The Influence of Rotation on the Heat Transfer Characteristics of Circular, Triangular, and Square-Sectioned Coolant Passages of Gas Turbine Rotor Blades," ASME *Journal of Turbomachinery,* Vol. 110, pp. 44–50.

Hwang, G. J., and Jen, T. C., 1990, "Convective Heat Transfer in Rotating Isothermal Ducts," *Int. J. Heat Mass Transfer*, Vol. 33, No. 9, pp. 1817–1828.

Hwang, G. J., and Soong, C. Y., 1989, "Experimental Automation and Heat Transfer Measurement on a Rotating Thermal System," *Transport Phenomena in Thermal Control,* G. J. Hwang, ed., Hemisphere Publishing Corp., New York, pp. 375–388.

Iskakov, K. M., and Trushin, V. A., 1985, "The Effect of Rotation on Heat Transfer in the Radial Cooling Channels of Turbine Blades," *Thermal Engineering,* Vol. 32, No. 2, pp. 93–96.

Ito, H., and Nanbu, K., 1971, "Flow in Rotating Straight Pipes of Circular Cross Section," ASME *Journal of Basic Engineering,* Vol. 93, pp. 383–394.

Lokai, V. I., and Gunchenko, E. I., 1979, "Heat Transfer Over the Initial Section of Turbine Blade Cooling Channels Under Condition of Rotation," *Thermal Engineering,* Vol. 26, No. 2, pp. 93–95.

Lokai, V. I., and Limanskii, A. S., 1975, "Influence of Rotation on Heat Transfer in Radial Cooling Channels of Turbine Blades," *Izvestiya VUZ. Aviatsionnaya Tekhnika,* Vol. 18, No. 3, pp. 69–72.

Metzger, D. E., and Stan, R. L., 1977, "Entry Region Heat Transfer in Rotating Radial Tubes," AIAA Paper No. 77–189.

Mori, Y., Fukada, T., and Nakayama, W., 1971, "Convective Heat Transfer in Rotating Radial Circular Pipe (2nd Report)," *Int. J. Heat Mass Transfer,* Vol. 11, pp. 1807–1824.

Mori, Y., and Nakayama, W., 1968, "Convective Heat Transfer in Rotating Radial Circular Pipes (1st Report, Laminar Region)," *Int. J. Heat Mass Transfer,* Vol. 11, pp. 1027–1040.

Morris, W. D., 1977, "Flow and Heat Transfer in Rotating Coolant Channels," *High Temperature Turbines,* AGARD CP-229, pp. 38-1 to 38-14.

Morris, W. D., 1981, *Heat Transfer and Fluid Flow in Rotating Control Channels,* Wiley, Chichester, United Kingdom.

Morris, W. D., and Ayhan, T., 1979, "Observation on the Influence of Rotation on Heat Transfer in the Coolant Channel of Gas Turbine Rotor Blade," *Proc. Inst. Mech. Engrs.,* Vol. 193, pp. 303–311.

Schlichting, H., 1979, *Boundary Layer Theory,* 7th ed., McGraw-Hill, New York, pp. 335 & 714.

Shah, R. K., and London, A. L., 1978, *Advances in Heat Transfer, Supplement 1, Laminar Flow Forced Convection in Ducts,* Academic Press, New York, p. 214.

Siegel, R., 1985, "Analysis of Buoyancy Effect on Fully Developed Laminar Heat Transfer in a Rotating Tube," ASME JOURNAL OF HEAT TRANSFER, Vol. 107, pp. 338–344.

Skiadaressis, D., and Spalding, D. B., 1977, "Heat Transfer in Ducts Rotating Around a Perpendicular Axis," ASME Paper No. 77-WA/HT-39.

Soong, C. Y., and Hwang, G. J., 1990, "Laminar Mixed Convection in Radially Rotating Semiporous Channel," *Int. J. Heat Mass Transfer*, Vol. 33, No. 9, pp. 1805–1816.

Spezial, C. G., and Thangan, S., 1983, "Numerical Study of Secondary Flow and Roll-Cell Instabilities in Rotating Channel Flow," *J. Fluid Mech.,* Vol. 130, pp. 377–395.

Swanson, L. W., and Catton, I., 1987, "Enhancement Heat Transfer Due to Secondary Flows in Mixed Turbulent Convection," ASME JOURNAL OF HEAT TRANSFER, Vol. 109, pp. 943–946.

Wagner, J. H., Johnson, B. V., and Hajek, T. J., 1991, "Heat Transfer in Rotating Passages With Smooth Walls and Radial Outward Flow," ASME *Journal of Turbomachinery*, Vol. 113, pp. 42–51.

Woods, J. L., 1975, "Heat Transfer and Flow Resistance in a Rotating Duct System," Ph.D. Thesis, School of Applied Science, Univ. Sussex, United Kingdom.

Youset, W. W., and Tarasuk, J. D., 1982, "Free Convection Effects on Laminar Forced Convective Heat Transfer in a Horizontal Tube," ASME JOURNAL OF HEAT TRANSFER, Vol. 104, pp. 145–152.

Zysina-Molozhen, L. M., Dergach, A. A., and Kogan, G. A., 1976, "Experimental Investigation of Heat Transfer in a Radially Rotating Pipe," *Teplofizika Vysokikh Temperatur,* Vol. 14, No. 5, pp. 1108–1111.

Numerical Simulation of Thermal Transport Associated With a Continuously Moving Flat Sheet in Materials Processing

M. V. Karwe
Center for Advanced Food Technology,
Cook College, Rutgers University,
New Brunswick, NJ 08903

Y. Jaluria
Department of Mechanical and Aerospace Engineering,
Rutgers University,
New Brunswick, NJ 08903

The thermal transport that arises due to the continuous motion of a heated plate or sheet in manufacturing processes such as hot rolling, extrusion, continuous casting, and drawing is numerically investigated. The resulting temperature distribution in the solid is influenced by the associated flow in the ambient fluid, which is taken as stationary far from the moving surface, and is of particular interest in this work. A numerical study is carried out, assuming a two-dimensional, steady circumstance with laminar flow in the fluid. The full governing equations, including buoyancy effects, are solved, employing finite-difference techniques. The effect of various governing parameters, such as the Peclet number, Pe, the mixed convection parameter, Gr/Re^2, and the conductivity parameter, K_f/K_s, which determine the temperature and flow fields, is studied in detail. Also, the effect of the boundary conditions, particularly at the location of the emergence of the plate, on the downstream thermal transport is investigated. The penetration of the conductive effects, upstream of the point of emergence, is found to be significant. The effect of buoyancy is found to be more prominent when the plate is moving vertically upward than when it is moving horizontally. The appropriate boundary conditions and their imposition in the numerical scheme are discussed for a variety of practical circumstances.

Introduction

Thermal transport from a heated moving surface to a quiescent ambient medium is of interest in many manufacturing processes, such as hot rolling, extrusion, wire drawing, and continuous casting; see, for instance, Altan et al. (1979), Tadmor and Klein (1970), and Fisher (1976). In most cases, the moving material is at a temperature higher than that of the ambient medium and energy transfer occurs at the surface of the moving material. Generally, the thermal energy is supplied in an upstream thermal system, for instance, in a furnace, an oven, or an extruder. This is the main source of high temperatures in the moving material. Plastic deformation of the material and friction between the flowing material and the system surfaces also contribute to the heating. In the case of hot extrusion, a portion of the heat input may be lost to the die, with the rest being dissipated to the ambient medium.

Consider, for example, the schematic representation of a hot rolling process shown in Fig. 1. A heated metallic plate passes through multiple rolling stations. At each station, the thickness of the plate is reduced. In such a process, the distance separating any two consecutive rolling stations is dependent upon the allowable temperature drop that the material can undergo to remain above the recrystallization temperature. The typical longitudinal temperature variation within the sheet is also shown schematically in Fig. 1. If the temperature of the sheet drops below the recrystallization temperature, the microstructure of the material changes, resulting in properties that may be different from those desired. The required force for rolling will also be much larger. Therefore, knowledge of the thermal transport is necessary for the design and control of the process and of the relevant system. In the case of an extrusion process, for example, metal drawing, the extrudate is passed through a cooling trough. The length of the cooling bath can be calculated as a function of the properties of the material, the conditions of extrusion, i.e., speed, temperature, etc., and the temperature of the cooling fluid. With an increase in the extrusion speed in recent years, the amount of time spent by the material in the cooling fluid has become progressively smaller, leading to longer cooling troughs.

The transport process is time dependent at the onset of the process, when the material starts emerging from the die or furnace. However, at a longer time, it can generally be treated as a steady-state convective circumstance. This is due to the fact that, during the initial stages, after the onset of the process, the thermal field has not been established and the process is transient. At a longer time, the process generally attains a steady flow situation, because the end effects, stemming from energy losses at the end, do not affect the transport over much of the moving surface. For instance, in hot rolling, if the tip of the material is sufficiently far from the rollers, then the effect of end conduction on the flow and on the heat transfer in the region near the rollers in negligible (Jaluria and Singh, 1983). Therefore, a steady-state situation may be assumed over most of the material, once the end is far from the point of emergence.

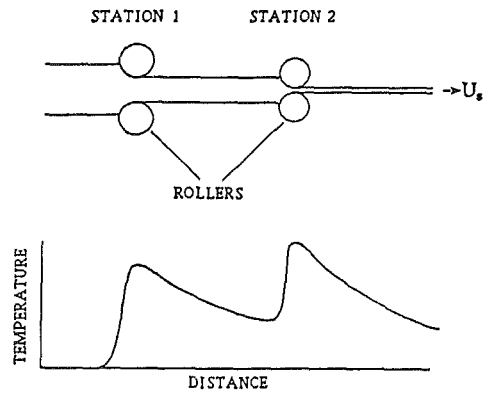

Fig. 1 Schematic of a hot rolling process and the corresponding temperature variation along the centerline of the plate or sheet

Contributed by the Heat Transfer Division and presented at the National Heat Transfer Conference, Houston, Texas, July 24–27, 1988. Manuscript received by the Heat Transfer Division April 22, 1990; revision received February 1, 1991. Keywords: Conjugate Heat Transfer, Materials Processing and Manufacturing Processes, Mixed Convection.

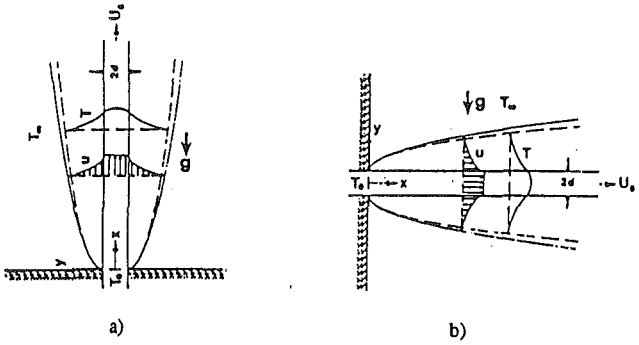

a) b)

Fig. 2 Flow geometry near the die showing the plate, the slot, and the walls: (*a*) plate moving vertically upward; (*b*) plate moving horizontally

The essential features of the two-dimensional flow induced by a long, continuously moving flat plate or sheet are shown schematically in Fig. 2, for both vertical and horizontal movement of the material. The plate moves out of the slot in an extrusion die or between the rollers, and proceeds at constant speed through an otherwise quiescent medium. Due to the viscous drag exerted on the ambient fluid near the surface of the plate, flow is induced in the fluid. The plate, if warmer than the fluid, also loses heat to the fluid. Depending upon the temperature difference between the plate and the fluid, a significant effect on the flow may arise due to thermal buoyancy. This effect will also depend upon the orientation of the plate with respect to gravity; see Jaluria (1980).

The resulting flow was assumed to be a boundary layer by Sakiadis (1961a, 1961b), who obtained a numerical solution for the flow field, using a similarity transformation. The velocity boundary layer was found to grow in the direction of the motion of the flat plate. Tsou et al. (1967) showed experimentally that such a flow indeed arises and studied its basic characteristics. Koldenhof (1963) solved the laminar boundary layer equations for flow on continuously moving flat plate and cylinders, using integral techniques. Fox et al. (1968) also followed an integral approach, but they included suction and injection at the surface in their model. Griffin and Thorne (1967) observed the growth of the thermal boundary layer over a continuously moving, flat belt. They also discussed the effect of the presence of walls near the slot on the heat transfer in this region. Tsou et al., as well as Griffin and Thorne, assumed the surface of the plate to be isothermal and the thickness to be small. However, in actual practice, the thickness of the moving plate is finite. The temperature distribution in the material can be important from the viewpoint of microstructure within the solid. This, in turn, determines the properties of the material of the plate after the thermal process. This consideration is particularly relevant to the continuous casting process, as discussed by Fisher (1976). In the case of glass fiber drawing, the temperature distribution within the fiber determines the solid–liquid interface and, thereby, the relevant properties of the fiber and also the maximum rate at which the fiber can be drawn.

Assuming typical values for the surface convective heat transfer coefficient, Jaluria and Singh (1983) obtained the temperature distribution in a moving plate and in a circular rod. They also considered transient effects and computed the time taken to attain steady-state conditions in the moving material. The length required to bring the temperature of the moving material to the ambient level was also determined. Such information is useful in the design of the thermal system. For instance, the optimum distance where the take-up spool should be located can be calculated. Chida and Katto (1976) have computed the flow and temperature fields for a plate of finite thickness, employing boundary layer approximations. Ignoring the effects of buoyancy, they obtained the downstream temperature variation at high values of Peclet number, Pe. In

Nomenclature

C = specific heat at constant pressure
2d = thickness of the moving flat sheet
g = magnitude of gravitational acceleration
Gr = Grashof number when surface radiation was not included = $g\beta(T_o - T_\infty)d^3/\nu_f^2$
h = surface heat transfer coefficient
K = thermal conductivity
Nu_x = local Nusselt number, Eq. (15)
p = pressure
Pe = Peclet number = $U_s d/\alpha_s$
Pr = Prandtl number = ν_f/α_f
Re = Reynolds number = $U_s d/\nu_f$
R_p = surface radiation parameter = $\epsilon\sigma d T_\infty^3/K_s$
t = physical time
T = local physical temperature
T_o = specified temperature at $x = 0$ or at $x = -x_b$
u = velocity component in x direction
U = dimensionless velocity component in x direction = u/U_s
U_s = velocity of the plate
v = velocity component in y direction
V = dimensionless velocity component in y direction = v/U_s
$\bar{v}$ = velocity vector = $\hat{i}u + \hat{j}v$
$\bar{V}$ = dimensionless velocity vector
x = coordinate distance along the length of the plate
X = dimensionless coordinate distance along the length of the plate = x/d
x_b = upstream conductive penetration distance where $T = T_o$
X_b = dimensionless x_b, $X_b = x_b/d$
y = coordinate in the fluid, perpendicular to the plate surface
Y = dimensionless coordinate in the fluid, perpendicular to the plate surface = y/d
y_s = coordinate inside the plate, normal to the plate surface
Y_s = dimensionless coordinate inside the plate, normal to the plate surface = y_s/d
α = thermal diffusivity = $K/\rho C$
β = coefficient of thermal expansion of the fluid
ϵ = emissivity of the plate surface
θ = dimensionless local temperature = $(T - t_\infty)/(T_o - T_\infty)$
$\hat{\theta}$ = dimensionless local temperature when surface radiation loss was included = T/T_∞
ν = kinematic viscosity
ρ = density
σ = Stefan–Boltzmann constant
ψ = stream function
Ψ = dimensionless stream function = $\psi/U_s d$
ω = vorticity
Ω = dimensionless vorticity = $\omega d/U_s$
∇, ∇_s = gradient operators
∇^*, ∇_s^* = dimensionless gradient operators

Subscripts

∞ = ambient medium
f = fluid
s = solid, i.e., plate material
c = centerline of the plate

these studies, thermal transport within the solid was included. However, axial conduction was ignored. Horvay (1961) calculated the temperature distribution in a slab moving from a chamber at one temperature to a chamber at another temperature, for a given surface heat transfer coefficient at the surface of the plate. Kuiken (1974) considered the cooling of a low-heat-resistance sheet moving through quiescent ambient fluid in which the transverse temperature variation within the sheet was neglected. Conditions under which such assumptions can be made were identified. There are a few other studies, such as those by Glicksman (1968), Bourne and Dixon (1971), and Kuiken (1975), which have considered the cooling of glass or polymer fibers by convection. Chen and Strobel (1980), Moutsoglou and Chen (1980), and Khader (1981) have all considered the effects of buoyancy in the case of a continuously moving flat surface. In some cases, the surface was assumed to be isothermal, and in others a uniform heat flux condition was applied. In all these cases, the boundary layer approximations were employed. More recently, Karwe and Jaluria (1988) have considered the effect of thermal buoyancy on the heat transfer from a plate of finite thickness to the ambient medium.

The present work considers the heat transfer from a continuously moving flat plate including the effects of buoyancy, thermal radiation, conduction within the plate, and non-boundary layer effects near the slot from which the plate emerges. The plate is assumed to move at a uniform speed U_s and to be maintained at a given uniform temperature far upstream of the point where it emerges from a slot, representing an extrusion die, furnace outlet, etc. Effects of thermal boundary conditions applied in the upstream region, on the downstream temperature variation, are investigated. Numerical calculations are carried out using a formulation based upon the full elliptic equations for laminar flow in the fluid and for conduction within the solid. The effects of thermal buoyancy, for the vertical and horizontal cases, are included. The effects of various dimensionless parameters such as the Peclet number, Pe, the ratio of the thermal conductivity of the fluid K_f to that of the material K_s, the Grashof number, Gr, and the radiation parameter, R_p, are considered. The relevance of the results obtained to the design of the systems for extrusion and rolling is also outlined in the paper.

Analysis

Consider the flow situation shown in Fig. 2, where a continuously moving plate emerges from the slot of, say, an extrusion die at a constant velocity U_s. The temperature of the plate is initially assumed to be at a uniform value of T_o at the slot, $x = 0$. The situations where the condition of uniform temperature is applied at some upstream distance x_b away from the origin, i.e., at $x = -x_b$, are discussed later. When the axial temperature gradients are large, for instance at small values of Peclet number Pe and near the slot (Karwe and Jaluria, 1988), the axial diffusion within the plate and the fluid must be taken into account. Therefore, the full governing equations, which are elliptic in nature, must be solved. The situations, in which the boundary layer approximations may be employed, are discussed in detail by Karwe and Jaluria (1986a, 1986b). The full governing equations, for the fluid and for the plate, including the transient terms, are:

For the fluid

$$\nabla \cdot \bar{v} = 0 \tag{1}$$

$$\frac{\partial \bar{v}}{\partial t} + \bar{v} \cdot \nabla \bar{v} = -\frac{\nabla p}{\rho_f} + \nu_f \nabla^2 \bar{v} - \bar{g}\beta(T - T_\infty) \tag{2}$$

$$\frac{\partial T}{\partial t} + \bar{v} \cdot \nabla T = \alpha_f \nabla^2 T \tag{3}$$

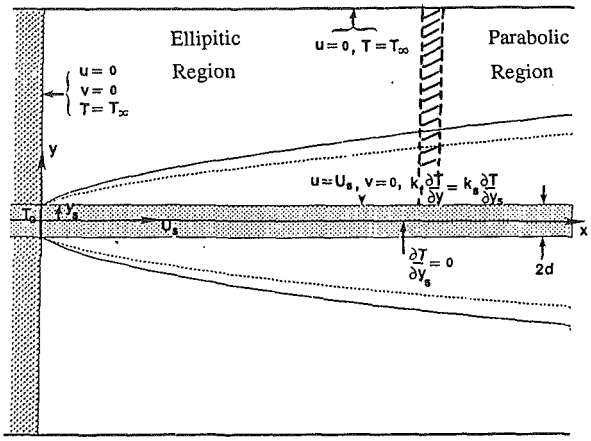

Fig. 3 Typical boundary conditions for a continuously moving material in a quiescent ambient medium

For the plate

$$\rho_s C_s \frac{\partial T}{\partial t} + \rho_s C_s U_s \frac{\partial T}{\partial x} = K_s \nabla_s^2 T \tag{4}$$

where the subscripts f and s refer to the fluid and the solid, respectively. The various symbols that appear in Eqs. (1)–(4) are given in the Nomenclature.

The boundary conditions on u, v, and T arise from the physical considerations and are shown in Fig. 3. These are due to the no-slip conditions at the moving surface of the plate and at the walls adjacent to the die, zero flow in the ambient medium far from the surface, temperature and heat flux continuity between the fluid and the solid at the surface of the plate, and symmetry about the x axis. When buoyancy effects are included, the symmetry condition at the axis of the plate is applicable only when the plate is moving vertically upward or when one surface is insulated, with this surface being taken as the x-coordinate axis. For further details on the boundary conditions, see Karwe (1987).

The pressure term in Eq. (2) is eliminated by taking the curl of the equation and, thus, transforming it into the vorticity transport equation. The stream function ψ and the vorticity ω are defined as

$$u = \frac{\partial \psi}{\partial y}, \quad v = -\frac{\partial \psi}{\partial x}, \text{ and } \omega = \frac{\partial v}{\partial x} - \frac{\partial u}{\partial y} \tag{5}$$

Equations (1)–(5) are nondimensionalized by employing the following transformations:

$$X = x/d, \quad Y = y/d, \quad Y_s = y_s/d, \quad \tau = tU_s/d, \quad U = u/U_s,$$

$$V = v/U_s, \quad \Psi = \psi/U_s d, \quad \Omega = \omega d/U_s, \quad \theta = \frac{T - T_\infty}{T_o - T_\infty},$$

$$\mathrm{Re} = U_s d/\nu_f, \quad \mathrm{Pe} = U_s d/\alpha_s, \quad \mathrm{Gr} = \frac{g\beta(T_o - T_\infty)d^3}{\nu_f^2}, \quad \mathrm{Pr} = \nu_f/\alpha_f \tag{6}$$

In the above equations d is the half plate thickness. In the earlier work by Karwe and Jaluria (1986, 1988), boundary layer formulation was employed wherein L, the distance along the x axis, was used as the length scale, instead of d. The dimensionless equations thus obtained, in the vorticity-stream function formulation, for a plate moving vertically upward, become:

For the fluid

$$\nabla^{*2}\Psi = -\Omega \tag{7}$$

$$\frac{\partial \Omega}{\partial \tau} + \bar{V} \cdot \nabla^* \Omega = \frac{1}{\mathrm{Re}}(\nabla^{*2}\Omega) - \frac{\mathrm{Gr}}{\mathrm{Re}^2}\frac{\partial \theta}{\partial Y} \tag{8}$$

$$\frac{\partial \theta}{\partial \tau} + \bar{V} \cdot \nabla^* \theta = \frac{1}{\mathrm{Re} \cdot \mathrm{Pr}}(\nabla^{*2}\theta) \tag{9}$$

For the case of a plate moving horizontally, the thermal buoyancy gives rise to a pressure gradient normal to the plate surface (Jaluria, 1980). This pressure gradient is aligned with the plate surface in the vertical case. Therefore, in the horizontal case, only Eq. (8) is changed, with the applicable equation for the upper surface being

$$\frac{\partial \Omega}{\partial \tau} + \overline{V} \cdot \nabla^* \Omega = \frac{1}{\mathrm{Re}} (\nabla^{*2} \Omega) + \frac{\mathrm{Gr}}{\mathrm{Re}^2} \frac{\partial \theta}{\partial X} \tag{10}$$

The energy equation for the plate is

$$\frac{\partial \theta}{\partial \tau} + \frac{\partial \theta}{\partial X} = \frac{1}{\mathrm{Pe}} (\nabla_s^{*2} \theta) \tag{11}$$

When radiative loss from the surface is also taken into account, the temperature may be nondimensionalized by T_∞. Because of the appearance of the T^4 terms in radiation, the nondimensionalization of temperature as done in Eq. (6), is inconvenient, as outlined by Jaluria (1982). The dimensionless temperature is denoted by $\hat{\theta} = T/T_\infty$ when radiative loss is included. Therefore, the boundary condition of $T = T_o$ at $x = 0$ or at $x = -x_b$ yields an additional parameter $\hat{\theta}_o = T_o/T_\infty$, which is obviously greater than unity. Assuming the walls at the slot and the environment to be black at T_∞, the boundary condition at the surface of the plate may be written as:

For $X > 0$, at $Y_s = 1$ or at $Y = 0$: $U = 1$, $V = 0$ and

$$\frac{\partial \hat{\theta}}{\partial Y_s} = \frac{K_f}{K_s} \frac{\partial \hat{\theta}}{\partial Y} - R_p(\hat{\theta}^4 - 1) \tag{12}$$

where R_p is termed the radiation parameter and is defined as $R_p = \epsilon \sigma d T_\infty^3 / K_s$. Similarly, other more complicated conditions for radiative transport may be simulated (Jaluria and Torrance, 1986).

The boundary condition of uniform temperature, i.e., $\theta = 1.0$ at $X = 0$, over the entire thickness of the plate, assumes that it is possible to maintain the temperature uniform over the entire cross section of the plate at the location where the plate emerges from the upstream heated region. However, in actual circumstances, the cooling effect occurring downstream often penetrates upstream of the point of emergence into the furnace or the heating zone. To simulate the conditions upstream, two cases were considered. These were adiabatic and uniform temperature conditions at the plate surface, for $X < 0$. The numerical value of the dimensionless distance X_b, where the temperature θ_o is specified, was varied. The distance X_b was not known a priori and thus was treated as a numerical parameter. The value of X_b was varied until the numerical results were largely unaffected by a further increase, as discussed later.

The boundary conditions, in terms of dimensionless quantities Ω and Ψ, were obtained by employing the appropriate transformation of the physical boundary conditions shown in Fig. 3; see Roache (1976). Note that additional boundary conditions downstream, in x, are needed because of the elliptic nature of the governing equations. This is achieved by dividing the physical domain under consideration in two regions: (I) an elliptic region near the slot or the die, and (II) parabolic region far downstream. Near the slot, the boundary layer approximations are not valid and, therefore, the full equations are solved in Region I. In the parabolic region, region II, which is taken far from the slot, the boundary layer approximations are employed. To solve for the elliptic region, boundary conditions are specified at the interface between the two regions numerically. This procedure is discussed in greater detail in the next section.

In the horizontal case, the problem is not symmetric about the x axis, since the buoyancy forces are directed away from the plate, in the flow, on the upper side, and are toward the plate on the lower side. We have considered only the upper half of the domain and applied the condition of symmetry at the centerline of the plate. The conditions under which this assumption is applicable are when the bottom surface of the plate is insulated, with the x axis being taken as this surface, or when the buoyancy forces are relatively small; see Karwe and Jaluria (1988). It should also be pointed out that in the horizontal case, it will not be possible to employ the boundary layer approximations far away from the point of emergence if the flow separates from the plate. However, if the plate has cooled sufficiently to ignore the effect of thermal buoyancy far downstream, boundary layer approximations may be employed, provided separation of the flow does not occur. This requires experimental information on similar flow situations (Jaluria, 1980). The discussion on the numerical procedure is given in the next section.

Numerical Solution

In all the cases considered here, the numerical calculations were carried out over one side of the plate. The extent of the domain in the y direction was chosen to be at least twice the estimated boundary layer thickness evaluated at the maximum value of X in the computational domain. This boundary layer thickness was calculated from the similarity solution for a uniform surface temperature situation. As mentioned before, the computational domain was divided into two regions, elliptic and parabolic. In the elliptic region, the transient vorticity transport Eq. (8) or (10) was solved along with the energy Eqs. (9) and (11) in the conservative form (Roache, 1976), for the flow and the plate, respectively, using the Alternate Direction Implicit (ADI) scheme of Peaceman and Rachford (1955). A second upwind differencing (Roache, 1976) was used for the convection terms in the x direction. The accuracy of such a scheme is of the order of $[\Delta X^2, \Delta Y^2, \Delta \tau^2]$. The Poisson Eq. (7) for the stream function was solved using the successive-over-relaxation (SOR) method (Carnahan et al., 1969). For the SOR method, optimum relaxation parameter was found to be close to 1.5, which gave the fastest convergence. At each time step, after advancing the solution for Eqs. (8), (9), and (11) by the ADI scheme, Eq. (7) was solved using the SOR method until the dimensionless stream function Ψ satisfied the following convergence criterion:

$$\max \left[\frac{\Psi_{i,j}^{k+1} - \Psi_{i,j}^{k}}{\Psi_{i,j}^{k+1}} \right] < 10^{-5} \tag{13}$$

where k stands for the kth iteration step and 10^{-5} is the chosen convergence parameter.

For the first time step in the elliptic region, the calculations are started with the ambient conditions at the interface between the two regions. Using the computed values of U, V, and θ at one grid point away from the interface, inside the elliptic region, the boundary layer equations are then solved in the remaining downstream region. The modified Crank-Nicolson scheme given by Karwe and Jaluria (1986b) is used to march in the downstream direction. Thus, the values of U, V, and θ are updated at the interface and are then used as boundary conditions for the calculations at the next time step in the elliptic region. Thus, the numerical procedure requires switching from one set of equations to the other set at the interface, at each time step. Such an approach has been shown to work successfully by Jaluria (1985).

The calculations were terminated when

$$\max \left[\frac{U_{i,j}^{n+1} - U_{i,j}^{n}}{U_{i,j}^{n+1}} \right] < 10^{-5} \text{ and } \max \left[\frac{\theta_{i,j}^{n+1} - \theta_{i,j}^{n}}{\theta_{i,j}^{n+1}} \right] < 10^{-5} \tag{14}$$

where n stands for the nth time step. This was taken as the steady-state situation. When the convergence parameter was reduced to values smaller than 10^{-5}, the solution essentially remained unchanged. The location of the interface between the elliptic and the parabolic regions was successively moved

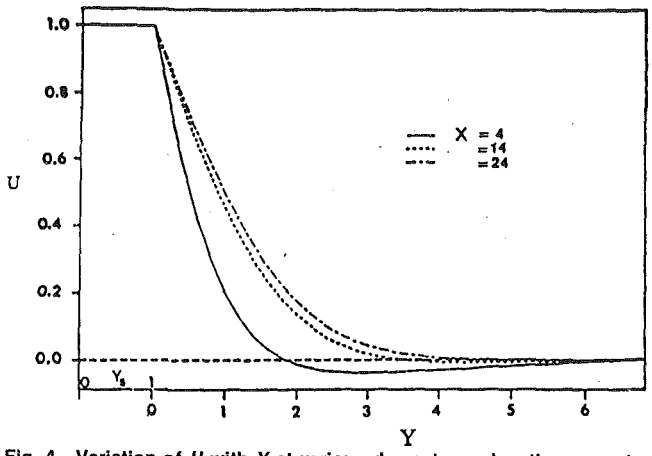

Fig. 4 Variation of U with Y at various downstream locations, as obtained from a solution of the full equations, for Pr = 0.7, Pe = 0.05, Re = 20.0, Gr = 0.0, K_f/K_s = 0.000127, R_p = 0

away from the wall until the final solution was only marginally affected by any further change. Similarly other numerical parameters like convergence criterion, grid size, etc., were varied. For further numerical details see Karwe (1987) and Karwe and Jaluria (1986b).

Numerical Results and Discussion

Numerical solutions to Eqs. (7)–(11) were obtained for wide ranges of governing parameters Pe, Re, R_p, K_f/K_s, and Gr/Re^2, the mixed convection parameter. The results for the solid materials such as glass, teflon, and aluminum, and the cooling fluids such as air and water, are presented later on. Some of the typical numerical results are presented here. Figure 4 shows the variation of the dimensionless velocity component U along the direction of the material motion with distance Y away from the surface at various downstream locations close to the die. These results are obtained from the solution of the full equations and indicate that the elliptic, or nonboundary layer, effects are important near the slot, as expected. These effects are found to decay downstream. Note that U even changes sign for $Y>2$ at smaller values of X, being $X=4$ in Fig. 4. This indicates that there is a small amount of flow toward the wall very close to the die. Far from the die, this effect dies down and the flow approaches the characteristics of a boundary layer flow over a continuously moving flat plate. This reverse flow very close to the die is a consequence of the large pressure gradients directed toward the corner, $X=Y=0$, due to the motion of the plate. This results in flow toward the corner yielding a weak reverse flow in the region. More details on this are given by Karwe (1988). Similar trends have been observed in the flow near the leading edge of a vertical plate in natural convection; see Jaluria (1980) and Jaluria and Agarwal (1986).

For the cases discussed above, the boundary condition θ = 1.0 was imposed at X = 0. As mentioned earlier, the effect of thermal diffusion penetrates upstream and, therefore, the relevant boundary condition must be applied at $X=-X_b$, where the value of X_b must be increased numerically until the results become essentially independent of a further increase. Figure 5 shows the centerline temperature variation for the circumstance when the plate surface is assumed to be adiabatic in the region $-X_b \le X \le 0$. The values of the parameters in Fig. 5 were chosen arbitrarily just to demonstrate the effect of X_b. The value of $\hat{\theta}_o$ is specified at a uniform value of $\hat{\theta}$ = 2.0 at $X=-X_b$, for $0 \le Y_s \le 1$. The final solution is dependent upon $\hat{\theta}_o$. Figure 5 shows the temperature distributions for different values of X_b. One can see that the value of X_b has a significant effect on the temperature distribution. The trends seen in Fig. 5 indicate that as the value of X_b is increased, the temperature

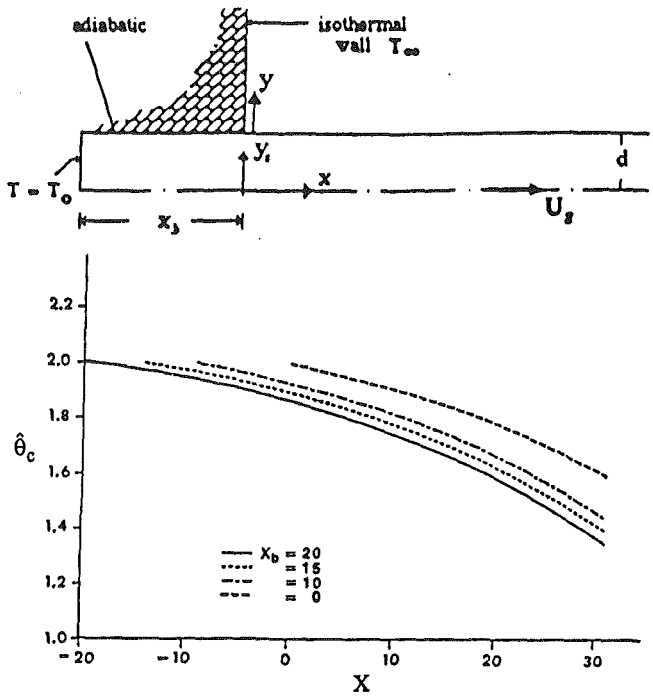

Fig. 5 Centerline temperature variation for the cases when the temperature $\hat{\theta}_o$ is specified at different locations $X=-X_b$ upstream. The plate surface is assumed to be adiabatic in the region $-X_b \le X \le 0$. Here, Pr = 0.7, Pe = 0.05, Re = 20.0, Gr = 0.0, K_f/K_s = 0.000127, R_p = 1.0 × 10^{-4}, $\hat{\theta}$ = 2.0.

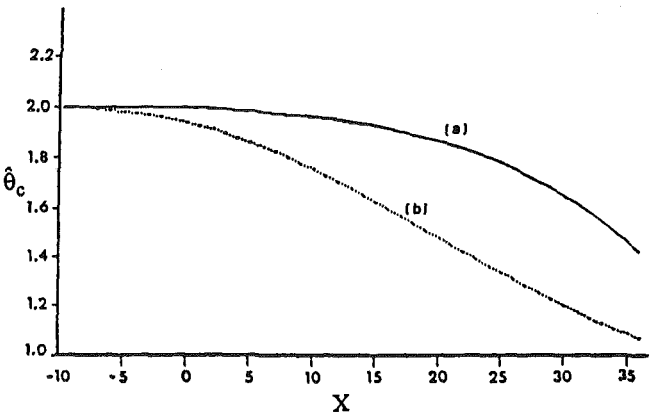

Fig. 6 Effect of the adiabatic and isothermal surface boundary conditions in the region $-X_b \le X \le 0$, on the downstream axial temperature variation: (a) $\hat{\theta} = \hat{\theta}_o$ at Y_s = 1, $-X_b \le X \le 0$; (b) $\partial\hat{\theta}/\partial Y_s = 0$ at Y_s = 1, $-X_b \le X \le 0$; the parametric values are: Pr = 0.7, Pe = 0.25, Re = 20.0, Gr = 0.0, K_f/K_s = 0.000127, R_p = 1.0 × 10^{-4}, $\hat{\theta}_o$ = 2.0

distribution approaches a definite variation for a given set of parameters. This variation, therefore, applies for $X_b \to \infty$ and is representative of the situation where the material emerges from a long heated zone or extruder. When radiation loss is neglected, the condition θ_o = 1.0 is applied at $X=-X_b$ and, again, X_b is increased until the results become largely independent of the value of X_b. It was found that $X_b>10$ was generally adequate to simulate conditions upstream. Several such results were obtained. However, only a few typical results are shown here for conciseness. Also, it is important to consider finite values of X_b for practical situations, as shown in Fig. 5 and discussed below.

To illustrate the effect of different boundary conditions at the plate surface in the upstream region $-X_b \le X \le 0$, numerical results are presented in Fig. 6 for the adiabatic and isothermal boundary conditions discussed earlier. It is seen that, for the isothermal boundary condition, the centerline temperature of the plate is higher everywhere than that for the

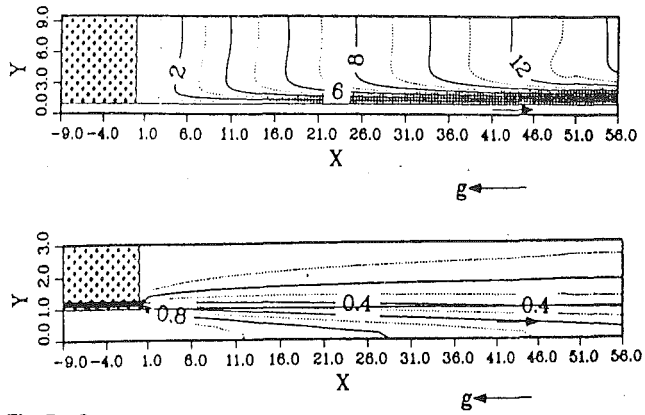

Fig. 7 Computed streamlines and isotherms for a teflon plate moving in air at Pe = 150.0, Pr = 0.7, K_f/K_s = 0.13, Gr = 1000.0, Re = 0.9, R_p = 0

corresponding adiabatic condition, implying that the back conduction effects are smaller in the isothermal case. In the adiabatic case, no heat is supplied or lost at the top and bottom surfaces in the upstream region. In the isothermal case, the temperature is maintained at a fixed value of T_o at $X = 0$ and on the plate surface in the upstream region. To achieve this, more heat must be supplied to maintain the fixed temperature, as compared to the adiabatic case. This results in higher downstream temperature levels in the isothermal case. The results shown in Figs. 5 and 6 are important from the point of view of design of an actual system. In many practical circumstances involving a furnace or an oven, the isothermal boundary condition is more appropriate. However, a longer length is required in this case, to bring the temperature level to a desired value. We have discussed only two of the typical boundary conditions that arise, depending upon the process under consideration. In some cases, for instance, in a process involving radiative or electrical heating, a uniform heat flux condition at the plate surface may be applied upstream of the slot. The type of boundary condition will influence the calculated length of the cooling trough, distance between the die and the take-up spool, etc. In the following results, the adiabatic boundary condition was used in the upstream region.

Typical computed streamlines and isotherms are shown in Fig. 7 for a heated teflon plate being cooled in air. The streamlines show that the ambient fluid flows toward the corner at $X = 0$. For $X > 0$, the fluid flows toward the plate surface, and then along the surface. The boundary layer thickness is seen to grow along the direction of motion. However, the isotherms indicate a significant axial temperature variation, especially within the solid plate. The presence of a high concentration of isotherms within the plate shows strong cooling effects. This is because for air and teflon, a higher value of the ratio K_f/K_s is obtained than that for air and steel, for example. Figure 8 shows the computed streamlines and isotherms for the cases of (*a*) aluminum plate moving in water and (*b*) glass plate moving in water, for a given plate velocity U_s, inlet temperature T_o, and ambient temperature T_∞. It can be seen from Fig. 8 that the conductivity parameter K_f/K_s strongly influences the thermal field, especially in the solid. The effect of downstream cooling on the temperature field upstream is seen to be significant in the case of aluminum. Strong temperature gradients are seen to occur in the solid, near the slot. Also, the temperature variation across the plate, i.e., along the y direction, is more uniform in the case of aluminum as compared to that in glass, whereas the isotherms indicate that the variation of temperature across the solid–liquid interface is less steep for the case of glass as compared to that of aluminum.

These results indicate that the temperature levels within the solid vary significantly, depending upon the properties of the

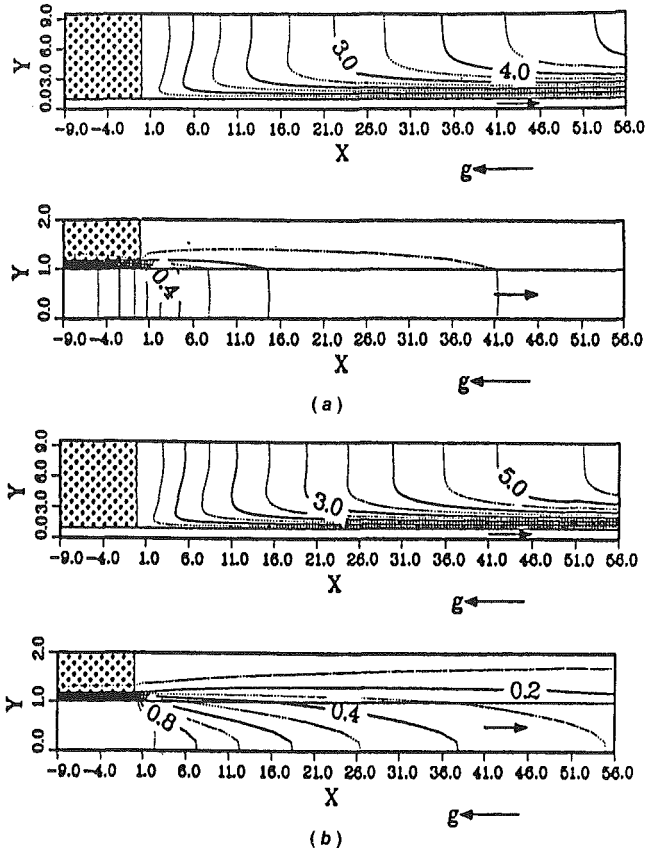

Fig. 8 Computed streamlines and isotherms for two different plate materials: (*a*) aluminum and water case at Pr = 7.0, Pe = 0.16, Gr = 1000, Re = 13.6, K_f/K_s = 0.0029, R_p = 0; (*b*) glass and water case at Pr = 7.0, Pe = 31.1, Gr = 1000, Re = 13.6, K_f/K_s = 0.62, R_p = 0

solid and the fluid. For example, for the case of water and aluminum strong temperature gradients exist near the surface of the plate and near the slot. This sharp cooling downstream may result in strong property variations over the plate. Surface hardening may occur at high rates of cooling, although it may not always be desirable. Also, the strong temperature gradients may give rise to large residual thermal stresses within the cooled material, leading to reduction in material ductility and machinability.

The parameter that determines the importance of thermal buoyancy is Gr/Re^2, as seen from the dimensionless governing equations. In addition, the orientation of the plate with respect to gravity determines whether buoyancy aids or opposes the flow induced by the plate motion. Results are presented here for two important cases. These are: (1) plate moving vertically upward, and (2) plate moving horizontally. In the first case, buoyancy forces aid the induced flow for heated surfaces and oppose it for cooled surfaces. In the second case, buoyancy forces are normal to the plate motion and generate pressure differences along the y direction; see Jaluria (1980). Thus, the flow is affected indirectly by the buoyancy through the pressure effects. Therefore, the resulting effect is expected to be smaller than that for the vertical, aiding circumstance. In Fig. 9, the numerical results for the two cases are compared in terms of the axial and transverse temperature distributions, and of the axial component of velocity U. As seen in Fig. 9(*a*, *c*), the temperature level in the vertical case is lower than that in the horizontal one. Figure 9(*b*) shows that the U velocity component in the fluid is higher for a plate moving vertically upward. Higher values of velocity in the flow indicate a higher rate of heat removal from the plate and, thus, lower temperature levels. This is, of course, the aiding circumstance. Buoyancy effects decrease the heat transfer rate for opposing natural

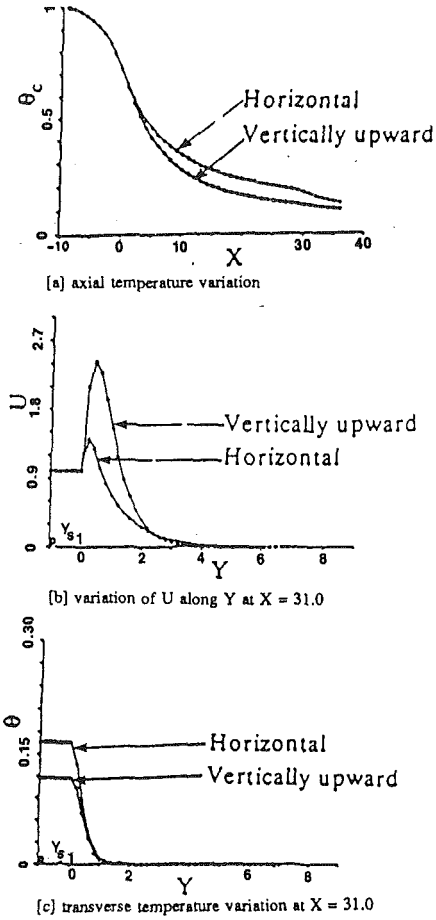

Fig. 9 Comparison between the results for a plate moving vertically upward and those for a plate moving horizontally; Pe = 0.25, Re = 25.0, Gr/Re^2 = 8.0, Pr = 7.0, K_f/K_s = 0.0127, R_p = 0.0

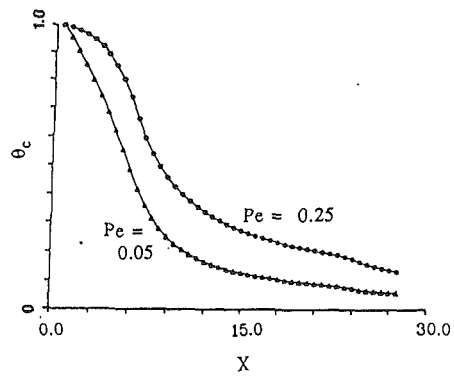

Fig. 10 Axial temperature variation for a plate moving horizontally at two different values of the Peclet number, Pe = 0.05 and 0.25, for Re = 25.0, Pr = 7.0, Gr/Re^2 = 8.0, K_f/K_s = 0.0127, R_p = 0.0

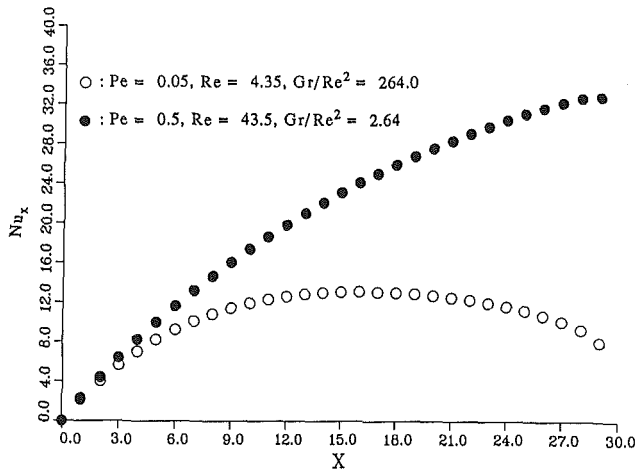

Fig. 11 Variation of the local Nusselt number Nu_x for the surface of a 5-mm-thick aluminum plate moving vertically upward in water at different values of the plate velocity U_s: ○ U_s = 1.5 mm/s; ● U_s = 15.0 mm/s

and forced flow situations, for instance, for a heated plate moving vertically downward (Merkin, 1969). Separation may also arise in this case, as observed qualitatively by Karwe (1987). However, the numerical analysis is much more complicated and was not carried out here for this circumstance. Some of these opposing mixed convection flow situations have been studied experimentally by Karwe (1987).

Figure 10 shows the axial temperature variation at two different values of the Peclet number Pe, for the horizontal case. As expected, at smaller values of Pe, conduction effects penetrate to a large upstream distance. Again, as mentioned earlier, temperature symmetry is assumed at the axis of the plate. This is done to restrict the computation to the upper region only. This assumption is valid when the buoyancy effects are small and also when the lower surface is insulated. Otherwise, the two regions on either side of the plate are coupled and must be considered together. The results for the horizontal case are important because in many of manufacturing processes, mentioned earlier, the material moves horizontally, generally for ease of handling. In a few circumstances, such as gravity casting, the material moves vertically downward. In continuous casting and in hot rolling, the heated solid material moves on a conveyor belt, which often provides an essentially insulated surface.

Figure 11 shows the variation of the local Nusselt number Nu_x with the downstream distance X. The Nusselt number Nu_x is defined as

$$Nu_x = \frac{h \cdot x}{K_f} = \frac{\left(-\frac{\partial \theta}{\partial Y}\right)_{Y=0} \cdot X}{\theta_{Y=0}} \qquad (15)$$

where h is the local heat transfer coefficient calculated at the surface of the plate and is given by $h = -K_f \partial T/\partial y|_{y=0}/(T_{y=0} - T_\infty)$. In Fig. 11, the curve represented by solid circles corresponds to a 5-mm-thick aluminum sheet moving at 15 mm/s in water and the curve shown by hollow circles corresponds to the case when the velocity of the sheet is about 1.5 mm/s. All other physical conditions are the same for both curves. As shown in Fig. 11, the value of the local Nusselt number, Nu_x, is smaller everywhere at the lower velocity. The value of Nu_x, as defined by Eq. (15), goes through a maximum for the case when the plate velocity was 1.5 mm/s. For the case when the plate velocity was 15 mm/s, this maximum occurred farther downstream. However, caution is needed in the interpretation of these results because eventually the plate will lose all its energy to the ambient medium and the temperature of the plate should approach the ambient temperature. As a result, $(T_s - T_\infty) \to 0$ far downstream, and the surface heat transfer rate approaches zero. For the values of Nu_x shown in Fig. 11, the definition given by Eq. (15) was applied for values of dimensionless surface temperature $\theta > 0.05$. At higher velocity, the induced flow in the fluid increases, which in turn results in an increase in the rate of heat removal. However, this increase in heat transfer rate is smaller than the corresponding increase in the convection due to the motion of the plate. Also, at higher velocity, less time is available for cooling up to a given distance. At lower velocity, the induced flow velocities decrease and natural convection effects dominate. The final temperature levels within the plate are lower because less energy is brought in by the plate motion. This indicates that in a given process, if the velocity of rolling or extrusion is increased, longer lengths would be required to cool the plate

to a certain level. Numerical results presented here have been compared, in some instances, with experimental results; see Karwe (1987) and Karwe and Jaluria (1991). These results have been found to be in fairly good agreement with the experimental results. However, further experimental work is needed on different flow configurations and materials. Some relevant investigations have recently been carried out by Kang (1990).

Conclusions

A detailed analytical and numerical study of the heat transfer and fluid flow arising from a continuously moving plate, relevant to several manufacturing processes such as hot rolling and extrusion, has been carried out. Numerical solutions for the flow and temperature fields, particularly in the vicinity of the die or a furnace from which the plate emerges, have been obtained. The temperature within the material is mainly governed by the thermal conductivity parameter K_f/K_s and the Peclet number Pe. At high values of K_f/K_s, strong temperature gradients within the plate are seen to occur. The cooling effects downstream of the die penetrate into the upstream region inside the die or furnace. The effects of various boundary conditions on the temperature in the upstream region are also considered. The effect of thermal buoyancy in the downstream thermal transport is found to be more significant when a heated plate is moving vertically upward than when it is moving horizontally, as expected. Larger values of the local Nusselt number Nu_x are observed at a higher velocity of the plate.

The results are valuable in the evaluation of various effects such as buoyancy, radiation, plate speed, temperature level, etc., on the overall thermal transport process. They are useful in determining the length of the system needed to cool the plate to a desired temperature level. For example, if the maximum allowable temperature of the material for it to be handled or further processed is known, then the minimum distance needed to cool the material to the desired temperature can be obtained from the computed axial temperature decay, for a given system. Also, if a limitation on the total distance is given, the results can be employed to determine whether additional cooling arrangements are needed or if the choice of the coolant, say water, is satisfactory to achieve a desired temperature level. In addition, the variation in material characteristics arising due to temperature gradients within the plate can be controlled, as well as estimated. Several such questions arise in the design of practical systems related to rolling and extrusion processes for which the results presented here are of interest and importance.

The results presented here are valid as long as the flow is laminar and does not separate from the plate surface, and the temperature levels are below the boiling point of the cooling medium. In the presence of strong buoyancy in the horizontal case, the flow may separate from the plate. Also, in the analysis presented here, the width of the plate was assumed to be infinite. In practical situations, due to the finite width of the plate, the edge effects may become important, especially in the horizontal case. Also, if the plate motion is vertically downward, in which case the buoyancy-induced flow is in the opposite direction of the plate motion, the flow may separate or become turbulent. These aspects have not been considered here and are presently being studied.

Acknowledgments

The authors acknowledge the financial support provided by the National Science Foundation, under Grant No. CBT-88-03049, for this work.

References

Altan, T., Oh, S., and Gegel, H., 1979, *Metal Forming Fundamentals and Applications*, American Society of Metals, Metals Park, OH.

Bourne, D. E., and Dixon, H., 1971, "The Cooling of Fibers in the Forming Process," *Int. J. Heat Mass Transfer*, Vol. 24, pp. 1323–1332.

Carnahan, B., Luther, H. A., and Wilkes, J. O., 1969, *Applied Numerical Methods*, Wiley, New York.

Chen, T. S., and Strobel, F. A., 1980, "Buoyancy Effects in Boundary Layer Flow Adjacent to a Continuous Moving Horizontal Flat Plate," ASME JOURNAL OF HEAT TRANSFER, Vol. 102, pp. 170–172.

Chida, K., and Katto, Y., 1976, "Conjugate Heat Transfer of Continuously Moving Surfaces," *Int. J. Heat Mass Transfer*, Vol. 19, pp. 461–470.

Fisher, E. G., 1976, *Extrusion of Plastics*, Wiley, New York.

Fox, V. G., Erickson, L. E., and Fan, L. T., 1968, "Methods for Solving Boundary Layer Equations for Moving Continuous Flat Surfaces With Suction and Injection," *AIChE Journal*, Vol. 14, pp. 726–736.

Glicksman, L. R., 1968, "Cooling of Glass Fibers," *Glass Technology*, Vol. 9, No. 5, pp. 131–138.

Griffin, J. F., and Thorne, J. L., 1967, "On Thermal Boundary Layer Growth on Continuous Moving Belts," *AIChE Journal*, Vol. 13, No. 6, pp. 1210–1211.

Horvay, G., 1961, "Temperature Distribution in a Slab Moving From a Chamber at One Temperature to a Chamber at Another Temperature," ASME JOURNAL OF HEAT TRANSFER, Vol. 83, pp. 391–402.

Jaluria, Y., 1980, *Natural Convection Heat and Mass Transfer*, Pergamon Press, New York.

Jaluria, Y., 1982, "Mixed Convection in a Wall Plume," *Computers and Fluids*, Vol. 10, pp. 95–104.

Jaluria, Y., and Singh, A. P., 1983, "Temperature Distribution in a Moving Material Subjected to Surface Energy Transfer," *Comp. Meth. Appl. Mech. Eng.*, Vol. 41, pp. 145–157.

Jaluria, Y., 1985, "Interaction of Natural Convection Wakes Arising From Thermal Sources on a Vertical Surface," ASME JOURNAL OF HEAT TRANSFER, Vol. 107, pp. 883–892.

Jaluria, Y., and Agarwal, R., 1986, "Computational Study of Nonboundary Layer External Natural Convection Flows," *Proceedings of the International Conference on Computational Mechanics*, May 26–29, Springer-Verlag, Tokyo.

Jaluria, Y., and Torrance, K. E., 1986, *Computational Heat Transfer*, Hemisphere, New York.

Kang, B. H., 1990, "Conjugate Heat Transfer From a Continuously Moving Material and From an Isolated Heat Source," Ph.D. thesis, Department of Mechanical and Aerospace Engineering, Rutgers University, New Brunswick, NJ.

Karwe, M. V., and Jaluria, Y., 1986a, "Thermal Transport From Heated Moving Surfaces," ASME JOURNAL OF HEAT TRANSFER, Vol. 108, No. 4, pp. 728–733.

Karwe, M. V., and Jaluria, Y., 1986b, "Numerical Simulation of the Conjugate Heat Transfer Process From a Heated Moving Surface," *Proceedings of the International Conference on Computational Mechanics*, May 26–29, Springer-Verlag, Tokyo.

Karwe, M. V., 1987, "Thermal Transport Between a Continuously Moving Heated Plate and a Quiescent Ambient Medium," Ph.D. thesis, Department of Mechanical and Aerospace Engineering, Rutgers University, New Brunswick, NJ.

Karwe, M. V., and Jaluria, Y., 1988, "Fluid Flow and Mixed Convection Transport From a Plate In Rolling and Extrusion Processes," ASME JOURNAL OF HEAT TRANSFER, Vol. 110, No. 3, pp. 655–661.

Karwe, M. V., and Jaluria, Y., 1991, "Experimental Investigation of Thermal Transport From a Heated Moving Plate," *Int. J. Heat Mass Transfer*, to appear.

Khader, M. S., 1981, "Transient Laminar Mixed Convection From a Moving Vertical Plate," ASME Paper No. 81-HT-40.

Koldenhof, E. A., 1963, "Laminar Boundary Layer on a Continuous Flat and Cylindrical Surfaces," *AIChE Journal*, Vol. 9, No. 3, pp. 411–418.

Kuiken, H. K., 1974, "The Cooling of Low-Heat-Resistant Sheet Moving Through a Fluid," *Proc. R. Soc. London, A*, Vol. 341, pp. 233–252.

Kuiken, H. K., 1975, "The Cooling of Low-Heat-Resistance Cylinder Moving Through a Fluid," *Proc. R. Soc. London, A*, Vol. 346, pp. 23–35.

Merkin, J. H., 1969, "The Effect of Buoyancy Forces on the Boundary-Layer Flow Over a Semi-infinite Vertical Flat Plate in a Uniform Free Stream," *J. Fluid Mech.*, Vol. 35, Part 3, pp. 439–450.

Moutsoglou, A., and Chen, T. S., 1980, "Buoyancy Effects in Boundary Layers on Inclined, Continuous, Moving Sheets," ASME JOURNAL OF HEAT TRANSFER, Vol. 102, pp. 371–372.

Peaceman, D. W., and Rachford, H. H., Jr., 1955, "The Numerical Solution of Parabolic and Elliptic Partial Differential Equations," *J. Soc. Indust. Applied Mathematics*, No. 3, Vol. 1, pp. 28–41.

Roache, P. J., 1976, *Computational Fluid Dynamics*, Hermosa Publishers, New Mexico.

Sakiadis, B. C., 1961a, "Boundary Layer Behavior on Continuous Solid Surfaces: I. Boundary Layer Equations for Two-Dimensional and Axisymmetric Flow," *AIChE Journal*, Vol. 7, No. 1, pp. 26–28.

Sakiadis, B. C., 1961b, "Boundary Layer Behavior on Continuous Solid Surfaces: II. The Boundary Layer on Continuous Flat Surface," *AIChE Journal*, Vol. 7, No. 2, pp. 221–225.

Tadmor, Z., and Klein, I., 1970, *Engineering Principles of Plasticating Extrusion*, Polymer Science and Engineering Series, Van Nostrand Reinhold Company, New York.

Tsou, F. K., Sparrow, E. M., and Goldstein, R. J., 1967, "Flow and Heat Transfer in the Boundary Layer on a Continuous Moving Surface," *Int. J. Heat Mass Tranfer*, Vol. 10, pp. 219–235.

D. Naylor

J. M. Floryan

J. D. Tarasuk

The Department of Mechanical Engineering,
The University of Western Ontario,
London, Ontario, Canada N6A 5B9

A Numerical Study of Developing Free Convection Between Isothermal Vertical Plates

Steady two-dimensional laminar free convection between isothermal vertical plates including entrance flow effects has been numerically investigated. The full elliptic forms of the Navier-Stokes and energy equations are solved using novel inlet flow boundary conditions. Results are presented for Prandtl number Pr = 0.7, Grashof number range $50 \leq Gr_b \leq 5 \times 10^4$, and channel aspect ratios of L/b = 10, 17, 24. New phenomena, such as inlet flow separation, have been observed. The results cast doubt on the validity of previous elliptic solutions. Comparisons with the approximate boundary-layer results show that a full elliptic solution is necessary to get accurate local quantities near the channel entrance.

Introduction

Natural convection in a vertical channel has been studied extensively by many authors. Elenbaas (1942) conducted the first comprehensive experimental study, which has served as a benchmark for most subsequent work. Due to modern applications to the cooling of printed circuit boards, there has been a resurgence of interest in studies of vertical channels.

Bodia and Osterle (1962) obtained the first numerical solution of developing natural convective flow in an isothermal channel using boundary-layer approximations. The boundary-layer form of the governing equations is parabolic and requires the assumption of channel inlet conditions. Bodia and Osterle (1962) assumed a uniform velocity profile, a uniform temperature profile, and ambient pressure at the channel inlet; overall heat transfer results were in good agreement with the experimental data of Elenbaas (1942). Since this original study, their basic methodology has been widely used to solve free convective channel flows for various boundary conditions (Aung et al., 1972; Miyatake and Fujii, 1972; Dalbert et al., 1981; Oosthuizen, 1984). The most significant and widely adopted improvement to this method has been to approximate the pressure drop due to the fluid acceleration at the channel inlet (Aihara, 1973). Although the overall heat transfer from these parabolic solutions generally agrees with experimental data, the accuracy of the local temperature, velocity, and pressure information has not been shown.

Very few numerical solutions to free convection in the vertical channel have been carried out without using the boundary-layer approximations. Kettleborough (1972) and Nakamura et al. (1982) have presented data from finite difference solutions to the full elliptic problem. However, these results are limited to two values of Grashof number and are in poor agreement in many aspects.

This paper presents the results of a solution to the full elliptic Navier-Stokes and energy equations over a moderately wide range of parameters. A new method for handling inflow boundary conditions is presented that more realistically represents the entrance flow characteristics. Comparisons of the full elliptic and approximate boundary-layer results for the isothermal channel show the applicability and limitations of boundary-layer-type solutions. Calculations for air (Pr = 0.7) were carried out using the finite element code FIDAP (Fluid Dynamics International, 1989).

Contributed by the Heat Transfer Division for publication in the JOURNAL OF HEAT TRANSFER. Manuscript received by the Heat Transfer Division May 22, 1990; revision received December 14, 1990. Keywords: Natural Convection, Numerical Methods.

Problem Formulation

The geometry analyzed is shown in Fig. 1. Heat is transferred by natural convection from two isothermal vertical plates of length L with spacing $2b$. The flow in the channel is assumed to be steady, laminar, incompressible, and two dimensional. With these assumptions, and assuming all thermophysical properties to be constant, except density in the buoyancy term of the y-momentum equation (Boussinesq approximation), the governing equations are:

$$\partial u/\partial x + \partial v/\partial y = 0 \tag{1}$$

$$\rho(u\partial u/\partial x + v\partial u/\partial y) = -\partial p/\partial x + \mu(\partial^2 u/\partial x^2 + \partial^2 u/\partial y^2) \tag{2}$$

$$\rho(u\partial v/\partial x + v\partial v/\partial y) = -\partial p/\partial y + \rho g\beta(T - T_o) + \mu(\partial^2 v/\partial x^2 + \partial^2 v/\partial y^2) \tag{3}$$

$$\rho c_p(u\partial T/\partial x + v\partial T/\partial y) = k(\partial^2 T/\partial x^2 + \partial^2 T/\partial y^2) \tag{4}$$

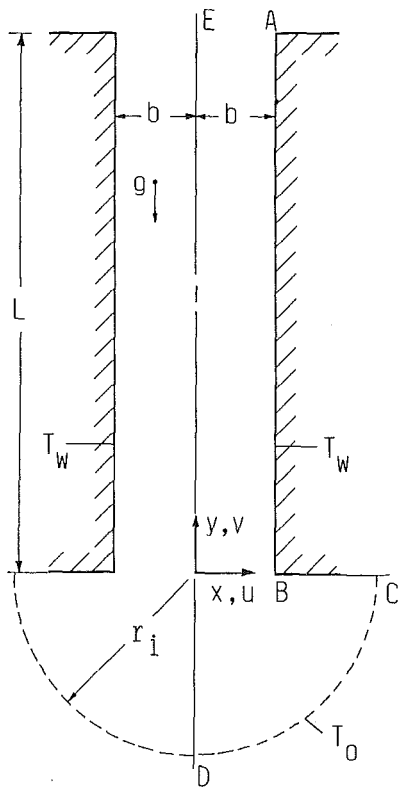

Fig. 1 Heat transfer model and coordinate system

The pressure (p) in the momentum equations is defined as the local channel-to-ambient pressure difference.

Methods of Solution

Equations (1)–(4) have been solved without further approximation. This will be referred to as the *elliptic solution*. Equations (1)–(4) have also been solved neglecting the second derivatives in the streamwise direction ($\partial^2/\partial y^2$); this is the standard boundary-layer approximation. The boundary-layer solution for the isothermal vertical channel has been reproduced in this study so that detailed comparisons could be made with the full elliptic solution. An explicit forward marching finite difference procedure, as described by Aung et al. (1972), was used to solve the parabolic form of the equations and need not be described here. The solution to the approximate equations will be referred to as the *parabolic solution*.

The boundary conditions, nondimensionalization, and method of solution for the elliptic equations are described below.

Elliptic Solution

The computational domain for the elliptic solution is shown in Fig. 1. Because of symmetry about the channel centerline, only half of the flow field was solved. In dimensional form, the centerline, wall, and channel exit boundary conditions are:

$$\partial T/\partial x = \partial v/\partial x = u = 0, \text{ for } -r_i \le y \le L, \quad x = 0 \text{ (DE)} \tag{5}$$

$$T = T_w, \quad u = v = 0, \text{ for } 0 \le y \le L, \quad x = b \text{ (AB)} \tag{6}$$

$$\partial T/\partial y = u = v = 0 \text{ for } b \le x \le r_i, \quad y = 0 \text{ (BC)} \tag{7}$$

$$\partial T/\partial y = \partial u/\partial y = \partial v/\partial y = 0, \text{ for } 0 \le x \le b, \quad y = L \text{ (EA)} \tag{8}$$

Boundary conditions corresponding to fully developed flow were used at the upper boundary (EA). Although this condition could affect the flow in the channel, it was the best assumption available short of extending the domain to consider the plume region outside the channel. The suitability of the exit boundary conditions will be discussed further when the results are presented.

In the present study, the channel inlet flow boundary conditions (CD) are nontrivial and have been given special consideration. The approach described here is entirely different from that used in previous elliptic solutions. Kettleborough (1972) and Nakamura et al. (1982) used boundary conditions that physically correspond to fully developed flow entering a channel with a large sudden expansion. Kageyama and Izumi (1979) used a similar approach to solve free convection between nonparallel plates.

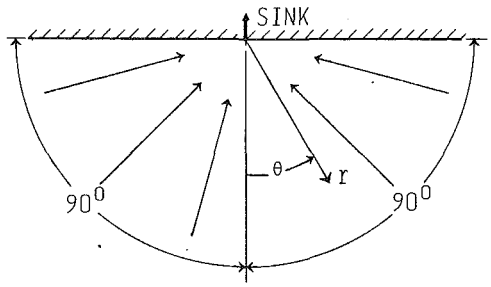

Fig. 2 Jeffrey-Hamel flow geometry applicable to the present study

Ramanathan et al. (1988) attempted to solve the inlet and outlet boundary condition problem (for constant heat flux plates) by enclosing the channel in a very large isothermal enclosure. This approach was only partially successful. Despite very large computational domains, enclosure effects were not entirely eliminated and corrections had to be applied for the preheating of the air entering the channel. The inlet boundary conditions used in the present case are based on Jeffrey–Hamel flow as shown in Fig. 2. Jeffrey–Hamel flow is a similarity solution of isothermal flow caused by the presence of a source or sink at the point of intersection of two walls. Solution details are given by Batchelor (1967). In the present study, converging flow caused by a sink and a wall half angle of 90 deg is of specific interest. The flow is purely radial and in cylindrical coordinates (r, θ) has the following form:

$$v_r = F(\theta)/r \tag{9}$$

$$v_\theta = 0 \tag{10}$$

where v_r and v_θ denote the radial and tangential velocity components.

The radial stress component for Jeffrey–Hamel flow is:

$$\sigma_{rr} = -p + 2\mu\partial v_r/\partial r = -p - 2\mu F(\theta)/r^2 \tag{11}$$

At large r ($r \to \infty$), far from the sink, the pressure approaches the ambient pressure ($p = 0$), v_r approaches zero, and the radial stress goes to zero. Hence, tangential velocity, radial

Nomenclature

b = half channel width
c_p = constant pressure specific heat
$F(\theta)$ = angular dependence of Jeffrey–Hamel flow
g = gravitational acceleration
Gr = Grashof number = $g\beta(T_w - T_o)b^3/\nu^2$
h = average heat transfer coefficient = $(H/L)/(T_w - T_o)$
h_y = local heat transfer coefficient = $(k\partial T/\partial x|_{x=b})/(T_w - T_o)$
H = rate of heat transfer from the half channel
k = thermal conductivity
L = channel length
Nu_y = local Nusselt number
Nu_{m1} = average Nusselt number defined by equation (26)
Nu_{m2} = average Nusselt number defined by equation (27)
p, P = pressure and dimensionless pressure
Pr = Prandtl number
Q = dimensionless half channel flow rate
r, R = radius and dimensionless radius
r_i, R_i = dimensional and dimensionless inlet domain radius
Ra* = Rayleigh number (modified) = GrPrb/L
T, T^* = temperature and dimensionless temperature
T_b^* = dimensionless bulk temperature at channel exit ($Y = L/b$)
T_o = ambient temperature
T_w = channel wall temperature
u, U = x velocity component and dimensionless x velocity component
U_{ref} = reference velocity scale
v, V = y velocity component and dimensionless y velocity component
v_r, v_θ = radial and tangential component of velocity
V_r, V_θ = dimensionless radial and tangential velocity components
x, y = Cartesian coordinates
X, Y = dimensionless Cartesian coordinates
α = thermal diffusivity
β = volumetric expansion coefficient
θ = cylindrical coordinate
μ = dynamic viscosity
ν = kinematic viscosity
ρ = density
σ_{rr} = radial stress component
ψ = dimensionless stream function

stress, and temperature inlet boundary conditions can be specified as:

$$v_\theta = \sigma_{rr} = 0, \quad T = T_o \text{ as } r \to \infty \tag{12}$$

On this physical basis, the above boundary conditions were imposed on a finite semicircular boundary (CD). For a sufficiently large inlet domain radius (r_i), the flow at the boundary (CD) will approach Jeffrey–Hamel flow. That is, with increasing radius (r_i), the channel will induce flow at the boundary that asymptotically approaches that produced by a point sink.

Now for the elliptic solution we introduce the following dimensionless quantities:

$$U = u/U_{\text{ref}}, \quad V = v/U_{\text{ref}} \tag{13}$$

$$X = x/b, \quad Y = y/b, \quad R = r/b \tag{14}$$

$$T^* = (T - T_o)/(T_w - T_o), \quad P = (pb)/(\mu U_{\text{ref}}) \tag{15}$$

where $U_{\text{ref}} = (\alpha \text{Pr}(\text{Gr})^{1/2})/b$, and $\text{Gr} = (g\beta(T_w - T_o)b^3)/\nu^2$. Using the above quantities, the governing equations become:

$$\partial U/\partial X + \partial V/\partial Y = 0 \tag{16}$$

$$\text{Gr}^{1/2}(U\partial U/\partial X + V\partial U/\partial Y) = -\partial P/\partial X + (\partial^2 U/\partial X^2 + \partial^2 U/\partial Y^2) \tag{17}$$

$$\text{Gr}^{1/2}(U\partial V/\partial X + V\partial V/\partial Y) = -\partial P/\partial Y + \text{Gr}^{1/2}T^* + (\partial^2 V/\partial X^2 + \partial^2 V/\partial Y^2) \tag{18}$$

$$\text{Pr Gr}^{1/2}(U\partial T^*/\partial X + V\partial T^*/\partial Y) = (\partial^2 T^*/\partial X^2 + \partial^2 T^*/\partial Y^2) \tag{19}$$

The dimensionless boundary conditions are:

$$\partial T^*/\partial X = \partial V/\partial X = U = 0, \text{ for } -R_i \le Y \le L/b, \quad X = 0 \text{ (DE)} \tag{20}$$

$$T^* = 1, \quad U = V = 0, \text{ for } 0 \le Y \le L/b, \quad X = 1 \text{ (AB)} \tag{21}$$

$$\partial T^*/\partial Y = U = V = 0, \text{ for } 1 \le X \le R_i, \ Y = 0 \text{ (BC)} \tag{22}$$

$$\partial T^*/\partial Y = \partial U/\partial Y = \partial V/\partial Y = 0, \text{ for } 0 \le X \le 1, \ Y = L/b \text{ (EA)} \tag{23}$$

and

$$V_\theta = 0, \ -P + 2\partial V_r/\partial R = 0, \ T^* = 0, \text{ on the semicircular boundary (CD)} \tag{24}$$

where $V_r = v_r/U_{\text{ref}}$, $V_\theta = v_\theta/U_{\text{ref}}$. The inlet boundary conditions (CD) are not valid for low Rayleigh number. At low Rayleigh number the fluid moves with very low velocity and becomes heated by conduction far upstream from the channel inlet. The buoyancy force affects the flow at the boundary and the conditions for the existence of Jeffrey–Hamel flow are no longer satisfied. From examination of stream function and isotherm contours in the inlet region, a conservative lower limit for which these boundary conditions are acceptable was found to be $\text{Gr} \approx 50$ ($\text{Ra}^* \approx 1.458$) for $L/b = 24$ and $\text{Pr} = 0.7$ (see Fig. 6).

The local and average Nusselt numbers, Nu_y and Nu_{m1}, are defined by:

$$\text{Nu}_y = \frac{h_y b}{k} = \left.\frac{\partial T^*}{\partial X}\right|_{X=1} \tag{25}$$

$$\text{Nu}_{m1} = \frac{hb}{k} = \frac{b}{L}\int_0^{L/b} \left.\frac{\partial T^*}{\partial X}\right|_{X=1} dY \tag{26}$$

The average Nusselt number (Nu_{m2}) was also computed using a heat balance as:

$$\text{Nu}_{m2} = \left[\text{Gr}^{1/2}\text{Pr}\,\frac{b}{L}\int_0^1 VT^* dX\right]_{Y=L/b} - \left[\text{Gr}^{1/2}\text{Pr}\,\frac{b}{L}\int_0^1 VT^* dX\right]_{Y=0} + \int_0^1 \left.\frac{\partial T^*}{\partial Y}\right|_{Y=0} dX \tag{27}$$

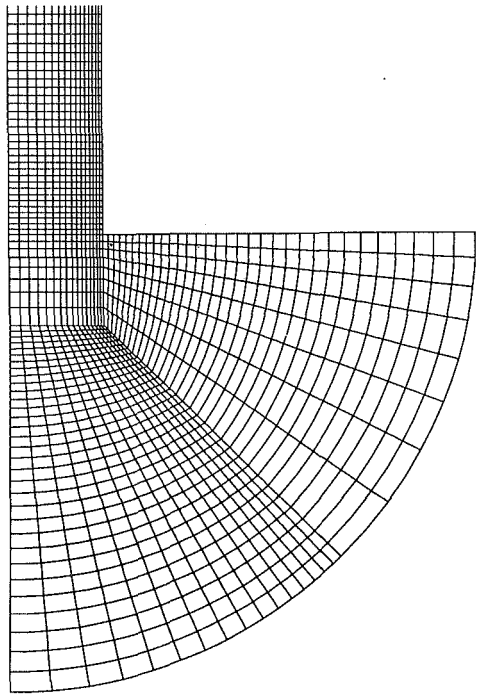

Fig. 3 Finite element mesh in the channel entrance region, $L/b = 24$, $R_i = 5$

Table 1 Partial results from grid tests (for $\text{Gr} = 10^4$, $\text{Ra}^* = 291.7$, $L/b = 24$)

Number of nodes	Inlet domain radius, R_i	Average Nusselt numbers Nu_{m1}	Average Nusselt numbers Nu_{m2}	Flow rate, Q
8465	3	2.346	2.4055	2.084
9249	4	2.346	2.4046	2.076
10,033	5	2.345	2.4040	2.073
14,369	5	2.357	2.4046	2.073

Special care was taken when computing the last two integrals of Nu_{m2}. These integrals were actually computed along a surface slightly outside the channel entrance, in order to avoid the singularity at the inlet corner. These two integrals are largest at low Ra^*. For the lowest Rayleigh number considered ($\text{Ra}^* = 1.458$), it was found that the heat conducted out of the channel entrance was equal to the heat convected back into the channel. Hence, Nu_{m2} was computed by:

$$\text{Nu}_{m2} = \left[\text{Gr}^{1/2}\text{Pr}\,\frac{b}{L}\int_0^1 VT^* dX\right]_{Y=L/b} \tag{28}$$

The dimensionless half channel flow rate was calculated by:

$$Q = \left[\int_0^1 V dX\right]_{Y=L/b} \tag{29}$$

The dimensionless bulk temperature at the channel exit was calculated by:

$$T_b^* = \left[\int_0^1 VT^* dX\right]_{Y=L/b} \Big/ \left[\int_0^1 V dX\right]_{Y=L/b} \tag{30}$$

Figure 3 is a close-up view of the finite element mesh in the channel entrance region (for $L/b = 24$, $R_i = 5$). Nine-node quadrilateral elements were used. Local interpolation functions for these elements are quadratic for velocity and temperature, and linear for pressure. The penalty formulation was used for pressure.

Tests were conducted on several grids to ensure that the results were independent of both grid density and the size of

Table 2 Comparison of major data with other elliptic solutions for Gr = 1250, Pr = 0.733, L/b = 10

	Average Nusselt numbers		Flow rate, Q	Exit bulk temperature, T_b^*
	Nu_{m1}	Nu_{m2}		
Kettleborough (1972)	2.75	2.38	2.079	0.442
Nakamura et al. (1982)	1.814	1.877	1.358	0.533
Present elliptic solution	1.802	1.867	1.439	0.501
Present parabolic solution	1.900	1.899	1.478	0.499

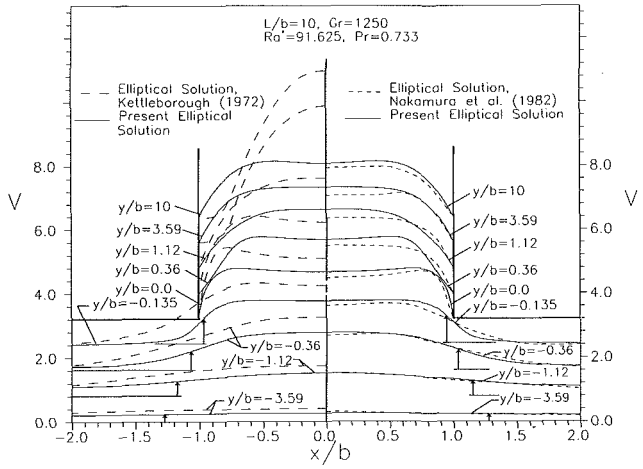

Fig. 4 Comparison of the streamwise velocity (V) profiles from the present elliptic solution with the work of Kettleborough (1972) and Nakamura et al. (1982)

the inlet computational domain (R_i). For all cases, the results were most grid sensitive at the upper limit of Grashof number (Gr = 10^4 for L/b = 24). Table 1 shows partial results from these tests. For the first three cases in Table 1, the grid density was held roughly constant and the inlet domain radius was varied. The last case in Table 1 shows the effect of increasing grid density with R_i = 5.

Based on the grid test results, the standard grid for L/b = 24 had inlet domain radius of R_i = 5 and 10,033 nodes (2,456 elements). With this grid, the flow rate (Q) is accurate to much better than 1 percent. For all cases, Nu_{m1} was 2–3 percent lower than Nu_{m2}. Nu_{m2} shows less grid dependence than Nu_{m1} (which tends toward Nu_{m2} with increasing grid density) and is a better estimate of the channel average Nusselt number. From this comparison, an estimate of the average Nusselt number (Nu_{m2}) accuracy is 3 percent. Local quantities, such as local Nusselt number, are much less accurate near the channel entrance than the exit. The local Nusselt number distributions along the channel wall (Ra* = 291.7, L/b = 24) for grids with 10,033 and 14,369 nodes (R_i = 5) had a maximum difference of about 3 percent near the leading edge. At the channel exit the difference becomes negligible. Despite these slight differences, the lower grid density was selected for subsequent runs since it required significantly less computing resources. For all runs, the convergence criteria were set such that the calculations were carried to four-digit accuracy.

Discussion of Results

There are two elliptic solutions (using finite difference methods) for the isothermal channel in the literature: those of Kettleborough (1972) and Nakamura et al. (1982) (hereafter, Nakamura). Each considered only two Grashof numbers (Gr = 12.5, 1250), an aspect ratio L/b = 10, and a Prandtl number Pr = 0.733. The results from these studies are in poor agreement in many aspects. Table 2 shows a comparison of the

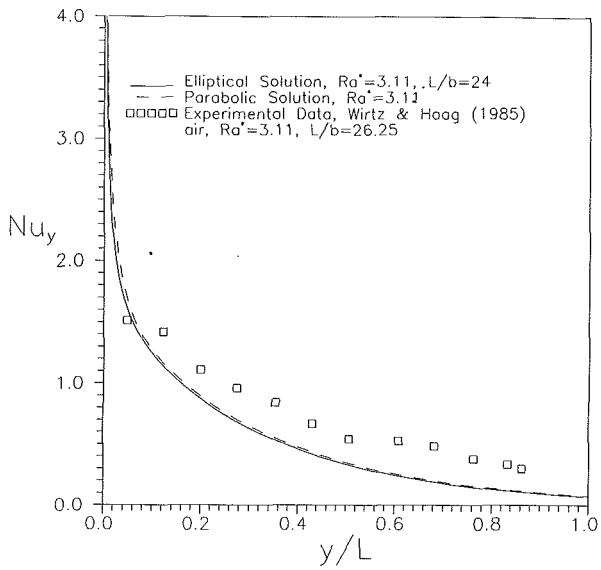

Fig. 5 Comparison of the local Nusselt number distributions with the experimental data of Wirtz and Haag (1985); see text for discussion of discrepancy

present results with these two solutions for Gr = 1250. The present work is in closer agreement with Nakamura than with Kettleborough. However, the close agreement with the average Nusselt number predicted by Nakamura is somewhat coincidental since the temperature and velocity profiles are not in close agreement.

Figure 4 shows a comparison of the streamwise velocity profiles from the present elliptic solution with those predicted by Kettleborough and by Nakamura. Again, the present work is closer to that of Nakamura, although significant disagreement does exist. Kettleborough predicts reverse flow in the channel with fluid being drawn far into the channel from the channel exit. This was not found in the present study nor in the study by Nakamura. Temperature profiles from the present elliptic solution (not shown) also do not agree with either of these previous studies.

A comparison has also been made of the centerline pressure distribution presented by Nakamura with the present solutions (Gr = 1250, L/b = 10). For the parabolic solution the inlet pressure is assumed to be $p = -\rho v_o^2/2$, where v_o is the assumed uniform inlet velocity. The pressure distribution presented by Nakamura is many times lower than that found by either of the present methods. The channel inlet pressure (y/b = 0.0) is reported by Nakamura to be about five times lower than that of the parabolic solution, whereas the centerline inlet pressure found by the present elliptic solution (P = −37.4) is only about 3 percent different from the parabolic solution (P = −38.6). Nakamura does not explain the large discrepancy between their inlet pressure and that predicted by Bernoulli's equation. Hence, it is likely that the present results more closely represent the actual channel pressure.

Figure 5 shows a comparison of the present data with the experimental local Nusselt distribution measured in air by Wirtz and Haag (1985). The experimental data correspond to Ra* = 3.11, L/b = 26.25. It should be noted that the aspect ratio for the elliptic solution is slightly different (L/b = 24) and the parabolic results are independent of aspect ratio. Although the general trends of the local heat transfer distributions are the same, both the numerical predictions are much lower than the experimental data, particularly near the channel exit. It is suspected that this may be due to experimental error, since the average Nusselt number given by Wirtz and Haag is about 20 percent higher than the experimental values given by Elenbaas (1942). Unfortunately, these were the only experimental data

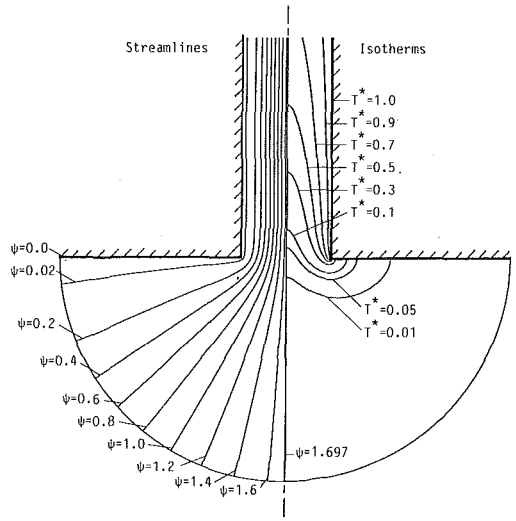

Fig. 6 Channel inlet streamline and isotherm contours from the elliptic solution for Gr = 50, L/b = 24, Pr = 0.7 (Ra* = 1.458)

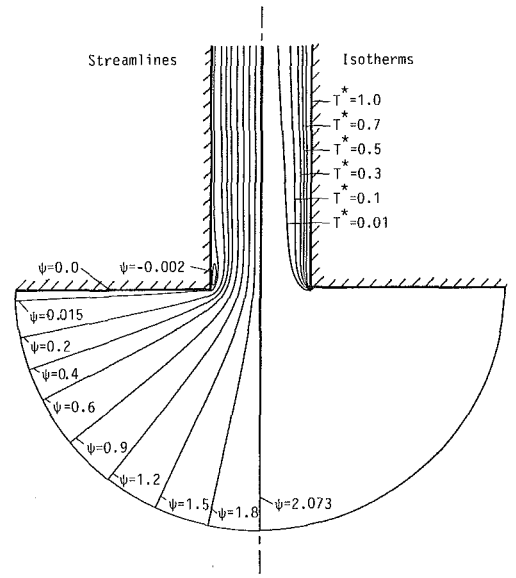

Fig. 7 Channel inlet streamline and isotherm contours from the elliptic solution for Gr = 10^4, L/b = 24, Pr = 0.7 (Ra* = 291.7)

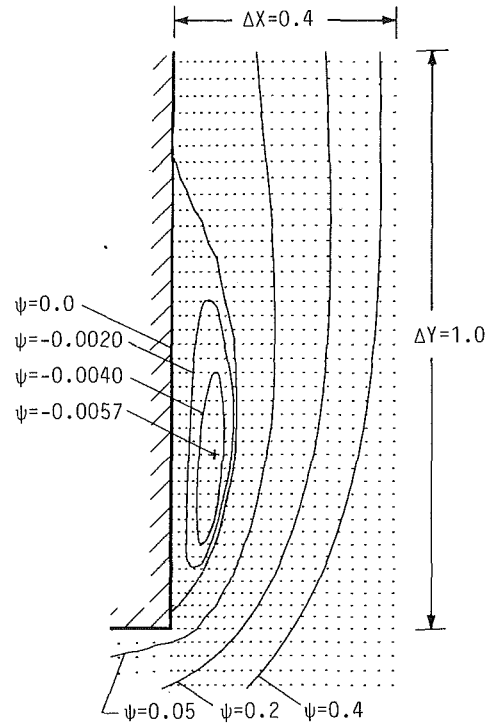

Fig. 8 Close-up view of the separated flow region for Gr = 10^4, L/b = 24, Pr = 0.7 (Ra* = 291.7)

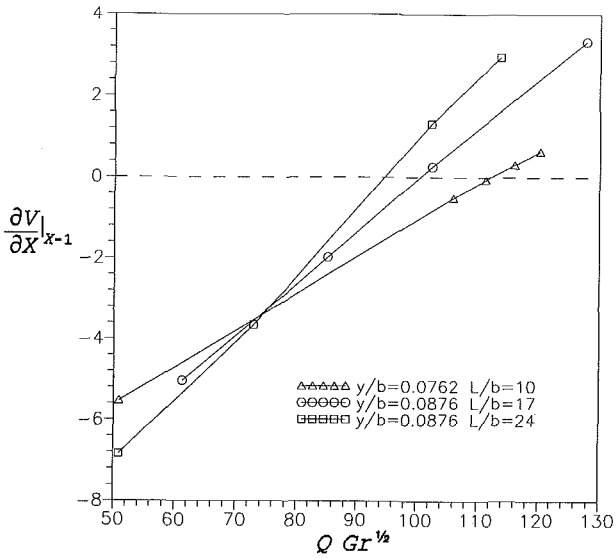

Fig. 9 Streamwise velocity gradient at the wall in the separated flow region versus Q $Gr^{1/2}$

available in the literature for the symmetrically heated isothermal channel.

Figures 6 and 7 show the streamline and isotherm contours of the inlet region for Gr = 50×10^4, L/b = 24 (Ra* = 1.458, 291.7). At low Rayleigh number the induced velocities are low and the flow enters the channel without separating. Also, due to the low velocities, the nonzero isotherms extend well outside the channel inlet and preheat the incoming air. At high Rayleigh number, fluid velocities are sufficiently high that the flow separates from the wall and there is a small eddy on the channel wall near the leading edge. A close-up view of the separated flow region is shown in Fig. 8. Dots are shown at each nodal point to illustrate the grid density in the vicinity of the eddy. The fluid re-attachment occurs at about y/b = 0.78, as determined from the wall shear stress distribution. Additional elliptic solutions were obtained for aspect ratios of L/b = 10, 17 so that the onset of inlet flow separation could be correlated. For L/b = 10, separation occurs at Gr ≈ 8200, Ra* ≈ 570 as determined from the wall shear stress distribution. For L/b = 17, separation occurs at Gr ≈ 2900, Ra* ≈ 120 and for L/b = 24, separation occurs at Gr ≈ 1700, Ra* ≈ 50. Figure 9 shows an attempt to correlate the onset of separation ($\partial V/\partial X|_{X=1} = 0$) with dimensional channel flow rate. (Note that dimensional channel flow rate is proportional to $Q\mathrm{Gr}^{1/2}$.) Velocity gradients at the wall were taken at several values of y/b near the channel entrance and the results were insensitive to the specific location chosen. Data at only one value of y/b (for each aspect ratio) are shown for clarity. This parameter is moderately successful in predicting separation; separation occurs within a 20 percent range of $Q\mathrm{Gr}^{1/2}$ for all three channel aspect ratios. Buoyancy effects can explain the slight delay of separation for channels with lower aspect ratios. Low aspect ratio channels require higher temperatures to induce the same flow rate as longer channels. The higher temperatures cause

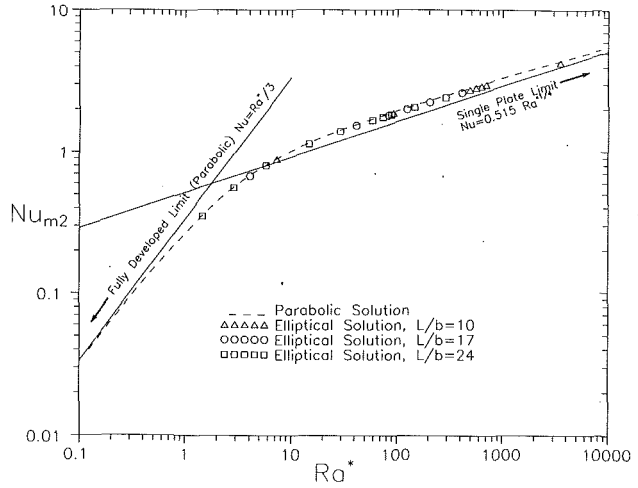

Fig. 10 Comparison of average Nusselt number results from the present elliptic and parabolic solutions

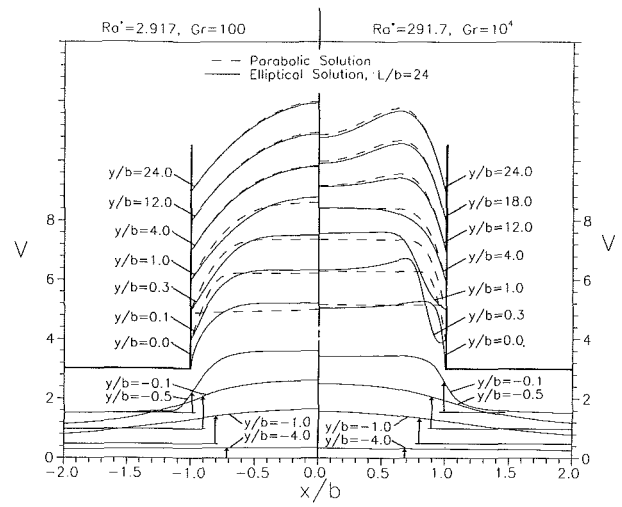

Fig. 11 Comparison of streamwise velocity (V) profiles from the present elliptic and parabolic solutions for Ra* = 2.917 and Ra* = 291.7

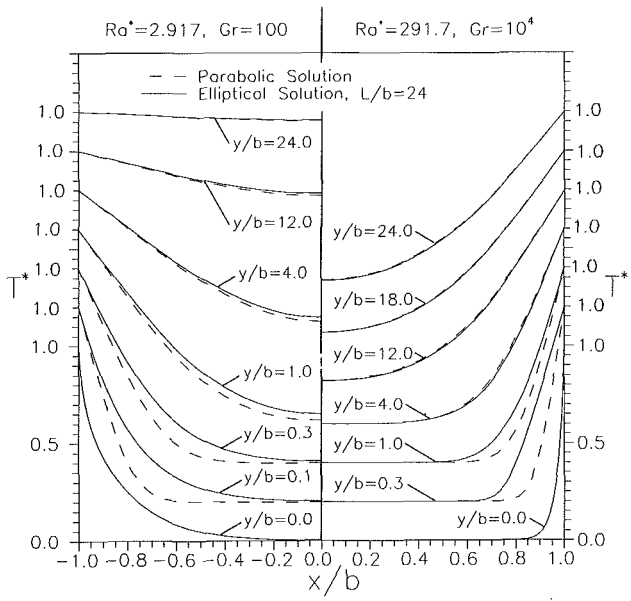

Fig. 12 Comparison of temperature profiles from the present elliptic and parabolic solutions for Ra* = 2.917 and Ra* = 291.7

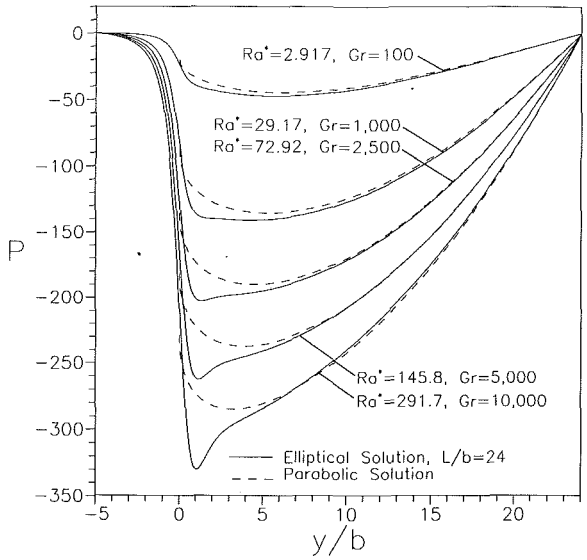

Fig. 13 Comparison of centerline pressure distributions from the present elliptic and parabolic solutions

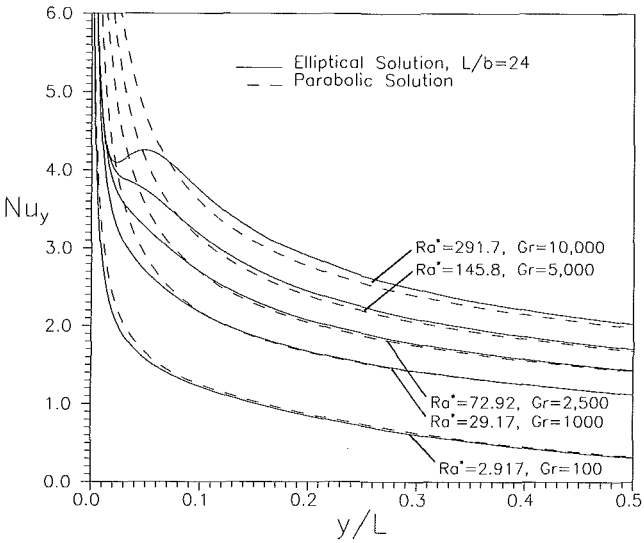

Fig. 14 Comparison of local Nusselt number distributions from the present elliptic and parabolic solutions

larger buoyancy forces at the wall, which act to oppose separation. Hence, slightly greater flow rates are required to induce separation in short channels.

The behavior of average Nusselt number (Nu_{m2}) with Rayleigh number for both of the present solutions is displayed in Fig. 10. The asymptotic limits of the parabolic solution for low and high Ra* are also shown. At low Ra*, the flow approaches the fully developed limit (Bodia and Osterle, 1962). At high Ra* the single isolated plate limit (Ostrach, 1953) is approached. The parabolic and elliptic solutions are in excellent agreement at low Ra* and at higher Ra* they differ by about 3 percent. Also, Aihara (1973) has shown that the experimental data of Elenbaas (1942) and Aihara (1963) are in good agreement with the parabolic solution over the range given in Fig. 10. Hence, the close agreement of the two solutions gives confidence in the present elliptic results.

Figures 11 and 12 show comparisons of the developing velocity and temperature profiles for Ra* = 2.917 and Ra* = 291.7. For the elliptic solution (L/b = 24), the developing velocity profiles outside the channel are also presented; for the parabolic solution the assumed inlet profiles (y/b = 0) are

uniform. In both figures, the parabolic profiles differ substantially from the elliptic profiles near the entrance. However, these differences diminish as the flow proceeds toward the channel exit. Exit velocity and temperature profiles (y/b = 24) are in close agreement. Considering the large differences near the channel entrance, it is somewhat surprising that the overall heat transfer and induced flow rate are in good agreement. These figures clearly show how insensitive the parabolic solution is to the assumed inlet conditions. It is also clear from these figures that derivative boundary conditions used at the channel exit for the elliptic solution are quite acceptable at $Ra^* = 2.917$; however, at $Ra^* = 291.7$ the velocity and temperature profiles are still developing and these conditions are less suitable.

The channel centerline pressure distributions for various values of Rayleigh number are displayed in Fig. 13. At low Rayleigh number, the parabolic and elliptic solutions are in fair agreement throughout the channel. However, at higher Rayleigh number there is a large difference near the channel entrance, which is due to entrance flow effects. At high Ra^* the fluid separation at the entrance has a "venturi" effect on the mainstream flow and causes a local reduction in pressure. Since the parabolic solution does not detect the inlet flow separation, it predicts higher pressures. Again, contrary to results presented by Nakamura et al. (1982), it was found that the inlet pressure assumption ($p = -\rho v^2/2$) used in the parabolic solution is a reasonable approximation over a wide range of Rayleigh number.

The fluid separation at the channel entrance has a profound effect on local heat transfer. Figure 14 shows the local Nusselt number (Nu_y) distributions in the lower half of the channel for various values of Rayleigh number. At $Ra^* = 2.917$, the fluid does not separate, and the local heat transfer distributions predicted by the parabolic and elliptic solutions are in good agreement. At higher Reynolds number, the discrepancy near the leading edge becomes large due to the fluid separation. The recirculating eddy predicted by the elliptic solution has an insulating effect on the channel wall. For $Ra^* = 291.7$, the elliptic solution shows a pronounced local minimum in Nu_y near the entrance. At this location, the parabolic solution predicts a local Nusselt number that is 65 percent higher than the elliptic solution. It must be kept in mind that the present elliptic solution is limited to two-dimensional flow. Following the onset of separation, three-dimensional effects may become significant, particularly at high Rayleigh number.

Conclusions

The full elliptic forms of the Navier–Stokes and energy equations have been solved using inlet flow boundary conditions based on Jeffrey–Hamel flow. The conditions allow a smaller computational domain and more realistically represent the entrance flow than previous methods.

Detailed comparisons of the parabolic and elliptic solutions show that an elliptic solution is necessary to get accurate local quantities, such as local heat transfer, near the channel entrance. However, global quantities predicted by the elliptic and parabolic solutions (such as total flow rate and average Nusselt number) are in good agreement.

The present elliptic solution is not in agreement with previous elliptic solutions. The close agreement of the present elliptic and parabolic solutions casts doubt on the validity of the results of Nakamura et al. (1982) and Kettleborough (1972). Also, the inlet pressure approximation ($p = -\rho v_o^2/2$) commonly used in parabolic solutions is validated by the present elliptic solution.

The present elliptic solution predicts fluid separation at the channel inlet, which approximately correlates with dimensional induced flow rate. Separation is shown to have an adverse effect on the local heat transfer near the channel entrance. For $Gr = 10^4$, $L/b = 24$ ($Ra^* = 291.7$), the local Nusselt number has a local minimum near the channel inlet.

Acknowledgments

The authors wish to acknowledge the support received from NSERC of Canada and computing funds provided by The University of Western Ontario.

References

Aihara, T., 1973, "Effects of Inlet Boundary-Conditions on Numerical Solutions of Free Convection Between Vertical Parallel Plates," *Report of the Institute of High Speed Mechanics*, Tohoku University, Sendai, Japan, Vol. 28, pp. 1–27.

Aihara, T., 1963, "Heat Transfer Due to Natural Convection From Parallel Vertical Plates," *Trans. JSME*, Vol. 29, pp. 903–909.

Aung, W., Fletcher, L. S., and Sernas, V., 1972, "Developing Laminar Free Convection Between Vertical Flat Plates With Asymmetric Heating," *Int. J. Heat Mass Transfer*, Vol. 15, pp. 2293–2308.

Batchelor, G. K., 1967, *An Introduction to Fluid Dynamics*, Cambridge University Press, United Kingdom.

Bodia, J. R., and Osterle, J. F., 1962, "The Development of Free Convection Between Heated Vertical Plates," ASME JOURNAL OF HEAT TRANSFER, Vol. 84, pp. 40–44.

Dalbert, A.-M., Penot, F., and Peube, J.-L., 1981, "Convection Naturelle Laminaire Dans un Canal Vertical Chauffe a Flux Constant," *Int. J. Heat Mass Transfer*, Vol. 24, pp. 1463–1473.

Elenbaas, W., 1942, "Heat Dissipation of Parallel Plates by Free Convection," *Physica*, Vol. 9, No. 1, pp. 1–28.

Fluid Dynamics International Inc., 1989, Evanston, IL, U.S.A., FIDAP version 4.51.

Kageyama, M., and Izumi, R., 1979, "Non-steady Natural Heat Convection in a Nonparallel Plane Walled Channel," *Trans. JSME*, Vol. 45, No. 393, pp. 682–693.

Kettleborough, C. F., 1972, "Transient Laminar Free Convection Between Heated Vertical Plates Including Entrance Effects," *Int. J. Heat Mass Transfer*, Vol. 15, pp. 883–896.

Miyatake, O., and Fujii, T., 1972, "Free Convection Heat Transfer Between Vertical Parallel Plates—One Plate Isothermally Heated and the Other Thermally Insulated" [in Japanese], *Kagaku Kogaku*, Vol. 36, pp. 405–412.

Nakamura, H., Yutaka, A., and Naitou, T., 1982, "Heat Transfer by Free Convection Between Two Parallel Flat Plates," *Numerical Heat Transfer*, Vol. 5, pp. 95–106.

Oosthuizen, P. H., 1984, "A Numerical Study of Laminar Free Convective Flow Through a Vertical Open Partially Heated Plane Duct," *Fundamentals of Natural Convection—Electronic Equipment Cooling*, ASME HTD-Vol. 32, pp. 41–48.

Ostrach, S., 1953, "An Analysis of Laminar Free-Convection Flow and Heat Transfer About a Flat Plate Parallel to the Direction of the Generating Body Force," NACA Technical Report No. 1111, pp. 1–17.

Ramanathan, S., Kumar, R., and Wang, T., 1988, "Natural Convection From Heated Plates in Large Enclosures," *Proceedings of the 1988 National Heat Transfer Conference*, Houston, TX, ASME HTD-96, Vol. 2, pp. 155–163.

Wirtz, R. A., and Haag, T., 1985, "Effect of an Unheated Entry on Natural Convection Between Vertical Parallel Plates," ASME Paper No. 85-WA/HT-14.

Axial Transport Effects on Natural Convection Inside of an Open-Ended Annulus

K. Vafai

J. Ettefagh

Department of Mechanical Engineering,
The Ohio State University,
Columbus, OH 43210

The present work centers around a numerical three-dimensional transient investigation of the effects of axial convection on flow and temperature fields inside an open-ended annulus. The transient behavior of the flow field through the formation of a three-dimensional flow field and its subsequent effect on the temperature distribution at different axial locations within the annulus were analyzed by both finite difference and finite element methods. The results show that the axial convection has a distinctly different influence on the temperature and velocity fields. It is found that in the midportion of the annulus a two-dimensional assumption with respect to the temperature distribution can lead to satisfactory results for $Ra < 10{,}000$. However, such an assumption is improper with respect to the flow field. Furthermore, it is shown that generally the errors for a two-dimensional assumption in the midportion of the annulus are less at earlier times ($t < 50\ \Delta t$) during the transient development of the flow and temperature fields.

1 Introduction

Consideration of the open boundary effects on heat transfer rate and the flow field is very limited in the open literature (Ettefagh and Vafai, 1988). One of the main characteristics of the buoyancy-induced flows in open-ended cavities is its basic geometry. This is because several complex geometries can be approximated or constructed from this basic geometry. The applications for open-ended cavities are several such as connections between reservoirs, solar thermal central receiver systems, some geothermal processes, nuclear waste repositories, brake housing of an aircraft, fire spread in rooms, etc. Previous investigations of open-ended geometries were based on a two-dimensional flow field. However, in practice, due to viscous shearing effects at the end walls, some problems require numerical simulation of the three-dimensional flow field.

Numerical investigation of fully three-dimensional flows, those that cannot physically be approximated by a two-dimensional model, are rare in the literature. A limited number of numerical procedures for three-dimensional flow and heat transfer computations have been proposed. Aziz and Hellums (1967) introduced a technique in which the full Navier–Stokes and energy equations were transformed and expressed in terms of vorticity and vector potential. Numerical integration of the Navier–Stokes equations for certain three-dimensional incompressible flows has been introduced by Williams (1969), which utilizes the primitive form of the governing equations plus a Poisson equation for the pressure.

Numerical methods, based on a nonstaggered grid system, for predicting three-dimensional, steady, incompressible flow in straight ducts (Briley, 1974), and in ducts of rectangular and polar cross sections (Ghia et al., 1976) have been used earlier. In these works, the parabolized equations were solved by stepwise integration in the primary flow direction from prescribed upstream conditions. However, it appears that no serious attempt has been made to apply this method to solve the full three-dimensional Navier–Stokes equations.

In this work, the complete Navier–Stokes equations are transformed and expressed in terms of vorticity and vector potential. The transformed equations with the energy equation are then solved by a modified three-dimensional alternating direction implicit method for the parabolic part, while the extrapolated Jacobi scheme is utilized for the numerical solution of elliptic equations. Some results were also obtained using a finite element code. The results from the finite element code were used to verify and enhance qualitatively the main theme proposed in this work, which is the effects of open boundary on the axial convection and its influence on temperature and flow fields. The existence of a core region, in which the temperature and/or the velocity fields are independent of the axial coordinate, is examined. It is found that a core region does exist in the midsection of the annulus. It is shown that within this core region the temperature field can be approximated as two dimensional for $Ra < 10{,}000$. However, this approximation is inappropriate for the flow field. It is also observed that the errors associated with a two-dimensional approximation within the core region are smaller at earlier times during the development of the flow and temperature fields within the annulus.

2 Analysis

In the present work a fluid layer is sandwiched between two

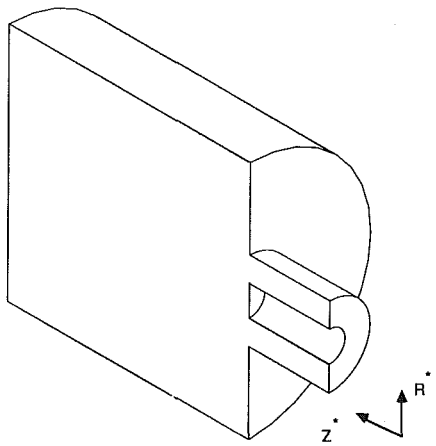

Fig. 1 Three-dimensional sketch of half of the open-ended horizontal annulus and the surrounding computational domain

Contributed by the Heat Transfer Division for publication in the JOURNAL OF HEAT TRANSFER. Manuscript received by the Heat Transfer Division June 6, 1990; revision received January 12, 1991. Keywords: Natural Convection, Numerical Methods; Transient and Unsteady Heat Transfer.

concentric cylinders with an inner radius R_1^*, outer radius R_2^*, and an axial length of L^* as shown in Fig. 1. The annulus is positioned horizontally so that the gravity acts in both the R^* and ϕ directions. The surrounding fluid communicating with the fluid inside the annulus through the opening is at ambient temperature T_∞. This temperature is lower than the heated inner cylinder and the cooled outer cylinder surfaces, which are kept at constant temperatures T_1 and T_2, respectively. The results are presented within the $0 \le \phi \le \pi$ region due to the symmetric nature of the flow field about the vertical plane. The nondimensional governing equations for this problem are

$$\nabla \cdot \mathbf{u} = 0 \tag{1}$$

$$\frac{\partial \mathbf{u}}{\partial t} + (\mathbf{u} \cdot \nabla)\mathbf{u} = -\nabla p + \mathrm{Pr}\nabla^2 \mathbf{u} - \mathrm{PrRa}\theta \begin{pmatrix} \cos\phi \\ -\sin\phi \\ 0 \end{pmatrix} \tag{2}$$

$$\frac{\partial \theta}{\partial t} + (\mathbf{u} \cdot \nabla)\theta = \nabla^2 \theta \tag{3}$$

where the nondimensional variables in the above equation are defined by

$$r = \frac{R^*}{R_2^*},\ z = \frac{Z^*}{R_2^*} \tag{4}$$

$$u = \frac{u^* R_2^*}{\alpha},\ t = \frac{t^* \alpha}{R_2^{*2}} \tag{5}$$

$$P = \frac{P^* R_2^{*2}}{\rho \alpha^2},\ \theta = \frac{T - T_\infty}{T_1 - T_\infty} \tag{6}$$

Equations (1)–(3) are transformed and expressed in terms of vorticity and a vector potential. The resultant transformed dimensionless governing equations are solved numerically in the present investigation. These governing equations are

$$\frac{\partial \theta}{\partial t} + (u \cdot \nabla)\theta = \nabla^2 \theta \tag{7}$$

$$\frac{\partial \zeta_r}{\partial g} + (u \cdot \nabla)\zeta_r - (\zeta \cdot \nabla)u_r = \mathrm{Pr}\left(\nabla^2 \zeta_r - \frac{\zeta_r}{r^2} - \frac{2}{r^2}\frac{\partial \zeta_\phi}{\partial \phi}\right) - \mathrm{PrRa}\sin\phi\frac{\partial \theta}{\partial z} \tag{8}$$

$$\frac{\partial \zeta_\phi}{\partial t} + (u \cdot \nabla)\zeta_\phi - (\zeta \cdot \nabla)u_\phi + \frac{u_\phi \zeta_r - u_r \zeta_\phi}{r} = \mathrm{Pr}\left(\nabla^2 \zeta_\phi - \frac{\zeta_\phi}{r^2} + \frac{2\zeta_r}{\partial \phi}\right) - \mathrm{PrRa}\cos\phi\frac{\partial \theta}{\partial z} \tag{9}$$

$$\frac{\partial \zeta_z}{\partial t} + (u \cdot \nabla)\zeta_z - (\zeta \cdot \nabla)u_z = \mathrm{Pr}\nabla^2 \zeta_z + \mathrm{PrRa}\left(\sin\phi\frac{\partial \theta}{\partial r} + \frac{1}{r}\cos\phi\frac{\partial \theta}{\partial \phi}\right) \tag{10}$$

$$\nabla^2 \psi_r + \frac{2}{r}\frac{\partial \psi_r}{\partial r} + \frac{\psi_r}{r^2} + \frac{2}{r}\frac{\partial \psi_z}{\partial z} + \zeta_r = 0 \tag{11}$$

$$\nabla^2 \psi_\phi - \frac{\psi_\phi}{r^2} + \frac{2}{r^2}\frac{\partial \psi_r}{\partial \phi} + \zeta_\phi = 0 \tag{12}$$

$$\nabla^2 \psi_z + \zeta_z = 0 \tag{13}$$

$$u_r = \frac{1}{r}\frac{\partial \psi_z}{\partial \phi} - \frac{\partial \psi_\phi}{\partial z} \tag{14}$$

$$u_\phi = \frac{\partial \psi_r}{\partial z} - \frac{\partial \psi_z}{\partial r} \tag{15}$$

$$u_z = \frac{\psi_\phi}{r} + \frac{\partial \psi_\phi}{\partial r} - \frac{1}{r}\frac{\partial \psi_r}{\partial \phi} \tag{16}$$

The above ten coupled partial differential equations for ten unknowns along with the specification of the proper boundary conditions describe the physics of the convective flow and heat transfer processes in the open-ended annulus and complete the formulation of the problem.

3 Boundary Conditions

The boundary conditions on velocity and temperature are based on the physical conditions. The boundary conditions on the vorticity follow from those on the velocity using the no-slip condition. The boundary conditions on the vector potential are based on the work of Hirasaki and Hellums (1968) who have verified that the proper boundary conditions on the normal component of velocity are satisfied if the normal derivative of the normal component of the vector potential and the components of the vector potential tangential to the surface vanish.

On the inner and outer cylinder surfaces, the dimensionless temperatures are θ_1 and θ_2, respectively. On all rigid and impermeable surfaces, the three components of the velocity are zero. The boundary conditions at $r = R_1^*/R_2^*$ or $r = 1$ are then found to be

$$u_r = u_\phi = u_z = 0 \tag{17}$$

$$\frac{\partial}{\partial r}(r\psi_r) = \psi_\phi = \psi_z = 0 \tag{18}$$

Nomenclature

$\mathbf{g}$ = body force vector, m/s^2
g = gravitational acceleration, m/s^2
L^* = axial length of the annulus, m
P^* = pressure, N/m^2
P = dimensionless pressure $= P^* R_2^{*2}/\rho\alpha^2$
Pr = Prandtl number $= \nu/\alpha$
R^* = radial coordinate, m
r = dimensionless radial coordinate $= R^*/R_2^*$
Ra = Rayleigh number $= g\beta R_2^{*2}\,\Delta T/\alpha\nu$
t^* = time, s
t = dimensionless time $= t^*\alpha/R_2^{*2}$
T = temperature, K
ΔT = temperature difference $= T_1 - T_2$, K
$\mathbf{u}$ = dimensionless velocity vector $= \mathbf{u}^* R_2^*/\alpha$
$\mathbf{u}^*$ = velocity vector, m/s
Z^* = axial coordinate, m
z = dimensionless axial coordinate $= Z^*/R_2^{*2}$
α = thermal diffusivity, m^2/s
β = thermal expansion coefficient of fluid, K^{-1}
ζ = vorticity
θ = dimensionless temperature $= (T - T_\infty)/(T_1 - T_\infty)$
μ = dynamic viscosity, kg m^{-1}s^{-1}
ν = kinematic viscosity, m^2/s
ρ = density, kg/m^3
ϕ = angular coordinate
ψ = vector potential

Subscripts

1 = inner cylinder
2 = outer cylinder
i = nodal index in r direction
j = nodal index in ϕ direction
k = nodal index in z direction
r = radial component
z = axial component
ϕ = angular component

$$\frac{\partial}{\partial r}(r\psi_r)=\psi_\phi=\psi_z=0 \tag{19}$$

$$\theta=1 \text{ or } \theta=0 \tag{20}$$

The angular velocity is zero at the top and bottom angular symmetry planes since there is no flow through those planes. The angular derivatives of the remaining velocity components and the temperature are also zero along the angular symmetry planes. The boundary conditions at the symmetry planes $\phi=0$ or $\phi=\pi$ are then

$$\frac{\partial u_r}{\partial \phi}=u_\phi=\frac{\partial u_z}{\partial \phi}=0 \tag{21}$$

$$\zeta_r=\frac{\partial \zeta_\phi}{\partial \phi}=\zeta_z=0 \tag{22}$$

$$\psi_r=\frac{\partial \psi_\phi}{\partial \phi}=\psi_z=0 \tag{23}$$

$$\frac{\partial \theta}{\partial \phi}=0 \tag{24}$$

At the symmetry plane, the axial velocity and the temperature as well as the normal gradients of the remaining velocity components are taken to be zero. So at $z=0$

$$\frac{\partial u_r}{\partial z}=\frac{\partial u_\phi}{\partial z}=u_z=0 \tag{25}$$

$$\zeta_r=\zeta_\phi=\frac{\partial \zeta_z}{\partial z}=0 \tag{26a}$$

$$\psi_r=\psi_\phi=\frac{\partial \psi_z}{\partial z}=0 \tag{26b}$$

$$\frac{\partial \theta}{\partial z}=0 \tag{27}$$

Since there are two kinds of temperature boundary condition (specified temperature on the cylindrical surface portion and adiabatic on the axial plane portion) imposed on the convex corners in the angular direction, a multivalued procedure similar to one used in the work of Ettefagh and Vafai (1988) and Ettefagh et al. (1991) has been utilized here. The same approach is also employed for treating the vorticity discontinuity at these locations.

It is impractical to impose known physical conditions on the open boundary. Therefore, the numerical simulation should include calculations in an enlarged computational domain to partially overcome the problem of unknown physical conditions at the opening. In the present study, the computational domain is successively extended in the radial and axial directions by enclosing it with a cylinder of radius R_3^* and length L_3^*. It should be mentioned that the position of the outer boundaries is not fixed. They are chosen such that further extensions will no longer produce any significant changes in the temperature or flow field inside the annuli and near the aperture plane. In this work, it was found that extensions of at least three times the annulus gap in both the axial and radial directions should be used to implement the far field boundary conditions properly.

Without any prescribed boundary conditions at the opening, one is left with three possible choices for specifications of the far field boundary conditions. These are zero value for the function, its normal gradient, or its second derivative in the normal direction. The third choice requires some type of extrapolation scheme and it cannot be used in an implicit routine that simultaneously incorporates the boundary and internal points into the solution algorithm at each time step. The first and second choices were considered as good candidates since they could be directly incorporated in the vector potential and energy equations. The first choice is obviously a valid one provided that we have extended the open boundaries far enough. However, such extensions in the computational domain are not desirable due to unreasonable increases in memory and computational time. The second choice places a far lesser degree of restriction on the flow field simultaneously and it can be implicitly incorporated into the solution algorithm at each time step. Therefore, in this work the far field boundary conditions are approximated by specifying zero normal gradients for temperature, vorticity, vector potential, and normal component of the velocity, while the remaining velocity components are set to zero. The following boundary conditions are then obtained at the outer boundaries:

$$r=\frac{R_3^*}{R_2^*} \qquad z=\frac{L_3^*}{R_2^*}$$

$$\frac{\partial u_r}{\partial r}=u_\phi=u_z=0 \qquad u_r=u_\phi=\frac{\partial u_z}{\partial z}=0 \tag{28}$$

$$\frac{\partial \zeta_r}{\partial r}=\frac{\partial \zeta_\phi}{\partial r}=\frac{\partial \zeta_z}{\partial r}=0 \qquad \frac{\partial \zeta_r}{\partial z}=\frac{\partial \zeta_\phi}{\partial z}=\frac{\partial \zeta_z}{\partial z}=0 \tag{29}$$

$$\frac{\partial \psi_r}{\partial r}=\frac{\partial \psi_\phi}{\partial r}=\frac{\partial \psi_z}{\partial r}=0 \qquad \frac{\partial \psi_r}{\partial z}=\frac{\partial \psi_\phi}{\partial z}=\frac{\partial \psi_z}{\partial z}=0 \tag{30}$$

$$\frac{\partial \theta}{\partial r}=0 \qquad \frac{\partial \theta}{\partial z}=0 \tag{31}$$

4 Results and Discussion

The four parabolic Eqs. (7)–(10) are solved by a modified form of the three-dimensional ADI method developed by Brian (1961) and the three elliptic Eqs. (11)–(13) are solved by the three-dimensional extrapolated Jacobi scheme. The remaining Eqs. (14)–(16) are solved by the central difference approximation technique. The updated values are used to advance the numerical solution in time and the sequence is repeated until steady-state conditions are obtained. It is assumed steady-state conditions have been reached when the following criterion:

$$\frac{\xi_{i,j,k}^{n+1}-\xi_{i,j,k}^{n}}{\xi_{i,j,k}^{n}}\le 10^{-3}$$

for temperature, vorticity components, and vector potential components has been met. In the above equation, n refers to any particular time level and ξ represents any one of the seven dependent variables.

In this work, the accuracy of the numerical scheme was checked quite carefully. Some of the accuracy tests described in detail by Vafai and Ettefagh (1990) for the open-ended structures were adopted here. Essentially, it was ensured that the results were grid (in all three directions) and time step size independent. Various combinations of mesh sizes were used to obtain grid independent results. Initially, the number of grids in the angular direction was fixed to examine the grid dependency of the results in the other directions. The number of grids in the radial direction was then increased successively with a fixed number of grids in the axial direction. Next, to check the grid dependency in the axial direction, the number of grids in the axial direction was successively increased using the number of grids in the radial direction obtained from the previous step. The number of grids in the angular direction was then increased successively using the number of grids in the radial and axial directions obtained in previous steps. Finally, the number of grids in all directions was increased from the values obtained from the above-described procedure. To ensure that we have indeed a totally grid-independent solution, this procedure was repeated for different cases analyzed in this work.

From the above-mentioned investigation it was found that 61 points in the radial direction, 19 points in the angular direction, and 61 points in the axial direction provide us with a high degree of accuracy for the lower range of Rayleigh numbers (less than 0.5 percent change in the field variables). For

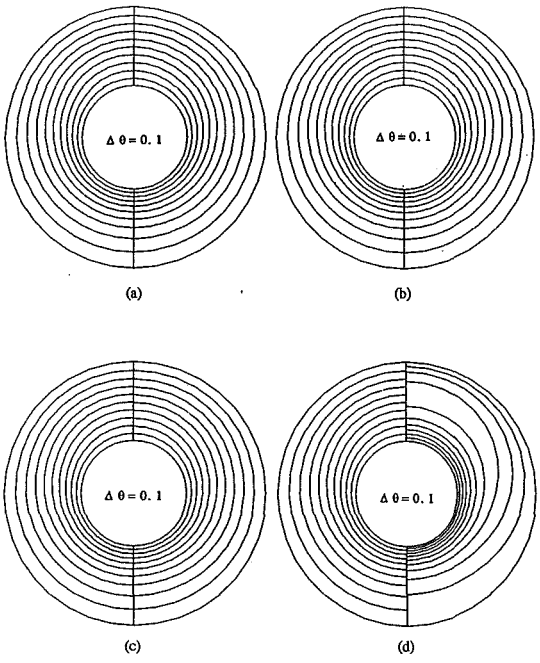

Fig. 2 Isotherms for Ra = 4.3 × 10^3 at different axial positions in the right and at midaxial plane in the left: (*a*) $z = 0$, $L/8$; (*b*) $z = 0$, $L/4$; (*c*) $z = 0$, $3L/8$; (*d*) $z = 0$, $L/2$

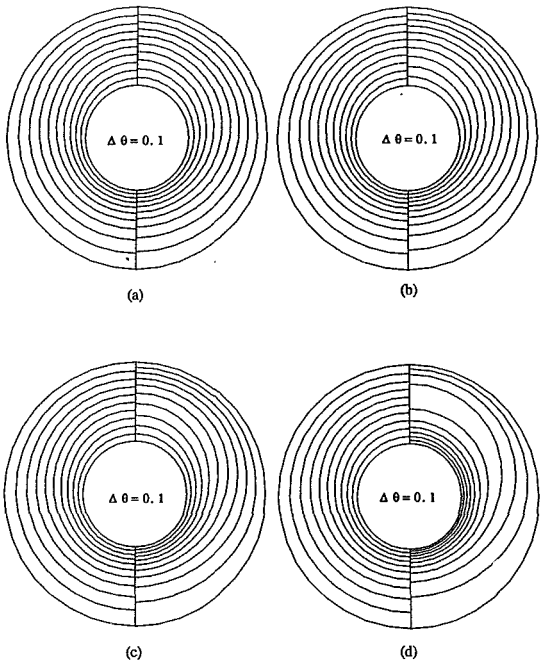

Fig. 4 Isotherms for Ra = 4.3 × 10^3 at different axial positions in the right and at midaxial plane in the left: (*a*) $z = 0$, $17L/40$; (*b*) $z = 0$, $18L/40$; (*c*) $z = 0$, $19L/40$; (*d*) $z = 0$, $L/2$

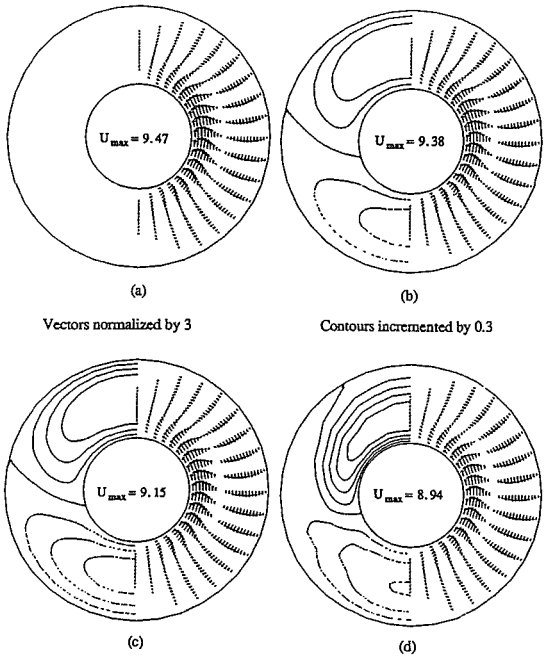

Fig. 3 Flow patterns for Ra = 4.3 × 10^3 at different axial positions: (*a*) $z = 0$; (*b*) $z = L/8$; (*c*) $z = L/4$; (*d*) $z = 3L/8$

higher Rayleigh numbers, the numbers of grids in the angular and axial directions were increased to 37 and 81 points, respectively, to accommodate the same level of accuracy. Numerical tests were also performed with different sizes of time step using the quoted grid distribution. It was found that a time increment of 2×10^{-4} would give us a time-dependent solution. In all the numerical simulations, the initial conditions were based on a quiescent air at the same temperature as that of the surrounding environment. The numerical algorithm was also used to generate the steady-state three-dimensional numerical results reported by Takata et al. (1984) and the two-dimensional results reported by Kuehn and Goldstein (1976). Excellent agreements were found between results generated by the present transient three-dimensional algorithm and the results reported in the cited references.

The streamlines and isotherms at the midaxial plane for a Rayleigh number of Ra = 4.3 × 10^3 displayed a crescent-shaped flow pattern, which was symmetric about a horizontal plane passing through the center of rotation. At this Rayleigh number, conduction was the dominant mode of heat transfer. To investigate the effects of axial convection, temperature and flow field distributions inside the annulus at axial positions 1/8 of the annulus length apart, including and away from the midaxial plane, are compared in Figs. 2 and 3. Figure 2 consists of two parts. The midaxial plane is displayed on the left-hand side while temperature distributions at different axial locations are displayed on the right-hand side. As seen clearly in Fig. 2, the temperature distribution essentially remains unchanged over a core region, which extends approximately 3/8 of the annulus length on each side of the midaxial plane. This is the core region in which the effect of axial convection on the temperature field is small. In Fig. 3, the radial and angular components of the velocity field are displayed on the right while the contours for the axial component of the velocity are shown on the left-hand side of that figure. The negative or positive contours illustrate regions within which the direction of axial velocity is into (negative z direction) or out of the R-ϕ plane, respectively. The dotted contour lines of the axial component of the velocity represent the negative contours while the positive contours are drawn as solid lines. The maximum values of velocity vectors at these locations are 9.47, 9.38, 9.15, and 8.94, respectively. The velocity vectors were normalized by a factor of 3 and vectors with values less than 0.01 are not shown in Fig. 2. Maximum axial velocities at these locations are 0.0, 0.73, 1.1, and 1.2, while their minimum values are 0.0, -0.75, -1.1, and -0.92, respectively. The strength of the recirculating region in the R-ϕ plane decreases slightly along the positive axial direction because the axial component of the velocity field increases along the positive axial direction. As seen in Fig. 3 the hot buoyant fluid rises above the inner cylinder and impinges on the outer cylinder. At this stage, this hot fluid enters the thermal boundary layer along the outer cylinder. As this fluid travels downward, it loses energy and

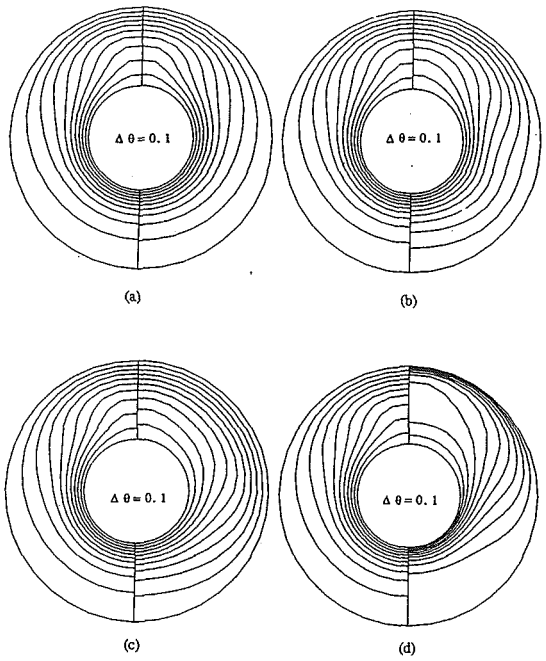

Fig. 5 Isotherms for Ra = 1 × 10^4 at different axial positions in the right and at midaxial plane in the left: (*a*) $z = 0$, $L/8$; (*b*) $z = 0$, $L/4$; (*c*) $z = 0$, $3L/8$; (*d*) $z = 0$, $L/2$

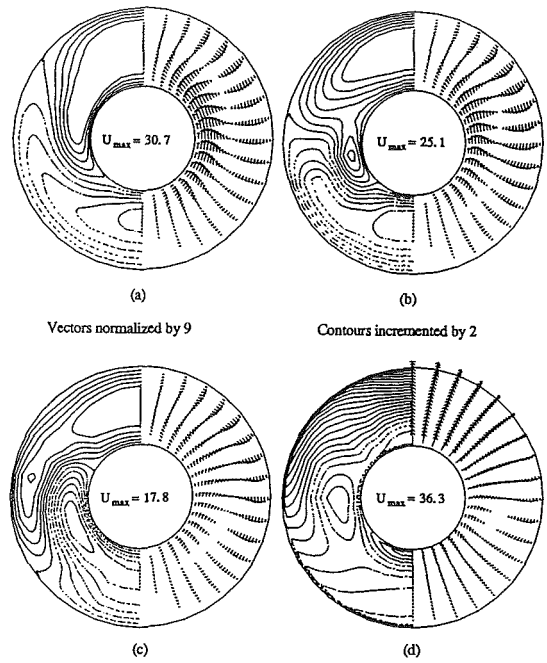

Fig. 6 Flow patterns for Ra = 1 × 10^4 at different axial positions: (*a*) $z = L/8$; (*b*) $z = L/4$; (*c*) $z = 3L/8$; (*d*) $z = L/2$

it eventually forces the separation of the thermal boundary layer along the outer cylinder. The cool fluid then enters the inner cylinder thermal boundary layer and completes the recirculating pattern. As can be clearly seen in Fig. 3, the velocity field does not enjoy the same axial independence as the temperature field.

The isotherms at the aperture plane are quite different from the isotherms at the midaxial plane as seen in Fig. 2(*d*). This is due to the influence of the outer region (outside the annulus) on the inner region (inside the annulus), which causes a significant distortion of the temperature field outside the cited core region. It should also be noted that the axial convection exerts a stronger influence on the inner cylinder.

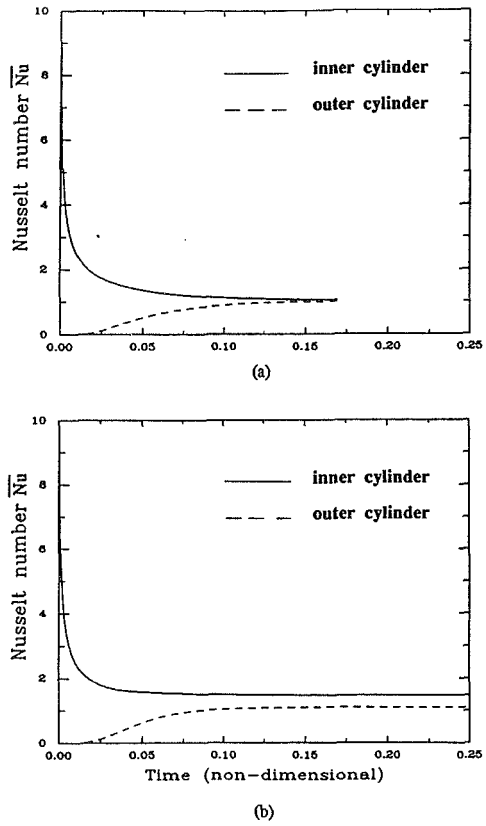

Fig. 7 Temporal variations of the mean Nusselt number at midaxial plane for Ra = 4.3 × 10^3 and Ra = 1 × 10^4

Temperature distributions at four other axial planes inside the annulus for the same Rayleigh number are shown in Figs. 4(*a–d*). The axial locations at which these distributions are presented are at $3\Delta z$, $2\Delta z$, Δz away from (and into the annulus) the aperture plane. The isotherms at the above axial planes are presented on the right-hand side of Figs. 4(*a–d*). The isotherms at the midaxial plane are plotted on the left-hand side of the above figures to make their relative differences more apparent. As seen in Figs. 4(*a–c*), at these axial locations, the isotherms near the inner cylinder in the upper angular part are spaced farther apart than the corresponding isotherms at the midaxial plane. Consequently, the heat transfer from the inner cylinder is reduced over this region. A closer inspection of these figures reveals that the main differences in the isotherm spacings occur in the $\pi/3 \leq \phi \leq \pi$ angular region. Therefore, the local heat transfer over this region is reduced in comparison with the heat transfer over the midaxial plane. Comparison of Figs. 4(*b*) and 4(*c*) shows that heat transfer from the inner cylinder increases in the positive axial direction. The clustering of isotherms near the inner cylinder as seen in Fig. 4(*d*) clearly shows that the heat transfer from the inner cylinder is considerably enhanced at the aperture plane. The heat transfer over the upper part of the outer cylinder also increases in the positive axial direction as seen by the closer spacing of the isotherms near the outer cylinder.

Figures 5(*a–d*) show the isotherms at four axial positions including and away from the midaxial plane set 1/8 of the annulus length apart for Ra = 1 × 10^4. The left-hand side of each figure displays the midaxial plane temperature distribution while the right-hand side shows the temperature distribution at the selected axial planes. It is observed that as the Rayleigh number increases, the effects of an open boundary penetrate much farther inside the annulus, resulting in stronger convective flow at the aperture plane. As a result, the extent of the core region within which the temperature distribution is independent of the axial position decreases as the Rayleigh

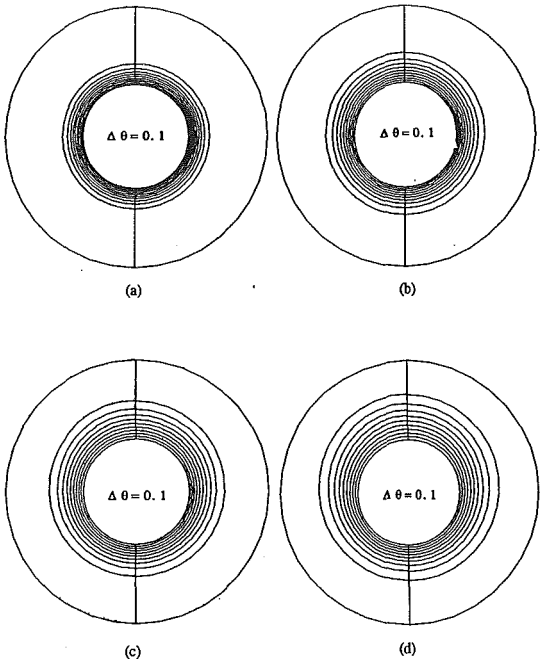

Fig. 8 Isotherms for Ra = 1×10^4 at $z = 17L/40$ in the right and at midaxial plane in the left side for different time steps: (*a*) $t = 10\Delta t$; (*b*) $t = 20\Delta t$; (*c*) $t = 30\Delta t$; (*d*) $t = 40\Delta t$

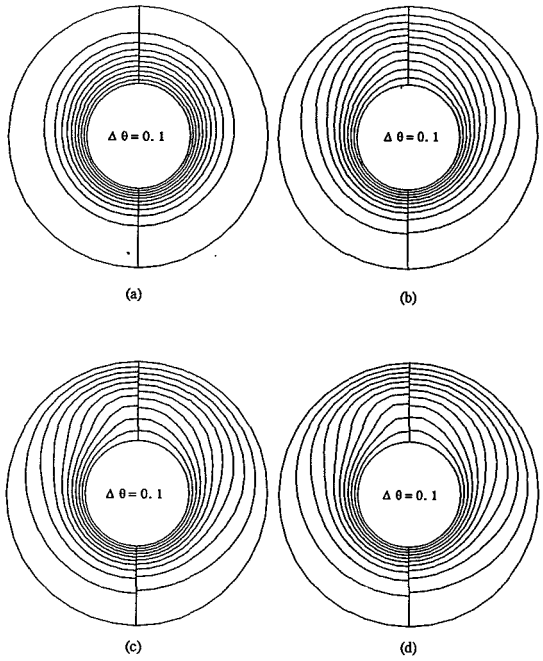

Fig. 9 Isotherms for Ra = 1×10^4 at $z = 17L/40$ in the right and at midaxial plane in the left side for different time steps: (*a*) $t = 50\Delta t$; (*b*) $t = 100\Delta t$; (*c*) $t = 150\Delta t$; (*d*) $t = 200\Delta t$

number increases. This is primarily due to strong axial convection associated with higher Rayleigh number flows in regions near the lower part of inner cylinder and the upper part of outer cylinder.

The flow field structure for Ra = 1×10^4 at the same locations as those given in Fig. 5 are displayed in Fig. 6. The axial velocity contours at these locations are presented on the left-hand side while the radial and angular components of the velocity field are shown on the right side. The maximum values of velocity vectors on these planes are 30.7, 25.1, 17.8, and 36.3, respectively. Maximum values of the axial velocities are 9.8, 14, 11, and 31 while minimum values are -11, -14, -14, and -11, respectively. Comparing Figs. 6(*a*), 6(*b*), and 6(*c*) with Figs. 3(*b*), 3(*c*), and 3(*d*) reveals that for higher Rayleigh numbers, the three-dimensional structure of the flow field becomes much more pronounced. The existence of axial velocities clearly is indicative of three-dimensional nature of the velocity field. As the hot fluid rises up around the inner cylinder, the axial component of its velocity ejects it out of the R–ϕ plane. Once it impinges on the outer cylinder it loses energy and starts to descend. Due to the recirculating nature of the flow, the cold fluid enters a new R–ϕ plane through the lower part of the annulus farther downstream. The basic flow pattern involved in this process can be seen in Figs. 6(*a–c*). It should be noted that the strength of the recirculating region in the R–ϕ plane decreases substantially in the axial direction due to the penetration of the open boundary effects. The basic physical mechanisms resulting in the complex flow field (shown in Fig. 6) are discussed by Ettefagh and Vafai (1991).

The temporal variations of the mean Nusselt numbers at the midaxial plane for Ra = 4.3×10^3 and Ra = 1×10^4 are presented in Figs. 7(*a*) and 7(*b*), respectively. In these figures, the solid line represents the inner cylinder mean Nusselt number, while the dotted line represents the mean Nusselt number for the outer cylinder. These mean (averaged over the angular direction) Nusselt numbers, $\overline{\mathrm{Nu}_1}$ and $\overline{\mathrm{Nu}_2}$, for the inner and outer cylinders are respectively defined as

$$\overline{\mathrm{Nu}_1} = \frac{-1}{\pi} \int_0^{\pi} R \ln (R) \left. \frac{\partial \theta}{\partial r} \right|_{r=R} d\theta \qquad (32)$$

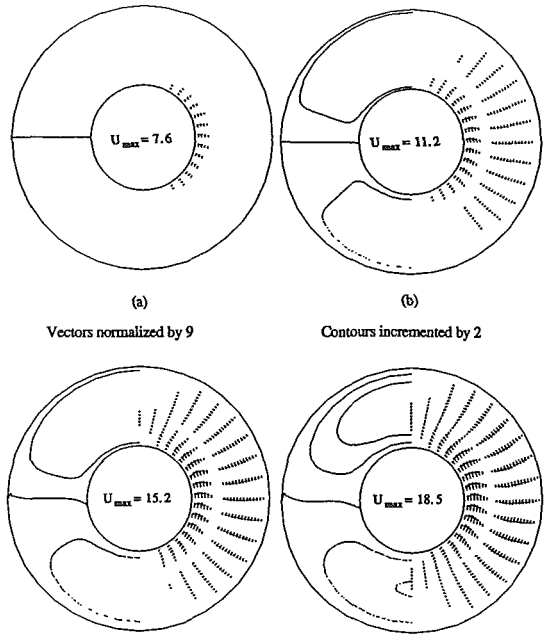

Fig. 10 Flow patterns for Ra = 1×10^4 and different time steps at $z = 17L/40$: (*a*) $t = 10\Delta t$; (*b*) $t = 20\Delta t$; (*c*) $t = 30\Delta t$; (*d*) $t = 40\Delta t$

$$\overline{\mathrm{Nu}_2} = \frac{-1}{\pi} \int_0^{\pi} \ln (R) \left. \frac{\partial \theta}{\partial r} \right|_{r=1} d\theta \qquad (33)$$

where $R = R_2^*/R_1^*$. Physically the above-defined Nusselt number expresses the ratio of the actual heat transfer to conduction in the radial direction between the inner and outer cylinders.

As expected, the transient response shows a decrease in the inner cylinder mean Nusselt number and an increase in the outer cylinder mean Nusselt number followed by their approach to the steady-state values. In theory, due to energy loss through the aperture plane, steady-state asymptotic values of the Nusselt numbers should not converge to the same value. Figure 7 reveals that an increase in the Rayleigh number in-

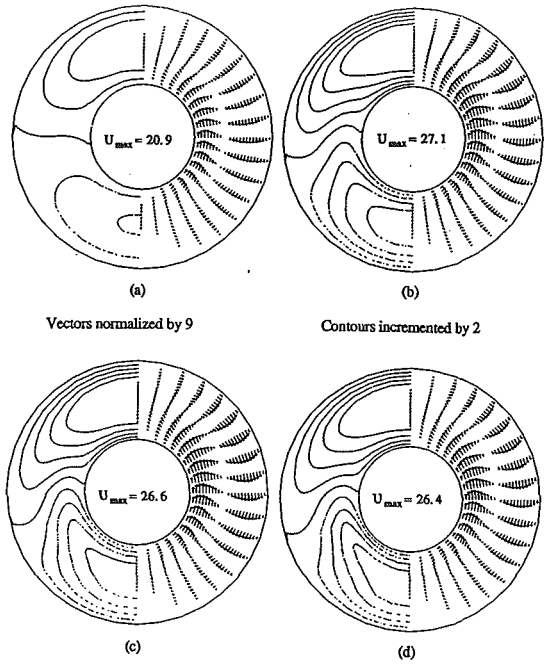

Fig. 11 Flow patterns for Ra = 1×10^4 and different time steps at $z = 17L/40$: (*a*) $t = 50\Delta t$; (*b*) $t = 100\Delta t$; (*c*) $t = 150\Delta t$; (*d*) $t = 200\Delta t$

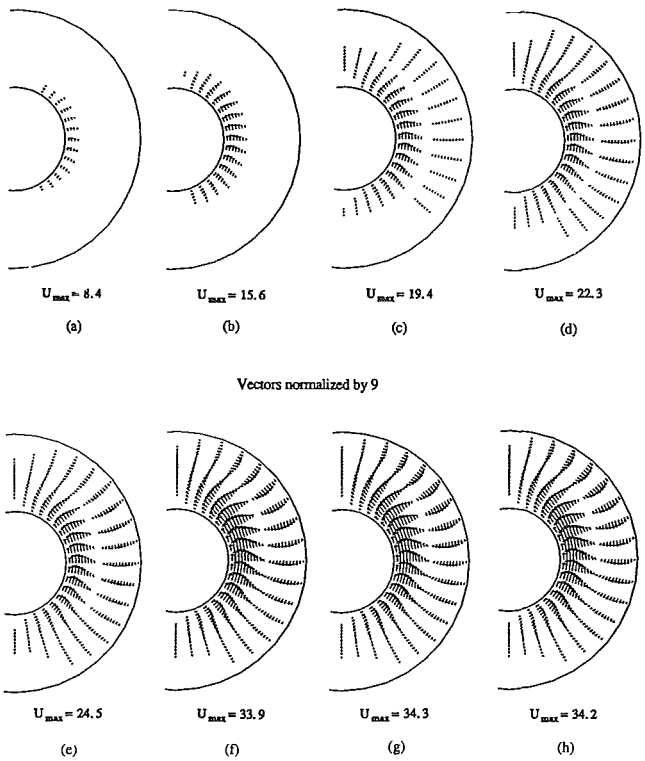

Fig. 12 Flow patterns for Ra = 1×10^4 at different time steps at midaxial plane: (*a*) $t = 10\Delta t$; (*b*) $t = 20\Delta t$; (*c*) $t = 30\Delta t$; (*d*) $t = 40\Delta t$; (*e*) $t = 50\Delta t$; (*f*) $t = 100\Delta t$; (*g*) $t = 150\Delta t$; (*h*) $t = 200\Delta t$

creases energy losses to the outer domain. The relative differences between the steady-state mean Nusselt numbers are 4 and 25 percent for Ra = 4.3×10^3 and Ra = 1×10^4, respectively.

Next, results of a transient investigation of flow and temperature fields inside the open-ended annulus are presented. These results further reveal the effects of axial transport on transient natural convection characteristics inside the annulus region. Temporal variations of the flow and temperature fields for Ra = 1×10^4 at an axial location 3 Δz away (into the annulus) from the opening are presented in Figs. 8–11. The temperature distributions at this location for eight different time steps are shown on the right side of the Figs. 8 and 9, while the corresponding isotherms at the midaxial plane are depicted on the left-hand side of these figures. The temporal development of the corresponding flow field structure at this location is displayed in Figs. 10 and 11. The maximum values of velocity vectors in the R-ϕ plane at the consecutive time steps displayed in Figs. 10 and 11 are 7.6, 11.2, 15.2, 18.5, 20.9, 27.1, 26.6, and 26.4, respectively. The velocity vectors are normalized by a factor of 9 and the vectors with values less than 0.01 are not plotted. The maximum values of axial velocity are 0.7, 3.6, 3.9, 4.1, 4.3, 9.6, 9.9,and 9.8, while their minimum values are −0.7, −3.6, −3.9, −4.2, −9.4, −9.5,and 9.4. In Figs. 10 and 11 contours are incremented by 2 and velocity vectors are normalized by 9 to preserve clarity of these figures.

As seen in Figs. 8(*a*), 8(*b*), 8(*c*), 8(*d*), and 9(*a*) for the period of $0 \le t \le 50\ \Delta t$, the temperature distribution at the cited axial location is almost identical to the one at the midaxial plane. This is due to the weak axial component of velocity field, as seen in Figs. 10(*a*), 10(*b*), 10(*c*), 10(*d*), and 11(*a*), which is not strong enough to influence the temperature distribution on this plane. In turn, this is because the open boundary effects have been confined mainly near the aperture plane for this period of time. For later times, $t \ge 50\ \Delta t$, the open boundary influences become more pronounced, resulting in a higher axial velocity, as clearly seen in Figs. 11(*b–d*). So, the effect of axial transport becomes more pronounced as can be seen in Figs. 11(*b–d*). It is exactly this increase in the axial transport that reduces the extent of the core region. However, although for $0 \le t \le 50\ \Delta t$, the axial transport has become significantly larger, its influence over the heat transfer characteristics within the core region is still quite limited.

Temporal characteristics of the flow and temperature fields for Ra = 1×10^4 at the midaxial plane are presented in Fig. 12. The maximum values of velocity vectors at the midaxial plane at the consecutive time steps are 8.4, 15.6, 19.4, 22.3, 24.5, 33.9, 34.3, and 34.2, respectively. In these figures, the velocity vectors are normalized by a factor of 9 and vectors with values less than 0.01 are not plotted to preserve the clarity of these figures. The flow and temperature fields were also investigated at several other locations. As mentioned earlier, a finite element code was also used further to verify and enhance the main theme that has been proposed in this work, which is the effects of open boundary on the axial convection and its influence on the temperature and the flow field. The results of all our investigations have shown the existence of a core region for Ra < 10,000 (the extent of which decreases with an increase in the Rayleigh number) in which the thermal characteristics are weakly dependent on the axial location. However, the three-dimensional flow field characteristics within this core region cannot be ignored.

5 Conclusions

The effects of axial convection on transient buoyancy-driven convection in an open-ended annulus have been numerically investigated in this work. The temporal three-dimensional flow field structure and its effects on the temperature distribution at different axial locations are investigated. The present investigation has revealed the existence of a core region for Ra < 10,000, in which the thermal characteristics are weakly dependent on the axial direction. It has been observed that a two-dimensional approximation within the core region yields accurate results for early time ($t < 50\ \Delta t$) during the flow field development. Furthermore, the results show that the influence of the axial transport on the flow field is quite different from that of the temperature field.

Acknowledgements

A grant from the Ohio Supercomputer Center is gratefully acknowledged.

References

Aziz, A., and Hellums, J. D., 1967, "Numerical Solution of the Three-Dimensional Equations of Motion for Laminar Natural Convection," *Physics of Fluids*, Vol. 10, pp. 314–324.

Brian, P. L. T., 1961, "A Finite-Difference Method of High-Order Accuracy for the Solution of Three-Dimensional Transient Conduction Problems," *AIChE Journal*, Vol. 7, pp. 367–370.

Briley, W. R., 1974, "Numerical Methods for Predicting Three-Dimensional Steady Viscous Flow in Ducts," *Journal of Computational Physics*, Vol. 14, pp. 8–28.

Ettefagh, J., and Vafai, K., 1988, "Natural Convection in Open-Ended Cavities With a Porous Obstructing Medium," *International Journal of Heat and Mass Transfer*, Vol. 31, pp. 673–693.

Ettefagh, J., Vafai, K., and Kim, S. J., 1991, "Non-Darcian Effects in Open-Ended Cavities Filled With a Porous Medium," ASME JOURNAL OF HEAT TRANSFER, Vol. 113, pp. 747–756.

Ettefagh, J., and Vafai, K., 1991, "An Investigation of Ejection, Mixing, and Suction Mechanisms in an Open-Ended Horizontal Annulus," ASME JOURNAL OF HEAT TRANSFER, in press.

Ghia, U., Ghia, K. N., and Studerus, C. J., 1976, "A Study of Three-Dimensional Laminar Incompressible Flow in Ducts," AIAA Paper No. 76-424.

Hirasaki, G. J.,and Hellums, J. D., 1968, "A General Formulation of the Boundary Conditions on the Vector Potential in Three-Dimensional Hydrodynamics," *Quarterly of Applied Mathematics*, Vol. 26, pp. 331–342.

Kuehn, T. H., and Goldstein, R. J., 1976, "An Experimental and Theoretical Study of Natural Convection in the Annulus Between Horizontal Concentric Cylinders," *Journal of Fluid Mechanics*, Vol. 74, pp. 695–719.

Takata, Y., Iwashige, K., Fukuda, K., and Hasegawa, S., 1984, "Three-Dimensional Natural Convection in an Inclined Cylindrical Annulus," *International Journal of Heat and Mass Transfer*, Vol. 27, pp. 747–754.

Vafai, K., and Ettefagh, J., 1990, "The Effects of Sharp Corners on Buoyancy-Driven Flows With Particular Emphasis on Outer Boundaries," *International Journal of Heat and Mass Transfer*, Vol. 33, pp. 2311–2328.

Williams, G. P., 1969, "Numerical Integration of the Three-Dimensional Navier–Stokes Equations for Incompressible Flow," *Journal of Fluid Mechanics*, Vol. 37, pp. 727–750.

D. A. Olson[1]
Graduate Student,
Department of Mechanical Engineering.
Assoc. Mem. ASME

L. R. Glicksman
Professor,
Department of Architecture and
Mechanical Engineering.
Mem. ASME

Massachusetts Institute of Technology,
Cambridge, MA 02139

Transient Natural Convection in Enclosures at High Rayleigh Number

Transient natural convection at Rayleigh numbers of 10^{10} was studied experimentally in two enclosures of aspect ratio 1/3, one a 1:5.5 physical scale model containing the dense refrigerant gas R114, and the second a full-scale room containing air. In one type of transient the vertical endwall temperature was suddenly changed, while in a second type of transient the isothermal, well-mixed gas was suddenly exposed to hot and cold vertical endwalls. The experiments indicated that the dominant time constant was a convective one. Comparisons between the scale model and full scale show that R114 gas can simulate the transient behavior of air-filled enclosures.

Introduction

Steady-state natural convection in enclosures driven by heat transfer at the vertical walls has been studied extensively in the past in the regimes appropriate to the flow in building interiors. However, it has not been shown whether "steady-state" natural convection will ever occur in a real building. That is, the time constants for the development of steady-state flow have not been determined or compared with common building time constants (e.g., those due to forced ventilation patterns, opening of doors and windows, or occupant movement). This paper is concerned with the onset of natural convection flow in enclosures where the primary driving mechanism for the flow is heat transfer at the vertical walls. The application of interest is the natural convection flow in buildings, in which the Rayleigh (Ra) number is 10^{10}, the Prandtl number (Pr) is less than 1.0, and the aspect ratio (height to length) is usually less than 1.0. The objective of this work is to determine the dominant time constant for the onset of natural convection flow in an enclosure by making experimental measurements on a 1:5.5 physical scale model of a building space.

In a previous study, Olson et al. (1990) demonstrated that this scale model, which uses refrigerant 114 gas instead of air, can accurately simulate steady-state natural convection driven by heated and cooled opposing endwalls. A second objective is to confirm that this scale model is also accurate for transient natural convection flow. This will be done by making comparisons with measurements on a full-scale room at similar geometry, Ra, and transient conditions. A final objective is to understand better the mechanisms of steady-state natural convection from the results of the transient experiments. This paper is based on the work of Olson (1986).

The enclosure studied is shown in Fig. 1 and was a rectangular space one third as high as it was long, and one-half as wide as it was long. For the small-scale model, the height, H, was 47 cm and the length, L, was 136 cm, corresponding to the full-scale room of $H=2.5$ m and $L=7.9$ m. The ceiling, floor, and side walls were well insulated. Two types of experiment were conducted. In one type of test, the flow was initially motionless and all the walls were at constant temperature T_0. The temperature of one or both endwalls was then "instantaneously" increased or decreased to $T_0 \pm \Delta T$, generating a temperature difference between the endwalls. Observations were made of the developing temperatures and flow patterns.

The second type of transient test involved disturbing a previously established steady-state flow, and observing the return to the steady natural convection pattern after the disturbance was discontinued. In the steady-state flow, the opposing endwalls were isothermal at different temperatures. The disturbance was one that provided a great deal of turbulent motion to the core, mixing the core so much that temperatures were uniform and the horizontal core flows were overwhelmed; however, the temperatures of the hot and cold walls, T_H and T_C, remained constant before, during, and after the disturbance.

Literature Review

A baseline for understanding the experimental results that follow is a description of the flow patterns and temperature

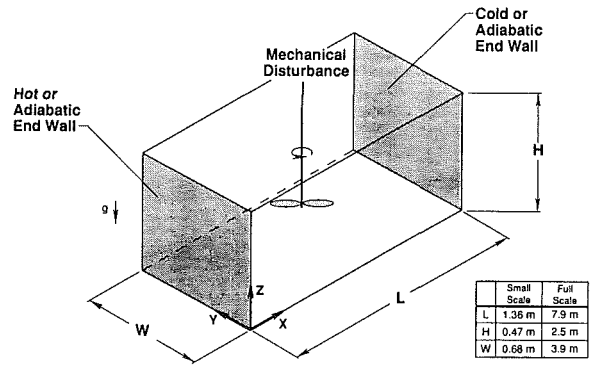

Fig. 1 Enclosure geometry

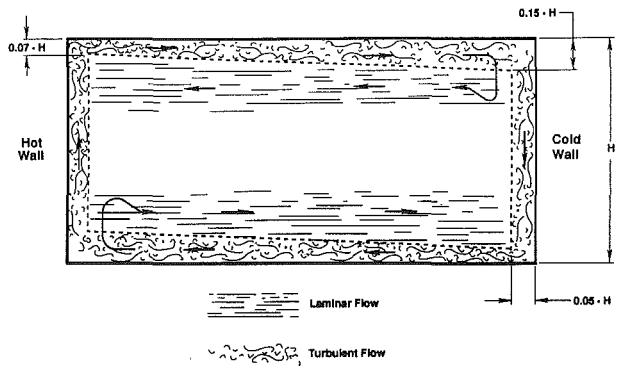

Fig. 2 Steady-state flow pattern in an empty enclosure at Ra ~ 10^{10}

[1]Present address: National Institute of Standards and Technology, Boulder, CO.

Contributed by the Heat Transfer Division for publication in the JOURNAL OF HEAT TRANSFER. Manuscript received by the Heat Transfer Division May 16, 1990; revision received April 23, 1991. Keywords: Enclosure Flows, Natural Convection, Transient and Unsteady Heat Transfer.

distributions of steady-state natural convection at $Ra \sim 10^{10}$ with isothermal opposing endwalls at different temperatures. This serves as a "final condition" that the transient natural convection approaches as time increases, and also places the past work on transient natural convection in perspective. For steady-state conditions typical to building interiors with heated and cooled opposing endwalls, the flow patterns are as shown in Fig. 2 (Olson et al., 1990). This would be a 2.5-m-high, 7.9-m-long room with a 10°C temperature difference between the endwalls. This flow pattern was observed both in an actual air-filled room and on a reduced scale model containing R114 gas. Turbulent boundary layers form on the hot and cold endwalls. Two horizontal recirculating flow loops form in the core, one near the floor and one near the ceiling. After the hot wall boundary layer reaches the ceiling, it makes a 90 deg turn and flows along the ceiling toward the cold vertical wall. Upon reaching the cold wall the flow divides and the majority reverses direction, flowing back to the hot wall. The floor loop is formed in a fashion similar to the ceiling loop. The horizontal layers closest to the ceiling and floor appear to be turbulent, with velocities about 1/10 of the velocities in the vertical boundary layers. Temperatures in the core are approximately linearly stratified from the ceiling to the floor, and constant horizontally from the hot wall to the cold wall once outside the vertical boundary layers. Temperatures do not vary by more than 0.5 percent (of $T_H - T_C$) in the spanwise direction, and flow visualization indicates the flow is primarily two dimensional.

Past works on transient natural convection in enclosures have studied the response of the flow to the instantaneous heating and cooling of the vertical walls (Yewell et al., 1982; Worster and Leitch, 1985; Patterson and Imberger, 1980), or the development of flow patterns due to a buoyancy source in the center of the enclosure (Baines and Turner, 1969; Worster and Huppert, 1983). More recently, Litsek and Bejan (1988) have investigated analytically an enclosure in which the left half is initially at a higher uniform temperature than the right half, then the "partition" is instantaneously removed. In the cases where the flow is driven by instantaneous heating or cooling of the vertical walls, configurations have been studied with $Pr > 1$ (usually water) and $Ra \leq 10^{10}$. The experimental studies have shown that laminar boundary layers develop on the vertical walls, which then spill out into the core to form "intrusion layers" (Yewell et al., $A_L < 1$) or "gravity currents" (Worster and Leitch, $A_L \leq 1$). Patterson and Imberger (1980) used scaling arguments based on laminar flow with $Pr > 1$ and $A_L < 1$ to identify flow regimes and time scales. Their work and the laminar flow experiments indicate that the boundary layers on the vertical surface reach steady state much faster than does the core flow. The boundary layer time constant is roughly the time for thermal diffusion across the boundary layer thickness, or for laminar flow,

$$\tau_{bl} = H^2/(\alpha \mathrm{Ra}^{1/2}). \quad (1)$$

When the boundary layers are laminar, the time constant for the core is argued to be the time for the fluid volume in the core to circulate through the boundary layers, or

$$\tau_{\mathrm{core}} = (HL)/(\alpha \mathrm{Ra}^{1/4}). \quad (2)$$

This time constant was confirmed by Yewell et al. (1982) for a water-filled enclosure of aspect ratios 0.0625 and 0.112, and $Ra = 1.5 \times 10^9$.

These past studies have not explored the conditions of $Pr \leq 1$ or used a gas as the working fluid. It has been shown that steady-state experiments using water do not predict the observed turbulent vertical boundary layers or horizontal recirculating flows of building natural convection, even though the Rayleigh number and aspect ratio have been scaled properly (Olson et al., 1990). The steady-state water models also do not predict the proper temperature stratification levels. It is therefore possible that transient natural convection in building enclosures cannot be extrapolated from the past transient models, which used water.

Baines and Turner (1969) and later Worster and Huppert (1983) looked at the onset of flow, which is driven by a turbulent source of buoyancy at the floor in the center of the enclosure. A plume rises to the ceiling and is then assumed to spread infinitely quickly horizontally to the enclosure vertical walls. The spread-out plume then flows downward at a velocity equal to the plume upward flow rate divided by the core area outside the plume. The core time constant is the time for the core fluid volume to circulate through the driving plume. The

Nomenclature

a = mean radiation absorption coeficient
A = area
A_L = height-to-length aspect ratio $= H/L$
A_W = height-to-width aspect ratio $= H/W$
c = constant used in evaluating thermal time constants
c_p = specific heat
F = view factor from ceiling to floor
g = acceleration to gravity
Gr = Grashof number $= g\beta(T_H - T_C)H^3/\nu^2$
H = height of enclosure
k = thermal conductivity
k_r = ceiling/floor radiation to wall convection $= 4\sigma T_m^3 LF/(k\mathrm{Nu})$
L = length of enclosure
Pr = Prandtl number $= \nu/\alpha$
Ra = Rayleigh number $= g\beta(T_H - T_C)H^3/\nu\alpha)$
Re = Reynolds number $= V\delta/\nu$
t = time
t^* = dimensionless time $= t/\tau_{\mathrm{conv}}$
T = temperature
T_C = temperature of coldest wall in enclosure
T_{CBL} = temperature of cold wall boundary layer
T_H = temperature of hottest wall in enclosure
T_{HBL} = temperature of hot wall boundary layer
T_m = mean gas temperature
T_{ss} = steady-state temperature
T_0 = initial temperature
T_1 = experimental temperature of a specific thermocouple
T_2 = experimental temperature of a specific thermocouple
T_3 = experimental temperature of a specific thermocouple
V_c = characteristic velocity $= [g\beta(T_H - T_m)H]^{1/2}$ or $[g\beta(T_m - T_H)H]^{1/2}$
W = width of enclosure
X = horizontal coordinate
Z = vertical coordinate
α = thermal diffusivity
β = coefficient of thermal expansion
δ = boundary layer width
θ = dimensionless temperature $= (T - T_C)/(T_H - T_C)$
ν = kinematic viscosity
σ = Stefan–Boltzmann constant
τ_{bl} = thermal time constant for laminar boundary layer on a vertical wall
τ_{conv} = convective time constant for enclosure $= (H + 2L)/V_c$
τ_{core} = time constant for core in an enclosure with laminar boundary layers
τ_{th} = measured experimental thermal time constant

assumption of instantaneous horizontal spreading of the plume at the ceiling may be valid for tall enclosures but is questionable for shallow enclosures. For building enclosures, the steady-state horizontal recirculation appears to exist over at least 60 percent of the core height (Olson et al., 1990).

Experimental Apparatus

The experimental facilities were the same as those reported by Olson et al. (1990) in their steady-state natural convection experiments. One was a small-scale physical model containing R114, and the other was a full-scale room of a building.

Physical Scale Model. The scale model was a 1:5.5 reduction of the full-scale room. The Rayleigh number and Prandtl number of air were matched by using a dense refrigerant gas, R114, as the scaling fluid. We note that a radiation to convection *conductance* ratio (Olson et al., 1990), k_r, is 20 for the full scale and 10 for the scale model. Thus, the radiation does not scale exactly. R114 was chosen for its high density, nontoxicity, low cost, and 3.3°C boiling point at atmospheric pressure. The inner dimensions of the scale model were H = 47 cm, W = 68 cm, and L = 136 cm, making A_L = 0.35 and A_W = 0.69. All vertical walls consisted of 0.6-cm-thick aluminum plates (emissivity of 0.05). Electric resistance strip heaters attached to the back side of one end wall were used for heating. Cooling water was circulated through copper tubes, soldered to the back side of the opposing end wall, when a cold wall was needed. The ceiling was a double-pane plexiglass window with a 2.5-cm-thick gap between the panes, and the floor was plexiglass (emissivity of about 1.0 for both). The walls, ceiling, and floor were surrounded with 15 cm of rigid polyurethane boards (R7.5 $m^2-°C/W$).

Wall surface temperatures were measured with 30 gage type T thermocouples imbedded in small holes in the aluminum. The uncertainty in T_H and T_C was ±0.5°C. Temperatures in the interior were measured with a movable rake containing seven thermocouples (type T, 40 gage) arranged in a vertical line. The rake could be moved horizontally from endwall to endwall. Another thermocouple probe was mounted on the end of a 1.2-cm tube, which penetrated the test cell through the ceiling and could be be traversed vertically. Three ports were available in the ceiling to insert this probe. The endwall boundary layer temperatures were measured at midheight with probes that could be traversed across the boundary layer but not vertically. The hot wall probe was mounted on a fork assembly, which eliminated conduction errors, and was made of 0.025-mm-dia type T thermocouple wire, bead size approximately 0.075 mm. The frequency response of this probe was about 10 Hz. The opposing cold endwall boundary layer temperature was measured with a 40 gage thermocouple (bead size 0.25 mm) mounted on a similar fork assembly attached to the interior rake. The absolute uncertainty of the interior gas temperature was ±0.2°C, while the relative uncertainty from probe to probe was ±0.05°C.

Flow motions were made visible by injecting light-reflecting smoke into the enclosure and illuminating the smoke with a planar light source. The smoke used was ammonium chloride (NH_3Cl) particles, mixed with R114 gas. The temperature of this gas was controlled so that it was neutrally buoyant. Illumination and video recording of the flow motions was done through the ceiling after removing the top pieces of insulation.

To generate a disturbance, a stirring mechanism was inserted into the interior through a port in the ceiling midway between the hot and cold walls. This mechanism was rotated for 4–5 min using a 3/8 in. drill at about 600 rpm. The mechanism was a 35-cm-long rod with two 14-cm-long by 1-cm-wide vanes attached to the tip. When rotated by the drill, the vanes flipped up to a horizontal position. During rotation, the stirring mechanism was moved up and down by the drill.

To heat the endwall rapidly, we applied a large pulse of electric power for a short period of time to increase the wall temperature quickly, then reduced the heat input to a lower steady value to maintain constant temperature. This heating cycle could change the hot wall from ambient temperature to 80–90 percent of the steady-state value in about one minute. To cool the endwall rapidly, water was precooled in a reservoir, then pumped rapidly through the cooling tubes. The endwall cooling time constant was about two minutes.

Full-Scale Room. The full-scale room was a rectangular room with H = 2.5 m, W = 3.9 m, and L = 7.9 m, constructed by Ferm (1985), making A_L = 0.32 and A_W = 0.64. The effective insulating values of the floor, walls, and ceiling were R3.0, R2.8, and R11.5 ($m^2-°C/W$), respectively. Electric radiant heat panels were mounted on the inner wall surface of one of the 3.9-m-wide endwalls for heating. 1.6-mm-thick aluminum sheeting was attached to the heating panels to make the hot wall isothermal and reflective (emissivity of 0.05). The opposing 3.9-m-wide endwall was cooled by copper solar collector panels (emissivity of 0.12), also mounted on the inner surface. Chilled water was pumped from a storage reservoir through the collector panels.

The air temperatures in the full-scale room were measured with a vertical array of 24 gage type T thermocouples, uncertainty ±0.3°C, mounted on a movable post. The post was located midway between the two side walls and could be moved from the hot to the cold wall from outside the room. Thermocouples were attached to the hot and cold walls to measure their temperatures, with an uncertainty of ±1.0°C. A disturbance was generated by a 50-cm-dia fan, displacing roughly 2000 to 3000 cfm, which had been placed midway between the hot and cold walls. The fan was positioned 30 cm above the floor and facing the side walls. The fan was operated for about 5 min to disturb the flow field. Flow visualization was not done.

Experimental Procedure. Four different experiments were performed on the small scale model; three involved combinations of rapid heating or cooling of the endwalls, and one was a mechanical disturbance of a steady-state flow. A single experiment was performed on the full-scale room, which was the mechanical disturbance of a steady-state flow. The experimental conditions are summarized in Table 1. During a transient heating experiment, the hot wall was heated to about 10°C above ambient temperature, and during a transient cooling experiment the cold wall was cooled to about 10°C below ambient temperature. Based on $T_H - T_C$ at the completion of the experiment, this corresponds to a *steady-state* Ra of about 2.5×10^{10}. The uncertainty on the Rayleigh number was ±5 percent. A range of Rayleigh numbers for each type of experiment was not tested. For all experiments except experiment 1, Ra was varied from 2.5 to 2.9×10^{10}. If Ra were based on

Table 1 Summary of transient experiments in an empty enclosure

Expt. #	Type of Experiment	Model Size	Wall Temperatures (°C) Initial T_H	Initial T_C	Final T_H	Final T_C	Ra x10^{10}	Pr	τ_{conv}[1] (s)
1	Transient Heating, No Cooling	Small, R114	22.5	22.3	36.9	22.5	1.54	0.80	6.46
2	Mechanical Disturbance	Small, R114	32.5	9.2	32.3	9.1	2.51	0.80	7.12
3	Mechanical Disturbance	Large, Air	26.0	8.7	26.0	8.7	2.92	0.71	17.3[2] 31.0[3]
4	Steady Heating, Transient Cooling	Small, R114	36.8	23.2	35.8	10.4	2.70	0.80	6.85
5	Transient Heating, Steady Cooling	Small, R114	18.3	9.3	32.0	9.1	2.48	0.80	7.15

(1) Calculated from eq (4).
(2) T_m=22.2°C; this is for cold wall and floor region.
(3) T_m=22.2°C; this is for hot wall and ceiling region.

$T_H - T_m$ instead of $T_H - T_C$, the range for all experiments (including #1) would be 1.25 to 1.5×10^{10}. An experimental run continued for about 1 h after it was initiated, much longer than the convective or thermal time constants of the interior flow. Each experiment was repeated several times with the flow visualization system and temperature probes in different locations.

Experimental Results

Response Due to a Single Heat Transfer Wall. The manner by which a natural convection flow develops is seen by examining the flow visualization results for experiment 1 on the small-scale model. One endwall was heated rapidly and the opposing endwall was adiabatic. Prior to heating the wall, all walls and the gas were isothermal. A cloud of smoke was injected next to the vertical wall before heating it. After waiting for the motions produced by the injection to decay, the power to the hot wall heaters was turned on. The ensuring motions of the smoke are shown in Fig. 3, which contains sketches of the observed flow patterns at several times into the experiment. Each sketch is marked by the absolute time, t, and the dimensionless time, t^*, where the dimensionless time is the absolute time divided by the convective time constant:

$$t^* = t/\tau_{\text{conv}}. \tag{3}$$

The convective time scale used is discussed below. The uncertainty on the time for the flow to look as sketched is ±10 percent.

Almost as soon as the heating started (within a few seconds) vertical motion next to the wall was observed. Because this motion occurs before the hot wall has achieved a steady-state temperature, this heating cycle cannot be termed "instantaneous" compared to the vertical boundary layer time constant. At about 10 s into the transient (Fig. 3*a*), the smoke began to push across the ceiling. At 40–60 s (Fig. 3*b*) the smoke had nearly reached the opposing vertical wall. At 70–90 s (Fig. 3*c*) the secondary flow had become visible below the primary horizontal flow. After 3 min. (Fig. 3*d*), the full recirculating flow pattern looked nearly identical to that seen at steady state (Fig. 2) in the top half of the enclosure. All of the smoke cloud injected next to the heated wall was eventually entrained into the vertical boundary layer, and no motion was seen in the lower half of the enclosure.

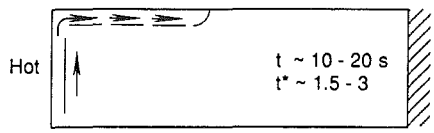

Figure 3a

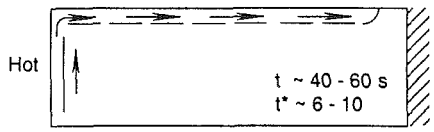

Figure 3b

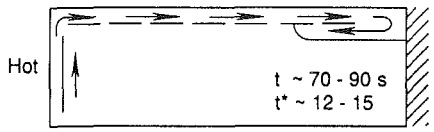

Figure 3c

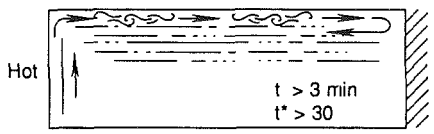

Figure 3d

Fig. 3 Development of flow patterns in response to sudden heating of one vertical wall in small-scale apparatus (experiment 1)

Close examination of the vertical boundary layer next to the hot wall indicated that the boundary layer was laminar rather than turbulent. The path-lines of the smoke next to the surface were vertical and parallel to it, with no random motion or disorder that characterizes turbulence. Additional smoke injected 7 min after the heating commenced also revealed a laminar boundary layer. This is in contrast to the turbulent boundary layer, which occurs at steady state with a vertical hot wall opposing a vertical cold wall (Fig. 2).

The same experiment was repeated with the smoke injected at other locations in the enclosure. Regardless of the injection location, or how long observations were continued after heating was initiated, the horizontal flow loop along the ceiling developed in the fashion shown in Fig. 3, and no flow was observed near the floor. Although motion was not observed with this flow visualization technique in the lower half of the enclosure, continuity requires that the vertical boundary layer entrain fluid along its height and set up a horizontal flow near the floor. Core velocities on the order of 1 mm/s would be expected due to entrainment, equivalent to the length of the enclosure divided by τ_{core}.

The reverse set of boundary conditions was also tested; that is, a transiently cooled endwall with the opposing wall adiabatic. In this case, the horizontal flow loop developed along the floor and flow was not observed near the ceiling. In both of these configurations, steady-state conditions were never truly achieved, since the heat flow at the walls was unbalanced and the enclosure temperatures drifted up (or down) with time. However, the flows patterns did not change qualitatively after the secondary flow returned to the driving vertical wall. The dominant flow time constant therefore appears to be a convective one, which is the time for the fluid to flow up through the vertical boundary layer and through the horizontal flow loop.

As the flow development appears to be convection dominated, we propose a convection time constant to scale time. The characteristic length scale is the distance traveled up the vertical wall and through the horizontal flow loop, or $H + 2L$. The velocity scale is the characteristic buoyant velocity in the steady-state vertical wall boundary layers, V_c. Steady-state natural convection experiments (Olson et al., 1990) show that both the vertical boundary layer velocities and the horizontal flow velocities scale well with V_c. Or,

$$\tau_{\text{conv}} = (H + 2L)/V_c, \quad \text{with } V_c = [g\beta(T_H - T_m)H]^{1/2}. \tag{4}$$

The uncertainty on τ_{conv} is ±3 percent for the small scale, and ±14 percent for the large scale. For experiment 1, τ_{conv} is about 6.5 s. For comparison, the boundary layer time constant (Eq. (1)) is 1 s, the core time constant (Eq. (2)) is 15.6 min, while a diffusive time constant (H^2/α) is 31 h. Referring to Fig. 3, the flow is established at $t^* = 30$. Since the velocity over most of the horizontal portion of the convection length is of the order of $0.1 V_c$, it is not surprising that the flow takes several multiples of $10 \times \tau_{\text{conv}}$ to become steady.

This simple transient experiment indicates that the core can be split conceptually into two separate regions, each substantially unaffected by the flow in the other region. Each horizontal flow loop is driven by the upstream vertical wall boundary layer; the ceiling loop requires a heated vertical wall, and the floor loop requires a cooled vertical wall. If the upstream vertical wall is not "active," there will be no significant motion in the "downstream" core region. The vertical wall

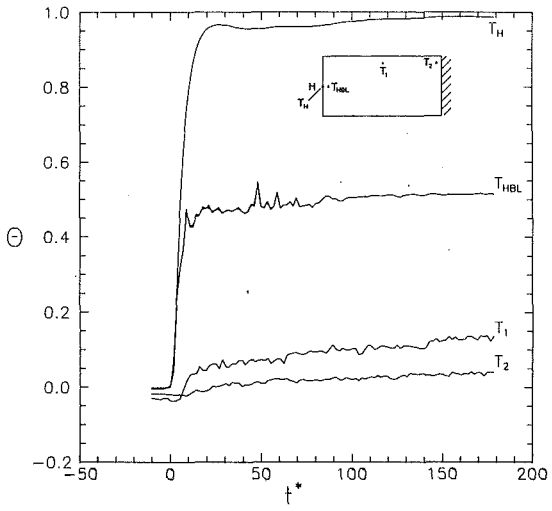

Fig. 4 Temperature response of the scale model for transient heating with no cooling (experiment 1); interior probe locations: T_{HBL}: $X/H = 0.004$, $Z/H = 0.5$; T_1: $X/L = 0.5$, $Z/H = 0.98$; T_2: $X/L = 0.96$, $Z/H = 0.96$

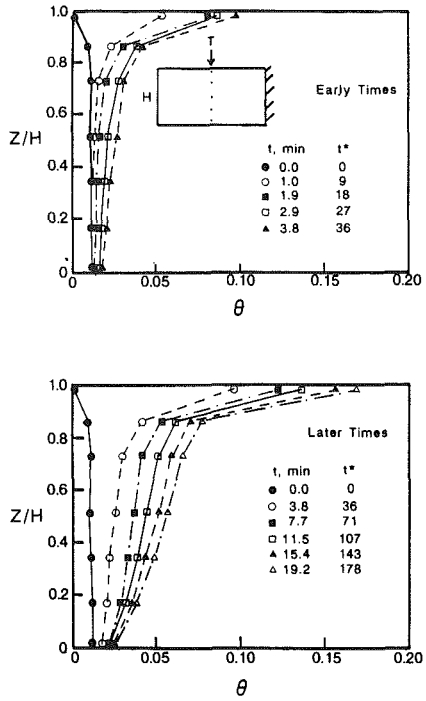

Fig. 5 Scale model vertical temperature profiles for transient heating with no cooling (experiment 1) at $X/L = 0.5$

conditions downstream of the horizontal loops have little effect on the horizontal flow.

Temperatures measured during experiment 1 (the rapidly heated wall with the opposing endwall adiabatic) are shown in dimensionless form in Figs. 4 and 5. Figure 4 is a trace of temperature versus time for probes located on the hot wall, in the hot wall boundary layer ($X/H = 0.004$, $Z/H = 0.5$), and two locations near the ceiling, denoted T_1 ($X/L = 0.5$, $Z/H = 0.98$) and T_2 ($X/L = 0.96$, $Z/H = 0.96$). The nondimensional temperature is referenced to the adiabatic endwall temperature since there was no cooling. The boundary layer temperature tracked the hot wall temperature very closely until the boundary layer temperature reached about 0.5; for later times the boundary layer temperature was roughly constant. This is believed to be a result of the vertical boundry layer having reached a steady temperature profile. (The value of $\theta = 0.5$ is due to the location of the probe; if the probe were closer to or farther from the wall the temperature at steady state would be different.) Some fluctuations were measured in the early part of the transient, but these were smaller in magnitude than those observed by Olson et al. (1990) in the turbulent boundary layer of the steady-state enclosure, which were at least 30 percent of $T_H - T_m$. The temperatures along the ceiling rose very slowly, although at $X/L = 0.5$, there appeared to be a slight jump at about 1 min, which could correspond to the horizontal flow front passing the probe.

Vertical temperature profiles are shown for equally spaced times in Fig. 5. Seven probes were positioned in a vertical line halfway between the two endwalls ($X/L = 0.5$); the top half of the figure shows time increments of about 1 min ($t^* = 9$), and the bottom half of the figure is for time increments of about 4 min ($t^* = 36$). The temperatures in the top 20 percent of the core increased rapidly in the first couple of minutes, then gradually drifted up. This was the region within the ceiling flow loop. This indicates a thermal time constant that is qualitatively similar to the convective time constant. Temperatures in the lower half of the core drifted up gradually for all times; since the only horizontal flow was due to boundary layer entrainment, the thermal time constant in this region should be different from the convection time constant (Eq. (3)). The gradual drift in temperature with time in the lower core for all times and in the upper core after the development of the horizontal flow loop is due to the imbalance of heat flow at the vertical walls.

Response Following a Disturbance. Results from experiments on both the small and large scale (experiments 2 and 3, respectively) for the response following a mechanical stirring of the gas were used to verify the accuracy of the scale model for transient conditions. Prior to the disturbance, a steady-state natural convection flow was established with an isothermal vertical hot wall opposing an isothermal vertical cold wall. The disturbance left the temperatures of all six walls unchanged, while equalizing the temperature of the fluid in the core. This type of experiment was a method of imposing the wall temperatures of the true steady-state flow instantaneously on an enclosure volume, with internal temperatures and flow patterns very different from the steady condition. The transient behavior after the disturbance stops will be due to the fluid accommodating itself to the steady wall temperatures, with no further drift in wall temperatures with time. We emphasize that the flow velocities were not zero when the disturbance stopped.

Flow visualization in the small-scale disturbance test (experiment 2) indicated the same mechanism for the flow development as for the transient hot wall test (experiment 1). Smoke was injected before the disturbance started, during the disturbance, and after the disturbance ended. Before the disturbance, the flow pattern was as shown in Fig. 1. When viewing at the location of the stirring mechanism ($X/L = 0.5$), upon disturbing the flow with the stirring vanes, the horizontal flow loops were overwhelmed by the mechanical disturbance. About 40 s ($t^* = 6$) after the disturbance stopped, wisps of smoke in the ceiling layer were visible moving from the hot wall to the cold wall at $X/L = 0.5$. At about 1 min 20 s ($t^* = 11$), smoke was first seen at $X/L = 0.5$ in the ceiling layer returning from the cold wall to the hot wall. By this time, the flow speed and layer thickness looked very similar to that of steady-state flow. Since the time for the natural convection flow loop to first be seen again was on the order of several convective time constants, it appears convection dominated the flow development.

The thermal time constant can be evaluated by examining the temperature measurements before, during, and after the disturbance transient. Figures 6 and 7 are plots of temperature versus time for the disturbance tests in the scale model and the full-scale room, respectively. Temperature measurements

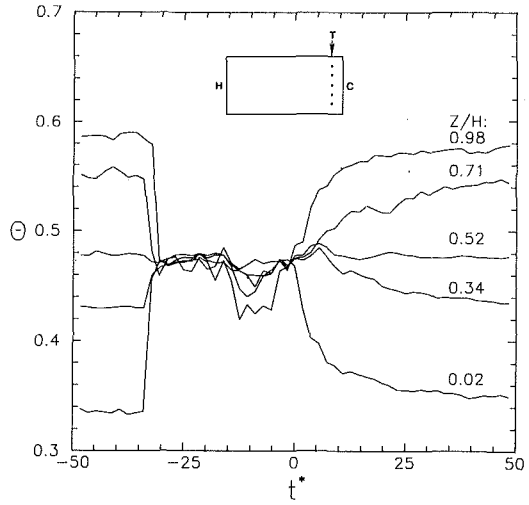

Fig. 6 Temperature response of the scale model during the recovery from a mechanical disturbance (experiment 2) at $X/L = 0.93$

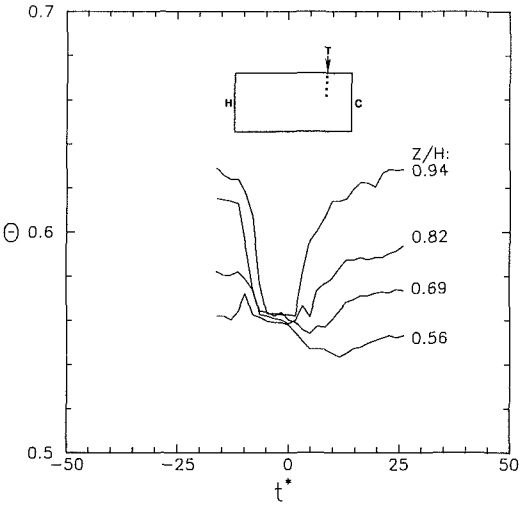

Fig. 7 Temperature response of the full-scale room during the recovery from a mechanical disturbance (experiment 3) at $X/L = 0.6$

are shown for the vertical array of thermocouples for the small scale at horizontal location $X/L = 0.93$ (the probes were placed here to avoid obstructing the stirring mechanism) and for the large scale at $X/L = 0.6$. Temperatures for the large scale are shown for the upper half of the enclosure only due to limitations in the number of channels that could be recorded on the data acquisition system. For both experiments, the disturbances were strong enough to overwhelm the steady-state natural convection, as evidenced by the temperature for all heights reaching a uniform level during the disturbance. After the disturbances were discontinued, the temperatures returned to their previous levels after only a few minutes, perhaps 3–5 min in the scale model and 5–10 min for the full scale. Especially noticeable in the scale model, the temperatures nearest the floor and ceiling seemed to reach steady state first, locations that would be within the horizontal flow layers. For the small scale, the thermal time constant was on the same order as the flow establishment time constant observed in flow visualization.

A more quantitative estimate of the experimental thermal time constant, τ_{th}, was made by examining the individual thermocouple traces, and defining the time constant as the time for the temperature to return to within e^{-1} of the "steady-state" temperature. Or,

$$\frac{T(\tau_{th}) - T_0}{T_{ss} - T_0} = 1 - e^{-1} \tag{5}$$

Table 2 Time constants for the mechanical disturbance experiments

Expt. #	Model Size	Time Constants (min) τ_{th}(1)	τ_{conv}(2)	τ_{th}/τ_{conv}
2	Small, R114	1.56±0.7	0.12	13.1±6.2
3	Large, Air, Ceiling Region	5.04±2.9	0.52	9.7±5.6
3	Large, Air, Floor Region	3.51±1.8	0.29	12.2±6.1

(1) Measured in experiment from temperatures.
(2) Calculated from eq (4).

where T_{ss} = the steady-state temperature of the probe,
T_0 = the temperature immediately after the disturbance is discontinued.

Averaging the time constants calculated for the individual probes over the height of the enclosure gives an estimate for the entire core. The disturbance test for the large scale was repeated with the probes placed in the lower half of the core. Table 2 lists these measured thermal time constants for the large and small scale, along with the convective time constants obtained by the scaling arguments. Also listed is the ratio of the measured thermal time constant to the convective time constant. In the large scale, since the mean core temperature was higher than the average of the hot and cold wall temperatures, convective and thermal time constants were calculated for both the hot wall/ceiling region, and the cold wall/floor region. The large uncertainties in the thermal time constants are due to the fluctuations in the gas temperatures (seen in Figs. 6 and 7).

Since the ratios of the measured thermal to convective time constants for the small and large scale agree to within experimental uncertainty (on the order of 10 for both), the small scale is a valid transient model of the full scale. Also, since the time constant ratios in Table 1 are of the same order as the dimensionless time for flow development ($t^* = 30$), it further confirms the thermal behavior, even in the core, is driven by a convective time scale rather than a diffusive time scale.

We note that although the natural convection has been scaled between the two models, radiation heat transfer is significant between the ceiling and floor and is not scaled. For the small scale, we estimate that 77 percent of the heat added at the vertical wall was radiated from the ceiling to the floor; for the large scale the same radiated heat was 62 percent. However, the agreement in the ratio of thermal to convective time scales for the two models indicates that this lack of radiation scaling is not significant in determining the transient behavior.

Figure 8 shows the vertical temperature profiles in the small scale (experiment 2) for several equally spaced times after the disturbance was turned off. The probes were located at $X/L = 0.8$. The top half of the figure shows the vertical profiles at time intervals of about 0.6 min ($t^* = 5$), and the lower figure shows the profiles at intervals of about 2.5 min ($t^* = 21$). The figure shows the re-establishment of the core temperature profile after only a few minutes, corresponding to a several multiples of the convective time constant.

Response Due to Two Heat Transfer Walls. In experiments 4 and 5, one endwall had been either hot or cold at steady temperature for several hours while the opposing wall was adiabatic. The previously adiabatic endwall was then cooled or heated rapidly. Due to the vertical wall conditions before the transient, one of the core horizontal flow loops was active while the other was absent. The rate of change of gas temperatures before the transient, due to an imbalance of heat added and removed, was approximately 0.2 to 0.4°C/h.

Flow observations show that the development of the horizontal flow loop in response to the vertical wall transient is

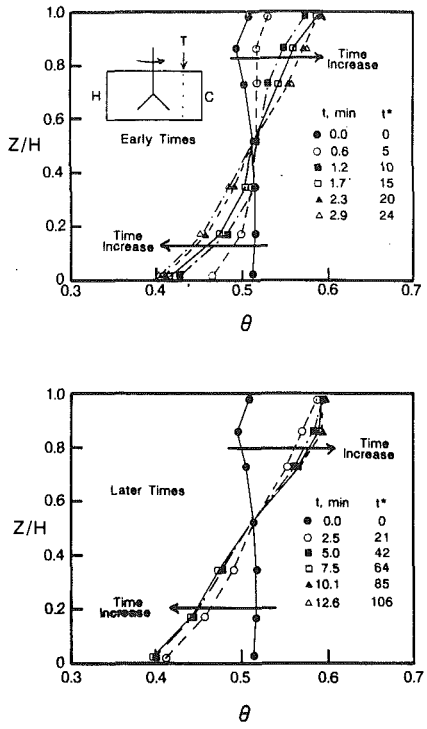

Fig. 8 Scale model vertical temperature profiles for the recovery from a mechanical disturbance (experiment 2) at $X/L = 0.8$

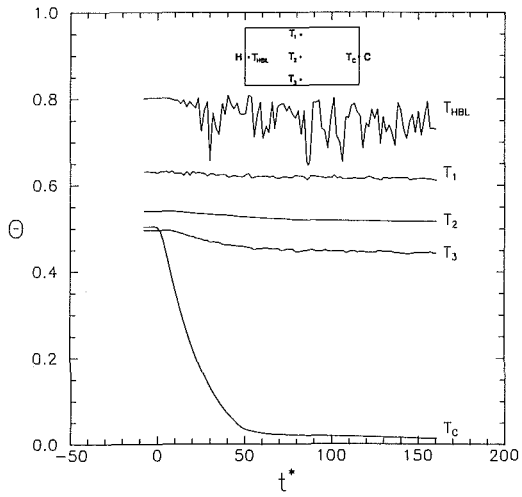

Fig. 9 Temperature response of the scale model for transient cooling with steady-state heating (experiment 4); T_{HBL}: $X/H = 0.004$, $Z/H = 0.5$; T_1: $X/L = 0.5$, $Z/H = 0.98$; T_2: $X/L = 0.5$, $Z/H = 0.5$; T_3: $X/L = 0.5$, $Z/H = 0.02$

again convection dominated. With the transient heating of the hot wall (experiment 5), the ceiling loop achieved what looks like steady-state conditions in a few minutes, corresponding to $t^* \sim 30$. Flow visualization for two active walls indicated that the vertical wall boundary layers were turbulent (which occurs in the steady-state flow of Fig. 1) instead of laminar as in the transient configuration with one endwall active.

Figure 9 shows a temperature versus time history for experiment 4, the configuration with transient cooling and steady-state heating. Shown are temperatures of the cold wall, the hot wall boundary layer, and three vertical positions in the core at $X/L = 0.5$ (Z/H coordinates are given in the figure caption). Before endwall cooling began, there were no fluctuations in the hot wall boundary layer temperature. In response to the cooling, the hot wall boundary layer temperature began to fluctuate with an amplitude of about 30 percent of $T_H - T_m$, similar to the fluctuations observed during steady-state conditions. Note that there has been *no change* in the hot wall boundary conditions to cause the fluctuations. This boundary layer fluctuation began about one minute after initiating the cooling, which should be about the time that the floor horizontal jet reached the bottom of the hot wall. The hot wall thermocouple was well above the vertical location where the upflowing horizontal floor jet formed a return layer to the cold wall. The transition from steady temperatures to highly fluctuating temperatures was also observed in the cold wall boundary layer for experiment 5. In this experiment, endwall cooling was steady and heating was begun rapidly.

The character of the vertical boundary layer, then, appeared to be related to whether or not a horizontal flow was approaching from "upstream." Presumably, the approaching jet flow had enough momentum to trip the vertical boundary layer from laminar to turbulent. An estimate of this effect was made by comparing the Reynolds number of the approaching horizontal jet to the vertical boundary layer Reynolds number. For a vertical natural convection boundary layer in an isolated fluid, transition to turbulence occurs anywhere from $Gr = 10^8$–10^{10} (Rohsenow and Choi, 1961). An effective Reynolds number of this flow can be estimated using the boundary layer width and velocity of laminar flow (Bejan, 1984). For $Pr < 1$:

$$\delta \sim H/(\mathrm{RaPr})^{1/4}, \tag{6}$$

$$V \sim [g\beta(T_H - T_C)H]^{1/2}, \tag{7}$$

$$\mathrm{Re} \sim V\delta/\nu \sim (\mathrm{Ra}^{1/4})/(\mathrm{Pr}^{3/4}). \tag{8}$$

For this Rayleigh number, Re of the laminar vertical boundary layer is on the order of 300. For the approaching horizontal flow, based on the jet velocity and thickness, Re is 500 to 1500. If the boundary layer in the absence of the approaching jet is laminar, the Reynolds number of the approaching floor jet seems enough higher so that transition to turbulence is assured.

Cheesewright and Zial (1986), in a steady-state experiment with air in a tall enclosure with hot and cold vertical walls ($A_L = 6$, $\mathrm{Ra} \sim 10^{10}$), also speculated that the turbulent temperature characteristics at the bottom of the hot wall boundary layer were carried over from the cold wall. The absence of a strong horizontal flow approaching the vertical boundary layer to promote turbulence could explain why Nansteel and Greif (1981) or Bohn et al. (1984) did not see turbulent boundary layers in steady-state water experiments with $\mathrm{Ra} \sim 10^{10}$.

We do not believe that the laminar or turbulent character of the wall boundary layers was due to differing stratification levels in the core, core temperatures changing with time, or the wall-to-core temperature difference. Using a linear stability analysis, Jaluria and Gebhart (1974) showed that ambient stratification tended to delay the onset of transition to turbulence for a vertical natural convection boundary layer. However, the transition from laminar to turbulent flow in experiments 4 and 5 occurred much more quickly than did changes in the core temperatures or stratification levels. This can be seen by comparing core temperatures T_1 and T_2 to T_{HBL} in Fig. 9. Hence both laminar and turbulent flow could occur for the *same* wall temperature and core temperature, the difference being the absence or presence of the incoming horizontal flow. In addition, for the steady-state experiments of Olson et al. (1990), turbulent vertical boundary layers were observed at the lowest Ra tested, $\mathrm{Ra} = 1.3 \times 10^{10}$ ($\mathrm{Ra} = 0.65 \times 10^{10}$ based on $T_H - T_m$). Experiment 1 of this work had laminar vertical boundary layers, even though the Rayleigh number and wall-to-core temperature difference was twice that of the steady-state experiment.

Profiles of temperature versus height for the core during transient cooling with the opposing endwall at steady-state heating (experiment 4) are shown in Fig. 10. The probes are located at $X/L = 0.5$. Most of the change in temperature occurred in the lower part of the core, which was expected since the ceiling flow loop was established before the cooling

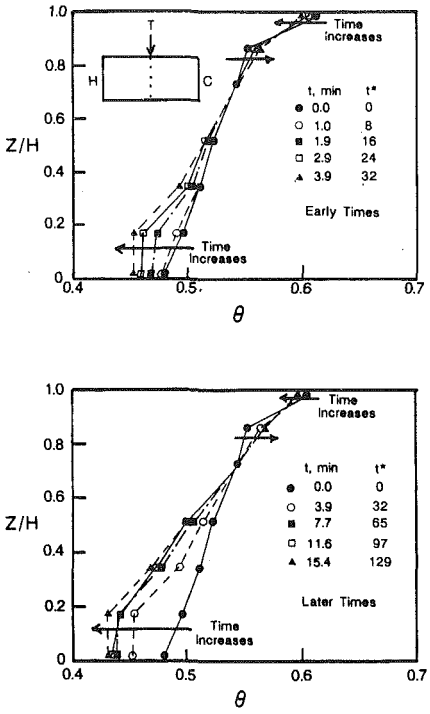

Fig. 10 Scale model vertical temperature profiles for transient cooling with steady-state heating (experiment 4) at $X/L = 0.5$

began. The accommodation of the temperatures to the new wall boundary conditions occurred after several increments of the convective time constant. A curious observation is that the temperature at $Z/H = 0.85$ appeared to rise slightly in response to the cooling of the cold wall. Pure speculation is that the cold wall may have some very minor effect on the ceiling flow loop; perhaps the primary ceiling jet thickens somewhat due to entrainment from the cold wall, and a probe that was previously within the cooler return layer is now inside the warmer primary layer. A similar effect was observed at height $Z/H = 0.1 - 0.2$ (near the floor) for transient heating and steady-state cooling; the temperature remained steady or dropped in response to transient heating.

Conclusions

Two kinds of transient natural convection experiment were performed: the establishment of steady-state convection starting from a well-mixed, isothermal gas with isothermal opposing endwalls at different temperatures; and the change in convective flow due to a sudden change in the temperature of one vertical endwall. All experiments indicated that the dominant time constant was a convective one. For both the large and small-scale experiments, the time constant was approximately the time for flow to travel up (or down) the adjacent vertical wall and through the horizontal flow loop. This time is on the order of 5–10 min for a room, which means natural convection flows re-establish themselves relatively quickly once a forced convection disturbance is stopped. This suggests that natural convection is important as a transport mechanism and in establishing comfort levels in many practical building situations.

Since we did not test a wide range of Rayleigh numbers, we do not know how extensive this time scaling is. However, steady-state experiments indicate the convective behavior does not change from $Ra = 1.3$ to 3.4×10^{10}; hence over this range in Ra we are confident the transient behavior is the same as that reported here.

The transient experiments confirmed that the horizontal flow loops were driven solely by the vertical boundary layer on the wall upstream, and were unaffected by the condition of the vertical wall downstream. The nature of the vertical boundary layer, however, was coupled to the horizontal flow upstream of it. For these flow conditions and room geometries, if there was a horizontal flow approaching the vertical wall, the boundary layer on the wall was turbulent. If there was no approaching flow, the boundary layer was laminar.

Finally, the agreement in scaled temperature profiles between the small and large-scale experiments for the disturbance-type transients confirms that a 1:5.5 scale model using R114 can accurately reproduce the transient behavior of building enclosures.

References

Baines, W. D., and Turner, J. S., 1969, "Turbulent Natural Convection From a Source in a Confined Region," *Journal of Fluid Mechanics*, Vol. 37, pp. 51–80.

Bejan, A., 1984, *Convection Heat Transfer*, Wiley, New York.

Bohn, M. S., Kirkpatrick, A. T., and Olson, D. A., 1984, "Experimental Study of Three Dimensional Laminar Convection at High Rayleigh Number," ASME JOURNAL OF HEAT TRANSFER, Vol. 106, pp. 339–345.

Cheesewright, R., and Zial, S., 1986, "Distributions of Temperature and Local Heat-Transfer Rate in Turbulent Natural Convection in a Large Rectangular Cavity," *Proceedings of the 8th International Heat Transfer Conference*, Vol. 4, pp. 1465–1470.

Ferm, H. M., 1985, "Measurements and Analysis of Natural Convection in Building Enclosures," S. M. Thesis, Massachusetts Institute of Technology, Cambridge, MA.

Jaluria, Y., and Gebhart, B., 1974, "Stability and Transition of Buoyancy-Induced Flows in a Stratified Medium," *Journal of Fluid Mechanics*, Vol. 66, pp. 593–612.

Litsek, P. A., and Bejan, A., 1988, "Transient Natural Convection Between Two Zones in an Insulated Enclosure," ASME JOURNAL OF HEAT TRANSFER, Vol. 110, pp. 116–125.

Nansteel, M. W., and Greif, R., 1981, "Natural Convection in Undivided and Partially Divided Rectangular Enclosures," ASME JOURNAL OF HEAT TRANSFER, Vol. 103, pp. 623–629.

Olson, D. A., 1986, "Scale Model Studies of Natural Convection in Enclosures at High Rayleigh Number," Ph.D. Thesis, Massachusetts Institute of Technology, Cambridge, MA.

Olson, D. A., Glicksman, L. R., and Ferm, H. M., 1990, "Steady-State Natural Convection in Empty and Partitioned Enclosures at High Rayleigh Numbers," ASME JOURNAL OF HEAT TRANSFER, Vol. 112, pp. 640–647.

Patterson, J., and Imberger, J., 1980, "Unsteady Natural Convection in a Rectangular Cavity," *Journal of Fluid Mechanics*, Vol. 100, part 1, pp. 65–86.

Rohsenow, W. M., and Choi, H., 1961, *Heat, Mass, and Momentum Transfer*, Prentice-Hall, Inc., Englewood Cliffs, NJ.

Worster, M. G., and Huppert, H. E., 1983, "Time-Dependent Density Profiles in a Filling Box," *Journal of Fluid Mechanics*, Vol. 132, pp. 457–466.

Worster, M. G., and Leitch, A. M., 1985, "Laminar Free Convection in Confined Regions," *Journal of Fluid Mechanics*, Vol. 156, pp. 301–319.

Yewell, R., Poulikakos, D., and Bejan, A., 1982, "Transient Natural Convection Experiments in Shallow Enclosures," ASME JOURNAL OF HEAT TRANSFER, Vol. 104, pp. 533–538.

Factors Affecting Nugget Growth With Mushy-Zone Phase Change During Resistance Spot Welding

P. S. Wei
Professor.
Mem. ASME

F. B. Yeh
Graduate Student.

Institute of Mechanical Engineering,
National Sun Yat-Sen University,
Kaohsiung, Taiwan

An unsteady, axisymmetric model is first proposed to investigate extensively effects of the physical, thermal, and metallurgical properties and welding conditions on nugget growths with mushy-zone phase change during resistance spot welding. The electromagnetic force, joule heat and interfacial heat generation, and cooling effects of electrodes are taken into account. Fluid patterns, temperature fields, and solute distributions in the liquid, solid, and mushy zones are determined. Results show that the computed nugget growths and temperature fields are consistent with experimental data. Variations of properties strongly affect the nugget growth. The maximum velocity in the weld nugget is found to be small and around 5 mm/s.

Introduction

Resistance spot welding has been widely used in joining workpieces. The materials to be joined are brought together under pressure by a pair of electrodes (see Fig. 1). A high electric current (usually greater than 8000 amp) passes through the workpieces between the electrodes and melts the weldments. Workpieces are thus joined as solidification of the weld pool occurs. Resistance spot welding is, therefore, a complicated process involving interactions of electrical, thermal, and metallurgical phenomena.

Heat transfer analysis is essentially required to investigate resistance spot welding. Nied (1984) proposed a highly flexible unsteady heat-conduction model and used the ANSYS finite-element computer code to determine temperature changes. The available numerical results were then applied to calculate deformation of electrodes and workpieces. Gould (1987) utilized a metallographic technique to measure weld nugget growths and developed a one-dimensional thermal model for comparison. Due to the breakdown of oxide layers and other insulating contaminants at the faying surfaces (Dickinson et al., 1980), electric contact resistance was assumed to be a linearly decreasing function of temperature. It was found that the predicted results exhibited a correct trend for the nugget development.

Wei and Ho (1990) modified the model of Gould (1987) to evaluate interfacial heat generation and joule heat. By accounting for effects of phase change, computed results showed surprisingly good agreement of the nugget thickness, nugget growth, and shape of the fusion zone with experimental data. Although the predicted nugget growths and temperatures have been achieved satisfactorily (Nied, 1984; Cho and Cho, 1989; Han et al., 1989; Wei and Ho, 1990), it is believed that the successes may be due to compensating effects of many unknown parameters, as can be seen later.

Recently, Alcini (1990) measured temperatures in the weld nugget by using beadless microthermocouples. Temperatures in the liquid nugget zone were found to be very uniform. Hence, it was concluded that strong convection occurred within the liquid nugget and the proposed swirling pattern was believed to be caused by a magnetic force. The importance of convection, however, appears to be questionable due to axisymmetry in shapes and forces for a resistance spot welding. For the sake of clarification, convection will be considered in this study.

Workpieces usually contain alloying elements. Melting or solidification of multiconstituent systems, unlike that of pure substances, is characterized by the existence of a multiphase or mushy region that separates the pure solid and liquid regions. Properties of the mushy zone control the microstructure and strength of workpieces. Savage et al. (1965) observed the microstructure and determined the conditions for occurrence of the mushy zone in resistance spot welding. A general understanding of the growth of the mushy zone as a function of the thermal, physical, and metallurgical properties and welding conditions, which are grouped by dimensionless parameters, however, has not been presented. Which factors they are and how these factors affect resistance spot welding will be investigated in this study.

In the present work, a continuum model, developed by Bennon and Incropera (1987), is used to predict the weld nugget growth by accounting for momentum, heat, and species transports in a binary solid–liquid phase-change system. A clearer understanding on resistance spot welding will be provided.

System Model and Analysis

Resistance spot welding is shown schematically in Fig. 1, as described previously. In this study, a cylindrical coordinate system is adopted to determine unsteady, axisymmetric momentum, energy, and species transport between solid, liquid and mushy zones. The major assumptions made are the following:

1 A uniform and axial electric current density is assumed for simplicity. Joule heat in the mushy zone is evaluated by using a mass-averaged electrical conductivity. Interfacial heat generation is, in fact, strongly affected by the pressure exerted by the electrodes and the surface condition of the workpieces. These factors, unfortunately, are very uncertain. A simple way to account for these factors is to introduce an effective heat transfer coefficient h_e at the contact surface between the electrode and the workpiece. Cooling effects and interfacial heat generation resulting from the workpiece–electrode contact thus can be determined. On the other hand, heat generation at the faying surface can be considered as a volumetric heat source with a small effective thickness ϵ_f (Wei and Ho, 1990). By increasing electrode pressure the effective thickness is decreased and interfacial heat becomes more concentrated. The contact resistance at ambient temperature, R_0, however, is reduced. Contact resistance also varies with temperature. In this study, contact resistance is assumed to decrease linearly

Contributed by the Heat Transfer Division for publication in the JOURNAL OF HEAT TRANSFER. Manuscript received by the Heat Transfer Division July 27, 1990. Keywords: Materials Processing and Manufacturing Processes, Phase-Change Phenomena, Transient and Unsteady Heat Transfer.

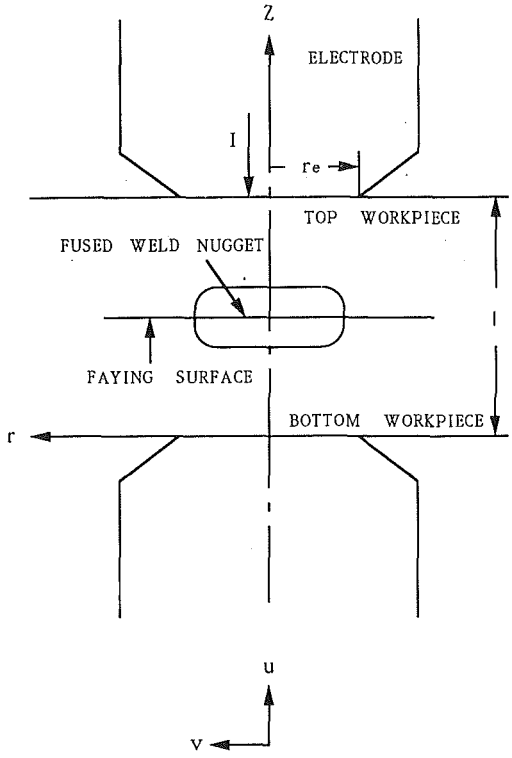

Fig. 1 Resistance spot welding process and coordinate system

with temperature to a first approximation, as suggested by Gould (1987) and Wei and Ho (1990).

2 Convection is considered. Darcy's law, which suggests that phase interaction forces are proportional to the liquid velocity relative to the velocity of the porous solid, is assumed to be applicable for modeling laminar momentum and energy transfers in the mushy zone (Ridder et al., 1981).

3 The workpieces are binary alloys. The solid and liquid in the mushy zone are assumed to be in a local thermal and phase equilibrium to a first approximation. The local equilibrium, however, does not preclude the existence of nonequilibrium conditions on a macroscopic scale (Bennon and Incropera, 1987). The solute diffusion in solid is also neglected due to a small solute diffusivity coefficient.

4 Properties of the liquid, solid, and mushy phases are assumed to be homogeneous and isotropic. Thermophysical properties are constant but different between phases.

Governing Equations. With the above assumptions, the continuity and momentum equations (Bennon and Incropera, 1987) become, respectively,

$$\frac{\partial \rho}{\partial t} + \nabla \cdot (\rho \mathbf{V}_m) = 0 \tag{1}$$

$$\frac{\partial \rho u_m}{\partial t} + \nabla \cdot (\rho \mathbf{V}_m u_m) = \mathrm{Pr} \nabla \cdot (\rho \nabla u_m) - \mathrm{Pr} \frac{\rho (1-g_l)^2}{\mathrm{Da} g_l^3} (u_m - u_s) - \frac{\partial p}{\partial z} + \mathrm{Pr}^2 \mathrm{Gr} [\theta_0 (T - T_{\mathrm{sol}}) + BF_0 (f_l^{\alpha} - f_{l, T=T_{\mathrm{sol}}}^{\alpha})] \tag{2}$$

Nomenclature

B = dimensionless parameter defined in equation (4)
$\mathbf{B}$ = magnetic flux vector, We/m^2
Bi_a, Bi_e = Biot number; $\mathrm{Bi}_a = \bar{h}_a r_e / k_s$, $\mathrm{Bi}_e = \bar{h}_e r_e / k_s$
c, C = specific heat and specific heat ratio; $C = c_l / c_s$
D = solute diffusivity, m^2/s
Da = Darcy number, defined in equation (4)
E = dimensionless electric contact resistance parameter defined in equation (10)
$\mathbf{F}$, F_r = force vector and component in r direction, N/m^3
f = mass fraction of liquid or solid
F_0 = dimensionless parameter defined in equation (4)
f^{α} = normalized solute mass fraction $= \tilde{f}^{\alpha} / \tilde{f}^{\alpha}_{m,0}$
$\tilde{f}^{\alpha}$ = solute mass fraction
$\tilde{f}^{\alpha}_{m,0}$ = initial solute content
g = volume fraction (= f for equal density between phases), or gravitational acceleration
Gr = Grashof number defined in equation (4)
h = enthalpy $= \tilde{h} / h_f$
$\bar{h}_a$, $\bar{h}_e$ = heat transfer coefficient, W/m^2-K
h_f = fusion latent heat at eutectic point, J/kg
I = welding current, amp
j = electric current density, amp/m^2
k, K = thermal conductivity and mixture thermal conductivity; $K = g_l + g_s K_h$
K_D = permeability, m^2
K_h = thermal conductivity ratio $= k_s / k_l$
k_p = equilibrium partition coefficient
K_0 = permeability constant, m^2
l, L = double workpiece thickness; $L = l / r_e$
La = dimensionless joule heat, defined in equation (4)
m = liquidus and solidus line slope parameter
p = pressure $= \tilde{p} r_e^2 / \tilde{\rho}_l \alpha_l^2$
Pr = Prandtl number
r = radial coordinate $= \tilde{r} / r_e$
R = $c_s \tilde{T}_0 / h_f$
r_e = electrode radius, m
R_f, R_0 = electrical contact resistance at any temperature and ambient temperature; $R_f = \tilde{R}_f / \tilde{R}_0$
Sc = Schmidt number
t = time $= \tilde{t} \alpha_l / r_e^2$
T, T_e = temperature and eutectic temperature; $T = \tilde{T} / \tilde{T}_0$
T_m, T_0 = melting and initial temperature
u = radial velocity $= \tilde{u} r_e / \alpha_l$
v = axial velocity $= \tilde{v} r_e / \alpha_l$
$\mathbf{V}$ = velocity vector
z = axial coordinate $= \tilde{z} / r_e$
α = thermal diffusivity, m^2/s
β_S, β_T = solutal and thermal expansion coefficient
δ_{liq}, δ_{sol} = dimensionless thickness of region surrounded by liquids and solidus line at $r = 0$
ϵ_f = effective thickness of heat source at faying surfaces, m
θ_0 = dimensionless parameter defined in equation (4)
μ_0, μ_r = free and relative magnetic permeability, N/amp^2
ν = kinematic viscosity, m^2/s
ρ = density $= \tilde{\rho} / \tilde{\rho}_l$
σ = electrical conductivity $= \tilde{\sigma} / \tilde{\sigma}_s = g_s + g_l \tilde{\sigma}_l / \tilde{\sigma}_s$
Σ = dimensionless parameter defined in equation (10)

Superscripts

α = solute
$\sim$ = dimensional quantity

Subscripts

l = liquid
liq = liquidus
m = mixture
s = solid
sol = solidus

$$\frac{\partial \rho v_m}{\partial t} + \nabla \cdot (\rho \mathbf{V}_m v_m) = \mathrm{Pr} \nabla \cdot (\rho \nabla v_m) - \mathrm{Pr} \frac{\rho (1-g_l)^2}{\mathrm{Da} g_l^3} (v_m - v_s) - \frac{\partial p}{\partial r} - La \frac{r}{2\pi^2} \quad (3)$$

where the dimensionless parameters are defined as

$$\mathrm{Pr} = \frac{\nu_l}{\alpha_l}, \quad \mathrm{Da} = \frac{K_0}{r_e^2}, \quad \mathrm{Gr} = \frac{g\beta_T (\tilde{T}_{\mathrm{sol}} - \tilde{T}_e) r_e^3}{\nu_l^2}, \quad \theta_0 = \frac{\tilde{T}_0}{\tilde{T}_{\mathrm{sol}} - \tilde{T}_e},$$
$$B = \frac{\beta_s (\hat{f}^{\alpha}_{l,e} - \hat{f}^{\alpha}_{m,0})}{\beta_T (\tilde{T}_{\mathrm{sol}} - \tilde{T}_e)}, \quad F_0 = \frac{\hat{f}^{\alpha}_{m,0}}{\hat{f}^{\alpha}_{l,e} - \hat{f}^{\alpha}_{m,0}}, \quad La = \frac{I^2 \mu_0 \mu_r}{\tilde{\rho}_l \alpha_l^2} \quad (4)$$

The second terms on the right-hand side of equations (2) and (3) are related to interactions between phases in the porous mushy zone. The isotropic permeability, according to the Kozeny–Carman equation, is

$$K_D = \frac{K_0 g_l^3}{(1-g_l)^2} \quad (5)$$

Equation (5) is generally considered valid in the laminar flow regime and applicable in this case as can be seen later. The last terms in equations (2) and (3) represent the buoyancy force resulting from the temperature and composition differences and electromagnetic force, respectively. The electromagnetic force can be found to be (Shercliff, 1965)

$$\mathbf{F} = \mathbf{j} \times \mathbf{B} \quad (6)$$

where the magnetic flux $\mathbf{B}$ can be calculated from Ampere's law

$$\nabla \times \frac{\mathbf{B}}{\mu_0 \mu_r} = \mathbf{j} \quad (7)$$

By substituting equation (7) into equation (6), the electromagnetic force becomes

$$F_r = -\frac{\mu_0 \mu_r j^2 \tilde{r}}{2} \quad (8)$$

In view of phase change in the mushy zone, the enthalpy formation for the energy equation can be conveniently used (Bennon and Incropera, 1987)

$$\frac{\partial \rho h_m}{\partial t} + \nabla \cdot (\rho \mathbf{V}_m h_m) = C \nabla \cdot (K \nabla h_m) + C \nabla \cdot [K \nabla (h_s - h_m)] - \nabla \cdot [\rho (h_l - h_m)(\mathbf{V}_m - \mathbf{V}_s)] + \frac{LaER_f}{\pi} + \frac{La\Sigma}{\sigma \pi^2} \quad (9)$$

where

$$E = \frac{\tilde{R}_0 \alpha_l}{h_f \epsilon_f \mu_0 \mu_r}, \quad \Sigma = \frac{\alpha_l}{r_e^2 h_f \tilde{\sigma}_s \mu_0 \mu_r} \quad (10)$$

and

$$h_s = RT; \quad h_l = RCT + R(1-C)T_e + 1 \quad (11)$$

The first two terms on the right-hand side of equation (9) represent the net Fourier diffusion flux; the third term is the energy flux associated with relative phase motion. The fourth term suggested by Wei and Ho (1990) is related to heat generation at the faying surface. As mentioned previously, the dimensionless electrical contact resistance at the faying surface can be expressed by

$$R_f = \frac{T_{\mathrm{liq}} - T}{T_{\mathrm{liq}} - 1} \quad (12)$$

Equation (12) indicates that contact resistance is a linearly decreasing function of temperature and it vanishes when the full-liquid weld pool occurs. The last term in equation (9) is joule heating occurring in the bulk workpieces.

The conservation requirement for species α is

$$\frac{\partial \rho f_m^{\alpha}}{\partial t} + \nabla \cdot (\rho \mathbf{V}_m f_m^{\alpha}) = \frac{\mathrm{Pr}}{\mathrm{Sc}} \nabla \cdot (\rho f_l \nabla f_m^{\alpha}) + \frac{\mathrm{Pr}}{\mathrm{Sc}} \nabla \cdot [\rho f_l \nabla (f_l^{\alpha} - f_m^{\alpha})] - \nabla \cdot [\rho (f_l^{\alpha} - f_m^{\alpha})(\mathbf{V}_m - \mathbf{V}_s)] \quad (13)$$

where the Schmidt number $\mathrm{Sc} \equiv \nu_l / D_l^{\alpha}$.

Boundary and Initial Conditions. The top workpiece surface is assumed to remain solid during the welding process

$$u_m = v_m = 0, \quad f_m^{\alpha} = 1 \qquad z = L, \quad 0 \le r < \infty \quad (14)$$

The heat loss to the top electrode is

$$-\frac{\partial h_m}{\partial z} = \mathrm{Bi}_e (h_m - R) \qquad 0 \le r \le 1 \quad (15)$$

and heat transfer loss to the surroundings is

$$-\frac{\partial h_m}{\partial z} = \mathrm{Bi}_a (h_m - R) \qquad 1 < r < \infty \quad (16)$$

Similarly, boundary conditions for the bottom workpiece are

$$u_m = v_m = 0, \quad f_m^{\alpha} = 1 \quad z = 0, \quad 0 \le r < \infty \quad (17)$$

$$\frac{\partial h_m}{\partial z} = \mathrm{Bi}_e (h_m - R) \quad 0 \le r \le 1 \quad (18)$$

$$\frac{\partial h_m}{\partial z} = \mathrm{Bi}_a (h_m - R) \quad 1 < r < \infty \quad (19)$$

The axisymmetric boundary conditions at $r = 0$ are

$$\frac{\partial u_m}{\partial r} = \frac{\partial v_m}{\partial r} = \frac{\partial f_m^{\alpha}}{\partial r} = \frac{\partial h_m}{\partial r} = 0 \qquad r = 0, \quad 0 \le z \le L \quad (20)$$

The initial temperature and temperatures of workpieces far from the weld nugget remain at the surrounding temperature $\tilde{T}_0$

$$u_m = v_m = 0, \quad f_m^{\alpha} = 1, \quad h_m = R \qquad r \to \infty, \quad 0 \le z \le L \quad (21)$$

Temperature/Enthalpy Relationships. Temperature can be determined provided that enthalpy is known. As illustrated in Fig. 2, the liquidus and solidus curves can be approximated as straight lines. Temperature versus enthalpy relationships found by Bennon and Incropera (1988) are:

1 For an enthalpy $h_m \le h_{\mathrm{sol}}$, temperature and solid fractions can be obtained to be

$$T = \frac{h_m}{R}, \quad f_s = 1 \quad (22)$$

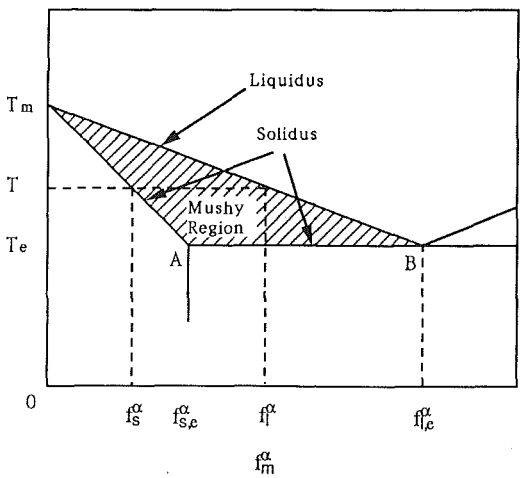

Fig. 2 Phase diagram for a binary system

where $R = c_s\bar{T}_0/h_f$ and $h_{sol} = RT_{sol}$.

2 For enthalpy $h_{sol} < h_m \le h_e$,

$$T = T_{sol}, \quad f_s = 1 - (h_m - h_{sol}) \tag{23}$$

where

$$h_e = h_{sol} + \left[1 - \frac{1}{1-k_p}\left(\frac{T_{sol}-T_{liq}}{T_{sol}-T_m}\right)\right] \tag{24}$$

3 For enthalpy $h_e < h_m < h_{liq}$, temperature and solid fractions become

$$T^2 + \gamma_1 T + \gamma_2 = 0, \quad f_s = \frac{1}{1-k_p}\left(\frac{T-T_{liq}}{T-T_m}\right) \tag{25}$$

where

$$h_{liq} = RCT_{liq} + R(1-C)T_e + 1 \tag{26}$$

and

$$\gamma_1 = \frac{1}{1-Ck_p}\left\{(C-1)T_{liq} - k_p\left[(1-C)T_e + \frac{1}{R}\right] - CT_m(1-k_p) - \frac{1-k_p}{R}h_m\right\} \tag{27}$$

$$\gamma_2 = \frac{1}{1-Ck_p}\left\{\left[(1-C)T_e + \frac{1}{R}\right]T_{liq} - (1-k_p)T_m\left[(1-C)T_e + \frac{1}{R}\right] + \frac{1-k_p}{R}T_m h_m\right\} \tag{28}$$

4 For enthalpy $h_m > h_{liq}$,

$$T = \frac{1}{C}\left\{\frac{h_m}{R} - \left[(1-C)T_e + \frac{1}{R}\right]\right\}, \quad f_s = 0 \tag{29}$$

Supplementary Relationships. By assuming an equilibrium state in the mushy zone, the fraction of the solute α in the solid and liquid can be found to be (Bennon and Incropera, 1987)

$$f_s^\alpha = \frac{k_p f_m^\alpha}{1 + f_s(k_p - 1)} \tag{30}$$

$$f_l^\alpha = \frac{f_m^\alpha}{1 + f_s(k_p - 1)} \tag{31}$$

where the equilibrium partition coefficient k_p represents the ratio of solute contents in the solid and liquid at the same temperature. That is

$$k_p = \frac{f_s^\alpha}{f_l^\alpha} \tag{32}$$

The mean solute concentration f_m^α appearing in equations (30) and (31) at any location then can be found from equation (13).

Solution Methodology. Each of conservation equations (1)–(3), (9), and (13) can be cast in the form

$$\frac{\partial \rho\phi}{\partial t} + \nabla\cdot(\rho \mathbf{V}_m\phi) = \nabla\cdot(\Gamma_\phi \nabla\phi) + S_\phi \tag{33}$$

where a general dependent variable ϕ denotes 1, u_m, v_m, h_m, and f_m^α, respectively, and Γ_ϕ and S_ϕ are the diffusion coefficient and source term, respectively. A control-volume, staggered grid, implicit finite-difference scheme (Patankar, 1980) was used to solve the governing equations. In this work, a successive underrelaxation method was adopted with a relaxation factor of 0.5 for momentum and species, and 0.8 for pressure and temperature fields. Results were obtained by using a 42 × 53 grid in the radial and axial directions, respectively. A uniform grid spacing in the axial direction and spacing ratio of adjacent grids of 1.17 in the radial direction were chosen. A dimensionless uniform time step was chosen to be 3.5×10^{-3}. A Cyber 840A computer required around 9800 seconds, CPU time, to complete computation for 71 time steps.

The convergence criterion was met by relative errors of dimensionless velocity components less than 1×10^{-2}, enthalpy and concentration less than 1×10^{-3}. The number of iterations for dimensionless results each time is around 70. In order to compare with experimental data, 150 iterations were used. The

Table 1 Values of dimensionless parameters

Biot number, Bi_a	1.4×10^{-3}
Biot number, Bi_e	0.72
Liquid specific heat parameter, C	1.4
Darcy number, Da	1.4×10^{-5}
Electrical contact resistance parameter, E	5.6×10^{-7}
Solid-to-liquid thermal conductivity ratio, K_h	1.0
Dimensionless workpiece thickness, L	0.5
Welding current parameter, La	1.1×10^{11}
Slope parameter of liquidus line, m_{liq}	4.0
Slope parameter of solidus line, m_{sol}	3.0
Prandtl number, Pr	0.1
Solid specific heat parameter, R	0.9
Schmidt number, Sc	140
Dimensionless eutectic temperature, T_e	5.0
Dimensionless melting temperature, T_m	6.0
Thermal-to-electrical property parameter, Σ	2.0×10^{-9}
Electrical conductivity ratio, σ	1.0

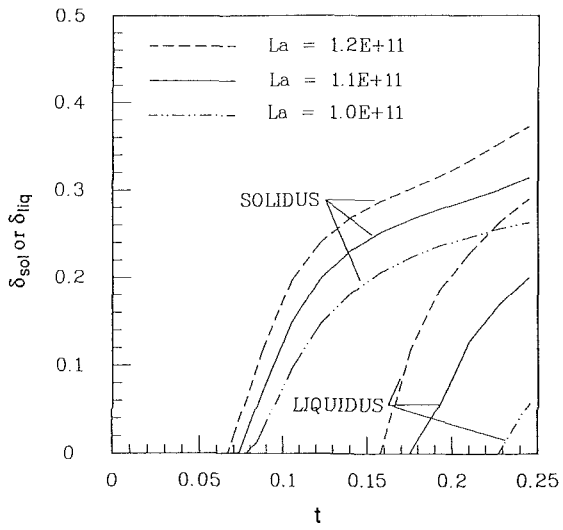

Fig. 3 Growths of the solidus and liquidus lines for different values of dimensionless welding current parameter

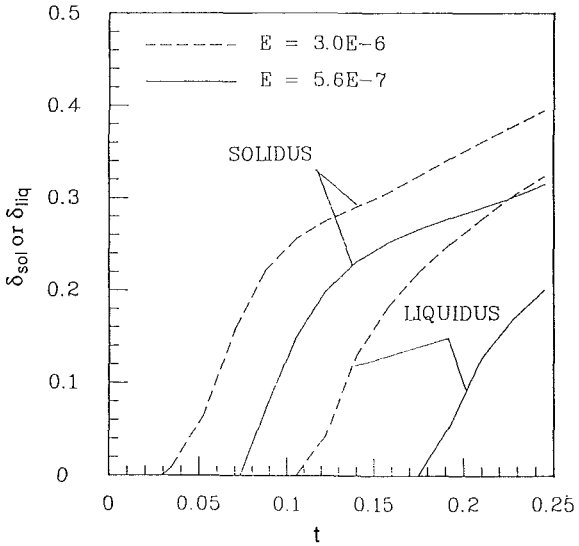

Fig. 4 Growths of the solidus and liquidus lines for different dimensionless electric contact resistances

global energy balance indicating that heat generations are balanced with the total internal energy rise and heat convected to the electrodes and surroundings is also required to assure convergence

$$\frac{\left|\int_{\nu} I^2\left(\frac{\tilde{R}_f}{\pi r_e^2 \epsilon_f}+\frac{1}{\tilde{\sigma}\pi^2 r_e^4}\right)d\nu-\int_{\nu_1}\tilde{\rho}c\frac{\partial\tilde{T}}{\partial\tilde{t}}\,d\nu_1-2\bar{h}_e\int_{A_e}(\tilde{T}_{\tilde{z}=1}-\tilde{T}_0)dA_e-2\bar{h}_a\int_{A_a}(\tilde{T}_{\tilde{z}=1}-\tilde{T}_0)dA_a\right|}{\int_{\nu} I^2\left(\frac{\tilde{R}_f}{\pi r_e^2 \epsilon_f}+\frac{1}{\tilde{\sigma}\pi^2 r_e^4}\right)d\nu} \le 10^{-2}$$

where ν is the volume where welding current passes between electrodes, ν_l denotes the volume of the heat-affected zone, A_e and A_a represent areas where energies dissipated to the electrode and surroundings, respectively.

Results and Discussion

In this study, resistance spot welding is found to be determined primarily by the welding current parameter $I^2\mu_0\mu_r/\tilde{\rho}_l\alpha_l^2$, dimensionless electric contact resistance $\tilde{R}_o\alpha_l/\epsilon_f h_f \mu_r\mu_0$, workpiece thickness l/r_e, Biot numbers $\bar{h}_e r_e/k_s$, solid-to-liquid thermal conductivity ratio k_s/k_l, liquid specific heat c_l/c_s, solid specific heat parameter $c_s\tilde{T}_0/h_f$, and the parameters m_{sol} and m_{liq} that are related to the slopes of the solidus and liquidus lines in the phase diagram, respectively. Values of them are chosen between pure iron and manganese to simulate a realistic resistance spot welding (Table 1).

The effect of the welding current parameter, which is related to heat generation, on the nugget growth is shown in Fig. 3. The vertical axis represents thicknesses δ_{sol} and δ_{liq} of the regions surrounded by the solidus and liquidus lines on the axisymmetric axis, respectively. For a welding current parameter $La = 1.2 \times 10^{11}$ the weld nugget or the solidus line is initiated at a dimensionless welding time of 0.0665. Thereafter, a mushy zone, that is, a mixture of solid and liquid, occurs and grows. After a welding time of 0.1575, the liquidus line appears and the weld nugget is then composed of the mushy and full-liquid regions. The thickness of the mushy zone, $(\delta_{\text{sol}} - \delta_{\text{liq}})/2$, becomes narrower as the welding time and welding current increase. This is because more energy is transferred to melt the solid. A slight increase in welding current gives rise to earlier onset, higher growth rate for both the liquid and solidus lines, and larger thicknesses of the weld nugget and full-liquid region.

As presented in Fig. 4, increasing electric contact resistance causes an early formation for both the solidus and liquidus lines, a decrease in the thickness of the mushy zone. Thickness of the weld nugget is also increased at a longer welding time.

The ratio of the workpiece thickness to electrode radius exhibits significant variations on the nugget growth and thickness, as shown in Fig. 5. Initiation times, growth rates, and movements of the solidus and liquidus lines decrease with decreasing workpiece thickness. The explanation is that the mass of a thin plate is small. Therefore, it is comparatively easy to raise temperatures in the workpieces and enhance the heat transfer rates to the electrodes (Wei and Ho, 1990).

The electrodes provide a cooling effect during the squeezing and welding cycles. Therefore, onsets of the solidus and liquidus lines are delayed, and growth rates and nugget thicknesses are reduced by increasing the Biot number, as can be seen from Fig. 6. Influence of the solid-to-liquid thermal conductivity ratio on the growth of the mushy zone is presented in Fig. 7. In view of an increase in heat transferred to melt the solid, increasing the liquid thermal conductivity results in an early formation and significant growth for both the solidus and liquidus lines. The full-liquid region does not appear in the case of the conductivity ratio above 1.25.

In view of a decrease in the energy absorbed per unit temperature rise in the liquid region and an increase of energy for melting, a low specific heat of liquid causes an early and rapid growth for both the solidus and liquidus lines, as shown in Fig. 8. Similarly, an increase in specific heat of solid delays the growth and reduces growth rate for both the solidus and liquidus lines, as presented in Fig. 9.

Characteristics of the phase diagram also have a significant influence on growths of the weld nugget and mushy zone, as shown in Fig. 10. The dimensionless parameter m_{sol} represents the ratio of the solute concentration at point A (see Fig. 2) to the initial solute content. The smaller the value of this dimensionless parameter, the steeper the solidus line is. It can be seen that decreasing the slope parameter results in an early growth for the solidus line and late formation of the liquidus

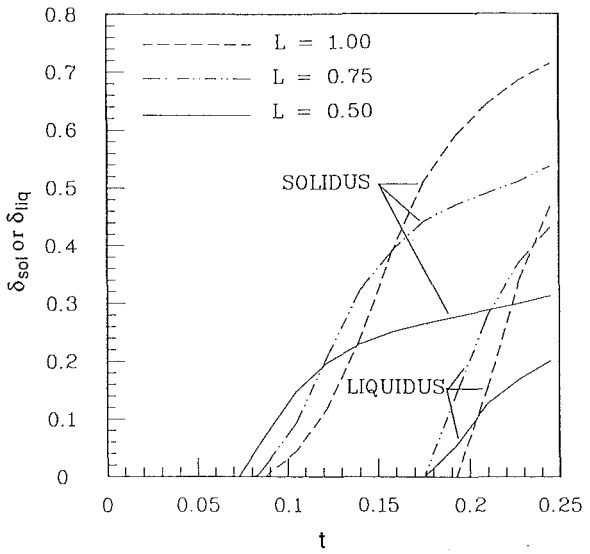

Fig. 5 Growths of the solidus and liquidus lines for different dimensionless workpiece thicknesses

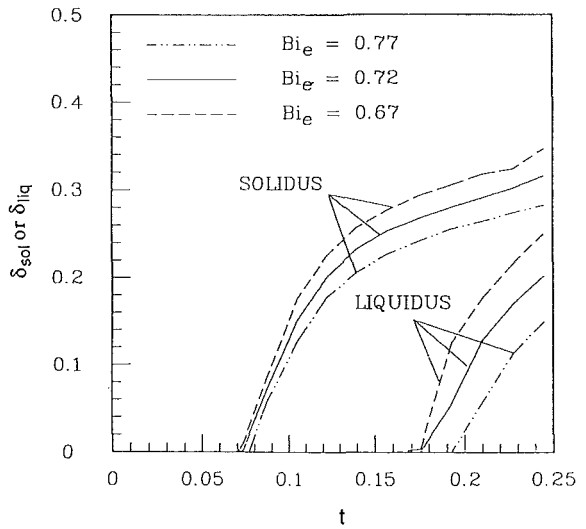

Fig. 6 Growths of the solidus and liquidus lines for different values of Biot number

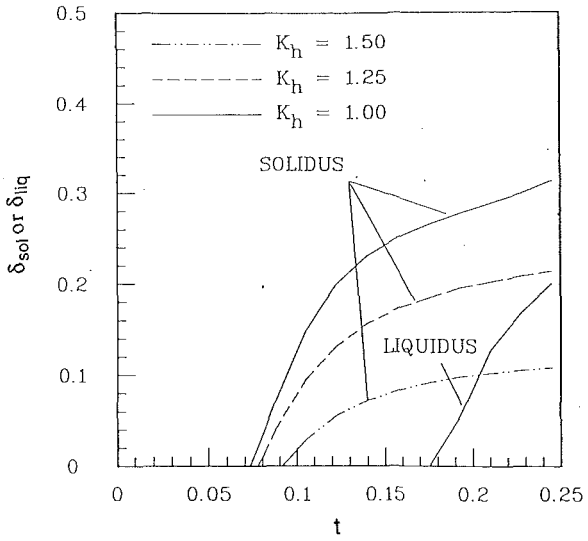

Fig. 7 Growths of the solidus and liquidus lines for different solid-to-liquid conductivity ratios

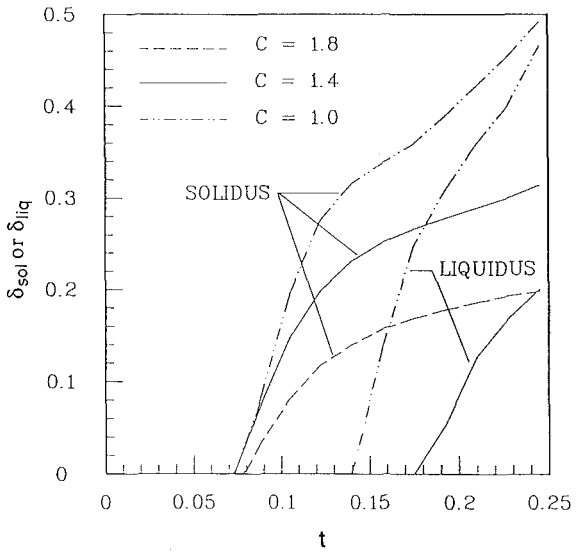

Fig. 8 Growths of the solidus and liquidus lines for different dimensionless liquid specific heats

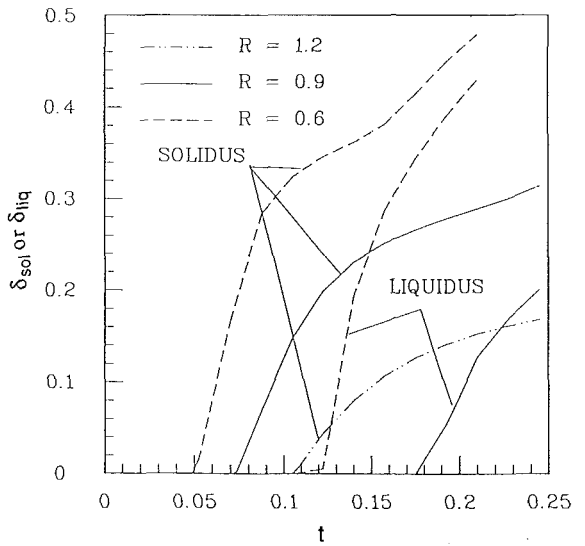

Fig. 9 Growths of the solidus and liquidus lines for different dimensionless solid specific heats

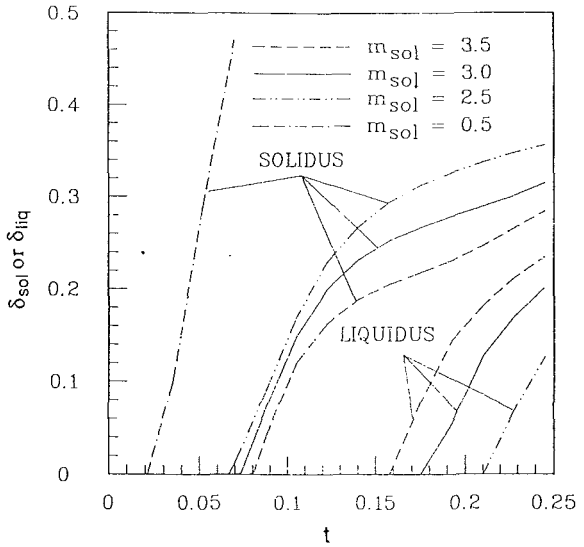

Fig. 10 Growths of the solidus and liquidus lines for different values of dimensionless slope parameter of the solidus line

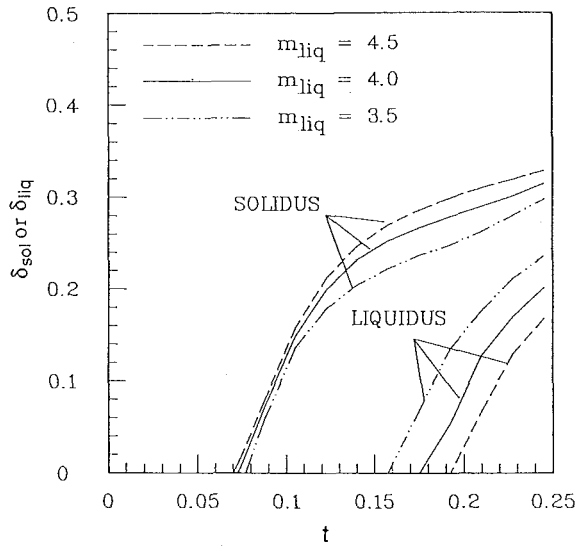

Fig. 11 Growths of the solidus and liquidus lines for different values of dimensionless slope parameter of the liquidus line

line. This is attributed to a decrease of the solidus temperature, which results in a wide range of the mushy zone and an increase of energy required for phase change (see Fig. 2). In the case of the dimensionless slope parameter equal to 0.5, the initial solute content lies between points A and B (see Fig. 2). Since the solidus temperature that corresponds to the eutectic temperature is lowest, the solidus line develops sooner.

The dimensionless parameter m_{liq} shown in Fig. 11 indicates the ratio of solute concentration at point B to the initial solute content. It can be seen that a steep liquidus line decreases the range of the mushy zone. As a result, initiation time for the liquidus line is reduced. The growth of the solidus line is found to be delayed slightly.

Referring to previous figures, it is seen that the general trend of nugget growths agrees with available experimental results for welding AISI 1008 (Gould, 1987). However, it is impossible to make an accurate comparison at the present time. The reason for this is that variations of properties have strong influence on the nugget growth, as can be seen in this study. Available data of properties such as the phase diagram with several components are also very limited. Since this study is a general

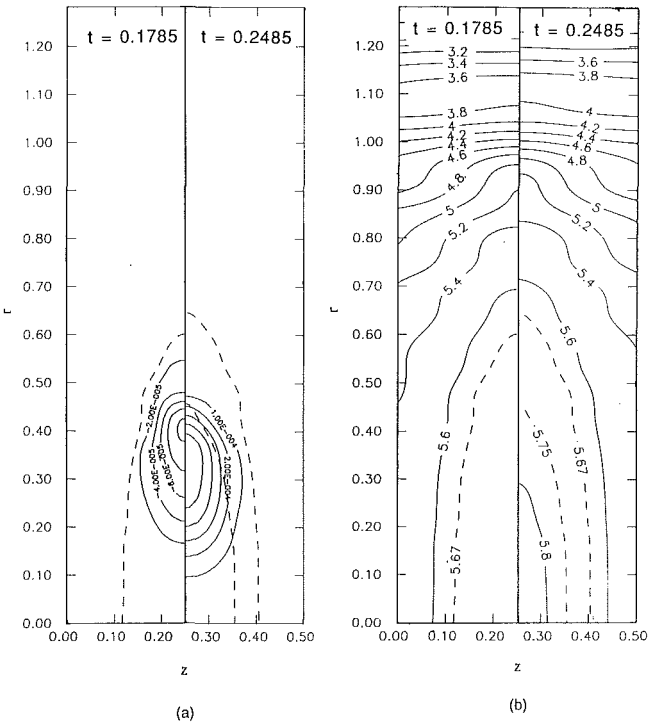

Fig. 12 *(a)* **The streamlines, and** *(b)* **isotherms at different welding times**

model that accounts for all the important factors previously indicated, the results will give a reliable and systematic insight into resistance spot welding.

The streamlines at different welding times are plotted in Fig. 12(*a*) to describe the flow pattern in the weld nugget. The dashed lines delineate the liquidus and solidus lines, respectively. It can be seen that the full-liquid region does not appear at a welding time of 0.1785. For a welding time of 0.2485 the weld nugget comprises the full-liquid and mushy regions. Motion of liquid is found to increase from the mushy zone to the full-liquid region. Liquid flows clockwise in the mushy zone due to the solute buoyancy and becomes counterclockwise in the full-liquid region as a result of thermal buoyancy. This result was qualitatively observed by Cunningham and Begeman (1965). The maximum liquid velocity was found to be around 5 mm/s, which is much smaller than the 20 cm/s and 5 m/s for the arc and high-energy beam weld pools, respectively, even though the welding current is typically 100 and 10^6 times as high. The explanation for this is that the electromagnetic force exerted on the fluid flow is nearly canceled due to axisymmetry of the resistance spot welding. Hence, fluid flow only causes a minor effect on the nugget growth and contradicts the proposition made by Alcini (1990). In the case of a radially distributed welding current density, it is noted that effects of the electromagnetic force are also small. This can be revealed by taking the curl of equation (6) and its value vanishes.

The corresponding isotherms in the solid, mushy, and liquid regions are shown in Fig. 12(*b*). It is found that the uniformity of temperatures agrees with experimental findings conducted by Alcini (1990) although convection is very small. Isotherms of 5.67 and 5.75 indicate the solidus and liquidus lines, respectively. The maximum temperature is located at the weld centerline. A significant temperature gradient occurs near the edge of electrodes ($r = 1$) and is in accord with the prediction made by Bentley et al. (1963), Wei and Ho (1990), and measurements conducted by Alcini (1990).

Since the fluid flow in the weld nugget is small, it is expected that influences of the Prandtl, Schmidt, and Darcy numbers on variations of the shape and growth of the mushy zone are insignificant and numerical computations confirm these.

Conclusions

1 Effects of the physical, thermal, and metallurgical properties and welding conditions on growths of the weld nugget and mushy zone during resistance spot welding are extensively investigated. The dimensionless parameters studied include the welding current parameter, electric contact resistance, workpiece thickness, Biot number, solid-to-liquid thermal conductivity and specific heat ratios, slopes of the solidus and liquidus lines defined in the phase diagram.

2 The solidus and liquidus lines, which define the weld nugget and mushy zone, are initiated earlier and grow more rapidly by increasing the welding current, electric contact resistance and reducing Biot number, solid-to-liquid thermal conductivity ratio, liquid and solid specific heat parameters. A steep solidus line results in an early onset of the solidus line and a late formation for the liquidus line. Increasing the slope of the liquidus line (i.e., small m_{liq}), however, causes the opposite results.

3 Convection in the weld nugget is very small. The maximum velocity is generally less than 5 mm/s even though the welding current is higher than 8000 amp.

4 Variations in the growth rate, nugget, and mushy zone thicknesses with thermal, physical, and metallurgical properties and welding conditions are pronounced. It is impossible to make an appropriate model without accounting for these factors.

References

Alcini, W. V., 1990, "Experimental Measurement of Liquid Nugget Heat Convection in Spot Welding," *Welding Journal*, Vol. 69, pp. 177-s-180-s.

Bennon, W. D., and Incropera, F. P., 1987, "A Continuum Model for Momentum, Heat and Species Transport in Binary Solid-Liquid Phase Change Systems—I. Model Formulation," *Int. J. Heat Mass Transfer*, Vol. 30, pp. 2161-2170.

Bennon, W. D., and Incropera, F. P., 1988, "Numerical Analysis of Binary Solid-Liquid Phase Change Using a Continuum Model," *Numerical Heat Transfer*, Vol. 13, pp. 277-296.

Bentley, K. P., Greenwood, J. A., Knowlson, P. Mck., and Baker, R. G., 1963, "Temperature Distributions in Spot Welds," *British Welding Journal*, Vol. 10, pp. 613-619.

Cho, H. S., and Cho, Y. J., 1989, "A Study of the Thermal Behavior in Resistance Spot Welds," *Welding Journal*, Vol. 68, pp. 236-s-244-s.

Cunningham, A., and Begeman, M. L., 1965, "A Fundamental Study of Projection Welding Using High Speed Photography," *Welding Journal*, Vol. 44, pp. 381-s-384-s.

Dickinson, D. W., Franklin, J. E., and Stanya, A., 1980, "Characterization of Spot Welding Behavior by Dynamic Electrical Parameter Monitoring," *Welding Journal*, Vol. 59, pp. 170-s-176-s.

Gould, J. F., 1987, "An Examination of Nugget Development During Spot Welding, Using Both Experimental and Analytical Techniques," *Welding Journal*, Vol. 66, pp. 1-s-10-s.

Han, Z., Orozco, J., Indacochea, J. E., and Chen, C. H., 1989, "Resistance Spot Welding: A Heat Transfer Study," *Welding Journal*, Vol. 68, pp. 363-s-371-s.

Nied, H. A., 1984, "The Finite Element Modelling of the Resistance Spot Welding Process," *Welding Journal*, Vol. 63, pp. 123-s-132-s.

Patankar, S. V., 1980, *Numerical Heat Transfer and Fluid Flow*, Hemisphere Publishing Corp., New York, Chaps. 5 and 6.

Ridder, S. D., Kou, S., and Mehrabian, R., 1981, "Effect of Fluid Flow on Macrosegregation in Axi-symmetric Ingots," *Metallurgical Transactions*, Vol. 12B, pp. 435-447.

Savage, W. F., Lundin, C. D., and Aronson, A. H., 1965, "Weld Metal Solidification Mechanics," *Welding Journal*, Vol. 44, pp. 175-s-181-s.

Shercliff, J. A., 1965, *A Textbook of Magnetohydrodynamics*, Pergamon Press, New York, p. 23.

Wei, P. S., and Ho, C. Y., 1990, "Axisymmetric Nugget Growth During Resistance Spot Welding," ASME JOURNAL OF HEAT TRANSFER, Vol. 112, pp. 309-316.

The Weighted-Sum-of-Gray-Gases Model for Arbitrary Solution Methods in Radiative Transfer

M. F. Modest
Professor of Mechanical Engineering,
Department of Mechanical Engineering,
The Pennsylvania State University,
University Park, PA 16802
Fellow ASME

The weighted-sum-of-gray-gases approach for radiative transfer in nongray participating media, first developed by Hottel in the context of the zonal method, has been shown to be applicable to the general radiative equation of transfer. Within the limits of the weighted-sum-of-gray-gases model (nonscattering media within a black-walled enclosure), any nongray radiation problem can be solved by any desired solution method after replacing the medium by an equivalent small number of gray media with constant absorption coefficients. Some examples are presented for isothermal media and media at radiative equilibrium, using the exact integral equations as well as the popular P-1 approximation for the equivalent gray media solutions. The results demonstrate the equivalency of the method with the quadrature of spectral results, as well as the tremendous computer times savings (by a minimum of 95 percent) that are achieved.

Introduction

The vast majority of radiative heat transfer analyses to date has been concerned with gray participating media. However, molecular gases below dissociation temperatures absorb and emit over a multitude of very narrow spectral lines, which may overlap and form so-called vibration–rotation bands. The result is an absorption coefficient that oscillates wildly within each band, and is zero between bands. Similarly, the radiative properties of suspended particles may oscillate strongly across the spectrum. Only if particles of varying sizes are present, as is often the case, do the spectral oscillations tend to be dampened out, and the assumption of a gray medium may become a reasonable one. Like molecular gases, semitransparent solids and liquids often display strong absorption bands in the infrared due to photon–phonon coupling, with weak absorption coefficients between bands. Therefore, the simplification of a gray participating medium is, except for particle suspensions with variable sizes, a poor assumption, which may lead to very significant errors in the analysis. It behooves the engineer to realize that accurate solutions to the equation of transfer (such as exact solutions in two or three dimensions), as opposed to simple approximate ones (such as the P-1 approximation in one or two dimensions), may be meaningless unless the spectral variation of radiation properties is taken into account.

Unfortunately, consideration of spectral variations of radiation properties tends to increase considerably the difficulty of an already extremely difficult problem, or at least make their numerical solution many times more computer time intensive. Nearly all solution methods, whether exact or approximate, are poorly suited for the consideration of nongray properties. In general, radiative flux, divergence of flux, and/or incident radiation must be evaluated for many, many spectral locations, followed by numerical quadrature of the spectral results.

Only the exact integral equation lends itself to an *a priori* spectral integration, using the wide-band model or total emissivity correlations. Such a solution approach quickly becomes intractable for all but the simplest geometries. On the other hand, a number of approximate methods such as the *P-N approximation* (including the most popular *P-1 approximation*) and the *discrete ordinates method* are readily applied to complicated geometries—as long as the medium is gray. *A priori* spectral integration of these popular methods—while attempted by many—had until now proven elusive.

The concept of a weighted-sum-of-gray-gases approach was first presented by Hottel and Sarofim (1967) within the framework of the zonal method. The method may be applied to arbitrary geometries with varying absorption coefficients, but is limited to nonscattering media confined within a black-walled enclosure. In this paper it is demonstrated that this approach can be applied to the directional equation of transfer and, therefore, to any solution method for the equation of transfer (exact, P-N approximation, discrete ordinates method, etc.). In this method the nongray gas is replaced by a number of gray gases, for which the heat transfer rates are calculated independently. The total flux is then found by adding the fluxes of the gray gases after multiplication with certain weight factors. The present method may be used in conjunction with any spectral model (line-by-line, narrow band, wide-band, or total emissivity correlations), and may be carried out to any desired accuracy. Since no spectral flux evaluations, followed by spectral integration, are required, computer time savings amount to factors of hundreds and even thousands for comparable accuracy. The accuracy and extreme numerical efficiency of the method are demonstrated with a few simple one-dimensional examples.

While the method is presently limited to black-walled enclosures and to nonscattering media, this covers a large number of important applications (Hottel and Sarofim, 1967). In a follow-up paper it will be shown how these restrictions may be relaxed.

Analysis

The equation of transfer for the radiative intensity I_η at a wavenumber η and along a path s is, for a nonscattering medium with spectral absorption coefficient κ_η,

$$\frac{dI_\eta}{ds} = \kappa_\eta (I_{b\eta} - I_\eta) \tag{1}$$

with the formal solution

$$I_\eta(s) = I_{bw\eta} e^{-\int_0^s \kappa_\eta ds'} + \int_0^s I_{b\eta}(s') e^{-\int_{s'}^s \kappa_\eta ds''} \kappa_\eta(s') ds' \tag{2}$$

where $I_{bw\eta} = I_{b\eta}(T_w)$ is the intensity emitted into the medium from the (black) wall at $s = 0$, as shown in Fig. 1. Integrating

Contributed by the Heat Transfer Division for publication in the JOURNAL OF HEAT TRANSFER. Manuscript received by the Heat Transfer Division March 28, 1990; revision received October 1, 1990. Keywords: Radiation, Radiation Interactions.

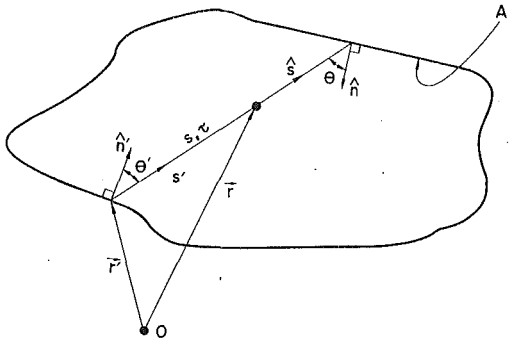

Fig. 1 Spectral intensity within an arbitrary black-walled enclosure

this over the entire spectrum we obtain the total intensity as

$$I(s)=\int_0^\infty I_\eta d\eta=\int_0^\infty I_{bw\eta}e^{-\int_0^s\kappa_\eta ds'}d\eta + \int_0^s\int_0^\infty I_{b\eta}(s')e^{-\int_{s'}^s\kappa_\eta ds''}\kappa_\eta(s')d\eta ds' \quad (3)$$

The spectral absorptivity and emissivity of a participating medium are defined as

$$\alpha_\eta(0\to s)=\epsilon_\eta(0\to s)=1-e^{-\int_0^s\kappa_\eta ds'} \quad (4)$$

For a constant absorption coefficient the absorptivity depends on the thickness of the gas layer as well as the (constant) absorption coefficient. If κ_η is not constant but varies spatially and/or with temperature, the absorptivity depends on the variation of κ_η along the entire path, here denoted by the argument $0\to s$. Substituting equation (4) into (3) we get

$$I(s)=\int_0^\infty I_{bw\eta}[1-\alpha_\eta(0\to s)]d\eta - \int_0^s\int_0^\infty I_{b\eta}(s')\frac{\partial\alpha_\eta}{\partial s'}(s'\to s)d\eta ds' \quad (5)$$

With the definition of the *total absorptivity* as

$$\alpha(T,s'\to s)=\frac{1}{I_b(T)}\int_0^\infty\alpha_\eta(s'\to s)I_{b\eta}(T)d\eta =\frac{1}{I_b(T)}\int_0^\infty\left[1-e^{-\int_{s'}^s\kappa_\eta ds''}\right]I_{b\eta}(T)d\eta \quad (6)$$

we may consolidate equation (5) as[1]

$$I(s)=[1-\alpha(T_w,\,0\to s)]I_{bw} - \int_0^s\frac{\partial\alpha}{\partial s'}[T(s'),\,s'\to s]I_b(s')ds' \quad (7)$$

For isothermal molecular gases correlations for the total absorptivity (or emissivity) can often be found in the literature, e.g., see Leckner (1972) for steam and carbon dioxide. If the gas is mixed with particles and/or is nonisothermal the absorptivity can be found from wide-band correlations (see, for example, Edwards, 1976). If the molecular gas contains a suspension of nonscattering particles, the absorption coefficient may be written as

$$\kappa_\eta=\kappa_{p\eta}+\kappa_{g\eta}=\kappa_{p\eta}+\sum_{n=1}^N\kappa_{n\eta} \quad (8)$$

We will now assume that the N gas bands are narrow and nonoverlapping, and that the absorption of the particles, $\kappa_{p\eta}$, does not vary appreciably over each band. Then

$$\alpha(T,s'\to s)=\frac{1}{I_b(T)}\int_0^\infty\left[1-e^{-\int_{s'}^s\kappa_{p\eta}ds''}e^{-\int_{s'}^s\kappa_{g\eta}ds''}\right]I_{b\eta}(T)d\eta$$
$$=\frac{1}{I_b(T)}\int_0^\infty\left[1-e^{-\int_{s'}^s\kappa_{p\eta}ds''}\right]I_{b\eta}(T)d\eta$$
$$+\frac{1}{I_b(T)}\int_0^\infty e^{-\int_{s'}^s\kappa_{p\eta}ds''}\left[1-e^{-\int_{s'}^s\kappa_{g\eta}ds''}\right]I_{b\eta}(T)d\eta$$
$$\simeq\alpha_p(T,s'\to s)+\sum_{n=1}^N\frac{\omega_n I_{b\eta_n}}{I_b}(T)e^{-\int_{s'}^s\kappa_{p\eta_n}ds''}A_n^*(s'\to s) \quad (9)$$

where ω_n is the band width parameter, η_n is the spectral position of the band center or head, and A_n^* is the nondimensional band absorptance. The evaluation of band absorptances for isothermal and nonisothermal gases has been summarized by Edwards (1976).

We will now assume that the absorptivity of equation (9) may be approximated by a *weighted sum of gray gases*, or

$$\alpha(T,s'\to s)\simeq\sum_{k=0}^K\alpha_k(T,\mathbf{r},\hat{\mathbf{s}})[1-e^{-\kappa_k(s-s')}] \quad (10)$$

For mathematical simplicity we have chosen the gray-gas ab-

[1]Note that, in concurrence with the definition of total absorptivity, the derivative in $\partial\alpha/\partial s'$ is only with respect to the path $s'\to s$, and *not* with respect to the s' in the temperature $T(s')$.

Nomenclature

A = gas band absorptance, cm^{-1}
A^* = nondimensional gas band absorptance
a = absorptivity fit coefficient
b = absorptivity fit parameter
c = absorptivity fit parameter
D = diameter of sphere, cm
E_n = exponential integral functions
G = incident intensity, W/cm^2
I = intensity, W/cm^2sr
K = number of terms in absorptivity fit
L = number of terms in band absorptance fit
L = distance between parallel plates, cm
N = number of gas bands
r = radial distance, cm
R = radius of sphere, cm
s = path length, cm
T = temperature, K
q = radiative flux, W/cm^2
z = coordinate between parallel plates, cm
α = slab absorptivity
β = line overlap parameter
ϵ = slab emissivity
η = wavenumber, cm^{-1}
θ = polar angle
κ = absorption coefficient, cm^{-1}
ξ = nondimensional coordinate between plates
σ = Stefan–Boltzmann constant = 5.6699×10^{-12} W/cm^2K^4
τ = optical thickness
ψ = azimuthal angle
ψ = nondimensional gas band blackbody intensity
Ψ = nondimensional radiative flux
ω = gas band width parameter, cm^{-1}

Subscripts

b = blackbody
g = gas
k = pertaining to kth gray gas
L = wall at $z=L$
m = medium
n = pertaining to nth gas band
p = particle
w = wall
η = spectral value at η
0 = wall at $z=0$, or at band center

sorption coefficients κ_k to be constants, while the weight factors α_k may be functions of temperature and, for media with locally varying absorption coefficient (due to concentration and/or temperature changes), also of position $\mathbf{r}$ as well as direction $\hat{\mathbf{s}}$. Neither α_k nor κ_k are allowed to depend on path length s. Depending on the material, the quality of the fit, and the accuracy desired, a K of 2 or 3 usually gives results of satisfactory accuracy (Hottel and Sarofim, 1967). Since, for an infinitely thick medium, the absorptivity approaches unity, we find

$$\sum_{k=0}^{K}\alpha_k(T, \mathbf{r}, \hat{\mathbf{s}})=1. \tag{11}$$

Still, for a molecular gas with its "spectral windows" it would take very large path lengths indeed until the absorptivity would be close to unity. For this reason equation (10) starts with $k = 0$ (with an implied $\kappa_0 = 0$), to allow for spectral windows.

Substituting equation (10) into equation (7) leads to

$$I(s)=\sum_{k=0}^{K}\alpha_k(T_w, \mathbf{r}_w, \hat{\mathbf{s}})e^{-\kappa_k s}I_{bw} + \int_0^s\sum_{k=0}^{K}a_k[T(s', \mathbf{r}', \hat{\mathbf{s}})]\kappa_k e^{-\kappa_k(s-s')}I_b(s')ds'$$

$$=\sum_{k=0}^{K}\left\{[a_kI_b](T_w), \mathbf{r}_w, \hat{\mathbf{s}}e^{-k_k s}+\int_0^s[a_kI_b](s', \hat{\mathbf{s}})e^{-\kappa_k(s-s')}\kappa_k ds'\right\} \tag{12}$$

Setting

$$I(s)=\sum_{k=0}^{K}I_k(s) \tag{13}$$

and comparing equations (12) and (2) we find that I_k satisfies the equation of transfer

$$\frac{dI_k}{ds}=\kappa_k([a_kI_b]-I_k) \tag{14}$$

subject to the boundary condition

$$s=0: \quad I_k=[a_kI_b](T_w) \tag{15}$$

This is, of course, the equation of transfer for a gray gas with constant absorption coefficient κ_k, with blackbody intensity I_b (for medium as well as surfaces) replaced by a weighted intensity a_kI_b [where, as indicated in equation (10), for media with variable absorption coefficients, the weighted Planck function is also a function of direction, corresponding to nonisotropic emission]. Thus, if the temperature field is known (or assumed), the intensity field (or simply the fluxes) must be determined for $k = 0, 1, \ldots, K$, using any standard solution method such as the exact integral equations, the P-N approximation, the discrete ordinates method, etc. The results are then added to give the total intensity (or radiative flux). Note that it will always be necessary to know or assume a temperature profile: For radiative equilibrium the condition $\nabla\cdot\mathbf{q} = 0$ applies to the total flux only and, in general, $\nabla\cdot\mathbf{q}_k \neq 0$.

Normally, the curve fit of the total absorptivity of the medium should be tailored to the medium at hand, and depends on composition, pressure levels, temperature levels, number of molecular gas bands, etc. Only if the fit is optimized will one be able to achieve acceptable accuracy with a weighted sum of two or three gray gases. Unfortunately, the curve fit indicated in equation (10) is a nonlinear one, further complicated by the fact that the α_k may be functions of temperature, pressure, composition, etc. Due to these difficulties the curve fitting effort may become more involved than the heat transfer calculations themselves! While some correlations have been reported in the literature (for use with the zonal method), e.g., for isothermal CO_2 by Farag and Allan (1981) and for isothermal H_2O–CO_2 mixtures by Smith et al. (1982), it would be desirable to have a "cookbook" formula available, even at the expense of numerical efficiency.

Table 1 Weighted-sum-of-gray-gases parameters for bad absorptance at high pressures, $A^*(\tau, \infty)$

	L=2		L=2		L=3	
ℓ	c_ℓ	b_ℓ	c_ℓ	b_ℓ	c_ℓ	b_ℓ
1	2.997	0.2385×10^{-1}	3.308	0.3272×10^{-2}	2.741	0.1491×10^{-1}
2	2.416	0.2992	4.192	0.9466×10^{-1}	1.656	0.1101
3					1.397	0.5267
4						
RMS†	0.0285/100		0.0875/1000		0.0031/100	
	L=3		L=4		L=5	
ℓ	c_ℓ	b_ℓ	c_ℓ	b_ℓ	c_ℓ	b_ℓ
1	2.891	0.2046×10^{-2}	2.748	0.1522×10^{-2}	2.682	0.1216×10^{-2}
2	2.195	0.2092×10^{-1}	1.693	0.1144×10^{-1}	1.479	0.7984×10^{-2}
3	2.746	0.2409	1.769	0.6255×10^{-1}	1.361	0.3212×10^{-1}
4			1.868	0.4057	1.401	0.1269
5					1.357	0.5291
RMS†	0.0189/1000		0.0042/1000		0.0010/1000	

† RMS= a/b implies a root-mean-square error of a over the range of the fit between $\tau = 0$ and $\tau = b$.

We will limit ourselves here to the case of a gas–particulate mixture with gray particulates and spatially independent absorption coefficients. The total absorptivity of such a medium is described by equation (9), which reduces to

$$\alpha(T, s)=1-e^{-\kappa_p s}+\sum_{n=1}^{N}\frac{\omega_nI_{b\eta_n}}{I_b}(T)e^{-\kappa_p s}A_n^*(\kappa_n s, \beta_n) \tag{16}$$

where β_n is the line overlap parameter (Edwards, 1976).

Suppose the band absorptance $A^*(\tau, \beta)$ can be approximated by a weighted sum of gray gases, i.e.,

$$A^*(\tau, \beta)\simeq\sum_{l=1}^{L}c_l(\beta)[1-e^{-b_l(\beta)\tau}] \tag{17}$$

Substituting this into equation (16), and using the abbreviations

$$\psi_n=\frac{\omega_nI_{b\eta_n}}{I_b}(T), \quad b_{ln}=b_l(\beta_n), \quad c_{ln}=c_l(\beta_n)$$

leads to

$$\alpha(T, s)\simeq1-e^{-\kappa_p s}+\sum_{n=1}^{N}\psi_ne^{-\kappa_p s}\sum_{l=1}^{L}c_{ln}[1-e^{-b_{ln}\kappa_n s}]$$

$$=\left[1-\sum_{n=1}^{N}\sum_{l=1}^{L}c_{ln}\psi_n(T)\right][1-e^{-\kappa_p s}] + \sum_{n=1}^{N}\sum_{l=1}^{L}c_{ln}\psi_n(T)[1-e^{-(\kappa_p+b_{ln}\kappa_n)s}] \tag{18}$$

This is clearly of the same type as the desired form, equation (10). A number of curve fits for equation (17) for the high pressure limit ($\beta\to\infty$) are given in Table 1. In these approximations the least-mean-square error integrated between $\tau = 0$ and $\tau = 100$ or 1000 has been minimized. Inspection of equation (18) reveals that the nongray medium is represented by a weighted sum of $N \times L + 1$ gray gases. The advantage of the set of coefficients listed in Table 1 is that they may be applied to any rotational and/or vibration-rotational band of any molecular gas, making individual fits for a given gas (or mixture) unnecessary. Its drawbacks are that (*i*) Table 1 is limited to bands with strongly overlapped spectral lines ($\beta > 1$), and (*ii*) the resulting fit is not very efficient for gases with multiple bands.

Illustrative Examples

To demonstrate the accuracy and relative simplicity of the method we will consider a few simple one-dimensional situa-

tions (inasmuch as nongray media problems can be simple). Since we want to verify the accuracy of the *method*, we will not use correlations for, say, steam and carbon dioxide, with emissivities given by Leckner 1972) and weighted-gray-gas factors given by Smith et al. (1982), for which "exact" solutions cannot be obtained. Instead, we consider a hypothetical gas centered at $\eta_0 = 3000\ \text{cm}^{-1}$, mixed with gray nonscattering particles, and with a mixture absorption coefficient described by

$$\kappa_\eta = \kappa_p + \kappa_g e^{-2|\eta-\eta_0|/\omega} \tag{19}$$

For simplicity we will assume that the absorption coefficient is uniform throughout the entire medium, and a single band width parameter of $\omega = 200\ \text{cm}^{-1}$ will be considered. The gas absorption coefficient in equation (19) corresponds to the high-pressure limit of the exponential wide-band model (Edwards, 1976) for an isothermal gas (or with properties evaluated at some average temperature). The main advantages of an absorption coefficient given by equation (19) are (*i*) that weighted-sum-of-gray-gases coefficients are readily found from Table 1, and (*ii*) exact solutions may be obtained for comparison, using the integral formulation and/or the Monte Carlo method.

In the following we will discuss three one-dimensional examples. First an isothermal medium confined between cold, parallel plates is considered, followed by the same isothermal medium inside a cold spherical shell. Finally, the more complicated case of a medium at radiative equilibrium contained between parallel plates at different temperatures is presented.

In most of the examples the *P-1 approximation* is employed for spectral and weighted-sum-of-gray-gases (WSGG) calculations, since it is a very popular method with reasonable levels of effort and accuracy. In the first example the exact integral equation is also considered, only to show that the WSGG method can be used with any solution method and that it, indeed, rapidly approaches the exact solution with very few "gray gases." Normally, the WSGG method would not be used in conjunction with the exact integral relations since these integral relations may be integrated spectrally in terms of band absorptances.

Isothermal Plane-Parallel Slab—P-1 and "Exact." Consider an isothermal medium at temperature T_m, confined between parallel, cold and black plates $0 \le z \le L$. The temperature is such that $\psi = \omega I_{b\eta_0}(T_m)/I_b(T_m) = 0.05$.

For the case of $N = 1$ and $\psi_n = \psi$ equation (18) reduces to

$$\alpha(T_m, s) = \left[1 - \psi\sum_{l=1}^{L} c_l\right][1 - e^{-\kappa_p s}] + \psi\sum_{l=1}^{L} c_l[1 - e^{-(\kappa_p + b_l\kappa_g)s}] \tag{20}$$

$$= \sum_{k=0}^{L} \alpha_k[1 - e^{-\kappa_k s}] \tag{21}$$

where

$$\alpha_k = \begin{cases} 1 - \psi\Sigma_{l=1}^{L} c_l, & k = 0 \\ \psi c_l, & k \ge 1 \end{cases} \tag{22a}$$

$$\kappa_k = \begin{cases} \kappa_p, & k = 0 \\ \kappa_p + b_k\kappa_g, & k \ge 1 \end{cases} \tag{22b}$$

Thus the problem must be solved for L gray gases with absorption coefficients $(b_k\kappa_g)$ (gas only), or for $L + 1$ gray gases with absorption coefficients κ_p and $(\kappa_p + b_k\kappa_g)$ (gas and particulates).

For a gray medium (or on a spectral basis) with absorption coefficient κ, the local radiative flux is readily determined exactly as (Siegel and Howell, 1981)

$$q(z) = 2\pi I_{bm}\{E_3[\kappa(L-z)] - E_3(\kappa z)\} \tag{23}$$

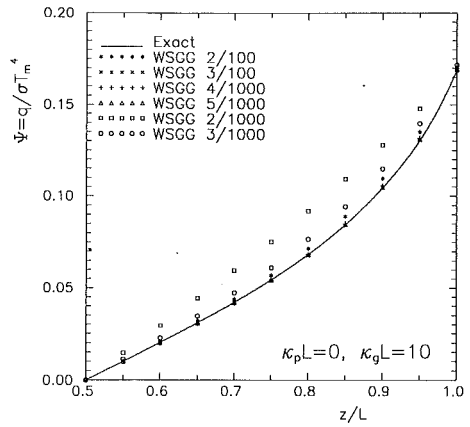

Fig. 2 Heat transfer rates through an isothermal gas layer ($\kappa_g L = 10$); WSGG *n/m* implies a total emissivity fit with *n* terms over the range $0 < \kappa_g s < m$ (*s* = geometric path length)

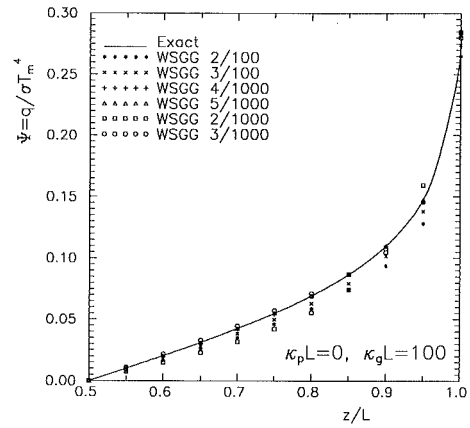

Fig. 3 Heat transfer rates through an isothermal gas layer ($\kappa_g L = 100$); WSGG *n/m* implies a total emissivity fit with *n* terms over the range $0 < \kappa_g s < m$ (*s* = geometric path length)

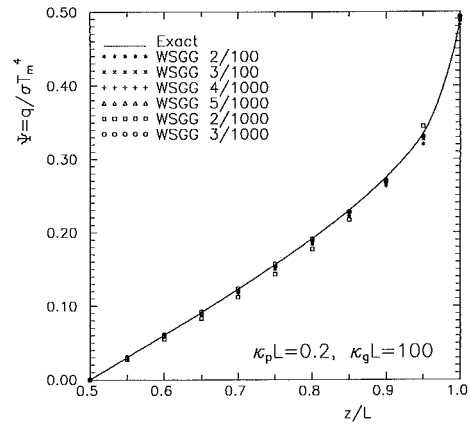

Fig. 4 Heat transfer rates through an isothermal mixture of gas and particles; WSGG *n/m* implies a total emissivity fit with *n* terms over the range $0 < \kappa_g s < m$ (*s* = geometric path length)

Thus, the heat flux for the weighted-sum-of-gray-gases method follows immediately as

$$\Psi(z) = \frac{q(z)}{\sigma T_m^4} = \frac{\Sigma_{k=0}^{L} q_k}{\sigma T_m^4} = 2\sum_{k=0}^{L} \alpha_k\{E_3[\kappa_k(L-z)] - E_3(\kappa_k z)\} \tag{24}$$

with α_k and κ_k as given by equation (22). Spectrally integrated results for the exact integral relations have been given by Modest (1981). Some results are shown in Figs. 2–4 for $\kappa_p L = 0$

and $\kappa_p L = 0.2$, for a number of absorptivity curve fits from Table 1. For the P-1 or differential approximation the spectral/gray flux for the same problem follows from Modest and Azad (1980), from which the weighted-sum-of-gray-gases flux is readily found. Spectrally integrated results for the P-1 method have to be obtained by numerical quadrature, resulting in similar curves (not shown) always predicting somewhat higher heat fluxes (up to 7 percent) as expected from the P-1 method (Modest and Azad, 1980). It is observed that even a crude fit with $L = 2$ (optimized over a range of optical thickness between 0 and 100) results in very acceptable accuracy, while the more accurate fits do, of course, approach the exact solution. For a gas optical thickness of $\kappa_g L = 10$ the simple 3/100 fit (i.e., $L = 3$ optimized for optical thickness between 0 and 100) gives nearly exact results (maximum error of < 1 percent), while the error is somewhat larger for $\kappa_g L = 100$ (maximum error < 10 percent), since the optical thickness of the gas layer exceeds 100 for all directions except the normal direction, falling outside of the fit. Thus, for this case the 3/1000 fit is more accurate (2–5 percent error). If a particle background is present, gas radiation diminishes in relative importance, and all fits give very accurate results. Covering the entire range of gas optical thickness between 0 and 100, the following statement can be made: For a molecular gas without particles the maximum error is approximately 20 percent for the 2/100 fit, 10 percent for the 3/100 and 3/1000 fits, 3 percent for the 4/1000 fit, and < 1 percent for 5/1000. If particles are added this maximum error decreases rapidly (by about a factor of five for $\kappa_p L = 0.2$).

Isothermal Sphere—P-1 Approximation. Next we consider the same isothermal medium as in the previous example, but in the form of a spherical body of radius R, again confined within cold black walls. The P-1 approximation for such a medium, for a gray or spectral absorption coefficient κ, is (Modest and Azad, 1980)

$$\frac{1}{r^2}\frac{d}{dr}(r^2 q) = \kappa(4\pi I_{bm} - G) \tag{25a}$$

$$\frac{dG}{dr} = -3\kappa q \tag{25b}$$

$$r=0: \quad q=0; \quad r=R: \quad 2q=G \tag{25c}$$

This set of equations is readily solved to yield a spectral/gray radiative flux of

$$q(r) = 2\pi I_{bm}\left(\frac{R}{r}\right)^2 \times \frac{\sinh\sqrt{3}\kappa r - \sqrt{3}\kappa r\cosh\sqrt{3}\kappa r}{\left(1-\frac{3}{2}\kappa R\right)\sinh\sqrt{3}\kappa R - \sqrt{3}\kappa R\cosh\sqrt{3}\kappa R} \tag{26}$$

Therefore, the total radiative flux for an absorption coefficient given by equation (19), using the present weighted-sum-of-gray gases, follows immediately as

$$\Psi(r) = \frac{q(r)}{\sigma T_m^4} = \left(\frac{R}{r}\right)^2 \sum_{k=0}^{L} \frac{2\alpha_k[\sinh\sqrt{3}\kappa_k r - \sqrt{3}\kappa_k r\cosh\sqrt{3}\kappa_k r]}{\left(1-\frac{3}{2}\kappa_k R\right)\sinh\sqrt{3}\kappa_k R - \sqrt{3}\kappa_k R\cosh\sqrt{3}\kappa_k R} \tag{27}$$

Exact spectral integration of equation (26) must be carried out using numerical quadrature. To this purpose we separate the gray particle radiation from the gas band by writing the spectral flux as

$$q_\eta(r) = \pi I_{bm\eta} f(\kappa_\eta, r) \tag{28}$$

where the $f(\kappa_\eta, r)$ is identified by comparison with equation (26). Integrating over the spectrum, this may be expressed as

$$q(r) = \int_0^\infty q_\eta(r)\,d\eta = \pi I_{bm} f(\kappa_p, r) + \int_0^\infty \pi I_{bm\eta}[f(\kappa_\eta, r) - f(\kappa_p, r)]\,d\eta \tag{29}$$

for which the integral vanishes outside the gas band. Using the narrow band assumption and the absorption coefficient from equation (19), this becomes

$$\Psi(r) = \frac{q(r)}{\sigma T_m^4} = f(\kappa_p, r) + \int_0^\infty \frac{I_{bm\eta}}{I_{bm}}[f(\kappa_p + \kappa_g e^{-2|\eta-\eta_0|/\omega}, r) - f(\kappa_p, r)]\,d\eta = f(\kappa_p, r) + \psi\int_0^1 [f(\kappa_p + \kappa_g y, r) - f(\kappa_p, r)]\frac{dy}{y} \tag{30}$$

where $\psi = 0.05$ as in the previous example. The integral must be evaluated through quadrature.

At $r = R$ (i.e., the location where—due to the temperature discontinuity—the P-1 approximation tends to be least accurate) the flux leaving the surface of the sphere is readily calculated from exact relationships as

$$q(R) = \int_{\eta=0}^\infty \int_{\psi=0}^{2\pi} \int_{\theta=0}^{\pi/2} I_\eta(R, \eta, \theta, \psi)\cos\theta\sin\theta\,d\theta\,d\psi\,d\eta = 2\pi\int_{\eta=0}^\infty \int_{\theta=0}^{\pi/2} I_{b\eta}(T_m)(1-e^{-2\kappa_\eta R\cos\theta})\cos\theta\sin\theta\,d\theta\,d\eta = \pi\int_0^\infty I_{b\eta}(T_m)\left\{1-\frac{2}{(\kappa_\eta D)^2}\left[1-(1+\kappa_\eta D)e^{-\kappa_\eta D}\right]\right\}d\eta \tag{31}$$

where $D = 2R$ is the diameter of the sphere. This expression may be integrated for the absorption coefficient given in equation (19), leading to

$\kappa_p = 0$:

$$\Psi(R) = \psi\left\{E_1(\kappa_g D) + \ln(\kappa_g D) + \gamma - \frac{1}{2} + \frac{1}{(\kappa_g D)^2}\left[1-(1+\kappa_g D)e^{-\kappa_g D}\right]\right\} \tag{32a}$$

$\kappa_p > 0$:

$$\Psi(R) = 1 - \frac{2}{(\kappa_p D)^2} \times \left\{1-(1+\kappa_p D)e^{-\kappa_p D}\left[1-\psi\left(E_1(\kappa_g D) + \ln(\kappa_g D) + \gamma\right)\right]\right\} + \frac{2\psi}{(\kappa_p D)^2}\left[E_1\left((\kappa_p+\kappa_g)D\right) - E_1(\kappa_p D) + \ln\frac{\kappa_p+\kappa_g}{\kappa_p}\right] + \frac{2\psi}{\kappa_p D}\left[\frac{1}{\kappa_p D}\left(1-e^{-\kappa_p D}\right) - \frac{1}{(\kappa_p+\kappa_g)}\left(1-e^{-(\kappa_p+\kappa_g)D}\right)\right] \tag{32b}$$

where $\gamma = 0.57721\ldots$ is Euler's constant.

Results for nondimensional fluxes are compared in Fig. 5. It is observed that the P-1 approximation does extremely well for this problem with a maximum error of < 4 percent. This is probably due to the fact that, in a sphere, the intensity varies gradually with direction while in a slab the intensity has a discontinuity at $\theta = \pi/2$. It is also seen that the weighted-sum-of-gray-gases fits perform even better than for the plane layer: The 3/100 fit gives basically exact results. This is not surprising since the maximum optical path through a sphere is κD, while it is infinite in the slab (taxing the quality of the fit). Consequently, the 3/100 fit or even the 2/100 fit should be more than adequate for most three-dimensional geometries.

To demonstrate the numerical efficiency of the present

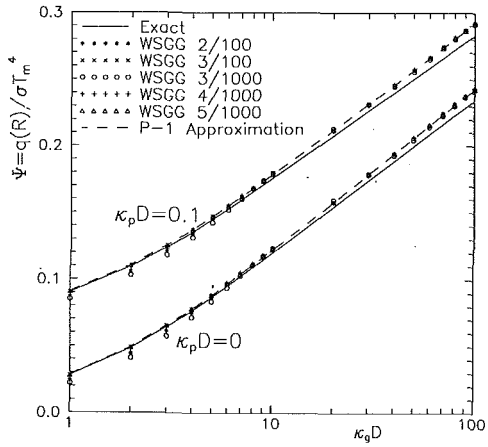

Fig. 5 Heat loss from an isothermal gas-particulate sphere; WSGG *n/m* implies a total emissivity fit with *n* terms over the range $0 < \kappa_g s < m$ (s = geometric path length)

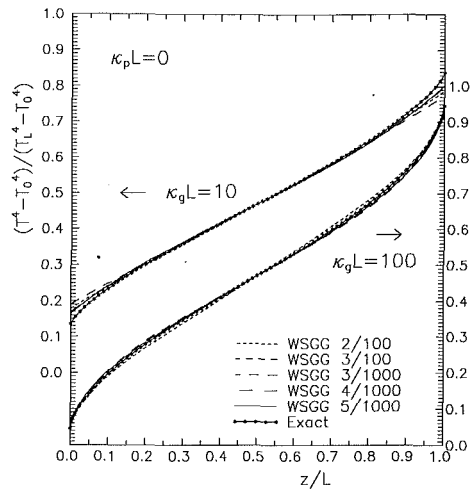

Fig. 6 Nondimensional temperature distribution in a slab at radiative equilibrium ($\kappa_g L = 0.0$); WSGG *n/m* implies a total emissivity fit with *n* terms over the range $0 < \kappa_g s < m$ (s = geometric path length)

Table 2 Nondimensional heat loss from an isothermal gas-particulate sphere, $\Psi = q(R)/\sigma T_m^4$; comparison between weighted sum of gray gases and spectral, numerical quadrature

		$\kappa_g D$ 1	10	100	CPU time [ms]
$\kappa_p D = 0$	WSGG 2/100	0.02396	0.12105	0.23412	0.29
	WSGG 3/100	0.02749	0.11951	0.23414	0.38
	WSGG 3/1000	0.02190	0.12062	0.23385	0.38
	WSGG 4/1000	0.02619	0.12013	0.23410	0.47
	WSGG 5/1000	0.02739	0.11957	0.23419	0.55
	NC/10^{-1}	0.02771	0.11923	0.23832	4.2
	NC/10^{-2}	0.02782	0.11924	0.23466	7.7
	NC/10^{-3}	0.02794	0.11933	0.23418	17.5
	NC/10^{-4}	0.02801	0.11943	0.23410	66.3
	NC/10^{-5}	0.02804	0.11947	0.23409	445.4
$\kappa_p D = 0.1$	WSGG 2/100	0.08647	0.17696	0.28279	0.29
	WSGG 3/100	0.08475	0.17556	0.28281	0.38
	WSGG 3/1000	0.08456	0.17651	0.28252	0.38
	WSGG 4/1000	0.08855	0.17613	0.28277	0.47
	WSGG 5/1000	0.08966	0.17561	0.28285	0.55
	NC/10^{-1}	0.09027	0.17555	0.28681	4.2
	NC/10^{-2}	0.09027	0.17555	0.28337	7.3
	NC/10^{-3}	0.09027	0.17555	0.28291	11.7
	NC/10^{-4}	0.09027	0.17555	0.28280	21.9
	NC/10^{-5}	0.09027	0.17555	0.28279	34.3

WSGG n/m: weighted sum of gray gases with n terms, fitted over $0 < \tau_g < m$

NC/10^{-q}: Newton-Cotes (6-point) quadrature with relative error (for integral) of 10^{-q}.

method a comparison of CPU times with results obtained from spectral numerical quadrature is given in Table 2. The CPU times given are the total time required for all three optical thicknesses ($\kappa_g D$ = 1, 10, and 100) on a Silicon Graphics personal Iris 4D/25 (a 1.6 Mflop machine). Differences in CPU time between the two methods, for similar accuracies, are tremendous, with numerical quadrature requiring longer CPU times by factors of 20 or more. This is particularly true for optically thick situations, for which the numerical quadrature CPU times increase, but not those for the present method (resulting in larger CPU times by factors of 50 or more). The results in Table 2 are for a gas with a single vibration-rotation band: In the presence of N gas bands, the numerical effort for spectral quadrature will increase N-fold; for the present method the CPU time will remain unchanged provided a total emissivity fit for the gas (or mixture) is available, rather than using the parameters from Table 1.

Radiative Equilibrium in a One-Dimensional Slab—P-1 Approximation. As a last example we will consider the somewhat more involved case of radiative equilibrium in a slab confined between two isothermal, parallel, black plates. The medium between the slabs has an absorption coefficient as described in equation (19), and the two slabs are kept at temperatures T_0 = 800 K and T_L = 1200 K, respectively. The P-1 approximation for such a medium is, with gray absorption coefficient κ_k and blackbody intensity $\alpha_k I_b$

$$\frac{dq_k}{dz} = \kappa_k(4\pi[\alpha_k I_b] - G_k) \tag{33a}$$

$$\frac{dG_k}{dz} = -3\kappa_k q_k \tag{33b}$$

$$z=0: \quad 2q_k = 4\pi[a_k I_b](T_0) - G_k \tag{33c}$$

$$z=L: \quad -2q_k = 4\pi[a_k I_b](T_L) - G_k \tag{33d}$$

where the $[a_k I_b]$ in the first equation depends on local temperature. The local temperature, in turn, is determined from the condition of radiative equilibrium

$$\frac{d}{dz}\int_0^\infty q_\eta d\eta = 0 = \int_0^\infty \kappa_\eta(4\pi I_{b\eta} - G_\eta)d\eta \tag{34}$$

or, for a weighted sum of gray gases,

$$\sum_{k=0}^{L}\frac{dq_k}{dz} = \sum_{k=0}^{L}\kappa_k(4\pi[a_k I_b] - G_k) = 0 \tag{35}$$

The a_k and κ_k are again determined from equation (22), but with a temperature-dependent ψ:

$$\psi(T) = \frac{\omega I_{b\eta o}(T)}{I_b(T)} \tag{36}$$

Since the temperature field is unknown, and since the temperature dependence of the $[a_k I_b]$ is nonlinear, an iterative solution procedure must be employed: (1) A temperature field is assumed and the values for $[a_k I_b]$ are calculated for a number of nodal points; (2) equations (33) are solved by a simple finite difference scheme (after elimination of q_k) for all k = 0, 1, . . . , L; (3) a new temperature field is calculated by solving equation (35) for I_b, or

$$4\pi I_b = 4\sigma T_{\text{new}}^4 = \sum_{k=0}^{L}\kappa_k G_k \Big/ \sum_{k=0}^{L}\kappa_k a_k(T_{\text{old}}) \tag{37}$$

The procedure is then repeated a few times until convergence is achieved.

For comparison with the results obtained from the P-1 approximation/weighted-sum-of-gray-gases model an exact so-

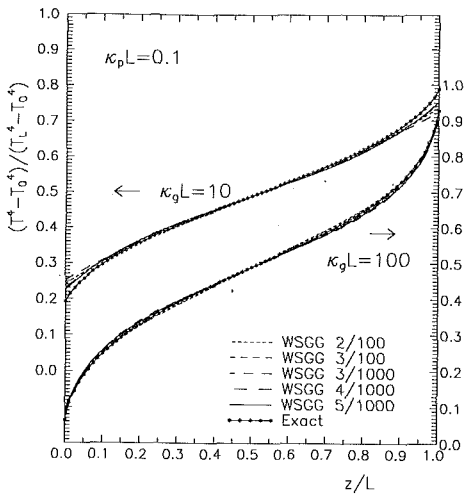

Fig. 7 Nondimensional temperature distribution in a slab at radiative equilibrium ($\kappa_p L$ = 0.1); WSGG *n/m* implies a total emissivity fit with *n* terms over the range $0<\kappa_g s < m$ (*s* = geometric path length)

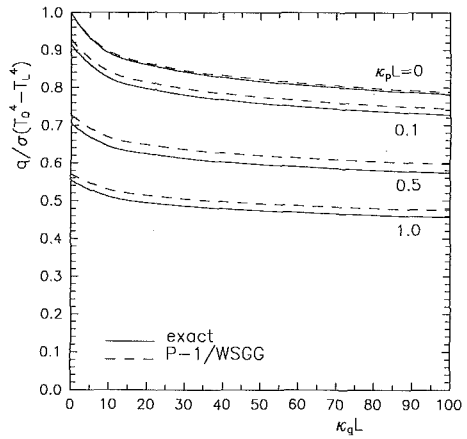

Fig. 8 Nondimensional heat flux through a slab at radiative equilibrium

lution has also been obtained. The development of the exact solution is quite lengthy and involved, and will not be presented here. Suffice it to say that this solution is based on the expression for spectral flux, which may be obtained by integration-by-parts from the standard form given in textbooks such as Siegel and Howell (1981),

$$q_\eta(\xi)=2\pi\{[I_{b\eta 0}-I_{b\eta}(0)]E_3(\kappa_\eta L\xi)-[I_{b\eta L}-I_{b\eta}(1)]E_3(\kappa_\eta L(1-\xi))$$
$$-\int_0^1 \frac{dI_{b\eta}}{d\xi'}(\xi')E_3(\kappa_\eta L|\xi'-\xi|)d\xi'\} \quad (38)$$

where $\xi = z/L$. Differentiation of equation (38) and subsequent integration over all wavenumbers gives the temperature profile. Once the temperature distribution is known, the radiative flux is calculated by spectrally integrating equation (38). The development of the necessary formulations suitable for numerical solution has been given by Modest (1981).

Some sample results for the nondimensional temperature distribution within the medium are given in Figs. 6 (gas only, $\kappa_p L = 0$) and 7 (gas with gray particle background, $\kappa_p L = 0.1$). The accuracy of the P-1 approximation is rather astounding. For a $\kappa_g L = 100$ with or without particle background the P-1 and exact solutions virtually coincide. Even poor weighted-sum-of-gray-gases fits, such as the 2/100 fit, give results of excellent accuracy. Obviously, it is the center of the gas band that determines the temperature distribution within the medium, and the center of the band is optically thick (even if $\kappa_g L = 10$), for which the P-1 approximation is expected to give excellent results. Note that the temperature distributions as shown are nondimensional in T^4, i.e., for a gray absorption coefficient the P-1 approximation would predict a straight line. This trend is observed in the $\kappa_g L = 10$ cases, where the P-1 approximation cannot follow the curvature of the exact solution near the walls, especially for the poorer weighted-sum-of-gray-gases fits.

Heat transfer rates between the two plates are shown in Fig. 8. As expected, agreement between the P-1 approximation and exact results is excellent. The P-1 results for the different weighted-sum-of-gray-gases fits all agree to within three significant figures and, therefore, only a single line is shown. Agreement between exact and P-1 is better in the absence of particles (~0.5 percent deviation) than with particle background (~2.0 percent for $\kappa_p L = 0.1$ and ~3.5 percent for $\kappa_p L = 1.0$). This affirms the earlier statement that the large optical thickness at the band center improves the accuracy of the P-1 method. The errors for the particle background cases are dominated by the optically thin ($\kappa_p L = 0.1$) to intermediate ($\kappa_p L = 1.0$) spectral windows (i.e., outside the gas band). In these cases the absolute error remains almost constant for varying $\kappa_g L$, being equal to the error at $\kappa_g L = 0$ (P-1 approximation for a gray medium).

Conclusions

It has been demonstrated that the concept of a weighted sum of gray gases, first introduced by Hottel and Sarofim (1967) for the zonal method, may be generalized for use with any arbitrary solution method, such as P-N approximations, discrete ordinates, etc. Comparison of sample results with exact results, obtained by numerical quadrature of spectral relations, proves not only the equivalence of the weighted-sum-of-gray-gases approach, but also shows that very simple fits give very accurate results. Thus, with the present approach the very complicated case of an arbitrary nongray gas-particulate mixture may be reduced to the simultaneous solution of three or four representative gray media. Computer CPU time savings over results of similar accuracy as obtained from spectral quadrature range from a minimum of 95 percent to as high as 99.5 percent (for optically thick gases with multiple bands). While at present limited to nonscattering media within black-walled enclosures, this new method makes it possible to include nongray radiation effects in many complicated and/or multidimensional situations.

References

Edwards, D. K., 1976, "Molecular Gas Band Radiation," *Advances in Heat Transfer*, Vol. 12, pp. 115–193, Academic Press, New York.

Farag, I. H., and Allam, T. A., 1981, "Gray-Gas Approximation of Carbon Dioxide Standard Emissivity," ASME JOURNAL OF HEAT TRANSFER, Vol. 103, pp. 403–405.

Hottel, H. C., and Sarofim, A. F., 1967, *Radiative Transfer*, McGraw-Hill, New York.

Leckner, B., 1972, "Spectral and Total Emissivity of Water Vapor and Carbon Dioxide," *Combustion and Flame*, Vol. 19, pp. 33–48.

Modest, M. F., 1981, "Radiative Heat Transfer in a Plane-Layer Mixture of Non-gray Particulates and Molecular Gases," *Journal of Quantitative Spectroscopy and Radiative Transfer*, Vol. 26, pp. 523–533.

Modest, M. F., and Azad, F. H., 1980, "The Differential Approximation for Radiative Transfer in an Emitting Absorbing and Anisotropically Scattering Medium," *Journal of Quantitative Spectroscopy and Radiative Transfer*, Vol. 23, pp. 117–120.

Siegel, R., and Howell, J. R., 1981, *Thermal Radiation Heat Transfer*, 2nd ed., Hemisphere Publ. Corp., New York.

Smith, T. F., Shen, Z. F., and Friedman, J. N., 1982, "Evaluation of Coefficients for the Weighted Sum of Gray Gases Model," ASME JOURNAL OF HEAT TRANSFER, Vol. 104, pp. 602–608.

C. P. Grigoropoulos[1]

W. E. Dutcher, Jr.[2]

K. E. Barclay[3]

Department of Mechanical Engineering,
University of Washington,
Seattle, WA 98195

Radiative Phenomena in CW Laser Annealing

Recrystallization of thin semiconductor films can yield improved electrical and crystalline properties. Recrystallization is often effected by using a laser source to melt the semiconductor film, which has been deposited on an amorphous insulating substrate. Although temperature measurement data would be valuable for the processing of materials on a microscopic scale, very few such measurements have been presented. It is the intent of this paper to demonstrate work toward the development of completely noninvasive experimental methods for in situ quantitative analysis of the laser annealing process, based on the acquisition of surface radiative data.

I Introduction

This study concerns the use of optically induced crystal growth of thin semiconductor films on amorphous insulators in the fabrication of high-performance electronic devices. Melting and recrystallization of such layers by light sources is used to improve their electrical and crystalline properties. Electronic devices fabricated by using recrystallized silicon films have shown good performance and reliability (Tsaur, 1986). In order to improve these techniques, it is necessary to address the issues that result from small length scales, high temperature gradients, and the mechanics of light interaction with thin film structures.

Despite their importance, very few experimental temperature measurements have been reported for laser annealing of thin films. Sedgwick (1981) measured the maximum temperature during CW laser silicon film annealing by using a modified optical pyrometer. The range of these measurements was 1300–1680 K with an estimated accuracy of a few tens of degrees. Lemons and Bosch (1982) measured the power spectra of the light emitted from molten silicon spots. These emissive power spectra were then correlated to temperature. This type of analysis is limited by the measurement resolution. The single temperature value they assigned to the spectral data with an accuracy of ± 50 K can provide an average temperature over the molten silicon region. Inoue et al. (1984) used thermal vision to obtain temperature profiles in electron-beam recrystallization of thin silicon layers. This technique is limited by the magnification requirements and the vision sensing resolution. Kodas et al. (1987) used micron-sized thin-film thermocouples made of intersecting nickel and gold lines embedded in a Si–SiO_2 structure to obtain surface temperatures during heating with a focused laser beam. It was found that the high thermal conductivity of the thermocouples provides heat flow paths that greatly alter the temperature field.

The work described in this paper explores the use of spatially resolved surface reflectivity measurements as a basis for further analysis. Time-resolved reflectivity measurements provide a useful diagnostic tool in laser materials processing. Olson et al. (1980, 1983) determined epitaxial solid phase crystallization rates in CW laser silicon annealing by analyzing optical interference effects from time-resolved surface reflectivity measurements. Murakami et al. (1984) demonstrated a technique for obtaining surface reflectivity measurements in CW Kr annealing of thin silicon samples.

If the temperature dependence of the material complex refractive index is known, surface reflectivity measurement can, in principle, be used in conjunction with thin film optics models to determine the semiconductor film temperature. The bulk silicon surface reflectivity between 1440 and 1680 K for the solid phase and up to 1950 K for the liquid phase has been measured for HeNe light of 632.8 nm wavelength incident on the surface of a bulk silicon slab (Lampert et al., 1981). Van der Meulen and Hien (1974) used an ellipsometric system to measure the complex refractive index of silicon for temperatures up to approximately 1550 K. Their experimental results for the silicon extinction coefficient do not correlate with the measurements of the silicon complex refractive index for temperatures below 1000 K given by Jellison and Modine (1983). More recent experiments by Jellison and Burke (1986) improved the measurement of the real part of the silicon complex refractive index and will be used in this work.

Thin film optical properties are strong functions of the microstructure (Aspnes, 1982). Chandrasekhar et al. (1988) reported the anomalous, with respect to the beam irradiance, and thus to the material temperature, behavior of the complex refractive index of silicon polycrystalline films irradiated by Ar^+ laser beams. They found that the observed changes of sign of the material thermo-optic coefficient, dn/dT, may be attributed to the presence of internal surfaces in films with large amorphous components.

II Description of the Experimental Apparatus

The experiments were performed on 0.5-μm-thick polysilicon films deposited on bulk, fused silica wafers of 7.6-cm diameter and 0.5-mm thickness. The silicon films were encapsulated by 0.5-μm-thick SiO_2 layers. A sketch of the laser annealing experimental apparatus is shown in Fig. 1.

A Spectra-Physics 164-08 4W Argon Laser is used as the annealing source. This laser operates in the fundamental mode, TEM_{00}, with a Gaussian intensity distribution across the multiline laser beam. The annealing laser beam is directed toward the silicon sample, which is mounted on a precision translation stage. The laser beam passes through the substrate, which is transparent in the visible spectrum, and is partially reflected and absorbed by the silicon layer, while the remaining portion is transmitted through the layer thickness. The annealing laser beam power intensity is assumed to be Gaussian and circular

$$Q_{an}(r) = \sum_{i=1}^{n_w} Q_{\lambda i}^{o} \exp\left[-\frac{r^2}{w_{\lambda i}^2}\right] \tag{1}$$

The positions of the translation stage and of the spherical lens are controlled using micrometers. Figure 2 shows the experimentally measured, $1/e$ irradiance radius of the blue (λ_b =

[1]Present address: Department of Mechanical Engineering, University of California, Berkeley, CA 94720.

[2]Present address: Advanced Programs, Boeing Commercial Airplane Group, Seattle, WA 98124-2207.

[3]Present address: Computer Dynamics Incorporated, Auburn Hills, MI 48326.

Contributed by the Heat Transfer Division and presented at the ASME Winter Annual Meeting, San Francisco, California, December 10–15, 1989. Manuscript received by the Heat Transfer Division June 13, 1990; revision received November 8, 1990. Keywords: Laser Processing, Materials Processing and Manufacturing Processes, Measurement Techniques.

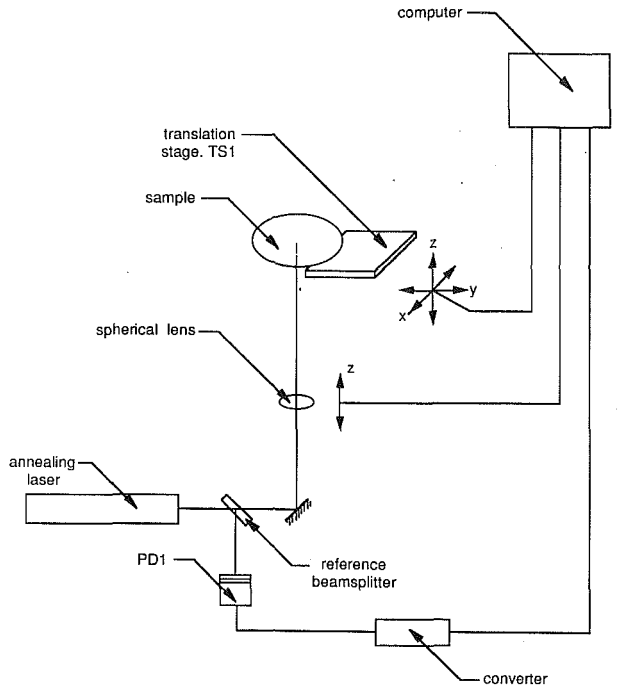

Fig. 1 Schematic of the laser annealing experimental apparatus

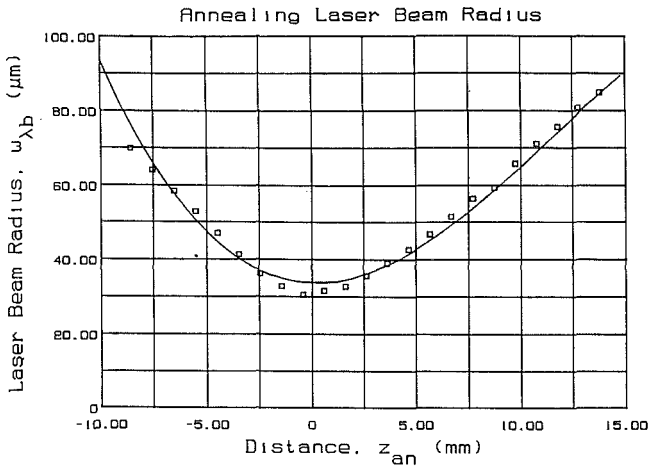

Fig. 2 Graph of the annealing laser beam 1/e irradiance radius, $w_{\lambda b}$, as a function of the distance along the beam axis. The marked points indicate the experimentally measured data. The solid line is a least-squares polynomial fit.

488 nm) component of the laser beam, $w_{\lambda b}$, as a function of the distance along the laser beam axis measured from its focal waist. Near the focal waist ($z = 0$), the beam radius was found to be not perfectly symmetric. A cubical polynomial was fitted to the experimental points.

The experimental setup for normal incidence reflectivity measurements is shown in Fig. 3. A low-power (5 mW) HeNe laser emits the red ($\lambda = 632.8$ nm) probing laser beam. The orientation of the probing laser light field vector is controlled by a broadband polarizer. A polarizing cube beamsplitter is installed inside a square beamsplitter microscope tube. A quarter-wave retarder plate is placed underneath this beamsplitter. This plate converts the linearly polarized input light into circularly polarized if the angle between the input electrical field vector and the retarder principal plane is $\pi/4$. The $\pi/2$ phase shift upon reflection converts this angle to $-\pi/4$. Hence, the sense of the polarization is reversed for the reflected beam. This beam can then be transmitted through the polarizing beamsplitter to the silicon diode photodetector, PD3. A 632.8-nm red light interference filter is used to block stray light and transmission from the annealing laser beam, with the aid of yellow Schott glass filters to attenuate the annealing laser beam light that is transmitted through the sample. The probing laser and the cube beamsplitter assembly are mounted on the precision translation stage TS2. Both the sample translation stage, TS1, and the probing apparatus translation stage, TS2, are driven by piezoelectric encoder motors, which are interfaced to a personal computer. The repeatable positioning accuracy of these motors is 1 μm and the maximum constant

Nomenclature

a_n = linear coefficient of temperature dependence of real part of silicon complex refractive index
d_{enc} = encapsulating layer thickness
d_{si} = silicon layer thickness
f = filter function
f^0 = peak filter strength
$k_{ext}(T)$ = extinction coefficient of silicon at temperature T
k_o = extinction coefficient of silicon at 300 K
$n(T)$ = real part of the silicon complex refractive index at temperature T
n_o = real part of the silicon complex refractive index at 300 K
n_w = number of annealing laser beam peak wavelengths
P_T = laser beam total power
Q = laser beam light source intensity distribution
Q^o = peak power intensity of the laser beam
r = radial distance from the center of the laser beam
R = thin film reflectivity
T = temperature
T_m = silicon melting temperature = 1685 K
V = material translation speed
$w_{\lambda b}$ = distance from laser beam center to point where irradiance intensity of blue ($\lambda = 488$ nm) component of the laser beam drops to $1/e$ of peak value
$w_{\lambda i}$ = distance from laser beam center to point where irradiance of λ_i wavelength component of the laser beam drops to $1/e$ of its peak value
x = coordinate along the direction of the sample motion
y = coordinate in the transverse direction
z = distance along the laser beam axis measured from the beam focal waist
Δx = raster scan step increment in x direction
Δy = distance between sampled points in y direction
λ = laser light wavelength
λ_b = blue ($\lambda = 488$ nm) annealing laser light wavelength
λ_i = wavelength of annealing laser line center ($i = 1, \ldots, n_w$)
ρ_{si} = silicon density
$\rho_{si,o}$ = silicon density at 300 K
τ = thin-film transmissivity

Subscripts

an = annealing laser beam
f = filtered data
l = liquid silicon
pr = probing laser beam
r = raw data

Superscripts

fp = laser beam parameter at its focal waist

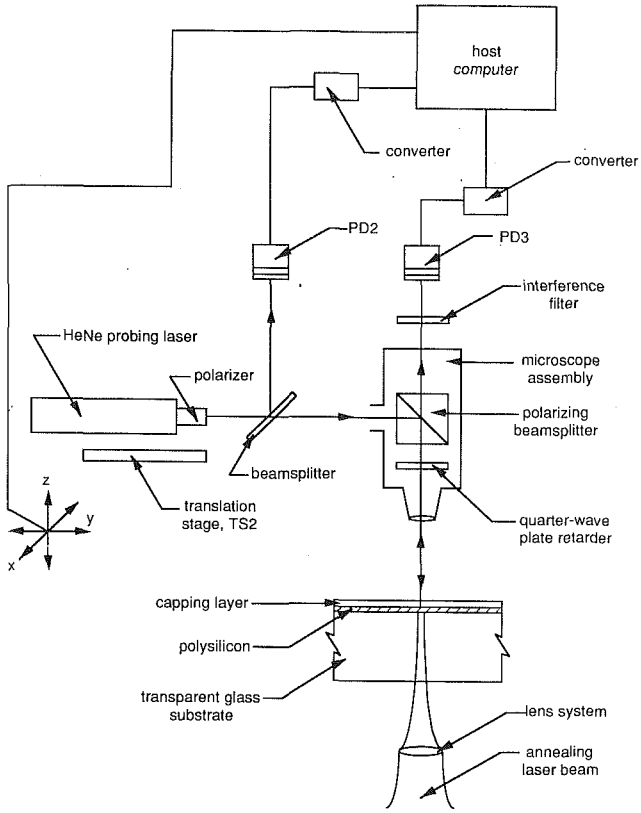

Fig. 3 Schematic of the experimental setup for normal incidence reflectivity measurements

translational speed is 2 mm/s. The probing laser translation stage, TS2, can be programmed to scan in a raster motion over the heated region.

A data acquisition system collects signals from the main laser reference arm, PD1, the probing laser reference, PD2, and the reflected beam, PD3. The laser beam total power at the sample surface is measured by a thermopile detector. The signal PD3/PD2 is calibrated to yield the reflectivity signal. The probing laser beam is focused on the silicon sample surface through the encapsulating SiO_2 layer via a 10× microscope objective lens. The probing laser beam light intensity distribution is also Gaussian and circular

$$Q_{pr}(r) = Q_{pr}^{o} \exp\left[-\frac{r^2}{(w_{pr}^{fp})^2}\right] \tag{2}$$

The variation of the probing laser beam $1/e$ irradiance radius, w_{pr}, with the distance from the focal waist, z_{pr}, was experimentally measured, as is shown in Fig. 4. The $1/e$ laser beam irradiance envelope (Kogelnik and Li, 1966) was fitted to the experimental points

$$w_{pr}(z_{pr}) = w_{pr}^{fp}\{1 + [\lambda z_{pr}/(2 \cdot \pi \cdot (w_{pr}^{fp})^2)]^2\}^{1/2} \tag{3}$$

The computed probing laser radius at the focal waist was found as $w_{pr}^{fp} \cong 5$ μm. Care was taken in the experiment to intercept the silicon layer with the probing laser beam in the vicinity of the focal waist. The experimental results show an increase from the theoretically minimum spot size by a factor of almost 2. This deviation can be attributed to the focusing microscope objective lens aberrations.

III Experimental Results

The laser annealing process is controlled by: (1) the total power of the laser beam, (2) the laser beam intensity distribution, and (3) the material translation speed. Experimental observations conducted with the same experimental apparatus

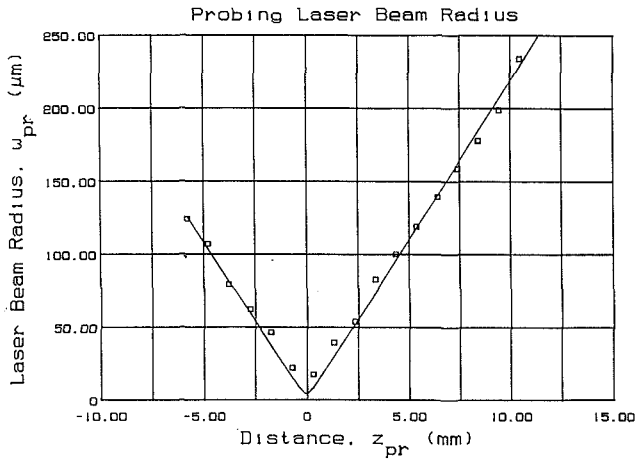

Fig. 4 Graph of the probing laser beam $1/e$ irradiance radius, w_{pr}, as a function of the distance from the focal waist. The marked points indicate the experimentally measured data.

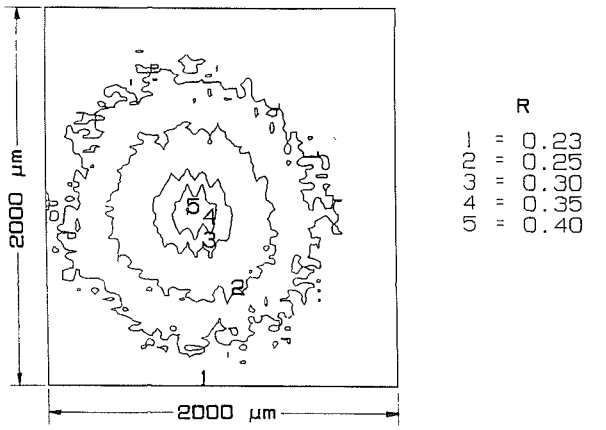

Fig. 5 Contour plot of the measured silicon film reflectivity, *R*. The annealing laser beam total power P_T = 0.3 W and the $1/e$ irradiance radius $w_{\lambda b}$ = 40 μm. The sample is not moving.

(Grigoropoulos et al., 1989) recorded the onset of silicon layer melting and the development of various phase change patterns. Based on this information, a first set of experiments analyzed light reflection from solid silicon, when heated below the melting temperature. In these experiments, the laser power, P_T, was varied from 0.3 to 1.5 W, and the laser beam $1/e$ irradiance radius, $w_{\lambda b}$, was varied from approximately 34 μm to 100 μm. The reflectivity probe was scanned at a constant speed of 1 mm/s, over a 2 mm × 2 mm area covering the heated polysilicon spot. The raster scan step increment in the x direction was set to Δx = 40 μm, and the data acquisition sampling frequency was 1 kHz. The acquired continuous reflectivity signal was postprocessed to yield the reflectivity spatial distribution over the annealed region.

Figure 5 shows the thin film reflectivity contour plot for an annealing laser beam of average total power, P_T = 0.3 W, and $1/e$ irradiance radius, $w_{\lambda b}$ = 40 μm. The data scatter is largely attributed to local variations in the thin film thickness (the reflectivity is a strong function of the thin film thickness), to film surface and internal roughness, and to the presence of local material imperfections. These defects may cause diffraction, as well as surface and volume scattering effects (Hunderi, 1979). As the laser beam total power was increased to P_T = 0.6 W, the reflectivity contour plot showed an expanded heated area (Fig. 6). The raw experimental data can be smoothed using a spatial-convolution-based digital fiter

$$R_f(x, y) = \int_{-\infty}^{+\infty}\int_{-\infty}^{+\infty} R_r(\alpha, \beta) f(x-\alpha, y-\beta)\, d\alpha d\beta \tag{5}$$

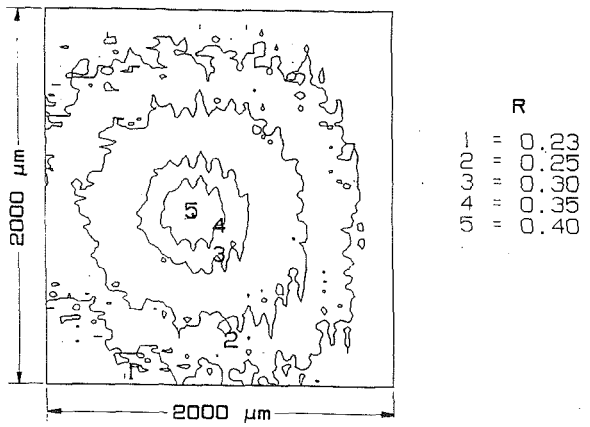

Fig. 6 Contour plot of the measured silicon film reflectivity, *R*. The annealing laser beam total power P_T = 0.6 W and the 1/*e* irradiance radius $w_{\lambda b}$ = 40 μm. The sample is not moving.

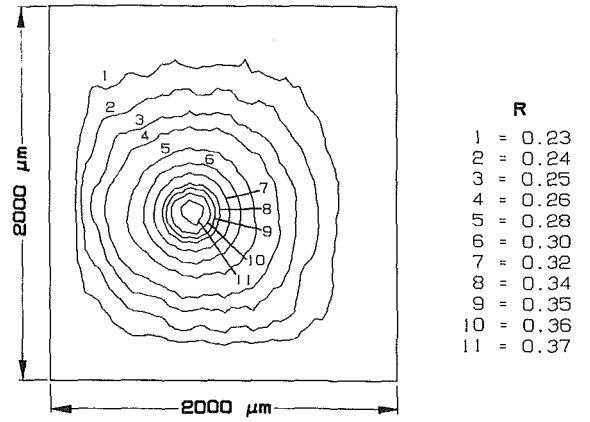

Fig. 7 Filtered reflectivity contours corresponding to Fig. 6

The function $f(x, y)$ represents a Gaussian filter

$$f(x, y) = f^0 \exp\left[-\left(\frac{x^2}{(3\cdot\Delta x)^2}+\frac{y^2}{(3\cdot\Delta y)^2}\right)\right] \quad (6)$$

The filter peak strength, f^0, yields a filter volume of unity over the x-y plane. The filtering is performed using standard two-dimensional discrete FFT and inverse FFT methods.

The experimental results can best be interpreted with the aid of computational analysis (Grigoropoulos et al., 1991). This model employs a three-dimensional ADI transient algorithm for the solution of conductive heat transfer in the encapsulating layer, the glass substrate, and the solid phase silicon layer, and an enthalpy formulation for the analysis of phase change in the silicon layer. Figure 8 gives the calculated steady-state temperature distributions in the thin silicon layer along an axis through the center of the laser beam for laser beam powers P_T = 0.3 W and 0.6 W and a laser beam 1/*e* irradiance radius, $w_{\lambda b}$ = 40 μm. These values correspond to the experimental data shown in Figs. 5 and 6. Thin film optics (Born and Wolf, 1970) are used to calculate the film optical parameters for normal incidence of red (λ = 632.8 nm) light. Density data (i.e., Yaws et al., 1981) show a linear relationship between density and temperature for solid silicon between the ambient temperature and the melting point.

$$\rho_{si} = \rho_{si,o}[1 - 0.03(T - 273)/1412] \quad (7)$$

The thickness of the solid silicon film was assumed also to vary linearly with temperature. The real part of the silicon complex refractive index is a linear function of temperature between approximately 300 and 1000 K (Jellison and Burke, 1986)

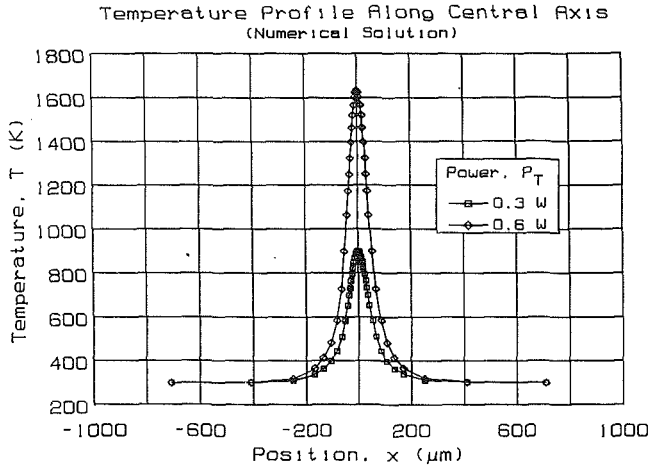

Fig. 8 Predicted steady-state temperature distributions in the silicon layer for laser beam powers P_T = 0.3 W and 0.6 W and $w_{\lambda b}$ = 40 μm. The sample is not moving.

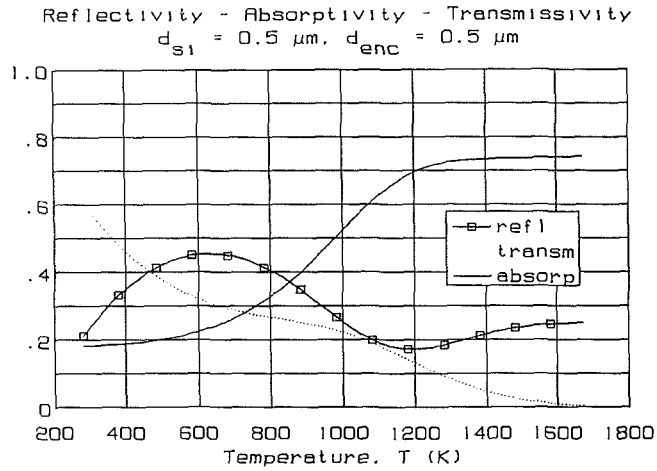

Fig. 9 Calculated thin film reflectivity, *R*, as a function of the silicon layer temperature

$$n(\lambda, T) = n_o(\lambda) + a_n(\lambda)(T - 300) \quad (8)$$

The coefficient $a_n(\lambda)$ is a fifth-order polynomial of the wavelength. The extinction coefficient, k_{ext}, is given by the following expression:

$$k_{ext}(\lambda) = k_o(\lambda) \exp[(T - 273)/430] \quad (9)$$

The liquid silicon complex refractive index has been measured by Shvarev et al. (1975). The reflectivity for molten silicon is found, R_l = 0.569. The thin film transmissivity, reflectivity, and absorptivity are calculated using thin film optics (Born and Wolf, 1970) and are shown as functions of temperature in Fig. 9. The simple heater assembly shown in Fig. 10 was constructed to check the reflectivity response of the optical microprobe to variations of the sample temperature. The temperature of the sample, which was monitored by thermocouples embedded in the sample stage, was raised to 700 K. The sample reflectivity as a function of temperature is shown in Fig. 11. This curve shows the reflectivity peak that occurs at a temperature of about 600 K. Figures 12 and 13 give the comparison between the computed and the experimentally measured reflectivity values for laser beam powers of P_T = 0.3 W and 0.6 W, respectively. It appears that the experimental signal is wider than the computed distribution, and that the calculated peak reflectivity values are higher than the experimentally obtained. It is, however, clear that the thin film optical interference effects responsible for the reflectivity peaks are captured by the experiment.

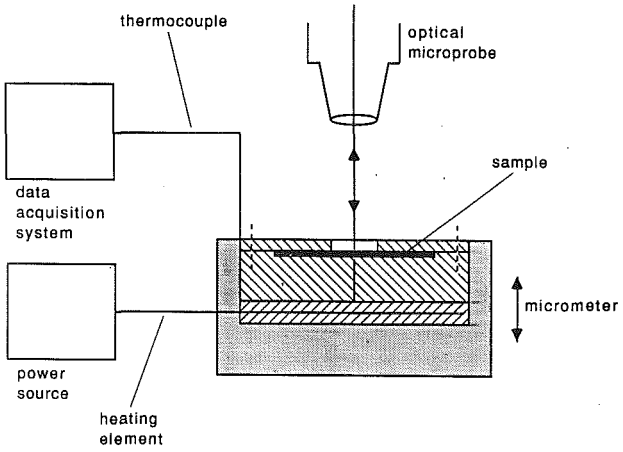

Fig. 10 Sketch of the sample heater arrangement

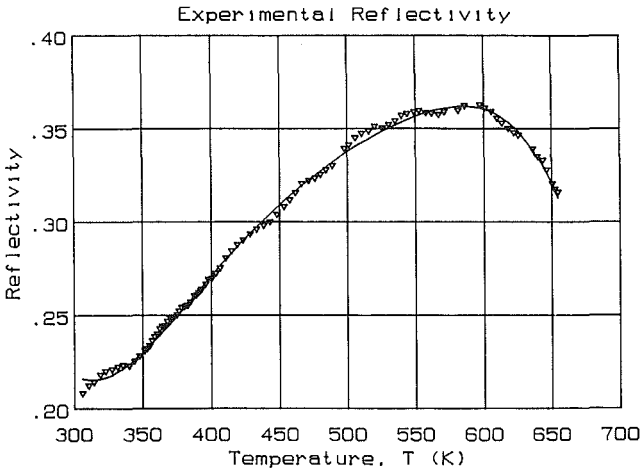

Fig. 11 Optical microprobe reflectivity signal as a function of the sample temperature. The marked points indicate experimental data. The solid line is a least-squares polynomial fit.

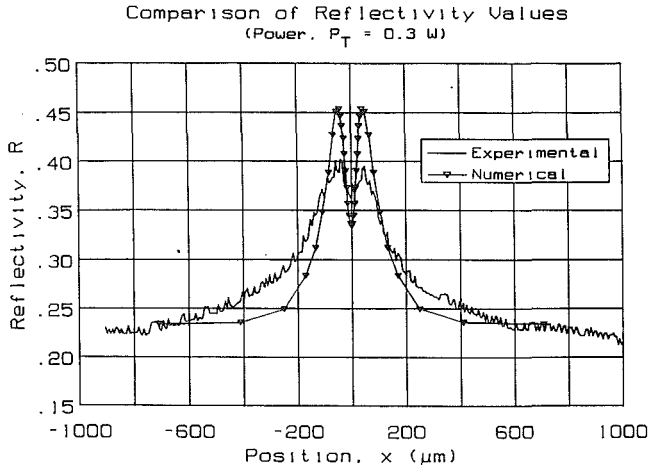

Fig. 12 Comparison between the experimentally obtained and the calculated thin film reflectivity along an axis through the center of the laser beam. The operating conditions are those of Fig. 5.

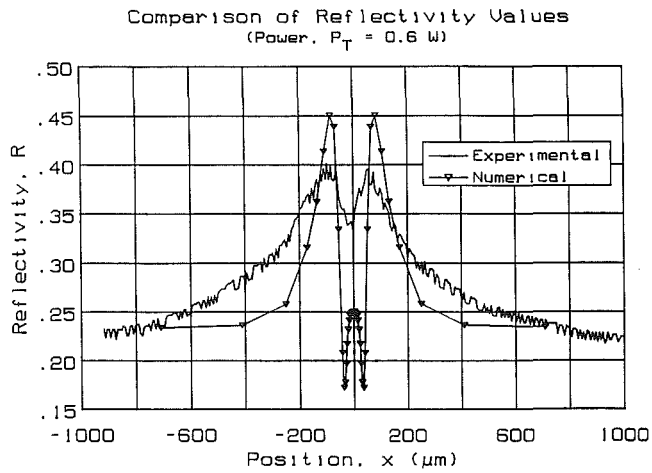

Fig. 13 Comparison between the experimentally obtained and the calculated thin film reflectivity along an axis through the center of the laser beam. The operating conditions are those of Fig. 6.

The same trends were recognized in all the experimental results for solid phase silicon laser annealing. No data, even for increased radii, $w_{\lambda b}$, showed a reflectivity drop to 0.16, a value that is predicted for a film temperature of approximately 1200 K. The minimum film reflectivity was found to be in the neighborhood of 0.3. The measured reflectivity signal represents an integrated reflectivity, which follows the Gaussian intensity distribution across the probing laser beam. Hence, in general, the measured signal underestimates the sampled point reflectivity, with error increasing as the probing beam radii, w_{pr}, becomes larger. This factor alone cannot fully explain the observed discrepancy. The data used for the calculation of the thin film reflectivity were based on measured bulk silicon optical properties for temperatures below 1000 K and extrapolated to the melting temperature of 1685 K. The experimental evidence presented in this paper suggests that the behavior of the polycrystalline film optical properties at high temperatures, in particular as these properties depend upon the film microstructure, should be independently studied. The film thickness and microstructure and the semiconductor electrical transport properties are affected by the stress field in the material. The extent to which the thermal stresses developed during annealing influence the optical properties should also be examined.

The experimental method was applied to the investigation of the phase change process. The sample material translation speed, V, was 0.5 mm/s, with the power ranging from P_T = 1.0 W to 2.0 W, and the laser beam $1/e$ radius, $w_{\lambda b}$, varying from 34 μm to 75 μm. Figure 14 shows the predicted temperature solution in the silicon layer for a laser beam of $1/e$ radius, $w_{\lambda b}$ = 60 μm and total power, P_T = 1.5 W at a time t = 40 ms after the laser beam is turned on and focused on the moving sample. At that time, a steady-state temperature field, with respect to a fixed frame of coordinates assigned to the laser beam, is developed in the silicon layer. Figure 15 compares the predicted silicon layer reflectivity with the measured reflectivity signal on an axis close to the center of the laser beam, along the direction of motion. There is a sharp reflectivity increase that clearly indicates melting. Ahead of the molten pool, $x<0$, the measured reflectivity signal is relatively smooth. The reflectivity of the recrystallized track, which is left in the wake of the molten pool, $x>0$, is not smooth, and it is not possible to observe the interference effects that characterize the polycrystalline silicon annealing. Etching of the encapsulating SiO_2 layer and subsequent contrast interference microscopic analysis of the recrystallized material reveal a "chevron" type of pattern. This pattern is formed of relatively long crystallites, typically 15–20 μm wide, separated by low angle grain boundaries. On the contrary, the polycrystalline silicon layer grains have an average characteristic dimension of about 2 μm, and are significantly smaller than the sensing probing laser beam diameter.

IV Conclusions

A new method for in situ analysis of radiative phenomena

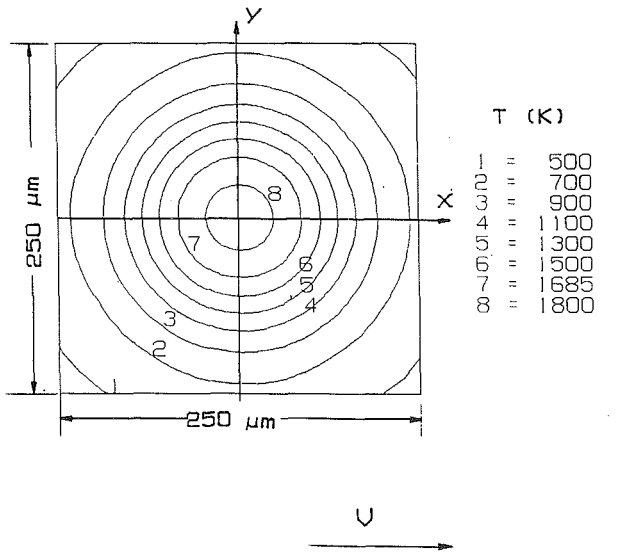

Fig. 14 Predicted temperature distribution in the silicon layer at t = 40 ms. The laser beam total power P_T = 1.5 W, the laser beam 1/e intensity radius $w_{\lambda b}$ = 60 μm, and the material translation speed V = 0.5 mm/s.

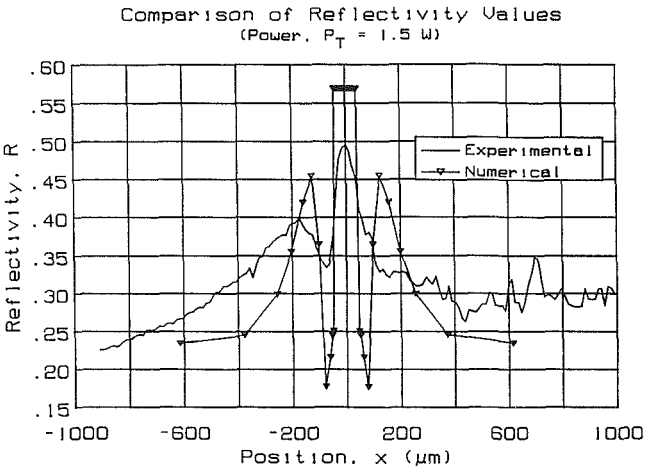

Fig. 15 Comparison between the calculated and experimentally obtained reflectivity values that correspond to the conditions of Fig. 10 along an axis in the direction of motion passing through the center of the laser beam

in laser annealing of thin semiconductor films has been presented. Spatially resolved thin film reflectivity measurements were obtained and correlated with theoretical modeling. Further work is focused on the improvement of both the measurement resolution and the postprocessing analysis. This method can also be applied to the experimental analysis of laser-induced transient thermal distributions. Research is also conducted to understand and establish thin film optical properties at high temperatures.

Acknowledgments

Support by the National Science Foundation, under Grant No. MSM-8708757, is gratefully acknowledged.

References

Aspnes, D. E., 1982, "Optical Properties of Thin Films," *Thin Solid Films*, Vol. 89, pp. 249–262.

Born, M., and Wolf, E., 1970, *Principles of Optics*, 6th ed., Pergamon, Exeter, Great Britain, pp.55–60, 611–624.

Chandrasekhar, S., Vengurlekar, A. S., Roy, S. K., and Karulkar, V. T., 1988, "Nonlinear Temperature Dependence of the Refractive Index Polycrystalline Silicon Films and the Influence of Microstructural Disorder," *Journal of Applied Physics*, Vol. 63, No. 6, pp. 2072–2076.

Grigoropoulos, C. P., Dutcher, W. E., and Emery, A. F, 1991, "Experimental and Computational Analysis of Laser Melting of Thin Silicon Films," ASME JOURNAL OF HEAT TRANSFER, Vol. 113, pp. 21–29.

Hunderi, O., 1979, "Thin Film Optical Properties in Relation to Film Structure," *Thin Solid Films*, Vol. 57, pp. 15–32.

Inoue, T., et al., 1984, "Electron-Beam Recrystallization of Silicon Layers on Silicon Dioxide," *Proceedings, Materials Research Society*, J. C. C. Fan and N. M. Johnson, eds., North-Holland, New York, Vol. 23, pp. 523–531.

Jellison, G. E., Jr., and Burke, H. H., 1986, "The Temperature Dependence of the Refractive Index of Silicon at Elevated Temperatures at Several Laser Wavelengths," *Journal of Applied Physics*, Vol. 60, No. 2, pp. 841–843.

Jellison, G. E., Jr., and Modine, F. A., 1983, "Optical Functions of Silicon Between 1.7 and 4.7 eV at Elevated Temperatures," *Physical Review B*, Vol. 27, No. 12, pp. 7466–7472.

Kodas, T. T., Baum, T. H., and Comita, P. B., 1987, "Surface Temperature Rise in Multilayered Solids Induced by a Focused Laser Beam," *Journal of Applied Physics*, Vol. 61, No. 8, pp. 2749–2753.

Kogelnik, H., and Li, T., 1966, "Laser Beams and Resonators," *Applied Optics*, Vol. 5, No. 10, pp. 1550–1567.

Lampert, M. O., Koebel, J. M., and Siffert, P., 1981, "Temperature Dependence of the Reflectance of Solid and Liquid Silicon," *Journal of Applied Physics*, Vol. 52, No. 8, pp. 4975–4976.

Lemons, R. A., and Bosch, M. A., 1982,"Microscopy of Si Films During Melting," *Appl. Phys. Lett.*, Vol. 40, No. 8, pp. 703–706.

Murakami, K., Itoh, H., Tomiya, Y., Takita, K., and Masuda, K., 1984, "Time-Resolved Si Lattice Temperature Measurement on Wide Time Scale (10^{-9}–10^{0} sec) During Laser Annealing," *Proceedings, Materials Research Society*, J. C. C. Fan and N. M. Johnson, eds., North-Holland, New York, Vol. 23, pp. 167–172.

Olson, G. L., Kokorowski, S. A., McFarlane, R. A., and Hess, L. D., 1980, "Direct Observation of Time-Resolved Optical Reflectivity," *Appl. Phys. Lett.*, Vol. 37, No. 11, pp. 1019–1021.

Olson, G. L., Kokorowski, S. A., Roth, G. A., and Hess, L. D., 1983, "Laser-Induced Solid Phase Crystallization on Amorphous Silicon Films," *Proceedings, Materials Research Society*, J. Narayan, W. L. Brown, and R. A. Lemons, eds., North-Holland, New York, Vol. 13, pp. 141–154.

Sedgwick, T. O., 1981, "A Simple Optical Pyrometer for in-situ Temperature Measurement During CW Laser Annealing," *Proceedings, Materials Research Society*, J. F. Gibbons, L. D. Hess, and T. W. Sigmon, eds., North-Holland, New York, Vol. 1, pp. 147–153.

Shvarev, K. M., Baum, B. A., and Gel'd, P. V., 1975, "Optical Properties of Liquid Silicon," *Sov. Phys. Solid State*, Vol. 16, No. 11, pp. 2111–2112.

Tsaur, B. Y., 1986, "Assessment of Silicon on Insulator Technologies for VLSI," *Proceedings, Materials Research Society*, A. Chiang, M. W. Geis, and L. Pfeiffer, eds., MRS, Pittsburgh, PA, Vol. 53, pp. 365–373.

Van der Meulen, Y. J., and Hien, N. C., 1974, "Design and Operation of an Automated High-Temperature Ellipsometer," *Journal of Optical Society of America*, Vol. 64, No. 6, pp. 804–811.

Yaws, C. L., Dickens, L. L., Lutwack, R., and Hsu, G., 1981, "Semiconductor Industry Silicon: Physical and Thermodynamic Properties," *Solid State Technology*, pp. 80–85.

Multiple Reflection Effects on Evaporative Cutting With a Moving CW Laser

S. Y. Bang
Student Mem. ASME

M. F. Modest
Fellow ASME

Department of Mechanical Engineering,
Pennsylvania State University,
University Park, PA 16802

Multiple reflection and beam guiding effects during laser machining are analyzed numerically. The surface of the treated material is considered to reflect the laser irradiation in a fully diffuse fashion, limiting the analysis to bodies that have a rough surface during laser evaporation (e.g., micro-explosive removal, violent surface boiling, etc.). For local irradiation calculations the material surface is divided into a number of triangular elements with linear interpolation functions. The net radiative flux for these elements is obtained from standard view factor theory. The irradiation calculations are combined with a simple integral method governing conduction losses into the medium, and the resulting groove shape and depth are found through an iterative procedure. Considering multiple reflection results in increased material removal rates and deeper grooves, accompanied by a flatter profile near the centerline and steeper slopes in the other parts of the groove cross section.

Introduction

Lasers have a variety of applications in modern technology because of their ability to produce high-power beams. Applications include welding, drilling, cutting, machining, medical surgery, and others.

Most of the theoretical work on laser-processing heat transfer to date has centered on the solution of the classical heat conduction equation for a stationary or moving semi-infinite solid. Cases with and without phase change and for a variety of irradiation conditions have been studied. The simplest case without phase change was first treated by Carslaw and Jaeger (1959), while a pulsed heat source was addressed by Carslaw and Jaeger (1959), White (1963a, 1963b) and Rykalin et al. (1967). A disk-shaped source was first treated by Paek and Gagliano (1972), and a Gaussian power distribution was investigated by Ready (1971). The case of a semi-transparent solid was first addressed by Brugger (1972) and Maydan (1970, 1971) for the one-dimensional case. A general heat conduction solution is given by Modest and Abakians (1986a), who looked at a moving semi-transparent body irradiated by a Gaussian laser source either uniformly in time or in a pulsed mode.

The problem is considerably more complicated when phase change takes place. Soodak (1943) was the first to study the problem of melting with complete removal of melt for a one-dimensional slab. Landau (1950) considered the same problem for the case where one surface was subjected to time-varying heating. Dabby and Paek (1972) considered laser penetration into the solid for a stationary semi-infinite solid. To model the laser drilling process von Allmen (1976) found a quasi-one-dimensional solution that showed considerable agreement with experiments. Bar-Isaac and Korn (1974) used a three-dimensional moving-heat-source model to describe the effects of a focused laser beam in the drilling process. Mazumder et al. have done considerable research on welding and melt pool behavior. Using a finite volume method, they developed a three-dimensional heat transfer model for laser welding (Mazumder, 1987; Mazumder and Steen, 1980; Chande and Mazumder, 1984) that allows for temperature-dependent properties, spatial distribution of the heat source, radiative and convective heat losses, and latent heat of fusion. Laser cutting or shaping with a moving laser was modeled by Modest and Abakians (1986b), for irradiation by a CW laser with Gaussian distribution onto an opaque, semi-infinite solid. They assumed one-step evaporation of the material (without beam interference), parallel laser beams, negligible reflection effects, and small heat losses (in order to employ a simple integral method for conduction losses). In a follow-up paper by Biyikli and Modest (1988), the assumption of parallel laser beams was relaxed showing that beam focusing has a strong influence on the laser shaping process. In another paper by Abakians and Modest (1988), they considered semi-transparent bodies, demonstrating that materials would have to be very transparent to show substantially different behavior.

In the model developed by Roy and Modest (1990) one of the weakest assumptions made by Modest and Abakians (1986b), Biyikli and Modest (1988), and Abakians and Modest (1988) was relaxed: Rather than treating conduction losses in a quasi-one-dimensional fashion, the full three-dimensional conduction equation was solved. Roy and Modest (1990) reported that a more accurate treatment of the conduction losses has a considerable effect on the size of the groove formed by evaporation if the scanning velocity is fairly low (resulting in large conduction losses). Ramanathan and Modest (1990) relaxed the assumption of constant properties with the simplified one-dimensional integral formulation and found good agreement with experimental data for silicon nitride ceramics. Though considering diffuse or specular reflections is well established in standard radiation problems, it has not been applied extensively to laser-related processes. Baily and Modak (1989) used the Monte Carlo method to simulate laser ablation with cavity reflections. To reduce the noise from the Monte Carlo method and still conserve power, they used Legendre polynomial smoothing. They reported that ignoring multiple reflections may give discrepancies up to 30 percent in predicted results. Minamida et al. (1986) used the multiple reflection effects of high-power CO_2 laser beams for wedge shape welding and developed a simple simulation model using the ray tracing method. They achieved fairly good prediction of the temperature profile in the sample.

Multiple reflection and beam guiding effects become important for highly reflective materials or for deep grooves with aspect ratios greater than one where large off-normal incidence causes high reflectivity values. Wallace (1983, 1986) found in his experiments that many of his grooves exhibited strongly

Contributed by the Heat Transfer Division and presented at the Joint AIAA/ASME Thermophysics and Heat Transfer Conference, Seattle, Washington, June 18–20, 1990. Manuscript received by the Heat Transfer Division June 14, 1990; revision received November 8, 1990. Keywords: Conduction, Laser Processing, Radiation.

curved cross sections that apparently resulted from beam guiding effects of partially polarized laser irradiation in the groove. Anthony (1980) also concluded that the non-straight holes in his experiments resulted partly from beam channeling along side walls. In the present study the surface of the treated material is assumed to reflect laser irradiation in a fully diffuse fashion. Considering multiple reflections of the laser beam shows how beam channeling can increase the effective absorptivity of the material.

Theoretical Background

In order to obtain a realistic yet feasible mathematical description of the evaporation front in a moving solid subjected to a concentrated laser beam, the following assumptions will be made:

1 The solid moves with constant velocity u and the frame of reference is fixed to the laser.

2 The solid is isotropic with constant properties. Because the main emphasis of the present work is to study the effect of multiple reflections and beam guiding as compared to the previous model (Biyikli and Modest, 1988) where only direct irradiation is considered, this assumption is made mainly for simplifying the presentation of results.

3 The material is opaque, i.e., the laser beam does not penetrate appreciably into the medium. Abakians and Modest (1988) showed that the absorption coefficient would have to be very small to make this a poor assumption.

4 The change of phase from solid to vapor occurs in a single step at the evaporation temperature T_{ev}. Real materials may display significantly different behavior (Modest and Abakians, 1986b; Abakians and Modest, 1988), such as liquefaction followed by evaporation, decomposition into liquid and gas, gradual evaporation over a wide range of temperatures, outgassing followed by microexplosive removal of solid particles, and so forth. Assuming that the most important parameter is the total amount of energy required to remove material, referred to as "heat of removal," the present model should do quite well.

5 The evaporated material does not interfere with the incoming laser beam, and ionization of the gas does not occur, both of which are true for many applications at moderate power levels. The gas is assumed transparent and there are no droplets or particles (or they are removed by an external gas jet).

6 Heat losses by convection and radiation are negligible (as compared to conduction and change-of-phase losses). This was shown to be accurate under all conditions by Modest and Abakians (1986b).

7 At the surface, the laser beam is reflected in a fully diffuse fashion with reflectivity $\rho^d = 1 - \alpha$. This limits the analysis to bodies that have a rough surface during laser evaporation (e.g., micro-explosive removal, violent surface boiling, etc.).

The laser beam is assumed to have a Gaussian power distribution with an effective radius $R(z)$, which is given by Kogelnik and Li (1956) as

$$R(z) = R_0\left[1 + \left(\frac{w+z}{\pi R_0^2/\lambda}\right)^2\right]^{1/2} \tag{1}$$

where R_0 is the effective radius at the focal plane, w is the distance between the focal plane of the lens and the material surface ($w > 0$ for focal point above surface, and $w < 0$ for focal point below surface), and λ is the wavelength of the laser. Since laser power for the expanding laser beam must be conserved, the direct irradiation from the laser beam may then be expressed as (Biyikli and Modest, 1988)

$$\mathbf{F} = (\hat{\mathbf{k}} + \tan\beta\cos\phi\hat{\mathbf{i}} + \tan\beta\sin\phi\hat{\mathbf{j}})F_0\frac{R_0^2}{R^2(z)} \times e^{-(x^2+y^2)/R^2(z)} \tag{2}$$

where β is the angle between a laser ray and the z-axis, ϕ is the azimuthal angle for the ray measured from the x-axis in the x-y-plane, and F_0 is the flux density at the beam center. Under the above conditions the heat transfer problem is expressed in nondimensional form as (see Fig. 1)

$$U\frac{\partial\theta}{\partial\xi} = \frac{\partial^2\theta}{\partial\xi^2} + \frac{\partial^2\theta}{\partial\eta^2} + \frac{\partial^2\theta}{\partial\zeta^2} \tag{3}$$

$$\xi \to \pm\infty, \quad \eta \to \pm\infty, \quad \zeta \to +\infty: \quad \theta = 0 \tag{4}$$

$$\zeta = S(\xi, \eta): \quad \left(\frac{\alpha}{\alpha_0}\right)\mathcal{H}(\xi, \eta) = -N_k\hat{\mathbf{n}}\cdot\nabla\theta - N_e(\hat{\mathbf{i}}\cdot\hat{\mathbf{n}}) \tag{5a}$$

$$\theta(\xi, \eta) = 1 \text{ if } \hat{\mathbf{i}}\cdot\hat{\mathbf{n}} < 0 \tag{5b}$$

Nomenclature

c = specific heat
D = thermal diffusivity
F_{i-j} = view factor
F_0 = radiation flux density at center of beam
$\mathbf{F}$ = direct irradiation flux vector
h_{ig} = "heat of removal"
H = total irradiation
$\mathcal{H}$ = nondimensional total irradiation
$\mathcal{H}_r$ = irradiation component due to diffuse reflections
$\mathcal{H}_0$ = direct irradiation component
k = thermal conductivity
$\hat{\mathbf{n}}$ = inward unit surface normal
N_e = evaporation-to-laser power parameter
N_k = conduction-to-laser power parameter
N_λ = beam divergence parameter
N_w = beam focusing parameter
P = laser power
R_0 = effective radius of laser beam at focal plane
$R(z)$ = radius of laser beam
s, S = groove depth
s_∞, S_∞ = fully developed groove shape
T_{ev} = evaporation temperature
T_∞ = ambient temperature
u = laser scanning speed
U = laser speed-to-diffusion parameter
$\dot{V}$ = material removal rate
x, y, z = Cartesian coordinates
$\alpha(x, y)$ = local effective absorptivity at laser wavelength
α_0 = reference absorptivity
Γ = ratio of $R(z)$ and R_0
δ = conduction penetration depth
θ = nondimensional temperature
θ_0 = nondimensional surface temperature
ξ, η, ζ = nondimensional x, y, z coordinates
ρ = density of the medium, or reflectivity

Subscripts
ev = evaporation temperature

Superscripts
d = diffuse

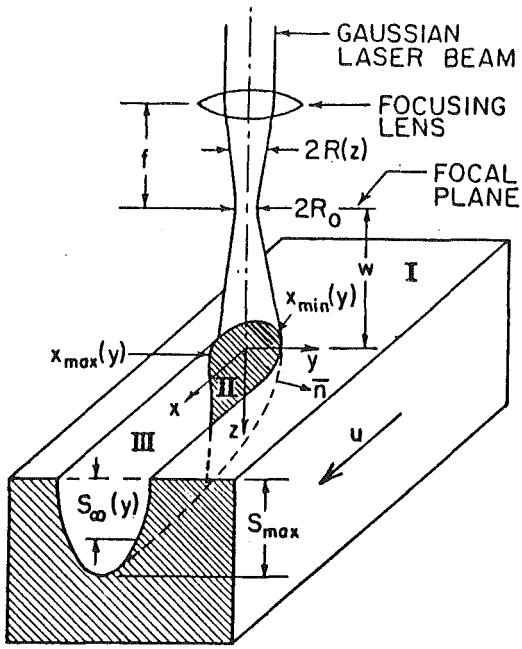

Fig. 1 Cross-sectional view of laser evaporation setup and regime

where the following nondimensional variables have been introduced (Modest and Abakians, 1986b; Biyikli and Modest, 1988)

$$\xi = x/R_0, \quad \eta = y/R_0, \quad \zeta = z/R_0 \tag{6a}$$

$$S = \frac{s(x, y)}{R_0}, \quad \theta = \frac{T - T_\infty}{T_{ev} - T_\infty}, \quad \mathfrak{H} = \frac{H(x, y)}{F_0} \tag{6b}$$

$$N_e = \frac{\rho u h_{ig}}{\alpha_0 F_0}, \quad N_k = \frac{k(T_{ev} - T_\infty)}{\alpha_0 F_0 R_0}, \quad U = \frac{uR_0}{D} \tag{6c}$$

$$N_\lambda = \frac{\lambda}{\pi R_0}, \quad N_w = \frac{w}{R_0} \tag{6d}$$

Here ρ is the density of the medium, c its specific heat, k its thermal conductivity, $D = k/(\rho c)$ is the thermal diffusivity, h_{ig} its heat of removal (i.e., the energy required to remove an amount of solid, either by melting followed by evaporation, by sublimation, by partial evaporation combined with microexplosive removal of particulates, or some other mechanism), $s(x, y)$ is the local groove depth, α_0 is its reference absorptivity (taken to be the maximum value of 1), and $\alpha(x, y) = 1 - \rho^d(x, y)$ is the local absorptivity and is assumed to be constant for the present study. Physically, N_e gives the ratio of power required to evaporate material normal to the irradiation, and absorbed laser flux. N_k approximates the ratio of conduction losses, again for a surface normal to irradiation, and absorbed laser flux. U relates the laser scanning speed to that of thermal diffusion (D) into the medium. N_λ represents the degree of beam divergence and N_w is a nondimensional lens focal position measured from the material surface. Equation (5a) states that the absorbed total laser irradiation is partially converted into conduction losses and partially used for evaporating material. A nondimensional material removal rate may be defined as

$$\frac{\dot{V}}{\dot{V}_{wc}} = \alpha_0[N_e + N_k U]\frac{2}{\pi}\int_0^\infty S_\infty d\eta \tag{7}$$

where

$$\dot{V}_{wc} = \frac{P}{\rho[c(T_{ev} - T_\infty) + h_{ig}]} \tag{8}$$

is the dimensional material removal rate for the case of no conduction losses and maximum absorptivity ($\alpha = 1$), and P ($= \pi R_0^2 F_0$) is the total laser power.

The total irradiation at a point on the groove surface may be determined from

$$\mathfrak{H}(\xi, \eta) = \mathfrak{H}_0(\xi, \eta) + \int_{\text{groove}} \rho^d(\xi', \eta')\mathfrak{H}(\xi', \eta')dF_{dA-dA'} \tag{9}$$

where the first term on the right-hand side is the dimensionless direct irradiation ($= \mathbf{F}\cdot\hat{\mathbf{n}}/F_0$), and the integral term is the contribution of diffuse reflections from the groove and $F_{dA-dA'}$ is a standard view factor as described, e.g., by Siegel and Howell (1981). Equation (3) with its boundary conditions (4), (5a), and (9) forms a complete set for the solution of the temperature field θ. The additional boundary condition (5b) over the evaporation region is required for the determination of the groove depth S. To solve the above set of equations, the following additional assumptions are made:

8 The temperature drop will be strongest normal to the surface, so that the diffusion term may be replaced by one-dimensional conduction into the normal direction, i.e., $\nabla^2\theta \simeq \partial^2\theta/\partial n^2$, where n is distance along the unit surface normal $\hat{\mathbf{n}}$.

9 The conduction equation can be solved by an integral method for which the temperature profile normal to the surface may be approximated by a quadratic polynomial, i.e., $\theta \simeq \theta_o(1 - n/\delta)^2$, where θ_o is the nondimensional surface temperature and δ is the conduction penetration depth.

The resulting simplified set of equations is similar to the one used by Modest and Abakians (1986b) as well as by Biyikli and Modest (1988), except that the present irradiation model is considerably more complex. The conduction simplification is made for computational efficiency, since it is the effects of beam guiding that are of interest here. Three-dimensional conduction effects have been modeled by Roy and Modest (1990). They showed that the one-dimensional model gives excellent results as long as the laser scanning speed is not too low ($U > 10$); only for $\xi > 0$ near the centerline is the one-dimensional model appreciably in error (since $\partial S/\partial\eta$ at $\eta = 0$ cannot be enforced). It was felt that the accuracy of the one-dimensional model was adequate for the present purpose, i.e., to evaluate the effects of multiple reflections in a laser-formed groove.

Solution Approach

The nature of beam guiding has a strong influence on the shape of the hole or groove formed by the laser; this shape, in turn, has a strong influence on beam guiding. Therefore, the radiation problem must be solved iteratively together with the quasi-one-dimensional conduction problem. In order to predict the total irradiation at each node, the entire groove shape, or groove depth $S(\xi, \eta)$, needs to be known. The solution for the case with correct absorptivity but without reflections is used as initial guess. Based on this groove the total irradiance is calculated, and an updated groove shape is determined, etc., until convergence is achieved.

In order to determine irradiation due to multiple reflections inside the groove, the surface is subdivided into triangular and rectangular linear elements, as depicted in Fig. 2, where interior positions are expressed through linear interpolation of nodal values. The local irradiation terms are then calculated using standard view factor theory (Siegel and Howell, 1981). Both contour integration and numerical quadrature of triangular elements are used to evaluate the view factors. For narrow, deep grooves only a small number of view factors will be significant. Re-emission from the surface has already been shown to be negligible by Modest and Abakians (1986b). Assuming uniform properties across each subsurface, equation (9) may be rewritten as

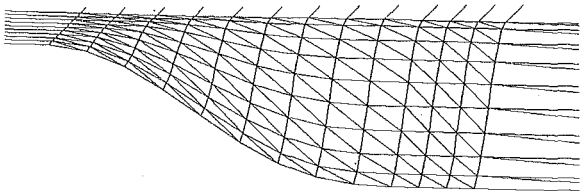

Fig. 2 Grid system for groove

$$\mathcal{H}_i = \mathcal{H}_{0i} + \sum_{j=1}^{m} \rho_j^d F_{i-j} \mathcal{H}_j \quad \text{for } i = 1, 2, \ldots, m \qquad (10a)$$

$$\mathcal{H}_{ri} = \mathcal{H}_i - \mathcal{H}_{0i} \qquad (10b)$$

where $\mathcal{H}_i$ is the total irradiation for subsurface i, and F_{i-j} is the view factor between subsurfaces i and j and is a function of geometry only. The unknown $\mathcal{H}_i$ are determined by solving the set of simultaneous equations using a standard equation solver. The diffuse reflection term is then calculated from equation (10b).

The diffuse reflection term calculated above is incorporated into the differential equations governing the groove shape, using bilinear interpolation within each linear element. The calculation of the configuration factors is the most CPU time-consuming part and, therefore, a somewhat coarse grid system has to be used sometimes for those calculations, while a finer grid system is used for the differential equation for the calculation of the groove shape. The bilinear variation insures first-order continuity at the element boundaries. In order to perform the interpolation, diffuse reflection energy values must be transferred from the elements themselves to each vertex of the elements. This is achieved by weighted averaging of surrounding subsurfaces similar to the method used by Cohen and Greenberg (1985). A typical number of surface elements is about 800 ~ 900. The final result is within 0.5 percent of the results obtained with 1200 elements (which was the maximum possible for the present computer).

The solution steps for the simplified conduction equations are similar to the ones used by Biyikli and Modest (1988). While only the solution to Regime II (ablation zone) is of interest, Regime I (preheat zone) must first be solved in order to provide the boundary between the two regimes, $\xi_{\min}(\eta)$, and a beginning value for the conduction penetration depth $\delta(\xi_{\min})$. Although only purely diffuse reflection is considered here, the absorptivity and reflectivity for the diffuse irradiation could be allowed to vary with direction of incidence to account for the effects such as the polarization of the laser beam on the groove formation. For Regime I, since the surface is flat and the beam divergence is assumed small, the direct irradiation angle is nearly normal. Therefore, $\alpha/\alpha_0 \simeq$ const over this regime, and the solution for Regime I is exactly the same as given by Biyikli and Modest (1988)

$$\theta_o^2 = \frac{3\sqrt{\pi}}{4UN_k^2\Gamma^3} \left(\frac{\alpha}{\alpha_o}\right)^2 e^{-(\xi^2+2\eta^2)/\Gamma^2} [1 + \operatorname{erf}(\xi/\Gamma)] \qquad (11)$$

Solving for η as a function of ξ in equation (11) for $\theta_o = 1$ establishes the boundary between Regimes I and II.

The groove depth $S(\xi, \eta)$ is found from the equations for Regime II using the Regime I solution as boundary conditions. The governing equation for the integral method is of first order and, thus, hyperbolic in nature (Modest and Abakians, 1986b). It is readily found that $\eta = 0$ is a characteristic line, and that $\partial S/\partial\eta$ may be discontinuous across that line. Here groove depth, S, and penetration depth, δ, at a node (ξ, η) were evaluated with a simple explicit-implicit method, where it is assumed that S and δ are known for all nodes with $\xi < \xi_i$ and $\eta > \eta_j$. Therefore, the solution for a given ξ_i is started at the outer boundary at $\eta = \eta_{\max}(\xi_i)$ (where $S = 0$ and δ has the value determined from the Regime I calculations), marching inward toward $\eta = 0$. More details on the conduction solution can be found in the papers by Modest and Abakians (1986b) and Biyikli and Modest (1988).

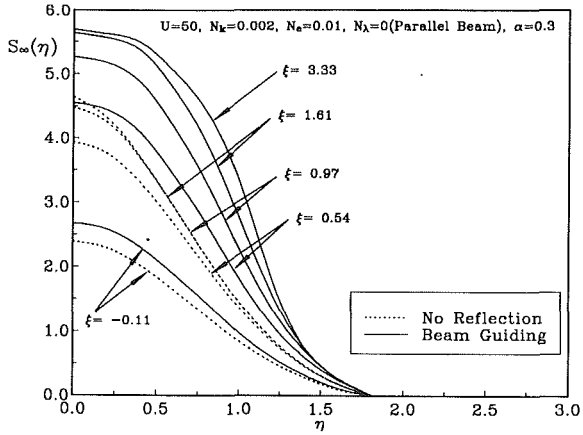

Fig. 3 Groove cross section at different ξ locations in the evaporating region

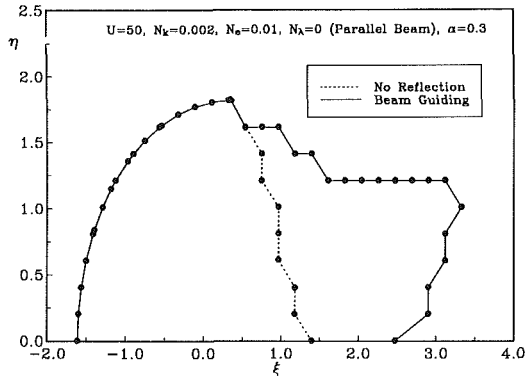

Fig. 4 Top view of evaporating region

A first approximation of S (i.e., the groove shape) is obtained by neglecting multiple reflections while using the given absorptivity. Using this groove shape, the local irradiation due to diffuse reflections is calculated and added to the boundary condition of the quasi-one-dimensional conduction equation to update the groove shape. The governing equations and boundary conditions are extremely nonlinear and very sensitive to the added reflected energy. This is especially true for deep grooves with high reflectivity. To overcome this difficulty, a pseudo-reflectivity $\rho^*(\leq\rho)$ is introduced in equation (10a) as follows:

$$\mathcal{H}_{ri} = \sum_{j=1}^{m} F_{i-j} (\rho_j^d \mathcal{H}_{rj} + \rho_j^* \mathcal{H}_{0j}) \quad \text{for} \quad i = 1, 2, \ldots, m \qquad (12)$$

After reaching intermediate converged results (corresponding physically to a case of weaker irradiation), ρ^* is increased and the above step is repeated until final convergence is obtained with $\rho_j^* = \rho_j^d$.

Discussion of Results

Figure 3 shows how a typical groove develops along the ξ-direction for the case of $U = 50$, $N_k = 0.002$, $N_e = 0.01$. For this set of parameters the groove undergoes evaporation over more than 90 percent of its width until $\xi = 0.54$, if multiple reflections are neglected. If beam guiding is accounted for, this region extends to $\xi = 1.1$–1.2. At $\xi = 1.61$ evaporation still takes place for $\eta < 1.41$, while without reflections the final groove shape has been reached. Figure 4 shows a top

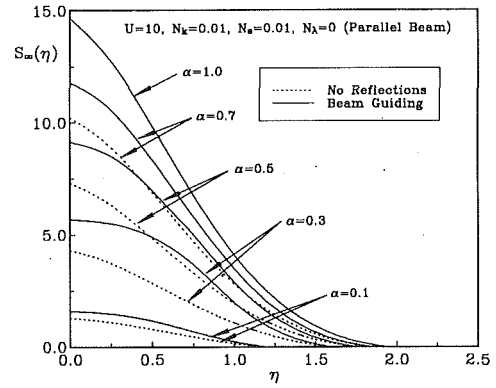

Fig. 5 Effects of absorptivity on groove depth

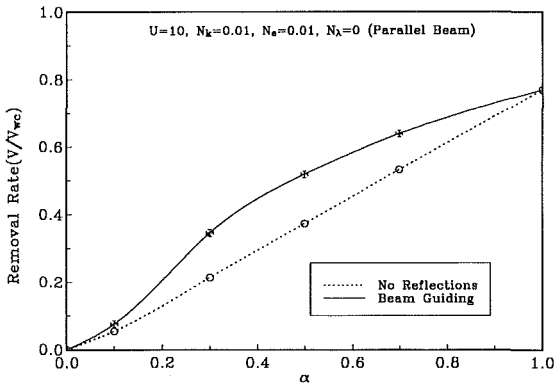

Fig. 6 Effects of absorptivity on removal rate

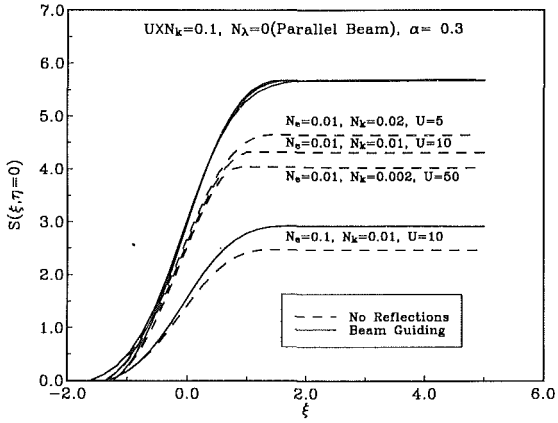

Fig. 7 Effects of N_e and N_k on groove development along centerline

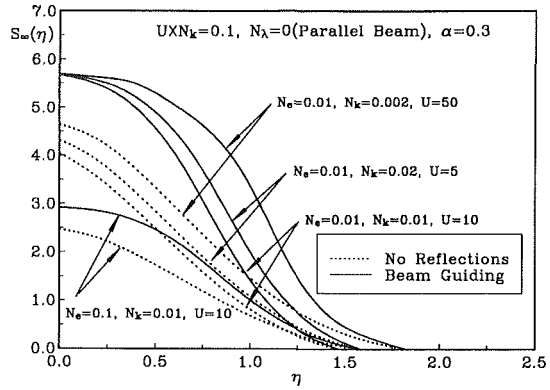

Fig. 8 Influence of N_e and N_k on groove depth

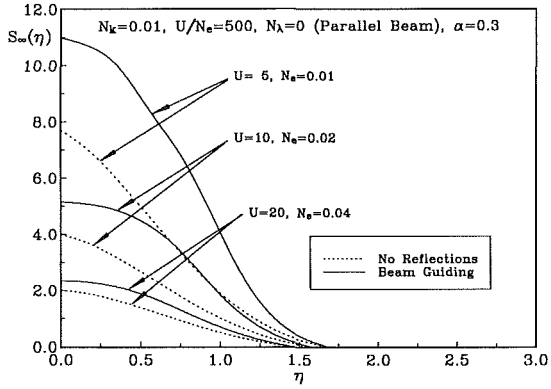

Fig. 9 Influence of scanning velocity on groove depth

view of the evaporating zone under a laser beam striking the surface of the material. Exact boundary points have been calculated using equation (11) for the onset of evaporation. For a given η-coordinate evaporation will occur until such ξ-location where the surface temperature drops below the evaporation temperature, $\theta_0 < 1$. Since this location tends to fall between nodes, only the maximum ξ-location (for each η) is indicated in Fig. 4, for which $\theta_0 = 1$. This results in a somewhat un-smooth evaporation tail picture because of the relatively crude nodal system employed (to limit the large CPU requirements for the calculation of view factors). This graph demonstrates how reflections, particularly from the steep walls near the centerline just ahead of the laser ($\xi < 0$, $|\eta|$ small), cause strong irradiation downstream, extending the evaporation zone. Note that, for this case, the farthest downstream evaporation point no longer falls on top of the centerline, since the peaks of reflected radiation (due to reflection from $\xi \simeq 0$, $|\eta| > 0$) are not near the centerline. For all cases beam guiding extends the evaporation zone downstream compared to the no-beam-guiding model. Thus, multiple reflections tend to carve out the bottom of the grooves, resulting in steeper grooves, which stay more equally wide over much of their depth.

The influence of the absorptivity α on the importance of multiple reflections is shown in Fig. 5. Here $U = 10$, $N_k = 0.01$, and $N_e = 0.01$ have been selected as representative values. Without reflections, large values of α result in deeper grooves with large nonzero slopes at the centerline, while small values of α form shallow grooves with flatter center zones. By considering multiple reflections, the present model shows a significant increase in groove depth and the formation of different groove shapes. If α is very small, the groove formed by direct irradiation becomes so shallow that most reflected energy leaves the cavity, reducing the effects of beam guiding. For intermediate values of α, the reflections from the wall produce a wider flat center region and steeper groove walls. As α becomes large, the effect of reflections is reduced, and the groove shapes become identical for $\alpha = 1$. This tendency is clearly seen in Fig. 6, which shows removal rate as function of absorptivity.

Figure 7 shows the development of centerline groove depth for different scanning speeds, but keeping energy deposition per unit area ($U \times N_k$) constant. It is observed that the beam-guiding model and previous model predictions are close for negative ξ-locations. For positive values of ξ the models diverge since the old model neglects the large amount of energy reflected from the groove walls into the downstream direction. Interestingly, the current model gives nearly the same maximum groove depth at the centerline for all scanning velocities as long as the energy deposition rate remains constant. There appears to be no logical explanation for this and, therefore, this statement cannot be generalized. However, the groove cross sections are different, as seen from Fig. 8: Increasing U decreases conduction losses and the removed material volume increases, resulting in grooves that are wider and flatter at the

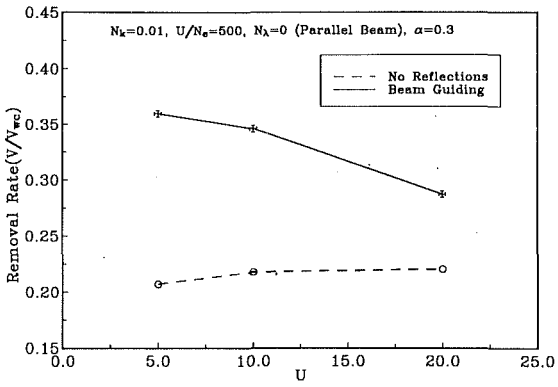

Fig. 10 Effects of scanning velocity on removal rate

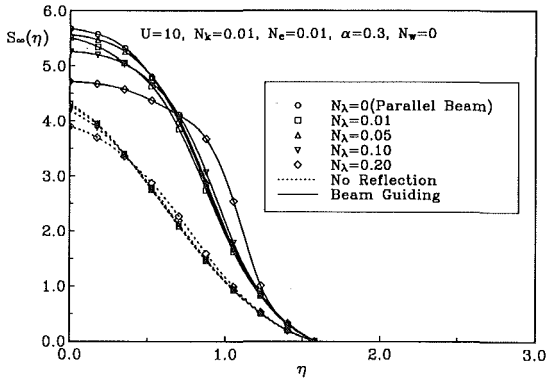

Fig. 11 Effects of N_λ on the groove, for beam focused on the surface

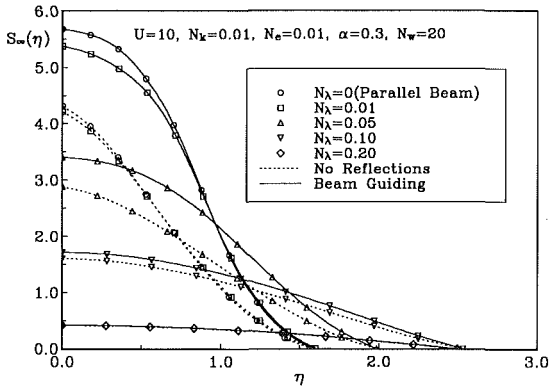

Fig. 12 Effects of N_λ on the groove, for beam focused above the surface

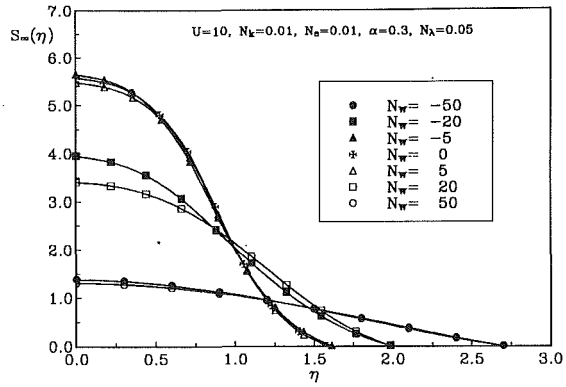

Fig. 13 Effects of lens distance in focusing beam

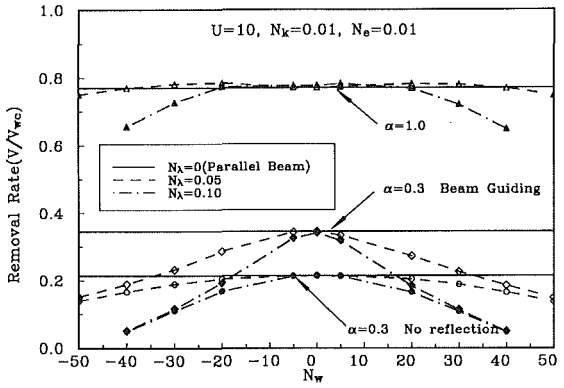

Fig. 14 Influence of N_λ and N_w on material removal rate

bottom. The previous model without reflections, on the other hand, predicts different groove depths with similar cross sections.

Figure 9 shows the effects of u, the laser scanning speed, on the fully developed groove shape S_∞. Here $\alpha = 0.3$, $N_k = 0.01$, and $U/N_e = 500$ have been selected. As the velocity is reduced, the irradiation produces deeper grooves resulting in an increased beam-guiding effect, while increased velocities give shallow grooves with reduced beam-guiding effects. The material removal rate increases as u increases if multiple reflections are neglected as depicted in Fig. 10. In contrast, the beam guiding model shows a decrease of material removal rate as u increases. This is apparently due to the fact that, for larger scanning velocities with the resulting shallow grooves, the effective absorptivity (total beam trapping) decreases faster than the diminishing conduction losses.

For the case of focusing beams, the nondimensional beam divergence number, N_λ, shows the rate of beam expansion, and N_w indicates the position of the beam waist relative to the solid surface. N_w is negative if the focal point of the lens is below the surface of the material. The effect of the beam expansion rate on the size and shape of fully developed grooves is depicted in Figs. 11 and 12 for different beam divergence numbers, N_λ. With increasing beam divergence the groove depth decreases, since the beam expands beyond the focal point, resulting in less concentrated laser energy at the groove surface. As N_λ becomes larger, the groove becomes shallower with a flatter center region if beam guiding is considered. For $N_\lambda = 0.2$, a significantly different groove profile with flat center region and steeper groove walls is obtained. On the other hand, only a slightly changed profile is obtained if multiple reflections are neglected. This implies that significantly different groove shapes may be obtained for the same material and operating conditions just by using a different focal-length lens. The decrease in depth is rather minor (Fig. 11) if the beam is well focused, but can be very substantial if the beam is poorly focused (Fig. 12).

The influence of beam waist position on fully developed groove shape and depth is shown in Fig. 13 for different focal points. It is observed that the depth of the groove increases and passes through a maximum when the beam is focused slightly inside the material. This type of behavior has been observed by Bar-Isaac and Korn (1974) for laser drilling and by Biyikli and Modest (1988). The increase in groove depth by focusing the beam slightly inside the material is apparently due to better average focusing of the laser energy, hence utilizing the energy more efficiently for evaporation rather than conduction. The groove gets shallower and wider when the focal point is moved further away from the surface of the material. To avoid crowding of the figure no results without beam guiding are shown. The behavior, however, is similar to that in Fig. 12.

The influence of N_λ and N_w on the material removal rate is shown in Fig. 14. In the vicinity of $N_w = 0$, the material

removal rate is relatively flat while it drops off rapidly for laser beams with their focal points far above or below the surface. The curves with $\alpha = 1$ showing maximum removal rate for a few focal positions above and below the surface correspond to the results of Biyikli and Modest (1988). The beam guiding model shows a much stronger dependence on focal position, especially in the vicinity of $N_w = 0$. This implies that as N_w gets smaller, the groove becomes deeper, resulting in increased beam guiding effects.

Summary

Multiple reflections and beam guiding effects on evaporative cutting with a CW laser have been studied by combining irradiation calculations, using view factor theory, with a quasi-one-dimensional conduction model. It is observed that beam guiding plays an important role in forming the fully developed groove, resulting in an increased effective absorptivity.

Due to beam channeling from the upstream wall as well as the side walls, the evaporation zone extends farther downstream and the fully developed groove cross sections have steeper groove walls with a flatter center region as compared to that predicted by the previous model without reflection effects. For materials with relatively large reflectivity, the material removal rate is increased significantly, resulting in an increased effective absorptivity. Generally, the beam guiding effects become significant for high-reflectivity materials and/or deep groove cases. For the cases of present study, the removal rate is increased by 20 percent for low-reflectivity materials and by up to 70 percent for high-reflectivity materials.

The groove depth can be increased by using lenses with larger focal lengths focused slightly inside the material. Larger focal length lenses have larger minimum beam radii at the focal plane, but with a lower beam divergence focused near the surface. On the other hand, flatter grooves with steeper walls can be obtained by using lenses with shorter focal lengths.

Acknowledgments

Support for this work by National Science Foundation Grant No. CBT-8711255 is gratefully acknowledged.

References

Abakians, H., and Modest, M. F., 1988, "Evaporative Cutting of a Semi-transparent Body With a Moving CW Laser," ASME JOURNAL OF HEAT TRANSFER, Vol. 110, pp. 924–930.

Anthony, T. R., 1980, "The Random Walk of a Drilling Laser Beam," *Journal of Applied Physics*, Vol. 51, pp. 1170–1175.

Bailey, A. W., and Modak, A., 1989, "Numerical Simulation of Laser Ablation With Cavity Reflections," *Journal of Thermophysics and Heat Transfer*, Vol. 3, No. 1, pp. 42–45.

Bar-Isaac, C., and Korn, U., 1974, "Moving Heat Source Dynamics in Laser Drilling Processes," *Journal of Applied Physics*, Vol. 3, pp. 45–54.

Biyikli, S., and Modest, M. F., 1988, "Beam Expansion and Focusing Effects on Evaporative Laser Cutting," ASME JOURNAL OF HEAT TRANSFER, Vol. 110, pp. 529–532.

Brugger, K., 1972, "Exact Solutions for the Temperature Rise in a Laser Heated Slab," *Journal of Applied Physics*, Vol. 43, pp. 577–583.

Carslaw, H. S., and Jaeger, J. C., 1959, *Conduction of Heat in Solids*, 2nd ed., Oxford University Press, United Kingdom.

Chande, T., and Mazumder, J., 1984, "Estimating Effects of Processing Conditions and Variable Properties Upon Pool Shape, Cooling Rates, and Absorption Coefficient in Laser Welding," *Journal of Applied Physics*, Vol. 56, pp. 1981–1986.

Cohen, M. F., and Greenberg, D. P., 1985, "The Hemi-Cube: A Radiosity Solution for Complex Environments," *Siggraph 85*, Vol. 19, No. 3, pp. 31–40.

Dabby, F. W., and Paek, U.-C., 1972, "High-Intensity Laser-Induced Vaporization and Explosion of Solid Material," *IEEE Journal of Quantum Electronics*, Vol. QE-8, pp. 106–111.

Kogelnik, H., and Li, T., 1956, "Laser Beams and Resonators," *Applied Optics*, Vol. 5, No. 10, pp. 1550–1565.

Landau, H. G., 1950, "Heat Conduction in a Melting Solid," *Quarterly of Applied Mathematics*, Vol. 8, pp. 81–94.

Maydan, D., 1970, "Fast Modulator for Extraction of Internal Laser Power," *Journal of Applied Physics*, Vol. 41, pp. 1552–1559.

Maydan, D., 1971, "Micromachining and Image Recording on Thin Films by Laser Beams," *Bell System Technical Journal*, Vol. 50, pp. 1761–1789.

Mazumder, J., 1987, "An Overview of Transport Phenomena in Laser Materials Processing," in: *International Conference on Laser Advanced Materials Processing—Science and Applications*, pp. 613–624, High Temperature Society of Japan, Japan Laser Processing Society, Osaka, Japan.

Mazumder, J., and Steen, W. M., 1980, "Heat Transfer Model for CW Laser Material Processing," *Journal of Applied Physics*, Vol. 51, pp. 941–947.

Minamida, K., Takafuji, H., Hamada, N., Haga, H., and Mizuhashi, N., 1986, "Wedge Shape Welding With Multiple Reflection Effects of High Power CO_2 Laser Beam," in: *5th International Congress on Applications of Lasers and Electro-optics*, pp. 97–104.

Modest, M. F., and Abakians, H., 1986a, "Heat Conduction in a Moving Semi-infinite Solid Subjected to Pulsed Laser Irradiation," ASME JOURNAL OF HEAT TRANSFER, Vol. 108, pp. 597–601.

Modest, M. F., and Abakians, H., 1986b, "Evaporative Cutting of a Semi-infinite Body With a Moving CW Laser," ASME JOURNAL OF HEAT TRANSFER, Vol. 108, pp. 602–607.

Paek, U.-C., and Gagliano, F. P., 1972, "Thermal Analysis of Laser Drilling Processes," *IEEE Journal of Quantum Electronics*, Vol. QE-8, pp. 112–119.

Ramanathan, S., and Modest, M. F., 1990, "Effect of Variable Properties on Evaporative Cutting With a Moving CW Laser," ASME HTD-Vol. 135, pp. 101–108.

Ready, J. F., 1971, *Effects of High Power Laser Radiation*, Academic Press, New York.

Roy, S., and Modest, M. F., 1990, "Three-Dimensional Conduction Effects During Scribing With a CW Laser," *Journal of Thermophysics and Heat Transfer*, Vol. 4, No. 2, pp. 199–203.

Rykalin, N. N., Uglov, A. A., and Makarov, N. I., 1967, "Effects of Peak Frequency in a Laser Pulse on the Heating of Metal Sheets," *Soviet Physics—Doklady*, Vol. 12, pp. 644–646.

Siegel, R., and Howell, J. R., 1981, *Thermal Radiation Heat Transfer*, 2nd ed., McGraw-Hill, New York.

Soodak, H., 1943, "Effects of Heat Transfer Between Gases and Solids," Ph.D. thesis, Duke University, Durham, NC.

von Allmen, M., 1976, "Laser Drilling Velocity in Metals," *Journal of Applied Physics*, Vol. 47, pp. 5460–5463.

Wallace, R. J., 1983, "A Study of the Shaping of Hot Pressed Silicon Nitride With a High Power CO_2 Laser," Ph.D. thesis, University of Southern California, Los Angeles, CA.

Wallace, R. J., and Copley, S. M., 1986, "Laser Machining of Silicon Nitride: Energetics," *Advanced Ceramic Materials*, Vol. 1, No. 3, pp. 277–283.

White, R. M., 1963a, "Elastic Wave Generation by Electron Bombardment or Electromagnetic Wave Absorption," *Journal of Applied Physics*, Vol. 34, pp. 2123–2124.

White, R. M., 1963b, "Generation of Elastic Waves by Transient Surface Heating," *Journal of Applied Physics*, Vol. 34, pp. 3559–3567.

S. Bhattacharjee
Department of Mechanical Engineering,
San Diego State University,
San Diego, CA 92182-0191

R. A. Altenkirch
Department of Mechanical and Nuclear Engineering,
Mississippi State University,
Mississippi State, MS 39762

S. L. Olson

R. G. Sotos

NASA-Lewis Research Center,
Cleveland, OH 44135

Heat Transfer to a Thin Solid Combustible in Flame Spreading at Microgravity

The heat transfer rate to a thin solid combustible from an attached diffusion flame, spreading across the surface of the combustible in a quiescent, microgravity environment, was determined from measurements made in the drop tower facility at NASA-Lewis Research Center. With first-order Arrhenius pyrolysis kinetics, the solid-phase mass and energy equations along with the measured spread rate and surface temperature profiles were used to calculate the net heat flux to the surface. Results of the measurements are compared to numerical solution of the complete set of coupled differential equations that describes the temperature, species, and velocity fields in the gas and solid phases. The theory and experiment agree on the major qualitative features of the heat transfer. Some fundamental differences are attributed to the neglect of radiation in the theoretical model. A scale analysis is developed that makes use of the experimental data at different ambient conditions to support the notion that radiation is important and to investigate the effect of pressure on the spread rate.

Introduction

With respect to fire safety in spacecraft, it is important to know the mechanisms of flame spread across a solid combustible in a low-gravity environment. In the absence of gravity, or buoyancy (Altenkirch et al., 1980), and any forced flow (Fernandez-Pello et al., 1981), the flow field is established by the fact that the flame is moving with respect to the solid and the pyrolysis process at the surface, which results in flow fields with velocities of the order of the spread rate. Heat transfer forward of the flame is responsible for allowing the flame to propagate, and, for a thin fuel, this heat transfer occurs via conduction in the gas or radiation. Most analyses for flames spreading into an opposing flow are for the situation where the flow velocities are large compared to the spread rate; radiation heat transfer in these analyses is neglected because the view factor from the flame to the unburned fuel is small, and, for most situations, the optical depth of the flame gases is also small (Sibulkin et al., 1981). Solid surface reradiation appears to be unimportant except for very slow flows (T'ien, 1986; Chen, 1986; Fakheri and Olson, 1989).

Although a substantial number of experimental studies on flame spread under normal gravity has been conducted, similar studies in a microgravity environment are substantially fewer in number. Such experiments, besides having implications for fire safety in space vehicles and future space stations, provide a means for uncovering some of the physics of the flame spread process at reduced gravity that may be masked in the gravitationally induced flows that exist in the normal gravity environment. To date, most quantitative flame spread studies conducted at reduced gravity have been carried out in drop tower facilities that generate a short period, a few seconds, of microgravity (see, e.g., Olson et al., 1989, and Andracchio and Cochran, 1976). Even though the experimental time available in drop towers does limit the conditions that can be studied, useful quantitative results can be obtained for selected combustibles and environments. Other means of developing low-gravity environments have heretofore not been available, e.g., the Space Shuttle (Bhattacharjee et al., 1990; Vento et al., 1989), or produce a gravitational field that might not be low enough or of sufficient quality to allow quantitative studies, e.g., aircraft flying Keplerian trajectories (Altenkirch, 1985).

Here we use surface temperature measurements for flame spread across ashless filter paper obtained in a drop tower at NASA-Lewis Research Center to obtain the net heat transfer rate from the gas-phase flame to the solid. The results are compared to the results of an analysis (Bhattacharjee et al., 1990) for flame spread at zero gravity that neglects all effects of radiation. Detailed presentation of the measured and computed spread rates from the analysis as a function of percent oxygen in the environment and pressure as well as a dimensionless presentation of spread rate versus Damkohler number (Altenkirch et al., 1980) for the computed spread rates appear elsewhere (Bhattacharjee et al., 1990). Differences between the results of the experiments and numerical solution are utilized to evaluate qualitatively the importance of radiation heat transfer in flame spreading at reduced gravity. A scale analysis is used to compare surface radiation with conduction heat transfer and to establish the relative importance of gas-phase radiation to solid-surface reradiation. The observed dependence of spread rate on ambient pressure is explained through phenomenological arguments stemming from the scale analysis.

Experimental

Diffusion flames spreading over thin solid fuels were studied in a quiescent, microgravity environment through the use of the 5.18 s Zero Gravity Facility at NASA-Lewis Research Center (Olson, 1987). Samples of vacuum-dried, ashless filter paper 10 cm long by 3 cm wide by 0.0826 mm half-thickness with an area density of 4.28×10^{-2} kg/m^2 were used.

Upon entering microgravity, the sample was ignited inside a cylindrical chamber filled with an O_2/N_2 mixture and whose volume is large enough to provide an unchanging ambient oxidizer environment during combustion. The ignitor was deactivated after 0.3 s to minimize the energy input to the system from the ignitor. A description of the apparatus and some of the procedures used is given by Olson (1987). A 16 mm cine camera was used to record the flame spread process. The films were later analyzed using a film motion analyzer

Contributed by the Heat Transfer Division for publication in the JOURNAL OF HEAT TRANSFER. Manuscript received by the Heat Transfer Division March 14, 1990; revision received January 12, 1991. Keywords: Combustion, Fire/Flames, Microgravity Heat Transfer.

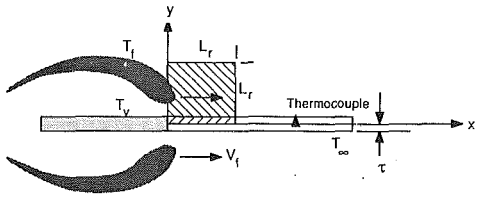

Fig. 1 Flame spread configuration

connected to a microcomputer to determine flame spread rate and flame dimensions. Estimated uncertainty in flame spread rate is ±6 percent except for the 30 percent O_2 test, where the uncertainty is ± 11 percent due to difficulty in measuring the position of the very dim blue flame.

Fine type-R, bare-wire thermocouples (0.013 cm in wire diameter) were positioned in the gas phase approximately 7 mm (± 1 mm) from the fuel surface and imbedded within the fuel surface to record the pyrolysis process as the flame passes. The location of the thermocouples with respect to the ignitor varied with percent oxygen and pressure to insure that the flame would reach the thermocouples during the 5 s of low-gravity test time. All were within 1.0 to 2.5 cm of the ignitor. The gas-phase flame shape did not have time to reach steady state during the short test time, so the gas-phase temperature measurements can only provide qualitative information.

Thermocouple data were referenced to room temperature. Potential outputs were recorded during the test at a frequency of approximately 15 Hz. No radiation or conduction corrections have been made to the temperature data; an estimate of the uncertainty associated with a radiation correction gives a worst-case uncertainty in the temperature measurements of approximately 20 K at the highest temperatures recorded.

Tests considered in detail here were conducted at 1.5 atm with oxygen molar percentages of 30, 50, 70, and 90 percent. An additional test conducted at 0.5 atm is used to investigate the effects of pressure on the flame spread process.

Experiment Analysis

Figure 1 shows a sketch of the flame as it approaches the imbedded thermocouple at speed V_f. The spread rate is determined from flame position versus time data, an example of which is shown in Fig. 2.

With respect to the flame, there is a steady flow of gas and solid fuel into the flame at a speed equal to the spread rate.

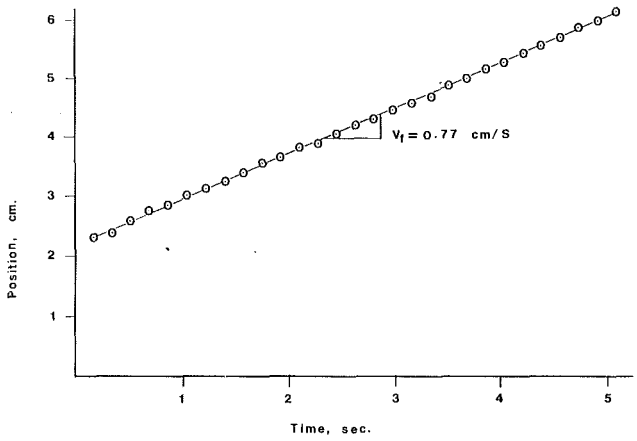

Fig. 2 Position (x) versus time (t) for 70 percent O_2 in N_2 at 1.5 atm

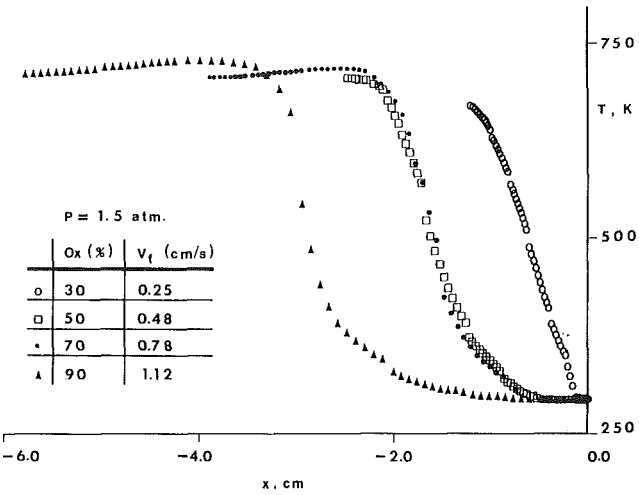

Fig. 3 Experimental surface temperature profiles with the origin equivalent to time zero, i.e., the instant the drop is initiated

The time-temperature data obtained from the thermocouple are converted to x-T data using the transformation $x = -V_f t$. An example of such data after application of the transformation is shown in Fig. 3. The origin in Fig. 3 is fixed at the

Nomenclature

A = surface area covered by the flame, m^2
a_p = Planck mean absorption coefficient, m^{-1}
A_s = pre-exponential factor for solid pyrolysis = $5 \times 10^{10} s^{-1}$ (Bhattacharjee et al., 1990)
C_1 = constant of order unity
C_p = specific heat of gas at constant pressure, kJ/kg·K (Bhattacharjee et al., 1990)
C_s = specific heat of solid fuel, kJ/kg·K, set equal to C_p
E_s = activation energy for pyrolysis = 139.6 kJ/mol (Bhattacharjee et al., 1990)
f = fraction of gas-phase emission that hits fuel surface
$I_1(x)$ = integrated quantity from x to infinity, Eq. (2)
$I_2(x)$ = integrated quantity from x to infinity, Eq. (4)
L_r = reference thermal length = α_r/V_f, m
$L_{r,e}$ = reference thermal length based on the experimental spread rate = $\alpha_r/V_{f,e}$, m
$L_{r,t}$ = reference thermal length based on the theoretical spread rate = $\alpha_r/V_{f,t}$, m
L_v = heat of evaporation for fuel at 298 K = 368.5 kJ/kg (Bhattacharjee et al., 1990)
$\dot{m}''$ = mass flux, $kg/m^2 \cdot s$
$Q(x)$ = cumulative heat transfer, per unit width, from x to infinity, W/m
q = heat flux, W/m^2
Q_c = conductive heat transfer, per unit width, from gas to solid, W/m
Q_g = radiative gas emission, per unit width, W/m
Q_l = heat loss from the flame and fuel surface, per unit width, due to gas and solid radiation, W/m
Q_{net} = net heat transfer to the surface, per unit width, W/m
Q_r = heat lost by radiation from the surface, per unit width, W/m
Q_s = surface emission loss, per unit width, W/m
R = radiation/conduction parameter, Eq. (11)

location of the thermocouple, and the location of the sharp temperature rise signifies the flame position. The changes in flame position for different environments are due to the fact that the flame spreads at different rates, and the thermocouples were placed at appropriate distances from the ignition source (1.0, 1.5, 1.5, and 2.5 cm for 30, 50, 70, and 90 percent O_2, respectively) to capture the maximum amount of information.

For a thermally thin fuel there is no variation of any property across the fuel thickness. This situation occurs when the half-thickness of the fuel, τ, is much less than the characteristic length for conduction in the solid, which, for gas-phase conduction dominant over solid-phase conduction, is $\{\alpha_r/V_f\}\{\lambda_s(T_v-T_\infty)\}\ /\ \{\lambda_g(T_f-T_v)\}$. Because $\lambda_s(T_v-T_\infty)/\lambda_g(T_f-T_v)$ is usually small for cellulosic fuels, $\tau << \alpha_r/V_f$ is a sufficient criterion to establish that the fuel is thin (Chen and T'ien, 1986; Altenkirch and Bhattacharjee, 1990). A first-order Arrhenius decomposition law for pyrolysis then yields the following ordinary differential equation for mass conservation in the solid:

$$\dot{m}'' = \frac{d}{dx}(\rho_s \tau V_f) = A_s \rho_s \tau e^{-E_s/RT_s} \tag{1}$$

Here ρ_s and T_s are the density and temperature, respectively, at any location x along the solid. Becasue pyrolysis occurs throughout the thickness, it is reasonable to assume that the thickness remains constant while ρ_s decreases due to depletion of volatiles. This assumption has been used before (Chen, 1986; Bhattacharjee et al., 1990), and with it Eq. (1) can be integrated to yield an expression for ρ_s.

$$\rho_s/\rho_{s,\infty} = e^{I_1(x)}, \text{ where } I_1(x) = -\int_x^\infty \frac{A_s}{V_f} e^{-E_s/RT_s} dx \tag{2}$$

The integral $I_1(x)$ is numerically evaluated after curve fitting the integrand with cubic splines.

The energy equation for the solid expresses a balance between the net heat flux to an element in the solid, the rise in its enthalpy, and the energy needed to vaporize the solid as dictated by Eq. (1).

$$q = -\frac{d}{dx}(\rho_s \tau V_f C_s T_s) + \dot{m}''(L_v + C_p(T_s - T_\infty) + C_s T_\infty) \tag{3}$$

Although $q(x)$ can be evaluated from Eq. (3), it is best to avoid direct numerical differentiation of experimental data by first evaluating the cumulative heat transfer up to a location x by integrating Eq. (3).

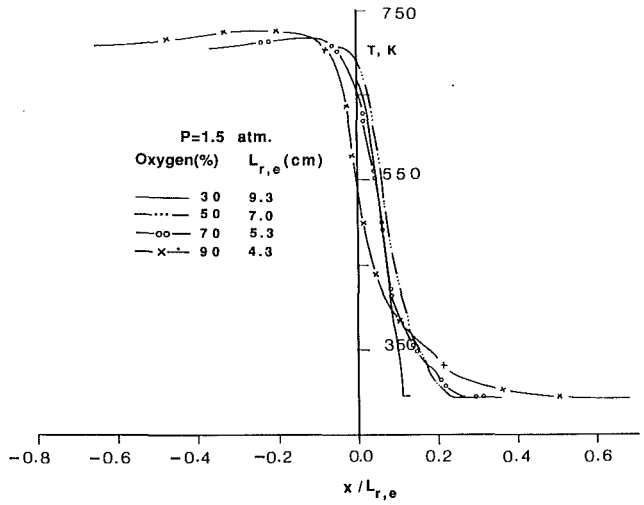

Fig. 4 Experimental surface temperature profiles with the origin situated at the peak of the heat flux profile

$$Q(x) = -\int_x^\infty q dx = V_f C_s(\tau \rho_s T_s|_{X=\infty} - \tau \rho_s T_s) + I_2(x) \tag{4}$$

where the integral $I_2(x) = \int_x^\infty \dot{m}''(L_v + C_p(T_s - T_\infty) + C_s T_\infty)\, dx$ is evaluated in a similar manner as $I_1(x)$. The resulting heat transfer $Q(x)$ may contain behavior that should be removed by smoothing before differentiating to yield the heat flux $q(x)$. While a low degree of smoothing cannot eliminate physically unrealistic behavior, a high degree of smoothing reduces the peak heat flux. The optimum degree of smoothing was obtained by trial and error for each individual case. After evaluation of the heat flux, a new origin is selected as the location of the peak flux.

Results

Whenever possible, the experimental results are compared to results of the theoretical model that has been formulated and solved numerically (Bhattacharjee et al., 1990). In the model, conservation equations for mass, momentum, species, and energy in the gas phase and mass and energy in the solid phase are solved numerically to yield the spread rate and the flame structure. First-order, solid-phase pyrolysis and second-

Nomenclature (cont.)

R = universal gas constant, 8.314 J/mol·K
S = inverse Stark number, Eq. (12)
t = time, s
T = temperature, K
T_{en} = equivalent environment temperature for gas-phase radiation, K
T_f = flame temperature, K
T_r = reference temperature, K
T_s = solid temperature, K
T_v = vaporization temperature, K
T_∞ = initial fuel temperature, 298 K
V_f = spread rate m/s
$V_{f,e}$ = experimental spread rate, m/s
$V_{f,t}$ = theoretical spread rate, m/s
W = fuel width, m
x = coordinate along the solid surface, m
α = absorptance of the fuel surface = ϵ
α_r = reference thermal diffusivity of the gas = $\lambda_g/\rho_g C_p$, m^2/s
ϵ = surface emittance, value used is unity
κ = optical depth
λ_g = thermal conductivity of the gas, W/m·K
λ_s = thermal conductivity of the solid, W/m·K
ρ_g = gas density, kg/m^3
ρ_s = solid density, kg/m^3
$\rho_{s,\infty}$ = initial solid density, kg/m^3
$\rho_{s,\infty}\tau$ = 4.282×10^{-2} kg/m^2
σ = Stefan-Boltzmann constant = 5.67×10^{-8} $W/m^2 \cdot K^4$
τ = invariant half-thickness of the fuel sheet, m

Subscripts

e = experimental value
f = fuel
g = gas
p = preheat
r = reference or radiation
s = solid
t = theoretical value
∞ = ambient condition

Superscript

= in the units of T_∞

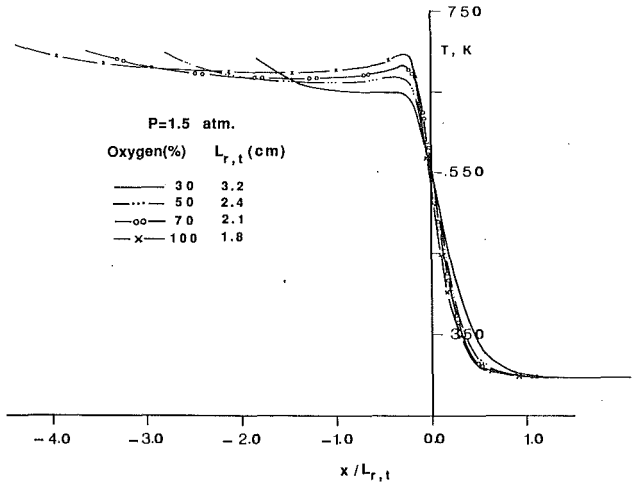

Fig. 5 Theoretical surface temperature profiles from Bhattacharjee et al. (1990) with the origin situated at the peak of the heat flux profile

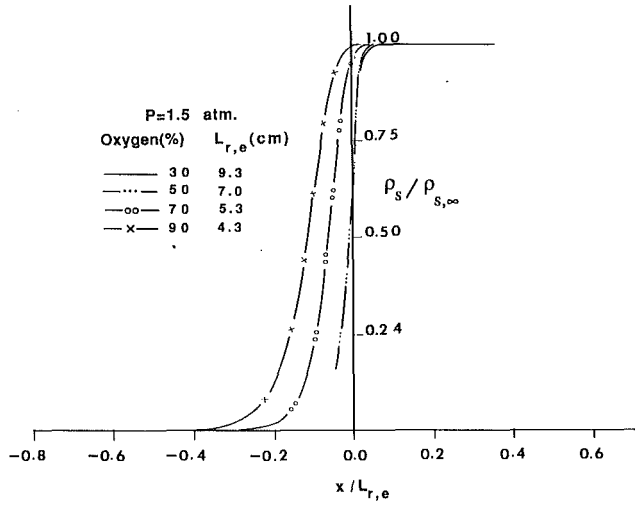

Fig. 6 Experimental fuel density profiles consistent with Fig. 4

order, gas-phase kinetics are used. Missing in the theory are gas and solid surface radiation effects. For consistency, the properties used here are the same as those used by Bhattacharjee et al. (1990).

Steady spread rates were calculated from the x–t diagrams. A steady spread rate is obtained in a short period of time after ignition, as can be seen from the linear x–t relation in Fig. 2. In the absence of any induced motion, the velocity scale is defined by the spread rate V_f. For a thermally thin fuel (Altenkirch et al., 1980), the length scale of importance is established by the gas phase, and if radiation is neglected, a balance between conduction and convection generates the thermal length scale $L_r = \alpha_r/V_f$, where α_r is the thermal diffusivity of the gas at a reference temperature T_r, which may conveniently be taken as an average of the ambient temperature and the adiabatic, stoichiometric, flame temperature for complete combustion. The spread rate increases with increasing oxygen content, and so the length scale is smaller for the higher ambient oxygen concentrations. The time scale, $L_r/V_f = \alpha_r/V_f^2$, is, therefore, much larger for the slower moving flames. Because the available microgravity time is the same for all cases studied, the extent of information collected is greater for the cases with the higher oxygen level. This is evident in Fig. 3 where the experiment for 90 percent oxygen is seen to cover the greatest span on the x axis.

The temperature profiles of Fig. 3 are replotted in Fig. 4 after aligning the flame tip locations to a common origin. This location for each flame is, as mentioned earlier, the position of peak heat flux. The thermal length scale $L_{r,e}$, where the subscript e implies use of the experimental spread rate $V_{f,e}$ in calculating $L_{r,e}$, was used to nondimensionalize the x coordinate. Corresponding theoretical profiles are shown in Fig. 5 where the computed spread rates $V_{f,t}$ (t for theory) were used in determining the length scale $L_{r,t}$. The reference temperature used in evaluating α_r was kept the same for theory and experiment for consistency. The spread rates predicted by the theory, which increase linearly with increasing percent oxygen at fixed pressure (Bhattacharjee et al., 1990), are higher than the experimental values, and this is reflected in the disparity of length scales between theory and experiment. The apparent nonlinearity of $V_{f,t}$ with O_2 percent reflected in the dependence of $L_{r,t}$ on O_2 percent is due to the increase of α_r with increasing flame temperature. Both Figs. 4 and 5 show a preheat zone followed by a relatively constant temperature pyrolysis zone. The preheat zone spans a length of approximately unity in the theoretical profiles, which is expected because conduction and convection are the only two mechanisms of heat transfer in the theory.

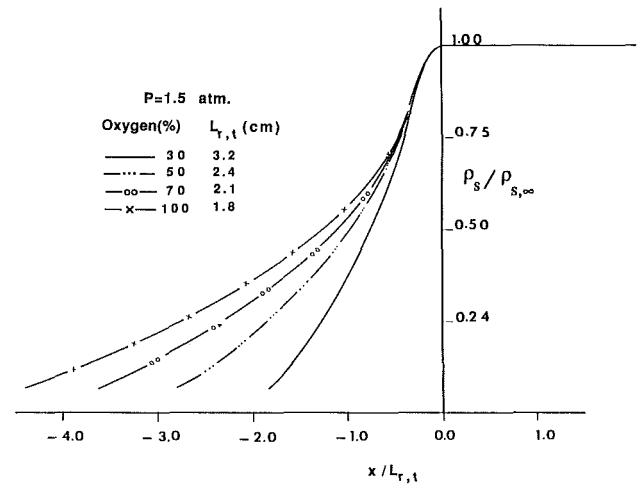

Fig. 7 Theoretical fuel density profiles from Bhattacharjee et al. (1990) consistent with Fig. 5

The preheat zones for the experimental results are much shorter than unity, implying that the actual length scale might be smaller than the thermal length $L_{r,e}$, which is established by a balance between conduction and convection. This observation suggests a higher conductive heat flux, at the same flame temperature, than that required for heating of the incoming gases. The only ways to account for this higher than expected conductive flux are radiation losses from the flame and/or surface and/or enhanced convective cooling due to an induced flow. The gravity levels present in the drop tower and the observed symmetry of the flame suggest a lack of induced motion. Hence, it seems likely that radiation losses play an important role here due to an enhanced effect of residence time. We further notice in Fig. 4 that the preheat length becomes shorter for slower flames. The residence time being greater in slower spreading flames, it can be expected that the importance of radiation losses is greatest for such flames, and the conduction length scale $L_{r,e}$ becomes inappropriate for characterizing the flame. Elaboration on this point is provided later.

The density profiles evaluated using Eq. (2) are shown in Fig. 6. The solid density decreases steadily because of the depletion of fuel by evaporation. The faster the flame spreads, the longer is the pyrolysis zone in order to accommodate the fuel that must be evaporated. For the same reason, the theoretical flames, having higher spread rates, show larger py-

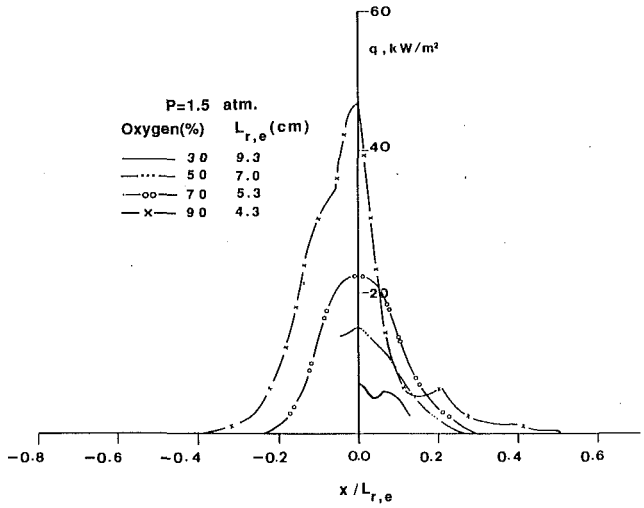

Fig. 8 Experimental surface heat flux profiles

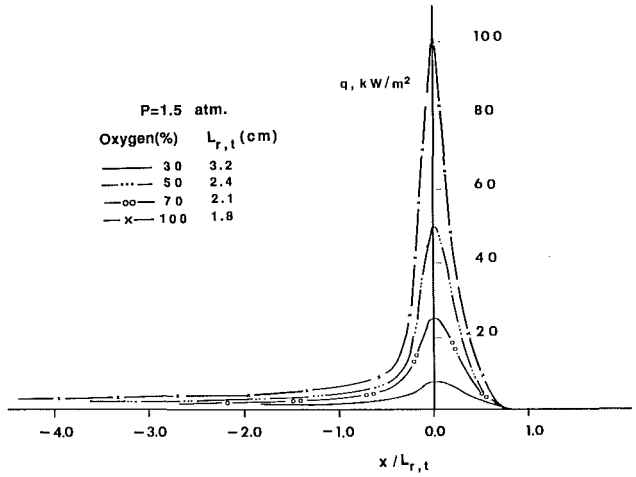

Fig. 9 Theoretical surface heat flux profiles from Bhattacharjee et al. (1990)

rolysis zones (see Fig. 7). Another distinction between experiment and theory emerges with respect to the location of the onset of pyrolysis. The theory predicts that pyrolysis starts at about the same location as that of the peak of the flux ($x=0$) whereas in Fig. 6 this location can be seen to migrate upstream as the ambient oxygen level decreases.

The conductive heat flux profiles from theory and the net heat flux profiles from experiment and Eq. (3) are compared in Figs. 8 and 9. The theoretical conductive flux levels are about 20–40 percent higher than the experimentally derived net ones. The net flux consists of conduction and radiation from the gas to the solid less the radiation lost from the surface. Consistent with the above discussion, the absence of a radiative loss in the theoretical description is likely to contribute to the differences seen between theory and experiment.The flame is physically much smaller than that predicted by theory. As a result, radiation loss from a long tail cannot be sustained by the smaller flame, and so the long pyrolysis tail evident in the theoretical flame is not found experimentally.

Discussion

Radiation interacts with the spreading flame in complicated ways. Radiation emitted from the surface, Q_s, interacts with the radiating flame in the gas before escaping to the environment. A fraction f of the emitted radiation Q_g from the gas phase is directed toward the surface, a part is absorbed, and the rest is reflected back to the gas phase to complicate the situation further. The net heat transfer rate to the surface, Q_{net}, thus consists of heat conduction and part of the gas-phase radiation minus radiation emitted and reflected from the surface.

For flames of small optical depth, which constitute the class of flame in which we are interested here, the emission approximation may be invoked. The total heat lost from the flame and fuel surface due to radiation, Q_l, and the net heat transfer to the fuel, Q_{net}, can then be expressed as

$$Q_l = Q_s + (1-f)Q_g + f(1-\epsilon)Q_g = Q_s + (1-\epsilon f)Q_g \quad (5)$$

$$Q_{\text{net}} = Q_c - Q_r \quad (6)$$

where $Q_r = Q_s - \epsilon f\, Q_g$. The surface absorptance has been taken equal to the emittance in Eq. (5).The spread rate depends on the net heat transferred to the solid from the gas, and radiation, from both the gas and solid phases, will have a direct influence on it via Eq. (6). The radiation loss Q_l tends to depress the flame temperature and hence has a secondary influence in reducing the net heat transfer rate to the surface. If gas-phase radiation is negligible, then surface radiation, acting alone, reduces Q_{net} and is the source of Q_l. Both these loss effects tend to retard flame spread. Because these effects are neglected in the theory, it is reasonable to expect predicted spread rates to be higher than those observed experimentally (Bhattacharjee et al., 1990).

Gas-phase radiation does have opposing influences. While it plays the role of a loss to reduce the flame temperature and hence the conductive flux to the surface, it also augments the net heat transfer rate to the surface ($\epsilon f Q_g$). Which effect dominates will determine whether gas-phase radiation acts to increase or decrease the spread rate.

It will be useful in the discussion that follows to estimate a length scale that contains the effects of radiation. Consider a control volume in the gas phase at the leading edge of the flame in the gas phase (cross-hatched area in the gas in Fig. 1). If radiation from the tail of the flame directed toward this control volume and absorbed is considered to be a perturbation and neglected, then the only source of heating is forward heat conduction, $\lambda_g(T_f - T_\infty)$. This conduction accounts for (*i*) the enthalpy rise of the gas, $\rho_g C_p V_f (T_f - T_\infty)\, L_r$, (*ii*) conduction to the solid, $\lambda_g\,(T_f - T_v)$, and (*iii*) radiation from the gas that, with the emission approximation, can be written as $Q_g = 4a_p \sigma(T_f^4 - T_\infty^4)\, L_r^2$.

Now consider a control volume in the solid phase (cross-hatched area in the solid in Fig. 1). Forward conduction through the solid can be shown to be negligible in comparison to gas-to-solid conduction (Altenkirch and Bhattacharjee, 1990). Consequently, the solid is heated by conduction at a rate approximately equal to $\lambda_g(T_f - T_v)$ and the fraction of the gas radiation, $\epsilon f Q_g$, that is directed toward the solid and absorbed. This heat transfer is balanced by (*i*) the rise in enthalpy of the solid, $\rho_s C_s V_f \tau (T_v - T_\infty)$, (*ii*) emission from the surface, $\epsilon\sigma(T_v^4 - T_\infty^4)\, L_r$, and (*iii*) reflected radiation from the surface, $(1-\epsilon)\, f Q_g$. The energy balance in the solid phase can be used to obtain an expression for $\lambda_g(T_f - T_v)$, which, when substituted into the gas-phase energy balance, produces the following expression for L_r:

$$L_r = \frac{\alpha_r}{V_f}\left[1 - \frac{\rho_s C_s \tau}{\lambda_g}\left(\frac{T_v - T_\infty}{T_f - T_\infty}\right) V_f - \frac{\epsilon\sigma}{\lambda_g}\left(\frac{T_v^4 - T_\infty^4}{T_f - T_\infty}\right) L_r - (1-\epsilon f)\frac{4a_p\sigma}{\lambda_g}\left(\frac{T_f^4 - T_\infty^4}{T_f - T_\infty}\right) L_r^2\right] \quad (7)$$

Equation (7) can be simplified somewhat by treating radiation as a perturbation to conduction and approximating, on the right-hand side, L_r by α_r/V_f and V_f by the classical conduction-dominated approximation $V_f = \lambda_g\ (T_f - T_v)/$

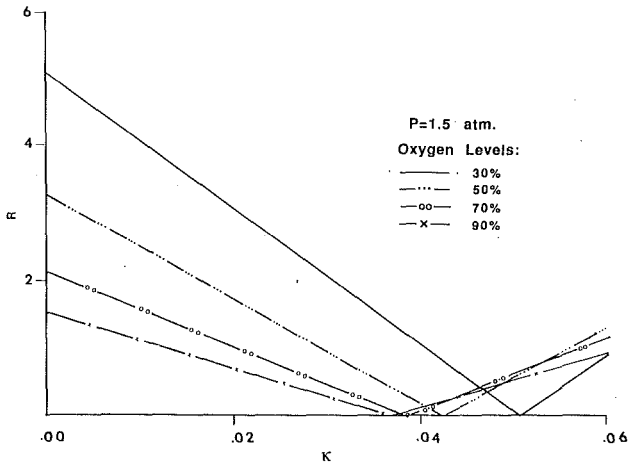

Fig. 10 Absolute value of the radiation/conduction parameter (Eq. (12)) versus optical depth. Values of R to the left of the discontinuity in slope imply a heat loss; values to the right of the discontinuity imply a heat gain.

$\rho_s C_s \tau (T_v - T_\infty)$ (de Ris, 1969; Altenkirch and Bhattacharjee, 1990) to give:

$$L_r = \frac{\alpha_r}{V_f}\left[C_1 - \frac{\epsilon\sigma T_\infty^3}{\rho_g C_g V_f}\left(\frac{\bar{T}_v^4 - 1}{\bar{T}_f - 1}\right) - (1-\epsilon f)\frac{4a_p\sigma T_\infty^3 \alpha_r^2}{\lambda_g V_f^2}\left(\frac{\bar{T}_f^4 - 1}{\bar{T}_f - 1}\right)\right] \quad (8)$$

where $C_1 = (\bar{T}_v - 1)/(\bar{T}_f - 1)$ is a constant somewhat smaller than unity, and the bar over T implies temperature measured in the units of T_∞. It is clear from Eq. (8) that $L_r = \alpha_r/V_f$ results in an overestimation of the length scale in all situations and particularly when radiation effects are important.

The length of the preheat zone found in experiment as compared to theory should provide an indication of the actual length scale for the flame spread phenomenon. In the theory applied here (Bhattacharjee et al., 1990) radiation was neglected, and so the preheat zone determined from computational results should be of length equal to approximately $L_{r,t} = \alpha_r/V_{f,t}$, which is the case as demonstrated by the length of the preheat zone in Fig. 9. However, experimental preheat zone lengths are substantially less than $\alpha_r/V_{f,e}$ as can be seen in Fig. 8.

Use of the equilibrium flame temperature rather than the flame temperature for complete combustion in establishing T_r for property determination results in a reduction in $L_{r,e}$ of about 15 percent, but α_r in $L_{r,t}$ is affected similarly such that the disparity in lengths remains regardless of the flame temperature used in T_r. Additionally, the disparity between the actual length and $\alpha_r/V_{f,e}$ increases as the oxygen level is reduced. This trend is consistent with Eq. (8), which predicts a higher impact of radiation at lower V_f. Given the complexity of Eq. (8) and the fact that any physically reasonable scale can be used for comparison purposes, we continue to use the thermal length α_r/V_f for scaling.

In order to determine how significant the above-mentioned radiation effects are, it is instructive to compare the radiative transfer, Q_r, to the conductive transfer, Q_c, where Q_c is approximately

$$Q_c \approx (A/W)\lambda_g (T_f - T_v)/L_r \quad (9)$$

To approximate Q_r, the flame is replaced by an equivalent hemispherical shell of optical depth κ. For small κ, the radiating gas can be replaced with a black surface radiating at an equivalent temperature T_{en} given by

$$T_{en}^4 \equiv T_\infty^4 + \kappa T_f^4 \quad (10)$$

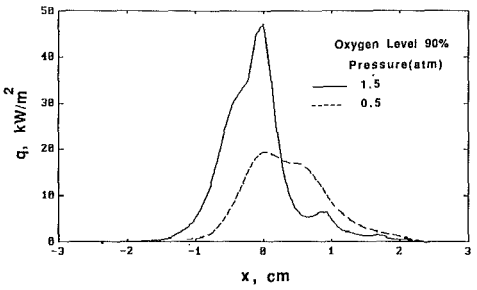

Fig. 11 Effect of pressure on experimental surface heat flux

The net radiation lost from the fuel surface can, therefore, be written as

$$Q_r \approx (A/W)\epsilon\sigma(T_v^4 - T_{en}^4) \quad (11)$$

Dividing Eq. (11) by Eq. (9) we obtain the radiation/conduction parameter

$$R = S\left|\frac{\bar{T}_v^4 - \bar{T}_{en}^4}{\bar{T}_f - \bar{T}_v}\right| \quad (12)$$

where $S = \epsilon\sigma T_\infty^3/\rho_g C_g V_f$ is the inverse of the usual Stark number.

A small value of R implies that radiation heat transfer is relatively unimportant. This occurs when there is a forced or induced flow that provides a velocity scale large compared to V_f that would replace V_f in the expression for S and thus reduce S. In a quiescent, microgravity environment, the spread rate itself is the velocity scale of interest as in Eq. (12), and S usually turns out to be large. For small flames, κ is small, and, therefore, T_{en} is small compared to T_v. In this case, a large value of R results in a radiative loss from the surface and a retarded rate of flame spread. On the other hand, if the flame is large enough that T_{en} may be greater than T_v, gas radiation will overwhelm the surface radiation loss, and any increase in the magnitude of R will increase the net flux to the surface to increase the flame spread rate.

In Fig. 10, the experimental information, i.e., $V_{f,e}$ and the measured vaporization temperature, is used to evaluate the absolute value of R for various ambient conditions. Quantities not known are the flame temperature T_f and the optical depth κ. The equilibrium flame temperature for stoichiometric combustion was used for T_f where T_f appears explicitly in T_{en} and R, and κ is made a variable. Because gas radiation is sensitive to T_f, inaccuracy in estimating T_f is magnified. The equilibrium temperature was chosen then in evaluating T_{en} and R because of the effects of dissociation on the flame temperature at the higher oxygen levels. T_r as previously defined though is used for property determination for consistency with theory and because property values are not nearly as sensitive to temperature as is the radiative effect.

For κ smaller than the κ for which R is zero, the net effect of radiation is a heat loss for the surface while for larger κ, the net effect is a gain. For small κ, which is likely for the flames under consideration here (Sibulkin et al., 1981), Fig. 10 shows clearly that the importance of a radiative loss increases with decreasing oxygen concentration in the environment. Recent theoretical results indicate that computed spread rates including only surface radiation, with $\kappa = 0$, normalized with computed spread rates neglecting all radiative effects, correlate with S (Bhattacharjee and Altenkirch, 1991).

The radiation/conduction parameter can be used to explain qualitatively the observed dependence of spread rate on pressure. While theory predicts almost no dependence of spread rate on pressure, the drop tower experiments show an increase of spread rate with pressure (Bhattacharjee et al., 1990). The net heat flux calculated from the surface temperature measurements for ambient pressures of 0.5 atm and 1.5 atm at 90

percent O_2 are shown in Fig. 11. The length scale $L_{r,e}$ is reduced at higher pressure because of the inverse dependence of α_r on pressure and the increase in $V_{f,e}$. If that were the only effect, we would expect the total heat transfer to remain unchanged because the area over which the flux is incident concomitantly decreases with a decrease in length scale. However, the areas under the curves in Fig. 11 are such that the heat transfer is higher at higher pressure. Additionally, from Fig. 11, it is clear that the actual length over which heat is transferred upstream, $L_{r,p}$, is comparable for the two pressures even though the value of $\alpha_r/V_{f,e}$ for 0.5 atm is nearly 4.5 times that for 1.5 atm. The fact that the preheat length does not decrease in proportion to the decrease in $L_{r,e}$ as the pressure increases indicates the presence of an effect other than conduction and convection alone, providing further evidence of the inappropriateness of using L_r to characterize these flames.

An explanation of the effect of pressure may be found in the role played by gas radiation in the radiation/conduction parameter. An increase in gas density decreases S. In addition, the equivalent optical depth κ may increase with pressure causing T_{en} to rise following Eq. (10). Both these effects combine to lower R, which implies that the radiation lost from the surface is now smaller at higher pressure resulting in a higher net heat flux and spread rate. In normal gravity, the buoyancy-induced flow dilutes the radiative effect, and a slight increase in spread rate with increasing pressure, when kinetic effects are important, can be explained by the effect of pressure on the viscous flow field alone (Altenkirch et al., 1980), providing indirect support of the explanation here as to the role played by gas radiation.

Conclusions

Measured surface temperature and spread rate for flame spread over ashless filter paper in a microgravity environment were used along with the solid-phase mass and energy balance equations to determine the heat flux profile along the surface and the fuel density distribution. The spread rate, peak heat flux, and net heat transferred from the gas to the solid increase with an increase in ambient oxygen concentration. For a given oxygen level, these same quantities increase with pressure.

Experimental results compare only qualitatively with respect to the effects of oxygen concentration on the spread process to those of a theoretical model that completely neglects the effects of radiation.There is quantitative disparity between experiment and theory with respect to spread rate, flame size, peak heat flux, and cumulative heat transfer. The observed increase in spread rate with an increase in pressure is not predicted theoretically.

A simplified analysis was used to demonstrate the importance of both surface and gas-phase radiation to explain an apparent disparity between theory neglecting radiation and experiment. Without any radiative effects, the heat flux received by the fuel that is responsible for flame spread is conducted to the solid from the gas phase. Surface radiation reduces this heat flux and also contributes to cooling the flame, the effects of both tending to slow the spread. Gas-phase radiation, on the other hand, has two opposing effects as part of it is fed back to the surface to increase the heat flux, while the rest is lost to the environment, thus reducing the flame temperature and hence the conductive flux. The characteristic gas-phase length is also reduced due to radiative effects. A radiation/conduction parameter was defined to include these effects. The relative importance of radiation increases with a decrease in the ambient oxygen level. The greatest disparity between theory and experiment occurs then at the lowest oxygen concentrations. It appears that increased gas-phase radiation may explain the observed increase in spread rate with increasing pressure through an increase in the optical depth of the flame and heat transfer back to the fuel surface.

Acknowledgments

This work was supported by NASA through Contract No. NAS3-23901. We thank Ralph Zavesky and Neil Rowe for their help in design of the experimental hardware and Kurt Sacksteder for serving as Contract Monitor during the early phase of the contract effort.

References

Altenkirch, R. A., Eichhorn, R., and Shang, P. C., 1980, "Buoyancy Effects on Flames Spreading Down Thermally Thin Fuels," *Comb. Flame*, Vol. 37, pp. 71–83.

Altenkirch, R. A., 1985, "Science Requirements Document for the Solid Surface Combustion Experiment," NASA Contract NAS3-23901 Report.

Altenkirch, R. A., and Bhattacharjee, S., 1990, "Opposed-Flow Flame Spread With Implications for Combustion at Microgravity," *AIAA Prog. Astro. Aero. Sci.*, Vol. 130, pp. 723–740.

Andracchio, C. R., and Cochran, T. H., 1976, "Gravity Effects on Flame Spreading Over Solid Surfaces," NASA TN D-8288.

Bhattacharjee, S., and Altenkirch, R. A., 1991, "The Effect of Surface Radiation on Flame Spread in a Quiescent, Microgravity Environment," *Comb. Flame*, Vol. 84, pp. 160–169.

Bhattacharjee, S., Altenkirch, R. A., Srikantaiah, N., and Vedha-Nayagam, M., 1990, "A Theoretical Description of Flame Spreading Over Solid Combustibles in a Quiescent Environment at Zero-Gravity," *Comb. Sci. Technol.*, Vol. 69, pp. 1–15.

Chen, C. H., 1986, "Flame Propagation: Effect of Solid-Phase Heat Conduction," presented at the Eastern Section/The Combustion Institute meeting.

Chen, C. H., and T'ien, J. S., 1986, "Diffusion Flame Stabilization at the Leading Edge of a Fuel Plate," *Comb. Sci. Technol.*, Vol. 50, pp. 283–306.

de Ris, J. N., 1969, "Spread of a Laminar Diffusion Flame," *Twelfth Symposium (International) on Combustion*, The Combustion Institute, pp. 241–252.

Fakheri, A., and Olson, S., 1989, "The Effects of Radiative Heat Loss on Microgravity Flame Spread," AIAA Paper No. 89-0504.

Fernandez-Pello, A. C., Ray, S. R., and Glassman, I., 1981, "Flame Spread in an Opposed Forced Flow: The Effect of Ambient Oxygen Concentration," *Eighteenth Symposium (International) on Combustion*, The Combustion Institute, pp. 579–589.

Olson, S. L., 1987, "The Effect of Microgravity on Flame Spread Over a Thin Fuel," NASA TM-100195.

Olson, S. L., Ferkul, P. V., and T'ien, J. S., 1989, "Near-Limit Flame Spread Over a Thin Solid Fuel in Microgravity," *Twenty-Second Symposium (International) on Combustion*, The Combustion Institute, pp. 1213–1222.

Sibulkin, M., Kulkarni, A. K., and Annamalai, K., 1981, "Effects of Radiation on the Burning of Vertical Fuel Surfaces," *Eighteenth Symposium (International) on Combustion*, The Combustion Institute, pp. 611–617.

T'ien, J. S., 1986, "The Flame Front Problem: Combustion in Low-Reynolds-Number Flow," ASME Paper No. 86-WA/HT-49.

Vento, D., Zavesky, R., Sacksteder, K., and Altenkirch, R., 1989, "The Solid Surface Combustion Space Shuttle Experiment Hardware Description and Ground-Based Test Results," AIAA Paper No. 89-0503.

Group Ignition of a Cloud of Coal Particles

W. Ryan

K. Annamalai

Mechanical Engineering,
Texas A&M University,
College Station, TX 77843-3123

Ignition of an isolated single coal particle is known to occur either heterogeneously or homogeneously. While single-particle studies may be useful for dilute coal sprays, their application to burners is limited since ignition occurs in the vicinity of the burners where the spray is dense. Rather than considering an isolated particle, one must consider a collection of particles in order to determine the change in ignition characteristics resulting from particle interactions. Thus, group combustion models have been developed essentially to predict the ignition and combustion characteristics of a larger number of interacting drops/particles. This paper presents results of the ignition characteristics of a spherical cloud of uniformly distributed coal particles in quiescent surroundings using a simple group combustion model. For the conditions studied, the results are as follows: (1) Ignition is heterogeneous if the cloud is dilute and homogeneous if the cloud is dense under the same ambient conditions; (2) there is a minimum ignition time for a given set of initial conditions corresponding to a certain cloud denseness; (3) ignition time is less sensitive to the denseness of the cloud at higher ambient temperatures; and (4) decreased proximate volatile matter can result in either increased or decreased ignition time depending on the cloud denseness (ignition mode). Qualitative comparisons to experimental data are given; however, these comparisons should be approached with caution since the experimental conditions and geometries may be vastly different than those used in the numerical study presented here.

1 Introduction and Problem

Fundamental experiments on ignition and combustion of coal have been conducted for many decades. The ignition studies have been essentially motivated by the desire to obtain the ignitability characteristics of coal dust. Based on the premise that the ignitability of a suspension of coal particles must depend on the ignition characteristics of single particles, most of the theoretical and experimental studies have been concentrated on the ignition and combustion of single coal particles (Cassel and Liebman, 1959; Golovina and Khaustovich, 1962; Essenhigh, 1963; Bandyopadhyay and Bhaduri, 1972; Kurylko and Essenhigh, 1973; Ragaland and Yang, 1985). These studies have shown that ignition of a coal particle occurs by two modes. The first mode, heterogeneous ignition, refers to the rapid oxidation of carbon and in-situ volatile matter at the particle surface. The other mode, homogeneous ignition (sometimes referred to as the Faraday mechanism), occurs when volatiles released from the particles undergo rapid oxidation in the gas phase. Single particle studies reveal that heterogenous ignition normally occurs for smaller sized particles, while homogeneous ignition occurs for larger particles (Annamalai and Durbetaki, 1977). Although single-particle studies may be useful for the study of ignition and combustion of dilute sprays, their application to spray ignition is limited since most industrial spray burners use very dense clouds and ignition occurs in the vicinity of the burner where the particles are closely spaced and interactions are significant. Further, the flammability data for coal dust air mixtures are correlated in terms of the proximate volatile matter, which seems to suggest that homogeneous ignition governs the flammability behavior (Bradley et al., 1989). Thus, the collective behavior of a group of particles must be studied in order to interpret data involving coal dust:air mixtures.

Experiments on a collection of particles have been conducted using a stream of particles in laminar flow reactors (Howard and Essenhigh, 1967; Kimber and Gray, 1971; Hamor et al., 1973; Midkiff et al., 1986; Niksa et al., 1986), and batches of coal particles introduced in a furnace (Chen et al., 1984) and in shock tubes (Seeker et al., 1979; Lester et al., 1981). Ignition experiments conducted using a cloud of metal particles reveal lower ignition temperatures than those of isolated particles with ignition temperatures decreasing as dust concentration increased (Cassel and Liebman, 1959). Recent experiments of Chen et al. (1984) on a cloud of char and coal particles reveal ignition temperatures of 620 K to 700 K, while single-particle experiments yield values around 1050 K to 1200 K (Bandyopadhyay and Bhaduri, 1972). Recently, group combustion (GC) models have been proposed to obtain the ignition and combustion characteristics of clouds of liquid drops, char particles, and coal particles (Chiu and Liu, 1977; Correa and Sichel, 1982; Bellan and Cuffel, 1983; Bellan and Harstad, 1987a, 1987b, 1988, 1990; Annamalai and Ramalingam, 1987; Annamalai et al., 1984, 1988a, 1988b). Theoretical group ignition studies on a cloud of dodecane liquid drops reveal ignition temperatures of 475 K to 700 K for a collection of drops (Correa and Sichel, 1982; Annamalai et al., 1984), while wire-supported isolated drops reveal an ignition temperature of 1400 K for 100-μm-dia drops (extrapolated from Lemott et al., 1971).

The present paper deals with the development of a transient group ignition model for a cloud of coal particles and presents ignition results for both dilute and dense clouds. Limitations of the model under dilute conditions are discussed. For a given particle diameter in the cloud, it is shown that homogeneous ignition occurs for a dense cloud while heterogeneous ignition occurs for a dilute cloud. Qualitative comparisons of the results with experimental findings are given.

2 Background

A single drop burning in air has its own envelope flame. If another burning drop is brought near the drop, then a common flame is formed around both drops. This is the simplest example of interactive combustion. If a dense cloud of droplets is ignited and burned, a common flame is expected to be formed

Contributed by the Heat Transfer Division for publication in the JOURNAL OF HEAT TRANSFER. Manuscript received by the Heat Transfer Division March 22, 1990; revision received February 15, 1991. Keywords: Combustion, Fire/Flames, Sprays/Droplets.

around the cloud. This is conventionally termed group combustion.

Analytical studies on the ignition of a dust cloud of char/carbon particles under quiescent conditions have been conducted by Rumanov and Khalkin (1969) and Krishna and Berlad (1980) using the steady-state thermal theory of ignition and assuming uniform properties throughout the cloud. However, there is no prior literature on the group ignition of a cloud of coal particles. As opposed to the ignition of a cloud of drops where the gasification of drops is total and is a purely physical process, ignition of a cloud of coal particles is somewhat complex in that the gasification of coal is partial and is a chemical decomposition process; further, ignition can be a result of heterogeneous reactions or the rapid oxidation of released volatiles in the gas phase. While a cloud containing a large number of closely spaced particles (dense cloud) can readily form a flammable mixture leading to homogeneous ignition, a cloud of widely spaced small particles (dilute cloud) may lead to heterogeneous ignition. As seen later, the two ignition modes lead to interesting results for ignition time. In the subsequent sections, the model will be described followed by a brief summary of the assumptions, conservation equations, and method of solution. Results for ignition time are then presented as a function of various parameters.

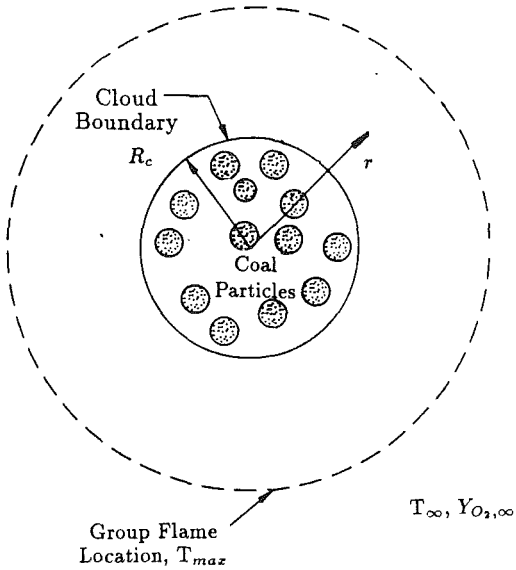

Fig. 1 Illustration of the group combustion model

3 The Model

In order to analyze the group ignition phenomenon of a cloud of coal dust and to keep the physics in tractable form, a simple model of the ignition process of a spherical cloud of coal particles in quiescent surroundings is analyzed here. The assumption of quiescent surroundings provides a basis for comparison with single-particle results and aids in ascertaining the effect of interactions on the ignition process.

Consider a cloud of uniformly distributed coal particles of radius a within a sphere of radius R_c (Fig. 1). The region adjacent to the particles is termed the bulk gas zone, within which properties are assumed uniform with respect to the θ and ϕ directions (spherical symmetry), but vary in the r direction. If this cloud is placed in a hot furnace, a thermal wave propagates from the ambience into the cloud. The bulk gas temperature increases, which in turn supplies heat to the particles. When the temperature of the particles reaches the pyrolysis level, thermal decomposition of coal occurs, releasing volatiles. The volatiles diffuse into the bulk gas zone, establishing a mixture of volatiles and oxygen in the bulk gas. If the cloud is dense, then homogeneous ignition may occur, provided that the gas phase temperature is high enough. On the other hand, if the cloud is dilute, a flammable mixture in the gas phase may not be formed and the carbon in the coal reacts with the oxygen adjacent to the particles resulting in heterogeneous ignition. Thus, the ignition mode may be either homogeneous or heterogeneous depending upon the denseness of the cloud.

3.1 Assumptions. The assumptions are briefly summarized below. A more detailed accounting of the assumptions and justification is given elsewhere (Annamalai et al., 1988b).

(*i*) Spherical symmetry exists.
(*ii*) $\rho D = \text{const.}$
(*iii*) $\text{Le} = 1$.
(*iv*) The particles are fixed in space.
(*v*) The particles act as point heat and mass sources.
(*vi*) The particle temperature is uniform.
(*vii*) The mass/heat generated from the particles is distributed rapidly in the interstitial space between the particles (top hat profile).
(*viii*) Pyrolysis occurs volumetrically with no swelling,

Nomenclature

a = particle radius, m
B = pre-exponential frequency factor, 1/s
C_p = gas specific heat, kJ/kg K
C_s = solid specific heat, kJ/kg K
D = diffusion coefficient, m^2/s
d = diameter, m
E = activation energy, kJ/kmole
G = G number
G_0 = initial G number
h = particle heat transfer coefficient, W/m^2K
HV = Heating Value, kJ/kg
h_T = thermal enthalpy, kJ/kg
$h_{T,\text{ref}}$ = reference enthalpy = $(h_{T,\text{ref}} = C_p T_{\text{ref}})$, kJ/kg
h_T^* = nondimensional enthalpy = $h/h_{T,\text{ref}}$
k = specific reaction rate constant
l = interparticle spacing, m
Le = Lewis number
m = mass, kg
$\dot{m}$ = mass flow rate, kg/s
m_{cu} = undecomposed particle mass, kg
$\dot{m}_C$ = heterogeneous mass burning rate, kg/s
$\dot{m}_{ch,p}$ = individual particle mass loss rate, kg/s
$\dot{m}'''_{ch,p}$ = volumetric particle mass loss rate, kg/m^3s
m_p = particle mass, kg
$\dot{m}_p$ = particle mass loss rate, kg/s
$\dot{m}_{\text{ref},g}$ = reference mass flow rate = $4\pi\rho D R_{c,0}$, kg/s
$\dot{m}_V$ = mass loss rate due to pyrolysis, kg/s
n = particle number density, m^{-3}
P = pressure, kPa
$\dot{q}_{ch}$ = heat source resulting from gas phase reactions, kW
$\dot{q}_{\text{conv}}$ = heat sink due to convective heat transfer to the particle, kW
$\dot{q}_m$ = heat source resulting from mass flow out of the particle, kW
$\dot{q}_{\text{rad}}$ = heat source resulting from radiation to the particle, kW
R_c = cloud radius, m
R_u = universal gas constant, kJ/kmole K
r = radial distance from the cloud center, m
T = temperature, K
T_{ref} = reference temperature = 300 K
t = time, s

while heterogeneous reactions occur at the external surfaces of the coal particles. Hence during pyrolysis, particle density decreases at constant diameter and for heterogeneous reactions, particle diameter decreases at constant density.

(*ix*) All gas phase chemical reactions for volatiles and CO occur by a single-step global reaction.

(*x*) The reactions included in the present analysis are as follows:

(*a*) Heterogeneous Reaction

$$C+\frac{1}{2}O_2\rightarrow CO \tag{I}$$

(*b*) Pyrolysis via Competing Reaction (Ubhayakar et al., 1977)

$$\text{Coal}\rightarrow\begin{cases}\alpha_{\mathrm{I}}\ \text{Volatiles}-\mathrm{I}+(1-\alpha_{\mathrm{I}})\mathrm{C} & \text{(II-1)}\\ \alpha_{\mathrm{II}}\ \text{Volatiles}-\mathrm{II}+(1-\alpha_{\mathrm{II}})\mathrm{C} & \text{(II-2)}\end{cases}$$

where $\alpha_{\mathrm{II}}\simeq 2\alpha_{\mathrm{I}}$ (Wall, 1987).

(*c*) Homogeneous (Gas Phase) Reactions

$$CO+\frac{1}{2}O_2\rightarrow CO_2 \tag{III}$$

$$\text{Volatiles}\ (V)+O_2\rightarrow V\cdot O_2$$

(*xi*) The radiative heat transfer between the particles and the wall is assumed to be negligible. For typical boiler burners, the radiative wall temperature is of the order 600–700 K and at these temperatures, radiation effects on ignition time can be considered negligible.

3.2 Gas Phase Conservation Equations. The estimation of various time scales, calculated for a cloud of 1 cm radius, reveal that the thermal penetration time into the cloud is the dominant time scale during the ignition process and as such ignition and combustion are essentially transient. The non-steady conservation equation used are:

3.2.1 Mass

$$4\pi r^2\left(\frac{\partial\rho}{\partial t}\right)+\left(\frac{\partial\dot{m}}{\partial r}\right)=\dot{w}_m'''(4\pi r^2) \tag{1a}$$

where

$$\dot{w}_m'''=\dot{m}_{ch,p}'''=n\dot{m}_{ch,p}=n\dot{m}_p,\quad r<R_c \tag{1b}$$

$$\dot{w}_m'''=0,\quad r>R_c \tag{1c}$$

where $\dot{w}_m'''$ is the mass added to the gas phase by the particles per unit volume and $\dot{m}_{ch,p}$ is the mass added to the gas phase per particle.

3.2.2 Species

$$4\pi r^2\left[\frac{\partial(\rho Y_k)}{\partial t}\right]+\left[\frac{\partial(\dot{m}Y_k)}{\partial r}\right]-\left(\frac{\partial}{\partial r}\left[4\pi r^2\rho D\left(\frac{\partial Y_k}{\partial r}\right)\right]\right)=\dot{w}_k'''(4\pi r^2),\quad k=O_2,\ CO,\ CO_2,\ H_2O,\ V_{\mathrm{I}},\ V_{\mathrm{II}} \tag{2a}$$

where $\dot{w}_k'''$ is the mass production rate of species k per unit volume. Thus

$$\dot{w}_k'''=(\dot{m}_{ch,p,k}'''+\dot{m}_{ch,k}'''),\quad r<R_c \tag{2b}$$

$$\dot{w}_k'''=\dot{m}_{ch,k}''',\quad r>R_c \tag{2c}$$

where $\dot{m}_{ch,p,k}'''$ is the rate at which species k is added to the gas phase per unit volume due to chemical reactions at the particle and $\dot{m}_{ch,k}$ is the creation (destruction) rate of species k due to gas phase chemical reactions.

3.2.3 Energy

The energy conservation equation is obtained by considering a control volume bounded by surfaces of radii r and $r+dr$ and by the surfaces surrounding all the particles within r and $r+dr$

$$4\pi r^2\left[\frac{\partial(\rho h_T)}{\partial t}\right]+\left[\frac{\partial(\dot{m}h_T)}{\partial r}\right]-\left(\frac{\partial}{\partial r}\left[4\pi r^2\rho D\left(\frac{\partial h_T}{\partial r}\right)\right]\right)=\dot{w}_h'''\ (4\pi r^2) \tag{3a}$$

where $\dot{w}_h'''$ is the enthalpy production rate per unit volume of bulk gas phase. It is a combination of the convective heat transfer between the gas phase and the particles ($\dot{q}_{\mathrm{conv}}'''$), the enthalpy produced as a result of chemical reactions in the gas phase ($\dot{q}_{ch}'''$) and the enthalpy gained by the gas phase due to the addition of mass from the particles ($\dot{q}_m'''$). Thus

$$\dot{w}_h'''=(\dot{q}_{\mathrm{conv}}'''+\dot{q}_{ch}'''+\dot{q}_m'''),\quad r<R_c \tag{3b}$$

$$\dot{w}_h'''=\dot{q}_{ch}'''\quad r>R_c \tag{3c}$$

where

$$\dot{q}_{ch}'''=\dot{m}_{V_{\mathrm{I}},ch}'''HV_{V_{\mathrm{I}}}+\dot{m}_{V_{\mathrm{II}},ch}'''HV_{V_{\mathrm{II}}}+\dot{m}_{CO,ch}'''HV_{CO} \tag{3d}$$

$$\dot{q}_{\mathrm{conv}}'''=n\dot{q}_{\mathrm{conv}} \tag{3e}$$

$$\dot{q}_m'''=n\dot{q}_m \tag{3f}$$

$$\dot{q}_{\mathrm{conv}}=\bar{h}\pi d_p^2(T_p-T_g) \tag{3g}$$

$$\dot{q}_m=\dot{m}_pC_p(T_p-T_{\mathrm{ref}}) \tag{3h}$$

Nomenclature (cont.)

t_{ref} = reference time = $\rho_{\mathrm{ref}}R_{c,0}^2/\rho D$, s
V = volatiles
w = source for mass, species, and enthalpy, kg/s
$\dot{w}_h'''$ = volumetric gas phase enthalpy source, kW/m^3
$\dot{w}_k'''$ = volumetric gas phase source of species k, kg/m^3 s
w_m = normalized volumetric mass source (Eq. 9(*b*))
$\dot{w}_m'''$ = volumetric mass source, kg/m^3 s
Y = species mass fraction
α = nondimensional mass flow = $\dot{m}/\dot{m}_{\mathrm{ref}}$
α_{I}, α_{II} = Maximum volatile matter via pyrolysis routes I and II
ξ = normalized inverse radius = $R_{c,0}/r$
ρ = density, kg/m^3
ρ_{ref} = reference density = P/RT_{ref}, kg/m^3
ρ^* = nondimensional density = ρ/ρ_{ref}
τ = nondimensional time = t/t_{ref}
∞ = infinite values of r

Subscripts

C = carbon, char
c = cloud
ch = gas phase chemical reaction
ch,p = particle chemical reaction
conv = due to convection
cu = coal undecomposed
g = gas phase
h = enthalpy
ig = ignition
k = species k
I = volatiles due to route I
II = volatiles due to route II
m = mass
max = maximum
O_2 = oxygen
p = particle
p,p = produced at the particle surface
rad = due to radiation
ref = reference condition
s = solid
T = thermal
V = volatiles
w = surface of the particle
0 = at time $t=0$
∞ = infinity

Superscripts

= per unit time
$'''$ = per unit volume
* = nondimensional variable

Table 1 Base case data

Ambience:
Air, $T_\infty =$ 1500 K, $Y_{O_2} = 0.23$

Cloud:
$T_{g,c,0} =$ 300 K, $Y_{O_2} = 0.23$, $R_c = 1$ cm, $d_p = 100$ μm
$\rho D = 5 \times 10^{-5}$, $C_p = 1.18$ kJ/kg K

Coal composition (percent mass):
C—84.63, H—5.47, N—2.13, O—7.77

Volatile composition:
$V_I =$ $CH_{2.64}N_{0.074}O_{0.24}$, $V_{II} = CHN_{0.028}O_{0.09}$
$HV_I = 3.95 \times 10^4$ kJ/kg, $HV_{II} = 3.72 \times 10^4$ kJ/kg

Kinetics:

Pyrolysis (Ubhayakar et al., 1977):
$\alpha_I =$ 0.4, $\alpha_{II} = 0.8$, $E_I = 7.37 \times 10^4$ kJ/K kmole
$E_{II} = 25.1 \times 10^4$ kJ/K kmole, $B_I = 3.7 \times 10^5$ m/s
$B_{II} = 1.46 \times 10^{13}$ m/s

Heterogeneous reactions (Smith, 1971):
$E_{c,1} = 6.64 \times 10^4$ kJ/K kmole, $B_{c,1} = 4.5 \times 10^3$ m/s
$n_{O_2} = 1.0$

Volatiles and CO gas phase reactions (Howard et al., 1973):
$A = 5 \times 10^9$ m^3/kg s, $E = 1.26 \times 10^5$ kJ/K kmole
$n_{O_2} = 1.0$

Condensed Phase Equations

3.3.1 Particle Mass (m_p)

$$\frac{dm_p}{dt} = -\dot{m}_p \tag{4a}$$

where dm_p/dt is the total rate of change of particle mass due to pyrolysis and heterogeneous reactions. Thus, the mass loss rate, $\dot{m}_p$, is the sum of the volatile liberation rate $\dot{m}_V$ and the carbon consumption rate $\dot{m}_C$ due to heterogeneous reactions. This is expressed as

$$\dot{m}_p = \dot{m}_V + \dot{m}_C \tag{4b}$$

The mass loss rate of volatiles is evaluated using the competing reaction pyrolysis model (reactions II). The competing reaction model assumes that the pyrolysis products consist of a lighter component (V_I) and a heavier component (V_{II}). The lighter component is released at low temperatures, while the heavier component is the predominant pyrolysis product at high temperatures. The values of α_I and α_{II} used in the model represent the fraction of coal that would be converted to volatiles if all the volatiles are released by either reaction I or II. If the coal composition is represented as $CH_{0.8}$, then the approximate compositions of the lighter and heavier volatiles are CH_2 and CH respectively. The actual composition of the released volatiles depends on the initial coal composition and the values of α_I and α_{II}. The volatile composition for the coal composition used in the current study is presented in Table 1. A complete description of the competing reaction model is given by Ubhayakar et al. (1977) and Stickler et al. (1974). According to the competing reaction model

$$\dot{m}_V = \dot{m}_{V,I} + \dot{m}_{V,II} \tag{4c}$$

where

$$\dot{m}_{V,i} = \alpha_i k_{V,i} m_{cu}, \quad i = \text{I, II} \tag{4d}$$

$$k_{V,i} = B_{V,i} \exp\left(\frac{-E_{V,i}}{R_u T_p}\right) \tag{4e}$$

As volatiles are released, a portion of the coal is decomposed. The rate of change of the undecomposed coal mass due to both reactions in the competing reaction model is given as

$$-\frac{dm_{cu}}{dt} = \left(\frac{\dot{m}_{V,I}}{\alpha_I}\right) + \left(\frac{\dot{m}_{V,II}}{\alpha_{II}}\right) \tag{4f}$$

where, at $t = 0$, m_{cu} is the initial particle mass ($m_{p,0}$).

The mass loss rate $\dot{m}_C$ due to heterogeneous char reactions is evaluated as follows. For the first-order heterogeneous reaction $\left(C + \frac{1}{2} O_2 \rightarrow CO\right)$ at constant density

$$\dot{m}_C = \rho_w k_C Y_{O_2,w} \pi d_p^2 \tag{4g}$$

where

$$k_C = B_C \exp(-E_C/R_u T) \tag{4h}$$

The oxygen mass fraction at the particle surface ($Y_{O_2,w}$) is calculated in terms of the bulk gas mass fraction (Y_{O_2}) adjacent to the particles using a mass balance that accounts for the blowing effects (Stefan flow) from the particle and chemical reactions at the particle surface (Ryan, 1988). If T_p and d_p are known, $\dot{m}_p$ can be evaluated using Eqs. (4*b*)–(4*h*).

3.3.2 Particle Diameter (d_p). Heterogeneous oxidation occurs at the particle surface with density constant. Hence, the diameter of the particle shrinks. The relation between $\dot{m}_C$ and d_p is given as

$$\frac{d(d_p)}{dt} = \frac{-2\dot{m}_C}{\pi \rho_p d_p^2} \tag{5}$$

3.3.3 Particle Density (ρ_p). Pyrolysis occurs volumetrically at constant particle size. Hence, the particle density changes as

$$\frac{d(\rho_p)}{dt} = \frac{-6\dot{m}_V}{\pi d_p^3} \tag{6}$$

3.3.4 Particle Temperature (T_p). From an energy balance around an individual particle,

$$m_p C_s \left(\frac{d(T_p)}{dt}\right) = -(\dot{q}_{conv} + \dot{q}_{rad}) + \dot{q}_{ch,p} \tag{7}$$

where $\dot{q}_{ch,p}$ is the heat released (absorbed) due to heterogeneous reactions and pyrolysis.

3.4 Boundary and Initial Conditions. At $t = 0$,

$$Y_k = Y_{k,c,0}, \; T = T_{g,c,0} \quad r < R_c \tag{8a}$$
$$Y_k = Y_{k,\infty}, \; T = T_\infty \quad r > R_c$$
$$\dot{m} = 0 \quad 0 < r < \infty$$

For $t > 0$,

$$\text{as } r \rightarrow \infty, \quad T = T_\infty, \quad Y_k = Y_{k,\infty} \tag{8b}$$

$$\text{as } r = \infty, \quad \frac{\partial T}{\partial r} = \frac{\partial Y_k}{\partial r} = \dot{m} = 0 \tag{8c}$$

3.5 Normalized Gas Phase Conservation Equations. Introducing the nondimensional form of time, radius, etc. (see nomenclature), the following gas phase conservation equations are obtained:

3.5.1 Mass

$$\frac{\partial \rho^*}{\partial \tau} - \xi^4 \left(\frac{\partial \alpha}{\partial \xi}\right) = w_m \tag{9a}$$

where

$$w_m = \frac{G_0 \dot{m}'''_{ch,p}}{4\pi n a_0 \rho D} = \left(\frac{R_{c,0}^2}{\rho D}\right) \dot{w}'''_m \tag{9b}$$

and the initial group combustion number (G_0) is defined as

$$G_0 = 4\pi n a_0 R_{c,0}^2 \tag{9c}$$

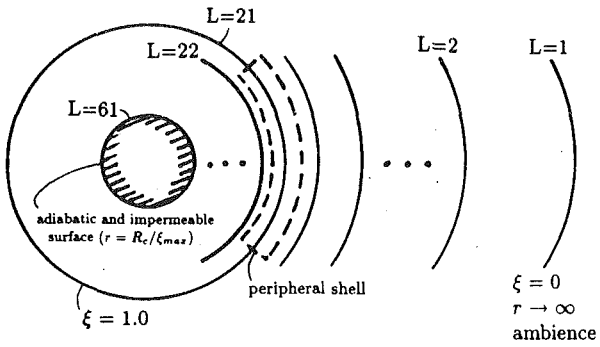

Fig. 2 Illustration of numerical scheme

3.5.2 Species

$$\rho^*\left(\frac{\partial Y_k}{\partial \tau}\right) - \alpha\xi^4\left(\frac{\partial Y_k}{\partial \xi}\right) - \xi^4\left(\frac{\partial^2 Y_k}{\partial \xi^2}\right) = w_m\left[\left(\frac{\dot{m}_{ch,p,k}}{\dot{m}_{ch,p}}\right) - Y_k\right] + \frac{\dot{m}'''_{ch,k}}{\dot{m}'''_{\text{ref},g}} \quad (10)$$

The ratio $\dot{m}'''_{ch,k}/\dot{m}'''_{\text{ref},g}$ is similar to Damkohler number III for a cloud, which is a ratio between the chemical reaction rate and the diffusion rate of species k into the cloud.

3.5.3 Energy

$$\rho^*\frac{\partial h_T{}^*}{\partial \tau} - \alpha\xi^4\frac{\partial h_T{}^*}{\partial \xi} - \xi^4\frac{\partial^2 h_T{}^*}{\partial \xi^2} = w_m\left(\frac{\dot{q}_{\text{conv}}}{\dot{m}_{ch,p}h_{T,\text{ref}}} - h_T{}^*\right) + \frac{\dot{q}'''_{ch} + \dot{q}'''_m}{\dot{m}'''_{\text{ref},g}h_{T,\text{ref}}} \quad (11)$$

The ratio $\dot{q}'''_{ch}/\dot{m}'''_{\text{ref},g}h_{T,\text{ref}}$ is similar to Damkohler number IV for a cloud, which is a ratio between the heat liberation rate due to chemical reactions and the diffusion rate of enthalpy into the cloud.

The initial and boundary conditions can be appropriately converted in the nondimensional form. It should also be noted that the term α represents the bulk mass convection from the cloud to the ambient due to the heating of the cloud and the gaseous mass generated by the particles in the cloud. It is determined by integrating the mass continuity equation (Eq. 9(*a*)) in the radial direction.

It is seen from Eqs. (9), (10), and (11) that the solutions are functions of the initial group combustion number, G_0, in addition to the heterogeneous and homogeneous kinetic parameters.

4 Results and Discussion

An explicit upwind scheme is used to solve the parabolic Eqs. (9), (10), and (11). The domain is divided into 60 spherical shells in the radial direction with 1/3 of the shells outside of the cloud (Fig. 2). If the particles are completely burned in the shell at the cloud periphery, the cloud is allowed to shrink to the adjacent shell; however, the cloud radius remains unchanged during the ignition process. Half of the shell at the cloud periphery is inside the cloud and contains particles, while the other half is outside the cloud and contains no particles. Thus, only half of the volumetric source terms (Eqs. (1*b*), (2*b*), (3*b*)) due to the presence of particles are used in the mass, species, and enthalpy conservation equations for the peripheral shell. Initially, the temperature and species mass fractions in the peripheral shell are an average value of the initial cloud and ambient values. The gas phase and particle temperatures in each shell are tracked as a function of time. Since $\xi \to \infty$ at the center of the cloud, computations were performed between $\xi = 0$ and $\xi = \xi_{\max} = 3$. Thus, the adiabatic and impermeable boundary conditions given in Eq. (8*c*) are imposed at $r = R_c/\xi_{\max}$ rather than at $r = 0$ (Carnahan et al., 1969). Also, the particles within $r = R_c/3$ were neglected in the calculations; however, they only comprise 3.7 percent of the initial cloud mass. Inclusion of the core using a coordinate transform did not result in any significant changes in the results. Additional details of the model and the numerical scheme are given by Annamalai et al. (1988b). A source correction method that overcomes the difficulties encountered when a flame is formed and oxidation becomes extremely rapid is discussed by Ryan and Annamalai (1990a). The base data used in the calculations are tabulated in Table 1.

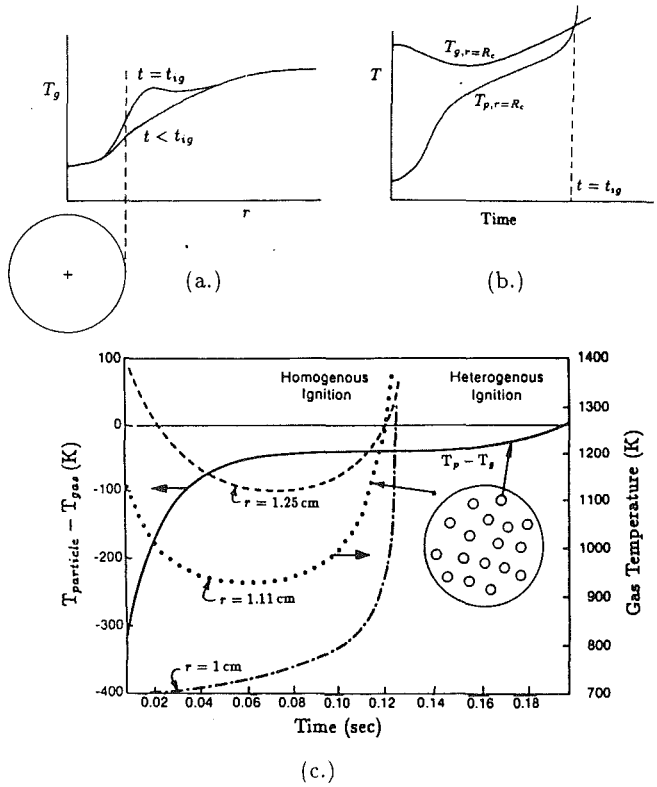

Fig. 3 Illustration of ignition criteria

4.1 Ignition Criteria. While flaming conditions in the experiments are indicative of ignition, the theoretical analyses adopt different thermal models for the occurrence of ignition. These are summarized by Annamalai and Durbetaki (1976). In the present work, two different criteria for ignition were established in order to distinguish between heterogeneous and homogeneous ignition. Homogeneous ignition is said to occur when the gas phase temperature shows a peak at some radial location (Fig. 3*a*). When the particle temperature rises above its local gas temperature anywhere in the cloud, the cloud is said to have ignited heterogeneously (Fig. 3*b*). The criteria that are satisfied first during the transient ignition process determine the ignition mode. Figure 3(*c*) illustrates the ignition criteria for both heterogeneous and homogeneous ignition. The dashed curves show the gradual development of the gas phase temperature profile just outside the cloud, while the solid curve shows the temperature difference between the particles located at the cloud periphery (heterogeneous ignition location) and the gas phase surrounding the particles. This curve becomes greater than zero at about 190 ms, signaling heterogeneous ignition. Referring to the other set of curves, a temperature peak in the gas phase occurs at 120 ms at $r \approx 1.1$ cm (outside the cloud), which is indicative of homogeneous ignition.

Note that Fig. 3(*c*) depicts the transient development of

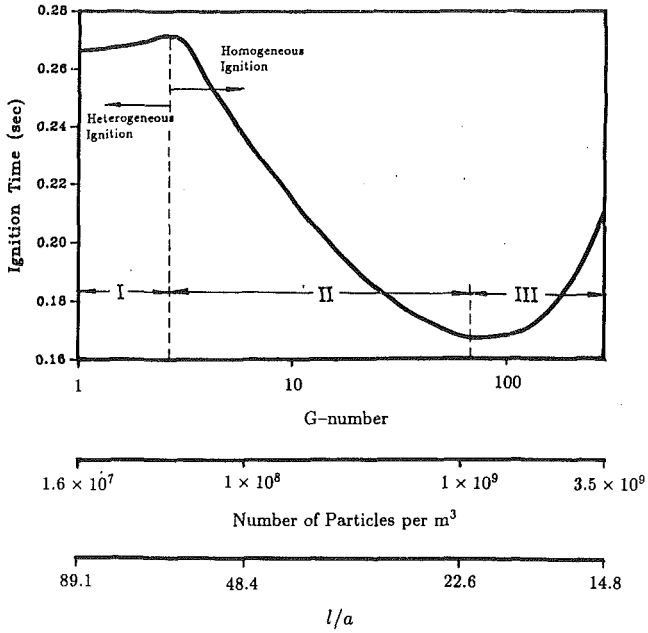

Fig. 4 Effect of cloud denseness on ignition time for the base case

temperature profiles and as such it will not reveal the S-type curve traditionally obtained using Semenov's steady-state thermal theory. The criteria based on the Semenov's classical thermal theory of ignition involve (*i*) the equality of the heat generation to the heat loss, and (*ii*) the equality of the rate of change of heat generation with temperature to the rate of the change of heat loss with temperature. As such the theory provides the conventional S-type stationary solution to the steady-state problem. The reader is referred to the recent review article by Essenhigh et al. (1989) for the discussion of the steady-state thermal theory of ignition. The steady-state solution provides information on the minimum ignition temperature to ignite the particle regardless of the amount of time required. In practical systems, the residence time is limited. If a laminar flow reactor is used, the condition of no ignition within the fixed residence time is construed as the particle being unignitable at the given gas temperature. Thus, even though the gas temperature may be higher than the required ignition temperature evaluated under steady-state conditions, the particle was said to be nonignitable because of limitations in residence time! Hence, a transient analysis is more realistic than a steady-state analysis since most combustion devices are time limited.

4.2 Group Combustion Number. Steady-state group combustion analyses reveal that most of the results can be correlated with a dimensionless parameter, G, called the group combustion number, which is a nondimensional measure of the denseness of the cloud. The dimensionless group obtained by Krishna and Berlad (1980) for the steady-state ignition analysis of a cloud of char particles assuming the cloud temperature is uniform is found to be equal to $G/3$. The analysis is similar to the steady-state solution for a large single particle of infinite thermal conductivity with the particle density equal to the cloud density. They obtained single char particle ignition when $G/3 \ll 1$ (characterized by the absence of cloud parameters influencing ignition) and cloud ignition of char particles when $G/3 \gg 1$ (characterized by a decrease in ignition temperature with increased cloud denseness). As opposed to the steady-state combustion model, nonsteady results cannot be correlated with a single dimensionless group. For the transient condition, the G number changes with time due to changing cloud radius and decreasing particle diameter and an initial group combustion number is defined as in Eq. (9*c*). However, during the ignition process the G number does not change much from G_0.

4.3 Effect of Cloud Denseness. Using the data shown in Table 1, results were generated for the variation of ignition time with cloud denseness by varying the particle number density. Results are presented as a function of the G number, particle number density, and normalized interparticle spacing [l/a; where $l/a \approx 22{,}500/n^{1/3}$ (Ryan and Annamalai, 1990b) with $a = 50 \times 10^{-6}$ m] (Fig. 4). At low dust concentrations (regime I), ignition is determined to be heterogeneous and ignition time increases slightly as the particle number density is increased from 1.6×10^7 to 4.0×10^7 particles/m^3. As the particle number density is increased beyond 4.0×10^7, ignition becomes homogeneous and the ignition time first decreases (regime II) and then increases (regime III). This behavior can be explained by considering the processes involved in the ignition of an initially cold cloud of coal particles introduced into a hot environment.

Ignition time can be considered to be a combination of several shorter time periods. These periods consist of t_{TH}—the thermal wave penetration time into the cloud, t_H—the particle heat-up time, t_F—the flammable mixture formation time, and t_I—the induction time. Since the induction time is normally very small, it is neglected in interpreting the results. Thus

$$t_{ign} = t_{TH} + t_H + t_F \quad \text{(homogeneous ignition)}$$

$$t_{ign} = t_{TH} + t_H \quad \text{(heterogeneous ignition)}$$

It should be mentioned that these times overlap and are not additive. As the G number increases (i.e., increasing the number of particles), there are two competing effects:

(*i*) The increased number of particles act as a heat sink lowering the local gas temperature and slowing the propagation rate of the thermal wave into the cloud and thereby delaying the heating of the particles and the onset of pyrolysis.

(*ii*) On the other hand, once pyrolysis has begun the increased number of particles provide more volatiles per unit volume, which can rapidly form a flammable mixture outside the cloud resulting in a decreased formation time.

For low G numbers (Regime I, $G < 3$), the flammable mixture cannot be formed easily since the volatile concentration remains low due to the small number of particles available for pyrolysis and due to the diffusion of released volatiles away from the cloud. Thus, cloud ignition is heterogeneous. Heterogeneous ignition is normally characterized by the completion of the pyrolysis process at the ignition location, which lends credence to the theory that a flammable mixture could not be formed. It is noted that ignition times for dilute clouds (low G numbers) are significantly higher compared to single particle ignition times. As opposed to a single particle exposed to the hot ambience, the particles in the cloud are initially surrounded by cold gas. Thus, although the particle diameter may be small, ignition time is controlled by the heat-up time of the surrounding gas in the cloud rather than the heat-up time of the particle. Hence, as $n \to 0$, the ignition time scale approaches the limit of the thermal penetration time for an initially cold cloud of radius R_c, rather than the individual particle ignition time. For the same reason, ignition time appears to remain insensitive to changes in G number in the dilute limit. However, the ignition time of a preheated cloud can reach the individual particle ignition time in the dilute limit.

For larger G numbers ($G > 3$, $l/a < 62$), the cloud ignited in the gas phase outside the cloud since higher gas phase temperatures exist outside the cloud and there are enough particles to form a flammable mixture. In regime II ($3 < G < 65$), the flammable mixture formation time, which includes the time for pyrolysis and diffusion of released volatiles to the hot ambience, decreases more rapidly than the thermal wave penetration time increases as the particle number density is increased, thereby resulting in decreased ignition times as the particle number density is increased. In regime III ($G > 65$),

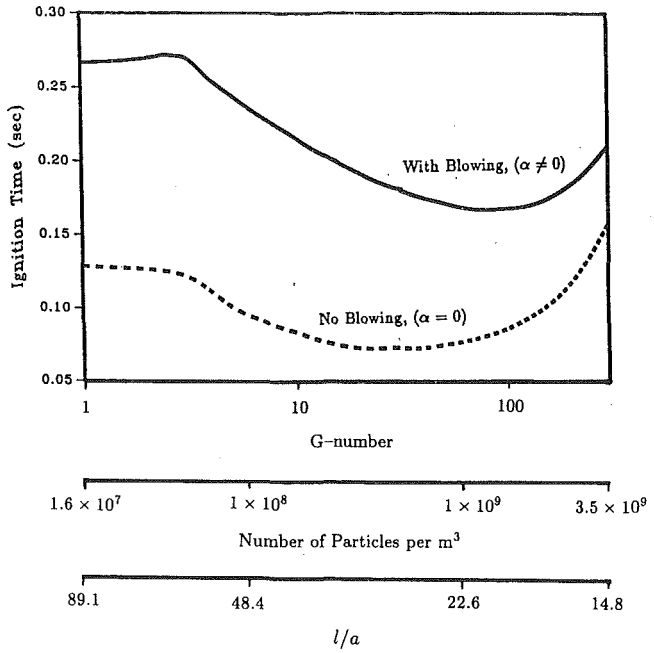

Fig. 5 Effect of blowing (α) on ignition time for the base case

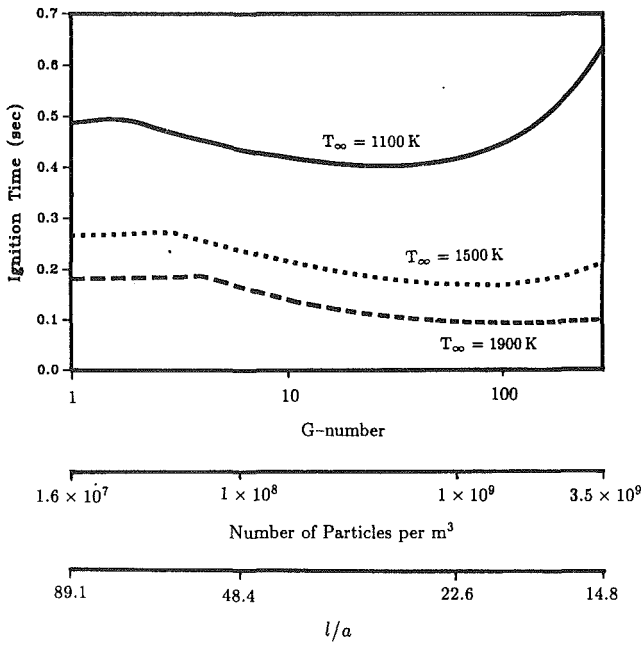

Fig. 6 Effect of ambient temperature on ignition time

the thermal wave penetration time becomes dominant and ignition time increases. Under this condition, one can visualize the cloud to be a large single porous particle with the particle density and radius equal to the cloud density and radius.

Group theory assumes a point source approximation with a top hat profile (uniform temperature between the particles) in the interstitial space between the particles. The top hat profile may be justified for dense clouds while the point source approximation may become invalid. However, Ryan and Annamalai (1990b) corrected the point source approximation due to finite size by suitably modifying the transfer coefficients. For dilute clouds, the point source approximation may be valid, but the top hat profile may not be justified. In order to investigate limits of group theory, the following order of magnitude analysis is conducted. If an impermeable membrane exists around each particle, the vapors/volatiles accumulate around the particle and eventually establish a top hat profile in a time scale on the order of $l^2/4D$. Hence, the top hat profile may be justified if

$$t_{ign} \gg l^2/4D \tag{12}$$

Upon rearrangement, an equation for the interparticle spacing can be found as

$$l \ll \sqrt{4Dt_{ign}} \tag{13}$$

With $t_{ign} = 0.27$ s and $D = 1.0 \times 10^{-4}$ m^2/s, $l \ll 1.0 \times 10^{-2}$ m, which corresponds to $l/a \ll 200$ for 100-μm-dia particles ($G \gg 0.09$). It should be noted that blowing from the particle surface as well as convective effects from within the cloud are expected to result in a more even distribution of gas phase profiles between particles. Thus, for the range of G numbers studied in this paper ($G > 1$), the assumption of rapid diffusion in the interstitial region (top hat profile) is justified for an initially cold cloud.

4.4 Effect of Blowing. Convection out of the cloud (blowing) occurs due to heating of the cloud, thus displacing mass at constant pressure, and due to the gaseous mass generated by the particles via pyrolysis and heterogeneous reactions. The term α in Eqs. (10) and (11) contains the blowing effect on heat and mass transfer. If α is artificially maintained equal to zero (no convective terms in the conservation equations), then results for ignition time can be obtained that neglect Stefan flow (blowing) out of the cloud. Figure 5 compares the results for ignition time with and without Stefan flow out of the cloud. Blowing reduces the heat transfer rate into the cloud and as such increases the ignition time since the thermal wave penetration time increases. For a dilute cloud, blowing is primarily a result of the heating of the gas mass within the cloud, while for a dense cloud, the entire cloud remains at low temperatures except those particles near the cloud periphery. Thus, the effect of blowing is less for a dense cloud. Qualitatively, both curves follow similar trends.

Assumption (*iv*) states that the particles are fixed within the cloud; however, in actuality the outward moving gases would tend to move the particles outward toward the hot ambience. Thus, if the model was modified to allow the particles to move, the results would be expected to lie somewhere between the curves for $\alpha = 0$ and $\alpha \neq 0$ in Fig. 5.

4.5 Effect of Ambient Temperature. Figure 6 shows that as the ambient temperature increases, ignition time decreases since the thermal wave penetration time is greatly reduced. The size of the heterogeneous regime extends to higher G numbers with increasing temperature. For example, if $T_\infty = 1900$ K with $G = 5$, ignition is heterogeneous; however, if $T_\infty = 1100$ K with $G = 5$, ignition is homogeneous. As the ambient temperature is increased, the thermal penetration depth may remain the same within the time of ignition. However, the high ambient temperatures provide a high-temperature environment around the reacting particles resulting in rapid char oxidation. The G number corresponding to the minimum ignition time also increases as temperature increases since the thermal wave penetration time becomes dominant at higher G numbers for higher temperatures. It is also observed that the homogeneous ignition portion of the curve is flatter for higher ambient temperatures. At low temperatures ($T = 1100$ K) and high G numbers ($G > 100$), the heat capacity of the cold cloud lowers the temperature of the gas surrounding the cloud below that at which significant volatile liberation can occur. The additional time required to "reheat" the surrounding gas results in rapidly increasing ignition times as the mass loading is increased for very dense clouds ($G > 100$). For high ambient temperatures ($T = 1900$ K), the temperature of the surrounding gas remains high enough to liberate volatiles and ignition time increases only slightly as the mass loading is increased for very dense clouds.

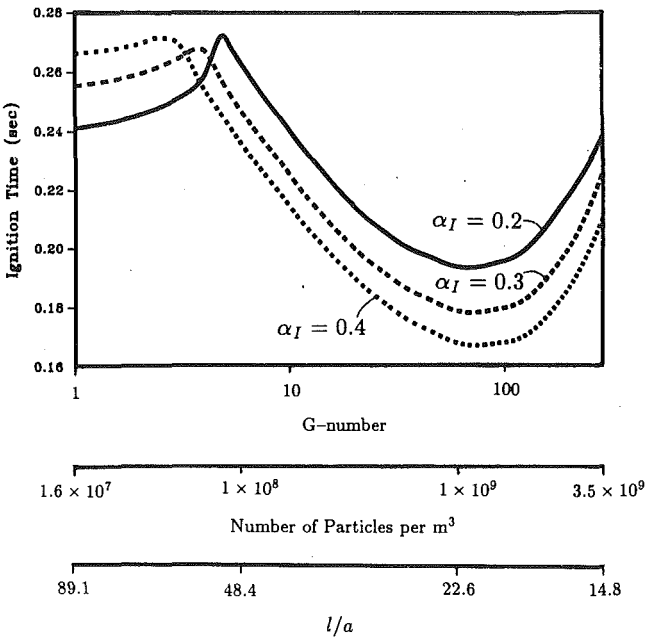

Fig. 7 Effect of volatile matter on ignition time

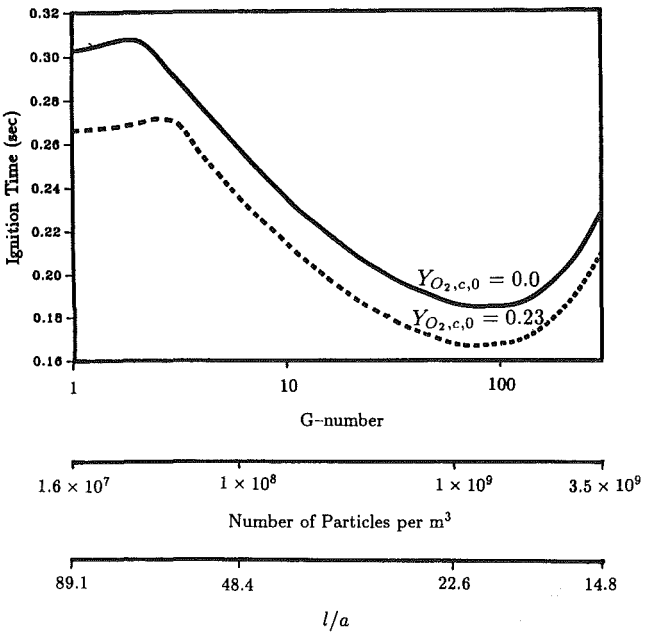

Fig. 8 Effect of initial cloud gas phase oxygen mass fraction on ignition time

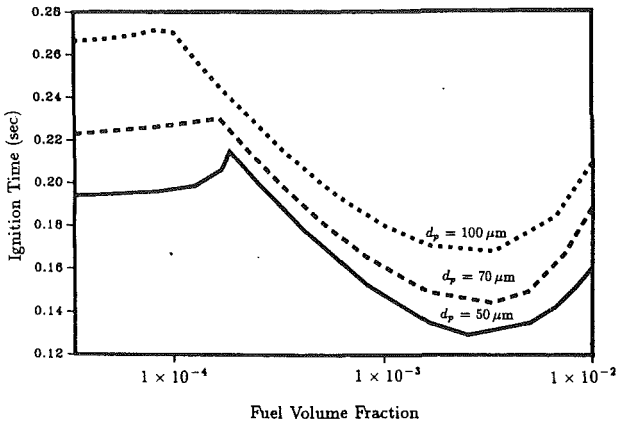

Fig. 9 Effect of particle diameter on ignition time

4.6 Effect of Volatile Matter. Figure 7 shows the variation of ignition time as a function of G number for three different values of proximate volatile matters. For low G numbers (heterogeneous ignition, Regime I), ignition time increases with increasing proximate volatile matter. This result stems from increased heat required to completely pyrolyze the particles at the cloud surface in order to ignite the cloud heterogeneously. Also, as the proximate volatile matter decreases, the size of heterogeneous ignition region increases as expected. At higher G numbers (homogeneous ignition, Regimes II and III), increased proximate volatile matter results in decreased ignition time since the flammable mixture can be formed readily.

4.7 Effect of Initial Cloud Oxygen Concentration. Figure 8 shows the effect of initial cloud oxygen gas phase mass fraction on ignition time. When the initial cloud oxygen mass fraction is zero, the cloud gas phase initially consists of only inert gases. Although the G number corresponding to the transition from the heterogeneous to the homogeneous regime remains essentially unchanged, ignition time increases with decreasing oxygen mass fraction as expected. In the heterogeneous region, the increase in ignition time results from the additional time for oxygen to diffuse into the cloud and reach the particles. However, in the homogeneous region, the increase is less significant since volatiles ignite outside the cloud in the oxygen rich ambience. Thus, ignition time increases more rapidly in the heterogeneous region than in the homogeneous region as the initial cloud oxygen mass fraction is decreased.

4.8 Effect of Particle Diameter. Figure 9 shows the effect of particle diameter on ignition time in both the heterogeneous and homogeneous ignition regimes. Since fuel volume fraction was used as the independent variable (abscissa), Fig. 9 shows the effect of increased pulverization at the same cloud fuel mass loading. Ignition time decreases with decreasing particle diameter. A single particle analysis would predict ignition time increasing in proportion to (diameter)^2. However, the rate of increase of ignition time with particle diameter is less under cloud conditions since the thermal penetration time into the cloud forms a significant proportion of the ignition time. It is also noted that the fuel volume fraction at which ignition time is a minimum is almost independent of the particle size for the range of particle sizes considered. Since the effect of particle diameter is more significant in the heterogeneous region, this suggests that low VM particles should be pulverized to a greater extent to obtain desirable ignition characteristics than high VM particles.

4.9 Effect of Cloud Radius. Figure 10 shows that the cloud radius is one of the significant parameters in reducing ignition time since it reduces the thermal wave penetration time. As the cloud radius is reduced the temperature gradient surrounding the cloud increases (quasi-steady theory shows that temperature gradient is proportional to R_c^{-1}). Thus, not only does the cloud heat faster, but higher temperatures exist closer to the cloud resulting in homogeneous ignition closer to the cloud surface. Since volatiles don't have as far to diffuse to ignite, the homogeneous region extends to lower G numbers for smaller cloud radii.

4.10 Ignition Temperature. The steady-state analysis of single char particles and measurements shows the ignition temperatures to be 1050 K to 1200 K (Bandyopadhyay and Bhaduri,

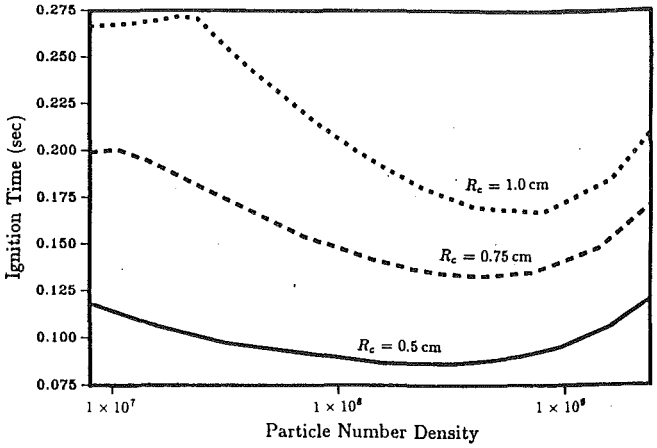

Fig. 10 Effect of cloud radius on ignition time

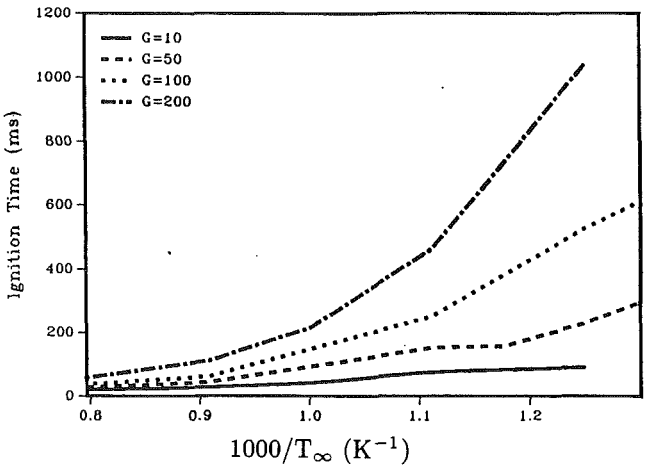

Fig. 12 Variation of ignition time with reciprocal temperature for an initially hot cloud (gas phase) with heat sink due to particles

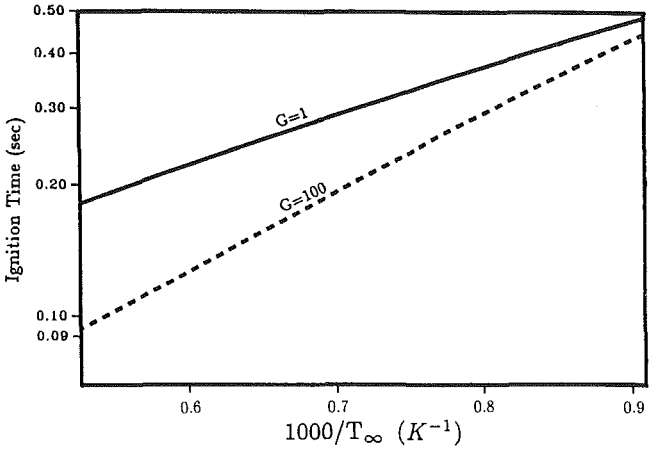

Fig. 11 Variation of ignition time with reciprocal temperature for an initially cold cloud

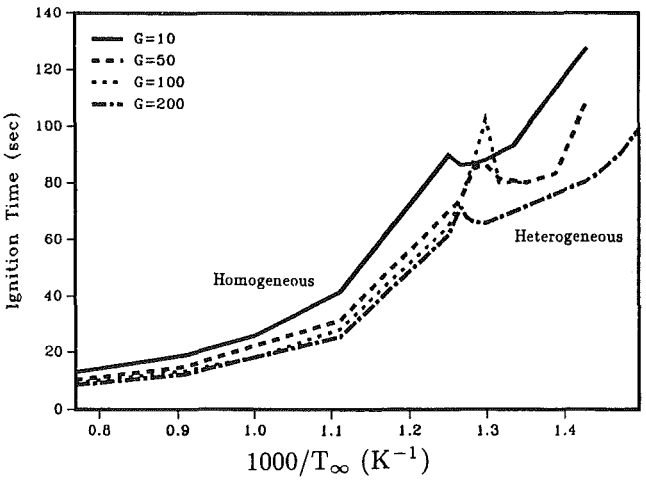

Fig. 13 Variation of ignition time with reciprocal temperature for an initially hot cloud (gas phase) without heat sink due to particles

1972). On the other hand, experiments conducted on coal and char particles using a TGA apparatus (Tognotti et al., 1985) and the Cassel and Liebman technique (Chen et al., 1984) show that ignition temperatures of particle clouds are in the range of 650 K to 700 K. In order to study the effect of interactions on the ignition temperature, the following cases were studied.

4.10.1 Initially Cold Cloud. Figure 11 presents results for ignition time with reciprocal temperature for an initially cold cloud. This plot seems to suggest an Arrhenius type law for ignition time for both heterogeneous ($G = 1$) ignition and homogeneous ($G = 100$) ignition of a cloud of coal particles. Consider a reactor into which a stationary cold cloud (gas phase and particles) is introduced. If the experimental duration is 0.2s, then from Fig. 11, ignition occurs at $T_\infty = 1800$ K for $G = 1.0$ and at $T_\infty = 1400$ K for $G = 100$. On the other hand if the experimental duration is 0.4 s, ignition occurs at $T_\infty = 1300$ K for $G = 1$ and $T_\infty = 1050$ K for $G = 100$. Thus, ignition temperature is dependent on the residence time of the cloud within the reactor. It should not be construed that ignition temperature for an initially cold cloud decreases monotonically with particle number density. In fact, as G is increased to large values ($G \gg 100$) ignition temperature for a given experimental duration time may increase (see Fig. 6).

4.10.2 Initially Hot Cloud. Now consider a hot cloud (gas phase) containing initially cold particles introduced into a furnace. As the cloud falls downward through the furnace, two extremes exist. In the first extreme, the cloud carries gas that was initially present in the cloud downward with it. This gas contributes some of its enthalpy to heat the particles within the cloud and as such the cloud gas phase temperature decreases. The extent of this decrease is dependent on the mass loading of particles within the cloud. In the other extreme, none of the gas phase within the cloud travels downward with the particles and the gas phase within the cloud is continually replaced with hot gases from the reactor.

The first extreme was modeled by setting the initial cloud gas phase temperature equal to the ambient temperature, while the particle temperature is initially 300 K. Figure 12 shows the results for ignition time with inverse ambient temperature. Ignition time increases as the cloud denseness (G number) increases since the increased mass loading lowers the temperature of the cloud more for higher mass loadings than for lower mass loadings. The second extreme was modeled by setting the gas phase heat sink due to the presence of the particles ($\dot{q}'''_{conv}$) equal to zero; thus the gas phase temperature within the cloud does not decrease due to the presence of the particles. Figure 13 shows the variation of ignition time with reciprocal temperature for various values of G number. It is seen that ignition time decreases with increased mass loading at constant temperature. For high temperatures, homogeneous ignition occurs, while for low temperatures, heterogeneous ignition occurs since the temperature drops below that required for significant pyrolysis to occur.

4.11 Experimental Data. While the geometry and physics

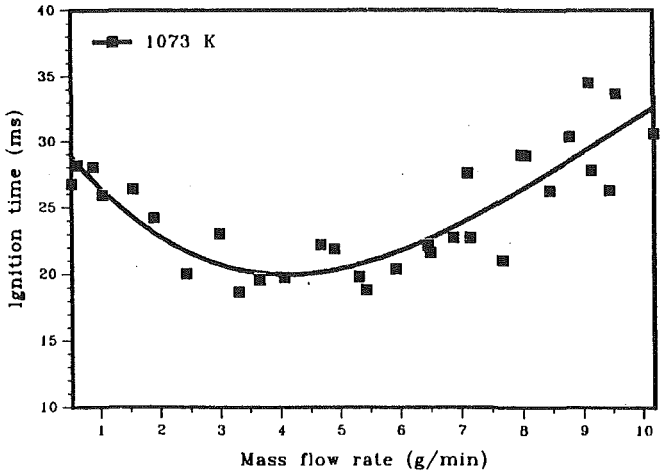

Fig. 14 Experimental variation of ignition time with coal mass using a laminar flow reactor

of the model in the current work are highly simplified (spherical geometry, no turbulence, etc.) some comparisons with experimental results can be made; however, these comparisons are only qualitative and should be viewed as such.

Ruiz and Annamalai (1990) conducted experiments in a laminar flow reactor at a temperature of 1073 K using cylindrical clouds of pulverized coal particles to determine the flame standoff distance from the injector. These results were translated into ignition times by dividing the flame standoff distance by the gas flow velocity. Their results show a minimum in ignition time as the coal loading is varied with the reactor temperature fixed (Fig. 14) in agreement with the model predictions. Chen et al. (1984) used the Cassel and Liebman technique (1959) to determine the ignition temperatures of char and coal particles. These experiments involve dropping a small sample of coal into a hot reactor with gases flowing upward such that the particles are suspended in the flow. Their results seem to suggest that the ignition temperature of a cloud of particles is lower than that of a single particle. This agrees qualitatively with the results shown in Fig. 13.

5 Summary

1 A group ignition model is presented for a cloud of coal particles that accounts for pyrolysis, and heterogeneous and homogeneous reactions.

2 Results reveal heterogeneous ignition for dilute clouds and homogeneous ignition for dense clouds.

3 Ignition time increases as the number of particles per unit volume is increased from the dilute limit (heterogeneous ignition, Regime I). Once homogeneous ignition occurs, ignition time initially decreases as the mass loading is increased (Regime II) and then increases again once the cloud becomes very dense (Regime III). Thus, a minimum is observed in ignition time for a particular mass loading.

4 Parametric studies reveal that while heterogeneous ignition time decreases with an increase in initial cloud oxygen mass fraction, the decrease is not as significant for homogeneous ignition.

Acknowledgments

This material was prepared with the support of the U.S. Department of Energy, Grant No. DE-FG 22-88 PC 88937, and the Center for Energy and Mineral Resources (CEMR) of the State of Texas. However any findings, conclusions, or recommendations expressed herein are those of the authors and do not necessarily reflect the views of the DOE or CEMR.

References

Annamalai, K., and Durbetaki, P., 1976, "Ignition of Thermally Thin Porous Pyrolyzing Solids Under Normally Impinging Flames," *Combustion and Flame*, Vol. 27, pp. 253–266.

Annamalai, K., and Durbetaki, P., 1977, "A Theory on Transition of Ignition Phase of Coal Particles," *Combustion and Flame*, Vol. 29, pp. 193–208.

Annamalai, K., Madan, A., and Mortada, Y. I., 1984, "Ignition of a Cloud of Droplets," presented as the ASME Winter Annual Meeting, New Orleans, LA, Paper No. 84-WA/HT-18.

Annamalai, K., and Ramalingam, S., 1987, "Distinctive Burning Characteristics of Carbon Particles," *Combustion and Flame*, Vol. 70, pp. 307–332.

Annamalai, K., Ramalingam, S., Dahdah, T., and Chi, D., 1988a, "Group Combustion of a Cylindrical Cloud of Char Particles," ASME JOURNAL OF HEAT TRANSFER, Vol. 110, pp. 190–200.

Annamalai, K., Ramalingam, S. C., and Ryan, W. R., 1988b, "Group Combustion of Coal Particles," Annual Report No. 2, PETC/DOE, Pittsburgh, PA.

Bandyopadhyay, S., and Bhaduri, D. B., 1972, "Prediction of Ignition Temperature of a Single Coal Particle," *Combustion and Flame*, Vol. 18, pp. 411–415.

Bellan, J., and Cuffel, R., 1983, "A Theory of Non-dilute Spray Evaporation Based Upon Multiple Drop Interactions," *Combustion and Flame*, Vol. 51, pp. 55–67.

Bellan, J., and Harstad, K., 1987a, "Analysis of the Convective Evaporation of Nondilute Clusters of Drops," *International Journal of Heat and Mass Transfer*, Vol. 30, pp. 125–136.

Bellan, J., and Harstad, K., 1987b, "Ignition of Non Dilute Clusters of Drops in Convective Flows," *Combustion Science and Technology*, Vol. 53, pp. 75–87.

Bellan, J., and Harstad, K., 1988, "Turbulence Effects During Evaporation of Drops in Clusters," *International Journal of Heat and Mass Transfer*, Vol. 31, pp. 1655–1668.

Bellan, J., and Harstad, K., 1990, "Evaporation, Ignition, and Combustion of Nondilute Cluster of Drops," *Combustion and Flame*, Vol. 79, pp. 272–286.

Bradley, D., Dixon-Lewis, G., and Habik, E., 1989, "Lean Flammability Limits and Laminar Burning Velocities of CH_4–Air–Graphite Mixtures and Fine Coal Dusts," *Combustion and Flame*, Vol. 77, pp. 41–50.

Carnahan, B., Luther, H. A., and Wilkes, J. O., 1969, *Applied Numerical Methods*, Wiley, New York.

Cassel, H. M., and Liebman, I., 1959, "The Cooperative Mechanisms in the Ignition of Dust Dispersions," *Combustion and Flame*, Vol. 3, pp. 467–475.

Chen, M. R., Fan, L. S., and Essenhigh, R. H., 1984, "Prediction and Measurement of Ignition Temperature of Coal Particles," *Twentieth Symposium (International) on Combustion*, pp. 1513–1519.

Chiu, H. H., and Liu, T. M., 1977, "Group Combustion of Liquid Droplets," *Combustion Science Technology*, Vol. 17, pp. 127–142.

Correa, S. M., and Sichel, M., 1982, "The Group Combustion of a Spherical Cloud of Monodisperse Fuel Droplets," *Nineteenth Symposium (International) on Combustion*, pp. 981–991.

Essenhigh, R. H., 1963, "The Influence of Coal Rank on the Burning Times of Single Captive Particles," ASME *Journal of Engineering for Power*, Vol. 85, pp. 183–190.

Essenhigh, R. H., Misra, M. K., and Shaw, D. W., 1989, "Ignition of Coal Particles: A Review," *Combustion and Flame*, Vol. 77, pp. 3–30.

Golovina, E. S., and Khaustovich, G. P., 1962, "The Interaction of Carbon With Carbon Dioxide and Oxygen at Temperature up to 3000 K," *Eighth Symposium (International) on Combustion*, pp. 784–792.

Hamor, R. J., Smith, I. W., and Taylor, R. J., 1973, "Kinetics of Combustion of Pulverized Brown Coal Char Between 630 and 2200 K," *Combustion and Flame*, Vol. 21, pp. 153–162.

Howard, J. B., and Essenhigh, R. H., 1967, "Pyrolysis of Coal Particles in Pulverized Fuel Flames," *Industrial Engineering Chemical Process Design and Development*, Vol. 6, pp. 74–84.

Howard, J. B., Williams, G. C., and Fine, D. H., 1973, "Kinetics of Carbon Monoxide Oxidation in Postflame Gases," *Proceedings 14th Symposium (International) on Combustion*, Combustion Institute, Pittsburgh, PA, pp. 975–986.

Kimber, G. M., and Gray, M. D., 1971, "Reaction Rates of Charcoal and Coal Char With Oxidizing Gases at 1800–2800 K," *3rd Conference on Industrial Carbon and Graphite*, London, pp. 278–298.

Krishna, C. R., and Berlad, A. L., 1980, "A Model for Dust Cloud Autoignition," *Combustion and Flame*, Vol. 37, pp. 207–210.

Kurylko, L., and Essenhigh, R. H., 1973, "Steady and Unsteady Combustion of Carbon," *Fourteenth Symposium (International) on Combustion*, pp. 1375–1386.

Lester, T. W., Seeker, W. R., and Merklin, J. F., 1981, "The Influence of Oxygen and Total Pressure on the Surface Oxidation Rate of Bituminous Coal," *Eighteenth Symposium (International) on Combustion*, The Combustion Institute, pp. 1257–1265.

LeMott, S. R., Peskin, R. L., and Levine, D. G., 1971, "Effect of Fuel Molecular Weight on Particle Ignition," *Combustion and Flame*, Vol. 16, pp. 17–27.

Midkiff, K., Altenkirch, R., and Peck, R., 1986, "Stoichiometry and Coal Type Effects on Homogeneous vs. Heterogeneous Combustion in Pulverized Coal Flames," *Combustion and Flame*, Vol. 64, pp. 253–267.

Niksa, S., Mitchell, R. E., Hencken, K. R., and Tichenor, D. A., 1986,

"Optically Determined Temperatures, Sizes, and Velocities of Individual Carbon Particles Under Typical Combustion Conditions," *Combustion and Flame*, Vol. 60, pp. 183–193.

Ragaland, K. W., and Yang, J. T., 1985, "Combustion of Millimeter Sized Coal Particles in Convective Flow," *Combustion and Flame*, Vol. 60, pp. 285–297.

Rumanov, E. N., and Khalkin, B. I., 1969, "Critical Autoignition Conditions for a System of Particles," *Combustion, Explosion and Shockwaves*, Vol. 5, pp. 129–136.

Ruiz, M., Annamalai, K., and Dahdah, T., 1990, "An Experimental Study on Group Ignition of Coal Particle Streams," *Heat and Mass Transfer in Fires and Combustion Systems*, W. L. Grosshandler and H. G. Semerjian, eds., ASME HTD Vol. 148, pp. 19–26.

Ryan, W., 1988, "Group Pyrolysis, Ignition, and Combustion of a Spherical Cloud of Coal Particles," Masters Thesis, Texas A&M University, College Station, TX.

Ryan, W., and Annamalai, K., 1990a, "Group Combustion of a Cloud of Coal Particles," presented as the Central States Section, The Combustion Institute, Paper #90-50.

Ryan, W., and Annamalai, K., 1990b, "Relation Between Group Combustion and Drop Array Studies," *Combustion and Flame*, Vol. 80, pp. 313–321.

Seeker, W. R., Wegenter, D. C., Lester, T. W., and Merklin, J. F., 1979, "Single Pulse Shock Tube Studies of Pulverized Coal Ignition," *Seventeenth Symposium (International) on Combustion*, pp. 155–166.

Smith, I. W., 1971, "Kinetics of Combustion of Size Graded Pulverized Fuels in the Temperature Range 1200–2270 K," *Combustion and Flame*, Vol. 17, pp. 303–314.

Stickler, D. B., Gannon, R. E., and Kobayashi, H., 1974, "Rapid Devolatization Modeling of Coal," presented at the Eastern Section of the Combustion Institute, Silver Srpings, MD.

Tognotti, L., Malotti, A., Petarce, L., and Zanetti, S., 1985, "Measurement of Ignition Temperature of Coal Particles Using Thermogravimetric Technique," *Combustion Science and Technology*, Vol. 44, pp. 15–28.

Ubhayakar, S. K., Sticker, D. B., Von Rosenberg, C. W., and Gannon, R. E., 1977, "Rapid Devolatization of Pulverized Coal in Hot Combustion Gases," *16th Symposium (International) on Combustion*, The Combustion Institute, pp. 427–436.

Wall, T. F., 1987, "Principles of Combustion Engineering for Boilers," C. K. Law, ed., Chap. 3, Academic Press, NY.

Buoyancy, Soret, Dufour, and Variable Property Effects in Silicon Epitaxy

R. L. Mahajan

C. Wei[1]

AT&T Bell Laboratories,
Princeton, NJ 08540

In most of the previous numerical and semi-analytical studies of silicon epitaxial deposition, a common practice has been to neglect the buoyancy flow, Dufour, Soret, and property variation effects. In this paper, we take a critical look at the validity of that approach and point out some fallacies. The geometric configuration studied is a horizontal reactor for the susceptor tilt angles of 0 and 2.9 deg. The full Navier–Stokes equations coupled with those for the energy and species transfer are solved numerically for a range of parameters typical of commercial silicon epitaxial deposition systems. The effects of ignoring terms due to buoyancy, Dufour, Soret, and variable properties on the mass transfer rate are systematically evaluated. The results indicate that for typical horizontal epitaxial deposition parameters, the buoyancy and Dufour effects have negligible effect on the mass transfer rate, while the Soret and property variation have a large impact. In light of this information, it is shown that the agreement reported in the past between the experimental and numerical/analytical studies is coincidental. The implication is that these assumptions must be critically examined for a given CVD system and not ignored a priori. Finally, the effects of important parameters—reactor height, inlet velocity, inlet concentration, and susceptor temperature—on the deposition characteristics are included to provide guidelines for controlling the epitaxial layer thickness and uniformity.

1 Introduction

The epitaxial growth of silicon by chemical vapor deposition (CVD) techniques is widely used in the production of a variety of solid-state device structures, including discrete bipolar transistors, junction field-effect transistors, dynamic random access memory (DRAM) devices, and complimentary metal-on-oxide (CMOS) integrated circuits (ICs). This is primarily due to the flexibility that the epitaxial layers provide to the designer to grow the doping profile in a controlled manner. In some circuits such as DRAM and CMOS, devices could be fabricated in bulk wafers. However, epitaxy provides essentially noise-free substrates that improve latch-up, near-surface impurity gettering, oxygen confinement, and increased trench capacitance; see Pearce (1983).

An important consideration in the epitaxial growth is the uniformity of layer thickness. Much experience has been accumulated over the years to improve the growth processes. Eversteyn et al. (1970) conducted epitaxial growth experiments and studied the effect of substrate tapering angle on film uniformity in a horizontal reactor. Also, they proposed a stagnation layer model to explain their experimental data. Following Eversteyn's work, several researchers (Takahashi et al., 1972; Berkman et al., 1978; Coltrin et al., 1984, 1986; Ristorcelli and Mahajan, 1987; Moffat and Jensen, 1988) have used analytical or numerical models to investigate epitaxial growth in horizontal reactors.

In the analytical studies by Eversteyn et al. (1970) and Berkman et al. (1978), constant physical properties are assumed and buoyancy, Soret (thermo-diffusion), and Dufour (diffusion-thermo) effects are neglected. The deposition rates obtained from these analyses are in fairly good agreement with the experimental data. As for the numerical studies, there are two-dimensional and three-dimensional models in the literature. In the two-dimensional model by Ristorcelli and Mahajan (1987), the variations of physical properties, Soret, and Dufour effects are neglected and the predicted growth rates show good agreement with the experimental data. Coltrin et al. (1984) considered gas phase and surface chemical reactions, the variation of physical properties, and buoyancy effect in their two-dimensional model; however, they did not include Soret and Dufour effects. The predicted growth rates agree with Eversteyn's experiments. Later, Coltrin et al. (1986) refined their model by adding Soret effect and found that at low temperatures (550–750° C), the addition of Soret effect reduces growth rates by about 50 percent. It can be inferred that had they included Soret effect in their earlier work (1984), disagreement between the predictions and experimental data would be quite significant. Assuming gas flow is fully developed in axial direction, Takahashi et al. (1972) computed two-dimensional velocity and temperature profiles and a three-dimensional concentration profile. Their model assumes constant physical properties and neglects Soret and Dufour effects. No comparison with experimental data is given. In a numerical study, Moffat and Jensen (1988) investigated three-dimensional flow effects in silicon CVD horizontal reactors. The buoyancy, Soret, and variation of physical properties were included. However, they provide no comparison of their results with the experimental data.

Clearly, in the modeling of silicon epitaxial growth, there are inconsistencies in the treatment of the effects of buoyancy, Soret, Dufour, and the variation of physical properties and discrepancies exist in the calculated growth rates. In this paper, we apply a two-dimensional finite element model to investigate systematically these effects and compare the computed growth rates with Eversteyn's experiments.

2 Mathematical Model

The physical parameters and dimensions used here are similar to those of Eversteyn (1970). A schematic diagram of the horizontal reactor is given in Fig. 1. The reactor consists of an entrance region, a deposition region and an exit region. The reactor height at the entrance (h) is 2.05 cm. The lengths of

[1]Current address: Bristol-Myers Squibb, New Brunswick, NJ 08903.

Contributed by the Heat Transfer Division for publication in the JOURNAL OF HEAT TRANSFER. Manuscript received by the Heat Transfer Division August 28, 1990; revision received January 17, 1991. Keywords: Materials Processing and Manufacturing Processes.

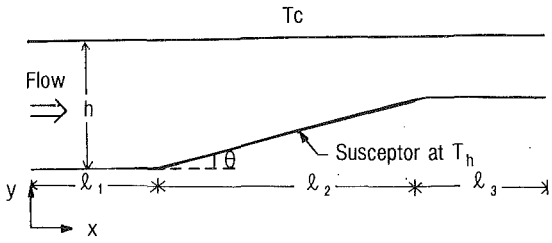

Fig. 1 Reactor schematics

the entrance region (l_1), the deposition region (l_2), and the exit region (l_3) are 14 cm, 30 cm, and 20 cm, respectively. The top wall of the reactor is flat, whereas the substrate on the bottom wall is either flat or tapered at 2.9 deg. The temperature at the top wall is set at 300 K, which is also the gas temperature at the inlet. The substrate is assumed heated to 1323 K or 1350 K, for $\theta = 0$ and 2.9 deg, respectively, corresponding to the experimental conditions of Eversteyn et al.; see Table 1. The entrance and exit regions are thermally insulated. The precursor is silane (SiH_4) and the carrier gas is atmospheric pressure hydrogen. Gas flow rates and inlet reactant concentration are given in Table 1.

Note that the reactant concentration is very small. The bulk flow is treated as though it were composed only of hydrogen (typically > 97 percent). We also assume that silicon deposition is diffusion-limited. This assumption has been employed in previous studies of Eversteyn et al. (1970), Takahashi et al. (1972), Berkman et al. (1978), and Ristorcelli and Mahajan (1987), and experimentally validated by the kinetic studies of Bloem and Giling (1985) at high temperature and atmospheric pressure conditions.

For a steady-state nonreacting process, two-dimensional momentum, continuity, and mass transfer and energy equations can be written as follows:

Momentum equation in x direction:

$$\rho\left(u\frac{\partial u}{\partial x}+v\frac{\partial u}{\partial y}\right)=-\frac{\partial p}{\partial x}+\frac{\partial}{\partial x}\left(2\mu\frac{\partial u}{\partial x}-\frac{2}{3}\mu\nabla\cdot\mathbf{v}\right)+\frac{\partial}{\partial y}\left[\mu\left(\frac{\partial u}{\partial y}+\frac{\partial v}{\partial x}\right)\right]+\rho g_x \quad (1)$$

Table 1 Reactor parameters for two experimental cases

Substrate tapering angle	u_o, cm/s	p_{silane}, dyne/cm^2	T_h, K
0 deg	17.5	1241	1323
2.9 deg	34.0	639	1350

Momentum equation in y direction:

$$\rho\left(u\frac{\partial v}{\partial x}+v\frac{\partial v}{\partial y}\right)=-\frac{\partial p}{\partial y}+\frac{\partial}{\partial x}\left[\mu\left(\frac{\partial u}{\partial y}+\frac{\partial v}{\partial x}\right)\right]+\frac{\partial}{\partial y}\left(2\mu\frac{\partial v}{\partial y}-\frac{2}{3}\mu\nabla\cdot\mathbf{v}\right)+\rho g_y \quad (2)$$

where ρ denotes gas density, u the velocity component in the x direction, v the velocity component in the y direction, p pressure, and μ viscosity. Also, $\mathbf{v} = (u, v)$, and g_x and g_y are gravity components in the x and y directions, respectively.

Continuity equation:

$$\frac{\partial}{\partial x}(\rho u)+\frac{\partial}{\partial y}(\rho v)=0 \quad (3)$$

Mass transfer equation:

$$Cu\frac{\partial x_1}{\partial x}+Cv\frac{\partial x_1}{\partial y}=-\frac{\partial J_{1x}}{\partial x}-\frac{\partial J_{1y}}{\partial y} \quad (4)$$

where C denotes molar concentration and x_1 the mole fraction of silane. J_{1x} and J_{1y} are the x and y components of the molar flux, $\mathbf{J}_1$, which, driven by both concentration gradient (molecular diffusion) and temperature gradient (Soret effect), is given by

$$\mathbf{J}_1=-CD\nabla x_1-CD\alpha x_1(1-x_1)\nabla \ln T. \quad (5)$$

Here, D is the diffusion coefficient of silane in hydrogen and α is the thermal diffusion factor. For derivation of the expression, the reader is referred to Baron (1962), Hirschfelder et al. (1954) and Grew and Ibbs (1952).

Energy equation:

$$\rho c_p\left(u\frac{\partial T}{\partial x}+v\frac{\partial T}{\partial y}\right)=-\frac{\partial q_x}{\partial x}-\frac{\partial q_y}{\partial y} \quad (6)$$

where c_p denotes the heat capacity and T the temperature, and

Nomenclature

C = molar concentration
C' = dimensionless molar concentration = C/C_o
c_p = heat capacity
D = diffusion coefficient
g = gravity
Gr = Grashof number = $g\beta(T_h-T_c)h^3/\nu^2$
Gr_x = local Gr based on downstream distance x
h = reactor height
$\mathbf{J}$ = molar flux
k = thermal conductivity
l = length
M = molecular weight
$\dot{m}$ = growth rate of monocrystalline silicon
p = pressure
p_{silane} = partial pressure of silane at inlet
Pr = Prandtl number = $\mu c_p/k$
$\mathbf{q}$ = heat flux
Ra = Rayleigh number = GrPr
R = gas constant
Re = Reynolds number = uh/ν
Re_x = local Re based on downstream distance x
$\mathbf{T}$ = stress tensor
T = temperature
T' = dimensionless temperature = $(T-T_c)/(T_h-T_c)$
u = velocity component in x direction
v = velocity component in y direction
x, y = Cartesian coordinates
x_1 = mole fraction of component 1
α = thermal diffusion factor
β = volumetric coefficient of thermal expansion
θ = substrate tapering angle
κ = thermal diffusivity
μ = dynamic viscosity
ν = kinematic viscosity
ρ = density
ψ = stream function
ψ' = normalized stream function = $\psi/\psi_{\max}$

Subscripts

c = cold wall
f = film or average value
h = hot susceptor
o = reference value
t = total

q_x and q_y are the x and y components of the thermal flux $\mathbf{q}$, given by

$$\mathbf{q} = -k\nabla T + \alpha RT\frac{M}{M_2}\mathbf{J}_1 \tag{7}$$

where k is the thermal conductivity, R the gas constant, M the averaged molecular weight, and M_2 is the molecular weight of hydrogen. In Eq. (7), the first term is the heat flux due to conduction and the second term is the contribution due to Dufour effect. For derivation of this equation, see Baron (1962).

Over the range of room to the susceptor temperature, the variation in the transport properties of hydrogen is significant and must be taken into account. For example, from 300 K to 1333 K, thermal conductivity, k, and absolute viscosity, μ, increase by factors of 2.85 and 2.73, respectively; see Eckert and Drake (1972). Appropriate expressions for ρ, μ, k, of hydrogen, and for D, diffusion of silane in hydrogen, as a function of temperature, are as follows:

$$\rho = \frac{pM}{RT} \tag{8}$$

$$\frac{\mu}{\mu_0} = \left(\frac{T}{T_0}\right)^{0.648} \tag{9}$$

$$\frac{k}{k_0} = \left(\frac{T}{T_0}\right)^{0.691} \tag{10}$$

$$\frac{D}{D_0} = \left(\frac{T}{T_0}\right)^{1.75} \tag{11}$$

The power law expressions in Eqs. (9) and (10) are taken from Moffat and Jensen (1988), and are valid over the whole range of temperature in the epi reactor. Equation (11) is derived from the Fuller correlations; see Reid et al. (1987). Note a sharp dependence of D on T; from 300 K to 1323 K, it increases by a factor of ≈ 13. Experimental values of viscosity and thermal conductivity at the reference temperature, 300 K, are used here; they are $\mu_0 = 8.963 \times 10^{-5}$ poise and $k_0 = 0.182 \times 10^5$ erg/s/cm/K; see Eckert and Drake [1972]. The reference diffusivity is calculated from the Fuller correlation assuming that the atomic diffusion volume of silicon is identical to that of argon. The calculation gives $D_0 = 0.698$ cm^2/s. The values of thermal diffusion factor, α, for silane in hydrogen are 0.54, 0.69, 0.74, 0.78, and 0.79 at 300 K, 500 K, 700 K, 900 K, and 1100 K, respectively; see Holstein (1988).

The boundary conditions for the differential equations are listed below:

At $x=0$; $0<y<h$

$$u = 6u_0[y/h - (y/h)^2];\ v=0;\ T=T_c;\ x_1=x_0 \tag{12}$$

At $0\le x<l_1$; $y=0$

$$u=0;\ v=0;\ q_y=0;\ J_{1y}=0 \tag{13}$$

At $l_1\le x\le l_1+l_2$; $y=(x-l_1)\tan\theta$

$$u=0;\ v=0;\ T=T_h;\ x_1=0 \tag{14}$$

At $l_1+l_2<x\le l_t$; $y=l_2\tan\theta$

$$u=0;\ v=0;\ q_y=0;\ J_{1y}=0 \tag{15}$$

At $0\le x\le l_t$; $y=h$

$$u=0;\ v=0;\ T=T_c;\ J_{1y}=0 \tag{16}$$

At $x=l_t$; $l_2\tan\theta<y<h$

$$\mathbf{n}\cdot\mathbf{T}=0;\ q_x=0;\ J_{1x}=0 \tag{17}$$

where l_t represents the length of the reactor and $\mathbf{T}$ is the stress tensor. The condition $x_1=0$ in Eq. (14) implies that surface reaction is much faster than the diffusion of silane to the hot surface.

Noting that $x_1=0$ at the susceptor, the growth rate of monocrystalline silicon on the substrate surface, $\dot{m}$, can be derived from Eq. (5) and is given by:

$$\dot{m} = -\frac{M_{\mathrm{Si}}CD}{\rho_{s,\mathrm{Si}}}\nabla x_1|_{\mathrm{s.s.}} \tag{18}$$

where M_{Si} is the molecular weight of Si and $\rho_{\mathrm{s,Si}}$ is the density of solid silicon.

3 Finite Element Method

In the Galerkin finite method, Zienkiewicz (1979),the irregular physical domain is divided into subdomains, called elments. Here we have 280 elements in the x direction and 10 elements in the y direction. Variable mesh size is used. In the regions of steep gradients, near the susceptor ($y=0$), and close to the leading edge ($x=l_1$), mesh size is more refined. The dependent variables are approximated locally over each element by basis functions that are low-order polynomials. Here, biquadratic basis functions are used for velocity, temperature, and partial pressure, and three-node linear basis functions are used for pressure. The governing differential equations are multiplied by the basis functions and integrated over the physical domain. To facilitate area integration, isoparametric transformation is used to map the irregular elements to square elements. The resulting algebraic equations, most of them nonlinear, are then linearized by the Newton–Raphson method. A modified version of the frontal matrix solver by Hood (1977) is applied to obtain v, p, T, x_1. The convergence criterion is that the absolute value of the difference of each dependent variable between consecutive iterations is $\le 10^{-10}$. The growth rates along the substrate surface are computed with a method similar to that given by Marshal et al. [1978] for heat flux computations. The sensitivity of the growth rates to grid spacing is tested by reducing the element number in the y direction to 5 and that in the x direction to 140. For the two cases listed in Table 1, no visible difference ($< \approx 1$ percent) is found between the growth rates using the two grids.

4 Results and Discussion

Before presenting any computational results, it should be noted that the two-dimensional analysis is in principle only valid for describing the transport between two plates of infinite width. In the epitaxial reactor considered here, typical of production reactors, presence of the side walls may induce buoyancy-induced rolls resulting in a three-dimensional flow. A pertinent question is: Under what conditions can the two-dimensional analysis predict accurately the silicon layer deposition in production reactors?

First, for the base case considered here corresponding to the experimental conditions of Eversteyn et al. (1970), the Rayleigh number is only 209. For low values of Ra, Giling's (1982) holograms in a horizontal epitaxial reactor showed the isotherms to be perfectly parallel to the susceptor. The gas flow patterns were found to be stable, indicating negligble effects of buoyancy-induced motion. A Rayleigh number limit of 1708 was indicated for the onset of buoyancy-induced motion. Houtman et al. (1985), on the other hand, observed vortex motions at values of Ra <1708. These motions, however, did not affect temperature distributions because of the high thermal conductivity of the hydrogen gas. Van de Ven et al. (1986) in their experimental study of epitaxial growth of gallium arsenide in horizontal MOCVD (Metal-Organic Chemical Vapor Deposition) addressed the issue of buoyancy-induced convective rolls. On the basis of their measurements of velocity and thickness of the deposited layer, they concluded that at low Ra, even if the buoyancy-induced convective motions are present, they do not affect the mass transfer.

Moffat and Jensen (1986) obtained three-dimensional numerical simulations of flow in a horizontal MOCVD reactor.

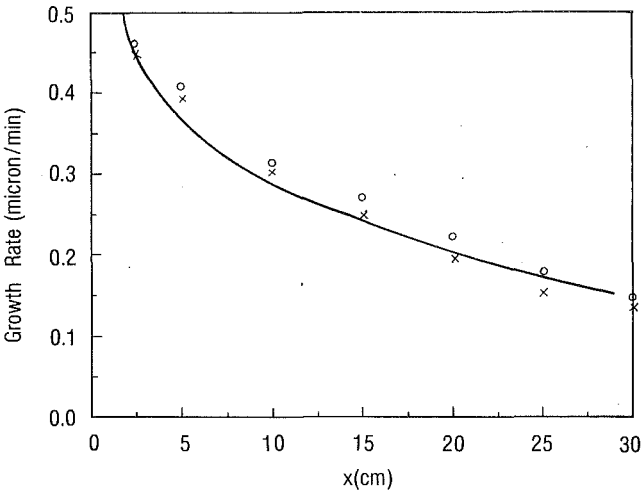

Fig. 2 Comparison of present results to those in the literature for θ = 0 deg; for other reactor parameters, see Table 1; xxx, Everstyn et al. (1970); ooo, Ristorcelli and Mahajan (1987); -, present work

Buoyancy-driven secondary flows were included. The side walls were assumed either insulated or kept cooled to the top wall temperature. For fully developed flow in a reactor with insulated side walls, the computations showed that the buoyancy-driven rolls did not develop for Ra $\approx$ 2000. For a reactor with cooled side walls, buoyancy-induced rolls developed at much lower Ra. However, even in this case, for reactors with smaller cross-section aspect ratio (height/width), a comparison of both the two-dimensional and three-dimensional computations with the experimental results of Van de Ven et al. (1986) showed very good agreement with experimental growth rates. It was concluded that the effects of buoyancy-driven flow are absent in the low cross-section aspect ratio reactors and that the two-dimensional and three-dimensional models produce very similar results.

Giling (1982) and Van de Ven et al. (1986) noted that the effect of buoyancy-induced motions at low Ra, if present, is felt toward the edges of the susceptor near the side walls. A solution to avoid nonuniform epitaxial deposition is then to place wafers away from the side walls. Giling recommends this distance to be equal to the height of the reactor. In commercial reactors, the intent of this recommendation is followed for achieving uniform deposition.

It is concluded from the above discussion that the two-dimensional analysis and results presented in this paper are applicable to the production epitaxial reactors.

Buoyancy, Soret, Dufour, and Variable Property Effects. To assess the validity of the various assumptions mentioned in Section 1 systematically, Eqs. (1)–(7) subject to boundary conditions (12)–(17) were solved for the following cases:

Case A: No buoyancy effect, no Dufour and Soret effects, and the transport properties are evaluated at the film temperature, $T_f = (T_h + T_c)/2$.

Case B: Same as A, with the buoyancy effects included.

Case C: Same as B, but with the Dufour and Soret effects included.

Case D: Same as C, and with the inclusion of the variable properties given in Eqs. (8)–(11).

Two susceptor tilt angles, θ = 0 and θ = 2.9 deg are considered. The results for the horizontal susceptor, θ = 0 deg, are presented first.

Horizontal Susceptor

Case A. Figure 2 shows the calculations for the deposition rate $\dot{m}$ versus x along with the experimental data of Eversteyn et al. (1970). The growth rate in their experiments was obtained by measuring both the time of growth and the thickness of the deposited layer. The accuracy in time measurement was ± 0.2 percent while that in thickness measurement was ± 0.5 percent. Thus, the maximum uncertainty in the experimental measurements of the deposition rate is $\approx \pm 0.7$ percent. The very good agreement seen in Fig. 2 between these experimental data and similar numerical results of Ristorcelli and Mahajan (1987) confirms the accuracy of the numerical scheme used here.

Case B: Buoyancy Effects. There have been several studies dealing with the buoyancy-induced flow in epitaxial deposition systems. The main consideration is: Under what flow circumstances does the buoyancy-induced flow start affecting the forced convection flow and deposition characteristics in a reactor?

For the flow adjacent to a vertical surface, of length L, Sparrow et al. (1959) suggested that for $Gr_x/Re_x^2 > 16$, the flow is buoyancy dominated; for $Gr_x/Re_x^2 < 0.3$, it is essentially forced flow; while for $16 > Gr_x/Re_x^2 > 0.3$, both buoyancy and forced flow are comparable. In a related numerical study, Sparrow and Gregg (1959) found that the effect of buoyancy on the local heat transfer coefficient is less than 5 percent if $Gr_x/Re_x^2 \leq 0.0075$. The effect on the average heat transfer coefficient was predicted to be within 5 percent of the forced flow results for $Gr_L/Re_L^2 \leq 0.225$. For horizontal boundary layer combined flows, analysis indicates that the parameter characterizing the relative vigor of buoyancy and forced flow is $Gr/Re^{2.5}$; see for example, Mori (1961), Sparrow and Minkowycz (1962), Hieber (1973), and Gebhart et al. (1988). Criteria similar to those for vertical flows are suggested.

Some of the earlier studies dealing with epitaxial deposition systems used the parameter Gr/Re^2 and the criteria proposed by Sparrow et al. (1959) to characterize the transition of flow from forced to mixed convection; see Takahashi et al. (1972), Hanzawa et al. (1977), and Ban (1978). Values of Gr/Re^2 ranging from 0.4 to 8.6 (0.4–4.1, Takahashi et al; 0.5, Ban; 0.8–8.6, Hanzawa et al.) were found to indicate the transition. This wide range in the transitional value of Gr/Re^2 suggests the inadequacy of the application of the parameter to epitaxial deposition systems, as has been demonstrated in the experiments of Giling (1982) and the numerical study of Moffat and Jensen (1988) for horizontal silicon epitaxy. In these studies no correlation was found between the flow characteristics and the parameter Gr/Re^2. Similar conclusions were drawn in the experimental study of Van De Ven (1986) in an MOCVD reactor.

The lack of correlation is not surprising, since the flow configuration in a horizontal reactor is quite different from the boundary layer flow over a vertical or even a horizontal surface. The classical Benard problem, of thermal instability of a layer enclosed between two infinite plates heated from below, is more likely a much closer representation of the reactor flow. The appropriate parameter, then, is Ra = GrPr, which for a fluid layer between two rigid horizontal surfaces has a value of 1708 for the onset of instability marked by longitudinal rolls; see Reid and Harris (1958, 1959). In this context, studies of Hwang and Cheng (1973) and Kamotani and Ostrach (1976) are pertinent. The former is a numerical investigation of the conditions for the onset of longitudinal vortex rolls due to buoyancy forces in the thermal entrance region of a horizontal parallel plate channel heated from below. The findings were that for Pr > 0.7, the theoretical value of Rayleigh number, Ra = GrPr = 1708, corresponding to the classical Benard problem, is a conservative estimate of the critical Rayleigh number. The opposite is true for Pr < 0.2. The experimental study of Kamotani and Ostrach for the same flow circumstance and for working fluid of air, Pr $\approx$ 0.7, indicated even higher values of Ra for onset of instability than predicted by the theoretical predictions of Hwang and Cheng.

Giling (1982), as mentioned earlier, used 1708 as the critical value of Rayleigh number for the onset of buoyancy-driven

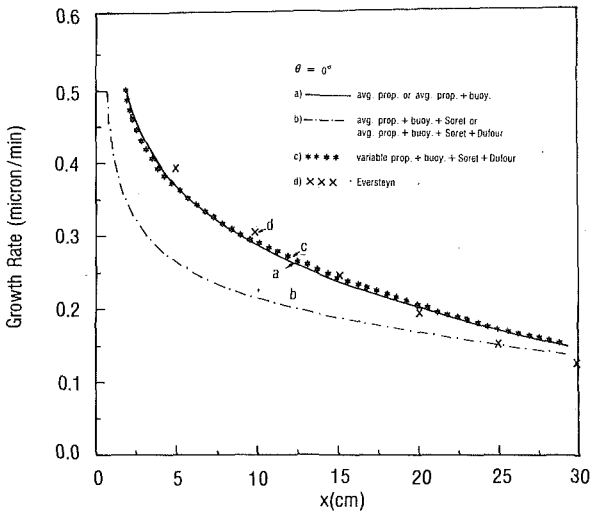

Fig. 3 Growth rate plots for horizontal susceptor for cases A, B, C, and D

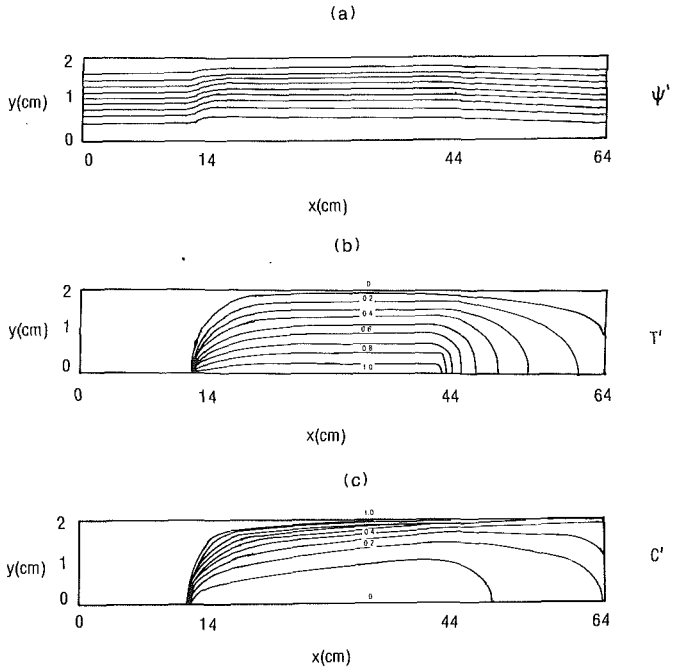

Fig. 4 Stream function, temperature, and concentration plots for horizontal susceptor for case D

axial rolls. At low Ra, the effect of buoyancy-induced flow was found to be negligible. However, in his experiments at Ra = 2295 and 2220 using nitrogen and argon respectively, the forced flow was found to be significantly affected by the buoyancy-driven flow. Moffat and Jensen (1988) in their numerical study of three-dimensional flow effects echo similar thoughts. With the side walls of the reactor assumed insulated, buoyancy-driven rolls first appeared when Ra was 1816.

Our numerical results for the horizontal susceptor for Case B, that is, with the buoyancy effects included, are shown in Fig. 3, as curve *a*. The Gr and Ra are 298.5 and 209, respectively. This curve is indistinguishable from that for Case A, indicating a negligible effect of buoyancy-induced flow on the mass transfer rate for Ra = 209. The fact that buoyancy does not play a role in the present case does not preclude it from being important in other operating conditions or other CVD systems.

Case C: Dufour and Soret Effects. Figure 3 also shows the results obtained with the inclusion of Dufour and Soret effects, curve *b*. Two conclusions are readily drawn. Of the Soret and Dufour effects, the former is dominant and accounts for almost all of the total diffusive effects. Secondly, the effect on the mass transfer rate is appreciable, with the mass transfer rate being lower by as much as 28 percent. This decrease can be easily understood form an examination of Eq. (5). For this discussion, only the gradients in the y direction, being much larger than those in the x direction, will be considered. In Eq. (5), concentration of silane at the susceptor is lower than in the bulk. Therefore, $\partial x_1/\partial y$ is positive. Whether the terms due to Soret effect aid or oppose the first term depends on the sign of the product $\alpha\ \partial T/\partial y$. For hydrogen, α is positive. For $T_h > T_c$, the contribution $\partial T/\partial y$ is negative and thus opposes the first term.

The Dufour effect is the contribution to the thermal flux due to the concentration gradient. Its impact on the temperature field and hence on the mass transfer rate is rather small.

Recall that in Fig. 3, curve *b* represents Case C when the buoyancy flow as well as the Soret and Dufour effects are included. These are typically the effects ignored in the earlier analyses as discussed in Section 1. The expectation was that the agreement between the experimental results and the improved analysis would be better. However, as seen in Fig. 3, the numerical results are now substantially lower than the experimental data. On the other hand, the previous approximate analyses are much closer to the experimental data. The unresolved question is: Is there any other effect ignored in the previous approximate analyses that compensates for the error introduced due to neglect of the Soret effect?

Case D: Variable Property Effect. The computational results when property variations are taken into account, curve *c* in Fig. 3, provide an answer to the above question. For these calculations, instead of the past practice of evaluating properties at the average temperature, the actual variation of the transport properties with temperature is taken into account. The results of the improved analysis are now in close agreement with the experimental data. It is noted parenthetically that the growth rate was found to be most sensitive to variation of D with temperature.

The clear indication is that the agreement between the experimental data and the past numerical/semi-analytical results was coincidental. It so happened that for this particular problem, the undercorrection due to miscalculation of the transport properties compensates for the overcorrection due to neglect of the Soret effects. One should not assume similar good luck (!) in other deposition systems.

Stream Function, Temperature, and Concentration Plots. The calculated normalized stream function, ψ', dimensionless isotherm, T', and dimensionless isoconcentration, C', plots are shown in Figs. 4(*a*, *b*, *c*), respectively, for Case D. The ψ' plots indicate uniform velocity with x in the heated section as evidenced by the almost uniform spacing between the streamlines, with x. Figure 4(*b*) indicates that barring the vicinity of the leading edge of $x = 14$ cm, the temperature gradient also stays uniform with increase in x. The concentration gradient, $\partial C/\partial y\ |_{(y=0)}$ on the other hand changes continuously with x, being larger at lower values of x.

Two conclusions are noteworthy from these plots. First, the temperature gradient uniformity cannot be taken as a measure of concentration gradient; hence the deposition rate uniformity, as used by Stock and Richter (1986). Only when the Lewis number Le = $D/\kappa = 1$, are the temperature and concentration plots the same. However, in the typical silicon deposition system as considered here, thermal diffusivity, κ, is about three times larger than the molecular diffusivity, D, of silane in hydrogen. This results in more uniformity in temperature profile than in the concentration profile. Secondly, Fig. 4(*c*) clearly

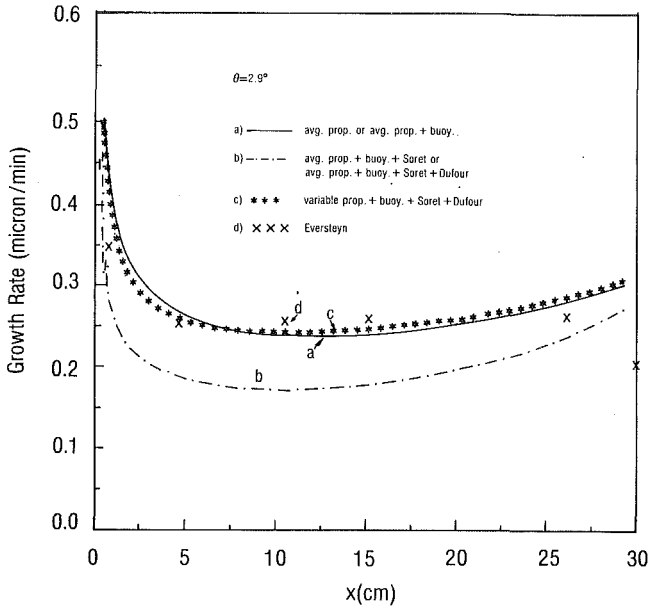

Fig. 5 Growth rate plots for inclined susceptor for cases A, B, C, and D

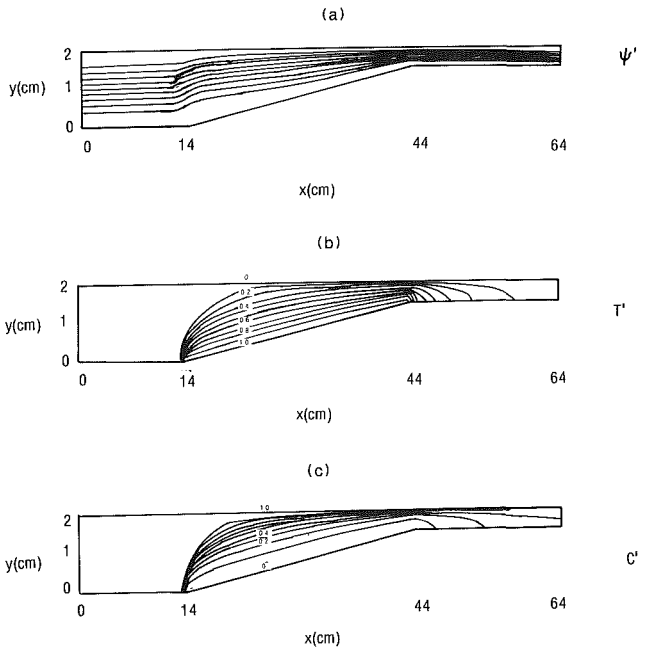

Fig. 6 Stream function, temperature, and concentration plots for tilted susceptor, θ = 2.9 deg for case D

shows the depletion effect characteristic of horizontal deposition systems; see Ban (1976), Berkman et al. (1978), Eversteyn et al. (1970), and Ristorcelli and Mahajan (1987).

Inclined Susceptor, $\theta = 2.9$. The most common practice to overcome the depletion effect, seen in Fig. 3 as well as in Fig. 4(*c*), is to tilt the susceptor by about 3 deg. The mass deposition rate calculations for the four cases, A, B, C, and D, discussed earlier are shown in Fig. 5. The numerically computed stream function, temperature, and concentration plots for θ = 2.9 deg and the susceptor temperature of 1350 K used in the experiments of Eversteyn et al. (1970) are shown in Fig. 6.

Figure 6 shows, as expected, an increase in velocity with x. Barring the leading edge region, the concentration gradient, $\partial C/\partial y \mid_{(y=0)}$, is relatively much more uniform in x. The $\dot{m}$ plot collaborates these results. Increased mass transport due to the increased flow velocity compensates for the decreased

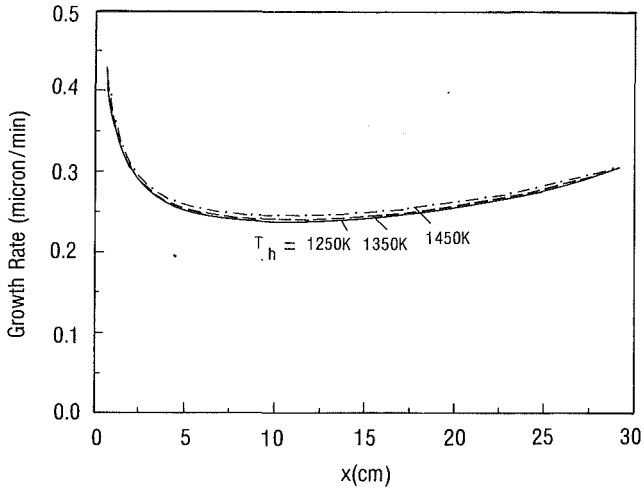

Fig. 7 Effect of susceptor temperature on deposition rate

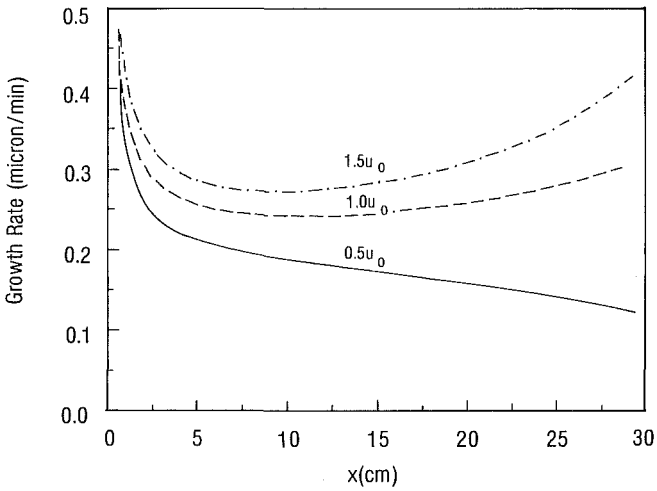

Fig. 8 Effect of inlet velocity on deposition rate

mass transport due to the depletion effect. Like those at θ = 0 deg, the calculations for the Cases A, B, C, and D indicate similar conclusions as related to the role of buoyancy flow, Soret, Dufour, and property variation effects.

5 Growth Rate and Reactor Parameters

This section describes the growth rate as a function of various parameters of interest. These include reactor height, flow velocity, inlet concentration of silicon-carrying species, and susceptor temperature. The results are presented for θ = 2.9 deg. Reference values of these parameters are those used in the experiments of Everstyn et al. (1970) (see Table 1), that is, h = 2.05 cm, u_0 = 34.0 cm/s, T_h = 1350 K, and C_o corresponds to p_o of 639 dynes/cm^2.

Influence of Susceptor Temperature. The growth rates when the susceptor temperature is raised or lowered by 100 K from the reference value of 1350 K are shown in Fig. 7. Clearly in this temperature range, the effect of substrate temperature on the deposition rate is small. The trend is for higher deposition at higher substrate temperature. This is in agreement with past studies; see Ristorcelli and Mahajan (1987) and Bloem and Giling (1985). The relative small variation with temperature is again indicator of the diffusion-controlled nature of the deposition at these temperatures. Also note that the variation of $\dot{m}$ downstream remains almost unaffected.

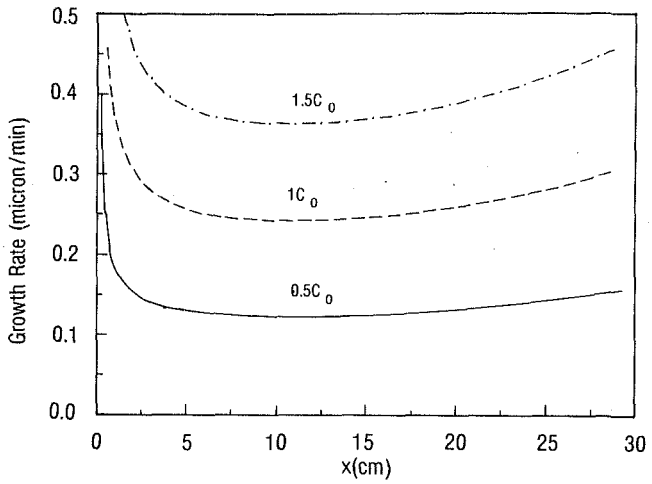

Fig. 9 Effect of inlet concentration on deposition rate

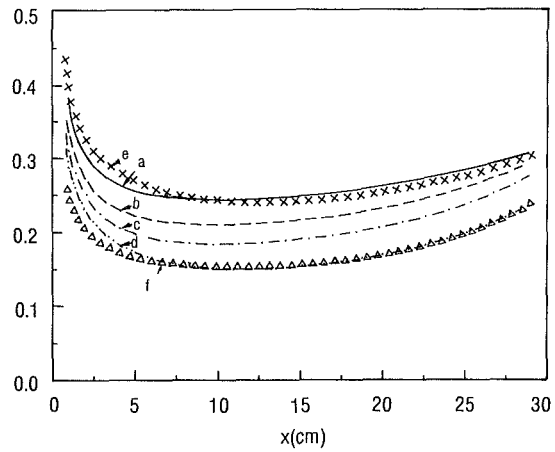

Fig. 10 Effect of reactor height on growth rate; curves *a–d* (*h* = 2.05 cm, 2.5 cm, 3 cm, 4 cm, respectively), with buoyancy included, curves *e* and *f* (*h* = 2.05 cm and 4 cm, respectively) with buoyancy neglected

Influence of Inlet Velocity. The downstream variation of $\dot{m}$ when u_0 is increased or decreased by 50 percent is shown in Fig. 8. The partial pressure of silane is assumed to be kept constant. As expected from fluid dynamic considerations, the deposition rate increases with increase in Reynolds number (or velocity). In addition, variation in flow rate has a large impact on the uniformity in the deposition rate. At higher flow rates, the curves tend to be more skewed upward at larger x. As flow rate increases, larger quantities of unreacted silicon-bearing species, silane in this case, are carried downstream, resulting in an increase in the concentration of silane in the bulk flow at larger x. Larger gradients in silane, therefore, lead to increased deposition rate of silicon as seen in the curves in Fig. 8. The reverse is true for lower velocities.

Influence of Inlet Concentration. Three curves for C_o corresponding to p_o of 639 dynes/cm^2, 0.5 p_o, and 1.5 p_o are shown in Fig. 9. The curves clearly indicate a linear dependence of the growth rate on the input concentration. Until the onset of gas-phase decomposition, such a linear relationship is observed for silane; see Bloem and Giling (1985).

Influence of Reactor Height. For a given reactor, h is generally not a parameter available to an epitaxial engineer to manipulate for controlling the deposition rate. However, it is one of the important design considerations and it is of interest to know how reactors of different heights (or of different aspect ratios, L/h) perform with respect to deposition characteristics. First, it is to be noted that Ra varies as h^3 so that change in

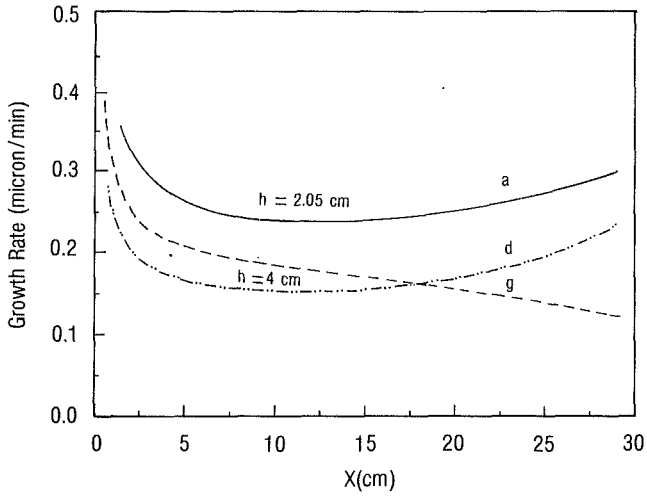

Fig. 11 Effect of *h* on deposition rate: Curves *a* and *d* are the same as in Fig. 10 and curve *g* corresponds to the $0.5u_0$ curve in Fig. 8 for *h* = 2.05 cm

h can impact the buoyancy flow effects substantially. To study this, we performed numerical calculations for h = 2.05 (standard case), 2.5, 3.0, and 4.0 cm, with the corresponding Ra being 209, 408, 655, and 1553, respectively. The flow velocity u_0 was changed so that Re was constant. With the buoyancy term included it is assumed that the buoyancy rolls have not set in yet so that our two-dimensional model is still applicable. These results are shown in Fig. 10, as curves *a–d*. Also shown are the calculations for these values of h when the buoyancy term is neglected in the momentum equation (for clarity, the calculations for no buoyancy are shown only for h = 2.05 and 4.0 cm, as curves *e* and *f*). The results confirm again that until the onset of Benard convective instability, expected around Ra = 1708, the effect of buoyancy on the growth rate is very small.

Note that in Fig. 10 the growth rate decreases with increase in h. This decrease partially reflects the effect of decrease in u_0, similar to that seen in Fig. 8. For h = 4 cm, the inlet velocity is approximately 0.5 of u_0. For comparison, the calculations for h = 2.05 cm for $0.5u_0$ from Fig. 8, curve *g*, along with the curves *a* and *f* from Fig. 10, are shown plotted together in Fig. 11. The residual difference between the two curves, *d* and *g*, is the effect of changing the aspect ratio. The indication is that the effect of increasing h or decreasing the aspect ratio is increased uniformity in deposition. At higher aspect ratios, the depletion of bulk concentration is faster, which results in larger nonuniformities. A similar conclusion was drawn by Ristorcelli and Mahajan (1987).

5 Summary

Numerical calculations have been carried out to investigate the role of buoyancy flow, Dufour, Soret, and variable property effects on the transport in horizontal silicon epitaxial deposition systems. The susceptor tilt angles of θ = 0 and 2.9 deg are considered and the impact of each of these effects on the silicon deposition rate is studied. The stream function, temperature, and concentration plots are also presented for the two values of θ, with all of these effects included in the governing equations. For the typical epitaxial reactor parameters, the results show that the former two effects have a negligible impact on the mass transfer rate while the latter two have a large influence. Based on these results, it is shown that the agreement between the previous numerical/semi-analytical calculations and the experimental data is fortuitous. Finally the numerical calculations detailing the effects of varying reactor height, inlet velocity, inlet concentration, and susceptor

temperature on the growth rate are presented. The results indicate that in the normal operating range of susceptor temperatures used in practice, the effect of varying susceptor temperature is small; the change in flow velocity has a large influence both on the growth rate and uniformity of the layer; the growth rate varies linearly with inlet concentration; and that narrower reactors (larger aspect ratio) result in increased nonuniformity in deposition.

References

Ban, V. S., 1978, "Transport Phenomena Measurements in Epitaxial Reactors," *Journal of Electrochemical Society*, Vol. 125, No. 2, p. 317.

Baron, J. R., 1962, "Thermodynamic Coupling in Boundary Layers," *ARS Journal*, Vol. 32, p. 1053.

Berkman, S., Ban, V. S., and Goldsmith, N., 1978, "An Analysis of the Gas Flow Dynamics in a Horizontal CVD Reactor," *Heteropitaxial Semiconductors for Electronic Devices*, G. W. Cullen and C. C. Wang, eds., Springer, New York, Chap. 7, p. 264.

Bloem, J., and Giling, L. J., 1985, "Epitaxial Growth of Silicon by Chemical Vapor Deposition," *VLSI Electronics: Microstructure Science*, Vol. 12, N. G. Einspruch and H. R. Huff, eds., Chap. 3, p. 89.

Coltrin, M. E., Kee, R. J., and Miller, J. A., 1984, "A Mathematical Model of the Coupled Fluid Mechanics and Chemical Kinetics in a Chemical Vapor Deposition Reactor," *Journal of Electromechanical Society*, Vol. 131, No. 2, p. 425.

Coltrin, M. E., Kee, R. J., and Miller, J. A., 1986, "A Mathematical Model of Silicon Chemical Vapor Deposition: Further Refinement and Effects of Thermal Diffusion," *Journal of Electrochemical Society*, Vol. 133, No. 6, p. 1206.

Eckert, E., and Drake, R. M., 1972, *Analysis of Heat and Mass Transfer*, McGraw-Hill, New York.

Eversteyn, F. C., Severin, P. J. W., Brekel, C. H. J. v.d., and Peek, H. L., 1970, "A Stagnation Layer Model for the Epitaxial Growth of Silicon From Silane in a Horizontal Reactor," *Journal of Electrochemical Society*, Vol. 117, No. 7, p. 925.

Gebhart, B., Jaluria, Y., Mahajan, R. L., and Sammakia, B., 1988, *Buoyancy Induced Flows and Transport*, Hemisphere Publishing Corp., New York.

Giling, L. J., 1982, "Gas Flow Patterns in Horizontal Epitaxial Reactor Cells Observed by Interference Holography," *Journal of Electrochemical Society*, Vol. 129, No. 3, p. 634.

Grew, K. E., and Ibbs, T. L., 1952, *Thermal Diffusion in Gases*, Cambridge University Press, London.

Hanzawa, T., Sakauchi, K., Kato, K., and Tadaki, J., 1977, "Velocity Profile and Temperature Distribution in the Horizontal Epitaxial Reactor," *J. Chem. Eng., Japan*, Vol. 10, p. 313.

Hieber, C. A., 1973, "Mixed Convection Above a Heated Horizontal Surface," *Int. J. Heat Mass Transfer*, Vol. 16, p. 769.

Hirschfelder, J. O., Curtis, C. F., and Bird, R. F., 1954, *Molecular Theory of Gases and Liquids*, Wiley, New York.

Holstein, W. L., 1988, "Thermal Diffusion in Metal-Organic Chemical Vapor Deposition," *Journal of Electrochemical Society*, Vol. 135, p. 1788.

Hood, P., 1977, "Frontal Solution Program for Unsymmetric Matrices," *International Journal for Numerical Methods in Engineering*, Vol. 10, p. 379; Errata, Vol. 11, p. 1055.

Houtman, C., Moffat, H., and Jensen, K. F., 1985, *Proc. 6th European Conference on CVD*, Uppsala, p. 73.

Hwang, G. J., and Cheng, K. C., 1973, "Convective Instability in the Thermal Entrance Region of a Horizontal Parallel Plate Channel Heated From Below," ASME JOURNAL OF HEAT TRANSFER, Vol. 95, p. 72.

Kamotani, Y., and Ostrach, S., 1976, "Effect of Thermal Instability on Thermally Developing Laminar Channel Flow," ASME JOURNAL OF HEAT TRANSFER, Vol. 98, p. 62.

Marshall, R. S., Heinrich, J. C., and Zienkiewicz, O. C., 1978, "Natural Convection in a Square Enclosure by a Finite-Element, Penalty Function Method Using Primitive Fluid Variables," *Numerical Heat Transfer*, Vol. 1, p. 315.

Mori, Y., 1961, "Buoyancy Effects in Forced Laminar Convection Flow Over a Horizontal Flat Plate," ASME JOURNAL OF HEAT TRANSFER, Vol. 83, p. 479.

Moffat, H., and Jensen, K. F., 1986, "Complex Flow Phenomena in MOCVD Reactors," *J. Crystal Growth*, Vol. 77, p. 108.

Moffat, H., and Jensen, K. F., 1988, "Three-Dimensional Flow Effects in Silicon CVD in Horizontal Reactors," *Journal of Electrochemical Society*, Vol. 135, p. 459.

Pearce, C. W., 1983, *VLSI Technology*, S. M. Tse, ed., McGraw-Hill, New York, Chap. 2.

Reid, R. C., Prausnitz, J. M., and Poling, B. E., 1987, *The Properties of Gases and Liquids*, 4th ed., McGraw-Hill, New York, p. 587.

Reid, W. K., and Harris, D. L., 1958, "Some Further Results on the Bernard Problem," *J. Phys. Fluids*, Vol. 1, p. 102.

Reid, W. K., and Harris, D. L., 1959, "Similarity Spectra in Isotropic Turbulence," *J. Phys. Fluids*, Vol. 2, p. 139.

Ristorcelli, J. R., and Mahajan, R. L., 1987, "Silicon Deposition and Dopant Incorporation in Epitaxial Processes," *Proceedings of 2nd ASME-JSME Thermal Engineering Joint Conference*, Hawaii, Mar. 22–27.

Sparrow, E. M., Eichhorn, R., and Gregg, J. L., 1959, "Combined Forced and Free Convection in a Boundary Layer Flow," *Phys. Fluids*, Vol. 2, p. 319.

Sparrow, E. M., and Gregg, J. L., 1959, "Buoyancy Effects in Forced-Convection Flow and Heat Transfer," *J. Appl. Mech.*, Vol. 81, p. 133.

Sparrow, E. M., and Minkowycz, W. J., 1962, "Buoyancy Effects on Horizontal Boundary Layer Flow and Heat Transfer," *Int. J. Heat Mass Transfer*, Vol. 5, p. 505.

Stock, L., and Richter, W., 1986, "Vertical Versus Horizontal Reactor: An Optical Study of the Gas Phase in a MOCVD Reactor," *J. Crystal Growth*, Vol. 77, p. 144.

Takahashi, R., Koza, Y., and Sugawara, K., 1972, "Gas Flow Pattern and Mass Transfer Analysis in a Horizontal Flow Reactor for Chemical Vapor Deposition," *Journal of Electrochemical Society*, Vol. 119, p. 1406.

Van de Ven, J., Rutten, G. M. J., Raaijmakers, M. J., and Giling, L. J., 1986, "Gas Phase Depletion and Flow Dynamics in Horizontal MOCVD Reactors," *J. Crystal Growth*, Vol. 76, p. 352.

Zienkiewicz, O. C., 1979, *The Finite Element Method*, McGraw-Hill, London.

T. A. Trabold[1]
Research Associate.
Mem. ASME

N. T. Obot
Associate Professor.
Mem. ASME

Fluid Mechanics, Heat and Mass Transfer Laboratory,
Department of Chemical Engineering,
Clarkson University,
Potsdam, NY 13699

Evaporation of Water With Single and Multiple Impinging Air Jets

An experimental investigation of impingement water evaporation under a single jet and arrays of circular jets was made. The parametric study included the effects of jet Reynolds number and standoff spacing for both single and multiple jets, as well as surface-to-nozzle diameter ratio and fractional nozzle open area for single and multiple jets, respectively. The nozzle exit temperature of the air jet, about the same as that of the laboratory, was 3-6°C higher than that of the evaporating water. Predictive equations are provided for mass transfer coefficient in terms of the flow and geometric conditions.

1 Introduction

Evaporation from liquid surfaces exposed to heated and unheated jets is important in the design of various industrial equipment: cooling of air by water and vice versa, design of scrubbers, spray towers, and various drying equipment. Although the problem has attracted the attention of researchers for nearly a century, there are few reliable mass transfer data. By contrast, the hydrodynamic aspects of gas jets impinging on liquid surfaces have been studied by many researchers (Collins and Lubanska, 1954; Banks and Chandrasekhara, 1963; to mention a few). The general features are briefly noted here because they have a direct bearing on the results to be presented subsequently. A gas jet striking a liquid surface deforms it by creating a depression, the width and depth of which depend largely on the jet momentum and spacing, $\overline{Z}_n$. For a high velocity jet, the depression is usually referred to as a cavity and is characterized by a lip of definite height. Beyond some critical velocity, the phenomenon of sputtering occurs (i.e., the creation or ejection of drops). Eventually, gas bubbles are generated within the liquid below the cavity.

The study by Coffey and Horne (1916) on humidifying towers probably provided the first indication of the importance of air direction on evaporation rates. This fact was established by Carrier (1921) who reported nearly twofold increases in evaporation rates with single jet impingement over parallel flow under identical conditions. Carrier provided no details of the experimental apparatus or measurement technique. Subsequent heat transfer studies (Friedman and Mueller, 1951) indicated similar differences between parallel flow and normal impingement.

Molstad et al. (1938) considered evaporation of water from various sized vessels exposed to a heated circular jet. Their finding was that the differences in evaporation rates between normal impingement and parallel flow were not as large as reported by Carrier, being 50 percent and 10 percent for low and high flow rates, respectively. There were problems with their experimental design and data reduction: the existence of edge effects due to the absence of an extended surface for jet flow away from the surfaces, especially since the jet diameter was larger than the diameters of the small vessels; the use of the wet-bulb temperature instead of the actual water temperature for uninsulated vessels; and the fact that evaporative losses were neglected in the analysis.

The only paper published since 1940 (Sparrow et al., 1986) dealt with isothermal jets impinging on circular free water surfaces for $7.68 \le D/d \le 23.47$, $\overline{Z}_n = 5$, 10, and 15, and $3800 \le \mathrm{Re} \le 15000$. The authors reported that, over the entire Re range, the nondimensional mass transfer coefficient varied as the 0.8 power of Re, a value that is much higher than the 0.574 power determined empirically by Martin (1977) for single impingement on solid surfaces.

Although multiple jet impingement heat and mass transfer from solid surfaces has been extensively studied (Trabold, 1989; Obot et al., 1980), little information is available on free surface evaporation with arrays of jets. In fact, the only relevant study uncovered during the literature search, that by Lyman (1965), dealt with the effect of air velocity on heat transfer from a smooth copper plate and water evaporation from a saturated felt mat. In that study, the heat transfer area was about the same as that for mass transfer and tests were made with two nozzle plates having square circular hole arrangement. Four standoff spacings $\overline{Z}_n$ = 3, 6, 12, and 24 were tested for values of Re between 3000 and 15,000. The values for the fractional nozzle open area (A_f) and the number of jet holes were 0.0123 and 36, and 0.0218 and 64, with d = 3.175 mm. The finding was that heat and mass transfer coefficients varied as the 0.644 and 0.776 power of the jet velocity, respectively.

The objectives of this study were twofold: first, to make measurements of evaporation rates for the central impingement region of laminar and turbulent single jets; thus, of the twelve values of D/d tested, nine were within the $2 \le D/d \le 7$ range for which there are no reliable data; second, to measure evaporative fluxes from a free water surface exposed to arrays of circular jets, a problem that has received meager treatment.

2 Experimental Apparatus, Test Procedures, and Data Reduction

Apparatus. A schematic of the apparatus for the single and multiple jet studies is given in Fig. 1. Since the air supply system was the same as given previously (Obot and Trabold, 1987; Trabold and Obot, 1987a; Obot et al., 1986), it is only

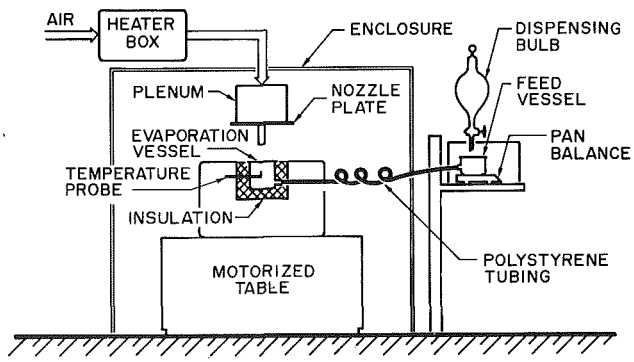

Fig. 1 Schematic of mass transfer apparatus

[1]Present address: Knolls Atomic Power Laboratory, Schenectady, NY 12309.

Contributed by the Heat Transfer Division for publication in the JOURNAL OF HEAT TRANSFER. Manuscript received by the Heat Transfer Division December 4, 1989; revision received August 8, 1990. Keywords: Direct-Contact Heat Transfer, Evaporation, Jets.

noted here that the air approaching the heater box was metered using calibrated orifices. The two $L/d = 5$ and the $L/d = 0.5$ single jet nozzles had a square-edged entrance configuration. The three multiple jet nozzle plates, each of which had an in-line hole arrangement, are best characterized by (X_n, Y_n, N_T, A_f,) = (10, 8, 48,0.0098), (10, 4, 90, 0.0196), and (5.6, 4, 180, 0.0352), where X_n, Y_n, are the center-to-center hole spacings (scaled with d) in the streamwise and spanwise directions, respectively, N_T is the number of jet holes in a plate, and A_f is the fractional nozzle open area. The jet hole diameter was 3.175 mm for all plates. Additional details were given in the 1987 papers cited above.

The central impingement target consisted of a free liquid surface created by filling a cylindrical (single jets) or rectangular (multiple jets) vessel with distilled water. The six circular vessels had internal diameters of 52.8, 64.8, 82.6, 106.4, 126.0, and 147.7 mm, and the vessel depth increased monotonically with the diameter from 51.0 mm to 169 mm for $d = 52.8$ and 147.7 mm, respectively. The length and width of the rectangular vessel were 209.6 and 203.3 mm, respectively, the same as those for the smooth heat transfer plate in the aforementioned 1987 papers, and the depth was 81.0 mm. Each vessel had two water-tight outlets for the installation of a chromel-constantan temperature probe and the polystyrene tube from the feed. An insulated vessel was supported within a wooden box, the top of which was perfectly flush with the edges of the vessel and served as an extended surface for flow away from the liquid surface (Fig. 1). The entire assembly was mounted atop a motorized cast iron table that could be raised or lowered by means of a three-phase AC motor, thereby affording variations in standoff spacing.

A segment of the apparatus (Fig. 1) was enclosed in a square housing consisting of a wooden frame enveloped in 0.25-mm-thick polystyrene sheeting. Small gaps between apparatus and sheeting were covered with thick tape. The laboratory floor was the bottom of the housing, and small gaps between the lower frame and the floor provided exhaust ports for spent air. On one side of the housing was a 635 × 500 mm air-tight Plexiglas door, above which was located a panel for the instrumentation.

Located outside of the large housing was a 250 × 270 × 505 mm wooden enclosure, the top of which was made of Plexiglas. This contained an Ainsworth Model A-400 pan balance on which the 59.2-mm-dia. Nalgene feedwater container was placed. The top of this enclosure had a water-filled glass dispensing bulb fitted with a Teflon valve (Fig. 1), from which distilled water could readily be added to the feed vessel prior to the start of a test run. The latter was covered with clear plastic wrap having several air holes to eliminate extraneous water losses. The feed vessel, balance, and enclosure were also mounted on a separate motorized platform. Since the evaporation and feed vessel were connected by a continuous line, water would flow between them whenever a difference in pressure (level of air–water interface) existed. A simple expression related change of mass of water in the feed vessel (measured directly by means of the pan balance) to change of mass of water in the evaporation vessel over time, the evaporation rate.

The relative humidity of the jet at any $\overline{Z_n}$ was measured using a YSI Model 91 dew point hygrometer or Wihl-Lambrecht Model 761 Assmann psychrometer. The latter was used to determine water vapor partial pressure for most of the trials while the former was used only for situations where localized measurements were required or the $\overline{Z_n}$ range precluded use of the larger Assmann psychrometer. A Wihl-Lambrecht 8889 barometer gave values of temperature and pressure within the evaporation chamber. The feed vessel water temperature was measured with a chromel-alumel thermocouple.

Test Procedures. Prior to each trial, distilled water was added to the vessel so that a meniscus cap was formed, protruding 3–4 mm above the top plane of the insulating box. This ensured that the water level did not drop appreciably below the cup's rim during the ensuing run, thereby avoiding any edge effects. The air flow was adjusted to give the desired Reynolds number and the free water surface was allowed to attain a constant temperature, a process that took 1½–2 hours depending on Re and $\overline{Z_n}$. Then, relative humidity of the jet at the particular $\overline{Z_n}$ was measured. A 203 mm square covering was placed over the evaporation vessel during this measurement to eliminate distortion of the humidity reading due to vapor

Nomenclature

A = surface area available for mass transfer, m^2
A_f = fractional nozzle open area = $\pi d^2 (4x_n y_n)^{-1}$
A_n = total jet flow area, m^2
d = nozzle diameter, m
D = diameter of evaporation vessel, m
$\mathfrak{D}$ = moisture diffusivity, m^2/s
E = blower power, W
$\bar{h}$ = average heat transfer coefficient, $W/m^2°C$
k = fluid thermal conductivity, W/m°C
k_c = mass transfer coefficient, kg/m^2s Pa
k' = modified mass transfer coefficient, kg/m^2s
K = jet momentum, N
L = jet nozzle length, m
$\dot{m}$ = air flow rate as measured at orifice, kg/s
MW_a = molecular weight of air = 29 kg/kmol
MW_w = molecular weight of water = 18 kg/kmol
N_T = number of jet holes in a nozzle plate
$\overline{Nu_m}$ = average mass transfer Nusselt number $k'/\rho\mathfrak{D}$
$\overline{Nu_{my}}$ = average mass transfer Nusselt number based on spanwise jet hole spacing = $k' y_n/\rho\mathfrak{D}$
$\overline{Nu_y}$ = Nusselt number $\bar{h} y_n/k$
P = pressure, Pa
Re = Reynolds number = $\dot{m}d/A_n\mu$
Re_y = Reynolds number = $\dot{m}y_n/A_n\mu$
$\overline{Re}$ = Reynolds number based on flow rate per unit transfer area = $Re \times A_f$
Sc = Schmidt number = $\nu/\mathfrak{D}$
T = temperature, K
$\dot{w}$ = evaporation rate, kg/s
x_n = streamwise jet hole spacing (x direction), m
y_n = spanwise jet hole spacing (y direction), m
z_n = standoff spacing, = m
$\overline{Z_n}$ = dimensionless nozzle-to-surface spacing = z_n/d
μ = fluid viscosity, Pa s
ν = kinematic viscosity, m^2/s
ρ = density, kg/m^3

Subscripts

amb = ambient condition
c = convective transfer rate or coefficient
ev = evaporating water
L = evaporative losses
sat,ev = saturation pressure at evaporating water temperature
T = total mass transfer
v,amb = ambient water vapor partial pressure

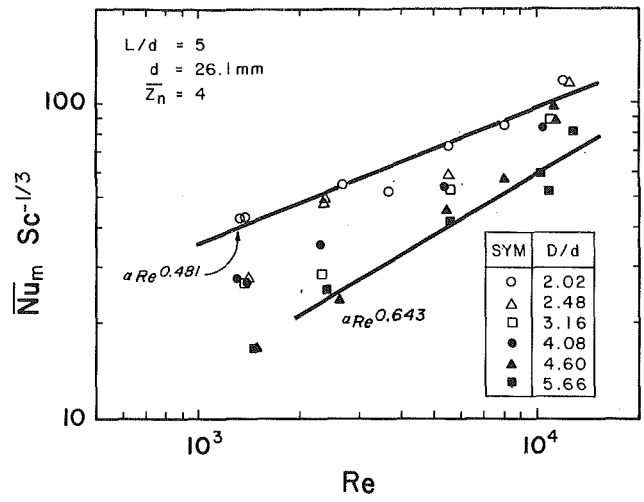

Fig.2 Variation of $\overline{Nu_m}Sc^{1/3}$ with Re for d = 26.1 mm at $\overline{Z_n}$ = 4

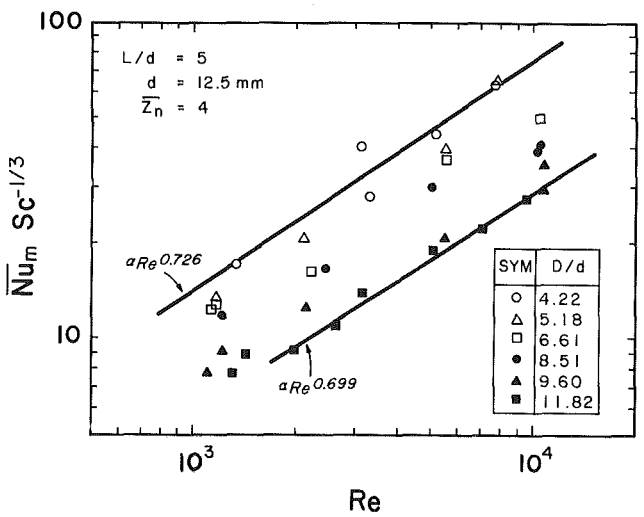

Fig.3 Variartion of $\overline{Nu_m}Sc^{1/3}$ with Re for d = 12.5 mm at $\overline{Z_n}$ = 4

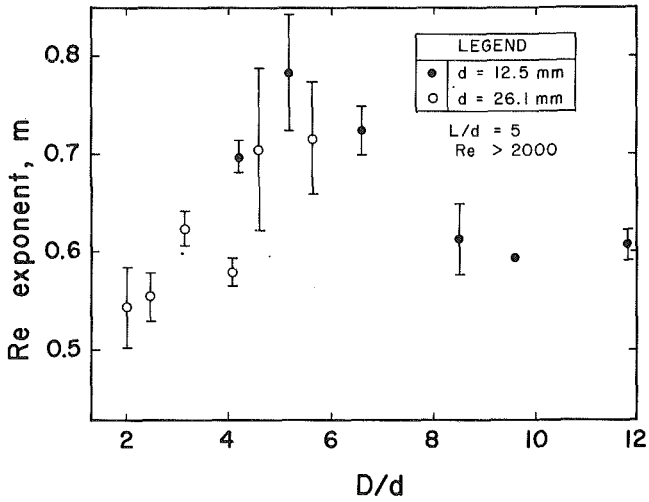

Fig.4 Variation of exponent on Re with D/d

originating at the water surface. Next, the pertinent temperature readings and ambient pressure were recorded.

At the beginning of the evaporation rate measurement, the mass of the feed vessel and contents were recorded as well as the evaporating water surface temperature. For the initial and final readings; the thermocouple probe was traversed radially, giving 6–20 values of T_{ev}, depending on the diameter of the cylindrical vessel. For the rectangular vessel, 20 temperature readings were standard. Typically, T_{ev} varied by no more than ± 0.2°C during an experiment. The feed vessel mass and T_{ev} were obtained every 10 or 20 minutes depending on the Re value being tested. Total time for a test trial was about 60 minutes, but somewhat longer for low Re and large $\overline{Z_n}$. The mass of water evaporated varied between 2 and 60 g depending, of course, on the test conditions. At the end of a test run, humidity of the impinging jet as well as all temperatures and pressures were recorded again. During an experiment, relative humidity varied by no more than a few percent.

There are several comments. First, the maximum attainable Re was the value beyond which there would be loss of water due to splashing from the free surface. Conversely, the lower Re limit was determined by the ability to meter small air flow rates accurately. Even at these relatively low flow rates, the water surface was characterized by small deformations. So, the physical state of the free water surface varied with geometric and flow conditions. From visual observations, well-shaped deformations were present for Re $\geq$ 2000 and Re $\geq$ 150 for single and multiple jets, respectively. Hence, for most of the test results, $\overline{Nu_m}$ data were acquired in the presence of varying degrees of surface deformations.

Another comment relates to the range of standoff spacings tested with a cylindrical evaporation vessel. The condition was that the jet be wholly contained over a vessel at a given $\overline{Z_n}$. The extensive mean velocity data for the L/d = 5 nozzle (Trabold et al., 1985) were used to determine the applicable spacings. For instance, with the smallest D/d = 2.02 vessel, data were acquired up to $\overline{Z_n}$ = 6 for Re = 1300 since the jet periphery would have extended beyond the edges of the vessel for $\overline{Z_n} > 6$.

Data Reduction. The convective mass transfer rate was evaluated from the relation

$$\dot{w}_c = k_c A \Delta P = \dot{w}_T - \dot{w}_L \tag{1}$$

where $\Delta P = P_{\text{sat},ev} - P_{v,\text{amb}}$ and $\dot{w}_T$ is the total measured evaporation rate obtained from the change in mass of water in the feed vessel over an elapsed time, with allowances for variation in water density and the cross-sectional areas of the evaporation and feed vessels. The density correction was nearly unity because the difference in water temperature between the evaporation and feed vessel was no more than a degree. Although the loss term was determined experimentally, it was necessary to generalize the results in order to facilitate experimentation as well as data reduction, notably because of the variation in both ambient and test conditions. In this regard, the extensive results of Sharpley and Boelter (1938) for evaporation into quiescent air were re-analyzed; these together with the losses determined experimentally from the present study were closely approximated by the relations

$$\frac{\dot{w}_L}{A} = 1.009 \times 10^{-5}; \text{ for } 405.3 \leq \Delta P \leq 891.7 \text{ Pa} \tag{2}$$

$$\frac{\dot{w}_L}{A} = [-1.951 + 0.00332\Delta P] \times 10^{-5};$$

$$\text{for } 891.7 < \Delta P \leq 4053 \text{ Pa} \tag{3}$$

For most test trials, $\dot{w}_L$ was evaluated from equation (2). The exceptions occurred for some trials with high Re. Expressed as percentages, $\dot{w}_L$ ranged from 1.8 to 16.0 percent and 3 to 32 percent of $\dot{w}_T$ for single and multiple jets, respectively. In general, the lower percentages were applicable to high Re while the larger corrections were encountered with low Re.

The mass transfer Nusselt numbers were calculated from the relation

$$\overline{Nu_m} = \frac{k' d}{\rho \mathfrak{D}} \tag{4}$$

where $k' = k_c\ (MW_a/MW_w)\ P_{amb}$. The moist air density is the average of the values at the nozzle exit and the evaporation surface. The diffusion coefficient was calculated from the empirical correlation of Spalding (1946) for several reasons. First, it is based solely on air–water experimental data; second, the effect of temperature and pressure are correctly represented with no dependence on mixture composition. Finally, it has been verified experimentally (see, for example, Mason and Monchick, 1962). Additional details on all aspects of the presentation in this section are given by Trabold (1989).

During the course of these experiments, about 284 and 144 test runs were made with single and multiple jets, respectively. Of these, about 8 and 20 percent, respectively, were replicate trials with single and multiple jets. For the former, the variations about the mean values ranged from 6 to 10 percent while those for the latter were between 4 and 12 percent.

3 Results and Discussion

It is emphasized at the outset that the water and air temperatures were 15–21°C and 19–27°C, respectively. In general, the differences between the steady-state temperature of the evaporating water at the onset of a test run and that of the jet just before impingement were between 3 and 6°C. Also, for the air–water system, the Schmidt number (Sc) is about 0.6, and a 1/3 power dependence on Sc was assumed for the data analysis.

3.1 Single Jets. Typical effects of Re are shown in Figs. 2 and 3 where, in each case, $\overline{Nu}_m\ Sc^{-1/3}$ is plotted against Re. The first figure gives results obtained with $d = 26.1$ mm, $2.02 \le D/d \le 5.66$, at $\overline{Z}_n = 4$, while the second shows the effect of nearly halving the nozzle diameter which, in turn, amounts to almost doubling the D/d value. The variation of the Re exponent (m) with D/d is presented in Fig. 4. The exponents on Re that are quoted on Figs. 2 and 3 were determined from regression analysis, and these are for the smallest and largest D/d in a figure. For the latter, regression was carried out using data for Re $\ge$ 2000, while exponents on Re for the smallest D/d were established using all Re data for the particular D/d ratio. Given the generally expected dependence of the Reynolds number exponent on the Re range tested, these are approximations that are intended to illustrate the magnitudes of their variation with D/d.

In general, the results indicate a steady decrease in $\overline{Nu}_m$ with increasing diameter ratio (D/d), in agreement with nearly all of the available literature for impingement heat and mass transfer. This consistent effect of D/d is a direct consequence of the variation in local heat or mass transfer coefficient, which is usually observed when moving from the stagnation point outward in the radial direction. For a given $\overline{Z}_n$ and Re, note that a typical profile for local heat/mass transfer coefficient for solid surface impingement is characterized by values that are largest over the central impingement region. The local coefficients decrease with increasing radial distance away from the impingement zone. Since the average mass transfer coefficient is essentially the area-integrated value of the local coefficients, a smaller averaging area must yield higher results.

Another observation is that the exponent on Re initially increases with D/d. This is consistent with the available local heat transfer data (Murray and Patten, 1978). For relative radial locations $r/d \le 0.75$ and $3000 < Re < 20000$, their nondimensional heat transfer coefficient was proportional to Re^m, where $m = 0.5$. This result is expected due to the existence of a laminar boundary layer in the immediate vicinity of the stagnation point. However, for $1.5 \le r/d \le 3.5$, which includes transition and turbulent boundary regions, the m values were 0.5 and 0.8 for $3000 \le Re \le 8000$ and $8000 < Re < 20000$, respectively.

In Fig. 4, m is plotted against D/d. Each m value is the average of the results obtained at $\overline{Z}_n = 2$ and 4 with $d = 12.5$ or 26.1 mm. The variations about the mean values, the result of the moderate dependence on $\overline{Z}_n$, are clearly indicated in this figure. The profile for m exhibits a maximum around $D/d = 5$, beyond which it decreases to approach nearly a constant value of 0.6 for $D/d \ge 8$. The existence of a peak value for m is a natural consequence of the fact that the radial velocity close to an impingement surface increases with radial distance, passes through a maximum between $r = 1.2d$ and $r = 3d$ depending on the $\overline{Z}_n$, and then falls off gradually with increasing radial distance (Hrycak et al., 1970). As the averaging area encompasses more and more of the high-velocity zone, m increases steadily and attains its maximum value when the high velocity zone is wholly contained within the averaging area. The fact that m falls off with D/d is also consistent with the general behavior of the radial velocity. It is also of interest to note that for impingement mass transfer from a solid surface to a single jet, Chin and Tsang (1978) observed that average Sherwood numbers vary as $Re^{0.68}$ for $D/d = 6$ and the same range of Re as encountered in the present experiments.

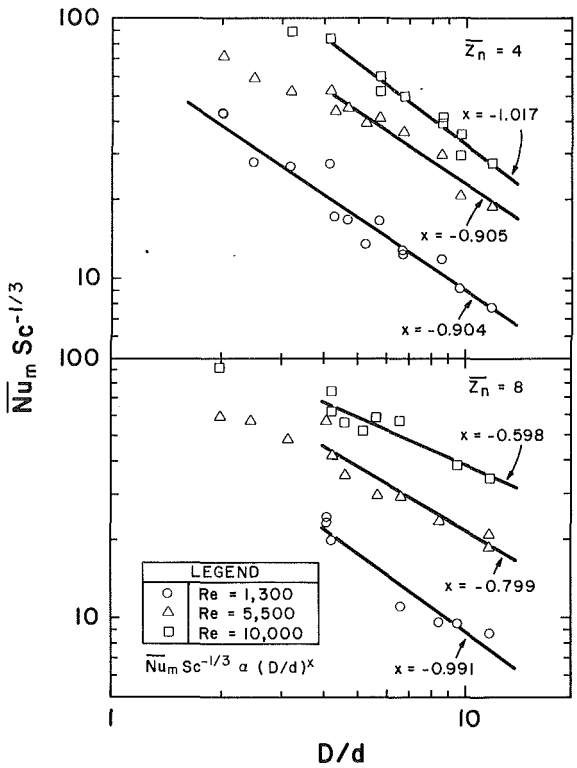

Fig.5 Variation of $\overline{Nu}_m Sc^{1/3}$ with D/d at $\overline{Z}_n$ = 4 and 8

Consistent with the heat transfer trends noted earlier, the average mass transfer data indicate a distinct change in slope of a typical $\overline{Nu}_m Sc^{1/3}$ versus Re profile and this occurs in the $2000 < Re < 4000$ range for nearly all values of D/d. For example, at $\overline{Z}_n = 2$ and $D/d = 2.02$, a break in the $\overline{Nu}_m$ versus Re profile was observed at Re $\approx$ 2300 with only slight increase in $\overline{Nu}_m Sc^{1/3}$ up to Re $\approx$ 4000. Beyond this transition region, another linear segment extended up to Re $\approx$ 10,000. Vestiges of this break are also in evidence on Figs. 2 and 3. This observation is in line with the results of Chin and Tsang (1978) who, for mass transfer experiments (electrochemical technique) with $D/d = 1$ and $\overline{Z}_n = 1$, observed inflection points at about the same Re as noted above for $D/d = 2.02$.

For nearly the same D/d, the effect of nozzle diameter is established from comparison of the $D/d = 4.06$ and 5.66 results of Fig. 2 with those on Fig. 3 for $D/d = 4.22$ and 5.18, respectively. The conclusion is that the jet hole opening is unimportant when the data are reduced in terms of $\overline{Nu}_m$ and

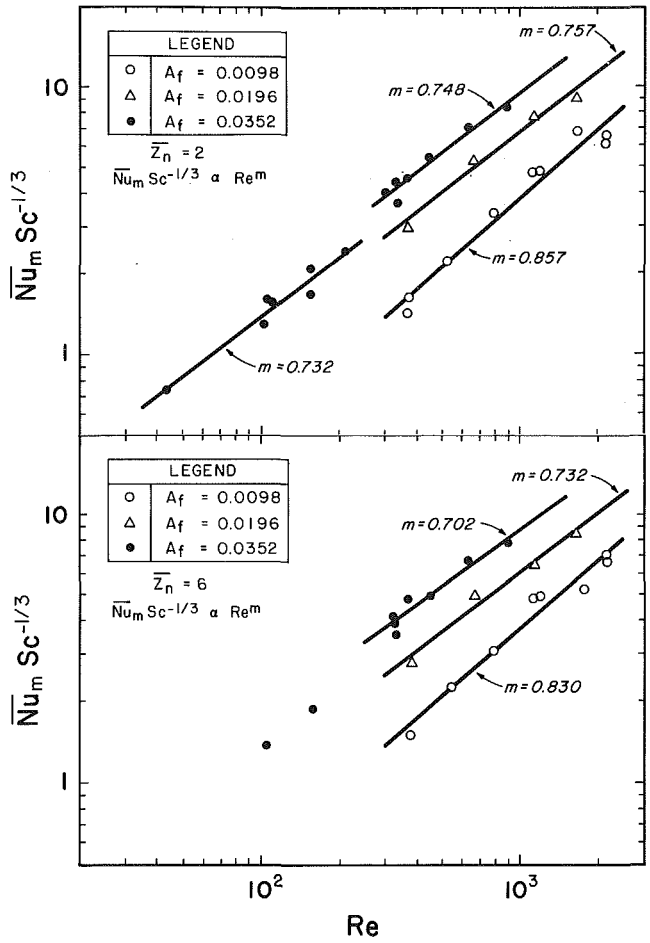

Fig.6 Variation of $\overline{Nu_m}Sc^{1/3}$ with Re at $\overline{Z_n}$ = 2 and 6

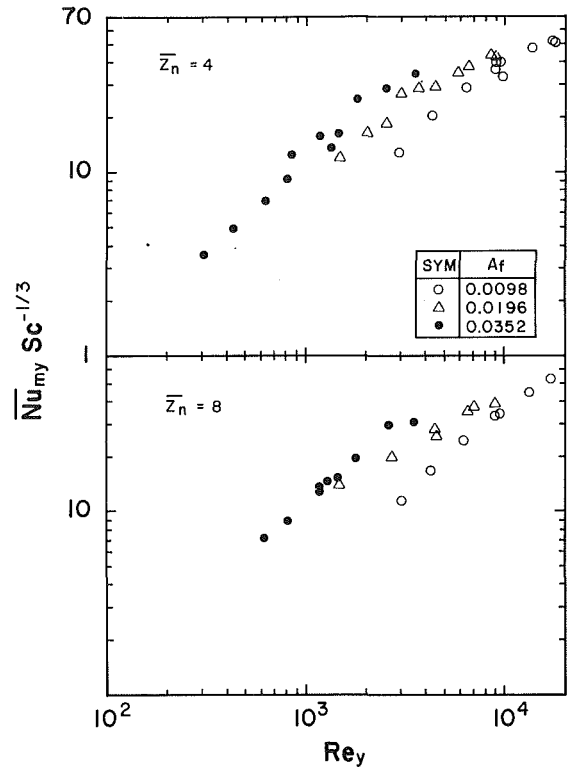

Fig.7 Effect of spanwise jet hole spacing on mass transfer Nusselt number

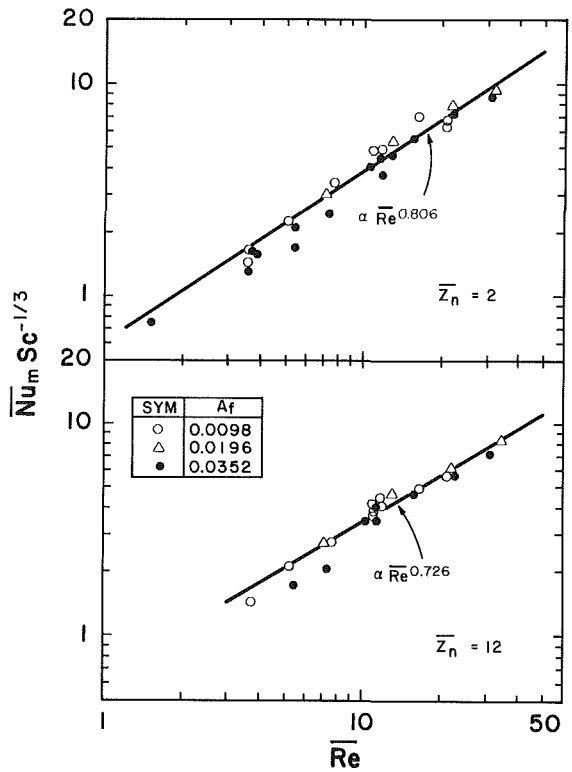

Fig.8 Average mass transfer Nusselt number versus Reynolds number based on flow rate per unit area

Re, a fact that was established for all $\overline{Z_n}$. However, since the diameter and depth of the liquid surface depression increases with increasing nozzle exit momentum, $K = \dot{m}/\rho A$ (Banks and Chandrasekhara, 1963), and since the downstream similarity of jets of comparable nozzle design occurs so long as K remains constant, the effect of d should probably be evaluated by plotting $\overline{Nu_m}$ against the blower power per unit transfer area. The results of such calculations, which are documented by Trabold (1989), favor the conclusion that $\overline{Nu_m}$ increases with increasing d for a given blower power per unit area. For a given $\dot{m}$, since doubling d results in fourfold decrease in average velocity and jet momentum at the nozzle exit, the same $\overline{Nu_m}$ is obtained with a reduced power rating.

Figure 5 shows typical variations of $\overline{Nu_m}Sc^{1/3}$ with D/d for $\overline{Z_n}$ = 4 and 8. The exponents on D/d, determined via a logarithmic best fit technique, are given in this figure for $D/d >$ 4.0. For $2 \leq \overline{Z_n} \leq 10$, only small variations in $\overline{Nu_m}Sc^{1/3}$ were observed over the range $2.02 \geq D/d \leq 3.16$ for any Re. This is, of course, consistent with the observation that in the neighborhood of the stagnation point for a single impinging jet, there is weak dependence of local heat/mass transfer coefficient on radial position over the range $0.2 \leq D/d \leq 2$. The presence of a maximum in the range of D/d between 2 and 3 is suggested by some of the results, but the evidence is not conclusive.

For $D/d \geq 4.08$, the decrease in $\overline{Nu_m}$ with increasing target surface size is substantial, and this general trend prevails for all Re and $\overline{Z_n}$. The exponent on D/d decreases with increasing $\overline{Z_n}$ for given Re, paralleling the trend observed by Banks and Chandrasekhara (1963) for water surface cavity depth. For impingement heat/mass transfer from solid surfaces, previous studies give values between -0.3 and -0.5 for the exponent on D/d (Obot et al., 1980). Hence, there is greater sensitivity of $\overline{Nu_m}$ to D/d for liquid than solid surface impingement. This is largely the result of the existence of a wavy surface structure, which favors mass transfer over the central impingement re-

gion. Since the size of this active region is fixed for a given nozzle diameter and $\overline{Z_n}$ and since the mass transfer rate in this region is independent of the vessel diameter, the effect of varying the averaging area is to lower the transfer coefficient markedly. With increasing $\overline{Z_n}$ both the size of the active zone and the mass transfer rate increase, and the dependence on D/d also decreases to approach that for heat/mass transfer from a solid surface, the entire transfer area of which is almost always active.

With regard to the effects of $\overline{Z_n}$ on $\overline{\mathrm{Nu}_m}$, these were small and, hence, are not illustrated graphically. The magnitudes of the effect are reflected in the correlations given later in Section 5. It may be noted that, for a comparable $\overline{Z_n}$ range (i.e., $5 \leq \overline{Z_n} \leq 10$), the trends with increasing $\overline{Z_n}$ for $D/d > 4$ are qualitatively in agreement with the results of Sparrow et al. (1986).

3.2 Multiple Jets. The multiple jet results were obtained in the presence of minimum crossflow, that is, for the situation where the spent air flows freely away from the target surface. Given the well-known effects of crossflow on impingement heat/mass transfer from solid surfaces (Obot and Trabold, 1987), its influence on evaporation rates may be significant, especially since the presence of crossflow may lead to early saturation of the evaporation chamber. For this reason, the results of this study may not be applicable to situations where the air flow is allowed to exit through two opposite sides or one side of a rectangular impingement surface.

The effects of Reynolds number on $\overline{\mathrm{Nu}_m}\mathrm{Sc}^{1/3}$ are presented differently on Figs. 6–8. For the upper and lower plots of Fig. 6, $\overline{\mathrm{Nu}_m}\mathrm{Sc}^{1/3}$ is plotted against Re and the exponents on Re quoted thereon are based on regression analysis using data for $\mathrm{Re} > 210$. For Fig. 7, the characteristic length in the definitions of Reynolds and Nusselt number is y_n, while Fig. 8 gives plots of $\overline{\mathrm{Nu}_m}\mathrm{Sc}^{1/3}$ versus $\overline{\mathrm{Re}}$, where $\overline{\mathrm{Re}} = \mathrm{Re} \times A_f$ (i.e., Reynolds number based on the mass flow rate per unit mass transfer area). The presentation format parallels that for heat transfer data (Obot and Trabold, 1987). Although the Re range covered in the mass transfer experiments is much lower than for the heat transfer results of that paper, Figs. 6–8 should afford qualitative comparison of heat and mass transfer trends.

To begin discussion of these results attention is drawn to Fig. 6. Although it was not possible to extend measurements below $\mathrm{Re} < 300$ with $A_f = 0.0098$ ($N_T = 48$) or 0.0196 ($N_T = 90$), data were obtained for Reynolds numbers as low as about 50 with $A_f = 0.0352$ ($N_T = 180$). For any of the five $\overline{Z_n}$ tested, a definite increase in $\overline{\mathrm{Nu}_m}\mathrm{Sc}^{1/3}$ was observed with increasing A_f at any given Re. This observation, which is in agreement with published heat transfer results, requires no elaboration beyond noting that this is a direct consequence of maintaining about the same pressure drop across the nozzle plates with varying flow rate.

The results show that, even for the relatively low Re range of these figures, some of the exponents on Re are either about the same or higher than those deduced from heat transfer data for $1000 < \mathrm{Re} \leq 21{,}000$ (Obot and Trabold, 1987). Also, it is evident from comparisons between the single jet results and those on Fig. 6 that the m values associated with the latter are significantly higher than the mean single jet value of 0.534 for $500 \leq \mathrm{Re} \leq 2000$. This is readily explained. A single jet gives rise to a single cavity on the liquid surface, the relative size of which is almost fixed for a given $\overline{Z_n}$. By contrast, for any particular array of jets, the number of cavities is the same as the number of jets in the array. Due to interactions of the liquid–air layers between adjacent nozzles, a wavy surface structure exists, the overall effect of which is similar to that of surface roughness (Trabold and Obot, 1987). The interfacial area available for mass transfer is markedly increased and this gives rise to a stronger dependence of transfer coefficients on Re.

Indirect support for this explanation as well as the effects of flow velocity comes from the work of Gilliland and Sherwood (1934). They found that, for vaporization of thin films of nine different liquids into air in a wetted-wall column, the dimensionless mass transfer coefficient varied as the 0.83 power of the Reynolds number over the entire 2000–25,000 Re range. This situation is one in which liquid falling films flow down the inside surface of the tube, while the gas (air) flows upward. Under these conditions, the characteristic features of the liquid surface are rippling and wave formation, not much different from the general picture given above for multiple jet impingement on a liquid surface. The transfer mechanisms associated with multiple jet impingement seem to be similar to those for liquid falling films.

A search of the literature revealed only three relevant heat transfer studies for the low Re range. The most recent one (Andrews et al., 1987) covered a wide Re range. Using the five data points of that study ($\overline{Z_n} = 4.5$, $300 < \mathrm{Re} < 2000$, and $A_f = 0.0086$), it was established that $\overline{\mathrm{Nu}} \propto \mathrm{Re}^m$ where $m = 0.771$, a value that is not markedly different from those on Fig. 6. The second study (Novikov and Malenko, 1980) considered the rather narrow, $\mathrm{Re} = 3.8$–18.9 range. Their results indicated that heat transfer coefficient varied as the 0.55 power of Re. This value is lower than those obtained in the present study for $40 < \mathrm{Re} < 200$. According to Lyman (1965), heat and mass transfer coefficients, averaged over roughly the same transfer area with identical nozzle geometries, vary as the 0.644 and 0.776 power of the jet velocity, respectively. From the results of Lyman, Andrews et al., and those of this study, it appears that the differences in the Re exponent between heat and mass transfer coefficients are small.

Another observation, one that derives from a study of the $A_f = 0.0352$ results, is that there is a sudden break in the $\overline{\mathrm{Nu}_m}\mathrm{Sc}^{1/3}$ versus Re profile somewhere between $\mathrm{Re} = 200$ and 300. Expressed as the jet hole average velocity, this range is between 1.0 and 1.5 m/s. It was already remarked that, based on visual observations, $\mathrm{Re} \geq 150$ marked the onset of a pronounced wavy surface. The discontinuity in the $\overline{\mathrm{Nu}_m}\mathrm{Sc}^{1/3}$ versus Re profile is a reflection of the change from moderate to significant surface deformations. For single jets, it was noted that a similar break in the mass transfer profile occurred between $\mathrm{Re} = 2000$ and 4000, i.e., between 1.2 and 2.4 m/s with $d = 26.1$ mm. So, the range of exit velocity that brings about this change in the mass transfer profile is about the same for both single and multiple jets, but the nozzle exit momentum for the former is much greater than that of an individual jet in an array. On the other hand, the total momentum for $A_f = 0.0352$ is nearly double that for the $d = 26.1$ mm single jet. Hence, the cumulative effect on surface deformation is always more pronounced with multiple than with single isolated jets, in support of the stronger dependence of mass transfer coefficient on Re for multiple jets.

In Obot and Trabold (1987), the advantage of having a greater number of jets over a given target area was examined by plotting $\overline{\mathrm{Nu}_y}$ versus Re_y. It was shown that all minimum and maximum crossflow data for $A_f = 0.0098$ and 0.0196 at $\overline{Z_n} = 4$ were adequately represented by a single regression line. That such a degree of concurrence is not realized in the corresponding treatment of mass transfer data is illustrated in Fig. 7, which also shows the break in the $A_f = 0.0352$ profiles. The general trend is one of increasing $\overline{\mathrm{Nu}_m}\mathrm{Sc}^{1/3}$ with open area. The conclusion is that the mass transfer coefficient increases with the number of jets in an array over a target surface. However, as with the use of the conventional Re (Fig. 6), this advantage of open area is a consequence of maintaining about the same pressure drop across the nozzle plate with varying air flow rate.

On Fig. 8, which gives another treatment of the mass transfer data, the exponents on $\overline{\mathrm{Re}}$ were obtained using all data for a comparable Re range at a given $\overline{Z_n}$, excluding the $A_f = 0.0352$

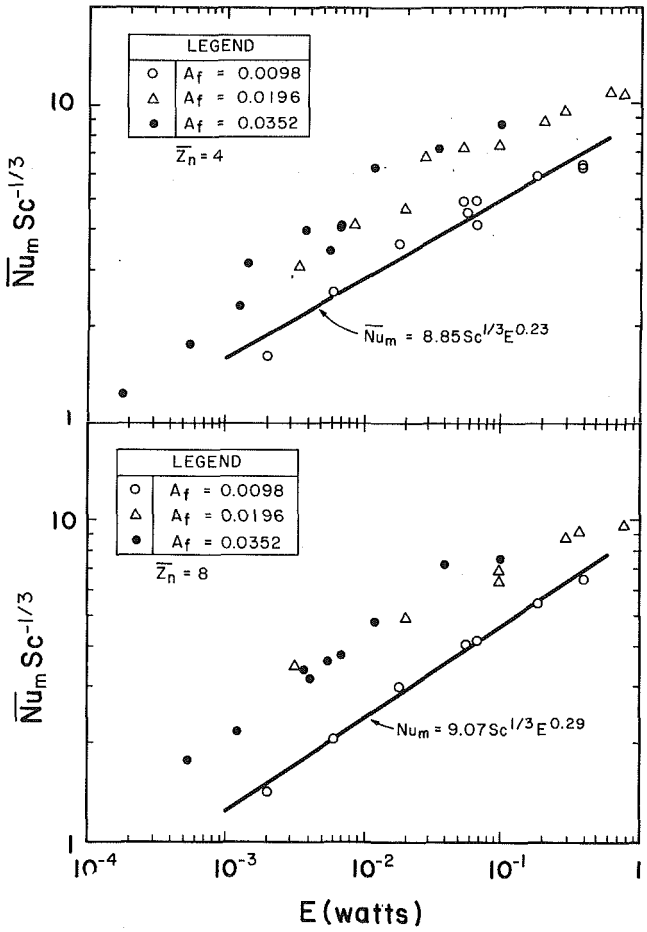

Fig.9 Variation of $\overline{Nu_m}Sc^{1/3}$ with blower power at $\overline{Z_n}$ = 4 and 8

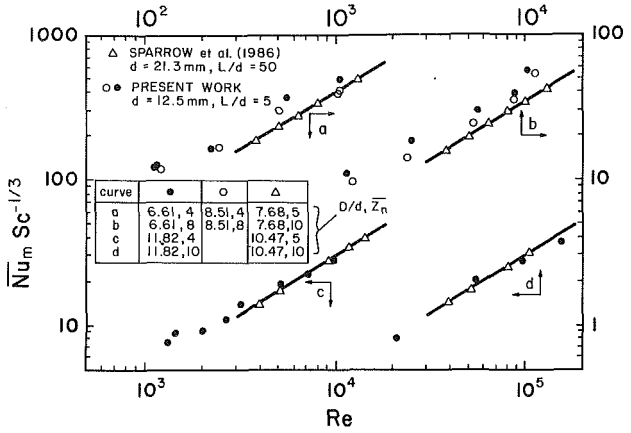

Fig.10 Comparison of present results with those of Sparrow et al. (1986)

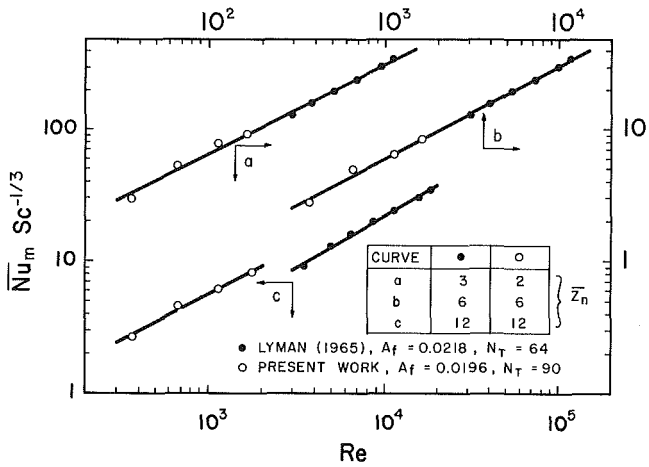

Fig.11 Comparison of present results with those of Lyman (1965)

data for $\overline{Re} \leq 10$, which belong to a separate regime. This approach provides the basis for the comparison of the transfer performance of nozzle plates of varying open areas by using coolant flow rate per unit transfer area. However, as with Re or Re_y, for a given $\overline{Re}$, the air mass flow rate varies with changes in A_f when d is held fixed. Although the previous heat transfer results indicated better performance per unit surface area for the least densely spaced nozzle configuration, with lower but nearly coincident results for $A_f = 0.0196$ and 0.0352, Fig. 8 shows that the results at each $\overline{Z_n}$ are closely approximated with a single straight line. This figure also highlights the lack of strong effect of $\overline{Z_n}$ on the Reynolds number exponent. For $2 \leq \overline{Z_n} \leq 12$ and based on plots of $\overline{Nu_m}$ versus $\overline{Re}$, the average value for this exponent is 0.759 ± 0.031.

For mass transfer, it is demonstrated that plots of $\overline{Nu_m}Sc^{1/3}$ versus $\overline{Re}$, Re_y, or $\overline{Re}$ modify the conclusions reached for heat transfer. It is, therefore, instructive to bring the discussion of the effects of jet velocity and open area to a logical conclusion, insofar as the advantage of having a greater number of jet holes is concerned, by considering plots of $\overline{Nu_m}Sc^{-1/3}$ versus E, typical results of which are given on Fig. 9 for $\overline{Z_n} = 4$ and 8. Similar trends were obtained at $\overline{Z_n} = 2$, 6, and 12. The solid line on each plot represents a logarithmic best fit through the $A_f = 0.0098$ data. From our previous results for heat transfer, the $A_f = 0.0352$ data at $\overline{Z_n} = 4$ were approximately 40 percent higher than for $A_f = 0.0098$ over the range $0.4 < E < 40$ watts. By contrast, Fig. 9 illustrates greater improvement in transfer coefficient for the case of evaporation. The large increases in mass transfer are due to the monotonic decrease of the nozzle plate pressure drop as well as the increase in the number of cavities with A_f.

Table 1 Summary of correlations

Single Jets

$$\overline{Nu_m} = 0.984\,Re^{0.534}\,Sc^{1/3}\,\overline{Z_n}^{0.155}\,(D/d)^{-0.484} \quad (5)$$

for $500 \leq Re \leq 2000$, $4.22 \leq D/d \leq 11.82$, and $2 \leq \overline{Z_n} \leq 10$

$$\overline{Nu_m} = 1.0\,Re^{0.7}\,Sc^{1/3}\,(D/d)^{-1.23}\,\overline{Z_n}^{n} \quad (6)$$

$$n = -0.381 + 0.041\,(D/d) - 7.34 \times 10^{-4}\,(D/d)^2 \quad (7)$$

for $2000 < Re \leq 15{,}000$, $4.60 \leq D/d \leq 11.82$ and $2 \leq \overline{Z_n} \leq 10$

Multiple Jets

$$\overline{Nu_m} = 0.646\,Sc^{1/3}\,Re^{0.755}\,\overline{Z_n}^{n}\,A_f^{0.720} \quad (8)$$

$$n = 117.64\,A_f^2 - 5.805\,A_f - 0.0284 \quad (9)$$

for $210 \leq Re \leq 2300$, $2 \leq \overline{Z_n} \leq 12$, and $0.0098 \leq A_f \leq 0.0352$.

From the alternative representations of the mass transfer data (Figs. 6–9) and the similar treatment of heat transfer (Obot and Trabold, 1987), it is established that conclusions derived from heat transfer measurements may not, in general, be extended to mass transfer coefficients for evaporation from a free liquid surface. In fact, even when profiles for both heat and mass transfer coefficient exhibit the same general features, it is established that the magnitudes of the effects of Reynolds number, open area, or standoff spacing on the transfer coefficients can be markedly different.

Finally, the effect of $\overline{Z_n}$ on $\overline{Nu_m}$ is briefly discussed. Although the original work contained graphic illustrations of the influence of $\overline{Z_n}$ (Trabold, 1989), none is given in this paper due to space limitations and the fact that the influence of $\overline{Z_n}$ is, as can be inferred from Figs. 6–8, small for $2 \leq \overline{Z_n} \leq 12$. For any Re or A_f, the general feature was one of gradual decrease of $\overline{Nu_m}Sc^{1/3}$ with $\overline{Z_n}$. The magnitudes of the effect of $\overline{Z_n}$ were smaller than those established for heat transfer. Another distinction between heat and mass transfer results relates to the nature of the variation with $\overline{Z_n}$ for the most compact array ($A_f = 0.0352$, $N_T = 180$). Whereas $\overline{Z_n} = 4$ afforded a maximum in average heat transfer coefficient, a typical $\overline{Nu_m}Sc^{1/3}$ versus $\overline{Z_n}$ profile exhibited no maximum.

4 Comparison With Available Data

For single jets, comparison of the present results with those of Sparrow et al. (1986) is provided in Fig. 10 for several $\overline{Z_n}$ and D/d and Sc = 0.6. The small differences are explained by the residual effects of nozzle geometry and D/d. In connection with the influence of nozzle geometry, note that although a jet generated with the $L/d = 5$ sharp-edged inlet nozzle possesses about the same exit mean velocity profile as that with $L/d = 50$, the former is characterized by nozzle exit turbulence intensities that are significantly higher than those for $L/d = 50$ (Obot et al., 1979).

For multiple jets, it is clear from the discussion in the introductory section that the work by Lyman (1965) is similar to the present study. Since the felt mat of that study was completely saturated with water during a test run, it is reasonable to suppose that Lyman's test conditions were analogous to evaporation from the pool of water of the present situation. To effect direct comparison of the two sets of data, and in the absence of Lyman's data for surface and nozzle temperatures, a linear variation of water temperature with nozzle exit temperature was assumed. For the $A_f = 0.0098$ or 0.0352 and $\overline{Z_n} = 4$ or 8 trials of Trabold (1989), a 30°C increase in nozzle exit temperature resulted in a 12°C change in water temperature. Hence, for an exit temperature of 90°C, a rough estimate of Lyman's value for air heated with a steam jacket, the water temperature would be around 42°C. Since the results of that study were presented in dimensional form, the latter temperature value was used for the evaluation of the physical properties. A comparison of the two sets of data is shown in Fig. 11. Since Lyman's tests covered the Re > 3000 range, the results of $\overline{Z_n} = 3$ and 6 are almost perfectly on the extrapolated regression lines for the present data, with a slight departure at $\overline{Z_n} = 12$. Given the magnitudes of the effects of A_f and N_T (Fig. 6), the outcome of the comparison is consistent with expectations.

5 Correlation of Mass Transfer Data

The predictive equations developed using the present data are summarized in Table 1. For single jets, equations (5) and (6) predicted 85 percent of the data points to within ±20 percent. Although the correlations were based on the data obtained with the $L/d = 5$ sharp-edged inlet nozzles, the fact that differences in measured $\overline{Nu_m}$ values between $L/d = 5$ and the relatively short $L/d = 0.5$ nozzle of comparable inlet geometry were no more than ±20 percent for 2000 < Re < 15,000 suggests that the predictive equations can be used for $L/d \geq 0.5$. Comparison of the present results with those of Sparrow et al. (1986) tends to support this view. However, for Re < 2000, these correlations are not recommended for other nozzle geometries because the combined effects of nozzle geometry and Re are significant (Trabold, 1989).

For multiple jets, there were two options: the use of Re_y in which a separate dependence on A_f probably will not occur, or the use of the conventional Re based on d. The latter is adopted to permit comparison with the results for impingement heat transfer. Although the Re exponent varied somewhat with A_f and $\overline{Z_n}$ (Figs. 6–8), the variations were such that a single value was sufficiently accurate for the present purpose. In contrast to the pronounced effect of $\overline{Z_n}$ with increasing A_f for the smooth surface heat transfer (Obot and Trabold, 1987), the influence of $\overline{Z_n}$ for $A_f = 0.0352$ is intermediate those for the other two open areas. This relatively weak dependence of $\overline{Nu_m}$ on $\overline{Z_n}$ for the most compact jet hole arrangement is most likely due to the effects of roughness, which are sustained over the entire $\overline{Z_n}$ range. The 0.72 power on A_f is not significantly different from the value of 0.82 deduced from the smooth surface heat transfer data for minimum crossflow. Equations (8) and (9), which are applicable for the minimum crossflow scheme, predicted about 90 percent of the large number of data points to within ±15 percent of the experimentally determined values (Trabold, 1989).

6 Concluding Remarks

An extensive investigation was made to determine the effects of jet Reynolds number and geometric parameters on evaporation rates from free water surfaces exposed to normally impinging single and multiple unheated air jets.

For single jets, the mass transfer Nusselt number is proportional to Re^m, where m is between 0.5 and 0.6 for $500 \leq Re \leq 2000$ and about 0.7 for $2000 < Re \leq 15{,}000$. At $\overline{Z_n} = 2$ and 4, the exponent on Re attains a maximum value around $D/d = 5$ and then drops off with increasing D/d to approach a nearly constant value of 0.6 for $D/d \geq 8$. There is little effect of D/d for $D/d \leq 4$, but $\overline{Nu_m}$ decreases markedly with increasing D/d for $D/d > 4$, and the magnitudes of this effect are more pronounced than for impingement heat/mass transfer from solid surfaces. In general, there are minimal effects of standoff spacing on mass transfer coefficient.

For multiple jets, $\overline{Nu_m}$ increases monotonically with nozzle open area for a given Re, reflecting the effect of maintaining about the same pressure drop across the nozzle plates with varying air flow rates. However, for a fixed air mass flow rate, $\overline{Nu_m}$ decreases with increasing A_f, due to the reductions in velocities at the nozzle exit and at impingement. For the $40 < Re < 2500$ range, $\overline{Nu_m} \propto Re^m$, where m varies between 0.6 and 0.98 depending on A_f, $\overline{Z_n}$, and the Re range. In terms of the blower power, $\overline{Nu_m}$ increases with increasing N_T for a given E and $\overline{Z_n}$, an indication that it is beneficial to have a greater number of jet holes over a given target area.

Acknowledgments

The initial phase of this work, including the construction of the test facility, was supported by the U.S. Army Chemical Research, Development, and Engineering Center (CRDEC) under Contract No. DAAK11-85-C-0001.

References

Andrews, G. E., Durance, J., Hussain, C. I., and Ojobor, S. N., 1987, "Full Coverage Impingement Heat Transfer: The Influence of the Number of Holes," ASME *Journal of Turbomachinery*, Vol. 109, pp. 557–563.

Banks, R. B., and Chandrasekhara, D. V., 1963, "Experimental Investigation of the Penetration of a High-Velocity Gas Jet Through a Liquid Surface," *Journal of Fluid Mechanics*, Vol. 15, pp. 13–34.

Carrier, W. H., 1921, "The Theory of Atmospheric Evaporation—With Special Reference to Compartment Dryers," *Journal of Industrial and Engineering Chemistry*, Vol. 13, pp. 432–438.

Chin, D.-T., and Tsang, C.-H., 1978, "Mass Transfer to an Impinging Jet Electrode," *Journal of the Electrochemical Society*, Vol. 125, pp. 1461–1470.

Coffey, B. H., and Horne, G. A., 1916, "A Theory of Cooling Towers Compared With Results in Practice," *ASRE Journal*, Vol. 2, pp. 5–32.

Collins, R. D., and Lubanska, H., 1954, "The Depression of Liquid Surfaces by Gas Jets," *British Journal of Applied Physics*, Vol. 5, pp. 22–26.

Friedman, S. J., and Mueller, A. C., 1951, "Heat Transfer to Flat Surfaces," *Proceedings, General Discussion on Heat Transfer*, IMECHE/ASME, pp. 138–142.

Gilliland, E. R., and Sherwood, T. K., 1934, "Diffusion of Vapors Into Air Streams," *Journal of Industrial and Engineering Chemistry*, Vol. 26, pp. 516–523.

Hrycak, P., Lee, D. T., Gauntner, J. W., and Livingood, J. N. B., 1970, "Experimental Flow Characteristics of a Single Turbulent Jet Impinging on a Flat Plate," NASA TN D-5690.

Lyman, L. C., 1965, "Effect of Air Flow on Heat Transfer and Water Evaporation in Jet-Drying Systems," *Forest Products Journal*, Vol. 15, pp. 453–458.

Martin, H., 1977, "Heat and Mass Transfer Between Impinging Gas Jets and Solid Surfaces," *Advances in Heat Transfer*, Vol. 13, pp. 1–60, Academic Press, New York.

Mason, E. A., and Monchick, L., 1962, "Transport Properties of Polar-Gas Mixtures," *Journal of Chemical Physics*, Vol. 36, pp. 2746–2757.

Molstad, M. C., Farevaag, P., and Farrell, J. A., 1938, "Rate of Evaporation From a Free Water Surface by a Perpendicular Stream," *Journal of Industrial and Engineering Chemistry*, Vol. 30, pp. 1131–1138.

Murray, B. G., and Patten, T. D., 1978, "Heat Transfer Under an Array of Impinging Jets," *Proceedings, 6th International Heat Transfer Conference*, Toronto, Vol. 4, pp. 207–212.

Novikov, P. A., and Malenko, G. L., 1980, "Convective Heat Exchange on a Plane Surface in the Case of a Perpendicular Jet Flow of Air Through a Perforated Wall for Small Re Numbers," *Journal of Engineering Physics*, Vol. 39, pp. 973–975.

Obot, N. T., Mujumdar, A. S., and Douglas, W. J. M., 1979, "The Effect of Nozzle Geometry on Impingement Heat Transfer Under a Round Turbulent Jet," ASME Paper No. 79-WA/HT-53.

Obot, N. T., Mujumdar, A. S., and Douglas, W. J. M., 1980, "Design Correlations for Heat and Mass Transfer Under Various Turbulent Jet Configurations," *Drying '80*, Hemisphere Publishing Co., pp. 388–402.

Obot, N. T., Trabold, T. A., Graska, M. L., and Gandhi, F., 1986, "Velocity and Temperature Fields in Turbulent Air Jets Issuing From Sharp-Edged Inlet Round Nozzles," *Industrial and Engineering Chemistry Fundamentals*, Vol. 25, pp. 425–433.

Obot, N. T., and Trabold, T. A., 1987, "Impingement Heat Transfer Within Arrays of Circular Jets: Part I—Effects of Minimum, Intermediate, and Complete Crossflow for Small and Large Spacings," ASME JOURNAL OF HEAT TRANSFER, Vol. 109, pp. 872–879.

Sharpley, B. F., and Boelter, L. M. K., 1938, "Evaporation of Water Into Quiet Air From a One-Foot Diameter Surface," *Journal of Industrial and Engineering Chemistry*, Vol. 30, pp. 1125–1131.

Spalding, J. D., 1946, S.B. Thesis, Massachusetts Institute of Technology, Cambridge, MA.

Sparrow, E. M., Celere, S. W., and Azevedo, L. F. A., 1986, "Evaporation at a Liquid Surface Due to Jet Impingement," ASME JOURNAL OF HEAT TRANSFER, Vol. 108, pp. 411–417.

Trabold, T. A., Esen, E. B., and Obot, N. T., 1985, "Entrainment by Turbulent Jets Issuing From Sharp-Edged Inlet Round Nozzles," *Jets and Cavities—International Symposium*, J. H. Kim et al., eds., ASME FED-Vol. 32, pp. 101–109.

Trabold, T. A., and Obot N. T., 1987a, "Impingement Heat Transfer Within Arrays of Circular Jets: Part II—Effects of Crossflow in the Presence of Roughness Elements," ASME *Journal of Turbomachinery*, Vol. 109, pp. 594–601.

Trabold, T. A., Esen, E. B., and Obot, N. T., 1987b, "Entrainment by Turbulent Jets Issuing From Sharp-Edged Inlet Round Nozzles," ASME *Journal of Fluids Engineering*, Vol. 109, pp. 248–254.

Trabold, T. A., 1989, "Impingement Evaporation and Heat Transfer From Complex Surface Geometries," Ph.D. Thesis, Clarkson University, Potsdam, NY.

Heat Transfer With Vaporization of a Liquid by Direct Contact in Another Immiscible Liquid: Experimental and Numerical Study

L. Tadrist

J. Sun

R. Santini

J. Pantaloni

Institut Universitaire des Systèmes Thermiques Industriels, Université de Provence, Marseille, France

An experimental setup was designed to study direct-contact evaporators using a liquid dispersed in another immiscible liquid. The study was carried out on an n-pentane–water system to determine the influence of different parameters on these systems, and consequently to construct a model for this type of evaporator. An optical probe was used to measure the local void fraction. At different column abscissas along a selected diameter, the local void fraction variations were determined. The shape of the curves can be attributed to the different processes occurring in the spray column. A one-dimensional heat transfer model in the spray column was established. Simplifying assumptions were used to establish and resolve the set of equations governing heat transfer and two-phase flow. The vaporization process induces a volumetric expansion of the two-phase mixture. A theoretical model was used, in which the coalescence between the spherical fluid particles is taken into account. Different coalescence laws dependent on particle density were introduced into the theoretical model and then tested. The numerical results are discussed and compared with the experimental data obtained for the n-pentane–water system.

1 Introduction

Direct-contact heat exchangers operate by injecting a substance A (dispersed phase) into a still or flowing fluid B (continuous phase). These heat exchangers offer considerable advantages over conventional wall-type exchangers. The absence of an exchange wall leaves the system free of wall-related problems such as fouling, scaling, and corrosion. The large exchange surface improves thermal performance. However, direct-contact heat exchangers do impose some restrictions (e.g., the substances in contact should be immiscible and chemically inert) that have limited the development of such exchangers. One such system causes a liquid to be vaporized into another immiscible liquid. These systems are used in geothermal energy applications in which the continuous phase is generally dirty and corrosive, and they are especially suitable for recovering low and intermediate level thermal waste.

Experimental thermal loops have been used to exploit intermediate level geothermal energy (Arkansas and East Mesa). Certain authors have pointed out that phase entrainment and two-phase flow problems have not yet been solved. Studies are underway to develop this type of thermal process as it eliminates the fouling and scaling problems found in the conventional wall-type heat exchangers (Boehm and Kreith, 1986; Jacobs, 1988). The widespread use of direct-contact processes in industry provides a considerable incentive for continued experimental as well as theoretical research. Numerous authors have shown interest in the phenomena occurring in these exchangers (Kreith and Boehm, 1988).

The two-phase flow observed in the vaporization process of multidroplets into another immiscible liquid took the form of independent and/or agglomerated droplets. Simple two-phase flow (uniform flow) or flow with recirculation were observed, depending on the inlet parameters and the properties of the fluids in use.

In the first model proposed by Battya et al. (1983), only the latent heat of vaporization was exchanged; dynamic effects were not taken into account. The velocity of the two-phase drop was assumed to be constant. This simplified model was designed to describe the continuous temperature profile, but it cannot be used to describe accurately the thermal and hydrodynamic variables in the column given the numerous simplifying assumptions in this model.

Mermet (1986) studied the water–gilotherm system in which the water droplets vaporize while moving downward. In his model it is assumed that vapor, after its formation, is separated from the droplets and that it rises countercurrently to the continuous phase. In numerical simulation, Mermet studied only the latent heat of water vaporization. The drops and bubbles were assumed to remain at their terminal velocity throughout the column.

Coban and Boehm (1986) studied local heat transfer in the n-pentane–water system using a large industrial-type column. The coalescence effect, which is capable of modifying the energy equation of the vaporization zone, was not taken into account.

The continuous variations of temperature of each phase and of the void fraction, which is dependent on the distance from the nozzle, are due to the vaporization, which also induces a variation of the two-phase drop velocity. The boiling process leads to an expansion in the volume of the two-phase mixture. A model in which the "coalescence" effect among the drops (or bubbles) was not taken into account gave a calculated two-phase exchange length that was much higher than those observed in experiments (Tadrist et al., 1987). The discrepancy between experimental and theoretical results becomes greater as the dispersed-phase flow rate increases. This is attributed to the effect of coalescence on the hydrodynamic and thermal state in the spray column.

As previously noticed, coalescence effects must be taken into consideration to achieve a realistic model of the two-phase flow and heat transfer in the spray column. To our knowledge, there is no mathematical formulation capable of establishing a coalescence law and of taking into account the different effects found in our system or in similar systems.

This paper deals with the experimental results and the modeling of moving drops that vaporize in immiscible liquid. The

Contributed by the Heat Transfer Division for publication in the JOURNAL OF HEAT TRANSFER. Manuscript received by the Heat Transfer Division March 7, 1990; revision received November 8, 1990. Keywords: Direct-Contact Heat Transfer, Heat Exchangers, Multiphase Flows.

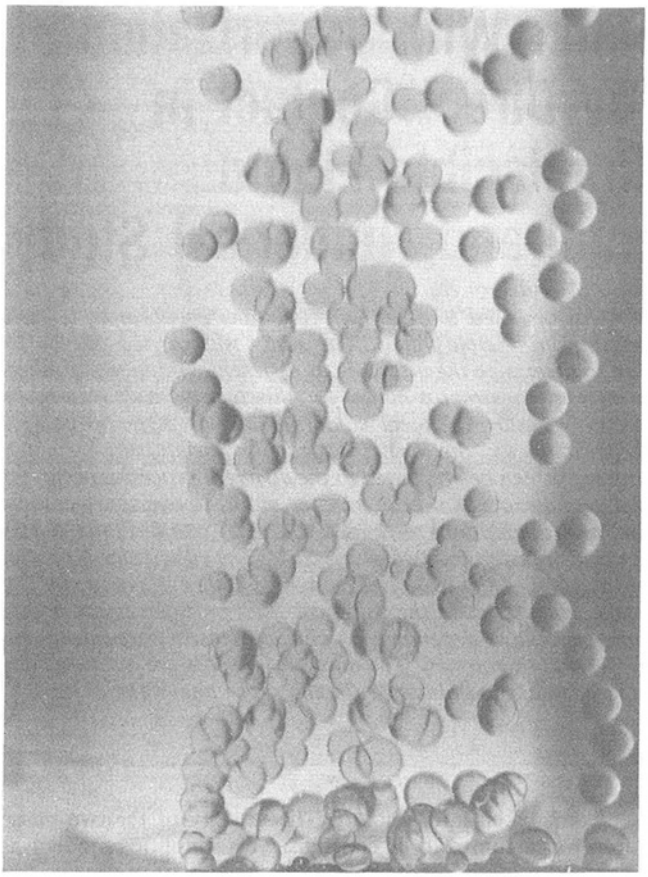

Fig. 1 An example of droplets obtained by injecting n-pentane into water near nozzle zone

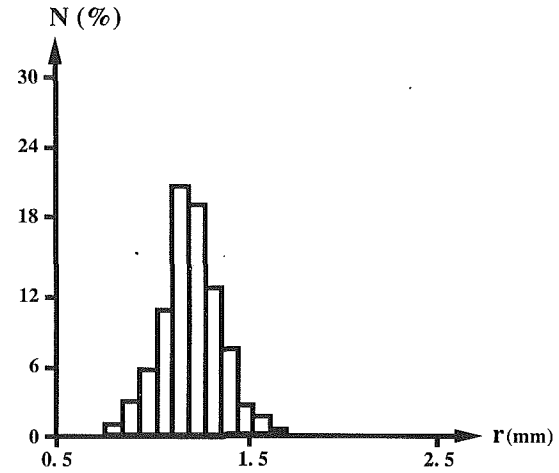

Fig. 2 Example of the injected drop size distribution, obtained with a 37-hole injector of 1 mm diameter, ψ_d = 8.06 cm^3/s, ψ_c = 83.33 cm^3/s, L_c = 20 cm. There are 301 samples in this case. The average radius of the drops is 1.1 mm with a standard deviation of 0.15 mm.

objective of the present study is to establish a heat transfer model for a dispersed phase that vaporizes in a spray column.

To conduct this study, an experimental analysis of direct contact evaporation is carried out to determine the system's behavior. A parametric study is carried out, and a one-dimensional heat transfer model is established for the exchange column. A set of equations governing the heat transfer and the two-phase flow are proposed and then solved numerically using simplifying assumptions. The equation system is not closed and lacks a source term corresponding to the coalescence of bubble-droplets. This source term is introduced as a simple phenomenological law of coalescence in which the proportionality constant is determined experimentally.

II Experimental Apparatus

The exchanger consisted of a vertical cylindrical Pyrex column with two stainless steel bridles. The internal diameter of the column was 100 mm and its length 1000 mm. The upper bridle was used to hold the inlet of the continuous phase and the outlet of the dispersed phase. The continuous phase was discharged through the lower bridle and the dispersed phase was injected through the same bridle. The fluids flowed countercurrently.

A pyrex jacket surrounding the spray column was used to ensure thermal insulation, obtained either by circulating hot water in the annular zone, or by maintaining a vacuum in this zone. The second solution is preferable as it is more efficient and easier to implement. Nevertheless, some heat loss was observed when working temperatures exceeded 60°C, though the loss did not exceed 15 percent of the total exchanged power.

A multiple-hole nozzle was used, consisting of a circular nozzle with 37 regularly distributed 1 mm holes. Special care was taken in manufacturing the injector so as to minimize the inlet effects, with particular care to eliminate hole defects.

The method used to determine the drop size distribution consisted in measuring the diameter of the drop on photographs of the injection zone. Figure 1 shows an example of the dispersed phase in the injection zone and Fig. 2 shows a histogram of the drop in the same regime derived from several photographs. In all the working conditions studied here, the mean diameter of the drops was constant, or 2.2 mm ± 0.2 mm.

The mean void fraction in the spray column can be expressed as

Nomenclature

A = column cross section
c = coalescence coefficient
C_d = drag coefficient
C_p = specific heat
g = gravitational acceleration = 9.81 m/s^2
h = superficial heat transfer coefficient
H_v = volumetric heat exchange coefficient
Ja = Jakob number
L_c = continuous-phase length
L_d = two-phase exchange length
L_v = latent vaporization heat of dispersed phase
m = mass of a fluid particle
n = particle density
Nu = Nusselt number
Pr = Prandtl number
Q = heat flux between a particle and the continuous phase
R = radius of drops or bubbles
Re = Reynolds number = $\mu_d D/\nu_c$
R_{lc} = spray column radius
t = time
T = temperature
u = velocity
V = volume
z = abscissa
α = void fraction
ΔT = temperature difference
ρ = density
ψ = volumetric flow rate

Subscripts

b = low signal
c = continuous phase
d = dispersed phase
e = inlet
h = high signal
l = liquid
s = outlet
sat = saturation
v = vapor

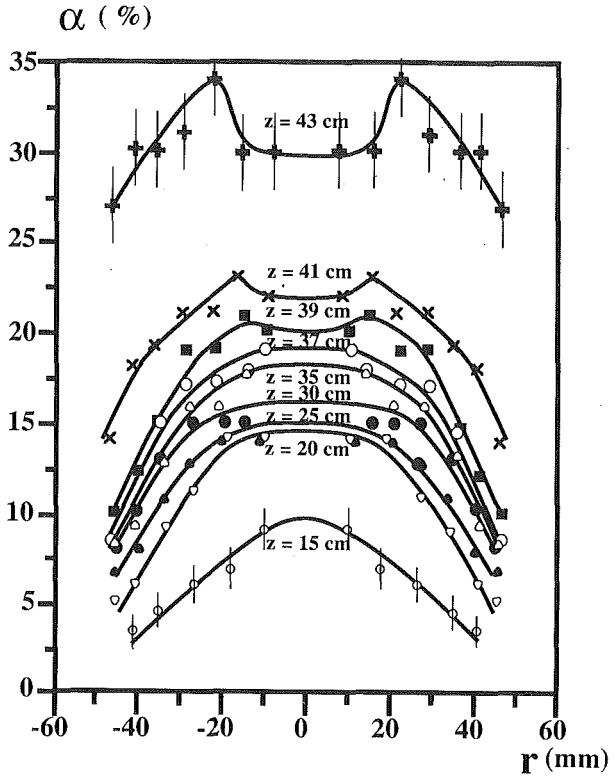

Fig. 3 Variation of the void fraction of the dispersed phase as a function of distance from column centerline and various height. ψ_c = 39.72 cm³/s, T_{de} = 17.9°C, T_{ce} = 46.2°C, ψ_d = 4.44 cm³/s, L_c = 40 cm. The relative errors are 3 percent, and are represented by error bars on the highest and lowest curves.

$$\bar{\alpha} = \frac{2}{L_d R_{lc}^2} \int_0^{R_c} \int_0^{L_d} r\alpha(r, z)\, dr\, dz$$

In the steady state, the average void fraction is also defined as the ratio of dispersed-phase volume V' to the total volume V and for a cylindrical spray column, the mean void fraction is thus

$$\bar{\alpha} = \frac{L_d - L_c}{L_d} \tag{1}$$

An optical probe is used to measure the local void fraction. This probe contains an optical fiber 0.1 mm in diameter with tapered and rounded ends. An infrared laser emits a beam, which propagates along the fiber and is reflected at its end. The intensity of the reflected light is a function of the reflective index of the medium in contact with the fiber ends. The device can therefore detect the bubbles touching the probe.

The detection circuit gives a high or low signal depending on whether the probe is in contact with the dispersed phase or the continuous phase. Measurement of high-signal (t_h) and low-signal (t_b) durations gives the local void fraction

$$\alpha(r, z) = \frac{t_b}{t_b + t_h}$$

Measurement can be conducted either by using an integrator, giving the average void fraction for a fixed duration of 10 or 100 s, or by working with a shorter time integration, recording continuously. The second technique is obviously more precise, because it allows the temporal stability of the void fraction to be verified. The measurement is easy to realize when the difference between the reflective index of the dispersed phase and that of the continuous phase is quite large.

There are two different reasons for decreased measurement precision of the void fraction. The first is related to the probe's surface state, which can modify the high and low voltage levels; the second is related to the probe's response time. In all experiments, we made sure that the high and low levels, indicating the presence of either pentane vapor or of liquid on the probe, were not modified. When these levels were found to be modified, the probe was dipped in a solvent, then soaked in hydrochloric acid for several minutes. This insures that the nominal characteristics of the probe are respected and thus that the sensitivity remains constant for all experiments.

With this system, the probe had a response time of several microseconds. We analyzed the influence of this response time on the precision of the void fraction by varying the value of the threshold voltage between the voltage limits that correspond to the presence or absence of either of the phases. The experimental results indicate that the measurement error for the void fraction did not exceed 12 percent of the measured value in extreme conditions. The threshold voltage in our working conditions was the median between the high and low voltages. In this case, the void is measured with a precision of ± 6 percent.

The measurement of void fraction, as a function of height, at the center and at the edge of the column, showed a nonuniform distribution at the cross section (Fig. 3).

- In the liquid–liquid zone, the void fraction could not be measured with our probe because the index difference between the two fluids was too small (less than 1.5 percent).
- In the second zone, this quantity increases slightly but varies within the cross section.
- In the third zone, the void fraction increases rapidly due to the accumulation of vapor bubbles.
- In the last zone, near the interface, the local void fraction is very difficult to determine correctly since the interface is greatly disturbed and the measured values have no real signification.

With a direct-contact exchanger using vaporization, certain conditions can lead to considerable superheating of the droplets. Consequently, the vaporization of these droplets can be explosive. In our study, the droplets vaporized at low superheat temperatures. With extremely low superheat conditions ($T_c - T_v < 5$°C), the exchanger works irregularly. Smith et al. (1982) also observed limit conditions for superheating, below which the vaporization of the cyclopentane in water becomes erratic.

III Theoretical Model

III.1 Introduction. The experiments showed that the following zones exist in the column:

- a liquid–liquid zone;
- a liquid–vapor zone;
- a vapor accumulation zone, in the form of foam, near the continuous-phase inlet.

This flow is observed when the difference between the temperatures of the two phases is not excessive (i.e., in the conditions of boiling without thermal shock), the injection velocities of the fluids are not excessive, and the density of the dispersed phase is lower than that of the continuous phase regardless of its state (liquid or gas). In the opposite case, the flow may be turbulent and is characterized by recirculation in the two-phase mixture.

The behavior of heat transfer in the spray column needed to be understood; thus we developed a simplified model in which the essential parameters are considered to determine the local parameters characterizing the vaporization column. Figure 4 shows the scheme of this simplified physical model. The upper foam layer is not taken into consideration. In the following chapters, the simplification hypothesis and the development of the model will be presented in detail.

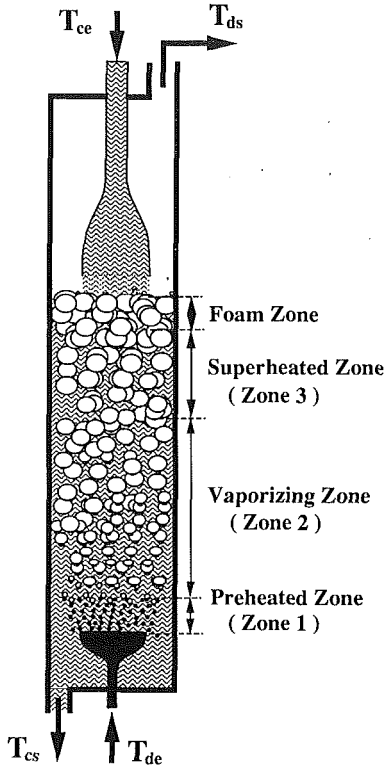

Fig. 4 Scheme of the physical model

III.2 Assumptions. The following assumptions were made:

1 The flow is steady and one-dimensional;
2 The droplets, bubbles, and bubble-droplets are spherical;
3 There are three distinct zones in the spray column:
liquid (c.p.)-drop (d.p.) zone
liquid (c.p.)-two-phase drop (d.p.) zone
liquid (c.p.)-bubble (d.p.) zone;
4 The particles are considered to be of the same size at a given height;
5 The drops were injected at their limiting velocity;
6 The system was assumed to be adiabatic;
7 The wall effects were considered to be negligible;
8 In zone 1, the coalescence effect was neglected.

III.3 Equations. The particle density conservation equation for the dispersed phase and coalescence function is

$$\frac{d}{dz}(nu_d) = f(n, d, \ldots) \tag{2}$$

where $f(n, d, \ldots)$ is the source term of the particle density. This term equals zero when the coalescence effect is excluded. In the opposite case, however, this term must be determined in order to solve the equation set.

With this system, we used a law similar to the collisional laws in the kinetic theory of gas. The coalescence function is assumed to be proportional to the square of the fluid's particle density. The law is written as

$$f(n) = -c\,n^2 \tag{3}$$

The proportional constant c corresponds to the coalescence intensity of the fluid particles. It is related to the physical properties of the fluids and flow conditions. Given that no physical model is able to give an accurate evaluation of this constant, it is derived from the experimental data.

Radovcich and Moissis (1962) calculated the collision frequency using a simple model in which the bubbles are disposed in a cubic system moving at a randomly fluctuating velocity. They found that the collision frequency is a polynomial function of the void fraction and it becomes significant for a void fraction of greater than 20 percent. From this frequency law, the source term in equation (2) can be approximated as

$$f(\alpha) = -A(\exp(C_1\alpha) - 1) \tag{4}$$

where A and C_1 are the coefficients indicating the coalescence intensity.

Park and Blair (1975) observed that in an agitated tank only 10 percent of the collisions led to coalescence. They concluded that the coalescence rate might be proportional to the turbulence level, with the highest coalescence rate occurring near the agitator. The coalescence process can be affected by a large number of variables (surface area of impact, interfacial tension, vibration, impurities . . .), many of which are difficult to control. As there is no model to evaluate the coalescence function, simple phenomenological laws are considered:

- The mass conservation equation of the dispersed phase:

$$\frac{d}{dz}(\alpha r_d u_d) = 0 \tag{5}$$

- The mass conservation equation of the continuous phase:

$$\frac{d}{dz}[(1-\alpha) r_c u_c] = 0 \tag{6}$$

- The momentum equation of a particle (Tadrist et al., 1987):

$$\left(\rho_d + \frac{1}{2}\rho_c\right) u_d V \frac{du_d}{dz} + \frac{3}{2}\rho_c u_d V \frac{du_c}{dz} + \frac{1}{2}\rho_c u_d (u_c + u_d)\frac{dV}{dz} - (\rho_c - \rho_d) V g + \frac{1}{2}\pi\rho_c R^2 (u_c + u_d)^2 C_d = 0 \tag{7}$$

- The momentum equation of the continuous phase.

In principle, the momentum equation for the continuous phase must be resolved to determine the velocity field. Thus the interactions between the phases must be known for this type of two-phase flow. However, these terms can be determined neither from theoretical analysis nor from current experimental methods. Consequently, the momentum equation of the continuous phase cannot be solved, and it is assumed that the edge effect and the dispersed-phase effect are negligible in this problem and that the continuous phase velocity is uniform. The velocity is then found using the conservation equation of the continuous phase (equation (6)).

- The energy equation of the dispersed phase:

-In zone 1 and 3 the energy equilibrium is

$$\rho_d C_{pdl} u_d \alpha \frac{dT_d}{dz} = n 4\pi R^2 h (T_c - T_d) \tag{8}$$

-In zone 2, the drops vaporize as they rise. It is supposed that the vapor part is always attached to its liquid part. This hypothesis is verified in the *n*-pentane–water system.

The energy equation can be written as follows (Sun, 1989):

$$\frac{d}{dz}\left(nV - \frac{\psi_d}{u_d S}\right) = \frac{\rho_l - \rho_v}{\rho_l \rho_v L_v u_d} nQ \tag{9}$$

- The energy equation of the continuous phase:

$$\rho_c C_{pc} u_c (1 - nV_d)\frac{dT_c}{dz} = nQ \tag{10}$$

III.4 Heat Exchange and Drag Coefficients

Heat Exchange Coefficients. To complete the set of equations it is necessary to determine the heat exchange coefficient between the two fluids and the drag coefficient of the particles. Correlations have been proposed, most of which are derived from the experimental results. The total heat exchange coefficient can be expressed by the following relation:

$$\frac{1}{h} = \frac{1}{h_c} + \frac{1}{h_d} \tag{11}$$

The common heat exchange coefficients for a particle moving in another moving fluid are applied to solve the set of equations.

The heat exchange laws used in each zone are: in the liquid-liquid zone, the Rowe et al. (1965) relation was used

$$\mathrm{Nu}_c = 2 + 0.79\mathrm{Re}^{0.5}\mathrm{Pr}^{0.33} \tag{12}$$

For the dispersed phase, several correlations have been proposed. Moresco and Marshall (1980) considered the internal convection of the drop and gave the following correlation:

$$\mathrm{Nu}_d = 0.0178\mathrm{Re}_d^{0.5}\,\mathrm{Pr}_d^{0.33} \tag{13}$$

In the vaporization zone, less work has been done on the exchange coefficient of a bubble-droplet. Sideman and Taitel (1964) gave an exchange coefficient in this case

$$\mathrm{Nu}_c = 0.272\mathrm{Pe}^{0.5} \tag{14}$$

Battya et al. (1984) introduced a corrective factor in their relation (20). The following relation was derived from their experimental results:

$$\mathrm{Nu}_c = 0.64\mathrm{Ja}^{-0.35}\mathrm{Pe}^{0.5} \tag{15}$$

In the liquid–vapor zone, the heat exchange occurs between the liquid and the gas. The correlations in this case are limited. We use the correlation of Ruckenstein (1959):

$$\mathrm{Nu} = 0.37\mathrm{Re}^{0.6}\mathrm{Pr}^{0.33} \tag{16}$$

Drag-Coefficient. The drag coefficient proposed by Haberman and Morton (1956) was chosen for our work. From their experimental results, an analytical expression is derived using curve fitting:

$$C_d = \exp(2.4397 - 0.2702\log \mathrm{Re} - 0.0756(\log \mathrm{Re})^2) \quad \mathrm{Re} < 450$$

$$C_d = \exp(-160.3 + 64.742\log \mathrm{Re} - 9.619(\log \mathrm{Re})^2) - 0.62529(\log \mathrm{Re})^3 - 0.01496(\log \mathrm{Re})^4 \quad \mathrm{Re} > 450 \tag{17}$$

III.5 Boundary Conditions.

$z = 0$:

$$T_d(0) = T_{de}; \qquad u_l(0) = \left[\frac{2Vg(\rho_c - \rho_d)}{\rho_d S C_d}\right]^{1/2};$$

$$u_c(0) = \frac{\psi_c}{(1 - n_0 v_0)S}; \quad n(0) = \frac{\psi_d}{\frac{4}{3}\pi R_0^3 u_0 S}$$

$z = L_c$: $$T_c(L_c) = T_{ce} \tag{18}$$

The differential equation system thus obtained is integrated using the second-order Runge-Kutta method. The space increment that ensures sufficient convergence is 0.06 mm. The consistency of this numerical scheme is verified by dividing the increment by 2; the difference between the two results is found to be less than 0.5 percent. The computations were performed on VAX/VMS 750 minicomputer. Processing time was about 90 s for each calculation.

Solving the system of differential equations (2), (3), (6)–(10) provides the evolution of temperature and speed for each of the phases $T_c(z)$, $T_d(z)$, $U_c(z)$, $U_d(z)$, the volume of the bubbles $V(z)$, the density, $n(z)$, and the void fraction of the dispersed phase $\alpha(z)$. The two-phase exchange length L_d can then be deduced. Under experimental conditions, column inlet and outlet temperatures $T_c(L)$, $T_d(L)$, $T_c(0)$, $T_d(0)$, the void fraction, and the length of the two-phase exchange L_d are measured. A comparison between the model and experimental results is carried out using the values $T_c(0) = T_{cs}$, $T_d(L) = T_{ds}$, $\alpha(z)$, and L_d.

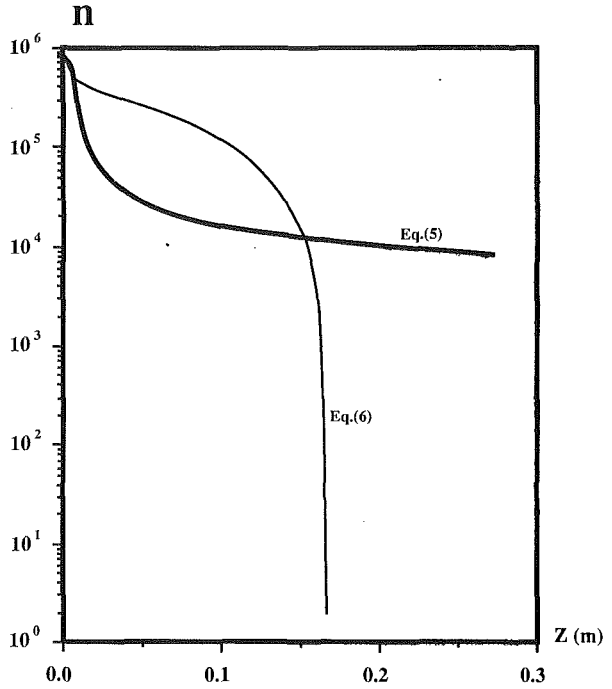

Fig. 5 Particle number density versus the abscissa z in the spray column; ψ_c = 56 cm³/s, ψ_d = 8.3 cm³/s, L_c = 20 cm, L_d = 24 cm

IV Results

IV.1 Selecting the Coalescence Law. The coalescence coefficient c of formula (5) can be estimated by determining the particle density as a function of the height z. Measuring coalescence along the column, however, is not possible with existing techniques. Therefore this constant is determined using a global approach. An arbitrary value of this coefficient is introduced, and the equation system is solved for the inlet parameters corresponding to one of the experiments. By comparing the measured and calculated two-phase exchange lengths L_d, the best coefficient value can be selected. This value is then used in all simulations with that fluid-pair system.

In this analysis, the constant c includes all parameters involved in the coalescence phenomenon. A study of the influence of exchanger parameters (inlet temperature, flow rate, thermal exchange, and drag laws) has shown their role to be secondary to that of the coalescence effect along the two-phase exchange (Sun, 1989).

Figure 5 shows the particle density variations derived from the collisional law (equation (3)) and the exponential law (equation (4)). Different behavior was found depending on which law was used. The second law causes the coalescence rate to increase so rapidly that at a certain height, the coalescences become to strong and the particle density reaches a very small value (approaching a unitary value); this would correspond to an annular (or semi-annular) flow. However, this flow was never observed experimentally. Therefore, it can be concluded that this law is not suitable to our system. In fact, using this law the coalescence at the beginning of the spray column is underestimated and the coalescence in the middle of the column is overestimated.

On the other hand, the coalescence rate decreases gradually when using the collisional law, because the particle density decreases gradually with the coordinate. This density also decreases rapidly at the beginning of the spray column, approaching a limiting value at the end of the column. The numerical results generally agree with the experimental data. Therefore, in the following numerical simulation equation (3) was used as the coalescence law.

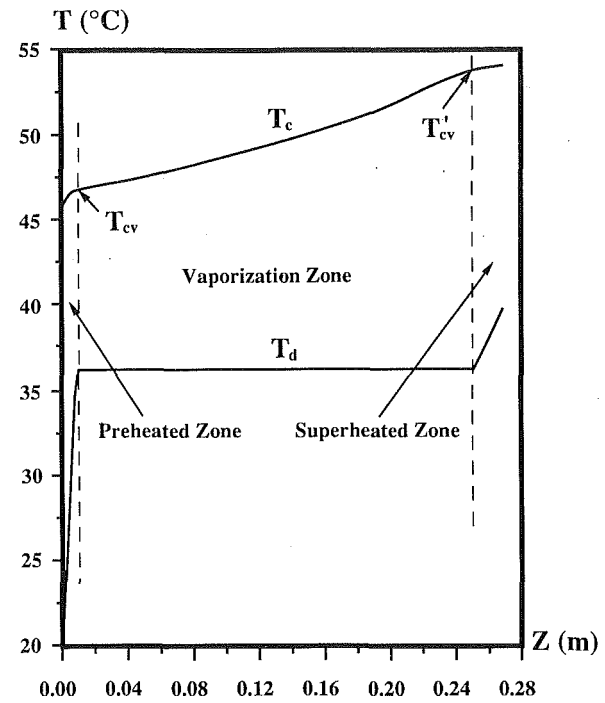

Fig. 6 Temperature of the dispersed phase and the continuous phase variations versus the distance from the injection nozzle; ψ_c = 56 cm^3/s, ψ_d = 8.3 cm^3/s, L_c = 20 cm

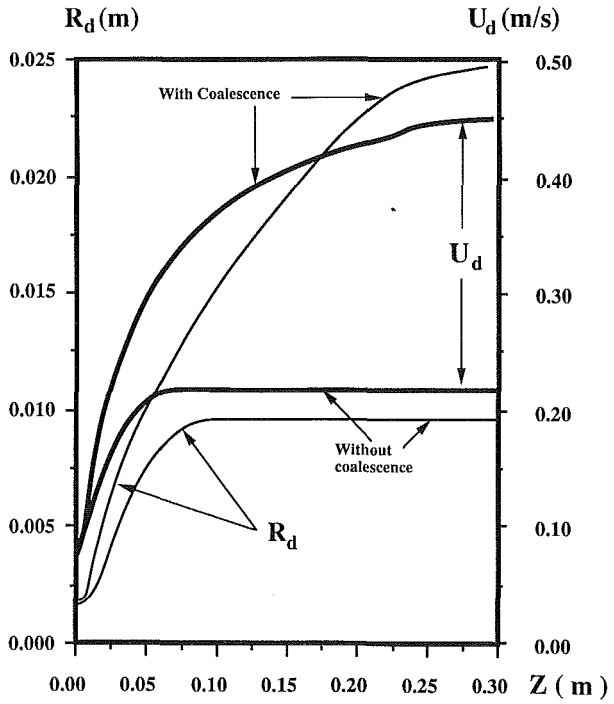

Fig. 7 Particle radius and velocity versus the distance from the injection nozzle; ψ_c = 83.3 cm^3/s, ψ_d = 8.3 cm^3/s, L_c = 20 cm

IV.2 Temperature Variations of the Phases. The calculated temperatures of the dispersed phase and of the continuous phase are plotted against the distance from the injection nozzle in Fig. 6. Three distinct zones, corresponding to the different transfer modes, can be clearly seen. The shortest zone obviously corresponds to the liquid–liquid exchange zone. In the second zone, the heat exchange is affected by vaporization, and the dispersed-phase temperature remains constant. In the third zone, the exchange occurs between the liquid (C.P.) and the dry vapor (D.P.). Less temperature variation of the continuous-phase was observed in zones 1 and 3.

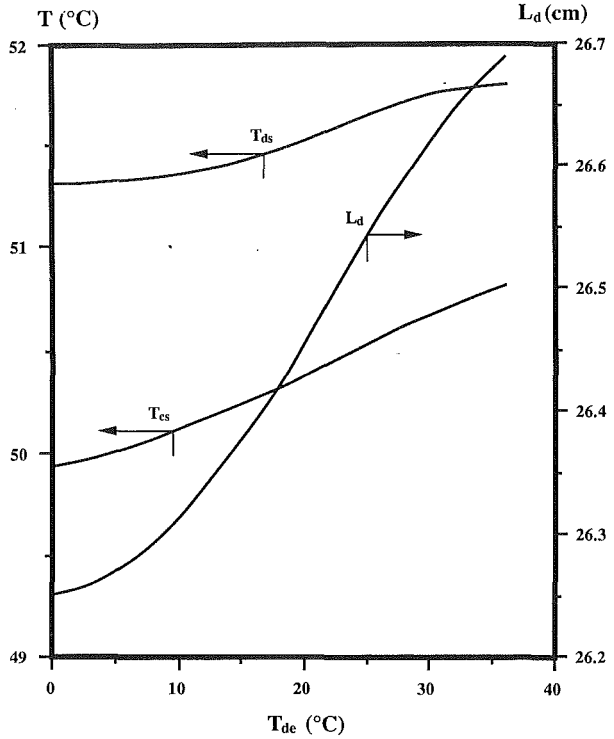

Fig. 8 Outlet temperatures and the two-phase heat exchange length L_d versus the inlet temperature of the dispersed phase, ψ_c = 83.3 cm^3/s, ψ_d = 5.6 cm^3/s, T_{cs} = 54°C, L_c = 20 cm

IV.3 Particle Size, Velocity, Density, and Void Fraction. The size of the particles, calculated as a function of the distance from the injector, is reported in Fig. 7 with and without the coalescence effect. The variation laws differ from zone to zone. The bubble-droplet size increases continuously throughout the spray column, except in the liquid–liquid zone where the drop diameter remains constant. In the second zone, the drop size changes greatly. This is due to the combination of two effects: the continuous vaporization and the coalescence between the bubble-droplets. It seems that the vaporization effect dominates in this zone, and the coalescence effect tends to diminish the heat exchange surface, resulting in a greater vaporization length. In the third zone, the increase in bubble volume can be attributed mainly to the coalescence effect.

The variation of particle velocity possesses the same characteristics as that of particle size, because both quantities are directly correlated (Fig. 7). Coalescence and vaporization tend to increase the particle size by a factor of 15 and the velocity by a factor of 7; without coalescence, the particle radius increases only by a factor of 6.

Figure 5 shows the variation of particle density as a function of height. Particle density decreases considerably in the beginning of the vaporization zone and becomes smaller toward the end of the column. This decreasing aspect is due to coalescence and to the acceleration of the particles.

IV.4 Inlet Parameter Sensitivity. The influence of the inlet temperature for each phase on the heat exchange of the system is investigated in this section. The influence of phase flow rate and of the length of the continuous-phase will be studied in the next section, in which the numerical results are compared with experimental data.

Increasing the inlet temperature of the dispersed phase results in an increase in the outlet temperature of both phases as well as a slight increase in the two-phase exchange length (Fig. 8). Increasing the inlet temperature of the dispersed phase

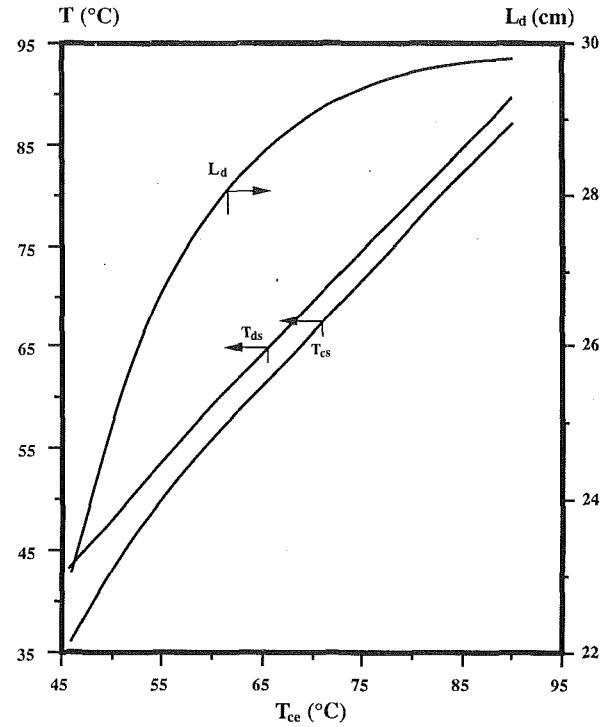

Fig. 9 Outlet temperatures and the two-phase heat exchange length L_d versus the inlet temperature of the continuous phase for ψ_c = 83.3 cm^3/s, ψ_d = 5.6 cm^3/s, T_{de} = 20°C, L_c = 20 cm

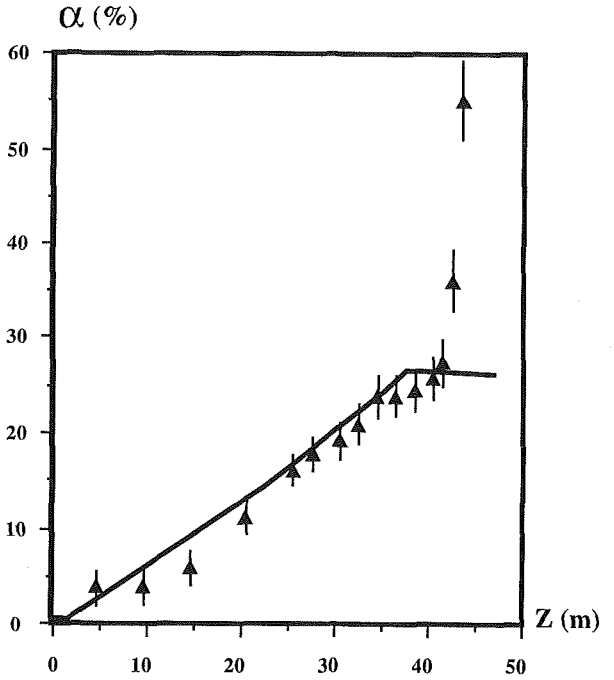

Fig. 10 Void fraction of the dispersed phase in the spray column versus the abscissa z. A comparison between the experimental measurements (▲) and the numerical results (——). ψ_c = 39.7 cm^3/s, ψ_d = 4.2 cm^3/s, T_{de} = 17.9°C, T_{ce} = 46.2°C

leads to a shorter exchange length upstream from the vaporization zone and to a longer superheated exchange length. Consequently, the averaged void fraction and the outlet temperatures of each phase become greater. Changing the inlet temperature of the dispersed phases causes only a slight change in outlet quantities. This can be explained by the preponderance of the vaporization in the heat exchange and the difference between the phases of the specific heat capacities.

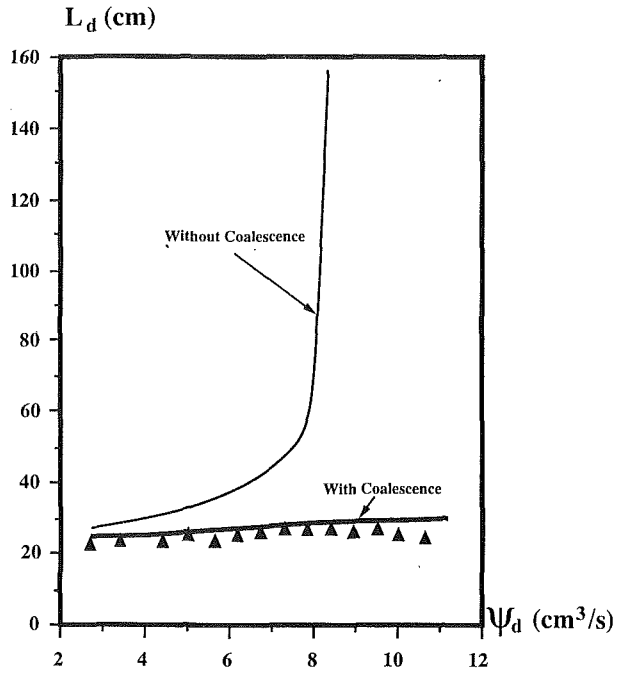

Fig. 11 Two-phase exchange length versus the dispersed phase flow rate ψ_d. Comparison between the experimental measurements (▲) and the numerical results with coalescence (——) and without coalescence (——). ψ_c = 83.3 cm^3/s, T_{de} = 20°C, T_{ce} = 54°C, L_c = 20 cm

Increasing the continuous-phase inlet temperature results in an increase in the temperature of each phase and in their outlet temperatures (Fig. 9). For given flow conditions, the outlet temperature of the dispersed phase increases continuously with T_{ce} and tends asymptotically toward this value, which corresponds to perfect heat exchange between the two phases. The outlet temperature of the continuous phase increases with T_{ce}, and the heat exchanged between the two phases increases until it reaches the limit value.

The two-phase exchange length increases with T_{ce} and tends toward its limit value with high T_{ce} values (Fig. 9). Beyond the critical value for T_{ce} (approximately 85°C), the heat transfer in the spray column can no longer be modified and the volume expansion remains constant. The same behavior is observed for heat exchange efficiency, but with a lower critical value for T_{ce} (60°C).

V Comparison Between the Numerical Results and the Experimental Data.

V.1 Void Fraction. The calculation of the void fraction is represented in Fig. 10. In the liquid–liquid zone, this fraction is small. In the vaporization zone, the void fraction of the dispersed phase increases gradually. In the third zone, it remains nearly constant.

The void fraction was measured locally and plotted against the distance from the injector for different injection conditions. Experimental and numerical results were very similar for the main part of the column. The discrepancy observed for the top of the column corresponds to an accumulation of vapor; and this was not considered in our theoretical model.

V.2 Influence of the Inlet Parameters on Certain Factors.

Two-Phase Exchange Length. If the coalescence effect is not taken into consideration in the model, the calculated two-phase exchange length varies exponentially with ψ_d (Fig. 11). With small ψ_d values, the numerical and experimental results are very similar. As ψ_d increases, the numerical results diverge rapidly from the experimental values.

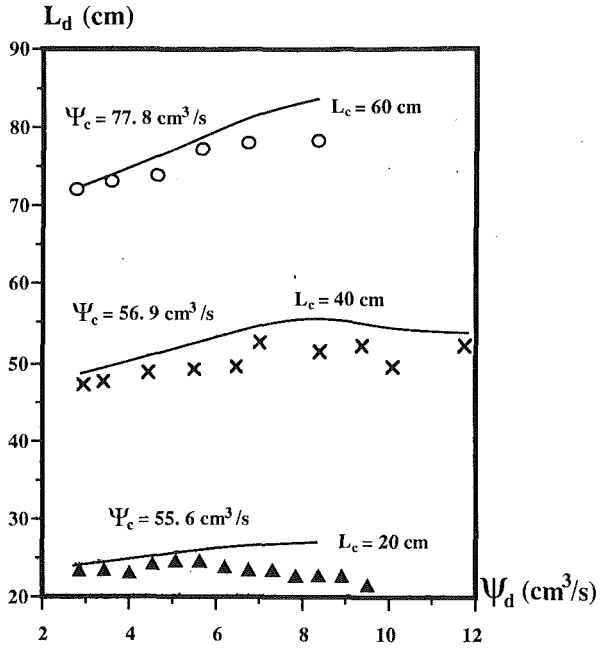

Fig. 12 Two-phase exchange length L_d versus the dispersed phase flowrate ψ_d for different continuous phase lengths L_c. Experimental and numerical results with coalescence. T_{de} = 20°C, T_{ce} = 54°C.

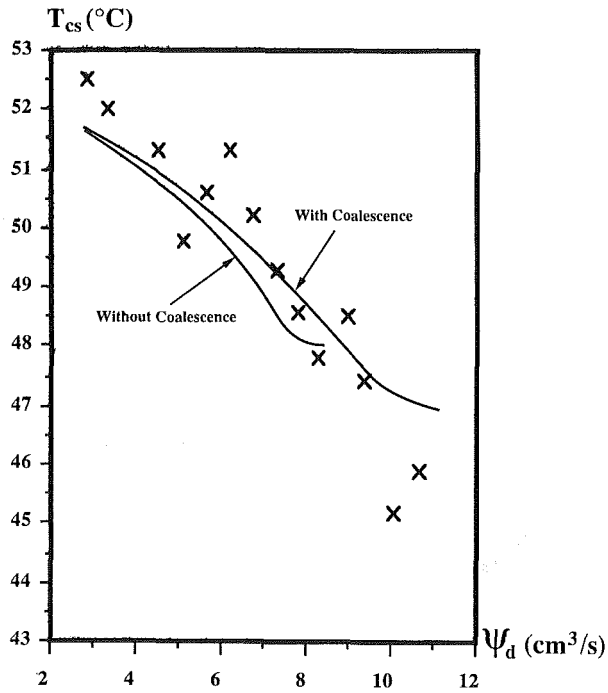

Fig. 13 Outlet temperature of the continuous phase T_{cs} versus the dispersed phase flow rate ψ_d. Experimental and numerical results with and without coalescence, with the same conditions as in Fig. 11.

By taking the coalescence phenomenon into consideration, the numerical results correspond quite well to the experimental data (Fig. 11). The coalescence effect tends to increase the particle volume and to decrease both the heat transfer surface and the residence time of the particle in the spray column. This leads to a reduction of the void fraction and of the exchange length.

The comparison was also carried out for experimental data using different L_c values (Fig. 12). The coalescence coefficient is found to be a linear function of the continuous-phase length. This relation can be expressed as follows:

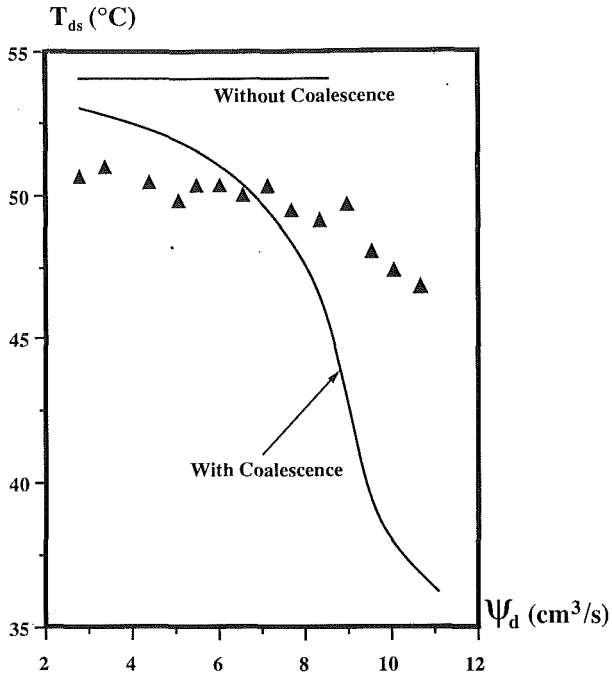

Fig. 14 Outlet temperature of the dispersed phase T_{ds} versus the dispersed phase in flow rate ψ_d. Experimental and numerical results with and without coalescence, with the same conditions as in Fig. 11.

$$c = 2.2\ 10^{-6} L_c \tag{19}$$

Using this formula, numerical and experimental results were quite similar. The linear variation of the coalescence constant in relation to the continuous-phase length can be attributed to the characteristics of the coalescence law that was used (equation (5)). This law is greatly simplified, as there are many parameters other than particle density that influence the coalescence phenomenon (e.g., the residence time of the particles in the spray column, the particle velocities, the interfacial tension, etc.). Thus equation (19) provides a correction coefficient for the residence time of the particles in the exchanger.

Temperatures of Dispersed Phase and Continuous Phase. The temperature of the continuous phase and of the dispersed phase vapor can be measured accurately at the outlet of the spray column, whereas the temperatures measured along the tube are simply mean values of the two-phase mixture. In the region where the void fraction of the dispersed phase is small (first zone), the measured temperature corresponds to the continuous-phase temperature (Tadrist et al., 1987). Yet, when the void fraction increases, experimental measurement of the temperature becomes sensitive and the value obtained corresponds to the true temperature of the two-phase mixture (Coban and Boehm, 1986). Due to the difficulty in conducting measurements, the numerical results were compared with the experimental data only for the outlet temperature of each phase.

The outlet temperature of the continuous phase decreases when ψ_d increases. Experimental results were found to agree with the model regardless of whether coalescence was taken into account (Fig. 13). The variation of the dispersed-phase heat exchange does not significantly modify the continuous-phase temperature because the continuous-phase heat capacity is very large (heat source). On the other hand, the outlet temperature of the dispersed phase is highly dependent on coalescence. If the coalescence effect is not taken into consideration, heat exchange is overestimated and the dispersed-phase outlet temperature is always found to be in equilibrium with the inlet continuous-phase temperature. When considering the coalescence effect, the numerical results correspond closely to the variation of the experimental values

(Fig. 14). It should be noted that the difference between the theoretical curve and the experimental points having a high ψ_d value results from the imprecision in experimental measurement. Indeed, when $\psi_d = 11$ cm^3 s^{-1}, a certain quantity of unevaporated pentane is observed at the outlet of the spray column. This can be seen in the calculated outlet temperature $T_{ds} = 36.2°C$, which corresponds to the boiling point of the n-pentane. Similar results are found for different L_c values.

Both the two-phase length and the temperature of each phase increase with the continuous-phase flow rate. This occurs because the increase in mass quantity of the hot phase results in an improvement of the heat exchange, thus increasing the temperature of each phase (Sun, 1989). This improvement, however, is limited and tends to saturate at the high ψ_c values.

VI Conclusion

In this paper, we have presented an experimental setup used to study the direct-contact vaporization of a dispersed liquid in another immiscible liquid. The experimental study allowed us to determine the void fraction variations in the spray column.

A two-phase heat exchange model was developed to determine the evolution of the hydrodynamic and thermal quantities in the spray column. It has been shown that vaporization results in a rapid variation of the void fraction, thus giving rise to significant interaction and coalescence between the particles. Different coalescence laws based on physical principles have been proposed. The variations are quite different depending on which law is selected. A simple law ($f = -c\, n^2$) was used in the present study as it provides the most reasonable results when compared with experimental values.

Experimental results and those derived from the model were found to agree closely. The measured and calculated local void fractions show similar variations, except in the region where an accumulation of vapor foam was observed in experiments.

It is assumed in the present model that there are three distinct zones, that the two-phase flow is uniform, and that the drop size is dependent only on the abscissa. These hypotheses are not entirely realistic. An improved model would consider the distribution of the particle size as well as the radial effect. This type of simulation requires precise knowledge of the laws of interaction between the phases. The coalescence law should be determined more precisely as it controls the particle density in the spray column. In experimental conditions, it seems that only local measurement can be used to establish a coalescence law truly characteristic of such a system.

References

Battya, P., Raghavan, V. R., and Seetharamu, K. N., 1983, "A Theoretical Analysis of Direct Contact Evaporation in a Spray Column," *International Communication of Heat Mass Transfer*, Vol. 10, pp. 533–543.

Battya, P., Raghavan, V. R., and Seetharamu, K. N., 1984, "Parametric Studies on Direct Contact Evaporation of a Drop in an Immiscible Liquid," *International Journal of Heat and Mass Transfer*, Vol. 27, pp. 263–272.

Boehm, R. F,. and Kreith, F., 1986, "Direct Contact Processes Promise High Performance Low Cost," *Mechanical Engineering*, Mar., pp. 79–81.

Coban, T., and Boehm, R., 1986, "Numerical and Experimental Modeling of Three Phase Direct Contact Heat Exchangers," *Proceedings of Eighth International Heat Transfer Conference*, pp. 3019–3024.

Haberman, W. L., and Morton, R. K., 1956, "An Experimental Study of Bubbles Moving in Liquids," *Trans. ASCE*, Vol. 121, pp. 227–252.

Jacobs, H. R., 1988, "Direct-Contact Heat Transfer for Process Technologies," ASME JOURNAL OF HEAT TRANSFER, Vol. 110, pp. 1259–1270.

Kreith, F., and Boehm, R. F., 1988, *Direct-Contact Heat Transfer*, Hemisphere Pub. Corp., New York.

Mermet, J. L., 1986, "Etude de l'Evaporation en Contact d'un Liquide Dispersé dans un autre Liquide non miscible chaud. Modélisation d'un Evaporateur à Contact Direct," Thèse I.N.P., Grenoble, France.

Moresco, L. L., and Marshall, E., 1980, "Liquid–Liquid Direct Contact Heat Transfer in Spray Column," ASME JOURNAL OF HEAT TRANSFER, Vol. 102, pp. 684–687.

Park, J. Y., and Blair, L. M., 1975, "The Effect of Coalescence on Drop Size Distribution in an Agitated Liquid–Liquid Dispersion," *Chem. Eng. Sci.*, Vol. 30, pp. 1057–1064.

Radovcich, N. A., and Moissis, R., 1962, "The Transition From Two Phase Bubble Flow to Slug Flow," M.I.T. Rept. No. 7-7673-22.

Rowe, P. N., Claxton, K. T., and Lewis, J. B., 1965, "Heat and Mass Transfer From a Single Sphere in an Extensive Flowing Fluid," *Trans. Inst. Chem. Eng.*, Vol. 43, pp. 14–31.

Ruckenstein, E., 1959, "On Heat Transfer Between Vapor Bubbles in Motion and the Liquid From Which They Are Generated," *Chem. Eng. Sci.*, Vol. 10, pp. 22–30.

Sideman, S., and Taitel, Y., 1964, "Direct Contact Heat Transfer With Change of Phase: Evaporation of Drops in an Immiscible Liquid Medium," *Int. J. Heat Mass Transfer*, Vol. 7, pp. 1273–1289.

Smith, R. C., Rohsenow, W. M., and Kasimi, M. S., 1982, "Volumetric Heat-Transfer Coefficients for Direct-Contact Evaporation," ASME JOURNAL OF HEAT TRANSFER, Vol. 104, pp. 264–270.

Sun, J., 1989, "Contribution à l'Etude des Transferts de Chaleur par Contact Direct entre Deux Liquides avec Changement d'Etat Liquide–Vapeur de la Phase Dispersée," Thèse de Docteur, l'Université d'Aix, Marseille, France.

Tadrist, L., Shehu Diso, I., Santini, R., and Pantaloni, J., 1987, "Vaporization of a Liquid by Direct Contact in Another Immiscible Liquid: Part 1: Vaporization of a Single Droplet; Part II: Vaporization of Rising Multidroplets," *Int. J. Heat Mass Transfer*, Vol. 30, No. 9, pp. 1773–1785.

Homogeneous Bubble Nucleation Predicted by a Molecular Interaction Model

Ho-Young Kwak

Sangbum Lee

Mechanical Engineering Department,
Chung-Ang University,
Seoul 156-756, Korea

The homogeneous bubble nucleation of various hydrocarbons was estimated by the modified classical nucleation theory. In this modification, the kinetic formalism of the classical theory is retained while the surface energy needed for the bubble formation is calculated from the interaction energy between molecules. With a nucleation rate value of $J_{n_c}=10^{22}$ nuclei/cm^{3}s, this modified model gives a very good prediction of the superheat limit of liquids. In another test of the model the complete evaporation time of a butane droplet at its superheat limit is compared with experiments and found to be in good agreement.

1 Introduction

The classical theory of homogeneous bubble nucleation is a mixture of macroscopic and molecular concepts. For the initiation of bubble formation, the classical theory initially assumes the formation of the critical size bubble. With the macroscopic interfacial tension, a condition for the formation of the critical bubble is given by

$$p_e - p_\infty = 2\sigma/r_c \tag{1}$$

Here r_c is termed the critical radius. The above equation, known as the Laplace equation, states that the critical bubble is in mechanical equilibrium with the liquid. To continue, one assumes that the critical bubble is in thermal and chemical equilibrium; the internal pressure of the bubble is equal to the vapor pressure p_v at the temperature of the liquid (Jarvis et al., 1975). With the condition given in Eq. (1), the free energy needed to form the critical size bubble becomes

$$F_{r_c}=\frac{4}{3}\pi r_c^2\sigma=\frac{16\pi}{3}\frac{\sigma^3}{(p_v-p_\infty)^2} \tag{2}$$

This expression, originally proposed by Gibbs, has been used previously for a wide variety of purposes (Skripov, 1974).

The classical molecular theory of nucleation, ascribed to Doering (1937, 1938), Volmer (1939), and Zeldovich (1943), supplies a steady state of nucleation for critical bubbles. With the use of Eq. (2), the nucleation rate may be written as (e.g., Blander and Katz, 1975)

$$J=N\left(\frac{\sigma}{\pi mB}\right)^{1/2}\exp\left[-\frac{16\pi\sigma^3}{3kT(p_v-p_\infty)^2}\right] \tag{3}$$

Here B is an arbitrary constant. Usually it is assumed that experimental observation of bubble nucleation in a liquid is possible when the nucleation rate is between $J=1$ and $J=10^6$ bubbles/cm^3 s.

The classical bubble nucleation theory fails to predict the amount of decompression for gaseous bubble formation in water-gas solutions (Hemmingsen, 1970, 1975). It also fails to predict the tensile strength of liquids (Briggs, 1950, 1951). In addition, this classical theory gives no information about the intensity of evaporation at the superheat limit (Avedisian, 1982). The theory, with the work of formation of the critical bubble Eq. (2), was widely accepted because it is quite successful in predicting the superheat limit of liquids with nucleation rate about $J=10^4$–10^6 bubbles/cm^{3}s (Blander and Katz, 1975).

The validity of the capillary approximation—the assumption that the value of surface tension, an equilibrium property of the macroscopic interface, is applicable to the nucleation phenomena—has often been discussed (Buckle, 1968). In fact, from a series of experiments, Hemmingsen (1977) realized that the surface tension at the gas-water boundary of the nucleus must be at least an order of magnitude lower than that obtained from the macroscopic bubble dimensions. Also Baidakov and Skripov (1982) noticed that for cryogenic liquids such as nitrogen, oxygen, and methane, the surface tension of vapor nuclei calculated from the experimental values of superheat limits is 6–7 percent lower than the macroscopic surface tension values.

The classical theory was modified to produce a gaseous bubble formation model (Kwak and Panton, 1983) and a vapor bubble formation model (Kwak and Panton, 1985). The essential element of these models is that the surface energy for the formation of the critical cluster is formulated using molecular concepts, while the kinetic formalism of the classical theory of nucleation is retained. For example, the surface energy for the vapor bubble formation, which is addressed in this paper, is assigned as the energy required to cut across a cluster (Feynman, 1972) composed of activated molecules. The modified model gives much better agreement with the experimental results of Briggs (1950) and Beams (1959) for the tensile strength of various simple liquids. Especially good agreement is attained for water, including the variation in the tensile strength with temperature.

In the present paper, the vapor bubble formation model (Kwak and Panton, 1985) is extended to estimate the superheat limit of various hydrocarbons. In applying the model, we introduce the van der Waals volume enclosed by the electron clouds of the molecules. For this kind of molecules, we also use a value of the dispersion energy averaged over all orientations. The reduced superheat limit of these fluids turns out to be about 0.89–0.90. In addition to the correct prediction of the superheat limit of liquids, the model makes it possible to calculate the evaporation rate of droplets at the superheat limit, which is directly related to the intensity of evaporation. Comparison was made for butane, a case for which good experiments are available (Shepherd and Sturtevant, 1982; McCann et al., 1988).

The detailed nature of the evaporation process at this limit may lead to the understanding of "vapor explosion," which poses a potential hazard in the transport of liquid natural gas and in the operation of liquid metal fast breeder reactors (Blander and Katz, 1975; Reid, 1976).

Contributed by the Heat Transfer Division for publication in the JOURNAL OF HEAT TRANSFER. Manuscript received by the Heat Transfer Division April 2, 1990; revision received November 21, 1990. Keywords: Boiling, Evaporation, Phase-Change Phenomena.

2 Stability Condition for a Cluster

Consider a system: a liquid at temperature T and under an ambient pressure p_∞. If the temperature of a liquid is well above the boiling point or the ambient pressure is well below the equilibrium vapor pressure, the system is in a metastable state. In such a system, one can imagine formation of clusters by activated liquid molecules.

A stability condition for a cluster and the corresponding minimum free energy for the cluster can be obtained by assuming that the liquid has a face centered cubic lattice (FCC) structure and that the London dispersion force is the only important interaction between molecules in their metastable state (Kwak and Panton, 1985):

$$-(p_\infty - p_v)n_c^{1/3} = \frac{z\epsilon_m}{3}/v_m \tag{4-1}$$

$$F_{n_c} = \frac{z\epsilon_m}{6} n_c^{2/3} = \frac{1}{2}(p_v - p_\infty)v_m n_c \tag{4-2}$$

These equations imply that the driving force for bubble formation is just the chemical potential difference between the metastable state and the saturation state; that is, $(p_\infty - p_v)v_m$. If any cluster, an aggregate of the activated molecules in the metastable state, meets the condition of Eq. (4-1), the liquid molecules in the cluster vaporize spontaneously by breaking the interaction between molecules. Thus Eq. (4-1) can be regarded as the equation of vapor state of the critical cluster. The evaporated state, retaining the molecular volume of the saturated liquid state v_m, is characterized by its very high pressure, p_n:

$$p_n = (p_v - p_\infty)n_c^{1/3} = \frac{z\epsilon_m}{3}/v_m \tag{4-1}'$$

For example, the value of p_n is about 136 atm for butane at its superheat limit. Such discontinuity in pressure is one of key features for nonequilibrium phase transition. For the equilibrium case, the dependence of volume on pressure is discontinuous along an isotherm. Of course, the internal pressure calculated from a realistic fluid model, such as the Lennard–Jones model, equals the equilibrium vapor pressure, p_v. However, the state with internal pressure of p_v can be achieved when the vapor molecule occupies the equilibrium molecular volume about $n_c^{1/3} v_m$. In the above equations, ϵ_m is the energy required to separate a pair of molecules from the given liquid state to the critical state. This is given by (Kwak and Panton, 1985) approximately

$$\epsilon_m = 4\epsilon_0\left[1 - \left(\frac{\rho_c}{\rho_m}\right)^2\right]\left[\left(\frac{d_w}{d_m}\right)^6 - \left(\frac{d_w}{d_m}\right)^{12}\right] \tag{5}$$

The average distance between molecules d_m in Eq. (5) and the effective molecular volume v_m in Eq. (4) can be found from the number density of liquid, N. The relation is

$$\frac{\pi}{6} d_m^3 N = v_m N = 0.7405 \tag{6}$$

where 0.7405 is the packing fraction of FCC lattice structure.

This stability condition of the cluster and the minimum free energy for vapor bubble formation turn out to be same for gaseous bubble formation in solution (Kwak and Panton, 1983) after a transformation such as

$$v_m = \left(\frac{4\epsilon_m}{kT}\right)^{3/2} v_m' \tag{7-1}$$

$$n_c = \left(\frac{kT}{4\epsilon_m}\right)^{3/2} n_c' \tag{7-2}$$

This is just a scaling transformation, which changes the mean value of the potential energy of a molecule in the cluster to be the translational energy of a molecule. The transformed forms of Eqs. (4-1) and (4-2) are:

$$-(p_\infty - p_v)n_c'^{1/3} = \frac{kT}{v_m'} \tag{8-1}$$

$$F_{n_c}' = \frac{1}{2} kT\, n_c'^{2/3} \tag{8-2}$$

Using the above expressions of the stability condition of the

Nomenclature

d_m = average distance between molecules
D_n = rate of molecules striking on the surface of n-mer cluster
d_w = van der Waals' diameter of liquid molecules
E_I = ionization potential
F_n = free energy needed to form n-mer cluster
F_r = free energy needed to form a bubble with radius of r
G = mass flux
j = nucleation probability, Eq. (13)
J = nucleation rate of bubble per unit volume
J_n = nucleation rate of n-mer cluster per unit volume
J_s = nucleation rate per unit area
k = Boltzmann constant
m = mass of molecule
M = molecular weight
n = number of molecules in a cluster
N = number density = ρ_m/m
N_A = Avogadro's number
n_b = number of molecules inside a bubble
n_D = refractive index of fluid
p_e = pressure inside a bubble
p_v = vapor pressure
p_∞ = ambient pressure
r = radius of bubble
R = gas constant
R_d = radius of evaporated sphere in the droplet
T = temperature of liquid
T_c = critical temperature
T_f = melting temperature of liquid
t_l = time lag of nucleation events
T_s = superheat limit of liquid
V = volume of a droplet
v_l = usual molecular volume of liquid
V_l = molar volume of liquid
v_m = effective molecular volume of liquid
V_w = van der Waals molar volume
z = coordination number
Z_f = Zeldovich nonequilibrium factor
α = polarizability of a liquid molecule
α_T = thermal expansion coefficient of liquid
β = accommodation coefficient
ΔH_{vap} = enthalpy of evaporation
ΔH_f = enthalpy of fusion
ϵ_0 = potential parameter of London dispersion attraction
ϵ_D = dielectric constant of liquid
ϵ_m = energy needed to separate a pair of molecules
ρ_m = density of liquid
ρ_c = critical density of liquid
σ = interfacial tension
τ = tensile strength of liquid
ϕ = number of molecules evolved in nucleation process in a volume of $4\pi r_m^2 \cdot 1$ cm (see Eq. (22)′)

Subscript

c = critical cluster or critical size bubble

cluster, Eq. (8-1), and the minimum free energy for the bubble formation, Eq. (8-2), one may treat the bubble formation by dissolved gas molecules and vapor molecules simultaneously (Kwak and Oh, 1988).

3 Nucleation Rate of the Critical Cluster

Using the customary kinetic theory argument (Frenkel, 1946), the steady state nucleation rate per unit volume, J_{n_c} (nuclei/cm^3•s), for critical clusters may be written as

$$J_{n_c} = N D_{n_c} Z_f \exp\left[-\frac{z}{6} \left(\frac{\epsilon_m}{kT} \right) n_c^{2/3} \right] \tag{9}$$

where the Zeldovich nonequilibrium factor (Feder et al., 1966), Z_f, is given by

$$Z_f = \left[-\frac{1}{2\pi kT} \left(\frac{\partial^2 F_n}{\partial n^2} \right)_{n=n_c} \right]^{1/2} = \left[\frac{z\epsilon_m}{18\pi kT} \right]^{1/2} n_c^{-2/3} \tag{10}$$

In Eq. (9), D_{n_c} is the rate molecules strike the surface of critical cluster. With appropriate assumptions this may be given by (Kwak and Panton, 1985)

$$D_{n_c} = \frac{\beta}{4} N \left(\frac{8kT}{\pi m} \right)^{1/2} \exp\left(-\frac{\Delta H_{\text{vap}}}{RT} - \frac{\Delta H_f}{RT_f} \right) 4\pi \left(\frac{3v_m}{4\pi} \right)^{2/3} n_c^{2/3} \tag{11}$$

It is important to note that Eq. (9) is valid in the steady state after the transient stage. The time lag t_l, which represents the duration of the transient state after the onset of nucleation occurs (see section 4) may be written as (Feder et al., 1966)

$$t_l = (4\pi D_{n_c} Z_f^2)^{-1} \tag{12}$$

Now the remaining problem is how to determine the nucleation rate of critical clusters, J_{n_c}, for the specific case of homogeneous nucleation. To estimate this value, one may use the nondimensional parameter (Feder et al., 1966) j from Eq. (9):

$$j = J_{n_c}/(N D_{n_c} Z_f) = \exp(-F_{n_c}/kT) \tag{13}$$

Lienhard and Karimi (1981) considered homogeneous nucleation corresponding to the spinodal line of the liquid. They assigned a value of F_{n_c}, which can be characterized as the potential energy (Tien and Lienhard, 1979), and may be expressed in terms of the critical temperature

$$F_{n_c}/kT_c = 11.5 \tag{14}$$

At the superheat limit, the reduced temperature is around 0.9; hence the above value becomes

$$F_{n_c}/kT_s \cong 13.0 \quad \text{or} \quad j \cong 10^{-6} \tag{14}$$

Now one can estimate the nucleation rate of critical clusters. With a typical number density of $N = 10^{21}$ molecules/cm^3 and a value $D_{n_c} Z_f = 10^7$/s, the nucleation rate at the superheat limit is approximately

$$J_{n_c} = jND_{n_c} Z_f = 10^{22} \text{ nuclei/cm}^3\text{s} \tag{15}$$

An even higher nucleation rate value of about $J = 10^{26}$ may be obtained by using the pre-exponential factor $(\sigma/\pi mB)^{1/2}$ defined in Eq. (3) and Lienhard's value for the homogeneous nucleation limits, $F_{n_c}/kT_c = 11.5$. In their recent work, Oxtoby and Evans (1988) also predicted the nucleation rate enhancement of 10 to 17 orders of magnitude over the classical prediction for bubble formation because the chemical potential difference between metastable state and the saturated state of liquid spinodal is smaller than at the gas spinodal.

The best method of finding the actual correct nucleation rate is by comparing experimental results on the evaporation of a droplet at its superheat limit.

4 Evaporation Phenomenon of a Droplet at the Superheat Limit

Recently Shepherd and Sturtevant (1982) observed the evaporation of a butane droplet at its superheat limit. They also measured the evaporation rate, as well as the far field pressure signal emanating from the evaporating droplet. Their photographic study revealed that the evaporation process (nucleation) first started at an asymmetric point in the droplet. Thereafter, the evaporation continued step by step to spread, eventually covering the whole droplet. This is a remarkable confirmation of the idea of L. Szilard (Farkas, 1927); the formation of a viable embryo is required to start the chain of evaporation. Indeed, such a chain reaction mechanism is in the context of the classical kinetic theory.

With a rather simple model we can predict the evaporation of a droplet at the superheat limit. Even though the nucleation center at first is found to be at an asymmetric position in the droplet, let us treat this problem symmetrically by assuming that the nucleation point at first coincides with the center of the droplet. Let R_d be the radius of the evaporated sphere in the droplet at time t. If the increment of the radius of the evaporated sphere is dR_d (assume $dR_d \ll R_d$) during dt, the total number of evaporated molecules in the volume $4\pi R_d^2 dR_d$ is

$$4\pi R_d^2 dR_d N \tag{16}$$

Since the evaporation rate, that is, the number of molecules evaporated per unit time and unit volume (Frenkel, 1946), is $J_{n_c} n_c$, then the number of molecules evaporated during dt in a volume $4\pi R_d^2$•1 cm becomes

$$(J_{n_c} \text{•} 1 \text{ cm}) n_c \text{•} 4\pi R_d^2 dt = J_s n_c \text{•} 4\pi R_d^2 dt \tag{17}$$

where J_s ($= J_{n_c}$•1 cm) is the nucleation rate with unit depth.

In the above equation, it is assumed that the surface area is covered with the critical nuclei. This assumption is valid for volume (bulk) nucleation (Afansa'ev and Krokhin, 1967), which occurs in the rapid solidification of undercooled Si (Stiffler et al., 1988). Such a nucleation process in two dimensions—the idea of surface area covered by critical nuclei with heterogeneity factor—was first considered by Alamgir and Lienhard (1981). Certainly this is the case in which no heterogeneous elements are present. By equating Eq. (16) to Eq. (17), one may obtain the velocity of the vapor sphere in the droplet for the one-dimensional evaporation case:

$$dR_d/dt = J_s n_c/N \tag{18}$$

In the case that nuclei generate in the droplet at random, the time needed for the droplet to evaporate completely is $4\pi R_d^3 N/3/(J_{n_c} n_c \text{•} 1 \text{ cm}^3)$, which is obviously shorter than that for one-dimensional evaporation case.

With the help of equation (8), we may write the above equation as

$$dR_d/dt = 1.3504\ v_m J_s n_c = v_l J_s n_c \tag{18}'$$

where $v_l = 1/N$, a usual molecular volume. This equation represents the evaporation of a unit layer with surface area of $4\pi R_d^2$ (one-dimensional approximation), which is clear if one compares this to the evaporation of a small metal drop (Samble et al., 1970), in which evaporation of molecules at the surface layer rather than bulk nucleation occurs.

Since J_{n_c} is constant during the steady-state nucleation process, the speed of growth of the vapor sphere remains constant. This is consistent with Shepherd and Sturtevant's observation: "the growth rate of the vapor sphere appears to be linear with a mean velocity of approximately 1.43×10^3 cm/s." Also McCann et al. (1988) measured a bubble growth rate of 1.39×10^3 cm/s for the evaporation of butane droplet at the superheat limit. With this observed value of dR_d/dt, Eq. (18) may be used to determine the nucleation rate at the superheat

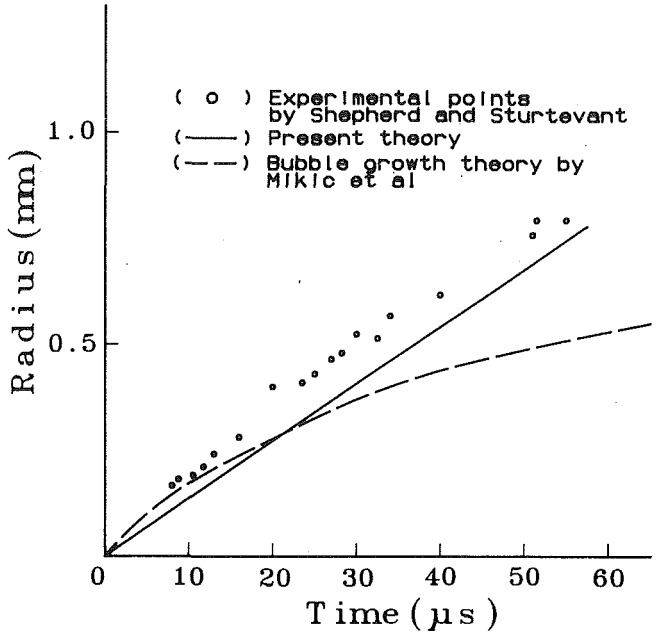

Fig. 1 Radius of evaporating droplet as a function of time

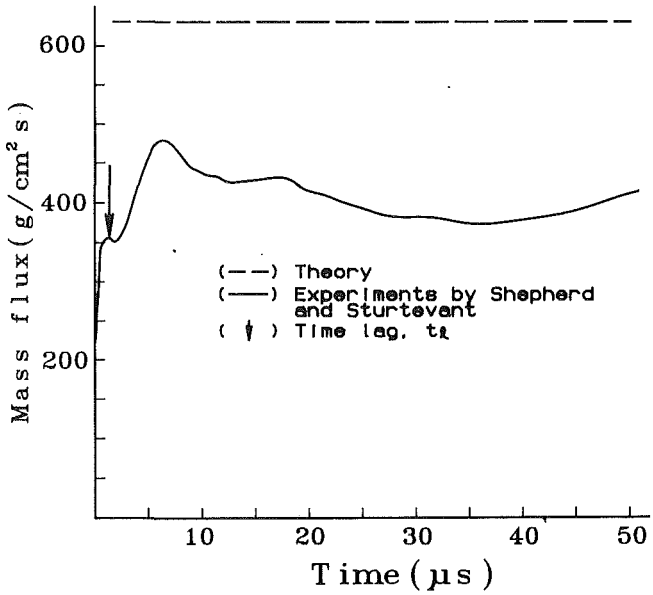

Fig. 2 Evaporative mass flux of a butane droplet at its superheat limit

limit. Also, one should be able to predict the superheat limit of the liquid with a nucleation rate evaluated from Eq. (18). The nucleation rate value that meets these conditions is about 10^{22} nuclei/cm^3 s for butane.

With an initial condition of $R_d = 0$ at $t = 0$, the time dependence of the radius of the vapor sphere becomes

$$R_d = v_l J_s n_c t \tag{19}$$

Experimental results and the curve obtained from Eq. (19) with $J_s = 10^{22}$ are shown in Fig. 1. As is apparent, conventional theory of bubble growth (Mikic et al., 1970) gives incorrect results when applied to this case. The bubble growth in the initial stage may be restricted by the condensation and evaporation process (Skripov, 1974). The above equation is valid until the droplet is fully evaporated (about 40 μs). After complete evaporation, the molecules become a gas bubble. The subsequent nonlinear growth and collapse mechanism of the gas bubble are governed by the well-known Rayleigh equation (Rayleigh, 1917; Kwak, 1984).

The evaporative mass flux G in this evaporation process may be written as

$$G = \rho_m \frac{dR_d}{dt} = m J_s n_c \tag{20}$$

Even though the observed values of the mass flux are somewhat below the value calculated from Eq. (20) and shown in Fig. 2, such a simple steady-state nucleation model is quite good after the time lag. For butane at 378 K, the time lag t_l calculated from Eq. (12) is about 16 μs, as marked in Fig. 2. Note that we have used the liquid density of butane at 378 K to evaluate the mass flux (see section 2). Rewriting the evaporative mass flux, Eq. (20), with help of Eqs. (9), (10), and (11), we have

$$G = \beta \rho_m \sqrt{\frac{kT}{2\pi m}} \exp\left(-\frac{\Delta H_{\text{vap}}}{RT} - \frac{\Delta H_f}{RT_f} \right) \phi \tag{20}'$$

where

$$\phi = n_c \, 4\pi r_m^2 \, N \exp\left[-\frac{z}{6} \left(\frac{\epsilon_m}{kT} \right) n_c^{2/3} \right],$$

which is the number of molecules involved in the nucleation process in a volume of $4\pi r_m^2 \cdot 1$ cm.

The absolute rate of evaporation, $\rho_m \sqrt{kT/2\pi m}$ (Schrage, 1953; liquid density rather than vapor density in this case), may be achieved for the case in which a cluster is constituted by one molecule. This absolute limit corresponds to molecular evaporation (Schrage, 1953). Certainly the rate of evaporation at the superheat limit (ϕ is on the order of n_c in this case) is much less than the absolute rate of evaporation because of the exponential term in Eq. (20)′, which distinguishes activated molecules (ΔH_{vap}) and reduces the mean velocity of molecules in liquid (ΔH_f; Faber, 1972).

To estimate the life time of the droplet at the limit, Sinitsyn and Skripov (1968) defined the time scale of the event, t_s, as

$$t_s = (JV)^{-1} \tag{21}$$

where V is the volume of the metastable phase or a droplet. For a 1-mm-dia droplet with the nucleation rate value $J = 10^6$ bubbles/cm^3 s, this time is on the order of microseconds, which turned out to be the time scale of the bubble oscillation after the complete evaporation (Shepherd and Sturtevant, 1982).

The nucleation rate is an important parameter to control the rate of nucleation process (Skripov, 1974). For example, Reid (1976) conjectured that the nucleation rate for a vapor explosion is about 10^{12} nuclei/cm^3 s. Stiffler et al. (1988) also estimated the nucleation rate at about 10^{23} events/cm^3 s from the measurement of the completion time in the solidification of supercooled Si following pulsed laser-induced melting of a thin film. Note that nucleation theory itself (Eq. (3) or Eq. (9)) does not allow an arbitrary value of nucleation rate; that is, if one knows the nucleation rate, one can determine the superheat limit and vice versa (Kwak, 1987; Stiffler et al., 1988). As is clear from Table 1, simultaneous prediction of these two quantities such as the superheat limit and the complete evaporation time of a droplet with a given nucleation rate is plausible. For pure liquids such as butane and pentane (Porteus and Blander, 1975) the deviation from the mean value of the measured superheat limit obtained by droplet explosion technique is less than 0.5°C. Such a narrow range of the superheat limit also lets us define the complete evaporation time of a droplet reasonably.

As mentioned earlier, the evaporation of a droplet at the superheat limit is a remarkable example of a nucleation event governed by kinetics. On the other hand, for the case of random generation of bubbles in pool of liquid, the diffusion process is a key factor for bubbles to grow to macroscopic size (Kwak and Kim, 1988) so that the time scale of this events is on the

Table 1 Number of molecules of critical cluster, n_c, the superheat limit, T_s, evaporation speed at the superheat limit, u, and the complete evaporation time of a 1-mm-dia butane droplet, t_c, for various values of the nucleation rate

J_{n_c}	$10^{21.5}$	$10^{21.75}$	10^{22}	$10^{22.25}$	$10^{22.5}$
n_c	733	707	681	650	620
T_s (K)	377.0	377.5	378.0	378.5	379.0
u (cm/s)	488	839	1440	2449	4157
t_c (μs)	100	60	35	20	12

order of a second. In such cases, the cluster that meets the stability conditions becomes stable and grows, as a cluster, until it becomes a critical size bubble. The corresponding nucleation rate is about 1 to 10^6 bubble/cm^3 s depending on the final volume occupied by bubbles in solution.

5 Molecular Properties of Liquids

For symmetric molecules, the potential parameter ϵ_0 in Eq. (5) (the London dispersion attraction at large separation) is given by

$$\epsilon_0 = \frac{3}{16}\frac{E_I \alpha^2}{d_w^6} \tag{22}$$

Even though the magnitude of the dispersion interaction between asymmetric molecules depends upon the relative orientation of the molecules, the potential parameter for the dispersion energy averaged over all orientations (Hirschfelder et al., 1954) is approximately as given in Eq. (22). In this case, the polarizability α is also the value averaged over all solid angles.

For the fluids whose polarizability data were not available, the Lorentz–Lorenz formula (Born and Wolf, 1975) (alternatively the Clausius–Mossotti equation) was used to evaluate the quantities

$$\alpha = \frac{3M}{4\pi N_A \rho_m}\left(\frac{n_D^2-1}{n_D^2+2}\right) \tag{23-1}$$

or

$$\alpha = \frac{3M}{4\pi N_A \rho_m}\left(\frac{\epsilon_D-1}{\epsilon_D+2}\right) \tag{23-2}$$

Since the Lorentz–Lorenz function $LL=(n_D^2-1)/[\rho_m(n_D^2+2)]$ is almost constant over the entire temperature range (Garside et al., 1968), the polarizability of liquids was obtained from the density and the refractive index data at the same temperature.

Another important physical property to be evaluated in Eq. (5) is the van der Waals diameter of liquid molecules (Streitwieser and Heathcock, 1981). The diameter may be obtained from the liquid molar volume (V_l) at the specified temperature. Since the average value of the thermal expansion coefficient, α_T, for organic solutions (Eley, 1939) is about 10^{-3}, one may use the following relationship between the liquid molar volume (V_l) and the van der Waals molar volume (V_w) for polymer liquids (Van Krevelen and Hoftyzer, 1976):

$$V_w = V_l(T)/[1.60+\alpha_T(T-298)]$$
$$\cong V_l(T)/[1.30+10^{-3}T] \tag{24}$$

With aid of Eqs. (6) and (24), the van der Waals diameter may be expressed in terms of the average distance between molecules at specified temperature, $d_m(T)$. It is

$$d_w = d_m(T)/[1.30+10^{-3}T]^{1/3} \tag{25}$$

Usually this parameter is evaluated at $T=293$ K. Physical parameters for typical hydrocarbons are shown in Table 2.

Table 2 Physical properties of hydrocarbons

Liquid	van der Waals' diameter d_w (Å)	Polarizability α (Å^3)	Ionization potential (eV)	Density (g/cm^3)
Ethane	4.5086	4.47[lb]	11.5	0.5090 (213.15 K)
Propane	5.0635	6.29[lb]	11.1	0.5005
Butane	5.2889	8.12[lb]	10.63	0.5788
Pentane	5.5370	9.95[lb]	10.35	0.6262
Hexane	5.7719	11.78[lb]	10.18	0.6603
Heptane	5.9991	13.61[lb]	9.90	0.6838
Octane	6.2107	15.44[lb]	10.24	0.7025
Nonane	6.4093	17.3813	10.21[lb]	0.7177
Decane	6.5977	19.1[lb]	10.19[lb]	0.7299
Isobutane	5.3564	8.14[lb]	10.57	0.5572
2,3-Dimethyl butane	5.7681	11.8207	10.0[lb]	0.6616
Cyclopropane	4.5559	5.64[lb]	10.09	0.6769
Cyclopentane	5.1749	9.1682	10.53	0.7457
Cyclohyexane	5.4204	10.87[lb]	11.0[lb]	0.7786
Benzene	5.0784	10.32[lb]	9.24[lb]	0.8787
1,3-Dimethyl benzene	5.6567	14.18[lb]	8.58	0.8642

Notes: (*a*) The ionization potential data, except those denoted lb (Landolt–Bornstein) and the density data at given temperature were obtained from the *CRC Handbook of Chemistry and Physics*, CRC Press Inc., 1979. The density data without temperature given are values at 20°C.

(*b*) The polarizabilities are taken from Landolt–Bornstein, *Zahlenwerte und Funktion*, 6th ed., Springer, 1951, and denoted lb in table. The other polarizability data are calculated from the Lorentz–Lorenz formula.

6 Calculation of the Superheat Limit

By regarding the equilibrium vapor pressure as a reference pressure, the liquid at temperature T, corresponding vapor pressure of p_v, and at an ambient pressure of p_∞ is considered to be under a tensile stress as given by Kwak and Panton (1985)

$$-\tau = p_v - p_\infty \tag{26}$$

With the aid of the stability condition for a cluster, Eq. (4-1), the intrinsic tensile strength of the liquid, τ, may be rewritten as

$$-\tau = \left(\frac{z\epsilon_m}{3}/v_m\right)/n_c^{1/3} \tag{27}$$

Since the pre-exponentional factor of Eq. (9) depends only on molecular properties such as ϵ_m, v_m, and N, which are slowly varying functions of temperature, the number of molecules in the critical cluster, n_c, can be determined from Eq. (9) with a specified value of the nucleation rate, J_{n_c}, at given temperature. With the value of n_c and the molecular properties known, the intrinsic tensile strength of liquid at given temperature is readily found from Eq. (27). Now the superheat limit corresponding to the vapor pressure, p_v, is determined from the intersection between the vapor pressure curve, Eq. (26) and the intrinsic tensile strength curve, Eq. (27). In other words, the liquid under a tensile stress equal to its intrinsic tensile strength ruptures to evaporate spontaneously. As an example, the superheat limit for butane (with nucleation rate $J_{n_c}=10^{22}$) is shown in Fig. 3. The nucleation rate, $J_{n_c}{}^{22}$ nuclei/cm^3 s (obtained from the observed evaporation speed of butane droplet at the superheat limit), was assumed for other fluids in predicting the results from droplet explosion experiments.

As shown in Fig. 3, one must know the temperature dependence of the tensile strength and the vapor pressure in order to determine the superheat limit of liquid. Assumptions used in the calculations are as follows. The temperature dependence of the saturated liquid density and the effective diameter of the molecules were estimated by the Gunn–Yamada (1971) method. The Frost–Kalkwarf (1953) method was employed to estimate the vapor pressure dependence on temperature. For

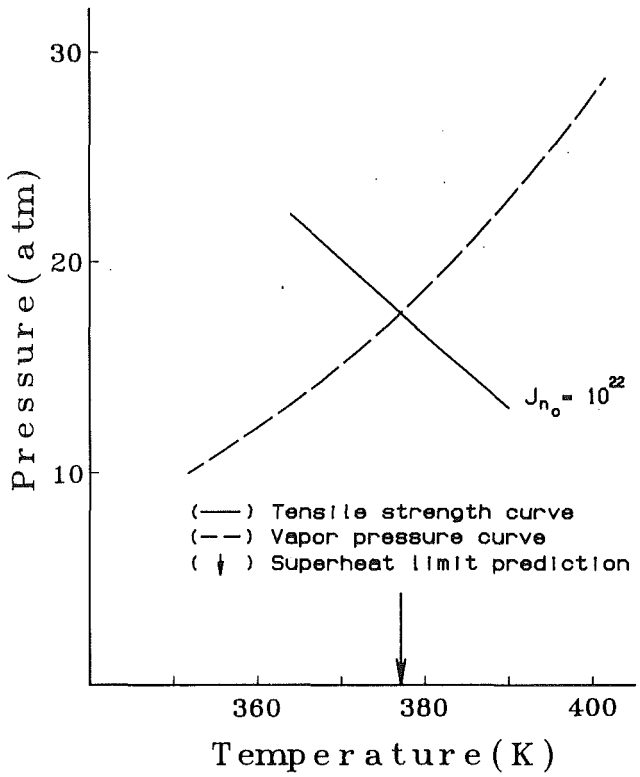

Fig. 3 Determination of the superheat limit of butane

the temperature dependence of the enthalpy of evaporation, Carruth and Kobayashi's (Reid et al., 1977) estimation method was used. The accommodation coefficient β was assumed to be unity in all calculations.

Our predictions for the superheat limit of hydrocarbons are shown in Table 3. In addition, the superheat limit calculated by the unmodified classical nucleation theory with a macroscopic surface tension is listed, as well as the experimental results by various authors (Porteus and Blander, 1975; Blander et al. 1971; Kenrick et al., 1924; Eberhart et al., 1975; Patrick-Yeboch and Reid, 1981). The new superheat limits of various hydrocarbons are shown to be in good agreement with the measurements by the droplet explosion technique, which verified that it is possible to predict the superheat limit of liquid as well as the evaporation phenomena at this limit avoiding the macroscopic capillarity approximation.

As noted briefly in the introduction, this modified model predicts the tensile strength of simple liquids such as helium, hydrogen, argon, oxygen, nitrogen, and water (Kwak and Panton, 1985). This model also predicts the tensile strength of organic liquids at 20°C (Kwak, 1983).

8 Discussion

The modified bubble formation model of classical nucleation theory, which is employed in this paper, predicts the superheat limit of liquids as well as the time scale of the evaporation process. Another merit of this modified model is that it can predict the tensile strength of liquids and gas bubble formation in liquids as noted in section 2. An essential feature of this bubble formation model is that the interface between liquid and vapor is not yet formed during the clustering process governed by kinetics. Therefore we cannot use the macroscopic surface tension value for the surface energy needed in the formation of the critical cluster (Kwak and Panton, 1983, 1985). Once the interface is formed, the diffusion process plays a dominant role in bubble growing (Kwak and Kim, 1988).

Recently, the nucleation rate has been measured for the

Table 3 Superheat limits of hydrocarbons

Liquid	Present theory $K(T_s/T_c)$ $J_{n_c}=1$	$J_{n_c}=10^{22}$	Classical theory ($J=10^6$)	Experiment	Reference (authors' initials)
Ethane	261.5 (0.8563)	275 (0.9005)	269.5	269.2	PB
Propane	311.0 (0.8410)	329.5 (0.8910)	328.5	326.2	PB
Butane	358.5 (0.8431)	377.5 (0.8878)	378.4	376.9	PB
Pentane	396.0 (0.8433)	421.0 (0.8965)	421.5	421.0	BHK
Hexane	430.0 (0.8475)	456.5 (0.8997)	457.5	457.0	BHK
Heptane	460.0 (0.8515)	485.5 (0.8987)	487.7	486.7	EKB
Octane	485.0 (0.8527)	517.5 (0.9098)	515.9	513.0	EKB
Nonane	507.5 (0.8535)	536.0 (0.9014)	535.0	538.5	EKB
Decane*	513.5 (0.8314)	557.5 (0.9027)	556.0	558.3	EKB
Isobutane	343.5 (0.8417)	363.0 (0.8895)	360.8	361.0	PB
2,3-Dimethyl butane	419.5 (0.8392)	439.0 (0.8782)	449.1	446.4	EKB
Cyclopropane	338.0 (0.8497)	356.5 (0.8962)	——	350.7	PB
Cyclopentane	432.5 (0.8454)	453.5 (0.8864)	446.4	456.7	EKB
Cyclohexane	468.0 (0.8457)	491.0 (0.8872)	489.5	492.8	EKB
Benzene	482.5 (0.8584)	507.0 (0.9020)	501.0	504.0	PR
1,3-Dimethyl benzene	522.5 (0.8468)	550.5 (0.8922)	——	(508.4)	KGW

*Superheat limits calculated by 6-9 potential type.

quantitative test of the classical nucleation theory in the case of homogeneous nucleation from vapor to liquid (Matthew and Steinwandel, 1983; Wagner and Strey, 1984; Kacker and Heist, 1985; Strey et al., 1985). In these experimental investigations, the dependence of nucleation rate on the supersaturation was found to be good agreement with the classical theory; however, the actual values of experimental and theoretical nucleation rate differ by several orders of magnitude or even more. Thus, the change in the value of macroscopic surface tension is necessary to bring the classical theory into agreement with experimental data. In fact, certain modifications to the classical theory were suggested in the homogeneous condensation case also. In these modifications, the free energies for formation of small clusters are calculated from the interaction potential directly while keeping the kinetic formalism of classical theory (McGinty, 1973; Hoare et al., 1980; Garcia and Torroja, 1981), which has been done for the homogeneous bubble nucleation case in this paper.

As noted in the introduction, one of the crucial assumptions in classical nucleation theory is that the critical size bubble is in mechanical and chemical equilibrium. This equilibrium theory, which may be applicable to the fluid at high ambient pressure (Skripov and Ermakov, 1964; Avedisian, 1982) cannot be applied to the phase transition at the superheat limit under an ambient pressure of 1 atm. The explosive character of the evaporation process in this case (Shepherd and Sturtevant, 1982; McCann et al., 1988) may be due to the very rapid evaporation process, corresponding to a very large nucleation rate, which makes the evaporated molecules keep their saturated liquid volume during this process so that the internal pressure of the vapor is very high (see sections 2 and 4). In fact, the driving force for nonlinear oscillation of a bubble after the complete evaporation of a droplet at the superheat limit depends on the difference in pressure between vapor within bubble and the surrounding liquid (Avedisian, 1982;

Table 4 Dielectric constant computed from Eq. (23-2) at the superheat limit T_s

Liquid	Molecular weight	Superheat limit (K)	Density at T_s (g/cm^3)	Dielectric constant at T_s
Propane	44.10	327.5	0.4382	1.5617
Butane	58.12	377.5	0.4577	1.5770
Pentane	72.15	421.0	0.4623	1.5748
Hexane	86.18	457.0	0.4668	1.5752
Heptane	100.21	485.5	0.4720	1.5787
Octane	114.23	517.5	0.4644	1.5642
Nonane	128.26	536.0	0.4734	1.5791

Kwak, 1987). Henry and Fauske (1979) also realized that the pressure inside the vapor space is higher than ambient pressure for a vapor explosion.

The equilibrium theory leads to the following unreasonable result. If one assumes that the critical size bubble is in mechanical equilibrium and the vapors in the bubble behave either ideally (Doering, 1983; Volmer, 1939) or nonideally, the free energy needed to form such a bubble is proportional to the number of molecules in the bubble, say n_b. That is

$$\frac{F_{r_c}}{kT}=\frac{4}{3}\pi r_c^2\sigma/kT=\frac{1}{2}(p_v-p_\infty)\cdot\frac{4}{3}\pi r_c^3/kT\sim n_b \qquad (28)$$

This is a consequence of the fact that the pressure of the bubble in mechanical equilibrium is two-thirds of the total translational energy of molecules inside the bubble (Batchelor, 1967). However, the free energy to form the critical cluster is supposed to be proportional to $n_c^{2/3}$, as can be seen in Eq. (4-2) because the driving force for bubble formation, $(p_v-p_\infty)v_m$ is approximately proportional to $kT/n_c^{1/3}$ (Kwak and Oh, 1988).

There is also an interesting side issue. It is known that the breakdown of molecular interactions at the superheat limit is accompanied by a dielectric breakdown of the liquid (Kraucki, 1966; Felix and Ellis, 1971). Remarkably, as shown in Table 4, the dielectric constant of hydrocarbons at the superheat limit have almost the same values. This implies that one might use the dielectric constant as a measure of the superheat limit.

We have shown that by using a vapor bubble formation model, one can predict the linear and nonlinear growth and the collapse mechanism of a bubble formed from the fully evaporated droplet at the superheat limit (Kwak, 1984). Also this model takes into account the intensity of evaporation depending on the ambient pressure (Kwak, 1987).

Acknowledgments

One of the authors (HK) was supported by the Korean Science and Engineering Foundation during this research. The authors thank Professor R. L. Panton for many discussions and suggestions. Also the author (HK) wishes to thank Professor C. T. Avedisian for financial support during his stay at Cornell University, where revision of this paper was done. The authors also thank the referee who informed us of the excellent works of Alamgir and Lienhard, and Schrage.

References

Afanas'ev, Yu. V., and Krokhin, O. N., 1967, "Vaporization of Matter Exposed to Laser Emission," *Sov. Phys. JETP*, Vol. 25, pp. 639-643.

Alamgir, Md., and Lienhard, J. H., 1981, "Correlation of Pressure Undershoot During Hot-Water Depressurization," ASME JOURNAL OF HEAT TRANSFER, Vol. 103, pp. 52-55.

Avedisian, C. T., 1982, "Effect of Pressure on Bubble Growth Within Liquid Droplet at the Superheat Limit," ASME JOURNAL OF HEAT TRANSFER, Vol. 104, pp. 750-757.

Baidakov, V. G., and Skripov, V. P., 1982, "Superheating and Surface Tension of Vapor Nuclei in Nitrogen, Oxygen, and Methane," *Russ. J. Phys. Chem.*, Vol. 56, pp. 499-501.

Batchelor, G. K., 1967, *An Introduction to Fluid Dynamics*, Cambridge University Press, United Kingdom, p. 39.

Beams, J. W., 1959, "Tensile Strengths of Liquid Argon, Helium, Nitrogen, and Oxygen," *Phys. Fluids*, Vol. 2, pp. 1-4.

Blander, M., Hengstenberg, D., and Katz, J. L., 1971, "Bubble Nucleation in *n*-Pentane, *n*-Hexane, *n*-Pentane+Hexadecane Mixtures, and Water," *J. Phys. Chem.*, Vol. 75, pp. 3613-3619.

Blander, M., and Katz, J. L., 1975, "Bubble Nucleation in Liquids," *AIChE J.*, Vol. 21, pp. 833-848.

Born, M., and Wolf, E., 1975, *Principles of Optics*, Pergamon, Oxford, United Kingdom, pp. 87-88.

Briggs, L. J., 1950, "Limiting Negative Pressure of Water," *J. Appl. Phys.*, Vol. 21, pp. 721-722.

Briggs, L. J., 1951, "The Limiting Negative Pressure of Acetic Acid, Benzene, Aniline, Carbon Tetrachloride, and Chloroform," *J. Chem. Phys.*, Vol. 19, pp. 970-972.

Buckle, E. R., 1968, "A Kinetic Theory of Cluster Formation in the Condensation of Gases," *Trans. Faraday Soc.*, Vol. 65, pp. 1267-1288.

Doering, W., 1937, "Die Ueberhitzungsgrenze und Zereissfestigkeit von Fluessigkeiten," *Z. Physikal Chem., B.*, Vol. 36, pp. 371-386.

Doering, W., 1938, "Berichtigung zu der Arbeit; Die Ueberhitzungsgrenze und Zerreissfestigkeit von Fluessigkeiten," *Z. Physikal Chem., B.*, Vol. 38, pp. 292-294.

Eberhart, J. G., Kremsner, W., and Blander, M., 1975, "Metastability Limits of Superheated Liquids," *J. Colloid Interface Sci.*, Vol. 50, pp. 369-378.

Eley, D. D., 1939, "On the Solubility of Gases, Part II—A Comparison of Organic Solvents With Water," *Farady Soc.*, Vol. 35, pp. 1421-1432.

Faber, T. E., 1972, *Introduction to the Theory of Liquid Metals*, Cambridge University Press, United Kingdom.

Farkas, L., 1927, "Keimbildungsschwindigkeit in Uebersaetingten Daempfen," *Z. Physikal Chem.*, Vol. 125, pp. 236-242.

Feder, J., Russel, K. C., Lothe, J., and Pound, G. M., 1966, "Homogeneous Nucleation and Growth of Droplets in Vapors," *Adv. Phys.*, Vol. 15, pp. 111-178.

Felix, M. P., and Ellis, A. T., 1971, "Laser-Induced Liquid Breakdown—a Step by Step Account," *Appl. Phys. Lett.*, Vol. 19, pp. 484-486.

Feynman, R. P., 1972, *Statistical Mechanics*, Benjamin, New York, pp. 125-126.

Frenkel, J., 1946, *Kinetic Theory of Liquids*, Oxford University Press, United Kingdom, p. 392.

Frost, A. A., and Kalkwarf, D. R., 1953, "A Semi-empirical Equation for the Vapor Pressure of Liquids as a Function of Temperature," *J. Chem. Phys.*, Vol. 21, pp. 264-267.

Garcia, N. G., and Torroja, J. M. S., 1981, "Monte Carlo Calculation of Argon Clusters in Homogeneous Nucleation," *Phys. Rev. Lett.*, Vol. 47, pp. 186-189.

Garside, D. H., Molgaard, H. V., and Smith, B. L., 1968, "Refractive Index and Lorentz-Lorenz Function of Xenon Liquid and Vapor," *J. Phys. B.*, Vol. 1, pp. 449-457.

Gunn, R. D., and Yamada, T., 1971, "A Corresponding States Correlation of Saturated Liquid Volumes," *AIChE J.*, Vol. 17, pp. 1341-1345.

Hemmingsen, E. A., 1970, "Supersaturation of Gases in Water," *Science*, Vol. 167, pp. 1493-1494.

Hemmingsen, E. A., 1975, "Cavitation in Gas-Supersaturated Solutions," *J. Appl. Phys.*, Vol. 46, pp. 213-218.

Hemmingsen, E. A., 1977, "Spontaneous Formation of Bubble in Gas Supersaturated Water," *Nature*, Vol. 267, pp. 141-142.

Henry, R. E., and Fauske, H. K., 1979, "Nucleation Processes in Large Scale Vapor Explosions," ASME JOURNAL OF HEAT TRANSFER, Vol. 101, pp. 280-287.

Hirschfelder, J. O., Curtis, C. F., and Bird, R. B., 1954, *Molecular Theory of Gases and Liquids*, Wiley, New York, Chap. 13.

Hoare, R., Pal, P., and Wegener, P. P., 1980, "Argon Clusters and Homogeneous Nucleation," *J. Colloid Interface Sci.*, Vol. 75, pp. 126-137.

Jarvis, T. J., Donohue, M. D., and Katz, J. L., 1975, "Bubble Nucleation Mechanism of Liquid Droplets," *J. Colloid Interface Sci.*, Vol. 50, pp. 359-368.

Kacker, A., and Heist, R. H., 1984, "Homogeneous Nucleation Rate Measurements I. Ethanol, *n*-Propanol, and *i*-Propanol," *J. Chem. Phys.*, Vol. 82, pp. 2734-2744.

Kenrick, F. B., Gilbert, C. S., and Wismer, K. L., 1924, "The Superheating of Liquids," *J. Phys. Chem.*, Vol. 28, p. 1297-1307.

Kraucki, Z., 1966, "Breakdown of Liquid Dielectrics," *Proc. Roy. Soc. A.*, Vol. 294, pp. 393-404.

Kwak, H., 1983, "Bubble Formation in Liquids," Technical report to Korean Science and Engineering Foundation.

Kwak, H., and Panton, R. L., 1983, "Gas Bubble Formation in Nonequilibrium Water-Gas Solutions," *J. Chem. Phys.*, Vol. 78, pp. 5795-5799.

Kwak, H., 1984, "Sound Radiation From the Evaporating Droplet and the Growing and Collapsing Bubble Formed From the Fully Evaporated Droplet," *J. Acoust. Soc. Am.*, Suppl. 1, Vol. 76, pp. S63-S64.

Kwak, H., and Panton, R. L., 1985, "Tensile Strength of Simple Liquids Predicted by a Model of Molecular Interactions," *J. Phys. D; Appl. Phys.*, Vol. 18, pp. 647-659.

Kwak, H., 1987, "Effect of Ambient Pressure on the Pressure Wave From the Rapidly Expanding Bubble," *J. Acoust. Soc. Am.*, Suppl. 1, Vol. 81, p. S26.

Kwak, H., and Kim, W., 1988, "Homogeneous Nucleation and Macroscopic

Growth of Gas Bubble in Organic Solutions," *Proceedings of the First KSME–JSME Thermal and Fluids Engineering Conference*, Vol. 1, pp. 125–131.

Kwak, H., and Oh, S., 1988, "Gas–Vapor Bubble Nucleation—a Unified Approach," ASME HTD-Vol. 96, Vol. 2, pp. 557–564.

Lienhard, J. H., and Karimi, A., 1981, "Homogeneous Nucleation and the Spinodal Line," ASME JOURNAL OF HEAT TRANSFER, Vol. 103, pp. 61–64.

Matthew, M. W., and Steinwandel, J., 1983, "An Experimental Study of Argon Condensation in Cryogenic Shock Tube," *J. Aerosol Sci.*, Vol. 14, pp. 755–763.

McCann, H., Clarke, L. J., and Masters, A. P., 1988, "An Experimental Study of Vapor Growth at the Superheat Limit Temperature," ASME HTD-Vol. 96, pp. 593–603.

McGinty, D. J., 1973, "Molecular Dynamics Studies of the Properties of Small Clusters," *J. Chem. Phys.*, Vol. 58, pp. 4733–4742.

Mikic, B. B., Rohsenow, W. M., and Griffith, P., 1970, "On Bubble Growth Rates," *Int. J. Heat Mass Transfer*, Vol. 103, pp. 657–666.

Oxtoby, D. W., and Evans, R., 1988, "Nonclassical Nucleation Theory for the Gas–Liquid Transition," *J. Chem. Phys.*, Vol. 89, pp. 7521–7530.

Patrick-Yeboch, J. R., and Reid, R. C., 1981, "Superheat-Limit Temperatures of Polar Liquid," *Ind. Eng. Chem. Fundam.*, Vol. 20, pp. 315–317.

Porteus, W., and Blander, M., 1975, "Limit of Superheat and Explosive Boiling of Light Hydrocarbons, Halocarbons, and Hydrocarbon Mixtures," *AIChE J.*, Vol. 21, pp. 560–566.

Rayleigh, L., 1917, "On the Pressure Developed in a Liquid During the Collapse of a Spherical Cavity," *Philo. Mag.*, Ser. 6, Vol. 34, pp. 94–98.

Reid, R. C., 1976, "Superheated Liquids," *American Scientist*, Vol. 64, pp. 146–156.

Reid, R. L., Prausnitz, J. M., and Sherwood, T. K., 1977, *The Properties of Gases and Liquids*, McGraw-Hill, New York.

Sambles, J. R., Skinner, L. M., and Lisgarten, N. D., 1970, "An Electron Microscope Study of Evaporating Small Particles," *Proc. Roy. Soc. A.*, Vol. 318, pp. 507–522.

Schrage, R. W., 1953, *A Theoretical Study of Interphase Mass Transfer*, Columbia University Press, New York.

Shepherd, J. E., and Sturtevant, B., 1982, "Rapid Evaporation at the Superheat Limit," *J. Fluid Mech.*, Vol. 121, pp. 379–402.

Skripov, V. P., and Ermakov, G. V., 1964, "Pressure Dependence of the Limiting Superheating of a Liquid," *Russ. J. Phys. Chem.*, Vol. 38, pp. 208–212.

Skripov, V. P., 1974, *Metastable Liquids*, Wiley, New York, Chap. 2.

Sinitsyn, E. N., and Skripov, V. P., 1968, "Kinetics of Nucleation in Superheat Liquids," *Russ. J. Phys. Chem.*, Vol. 42, pp. 440–443.

Stiffler, S. R., Thompson, M. O., and Peercy, P. S., 1988, "Supercooling and Nucleation of Silicon After Laser Melting," *Phys. Rev. Lett.*, Vol. 60, pp. 2519–2522.

Streitwieser, A., and Heathcock, C. H., 1981, *Introduction to Organic Chemistry*, Macmillan, London, p. 147.

Strey, R., Wagner, P. E., and Schmeling, T., 1986, "Homogeneous Nucleation Rates for *n*-Alcohol Vapors Measured in a Two-Piston Expansion Chamber," *J. Chem. Phys.*, Vol. 84, pp. 2325–2335.

Tien, C. L., and Lienhard, J. H., 1979, *Statistical Thermodynamics*, Hemisphere, Washington, DC, Chap. 9.

Van Krevelen, D. W., and Hoftyzer, P. J., 1976, *Properties of Polymers*, Elsevier, Amsterdam.

Volmer, M., 1939, *Kinetik der Phasenbildung*, translated by U.S. Department of Intelligence: refer to ATI No. 81935 from the Clearinghouse for Federal and Technical Information.

Wagner, P. E., and Strey, R., 1984, "Measurement of Homogeneous Nucleation Rates for *n*-Nonane Vapor Using a Two-Piston Expansion Chamber," *J. Chem. Phys.*, Vol. 80, pp. 5266–5275.

Zeldovich, J. B., 1943, "On the Theory of New Phase Formation; Cavitation," *Acta Physicochim., U.R.S.S.*, Vol. 18, pp. 1–22.

Critical Heat Flux in Saturated Forced Convective Boiling on a Heated Disk With Multiple Impinging Jets

M. Monde
Department of Mechanical Engineering,
Saga University,
1 Honjo Saga, Japan 840

T. Inoue
Department of Mechanical Engineering,
Kurume Institute of Technology,
2228 Kamitu Kurume, Japan 830

The existing data for critical heat flux (CHF) on a disk heater cooled by multiple impinging jets have been correlated successfully by deriving a generalized correlation that can predict the CHF on a disk heater cooled by a single impinging jet with high accuracy. The generalized correlation for the CHF for the single jet can be applied to predict the CHF for multiple jets with an accuracy of ±20 percent, in spite of a great difference in the flow situation on a disk between a single jet and multiple jets.

Introduction

Boiling provides an efficient heat transfer process for applications such as the cooling of electric components and fusion components. The critical heat flux (CHF), which defines the upper limit of the efficient range of boiling heat transfer, limits the maximum heat flux that may be dissipated from the components. Enhancement of the CHF becomes important to utilize the boiling heat transfer properly. An impinging liquid jet can, for example, be considered as a means of the CHF enhancement.

The critical heat flux in saturated convective boiling with an impinging jet has been studied rather extensively (Monde and Katto, 1978; Katto and Shimizu, 1979; Monde and Okuma, 1985; Monde, 1987; Monde and Furukawa, 1988). Generalized correlations, which are applicable for the CHF within a wide experimental range of the density ratio ρ_l/ρ_v = 5.3 to 1603 and the reciprocal of the Weber number $2\sigma/\rho_l u^2(D-d)$ = 2×10^{-7} to 10^{-3}, have been derived by Monde (1985, 1987), Sharan and Lienhard (1985), and Katto and Yokoya (1988). The generalized correlation (1) revised by Monde (1985, 1987) and the generalized correlation (2) by Katto and Yokoya (1988) have been reconsidered through the concept of Critical Liquid Film Thickness on the basis of a new hydrodynamic model of the mechanism of the CHF proposed by Haramura and Katto (1983). If this concept is applied to the boiling system with one jet, the following equation is readily derived without empirical constants and exponents (Monde, 1985):

$$\frac{q_{co}}{\rho_v H_{fg} u}=0.220(\rho_l/\rho_v)^{0.533}\left(\frac{2\sigma}{\rho_l u^2(D-d)\,(1+D/d)}\right)^{1/3}$$

Taking dimensional groups given in the above equation into account, Monde (1985) analyzed the existing data to give the following equations for the V and I regimes, respectively:

For the V regime (velocity-dependent):

$$\frac{q_{co}}{\rho_v H_{fg} u}=0.221(\rho_l/\rho_v)^{0.645}\left(\frac{2\sigma}{\rho_l u^2(D-d)\,(1+D/d)}\right)^{0.343}\cdot(1/(1+D/d))^{0.021} \quad (1a)$$

For the I regime (velocity-independent):

$$\frac{q_{co}}{\rho_v H_{fg} u}=0.691(\rho_l/\rho_v)^{0.466}\left(\frac{2\sigma}{\rho_l u^2(D-d)\,(1+D/d)}\right)^{0.421}\cdot(1/(1+D/d))^{-0.118} \quad (1b)$$

Monde (1985) and Monde and Okuma (1985) reported that the CHF for

$$\rho_l/\rho_v > 67.1$$

and

$$D/d < 18.4(\rho_l/\rho_v)^{-0.194}(d/\sigma/g(\rho_l-\rho_v))^{-0.76}\cdot(2\sigma/\rho_l u^2(D-d))^{-0.209}$$

can be predicted by equation (1*a*). In addition, Monde (1987) reported that the CHF that coexists in the V and I regimes for ρ_l/ρ_v < 67.1 at a moderate pressure is given by the smaller of the values calculated from equations (1*a*) and (1*b*). For the CHF at higher pressure, where ρ_l/ρ_v approaches 1, he has derived a different equation, which also is given in that reference.

Although equation (1*a*) is derived using data for a single jet experiment, it may be reasonable to assume that it can also predict the CHF data for multiple jets, the reason being that the multiple-jet data are measured in the region of ρ_l/ρ_v > 203 (see Table 1). The objective of the present study is to apply equation (1*a*) for the critical heat flux in a multiple-jet configuration.

In a separate study, Katto and Yokoya (1988) also analyzed the same single-jet existing data to derive the following equation:

$$\frac{q_{co}}{\rho_v H_{fg} u}=K\left(\frac{\sigma}{\rho_l u^2(D-d)\,(1+D/d)}\right)^{m} \quad (2)$$

where K and m are given as

$$K=(\rho_l/\rho_v)\,(0.0166+7.0(\rho_v/\rho_l)^{1.12})$$

and

$$m=0.374(\rho_v/\rho_l)^{0.0155},\ \text{for}\ \rho_l/\rho_v \geqq 248.1$$
$$m=0.532(\rho_v/\rho_l)^{0.0794},\ \text{for}\ \rho_l/\rho_v < 248.1$$

It may be necessary to mention that both equations (1*a*) and (2) are in good agreement for ρ_l/ρ_v > 100 because both equations are derived by analyzing the same CHF data. In addition, both equations (1) and (2) made the effect of the diameter ratio D/d on the CHF clearer and also made it possible to predict the CHF for a large value of D/d (Monde, 1985).

Contributed by the Heat Transfer Division for publication in the JOURNAL OF HEAT TRANSFER. Manuscript received by the Heat Transfer Division February 26, 1990; revision received November 9, 1990. Keywords: Boiling, Jets, Phase-Change Phenomena.

Table 1 Experimental range of CHF referred

FLUID	N	d mm	L mm	θ	2L/d	u m/s	$\sigma/[\rho_1 u^2(2L-d)(1+2L/d)]$	Ref.
WATER	2a	2.1	14.6	29.2	13.9	3.48 - 13.7	1.62×10^{-5} - 2.51×10^{-6}	[1,2]
	2*a	2.1	18.5	16.7	17.6	4.00 - 14.7	2.74 - 1.18	[1,2]
	2b	2.0	18.9	47.8	18.9	4.40 - 13.4	0.960 - 0.890	[1,2]
	2*b	2.0	24.6	23.7	24.6	4.00 - 13.5	0.557 - 5.25	[1,2]
	2c	2.0	18.0	45.0	18.0	2.34 - 14.0	0.969 - 3.47	[1,2]
	2*c	2.0	23.5	23.1	23.5	2.34 - 14.0	0.568 - 2.30	[1,2]
	2a	2.0	14.7	42.8	14.7	3.80 - 14.9	1.29 - 1.98	[2]
	2a	2.0	16.6	36.9	16.6	3.50 - 14.9	1.01 - 1.82	[2]
	2a	2.0	11.5	20.4	11.5	3.20 - 14.8	2.13 - 4.57	[2]
	2a	2.0	13.8	16.9	13.8	3.20 - 14.8	1.48 - 3.16	[2]
	2a	2.0	10.9	8.0	10.9	3.00 - 14.8	2.38 - 5.79	[2]
	2a	2.0	13.3	6.3	13.3	3.00 - 14.8	1.59 - 3.88	[2]
	2*a	2.0	15.9	5.2	15.9	3.00 - 14.9	1.10 - 2.71	[2]
	2*a	2.0	18.3	4.6	18.3	3.00 - 14.9	0.828 - 2.04	[2]
	2*a	2.0	17.5	25.5	17.5	3.90 - 15.1	0.882 - 1.32	[2]
	2*a	2.0	19.7	22.3	19.7	3.90 - 15.1	0.695 - 1.04	[2]
	3a	2.1	10.9	35.6	10.4	2.90 - 9.3	6.33 - 7.74	[1,2]
	3b	2.0	14.0	60.0	14.0	4.10 - 16.8	1.12 - 1.87	[1,2]
	4a	2.1	9.1	33.6	8.67	2.53 - 14.9	7.89 - 1.23	[1,2]
	4c	2.0	12.7	45.0	12.7	2.34 - 14.9	9.50 - 6.99	[1,2]
	4b	2.0	13.9	45.0	13.9	2.52 - 14.2	1.58 - 5.03	[1,2]
R113	2a	2.1	14.6	29.2	13.9	4.37 - 16.3	1.83×10^{-6} - 2.53×10^{-7}	[1,2]
	2*a	2.1	18.5	16.7	17.6	4.07 - 16.3	1.14 - 1.81	[1,2]
	2b	2.0	18.9	47.8	18.9	3.69 - 14.6	1.28 - 2.0	[1,2]
	2*b	2.0	24.6	23.7	24.6	3.66 - 14.6	0.769 - 1.21	[1,2]
	2c	2.0	14.7	42.8	14.7	4.00 - 13.8	2.38 - 2.84	[2]
	2*c	2.0	16.6	36.9	16.6	4.00 - 13.5	1.95 - 2.22	[2]
	2a	2.0	11.5	20.4	11.5	3.90 - 15.2	3.24 - 4.89	[2]
	2a	2.0	13.8	16.9	13.8	3.70 - 15.2	2.23 - 3.77	[2]
	2a	2.0	10.9	8.0	10.9	3.70 - 13.9	4.29 - 6.05	[2]
	2a	2.0	13.3	6.3	13.3	3.70 - 13.9	2.87 - 4.06	[2]
	2*a	2.0	15.9	5.2	15.9	3.40 - 13.9	2.01 - 3.35	[2]
	2*a	2.0	18.3	4.6	18.3	3.45 - 13.9	1.51 - 2.53	[2]
	2*a	2.0	17.5	25.5	17.5	4.30 - 13.9	1.66 - 1.73	[2]
	2*a	2.0	19.7	22.3	19.7	4.30 - 13.9	1.31 - 1.36	[2]
	3a	2.1	10.9	35.6	10.4	3.37 - 16.4	3.24 - 7.67	[1,2]
	3b	2.0	14.0	60.0	14.0	3.41 - 14.6	2.42 - 4.37	[1,2]
	4a	2.1	9.1	33.6	8.67	4.38 - 16.3	4.79 - 6.54	[1,2]
	4b	2.0	13.9	45.0	13.9	3.84 - 16.5	1.98 - 3.40	[1,2]

A symbol 2a in the column of N, for example, denotes two jets arranged on the center line within the disk as shown in Fig.1.
Numbers 1 and 2 in the column of Ref. are references showing Monde et. al(1980) and Monde(1980), respectively.
Density ratio ρ_l/ρ_v = 1603 for water and 203 for R113.

Incidentally, Lienhard and Eichhorn (1979), using another concept based on the Mechanical Energy Stability Criterion, and Lienhard and Hasan (1979) had made an effort to derive a generalized correlation predicting the CHF for disk heaters cooled by a liquid jet. Sharan and Lienhard (1985) finally proposed the following correlation:

$$\frac{\Phi\beta^{1/3}}{f(r)}=\left(\frac{1000}{\mathrm{We}}\right)^{A(r)} \tag{3}$$

where $f(r)$ and $A(r)$ were determined empirically as functions of r:

$$f(r)=0.00171r+0.21$$

and

$$A(r)=0.486+0.06052(\ln r)-0.0378(\ln r)^2+0.00362(\ln r)^3$$

It should be pointed out that equation (3) is applicable only within certain limits, namely:

$$\mathrm{Fr}=u/\sqrt{gD}>8 \tag{3a}$$

and

$$\beta/\mathrm{Re}^{1/3}<0.4 \tag{3b}$$

It may also be noted that it cannot predict the CHF for a large value of D/d, which equations (1a) and (2) can predict.

All generalized correlations show that the CHF decreases with increasing diameter of the disk heater and diameter ratio of D/d. As a result, the maximum heat flux provided by the impinging jet decreases with the increase in D. Therefore, in

Nomenclature

$A(r)$ = exponent in equation (3) and a function of r
C = constant in equation (4)
D = diameter of a disk heater
d = diameter of an impinging jet
Fr = Froude number = $u/\sqrt{gD}$
$f(r)$ = function of r in equation (3)
g = gravitational acceleration
H_{fg} = latent heat of evaporation
K = constant in equation (2) and a function of r
L = maximum distance from the jet position to the point in the domain controlled by the jet (see Fig. 1)
m = exponent in equation (2) and a function of r
N = number of impinging jets
n = exponent in equation (4)
q_{co} = critical heat flux for saturated boiling
Re = Reynolds number = ud/ν
r = density ratio = ρ_l/ρ_v
u = velocity of a liquid jet at the nozzle exit
We = Weber number = $\rho_l u^2 d/\sigma$
β = diameter ratio = D/d
θ = a half angle of radial flows colliding at the maximum length point
ν = kinematic viscosity
ρ_l = density of saturated liquid
ρ_v = density of saturated vapor
σ = surface tension
Φ = Kutateladze number = $q_{co}/\rho_v H_{fg} u$

order to cool a large surface effectively, it would be necessary to employ multiple impinging jets.

Monde et al. (1980) and Monde (1980) measured the critical heat flux of water and R113 in saturated forced convective boiling with multiple impinging jets at atmospheric pressure. They reported that the CHF can be predicted by

$$\frac{q_{co}}{\rho_v H_{fg} u} = C(\rho_l/\rho_v)^n(\sigma/\rho_l u^2 L)^{1/3}/(1+0.00113(2L/d)^2) \quad (4)$$

where C and n in equation (4) are given as:

For the CHF occurring at the boundary of the disk heater

$$C=0.150 \text{ and } n=0.615$$

For the CHF occurring at the center of the disk heater

$$C=0.0941 \text{ and } n=0.646$$

It is noted that this equation is in a form similar to the equation (see Monde, 1985) for the single jet, although the behavior of the liquid flow on the disk heater becomes very complicated compared to that of the single jet. However, since equation (4) was proposed before Haramura and Katto published their new hydrodynamic model of CHF, we were not able to clarify the effect of D and d on the CHF. Consequently it now is of interest to rearrange equation (4) in a form similar to equations (1) and (2), which yield

$$\frac{q_{co}}{\rho_v H_{fg} u} = C(\rho_l/\rho_v)^n\left(\frac{\sigma}{\rho_l u^2(2L-d)(1+2L/d)}\right)^{1/3} g(2L/d) \quad (4a)$$

where

$$g(2L/d) = \frac{((2L/d)^2-1)^{1/3}}{(d/L)^{1/3}(1+0.00113(2L/d)^2)}$$

The function $g(2L/d)$, whose characteristics were described by Monde (1985), gives the effect of $2L/d$ on the CHF.

In light of new CHF data, and the role of D and d having been clarified, the authors have concluded that equation (1a) is valid for a single jet as well as for multiple jets, and that it is more accurate than equation (4).

Relative Location of the Jets on the Disk Heater

Figure 1 shows possible locations of the jets on the disk heater and the domain controlled by a single jet. The distance L in Fig. 1 denotes the maximum flow length from the position of the jet to the boundary of the domain. The angle θ is defined by the common line to two domains and L. Table 1 shows experimental ranges of the CHF for a given number of jets (Monde et al., 1980; Monde, 1980).

Correlation of Critical Heat Flux

CHF for Two Impinging Jets (N = 2). To analyze the effect of D and d on the critical heat flux, one starts by testing the applicability of the dimensionless parameter $\sigma/\rho_l u^2(2L - d)(1 + 2L/d)$ obtained by replacing D with $2L$ in equations (1), (2), (3), and (4), where the length $2L$ plays the same role as the diameter. For the sake of comparison, equation (3) obtained by Sharan and Lienhard is plotted after rearrangement, which gives

$$\frac{q_{co}}{\rho_v H_{fg} u} = f(r)\left[\left(\frac{d}{2L}\right)^{1/3}\left(1000\left(\left(\frac{2L}{d}\right)^2-1\right)\right)^{A(r)}\right] \cdot\left[\left(\frac{\sigma}{\rho_l u^2(2L-d)(1+2L/d)}\right)^{A(r)}\right] \quad (5)$$

We note that $A(r)$ needs be specified and in the present study, $A(r)$ is calculated for water and R113. Equations (1a) and (4) are also reported on Figs. 2 and 3. The parameter D/d in all three equations (1), (4), and (5) must be fixed and is chosen to be equal to 10 throughout the discussion, which is within the experimental range.

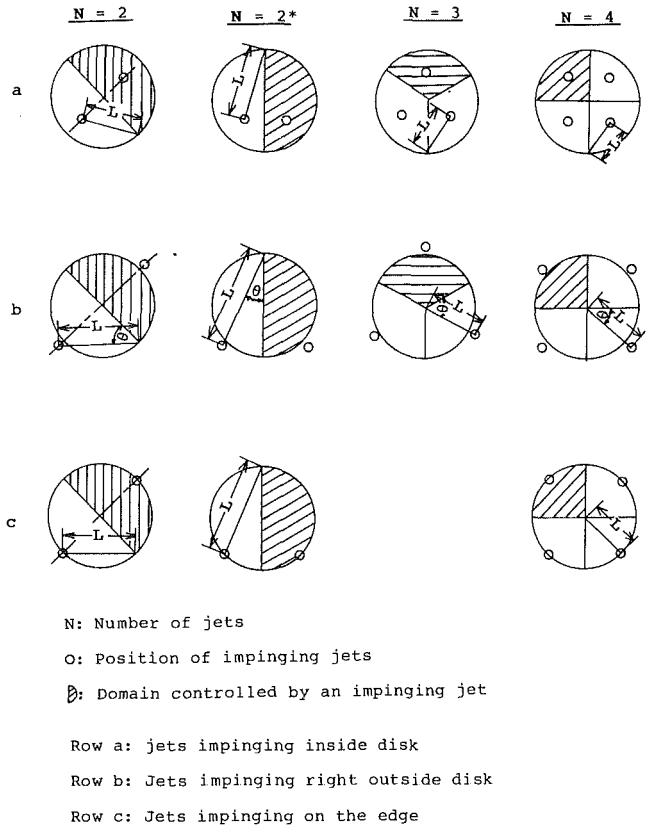

Fig. 1 Relative location of the jets on the disk heater (note: * means that the two jets are not located on a diameter)

Figure 2 shows the CHF data for N = 2 and N = 2*, where $q_{co}/\rho_v H_{fg} u$ are plotted against $\sigma/\rho_l u^2(2L - d)(1 + 2L/d)$. The dot-dash line is a plot of equation (2), the heavy solid line shows equation (1a), the broken line equation (4), and the light solid line equation (3).

The terms in the first brackets of equation (5) turned out to play a minor effect on the CHF, which changes by only 0.6 percent for water and by 6.0 percent for R113, as $2L/d$ varies from 5 to 20. For the same variation of $2L/d$, the term $(1 + 2L/d)$ in equation (1a) decreases by almost 3 percent, and $g(2L/d)$ in equation (4a) decreases by about 34 percent (see Monde, 1985, for details). A complete comparison of the four generalized correlations is presented in Table 2.

Figure 2 and Table 2 reveal that the CHF data for N = 2 and N = 2* can be predicted with an accuracy of ±20 percent by equation (1a). However, equations (3) and (4) give a better fitting for the CHF of water for small values of $2L/d$. For large $2L/d$, it should be recalled that equation (3) is not applicable (see equation (3a) in Fig. 2) and it is noted that equation (4) is less accurate for the reasons given by Monde (1985, 1987). Table 2 shows that the maximum deviations of data from correlation (2) are higher than that from correlation (1a). As we will see later, the deviations get worse for N = 3 and 4, and consequently, correlation (1a), which was derived from single-jet data, is valid for a two-jet configuration. It is interesting to note that it is accurate enough even if the jets impinge very close to the edge of the disk heater.

CHF for Three or Four Impinging Jets (N = 3 or 4). Figure 3 shows the CHF data for N = 3 and 4 where $q_{co}/\rho_v H_{fg} u$ are plotted against $\sigma/\rho_l u^2(2L - d)(1 + 2L/d)$. The same heavy solid, light solid, dot-dash, and broken lines shown in Fig. 2 are reported in Fig. 3. The case of three or four impinging jets differs from the case of two jets in that CHF can occur at the

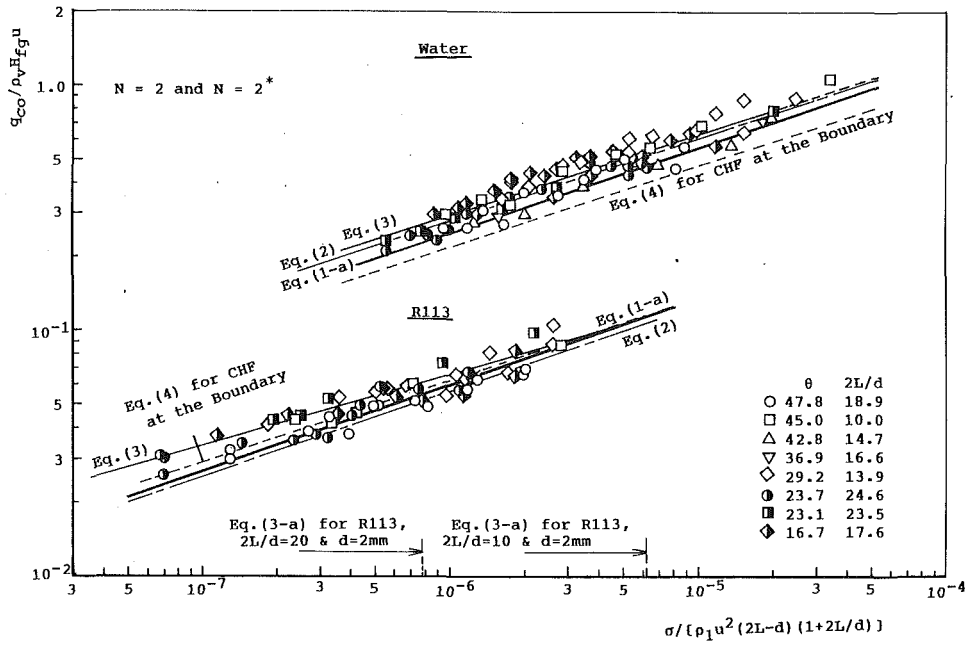

Fig. 2(*a*) Correlation of CHF data for $N = 2$ and $N = 2^*$

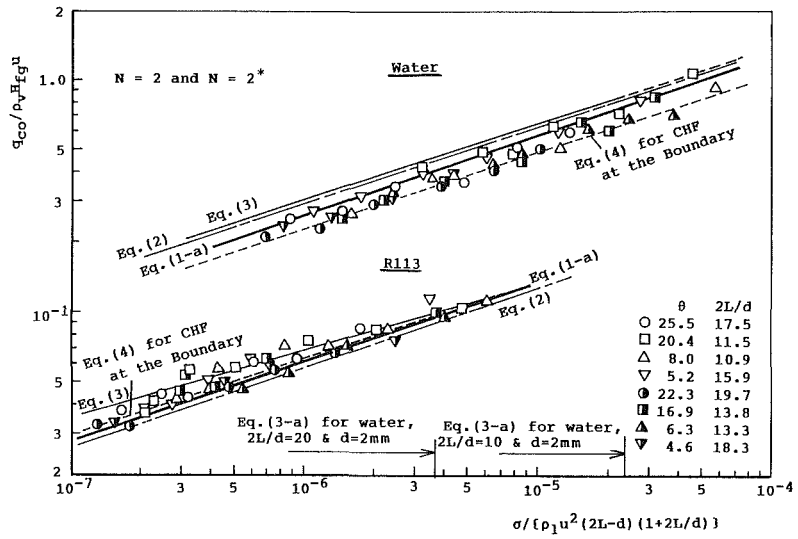

Fig. 2(*b*) Correlation of CHF data for $N = 2$ and $N = 2^*$

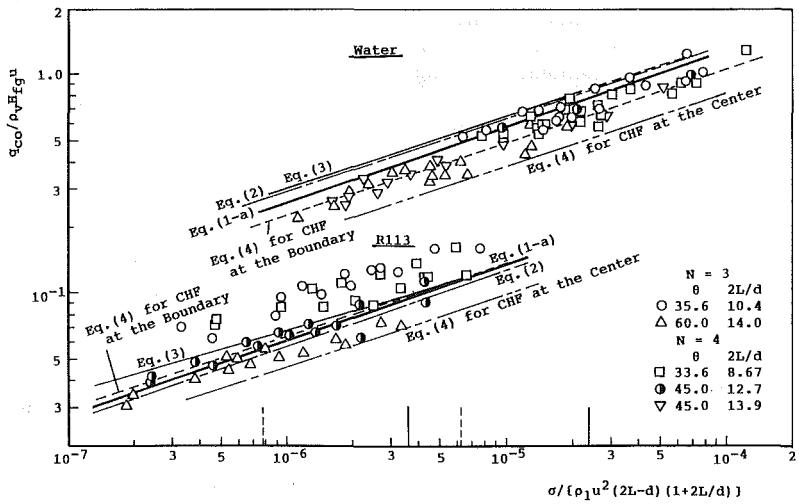

Fig. 3 Correlation of CHF data for $N = 3$ and 4

Table 2 Average (AVG) and root-mean-square (RMS) errors with various predictions

Fluid	N	θ	2L/d	NUM	Eq.(1-a)		Eq.(2)		Eq.(3)		Eq.(4)	
					AVG	RMS	AVG	RMS	AVG	RMS	AVG	RMS
Water	2a	29.2	13.9	13	15.8	18.6	8.4	12.5	34.4(7)	35.5	14.8	17.7
	2*a	16.7	17.6	23	11.8	16.9	3.6	11.5	33.4(1)	33.4	12.2	17.0
	2b	47.8	18.9	11	-2.0	8.8	-9.4	12.3	- (0)	-	-0.4	8.6
	2*b	23.7	24.6	14	2.2	8.2	-6.3	9.7	- (0)	-	13.0	15.7
	2c	45.0	18.0	7	13.8	15.1	5.6	8.0	- (0)	-	14.9	16.3
	2*c	23.1	23.5	7	4.7	6.8	-3.9	6.3	- (0)	-	13.7	14.9
	2a	42.8	14.7	6	-10.3	10.9	-16.2	16.6	1.0(3)	3.3	-11.1	11.8
	2a	36.9	16.6	6	-3.1	6.2	-9.9	11.2	14.2(1)	14.2	-3.3	6.6
	2a	20.4	11.5	6	5.1	12.5	-1.0	10.2	22.1(5)	25.8	5.5	12.0
	2a	16.9	13.8	6	-11.8	13.4	-17.3	18.6	-5.2(3)	6.0	-12.5	14.4
	2a	8.0	10.9	6	-15.6	16.6	-20.2	20.9	-1.3(5)	6.7	-14.6	15.6
	2a	6.3	13.3	6	-16.8	17.5	-21.9	22.4	-2.7(4)	4.4	-17.4	18.0
	2*a	5.2	15.9	6	-2.5	3.1	-9.1	9.3	9.6(2)	9.7	-3.0	3.5
	2*a	4.6	18.3	6	-15.3	16.1	-21.6	21.9	- (0)	-	-14.4	15.0
	2*a	25.5	17.5	6	-9.7	11.5	-16.3	17.2	11.1(1)	11.1	-9.4	11.1
	2*a	22.3	19.7	6	-17.0	17.3	-23.3	23.5	- (0)	-	-14.8	15.2
	3a	35.6	10.9	17	-5.9	12.0	-10.4	14.3	12.9(13)	17.3	-3.5	11.1
	3b	60.0	14.0	18	-20.8	22.2	-26.0	27.0	-7.6(11)	11.2	-0.7	9.7
	4a	33.6	8.67	21	-16.5	18.4	-20.1	21.5	-0.3(19)	9.5	-11.5	14.2
	4c	45.0	12.7	3	-8.7	11.0	-13.3	14.5	17.3(1)	17.3	7.6	9.4
	4b	45.0	13.9	14	-17.1	17.6	-22.4	22.8	-4.4(9)	7.2	4.2	6.8
R113	2a	29.2	13.9	14	-5.5	14.9	18.1	25.1	13.4(8)	21.5	-13.8	18.5
	2*a	16.7	17.6	8	-10.5	20.6	11.8	25.5	30.1(1)	30.1	-17.2	23.3
	2b	47.8	18.9	13	-17.2	18.5	3.2	9.3	- (0)	-	-22.2	23.0
	2*b	23.7	24.6	13	-7.4	13.1	15.1	20.4	- (0)	-	-5.6	12.0
	2c	42.8	14.7	6	-8.5	10.3	14.4	16.3	10.2(3)	11.4	-16.6	17.3
	2*c	36.9	16.6	6	6.1	7.3	32.5	32.9	18.2(1)	18.2	-2.6	4.7
	2a	20.4	11.5	5	-0.4	12.0	24.8	29.3	27.6(4)	28.6	-8.0	13.0
	2a	16.9	13.8	6	-7.6	9.7	15.7	17.6	14.1(4)	15.0	-15.8	16.6
	2a	8.0	10.9	6	-2.7	11.4	22.0	26.3	22.9(6)	24.4	-9.5	13.5
	2a	6.3	13.3	6	-13.7	14.7	8.0	10.6	4.8(4)	7.4	-21.1	21.6
	2*a	5.2	15.9	6	0.8	9.2	25.8	28.0	4.0(2)	4.1	-7.7	11.9
	2*a	4.6	18.3	6	-10.3	12.1	12.0	14.7	- (0)	-	-16.5	17.3
	2*a	25.5	17.5	6	-10.9	13.2	11.2	14.3	- (0)	-	-17.5	19.0
	2*a	22.3	19.7	6	-14.6	16.0	6.5	10.4	- (0)	-	-19.3	20.2
	3a	35.6	10.4	14	25.7	29.4	57.3	60.1	62.8(13)	65.4	18.1	22.5
	3b	60.0	14.0	14	-23.8	25.1	-4.7	11.3	-2.8(9)	7.6	-5.9	11.0
	4a	33.6	8.67	14	13.5	21.2	42.5	47.3	47.0(14)	50.2	10.3	18.4
	4b	45.0	13.9	15	-10.4	12.3	11.9	14.5	11.0(7)	13.1	8.9	13.3

Both average and r.m.s errors are presented in percentages.
NUM represents the number of the CHF data.
A number in the parenthesis gives the number of available data to which equation(3) can be applicable.

center; depending on the relative position of the three or four jets, CHF takes place either at the edge or at the center, in which case the two-dot-dash line illustrates equation (4).

In this configuration, equation (1*a*) again predicts the CHF for water within ±20 percent, as shown in Table 2 and Fig. 3. It gives the best fitting among the four equations.

For R113, there is a significant scatter between the data and the predicted values. However, for a given θ and $2L/d$, the trend in the set of data is conserved and given by equation (1*a*). A reason why the dispersion becomes larger for R113 than for water would be related to the splashed droplets, which are generated due to the strong ejection of vapor during the violent nucleate boiling near the CHF. In addition, this dispersion may be partly caused by possible contamination during experiments.

From visual observations (Monde and Katto, 1978; Monde et al., 1980; Katto and Ishii, 1978; Mudawwar et al., 1987), the angle of the splashed droplets for R113 is very small compared to that for water. As a result, the splashed droplets for $N = 3$ and 4 may play an important role in the enhancement of the CHF by the following fact: The droplets collide with each other above the disk heater due to the small splashed angle and some of them return to it. Incidentally, Baines et al. (1984) and Grimly et al. (1988a, 1988b) noted that the critical heat flux in flowing liquid film is increased by using a flow deflector, which returns the splashed portion of the liquid film to the surface.

Although equation (4) is slightly superior to equation (1*a*) in correlating the CHF data for $N = 3$ and 4, equation (1*a*) can predict the CHF for $N = 3$ and 4 with a tolerable agreement, in such case it can be applied to predict the CHF not only for the multiple impinging jets but also for the single impinging jet.

Characteristics of the CHF for Impinging Jets

The critical heat flux for the single jet as well as the multiple jets can be predicted by equation (1*a*). Consequently the correlation is independent of the number of the jets, though one must focus on the domain controlled by a single jet (see Fig. 1). This is correctly supported by the observation of the liquid flow on the disk heater just before the CHF takes place (Monde et al., 1980). In addition, it may also be estimated from the flow aspect just before CHF observed by Baines et al. (1984) and Grimly et al. (1988a).

Finally, it seems that the fact that the CHF not only for the single jet but also for the multiple jets can be predicted by equation (1*a*) would support the Haramura and Katto model for the CHF mechanism on the basis of the concept of Critical Liquid Film Thickness on a high heat flux nucleate boiling surface. Within its range of applicability, equation (3) derived from the concept of Mechanical Energy Stability Criterion predicts the data as well as does equation (1*a*).

Conclusions

The existing CHF data for the forced convective boiling with multiple impinging jets are analyzed, yielding the following results:

1 The characteristics of the CHF for the single jet and the multiple jets are totally similar in the domain controlled by

the jet, in spite of the difference in the appearance of the thin liquid film flow on the disk heater.

2 Equation (1*a*) predicting the CHF for the single jet can be extended to the CHF for the multiple jets and can correlate these data with an accuracy of ±20 percent.

References

Baines, R. P., El-Masri, M. A., and Rohsenow, W. M., 1984, "Critical Heat Flux in Flowing Liquid Film," *Int. J. Heat Mass Transfer*, Vol. 27, No. 9, pp. 1623–1629.

Grimley, T. A., Mudawwar, I., and Incropera, F. P., 1988a, "CHF Enhancement in Flowing Fluorocarbon Liquid Films Using Structured Surfaces and Flow Deflectors," *Int. J. Heat Mass Transfer*, Vol. 31, pp. 55–65.

Grimley, T. A., Mudawwar, I., and Incropera, F. P., 1988b, "Limits to Critical Heat Flux Enhancement in a Liquid Film Falling Over a Structured Surface That Simulates a Microelectronic Chip," ASME JOURNAL OF HEAT TRANSFER, Vol. 110, pp. 535–538.

Haramura, Y., and Katto, Y., 1983, "A New Hydrodynamic Model of Critical Heat Flux Applicable Widely to Both Pool and Forced Convection Boiling Submerged Bodies in Saturated Liquids," *Int. J. Heat Mass Transfer*, Vol. 26, pp. 389–399.

Katto, Y., and Ishii, K., 1978, "Burnout in a High Heat Flux Boiling System With a Forced Supply of Liquid Through a Plane Jet," *Proc. 6th International Heat Transfer Conference*, Vol. 1, pp. 435–440.

Katto, Y., and Shimizu, M., 1979, "Upper Limit of CHF in the Saturated Forced Convection on a Heated Disk With a Small Impinging Jet," ASME JOURNAL OF HEAT TRANSFER, Vol. 101, pp. 265–269.

Katto, Y., and Yokoya, S., 1988, "Critical Heat Flux on a Disk Heater Cooled by a Circular Jet of Saturated Liquid Impinging at the Center," *Int. J. Heat Mass Transfer*, Vol. 31, No. 2, pp. 219–227.

Lienhard, J. H., and Eichhorn, R., 1979, "On Predicting Boiling Burnout for Heaters Cooled by Liquid Jets," *Int. J. Heat Mass Transfer*, Vol. 22, pp. 774–776.

Lienhard, J. H., and Hasan, M. Z., 1979, "Correlation of Burnout Data for Disk Heaters Cooled by Liquid Jets," ASME JOURNAL OF HEAT TRANSFER, Vol. 101, pp. 383–384.

Monde, M., and Katto, Y., 1978, "Burnout in a High Heat Flux Boiling System With an Impinging Jet," *Int. J. Heat Mass Transfer*, Vol. 21, pp. 295–305.

Monde, M., 1980, "Unpublished CHF Data (Undergraduate Student Experiment at Saga University, 1980)."

Monde, M., Kusuda, H., and Uehara, H., 1980, "Burnout Heat Flux in Saturated Forced Convection Boiling With Two or More Impinging Jets," *Heat Transfer—Japanese Research*, Vol. 9, No. 3, pp. 18–31.

Monde, M., 1985, "Critical Heat Flux in Saturated Forced Convective Boiling on a Heated Disk With an Impinging Jet—A New Generalized Correlation," *Waerme- und Stoffuebertragung*, Vol. 19, No. 3, pp. 205–209.

Monde, M., and Okuma, Y., 1985, "Critical Heat Flux in Saturated Forced Convective Boiling on a Heated Disk With an Impinging Jet—CHF in L-regime," *Int. J. Heat Mass Transfer*, Vol. 28, No. 3, pp. 547–552.

Monde, M., 1987, "Critical Heat Flux in Saturated Forced Convective Boiling on a Heated Disk With an Impinging Jet," ASME JOURNAL OF HEAT TRANSFER, Vol. 109, No. 4, pp. 991–996.

Monde, M., and Furukawa, Y., 1988, "Critical Heat Flux in Saturated Forced Convective Boiling on a Heated Disk With an Impinging Jet—Coexistence of Pool and Forced Convective Boiling," *Heat Transfer—Japanese Research*, Vol. 17, No. 5, pp. 81–91.

Mudawwar, I. A., Incropera, T. A., and Incropera, F. P., 1987, "Boiling Heat Transfer and Critical Heat Flux in Liquid Films Falling on Vertically Mounted Heat Sources," *Int. J. Heat Mass Transfer*, Vol. 30, No. 10, pp. 2083–2095.

Sharan, A., and Lienhard, J. H., 1985, "On Predicting Burnout in the Jet-Disk Configuration," ASME JOURNAL OF HEAT TRANSFER, Vol. 107, pp. 398–401.

Experimental and Numerical Analysis of Low-Temperature Heat Pipes With Multiple Heat Sources

A. Faghri
Brage Golding Distinguished Professor.

M. Buchko
Graduate Research Assistant.

Department of Mechanical and Materials Engineering,
Wright State University,
Dayton, OH 45435

A numerical analysis and experimental verification of the effects of heat load distribution on the vapor temperature, wall temperature, and the heat transport capacity for heat pipes with multiple heat sources is presented. A numerical solution of the elliptic conjugate mass, momentum and energy equations in conjunction with the thermodynamic equilibrium relations and appropriate boundary conditions for the vapor region, wick structure, and the heat pipe wall are given. The experimental testing of a copper-water heat pipe with multiple heat sources was also made showing excellent agreement with the numerical results. An optimization of the heat distribution for such heat pipes was performed and it was concluded that by redistribution of the heat load, the heat capacity can be increased.

Introduction

Since the invention of the heat pipe by Grover et al. (1964), many investigations have been performed concerning heat pipe operating limits, heat pipe applications, and design modifications to improve heat pipe performance. Because of the simplicity of design and ease of manufacture and maintenance, heat pipes have found applications in a wide variety of areas (Chi, 1976; Dunn and Reay, 1982), such as energy conversion systems, cooling of nuclear and isotope reactors, cooling of electronic equipment, and high-performance space applications. The performance of a heat pipe is critical and is often judged in part by the amount of heat a unit length of the heat pipe can transport under a uniform heat load.

Advanced spacecraft electronic cooling systems will require heat transport loops and heat pipes that have multiple heat sources in series along the heat flow path separated by uniform and nonuniform distances. In addition, thermal management for advanced spacecraft and hypersonic vehicles also motivated the analysis and performance evaluation of heat pipes with multiple heat sources. Military applications of such heat pipes are the cooling of leading edges and nose cones of re-entry vehicles and cooling rail guns and laser mirrors. Future hypersonic vehicle structures will also require high-performance heat pipes with multiple evaporators for regions subjected to high-intensity heating, where large quantities of heat must be absorbed and the heating distribution is not uniform. In general, the conventional analytical methodology developed for single evaporator heat pipes cannot be applied to multiple evaporator heat pipes with nonuniform heat loads.

Many investigators have examined the problem of vapor flow in circular and annular heat pipes under uniform heating loads using numerical and analytical methods. The majority of these investigators neglected the effect of the wick and the heat conduction in the pipe wall. Compressible vapor flow analysis is also needed for the sonic conditions. A recent detailed literature survey concerning the thermal modeling of heat pipes is given by Chen and Faghri (1989). The review covers both analytical and numerical methods, transient and steady conditions as well as one- or two-dimensional modeling. Some of the most recent investigations are by Busse (1987), Faghri and Parvani (1988), Issacci et al. (1988), Bowman and Hitchcock (1988), Cao et al. (1989), Faghri and Thomas (1989), Faghri (1989), Chen and Faghri (1990), Faghri and Chen (1989), and Jang et al. (1990, 1991).

Gernert (1986) attempted the analysis of heat pipes with multiple heat sources with the use of superposition and the extension of the existing theories for a single evaporator heat pipe. It is clear that one cannot use superposition for fluid flow analysis due to the nonlinearity of the momentum equations. Furthermore, axial conduction is neglected, which can play an important role with multiple heat sources. The objective of this paper was to achieve the following:

1 The formulation of a detailed mathematical model with numerical results for predicting the performance of heat pipes with multiple evaporators. This was accomplished by solving numerically the complete mass, momentum, and energy equations in the vapor region, wick structure, and the heat pipe wall for heat pipes with multiple heat sources as a conjugate problem. This new model includes the effect of liquid flow in the wick, which is important for low-temperature heat pipes rather than assuming pure conduction through the wick as was done by Chen and Faghri (1990).

2 The experimental testing of a copper-water heat pipe with multiple evaporators using various heat loads in each evaporator for model verification as well as optimization of the heat distribution for such heat pipes.

Mathematical Modeling and Numerical Analysis

Fluid mechanics and heat transfer problems in heat pipes are categorized into three basic types: vapor flow in the core region; liquid flow in the wick; and heat conduction in the heat pipe wall. Most of the analytical and numerical studies on heat pipes have been done on the vapor region for the case of uniform heating and cooling with one evaporator section. In this study, all three effects are considered.

The physical problem under consideration is a conventional heat pipe with multiple heat sources, as shown in Fig. 1(*a*), which is divided into three regions, namely, the vapor flow region, the liquid-wick, and the solid wall. It is assumed that the vapor flow in all segments of the heat pipe, i.e., the evaporator, adiabatic, and condenser sections, is operating under laminar, subsonic, and steady conditions. Nonuniform radial inflow and outflow boundary conditions are needed to model evaporation and condensation. Since the heat pipe is closed at both ends, it is required that the vapor that flows out of the evaporator segments enter into the condenser section. The

Contributed by the Heat Transfer Division and presented at the ASME Winter Annual Meeting, Dallas, Texas, November 25-30, 1990. Manuscript received by the Heat Transfer Division February 15, 1990; revision received November 22, 1990. Keywords: Heat Pipes and Thermosyphons, Porous Media, Space Power Systems.

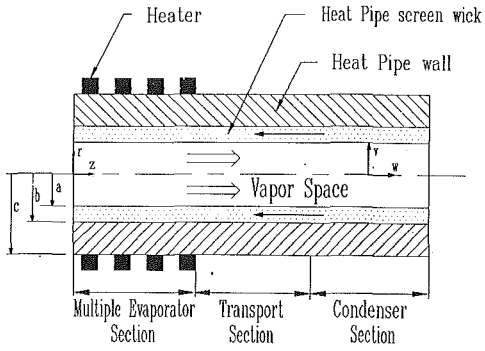

Fig. 1(*a*) Multiple evaporator heat pipe and coordinate system

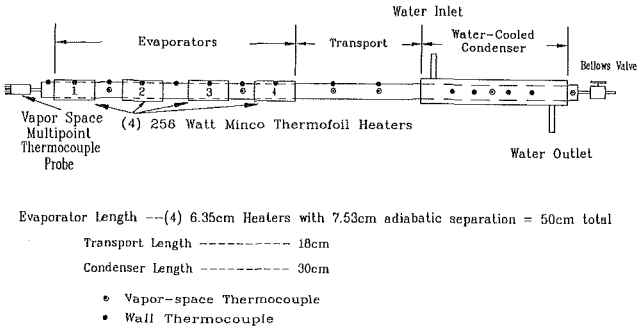

Fig. 1(*b*) Low-temperature heat pipe with multiple heat sources: thermocouple locations

equations for conservation of mass, momentum, and energy for the compressible vapor flow region including viscous dissipation are

$$\frac{\partial}{\partial z}(\rho_v w_v)+\frac{1}{r}\frac{\partial}{\partial r}(\rho_v r v_v)=0 \tag{1}$$

$$\rho_v\left(w_v\frac{\partial w_v}{\partial z}+v_v\frac{\partial w_v}{\partial r}\right)=-\frac{\partial p_v}{\partial z}+\mu_v\left[\frac{4}{3}\frac{\partial^2 w_v}{\partial z^2}+\frac{1}{r}\frac{\partial}{\partial r}\left(r\frac{\partial w_v}{\partial r}\right)+\frac{1}{r}\frac{\partial}{\partial r}\left(r\frac{\partial v_v}{\partial z}\right)-\frac{2}{3}\frac{\partial}{\partial z}\left(\frac{1}{r}\frac{\partial}{\partial r}(rv_v)\right)\right] \tag{2}$$

$$\rho_v\left(w_v\frac{\partial v_v}{\partial z}+v_v\frac{\partial v_v}{\partial r}\right)=-\frac{\partial p_v}{\partial r}+\mu_v\left[\frac{\partial^2 v_v}{\partial z^2}+\frac{4}{3r}\frac{\partial}{\partial r}\left(r\frac{\partial v_v}{\partial r}\right)-\frac{4}{3}\frac{v_v}{r^2}+\frac{1}{3}\frac{\partial^2 w_v}{\partial z\partial r}\right] \tag{3}$$

$$\rho_v c_{p,v}\left(w_v\frac{\partial T_v}{\partial z}+v_v\frac{\partial T_v}{\partial r}\right)=\times\frac{k_v}{r}\left[\frac{\partial}{\partial r}\left(r\frac{\partial T_v}{\partial r}\right)+r\frac{\partial^2 T_v}{\partial z^2}\right]+v_v\frac{\partial p_v}{\partial r}+w_v\frac{\partial p_v}{\partial z}+\mu_v\phi \tag{4}$$

where

$$\phi=2\left[\left(\frac{\partial v_v}{\partial r}\right)^2+\left(\frac{v_v}{r}\right)^2+\left(\frac{\partial w_v}{\partial z}\right)^2+\frac{1}{2}\left(\frac{\partial v_v}{\partial z}+\frac{\partial w_v}{\partial r}\right)^2-\frac{1}{3}(\nabla\cdot\mathbf{V})^2\right]$$

and

$$\nabla\cdot\mathbf{V}=\frac{1}{r}\frac{\partial}{\partial r}(rv_v)+\frac{\partial w_v}{\partial z}$$

The perfect gas law ($p_v=\rho_v R T_v$) is employed to account for the compressibility of the vapor.

The use of liquid capillary action is the unique feature of the heat pipe. From a fundamental viewpoint, the liquid capillary flow in heat pipes with screen wicks should be modeled as a flow through a porous medium. It is assumed that wicking material is isotropic and of constant thickness. In addition, the wick is saturated and the vapor condenses and the liquid evaporates at the vapor–liquid interface.

The averaging technique was applied by many investigators to obtain the general governing equation, which describes the conservation of momentum in a porous structure. Since the development of Darcy's semi-empirical equation, which characterizes the fluid motion under certain conditions, many scientists have tried to develop and extend Darcy's law in order to see the effect of the inertia terms. In this respect, those who have tried to model the flow with the Navier–Stokes equations were the most successful.

The general equations of motion and energy for steady-state laminar incompressible liquid flow in porous media in terms of the volume-averaged velocities (Bachmat and Bear, 1986) are

$$\rho_l v_l\frac{\partial w_l}{\partial r}+\rho_l w_l\frac{\partial w_l}{\partial z}=-\frac{\partial p_l}{\partial z}+\mu_l\left[\frac{1}{r}\frac{\partial}{\partial r}\left(r\frac{\partial w_l}{\partial r}\right)+\frac{\partial^2 w_l}{\partial z^2}\right]-\frac{\mu_l\epsilon_z w_l}{K_z} \tag{5}$$

$$\rho_l v_l\frac{\partial v_l}{\partial r}+\rho_l w_l\frac{\partial v_l}{\partial z}=-\frac{\partial p_l}{\partial r}+\mu_l\left[\frac{1}{r}\frac{\partial}{\partial r}\left(r\frac{\partial v_l}{\partial r}\right)+\frac{\partial^2 v_l}{\partial z^2}\right]-\frac{\mu_l\epsilon_r v_l}{K_r} \tag{6}$$

$$\rho_l c_{p,l}\left(v_l\frac{\partial T_l}{\partial r}+w_l\frac{\partial T_l}{\partial z}\right)=\frac{k_{\text{eff}}}{\epsilon}\left[\frac{1}{r}\frac{\partial}{\partial r}\left(r\frac{\partial T_l}{\partial r}\right)+\frac{\partial^2 T_l}{\partial z^2}\right] \tag{7}$$

For only a capillary jacket when the pores in the isotropic wicking material are completely filled with liquid,

$$\epsilon_r=\epsilon_z=\epsilon \qquad K_r=K_z=K \tag{8}$$

The above assumption was made in all the numerical results presented in this paper. The method of calculated the effective thermal conductivity of the wick, k_{eff}, from the thermal conductivity of the solid and liquid phases is given by Chi (1976),

$$k_{\text{eff}}=\frac{k_l[(k_l+k_s)-(1-\epsilon)(k_l-k_s)]}{[(k_l+k_s)+(1-\epsilon)(k_l-k_s)]} \tag{9}$$

Nomenclature

A = area, m^2
a = inner radius of vapor space, m
b = inner radius of heat pipe, m
c = outer radius of heat pipe, m
c_p = specific heat at constant pressure, J/kg-K
h_{fg} = latent heat of vaporization, J/kg
K = permeability, m^2
k = thermal conductivity, W/m-K
LT = total heat pipe length, m
$\dot{m}$ = mass flux, kg/m^2-s
p = pressure, N/m^2
p^* = modified pressure, N/m^2
Q = heat input, W
R = gas constant, J/kg-K
r = radial coordinate, m
S = source term
T = temperature, K
$\mathbf{V}$ = net velocity vector, m/s
v = radial velocity, m/s
w = axial velocity, m/s
z = axial coordinate, m
ϵ = porosity
μ = dynamic viscosity, kg/m-s
ρ = density, kg/m^3
ρ^* = modified density, kg/m^3

Subscripts

eff = effective
l = liquid or liquid-wick
o = properties at liquid–vapor interface
r = r direction
s = wick structure material
v = vapor
w = wall
z = z direction

The steady-state energy equation that describes the temperature in the heat pipe wall is

$$\frac{\partial}{\partial z}\left(k_w \frac{\partial T_w}{\partial z}\right)+\frac{1}{r}\frac{\partial}{\partial r}\left(k_w r \frac{\partial T_w}{\partial r}\right)=0 \tag{10}$$

where k_w is the local thermal conductivity of the heat pipe wall. The boundary conditions are

$$w(0, r)=v(0, r)=0 \tag{11}$$

$$w(LT, r)=v(LT, r)=0 \tag{12}$$

$$w(z, a)=0 \tag{13}$$

$$w(z, b)=0 \tag{14}$$

$$\frac{\partial w}{\partial r}(z, 0)=\frac{\partial v}{\partial r}(z, 0)=0 \tag{15}$$

$$v(z, a)=\frac{-k_{\text{eff}}\left.\frac{\partial T_l}{\partial r}\right|_{r=a}+k_v\left.\frac{\partial T_v}{\partial r}\right|_{r=a}}{\rho_v h_{fg}} \tag{16}$$

$$v(z, b)=0 \tag{17}$$

$$\frac{\partial T}{\partial z}(0, r)=\frac{\partial T}{\partial z}(LT, r)=0 \tag{18}$$

$$T(z, a)=\frac{1}{\frac{1}{T_o}-\frac{R}{h_{fg}}\ln\frac{p_v}{p_o}} \tag{19}$$

$$k_w \frac{dT_w}{dr}(z, c)=\pm\frac{Q}{A}(z) \tag{20}$$

In boundary condition (20), the heat flux was constant and positive under the active evaporators and zero in all adiabatic and transport sections and the inactive evaporators. In the condenser section, the heat flux was assumed to be uniform and negative based on the total heat input through the evaporators. The temperature along the vapor–liquid interface is taken as the equilibrium saturation temperature corresponding to its equilibrium pressure condition. By the above procedure, the effect of energy conduction in the heat pipe wall and the liquid flow in the wick is taken into account.

For simplicity and generality, the problem should be solved using conjugate heat transfer analysis as a single domain problem. To achieve this, one should generalize the conservation equations for mass, momentum, and energy such that each conservation equation should have the same source term for the energy equation in terms of temperature as a dependent variable for the three regions (i.e., wall, wick, and vapor). In addition, the continuity of temperature, heat flux, and mass flux should be satisfied at each of the interfaces, along with some special boundary conditions such as thermodynamic equilibrium. The following approach is not only very beneficial for those who develop their own computer program to solve this heat pipe problem, but also for those who wish to use the existing commercial codes to set up this problem.

The energy equation can be written in terms of temperature as

$$\rho\frac{DT}{Dt}=\frac{k}{c_p}\nabla^2 T+\frac{S}{c_p} \tag{21}$$

Here S is the source term, which includes viscous dissipation and pressure work. It should be noted that solving the problem in terms of enthalpy does not preserve the condition of temperature continuity at an interface when harmonic averaging is employed and leads to an incorrect calculation of diffusion.

For the vapor region, the energy equation is

$$\rho_v\frac{DT}{Dt}=\frac{k_v}{c_{p,v}}\nabla^2 T+\frac{S}{c_{p,v}} \tag{22}$$

Multiplying both sides of the energy equation for the liquid-wick region by $c_{p,l}/c_{p,v}$ results in

$$\rho_l\frac{c_{p,l}}{c_{p,v}}\frac{DT}{Dt}=\frac{k_l}{c_{p,v}}\nabla^2 T+\frac{S}{c_{p,v}} \tag{23}$$

Similarly, the energy equation for the heat pipe wall is

$$\rho_w\frac{c_{p,w}}{c_{p,v}}\frac{DT}{Dt}=\frac{k_w}{c_{p,v}}\nabla^2 T+\frac{S}{c_{p,v}} \tag{24}$$

It should be noted that since $u=v=0$ in the heat pipe wall, the term S is equal to zero.

From this transformation, we observe the following:

1 The source term for the energy equation is divided by $c_{p,v}$ for all three regions.

2 One needs to set up the density equal to the modified density ρ^* for different regions, i.e., ρ_v for vapor, $\rho_l c_{p,l}/c_{p,v}$ for liquid, and $\rho_w c_{p,w}/c_{p,v}$ for solid.

3 The diffusion coefficients contain only on c_p, namely, $c_{p,v}$. The transformation makes possible an exact representation of diffusion across an interface when the harmonic average is used for the diffusion coefficient at the interfaces.

The momentum equation for the vapor flow does not need any special treatment since $\rho^*=\rho_v$ in the vapor region. In the wick region, the momentum equation can be transformed in the same manner, giving

$$\rho^*\frac{D\mathbf{V}}{Dt}=-\nabla p^*+\nu_l\rho^*\mathbf{V}-\frac{\nu_l\rho^*\epsilon\mathbf{V}}{K} \tag{25}$$

We observe the following:

1 A source term should be added in the momentum equation for the porosity effect in the wick region.

2 The pressure solved for is the modified pressure p^*, which is proportional to the actual pressure. The actual pressure drop between two points in the flow fluid can be calculated as $\Delta p=(c_{p,v}/c_{p,l})\Delta p^*$.

The transformed continuity equation can be written as

$$\nabla\cdot(\rho^*\mathbf{V})=0 \tag{26}$$

The finite-difference iteration method of solution developed by Spalding (1980) is employed in the solution of the elliptic governing equations (1)–(10) subjected to the boundary conditions (11)–(20). In this methodology, finite-domain equations are derived by integration of the differential equations over a control volume surrounding a grid node. The source terms due to viscous dissipation and pressure work in the energy equation, and the source term due to the porous matrix in the momentum equation are linearized, and the "SIMPLEST" practice (Spalding, 1980) was employed for the momentum equations.

Table 1 Design summary of the low-temperature heat pipe with multiple heat sources

Container material	Copper
Wick material	Copper
End cap material	Copper
Length	1000 mm
Container o.d.	25.4 mm
Container i.d.	22.0 mm
End cap thickness	3.175 mm
Screen mesh number	$1.97\times10^3\,\text{m}^{-1}$ (50 mesh)
Screen wire diameter	0.178 mm
Screen wick thickness	0.712 mm
Vapor core diameter	20.5 mm
Working fluid	Distilled water
Fluid charge	40 cm^3
Evaporator length*	(4) @ 63.5 mm
Transport length	180 mm
Condenser length†	300 mm

*Evaporators separated by 75.3 mm adiabatic sections with a 20 mm adiabatic section between the evaporator end cap and evaporator 1.

†20 mm adiabatic section between the condenser and the condenser end cap.

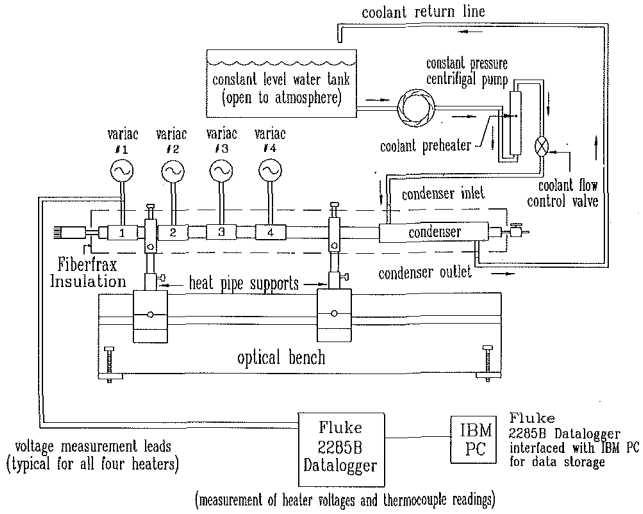

Fig. 2 Low-temperature heat pipe with multiple heat sources: experimental test setup

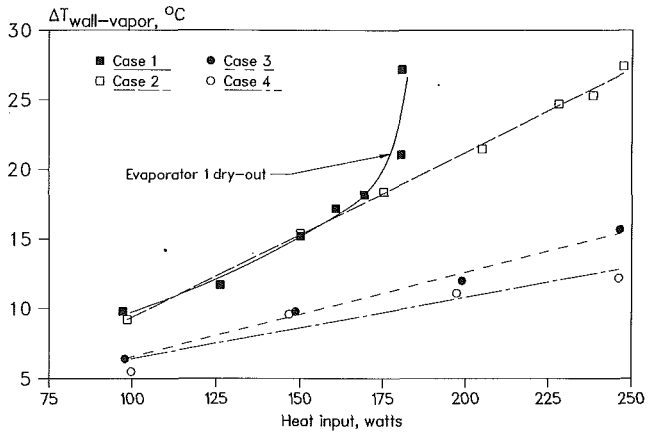

Fig. 3 $\Delta T_{wall\text{-}vapor}$ versus heat input for different single evaporator operations

The solution procedure is based on a line-by-line iteration method in the axial direction and the Jacobi point-by-point procedure in the radial direction.

The energy equation is not continuous at the vapor–liquid interface due to the latent heat of evaporation and condensation. The term $\dot{m}h_{fg}$ must be added as a source term in the energy equation at the vapor–liquid interface. For the first few iterations, it was assumed the heat flux at the liquid–vapor interface is equal to the outer wall heat flux. An exact energy balance given by equation (16) is satisfied after these initial iterations.

The computation proceeded until the sum of the absolute volumetric errors over the whole field was negligibly small ($\leq 10^{-6}$). The numerical results were also tested for grid independence by systematically varying the number of grids in both the r and z directions. This was done for both uniform and nonuniform grids in both directions in each radial component. For the numerical results presented here, the final grid sizes for all of the cases presented were chosen as follows: 100 × (20 + 5 + 10) = (axial) × [(radial vapor) + (radial liquid-wick) + (radial solid wall)]. The difference between this final grid specification and 50 × (10 + 5 + 5) = (axial) × [(radial vapor) + (radial liquid-wick) + (radial solid wall)] was less than 5 percent.

Experimental Apparatus and Procedure

The low-temperature heat pipe was a copper-water heat pipe designed to operate at a vapor temperature of 60–100°C. The compatibility and efficiency of the copper-water heat pipe is well documented in heat pipe literature.

The heat pipe shell and end caps were fabricated from standard composition copper (UNS-C12200). The heat pipe shell is 1000 mm in length with an outside diameter of 25.4 mm, and a wall thickness of 1.7 mm. The ends of the heat pipe shell were machined so that the end caps fit snugly. A simple circumferential screen wick consisting of two wraps of 50 per inch mesh copper screen was installed to provide a liquid return path to the evaporators. A summary of the design specifications for the heat pipe is given in Table 1.

All of the heat pipe parts were carefully fitted, cleaned, and deoxidized using standard procedures (Chi, 1976), and the end caps were brazed to the heat pipe shell using Harris 15 filler rod. The interior of the heat pipe was protected from oxidation during brazing with a cover layer of hydrogen. A bellows-type valve was attached to the heat pipe fill tube to facilitate sealing, purging, and charging of the fluid inventory inside the heat pipe.

The heat pipe has four independently controlled evaporators in the evaporator section. Each evaporator consists of a 63.5-mm-long 257-W Minco Thermofoil heater clamped to the heat pipe (Fig. 1*b*). Power input for each heater was supplied by a 120-V variable a-c transformer and measured with a Fluke 77 multimeter, which has an accuracy of approximately ±2 percent of the reading. Heat was removed from the condenser section by a 300-mm-long copper water-cooled manifold calorimeter mounted to the heat pipe. Thermocouples in the calorimeter inlet and outlet and mass flow measurements allow the power output from the calorimeter to be calculated and compared to the electrical input power so that accurate heat pipe power levels were obtained.

All heat pipe vapor and wall temperatures were measured with standard Type K thermocouples, which have been calibrated with an accuracy of ±0.3°C. There were thirteen wall thermocouples and six vapor space thermocouples (Fig. 1*b*). Wall temperatures in the adiabatic sections were measured with beaded thermocouples clamped to the heat pipe shell. Four sheathed thermocouples were soft-soldered to the heat pipe wall within the calorimeter. These thermocouples exit the calorimeter through shallow grooves machined in the heat pipe wall. Wall temperatures at the axial center of each evaporator were measured with sheathed thermocouples soft-soldered to the heat pipe shell. These thermocouples exit the evaporator sections through a shallow groove in the heat pipe wall. The heat pipe was evacuated to a pressure of 10^{-7} torr prior to wall thermocouple soldering to prevent interior oxidation. Vapor temperatures were measured with a 4.7-mm-dia type 316 stainless steel sheathed multipoint thermocouple mounted axially within the heat pipe vapor space. The multipoint thermocouple exits the heat pipe through a tube in the evaporator end cap and was swaged in place to provide a leak-tight seal.

After the installation of all thermocouples and heaters, the heat pipe was processed in a specially built heat pipe filling station. The heat pipe was evacuated to a pressure of 10^{-7} torr and filled with 40 cm^3 of degassed, distilled water.

A schematic of the test setup is shown in Fig. 2. The heat pipe was mounted horizontally on an optical bench. The optical bench was equipped with adjustable base plates to allow for precise leveling of the heat pipe assembly. The thermocouples were read by a Fluke 2285B Data Logger. Cooling water was supplied to the calorimeter by a centrifugal pump connected to a constant head reservoir in order to maintain a steady coolant flow. A coolant preheater was located prior to the calorimeter inlet to allow greater flexibility in the heat pipe operating temperature. The entire length of the heat pipe as-

Table 2 Low-temperature heat pipe with multiple heat sources test matrix; power listed is experimental capillary limit++; power in evaporator (W)

Case	1	2	3	4	Total power
1	181	–	–	–	181
2	–	>247*	–	–	>247*
3	–	–	>246*	–	>246*
4	–	–	–	>246*	>246*
5	119	118	–	–	237
6	112	112	110	–	334
7	97	98	99	98	392
8	161	–	160	–	321
9	150	–	–	149	299
10	97**	–	–	>245*	>342*
11	100**	–	250	–	350
12	102**	182	–	–	284

++The capillary limit for multiple evaporator operation was defined as a sudden, rapid, and continuous increase in the wall temperature in evaporator 1.

*The capillary limit was not reached in cases 2, 3, 4, and 10 due to the maximum power level limitations of the heaters.

**In cases 10, 11, and 12 evaporator 1 was held constant at 100 W (nominal).

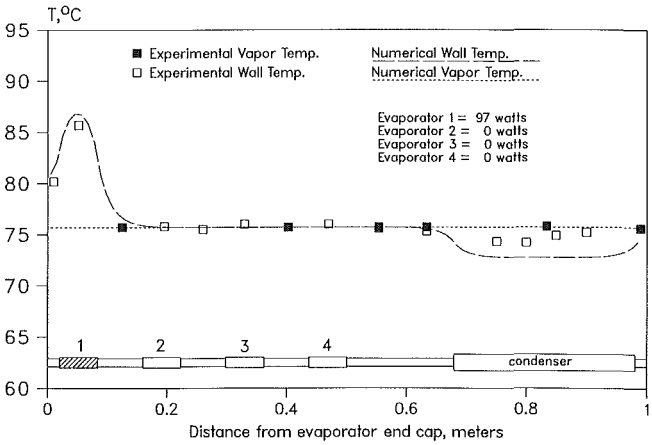

Fig. 4 Heat pipe wall and vapor temperatures versus axial location for Case 1

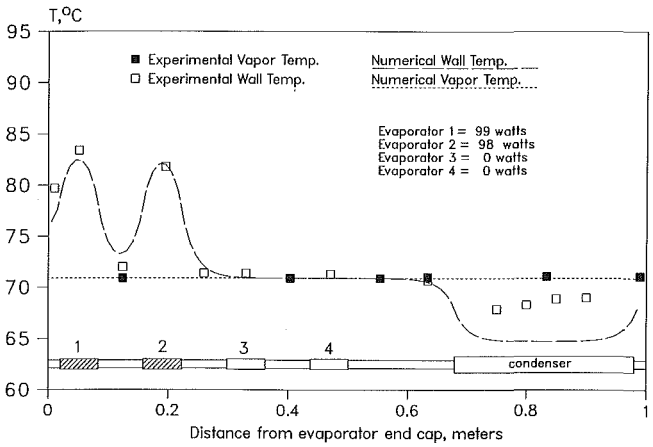

Fig. 5 Heat pipe wall and vapor temperatures versus axial location for Case 5

sembly was insulated with 2 inches of Fiberfrax ceramic fiber insulation.

Tests were performed to establish the maximum heat transport capacity of the heat pipe with variable heat input rates and locations when the heat pipe was horizontal. The operating vapor temperature was held between 65°C and 85°C. Energy balances between the heat input by the heaters and the heat

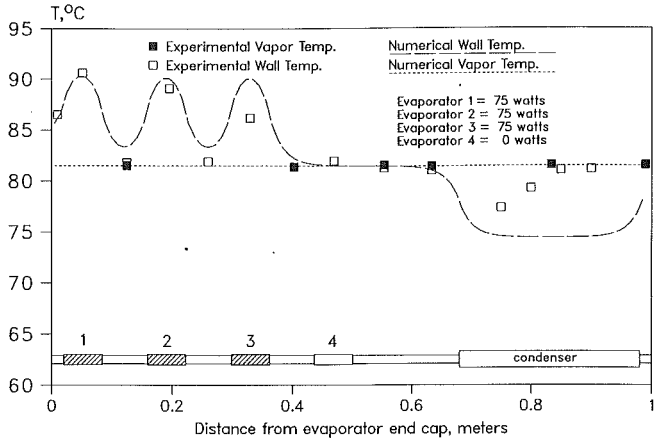

Fig. 6 Heat pipe wall and vapor temperatures versus axial location for Case 6

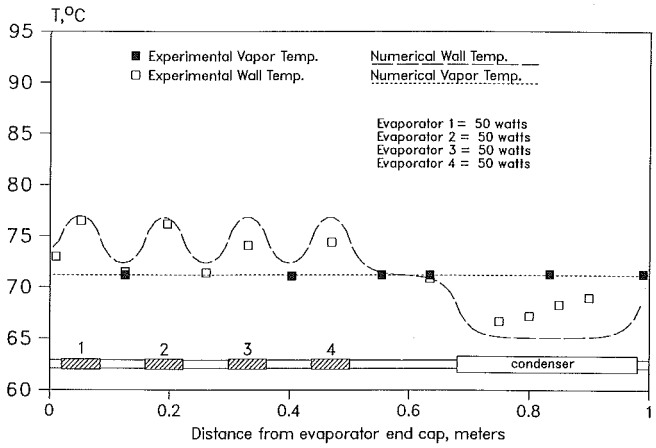

Fig. 7 Heat pipe wall and vapor temperatures versus axial location for Case 7

removed by the calorimeter were monitored to ensure an energy balance of at least 90 percent during steady-state operation.

The primary interest in these tests was to determine the wall and vapor temperature along the heat pipe as well as the capillary limit of the heat pipe in multiple evaporator operation. Because the evaporator located farthest from the condenser will experience dryout first, all multiple evaporator tests were performed with some combination of evaporator 1 and the other evaporators. The maximum heat transport capacity, or capillary limit, of the heat pipe was defined as a sudden, rapid, and continuous increase in the wall temperature of evaporator 1.

Results and Discussion

The heat pipe was first operated in the single evaporator mode in order to establish the capillary limits of the heat pipe at all four heat input locations. The capillary limit for the evaporator farthest from the condenser, evaporator 1, was found to be 181 W. Limits for evaporators 2, 3, and 4 were greater than the maximum power levels that the heaters could deliver, which was 257 W. Figure 3 shows the difference between the wall temperature at the center of the evaporator and the vapor temperature ($\Delta T_{\text{wall-vapor}}$) versus the power input for each single evaporator test. The single evaporator tests show that the $\Delta T_{\text{wall-vapor}}$ increases linearly with increasing power, and that the heat pipe can operate successfully with a high $\Delta T_{\text{wall-vapor}}$.

The test matrix (Table 2) shows the experimentally deter-

mined capillary limits for the heat pipe in the single and multiple evaporator operating modes for twelve different cases. All the multiple evaporator tests were performed with evaporator 1 in combination with other evaporators, since the single-evaporator tests indicated that the evaporator located farthest from the condenser had the lowest capillary limit. Figures 4–7 show typical plots of wall and vapor temperatures versus axial location for the heat pipe in multiple evaporator operation for cases 1, 5, 6, and 7, respectively, at power loads significantly less than the capillary limit. Numerical results based on the mathematical modeling presented in this paper are also shown in Figs. 4–7, which show excellent agreement with experimental data for the wall and vapor temperatures along the heat pipe. In the condenser section, it can be seen that the experimental and numerical values of the outer wall temperature do not coincide. This is due to the assumption of a constant heat flux along the condenser section at the outer wall, which is not precisely correct in this particular experimental design, and the fact that the thermocouples mounted on the condenser wall may be affected by the cooling water circulating in the calorimeter. Near the evaporator end cap, the outer wall temperature can be seen to decrease from the center of evaporator 1 to the end cap. The reason for this is the 20-mm unheated length between the evaporator end cap and evaporator 1. It should be noted, however, that even though the outer pipe wall is adiabatic in the unheated lengths, these sections still act as evaporators due to axial conduction.

In Figs. 5–7, the experimental wall temperatures in the center of the active evaporators decrease closer to the condenser, but the numerical model predicts that these peak temperatures are all nearly the same. Again, this is due to the assumption of a constant heat flux at the outer wall in the condenser section. Since the heat pipe is a closed system, the downstream boundary conditions can affect the temperature upstream.

In cases 5–9 the heat pipe was operated with uniformly increasing power to each evaporator until dryout occurred in evaporator 1. Cases 5, 6, and 7 indicate that the total heat load on the heat pipe can be significantly increased by adding evaporators, although the maximum heat flux for evaporator 1 decreases as evaporators are added downstream (i.e., toward the condenser section).

In cases 10–12 the power input to evaporator 1 was held at a constant 100 W, while the power input to evaporators 2, 3, or 4 was increased uniformly. Figures 8 and 9 show the $\Delta T_{\text{wall-vapor}}$ in evaporator 1 remains relatively constant as the total heat load on the heat pipe is increased for cases 11 and 12, respectively, then evaporator 1 suddenly dries out when a specific downstream power level is reached. This maximum downstream power level decreases as the second evaporator moves farther away from the condenser.

Bienert et al. (1977) demonstrated a jet-pump-assisted arterial heat pipe in which a venturi located in the vapor space maximized capillary pumping by providing a low pressure source to the evaporator end of the heat pipe artery. Similarly, the addition of one or more evaporators near the condenser of a heat pipe will provide a pressure drop in the wick and increase the liquid mass flow rate, while the loss of capillary pressure in the wick due to the additional evaporators is minimal given their proximity to the condenser. This argument can be applied to cases 8 and 9, which show that the addition of one downstream evaporator increases the heat capacity of the heat pipe by 40 percent over the single evaporator, case 1.

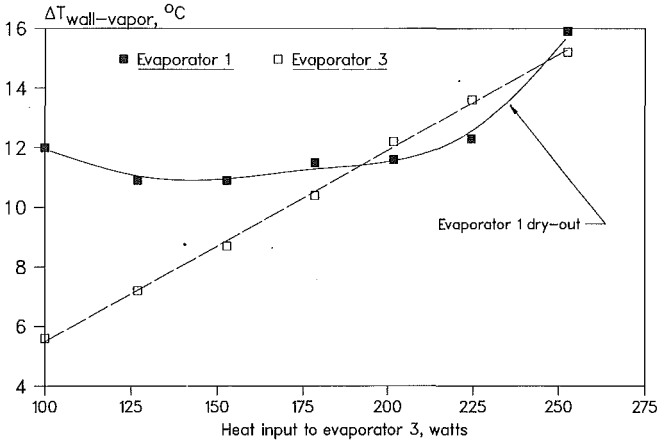

Fig. 8 $\Delta T_{\text{wall-vapor}}$ versus heat input to evaporator 3 with heat input to evaporator 1 held constant at 100 W for Case 11

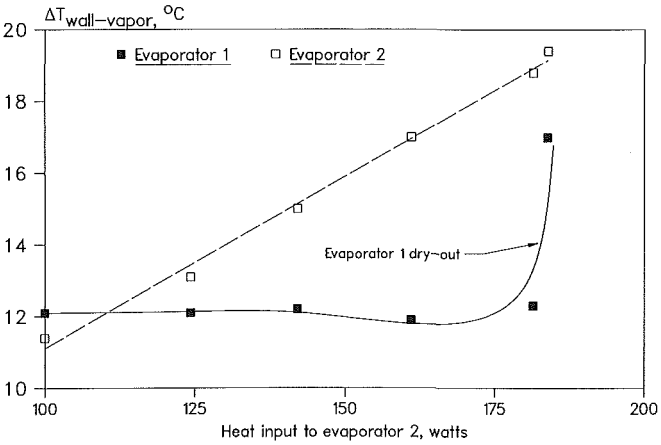

Fig. 9 $\Delta T_{\text{wall-vapor}}$ versus heat input to evaporator 2 with heat input to evaporator 1 held constant at 100 W for Case 12

Conclusions

A complete two-dimensional numerical model of heat pipes with multiple heat sources including heat conduction in the wall, fluid flow in the screen wick, and compressible vapor flow as a conjugate problem is given. This methodology can be easily extended to predict the performance of capillary pumped loops as well.

A simple circumferential screen-wick copper-water heat pipe with multiple heat sources has also been fabricated and successfully tested. These tests show that the maximum total heat load on the heat pipe varies greatly with the location of the local heat fluxes. Significant heat loads can be carried by evaporators close to the condenser without affecting the operation of upstream evaporators, but adding additional evaporators to the heat pipe lowers the maximum heat flux capacity of the evaporator located farthest from the condenser. The temperature difference between the evaporator wall and the vapor seems to be mainly a function of the local heat flux, and cannot be used to predict the maximum heat capacity of the heat pipe operating in the multiple evaporator mode. The numerical results agree with the experimental results for wall and vapor temperatures along the heat pipe for cases with different heat distributions along the evaporator section.

Acknowledgments

Funding for this work was provided by a joint effort of the NASA-Lewis Research Center and Thermal Energy Group of the Aero Propulsion Laboratory of the U.S. Air Force under contract No. F33615-89-C-2820.

References

Bachmat, Y., and Bear, J., 1986, "Macroscopic Modeling of Transport Phenomena in Porous Media, Parts 1 and 2," *Transport in Porous Media*, Vol. 1, pp. 213–269.

Bienert, W. B., Ducao, A. S., and Trimmer, D. S., 1977, "Development of a Jet Pump-Assisted Arterial Heat Pipe" (Final Report), Dynatherm Corp., Cockeysville, MD.

Bowman, J., and Hitchcock, J., 1988, "Transient Compressible Heat Pipe Vapor Dynamics," *Proc. 24th ASME National Heat Transfer Conf.*, Vol. 1, pp. 329–338.

Busse, C. A., 1987, "Subsonic Pressure Recovery in Cylindrical Condensers," personal communication.

Cao, Y., Faghri, A., and Mahefkey, E. T., 1989, "The Thermal Performance of Heat Pipes With Localized Heat Input," *Int. J. Heat Mass Transfer*, Vol. 32, No. 7, pp. 1279–1287.

Chen, M. M., and Faghri, A., 1990, "An Analysis of the Vapor Flow and the Heat Conduction Through the Liquid-Wick and Pipe Wall in a Heat Pipe With Single or Multiple Heat Sources," *Int. J. Heat Mass Transfer*, Vol. 33, No. 9, pp. 1945–1955.

Chi, S. W., 1976, *Heat Pipe Theory and Practice*, Hemisphere Publishing Corp., New York.

Dunn, P. D., and Reay, D. A., 1982, *Heat Pipes*, 3rd ed., Pergamon Press, New York.

Faghri, A., and Parvani, S., 1988, "Numerical Analysis of Laminar Flow in a Double-Walled Annular Heat Pipe," *J. Thermophysics Heat Transfer*, Vol. 2, No. 3, pp. 165–171.

Faghri, A., 1989, "Performance Characteristics of a Concentric Annular Heat Pipe: Part II—Vapor Flow Analysis," ASME JOURNAL OF HEAT TRANSFER, Vol. 111, No. 4, pp. 851–857.

Faghri, A., and Chen, M. M., 1989, "Numerical Analysis of the Effects of Conjugate Heat Transfer, Vapor Compressibility and Viscous Dissipation in Heat Pipes," *Numerical Heat Transfer*, Part A, Vol. 16, pp. 389–405.

Faghri, A., and Thomas, S., 1989, "Performance Characteristics of a Concentric Annular Heat Pipe: Part I—Experimental Prediction and Analysis of the Capillary Limit," ASME JOURNAL OF HEAT TRANSFER, Vol. 111, No. 4, pp. 844–850.

Gernert, N. J., 1986, "Analysis and Performance Evaluation of Heat PIpes With Multiple Heat Sources," presented at the AIAA/ASME 4th Joint Thermophysics and Heat Transfer Conference.

Grover, G. M., Cotter, T. P., and Erikson, G. F., 1964, "Structures of Very High Thermal Conductance," *J. Appl. Physics*, Vol. 6, pp. 1990–1991.

Issacci, F., Catton, I., Heiss, A., and Ghoniem, N. M., 1988, "Analysis of Heat Pipe Vapor Dynamics," *Proc. 24th ASME National Heat Transfer Conf.*, Vol. I, pp. 361–366.

Jang, J. H., Faghri, A., Chang, W. S., and Mahefkey, E. T., 1990, "Mathematical Modeling and Analysis of Heat Pipe Start-Up From the Frozen State," ASME JOURNAL OF HEAT TRANSFER, Vol. 112, No. 3, pp. 586–594.

Jang, J. H., Faghri, A., and Chang, W. S., 1991, "Analysis of the Transient Compressible Vapor Flow in Heat Pipes," *Int. J. Heat Mass Transfer*, in press.

Spalding, D. B., 1980, "Mathematical Modeling of Fluid-Mechanics," Heat Transfer and Chemical-Reaction Process, a lecture course, CFDU Report HTS/80/1, Imperial College, London.

Analytical Modeling of Calcium Carbonate Deposition for Laminar Falling Films and Turbulent Flow in Annuli: Part I—Formulation and Single-Species Model

S. H. Chan
Wisconsin Distinguished Professor and Chairman.

K. F. Ghassemi
Graduate Research Student

Department of Mechanical Engineering, University of Wisconsin—Milwaukee, Milwaukee, WI 53201

This is a two-part series to model scaling of heat transfer surfaces by calcium carbonate based on the first conservation principle approach. In Part I, general physical and chemical processes in $CaCO_3$ fouling are described and a single-species model is proposed whereby only Ca^{+2} species transport needs to be of concern. The deposition process is assumed to be controlled by the two processes of mass transport to and crystallization reaction on the heat transfer surface. The model is then used to solve for $CaCo_3$ scaling in a laminar falling film system and to assess which of the two types of prevailing reaction rate expressions is more appropriate for the $CaCO_3$ fouling analysis. The predicted deposition rate, scale thickness, and its profile are compared with experimental data. The comparison shows that the single-species model yields satisfactory predictions only for a limited range of concentrations. It reveals that the type of reaction rate expression used in the single-species model is less accurate than the other type used in the multispecies model. The latter is described in Part II of the series.

Introduction

Fouling is the process in which unwanted materials are deposited onto a surface. The process can occur either in the presence or absence of temperature gradients. Fouling on a heat transfer surface causes a decrease in the efficiency of the heat exchanger as well as impeding fluid flow. It "can typically degrade the performance of heat exchangers by as much as 80 percent, and can sometimes cause complete failure" (O'Callaghan, 1986). Therefore, it is important for designers of heat transfer equipment to understand the fundamental processes and parameters that affect the rate of fouling in heat exchangers (Somerscales, 1981; Taborek et al., 1972a, 1972b).

Most work on the analytical treatment of fouling assumes two simultaneous processes: deposition and removal. The focus, then, of fouling research has been directed toward establishing the functional relationship of deposition and removal terms on the various process parameters. One of the first such models was proposed by Kern and Seaton (1959). They assumed a constant deposition rate with time, and a removal rate proportional to the mass of the deposit. Epstein (1981) has reviewed other alternatives proposed for the evaluation of the deposition and removal terms.

In the present study, transport and formation in the deposition term are most significant for scaling of $CaCO_3$. Due to the hardness and adhesion characteristics of $CaCO_3$, it is agreed that any removal term would be insignificant. In most models the deposition term is given as the product of a concentration difference times a mass transfer coefficient. It is noted in passing that, compared to the deposition, the removal term is far less understood; thus, fewer models for this process are available (Taborek et al., 1972b).

Hasson et al. (1968), Hasson and Perl (1981), Sheikholeslami and Watkinson (1986), and Watkinson and Martinez (1975) have considered the deposition of $CaCO_3$ in laminar falling film or turbulent shell-and-tube flows. In the absence of removal processes, the deposition of $CaCO_3$ increases linearly with time under constant heat flux condition. They consider the fouling of this inverse solubility salt to be the result of the mass transport of chemical species from the bulk to the liquid–solid interface, followed by a crystallization reaction to form $CaCO_3$ scale. They use values of mass transfer coefficients based on nonfouling flow conditions for their studies. Although Hasson's model has been considered to be "the most successful model for predicting $CaCO_3$ scaling rates" (Sheikholeslami and Watkinson, 1986), recent experimental work (Sheikholeslami and Watkinson, 1986) aimed at determining the applicability of this model in predicting scaling on various materials has shown that shortcomings in terms of accuracy, as well as predicted fouling behavior, are present in this analytical formulation.

The purpose of the study is to improve Hasson's approach in an effort to provide a better prediction of $CaCO_3$ scaling. A mechanistic approach is to be proposed whereby the fundamental equations of mass transfer with appropriate boundary conditions are to be solved. This eliminates the use of mass transfer coefficients calculated for nonfouling conditions. The temperature dependency of most physical properties will be accounted for. In Part I of this study, a general theory of calcium carbonate fouling is described first, followed by a proposed single-species fouling model. It will be seen that, in the single species model, only the Ca^{+2} species needs to be considered. Thus the model is attractive due to its simplicity. The model will then be employed to predict $CaCO_3$ deposition from a laminar falling film. Results will be compared with experimental data to assess the accuracy of the model and to reveal which of the two prevailing expressions of reaction rate can provide better predictions.

Contributed by the Heat Transfer Division and presented at the National Heat Transfer Conference, Philadelphia, Pennsylvania, August 6–9, 1989. Manuscript received by the Heat Transfer Division July 7, 1989; revision received November 22, 1990. Keywords: Fouling, Heat Exchangers, Modeling and Scaling.

Calcium Carbonate Fouling Processes and Deposition

Physical and Chemical Aspects. To facilitate the description and modeling of $CaCO_3$ scale, a physical system similar to the

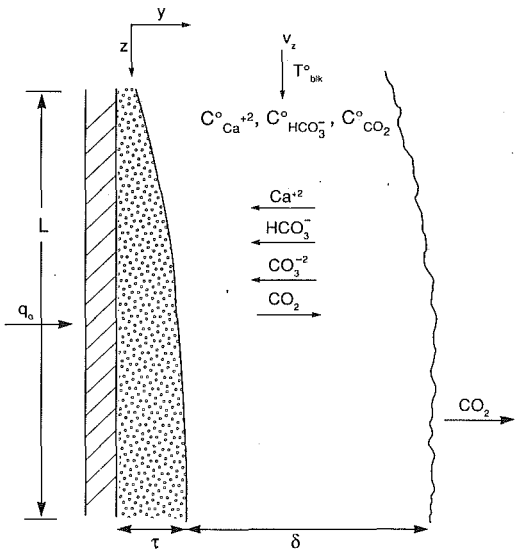

Fig. 1 Geometry for falling film deposition

scaling experiments performed by Hasson and Perl (1981) is illustrated in Fig. 1, in which a vertically falling film of scale-producing water is evaporated on the outside surface of a cylindrical tube. The diameter-to-film thickness ratio is assumed to be large so that the problem geometry can be approximated in rectangular coordinates as shown. The surface is heated at constant flux, q_o, while a constant flow of scale-producing water of known inlet temperature and chemical composition is maintained over it. The heat flux is low enough so that evaporation is in the nonboiling region. Due to the inverse solubility characteristic of the salt, precipitation of $CaCO_3$ from the solution creates a scale of increasing thickness on the heat transfer surface. The problem, then, is predicting the local rate of deposition of $CaCO_3$ given the known operating conditions, i.e., velocity and inlet temperature and composition.

In studies of $CaCO_3$ deposition, the equilibrium of the H_2O–CO_2 system must be considered. Although research on the equilibrium of this system is not the purpose of the present study, its essential concepts will be presented. A more complete review can be found in the literature (Plummer and Busenberg, 1982; Rau, 1982; Wiechers et al., 1975). Dissolved CO_2 gas in water exists as both aqueous CO_2 and as carbonic acid, H_2CO_3. It can also be found in the form of bicarbonate and carbonate ions, HCO_3^- and CO_3^{-2}, respectively. The following equilibrium reactions can be identified for the H_2O–CO_2 system:

$$CO_{2(g)} \underset{}{\overset{K_H}{\rightleftharpoons}} CO_{2(aq)} \tag{1}$$

$$CO_{2(aq)} + H_2O \overset{K_1}{\rightleftharpoons} H^+ + HCO_3^- \tag{2}$$

$$HCO_3^- \overset{K_2}{\rightleftharpoons} H^+ + CO_3^{-2} \tag{3}$$

The reactions in equations (2) and (3) are the first and second dissociation of CO_2 with dissociation constants K_1 and K_2, respectively. These equilibrium constants are temperature dependent and this functionality has been expressed by Plummer and Busenberg (1982) as:

$$\log(K_1) = -356.3094 - 0.06091964 * T + 21834.37/T + 126.8339 * \log T - 1684915./T^2 \tag{4a}$$

$$\log(K_2) = -107.8871 - 0.03252849 * T + 5151.79/T + 38.92561 * \log T - 563713.9/T^2 \tag{4b}$$

where K_1 and K_2 are on the molar basis and T is the temperature in K. The dissociation of the various ionic species in the H_2O–CO_2 system is quite sensitive to the pH of the solution. In the present analysis, a low pH solution (i.e., $6 < \text{pH} < 8.5$) is assumed so that most of the dissolved CO_2 in water is in the form of the bicarbonate species, HCO_3^- (Wahl, 1977).

Calcium carbonate crystals exist in three forms. These are aragonite, calcite, and vaterite. The salt in its aragonite form is considered here since this is the form found in the experimental studies of Hasson and Perl (1981). Calcium carbonate is an inverse solubility salt; therefore, its concentration in solution will tend to decrease as the temperature increases. Under

Nomenclature

A = kinetic constant, pre-exponential factor
A_o = polynomial coefficient
C_j or $[j]$ = concentration of species j
C_j^+ or C_j^* = nondimensional concentration
$\hat{C}_p$ = heat capacity of solution
D_i = mass diffusivity of species i in water
D_{turb} = turbulent mass diffusivity
D_{eff} = effective diffusivity
D^+ = nondimensional diffusivity
D_o = diameter of tube
E_a = reaction activation energy
g = gravitational constant
h = heat transfer coefficient
$j_i^{(x)}$ = mass flux due to concentration gradient
K_1, K_2 = dissociation constant of CO_2
K = the ratio of K_2 to K_1
K_{sp} = the solubility product of $CaCO_3$
k = thermal conductivity of solution
k_f = thermal conductivity of $CaCO_3$ scale
k_r = crystallization rate constant
L = length of heated section
M = molarity
M_i = molecular weight of species i
$\dot{m}_p$ = mass flow rate per unit perimeter
N = quantity defined in equation (35)
N_{CaCO_3} = calcium carbonate deposition flux
q_o = heat flux
R_f = fouling resistance
R_g = gas constant
R = residual
r_i = rate of consumption/generation by reaction
T_{blk}, T_{sc} = bulk and surface temperature
t = time
$\bar{v}_z$ = average or mean velocity in z direction
W = weighting function
y, z = rectangular coordinates
y^+ = dimensionless coordinate
α = nondimensional quantity defined in equation (28)
Γ = nondimensional reaction rate
δ = film thickness in laminar flow
μ = liquid viscosity for water
ρ = liquid density for water
ρ_f = scale density for $CaCO_3$
τ = scale thickness

Subscripts

eq = equilibrium
g = gas phase
s = solid phase

Superscripts

o = initial condition

equilibrium conditions the extent of the dissolution of $CaCO_3$ can be represented by the solubility product, K_{sp},

$$CaCO_{3(s)} \underset{\longleftarrow}{\xrightarrow{K_{sp}}} Ca^{+2} + CO_3^{-2} \tag{5}$$

where the subscript s denotes the solid phase. The solubility product is normally sensitive to temperature variations. For $CaCO_3$ this dependency has been given by Plummer and Busenberg (1982) as

Aragonite

$$\log(K_{sp}) = -171.9773 - 0.077993 * T + 2903.293/T + 71.595 * \log T \tag{6}$$

Calcite

$$\log(K_{sp}) = -171.9065 - 0.077993 * T + 2839.319/T + 71.595 * \log T \tag{7}$$

Vaterite

$$\log(K_{sp}) = -172.1295 - 0.077993 * T + 3074.688/T + 71.595 * \log T \tag{8}$$

where K_{sp} is in molar units and T is the absolute temperature in degrees Kelvin.

The inlet compositions, i.e., concentrations of Ca^{+2}, CO_2, and HCO_3^-, are assumed to be known. Since $CaCO_3$ has an inverse solubility characteristic, its equilibrium concentration will tend to decrease in the solution adjacent to the heated surface. Due to the concentration gradient, Ca^{+2} and HCO_3^- will be transported from the bulk of the film toward the surface. At the liquid–solid interface (and in the bulk), the HCO_3^- undergoes the following equilibrium reaction (Hasson et al., 1968):

$$2HCO_3^- \xrightarrow{K} H_2O + CO_{2(aq)} + CO_3^{-2} \tag{9}$$

It should be noted that the reaction in equation (9) is actually the net of the two dissociation reactions in equations (2) and (3); therefore, the equilibrium constant, K, is given by

$$K = K_2/K_1 \tag{10}$$

in which K_1 and K_2 are the dissociation constants given by equation (4). The CO_2 formed from the reaction given by equation (9) is transported through the liquid film and desorbed at the liquid–gas interface. The CO_3^{-2} species produced in the same reaction reacts with Ca^{+2}, which has been transported to the surface, to form $CaCO_{3(s)}$,

$$Ca^{+2} + CO_3^{-2} \xrightarrow{k_r} CaCO_{3(s)} \tag{11}$$

where k_r, the reaction rate constant, is given later (see equation (27)). This completes the precipitation of $CaCO_3$ scale on the heat transfer surface. Reactions in equations (1), (9) and (11) are sometimes combined in the form (Hasson and Perl, 1981)

$$Ca^{+2} + 2HCO_3^- \longrightarrow CaCO_{3(s)} + CO_{2(g)} + H_2O \tag{12}$$

Several proposals regarding the form of the reaction rate expression for $CaCO_3$ crystallization (equation (11)) have been made. Two of these will later be considered in this study (equations (25) and (26)).

Governing Transport Equations

Fluid Flow. For a laminar film flowing under the force of gravity, the only velocity component is in the downward or z direction. Assuming a fully developed velocity profile ($v_z = v_z(y)$), the z component of the momentum equation for the coordinate system shown in Fig. 1 can be readily solved to yield the velocity profile as (Bird et al., 1960)

$$v_z(y) = 3\bar{v}_z(2y/\delta - y^2/\delta^2)/2 \tag{13}$$

where $\bar{v}_z = \rho g \delta^2/3\,\mu$ is the mean velocity.

Heat Transfer. As will be seen, it is necessary to have expressions for the surface and bulk temperatures along the length of the heated section. A constant heat flux supplied to the surface and the bulk inlet temperature and mass flow rate are assumed to be given. A convective film heat transfer coefficient having negligible variation in the z direction is assumed. Then, a simple heat transfer analysis yields the bulk and surface temperature profiles as

$$T_{blk}(z) = q_o z/\dot{m}_p \hat{C}_p + T^o_{blk} \tag{14}$$

and

$$T_{sc}(z) = q_o z/\dot{m}_p \hat{C}_p + T^o_{blk} + q_o/h \tag{15}$$

The least justified assumption in developing the expression for the scale surface temperature is that of the existence of a constant convective heat transfer coefficient, which inevitably is calculated based on correlations for nonfouling conditions. However, this assumption does not seem significant enough to affect the results of the present analysis seriously. In fact, it provides at least a means of improvement by not using the mass transfer coefficient based on nonfouling condition, as will be seen later. The heat transfer coefficient used in the computations is calculated from the correlation developed by Chun and Seban (1971) in the form

$$h = 0.606\,(k^3\rho^2 g/\mu^2)^{1/3}(\dot{m}_p/\mu)^{-0.22} \tag{16}$$

which accounts for the effect of rippling at the liquid–gas interface.

Mass Transfer. The equation of continuity of species i of a multicomponent system, assuming the flux due to concentration differences is the only significant mass flux, is given as

$$\frac{\partial \rho_i}{\partial t} = -\{\nabla \cdot (\rho_i \mathbf{v} + j_i^{(x)})\} + r_i \tag{17}$$

For the present study, a steady state is assumed, since the experimental data to be compared with are obtained as such, and little would be gained by considering the unsteady-state behavior except for greatly complicating the solution. Also no reaction in the bulk is assumed. A crystallization reaction does occur to form the scale; however, this reaction is assumed to occur at the liquid–solid interface and must be handled as a boundary condition to the mass transport equations. The mass flux of species i in a dilute aqueous solution due to concentration gradients is

$$j_i^{(x)} = -M_i D_i \nabla C_i \tag{18}$$

Therefore, for steady state and no bulk reactions, the species equation reduces to

$$0 = -\nabla \cdot (M_i C_i \mathbf{v} - M_i D_i \nabla C_i) \tag{19}$$

For a laminar falling film with $v_z(y)$ as the only velocity component and assuming negligible diffusive mass transfer in the z direction relative to convective transport, the above equations are combined to give

$$\frac{3}{2}\bar{v}_z\left(\frac{2y}{\delta} - \frac{y^2}{\delta^2}\right)\frac{\partial C_j}{\partial z} = D_j \frac{\partial^2 C_j}{\partial y^2} \tag{20}$$

This is the governing mass transport equation for the four chemical species, Ca^{+2}, CO_3^{-2}, HCO_3^-, and CO_2, in the falling film system. The inlet concentration of all species is assumed to be known, i.e.,

$$\text{at } z = 0; \quad C_j = C_j^o \tag{21}$$

where j denotes any one of the four species. Except for CO_2, transport of the species occurs only in the liquid phase. This implies that at the gas–liquid interface no mass flux exists for these components, which is written as

$$\text{B.C.1:} \quad \text{at } y = \delta; \quad \frac{\partial C_j}{\partial y} = 0 \tag{22}$$

where j excludes CO_2. The carbon dioxide produced at the heated surface diffuses through the liquid phase and is desorbed at the gas–liquid interface. The film thickness is assumed to be constant. Depending upon the extent of the desorption of CO_2 in water, two types of boundary condition can be written for CO_2 at the gas–liquid interface, which are

$$\text{B.C.1 } (CO_2): \quad \text{at } y=\delta; \quad C_{CO_2}=O \tag{23a}$$

$$-D_{CO_2}\frac{\partial C_{CO_2}}{\partial_y}=k_{des}(C_{CO_2,liq}-C_{CO_2,g}) \tag{23b}$$

At the liquid–solid interface various species are being consumed and/or generated according to the reaction given in equations (11) and (12). Under steady-state conditions, mass flux to/from the surface must equal the consumption/generation by net chemical reactions. Let the rate of generation of $CaCO_3$ scale be denoted by r. Then from the stoichiometry in equations (11) and (12), a surface-reaction condition can be written for the various species as

$$\text{B.C.2:} \quad \text{at } y=0; \quad D_{Ca^{+2}}\frac{\partial C_{Ca^{+2}}}{\partial y}=r$$

$$D_{Ca\bar{}^2_3}\frac{\partial C_{CO\bar{}^2_3}}{\partial y}=r$$

$$D_{HCO\bar{}_3}\frac{\partial C_{HCO\bar{}_3}}{\partial y}=2r, \text{ and}$$

$$D_{CO_2}=\frac{\partial C_{CO_2}}{\partial y}=-r \tag{24}$$

In these expressions the mass diffusivities are temperature-dependent quantities, the exact form of which is discussed in the appendix.

Knowledge of the form of the crystallization reaction rate, r, though crucial to any predictive model of scaling, has been quite limited. Several studies in this area have been conducted (Nancollas and Reddy, 1971), and it seems that the most likely candidates for the form of the reaction rate are

$$r=k_r([Ca^{+2}]-[Ca^{+2}]_{eq})^2 \tag{25}$$

$$r=k_r([Ca^{+2}][CO_3^{-2}]-K_{sp}) \tag{26}$$

where the concentrations and other properties are evaluated at the surface conditions. The equilibrium concentration of calcium, Ca^{+2}_{eq}, is assumed to be given by the square root of the solubility product, K_{sp}, which is given by equation (6). It has been proposed that k_r, the reaction rate constant, would have an Arrhenius form (Hasson and Perl, 1981) such that its dependence on surface temperature is given as

$$k_r=A \exp(-E_a/R_gT_{sc}) \tag{27}$$

Attempts to determine the values of the pre-exponential factor and activation energy in equation (27) have been limited in success. One reason for the lack of a consistent set of values is the sensitivity of the two constants to the experimental measurements, since the constants are specific to the crystallizing salt and extremely sensitive to errors introduced by the presence of impurities, which would affect the crystal growth rate.

In the present analysis, both types of the reaction rate given by equations (25) and (26) are utilized in the boundary conditions in equations (24), and the results are compared with experimental data. This will provide a means to assess which of the forms is more realistic or probable.

In Part I, the first form of the reaction rate expression is used to predict the fouling behavior of a laminar falling film, while the second form is used in Part II to analyze the fouling in two systems: laminar falling films and turbulent annulus flow systems.

Single-Species Model. The mass transport equation for a laminar falling-film system, given in equation (20), can be solved to obtain the concentration profile of various species and from this the local deposition rate and other related quantities such as scale thickness can be determined. Selection of equation (25) to represent the form for the crystallization reaction rate would make it unnecessary to consider all the components in the solution, since it involves only the Ca^{+2} concentration. This is termed the single-species model. Therefore, solution of the transport equation for only Ca^{+2} with appropriate boundary conditions would allow calculation of the local deposition rate anywhere on the surface.

In accordance with the simple single-species model, the mass transport equation and its inlet and boundary conditions are summarized below:

$$\frac{3}{2}\bar{v}_z\left(2\frac{y}{\delta}-\frac{y^2}{\delta^2}\right)\frac{\partial C_1}{\partial z}=D_1(z)\frac{\partial^2 C_1}{\partial y^2} \tag{20}$$

$$\text{at } z=0; \quad C_1=C_1^o \tag{21}$$

$$\text{at } y=0; \quad D_1(z)\frac{\partial C_1}{\partial y}=k_r(z)(C_1-C_{1,eq})^2 \tag{24}$$

$$\text{at } y=\delta; \quad \frac{\partial C_1}{\partial y}=0 \tag{22}$$

where the subscript 1 designates Ca^{+2} species. Substituting the following dimensionless groups:

$$C^+=\frac{C_1-C_{1,eq}}{C_1^o-C_{1,eq}}, \quad y^+=\frac{y}{\delta}, \quad z^+=\frac{z}{L}$$

$$D^+(z^+)=\frac{2L\,D_1(z^+)}{3\delta^2\bar{v}_z}, \quad \alpha(z^+)=\frac{\partial C_{1,eq}/\partial z^+}{(C_1^o-C_{1,eq})}$$

and

$$\Gamma(z^+)=\frac{A\delta(C_1^o-C_{1,eq})}{D_1(z^+)}\exp(-E_a/R_gT_{sc}(z^+)) \tag{28}$$

into the previous equation yields the dimensionless form as

$$\partial^2 C^+/\partial y^{+2}-\frac{(2y^+-y^{+2})}{D^+(z^+)}[\partial C^+/\partial z^+ + \alpha(z^+)(1-C^+)]=0 \tag{29}$$

$$\text{at } z^+=0; \quad C^+=1 \tag{30a}$$

$$\text{at } y^+=0; \quad \partial C^+/\partial y^+=\Gamma(z^+)C^{+2} \tag{30b}$$

$$\text{at } y^+=1; \quad \partial C^+/\partial y^+=0 \tag{30c}$$

Due to the nonlinear nature of the reaction boundary condition, the Galerkin method (Finlayson, 1972; Villadsen and Michelsen, 1978) will be used. This approximate analytical approach could give some insight into the quantitative behavior of the deposition process. Accordingly, the approximation polynomial is chosen as a quadratic of the form

$$\bar{C}(y^+, z^+)=A_o(z^+)+\Gamma A_o^2(z^+)y^+-\Gamma A_o^2(z^+)y^{+2}/2 \tag{31}$$

which satisfies both boundary conditions already. The residue for $C(y^+, z^+)$ is given by

$$R[\bar{C}]=\partial^2\bar{C}/\partial y^{+2}-\frac{1}{D(z^+)}(2y^+-y^{+2})[\partial\bar{C}/\partial z^+ + \alpha(z^+)(1-\bar{C})] \tag{32}$$

and the weighting function is assigned as

$$W=1+2\Gamma(z^+)A_o(z^+)y^+-\Gamma(z^+)A_o(z^+)y^{+2} \tag{33}$$

To determine the coefficient $A_o(z^+)$, $R[C]$ is made orthogonal on the weighting function

$$\int_0^1 R[\bar{C}]W\,dy^+=0$$

The above residue can be minimized. After a tedious but straightforward integration and some rearrangement, the resulting unknown coefficient, $A_o(z^+)$, can be obtained from

$$\frac{dA_o}{dz} = \frac{-[D(\Gamma A_o^2(1+2\Gamma A_o/3)+N(z))+A_o^2 d\Gamma/dz(4/15+8\Gamma A_o/35))]}{[(2/3+8\Gamma A_o/15)+2\Gamma A_o(4/15+8\Gamma A_o/35)]} \quad (34)$$

where

$$N(z^+) = \frac{\alpha(z^+)}{D(z^+)}\,[2(1-A_o)/3+8\Gamma A_o/15 - 4\Gamma A_o^2/5 - 8\Gamma^2 A_o^3/35] \quad (35)$$

Analytical solution of the above differential equation appears unlikely and a numerical solution is possible provided that an initial condition exists. This initial condition can be obtained from the inlet condition, but it must be normalized over y^+, since $C(y^+, z^+)$ is only an approximation. The procedure is similar to that for the residue, except now equation (30*a*) is used and evaluation of the integral gives

$$\int_0^1 [1-\bar{C}(y^+, 0)](2y^+ - y^{+2})dy^+ = 0 \quad (36)$$

which results in the following initial condition on equation (34):

$$A_o(z^+=0) = [-5 \pm (25+40\Gamma(z^+=0))^{1/2}]/4\Gamma(z^+=0) \quad (37)$$

To evaluate equation (34) numerically, the z^+ and hence, temperature dependency of some physical constants such as $D(z^+)$ and Γ are necessary. $D(z^+)$ is given in the appendix and Γ can be found from equations (28) and (15). The ability to calculate $A_o(z^+)$ in equation (31) gives the approximate solution to the concentration profile at any position. From this profile, the local deposition rate can also be calculated

$$N_{CaCO_2} = D_1 \left.\frac{\partial C_1}{\partial y}\right|_{y=0} = D_1(C_1^o - C_{1,eq})\Gamma A_o^2(z)/\delta \quad (38)$$

and, from this, the local thickness could be determined from a simple mass balance on the surface

$$\tau = [-D_o + (D_o^2 + 4D_o t N_{CaCO_3} M_{CaCO_3}/\rho_f)^{1/2}]/2 \quad (39)$$

To compare the model with experimental data of Hasson and Perl (1981) for runs with a similar system, equation (34) was solved using a fourth-order Runge–Kutta procedure with 120 steps along the length of the heat transfer surface. The error analysis of using the fourth-order Runge–Kutta method indicates that the numerical error is less than 0.05 percent. At each z position, the relevant temperature dependent quantities and properties were elevated and the local deposition rate and thickness at the end of a run were calculated. Since accurate a priori values of the activation energy and pre-exponential constant in equation (27) were not available, a trial and error procedure was used to obtain agreement for run E-3 of Hasson and Perl (1981).

This procedure included choosing the experimental thickness at $z = 1$ m as the reference, and changing the values of E_a and A in increments so that close agreement of the calculated and experimental thickness would be obtained. Run E-3 was chosen because it is the only run for which the complete experimental thickness (and hence deposition) profile is given by Hasson and Perl (1981). This would provide a comparison for testing the predictions of local deposition over the entire surface, not just an average. The set of values, $E_a/R_g = 1720$ K and $\ln(A) = 8.95$ (A in units of cm^4/mole s), was then used in the computation for the other runs. The values of all physical properties, parameters, and initial conditions used in the calculations are given in Table 1. The results of these computations are summarized in Table 2 and Fig. 2.

Table 2 shows the prediction of the single-species model for the local deposition flux and thickness at $z = 1$ m for the nine runs performed by Hasson and Perl (1981). Experimental values are given for comparison. As seen in Table 2, the predictions of the model are extremely good for run numbers E-3, E-4, E-5, E-7, and E-8 with a maximum error of ±10 percent. However, these runs cover a limited concentration range only. Outside this range much larger errors are present in E-2, E-9,

Table 1 Physical properties and initial conditions used in the calculations for deposition from a falling film

Run Number	pH	Initial Concentrations (M x 10^3) $C^\circ_{Ca^{+2}}$	$C^\circ_{HCO_3^-}$	$C^\circ_{CO_2}$	$C^\circ_{CO_3^{-2}}$	T°_{blk}(K)	Length of Run (Hours)
E-3	7.75	6.30	4.60	0.119	0.030	318.5	52.5
E-2	7.55	4.25	8.00	0.330	0.033	319.0	65.4
E-9	7.25	8.15	4.40	0.343	0.010	320.0	84.5
E-11	7.10	14.60	4.40	0.431	0.009	320.5	82.5
E-10	7.20	10.25	4.40	0.370	0.010	321.0	83.0
E-5	7.55	6.20	4.40	0.178	0.020	326.0	78.75
E-7	7.20	6.20	4.40	0.411	0.009	335.5	84.5
E-4	7.25	6.30	4.50	0.374	0.011	336.0	32.2
E-8	7.25	6.05	4.20	0.359	0.010	339.5	61.0

δ	2.3 x 10^{-4} m	M_{CaCO_3}	0.1 kg/mol
$\bar{v}_z$	0.32609 m/s	g	9.8 m/s^2
q_o	420.16 w/m^2	k	0.628 w/m K
$\dot{m}_p$	0.075 kg/ms	k_f	2.25 w/m K
μ	1 x 10-3 kg/ms	ρ	10^3 kg/m3
C_p	4186 J/kg K	ρ_f	2.45 x 10^3 kg/m^3
Rg	8.33 J/mol K		

Table 2 Comparison of experimental data with predictions of the single-species model for thickness and deposition at $z = 1$ m

Run Number	C°_{Ca}(Mx10^3)	N_{CaCO_3}(kg/m^{2}s x 10^6) Exp.	Calc.	Thickness (μm) Exp.	Calc.
E-3	6.30	1.31	1.34	103	103
E-2	4.25	1.99	0.66	195	63
E-9	8.15	1.48	2.18	188	270
E-11	14.60	1.71	5.96	211	713
E-10	10.25	1.65	3.30	206	401
E-5	6.20	1.41	1.46	166	169
E-7	6.20	1.77	1.66	224	205
E-4	6.30	1.78	1.73	86	82
E-8	6.05	1.84	1.68	168	150

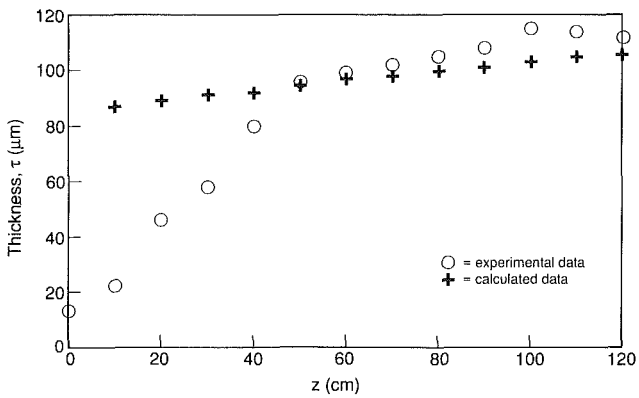

Fig. 2 Experimental and calculated thickness profiles for Hasson's run E-3

E-11, and E-12. This clearly indicates that consideration of only Ca^{+2} in the deposition process is inaccurate and that the selection of equation (25) to represent the form for crystallization reaction rate is unsatisfactory. The presence and participation of the other species such as CO_3^{-2} and HCO_3^- (which are related to solution pH) should be accounted for as shown in the later multispecies model.

Figure 2 shows the comparison of the experimental and predicted thickness profiles over the entire heat transfer surface for Hasson's run E-3. The model gives good agreement except for the one-third section near the inlet portion. This is quite likely because the fluid mechanics is not well known in this region and heat and mass transfer rates are difficult to predict. Another reason may be due to the neglect of the large solution acidity in the inlet section. The model does correctly predict an increasing thickness along the surface. Hasson attributes this to the decrease of pH; however, the present model shows that the increase in surface temperature can also result in this behavior.

The limited success of the single-species model in predicting $CaCO_3$ deposition in laminar falling film is also expected to be the case when applied to the case of turbulent flow in annuli. As will be seen in Part II of the series, the multispecies model provides a considerable improvement in accuracy; thus, repeating the solution in turbulent annulus flow systems using the single-species model is unwarranted here.

Conclusions

Physical and chemical processes pertaining to calcium carbonate fouling have been described. Then they have been incorporated in a simple single-species model to predict both the overall averaged fouling resistance and the fouling thickness profile along the flow direction of a heated surface in a laminar falling film system. The model is based on a transport equation subject to a surface reaction rate condition. An approximate, semi-analytical solution of concentration profile has been obtained. Deposition rate, fouling thickness, and its profile have also been predicted. Comparison with available experimental data shows that the single-species model yields limited success. It also reveals that among the two forms of reaction rate expression prevailing in the literature, the one used in the single-species model is inferior to the other one. The latter is to be used and examined in Part II of the analysis.

Acknowledgments

Support from the National Science Foundation under grant No. CBT-8807406 is gratefully acknowledged.

References

Bird, R. B., Stewart, W. E., and Lightfoot, E. N., 1960, *Transport Phenomena*, Wiley, New York.

Chun, K., and Seban, R., 1971, "Heat Transfer to Evaporating Liquid Films," ASME JOURNAL OF HEAT TRANSFER, Vol. 93, pp. 391–396.

Epstein, N., 1981, "Fouling: Technical Aspects," *Fouling of Heat Transfer Equipment*, E. F. C. Somerscales and J. G. Knudsen, eds., Hemisphere Publishing, Washington, DC.

Finlayson, B. A., 1972, *The Method of Weighted Residuals and Variational Principles*, Academic Press, New York.

Hasson, D., Avriel, M., Resnick, W., Rozenman, T., and Windreich, S., 1968, "Mechanism of Calcium Carbonate Deposition on Heat-Transfer Surfaces," *Industrial and Engineering Chemistry Fundamentals*, Vol. 7, No. 1, pp. 59–65.

Hasson, D., and Perl, I., 1981, "Scale Deposition in a Laminar Falling-Film System," *Desalination*, Vol. 37, pp. 279–292.

Kern, D. Q., and Seaton, R. E., 1959, "A Theoretical Analysis of Thermal Surface Fouling," *British Chemical Engineering*, Vol. 4, pp. 258–262.

Nancollas, G. H., and Reddy, M. M., 1971, "The Crystallization of Calcium Carbonate. II. Calcite Growth Mechanism," *Journal of Colloid and Interface Science*, Vol. 37, pp. 824–830.

O'Callaghan, M. G., 1986, "Fouling of Heat Transfer Equipment: Summary and Review," in: *Heat Exchanger Sourcebook*, J. W. Palen, ed., Hemisphere Publishing, Washington, DC.

Plummer, L. N., and Busenberg, E., 1982, "The Solubilities of Calcite, Aragonite, and Vaterite in CO_2-H_2O Solutions Between 0 and 90°C, and an Evaluation of the Aqueous Model for the System $CaCO_3$-CO_2-H_2O," *Geochimica et Cosmochimica Acta*, Vol. 46, pp. 1011–1040.

Rau, H., 1982, "Modeling of Calcium Carbonate and Silica Deposition in Geothermal Energy Systems," M.S. Thesis, Department of Mechanical Engineering, University of Wisconsin, Milwaukee, WI.

Sheikholeslami, R., and Watkinson, A. P., 1986, "Scaling of Plain and Externally Finned Heat Exchanger Tubes," ASME JOURNAL OF HEAT TRANSFER, Vol. 108., pp. 147–152.

Somerscales, E. F. C., 1981, "Introduction and Summary: The Fouling of Heat Transfer Equipment," in: *The Fouling of Heat Transfer Equipment*, E. F. C. Somerscales and J. G. Knudsen, eds., Hemisphere Publishing, Washington, DC.

Taborek, J., Aoko, T., Ritter, R. B., Palen, J. W., and Knudsen, J. G., 1972a, "Fouling: The Major Unresolved Problem in Heat Transfer," *Chemical Engineering Process*, Vol. 68, No. 2, pp. 59–67.

Taborek, J., Aoko, T., Ritter, R. B., Palen, J. W., and Knudsen, J. G., 1972b, "Predictive Methods for Fouling Behavior," *Chemical Engineering Progress*, Vol. 68, No. 7, pp. 69–78.

Villadsen, J., and Michelsen, M. L., 1978, *Solutions of Differential Equation Models by Polynomial Approximation*, Prentice-Hall, New Jersey.

Wahl, E. F., 1977, *Geothermal Energy Utilization*, Wiley, New York.

Watkinson, A. P., and Martinez, O., 1975, "Scaling of Heat Exchanger Tubes by Calcium Carbonate," ASME JOURNAL OF HEAT TRANSFER, Vol. 97, pp. 504–508.

Wiechers, H. N. S., Sturrock, P., and Marais, G. V. R., 1975, "Calcium Carbonate Crystallization Kinetics," *Water Research*, Vol. 9, pp. 835–845.

APPENDIX

Mass Diffusivity

A knowledge of the temperature variation of the mass diffusivity of the various species is important for various calculations in the mass transport models presented in the text. The assumption is made that the species, Ca^{+2}, HCO_3^-, and CO_3^{-2}, have equal diffusivities denoted by the subscript, $Ca(HCO_3)$. This temperature dependency was obtained using an approximate procedure. Knowledge of mass diffusivities of $Ca(HCO_3)$ and CO_2 was available at one temperature (Hasson and Perl, 1981). Using this information and the approximate relation (Bird et al., 1960):

$$D_{T_2} = D_{T_1}(T_2/T_1)(\mu_1/\mu_2) = D_{T_1}(T_2/T_1) \cdot \exp[3.8T_b(1/T_1 - 1/T_2)]$$

where T_b denotes boiling temperature of the liquid, the diffusivity can be calculated at any temperature. For water T_b = 373 K, it becomes

$$D_{T_2} = D_{T_1} \cdot (T_2/T_1) \cdot \exp[1417(1/T_1 - 1/T_2)]$$

In the model calculations the known values were:

$$T_1 = 336 \text{ K}; \quad D_{Ca(HCO_3)} = 2.29 \times 10^{-9} \text{ m}^2/\text{s}$$

$$D_{CO_2} = 3.67 \times 10^{-9} \text{ cm}^2/\text{s}$$

Analytical Modeling of Calcium Carbonate Deposition for Laminar Falling Films and Turbulent Flow in Annuli: Part II—Multispecies Model

S. H. Chan
Wisconsin Distinguished Professor and Chairman.

K. F. Ghassemi
Graduate Research Assistant.

Department of Mechanical Engineering, University of Wisconsin—Milwaukee, Milwaukee, WI 53201

The present study proposes a multispecies transport model to predict calcium carbonate deposition. The model has been applied to predict the deposition flux, the mean fouling layer thickness, and the profile of local fouling thickness along a heated plate of a laminar falling film. Good agreement is found when comparing with experimental data. Similarly, the model is applied to predict the fouling layer in a turbulent annulus flow system and a good agreement of the predicted results is also found with recent experimental data. Finally, solutions in dimensionless forms are presented to show the effects of various dimensionless parameters on calcium carbonate deposition.

Introduction

From the results obtained in the single-species model, it is clear that the neglect of chemical species other than calcium will not result in an accurate representation of the deposition process and that the first form of the reaction rate expression (equation (25), Part I, Chan and Ghassemi, 1991) provides only limited success. The next obvious approach is to solve a system of the species transport equations by using the second form of the reaction rate expression given by equation (26) in Part I. This approach would then include the contribution of all the species to the scaling process. Such a multispecies model is now employed to analyze the $CaCO_3$ fouling in a laminar falling film system. It is to be seen that only three of the four species present need be considered since the assumed chemical equilibrium at the interface gives an additional relation. The three transport equations, which are coupled through the boundary condition, are then solved simultaneously using a finite difference approach and the predicted results for deposition of calcium carbonate scale and the scale thickness are once again compared to the data of Hasson and Perl (1981). The results of calculations are also presented as plots of the nondimensional deposition flux versus various dimensionless groupings of the relevant operating parameters.

With demonstrated success of the multispecies model in the laminar falling system, the model is then extended to solve for the $CaCO_3$ deposition in a turbulent annulus flow system. Extensive comparison of the theoretical results with experimental data will be made and similar dimensionless results will be presented.

Deposition in Laminar Falling Film System

Governing Transport Equations. Reference should be made to the physical coordinate system shown in Part I. Assuming equation (9) in Part I to be an equilibrium reaction at the heated surface, the concentration of CO_3^{-2} at the interface can be written as

$$C_{CO_3^{-2}} = K \frac{C^2_{HCO^-_3}}{C_{CO_2}} \tag{1}$$

where K is given in equation (10) in Part I. This eliminates $C_{CO^{-2}_3}$ from the reaction rate expression given in equation (26) in Part I. The resulting reaction rate expression is to be used in the boundary condition at the scale deposition surface (see equation (5)). Since it is in terms of concentrations of Ca^{+2}, HCO_3^-, and CO_2 species, three conservation species equations will be needed to describe their mass transport processes. By defining the following groupings:

$$y^+ \equiv \frac{y}{\delta}; \quad z^+ = \frac{z}{L}; \quad D_j^+(z^+) \equiv \frac{2LD_j(z^+)}{3\bar{v}_z\delta^2}; \quad K_{R,j} \equiv \frac{k_r(z)\delta}{D_j(z)} \tag{2}$$

where Ca^{+2}, HCO_3^-, and CO_2 species are represented by the subscripts $j = 1$, 2, and 3, respectively, the three transport equations with appropriate conditions are summarized below:

$$(2y^+ - y^{+2}) \frac{\partial C_j}{\partial z^+} = D_j^+(z^+) \frac{\partial^2 C_j}{\partial y^{+2}}, \quad j = 1, 2, \text{ and } 3 \tag{3}$$

$$\text{at } z^+ = 0 \quad C_j = C_j^\circ, \quad j = 1, 2, \text{ and } 3 \tag{4}$$

$$\text{at } y^+ = 0 \quad \frac{\partial C_j}{\partial y^+} = n_j K_{R,j}(z^+) \left[K(z^+) \frac{C_1 C_2^2}{C_3} - K_{sp}(z^+) \right], \quad j = 1, 2, \text{ and } 3 \tag{5}$$

In equation (5), the constant $n_j = 1$, 2, and (-1) for $j = 1$, 2, and 3, respectively, in view of the combined chemical reaction given in equation (12) in Part I. Also, it is noted that the reaction rate constant, k_r, of an Arrhenius form (see equation (27), Part I) is built into the $K_{R,j}$ group. The other conditions, at $y^+ = 1$, are

$$\begin{aligned} &\text{for } j = 1, 2, && \frac{\partial C_j}{\partial y^+} = 0 \\ &j = 3, && (i) \quad C_3 = 0 \end{aligned} \tag{6}$$

or

$$(ii) \quad \frac{\partial C_3}{\partial y^+} = K_{des}(C_{3,liq} - C_{3,gas})/(-D_3) \tag{7}$$

In equation (7), two possible forms of the boundary condition of CO_2 at the film–air interface are listed. The first one assumes negligible CO_2 concentration at the interface, while the second one assumes that the diffusion rate is equal to the desorption rate. All of them are employed and tested in the present study.

Contributed by the Heat Transfer Division and presented at the National Heat Transfer Conference, Philadelphia, Pennsylvania, August 6–9, 1989. Manuscript received by the Heat Transfer Division July 7, 1989; revision received November 22, 1990. Keywords: Fouling, Heat Exchangers, Modeling and Scaling.

Table 1 Comparison of the data of Hasson and Perl (1981) with predictions of the multispecies model for deposition flux and scale thickness at $z = 1$ m

	$N_{CaCO_3} \times 10^7$ (g/cm^2•s)			Thickness, τ (μm)		
Run No.	Exp.	Calc. 1	Calc. 2	Exp.	Calc. 1	Calc. 2
E-3	1.31	1.39	1.37	103	107	106
E-2	1.99	2.02	1.99	195	193	189
E-9	1.48	1.46	1.42	188	180	175
E-11	1.71	1.77	1.73	211	212	208
E-10	1.65	1.62	1.58	206	196	192
E-5	1.41	1.63	1.60	166	187	184
E-7	1.77	2.03	1.98	224	250	243
E-4	1.78	2.13	2.07	86	100	98
E-8	1.84	2.12	2.07	168	189	184

Calculation 1 uses the boundary condition $C_{CO_2} = 0$ while calculation 2 uses $\partial C_{CO_2}/\partial y = -k_{des}\, C_{CO_2,liq}./D_{CO_2}$, k_{des} taken from Hasson and Perl (1981).

Solution Procedure, Results, and Discussion. The three species equations and their conditions are solved numerically using a finite difference technique. Once the concentration profiles are obtained at a position z^+, the concentration gradient at the wall is obtained using a quadratic polynomial fit

$$\frac{\partial C_j}{\partial y^+} = \frac{-9C_{j,1}^{K+1} + 10C_{j,2}^{K+1} - C_{j,3}^{K+1}}{8\delta\Delta y^+}$$

at $y^+ = 0$. The above equation together with equations (38) and (39) in Part I will then give the deposition rate and thickness of the calcium carbonate layer at any local position z.

The values of all physical properties and initial conditions used in the calculations for the multispecies model are the same as given in Table 1 in Part I. The diffusivities of Ca^{+2}, HCO_3^-, and CO_3^{-2} species are assumed to be equal as stated in Appendix A in Part I. The values of E_a and A were obtained as before, by trial and error. The set of values for E_a/R_g (in units of K) and $\ln(A)$ (A in units of cm^4/mole s) used were 8800 and 38.50, respectively. These values are close to those reported by Hasson and Perl (1981) of 10,300 and 38. A grid of 50 steps in y and 120 steps in z was used in the numerical computations. Increasing the grid size in both y and z steps gave little variation in results, indicating the stability and convergence of the computation. Furthermore, the numerical convergence of the finite

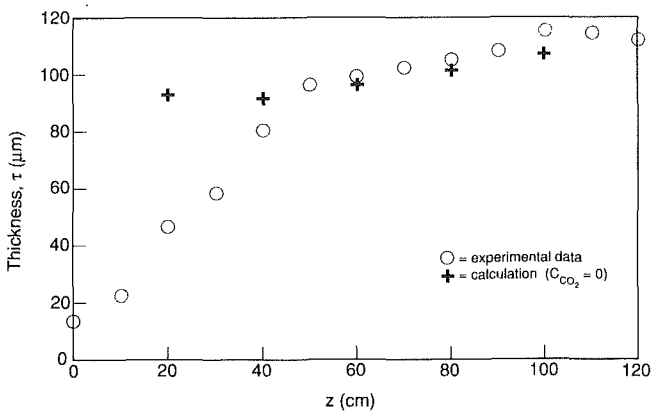

Fig. 1 Experimental and calculated thickness profiles for Hansson's Run E-3

Nomenclature

A_{flow} = flow area in the annulus
C_j or $[j]$ = concentration of species j
C_j^* = nondimensional concentration
$C_{CO_2,Sol}$ = solubility of CO_2 in water
D_i = mass diffusivity of species i in water
D_{turb} = turbulent mass diffusivity
D_{eff} = effective diffusivity
D^+ = nondimensional diffusivity
d_1, d_2 = inner and outer annulus diameter
d_e = equivalent diameter of annulus
d_r = reference diameter = $(d_1^2 - d_2^2)/d_1$
f_1, f_2 = friction factors for inner and outer annulus
H_1, H_2 = quantities defined in equations (17) and (18)
K = the ratio of K_2 to K_1
$K_{R,j}$ = quantities defined in equation (2)
K_{sp} = solubility product $CaCO_3$
k_{des} = desorption coefficient
k_f = thermal conductivity of $CaCO_3$ scale
k_r = crystallization rate constant
l_m = mixing length for turbulence model
L = length of heated section
M = molarity
M_i = molecular weight of species i
$\dot{m}$ = fluid mass flow rate
$\dot{m}_p$ = mass flow rate per unit perimeter
N_{CaCO_3} = calcium carbonate deposition flux
$N^*_{CaCO_3}$ = nondimensional deposition flux
Nu, Pr, Re = Nusselt, Prandtl, and Reynolds number
q_o = heat flux
q^* = nondimensional heat flux
R = outer annulus radius
R_f = fouling resistance
Re_f = flow Reynolds number
T_{blk}°, T_{sc} = initial bulk and surface temperature
t = time
$\bar{v}_z$ = average or mean velocity in z direction
$\bar{v}_{z,max}$ = average and maximum velocity
y, z = rectangular coordinates
y^+, z^+ = dimensionless coordinates
δ = film thickness in laminar flow
Δr, Δy = grid spacing in finite difference equations
κ = ratio of inner to outer annulus radii
κ_1 = von Karman constant = 0.418
λ = quantity defined in equation (9)
μ = liquid viscosity for water
ρ = liquid density for water
ρ_f = scale density for $CaCO_3$
τ_o = shear stress at the wall

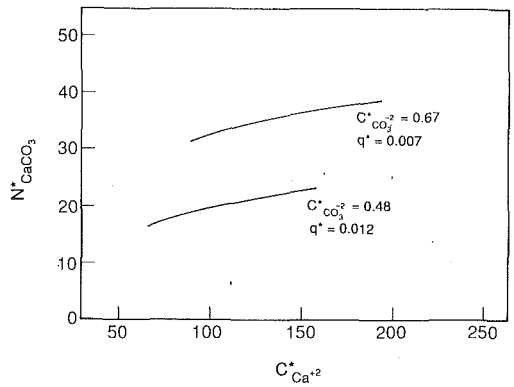

Fig. 2 Nondimensional mass flux versus pertinent dimensionless operating parameters

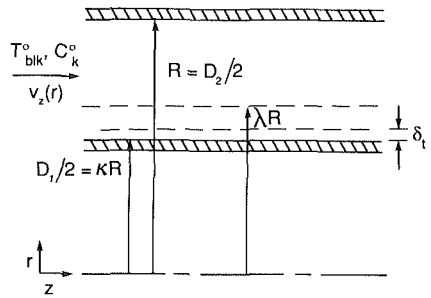

Fig. 3 Geometry for deposition in turbulent flow in an annulus

difference formulation is reconfirmed when a check is made indicating that the present calculations have satisfied the convergence criterion of a linear system of equations, namely, the magnitude of the coefficients of the main diagonal elements is indeed larger than the sum of the nondiagonal elements. The error analysis of the finite difference method shows an approximate error of less than 0.5 percent.

The mass deposition flux and scale layer thickness using two different boundary conditions for CO_2 (see (*i*) and (*ii*) in equation (7)) were calculated for the experiments of Hasson and Perl (1981) and are tabulated in Table 1. The experimental and calculated thickness profile for run E-3 is shown in Fig. 1. The results from the multispecies computations are also presented as plots of a dimensionless mass flux versus the dimensionless operating parameters of heat flux and inlet composition, as shown in Fig. 2. The nondimensional species concentration, molar deposition flux, and heat flux were defined as:

$$N^*_{CaCO_3} = \frac{N_{CaCO_3}\delta}{DK_{sp}^{1/2}}; \quad q^* = \frac{q_o\delta}{k_f(T^\circ_{blk} - T_{ref})}; \quad C_j^* = \frac{C_j^\circ}{K_{sp}^{1/2}}$$

where the temperature-dependent quantities such as K_{sp} and D are evaluated at the inlet temperature, T°_{blk}. The reference temperature, T_{ref}, is chosen for convenience at 273 K. The plots are for constant values of Schmidt and Reynolds numbers. From Part I (Table 1 and Appendix A), they are $Sc = \mu/\rho D = 436$ and $Re_f \equiv 4\,\delta\,V_z/\mu = 300$.

Comparison of predicted with experimental values in Table 1 indicates an excellent agreement with a maximum error of about ± 16 percent. It was found that the two boundary conditions given by equation (7) produced almost similar results. Clearly the use of equation (26) in Part I as the form for the crystallization reaction and accounting for the other species in the deposition process has been a great improvement over the single-species model in predicting deposition rates in laminar film flow. The model can predict local deposition with greater accuracy than Hasson's model; the latter only gives average values. However, predicted inlet behavior is still inconsistent with experimental data. The assumption of a fully developed velocity profile at the entrance region may be one reason. The importance of pH and its effect on the CO_3^{-2} concentration might also be a reason. Another, although less likely, reason is that the model is in effect a mass transport model. The processes such as nucleation, attachment, and removal, which have been assumed to be insignificant, could have some effects as well. They are the subjects for future studies. Finally, for the sake of generality, dimensionless mass flux of calcium carbonate deposition versus dimensionless inlet Ca^{+2} concentration is presented in Fig. 2 with the dimensionless heat flux and inlet CO_3^{-2} concentration as varying parameters.

Deposition in Turbulent Flow in an Annulus

With the encouraging success of the multispecies model in analyzing the laminar falling film system, the deposition of $CaCO_3$ in turbulent shell-and-tube flows with constant heat flux, such as that in the experiments of Sheikholeslami and Watkinson (1986), is considered. The process variables are essentially the same as in the laminar case, except that the flow is turbulent and that cylindrical coordinates must be used since calcium carbonate deposition occurs on the outside of the inner cylindrical surface in an annulus. The geometry of the problem is shown in Fig. 3. A constant flow of scale-producing water is maintained between the two concentric cylinders, while the inner cylinder is supplied with constant heat flux. The chemistry and equilibria of the system are similar to the laminar case and remain unchanged. Scale build-up on the surface on the inner tube causes the increase of fouling resistance. The prediction of the fouling resistance R_f as a function of time is desired, assuming inlet temperature and composition are known. Since the deposition rate of $CaCO_3$ scale is related to the increase of R_f, the determination of the $CaCO_3$ deposition rate allows calculation of R_f.

Governing Transport Equations

Fluid Flow. Due to the turbulent nature of the flow in this problem, an analytical derivation of the velocity profile from the fundamental Navier-Stokes equation would be impractical. However, assuming a fully developed profile ($v_z = v_z(r)$), the mean turbulent velocity distribution in annuli, using a semi-empirical approach, has been shown to be approximated by (Bird et al., 1960)

$$\bar{v}_{z,max} - \bar{v}_z = \frac{1}{\kappa_1}\left(\frac{\tau_o}{\rho}\frac{\lambda^2-\kappa^2}{\kappa}\right)^{1/2} \ln\frac{(\lambda-\kappa)R}{r-\kappa R} \quad \text{for } r<\lambda R \qquad (8)$$

$$\bar{v}_{z,max} - \bar{v}_z = \frac{1}{\kappa_1}\left(\frac{\tau_o}{\rho}(1-\lambda^2)\right)^{1/2} \ln\frac{R-\lambda R}{R-r} \quad \text{for } r>\lambda R \qquad (9)$$

where

$$\lambda^2 = \frac{1-\kappa}{2\ln(1/\kappa)}$$

The shear stress at the wall, τ_o, can be obtained if the friction factor for the inner wall is known. This factor, f_1, for annuli has been correlated to the flow Reynolds number (Perry et al., 1984) as

$$f_1 = f_2\frac{(\lambda^2-2\kappa^2)}{\kappa(1-\lambda^2)}$$

where f_2, the outer wall friction factor, is

$$f_2 = \frac{0.0791}{(Re_f(1-\lambda^2))^{1/4}}$$

Then the wall shear stress may be calculated using

$$\tau_o = f_1\rho\langle\bar{v}_z\rangle^2 \qquad (10)$$

Unfortunately, the velocity profile given above does not ac-

Table 2 Physical properties and initial conditions used in the calculations for deposition in turbulent flow

Run No.	$C^*_{Ca^{+2}}$ ($M\times10^{-3}$)	$C^*_{CO_3^{-}}$ ($M\times10^{3}$)	Q_o (J/s)	$\langle\bar{v}_z\rangle$ (m/s)
20	7.00	0.0090	11958	0.695
23	6.44	0.0080	11254	0.503
36	6.19	0.0092	13465	0.695
38	6.59	0.0082	9948	0.299

$d_1 = 1.91\times10^{-2}$ m; $\mu = 0.001$ kg/ms
$d_2 = 3.70\times10^{-2}$ m; $\rho = 1000$ kg/m^3
$T_{bik} = 298$ K; $\hat{C}_p = 4186$ J/kg K
$\rho_f = 2.65\times10^{3}$ kg/m^3; $k = 0.628$ W/m K
$k_f = 2.2$ W/m K; Section length = 1.15 m

Table 3 Calculated average deposition flux and fouling resistance for four experimental runs of Sheikholeslami and Watkinson (1986) over a 70-h period

	N_{CaCO_3}	R_f (m^{2}K/kW) at various times (h)						
	$\left(\frac{kg}{m^2 s}\times10^5\right)$	10	20	30	40	50	60	70
Run 20								
Experimental		0.01	0.02	0.03	0.04	0.05	0.06	0.07
Calc. (present)	0.167	0.010	0.021	0.031	0.041	0.052	0.062	0.072
Calc. (Hasson and Perl, 1981)	0.069	0.004	0.007	0.013	0.017	0.021	0.026	0.030
Run 23								
Experimental		0.08	0.12	0.15	0.17	0.18	0.18	0.19
Calc. (present)	0.368	0.023	0.045	0.068	0.091	0.114	0.136	0.159
Calc. (Hasson and Perl, 1981)	0.086	0.005	0.011	0.016	0.021	0.027	0.032	0.037
Run 36								
Experimental		0.02	0.05	0.07	0.09	0.12	0.14	0.16
Calc. (present)	0.444	0.027	0.055	0.082	0.110	0.137	0.165	0.192
Calc. (Hasson and Perl, 1981)	0.056	0.003	0.007	0.010	0.014	0.017	0.020	0.024
Run 38								
Experimental		0.05	0.07	0.07	0.07	0.07	0.07	0.07
Calc. (present)	0.268	0.017	0.033	0.050	0.066	0.083	0.099	0.116
Calc. (Hasson and Perl, 1981)	0.279	0.017	0.035	0.052	0.069	0.087	0.104	0.121

curately represent the profile for regions close to the annulus walls. For the region adjacent to the walls, approximated by a boundary layer thickness δ_t, one may use the following profile (Bird et al., 1960):

$$v^+ = y^+ \text{ for } r < \kappa R + \delta_t \text{ and } r > \kappa R - \delta_t \tag{11}$$

where

$$v^+ = \frac{\bar{v}_z/\langle\bar{v}_z\rangle}{f_1^{1/2}} \text{ and } y^+ = \frac{y\langle\bar{v}_z\rangle f_1^{1/2}\rho}{\mu}$$

The layer thickness can be approximated as the critical thickness over a plate such that, as obtained from experiments,

$$\delta_t = \frac{10.8\,\mu}{\langle\bar{v}_z\rangle f_1^{1/2}\rho}$$

Heat Transfer. The development of expressions for bulk and surface temperatures from heat transfer consideration is similar to the laminar case. Only $\dot{m}_p$ should be redefined as the mass flow rate per unit of inner tube perimeter and a different heat transfer correlation referring to the inner tube should be used. For diameter ratios $d_1/d_2 > 0.2$, the following correlation for turbulent heat transfer in annuli is recommended (Perry et al., 1984):

$$\text{Nu} = 0.02\ \text{Re}^{0.8}\ \text{Pr}^{1/3}\ (d_2/d_1)^{0.53} \tag{12}$$

for calculation of the heat transfer coefficient. The Reynolds number for heat transfer in an annulus is given as

$$\text{Re} = d_e\dot{m}/A_{\text{flow}}\mu$$

where

$$d_e = d_2 - d_1 \text{ and } A_{\text{flow}} = \pi(d_2^2 - d_1^2)/4 \tag{13}$$

Mass Transfer. For mass transfer in dilute solutions, the multicomponent equation for mass transport given in Part I is still valid. However, for turbulent flows, a time-averaged equation must be used with mean quantities $\bar{C}_j$ as the dependent variables and with an effective turbulent diffusivity replacing the molecular diffusivity. The mean mass transport equation written for species j, where j can be Ca^{+2}, CO_3^{-2}, HCO_3^-, or CO_2, in cylindrical coordinates is

$$\bar{v}_z(r)\frac{\partial\bar{C}_j}{\partial z} = \frac{1}{r}\frac{\partial}{\partial r}\left[rD_{j,\text{eff}}\frac{\partial\bar{C}_j}{\partial r}\right]$$

where

$$D_{j,\text{eff}} = D_j + D_{j,\text{turb}} \tag{14}$$

To determine the turbulent diffusivity, the mixing length hypothesis is used. Assuming the turbulent Schmidt number to be unity, i.e., $\text{Sc}_{\text{turb}} = \nu_{\text{turb}}/D_{\text{turb}} = 1$, $D_{j,\text{turb}}$ can be written as

$$D_{j,\text{turb}} = l_m^2\left|\frac{d\bar{v}_z}{dr}\right| \tag{15}$$

in which l_m, the mixing length, is approximated by l_m in turbulent pipe flows (Schlichting, 1955):

$$l_m/R = 0.14 - 0.08(1 - y/R)^2 - 0.06(1 - y/R)^4 \tag{16}$$

where y is the distance from the wall. Since the equation is being used for an annulus for which the axis of zero shear is not in the center, two separate regions must be considered: one from $r = \kappa R$ to λR and the other from $r = \lambda R$ to R. Equation (16) then becomes

$$r < \lambda R: \quad \frac{l_m}{R(\lambda - \kappa)} = 0.14 - 0.08H_1^2 - 0.06H_1^4; \quad H_1 = 1 - \frac{r - \kappa R}{R(\lambda - \kappa)} \tag{17}$$

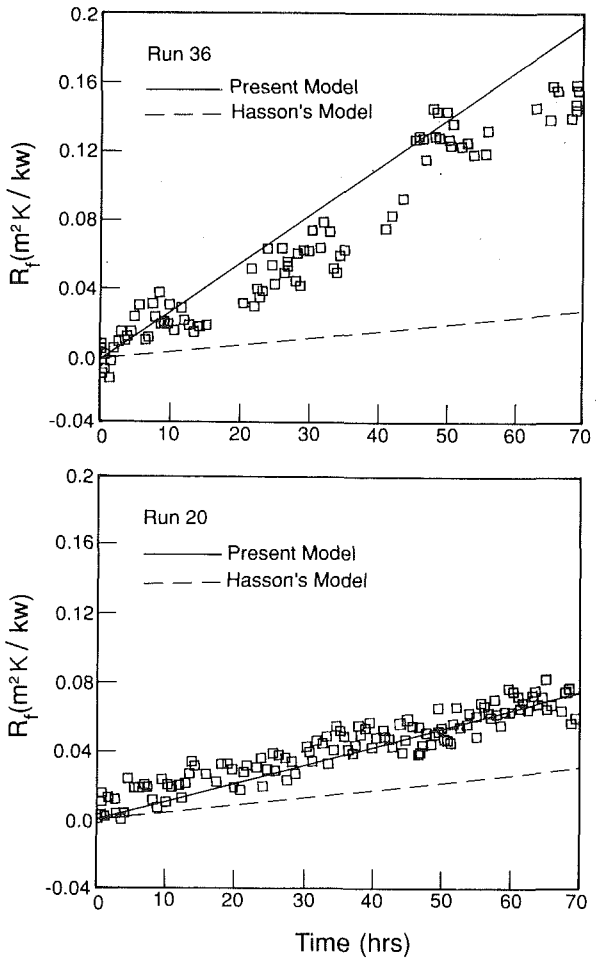

Fig. 4 Comparison of the present and Hasson's model with fouling data of Sheikholeslami and Watkinson (1986)

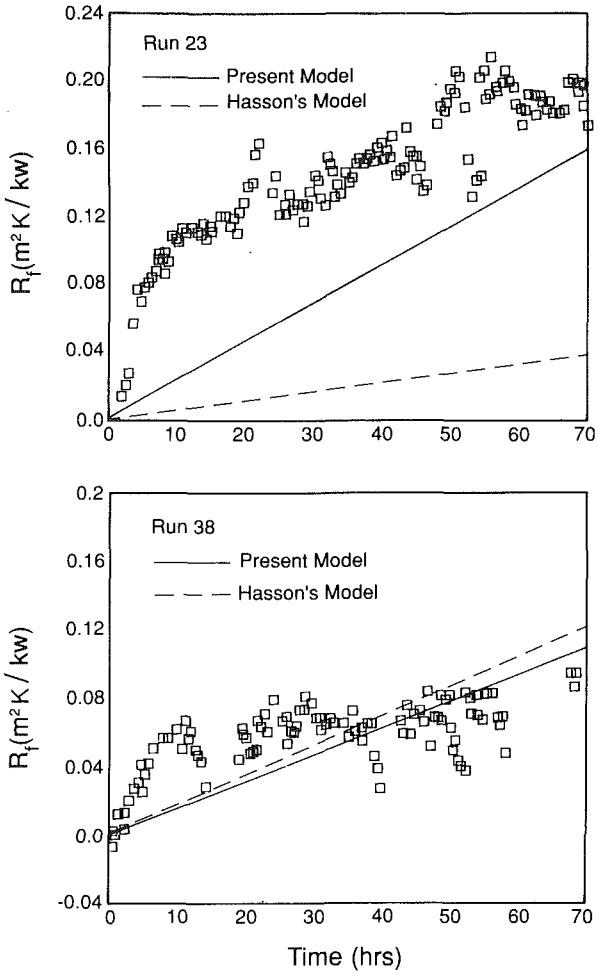

Fig. 5 Comparison of the present and Hasson's model with fouling data of Sheikholeslami and Watkinson (1986)

$$r>\lambda R: \quad \frac{1}{R(1-\lambda)}=0.14 - 0.08H_2^2-0.06H_2^4; \quad H_2=1-\frac{R-r}{R(1-\lambda)} \tag{18}$$

The reaction rate form of equation (26) in Part I is used, and only the Ca^{+2} and CO_3^{-2} species are considered. The reason for using only two species rather than three is that in the turbulent case, the composition of the inlet water is given as alkalinity and solution pH from which the other concentrations can be calculated from equilibrium relations (assuming equilibrium conditions exist). For the laminar case, all the relevant composition data are given for the experimental runs. The general initial and boundary conditions to equation (14) are then

$$\text{at } z=0; \quad \overline{C}_j=\overline{C}_j^{\circ} \tag{19}$$

$$\text{at } r=\kappa R; \quad D_j\,\partial\overline{C}_j/\partial r=k_r(z)\,(\overline{C}_1\,\overline{C}_2-K_{sp}(z)) \tag{20}$$

$$\text{at } r=R; \quad \partial\overline{C}_j/\partial r=0 \tag{21}$$

where $j=1$ and 2 to represent the Ca^{+2} and CO_3^{-2} species, respectively.

Calculation Procedure, Results, and Discussion. The calculational procedure used to solve for the concentration profiles of Ca^{+2} and CO_3^{-2} from equation (14) is the same as before. The concentration gradient at the wall is obtained from

$$\left.\frac{\partial C_j}{\partial r}\right|_{r=\kappa R}=\frac{-9C_{j,1}^{k+1}+10C_{j,2}^{k+1}-C_{j,3}^{k+1}}{8\Delta r} \tag{22}$$

and the mass deposition can be calculated as

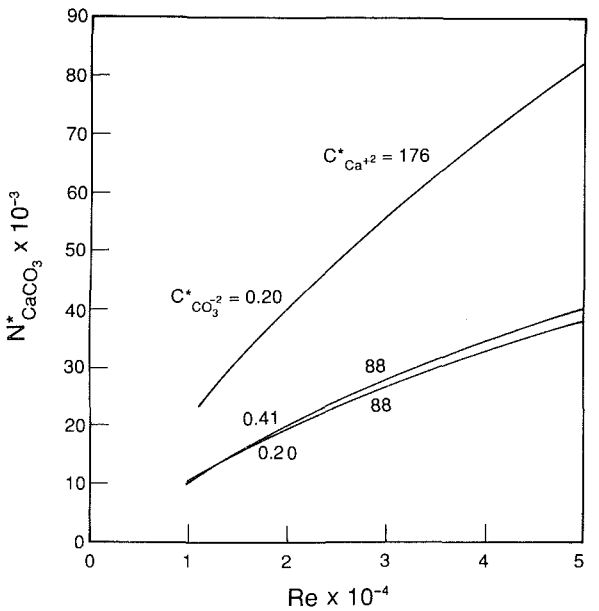

Fig. 6 Nondimensionless mass flux versus pertinent dimensionless operating parameters

$$N_{CaCO_3}=M_{CaCO_3}\,D_j\left.\frac{\partial C_j}{\partial r}\right|_{r=R} \tag{23}$$

The relation between the mass of deposit and the fouling resistance, R_f, can be expressed as

$$dR_f/dt = N_{CaCO_3}/\rho_f k_f \tag{24}$$

from which the fouling resistance at any time can be calculated, assuming the quantities on the right-hand side of equation (24) to be time independent.

The average value of the fouling resistance for several flows was calculated and compared with experiments (Sheikholeslami and Watkinson, 1986). The values of all physical properties and initial conditions used in the calculations for the turbulent model are given in Table 2. The values of E_a and A were obtained, as in the laminar case, by trial and error. The values for E_a/R_g (in units of K) and $\ln(A)$ (A in units of cm^4/mole s) used were 4800 and 46, respectively. It was found that the model is quite insensitive to the kinetic parameters (E_a and A) beyond these values. This is quite different from the laminar computations, which would increase without bound if the reaction kinetic parameters were continually increased. A grid of 95 steps in r and 1150 steps in z was used in the numerical computations. Convergence was examined in a similar manner as in the laminar case and the numerical error is estimated to be less than 0.5 percent.

The mean mass deposition flux averaged over the axial length of the fouling surface has been calculated for the conditions of Sheikholeslami's experiments and four representative results are given in Table 3. Also listed in the table are the calculated, average value of the fouling resistance at various time. The experimental as well as the predicted behavior of fouling resistance versus time from both the present model and Hasson's model (see Sheikholeslami and Watkinson, 1986, and Hasson and Perl, 1981) are all listed in Table 3 and compared in Figs. 4 and 5. The comparison shows that the current multispecies transport model has improved significantly over Hasson's model. The agreement between the present predictions and experimental data appears to be excellent for runs with linear fouling behavior (see runs 20 and 36 in Fig. 4). However, the agreement is not as good, especially during early stages of scaling, for the two runs (runs 23 and 38 shown in Fig. 5) with asymptotic behavior. However, Sheikholeslami and Watkinson (1986) pointed out that most of their experiments produced linear plots of R_f versus time. They further stated that "asymptotic behavior was noted only in a few instances such as when the mild steel tube was used for the first time (run 23) or with the noncorroding copper tube at the lowest velocity (run 38)." They also continued to state "that for both cases, the initial rate was very much higher than usual, and in the former case the ultimate scaling resistance was also abnormally high. In a repeated run on the mild steel tube, scaling was linear, and less extensive." Therefore for practical purposes, it was concluded that the predictions by the present transport model appears to be satisfactory for most applications.

It should be mentioned that in using the Hasson model, the calculation of Sheikholeslami and Watkinson (1986) is higher than ours. Hasson (1990) has kindly reviewed the manuscript and pointed out that the difference is partly from the use of different heat transfer coefficient correlations and mainly from having used different correlations of surface reaction coefficient K_R, which has an exponential dependence on temperature. They did not disclose in their paper what heat transfer correlation was used, while the present work uses the one given by equation (12). As for K_R, they used the earlier work of Hasson, namely, the Gazit–Hasson correlation (1975; cited by Sheikholeslami and Watkinson, 1986), which gives higher K_R values than that of the Hasson–Perl correlation (1981) adopted here. It is noted in passing that a typographical error appears in their Hasson expression, i.e., the term x^2 in their equation (4) should be replaced by x (the Ca^{++} concentration). In any case, the difference has no bearing on the model proposed here.

Like the previous laminar solution, the results from the turbulent model computations are also presented as plots of a nondimensional mass flux versus the dimensionless operating parameters of the inlet composition and flow Reynolds number, as shown in Fig. 6. The plots are for a constant laminar Schmidt number value of 500. The nondimensional molar flux, species concentration, and Reynolds number were defined as

$$N^* = \frac{N_{CaCO_3}\, d_r}{DK_{sp}^{1/2}}; \quad C_j^* = \frac{C_j^\circ}{K_{sp}^{1/2}}; \quad \mathrm{Re}_f = \frac{(d_2 - d_1)\langle \bar{v}_z \rangle \rho}{\mu}$$

where $d_r = (d_2^2 - d_1^2)/d_1$; the temperature-dependent quantities such as K_{sp} and D are evaluated at the inlet temperature, T°_{blk}. It is clearly seen that the calcium carbonate fouling increases significantly with Reynolds number and with the inlet Ca^{+2} ion concentrations but less with the inlet CO_3^{-2} ion concentrations.

Conclusions

The model proposed for calcium carbonate fouling is a mechanistic one, based on conservation equations and surface reaction kinetics. When applied to a laminar falling film system, comparisons of predicted deposition flux and fouling thickness with those of the experimental data indicate an excellent agreement with a maximum error of less than ± 16 percent. Similarly, the prediction of deposition in an annulus with turbulent flow is also excellent for the majority of fouling curves observed experimentally that exhibit linear time behavior, but prediction is less accurate for a few exceptional runs that exhibit asymptotic behavior. It has the capability of calculating not only the overall fouling resistance averaged over the entire heat exchanger, but also the local fouling profile along the length of the heat exchanger.

Acknowledgments

Support by the National Science Foundation under grant No. CBT-8807406 is gratefully acknowledged.

References

Bird, R. B., Stewart, W. E., and Lightfoot, E. N., 1960, *Transport Phenomena*, Wiley, New York.

Chan, S. H., and Ghassemi, K. F., 1991, "Analytical Model of Calcium Carbonate Deposition for Laminar Falling Films and Turbulent Flow in Annuli: Part I—Formulation and Single-Species Model," ASME JOURNAL OF HEAT TRANSFER, Vol. 113, pp. 735–740.

Gazit, E., and Hasson, D., 1975, "Scale Deposition From an Evaporating Falling-Film," *Desalination*, Vol. 17, p. 339.

Hasson, D., and Perl, I., 1981, "Scale Deposition in a Laminar Falling-Film System," *Desalination*, Vol. 37, pp. 279–292.

Hasson, D., 1990, private communication.

Perry, R. H., Green, D. W., and Maloney, J. O., 1984, eds., *Perry's Chemical Engineers' Handbook*, 6th ed., McGraw-Hill, New York.

Schlichting, H., 1955, *Boundary-Layer Theory*, McGraw-Hill, New York.

Sheikholeslami, R., and Watkinson, A. P., 1986, "Scaling of Plain and Externally Finned Heat Exchanger Tubes," ASME JOURNAL OF HEAT TRANSFER, Vol. 108, pp. 147–152.

Non-Darcian Effects in Open-Ended Cavities Filled With a Porous Medium

J. Ettefagh

K. Vafai
Professor.
Mem. ASME

S. J. Kim

Department of Mechanical Engineering,
The Ohio State University,
Columbus, OH 43210

The importance and relevance of non-Darcian effects associated with the buoyancy driven convection in open-ended cavities filled with fluid-saturated porous medium is analyzed in this work. Several different flow models for porous media, such as Brinkman-extended Darcy, Forchheimer-extended Darcy, and generalized flow models, are considered. The significance of inertia and boundary effects, and their crucial influence on the prediction of buouancy-induced flow and heat transfer in open-ended cavities, are investigated. Analysis is made on the proper choice of parameters that can fully determine the criteria for the range of validity of Darcy's law in this type of configuration. Critical values of the inertial parameter, Λ_{crit}, below which, for any given modified Rayleigh number, the Darcy flow model breaks down, have been investigated. It is shown that the critical value of the inertial parameter depends on the modified Rayleigh number and that this critical value increases as Ra increases. It is also observed that for higher modified Rayleigh number, the deviation from a Darcian formulation appears at Darcy numbers greater than 1×10^{-4}. The Prandtl number effects on convective flow and heat transfer are shown to be quite significant for small values of Pr. The Prandtl number effects are reduced significantly for higher values of the Prandtl number.*

1 Introduction

The buoyancy-induced flow in fluid-saturated porous media has been a major topic of many studies during the past 20 years. This is due to many engineering applications such as thermal insulation engineering, water movements in geothermal reservoirs, underground spreading of chemical waste, nuclear waste repository, grain storage, and enhanced recovery of petroleum reservoirs. Most of the previous investigations include natural convection in confined enclosures driven by horizontal temperature gradients, natural convection boundary layers, and convective flows in horizontal porous layers heated from below. However, consideration of the open boundary effects on the heat transfer rate and the flow field is limited. One of the main characteristics of the buoyancy-induced flows in the open-ended cavities is its basic geometry, which, among other aspects, reveals the interactions and the influence of the inner (inside the cavity) and the outer (the open region) flow and temperature fields. There has been very little work done on these types of interactions, which can occur in various practical applications.

Bejan and Tien (1978) developed an approximate analytical solution of the fluid flow and heat transfer in a shallow porous cavity with vertical, permeable walls subjected to an end-to-end temperature difference. Their results show that an end-to-end temperature difference gives rise to a horizontal counterflow pattern augmenting the heat transfer rate through the porous medium. The open boundary in the case of parallel plates is shown to enhance the heat transfer rate significantly through the porous medium. Later in an effort related to the conceptual design of porous winding structures for rotating superconducting electric machines, Bejan (1981) performed an analytical study of lateral penetration of natural convection into a horizontal porous layer in lateral communication with a heat reservoir. The study shows that the flow penetrates laterally to a distance of order $H \times \mathrm{Ra}^{1/2}$, where H is the height of the porous layer. The net heat exchange between the porous structure and the lateral heat reservoir is described by a Nusselt number of the type $\mathrm{Nu} \sim \mathrm{Ra}^{1/2}$.

Haajizadeh and Tien (1983) studied the same problem originally considered by Bejan and Tien (1978). In this work, the asymptotic solutions for a shallow open cavity including the numerical and experimental results are presented for an aspect ratio of 3.17 and Rayleigh numbers up to 120. They showed that the constant pressure and temperature assumptions at the permeable wall, as employed in the theoretical analysis, compare satisfactorily with the experimental data, although in principle the reservoir and the cavity flows are coupled. It should be mentioned that the boundary conditions and the driving mechanism in Haajizadeh and Tien's (1983) work are totally different from those in the work of Bejan and Tien (1978). For example, in contrast to Bejan and Tien's (1978) work in which the axial conduction was neglected, Haajizadeh and Tien (1983) considered the axial conduction as the main driving mechanism for the flow.

The latest study in this area is by Ettefagh and Vafai (1988) who conducted a numerical investigation of buoyancy-driven flow in open-ended cavities that are obstructed by a porous medium. The problem was modeled as a transient, two-dimensional natural convection and the stream function-vorticity formulation was employed in their analysis. The difficulty of specifying the appropriate boundary conditions at the opening was overcome by solving the governing equations in an extended computational domain outside the opening. A detailed study of the flow characteristics including the heat transfer analysis inside the open-ended cavity was performed. Steady-state and transient results were obtained for various modified Rayleigh numbers, aspect ratios, and temperature levels. Their results indicated that the flow field inside the open-ended cavity

Contributed by the Heat Transfer Division for publication in the JOURNAL OF HEAT TRANSFER. Manuscript received by the Heat Transfer Division January 30, 1990; revision received July 24, 1990. Keywords: Geophysical Heat Transfer, Natural Convection, Porous Media.

and near the aperture plane was relatively insensitive to the far field boundary conditions provided that the boundaries were set far enough from the opening. In this work, the crucial influence of the external corners on the flow pattern and heat transfer process in terms of vorticity generation and the flow instabilities was also observed. The presence of "humps" as well as the periodic behavior in the variation of the cavity Nusselt number with time were discussed in length. It was found that decreasing the aspect ratio had a stabilizing effect on the flow field. They also concluded that an increase in the temperature of the upper block considerably enhances the heat transfer from the upper block while slightly increasing that of the lower block.

The preceding literature survey suggests that very little research has been conducted in the area of natural convection in partial enclosures or open-ended cavities filled with fluid-saturated porous medium. In all of the above investigations, Darcy's law has been utilized as the governing momentum equation. The most common reason for the wide use of a Darcian formulation in recent investigations is its simplicity. However, the Darcian formulation breaks down when boundary and inertial effects become important. Such is the case for heat transfer through a porous layer in the convection-dominated regime, where the vertical velocity is quite large.

At higher velocities, inertial effects become appreciable, resulting in an increase in the form drag. Forchheimer (1901) recognized the breakdown of Darcy's law at high speeds and suggested the addition of a quadratic velocity term to Darcy's equation. The effect of a solid boundary on flow and heat transfer in a porous medium originates from vorticity diffusion caused by the boundary frictional resistance. This resistance is in addition to the bulk frictional drag induced by the solid matrix, which embodies Darcy's law. For the flow through a porous medium with a high permeability, Brinkman (1947) suggested that the momentum equation for porous media flow must be reduced to the viscous flow limit and suggested the addition of the classical frictional term to the Darcy flow model. The Brinkman—extended Darcy model includes the shear stress terms and makes it possible for the no-slip condition to be satisfied at the boundaries. Since Darcy's law is one order less than the Navier-Stokes equation, only the impermeable boundary condition at the surface can be satisfied, while the no-slip boundary condition cannot be satisfied. It should be emphasized that none of the above models account adequately for the transition from porous medium flow to pure fluid flow as the permeability increases. A model that bridges the entire gap between the Forchheimer-extended Darcy flow model and the Navier-Stokes equation was developed by Vafai and Tien (1981).

In recent years, several attempts have been made to examine the non-Darcy effects on buoyancy-induced flow and heat transfer in porous media. These studies generally concentrate on problems such as buoyancy-driven flow by horizontal temperature gradients in cavities, convective flow and heat transfer in porous cavity heated from below, and natural convection boundary layer flows. Most of these studies have investigated either the inertia or boundary effects individually while considerations of both effects simultaneously via generalized flow model are very limited in literature. However, since these studies have used geometric configurations other than a partially open or an open-ended cavity filled with a porous medium, they will not be reviewed here for the sake of brevity.

The purpose of the present study is to consider the generalized equation of motion, and examine the significance of both the Forchheimer and the Brinkman modifications on the predictions of buoyancy-induced flow and heat transfer in open-ended cavities filled with fluid-saturated porous medium. In the course of this study, an analysis will be made on the proper choice of a parameter or combination of parameters that can fully describe the criteria for the range of validity of Darcy's law in these type of configurations.

2 Mathematical Formulation

A schematic of the physical model and coordinate system is shown in Fig. 1. The problem is modeled as an incompressible transient two-dimensional buoyancy-induced flow through an isotropic, homogeneous, fluid-saturated porous medium. The thermophysical properties of the solid and fluid are assumed to be constant except for the density variation in the buoyancy

Nomenclature

A = aspect ratio = H/D
D = width of the open cavity, m
Da = Darcy number = K/H^2
F = inertial coefficient, an empirical function that depends on Reynolds number and the microstructure of the porous medium
$\mathbf{g}$ = gravitational acceleration vector, m^2/s
g = gravitational acceleration, m^2/s
H = open cavity height, m
K = permeability of the porous medium, m^2
Nu = Nusselt number, equation (11)
P = pressure, Pa
Pr = Prandtl number = $\nu_f/\alpha_{\text{eff}}$
Pr_m = modified Prandtl number = $\nu_f \sigma\delta/\alpha_{\text{eff}}$
Ra = Rayleigh number = $g\beta H^3\Delta T/\alpha_{\text{eff}}\nu_f$
Ra* = modified Rayleigh number for porous medium = $g\beta HK\Delta T/\alpha_{\text{eff}}\nu_f$
t = time, s
t^* = dimensionless time = $t\alpha/\sigma H^2$
T = temperature, K
ΔT = temperature difference = $T_1 - T_\infty$, K
$\mathbf{u}$ = velocity vector, m/s
u = x component of the velocity, m/s
u^* = dimensionless x component of the velocity = uH/α_{eff}
v = y component of the velocity, m/s
v^* = dimensionless y component of the velocity = $v H/\alpha_{\text{eff}}$
x = horizontal coordinate, m
x^* = dimensionless horizontal coordinate = x/H
y = vertical coordinate, m
y^* = dimensionless vertical coordinate = y/H
α = thermal diffusivity, m^2s^{-1}
β = thermal expansion coefficient of fluid, K^{-1}
δ = porosity
θ = dimensionless temperature = $(T - T_\infty)/(T_1 - T_\infty)$
Λ = dimensionless inertial parameter = $F\delta^2\sigma H/\sqrt{K}$
μ = dynamic viscosity, $kgm^{-1}s^{-1}$
ν = kinematic viscosity, m^2s^{-1}
ξ = vorticity
ξ^* = dimensionless vorticity = $\xi H^2/\alpha_{\text{eff}}$
ρ = density, kgm^{-3}
σ = thermal capacitance of the porous/fluid system
ψ = stream function
ψ^* = dimensionless stream function = ψ/α_{eff}

Subscripts

1 = lower block
2 = upper block
eff = refers to effective properties for a fluid-saturated porous medium
f = refers to the fluid
i = nodal index in the x direction
j = nodal index in the y direction
∞ = ambient conditions

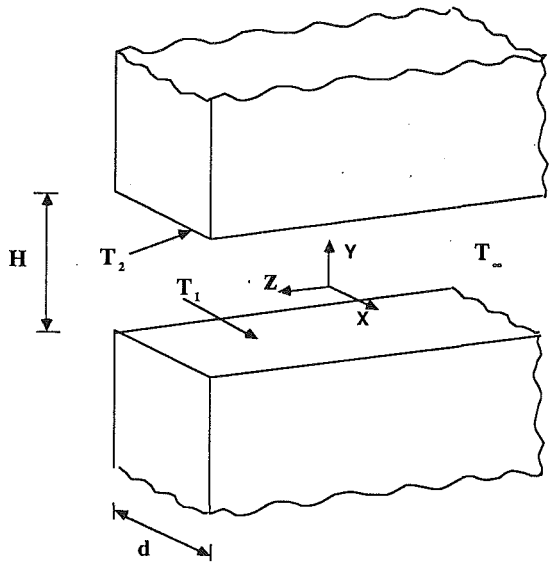

Fig. 1 Schematic of an open-ended cavity

term. Also, it is assumed that the solid matrix and the fluid are in local thermodynamic equilibrium. These equations governing the conservation of mass, momentum, and energy in their general form can be written as in Vafai and Tien (1981) and Vafai (1984)

$$\nabla \cdot \mathbf{u} = 0 \tag{1}$$

$$\frac{\rho_f}{\delta}\frac{D\mathbf{u}}{Dt} = -\nabla p + \mu_{\text{eff}}\nabla^2\mathbf{u} + \rho_f \mathbf{g}\,\beta(T - T_\infty) - \frac{\mu_f}{K}\mathbf{u} - \frac{\rho_f F\delta}{\sqrt{K}}|\mathbf{u}|\mathbf{u} \tag{2}$$

$$\sigma\frac{\partial T}{\partial t} + \mathbf{u}\cdot\nabla T = \alpha_{\text{eff}}\nabla^2 T \tag{3}$$

where

$$|\mathbf{u}| = \sqrt{u^2 + v^2}$$

In the above equations $\mathbf{u}$ is the velocity vector, p is the pressure, $\mathbf{g}$ is the gravitational vector, T is the temperature, ρ_f is the fluid density, K is the permeability of the porous medium, α_{eff} is the effective thermal diffusivity, μ_f is the viscosity of the fluid, μ_{eff} is the apparent viscosity of the medium, δ is the porosity of the porous medium, β is the volume thermal expansion coefficient of the fluid, σ the thermal capacitance of the porous matrix, and F is the inertial coefficient, an empirical function that depends on Reynolds number and the microstructure of the porous medium. While the effective viscosity of the fluid-saturated porous medium μ_{eff} associated with the Brinkman term in the momentum equation may have a different value than the fluid viscosity μ_f (Cheng, 1978), as a first approximation μ_{eff} is taken equal to μ_f in the present study. This approximation provides a good agreement with the experimental data reported by Lundgren (1972) and Neale and Nader (1974). It is worth noting that here, the thermal dispersion effect is accounted for by lumping it with the thermal conductivity. That is, we have taken one of the customary approaches in which thermal dispersion contribution is embedded into the effective thermal conductivity. Hence the effective thermal diffusivity can be decomposed into two parts: One stands for the stagnant thermal diffusivity of the fluid-saturated porous medium and the other incorporates the additional thermal transport due to the transverse mixing. The above approach has the advantage of not diluting our main goal for this investigation, i.e., boundary and inertial effects in open-ended cavities.

In two-dimensional Cartesian coordinates, upon cross differentiation and eliminating pressure in the momentum equations and introducing the stream function and vorticity, the vorticity transport and stream function equations in their general forms can be written as

$$\frac{\rho_f}{\delta}\frac{D\zeta}{Dt} = \mu_f\nabla^2\zeta - \frac{\mu_f}{\kappa}\zeta - \frac{\rho_f F\delta}{\sqrt{\kappa}}\left(\frac{\partial}{\partial y}(|\mathbf{u}|u) - \frac{\partial}{\partial x}(|\mathbf{u}|v)\right) - \rho_f g\beta\frac{\partial T}{\partial x}$$

$$\nabla^2\Psi = \zeta$$

where

$$\zeta = \frac{\partial u}{\partial y} - \frac{\partial v}{\partial x}$$

and

$$u = \frac{\partial\Psi}{\partial y}, \qquad v = -\frac{\partial\Psi}{\partial x}$$

In the above equations, ζ is the vorticity and Ψ is the stream function. It is convenient to cast the governing equations in dimensionless form by introducing the new nondimensional variables

$$x^* = \frac{x}{H}, \qquad y^* = \frac{y}{H}$$

$$u^* = \frac{uH}{\alpha_{\text{eff}}}, \qquad v^* = \frac{vH}{\alpha_{\text{eff}}}$$

$$\Psi^* = \frac{\Psi}{\alpha_{\text{eff}}}, \qquad \zeta^* = \frac{\zeta H^2}{\alpha_{\text{eff}}}$$

$$t^* = \frac{t\alpha}{\sigma H^2}, \qquad \theta = \frac{T - T_\infty}{T_1 - T_\infty}$$

The resultant nondimensional governing equations are written as

$$\frac{D\zeta}{Dt} = \text{Pr}_m\nabla^2\zeta - \text{Pr}_m\text{Ra}\frac{\partial\theta}{\partial x} - \frac{\text{Pr}_m}{\text{Da}}\zeta - \Lambda\left(\frac{\partial}{\partial y}(|\mathbf{u}|u) - \frac{\partial}{\partial x}(|\mathbf{u}|v)\right) \tag{4}$$

$$\nabla^2\Psi = \zeta \tag{5}$$

$$\frac{\partial\theta}{\partial t} + u\frac{\partial\theta}{\partial x} + v\frac{\partial\theta}{\partial y} = \nabla^2\theta \tag{6}$$

In the above equations the superscripts are dropped for convenience. The nondimensional parameters are defined as Rayleigh number $\text{Ra} = g\beta H^3\Delta T/\alpha_{\text{eff}}\nu_f$, Darcy number $\text{Da} = K/H^2$, the modified Prandtl number $\text{Pr}_m = \nu_f\sigma\delta/\alpha_{\text{eff}}$, the inertial parameter $\Lambda = F\delta^2\sigma H/\sqrt{K} = F\delta^2\sigma/\sqrt{\text{Da}}$, and the modified Rayleigh number for porous medium $\text{Ra}^* = g\beta HK\Delta T/\alpha_{\text{eff}}\nu_f$. It should be noted that when the convective terms in the momentum equation (Vafai and Tien, 1981) are neglected and under steady-state conditions $\text{Pr}_m = \text{Pr} = \nu_f/\alpha_{\text{eff}}$, $t^* = t\alpha/H^2$ and $\Lambda = F\delta H/\sqrt{K} = F\delta/\sqrt{\text{Da}}$.

Equation (4) is the vorticity transport equation in a fluid-saturated porous medium based on the general flow model, which incorporates both the boundary and inertial effects. The use of different models instead of the general flow model would result in essentially a total of three different limiting forms of this equation, which are given as

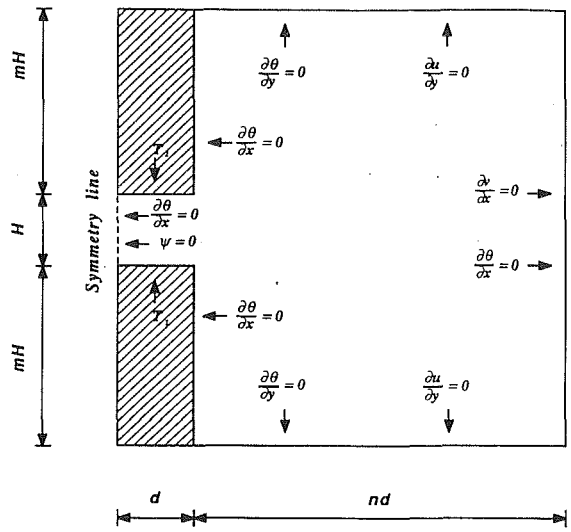

Fig. 2 The nonuniform grid distribution for the portion of the computational domain that concentrates on the cavity and its immediate surroundings

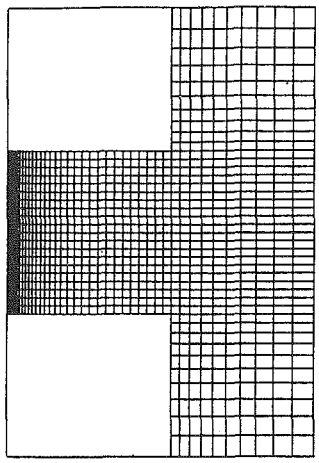

Fig. 3 Schematic of computational domain along with the extended boundary conditions

Darcy flow model

$$\nabla^2\Psi = -\mathrm{Ra}^* \frac{\partial\theta}{\partial x} \tag{7}$$

Forchheimer-extended Darcy flow model

$$\nabla^2\Psi = -\mathrm{Ra}\frac{\partial\theta}{\partial x} - \frac{\Lambda\mathrm{Da}}{\mathrm{Pr}_m}\left(\frac{\partial}{\partial y}(|\mathbf{u}|u) - \frac{\partial}{\partial x}(|\mathbf{u}|v)\right) \tag{8}$$

Brinkman-extended Darcy flow model

$$\frac{D\zeta}{Dt} = \mathrm{Pr}_m\nabla^2\zeta - \mathrm{Pr}_m\,\mathrm{Ra}\frac{\partial\theta}{\partial x} - \frac{\mathrm{Pr}_m}{\mathrm{Da}}\zeta \tag{9}$$

It should be noted that equation (9) would reduce to the vorticity transport equation in a regular medium in the limiting case of very high-permeability porous medium ($K\to\infty$).

$$\frac{D\zeta}{Dt} = \mathrm{Pr}_m\nabla^2\zeta - \mathrm{Pr}_m\mathrm{Ra}\frac{\partial\theta}{\partial x} \tag{10}$$

The lower and upper block Nusselt numbers are defined as the ratio of actual heat transfer rate to pure conduction heat transfer rate. The rate of heat transfer across the open-ended cavity was calculated in terms of a cavity Nusselt number, which represents the nondimensional total rate of heat transfer from the entire cavity, and is given as

$$\mathrm{Nu}_c = -A\int_0^{\frac{1}{2}}\frac{\partial\theta}{\partial y}\bigg|_{y=-\frac{A}{2}}dx + \frac{A}{\theta_2}\int_0^{\frac{1}{2}}\frac{\partial\theta}{\partial y}\bigg|_{y=\frac{A}{2}}dx \tag{11}$$

3 Boundary Conditions

Schematics of the computational domain including the proper boundary conditions are shown in Figs. 2 and 3. The stream functions along the impermeable block surfaces are taken to be zero. The vorticity along these surfaces is determined by invoking the no-slip conditions for the cases of Brinkman-extended Darcy and the general flow models. Temperature conditions are specified temperature at the base and adiabatic conditions along the vertical portion of the blocks. The stream function value and normal temperature gradient are set to zero at the symmetry line. In addition, the symmetry condition requires the vorticity to be zero in the cases of Brinkman-extended Darcy and the general flow models. The far field boundary conditions are approximated by setting the normal gradients of the velocity and the temperature to zero. The validity of these conditions is explored in more detail later on. The vorticity values at these locations are calculated from the stream function distribution in the cases of Brinkman-extended Darcy and the general flow models.

Since there are two kinds of temperature (specified temperature on horizontal portion and adiabatic on vertical portion) imposed on the convex corners, a multivalued procedure is used at the corners. Such discontinuous treatment for a field variable is discussed by Thom and Apelt (1961), Roache and Mueller (1970), and Kacker and Whitelaw (1970) and used by several different researchers. Here to model the mathematical limit of a sharp corner, the method of discontinuous vorticity values, as described by Ettefagh and Vafai (1988) and Vafai and Ettefagh (1990), has been utilized. In the cases of Brinkman-extended Darcy and the general flow models, due to discontinuity of vorticity at sharp corners, a multi-valued procedure similar to the temperature evaluation is employed for the vorticity calculation at the convex corners.

4 Numerical Solution; Stability and Accuracy of the Numerical Scheme

The governing equations (4)–(6) were approximated by finite-difference method and the discretized equations were solved numerically on a Cray-YMP via a highly vectorized scheme. The transient transport equations were solved in a variable grid mesh by a modified ADI method, which incorporates the upwind differencing and accounts for the convective instabilities. The treatment of the inertial term for the case of general flow model required a special consideration. In one approach the inertial term could be considered as a source term in the vorticity transport equation. Alternatively, this inertial term could be split into two parts: The first part would be combined with the Darcy term and taken to the left-hand side of the equation, while the other part would be treated as part of the source term. Both of the above procedures were considered and it was observed that there were no significant changes in the Nusselt numbers obtained from the above two methods. In this work, the inertial term was linearized and considered as a source term.

At each time step, the stream function equation was solved by an extrapolated Jacobi scheme, an iterative method with optimum overrelaxation. This scheme has some similarities with the original Jacobi scheme (Nakamura, 1990). However, unlike other iterative methods in which the entire grids are updated, in this scheme only half of the nodal points are updated for any given iteration level while the other half are updated at the next consecutive iteration level. Furthermore, before starting each iteration cycle the newly iterated nodal values are overrelaxed using the optimum overrelaxation pa-

rameter. It can be shown that the extrapolated Jacobi scheme has the same convergence rate as the conventional SOR method and even its spectral radius is the same as that of SOR. Hence, the algorithm for its optimum overrelaxation parameter is the same as the one for SOR (Nakamura, 1990). But, its advantage is that it can be vectorized, which makes it very efficient when used on a Cray-YMP. This efficiency is best explained when one realizes that most of the computer time spent results from the solution of the Poisson equation.

There are several important aspects of the numerical simulation of the flow field and heat transfer in these type of configuration that need to be explored. The problem of specifying the proper boundary conditions at the openings was overcome by extending the computational domain in both the horizontal and vertical directions. The open boundary conditions were approximated by specifying zero normal gradients for the velocities and temperature at the far field locations. These approximations supplied enough accuracy for the results provided that the computational domain was extended far enough. In this work, the extension of at least 16 times the cavity height was necessary so as to retard any significant changes in the flow field and heat transfer characteristics inside the open cavity and its immediate surroundings. The symmetry condition at the centerline of the cavity was validated by comparing the numerical results obtained for half of the open-ended cavity, using the symmetry conditions, versus the full numerical simulation of the entire open-ended cavity. In addition, the flow was extensively perturbed by employing different asymmetric initial conditions and again a return to a symmetric state was observed.

The energy equation is advanced in time according to the ADI method. The spatial derivatives are approximated in the nonuniform grid system by central differencing. The convective terms are represented by the second upwind differencing to avoid the stability problem associated with the central differencing and the inaccuracies caused by the artificial viscosity effects associated with the first upwind differencing. In the cases of Brinkman-extended Darcy and the general flow models, the vorticity is then advanced in time using the ADI method. The stream function is then updated by the Extrapolated Jacobi scheme. The heat flux is calculated by three-point differencing of the temperature gradients at the walls, and the cavity Nusselt number is found upon numerical integration of equation (7) using Simpson's rule. A convergence criterion 0.01 percent or less change in θ, Ψ, and ζ at all nodes in the domain has been used to test the steady-state conditions.

To resolve the flow field and heat transfer rate near the walls adequately, a variable grid system was used. Figure 3 displays the nonuniform grid distribution for the portion of the domain that concentrates on the cavity and its immediate surroundings. The grid distribution was chosen such that the criteria

$$\Delta x_i - \Delta x_{i-1} = O\{(\Delta x_{i-1})^2\}$$

and

$$\Delta y_j - \Delta y_{j-1} = O\{(\Delta y_{j-1})^2\}$$

would always be satisfied. In the above expressions Δx_i and Δy_j are the spatial distances between nodal locations x_i and x_{i+1}, and y_j and y_{j+1}, respectively. These criteria ensured that the truncation error for the utilized variable grid system would be locally second order accurate.

In our work it was ascertained that using larger spatial extensions or smaller time steps (relative to what was used to obtain the numerical results) have no influence on the transient or the steady-state results for the stream function, temperature, vorticity, and the temporal Nusselt number distributions. First, the open boundaries were systematically extended in both directions and it was determined that it was necessary to extend the computational domain at least 16 times the height of the cavity to eliminate the effects of the far field solution on the flow field and the heat transfer characteristics inside the open cavity and its surroundings. Next, we used consecutively smaller time step sizes to obtain time step independent solutions. The latter process was done with the proper extensions found from the first stage of our accuracy tests. Finally we have ascertained that simultaneous changes in the spatial domain and the magnitude of the time step have less than one half of a percent influence on any of our results.

Based on these tests, it was found that in order to resolve the flow field accurately near the boundaries, especially for higher modified Rayleigh number flows, a variable grid system having the smallest mesh size of (0.01) should be used inside the open cavity. The typical time increment for time step independent solutions was found to be 10^{-3} for lower and 5×10^{-4} for higher modified Rayleigh numbers. For cases with very small inertial parameters, the time increment of 2×10^{-5} had to be used in order to achieve time step independent solutions.

5 Results and Discussion

The influence of governing physical parameters such as the Rayleigh number, Darcy number, inertial parameter, and modified Rayleigh number on the heat transfer and flow field for natural convection in open-ended cavities was studied. The Forchheimer-extended Darcy equation of motion for flow through porous media was utilized to investigate the inertial effects on natural convection in an open-ended cavity. The boundary effects on buoyancy-driven flow and heat transfer were examined through the use of the Brinkman-extended Darcy flow model. Finally, the general flow model was utilized to demonstrate the significance of both the inertial and the boundary effects on the buoyancy-induced flow and heat transfer in open-ended cavities filled with porous medium.

An open-ended cavity with an aspect ratio of $A = 0.5$, a lower block surface temperature of $\theta_1 = 1$, an upper block surface temperature of $\theta_2 = 1$, and a working fluid with a modified Prandtl number, Pr_m, of 1 was considered as the general case in this work. In all cases, numerical results were obtained via a time-marching technique from an initial condition of stagnant isothermal fluid (at ambient temperature) to steady state. The results are illustrated in terms of streamlines and isotherms and only the portion that concentrates on the open-ended region and its close vicinity is presented. It should be noted that the values of isotherms start with 0.1 and are incremented by 0.1 for all figures presented in this work. In presenting the steady-state results the streamline contour values are set to zero on all solid boundaries and then each subsequent contour is incremented by 1.

5.1 Inertial Effects. Inertial effects on the buoyancy-induced flow and heat transfer in open-ended cavities were studied by invoking the Forchheimer-extended Darcy equation of motion for flow through fluid-saturated porous medium. It should be mentioned that the open-ended configuration is entirely different from a closed enclosure geometry and therefore the range of validity of Darcy's law must be established separately for it. The calculations were made for a range of modified Rayleigh numbers $\mathrm{Ra}^* \leq 350$, and a range of inertial parameters $0.09 \leq \Lambda \leq 200$. In this study, the experimental correlation of Beavers and Sparrow (1969) was employed. They propose that the expression of $F\delta = 0.074$ should be a valid representation for porous media made up of metallic fibers that do not have any free ends within the medium. In any case the chosen value represented a range of practical applications. The value cited for $F\delta$ is just a representative value. Therefore, it is immaterial whether the cited value (i.e., correlation for $F\delta$) is valid for higher Darcy numbers. In the present investigation a parametric investigation is performed on the inertial parameter, $\Lambda = F\delta^2\sigma/\sqrt{\mathrm{Da}}$. These types of inertial parameter

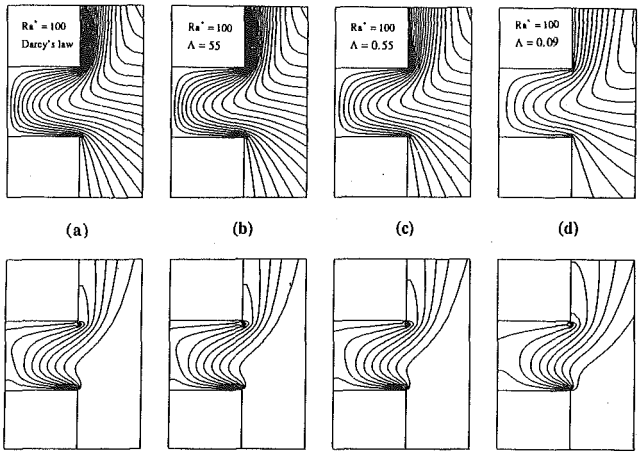

Fig. 4 Streamlines and isotherms for Ra* = 100, Pr_m = 1, and different inertial parameter

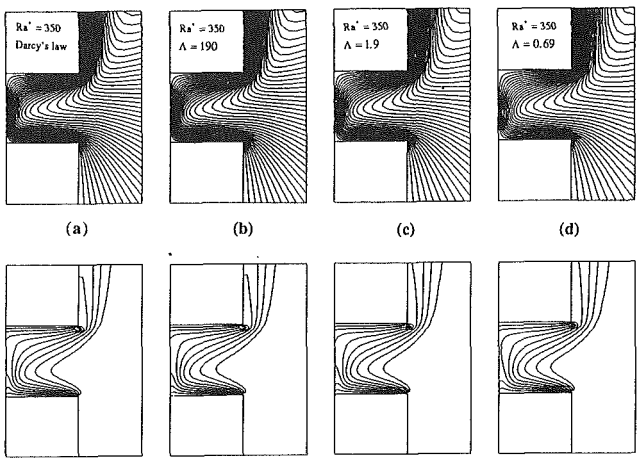

Fig. 5 Streamlines and isotherms for Ra* = 350, Pr_m = 1, and different inertial parameters

were first introduced and analyzed by Vafai and Tien (1981) and later used by other investigators such as Prasad and Tuntomo (1987), etc.

The temperature and flow fields for Ra* = 100 and using Darcy's law as the fluid flow model are illustrated in Fig. 4(*a*). Figures 4(*b–d*) present the streamlines and isotherms for Ra* = 100 and different inertial parameters in the range of $0.09 \le \Lambda \le 55$. A close examination of the results for $\Lambda = 55$ (Fig. 4*b*) shows the great amount of qualitative as well as quantitative similarities to the Darcy flow results (Fig. 4*a*). The stream function's maximum value of 19.55 in Fig. 4(*a*) is comparable to the corresponding value of 19.52 in Fig. 4(*b*). The heat transfer results for $\Lambda = 55$ also show that the inertial effects are negligible and the Nusselt number is only 0.18 percent lower than the value obtained without Forchheimer's extension. As the inertial parameter is increased, significant changes occur in velocity distributions as can be seen in Figs. 4(*c*) and 4(*d*). The flow rate decreases with a decrease in inertial parameter. In fact, the maximum value of stream function changes from 17.39 to 11.28 when the inertial parameter decreases from 0.55 to 0.09 for a modified Rayleigh number of Ra* = 100. The heat transfer results also follow the same trend, in which the Nusselt number changes from 2.029 to 1.530 for the same reduction in the inertial parameter. It should be pointed out that an increase in the inertial parameter in the above figures translates into a decrease in the Darcy number Da. This is because in this figure for a fixed value of, e.g., $F\delta = 0.074$, specifying a value for the Darcy number in effect fixes a value for the inertial parameter.

Figures 5(*a–d*) present the streamlines and isotherms for the similar range of inertial parameters but for a modified Rayleigh number of Ra* = 350. As illustrated by the above figures, the effects of a decrease in the inertial parameter appear to be quite similar to that of Ra* = 100. This trend in fact was found to be the case for all of the modified Rayleigh numbers that were investigated in this work. The boundary layer along the block surface becomes less pronounced as the inertial parameter is decreased as indicated in Fig. 5. Finally, the stratification along the upper block is reduced with a decrease in the inertial parameter as witnessed by the reduction in number of horizontal isotherms close to the upper block surface shown in Fig. 5(*d*). It should be mentioned that the critical value of the inertial parameter, Λ_{crit}, below which the Darcy flow model breaks down, increases for higher modified Rayleigh numbers. Indeed, as shown in Fig. 6, Λ_{crit} changes from 27 to about 190 with an increase in Ra* from 50 to 350, respectively.

5.2 Boundary Effects. The influence of impermeable boundaries on natural convection in open-ended cavities filled with fluid-saturated porous medium was investigated by utilizing the Brinkman-extended Darcy equation of motion. The calculations were performed for the wide ranges of Rayleigh number $10^3 \le Ra \le 2 \times 10^5$, modified Rayleigh number $10 \le Ra^* \le 10^4$, and Darcy number $5 \times 10^{-4} \le Da \le 10^{-1}$. It should be noted that, based on the definition of these dimensionless parameters, once any two of the above parameters are specified then the third one will be fixed. Although the analysis of high Darcy number cases is mainly of academic interest, nevertheless, the results from high Da have highlighted the significance of the boundary effects in drawing important conclusions regarding the fluid flow and heat transfer characteristics in these type of geometries. In what follows, the results from parametric studies for two different cases are reported.

5.2.1 Case 1: Fixed Modified Rayleigh Number. In this case, the modified Rayleigh number is kept constant, Ra* = 100, while the Darcy number is varied. The streamlines and isotherms using Darcy's law as the equation of fluid motion are presented in Fig. 7(*a*). The results for a wide range of Darcy number $5 \times 10^{-4} \le Da \le 10^{-1}$ and Ra* = 100 are illustrated in Figs. 7(*b–d*). Comparison of the results in Figs. 6(*a*) and 6(*b*) indicates that the flow is governed by Darcy's law for $Da \le 5 \times 10^{-4}$ and Ra* = 100. The maximum value of stream function changes from 19.55 to 19.56 as Da changes from zero to 5×10^{-4}, respectively. The Nusselt number for the case of $Da = 5 \times 10^{-4}$ indicates a very small reduction of 1.4 percent from the corresponding value obtained by Darcy's law.

As the Darcy number increases, the heat transfer mechanism inside the open-ended cavity changes from convection dominated to more of a conduction mode of energy transfer as witnessed by the shapes of the isotherms in Fig. 7. Consequently, the heat transfer rate inside the open-ended cavity decreases substantially. In fact, the Nusselt number experiences a 64.5 percent reduction as the Darcy number increases from 5×10^{-4} to 10^{-1}. Figure 7 also shows that as Da increases, the velocity of incoming and outgoing flows decrease considerably. It is interesting to note that as Da increases, the medium becomes more permeable and consequently, one would expect the flow to penetrate more inside the open cavity. However, the results actually show that the flow penetration decreases substantially. This is attributed to the fact that for fixed modified Rayleigh number, as the Darcy number increases, the Rayleigh number, which in this case is the main driving force, decreases. Hence, as a result, the velocity of incoming as well as outgoing flow decreases and the extent of flow penetration inside the open-ended cavity also decreases drastically.

Similar effects were also observed for cases with higher modified Rayleigh numbers. Although the boundary effects have common features for higher Ra*, the viscous diffusion effect

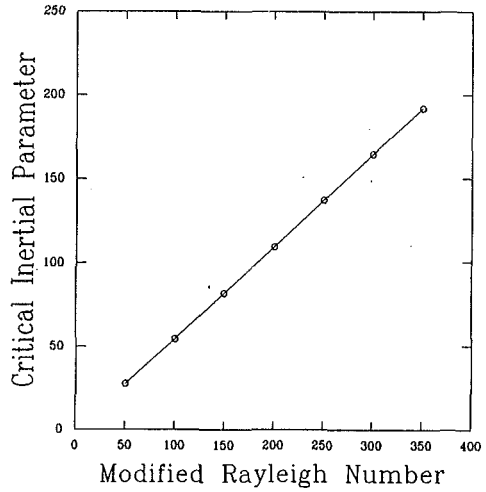

Fig. 6 Variations of critical inertial parameter as a function of different Darcy and Rayleigh numbers

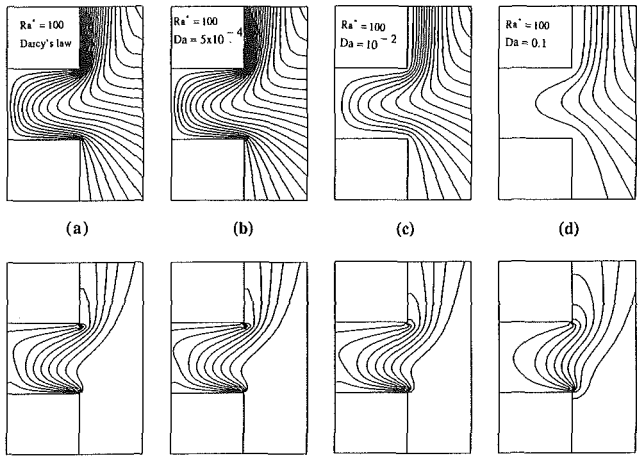

Fig. 7 Streamlines and isotherms for Ra* = 100, Pr_m = 1, and different Darcy numbers.

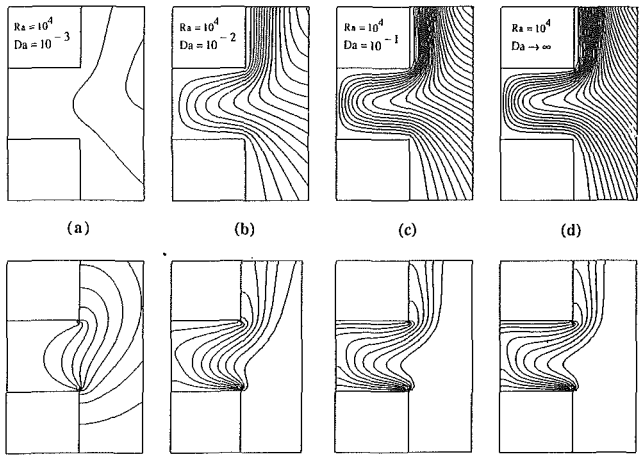

Fig. 8 Streamlines and isotherms for Ra = 10^4, Pr_m = 1, and different Darcy numbers

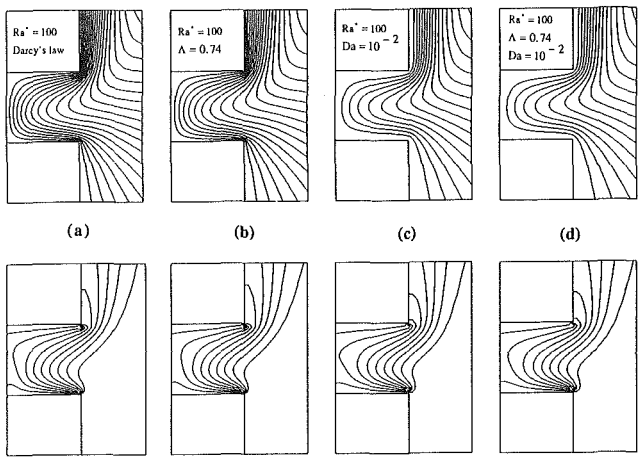

Fig. 9 Streamlines and isotherms for Ra* = 100, Pr_m = 1, Λ = 0.74, Da = 10^{-2}, and different flow models

in the wall region is of greater significance for higher Ra* flows. So, the deviation from Darcy flow model at higher Ra* appears at smaller Darcy number.

5.2.2. Case 2: Fixed Rayleigh Number. Here, the Rayleigh number is kept constant, Ra = 10^4, while the Darcy number is varied. Figures 8(*a–c*) depict the streamlines and isotherms for $10^{-3} \leq Da \leq 10^{-1}$ while Fig. 8(*d*) shows the corresponding results for the limiting case of regular medium ($K \rightarrow \infty$). It is clearly seen in Figs. 8(*a–c*) that as Darcy number increases, the speed of incoming and outgoing flows increase considerably. In fact, the maximum value of stream function undergoes a drastic increase (600 to 1200 percent) when Da is increased by one to two orders of magnitude respectively. Figure 8 shows that as the Darcy number increases, the flow penetration inside the open cavity also increases. For a fixed Rayleigh number, an increase in Darcy number results in an enhancement of the modified Rayleigh number, which is the main driving force in this case. Therefore, the flow penetration inside the open-ended cavity increases substantially.

The isotherms in Fig. 8 show that as the Da is increased, conduction-dominated heat transfer is changed to a convection-dominated mechanism inside the open-ended cavity. Indeed, the heat transfer rate increases considerably (223 or 302 percent enhancement) as Da increases by one or two orders of magnitude, respectively. Comparison of the Figs. 8(*c*) and 8(*d*) shows that when $Da = 10^{-1}$, the flow field and heat transfer characteristics in a porous medium approach those of the regular medium. Indeed, as Da is further increased, an asymptotic solution is obtained that is independent of the permeability of the porous matrix, or the Darcy number.

It should be emphasized that although the effect of an increase in the Darcy number appears to be very similar at all Rayleigh numbers, its effect is more important at higher Rayleigh number flows. However, the Brinkman-extended Darcy flow model is valid only at low velocities when the inertial effects are neglected.

5.3 Inertial and Boundary Effects. To predict the convective flow and heat transfer accurately in open-ended cavities filled with fluid-saturated porous medium, the generalized flow model of Vafai and Tien (1981) is used. Typical numerical results for a case with modified Rayleigh number Ra* = 100, Darcy number $Da = 10^{-2}$, modified Prandtl number, Pr_m, of 1, and the inertial parameter of Λ = 0.74 are reported.

Figures 9(*a–d*) illustrate the results for cases where Darcy, Forchheimer-extended Darcy, Brinkman-extended Darcy, and the generalized flow model have been utilized, respectively. Comparison of the streamline contours in Figs. 9(*a*) and 9(*b*) shows that the flow field is modified by the inclusion of the inertial term. In fact, the inertial effect has caused a decrease in flow rate (8.3 percent reduction in the maximum value of stream function). Hence, the heat transfer rate also undergoes a 7.3 percent reduction. Inspection of the streamlines near the

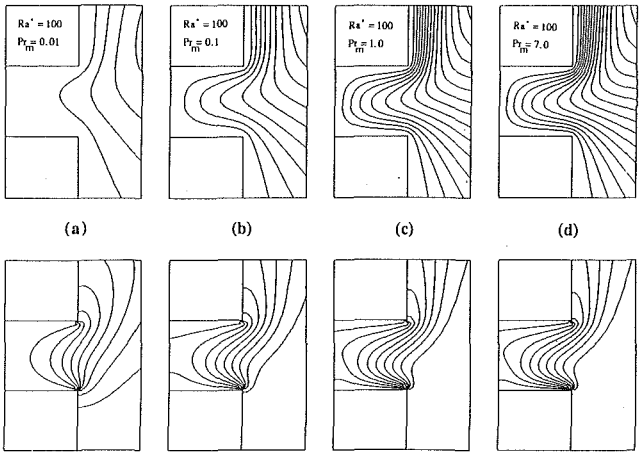

Fig. 10 Streamlines and isotherms for Ra* = 100, Λ = 0.74, Da = 10^{-2}, and different modified Prandtl numbers

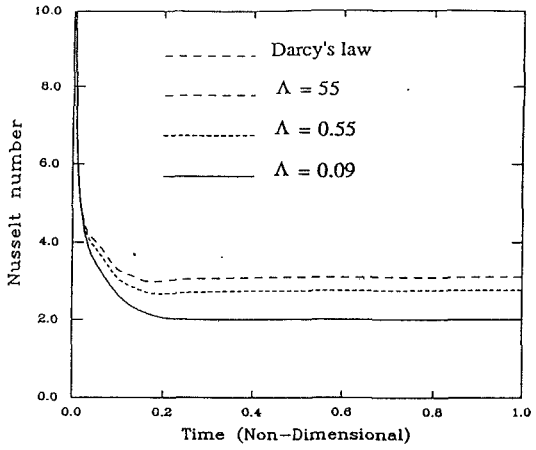

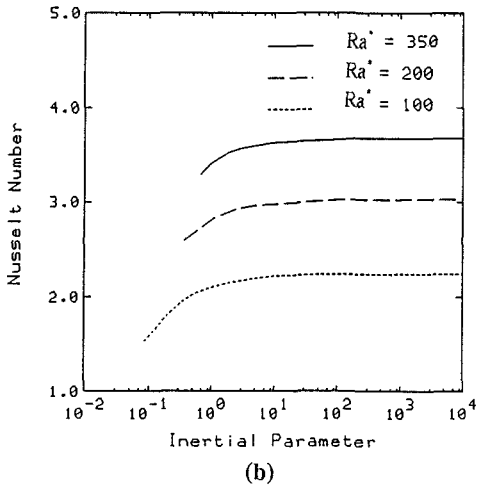

Fig. 11 (*a*) Temporal cavity Nusselt numbers for Ra* = 100, $Pr_m = 1$, and different inertial parameters; (*b*) variations of the Nusselt number as a function of inertial and Rayleigh numbers

solid boundaries in Figs. 9(*a*) and 9(*b*) and their comparison with Figs. 9(*c*) and 9(*d*) indicate that the viscous diffusion effects in the wall region are not present since the boundary effects were not included.

Figure 9(*c*) clearly depicts the influence of the boundary effects near the solid walls, which causes a decrease in flow rate compared to the corresponding Darcy results. In this case, 22 and 31.4 percent reductions in maximum value of stream function and heat transfer rate are observed, respectively. Comparison of the results in Figs. 9(*c*) and 9(*d*) indicates that the inclusion of inertial term does not influence the flow field considerably (5.7 percent reduction in maximum value of stream function). The calculated Nusselt number shows even smaller change in the magnitude of the heat transfer rate (2.3 percent reduction). This is attributed to the fact that although the inertial effects play a major role especially at Reynolds numbers (based on the particle diameter) greater than one, the viscous diffusion effects near the wall region are more important since the convective heat transfer is generally considered as a boundary phenomenon.

5.4 Modified Prandtl Number Effects. To study the effect of different working fluids on fluid flow and heat transfer characteristics in open-ended cavities, numerical results are obtained for the general case with $Ra^* = 100$, $\Lambda = 0.74$, $Da = 10^{-2}$, and different modified Prandtl numbers. Figures 10(*a–d*) present the streamlines and isotherms for cases with Pr_m = 0.01, 0.1, 1.0, and 7.0, respectively.

As Pr_m increases from 0.01 to 0.1, the speed of incoming and outgoing flows also increases substantially. The maximum value of stream function undergoes a 126 percent increase and the flow penetration inside the open-ended cavity increases as shown in Fig. 10(*b*). Consequently, the conduction-dominated heat transfer inside the open-ended cavity changes to partially convective heat transfer as illustrated by the shapes of the isotherms in Fig. 10(*b*). As a result, the heat transfer result experiences an 87.4 percent increase in the Nusselt number. Similar enhancements in flow rate and the heat transfer rate are observed as the modified Prandtl number increases from 0.1 to 1.0 (48.5 and 40.3 percent increase in maximum value of stream function and Nusselt number, respectively). As Pr_m is further increased (1.0 to 7.0), the relative increase in flow rate as well as the heat transfer rate is reduced. In fact, the maximum value of stream function is only increased by 8.4 percent while the Nusselt number increase is about 7 percent. This is attributed to the fact that in the high modified Prandtl number limit, the inertial effects are negligible and equation (4), the generalized model, reduces to the Brinkman-extended Darcy flow model, equation (9), which approaches an asymptotic solution that is independent of the modified Prandtl number.

5.5 Heat Transfer Results. The cavity Nusselt number defined as the sum of the lower block and upper block Nusselt numbers is evaluated by numerical integration of the equation (11). The time history of cavity Nusselt numbers from the onset of fluid flow to steady state for different case studies is reported. The crucial influences on inertial and boundary effects individually as well as the inclusion of both effects on the heat transfer rate inside the open-ended cavities are examined.

Figure 11(*a*) shows the temporal cavity Nusselt number for Darcy flow and Forchheimer-extended Darcy flow with a modified Rayleigh number of $Ra^* = 100$, modified Prandtl number of $Pr_m = 1.0$, and different inertial parameters. The heat transfer results for cases with $\Lambda_{crit} = 55$ and the corresponding one for Darcy flow, for $Ra^* = 100$, are almost identical as clearly illustrated in Fig. 11(*a*). It should be reiterated that the value of critical inertial parameter, Λ_{crit}, increases for higher modified Rayleigh flows. The plots in Fig. 11(*a*) also show that as the inertial parameter increases, the heat transfer rate inside the open-ended cavity increases. This trend is found to be the same for different values of modified Rayleigh numbers. Figure 11(*b*) shows that the Nusselt number increases with an increase in the inertial parameter up to a point, Λ_{crit}, beyond which it reaches its asymptotic value obtained by the Darcy's law formulation.

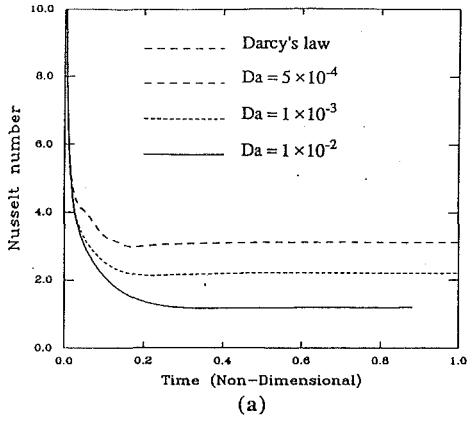

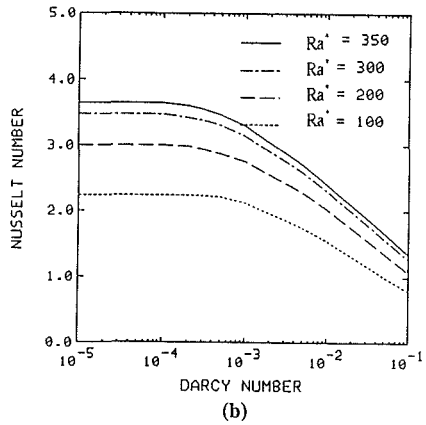

Fig. 12 (*a*) **Temporal cavity Nusselt numbers for Ra* = 100, Pr_m = 1, and different Darcy parameters; (*b*) variations of the Nusselt number as a function of different Darcy and Rayleigh numbers**

The temporal cavity Nusselt numbers for Darcy flow and Brinkman-extended Darcy flow with $Ra^* = 100$, $Pr_m = 1.0$, and a range of $5 \times 10^{-4} \le Da \le 1 \times 10^{-1}$ are presented in Fig. 12(*a*). In this case, the heat transfer results from the Darcy model and the corresponding ones from the Brinkman-extended Darcy model are identical provided that the critical Darcy number is less than 5×10^{-4}. Figure 12(*a*) clearly shows that as Da is increased, the heat transfer rate inside the open-ended cavity is decreased. Again, this trend is found to be the same for different values of modified Rayleigh numbers. Figure 12(*b*) indicates that for Darcy numbers less than 1×10^{-4}, there are no variations between the Nusselt numbers obtained from Darcy's law and the corresponding ones computed by the Brinkman-extended Darcy model.

Figure 13(*a*) presents the temporal cavity Nusselt numbers for Darcy flow with $Ra^* = 100$, Forchheimer-extended Darcy flow with $\Lambda = 0.74$, Brinkman-extended Darcy flow with $Da = 1 \times 10^{-2}$, and the generalized flow model with $Da = 1 \times 10^{-2}$, $\Lambda = 0.74$, and $Pr_m = 1.0$. The results clearly show that the inclusion of each individual term (inertial and boundary) as well as simultaneously incorporating both terms in the equation of fluid motion reduces the heat transfer results. In fact, in cases when both the boundary and inertial effects are important, utilization of Darcy flow model would overpredict the cavity Nusselt number considerably.

The modified Prandlt number effect on the heat transfer rate is illustrated in Fig. 13(*b*). Here, the temporal cavity Nusselt numbers for the generalized flow model with $Ra^* = 100$, $\Lambda = 0.74$, $Da = 1 \times 10^{-2}$, and different modified Prandtl numbers are presented. The plots in Fig. 13(*b*) clearly show that as Pr_m increases, the heat transfer rate inside the open-ended cavity also increases. It should be reiterated that in the limiting cases of high Pr_m, there exists an asymptotic cavity Nusselt number, which is independent of the magnitude of the modified Prandtl number. This behavior, which is expected (by examining the vorticity equation at the high Prandtl number limit), was also observed by Kladias and Prasad (1988) for a closed horizontal layer.

Table 1 Nusselt numbers for Ra* = 500, A = 1, and Pr = 1 (inertial effects) (Forchheimer-extended Darcy flow model)

Λ	∞	55	11	5.5	1.1	0.55	0.11	0.05
Fs / Pr*	0	10^{-4}	5×10^{-4}	10^{-3}	5×10^{-3}	10^{-2}	5×10^{-2}	10^{-1}
Present	8.98	8.92	8.67	8.44	7.24	6.46	4.55	3.80
Prasad and Tuntomo (1987)	9.27	9.17	8.84	8.52	7.51	6.36	4.67	3.87
Lauriat (1987)	8.96	8.90	8.60	8.45	7.31	6.56	4.60	3.82

Table 2 Nusselt numbers for A = 1 and Pr = 1 (boundary effects) (Brinkman-extended Darcy flow model)

Da	10^{-5}	10^{-5}	10^{-5}	10^{-3}	10^{-3}	10^{-3}
Ra*	10	100	1000	10	100	1000
Present	1.09	3.06	12.64	1.06	2.45	7.42
Prasad et al. (1988).	1.07	3.02	12.42	1.05	2.41	7.29

6 Validation and Comparison

The program developed for this study was validated for different cases of Forchheimer as well as Brinkman-extended Darcy flow models. Since there was no previous investigation of boundary and inertial effects in open-ended geometries, a systematic validation of results was made with cases of a vertical cavity filled with fluid-saturated porous medium. The geometry considered was a rectangular cavity with isothermal heated and cooled vertical walls in which the horizontal walls were maintained adiabatic. All the results were computed for an aspect ratio of $A = 1$ and Prandlt number of $Pr = \nu_f/\alpha_{eff} = 1$. Again when the convective terms in the momentum equation (Vafai and Tien, 1981) are neglected and under steady-state conditions $Pr_m = Pr$ and $\Lambda = F\delta H/\sqrt{K} = F\delta/\sqrt{Da}$. Of course, both of the abovementioned conditions are satisfied when Forchheimer-extended Darcy flow model is used. Therefore, in these comparisons, $Pr_m = Pr$ and $\Lambda = F\delta H/\sqrt{K} = F\delta/\sqrt{Da}$.

The numerical results for Forchheimer-extended Darcy flow model were benchmarked against the results presented by Prasad and Tuntomo (1987) and Lauriat's results reported via a personal communication with the same authors. As shown in Table 1, it is evident that the present Nusselt numbers are in an excellent agreement with those of Lauriat and they are at most up to 3 percent lower than the ones from Prasad and Tuntomo (1987).

In order to validate the Brinkman-extended Darcy flow results, the work of Prasad et al. (1988) was considered. Table 2 exhibits the Nusselt numbers obtained in both studies. In that table Fs/Pr^* is the ratio (Forchheimer number to Prandtl number) defined by Prasad and Tuntomo (1987), which is equivalent to $\Lambda Da/Pr$ in the present work. Again, the present Nusselt numbers show a very good agreement with the corresponding values computed by Prasad et al. (1988).

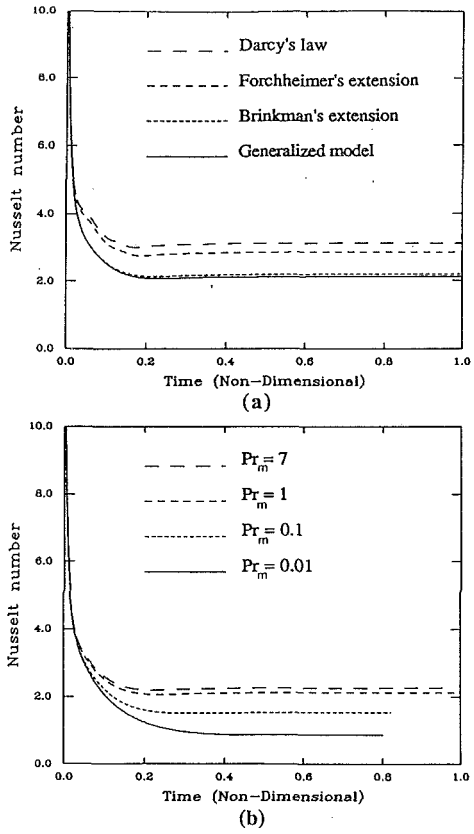

Fig. 13 Temporal cavity Nusselt numbers for Ra* = 100, Λ = 0.74, Da = 10^{-2}, and (*a*) different flow models with Pr_m = 1; (*b*) generalized flow model with different modified Prandtl numbers

7 Conclusions

The significance of the inertial and boundary effects and their crucial influence on predicting buoyancy-induced flow and heat transfer in open-ended cavities filled with fluid-saturated porous medium is investigated. This is accomplished by employing the generalized equation of motion in porous media along with three other commonly employed limiting approximations. In the course of this study, the appropriate choice of parameters that can fully determine the criteria for the range of validity of Darcy's law in this type of configuration was analyzed.

A critical value for the inertial parameter, $\Lambda_{crit} = 55$, is determined for cases with $Ra^* = 100$, beyond which there are no significant changes in convective flow and heat transfer from the Darcy flow results. It is also shown that the critical value of inertial parameter is a function of modified Rayleigh number and that its value increases as Ra* increases. The significant influence of the inclusion of Forchheimer velocity-square term is described by the reduction in flow rate and heat transfer inside the open-ended cavity.

The numerical results from the Brinkman-extended Darcy flow model show that the flow is governed by Darcy's law for $Da \leq 5 \times 10^{-4}$ at $Ra^* = 100$. It is also observed that for higher modified Rayleigh numbers the deviation from Darcy flow results appears at smaller Darcy numbers, i.e., $Da \leq 1 \times 10^{-4}$. The crucial influence of an increase in Darcy number is indicated by reduction of flow penetration and heat transfer rate inside the open-ended cavity for a fixed modified Rayleigh number. For cases with a fixed Rayleigh number, the effect of an increase in Darcy number is characterized by an increase in flow penetration and heat transfer enhancement inside the open-ended cavity. Furthermore, in the limiting case of high Darcy number, $Da \geq 10^{-1}$, an asymptotic solution (regular fluid medium solution) is obtained that is no longer dependent on the permeability of the porous matrix.

The influence of simultaneously including both inertial and boundary terms in the equation of motion is shown to follow a similar trend as in the case of Brinkman-extended Darcy flow results. This is attributed to the fact that even though inertial effects play a major role, especially at particle Reynolds number greater than one, the viscous diffusion effects near the wall region are more important since the convective heat transfer is generally considered as a boundary phenomenon.

The effect of modified Prandtl number or convective flow and heat transfer is shown to be quite significant at lower values of Pr_m. It is also observed that the magnitude of this effect reduces as the modified Prandtl number increases. This is attributed to the fact that in the high modified Prandtl number limit, the inertial effects are negligible and hence, the generalized flow model reduces to the Brinkman-extended Darcy flow model, which approaches an asymptotic solution that is independent of the modified Prandtl number.

The transient results have shown that the conclusions with respect to the effects of inertia parameter, Darcy number, modified Prandtl number, and different flow models on heat transfer results are true for transient states as well as the steady state. However, the influence of these quantities during the very early transient stage is quite limited.

Acknowledgments

A grant from OSC is gratefully acknowledged.

References

Beavers, G. S., and Sparrow, E. M., 1969, "Non-Darcy Flow Through Fibrous Porous Media," ASME *Journal of Applied Mechanics*, Vol. 36, pp. 711–714.

Bejan, A., 1981, "Lateral Intrusion of Natural Convection Into a Horizontal Porous Structure," ASME JOURNAL OF HEAT TRANSFER, Vol. 103, pp. 237–241.

Bejan, A., and Tien, C. L., 1978, "Natural Convection in a Horizontal Porous Medium Subjected to an End-to-End Temperature Difference," ASME JOURNAL OF HEAT TRANSFER, Vol. 100, pp. 191–198.

Brinkman, H. C., 1947, "A Calculation of the Viscous Force Exerted by a Flowing Fluid on a Dense Swarm of Particles," *Applied Science Research*, Vol. A1, pp. 27–34.

Cheng, P., 1978, "Heat Transfer in Geothermal Systems," *Advances in Heat Transfer*, Vol. 14, pp. 1–105.

Ettefagh, J., and Vafai, K., 1988, "Natural Convection in Open-Ended Cavities With a Porous Obstructing Medium," *Int. J. Heat Mass Transfer*, Vol. 31, pp. 673–693.

Forchheimer, P. H., 1901, *Z. Ver. Dtsch. Zucker-Ind.*, Vol. 45, pp. 1782–1788.

Haajizadeh, M., and Tien, C. L., 1983, "Natural Convection in a Rectangular Porous Cavity With One Permeable Endwall," ASME JOURNAL OF HEAT TRANSFER, Vol. 105, pp. 803–808.

Kacker, S. C., and Whitelaw, J. H., 1970, "Prediction of Wall-Jet and Wall-Wake Flows," *Journal Mechanical Science*, Vol. 12, pp. 404–420.

Kladias, N., and Prasad, V., 1988, "Natural Convection in a Horizontal Porous Layers: Effects of Darcy and Prandtl Numbers," *Proceedings, National Heat Transfer Conference*, Houston, Vol. 1, pp. 593–603, ASME, New York.

Lundgren, T. S., 1972, "Slow Flow Through Stationary Random Beds and Suspensions of Spheres," *Journal of Fluid Mechanics*, Vol. 51, pp. 273–299.

Nakamura, S., 1991, *Applied Numerical Methods With Software*, Prentice Hall.

Neale, G., and Nader, W., 1974, "Practical Significance of Brinkman's Extension of Darcy's Law: Coupled Parallel Flows Within a Channel and a Bounding Porous Medium," *Canadian Journal of Chemical Engineering*, Vol. 52, pp. 475–478.

Prasad, V., Lauriat, G., and Kladias, N., 1988, "Reexamination of Darcy-Brinkman Solutions for Free Convection in Porous Media," *Proceedings, National Heat Transfer Conference*, Houston, Vol. 1, pp. 569–579, ASME, New York.

Prasad, V., and Tuntomo, A., 1987, "Inertia Effects on Natural Convection in a Vertical Porous Cavity," *Numerical Heat Transfer*, Vol. 11, pp. 295–320.

Roache, P. J., and Mueller, T. J., 1970, "Numerical Solutions of Laminar Separated Flows," *AIAA Journal*, Vol. 8, pp. 530–538.

Thom, A., and Apelt, C. J., 1961, *Field Computations in Engineering and Physics*, C. Van Nostrand Company, New York.

Vafai, K., 1984, "Convective Flow and Heat Transfer in Variable-Porosity Media," *J. Fluid Mech.*, Vol. 147, pp. 233–259.

Vafai, K., and Tien, C. L., 1981, "Boundary and Inertia Effects on Flow and Heat Transfer in Porous Media," *Int. J. Heat Mass Transfer*, Vol. 24, pp. 195–203.

Vafai, K., and Ettefagh, J., 1990, "The Effects of Sharp Corners on Buoyancy-Driven Flows With Particular Emphasis on Outer Boundaries," *International Journal of Heat and Mass Transfer*, Vol. 33, pp. 2311–2328.

Drying of Porous Materials in a Medium With Variable Potentials

Jen Y. Liu
Research General Engineer,
USDA Forest Service,
Forest Products Laboratory,
Madison, WI 53705-2398
Mem. ASME

This paper presents an application of the Luikov system of heat and mass transfer equations in dimensionless form to predict the temperature and moisture distributions in a slab of capillary-porous material during drying. The heat and mass potentials of the external medium in the boundary conditions are assumed to vary linearly with time. The method of solution is illustrated by considering the drying of a slab of lumber. Numerical results based on the estimated thermophysical properties of spruce are presented.

Introduction

The Luikov system of heat and mass transfer equations (Luikov, 1966) has been applied to predict the temperature and moisture distributions in a slab of capillary-porous material during drying. The slab is subjected to boundary conditions of the third kind (Luikov and Mikhailov, 1965a), which relate the transfer potentials at the surfaces of the body being dried to the corresponding potentials of the external medium. The method of solution is illustrated by considering the drying of a slab of lumber. The transfer potentials of the external medium (that is, the dry-bulb temperature (DBT) and the relative humidity of the drying air corresponding to the equilibrium mass transfer potential (EMTP) of wood), are usually assumed to be constant for mathematical simplicity, but in application they can be controlled to vary with time to achieve economic purposes.

Analytical solutions for the Luikov system of equations with medium temperature varying linearly or exponentially with time were presented by Luikov and Mikhailov (1965a). These authors used the Laplace transform technique to obtain their solutions without considering the possible existence of complex eigenvalues. As pointed out by Liu and Cheng (1989, 1991), if complex eigenvalues do exist, their solutions can be grossly in error.

In the study reported here, we solved the Luikov system of equations in dimensionless form with boundary conditions of the third kind expanded to include the assumptions that both DBT and EMTP vary linearly with time. The complete solutions are composed of a homogeneous solution and a particular solution, the former being obtained by means of the same analytical technique developed by Liu and Cheng (1989, 1991), the latter by the method of undetermined coefficients (Hildebrand, 1962). When the boundary conditions change, the particular solution needs to be changed, but the homogeneous solution remains the same. Numerical results based on the estimated thermophysical properties of spruce (Thomas et al., 1980) reveal that by increasing DBT only, the heat absorption of lumber required to achieve a specified moisture content level in lumber is reduced in comparison with that in a constant drying environment, but the drying time is not. However, by simultaneously increasing DBT and decreasing EMTP, the heat absorption of lumber and the drying time can both be reduced. The method of solution presented in this paper should have a general application to problems of heat and mass transfer in capillary-porous bodies with variable boundary conditions.

Heat and Mass Transfer Equations

For the one-dimensional case shown in Fig. 1, heat and mass move along the x axis only. Under the constant pressure condition, the governing equations for porous media (Luikov and Mikhailov, 1965a) are as follows:

$$\frac{\partial T}{\partial \mathrm{Fo}}=\frac{\partial^2 T}{\partial X^2}-\epsilon \mathrm{Ko}\frac{\partial \Theta}{\partial \mathrm{Fo}} \qquad (-1<X<1;\ \mathrm{Fo}>0) \tag{1}$$

$$\frac{\partial \Theta}{\partial \mathrm{Fo}}=\mathrm{Lu}\frac{\partial^2 \Theta}{\partial X^2}-\mathrm{LuPn}\frac{\partial^2 T}{\partial X^2} \qquad (-1<X<1;\ \mathrm{Fo}>0) \tag{2}$$

where T is dimensionless temperature, Θ dimensionless mass transfer potential, Fo dimensionless time or Fourier number, X dimensionless space coordinate, ϵ phase transformation number, Ko Kossovich number, Lu Lukomskii number, and Pn Posnov number (see Nomenclature).

For constant DBT and EMTP in the boundary conditions

$$T=\frac{t-t_0}{t_c-t_0} \tag{3}$$

$$\Theta=\frac{\theta_0-\theta}{\theta_0-\theta_p} \tag{4}$$

$$\mathrm{Ko}=\frac{\lambda C_m(\theta_0-\theta_p)}{C_q(t_c-t_0)} \tag{5}$$

$$\mathrm{Pn}=\frac{\delta(t_c-t_0)}{\theta_0-\theta_p} \tag{6}$$

where the notations on the right-hand sides are dimensional and t is temperature, t_c dry-bulb temperature, t_0 initial temperature of lumber, θ moisture transfer potential, θ_p equilibrium mass transfer potential, θ_0 initial mass transfer potential of lumber, λ heat of phase change, C_m and C_q are moisture capacity and heat capacity, respectively, and δ is the thermogradient coefficient. Assuming that DBT and EMTP are time dependent so that

$$t_c=t_{c0}+b\tau \qquad (b\geq 0) \tag{7}$$

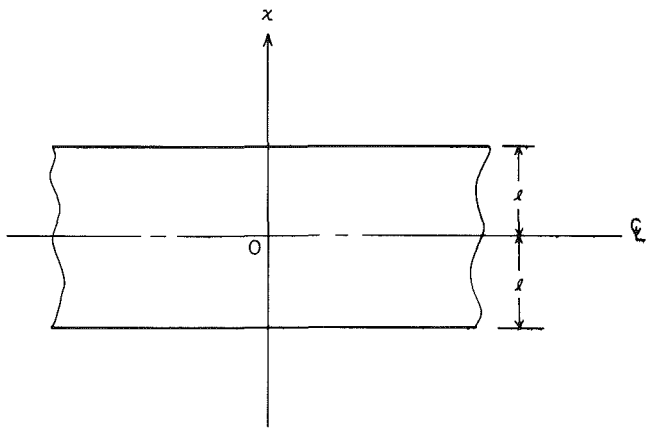

Fig. 1 Schematic representation of wood specimen (ML89 5580)

Contributed by the Heat Transfer Division and presented at the 5th AIAA/ASME Thermophysics and Heat Transfer Conference, Seattle, Washington, June 18–20, 1990. Manuscript received by the Heat Transfer Division April 25, 1990; revision received November 22, 1990. Keywords: Mass Transfer, Porous Media, Transient and Unsteady Heat Transfer.

$$\theta_p = \theta_{p0} - b'\tau \quad (b' \geq 0) \tag{8}$$

where t_{c0} is the initial value of t_c, θ_{p0} initial value of θ_p, τ time, and b and b' are constants denoting the rates of change of DBT and EMTP, respectively, t_c and θ_p in equations (3)–(6) must be replaced by t_{c0} and θ_{p0}:

$$T = \frac{t - t_0}{t_{c0} - t_0} \tag{9}$$

$$\Theta = \frac{\theta_0 - \theta}{\theta_0 - \theta_{p0}} \tag{10}$$

$$\mathrm{Ko} = = \frac{\lambda C_m(\theta_0 - \theta_{p0})}{C_q(t_{c0} - t_0)} \tag{11}$$

$$\mathrm{Pn} = \frac{\delta(t_{c0} - t_0)}{\theta_0 - \theta_{p0}} \tag{12}$$

Equations (9)–(12) are also true in equations (1) and (2). The boundary conditions of the third kind based on equations (7) and (8) are as follows:

$$\frac{\partial T}{\partial X} + \mathrm{Bi}_q T - (1-\epsilon)\mathrm{LuKoBi}_m\Theta = \mathrm{Bi}_q(1 + \mathrm{Pd}_q\mathrm{Fo})$$

$$-(1-\epsilon)\mathrm{LuKoBi}_m(1 + \mathrm{LuPd}_m\mathrm{Fo}) \quad (X = \pm 1;\ \mathrm{Fo} > 0) \tag{13}$$

$$\frac{\partial \Theta}{\partial X} - \mathrm{Pn}\frac{\partial T}{\partial X} + \mathrm{Bi}_m\Theta = \mathrm{Bi}_m(1 + \mathrm{LuPd}_m\mathrm{Fo}) \quad (X = \pm 1;\ \mathrm{Fo} > 0) \tag{14}$$

where Bi_q and Bi_m are the Biot heat and mass transfer numbers, respectively, Pd_q (the same Pd as in Luikov and Mikhailov (1965a, 1965b)) the Predvoditelev number for the case of linear time dependence of DBT and defined by

$$\mathrm{Pd}_q = \frac{bl^2}{a_q(t_{c0} - t_0)} \tag{15}$$

and Pd_m a new dimensionless number identified in this study for the case of linear time dependence of EMTP and defined by

$$\mathrm{Pd}_m = \frac{b'l^2}{a_m(\theta_0 - \theta_{p0})} \tag{16}$$

In equations (15) and (16), a_q and a_m are the thermal diffusivity coefficient and moisture diffusion coefficient, respectively, and l is half the specimen thickness.

For $\mathrm{Pd}_m = 0$, the boundary conditions (13) and (14) agree with those of Luikov and Mikhailov (1965a), which consider the time dependence of DBT only.

Because of symmetry, at $X = 0$ we should have

$$\frac{\partial T}{\partial X} = 0 \quad (X = 0;\ \mathrm{Fo} \geq 0) \tag{17}$$

$$\frac{\partial \Theta}{\partial X} = 0 \quad (X = 0;\ \mathrm{Fo} \geq 0) \tag{18}$$

The initial conditions are assumed to be constant and are represented by

$$T = 0 \quad (-1 \leq X \leq 1;\ \mathrm{Fo} = 0) \tag{19}$$

$$\Theta = 0 \quad (-1 \leq X \leq 1;\ \mathrm{Fo} = 0) \tag{20}$$

For the physical significance of the dimensionless numbers, see Luikov and Mikhailov (1965b).

Method of Solution

Because the boundary conditions (13) and (14) are nonhomogeneous, the solutions can be represented by two parts, a homogeneous solution and a particular solution.

Homogeneous Solutions. For the homogeneous solutions of T and Θ, we set the right-hand sides of equations (13) and (14) equal to zero and introduce a potential function $\phi(X, \mathrm{Fo})$ such that (Liu and Cheng, 1989, 1991)

$$T_H = \left(\frac{\partial}{\partial \mathrm{Fo}} - \mathrm{Lu}\frac{\partial^2}{\partial X^2}\right)\phi \tag{21}$$

$$\Theta_H = -\mathrm{LuPn}\frac{\partial^2 \phi}{\partial X^2} \tag{22}$$

We find that by substituting T_H for T and Θ_H for Θ in equation (2), the equation is automatically satisfied and equation (1) becomes

$$\left[\frac{\partial^4}{\partial X^4} - \left(1 + \frac{1}{\mathrm{Lu}} + \epsilon\mathrm{KoPn}\right)\frac{\partial^3}{\partial \mathrm{Fo}\partial X^2} + \frac{1}{\mathrm{Lu}}\frac{\partial^2}{\partial \mathrm{Fo}^2}\right]\phi = 0 \tag{23}$$

or

$$\left[\left(\frac{\partial^2}{\partial X^2} - \nu_1^2\frac{\partial}{\partial \mathrm{Fo}}\right)\left(\frac{\partial^2}{\partial X^2} - \nu_2^2\frac{\partial}{\partial \mathrm{Fo}}\right)\right]\phi = 0 \tag{24}$$

with

Nomenclature

a_m = moisture diffusion coefficient, m^2/s
a_q = thermal diffusivity coefficient, m^2/s
b = constant denoting rate of change of DBT, K/s
b' = constant denoting rate of change of EMTP, °M/s
Bi_m = Biot number of mass transfer $= \alpha_m l/\lambda_m$
Bi_q = Biot number of heat transfer $= \alpha_q l/\lambda_q$
C_m = moisture capacity, 1/°M
C_q = heat capacity, J/kg • K
Fo = Fourier number; dimensionless time $= a_q\tau/l^2$
Ko = Kossovich number $= \lambda C_m(\theta_0 - \theta_{p0})/C_q(t_{c0} - t_0)$
l = half specimen thickness, m
Lu = Lukomskii number $= a_m/a_q$
Pd_q = Predvoditelev number denoting rate of change of medium temperature $= bl^2/a_q(t_{c0} - t_0)$
Pd_m = Predvoditelev number denoting rate of change of equilibrium mass transfer potential $= b'l^2/a_m(\theta_0 - \theta_{p0})$
Pn = Posnov number $= \delta(t_{c0} - t_0)/(\theta_0 - \theta_{p0})$
t = temperature, K
T = dimensionless temperature $= (t - t_0)/(t_{c0} - t_0)$
x = space coordinate, m
X = dimensionless coordinate $= x/l$
α_m = convective mass transfer coefficient, $kg/m^2 \cdot s \cdot °M$
α_q = convective heat transfer coefficient $W/m^2 \cdot K$
δ = thermo-gradient coefficient, °M/K
ϵ = phase transformation number; ratio of vapor diffusion coefficient to coefficient of total moisture diffusion
θ = mass transfer potential, °M
Θ = dimensionless mass transfer potential $= (\theta_0 - \theta)/(\theta_0 - \theta_{p0})$
λ = heat of phase change, J/kg
λ_m = mass conductivity coefficient, $kg/m \cdot s \cdot °M$
λ_q = thermal conductivity coefficient, $W/m \cdot K$
τ = time, s

Subscripts

c = surrounding medium
m = mass transfer
p = equilibrium value
q = heat transfer
0 = initial condition

$$\nu_1^2=\frac{1}{2}\left(1+\frac{1}{\mathrm{Lu}}+\epsilon\mathrm{KoPn}\right) - \left[\frac{1}{4}\left(1+\frac{1}{\mathrm{Lu}}+\epsilon\mathrm{KoPn}\right)^2-\frac{1}{\mathrm{Lu}}\right]^{1/2} \quad (25)$$

$$\nu_2^2=\frac{1}{2}\left(1+\frac{1}{\mathrm{Lu}}+\epsilon\mathrm{KoPn}\right) + \left[\frac{1}{4}\left(1+\frac{1}{\mathrm{Lu}}+\epsilon\mathrm{KoPn}\right)^2-\frac{1}{\mathrm{Lu}}\right]^{1/2} \quad (26)$$

Equation (24) can be expressed as two equations:

$$\frac{\partial^2\phi_1}{\partial X^2}=\nu_1^2\frac{\partial\phi_1}{\partial \mathrm{Fo}} \quad (27)$$

$$\frac{\partial^2\phi_2}{\partial X^2}=\nu_2^2\frac{\partial\phi_2}{\partial \mathrm{Fo}} \quad (28)$$

which are of the diffusion type. The general solution of equation (24) is the sum of the solutions of equations (27) and (28):

$$\phi=\phi_1(X,\ \mathrm{Fo})+\phi_2(X,\ \mathrm{Fo})$$

in which

$$\phi_1=Ae^{-\mu^2\mathrm{Fo}}\cos\ \nu_1\mu X$$
$$\phi_2=Be^{-\mu^2\mathrm{Fo}}\cos\ \nu_2\mu X$$

Hence

$$\phi=e^{-\mu^2\mathrm{Fo}}(A\cos\ \nu_1\mu X+B\cos\ \nu_2\mu X) \quad (29)$$

where A and B are arbitrary constant coefficients. (Sine functions do not appear because of the conditions of symmetry represented by equations (17) and (18).)

Substituting equation (29) into equations (21) and (22) yields

$$T_\mathrm{H}=\mu^2e^{-\mu^2\mathrm{Fo}}(Aa_1\cos\ \nu_1\mu X+Ba_2\cos\ \nu_2\mu X) \quad (30)$$

$$\Theta_\mathrm{H}=\mu^2e^{-\mu^2\mathrm{Fo}}(Ab_1\cos\ \nu_1\mu X+Bb_2\cos\ \nu_2\mu X) \quad (31)$$

where

$$\begin{aligned} a_1&=\mathrm{Lu}\nu_1^2-1\\ a_2&=\mathrm{Lu}\nu_2^2-1\\ b_2&=\mathrm{LuPn}\nu_1^2\\ b_2&=\mathrm{LuPn}\nu_2^2 \end{aligned} \quad (32)$$

Using expressions (30) and (31) for T and Θ in the boundary conditions (13) and (14) with their right-hand sides equal to zero, we obtain

$$(c_1\mu\sin\ \nu_1\mu+c_2\cos\ \nu_1\mu)A+(c_3\mu\sin\ \nu_2\mu + c_4\cos\ \nu_2\mu)B=0 \quad (33)$$

$$(d_1\mu\sin\ \nu_1\mu+d_2\cos\ \nu_1\mu)A+(d_3\mu\sin\ \nu_2\mu + d_4\cos\ \nu_2\mu)B=0 \quad (34)$$

where

$$\begin{aligned} c_1&=\nu_1-\mathrm{Lu}\nu_1^3\\ c_2&=-\mathrm{Bi}_q+\mathrm{Bi}_q\mathrm{Lu}\nu_1^2-(1-\epsilon)\mathrm{Lu}^2\mathrm{KoBi}_m\mathrm{Pn}\nu_1^2\\ c_3&=\nu_2-\mathrm{Lu}\nu_2^3\\ c_4&=-\mathrm{Bi}_q+\mathrm{Bi}_q\mathrm{Lu}\nu_2^2-(1-\epsilon)\mathrm{Lu}^2\mathrm{KoBi}_m\mathrm{Pn}\nu_2^2\\ d_1&=\nu_1\\ d_2&=-\mathrm{Bi}_m\mathrm{Lu}\nu_1^2\\ d_3&=\nu_2\\ d_4&=-\mathrm{Bi}_m\mathrm{Lu}\nu_2^2 \end{aligned}$$

For nontrivial solutions of equations (33) and (34) to exist, the determinant of the coefficients of A and B must vanish, giving the characteristic equation

$$(\mu\nu_1\tan\ \nu_1\mu+\psi_1)(\mu\nu_2\tan\ \nu_2\mu+\psi_2)=\psi_3 \quad (35)$$

in which

$$\psi_1=[\mathrm{Bi}_q-\mathrm{Bi}_q\mathrm{Lu}\nu_1^2+(1-\epsilon)\mathrm{Lu}^2\mathrm{KoBi}_m\mathrm{Pn}\nu_1^2 - \mathrm{Bi}_m\mathrm{Lu}\nu_1^2(1-\mathrm{Lu}\nu_2^2)]/\mathrm{Lu}(\nu_1^2-\nu_2^2)$$

$$\psi_2=[\mathrm{Bi}_q-\mathrm{Bi}_q\mathrm{Lu}\nu_2^2+(1-\epsilon)\mathrm{Lu}^2\mathrm{KoBi}_m\mathrm{Pn}\nu_2^2 - \mathrm{Bi}_m\mathrm{Lu}\nu_2^2(1-\mathrm{Lu}\nu_1^2)]/\mathrm{Lu}(\nu_2^2-\nu_1^2)$$

$$\psi_3=-\mathrm{Bi}_m\mathrm{Bi}_q+\psi_1\psi_2$$

From equation (34) we can also derive

$$\frac{B}{A}=\frac{-\mu\nu_1\sin\ \nu_1\mu+\mathrm{Bi}_m\mathrm{Lu}\nu_1^2\cos\ \nu_1\mu}{\mu\nu_2\sin\ \nu_2\mu-\mathrm{Bi}_m\mathrm{Lu}\nu_2^2\cos\ \nu_2\mu}=g(\mu) \quad (36)$$

where the ratio B/A is set equal to $g(\mu)$ so that B can be expressed as the product of A and $g(\mu)$.

In equation (35) the constant parameter μ can take an infinite number of real values and may also take some complex values. These values are called the eigenvalues of μ. For each eigenvalue, corresponding values for A and B should exist. Therefore, equations (30) and (31) can be put in the following series form:

$$T_\mathrm{H}=\sum_{n=1}^{\infty}\mu_n^2e^{-\mu_n^2\mathrm{Fo}}A_n(a_1\cos\ \nu_1\mu_nX + a_2g(\mu_n)\cos\ \nu_2\mu_nX) \quad (37)$$

$$\Theta_\mathrm{H}=\sum_{n=1}^{\infty}\mu_n^2e^{-\mu_n^2\mathrm{Fo}}A_n(b_1\cos\ \nu_1\mu_nX + b_2g(\mu_n)\cos\ \nu_2\mu_nX) \quad (38)$$

where the function $g(\mu_n)$ from equation (36) is used to eliminate B_n. Because μ_n can be either positive or negative in the preceding equations without changing the results, we must take only the positive real values and complex values with positive real components in the numerical calculations.

Particular Solutions. For the particular solutions of T and Θ, we use the method of undetermined coefficients (Hildebrand, 1962) by assuming that

$$T_\mathrm{p}=h_1\mathrm{Fo}+h_2X^2+h_3 \quad (39)$$

$$\Theta_\mathrm{p}=f_1\mathrm{Fo}+f_2X^2+f_3 \quad (40)$$

By substituting T_p for T and Θ_p for Θ in equations (1), (2), (13), and (14), we obtain

$$\begin{aligned} h_1&=\mathrm{Pd}_q\\ h_2&=(\mathrm{Pd}_q+\epsilon\mathrm{LuKoPd}_m)/2\\ h_3&=1-\mathrm{LuKoPd}_m\left(\frac{1}{\mathrm{Bi}_q}+\frac{\epsilon}{2}\right)-\mathrm{Pd}_q\left(\frac{1}{\mathrm{Bi}_q}+\frac{1}{2}\right)\\ f_1&=\mathrm{LuPd}_m\\ f_2&=(\mathrm{Pd}_m+\mathrm{PnPd}_q+\mathrm{Pn}\epsilon\mathrm{LuKoPd}_m)/2\\ f_3&=1-\frac{\mathrm{Pd}_m}{\mathrm{Bi}_m}-f_2 \end{aligned} \quad (41)$$

Thus, we have from equations (37)–(40)

$$T=T_\mathrm{H}+T_\mathrm{p} \quad (42)$$

$$\Theta=\Theta_\mathrm{H}+\Theta_\mathrm{p} \quad (43)$$

Now we must evaluate the coefficients A_n in equations (37) and (38), which are the homogeneous solutions in equations (42) and (43). By setting Fo = 0 in the homogeneous and particular solutions in equations (37)–(40) and making use of the initial conditions (19) and (20), these coefficients can be evaluated using a least-squares technique (Cheng and Angsirikul, 1977; Hildebrand, 1974). First, we set up the following integral:

$$\Omega=\int_0^1\left\{\left[h_2X^2+h_3 + \sum_{n=1}^{\infty}\mu_n^2A_n(a_1\cos\ \nu_1\mu_nX+a_2g(\mu_n)\cos\ \nu_2\mu_nX)\right]\right.$$

$$\times\left[h_2X^2+h_3+\sum_{n=1}^{\infty}\bar{\mu}_n^2\bar{A}_n(a_1\cos\nu_1\bar{\mu}_nX+a_2g(\bar{\mu}_n)\cos\nu_2\bar{\mu}_nX)\right]$$

$$+\left[f_2X^2+f_3+\sum_{n=1}^{\infty}\mu_n^2A_n(b_1\cos\nu_1\mu_nX+b_2g(\mu_n)\cos\nu_2\mu_nX)\right]$$

$$\times\left[f_2X^2+f_3+\sum_{n=1}^{\infty}\bar{\mu}_n^2\bar{A}_n(b_1\cos\nu_1\bar{\mu}_nX+b_2g(\bar{\mu}_n)\cos\nu_2\bar{\mu}_nX)\right]\Bigg\}dX \quad (44)$$

which must be a minimum and in which the a and b values are defined by equation (32) and the h and f values by equation (41). The parameters $\bar{\mu}_n$ and $\bar{A}_n$ are complex conjugates of μ_n and A_n, respectively.

The condition that Ω be a minimum requires that its partial derivatives with respect to $\bar{A}_m$ or A_m shall be zero. We therefore have

$$\frac{\partial\Omega}{\partial\bar{A}_m}=\int_0^1\Bigg\{\left[h_2X^2+h_3+\sum_{n=1}^{\infty}\mu_n^2A_n(a_1\cos\nu_1\mu_nX+a_2g(\mu_n)\cos\nu_2\mu_nX)\right]\times\bar{\mu}_m^2(a_1\cos\nu_1\bar{\mu}_mX+a_2g(\bar{\mu}_m)\cos\nu_2\bar{\mu}_mX)$$

$$+\left[f_2X^2+f_3+\sum_{n=1}^{\infty}\mu_n^2A_n(b_1\cos\nu_1\mu_nX+b_2g(\mu_n)\cos\nu_2\mu_nX)\right]\times\bar{\mu}_m^2(b_1\cos\nu_1\bar{\mu}_mX+b_2g(\bar{\mu}_m)\cos\nu_2\bar{\mu}_mX)\Bigg\}dX$$

$$=0\quad(m=1,2,3,\ldots) \quad (45)$$

Note that the same results are obtained if we set $\partial\Omega/\partial A_m = 0$. In matrix form, equation (45) generates a Hermitian matrix as

$$[C_{mn}]\{A_n\}=\{R_m\} \quad (46)$$

in which

$$C_{mn}=\int_0^1\{[\bar{\mu}_m^2(a_1\cos\nu_1\bar{\mu}_mX+a_2g(\bar{\mu}_m)\cos\nu_2\bar{\mu}_mX)\times\mu_n^2(a_1\cos\nu_1\mu_nX+a_2g(\mu_n)\cos\nu_2\mu_nX)]+[\bar{\mu}_m^2(b_1\cos\nu_1\bar{\mu}_mX+b_2g(\bar{\mu}_m)\cos\nu_2\bar{\mu}_mX)\times\mu_n^2(b_1\cos\nu_1\mu_nX+b_2g(\mu_n)\cos\nu_2\mu_nX)]\}dX \quad (47)$$

$$R_m=-\int_0^1\bar{\mu}_m^2\{(h_2X^2+h_3)[a_1\cos\nu_1\bar{\mu}_mX+a_2g(\bar{\mu}_m)\cos\nu_2\bar{\mu}_mX]+(f_2X^2+f_3)[b_1\cos\nu_1\bar{\mu}_mX+b_2g(\bar{\mu}_m)\cos\nu_2\bar{\mu}_mX]\}dX \quad (48)$$

The coefficients A_n can be determined from the system of linear equations (46). We can then calculate T and Θ from equations (42) and (43) by means of equations (37)–(40).

The expressions for T and Θ, their averages $\overline{T}$ and $\overline{\Theta}$ across $0\le X\le 1$, and the derivatives of T, Θ, $\overline{T}$, and $\overline{\Theta}$ with respect to time Fo (that is, the heating rates and the drying rates) are summarized as follows:

$$T=h_1\mathrm{Fo}+h_2X^2+h_3+\sum_{n=1}^{\infty}\mu_n^2e^{-\mu_n^2\mathrm{Fo}}A_n(a_1\cos\nu_1\mu_nX+a_2g(\mu_n)\cos\nu_2\mu_nX) \quad (49)$$

$$\Theta=f_1\mathrm{Fo}+f_2X^2+f_3+\sum_{n=1}^{\infty}\mu_n^2e^{-\mu_n^2\mathrm{Fo}}A_n(b_1\cos\nu_1\mu_nX+b_2g(\mu_n)\cos\nu_2\mu_nX) \quad (50)$$

Table 1 Input data for three cases of drying environmental conditions

Case	Lu	Bi_q	Bi_m	ϵ	Pn	Ko	Pd_q	Pd_m	t_{c0}	θ_{p0}
1	0.008	0.4	1.4	0.3	2.4	8	0	0	$11t_0$	θ_{p0}
2(*a*)	0.008	0.4	1.4	0.3	0.24	80	>0	0	$2t_0$	θ_{p0}
2(*b*)	0.008	0.4	1.4	0.3	0.24	80	>0	0	$2t_0$	$0.1\theta_0$
3	0.008	0.4	1.4	0.3	0.43	44.44	>0	>0	$2t_0$	$0.5\theta_0$

$$\overline{T}=h_1\mathrm{Fo}+\frac{h_2}{3}+h_3+\sum_{n=1}^{\infty}\mu_ne^{-\mu_n^2\mathrm{Fo}}A_n\left(\frac{a_1}{\nu_1}\sin\nu_1\mu_n+\frac{a_2g(\mu_n)}{\nu_2}\sin\nu_2\mu_n\right) \quad (51)$$

$$\overline{\Theta}=f_1\mathrm{Fo}+\frac{f_2}{3}+f_3+\sum_{n=1}^{\infty}\mu_ne^{-\mu_n^2\mathrm{Fo}}A_n\left(\frac{b_1}{\nu_1}\sin\nu_1\mu_n+\frac{b_2g(\mu_n)}{\nu_2}\sin\nu_2\mu_n\right) \quad (52)$$

$$\frac{dT}{d\mathrm{Fo}}=h_1-\sum_{n=1}^{\infty}\mu_n^4e^{-\mu_n^2\mathrm{Fo}}A_n(a_1\cos\nu_1\mu_nX+a_2g(\mu_n)\cos\nu_2\mu_nX) \quad (53)$$

$$\frac{d\Theta}{d\mathrm{Fo}}=f_1-\sum_{n=1}^{\infty}\mu_n^4e^{-\mu_n^2\mathrm{Fo}}A_n(b_1\cos\nu_1\mu_nX+b_2g(\mu_n)\cos\nu_2\mu_nX) \quad (54)$$

$$\frac{d\overline{T}}{d\mathrm{Fo}}=h_1-\sum_{n=1}^{\infty}\mu_n^3e^{-\mu_n^2Fo}A_n\left(\frac{a_1}{\nu_1}\sin\nu_1\mu_n+\frac{a_2g(\mu_n)}{\nu_2}\sin\nu_2\mu_n\right) \quad (55)$$

$$\frac{d\overline{\Theta}}{d\mathrm{Fo}}=f_1-\sum_{n=1}^{\infty}\mu_n^3e^{-\mu_n^2\mathrm{Fo}}A_n\left(\frac{b_1}{\nu_1}\sin\nu_1\mu_n+\frac{b_2g(\mu_n)}{\nu_2}\sin\nu_2\mu_n\right) \quad (56)$$

Numerical Results and Discussion

We consider three cases of drying environmental conditions for comparison:

Case 1. Both DBT and EMTP are constant; Pd_q and Pd_m in equations (15) and (16) are then zero; DBT should maintain a high value while EMTP maintains a low value.

Case 2. DBT increases linearly with time while EMTP remains constant; Pd_q should then be positive and Pd_m zero; initial DBT or t_{c0} should take a low value, so should the EMTP.

Case 3. DBT increases linearly with time while EMTP decreases linearly with time; Pd_q and Pd_m should both be positive; initial DBT or t_{c0} should take a low value, but initial EMTP or θ_{p0} a high value.

To compare cases 1 and 2 conveniently, we express t_{c0} in terms of t_0, whereas θ_{p0} need not be specified. To compare cases 2 and 3, t_{c0} is expressed in terms of t_0, and θ_{p0} in terms of θ_0. Based on the estimated thermophysical properties of spruce (Thomas et al., 1980), the input data for the three cases are shown in Table 1 with case 2 denoted as case 2(a) for comparison with case 1 and case 2(b) for comparison with case 3. The numbers Ko in equation (11) and Pn in equation (12) both contain t_{c0}, t_0, θ_{p0}, and θ_0. They have been calculated for the three cases according to the assumed relationships between t_{c0} and t_0 and θ_{p0} and θ_0 in Table 1. For the numerical illustrations of this study, these data are also based on the assumption that the thermophysical properties remain constant during drying.

The real eigenvalues in equation (35) were obtained by means of a bisection procedure. As pointed out by Liu and Cheng (1989, 1991), when complex eigenvalues also exist in equation (35), they must be included in the calculations to satisfy the initial conditions. Using a method of Müller (1956), which was

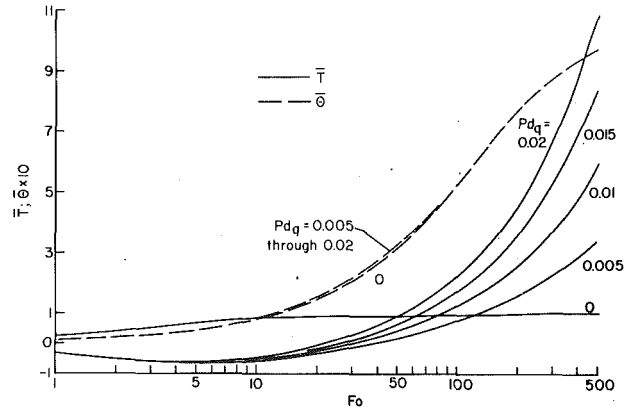

Fig. 2 Variations of average dimensionless temperature $\bar{T}$ and mass transfer potential $\bar{\Theta}$ as functions of time Fo for several values of Pd_q with Pd_m = 0 (Lu = 0.008, Bi_q = 0.4, Bi_m = 1.4, ϵ = 0.3; for Pd_q = 0, Pn = 2.4, Ko = 8; for $Pd_q > 0$, Pn = 0.24, Ko = 80)

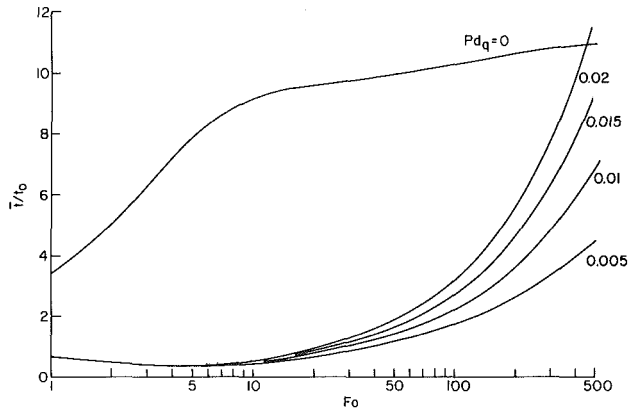

Fig. 3 Variations of average temperature ratio $\bar{t}/t_0$ as a function of time Fo for several values of Pd_q with Pd_m = 0 (Lu = 0.008, Bi_q = 0.4, Bi_m = 1.4, ϵ = 0.3; for Pd_q = 0, Pn = 2.4, Ko = 8; for $Pd_q > 0$, Pn = 0.24, Ko = 80)

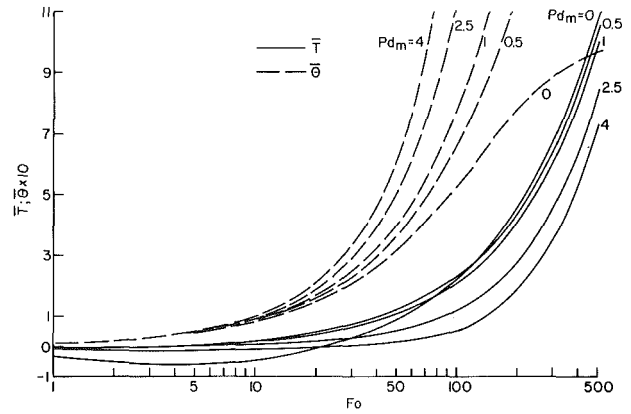

Fig. 4 Variations of average dimensionless temperature $\bar{T}$ and mass transfer potential $\bar{\Theta}$ as functions of time Fo for several values of Pd_m with Pd_q = 0.02 (Lu = 0.008, Bi_q = 0.4, Bi_m = 1.4, ϵ = 0.3; for Pd_m = 0, Pn = 0.24, Ko = 80; for $Pd_m > 0$, Pn = 0.43, Ko = 44.44)

included in IMSL (1987), we obtained a pair of complex eigenvalues for each case in Table 1. The eigenvalues in equation (35) are dependent on the product of Ko and Pn; therefore, we obtained the same complex eigenvalues for all cases. These values are $0.58311 \pm 0.0199078i$.

Equations (19) and (20) specify that initially the heat and mass transfer potentials are uniformly distributed in the specimen; however, as drying progresses, their distributions are known to be approximately parabolic. For the heat potential

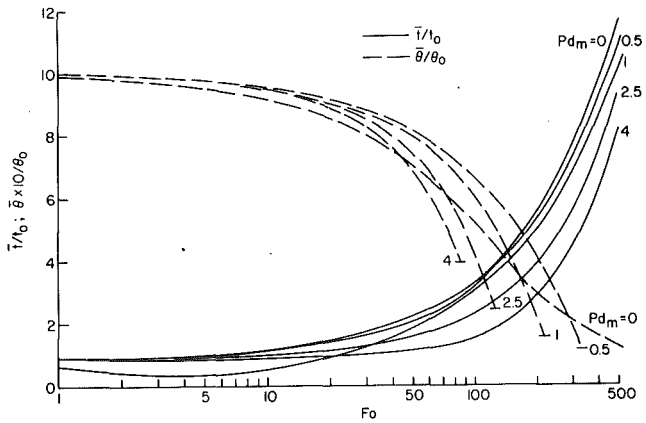

Fig. 5 Variations of average temperature ratio $\bar{t}/t_0$ and mass transfer potential ratio $\bar{\theta}/\theta_0$ as functions of time Fo for several values of Pd_m with Pd_q = 0.02; "—" indicates θ/θ_0 = 0 at $X = \pm1$ (Lu = 0.008, Bi_q = 0.4, Bi_m = 1.4, ϵ = 0.3; for Pd_m = 0, Pn = 0.24, Ko = 80; for $Pd_m > 0$, Pn = 0.43, Ko = 44.44)

or temperature distribution, the maximum value is at the surfaces ($X = \pm1$) and the minimum value at the center ($X = 0$); for the mass or moisture potential distribution, the opposite is true. For comparison, it is convenient to consider their average values across the specimen thickness.

Figure 2 shows the variations of average dimensionless temperature $\bar{T}$ and mass transfer potential $\bar{\Theta}$ as functions of Fo for several values of Pd_q with $Pd_m = 0$. For $Pd_q = 0$, we have case 1 in Table 1. The value $\bar{T}$ increases with Fo and approaches 1 when Fo > 200. For $Pd_q > 0$, we have case 2(a) in Table 1. The value $\bar{T}$ decreases initially with time until Fo = 6, when it starts to increase. This is because of the large value of Ko, which influences the internal temperature field strongly (Luikov and Mikhailov, 1965b). The value $\bar{T}$ also increases with increasing Pd_q. The combined effects of Pd_q, Ko, and Pn on $\bar{\Theta}$ are seen to be negligible. Therefore, by increasing DBT only, the drying time cannot be reduced according to Fig. 2.

According to equation (9), with t replaced by its average value $\bar{t}$ and T by $\bar{T}$, and cases 1 and 2(a) of Table 1, we obtain

$$\frac{\bar{t}}{t_0} = 1 + 10\bar{T} \quad (Pd_q = 0) \tag{57}$$

$$\frac{\bar{t}}{t_0} = 1 + \bar{T} \quad (Pd_q > 0) \tag{58}$$

The data for $\bar{T}$ as a function of Fo for the Pd_q values in Fig. 2 are transformed with $\bar{T}$ being replaced by the average temperature ratio $\bar{t}/t_0$ according to equations (57) and (58) (Fig. 3). Here we see for the same curves of $\bar{\Theta}$ as a function of Fo for the several values of Pd_q in Fig. 2 that the curve of the average temperature ratio $\bar{t}/t_0$ as a function of Fo for $Pd_q = 0$ is much higher than the curves for $Pd_q > 0$. This indicates that for $Pd_q > 0$, the heat absorption of lumber is less than that for $Pd_q = 0$ based on the assumed relations (57) and (58). Obviously, for equation (58) to be valid and to achieve the economic process objectives, Pd_q cannot be made arbitrarily small. The smallest allowable value for Pd_q can be determined only experimentally.

Figure 4 presents the variations of average dimensionless temperature $\bar{T}$ and mass transfer potential $\bar{\Theta}$ as functions of Fo for several values of Pd_m with Pd_q = 0.02. The curves of $\bar{T}$ and $\bar{\Theta}$ as functions of Fo for $Pd_m = 0$ (case 2(b) in Table 1) are the same as the corresponding curves for $Pd_q = 0.02$ in Fig. 2. As Pd_m increases from 0.5 to 4, $\bar{T}$ decreases only slightly, but $\bar{\Theta}$ increases drastically, for any specified value of Fo < 100.

The variations of average temperature ratio $\bar{t}/t_0$ as a function of Fo for the several values of Pd_m in Fig. 5 are obtained from

equation (58). For the average mass transfer potential ratio $\bar{\theta}/\theta_0$, we obtain the following from equation (10) with θ replaced by its average value $\bar{\theta}$, Θ by $\bar{\Theta}$, and cases 2(b) and 3 of Table 1:

$$\frac{\bar{\theta}}{\theta_0} = 1 - 0.9\bar{\Theta} \quad (\mathrm{Pd}_m = 0) \tag{59}$$

$$\frac{\bar{\theta}}{\theta_0} = 1 - 0.5\bar{\Theta} \quad (\mathrm{Pd}_m > 0) \tag{60}$$

The data for $\bar{\Theta}$ as a function of Fo for the values of Pd_m in Fig. 4 are transformed with $\bar{\Theta}$ being replaced by the average mass transfer potential ratio $\bar{\theta}/\theta_0$ according to equations (59) and (60) (Fig. 5). Here we see that by increasing the value of Pd_m within a certain limit, the drying time and the heat absorption of lumber can both be reduced to achieve a specified value for the average mass transfer potential ratio $\bar{\theta}/\theta_0$. For instance, for $\bar{\theta}/\theta_0 = 0.2$, Fo has dropped from 320 at $\mathrm{Pd}_m = 0$ to 203 at $\mathrm{Pd}_m = 1$, and $\bar{t}/t$ from 8 at $\mathrm{Pd}_m = 0$ to 5.1 at $\mathrm{Pd}_m = 1$.

However, for a given value of Pd_m, as time Fo increases the ratio θ/θ_0 at the surfaces ($X = \pm 1$) will approach 0 when the ratio $\bar{\theta}/\theta_0$ is still positive. The location when that occurs is marked for each curve of $\bar{\theta}/\theta_0$ versus Fo in Fig. 5. The larger the value of Pd_m, the larger the value of $\bar{\theta}/\theta_0$, and the smaller the time Fo, when the surfaces tend to dry out, that is, θ/θ_0 approaches 0. In a drying process, when θ/θ_0 approaches a specified low value, the process must be suspended and the environment altered to avoid material degrade. Thus, it appears that a drying process can be divided into several zones as suggested by Luikov and Mikhailov (1965b), in each of which the boundary conditions are different and properly controlled, in order to minimize heat absorption and drying time without compromising product quality.

Conclusions

This paper presents an analytical method for solving the Luikov system of heat and mass transfer equations with linearly time-dependent boundary conditions. The solutions are composed of a homogeneous solution and a particular solution. When the boundary conditions change, the homogeneous solution remains the same; only the particular solution needs to be changed. Numerical results from the example of lumber drying indicate that by simultaneously increasing the dry-bulb temperature and decreasing the equilibrium mass transfer potential with respect to time, the drying time and the heat absorption of lumber in the process can both be reduced to achieve a specified lumber moisture content level. However, to avoid material degrade, the magnitudes of the Predvoditelev numbers must be properly controlled. The solution approach should be useful for obtaining valuable information on drying environmental control to realize the economic and quality enhancement objectives in the drying of porous materials.

References

Cheng, S., and Angsirikul, T., 1977, "Three-Dimensional Elasticity Solution and Edge Effects in a Spherical Dome," ASME *Journal of Applied Mechanics*, Vol. 44, No. 4, pp. 599–603.

Hildebrand, F. B., 1962, *Advanced Calculus for Applications*, Prentice-Hall, Inc., Englewood Cliffs, NJ.

Hildebrand, F. B., 1974, *Introduction to Numerical Analysis*, McGraw-Hill, New York.

IMSL, Inc., 1987, Math/Library User's Manual, Version 1.0, ISML, Houston, TX.

Liu, J. Y., and Cheng, S., 1989, "Heat and Moisture Transfer in Wood During Drying," in: *Mechanics of Cellulosic and Polymeric Materials*, R. W. Perkins, ed., 3rd Joint ASCE/ASME Mechanics Conference, ASME AMD-Vol. 99, pp. 79–85.

Liu, J. Y., and Cheng, S., 1991, "Solutions of Luikov Equations of Heat and Mass Transfer in Capillary-Porous Bodies," *International Journal of Heat and Mass Transfer*, in press.

Luikov, A. V., and Mikhailov, Y. A., 1965a, *Theory of Heat and Mass Transfer*, Daniel Davey & Co., Inc., New York.

Luikov, A. V., and Mikhailov, Y. A., 1965b, *Theory of Energy and Mass Transfer*, Pergamon Press, Oxford, United Kingdom.

Luikov, A. V., 1966, *Heat and Mass Transfer in Capillary-Porous Bodies*, Pergamon Press, Oxford, United Kingdom.

Müller, D. E., 1956, "A Method for Solving Algebraic Equations Using an Automatic Computer," *Mathematical Tables and Aids to Computation*, Vol. 10, pp. 208–215.

Thomas, H. R., Lewis, R. W., and Morgan, K., 1980, "An Application of the Finite Element Method to the Drying of Timber," *Wood and Fiber*, Vol. 11, No. 4, pp. 237–243.

Journal of Heat Transfer

Technical Notes

This section contains shorter technical papers. These shorter papers will be subjected to the same review process as that for full papers.

Conjugate Heat Transfer for Simultaneously Developing Laminar Flow in a Circular Tube

G. Pagliarini[1]

Nomenclature

c = specific heat
Ⓗ = thermal condition referring to uniform heat flux at the boundary of the fluid phase
I = conduction influence parameter $= \Delta(1+\Delta)K/\mathrm{Pe}^2$
k = thermal conductivity
K = dimensionless wall thermal conductivity $= k_s/k_f$
Nu = Nusselt number $= 2\left.\dfrac{\partial\theta_f}{\partial r}\right|_{r=1} /(\theta_w - \theta_{fb})$
p = dimensionless pressure $= p'/(\rho\, U^2/2)$
Pe = Péclet number = Re Pr
Pr = Prandtl number $= \nu\, \rho\, c/k_f$
q_w = dimensionless heat flux at the wall-fluid interface $= \left.\dfrac{\partial\theta_f}{\partial r}\right|_{r=1}$
q_o' = uniform heat flux specified at the outer wall boundary
$Q_{w\infty}$ = dimensionless heat diffusing toward the inlet from far downstream because of wall axial conduction
r = dimensionless radial coordinate $= r'/R$
R = internal radius of the tube
Re = Reynolds number $= 2\,R\,U/\nu$
T = temperature
Ⓣ = thermal condition referring to uniform temperature at the boundary of the fluid phase
u = dimensionless fluid axial velocity $= u'/U$
U = fluid mean axial velocity
v = dimensionless fluid radial velocity $= v'/U$
x = dimensionless axial coordinate $= x'/R$
x^* = dimensionless axial coordinate $= x'/(2\,R\,\mathrm{Pe})$
x^+ = dimensionless axial coordinate $= x'/(2\,R\,\mathrm{Re})$
δ = wall thickness
Δ = dimensionless wall thickness $= \delta/(2\,R)$
θ = dimensionless temperature $= (T - T_e)k_f/(q_o'(R+\delta))$
θ_{fb} = dimensionless fluid bulk temperature $= \int_0^1 \theta\, u\, r\, dr / \int_0^1 u\, r\, dr$
ν = kinematic viscosity
ρ = density

Subscripts

e = initial value at $x = -\infty$
f = fluid
H = Ⓗ boundary condition
s = solid
T = Ⓣ boundary condition
x = local value
w = wall-fluid interface

Superscripts

$'$ = dimensional quantity

Introduction

Conjugate heat transfer for laminar flow in ducts has been widely analyzed in the past. An extensive review on this subject was presented by Barozzi and Pagliarini (1985). However, some recent papers should be added to the list.

Previously, only fully developed flow has been considered, while, in practical applications, velocity and temperature profiles frequently develop simultaneously. Except for high Prandtl number fluids, velocity development cannot be neglected with respect to temperature development

Conjugate heat transfer in a semi-infinite circular tube uniformly heated at the outer wall boundary is analyzed in the present paper. The fluid flow is laminar with simultaneous development of the profiles of both temperature and velocity. Axial diffusion of heat and momentum are included in the analysis, thus making the momentum and energy equations of the elliptic type.

Analysis and Solution

The conjugate problem analyzed in this paper concerns the steady laminar flow of a Newtonian constant property fluid through a circular tube of semi-infinite extent. Viscous dissipation is neglected.

By utilizing the dimensionless quantities defined in the Nomenclature, the dimensionless forms of the governing equations are as follows:

Continuity equation

$$\frac{\partial u}{\partial x} + \frac{\partial v}{\partial r} + \frac{v}{r} = 0 \tag{1}$$

Momentum equation

axial direction

$$u\frac{\partial u}{\partial x} + v\frac{\partial u}{\partial r} = -\frac{1}{2}\frac{\partial p}{\partial x} + \frac{2}{\mathrm{Re}}\left(\frac{\partial^2 u}{\partial r^2} + \frac{1}{r}\frac{\partial u}{\partial r} + \frac{\partial^2 u}{\partial x^2}\right) \tag{2}$$

[1]Istituto di Fisica Tecnica, Facoltà di Ingegneria, Università di Bologna, I-40136 Bologna, Italy.

Contributed by the Heat Transfer Division for publication in the JOURNAL OF HEAT TRANSFER. Manuscript received by the Heat Transfer Division June 11, 1990; revision received December 24, 1990. Keywords: Conjugate Heat Transfer, Forced Convection.

radial direction

$$u\frac{\partial v}{\partial x}+v\frac{\partial v}{\partial r}=-\frac{1}{2}\frac{\partial p}{\partial r}+\frac{2}{\mathrm{Re}}\left(\frac{\partial^2 v}{\partial r^2}+\frac{1}{r}\frac{\partial v}{\partial r}-\frac{v}{r^2}+\frac{\partial^2 v}{\partial x^2}\right) \quad (3)$$

Energy equation

$$u\frac{\partial \theta}{\partial x}+v\frac{\partial \theta}{\partial r}=\frac{2}{\mathrm{Pe}}\left(\frac{\partial^2 \theta}{\partial r^2}+\frac{1}{r}\frac{\partial \theta}{\partial r}+\frac{\partial^2 \theta}{\partial x^2}\right) \quad (4)$$

Upstream of the inlet the fluid flows inside a frictionless, impermeable, and thermally insulated stream tube, which allows upstream axial diffusion of heat and momentum. Far upstream the temperature is uniform and the velocity irrotational with a uniform axial component. Downstream of the inlet the wall verifies the usual impermeability and nonslip conditions. The velocity field is symmetric with respect to the tube axis and meets the fully developed parabolic distribution downstream of the hydrodynamic inlet.

For the temperature field the following boundary conditions are required:

$$\left.\frac{\partial \theta}{\partial x}\right|_{x=0}=0 \quad 1\le r\le 1+2\Delta \quad (5)$$

$$\left.\frac{\partial \theta}{\partial r}\right|_{r=1}=0 \quad -\infty\le x<0 \quad (6)$$

$$\left.\frac{\partial \theta}{\partial r}\right|_{r=0}=0 \quad -\infty\le x\le\infty \quad (7)$$

$$\theta(-\infty, r)=0 \quad 0\le r\le 1 \quad (8)$$

$$\left.\frac{\partial \theta}{\partial x}\right|_{x=\infty}=\frac{4}{\mathrm{Pe}} \quad 0\le r\le 1+2\Delta \quad (9)$$

$$\left.\frac{\partial \theta}{\partial r}\right|_{r=1+2\Delta}=\frac{1}{K(1+2\Delta)} \quad 0\le x\le\infty \quad (10)$$

Simultaneous handling of the energy equation in both the fluid and the solid, where the velocity field vanishes, requires no explicit compatibility condition for the temperature field at the interface. They are, nevertheless, specified all the same in order to complete the statement of the conjugate problem:

$$\theta_f|_{r=1}=\theta_s|_{r=1} \quad 0\le x\le\infty$$

$$\left.\frac{\partial \theta_f}{\partial r}\right|_{r=1}=K\left.\frac{\partial \theta_s}{\partial r}\right|_{r=1} \quad 0\le x\le\infty$$

The problem specified by the complete conservation Eqs. (1)–(4) and the related boundary conditions has been reformulated in integral form by the Galerkin weighted residuals method and then approximately solved in terms of primitive variables by the finite element technique. The nonlinearity in the momentum equation was handled by an iterative scheme in which at each iteration the convective terms are linearized by the velocity values obtained at the previous step. The resulting system of algebraic linear equations was then solved by the IMSL subroutine LEQT1B. The details of the solution procedure, explained elsewhere (Pagliarini, 1989), will be omitted here.

In applying the numerical procedure the integration domain has been discretized by means of axisymmetric elements having a triangular cross section. In each element the velocity components and temperature are approximated by quadratic polynomials and the pressure by linear polynomials. In this way the velocity components and temperature are each interpolated through six nodes located at the triangle vertices and their midsides while the pressure is interpolated only through the vertex nodes. The axial spacing was increased logarithmically in order to achieve greater accuracy near the tube entrance. Each decade was then subdivided into a constant number of elements starting from $x^*=0.00001$. Upstream of the inlet, the stream tube was discretized by a subdivision that is symmetric with respect to the origin. In the fluid domain the mesh becomes thicker and thicker near the interface, the better to approximate the fields of both velocity and temperature inside the hydrodynamic and thermal boundary layers. The integration domain (fluid and solid phases) has been subdivided into a maximum of 2376 elements with 4913 nodal points. Exclusion from the solving system of those nodal variables for which a value is prescribed by the boundary conditions allowed the order of the algebraic equation system to be lowered. In assembling the coefficient matrix deriving from the continuity and momentum equations, particular care was devoted to the semiband width, which was restricted to a maximum value of 111. Neglecting the fluid property variation with temperature allowed the hydrodynamic field to be solved independently of the thermal one. The energy equation was then simultaneously solved in both the fluid and the wall, where the convective terms vanish.

The numerical procedure has been verified by comparison with previous solutions. For Poiseuille flow, within the limits of the intelligibility of the graphic results, the present local Nusselt numbers are the same as that analytically obtained by Mori et al. (1974). The comparison is restricted to x^* values lower then 0.005. Farther downstream the two solutions cannot be compared, the tube of Mori et al. being of finite length ($L^*=0.02$). Without inclusion of the wall effect, further checks of the solution procedure are quoted in a previous paper (Pagliarini, 1989).

Results and Discussion

The conservation Eqs. (1)–(4) with the specified boundary and compatibility conditions point out that the dimensionless solution of the conjugate problem depends on the following dimensionless parameters: the Reynolds number, Re, the Péclet number, Pe, and the dimensionless thermal conductivity of the wall, K, in addition to the dimensionless wall thickness, Δ.

Considering fully developed flow in a tube of vanishing wall thickness, Cotton and Jackson (1985) showed that, for sufficiently high Pe values, the solutions of conjugate thermal problems characterized by the same value of the conduction influence parameter, I, are similar in the x^* and r coordinates. In the present paper the simplifying assumptions of Cotton and Jackson (vanishing wall thickness and high Pe) are dropped. Nevertheless, the conduction influence parameter, in connection with the dimensionless axial coordinate x^*, is used all the same in the presentation of the results because its close relation with the wall energy balance in the thermal entrance region allows further insight in their analysis to be given. Indeed, the dimensionless heat diffusing toward the inlet from far downstream ($Q_{w\infty}$) because of wall axial conduction depends on I only, being directly proportional to it. This statement can be verified by equating to $Q_{w\infty}$ the excess interface heat flux in the thermal entrance region:

$$Q_{w\infty}=4\,I=\int_0^{x^*_\infty}\left.\frac{\partial \theta_f}{\partial r}\right|_{r=1}dx^*-x^*_\infty$$

x^*_∞ is the dimensionless tube length where the interface heat flux redistribution takes place.

The considered conjugate entry problem has been solved for two Pe values, i.e., 5 and 500, and for Pr ranging from 0.01 to 100, while restricting Re between 5 and 714. The same conjugate problem was also solved for Pe = 50. Nevertheless, far from the immediate entrance the results do not differ substantially from those obtained with Pe = 500, thus confirming that for Pe > 50 the results of the conjugate problem may be obtained, at least in a first approximation, from those for Pe = 500 by entering x^* and I with the proper Pe value. In the considered range of Pe and Re values, axial diffusion of heat

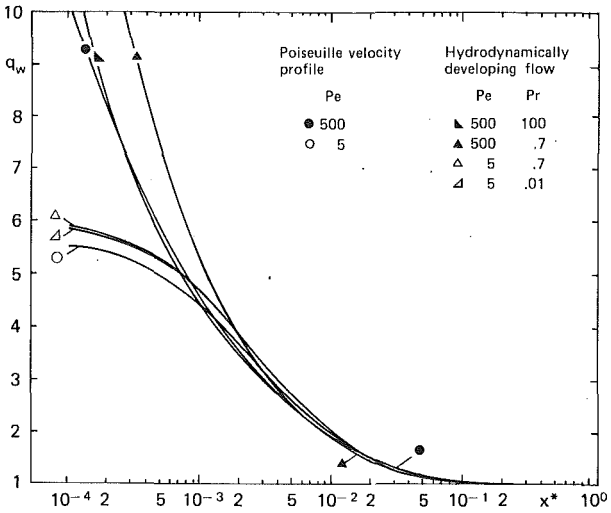

Fig. 1 Dimensionless heat flux at the fluid-wall interface: $I = 0.01$, $\Delta = 0.1$

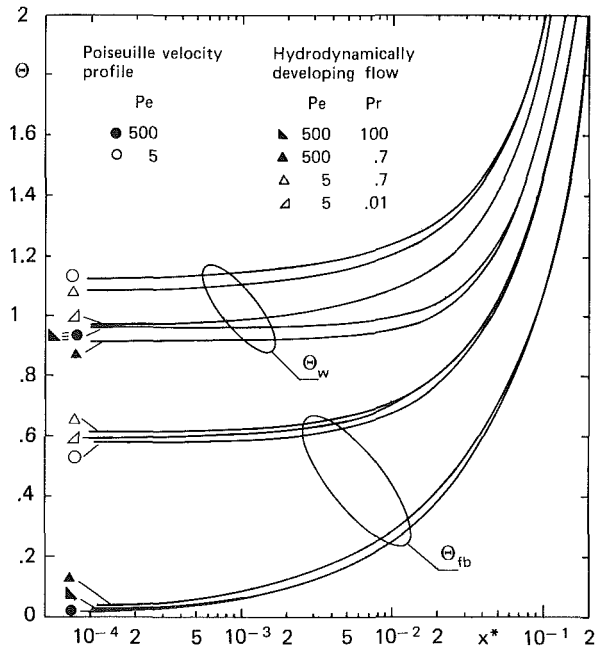

Fig. 2 Dimensionless interface and fluid bulk temperature distributions: $I = 0.01$, $\Delta = 0.1$

and momentum in the fluid can have a definite effect on the convective heat transfer. Nevertheless only the effect of axial heat diffusion is focused in the analysis of the results because it readily overwhelms the effect of momentum axial diffusion.

The distributions of the relevant dimensionless local parameters are presented in Figs. 1-3, for $\Delta = 0.1$ and $I = 0.01$.

The dimensionless heat flux at the wall-fluid interface is shown in Fig. 1. Since the temperature radial gradients in the fluid are reduced by the heat diffusion upstream of the inlet, in the neighborhood of $x^* = 0$ the interface heat flux decreases as Pe decreases. Farther downstream q_w assumes the opposite behavior because the overall heat exchanged at the interface must be the same for the same I value. On the contrary, due to the development of the velocity profile, the interface heat flux increases considerably at the inlet as Pr decreases, while it decreases farther downstream.

The distributions of the dimensionless interface temperature (Fig. 2) confirm the presence near the inlet of an isothermal zone whose extent, however, decreases as Pe decreases. At low Pe the wall-to-fluid bulk temperature difference decreases considerably not only in the tube portion where, because of the fluid axial conduction, q_w decreases, but also farther downstream. Also the development of the velocity profile results in a wall-to-fluid bulk temperature difference decrease.

Table 1 Fluid bulk temperature at the inlet for Pe = 5

	$I = 0.$	$I = 0.01$
Poiseuille velocity profile	0.35	0.58
Pr = 0.7	0.37	0.61
Pr = 0.01	0.34	0.59

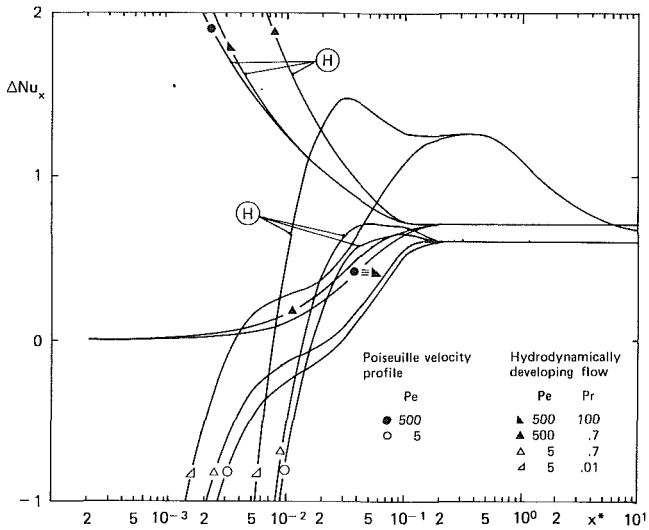

Fig. 3 Difference between the local Nusselt number, Nu_x, and the corresponding distributions for the (T) boundary condition, Nu_{xT}: $I = 0.01$, $\Delta = 0.1$

The effect of the axial heat diffusion in the stream is particularly demonstrated by the fluid bulk temperature distributions. From the downstream sections heat is diffused axially toward the entrance both in the wall and the fluid. To the heat upstream conducted in the wall at $x^* = +\infty$ ($Q_{w\infty} = 4I$), there corresponds an increment in θ_{fb} equal to $32\ I$. On the other hand the dimensionless heat upstream conducted in the fluid at $x^* = +\infty$ amounts to $1/Pe^2$. At the end of the thermal entry it causes a further increment in θ_{fb} equal to $8/Pe^2$. This is, of course, negligible for high Pe values, while for $Pe = 5$ it equals the increment due to the upstream axial heat conducted in the wall when assuming $I = 0.01$. The preheating due to the heat diffusion in the fluid upstream of the inlet section is shown in Table 1 by the inlet θ_{fb} values.

At $x^* = 0$ the preheating effect corresponds to an axial heat flux upstream of the inlet, which exceeds 90 percent of the overall heat flux upstream conducted at $+\infty$ in both the fluid and the wall, thus considerably exceeding the preheating effect that occurs when neglecting wall axial conduction ($I = 0.$).

In Fig. 3 the difference, ΔNu_x, between the actual local Nusselt number and the distributions obtained by specifying the (T) condition at the fluid boundary shows that, when accounting for the wall effect, Nu_x ranges between the distributions obtained for the fundamental cases of the (T) and (H) boundary conditions even when considering the velocity profile development and the axial heat diffusion in the fluid. However, at low Pe values, according to the interface temperature distributions, Nu_x does not coincide with Nu_T in the neighborhood of $x^* = 0$. For negligible axial heat diffusion in the fluid, ΔNu_x is always greater than zero, but, as Pe decreases, it becomes negative because Nu_{xT} exceeds Nu_{xH} along most of the thermal entrance region. For $Pe = 5$ the intersection between corresponding curves obtained with $\Delta = 0$ and $\Delta \neq 0$ does not occur exactly at $\Delta Nu_x = 0$; it shifts up slightly as Pr decreases. Nevertheless the last behavior may be meaningless because of the difficulty in stating whether it is to be ascribed

to a physical phenomenon or rather to the numerical approximation. Development of the velocity profile affects the local Nusselt number distribution as in the classical thermal entry problem, thus generally increasing its value. For $Pr = 0.01$ the dimensionless axial coordinate characteristic for the development of the velocity profile, that is x^+, is one hundred times lower than the actual one. Therefore, as shown by Pagliarini (1989), when $Re = 500$ the velocity profile is far from being fully developed at $x^* > 0.1$, which corresponds to $x^+ > 0.001$. For this reason the thermal entry length increases considerably. When the (H) thermal condition is specified at the fluid boundary, the fully developed Nu_x value is not even reached at $x^* = 10$ because the temperature profile is continuously altered by the changes in the velocity profile, while the wall effect vanishes near $x^* = 0.3$. On the contrary, in the case of the (T) boundary condition, the fluid does practically attain uniform temperature distribution already at $x^* = 1$.

Regarding the upstream axial momentum diffusion, no remarkable effect on the conjugate heat transfer is detectable from the results, not even when considering very low Re values. In fact, in the case characterized by $Pe = 500$ and $Pr = 100$, $x^* = 0.0001$ corresponds to $x^+ = 0.01$, an axial position where the velocity profile is not much affected by upstream axial momentum diffusion. In the case characterized by $Pe = 5$ and $Pr = 0.7$, the effect of axial heat diffusion in the fluid readily overwhelms that of the axial momentum diffusion.

Acknowledgments

Support of this work by the Italian Ministry of Education is gratefully acknowledged.

References

Barozzi, G. S., and Pagliarini, G., 1985, "A Method to Solve Conjugate Heat Transfer Problems: The Case of Fully Developed Laminar Flow in a Pipe," ASME JOURNAL OF HEAT TRANSFER, Vol. 107, pp. 77–83.

Cotton, M. A., and Jackson, J. D., 1985, "The Effect of Heat Conduction in a Tube Wall Upon Forced Convection Heat Transfer in the Thermal Entry Region," *Proceedings, 4th International Conference on Numerical Methods in Thermal Problems*, R. W. Lewis and K. Morgan, eds., Pineridge Press, Swansea, United Kingdom, Part 1, pp. 504–515.

IMSL Library, version 9.2, International Mathematical & Statistical Libraries, Inc., Huston.

Mori, S., Sakakibara, M., and Tanimoto, A., 1974, 'Steady Heat Transfer to Laminar Flow in a Circular Tube With Conduction in the Tube Wall," *Heat Transfer, Japanese Research*, Vol. 3, pp. 37–46.

Pagliarini, G., 1989, "Steady Laminar Heat Transfer in the Entry Region of Circular Tubes With Axial Diffusion of Heat and Momentum," *Int. J. Heat Mass Transfer*, Vol. 32, pp. 1037–1052.

The Effects of Free-Stream Turbulence and Flow Pulsation on Heat Transfer From a Cylinder in Crossflow

M. Gundappa[1] and T. E. Diller[1]

Introduction

The heat transfer from a circular cylinder is a fundamental problem with practical applications ranging from tubular heat exchangers to the leading edge of gas turbine blades. The flow field across the surface is often unsteady due to natural instabilities or forced oscillations of the fluid. Examples are the periodic natural shedding of vortices from cylinders and the wakes of rotor blades in gas turbine engines. In addition, active vibration of the fluid is a possible means of augmenting the heat transfer (Bergles, 1969). When the frequencies are near the natural shedding frequency of the cylinder, active fluid vibration also gives the possibility of frequency control through lock-on (Barbi et al., 1986).

Many previous researchers have reported measurements of the effects of free-stream turbulence on the heat transfer from a circular cylinder to a steady crossflow (VanFossen and Simoneau, 1987, and papers cited therein). It is clear that as the turbulence intensity is increased, the heat transfer increases at the forward stagnation point and in the boundary layer over the front of the cylinder. Fewer local heat transfer measurements have been reported in the wake region (Zukauskas and Ziugzda, 1985, and papers cited therein). With an increase in turbulence intensity the critical Reynolds number for the boundary layer is decreased substantially. This affects the position of the separation point and the shape of the heat transfer curve in the wake region.

A previous study of the effect of flow pulsation has shown very little effect on the local heat transfer at most positions around a circular cylinder (Andraka and Diller, 1985). This study covered a range of frequencies both above and below the natural shedding frequency with a low free-stream turbulence intensity ($Tu < 0.5$ percent). The pulsations were carefully created in the flow so as not to alter the turbulence. Other investigators, however, have found that the presence of flow unsteadiness increased transfer when turbulence was present (Marziale and Mayle, 1984; Simoneau et al., 1984). One of the important applications is the effect of rotor wakes on turbine stator blades. Time-resolved measurements of the heat transfer have shown that the passage of a rotor wake has an effect similar to that of a short burst of turbulence in the fluid (Doorly and Oldfield, 1985; O'Brien, 1988). Therefore, the effect of rotor wakes (Morehouse and Simoneau, 1986) is not the same as a clean flow pulsation.

The present work is an experimental study of the combined effects of flow pulsation and turbulence on the local heat transfer from a circular cylinder. In particular, the possibility of a coupling between the two effects is investigated.

Experimental Apparatus and Procedure

The experimental results were obtained with the same wind tunnel as previously reported by Andraka and Diller (1985). The wave amplitudes for the pulsating flow are listed in Table 1 for the different frequencies used. The amplitude ϵ is defined as

$$U = U_\infty[1 + \epsilon\sin(2\pi ft)] \quad (1)$$

where U is the instantaneous flow velocity, U_∞ is the time-averaged flow velocity, f is the pulsation frequency, and t is the time. Table 1 also lists the dimensionless frequencies, which included values above and below the natural shedding frequency of the test cylinder ($fD/U_\infty \simeq 0.20$), where D is the cylinder diameter. The corresponding length scale of the pulsation relative to the cylinder diameter (L/D) is the inverse of these values.

The turbulence was generated by placing grids at various locations in the test section upstream of the cylinder. The

Table 1 Pulsation characteristics at Re = 50,000

Frequency, f (Hz)	Amplitude, α (percent)	fD/U_∞	L/D
1.7	15.5	0.016	62.5
7.0	6.5	0.066	15.2
18.5	8.0	0.175	5.7
23.0	4.0	0.218	4.6

[1]Mechanical Engineering Department, Virginia Polytechnic Institute and State University, Blacksburg, VA 24061-0238.

Contributed by the Heat Transfer Division and presented at the ASME Winter Annual Meeting, Miami Beach, Florida, November 17–21, 1985. Manuscript received by the Heat Transfer Division June 9, 1989; revision received January 22, 1991. Keywords: Augmentation and Enhancement, Forced Convection, Transient and Unsteady Heat Transfer.

to a physical phenomenon or rather to the numerical approximation. Development of the velocity profile affects the local Nusselt number distribution as in the classical thermal entry problem, thus generally increasing its value. For $Pr = 0.01$ the dimensionless axial coordinate characteristic for the development of the velocity profile, that is x^+, is one hundred times lower than the actual one. Therefore, as shown by Pagliarini (1989), when $Re = 500$ the velocity profile is far from being fully developed at $x^* > 0.1$, which corresponds to $x^+ > 0.001$. For this reason the thermal entry length increases considerably. When the (H) thermal condition is specified at the fluid boundary, the fully developed Nu_x value is not even reached at $x^* = 10$ because the temperature profile is continuously altered by the changes in the velocity profile, while the wall effect vanishes near $x^* = 0.3$. On the contrary, in the case of the (T) boundary condition, the fluid does practically attain uniform temperature distribution already at $x^* = 1$.

Regarding the upstream axial momentum diffusion, no remarkable effect on the conjugate heat transfer is detectable from the results, not even when considering very low Re values. In fact, in the case characterized by $Pe = 500$ and $Pr = 100$, $x^* = 0.0001$ corresponds to $x^+ = 0.01$, an axial position where the velocity profile is not much affected by upstream axial momentum diffusion. In the case characterized by $Pe = 5$ and $Pr = 0.7$, the effect of axial heat diffusion in the fluid readily overwhelms that of the axial momentum diffusion.

Acknowledgments

Support of this work by the Italian Ministry of Education is gratefully acknowledged.

References

Barozzi, G. S., and Pagliarini, G., 1985, "A Method to Solve Conjugate Heat Transfer Problems: The Case of Fully Developed Laminar Flow in a Pipe," ASME JOURNAL OF HEAT TRANSFER, Vol. 107, pp. 77–83.

Cotton, M. A., and Jackson, J. D., 1985, "The Effect of Heat Conduction in a Tube Wall Upon Forced Convection Heat Transfer in the Thermal Entry Region," *Proceedings, 4th International Conference on Numerical Methods in Thermal Problems*, R. W. Lewis and K. Morgan, eds., Pineridge Press, Swansea, United Kingdom, Part 1, pp. 504–515.

IMSL Library, version 9.2, International Mathematical & Statistical Libraries, Inc., Huston.

Mori, S., Sakakibara, M., and Tanimoto, A., 1974, 'Steady Heat Transfer to Laminar Flow in a Circular Tube With Conduction in the Tube Wall," *Heat Transfer, Japanese Research*, Vol. 3, pp. 37–46.

Pagliarini, G., 1989, "Steady Laminar Heat Transfer in the Entry Region of Circular Tubes With Axial Diffusion of Heat and Momentum," *Int. J. Heat Mass Transfer*, Vol. 32, pp. 1037–1052.

The Effects of Free-Stream Turbulence and Flow Pulsation on Heat Transfer From a Cylinder in Crossflow

M. Gundappa[1] and T. E. Diller[1]

Introduction

The heat transfer from a circular cylinder is a fundamental problem with practical applications ranging from tubular heat exchangers to the leading edge of gas turbine blades. The flow field across the surface is often unsteady due to natural instabilities or forced oscillations of the fluid. Examples are the periodic natural shedding of vortices from cylinders and the wakes of rotor blades in gas turbine engines. In addition, active vibration of the fluid is a possible means of augmenting the heat transfer (Bergles, 1969). When the frequencies are near the natural shedding frequency of the cylinder, active fluid vibration also gives the possibility of frequency control through lock-on (Barbi et al., 1986).

Many previous researchers have reported measurements of the effects of free-stream turbulence on the heat transfer from a circular cylinder to a steady crossflow (VanFossen and Simoneau, 1987, and papers cited therein). It is clear that as the turbulence intensity is increased, the heat transfer increases at the forward stagnation point and in the boundary layer over the front of the cylinder. Fewer local heat transfer measurements have been reported in the wake region (Zukauskas and Ziugzda, 1985, and papers cited therein). With an increase in turbulence intensity the critical Reynolds number for the boundary layer is decreased substantially. This affects the position of the separation point and the shape of the heat transfer curve in the wake region.

A previous study of the effect of flow pulsation has shown very little effect on the local heat transfer at most positions around a circular cylinder (Andraka and Diller, 1985). This study covered a range of frequencies both above and below the natural shedding frequency with a low free-stream turbulence intensity ($Tu < 0.5$ percent). The pulsations were carefully created in the flow so as not to alter the turbulence. Other investigators, however, have found that the presence of flow unsteadiness increased transfer when turbulence was present (Marziale and Mayle, 1984; Simoneau et al., 1984). One of the important applications is the effect of rotor wakes on turbine stator blades. Time-resolved measurements of the heat transfer have shown that the passage of a rotor wake has an effect similar to that of a short burst of turbulence in the fluid (Doorly and Oldfield, 1985; O'Brien, 1988). Therefore, the effect of rotor wakes (Morehouse and Simoneau, 1986) is not the same as a clean flow pulsation.

The present work is an experimental study of the combined effects of flow pulsation and turbulence on the local heat transfer from a circular cylinder. In particular, the possibility of a coupling between the two effects is investigated.

Experimental Apparatus and Procedure

The experimental results were obtained with the same wind tunnel as previously reported by Andraka and Diller (1985). The wave amplitudes for the pulsating flow are listed in Table 1 for the different frequencies used. The amplitude ϵ is defined as

$$U = U_\infty[1 + \epsilon\sin(2\pi ft)] \quad (1)$$

where U is the instantaneous flow velocity, U_∞ is the time-averaged flow velocity, f is the pulsation frequency, and t is the time. Table 1 also lists the dimensionless frequencies, which included values above and below the natural shedding frequency of the test cylinder ($fD/U_\infty \simeq 0.20$), where D is the cylinder diameter. The corresponding length scale of the pulsation relative to the cylinder diameter (L/D) is the inverse of these values.

The turbulence was generated by placing grids at various locations in the test section upstream of the cylinder. The

Table 1 Pulsation characteristics at Re = 50,000

Frequency, f (Hz)	Amplitude, α (percent)	fD/U_∞	L/D
1.7	15.5	0.016	62.5
7.0	6.5	0.066	15.2
18.5	8.0	0.175	5.7
23.0	4.0	0.218	4.6

[1]Mechanical Engineering Department, Virginia Polytechnic Institute and State University, Blacksburg, VA 24061-0238.

Contributed by the Heat Transfer Division and presented at the ASME Winter Annual Meeting, Miami Beach, Florida, November 17–21, 1985. Manuscript received by the Heat Transfer Division June 9, 1989; revision received January 22, 1991. Keywords: Augmentation and Enhancement, Forced Convection, Transient and Unsteady Heat Transfer.

turbulence intensity in steady flow, defined as

$$Tu = \frac{\sqrt{\overline{(u')^2}}}{U_\infty} \tag{2}$$

was determined from the ratio of the true rms a-c and d-c components of a linearized hot-wire velocity signal. The symbol u' indicates the fluctuating component of flow velocity and the bar indicates time average. For pulsating flow, a Zonic 5003 digital signal analyzer was used to sample both a single time record and an ensemble-averaged signal of velocity. The subtraction of the two signals gave the turbulence of the pulsating flow. Without the grids the turbulence in the steady and pulsating flows was less than 0.5 percent and did not vary significantly with pulsation frequency.

The integral length scale of turbulence was measured by first determining the autocorrelation coefficient $\rho(\tau)$ of the fluctuating component of the velocity signal u'. This was then integrated over the time delay τ, to obtain the Eulerian integral time scale. Finally the integral length scale, L, was determined by multiplying the time scale by the mean velocity. The same procedure was followed for determining length scales in pulsating flow except that the ensemble-averaged signal was subtracted from the single time record (as explained earlier) before calculating the autocorrelation coefficient.

The turbulence characteristics with the grids are listed in Table 2. The pulsations did not significantly affect the measured turbulence intensity or integral length scales. This ensured that the pulsations did not introduce any additional turbulence in the free stream. The grids were standard 16 gage steel stamped with square holes. Grid 1 had a mesh size, M, of 12.7 mm (0.5 in.) with bars 3.17 mm (0.125 in.) in width. Grid 2 had a mesh size, M, of 17.5 mm (0.687 in.) with bars of 4.76 mm (0.187 in.). The open area of grid 1 was 56 percent and that of grid 2 was 53 percent. In the table, x represents the distance from the turbulence grid to the cylinder stagnation point.

Figure 1 shows the cylinder model used in this study. The heat transfer measurements were made with a 3.2-mm-o.d. Gardon heat flux gage that was mounted flush with the cylinder wall. The sensing element of the gage subtended a 2 deg arc on the cylinder. It was calibrated in a convective environment as described by Borell and Diller (1987). The calibration included the effects of radiation and the small temperature nonuniformities across the gage surface. The cylinder was heated from the inside to maintain a nearly isothermal boundary condition. Further details of the cylinder construction, related instrumentation, and the data reduction procedure are described in the paper by Andraka and Diller (1985). All measurements were make at a cylinder Reynolds number of Re = 50,000.

Steady Flow Results

Figure 2 shows the heat transfer distributions for different levels of free-stream turbulence. The entire attached boundary layer region has increased heat transfer due to the added free-stream turbulence. In addition, the point of minimum heat transfer is shifted farther back on the cylinder and its value is increased. In the wake region, heat transfer is increased up to an angle of about 130 deg and decreased thereafter, including the rear stagnation point. The large increase in heat transfer from θ = 90 to 130 deg for the 7.5 percent turbulence case is indicative of the critical flow regime. Similar results have been reported for mass transfer at Re = 75,000 by Kestin and Wood (1971).

Average heat transfer coefficients over the front (0 deg < θ < 90 deg), the back (90 deg < θ < 180 deg), and the entire cylinder (0 deg < θ < 180 deg) were evaluated by numerical integration of the local values using the trapezoidal rule. These values are listed in Table 3 for the steady flow cases. On the front of the cylinder, the average heat transfer increased progressively with increasing turbulence intensity. At a turbulence intensity of 7.5 percent, the average heat transfer on the front increased by about 45 percent. On the back, however, the addition of turbulence decreased the average heat transfer.

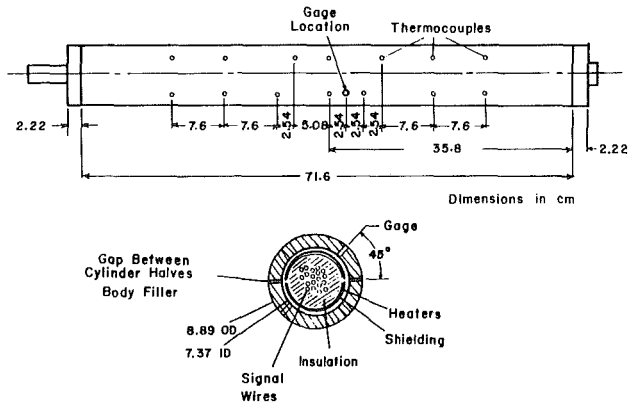

Fig. 1 The cylinder model used for the heat transfer measurements

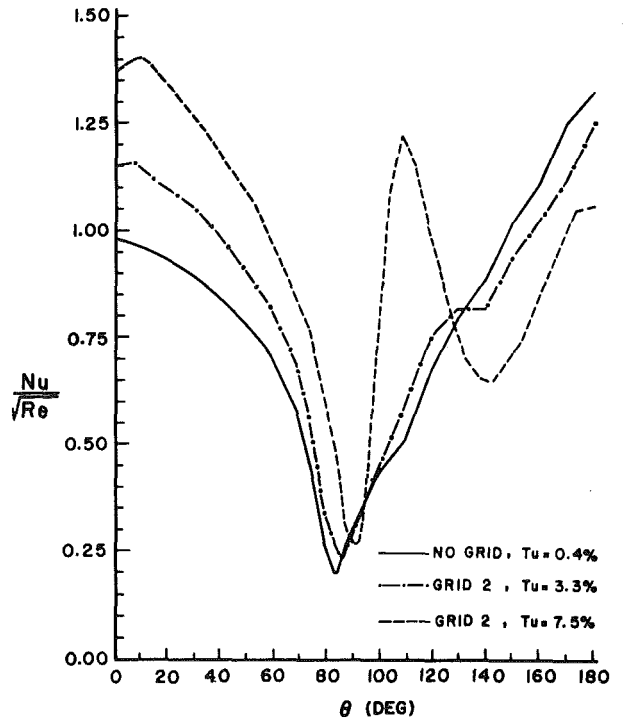

Fig. 2 Effect of free-stream turbulence on cylinder heat transfer

Table 2 Turbulence characteristics for pulsating and steady flow at Re = 50,000

	x/M	L/D	Tu (percent)
No grid	--	--	0.4
Grid 1	54	0.11	2.3
Grid 2	39	0.14	3.3
Grid 2	13	0.07	7.5

Table 3 Average heat transfer results for steady flow at Re = 50,000

Tu (percent)	$Nu/\sqrt{Re}$ (front)	$Nu/\sqrt{Re}$ (back)	$Nu/\sqrt{Re}$ (total)
0.4	0.740	0.836	0.788
2.3	0.828	0.788	0.808
3.3	0.871	0.803	0.837
7.5	1.070	0.822	0.946

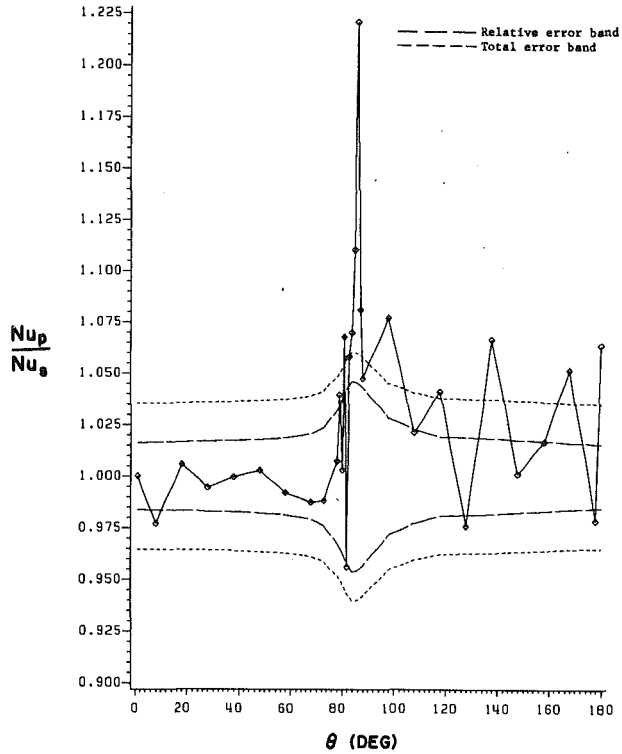

Fig. 3 Heat transfer results in pulsating flow (f = 18.5 Hz, Tu = 3.3 percent)

This decrease varied from 2 percent for the high-turbulence-intensity case (7.5 percent turbulence) to about 6 percent for the low-turbulence-intensity case (2.3 percent turbulence). In general, the addition of turbulence increased the average heat transfer over the entire cylinder by up to 20 percent.

Pulsating Flow Results

A representative sample of the local heat transfer results obtained for pulsating flow is presented in Fig. 3. The ordinate represents the ratio of the pulsating Nusselt number, Nu_p, to the steady Nusselt number, Nu_s. A steady-flow test was performed either immediately before or after each pulsating flow test to ensure the best possible comparison. The estimated error bands are also shown to indicate the confidence intervals for the data. The total error band reflects the estimated error in the results for each test by accounting for all possible errors sources. The relative error between a set of tests, on the other hand, is found by neglecting the errors that are common between the two measurement sets (e.g., the amplifier gain and the gage calibration).

Similar results were obtained at other pulsing frequencies and turbulence levels. In all of these cases the addition of flow pulsation did not measurably affect the heat transfer on the front of the cylinder except near the separation point. Because of the steep changes in heat transfer with θ in this region, small shifts in the location or size of the separation region result in large localized changes due to pulsation. In the wake region, however, the flow pulsation appeared to causes small increases in heat transfer at some locations for the low turbulence intensity cases.

Average heat transfer coefficients for the front, the back, and the whole cylinder were obtained from the local measurements by numerical integration using the trapezoidal rule. These values at various pulsing frequencies and turbulence levels are listed in Table 4 as average Nu_p/Nu_s ratios. All of these values (except for f = 7.0 Hz, Tu = 3.3 percent) are within 3 percent of the corresponding steady values, which is

Table 4 Average heat transfer results for pulsating flow at Re = 50,000

Frequency, f (Hz)	Tu (percent)	Nu_p/Nu_s (front)	Nu_p/Nu_s (back)	Nu_p/Nu_s (total)
1.7	2.3	0.997	0.973	0.985
1.7	3.3	0.984	0.994	0.989
1.7	7.5	0.967	0.995	0.981
7.0	2.3	1.011	0.967	0.989
7.0	3.3	1.025	1.076	1.050
7.0	7.5	0.996	0.956	0.976
18.5	2.3	1.014	1.016	1.015
18.5	3.3	0.990	1.029	1.010
18.5	7.5	0.958	0.978	0.968
23.0	3.3	0.999	1.030	1.015

within the estimated average relative error. The table shows that at frequencies both below and above the natural shedding frequency of the cylinder (21 Hz), the introduction of flow pulsation did not affect the average heat transfer. This indicates the absence of any interaction between the two effects, namely, flow pulsation and turbulence, in their influence on the heat transfer.

The results at a dimensionless frequency of 0.066 (f = 7.0 Hz, Tu = 3.3 percent) are particularly interesting because they are close to matching the conditions used by Marziale and Mayle (1984). The latter found a 10 percent increase in mass transfer at the stagnation point of a cylinder oscillating rotationally at nearly the same dimensionless frequency and mean Reynolds number used here. Their reported turbulence intensity was 2.65 percent with a value of L/D = 0.030. The amplitude of oscillation (± 6 deg) corresponds to a considerably smaller amplitude than used in the present experiments. However, the results here show only a small increase in heat transfer in the attached boundary layer region. Apparently, the difference in the type of the unsteadiness (flow pulsation versus cylinder rotation) affects the interaction with the flow turbulence. In the wake region of the present experiment, however, flow pulsation increased the average heat transfer by 7.6 percent.

The results presented here are also different from those of Simoneau et al. (1984), who found increases of up to 30 percent in the average heat transfer due to the presence of 10 percent unsteadiness created by simulated rotor wakes. The dimensionless frequencies and amplitude of this unsteadiness, the cylinder Reynolds number, and turbulence intensities were all close to the range presently studied. The difference between the present results and the previous results with rotor wakes is the separation of the effects of turbulence and flow unsteadiness. The observed heat transfer increase was subsequently shown to be caused by the increased turbulence in the rotor wakes rather than the flow pulsation introduced (Morehouse and Simoneau, 1986).

In a different geometry the effect of free-stream flow pulsation has been investigated for flow over a flat plate by Parikh et al. (1982) and Miller (1969). They found no pulsation effect on the time-averaged turbulent boundary layer. Later work by Miller and Pucci (1971) in flows with adverse pressure gradients demonstrated that flow pulsation promoted early transition and separation of the boundary layer. This increased or decreased the heat transfer correspondingly. The present results also indicate a shift of the separation and transition points when free-stream turbulence is added to the flow.

The present results indicate either no or small increases in heat transfer due to flow pulsation with turbulence, the same as without turbulence (Andraka and Diller, 1985). Consequently, there is no evidence of any coupling between the effects of the free-stream turbulence and a sinusoidal flow pulsation. It should be noted that the integral time scale of the turbulence is more than an order of magnitude smaller than that of the flow pulsations. A topic for further investi-

gation would be be investigate the possibility of interaction when these two time scales are more nearly matched.

Conclusions

The time-averaged local distributions of heat transfer were obtained around a heated cylinder placed in a turbulent and pulsating crossflow. The results showed the expected distribution of heat transfer due to free-stream turbulence alone. A large increase (up to 45 percent) on the front side of the cylinder and a small decrease (up to 6 percent) on the back side of the cylinder were as expected.

The addition of flow pulsation to the turbulent flow produced no significant change to the observed heat transfer on the front side of the cylinder. Small increases in the average heat transfer values (up to 7.5 percent) were measured on the back side of the cylinder. This is similar to the results obtained without turbulence (Andraka and Diller, 1985). Thus there appears to be no evidence of any coupling between the effects of free-stream turbulence and flow pulsation on the heat transfer. It is also apparent from these results that the nature of the flow unsteadiness (turbulence versus a well-organized flow pulsation) is very important in determining the resulting overall heat transfer augmentation.

Acknowledgments

The support of the Department of Energy, Grant No. DE-A505-82ER12022 is gratefully acknowledged. This is a project in the program of Dr. Oscar P. Manley, Division of Engineering and Geosciences of the Office of Basic Energy Sciences.

References

Andraka, C. E., and Diller, T. E., 1985, "Heat Transfer Distribution Around a Cylinder in Pulsating Crossflow," ASME *Journal of Engineering for Gas Turbines and Power*, Vol. 107, pp. 976–982.

Barbi, C., Favier, D., Maresca, C., and Telionis, D. P., 1986, "Vortex Shedding and Lock-on of a Circular Cylinder in Oscillating Flow," *J. Fluid Mechanics*, Vol. 170, pp. 527–544.

Bergles, A. E., 1969, "Survey and Evaluation of Techniques to Augment Convective Heat and Mass Transfer," *Progress in Heat and Mass Transfer*, Vol. 1, pp. 331–422.

Borell, G. J., and Diller, T. E., 1987, "A Convective Calibration Method for Local Heat Flux Gages," ASME JOURNAL OF HEAT TRANSFER, Vol. 109, pp. 83–89.

Doorly, D. J., and Oldfield, M. L. G., 1985, "Simulation of the Effects of Shock Wave Passing on a Turbine Rotor Blade," ASME *Journal of Engineering for Gas Turbines and Power*, Vol. 107, pp. 998–1006.

Kestin, J., and Wood, R., 1971, "The Influence of Turbulence on Mass Transfer From Cylinders," ASME JOURNAL OF HEAT TRANSFER, Vol. 93, pp. 321–327.

Marziale, M. L., and Mayle, R. E., 1984, "Effect of an Oscillating Flow Direction on Leading Edge Heat Transfer," ASME *Journal of Engineering for Gas Turbines and Power*, Vol. 106, pp. 222–227.

Miller, J. A., 1969, "Heat Transfer in the Oscillating Turbulent Boundary Layer," ASME *Journal of Engineering for Power*, Vol. 91, pp. 239–244.

Miller, J. A., and Pucci, P. F., 1971, "Heat Transfer to an Airfoil in Oscillating Flow," ASME *Journal of Engineering for Power*, Vol. 93, 1971, pp. 641–645.

Morehouse, K. A., and Simoneau, R. J., 1986, "Effect of a Rotor Wake on the Local Heat Transfer on the Forward Half of a Circular Cylinder," *Heat Transfer 1986*, Vol. 3, C. L. Tien et al., eds., Hemisphere Pub. Co., Washington, pp. 1249–1255.

O'Brien, J. E., 1988, "Effects of Wake Passing on Stagnation Region Heat Transfer," in: *Heat Transfer in Gas Turbine Engines and Three-Dimensional Flows*, E. Elovic et al., eds., ASME, NY, pp. 17–28.

Parikh, D. G., Jayaraman, R., and Reynolds, W. C., 1982, "Dynamics of an Unsteady Turbulent Boundary Layer," in: *Turbulent Shear Flows 3*, L. J. S. Bradbury, F. Durst, B. E. Launder, F. W. Schmidt, and J. H. Whitelaw, eds., Springer-Verlag, Berlin, pp. 34–45.

Simoneau, R. J., Morehouse, K. A., VanFossen, G. J., and Behning, F. P., 1984, "Effect of Rotor Wake on Heat Transfer From a Circular Cylinder," ASME Paper No. 84-HT-25.

VanFossen, G. J., and Simoneau, R. J., "A Study of the Relationship Between Free-Stream Turbulence and Stagnation Region Heat Transfer," ASME JOURNAL OF HEAT TRANSFER, Vol. 109, pp. 10–15.

Zukauskas, A., and Ziugzda, J., 1985, *Heat Transfer of a Cylinder in Crossflow*, Hemisphere Pub. Co., Washington, DC.

Measurement of Heat Transfer From a Supersonic Impinging Jet Onto an Inclined Flat Plate at 45 deg

Chan Lee,[1] Myung Kyoon Chung,[2] Kyung Bin Lim,[3] and Yoon Soo Kang[3]

Nomenclature

A_e, A_t = exit, throat area of nozzle
d = thickness of plate
D = jet exit diameter = 100 mm in present experiment
h = local heat transfer coefficient
k_g = thermal conductivity of hot gas
k_s = thermal conductivity of plate
L = distance from jet exit to plate surface
M = Mach number
Nu = Nusselt number = hD/k_g
ΔNu = uncertainty of Nusselt number
Pr = Prandtl number
Re = Reynolds number
t = measurement time
T_o = jet total temperature
U = mean velocity at jet exit
x, y, z = Cartesian coordinates, see Fig. 1
α = thermal diffusivity of plate

1 Introduction

The problem of heat and momentum transfer by the impingement of a jet on a solid object arises in a wide variety of engineering devices, such as multistage rocket separation, jet engine exhaust impingement of V/STOL aircraft, shock impingement heating, and so on.

Previous investigations of this problem were mainly conducted with subsonic impinging jets. Foss (1979) examined the flow field of an oblique jet with a jet Reynolds number of 48,000 and a jet spacing of $L/D=5$. A series of experimental studies by Goldstein et al. (1986) and Goldstein and Franchett (1988) revealed the effects of the jet impingement angle and jet spacing on heat transfer and they suggested a practical correlation of Nusselt number over the plate surface. Sparrow and Lovell (1980) measured the heat transfer of an oblique impinging circular jet using the naphthalene sublimation technique.

However, studies of momentum and heat transfer in the supersonic jet impingement are rarely found because of the complexities of interactions between shock waves and the boundary layer and also because of the difficulties in measurement of the high pressure and the temperature on the plate surface. Papers by Donaldson and Snedeker (1971) and Donaldson et al. (1971) were concerned with the free jet turbulent structure and the heat transfer of an impinging jet normal to a plate at Mach number near unity. Their results showed that at large distances from the stagnation point the heat transfer falls off inversely proportional to the distance. The impingement of underexpanded, axisymmetric jets on normal and in-

[1]Graduate Student, Department of Aerospace Engineering, Korea Advanced Institute of Science and Technology, Cheongryang, Seoul, Korea.

[2]Professor, Department of Mechanical Engineering, Korea Advanced Institute of Science and Technology, Cheongryang, Seoul, Korea.

[3]Senior Researcher, Agency for Defence Development, Daeduck Science Town, Daeduck, Korea.

Contributed by the Heat Transfer Division for publication in the JOURNAL OF HEAT TRANSFER. Manuscript received by the Heat Transfer Division March 28, 1990; revision received December 6, 1990. Keywords: Forced Convection, Jets, Measurement Techniques.

gation would be be investigate the possibility of interaction when these two time scales are more nearly matched.

Conclusions

The time-averaged local distributions of heat transfer were obtained around a heated cylinder placed in a turbulent and pulsating crossflow. The results showed the expected distribution of heat transfer due to free-stream turbulence alone. A large increase (up to 45 percent) on the front side of the cylinder and a small decrease (up to 6 percent) on the back side of the cylinder were as expected.

The addition of flow pulsation to the turbulent flow produced no significant change to the observed heat transfer on the front side of the cylinder. Small increases in the average heat transfer values (up to 7.5 percent) were measured on the back side of the cylinder. This is similar to the results obtained without turbulence (Andraka and Diller, 1985). Thus there appears to be no evidence of any coupling between the effects of free-stream turbulence and flow pulsation on the heat transfer. It is also apparent from these results that the nature of the flow unsteadiness (turbulence versus a well-organized flow pulsation) is very important in determining the resulting overall heat transfer augmentation.

Acknowledgments

The support of the Department of Energy, Grant No. DE-A505-82ER12022 is gratefully acknowledged. This is a project in the program of Dr. Oscar P. Manley, Division of Engineering and Geosciences of the Office of Basic Energy Sciences.

References

Andraka, C. E., and Diller, T. E., 1985, "Heat Transfer Distribution Around a Cylinder in Pulsating Crossflow," ASME *Journal of Engineering for Gas Turbines and Power*, Vol. 107, pp. 976–982.

Barbi, C., Favier, D., Maresca, C., and Telionis, D. P., 1986, "Vortex Shedding and Lock-on of a Circular Cylinder in Oscillating Flow," *J. Fluid Mechanics*, Vol. 170, pp. 527–544.

Bergles, A. E., 1969, "Survey and Evaluation of Techniques to Augment Convective Heat and Mass Transfer," *Progress in Heat and Mass Transfer*, Vol. 1, pp. 331–422.

Borell, G. J., and Diller, T. E., 1987, "A Convective Calibration Method for Local Heat Flux Gages," ASME JOURNAL OF HEAT TRANSFER, Vol. 109, pp. 83–89.

Doorly, D. J., and Oldfield, M. L. G., 1985, "Simulation of the Effects of Shock Wave Passing on a Turbine Rotor Blade," ASME *Journal of Engineering for Gas Turbines and Power*, Vol. 107, pp. 998–1006.

Kestin, J., and Wood, R., 1971, "The Influence of Turbulence on Mass Transfer From Cylinders," ASME JOURNAL OF HEAT TRANSFER, Vol. 93, pp. 321–327.

Marziale, M. L., and Mayle, R. E., 1984, "Effect of an Oscillating Flow Direction on Leading Edge Heat Transfer," ASME *Journal of Engineering for Gas Turbines and Power*, Vol. 106, pp. 222–227.

Miller, J. A., 1969, "Heat Transfer in the Oscillating Turbulent Boundary Layer," ASME *Journal of Engineering for Power*, Vol. 91, pp. 239–244.

Miller, J. A., and Pucci, P. F., 1971, "Heat Transfer to an Airfoil in Oscillating Flow," ASME *Journal of Engineering for Power*, Vol. 93, 1971, pp. 641–645.

Morehouse, K. A., and Simoneau, R. J., 1986, "Effect of a Rotor Wake on the Local Heat Transfer on the Forward Half of a Circular Cylinder," *Heat Transfer 1986*, Vol. 3, C. L. Tien et al., eds., Hemisphere Pub. Co., Washington, pp. 1249–1255.

O'Brien, J. E., 1988, "Effects of Wake Passing on Stagnation Region Heat Transfer," in: *Heat Transfer in Gas Turbine Engines and Three-Dimensional Flows*, E. Elovic et al., eds., ASME, NY, pp. 17–28.

Parikh, D. G., Jayaraman, R., and Reynolds, W. C., 1982, "Dynamics of an Unsteady Turbulent Boundary Layer," in: *Turbulent Shear Flows 3*, L. J. S. Bradbury, F. Durst, B. E. Launder, F. W. Schmidt, and J. H. Whitelaw, eds., Springer-Verlag, Berlin, pp. 34–45.

Simoneau, R. J., Morehouse, K. A., VanFossen, G. J., and Behning, F. P., 1984, "Effect of Rotor Wake on Heat Transfer From a Circular Cylinder," ASME Paper No. 84-HT-25.

VanFossen, G. J., and Simoneau, R. J., "A Study of the Relationship Between Free-Stream Turbulence and Stagnation Region Heat Transfer," ASME JOURNAL OF HEAT TRANSFER, Vol. 109, pp. 10–15.

Zukauskas, A., and Ziugzda, J., 1985, *Heat Transfer of a Cylinder in Crossflow*, Hemisphere Pub. Co., Washington, DC.

Measurement of Heat Transfer From a Supersonic Impinging Jet Onto an Inclined Flat Plate at 45 deg

Chan Lee,[1] Myung Kyoon Chung,[2] Kyung Bin Lim,[3] and Yoon Soo Kang[3]

Nomenclature

A_e, A_t = exit, throat area of nozzle
d = thickness of plate
D = jet exit diameter = 100 mm in present experiment
h = local heat transfer coefficient
k_g = thermal conductivity of hot gas
k_s = thermal conductivity of plate
L = distance from jet exit to plate surface
M = Mach number
Nu = Nusselt number = hD/k_g
ΔNu = uncertainty of Nusselt number
Pr = Prandtl number
Re = Reynolds number
t = measurement time
T_o = jet total temperature
U = mean velocity at jet exit
x, y, z = Cartesian coordinates, see Fig. 1
α = thermal diffusivity of plate

1 Introduction

The problem of heat and momentum transfer by the impingement of a jet on a solid object arises in a wide variety of engineering devices, such as multistage rocket separation, jet engine exhaust impingement of V/STOL aircraft, shock impingement heating, and so on.

Previous investigations of this problem were mainly conducted with subsonic impinging jets. Foss (1979) examined the flow field of an oblique jet with a jet Reynolds number of 48,000 and a jet spacing of $L/D=5$. A series of experimental studies by Goldstein et al. (1986) and Goldstein and Franchett (1988) revealed the effects of the jet impingement angle and jet spacing on heat transfer and they suggested a practical correlation of Nusselt number over the plate surface. Sparrow and Lovell (1980) measured the heat transfer of an oblique impinging circular jet using the naphthalene sublimation technique.

However, studies of momentum and heat transfer in the supersonic jet impingement are rarely found because of the complexities of interactions between shock waves and the boundary layer and also because of the difficulties in measurement of the high pressure and the temperature on the plate surface. Papers by Donaldson and Snedeker (1971) and Donaldson et al. (1971) were concerned with the free jet turbulent structure and the heat transfer of an impinging jet normal to a plate at Mach number near unity. Their results showed that at large distances from the stagnation point the heat transfer falls off inversely proportional to the distance. The impingement of underexpanded, axisymmetric jets on normal and in-

[1]Graduate Student, Department of Aerospace Engineering, Korea Advanced Institute of Science and Technology, Cheongryang, Seoul, Korea.

[2]Professor, Department of Mechanical Engineering, Korea Advanced Institute of Science and Technology, Cheongryang, Seoul, Korea.

[3]Senior Researcher, Agency for Defence Development, Daeduck Science Town, Daeduck, Korea.

Contributed by the Heat Transfer Division for publication in the JOURNAL OF HEAT TRANSFER. Manuscript received by the Heat Transfer Division March 28, 1990; revision received December 6, 1990. Keywords: Forced Convection, Jets, Measurement Techniques.

Table 1 Experimental conditions

Area ratio (A_e/A_t)	5.15
Chamber pressure (P_o)	8.96 MPa
Total temperature (T_o)	2871 K
Jet exit pressure (P_j)	0.263 MPa
Ambient pressure (P_∞)	0.101 MPa
Jet exit temperature (T_j)	1555 K
Ambient temperature (T_∞)	286 K
Jet exit Mach number (M)	2.82
Jet Reynolds number (Re)	8.47×10^5
Underexpansion ratio (P_j/P_∞)	2.604
Heat capacity of gas (C_p)	1.775 kJ/kg K
Thermal conductivity of gas (k_g)	0.0419 W/m K

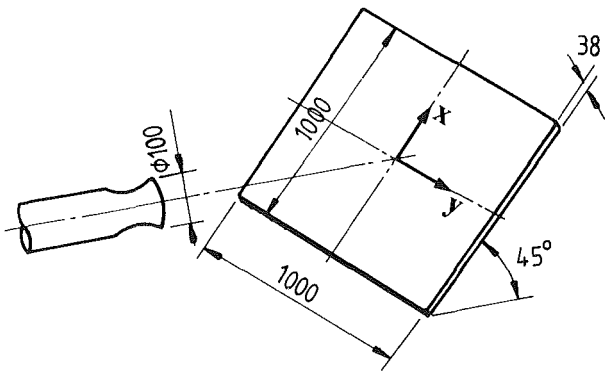

Fig. 1 Schematic diagram showing a supersonic jet impingement onto an inclined plate surface

clined flat plates was experimentally studied by Lamont and Hunt (1980). They observed that multiple shock waves are created by the plate in the stagnation region.

The present experiment was performed with a supersonic jet from a rocket nozzle. Since direct instantaneous measurements of high temperature and heat flux on the plate surface are nearly impossible in heated supersonic impinging jet by presently available techniques, local heat transfer was obtained by applying a locally quasi-one-dimensional heat conduction model to the temperature data measured beneath the plate surface. This indirect method was used to determine the Nusselt number, as will be explained in the following section.

2 Experimental Apparatus and Operational Procedure

Supersonic gas for the jet impingement was supplied by a rocket nozzle; operating conditions are listed in Table 1. The solid propellant contains about 82 percent ammonium perchlorate oxidizer, 12 percent carboxyl terminated polybutadiene binder, 2 percent aluminum metal fuel, and the remaining 4 percent additives. The composition of the combustion gas and its thermochemical properties under the conditions in Table 1 are calculated by using a thermodynamic calculation code from Gordon and McBride (1971). The major combustion products are CO (16.0 percent), CO_2 (10.6 percent), HCl (17.2 percent), H_2 (16.4 percent), H_2O (30.4 percent), and N_2 (8.6 percent), and its thermochemical properties are also included in Table 1.

The distance between the jet exit and the plate surface is 5 diameters, and the angle between the axis of the jet and the plate surface is set at 45 deg. The test plate used is a rectangular flat plate whose dimensions are 1000 mm high, 1000 mm wide, and 38 mm thick. This plate is made of aluminum and the back side of the plate is insulated. The test plate contains 25 thermocouple holes equally spaced in the x and y directions where x is pointing upward as shown in Fig. 1 along the x axis in the jet center plane. Five thermocouples are embedded at a depth of 20 mm from the plate surface. The holes are bored from the back side of plate. On the left side ten thermocouples are placed at a depth of 5 mm, and on the right side the depth of the ten thermocouples is 35 mm. The chromel-alumel thermocouples are used in the present study and the interior temperature variation with time at each probe location is obtained at time intervals of 0.01 s. With these measured temperature data, the local heat transfer at the surface can be determined by using a locally quasi-one-dimensional conduction model, which will be described below. This indirect method of determining the heat transfer is based upon the assumption that the conductive heat transfer in the direction of the plate depth (z direction) is much larger than those in any other lateral directions (x, y directions) when the test plate is heated by a high-temperature jet.

The mathematical model for heating of the test plate is represented by

$$\frac{\partial T}{\partial t} = \alpha \frac{\partial^2 T}{\partial z^2} \qquad 0 \le z \le d, \quad t \ge 0, \tag{1}$$

with initial and boundary conditions of

$$T = T_\infty \quad \text{at} \quad t = 0, \tag{2}$$

and

$$-k_s \frac{\partial T}{\partial z} = h(T_o - T) \quad \text{at} \quad z = 0, \tag{3}$$

$$-k_s \frac{\partial T}{\partial z} = 0 \quad \text{at} \quad z = d. \tag{4}$$

The solution of equations (1)–(4) is found by Luikov (1969) as

$$\frac{T - T_\infty}{T_o - T_\infty} = 1 - \sum_{n=1}^{\infty} A_n \cos\left[\mu_n\left(1 - \frac{z}{d}\right)\right] \exp\left(-\mu_n^2 \frac{t\alpha}{d^2}\right), \tag{5}$$

where

$$A_n = \frac{2 \sin \mu_n}{\sin \mu_n \cos \mu_n + \mu_n},$$

and the eigenvalues μ_n are obtained from the characteristics equation

$$\tan \mu_n = \frac{\mathrm{Nu}}{\mu_n}\left(\frac{dk_g}{Dk_s}\right). \tag{6}$$

Once the interior temperature variations in the test plate are measured during the heating transient, the time-dependent local Nusselt numbers are determined through the iterative calculations of Eqs. (5) and (6). During the hot jet impingement of about 3.2 s by the supersonic rocket nozzle, the surface of the aluminum plate is melted after about 1 s from the firing of the rocket. Therefore, only the measured data before melting of the surface are used in the present calculations.

3 Results and Discussions

Before computing the heat transfer coefficients by the locally quasi-one-dimensional heat conduction analysis, its validity must be verified. Using the temperature data obtained in a preliminary experiment, the lateral slope of the temperature (dT/dy or dT/dx) was found to be less than 5 percent of the depthwise temperature slope (dT/dz) at any time during the measurement, and thus, the lateral heat conduction can be neglected under the uncertainty of the present measurement.

In general, the local Nusselt number is a function of L/D, x/D, y/D, Pr, Re, and M. Therefore, in the present experiment, Nu is a function of location since Re, Pr, M, and L/D are fixed; $\mathrm{Nu} = f(x/D, y/D)$.

First, consider the distribution of Nusselt number along the x axis in the jet center plane. As shown in Fig. 2, the maximum

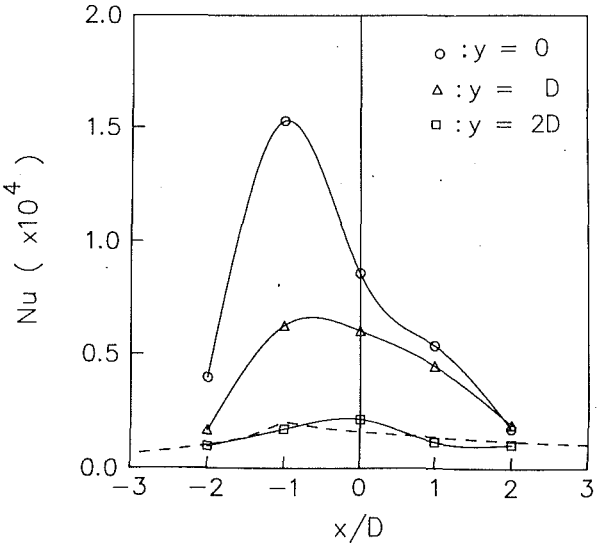

Fig. 2 Distributions of local Nusselt numbers at different y positions; dotted line represents the data of Goldstein (1988) for subsonic jet at $y=0$

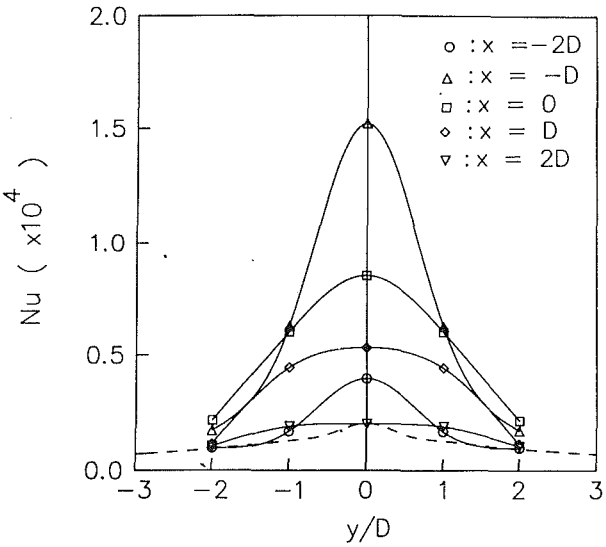

Fig. 3 Distributions of local Nusselt numbers at different x positions; dotted line represents the data of Goldstein (1988) for subsonic jet at $x=-D$

heat transfer occurs at the location displaced downstream ($x/D<0$) for given y, and the local Nusselt number in the downstream region away from the maximum point is more abruptly decreased than that in the upstream region ($x/D>0$). This may be attributed to the fact that shock-induced separation occurs near the stagnation point (Lamont and Hunt, 1980). The existence of an inflection point in the upward region indicates a small pressure hump due to the interactions between shock waves created by the plate. The upstream movement of the peak heat transfer point with the increase in y may be related to the crescent-shaped stagnation ridge. Comparison of our results with those of subsonic impinging jet observed by Goldstein and Franchett (1988) reveals that the shapes of the local Nusselt number variations along the x axis are similar. However, the maximum heat transfer coefficient of the supersonic jet is about 10 times higher than that of the subsonic jet.

Figure 3 represents the heat transfer distributions along the y direction. As was expected, the profiles are nearly symmetric with respect to the x axis. The Nusselt number sharply decreases with increasing distance y, and the value of the local Nusselt number of the supersonic impinging jet approaches that of the subsonic jet as the distance increases. Similar variations were found by Donaldson et al. (1971), who observed that away from the stagnation point on the plate, the heat transfer behaves in a manner similar to a normal turbulent boundary layer, which is developed in an external flow having a free-stream velocity equal to the local maximum velocity in the wall jet.

Figure 4 shows the contours of constant Nusselt numbers. Since the jet impinges on the surface at 45 deg inclination, the contours are quasi-elliptical. Also, these results have a tendency similar to the subsonic cases of Goldstein and Franchett (1988) and Sparrow and Lovell (1980).

Since only one data set is available in the present study, the reliable range of the Nusselt numbers obtained in this study must be estimated. In the present measurement, the Nusselt number is determined from three measured quantities: thermocouple temperature reading (T), measurement time (t), and probe position (z). Therefore, the uncertainty in the result of the Nusselt number is caused by uncertainties of t, z, and T as given by Holman (1966):

$$\Delta \mathrm{Nu} = \left[\left(\frac{\partial \mathrm{Nu}}{\partial h} \Delta h \right)^2 + \left(\frac{\partial \mathrm{Nu}}{\partial D} \Delta D \right)^2 + \left(\frac{\partial \mathrm{Nu}}{\partial k_g} \Delta k_g \right)^2 \right]^{1/2}, \quad (7)$$

where

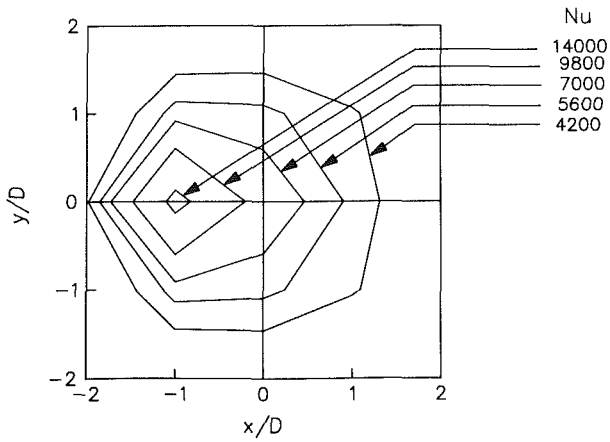

Fig. 4 Contours of constant Nusselt numbers

$$\Delta h = \left[\left(\frac{\partial h}{\partial t} \Delta t \right)^2 + \left(\frac{\partial h}{\partial z} \Delta z \right)^2 + \left(\frac{\partial h}{\partial T} \Delta T \right)^2 \right]^{1/2}. \quad (8)$$

The uncertainty Δt is due to the variation in the response time of the thermocouples and it is estimated to be about $\Delta t<0.03$ s. The positioning uncertainty Δz may be set equal to the tolerance of drilling; thus, $\Delta z=\pm 0.5$ mm. According to the specification of the K-type thermocouples provided by the manufacturer, the uncertainty in the temperature reading is about ± 0.7 K. In addition, $\Delta D=\pm 0.1$ mm and $\Delta k_g=\pm 0.0001$ W/mK.

On the other hand, the sensitivities in Eq. (8) were obtained by solving Eqs. (5) and (6) for finitely small variations in t, z, and T. The uncertainty analysis shows that the present experimental results are reliable within 15 percent uncertainty, which is comparable to those of other subsonic impinging jet experiments (Goldstein and Franchett, 1988).

References

Donaldson, C. D., and Snedeker, R. S., 1971, "A Study of Free Jet Impingement. Part 1. Mean Properties of Free and Impinging Jets," *J. Fluid Mech.*, Vol. 45, pp. 281-319.

Donaldson, C. D., Snedeker, R. S., and Margolis, D. P., 1971, "A Study of Free Jet Impingement. Part 2. Free Jet Turbulent Structure and Impingement Heat Transfer," *J. Fluid Mech.*, Vol. 45, pp. 477-512.

Foss, J. F., 1979, "Measurement in a Large-Angle Oblique Jet Impingement Flow," *AIAA Journal*, Vol. 17, pp. 801-802.

Goldstein, R. J., Behbahani, A., and Heppelmann, K. K., 1986, "Streamwise Distribution of the Recovery Factor and the Local Heat Transfer Coefficient to an Impinging Circular Air Jet," *Int. J. Heat Mass Transfer*, Vol. 29, pp. 1227–1235.

Goldstein, R. J., and Franchett, M. E., 1988, "Heat Transfer From a Flat Surface to an Oblique Impinging Jet," ASME JOURNAL OF HEAT TRANSFER, Vol. 110, pp. 84–90.

Gordon, S., and McBride, B. J., 1971, "Computer Program for Calculation of Complex Chemical Equilibrium Compositions, Rocket Performance, Incident and Reflected Shocks and Chapman-Jouguet Detonations," NASA SP-273.

Holman, J. P., 1966, *Experimental Methods for Engineers*, McGraw-Hill, New York, pp. 37–42.

Lamont, D. J., and Hunt, B. L., 1980, "The Impingement of Underexpanded, Axisymmetric Jets on Perpendicular and Inclined Flat Plates," *J. Fluid Mech.*, Vol. 100, pp. 471–511.

Luikov, A. V., 1969, *Analytical Heat Diffusion Theory*, Academic Press, New York, pp. 238–239.

Sparrow, E. M., and Lovell, B. J., 1980, "Heat Transfer Characteristics of an Obliquely Impinging Circular Jet," ASME JOURNAL OF HEAT TRANSFER, Vol. 102, pp. 202–209.

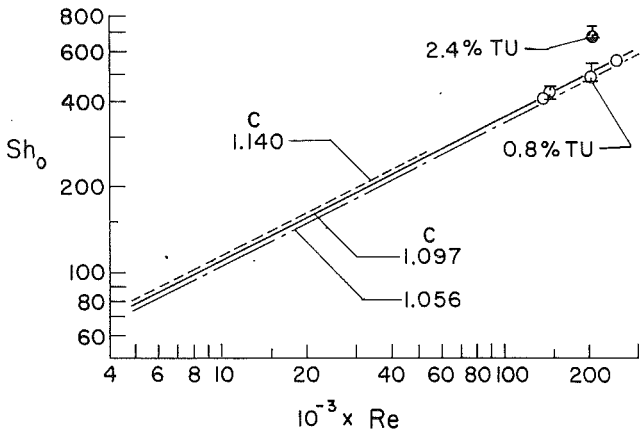

Fig. 1 Summary of stagnation point mass transfer results: Coefficient *C* refers to equation (1). *C* = 1.140 represents experimental work in [3] based on solid naphthalene specific gravity 1.146; *C* = 1.097 is a combination of the experimental work in both [3] and [4] based on specific gravity 1.068; and *C* = 1.056 represents the real flow solution of the laminar boundary layer equations. Influence of increasing wind tunnel turbulence intensity is also shown.

An Improved Correlation of Stagnation Point Mass Transfer From Naphthalene Circular Disks Facing Uniform Airstreams

H. H. Sogin[1]

Introduction

The basis and purpose of the heat–mass transfer experimental analog using subliming naphthalene is presumed to be well known [e.g., 1, 2]. Experiments like the ones described here and comparisons of their results with those of boundary layer theory serve to refine the calibration of the analog and to improve techniques. This technical note correlates the results of two studies [3, 4] on (local) stagnation point mass transfer from circular disks. It also provides some information about the influence of wind tunnel turbulence. We begin with an illustrative summary that will guide us through the remainder of the technical note.

Figure 1 is a composite bilogarithmic plot of three sets of results taken from [3, 4]. The stagnation point Sherwood number, $Sh_o = K_oD/\mathfrak{D}$, is plotted against the disk Reynolds number, $Re = U_\infty D/\nu$, where K_o is the stagnation point coefficient of mass transfer, $\mathfrak{D}$ is the diffusivity of naphthalene vapor in air, U_∞ is the velocity of the oncoming airstream; and ν is the kinematic viscosity of air. The disk diameter D was 3.493 cm in [3] and 10.2 cm in [4]. Each of the three straight lines in Fig. 1 is identified by a value of the coefficient C in the typical correlation equation

$$Sh_o = C \cdot Re^{1/2} \tag{1}$$

which represents both experimental and theoretical results. The next three sections explain the sources of these lines.

Experimental Results of Sparrow and Geiger (C = 1.140)

Local mass transfer is determined by measuring the local change of depth owing to sublimation and multiplying it by the density of the solid naphthalene. In [3] the nominal resolving power of the instrumentation for measuring the recession of the naphthalene was 0.00025 mm (0.00001 in.). The uppermost line in Fig. 1, spanning the range of Re from 5000 to 50,000, represents six data points correlated by the method of least squares [3]; the mean scatter is ±3 percent. The specific gravity of the solid naphthalene assumed in reducing the data was 1.146. For reasons explained in the next paragraph, this value must be considered high for naphthalene that has been poured into a mold exposed to the atmosphere.

One of the earliest and most meticulous determinations of specific gravity is due to Schröder [5, 6]. He used the method of weighing known volumes of samples in liquids of known density. Critical tables and handbooks quote his value for naphthalene, namely, 1.145 at 20°C. In the course of his measurements he identified two major difficulties: that all polycrystalline materials develop small cavities and that removing all of the gas bubbles is an onerous task often accompanied by side effects further complicating experimental procedure. In short, he had to overcome the effect of porosity. Dewar [7], who also measured the specific gravity of numerous compounds, reported 1.1589 for naphthalene at 17°C. He gave this description of the preparation of his samples:

> Salts were employed in the form of compressed blocks. The salt, previously reduced to a fine powder, was moistened with water and compressed in a cylindrical steel mould under great hydraulic pressure. ... In order to get cylindrical blocks of the salts showing no porosity ... the saturated salt solution...was found to be essential during the application of pressure. In the same way it was found to be an advantage in compressing such a substance as solid carbonic acid to moisten it with a fluid like ether before applying the hydraulic pressure.

Owing to the context, we must suppose that he treated naphthalene similarly to the way he treated the dry ice. Since none of these precautions are taken in preparing the naphthalene models, one must assume they are porous. Accordingly, the handbook values of specific gravity in the literature are upper limits. What aspects of the casting procedure affect the porosity and how much the porosity might be under any particular set of circumstances have not yet been systematically or satisfactorily determined.

Combining All the Experimental Results (C = 1.097)

The method of determining the stagnation point mass transfer in [4] was very much the same as the one in [3]. There were significant differences in the instrumentation and models. The least count of the profiling instrument was 0.0025 mm (0.0001 in.), ten times the value available in [3]. The specimens in [4]

[1]Emeritus Professor of Mechanical Engineering, Tulane University, New Orleans, LA 70118.

Contributed by the Heat Transfer Division of THE AMERICAN SOCIETY OF MECHANICAL ENGINEERS. Manuscript received by the Heat Transfer Division July 30, 1990; revision received November 26, 1990. Keywords: Analog Techniques, Forced Convection, Mass Transfer.

Goldstein, R. J., Behbahani, A., and Heppelmann, K. K., 1986, "Streamwise Distribution of the Recovery Factor and the Local Heat Transfer Coefficient to an Impinging Circular Air Jet," *Int. J. Heat Mass Transfer*, Vol. 29, pp. 1227–1235.

Goldstein, R. J., and Franchett, M. E., 1988, "Heat Transfer From a Flat Surface to an Oblique Impinging Jet," ASME JOURNAL OF HEAT TRANSFER, Vol. 110, pp. 84–90.

Gordon, S., and McBride, B. J., 1971, "Computer Program for Calculation of Complex Chemical Equilibrium Compositions, Rocket Performance, Incident and Reflected Shocks and Chapman-Jouguet Detonations," NASA SP-273.

Holman, J. P., 1966, *Experimental Methods for Engineers*, McGraw-Hill, New York, pp. 37–42.

Lamont, D. J., and Hunt, B. L., 1980, "The Impingement of Underexpanded, Axisymmetric Jets on Perpendicular and Inclined Flat Plates," *J. Fluid Mech.*, Vol. 100, pp. 471–511.

Luikov, A. V., 1969, *Analytical Heat Diffusion Theory*, Academic Press, New York, pp. 238–239.

Sparrow, E. M., and Lovell, B. J., 1980, "Heat Transfer Characteristics of an Obliquely Impinging Circular Jet," ASME JOURNAL OF HEAT TRANSFER, Vol. 102, pp. 202–209.

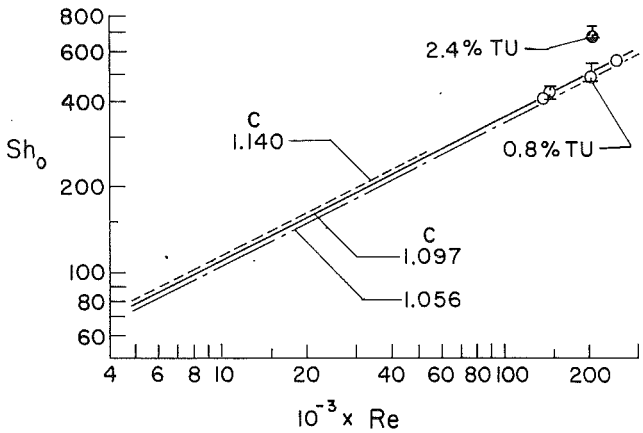

Fig. 1 Summary of stagnation point mass transfer results: Coefficient *C* refers to equation (1). *C* = 1.140 represents experimental work in [3] based on solid naphthalene specific gravity 1.146; *C* = 1.097 is a combination of the experimental work in both [3] and [4] based on specific gravity 1.068; and *C* = 1.056 represents the real flow solution of the laminar boundary layer equations. Influence of increasing wind tunnel turbulence intensity is also shown.

An Improved Correlation of Stagnation Point Mass Transfer From Naphthalene Circular Disks Facing Uniform Airstreams

H. H. Sogin[1]

Introduction

The basis and purpose of the heat–mass transfer experimental analog using subliming naphthalene is presumed to be well known [e.g., 1, 2]. Experiments like the ones described here and comparisons of their results with those of boundary layer theory serve to refine the calibration of the analog and to improve techniques. This technical note correlates the results of two studies [3, 4] on (local) stagnation point mass transfer from circular disks. It also provides some information about the influence of wind tunnel turbulence. We begin with an illustrative summary that will guide us through the remainder of the technical note.

Figure 1 is a composite bilogarithmic plot of three sets of results taken from [3, 4]. The stagnation point Sherwood number, $Sh_o = K_oD/\mathfrak{D}$, is plotted against the disk Reynolds number, $Re = U_\infty D/\nu$, where K_o is the stagnation point coefficient of mass transfer, $\mathfrak{D}$ is the diffusivity of naphthalene vapor in air, U_∞ is the velocity of the oncoming airstream; and ν is the kinematic viscosity of air. The disk diameter D was 3.493 cm in [3] and 10.2 cm in [4]. Each of the three straight lines in Fig. 1 is identified by a value of the coefficient C in the typical correlation equation

$$Sh_o = C \cdot Re^{1/2} \tag{1}$$

which represents both experimental and theoretical results. The next three sections explain the sources of these lines.

Experimental Results of Sparrow and Geiger (C = 1.140)

Local mass transfer is determined by measuring the local change of depth owing to sublimation and multiplying it by the density of the solid naphthalene. In [3] the nominal resolving power of the instrumentation for measuring the recession of the naphthalene was 0.00025 mm (0.00001 in.). The uppermost line in Fig. 1, spanning the range of Re from 5000 to 50,000, represents six data points correlated by the method of least squares [3]; the mean scatter is ±3 percent. The specific gravity of the solid naphthalene assumed in reducing the data was 1.146. For reasons explained in the next paragraph, this value must be considered high for naphthalene that has been poured into a mold exposed to the atmosphere.

One of the earliest and most meticulous determinations of specific gravity is due to Schröder [5, 6]. He used the method of weighing known volumes of samples in liquids of known density. Critical tables and handbooks quote his value for naphthalene, namely, 1.145 at 20°C. In the course of his measurements he identified two major difficulties: that all polycrystalline materials develop small cavities and that removing all of the gas bubbles is an onerous task often accompanied by side effects further complicating experimental procedure. In short, he had to overcome the effect of porosity. Dewar [7], who also measured the specific gravity of numerous compounds, reported 1.1589 for naphthalene at 17°C. He gave this description of the preparation of his samples:

> Salts were employed in the form of compressed blocks. The salt, previously reduced to a fine powder, was moistened with water and compressed in a cylindrical steel mould under great hydraulic pressure. ... In order to get cylindrical blocks of the salts showing no porosity ... the saturated salt solution...was found to be essential during the application of pressure. In the same way it was found to be an advantage in compressing such a substance as solid carbonic acid to moisten it with a fluid like ether before applying the hydraulic pressure.

Owing to the context, we must suppose that he treated naphthalene similarly to the way he treated the dry ice. Since none of these precautions are taken in preparing the naphthalene models, one must assume they are porous. Accordingly, the handbook values of specific gravity in the literature are upper limits. What aspects of the casting procedure affect the porosity and how much the porosity might be under any particular set of circumstances have not yet been systematically or satisfactorily determined.

Combining All the Experimental Results (C = 1.097)

The method of determining the stagnation point mass transfer in [4] was very much the same as the one in [3]. There were significant differences in the instrumentation and models. The least count of the profiling instrument was 0.0025 mm (0.0001 in.), ten times the value available in [3]. The specimens in [4]

[1]Emeritus Professor of Mechanical Engineering, Tulane University, New Orleans, LA 70118.

Contributed by the Heat Transfer Division of THE AMERICAN SOCIETY OF MECHANICAL ENGINEERS. Manuscript received by the Heat Transfer Division July 30, 1990; revision received November 26, 1990. Keywords: Analog Techniques, Forced Convection, Mass Transfer.

were about 8 mm deep, mounted in the wind tunnel on a thin sting. The disks in [3], besides being of smaller diameter than the ones in [4], were made integral with an inert afterbody, which served as a mount and protected the disk edges as well as the rear surfaces.

In [4] the value of the specific gravity of the solid naphthalene was determined by dividing the loss of weight by the integrated volume of recession. The mean value in twelve runs was found to be 1.068, 7 percent less than Schröder's value. Unfortunately, there is no record of the data spread for these measurements of specific gravity, which also included a systematic correction for edge losses from the disks.

The average results of the experiments in [4] at free turbulence intensity of the tunnel are shown by the open circles in Fig. 1. The bar at Re = 144,000 spans four points and the bar at 205,000 eight; the ends of the bars locate the extremes of the spreads. The total number of experimental points is 14, each representing the average of four determinations, as in [3]. The following method was used to correlate all 20 experimental points of the two studies.

In order to weigh all points uniformly, values of the Sherwood number were converted to values of the Frössling number:

$$\mathrm{Fg}_o \equiv \mathrm{Sh}_o/(\mathrm{Sc}\cdot\mathrm{Re}^{1/2}) = (K_o/U_\infty)\cdot\mathrm{Re}^{1/2} \qquad (2)$$

Clearly, Fg_o is independent of the Reynolds number in the present case, so averages are found by simple arithmetic. Thus, the experimental results of [3] correlate in accordance with $\mathrm{Fg}_o = 1.140/2.55 = 0.447 \pm 3$ percent on the average in the range of Re from 5000 to 50,000. In [4] the average value of Fg_o is 0.436 lying between extremes of 0.412 and 0.473 with a standard deviation of 4 percent of the average; Re ranges from 135,000 to 250,000. *Assuming* that the specific gravity of the solid in [3] was 1.068 as found in [4] and *then* averaging over the 20 experimental points, we find the average Frössling number of the combined studies to be 0.430. This translates to $C = 1.097$ in equation (1). Adjusting the value of the specific gravity for the results taken from [3] emphasizes the need to investigate the question of porosity where the experimental method is used to measure local rates of recession. If the results from [3] were not adjusted and the specific gravity 1.068 for the results in [4] were retained, the final correlation coefficient would be 1.120 instead of 1.097, hardly significantly different in view of the uncertainty of about ± 4 percent in the averages. The principal merit of the new correlation is that it bridges the gap between the two sets of data and broadens the applicable range of Reynolds number, the span now being 5000 to 250,000.

Real Flow Solution ($C = 1.056$)

The real flow solution is a solution of the boundary layer equations exactly like the so-called potential flow solution in [3], except that the velocity at the outer edge of the boundary layer is taken to be the distribution determined by measuring the pressure distribution on the forward surface of the disk and employing Bernoulli's principle. In general, for flow near a stagnation point, the velocity at the outer edge of the boundary layer is proportional to the oncoming velocity and virtually linear in the distance from the stagnation point. Thus in the case of a disk in axisymmetric flow,

$$v(r) = C'\cdot U_\infty (r/R) \qquad (3)$$

where $v(r)$ is the radial velocity component, r the local radius, R the disk radius, and C' is a constant of proportionality. The boundary layer solution shows that the mass transfer coefficient is proportional to the square root of the gradient of the velocity at the stagnation point, so that generally Sh_o is proportional to $(C'U_\infty/R)^{1/2}$. Pressure distributions were measured in [4] on two differently instrumented 10.2-cm-dia models. The results, consistent within themselves, yielded $C' = 0.480$ as compared with 0.454 in [8] and 0.637 for the potential flow solution. Barring significant changes of hydrodynamic conditions that might occur on account of disk profile owing to the nonuniform recession of the naphthalene surface or to effects of different afterbodies, the real flow solution for the slope of the velocity at the outer edge of the boundary layer yields $C = 1.056$ for the theoretical laminar transfer. The recommended line representing the data in Fig. 1 ($C = 1.097$) is about 4 percent higher than the prediction for the real flow solution. This difference perhaps could be rationalized in terms of the data spread, but it seems more likely ascribable to the influence of the mainstream turbulence and its effect on the boundary layers.

Influence of Turbulence in the Airstream

The turbulence intensity of the normal airstream in [4] was 0.8 percent. The cluster of points in Fig. 1 at Re = 205,000, $\mathrm{Sh}_o \approx 700$ was obtained in [4] by introducing a screen that raised the turbulence intensity to 2.4 percent. The mass transfer increased about 46 percent of the value predicted by the real flow solution. Overall, the trend of the increasing mass transfer rate with increasing turbulence intensity is consistent within itself and with other such findings [9]. There is no analysis that would serve to check these results.

Conclusions

The recommended correlation for the stagnation point mass transfer from circular naphthalene disks perpendicular to airstreams is

$$\mathrm{Sh}_o = 1.097\cdot\mathrm{Re}^{1/2} \pm 4 \text{ percent}; \quad 5000 < \mathrm{Re} < 250{,}000 \qquad (4)$$

Accordingly, a suitable interpolation to allow for a Schmidt number other than 2.55 is [3]

$$\mathrm{Sh}_o = 0.783\cdot\mathrm{Sc}^{0.36}\mathrm{Re}^{1/2} \qquad (5)$$

and by analogy the heat transfer would be calculated with

$$\mathrm{Nu}_o = 0.783\cdot\mathrm{Pr}^{0.36}\mathrm{Re}^{1/2} \qquad (6)$$

At Re = 205,000 (30.5 m/s) when the wind tunnel turbulence intensity is changed from 0.8 to 2.4 percent, the stagnation point transfer rate changes from about 4 to 46 percent in excess of the amount predicted by the real flow solution.

Finally, this study raises the following questions: How much is the porosity of naphthalene under various casting conditions? How do various afterbodies as well as mainstream turbulence affect the flow regime and transfer of mass or heat at the stagnation point region?

References

1 Incropera, F. P., and DeWitt, D. P., *Fundamentals of Heat Transfer*, 2nd ed., Wiley, New York, 1985, Chap. 6.

2 Sogin, H. H., "Sublimation From Disks to Air Streams Flowing Normal to Their Surfaces," ASME *Transactions*, Vol. 80, 1958, pp. 61–71.

3 Sparrow, E. M., and Geiger, G. T., "Local and Average Heat Transfer Characteristics for a Disk Situated Perpendicular to a Uniform Flow," ASME JOURNAL OF HEAT TRANSFER, Vol. 107, No. 2, 1985, pp. 321–326.

4 Sogin, H. H., and Oskay, V., "Heat Transfer From Surfaces on Nonuniform Temperature Distribution. Final Report Part II: Local Sublimation From Disks in Axisymmetric Flow," AFOSR TR-60-78, Air Force Office of Scientific Research, Contract No. AF49 (638)-46, Project No. 17500, 1960, pp. i–vi, 1–36, +5 figs.

5 Schröder, H., "Neue Beitrage zur Volumentheorie," Poggendorff's *Annal.*, Vol. 106, 1859, pp. 226–240.

6 Schröder, H., "Neue Dichtigkeitsmessungen fester, organisher Verbindungen," *Berichte der deutschen chemischen Gesellschaft*, Vol. 12, Jan.–June 1879, pp. 1611–1618.

7 Dewar, J., "Low Temperature Investigations," *The Chemical News and Journal of Physical Science*, Vol. 91, 1905, p. 217.

8 Fail, R., Lawford, J. A., and Eyre, R. C. W., "Low Speed Experiments on the Wake Characteristics of Flat Plates Normal to an Airstream," RAE Technical Note Aero 2516, 1957.

9 Sogin, H. H., and Subramanian, V. S., "Local Mass Transfer From Circular Cylinders in Cross Flow," ASME JOURNAL OF HEAT TRANSFER, Vol. 83, No. 4, 1961, p. 486.

An n-Bounce Method for Analysis of Radiative Transfer in Enclosures With Anisotropically Scattering Media

M. H. N. Naraghi[1] and Jianchun Huan[1]

Introduction

The intent of this note is to present an n-bounce approximate approach for analysis of radiative heat transfer in enclosures with anisotropic scattering media. This method is an extension of continuous and discrete exchange factor methods (Naraghi et al., 1988). It has been shown that the discrete exchange factor method is a very efficient method for analysis of radiative transfer in multidimensional enclosures with isotropic scattering media (Naraghi and Kassemi, 1989; Naraghi and Litkouhi, 1989). In the n-bounce method, the total exchange factor is approximated by the summation of direct radiative and higher order terms resulting from multiple wall reflection and medium scattering. The present approach is applied to a number of three-dimensional radiative transfer problems in isotropically and anisotropically scattering media. Results calculated based on the present method are compared to the existing solutions in the literature.

Formulation

Consider the enclosure shown in Fig. 1. The continuous differential direct exchange factors $\overline{dss}(\mathbf{r}_i, \mathbf{r}_j)$, $\overline{dsg}(\mathbf{r}_i, \mathbf{r}_j)$, $\overline{dgs}(\mathbf{r}_i, \mathbf{r}_j)$, and $\overline{dgg}(\mathbf{r}_i, \mathbf{r}_j)$ can be denoted by $\overline{dzz}(\mathbf{r}_i, \mathbf{r}_j)$. When $\mathbf{r}_i$ or $\mathbf{r}_j$ are located on the surface of the enclosure, then z represents surface; otherwise it represents medium. Similarly, the bidirectional surface reflectivity, $\rho(\theta, \phi; \theta', \phi')$, and the medium albedo-phase function product, $\omega_0\Phi(\theta, \phi; \theta', \phi')$, are analogous and can be represented by a single reflectance, $r(\theta, \phi; \theta', \phi')$. Based on these definitions, a unified total exchange factor can be expressed as:

$$\overline{DZZ}(\mathbf{r}_i, \mathbf{r}_j) = \overline{dzz}(\mathbf{r}_i, \mathbf{r}_j)a(\mathbf{r}_j) + \int_{r_{k_1}} \overline{dzz}(\mathbf{r}_i, \mathbf{r}_{k_1})r(\mathbf{n}_{ik_1}, \mathbf{n}_{k_1 j})\overline{dzz}(\mathbf{r}_{k_1}, \mathbf{r}_j)a(\mathbf{r}_j) + \int_{r_{k_1}}\int_{r_{k_2}} \overline{dzz}(\mathbf{r}_i, \mathbf{r}_{k_1})r(\mathbf{n}_{ik_1}, \mathbf{n}_{k_1k_2})\overline{dzz}(\mathbf{r}_{k_1}, \mathbf{r}_{k_2}) \times r(\mathbf{n}_{k_1k_2}, \mathbf{n}_{k_2 j})\overline{dzz}(\mathbf{r}_{k_2}, \mathbf{r}_j)a(\mathbf{r}_j) + \ldots \quad (1)$$

where $\mathbf{n}_{ij}$ is the unit vector along the direction of vector $\mathbf{r}_j - \mathbf{r}_i$ and $a(\mathbf{r}_j)$ is the absorptance (which is equal to the surface absorptivity when $\mathbf{r}_j$ is located on the surface of the enclosure and $1 - \omega_0$ when it is within the medium). The first term in Eq. (1) represents the differential fraction of energy emitted from a differential element located at $\mathbf{r}_i$, which is absorbed by a differential medium or surface at $\mathbf{r}_j$ via direct radiation (no reflection and scattering). The other terms have the same physical interpretation as that of the first term but include intermediate bidirectional reflection and/or anisotropic scattering.

If the surface is diffuse and the medium is isotropically scattering, Eq. (1) reduces to:

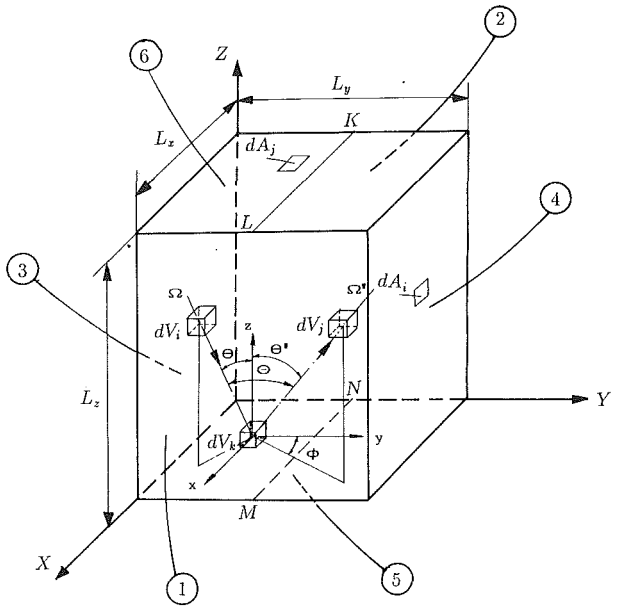

Fig. 1 Schematic of a three-dimensional rectangular enclosure

$$\overline{DZZ}(\mathbf{r}_i, \mathbf{r}_j) = \overline{dzz}(\mathbf{r}_i, \mathbf{r}_j)a + \int_{r_{k_1}} \overline{dzz}(\mathbf{r}_i, \mathbf{r}_{k_1})r\overline{dzz}(\mathbf{r}_{k_1}, \mathbf{r}_j)a + \int_{r_{k_1}}\int_{r_{k_2}} \overline{dzz}(\mathbf{r}_i, \mathbf{r}_{k_1})r\overline{dzz}(\mathbf{r}_{k_1}, \mathbf{r}_{k_2})r\overline{dzz}(\mathbf{r}_{k_2}, \mathbf{r}_j)a + \ldots \quad (2)$$

It can be shown via the procedure similar to that given by Naraghi et al. (1988) that Eq. (2) can be reduced to an integral equation of the form

$$\overline{DZZ}(\mathbf{r}_i, \mathbf{r}_j) = \overline{dzz}(\mathbf{r}_i, \mathbf{r}_j)a + \int_{r_k} \overline{dzz}(\mathbf{r}_i, \mathbf{r}_k)r\overline{DZZ}(\mathbf{r}_k, \mathbf{r}_j) \quad (3)$$

It is not possible to reduce Eq. (1), in its general form, to an integral equation similar to Eq. (3). Hence, for the case of bidirectionally reflecting surfaces and anisotropically scattering media, an approximate solution can be obtained by truncating higher order terms of Eq. (1). Since the radiation energy is attenuated as it travels through the media, the terms with the larger number of reflections and/or scattering become very small. The present approximate solution is based on the number of bounces (reflection and/or scattering) of the radiative energy. The lowest order approximation, 0-bounce solution, corresponds to only the first term in Eq. (1), i.e.,

$$\overline{DZZ}(\mathbf{r}_i, \mathbf{r}_j) = \overline{dzz}(\mathbf{r}_i, \mathbf{r}_j) \quad (4)$$

The one-bounce solution consists of the first two terms of Eq. (1) (i.e., one reflection or scattering),

$$\overline{DZZ}(\mathbf{r}_i, \mathbf{r}_j) = \overline{dzz}(\mathbf{r}_i, \mathbf{r}_j)a(\mathbf{r}_j) + \int_{r_{k_1}} \overline{dzz}(\mathbf{r}_i, \mathbf{r}_{k_1})r(\mathbf{n}_{ik_1}, \mathbf{n}_{k_1 j})\overline{dzz}(\mathbf{r}_{k_1}, \mathbf{r}_j) \quad (5)$$

Similarly, the two-bounce solution is given by

$$\overline{DZZ}(\mathbf{r}_i, \mathbf{r}_j) = \overline{dzz}(\mathbf{r}_i, \mathbf{r}_j)a(\mathbf{r}_j) + \int_{r_{k_1}} \overline{dzz}(\mathbf{r}_i, \mathbf{r}_{k_1})r(\mathbf{n}_{ik_1}, \mathbf{n}_{k_1 j})\overline{dzz}(\mathbf{r}_{k_1}, \mathbf{r}_j)a(\mathbf{r}_j) + \int_{r_{k_1}}\int_{r_{k_2}} \overline{dzz}(\mathbf{r}_i, \mathbf{r}_{k_1})r(\mathbf{n}_{ik_1}, \mathbf{n}_{k_1k_2})\overline{dzz}(\mathbf{r}_{k_1}, \mathbf{r}_{k_2}) \times r(\mathbf{n}_{k_1k_2}, \mathbf{n}_{k_2 j})\overline{dzz}(\mathbf{r}_{k_2}, \mathbf{r}_j) \quad (6)$$

[1]Department of Mechanical Engineering, Manhattan College, Riverdale, NY 10471.

Contributed by the Heat Transfer Division of the American Society of Mechanical Engineers. Manuscript received by the Heat Transfer Division March 7, 1990; revision received February 15, 1991. Keywords: Numerical Methods, Radiation.

Similar expressions can be written for three, four, . . . , n-bounce solutions. Note that in order to compensate for the neglected higher order terms in Eqs. (4)–(6) and to make the total exchange factors satisfy the energy conservation law, the absorptance $a(\mathbf{r}_j)$ is set to unity in the last terms of the right-hand side of these equations. This means that all radiative energy is absorbed after the last bounce. It should be noted that the direct exchange factors, depending on whether the emitting and receiving elements are surface or medium, are given by Naraghi et al. (1988). The n-bounce method yields the same results as those of multiple scattering theory as n approaches infinity.

Equations (5) and (6) must be solved numerically for general multidimensional cases. In the DEF method (Naraghi et al., 1988; Naraghi and Kassemi, 1989), it has been shown that the Gaussian quadrature method provides the most accurate results; however, since the nodal points are not evenly spaced, it is not a suitable method if finite difference compatible nodes are to be employed. Hence, for combined conduction/convection-radiation problems, other numerical integration methods must be adopted. A complete discussion of different discretization methods and treatment of singularities in evaluating direct exchange factors between nodes is presented elsewhere (Naraghi and Kassemi, 1989; Naraghi and Litkouhi, 1989). Furthermore, Saltiel and Naraghi (1989) have shown that arbitrarily selecting nodes can produce accurate results, which can be useful in problems with irregular configurations (finite element compatible nodes). Implementing one of the aforementioned numerical methods, the discretized forms of Eqs. (5) and (6), respectively, become:

$$\overline{DZ_iZ_j} = \overline{dz_iz_j}a_j + \sum_{k_1=1}^{N_s+N_g} \overline{dz_iz_{k_1}} r_{ik_1j} w_{k_1} \overline{dz_{k_1}z_j} \tag{7}$$

and

$$\overline{DZ_iZ_j} = \overline{dz_iz_j}a_j + \sum_{k_1=1}^{N_s+N_g} \overline{dz_iz_{k_1}} r_{ik_1j} w_{k_1} \overline{dz_{k_1}z_j} a_j + \sum_{k_1=1}^{N_s+N_g} \sum_{k_2=1}^{N_s+N_g} \overline{dz_iz_{k_1}} r_{ik_1k_2} w_{k_1} \overline{dz_{k_1}z_{k_2}} r_{k_1k_2j} w_{k_2} \overline{dz_{k_2}z_j} \tag{8}$$

where $\overline{DZ_iZ_j}$ and $\overline{dz_iz_j}$ are total and direct exchange factors between nodes i and j, and r_{ikj} is reflectance (reflectivity or scattering) of node k for radiative energy coming from node i and directed toward node j. The reflectance r_{ikj} is equal to the bidirectional reflectively if node k is on the surface ($r_{ikj} = \rho_k(\mathbf{n}_{ik}, \mathbf{n}_{kj})$) or it is equal to the product of the scattering albedo and phase function when node k is within the medium ($r_{ikj} = \omega_0\Phi(\mathbf{n}_{ik}, \mathbf{n}_{kj})$). The numerical integration weight factor w_k is either a surface weight factor w_s (when node k is a surface node) or a medium weight factor w_g (when node k is a medium node). Once the total exchange factors are determined using any of the n-bounce approximations, the heat flux and emissive powers are related via

$$q_s''(\mathbf{r}_i) = E_s(\mathbf{r}_i) - \int_S \overline{DS_jS_i} E_s(\mathbf{r}_j) ds(\mathbf{r}_j) - \int_V \overline{DG_jS_i} E_g(\mathbf{r}_j) dv(\mathbf{r}_j) \tag{9}$$

and

$$q_g'''(\mathbf{r}_i) = E_g(\mathbf{r}_i) - \int_S \overline{DS_jG_i} E_s(\mathbf{r}_j) ds(\mathbf{r}_j) - \int_V \overline{DG_jG_i} E_g(\mathbf{r}_j) dv(\mathbf{r}_j) \tag{10}$$

where $E_s(\mathbf{r}_j) = \epsilon_j\sigma T^4(\mathbf{r}_j)$ and $E_g(\mathbf{r}_j) = 4K_t(1 - \omega_0)\sigma T^4(\mathbf{r}_j)$ are surface and medium emissive power functions, respectively, $\overline{DS_jS_i}$, $\overline{DG_jS_i}$, $\overline{DS_jG_i}$, and $\overline{DG_jG_i}$ are the discrete total exchange factors between two different nodes. Making use of a numerical integration scheme, Eqs. (13) and (14) can then be discretized as

$$q_{s_i}'' = E_{s_i} - \sum_{j=1}^{N_s} w_{s_j} E_{s_j} \overline{DS_jS_i} - \sum_{j=1}^{N_g} w_{g_j} E_{g_j} \overline{DG_jS_i} \tag{11}$$

and

$$q_{g_i}''' = E_{g_i} - \sum_{j=1}^{N_s} w_{s_j} E_{s_j} \overline{DS_jG_i} - \sum_{j=1}^{N_g} w_{g_j} E_{g_j} \overline{DG_jG_i} \tag{12}$$

where $E_{s_j} = \epsilon_j\sigma T_j^4$ and $E_{g_j} = 4K_t(1 - \omega_0)\sigma T_j^4$ are surface and medium nodal emissive powers, respectively.

Results and Discussion

Consider the three-dimensional rectangular enclosure shown in Fig. 1. Dimensions of this enclosure in x, y, and z directions are L_x, L_y, and L_z, respectively. To compare the results of the n-bounce solution with those of the P-3 and discrete-ordinates method, the n-bounce method is also applied to an idealized furnace model given by Mengüç and Viskanta (1985). This enclosure has the following specifications:

$$L_x = 2 \text{ m}, \quad L_y = 2 \text{ m}, \quad L_z = 4 \text{ m}$$
$$K_t = 0.5 \text{ m}^{-1}, \quad \omega_0 = 1.0, \quad q_g''' = 5 \text{ kW/m}^3$$

and at the surfaces:

$$T_1 = T_2 = T_3 = T_4 = 900 \text{ K}, \quad \epsilon_1 = \epsilon_2 = \epsilon_3 = \epsilon_4 = 0.7$$
$$T_5 = 1200 \text{ K}, \quad \epsilon_5 = 0.85$$
$$T_6 = 400 \text{ K}, \quad \epsilon_6 = 0.7$$

This enclosure was analyzed by Mengüç and Viskanta (1985) using the P-3 and zonal method and by Fiveland (1988) using

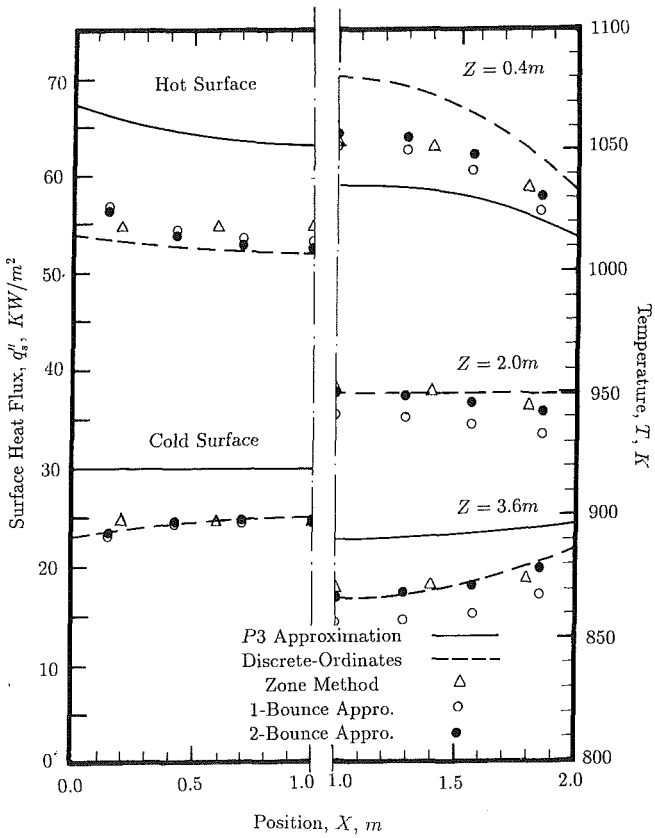

Fig. 2 Comparison between one-bounce and two-bounce solutions, the P-3 approximation, and the discrete-ordinates (S8) method for surface heat fluxes at hot and cold walls and gas temperature distributions at three axial locations (z = 0.4, 2.0, and 3.6 m)

the discrete-ordinates method. The resulting surface heat fluxes and gas temperatures based on the P-3, zonal, discrete-ordinates (S8), and the one- and two-bounce solutions are presented in Fig. 2. These results are based on a $7\times7\times10$ grid, and due to the symmetric configuration, only half of the curves are shown in this figure. The wall heat flux predictions for one- and two-bounce solutions are very close to each other and to those of the zonal and discrete-ordinates methods. The results of the P-3 approximation, however, appear to be off by 20 percent. For the gas temperature, the results of the one-bounce solution are at most 1.3 percent different from those of the two-bounce and zonal solutions. The prediction of the one-bounce solution close to the hot wall is better than those of the P-3 and discrete-ordinates method. Gas temperatures based on the two-bounce solution show an excellent agreement with the results of the zonal method. Further comparisons between the results of the present approach and those of the zonal method (Larsen, 1983) when the gas scatters isotropically are presented by Huan (1990) and Naraghi and Huan (1990). These results indicate that the one-bounce solution provides results with excellent accuracy for the wall heat flux, especially for those cases where the surface reflectivities are less than 0.5. For the gas temperature, however, the one-bounce is a little off, and two-bounce solutions may be required for better accuracy.

To examine the accuracy of the n-bounce method in solving radiative transfer problems with anisotropically scattering media, a comparison will be made with the results of the discrete-ordinates method (Fiveland, 1988).

The phase function $\Phi(\Omega' \rightarrow \Omega)$, which is the fraction of energy scattered into the outgoing direction Ω from the incoming direction Ω', can be represented by a Legendre series:

$$\Phi(\Theta)=\sum_{n=0}^{N}(2n+1)X_nP_n(\cos\Theta). \tag{13}$$

Here, Θ is the scattering angle, i.e., the angle between the incident and outgoing radiation (see Fig. 1). Introducing the general form of phase function (13) into the radiative analysis will make the calculation very complex. To simplify the analysis, the δ-function approximation (Wiscombe, 1977) is recommended to replace the forward peak scattering, which occurs when radiative energy is highly forward scattered from micron-sized particles like coal, char, and fly ash. Based on the approximation to the general phase function, Eq. (13) becomes:

$$\Phi(\Theta)=2f\delta(1-\cos\Theta)+(1-f)\sum_{n=0}^{2M-1}(2n+1)X_n^*P_n\cos\Theta \tag{14}$$

The coefficients of X_n^* in Eq. (14) and X_n in Eq. (13) are correlated by:

$$f=X_{2M} \tag{15}$$

$$X_n^*=\frac{X_n-f}{1-f}\quad\text{for}\quad n=0,\ 1,\ \ldots,\ 2M-1 \tag{16}$$

Physically, the δ-function approximation removes the forward peak scattering from the phase function and includes this effect in the extinction coefficient (Potter, 1970). Therefore the δ-function approximate phase function in Eq. (14) can be expressed alternatively as:

$$\Phi^*(\Theta)=\sum_{n=0}^{2M-1}(2n+1)X_n^*P_n(\cos\Theta) \tag{17}$$

with new extinction coefficient and scattering albedo:

$$K_t^*=K_t(1-f\omega_0) \tag{18}$$

$$\omega_0^*=\frac{\omega_0(1-f)}{1-f\omega_0} \tag{19}$$

In the n-bounce approximation, Eqs. (17)-(19) are used instead of directly using the δ-function approximation of Eq. (14). For $M = 1$, Eq. (21) becomes equivalent to the δ-Eddington approximation:

$$\Phi^*(\Theta)=1+3X_1^*\cos\Theta \tag{20}$$

together with Eqs. (18) and (19).

The results for the two cases, which were studied by Fiveland (1988), are evaluated using the n-bounce approximation. The anisotropic parameters are listed as:

Case 1: $f = 0.111$, $g = 0.215$
Case 2: $f = 0.781$, $g = 0.868$

where f and $X_1^* = g$ are defined in Eqs. (15) and (16), respectively. The radiative properties of the medium and surface are: $\omega_0 = 0.5$, $K_t = 1.0\ m^{-1}$, and $\epsilon = 0.8$. Other enclosure specifications are the same as the idealized furnace model considered in the previous isotropic scattering case. The resulting wall heat fluxes given in Fig. 3 are based on the one-bounce model and a $7\times7\times10$ grid. As shown in this figure, the results of the one-bounce solution are in excellent agreement with those of the discrete-ordinates (S4) method.

Next, the n-bounce method is used to analyze radiative transfer in a three-dimensional enclosure with a medium composed of diffusely reflecting spherical particles (non-δ-Eddington phase function). The scattering for this case is a backward one, and the corresponding phase function is given by Siegel and Howell (1981):

$$\Phi(\Theta)=\frac{8}{3\pi}(\sin\Theta-\Theta\cos\Theta) \tag{21}$$

All the known values are the same as those in the idealized furnace model studied earlier. The results for hot wall heat flux, cold wall heat flux, and centerline gas temperatures for albedo $\omega_0 = 0.25$, 0.5, and 0.75 are presented in Table 1. Because this case is backward scattering, as albedo ω_0 increases,

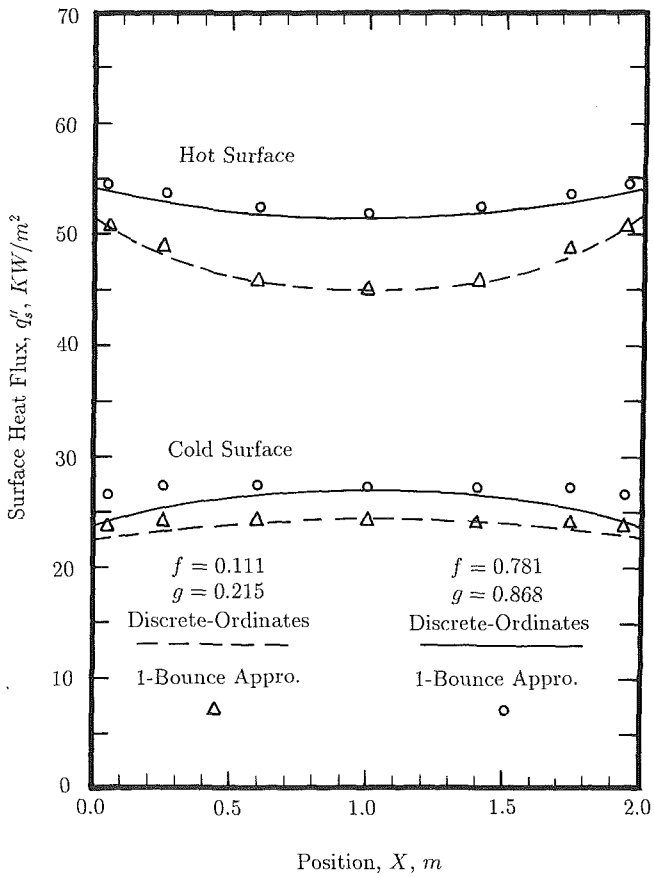

Fig. 3 Comparison between surface flux results by one-bounce approximation and discrete-ordinates (S4) method for some delta-function phase functions

Table 1 Results of centerline wall heat flux and temperature distribution when $\epsilon = 0.8$, $K_t = 1.0\ m^{-1}$, $\omega_0 = 0.5$, and the anisotropic phase function $\Phi(\Theta) = (8/3\pi)(\sin\Theta - \Theta\cos\Theta)$

	Position	one-bounce solution		
		$\omega_0 = 0.25$	$\omega_0 = 0.5$	$\omega_0 = 0.75$
Hot Surface Heat Flux (KW/m^2)	.05089	48.300	46.527	44.671
	.25847	45.114	42.603	40.126
	.59415	41.273	37.840	34.537
	1.0000	40.241	36.670	33.265
Cold Surface Heat Flux (KW/m^2)	.05089	-23.858	-23.285	-22.799
	.25847	-23.300	-22.388	-21.543
	.59415	-22.337	-21.243	-20.199
	1.0000	-22.110	-20.978	-19.888
Centerline Gas Temperature (K)	.05089	956.41	999.83	1128.64
	.25847	950.79	986.36	1095.82
	.59417	960.89	1000.00	1120.35
	1.0000	964.46	1004.35	1126.45

the hot wall loses less heat while the cold wall gains more heat. The medium temperatures always increase as the albedo ω_0 increases.

It should be noted that the computational time of the n-bounce method for anisotropically scattering media is much larger than that of isotropically scattering. For example, the CPU time on an IBM/RT-PC model 130 for a three-dimensional enclosure with an anisotropic medium and $5\times5\times7$ grid was about 40 min.

Concluding Remarks

An n-bounce method for analysis of radiative heat transfer in enclosures with anisotropically scattering media is developed. This method is based on the same principles as those of exchange factor methods (i.e., zone method and continuous and discrete exchange factor methods); hence, it is as versatile as these methods, especially in dealing with thermal radiation in complex geometries and combined mode heat transfer.

The n-bounce method provides a number of approximations (e.g., zero-, one-, two-, or higher bounce approximations). Depending on the problem in hand, each of these methods has its own applicability. For example, for an enclosure with black walls, a zero-bounce solution provides exact results for wall heat flux (only when the gas is isotropically scattering). The one-bounce solution can always provide wall heat fluxes accurately, except when the surface reflectivity is large ($\rho > 0.9$). For medium temperature, although the one-bounce solution provides acceptable results, the two-bounce solution provides much more accurate results.

References

Fiveland, W. A., 1988, "Three-Dimensional Radiative Heat Transfer Solution by the Discrete-Ordinate Method," *AIAA Journal of Thermophysics and Heat Transfer*, Vol. 2, No. 4, pp. 309-316.

Huan, J., 1990, "Exchange Factor Based Methods for Analysis of Radiative Transfer in Enclosures With Anisotropic Scattering Media," M.S. Thesis, Manhattan College, Riverdale, NY.

Larsen, M. E., 1983, "Exchange Factor Method and Alternative Zonal Formulation for Analysis of Radiating Enclosures Containing Participating Media," Ph.D. Thesis, Univ. of Texas, Austin.

Mengüç, M., and Viskanta, R., 1985, "Radiative Transfer in Three-Dimensional Rectangular Enclosures," *J. Quant. Spectrosc. Radiat. Transfer*, Vol. 33, pp. 533-549.

Naraghi, M. H. N., Chung, B. T. F., and Litkouhi, B., 1988, "A Continuous Exchange Factor Method for Radiative Exchange in Enclosures With Participating Media," ASME JOURNAL OF HEAT TRANSFER, Vol. 110, pp. 456-462.

Naraghi, M. H. N., and Kassemi, M., 1989, "Radiative Transfer in Rectangular Enclosures: A Discretized Exchange Factor Solution," ASME JOURNAL OF HEAT TRANSFER, Vol. 111, pp. 1117-1119.

Naraghi, M. H. N., and Litkouhi, B., 1989, "Discrete Exchange Factor Solution of Radiative Heat Transfer in Three-Dimensional Enclosures," *Heat Transfer Phenomena in Radiation, Conduction, and Fire*, R. K. Shah, ed., ASME HTD-Vol. 106, pp. 221-229.

Naraghi, M. H. N., and Huan, J., 1990, "An n-Bounce Method for Analysis of Radiative Transfer in Enclosures With Anisotropic Scattering Media," *Radiation Heat Transfer Fundamentals and Applications*, T. F. Smith et al., eds., ASME HTD-Vol. 137, pp. 107-115.

Potter, J. F., 1970, "The Delta Function Approximation in Radiative Transfer Theory," *J. Atmos. Sci.*, Vol. 27, pp. 943-949.

Saltiel, C., and Naraghi, M. H. N., 1990, "Analysis of Radiative Heat Transfer in Participating Media Using Arbitrary Nodal Distribution," *Numerical Heat Transfer, Part B: Fundamentals*, Vol. 17, pp. 227-243.

Siegel, R., and Howell, J. R., 1981, *Thermal Radiation Heat Transfer*, pp. 581-582.

Wiscombe, W. J., 1977, "The Delta-M Method: Rapid Yet Accurate Radiative Flux Calculations for Strongly Asymmetric Phase Functions," *J. Atmos. Sci.*, Vol. 34, pp. 1408-1422.

Condensation Heat Transfer Inside Vertical and Inclined Thermosyphons

J. C. Y. Wang[1] and Yiwei Ma[2]

Nomenclature

g = gravitational acceleration
k = thermal conductivity of condensate
L = axial length of condenser section
Mz = axial mass flow rate of condensate
P_s = vapor pressure
q = heat flux of condenser
r = latent heat of condensation
R = inside radius of thermosyphon
S = circumferential length
t = cooling water inlet temperature
ΔT = temperature difference between saturated vapor and wall
w = a dummy angle from 0 to ϕ for integration
W = cooling water mass flow rate
α = local condensation coefficient
α_c = mean condensation coefficient
α_n = mean condensation coefficient predicted by Nusselt
β = inclination angle of a thermosyphon from the horizontal
θ_o = subtended central angle of condensate stream
μ = absolute viscosity of condensate
ρ = density of condensate
ϕ = subtended central angle of condensate film
ψ = liquid filling as the ratio of working fluid volume to total volume of a thermosyphon

Introduction

In recent years, heat-pipe heat exchangers have played a significant role in waste heat recovery. In some cases, the heat-pipe heat exchangers are required to be inclined to gravity as several experimental investigations have reported (e.g., Groll et al., 1980; Hahne and Gross, 1981; Negishi and Sawards, 1983; Wen and Guo, 1984). Similarly to these cases, Chato (1962) studied laminar condensation inside inclined tubes. However, no uniform conclusion on optimum inclination angle can be made due to the differences among the operating con-

[1]Concordia University, Montreal, Canada.

[2]Harbin Institute of Technology, Harbin, People's Republic of China.

Contributed by the Heat Transfer Division and presented at the National Heat Transfer Conference, Philadelphia, Pennsylvania, August 6-9, 1989. Manuscript received by the Heat Transfer Division April 16, 1990; revision received January 17, 1991. Keywords: Condensation, Heat Pipes and Thermosyphons.

Table 1 Results of centerline wall heat flux and temperature distribution when $\epsilon = 0.8$, $K_t = 1.0\ m^{-1}$, $\omega_0 = 0.5$, and the anisotropic phase function $\Phi(\Theta) = (8/3\pi)(\sin\Theta - \Theta\cos\Theta)$

	Position	one-bounce solution		
		$\omega_0 = 0.25$	$\omega_0 = 0.5$	$\omega_0 = 0.75$
Hot Surface Heat Flux (KW/m^2)	.05089	48.300	46.527	44.671
	.25847	45.114	42.603	40.126
	.59415	41.273	37.840	34.537
	1.0000	40.241	36.670	33.265
Cold Surface Heat Flux (KW/m^2)	.05089	-23.858	-23.285	-22.799
	.25847	-23.300	-22.388	-21.543
	.59415	-22.337	-21.243	-20.199
	1.0000	-22.110	-20.978	-19.888
Centerline Gas Temperature (K)	.05089	956.41	999.83	1128.64
	.25847	950.79	986.36	1095.82
	.59417	960.89	1000.00	1120.35
	1.0000	964.46	1004.35	1126.45

the hot wall loses less heat while the cold wall gains more heat. The medium temperatures always increase as the albedo ω_0 increases.

It should be noted that the computational time of the n-bounce method for anisotropically scattering media is much larger than that of isotropically scattering. For example, the CPU time on an IBM/RT-PC model 130 for a three-dimensional enclosure with an anisotropic medium and $5\times5\times7$ grid was about 40 min.

Concluding Remarks

An n-bounce method for analysis of radiative heat transfer in enclosures with anisotropically scattering media is developed. This method is based on the same principles as those of exchange factor methods (i.e., zone method and continuous and discrete exchange factor methods); hence, it is as versatile as these methods, especially in dealing with thermal radiation in complex geometries and combined mode heat transfer.

The n-bounce method provides a number of approximations (e.g., zero-, one-, two-, or higher bounce approximations). Depending on the problem in hand, each of these methods has its own applicability. For example, for an enclosure with black walls, a zero-bounce solution provides exact results for wall heat flux (only when the gas is isotropically scattering). The one-bounce solution can always provide wall heat fluxes accurately, except when the surface reflectivity is large ($\rho > 0.9$). For medium temperature, although the one-bounce solution provides acceptable results, the two-bounce solution provides much more accurate results.

References

Fiveland, W. A., 1988, "Three-Dimensional Radiative Heat Transfer Solution by the Discrete-Ordinate Method," *AIAA Journal of Thermophysics and Heat Transfer*, Vol. 2, No. 4, pp. 309-316.

Huan, J., 1990, "Exchange Factor Based Methods for Analysis of Radiative Transfer in Enclosures With Anisotropic Scattering Media," M.S. Thesis, Manhattan College, Riverdale, NY.

Larsen, M. E., 1983, "Exchange Factor Method and Alternative Zonal Formulation for Analysis of Radiating Enclosures Containing Participating Media," Ph.D. Thesis, Univ. of Texas, Austin.

Mengüç, M., and Viskanta, R., 1985, "Radiative Transfer in Three-Dimensional Rectangular Enclosures," *J. Quant. Spectrosc. Radiat. Transfer*, Vol. 33, pp. 533-549.

Naraghi, M. H. N., Chung, B. T. F., and Litkouhi, B., 1988, "A Continuous Exchange Factor Method for Radiative Exchange in Enclosures With Participating Media," ASME JOURNAL OF HEAT TRANSFER, Vol. 110, pp. 456-462.

Naraghi, M. H. N., and Kassemi, M., 1989, "Radiative Transfer in Rectangular Enclosures: A Discretized Exchange Factor Solution," ASME JOURNAL OF HEAT TRANSFER, Vol. 111, pp. 1117-1119.

Naraghi, M. H. N., and Litkouhi, B., 1989, "Discrete Exchange Factor Solution of Radiative Heat Transfer in Three-Dimensional Enclosures," *Heat Transfer Phenomena in Radiation, Conduction, and Fire*, R. K. Shah, ed., ASME HTD-Vol. 106, pp. 221-229.

Naraghi, M. H. N., and Huan, J., 1990, "An n-Bounce Method for Analysis of Radiative Transfer in Enclosures With Anisotropic Scattering Media," *Radiation Heat Transfer Fundamentals and Applications*, T. F. Smith et al., eds., ASME HTD-Vol. 137, pp. 107-115.

Potter, J. F., 1970, "The Delta Function Approximation in Radiative Transfer Theory," *J. Atmos. Sci.*, Vol. 27, pp. 943-949.

Saltiel, C., and Naraghi, M. H. N., 1990, "Analysis of Radiative Heat Transfer in Participating Media Using Arbitrary Nodal Distribution," *Numerical Heat Transfer, Part B: Fundamentals*, Vol. 17, pp. 227-243.

Siegel, R., and Howell, J. R., 1981, *Thermal Radiation Heat Transfer*, pp. 581-582.

Wiscombe, W. J., 1977, "The Delta-M Method: Rapid Yet Accurate Radiative Flux Calculations for Strongly Asymmetric Phase Functions," *J. Atmos. Sci.*, Vol. 34, pp. 1408-1422.

Condensation Heat Transfer Inside Vertical and Inclined Thermosyphons

J. C. Y. Wang[1] and Yiwei Ma[2]

Nomenclature

g = gravitational acceleration
k = thermal conductivity of condensate
L = axial length of condenser section
Mz = axial mass flow rate of condensate
P_s = vapor pressure
q = heat flux of condenser
r = latent heat of condensation
R = inside radius of thermosyphon
S = circumferential length
t = cooling water inlet temperature
ΔT = temperature difference between saturated vapor and wall
w = a dummy angle from 0 to ϕ for integration
W = cooling water mass flow rate
α = local condensation coefficient
α_c = mean condensation coefficient
α_n = mean condensation coefficient predicted by Nusselt
β = inclination angle of a thermosyphon from the horizontal
θ_o = subtended central angle of condensate stream
μ = absolute viscosity of condensate
ρ = density of condensate
ϕ = subtended central angle of condensate film
ψ = liquid filling as the ratio of working fluid volume to total volume of a thermosyphon

Introduction

In recent years, heat-pipe heat exchangers have played a significant role in waste heat recovery. In some cases, the heat-pipe heat exchangers are required to be inclined to gravity as several experimental investigations have reported (e.g., Groll et al., 1980; Hahne and Gross, 1981; Negishi and Sawards, 1983; Wen and Guo, 1984). Similarly to these cases, Chato (1962) studied laminar condensation inside inclined tubes. However, no uniform conclusion on optimum inclination angle can be made due to the differences among the operating con-

[1]Concordia University, Montreal, Canada.

[2]Harbin Institute of Technology, Harbin, People's Republic of China.

Contributed by the Heat Transfer Division and presented at the National Heat Transfer Conference, Philadelphia, Pennsylvania, August 6-9, 1989. Manuscript received by the Heat Transfer Division April 16, 1990; revision received January 17, 1991. Keywords: Condensation, Heat Pipes and Thermosyphons.

Table 1 Optimum inclination angle obtained by other authors

REFERENCE	Chato	Wen and Guo	Negishi and Sawards	Hahne and Gross	Groll et al.
Optimum angle	10°-20°	15°	20°-40°	50°	60°-80°

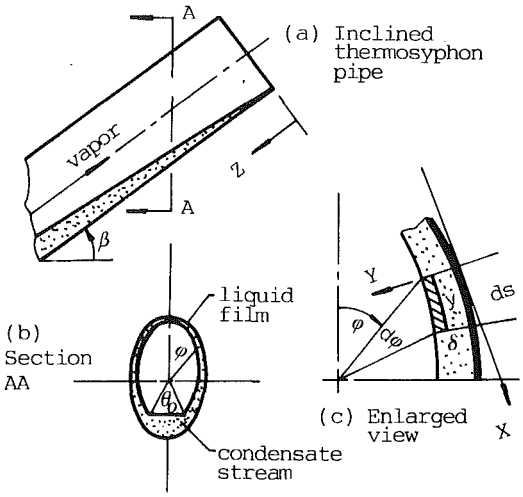

Fig. 1 Physical model

ditions, as shown in Table 1. Spendel (1981) has theoretically studied the condensation heat transfer in vertical thermosyphons and found that the average condensation coefficients differ from those predicted using Nusselt's theory by only 1–4 percent.

In this paper, both theoretical and experimental studies on vertical and inclined thermosyphons have been carried out. A semi-empirical correlation is presented for the purpose of designing heat pipe heat exchangers.

Theoretical Analysis

Condensation heat transfer in two-phase flow inside a thermosyphon is highly complex. As an initial step in gaining a basic understanding of this topic, several assumptions were made as follows:

1 The liquid filling of the thermosyphon is small enough that the working fluid cannot rush up into the condenser section.

2 The laminar film condensation is considered, as shown in Fig. 1.

3 The condensate in the liquid film does not flow directly along the Z direction due to the existence of the friction of the vapor flow. Rather, it first flows downward along the elliptical wall to the bottom of the ellipse, and subsequently returns back to the evaporator section. Furthermore, all other flow effects, interfacial interaction, and streamwise changes in liquid momentum are neglected.

4 The wall temperature is constant along the condenser section.

5 The condensate at the bottom of the ellipse is adiabatic.

6 The vapor density is ignored as comparing to the condensate density.

Similar to Nusselt's approach, the local condensation coefficient can be derived as:

$$\alpha = \left(\frac{\rho^2 grk^3}{4\mu R\Delta T}\right)^{1/4} \frac{\sin^{1/3}\phi}{(\cos^4\beta\cos^2\phi+\sin^2\phi)^{1/6}} \left[\int_0^{\phi} f(w,\beta)dw\right]^{-1/4} \quad (1)$$

where

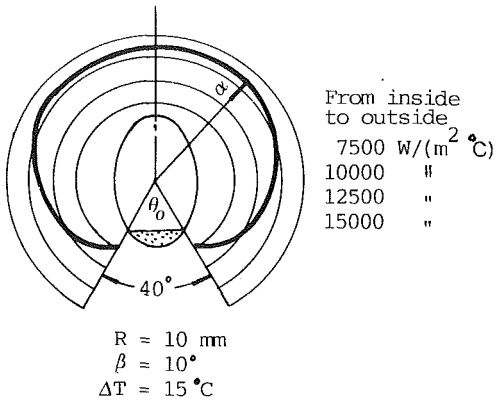

Fig. 2 Local condensation coefficient (for water)

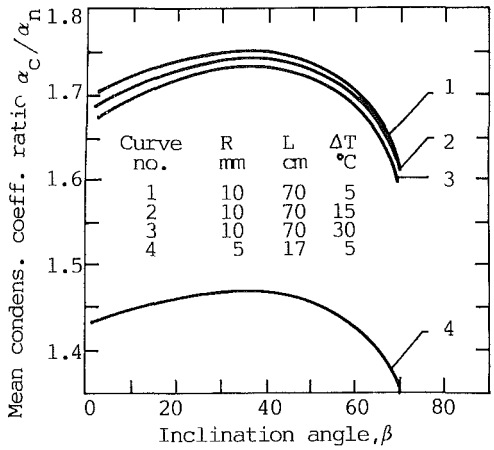

Fig. 3 Mean condensation coefficient ratio

$$f(w,\beta) = \frac{\sin^{1/3}w(\cos^4\beta\cos^2 w+\sin^2 w)^{1/3}}{(\cos^2\beta+\sin^2\beta\sin^2 w)^{3/2}} \quad (2)$$

Equation (1) may be calculated numerically; the results are illustrated in Fig. 2. It can be seen from this figure that the condensation coefficient decreases due to the increased thickness of the condensate film.

The mean condensation coefficient along the condenser may then be shown as follows:

$$\alpha_c = \frac{2R}{LS}\left(\frac{\rho^2 grk^3}{4\mu R\Delta T}\right)^{1/4} \int_0^L \int_0^{\pi-\theta_o/2} f(\phi,\beta) \left[\int_0^{\phi} f(w,\beta)dw\right]^{-1/4} d\phi dz \quad (3)$$

where $S = 2\int_0^{\pi} ds$ is the circumferential length of the ellipse, and $f(\phi, \beta)$ takes the same form as in Eq. (2).

Normalizing Eq. (3) with Nusselt's formula of film condensation for vertical plates (or cylinders) yields the following equation:

$$\frac{\alpha_c}{\alpha_n} = \frac{3}{2S}\left(\frac{R}{L}\right)^{3/4} \int_0^L \int_0^{\pi-\theta_o/2} f(\phi,\beta)[f(w,\beta)dw]^{-1/4} d\phi dz \quad (4)$$

It is found from Eq. (4) that the ratio α_c/α_n is related to L, R, and θ_o. The subtended angle θ_o may vary with tube inclination angle β, condensate rate Mz, tube size R, viscosity μ, and density ρ. Based on these considerations, a correlation of θ_o has been recommended as

$$tg\frac{\theta_o}{2} = \cos\beta tg\left[(41-1250R)\left(\frac{Mz\mu}{\rho^2 g\sin\beta}\right)^{0.15}\right] \quad (5)$$

Table 2 Parameters used in the experiments

Vapour pressure	P_s = 0.08 - 1.5 bar
Heat flux of condenser	q = 10 000 - 40 000 W/m^2
Inclination angle	β = 15°, 30°, 45°, 60°, 90°
Cooling water inlet temperature	t = 20 °C - 60°C
Cooling water mass flow rate	W = 0.005 - 0.03 kg/s

From the viewpoint of mass conservation, Mz can be calculated with the following equation:

$$Mz = \frac{2\Delta T}{r} \int_0^L \int_0^{\pi - \theta_o/2} \alpha dz ds \tag{6}$$

Consequently, the ratio α_c/α_n can be numerically computed. The computed results are shown in Fig. 3. The temperature differences of curves 1, 2, and 3 in Fig. 3 are 5°C, 15°C, and 30°C, respectively. It is clearly indicated that temperature difference ΔT has a weak, almost nonexistent effect on the ratio α_c/α_n since both α_c and α_n are proportional to $(\Delta T)^{-1/4}$. From curves 1 and 4, it can be further noted that the inside radius R and condenser length L have a strong influence on the ratio α_c/α_n. It should also be noted that the range of the optimum inclination angle is 20–50 deg from the horizontal.

Equation (4) may be further approximated as follows:

$$\frac{\alpha_c}{\alpha_n} = \left(\frac{L}{R}\right)^{\frac{\cos\beta}{4}} (0.54 + 5.86 \times 10^{-3}\beta) \tag{7}$$

When the thermosyphon operates vertically, i.e., β = 90 deg, from Eq. (7) one obtains:

$$\alpha_c = 1.06\alpha_n, \text{ i.e., } \alpha_c \approx \alpha_n$$

The results closely approximate those derived by Spendel (1981).

Experimental Studies

The experimental apparatus is quite simple and not shown here due to the space limitation. The test thermosyphon is made from a commercial steel tube. Its length is 1.8 m, while the inner and outer diameters are 20 mm and 25 mm, respectively. The working fluid is water and the liquid filling can be changed when necessary. This thermosyphon can be positioned with an inclination angle from 0 deg and 90 deg with respect to the horizontal.

The experiments are conducted with three liquid fillings, i.e., 10, 23, and 33 percent. The parameters and their ranges of working conditions are presented in Table 2.

From the experimental results, it is found that the ratio α_c/α_n increases with vapor pressure according to the following relationship:

$$\frac{\alpha_c}{\alpha_n} \propto P_s^{0.37}$$

It is also reaffirmed that the temperature difference ΔT and the heat flux q have little effect on the ratio α_c/α_n.

All the relevant experimental data are included in Fig. 4. It can be seen that the condensation coefficient increases as liquid filling becomes smaller and that the optimum inclination angle varies from 20 to 50 deg depending on the liquid filling.

Comparisons of Theoretical and Experimental Results

As mentioned above, both theoretical analysis and experimental studies have indicated that heat flux or temperature differences have no effects on the ratio α_c/α_n and that the optimum inclination angle is about 20–50 deg. However, there

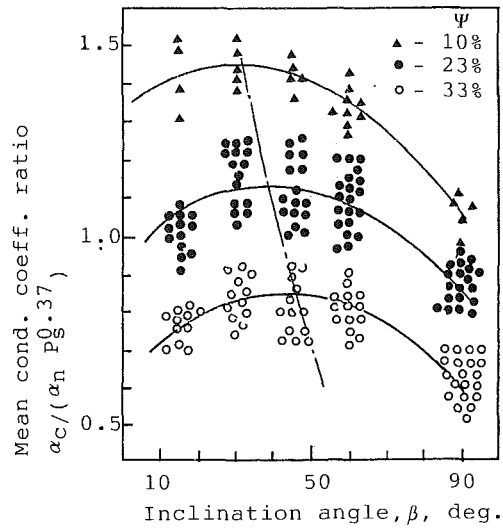

Fig. 4 Effects of liquid filling and inclination angle on condensation coefficient

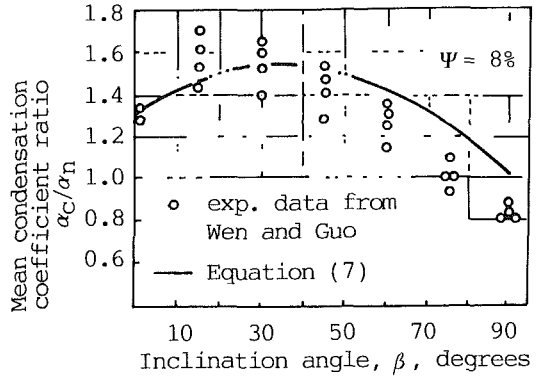

Fig. 5 Comparisons between Eq. (7) and the experimental data from Wen and Guo (1984)

are some differences between the theoretical and the experimental results. The main reason for this is that Eqs. (4) and (7) do not show the effects of vapor pressure and liquid filling on the condensation coefficient. It is therefore more desirable to modify Eq. (7) with these additional factors. As a result, the following semi-empirical correlation is obtained:

$$\frac{\alpha_c}{\alpha_n} = P_s^{0.37}\left(\frac{L}{R}\right)^{\frac{\cos\beta}{4}} [0.41 - 0.72\psi + (-62.7\psi^2 + 14.5\psi + 7.1)\beta/1000] \tag{8}$$

The maximum deviation of the test results from Eq. (8) is within 15 percent for all three liquid fillings.

Equation (8) is valid when the liquid filling is larger than 10 percent and the concerned parameters are within the ranges given in Table 2. As the liquid filling drops below 10 percent, Eq. (7) becomes available. This is demonstrated in Fig. 5 with the experimental results from Wen and Guo (1984).

Conclusions

1 The heat flux q or the temperature difference ΔT has little effect on the ratio α_c/α_n. However, the inclination angle of a thermosyphon has a notable influence on the condensation coefficient and the optimum inclination angle varies with liquid filling from 20 to 50 deg.

2 When the liquid filling is larger than 10 percent, the liquid filling and vapor pressure will affect the condensation heat transfer of a thermosyphon. Its condensation coefficient can be predicted from Eq. (8).

3 When the liquid filling is smaller than 10 percent, the influences of vapor pressure and liquid filling on condensation coefficient are diminished, and thus Eq. (7) should be applied.

References

Chato, J. C., 1962, "Laminar Condensation Inside Horizontal and Inclined Tubes," *ASHRAE Journal*, Vol. 4, No. 2, p. 52.

Groll, M., et al., 1980, "Heat Recovery Units Using Reflux Heat Pipe as Components," Report-IKE5-TF-38-80, Inst. for Kemtech and Energiewand Lang, Federal Republic of Germany.

Hahne, E., and Gross, U., 1981, "The Influence of the Inclination Angle on the Performance of a Closed Two-Phase Thermosyphon," *Proceedings of the 4th Int. Heat Pipe Conf.*, London, United Kingdom, p. 125.

Negishi, K., and Sawards, T., 1983, "Heat Transfer Performance of an Inclined Two-Phase Closed Thermosyphon," *Int. J. Heat Mass Transfer*, Vol. 26, No. 8.

Spendel, Th., 1981, "Laminar Film Condensation Heat Transfer in Closed Two-Phase Thermosyphons," *Proceedings of the 4th Int. Heat Pipe Conf.*, London, United Kingdom, p. 163.

Wen, Y. P., and Guo, S., 1984, "Experimental Heat Transfer Performance of Two-Phase Thermosyphons," *Proceedings of the 5th Int. Heat Pipe Conf.*, Tsukuba, Japan.